CODEN: JASMAN

The Journal of the Acoustical Society of America

ISSN: 0001-4966

Vol. 122, No. 3 September 2007

(Continued)

CONTENTS—*Continued from preceding page*

UNDERWATER SOUND [30]

ULTRASONICS, QUANTUM ACOUSTICS, AND PHYSICAL EFFECTS OF SOUND [35]

TRANSDUCTION [38]

STRUCTURAL ACOUSTICS AND VIBRATION [40]

NOISE: ITS EFFECTS AND CONTROL [50]

ARCHITECTURAL ACOUSTICS [55]

(Continued)

CONTENTS—*Continued from preceding page*

(Continued)

CONTENTS—*Continued from preceding page*

BIOACOUSTICS [80]

ERRATA

JASA EXPRESS LETTERS

CUMULATIVE AUTHOR INDEX

New Insights on Loudness and Hearing Thresholds

The letters published in this special issue of *JASA Express Letters* were originally presented at the session titled "New insights on loudness and hearing thresholds," which was organized by Rhona Hellman and Yôiti Suzuki for the Fourth Joint Meeting of the Acoustical Society of America and the Acoustical Society of Japan. This meeting took place from 28 November to 2 December, 2006 in Honolulu, Hawaii. The session was sponsored by the ASA Technical Committee on Psychological and Physiological Acoustics, the ASA Committee on Standards, and by the ASJ Committee on Psychological and Physiological Acoustics. Six of the eight participants in the session chose to submit articles for this special issue.

Although loudness precedes thresholds in the session title, the order of these topics was reversed for both the oral and written presentations. Thus, you will note that the three papers dealing with threshold effects precede those that deal with more complex processes involved in supra-threshold measures. The first paper by Ashihara presents recent free-field threshold data in normal hearing for pure tones between 16 and 30 kHz. Those results suggest that above 18 kHz the threshold curve may reflect the combined characteristic of the upper slope of the last auditory channel's tuning curve and the middle ear attenuation. The second paper by Aoyagi *et al.* provides an overall review of the auditory steady-state response (ASSR) elicted by a sinusoidally amplitude-modulated (SAM) tone for objective audiometry in children. This technique is shown to be useful for both awake adults and asleep children. The last paper dealing with threshold effects is by Yoshida *et al.* These authors investigated the effect of a previous sound presentation on both contralateral and ipsilateral thresholds. When both the previous and test sounds are at the same frequency of 500 Hz, thresholds decreased by 2 dB in the contralateral ear, whereas they increased slightly in the ipsilateral ear. These effects appear to be systematic, but the underlying mechanism is unclear.

Next we turn to the three loudness-related papers. Two of them provide new insights into loudness measures in normal hearing, whereas the third attempts to address the less well understood loudness issues involved in cochlear-impaired hearing. First, Leibold and Jesteadt review their recent work on the perceptual weight listeners assign to the loudness of individual components of a multitone complex centered on 1 kHz and report new data on intensity discrimination for the same stimulus set. Just as for the loudness measurements, the Moore *et al.* (1997) loudness model predicts greater improvement in intensity discrimination with increasing bandwidth than was observed in the data. This article is followed by Epstein's comprehensive overview of induced loudness reduction or ILR. A variety of data from loudness-matching to absolute magnitude estimation are examined. The pervasiveness of ILR in loudness measurements is clearly elucidated. In the sixth and final paper, Marozeau and Florentine attempt to evaluate and analyze loudness functions for individual listeners with cochlear-impaired hearing. Results from five different studies using different methods to obtain individual loudness functions are assessed. Overall, their analysis indicates that loudness functions of listeners with cochlear-impaired hearing can exhibit large individual differences. According to Marozeau and Florentine, methodological effects can only partly account for their results.

Taken together, the ensemble of articles highlight some of the threshold and loudness issues currently under investigation by American and Japanese researchers.

Rhona Hellman and Yôiti Suzuki, Guest Editors

Hearing thresholds for pure tones above 16 kHz

Kaoru Ashihara
National Institute of Advanced Science and Technology, AIST Tsukuba Central 6, Tsukuba, Ibaraki 3058566, Japan
ashihara-k@aist.go.jp

Abstract: Hearing thresholds for pure tones between 16 and 30 kHz were measured by an adaptive method. The maximum presentation level at the entrance of the outer ear was about 110 dB SPL. To prevent the listeners from detecting subharmonic distortions in the lower frequencies, pink noise was presented as a masker. Even at 28 kHz, threshold values were obtained from 3 out of 32 ears. No thresholds were obtained for 30 kHz tone. Between 20 and 28 kHz, the threshold tended to increase rather gradually, whereas it increased abruptly between 16 and 20 kHz.

PACS numbers: 43.66.Cb, 43.66.Dc [DKW]
Date Received: March 14, 2007 **Date Accepted:** May 14, 2007

1. Introduction

It has been warned since the 1960s that very high-frequency noises could cause subjective effects, such as discomfort and fullness in the ears, malaise, nausea, vestibular dysfunction, tinnitus, and persistent headaches. Extraordinarily high-level ultrasounds may also induce temporary threshold shifts.[1] Although a number of damage risk criteria and maximum permissible levels such as that introduced by Health Canada[2] have been proposed since the 1960s, these tentative recommendations were based on scant experimental and survey data.[1]

Absolute thresholds for pure tones have been studied by many groups of researchers.[3–11] The absolute threshold usually starts to increase sharply when the signal frequency exceeds about 15 kHz. It reaches about 80 dB SPL at the frequency of 20 kHz.[3,6,8,11] Above 20 kHz, however, only limited data have been reported. According to recent studies,[12,13] ultrasounds seem to be inaudible as long as their level does not exceed about 85 dB SPL.

To determine thresholds at very high frequencies, stimuli have to be presented at extremely high levels. It is not easy, however, to present pure tones at a level above 80 dB SPL with a good resolution. Factors that affect the maximum measurable threshold are the resolution of the signal, performance of the D/A converter, amplifiers, and loudspeakers. In particular, sufficient linearity of loudspeakers is definitely needed.[12,14]

Henry and Fast[4] used a sound delivery system that could deliver constant stimuli up to 124 dB SPL, and reported that most listeners had detected tones up to 24 kHz. They noted that thresholds increased abruptly as the signal frequency changed from about 14 to 20 kHz. Above 20 kHz, however, thresholds increased less rapidly. In Henry and Fast's study, however, the characteristics of acoustical stimuli were not fully described. They did not specify the amount of subharmonic distortions; they only referred to harmonic distortions. Listeners in their experiment might have been responding to low-frequency distortions or noises.

Ashihara *et al.*[15] made an attempt to measure threshold of hearing for pure tones up to 28 kHz. In their study, white noise was used to mask subharmonic distortions. They could obtain threshold values from some listeners for a 24 kHz tone. They also noted that hearing threshold increased gradually for tones from 20 to 24 kHz.

These studies show that some listeners can perceive tones up to at least 24 kHz. The highest frequency examined in Henry and Fast's study was 24 kHz. Ashihara *et al.* could not obtain threshold values above 26 kHz. The highest presentation level in their study was 99 dB SPL. Therefore, it is still an open question if tones above 26 kHz would be audible or not when their level exceeded 100 dB SPL.

The purpose of the present study is to obtain thresholds for tones up to 30 kHz. A transformed up-down method combined with a two-alternative forced choice (2AFC)

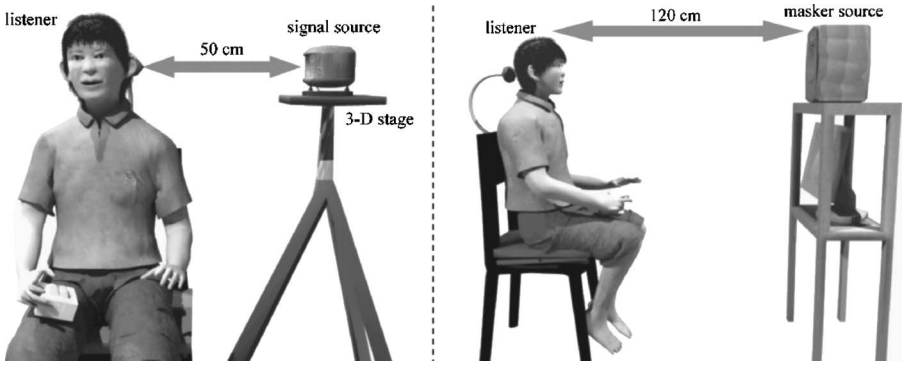

Fig. 1. Front view (left) and side view (right) of the listener. A 3D stage was adjusted so that the signal source directly faced to the entrance of the listener's ipsilateral ear and the distance between the signal source and the entrance of the listener's outer ear was 50 cm. The masking noise was presented by the masker source that directly faced to the listener's face. The distance between the masker source and the midpoint of the listener's head was 120 cm.

procedure[16] was employed in the present study. The hearing threshold was measured at every 2 kHz between 16 and 30 kHz. To prevent listeners from detecting subharmonic distortions in the lower frequency range, pink noise was used as a masker. To evaluate the masking effect caused by the pink noise, masked and the absolute thresholds were measured at 250 Hz, 1, 4, and 12 kHz.

2. Method

2.1 Listeners and equipment

Eight males and 8 females participated. None of them had a history of otological disease. Their ages ranged between 19 and 25 years. They were paid for their participation. Necessary information about the experiments was given to them and a written informed consent was obtained from each participant prior to the experiment. The study was approved by the Ethics Committee of National Institute of Advanced Industrial Science and Technology.

In the free-field measurement of the hearing threshold, the distance between the signal source and the listening point is recommended to be at least 1 m.[17] In the present study, however, a signal source was placed at a distance of 50 cm from the listener's ear to provide sufficient level at the listening point. A listener sat on a chair with the back of his or her head attached to a headrest in an anechoic room. The listener was instructed not to move his or her body during the measurement.

Two sound sources were used in the measurement. They were a signal source and a masker source. The signal source was either a super-tweeter (PIONEER PT-R100) or a loudspeaker (DENON SC-A33) and the masker source was a loudspeaker (DENON SC-A33). The signal source was set on a three-dimensional (3D) stage placed on either the right or left side of the listener. The stage was adjusted so that the signal source directly faced to the entrance of the listener's outer ear and the distance between the signal source and the entrance of the outer ear was 50 cm as can be seen in Fig. 1. The masker source was at a distance of 120 cm from the midpoint of the listener's head and it directly faced to the listener's face as shown in Fig. 1. A liquid crystal display was placed in front of the listener for instructions and a visual feedback.

2.2 Stimuli

Digitally synthesized sinusoids were used as signals. The signal was generated by a D/A converter (EDIROL UA-1000) at a sampling rate of 96 kHz and 16 bit resolution. The signals at 16 kHz and above were presented by a super-tweeter (PIONEER PT-R100) via a high-pass filter (PIONEER DN-100). A loudspeaker (DENON SC-A33) was used for the signals at 250 Hz, 1,

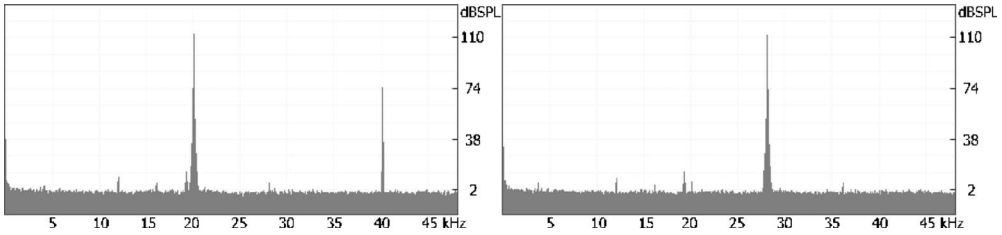

Fig. 2. Signals at the listening point. The power spectra of the signals at 20 kHz (left) and 28 kHz (right) are shown. The signals were recorded at a distance of 50 cm from the signal source when the listener was absent. Their level was 110 dB SPL. It was confirmed that there were no subharmonic distortions larger than 20 dB SPL.

4, and 12 kHz. The signal level was calibrated with a $\frac{1}{2}$ in. microphone (B&K type 4133) placed at a distance of 50 cm from the signal source when the listener was absent. The power spectra of the tones at the listening point are shown in Fig. 2. Although harmonic distortions were quite eminent at frequencies higher than the signals, subharmonic distortions in the lower frequency side of the signals were not larger than 15 dB SPL. It was confirmed that for any frequencies, subharmonic distortions never exceeded 20 dB SPL.

In the measurement of the hearing threshold, signal tones were amplitude modulated by a sinusoid of 2 Hz. They were, therefore, supposed to be heard as intermittent tones. The duration of the signal was 2000 ms.

A low-pass filtered pink noise was used to mask distortions in the lower frequency range. When the signal frequency was 16 kHz, pink noise low-pass filtered at 12 kHz was used, otherwise pink noise low-pass filtered at 15 kHz was used. The level of the masker was fixed at 60 dB SPL at a distance of 120 cm from the masker source. The masker duration was 2500 ms, including linear onset and offset ramps of 250 ms each. The masker was generated by a D/A converter (EDIROL UA-1000) at a sampling rate of 96 kHz and 16 bit resolution.

2.3 Procedure

The threshold was measured by a three-down one-up transformed up-down paradigm combined with a 2AFC procedure. Two test intervals of 2500 ms were presented to the subject. Both intervals contained the masker but only one of them contained the signal. A silent interval between the two test intervals was 300 ms. Duration of the signal was 2000 ms. The masker always started 250 ms prior to the signal onset and ended 250 ms after the signal offset. Subjects were asked to judge which test interval contained an intermittent tone and respond by pressing a key within 8 s. A visual feedback was given immediately after every response. The level of the stimulus varied adaptively according to a three-down one-up transformed up-down method so that the threshold was estimated automatically. The level of the masker was fixed.

A single run consisted of eight reversals. The threshold value was defined as the mean level at the last four reversal points. The minimum step size was 1 dB. If the level exceeded the maximum level of presentation before eight reversals were completed, the run automatically terminated and no estimation was made. As mentioned earlier, masked and absolute thresholds were also measured for tones at 250 Hz, 1, 4, and 12 kHz. Absolute thresholds were measured without using pink noise.

3. Results and Discussion

For all ears, masked threshold values at 12 kHz and below were higher than 20 dB SPL indicating that any distortions smaller than 20 dB SPL would be masked by the pink noise. As mentioned earlier, subharmonic distortions were always lower than 20 dB SPL in the present study. It can be said that pink noise sufficiently masked distortions in the present study.

Table 1 shows hearing threshold values for tones between 16 and 30 kHz. It also shows the absolute threshold values for tones at 250 Hz, 1, 4, and 12 kHz. Because 16 listeners participated and both sides were examined for each listener, the number of the measured ears was

Table 1. Threshold of hearing for pure tones. Threshold values for tones at 12 kHz and below are the absolute threshold values, otherwise the threshold values were measured with pink noise as the masker.

Frequency (kHz)	Maximum level of presentation (dB SPL)	Threshold values (dB SPL) Minimum	median	Maximum	Number of valid data	Number of tested ears
0.25	80	0.7	7.2	20.4	32	32
1	80	−9.4	−1.6	6.2	32	32
4	80	−13.8	−5.9	7.0	32	32
12	80	−3.6	9.7	25.1	32	32
16	110	22.1	41.8	84.0	32	32
18	105	28.0	64.0	99.5	32	32
20	110	66.4	89.9	···	29	32
22	111	87.6	102.7	···	25	32
24	110	91.9	···	···	16	32
26	112	95.3	···	···	10	32
28	111	101.3	···	···	3	32
30	110	···	···	···	0	32

32. Threshold values were measurable for most ears at 20 and 22 kHz. They were obtained from half of the ears at 24 kHz and from about one-third of the ears at 26 kHz. Although no threshold values were obtained for a tone at 30 kHz, they could be obtained from 3 ears out of 32 at 28 kHz. Above 24 kHz, threshold values were always higher than 90 dB SPL.

Figure 3 shows the maximum, median, and the minimum values of hearing threshold. It can be seen that the hearing threshold increased abruptly as signal frequency increased from 12 to 20 kHz. The actual threshold curve is not known here for threshold values at 16 kHz and above, especially the minimum values at 16 and 18 kHz, might be affected by the masker. Still there seems to be a steep increase of threshold between 16 and 20 kHz. Above 20 kHz, however, it increased relatively slowly. This is consistent with the findings of Henry and Fast[4] and Ashihara *et al.*[15]

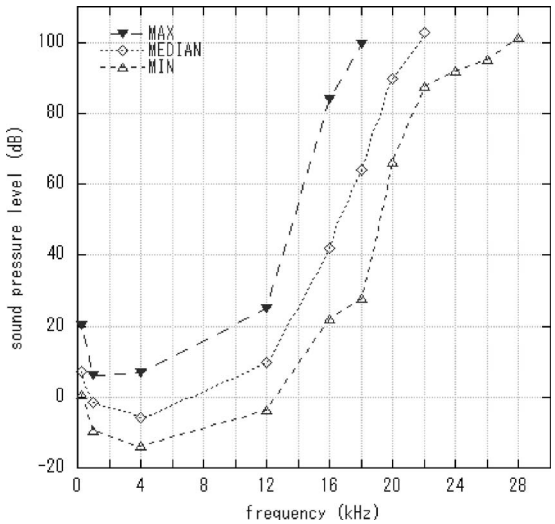

Fig. 3. Hearing threshold for tones. Hearing threshold values are shown as a function of the frequency. The minimum, median, and the maximum values are represented by open triangles, open diamonds, and closed triangles, respectively.

Although it has been repeatedly observed that the thresholds of hearing start to increase abruptly at about 14 kHz, what is responsible for this steep increase is not fully understood. Buus *et al.*[18] proposed three explanations for this steep increase of thresholds: (1) inefficient transmission of acoustic energy to the inner ear, (2) decreasing sensitivity of auditory channel tuned to high frequencies, and (3) running out of channels or the end of cochlea. Their tentative conclusion was that the abrupt increase of thresholds seemed to reflect the characteristics of the last (highest) auditory channel.

Yasin and Plack[19] suggested that the high-frequency limitation in humans would be imposed in part by the middle ear attenuation. Frequency characteristics of the middle ear have been studied and the amplitude at the stapes is known to fall off by 12–15 dB/ octave above 1 kHz.[20–23] In these studies, however, no reliable data are presented above 10 kHz, probably because the signal to noise ratio also falls off at high frequencies. Although further investigations are needed to clarify what the sharp increase of thresholds above 14 kHz represents and why the threshold curve changes its slope at around 20 kHz, the present results can be interpreted as follows.

The characteristic frequency (CF) of the last auditory channel of the cochlea is between 14 and 18 kHz as suggested by Buus *et al.*[18] The threshold curve above this frequency may reflect a combined characteristic of the upper side slope of the last auditory channel's tuning curve and the middle ear attenuation. The psychophysical tuning curve usually has a sharp dip around its CF and a shallower skirt at frequencies away from the CF. If this shallower skirt extends to the ultrasonic regions and the level of the ultrasound is sufficiently high, a part of the sound energy may activate the last auditory channel and thus the sound can be detected. The threshold, therefore, starts to increase rapidly above the CF of the last auditory channel and increase somewhat slowly at much higher frequencies.

4. Conclusion

Thresholds of hearing for pure tones between 16 and 30 kHz were measured. The maximum measurable level was more than 100 dB SPL. Although no threshold was obtained for a 30 kHz tone, it was obtained from 3 out of 32 ears at 28 kHz. The threshold values at 24 kHz and above were always more than 90 dB SPL.

The present results show that some humans can perceive tones up to at least 28 kHz when their level exceeds about 100 dB SPL. These findings would be useful for providing criteria for industrial and commercial use of ultrasounds.

The present data, however, may contain some errors. The signal level was calibrated in the absence of the listener. The actual sound pressure level of the signals at each ear is not known. Difference in size and shape of the heads and earlobes might have caused deviations that would not be negligible. Because the distance between the signal source and the listening point was not enough, a small movement of the head might seriously affect the sound pressure level. In addition, the contralateral ear canal was not sealed in the measurement. The data, therefore, may not precisely represent the actual hearing threshold values of the particular ear. Further investigations are needed to provide more accurate estimation of the hearing threshold values.

References and links

[1]B. W. Lawton, "Damage to human hearing by airborne sound of very high frequency or ultrasonic frequency," Contract Research Report 343, Health and Safety Executive (HSE books, Suffolk, 2001).
[2]Health Canada, "Guidelines for the safe use of ultrasound. II. Industrial and commercial applications," Minister of National Health and Welfare, EHDTR-158, Canadian Communication Group, Ottawa, 1991.
[3]S. A. Fausti, R. H. Fray, D. A. Erickson, B. Z. Rappaport, E. J. Cleary, and R. E. Brummett, "System for evaluating auditory function from 8,000-20,000 Hz," J. Acoust. Soc. Am. **66**, 1713–1718 (1979).
[4]K. R. Henry and G. A. Fast, "Ultrahigh-frequency auditory thresholds in young adults: Reliable responses up to 24 kHz with a quasi-free-field technique," Audiology **23**, 477–489 (1984).
[5]D. M. Green, G. Kidd, Jr., and K. N. Stevens, "High-frequency audiometric assessment of a young adult population," J. Acoust. Soc. Am. **81**, 485–494 (1987).
[6]P. G. Stelmachowicz, K. A. Beauchain, A. Kalberer, and W. Jesteadt, "Normative thresholds in the 8- to 20-kHz range as a function of age," J. Acoust. Soc. Am. **86**, 1384–1391 (1989).

[7]K. Betke, "New hearing threshold measurements for pure tones under free-field listening conditions," J. Acoust. Soc. Am. **89**, 2400–2403 (1991).
[8]H. Takeshima, Y. Suzuki, M. Kumagai, T. Sone, T. Fujimori, and H. Miura, "Threshold of hearing for pure tone under free-field listening conditions," J. Acoust. Soc. Jpn. (E) **15**, 159–169 (1994).
[9]T. Poulsen and L. A. Han, "The binaural free field hearing threshold for pure tones from 125 Hz to 16 kHz," Acust. Acta Acust. **86**, 333–337 (2000).
[10]M. Sakamoto, M. Sugawara, K. Kaga, and T. Kamio, "Average thresholds in the 8 to 20 kHz range in young adults," Scand. Audiol. **27**, 169–172 (1998).
[11]K. Kurakata, K. Ashihara, K. Matsushita, H. Tamai, and Y. Ihara, "Threshold of hearing in free field for high frequency tones from 1 to 20 kHz," Acoust. Sci. & Tech. **24**, 398–399 (2003).
[12]K. Ashihara, "Audibility of complex tones above 20 kHz," *Proceedings Internoise 2000* (Nice, 2000).
[13]K. Ashihara, "The higher limit of the audible area for complex sounds," *Proceedings of the 15th Triennial Congress of International Ergonomics Association*, pp. 524–537 (Seoul, 2003).
[14]K. Ashihara and S. Kiryu, "Audibility of components above 22 kHz in a complex tone," Acust. Acta Acust. **89**, 540–546 (2003).
[15]K. Ashihara, K. Kurakata, T. Mizunami, and K. Matsushita, "Hearing threshold for pure tones above 20 kHz," Acoust. Sci. & Tech. **27**, 12–19 (2006).
[16]H. Levitt, "Transformed up-down methods in psychoacoustics," J. Acoust. Soc. Am. **49**, 467–477 (1971).
[17]ISO 8253-2, "Acoustics - audiometric test methods. - 2 Sound field audiometry with pure tone and narrow-band test signals," International Organization for Standardization, Geneva Switzerland, 1992.
[18]S. Buus, M. Florentine, and C. R. Mason, "Tuning curves at high frequencies and their relation to the absolute threshold curves," in *Auditory Frequency Selectivity*, edited by B. C. J. Moore and R. D. Patterson (Plenum, New York, 1986).
[19]I. Yasin and C. J. Plack, "Psychophysical tuning curves at very high frequencies," J. Acoust. Soc. Am. **118**, 2498–2506 (2005).
[20]M. Kringlebotn and T. Gundersen, "Frequency characteristics of the middle ear," J. Acoust. Soc. Am. **77**, 159–164 (1985).
[21]M. S. Vlaming and L. Feenstra, "Studies on the mechanics of the normal human middle ear," Clin. Otolaryngol. **11**, 353–363 (1986).
[22]R. L. Goode, K. Nakamura, K. Gyo, and H. Aritomo, "Comments on 'Acoustic transfer characteristics in human middle ears studied by a SQUID magnetometer method' [J. Acoust. Soc. Am. **82**, 1646–1654 (1987)]," J. Acoust. Soc. Am. **86**, 2446–2449 (1989).
[23]H. Kurokawa and R. L. Goode, "Sound pressure gain produced by the human middle ear," Arch. Otolaryngol. Head Neck Surg. **113**, 349–355 (1995).

Reliability and frequency specificity of auditory steady-state response detected by phase spectral analysis

M. Aoyagi, T. Watanabe, T. Ito, and Y. Abe
Department of Otolaryngology, Yamagata University School of Medicine, 2-2-2 Iida-Nishi, Yamagata, 990-9585, Japan
aoyagi@med.id.yamagata-u.ac.jp, watanatm@med.id.yamagata-u.ac.jp, tuito@med.id.yamagata-u.ac.jp, yabe@med.id.yamagata-u.ac.jp

Abstract: Automatic threshold detection techniques are described for auditory steady-state response (ASSR) elicited with a sinusoidally amplitude-modulated tone. The reliability and frequency specificity of ASSR are discussed. When applied to awake adults and detected by phase spectral analysis, 40-Hz ASSR threshold patterns closely resemble their corresponding audiograms. However, 40-Hz ASSR is insufficiently reliable for determining hearing thresholds in young children during sleep. On the other hand, 80-Hz ASSR is detected clearly in sleeping children. Moreover, 80-Hz ASSR threshold patterns also closely resemble the corresponding audiograms. Therefore, 80-Hz ASSR appears to be useful for objective audiometry in children.

PACS numbers: 43.64.Ri, 43.66.Cb, 43.66.Sr [DKW]
Date Received: March 29, 2007 **Date Accepted:** June 26, 2007

1. Introduction

The initial goal of objective audiometry is to predict an audiogram in a frequency-specific manner. However, the frequency specificity of auditory brainstem response (ABR), which is the most popular device for objective audiometry, is insufficient to predict hearing accurately in the low-frequency range. The auditory steady-state response (ASSR) elicited by sinusoidally amplitude-modulated (SAM) tone[1] is considered to be a reflection of the synchronous discharge of auditory neurons that are phase-locked to the modulation frequency (MF) of the stimulus tone. Application of ASSR provides reliable frequency-specific hearing information because of the quite narrow band power spectrum of the SAM tone. When the carrier frequency (CF) is f_c and MF is f_m, the power spectrum of the SAM tone has three steep peaks at $f_c - f_m$, f_c, and $f_c + f_m$; the power spectrum is considerably narrower than the spectra of click and tone pips. This letter presents descriptions of the automatic detection technique of ASSR developed by the authors, the optimal MFs of stimulus tone in different arousal states, and the reliability and frequency specificity of ASSRs elicited by SAM tone. A summary of the contents of the author's former papers,[2–5] along with papers by other authors,[6–10] is given.

2. Automatic threshold detection

The ASSR wave form resembles a sinusoidal wave form corresponding to the MF of stimulus tone. For that reason, fast Fourier transform based computer analyses using the power[6] and phase spectral analysis[7] are useful for automatic detection of thresholds. For this study, we applied phase spectral analysis[2] developed by Fridman *et al.*,[8] which is called *synchrony measure method*. Mardia's equation[9] was used to compute the phase variance [φ (m)] of each Fourier component among ten averaged wave forms, called *group averages*, which are obtained under identical stimulus condition. Furthermore, the component synchrony measure (CSM) was calculated using

$$\mathrm{CSM(m)} = 1 - \mathrm{var}[\varphi(\mathrm{m})]. \quad (1)$$

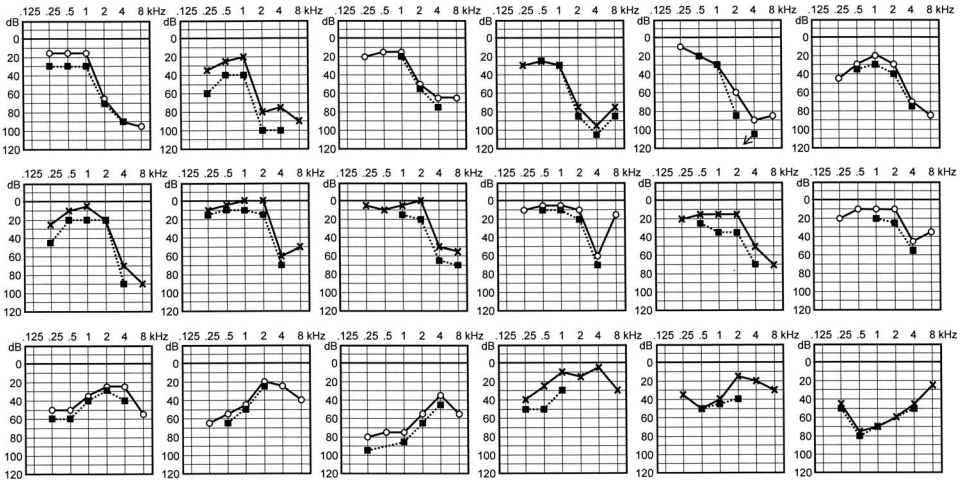

Fig. 1. Comparison between pure-tone audiograms and 40-Hz ASSR thresholds (closed squares) in hearing-impaired adults. In the audiograms, circles indicate air-conduction hearing thresholds for the right ear and crosses those for the left ear. An AD-02B (RION, Tokyo) earphone was used for the audiometric tests.

In Eq. (1), CSM represents the degree of synchronization of a frequency component for the ten group averages; it varies from 0 to 1. If the phases of a frequency component were exactly the same for all ten group averages, then CSM would be equal to 1. The CSM would then approach 0 if the phases change randomly from wave form to wave form. When the calculation procedure is performed for n group averages and if no response exists, then CSMs have a distribution with a mean CSM and a standard deviation (σ), which are defined by[2]

$$\text{Mean} = 1/n, \tag{2}$$

$$\sigma^2 = (n-1)/n^3. \tag{3}$$

The criterion for the presence of response (mean+3s.d.) is therefore set at 0.385 according to the above theoretical equations (2) and (3), when CSMs are calculated from ten group averages.

3. Optimal modulation frequency for ASSRs

To determine the optimal MF for ASSRs in different arousal states, the detectability of ASSR elicited by SAM tones, for which MF was varied from 20 to 200 Hz in 20 Hz steps, was examined using phase spectral analysis described earlier in awake adults, adults during sleep, and in children[3] during sleep. At the MF of 40 Hz, CSMs were very high in awake adults, although the CSMs at the 40-Hz component in children during sleep were significantly lower than those of awake and asleep adults. On the other hand, the CSMs at MFs of 80–100 Hz were high during sleep, especially in children. Consequently, when a response is detected using phase spectral analysis, ASSR can be detected clearly at the MF of 40 Hz (40-Hz ASSR) while awake, and at MFs of 80–100 Hz during sleep, especially in children. The frequency specificity of the SAM tone at the MF of 80 Hz is higher than that at the MF of 100 Hz. Therefore, 80-Hz ASSR is considered to be an optimal response for children during sleep.

4. 40-Hz ASSR thresholds versus audiograms

In Fig. 1, the 40-Hz ASSR thresholds at each CF examined while awake are plotted as closed squares in the audiograms for 20 adult patients with various types of hearing loss. Threshold patterns of 40-Hz ASSR very closely resemble the corresponding audiograms for all audiogram types. The correlation coefficients between the behavioral hearing thresholds and 40-Hz ASSR

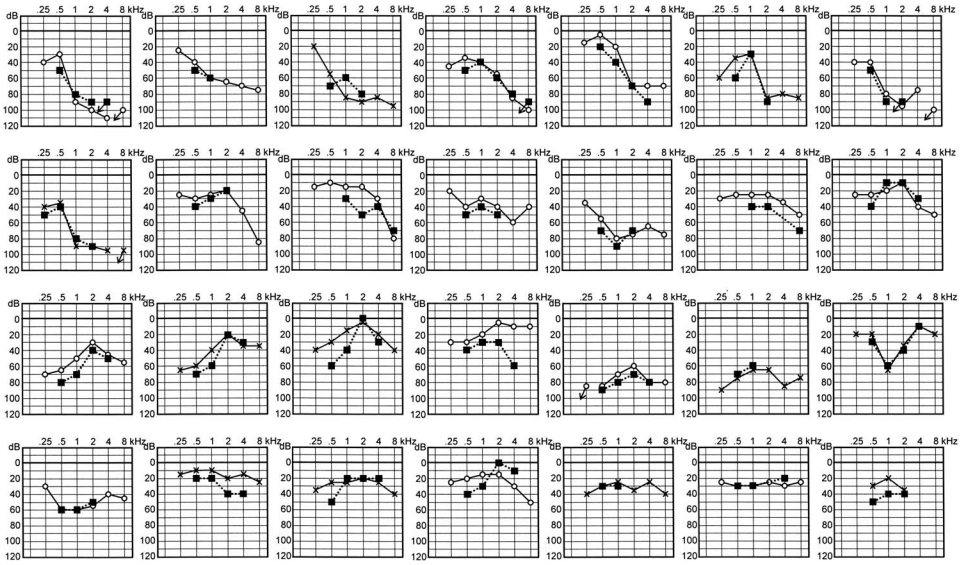

Fig. 2. Comparison between pure-tone audiograms and 80-Hz ASSR thresholds in hearing-impaired children. The symbols are the same as in Fig. 1.

thresholds in adult patients with hearing loss pooled across frequencies was 0.963.[4] These findings suggest that the reliability and the frequency specificity of 40-Hz ASSR is very high if the subject is an awake adult and the response is detected using phase spectral analysis.

5. 80-Hz ASSR thresholds versus audiograms

In Fig. 2, the 80-Hz ASSR thresholds at each CF are plotted as closed squares in the audiograms of 28 young children with various types of hearing loss. The 80-Hz ASSR were examined during sleep. The threshold patterns of 80-Hz ASSR also closely resemble the corresponding audiogram patterns in any type of hearing impairment. These results mean that 80-Hz ASSR provides accurate hearing information with a good frequency specificity in asleep children.

Comparison of the correlation between the behavioral hearing threshold and the threshold of ABR to 1000-Hz tone pips ($n=93$) with the correlation between the behavioral hearing threshold and the threshold of 80-Hz ASSR to 1000-Hz SAM tones ($n=169$), showed that the correlation coefficient for 80-Hz ASSR was significantly higher than the one obtained for ABR (0.863 vs 0.828).[5] That result suggests that 80-Hz ASSR is of greater use than ABR to tone pips in assessing hearing in young children during sleep. However, Figs. 1 and 2 show that the reliability of 80-Hz ASSR examined in asleep children is somewhat lower than that of 40-Hz ASSR examined in awake adults ($r=0.863$ vs 0.963).

To estimate the reliability of 80-Hz ASSR for the prediction of a hearing threshold in the low-frequency range, the correlations between the behavioral hearing threshold and the threshold of 80-Hz ASSR to SAM tones were calculated with each CF: 500, 1000, 2000, and 4000 Hz. The respective correlation coefficients at those tested frequencies were 0.729, 0.863, 0.879, and 0.915. The respective mean differences (±s.d.) in decibels between the 80-Hz ASSR threshold and the behavioral hearing threshold at those frequencies were 15(±15), 4(±13), 9(±16), and 2(±14) dB. Those results show that 80-Hz ASSRs at lower frequencies are less reliable than those at higher frequencies. Moreover, thresholds at lower frequencies are more elevated. In their recent review, Picton *et al.* (2003)[10] reported an almost identical finding using summarized results from many studies.

Picton indicated that the difficulty in the assessment of ASSR threshold at the lower frequency range, such as at 500 Hz, might be related to the width of the auditory filter. To detect

the amplitude modulation of a signal, the ear must process both the CF and two sidebands. Each sideband is separated from the carrier by an amount equal to the MF. The auditory filter at 500 Hz is sufficiently narrow (e.g., Glasberg and Moore)[11] that the sidebands might not be processed together with the CF. This might be particularly true at near-threshold intensities.

6. Conclusions

The ASSRs elicited by SAM tones and detected by phase spectral analysis are a useful audiometric device for the determination of hearing levels in a frequency-specific manner. The 40-Hz ASSR, or low-frequency ASSR, is applicable to awake adults; the 80-Hz ASSR, or high-frequency ASSR, is applicable to asleep children.

References and links

[1]F. W. Rickards and G. M. Clark, "Steady-state evoked potentials to amplitude-modulated tones," in *Evoked Potentials II*, edited by R. H. Nodar and C. Barer (Butterworth, Boston, MA, 1984), pp. 163–168.
[2]M. Aoyagi, T. Fuse, T Suzuki, Y. Kim, and Y. Koike, "An application of phase spectral analysis to amplitude-modulation following response," Acta Oto-Laryngol., Suppl. **504**, 82–88 (1993).
[3]M. Aoyagi, T. Kiren, Y. Kim, Y. Suzuki, T. Fuse, and Y. Koike, "Optimal modulation frequency for amplitude-modulation following response in young children during sleep," Hear. Res. **65**, 253–261 (1993).
[4]M. Aoyagi, T. Kiren, Y. Kim, Y Suzuki, T. Fuse, and Y. Koike, "Frequency specificity of amplitude-modulation following response detected by phase spectral analysis," Audiology **32**, 293–301 (1993).
[5]M. Aoyagi, Y. Suzuki, M. Yokota, H. Furuse, T. Watanabe, and T. Ito, "Reliability of 80-Hz amplitude modulation-following response detected by phase coherence," Audiol. Neuro-Otol. **4**, 28–37 (1999).
[6]H. Hotelling, "The generalization of Student's ratio," Ann. Math. Stat. **2**, 360–378 (1931).
[7]J. R. Jerger, R. Chimel, J D. Frost, Jr., and N. Coker, "Effect of sleep on the auditory steady state evoked potential," Ear Hear. **7**, 240–245 (1986).
[8]J. Fridman, R. Zappulla, M. Bergelson, E. Greenblatt, L. Malis, F. Morrell, and T. Hoeppner, "Application of phase spectral analysis for brain stem auditory evoked potential detection in normal subjects and patients with posterior fossa tumors," Audiology **23**, 99–113 (1984).
[9]K. V. Mardia, *Statistics of Directional Data* (Academic, New York, 1972).
[10]T. W. Picton, M S. John, A Dimitrijevic, and S Purcell"Human auditory steady-state responses," Int. J. Audiol. **42**, 177–219 (2003).
[11]B. R. Glasberg and B. C. Moore, "Derivation of auditory filter shaped from notched-noise data," Hear. Res. **47**, 103–138 (1990).

Frequency-dependent changes in absolute hearing threshold caused by perception of a previous sound

Junji Yoshida, Hiroshi Hasegawa, and Masao Kasuga
Graduate School of Engineering, Utsunomiya University, 7-1-2, Yoto, Utsunomiya-shi, Tochigi, 321-8585, Japan
yossy_j0223@yahoo.co.jp, hasegawa@is.utsunomiya-u.ac.jp, kasuga@is.utsunomiya-u.ac.jp

Abstract: This study investigated effects of a previous sound presentation at the absolute threshold of hearing. Changes in threshold were measured when a pure tone at 60 dB SPL preceded a test tone in the contra- or ipsilateral ear. When the previous and test sounds both had the same frequency of 500 Hz, threshold decreased approximately 2 dB in the contralateral ear, and increased slightly in the ipsilateral ear. On the other hand, when the frequency of the previous sound differed from that of the test sound, the threshold was decreased slightly in the ipsilateral ear.

PACS numbers: 43.66.Cb, 43.66.Ed [DKW]
Date Received: March 24, 2007 **Date Accepted:** June 8, 2007

1. Introduction

It is known that perception of a sound is changed by stimuli preceding it.[1–7] When a human hears a loud sound in one ear, the absolute threshold of hearing in the ipsilateral ear increases. This phenomenon is referred to as auditory fatigue.[2,3] Loudness adaptation has also been reported when a continuous sound becomes generally softer and an intermittent sound is heard in the contralateral ear.[4,5] Both of these phenomena are detectability or loudness decrease effects resulting from perception of an inducing sound. On the other hand, monaural detection contralateral cueing (MDCC) is a known detectability increase phenomenon in which the cueing sound has the same frequency and phase as the test sound presented simultaneously in the contralateral ear.[6,7]

In the present study, we measured changes of threshold due to presentation of a previous sound. The procedure is similar to auditory-fatigue experiments, except for the presentation ear. We presented the previous sound in the contralateral ear as a cueing sound similar to the MDCC experiment. Then, we investigated whether the threshold increases, as with auditory fatigue, or decreases, as with MDCC. We also measured changes to threshold in the ipsilateral ear to compare to the effect in the contralateral ear. In addition, to investigate the frequency dependence and to discuss the mechanism of the previous sound effect, we performed threshold change measurements when the frequency of the previous sound was varied.

2. Threshold change by perceiving previous sound

2.1 Experiment 1

The test apparatus consisted of a digital audio tape (DAT) player (SONY TCD-08) and an audiometer with headphones (GN Otometrics A/S ITERA). Pure tones at −15 to 20 dB SPL were used as the test sounds for measurement of the threshold. Pure tones at 60 dB SPL were used as the previous sounds. The previous and test sounds had the same duration of 3 s and frequency of 500 Hz. The interstimulus interval between the previous and test sounds was 0.5 s. These sounds were recorded onto a DAT and their SPLs were arranged using the audiometer when the sounds were reproduced from the DAT player.

In the general measurement of the threshold (without the previous sound), the test sound was first presented to the subject as an inaudible sound at −15 dB SPL. The SPL was then increased in a 5 dB step to the level at which subject response changed from "inaudible" to

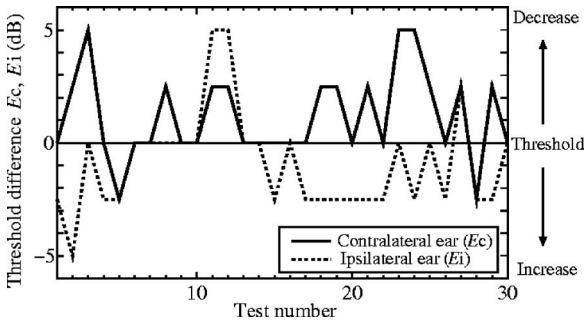

Fig. 1. Differences in absolute threshold of hearing averaged for left and right ears for each test for Subject A. Solid and dotted lines denote threshold differences in the contralateral ear (E_c) and in the ipsilateral ear (E_i), respectively.

"audible." For indicating test sound audibility, the subject pushes a button that is attached to the audiometer. Next, the SPL was decreased in a 5 dB step to the level at which subject response changed from audible to inaudible. We then performed the above-described procedure again. When the response changed at the same SPL in the previous upward sequence, we determined the level as the absolute threshold of hearing. If the response changed at a different SPL, the procedure was continued until the response changed at the same SPL in the previous upward sequence. In the measurement of the threshold for the case with the previous sound, we presented the previous sound 0.5 s before the test sound. The measurement procedure was the same for the case without the previous sound. The previous sound was presented either in the contralateral ear or in the ipsilateral ear (test ear). Each test session involved six types of tests: measurement of the threshold in each ear (left and right) for cases without the previous sound, with the previous sound in the contralateral ear, and with the previous sound in the ipsilateral ear. Then, we calculated the change in threshold originating from the previous sound presentation by subtracting the threshold with the previous sound from the threshold without the previous sound in each session, as follows:

$$E_c = T_g - T_c, \tag{1}$$

$$E_i = T_g - T_i, \tag{2}$$

where T_g is the threshold in the case without the previous sound, and T_c and T_i are the thresholds in cases with the previous sound in the contra- and ipsilateral ears, respectively. E_c and E_i, are threshold differences when the previous sound was presented in the contra- and ipsilateral ears, respectively. In cases where the threshold difference (E_c and/or E_i) becomes positive, this means the absolute threshold of hearing has decreased.

Five male subjects in their 20's, who had normal hearing acuity, participated in the experiments. Subjects were designated as Subject A through E. Each subject performed one session without break in about 15 min. And each subject carried out 30 sessions in total, taking a break between each one. Each subject thus performed 180 tests, and the five subjects performed 900 tests in total. Also, there are two patterns of presentation order in the 30 sessions. The first pattern is the presentation order of T_g in each ear, T_c in each ear, and T_i in each ear. The second pattern is the presentation order of T_g, T_i, and T_c. The number of each order pattern is the same in 30 sessions.

2.2 Result 1

Figure 1 shows the threshold differences (E_c and E_i) averaged in the left and right ears for each test of Subject A. The solid and dotted lines denote the threshold differences in the contralateral ear (E_c) and in the ipsilateral ear (E_i), respectively. In Fig. 1, E_c is generally positive, i.e., the threshold was decreased by perceiving the previous sound in the contralateral ear, whereas E_i shows slight tendency of the threshold increase. To obtain the value of the threshold change, we

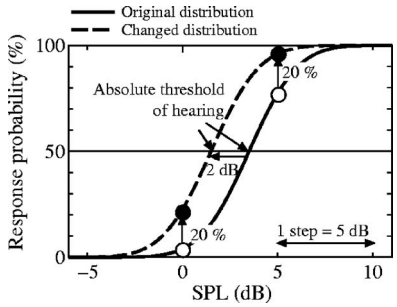

Fig. 2. Distributions when threshold changes. Response probability change at each step (0 and 5 dB) could be measured. Solid and dotted curves indicate original and changed distributions, respectively.

employed a psychometric function where the absolute threshold of hearing is assumed to vary depending on a Gaussian distribution with respect to the SPL. Figure 2 shows a change in the assumed distribution when the threshold was changed. The horizontal axis shows the SPL of the test sound, and the vertical axis shows the audible response probability to the presented test sound. The solid curve shows the distribution of the original threshold and the dotted curve shows the distribution of the changed threshold. The 50% point in each distribution indicates the threshold in a subject. Then, the audible response probability at the measurement point (in a 5 dB step) changes depending on the threshold change. As shown in Fig. 2, when the threshold changes by 2 dB, the audible response probability at 0 and 5 dB (measurement point) in the original distribution (open circles) increases by approximately 20% in the changed distribution (closed circles). Consequently, if we can measure the audible response probability change between the original distribution and the changed distribution at the measurement points, the value of threshold change could be estimated in the 5 dB step measurement. However, if the standard deviation of distributions is too small, the response probability change could not be measured at the measurement points and the threshold change could not be calculated correctly (the threshold change is calculated as 0 dB by the estimation using the response probability change). Figure 3 shows the threshold change estimated by the above-mentioned method in each subject and all subjects. In addition, the 95% confidence intervals were calculated using the number of session and the standard deviation for all sessions. Here, the gray and white bars indicate threshold differences when the previous sound was presented in the contralateral ear (E_c) and the ipsilateral ear (E_i), respectively. Error bars indicate 95% confidence intervals. As shown in Fig. 3, presentation of a previous sound changed the threshold by approximately 1 or 2 dB. This result indicates that the standard deviation of the distribution of the psychometric function was not too small to measure the response, probability change, and that E_c in all subjects displayed positive values in Figs. 3(a)–3(e). In Fig. 3(f), the averaged value was approximately 2 dB. This result indicates that the threshold was decreased for most subjects when the previous sound was presented in the contralateral ear. Conversely, E_i was negative in most subjects, and the averaged value was approximately 1 dB. This result indicates that the threshold increased slightly by presenting the previous sound in the ipsilateral ear. These results indicate that the previous sound effect in the contralateral ear works to decrease threshold, while that in the ipsilateral ear works to increase threshold.

3. Frequency dependence of threshold change

The absolute threshold of hearing was found to be decreased significantly by presenting the previous sound in the contralateral ear. In this experiment, to investigate the frequency dependence of threshold changes, we measured threshold changes when frequency of the previous sound was varied.

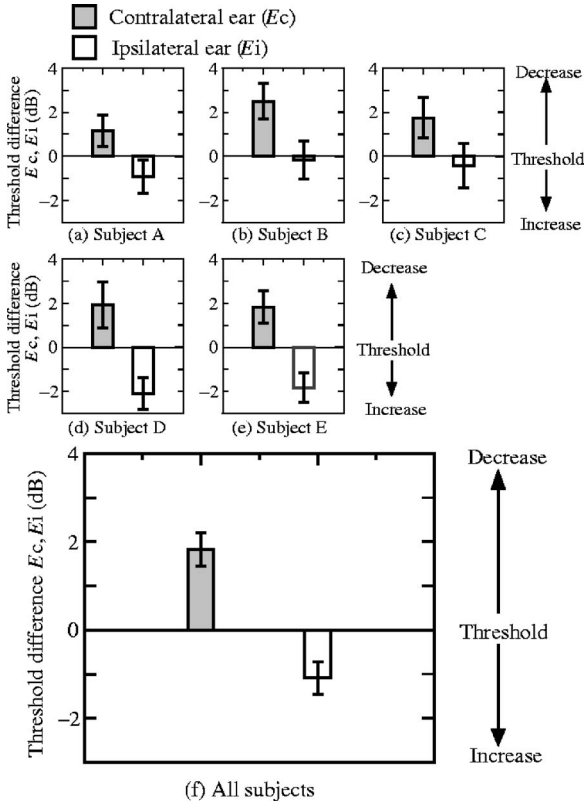

Fig. 3. Threshold differences in each subject and averaged in all subjects. Gray and white bars indicate threshold differences in the contralateral (E_c) and ipsilateral (E_i) ears, respectively. Error bars indicate 95% confidence intervals.

3.1 Experiment 2

Threshold with and without presentation of a previous sound was measured to determine threshold changes in the contra- or ipsilateral ear. The experimental procedure was identical to that in Experiment 1. The previous and test sounds were pure tones with a duration of 3 s. SPL of the previous sound was 60 dB and the frequency of the test sound was 500 Hz. The frequency of the previous sound was set at 500, 1 k, or 2 kHz. Interstimulus interval between the previous and test sounds was 0.5 s.

Five male subjects (Subject A through E) in their 20's, who had normal hearing acuity, participated in this experiment. These were the same subjects who participated in Experiment 1. Each subject performed 30 sessions comprising six types of tests: measurement of the threshold in each ear (left and right) for cases without previous sound, with previous sound in the contralateral ear, and with previous sound in the ipsilateral ear. In addition, there were three kinds of previous sound frequencies. Each subject thus performed 540 tests, and in total the five subjects performed 2700 tests.

3.2 Result 2

Figure 4 shows the threshold difference (E_c,E_i) in each subject and averaged in all subjects at each previous sound frequency. Horizontal and vertical axes show the previous sound frequency and threshold difference, respectively. Closed and open circles indicate threshold difference in the contralateral (E_c) and ipsilateral ear (E_i), respectively. Error bars indicate 95% confidence intervals. From the experimental results for each subject in Figs. 4(a)–4(e), thresholds were

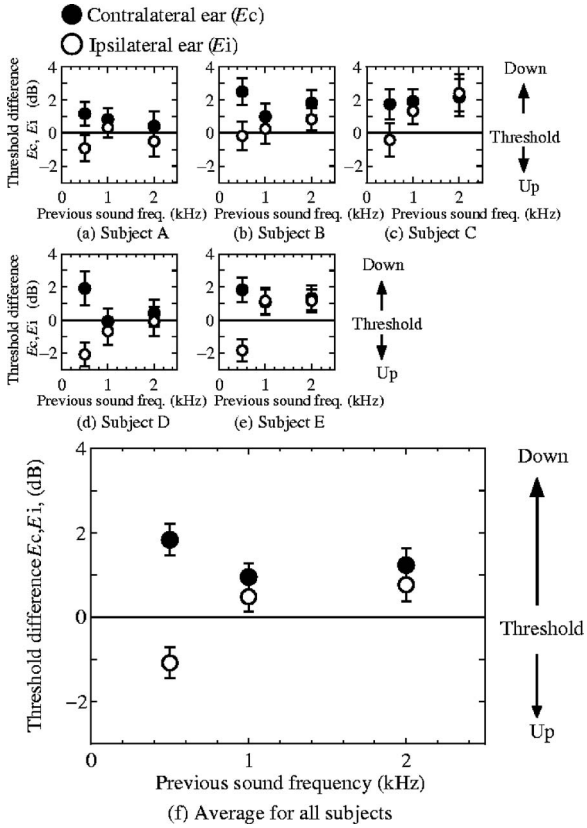

Fig. 4. Threshold differences in each subject and averaged in all subjects. Horizontal and vertical axes show the previous sound frequency and threshold difference, respectively. Closed and open circles indicate threshold difference in the contralateral (E_c) and ipsilateral ear (E_i), respectively. Error bars indicate 95% confidence intervals.

found to be decreased when the previous sound was presented in the contralateral ear (closed circle) at any frequency (500, 1 k, 2 kHz). Thresholds were increased in the ipsilateral ear (open circle) when the frequency of the previous sound was 500 Hz in most subjects, as in Experiment 1. By averaging subject results in Fig. 4(f), the threshold decrease in the contralateral ear (closed circle) at 500 Hz was found to be larger than that at 1 and 2 kHz, and the threshold decreased slightly by presenting the previous sound in the ipsilateral ear (open circle) at 1 and 2 kHz.

These results indicate that threshold decrease in the contralateral ear tends to be maximized when the frequency of the previous sound is the same as that of the test sound. Conversely, threshold change by perceiving the previous sound in the ipsilateral ear displays a different tendency, in which threshold is increased when the frequency of the previous sound is the same as that of the test sound, but threshold is decreased by presenting the previous sound at a different frequency to the test sound.

Next, we examined the significance of the frequency dependence of threshold change. We employed the Wilcoxon rank sum test, which is a nonparametric statistical test, to verify the significance of the threshold change as the threshold was measured in a discrete variable (5 dB step). The results (Table 1) show that the change in threshold decrease in the contralateral ear between 500 Hz and 2 kHz (0.6 dB) and between 500 Hz and 1 kHz (0.9 dB) were statistically significant but the change between 1 and 2 kHz (−0.3 dB) was not significant at a significance level of 5%. Consequently, the threshold decrease phenomenon was found to have a characteristic in which the decrease level is maximized significantly when the frequency is the same as

Table 1. Result of Wilcoxon rank sum test for verification of the dependence of threshold change on previous sound frequency.

	Contralateral		Ipsilateral	
Pair	Chng.Th.Df. (dB)	*P*(%)	Chng.Th.Df (dB)	*P*(%)
500 Hz vs 2 kHz	0.6	1[a]	−1.9	0[a]
500 Hz vs 1 kHz	0.9	0[a]	−1.6	0[a]
1 kHz vs 2 kHz	−0.3	25	−0.3	26

[a]Significance level 5%.

that of the test sound. In the ipsilateral ear, changes between 500 Hz and 2 kHz (−1.9 dB), and between 500 Hz and 1 kHz (−1.6 dB)were significant but the change between 1 and 2 kHz (−0.3 dB) was not significant. This result indicates that the threshold change in the ipsilateral ear became largest when the frequency of the previous sound is the same as that of the test sound as in the contralateral ear. However, the tendency of this change differs. When the frequency of the previous sound changes from the same frequency of the test sound to another frequency, the threshold changes from an increase to a decrease in the ipsilateral ear.

4. Discussion

In Experiment 1, the threshold was decreased approximately 2 dB by presenting the previous sound in the contralateral ear, and increased 1 dB in the ipsilateral ear. Regarding the effect in the ipsilateral ear, the threshold increase is considered to be related to the auditory fatigue.[2,3] In the auditory-fatigue experiment, threshold is reported to be increased approximately 1 dB by presenting a previous sound having 60 dB SPL in the ipsilateral ear.[3] Regarding the effect in the contralateral ear, auditory adaptation was reported as a phenomenon in which loudness of a continuous sound becomes softer when an intermittent sound was presented in the contralateral ear.[4,5] If the same phenomenon occurs in our experiment, loudness of test sound is decreased by the presentation of the previous sound in the contralateral ear. And when the loudness around the threshold decreases, the threshold is considered to be increased. The threshold, however, decreased in our experiment. From the result and characteristic of the adaptation, it is believed that adaptation was not the primary cause of the threshold decrease in the contralateral ear. Also, Taylor *et al.* reported that signal detection ability against noise was increased by presenting a cue signal in the contralateral ear (MDCC).[6,7] Although the investigation target of MDCC (signal detection ability) is not exactly the same as examined in this study (absolute threshold of hearing), the mechanisms underlying both phenomena might be similar because detection abilities in both phenomena are increased by perceiving a cue sound in the contralateral ear. However, important differences exist between these phenomena. In the MDCC experiment, the cue and test signals were presented simultaneously, and when the both signals had the same frequency, amplitude, and phase, detection ability increased.[6] When the cue signal preceded the test signal by at least 800 μs, detection ability did not increase at all.[7] Conversely, threshold was decreased by presenting the previous sound in the contralateral ear 500 ms before presenting the test sound in our experiment. Consequently, the threshold decrease in this study is considered to involve different mechanisms than MDCC. Therefore, few phenomena considered as a main factor of the threshold decrease observed in this experiment are reported at present. But the previous sound in the contralateral ear is considered to occur in the auditory central nervous system, since the phenomenon occurs mainly in the contralateral ear.

In Experiment 2, threshold decrease in the contralateral ear was maximized when the frequency of the previous sound was the same as that of the test sound. This phenomenon is thus considered to display a characteristic in which magnitude of the threshold decrease is maximized according to similarity between previous and test sounds. On the other hand, threshold increased by presenting the previous sound with the same frequency.as the test sound in the

ipsilateral ear. This phenomenon is considered to occur by the deterioration of loudness sensitivity due to auditory fatigue.[2,3] This threshold increase effect is considered to occur mainly in the peripheral nervous system, as the effect occurs only in the ipsilateral presentation pattern. However, when the frequency of the previous sound differed from that of the test sound at 1 and 2 kHz, threshold was not increased, instead decreasing slightly. These phenomena may occur due to the mutual effect of the threshold decrease effect in the central nervous system and the threshold increase effect in the peripheral nervous system. When the frequency of the previous sound was 1 or 2 kHz, the level of threshold decrease in the central system is believed to be larger than the threshold increase level in the peripheral system. As a result, threshold was found to be decreased even in the ipsilateral presentation pattern.

References and links

[1]B. Scharf, "Sequential effects in loudness," *Fechner Day 2001* (2001), pp. 1–6.
[2]I. J. Hirsh and W. D. Ward, "Recovery of the auditory threshold after strong acoustic stimulation," J. Acoust. Soc. Am. **24**, 131–141 (1952).
[3]I. J. Hirsh and R. C. Bilger, "Auditory-threshold recovery after exposures to pure tones," J. Acoust. Soc. Am. **27**, 1186–1194 (1955).
[4]M.-C. Botte, G. Canevet, and B. Scharf, "Loudness adaptation induced by an intermittent tone," J. Acoust. Soc. Am. **80**, 727–739 (1982).
[5]M.-C. Botte, C. Baruch, and B. Scharf, "Loudness reduction and adaptation induced by a contralateral tone," J. Acoust. Soc. Am. **80**, 73–81 (1986).
[6]M. M. Taylor and S. M. Forbes, "Monaural detection with contralateral cue (MDCC). I. Better than energy detector performance by human observers," J. Acoust. Soc. Am. **46**, 1519–1526 (1969).
[7]M. M. Taylor and D. P. J. Clarket, "Monaural detection with contralateral cue (MDCC). II. Interaural delay of cue and signal," J. Acoust. Soc. Am. **49**, 1243–1253 (1971).

Use of perceptual weights to test a model of loudness summation

Lori J. Leibold
The University of North Carolina at Chapel Hill, Chapel Hill, North Carolina 27599
leibold@med.unc.edu

Walt Jesteadt
Boys Town National Research Hospital, Omaha, Nebraska 68131
jesteadt@boystown.edu

Abstract: Leibold *et al.*[J. Acoust. Soc. Am. **121**, 2822–2831 (2007)] examined the perceptual weight subjects assigned to individual components of a multitone complex while performing a loudness-matching task. Weights agreed with the Moore *et al.* loudness model [J. Audio Eng. Soc. **45**, 224–237 (1997)], except when components were widely spaced in frequency. In an effort to account for the data, the just-noticeable-difference (jnd) for intensity discrimination was measured for each component and compared to the weight for that component. The model predicts greater improvement in intensity discrimination with increasing bandwidth than was observed in the data. jnds were not correlated with weights in the widest frequency-spacing condition.

PACS numbers: 43.66.Cb, 43.66.Lj [DKW]
Date Received: March 27, 2007 **Date Accepted:** May 23, 2007

1. Introduction

Complex sounds, such as speech, are made up of multiple components that vary in frequency and in level. If we hope to develop a complete understanding of loudness perception, we must determine how these individual components contribute to the overall loudness of the complex sound. For example, do individual components contribute equally or do some components influence our perception of loudness more than others?

We recently examined the contribution of individual components to judgments of overall loudness in the context of a band-widening experiment by estimating the perceptual weights subjects assign to the individual components of a multitone complex during a two-interval, loudness-matching task (Leibold *et al.*, 2007). Stimuli were five-tone complexes centered on 1000 Hz, with six different logarithmic frequency spacing conditions, ranging from a frequency ratio of 1.012 to 1.586. The perceptual weights were in good agreement with the predictions of a model of loudness summation (Moore *et al.*, 1997), except at the widest bandwidth. The model proposed by Moore *et al.* (1997) accounts for loudness summation by representing sounds as excitation patterns that are summed and then converted to specific loudness, as proposed in earlier models (e.g., Zwicker and Scharf, 1965). We will briefly review the original data and present new data on discrimination of the level of the individual components obtained from the same listeners. We will compare the new data to predictions obtained from the model and to predicted and obtained perceptual weights.[1]

2. Method

2.1 Subjects

The subjects were six adults (18–40 years), including author LL. All subjects had normal hearing sensitivity, with thresholds for 200-ms tones in quiet of 20 dB SPL or less at octave frequencies from 250 to 8000 Hz in both ears, measured using a two-interval, forced-choice (2IFC) adaptive procedure. All subjects participated in the experiments reported by Leibold *et al.*

(2007). Data for a seventh subject who participated in the earlier experiments were excluded from the analyses reported here because the intensity discrimination thresholds were abnormally high and variable.

2.2 Stimuli and equipment

The stimuli were five-tone complexes centered on 1000 Hz. All stimuli were presented for 300 ms. Six different frequency spacing conditions were examined, corresponding to bandwidths from 46 to 2119 Hz. The overall level of the complex was 60 dB SPL (53 dB SPL/component). Stimuli were digitally generated and presented monaurally over headphones as described in greater detail by Leibold *et al.* (2007).

2.3 Intensity discrimination procedure

Following collection of data for loudness matching, perceptual weights, and masked thresholds in the three experiments described by Leibold *et al.*, data were collected for intensity discrimination at each of the component frequencies in the presence of the five-tone complex for each of the six spacing conditions. The pedestal level of the five-tone complex was 60 dB SPL (53 dB SPL/component). Thresholds were estimated using a 2IFC, adaptive procedure that adjusted the level of an increment tone added in quadrature phase to one of the five tones to estimate the 71% point on the psychometric function (Levitt, 1971). Two 100-block trials were run for each component in each frequency-spacing condition. This procedure was identical to the procedure used by Leibold *et al.* (2007) to estimate masked thresholds, except that fewer threshold estimates were obtained in this case and the complex, or masker, contained five tones rather than four, where one of the five tones was identical in frequency to the increment tone, or signal. For reasons described below, we report the data in terms of the threshold level of the increment tone. Paraphrasing an explanation of this terminology given by Viemeister and Bacon (1988), the threshold level of the increment can be interpreted as the SPL of a waveform that, when added to the five-tone complex, produces a change in level that is detectable on 71% of the trials.

3. Results and discussion

3.1 Overview of results reported by Leibold et al.

Leibold *et al.* (2007) obtained loudness matching data consistent with the classic experiment by Zwicker *et al.* (1957) demonstrating that the loudness of the multitone complex was independent of bandwidth when components were within a critical band, but that the loudness of the complex increased as bandwidth increased beyond the critical band. The Moore *et al.* (1997) loudness model predicts a pattern of results consistent with the observed data and, also similar to the data, predicts no decrease in loudness growth with increasing bandwidth at the larger bandwidths. That is, the model assumes partial masking across several critical bands before conversion to loudness, with reduction in partial masking leading to increased loudness.

Leibold *et al.* examined mean perceptual weight as a function of component position for each bandwidth. The range of weights increased with increasing frequency spacing, with more weight assigned to the lowest and highest frequency components. Estimates of perceptual weight provided by the loudness model were largely in agreement with observed weights, except for the widest spacing condition. The discrepancy between the data and model in that condition suggests that central processes contribute to how subjects assign loudness judgments when components are widely spaced.

To determine the contribution of partial masking to loudness, Leibold *et al.* obtained mean masked thresholds for each component in the presence of the other four components for each spacing condition. Thresholds varied little across components for the two narrowest conditions, but the range of thresholds increased with increasing frequency spacing. Masked thresholds predicted by the loudness model were in good agreement with the data at all but the widest spacing condition, where the model predicted less masking than was observed.

Leibold *et al.* observed a strong correlation between masked threshold and weight for the two narrowest bandwidth conditions (46 and 92 Hz) and for the two intermediate conditions

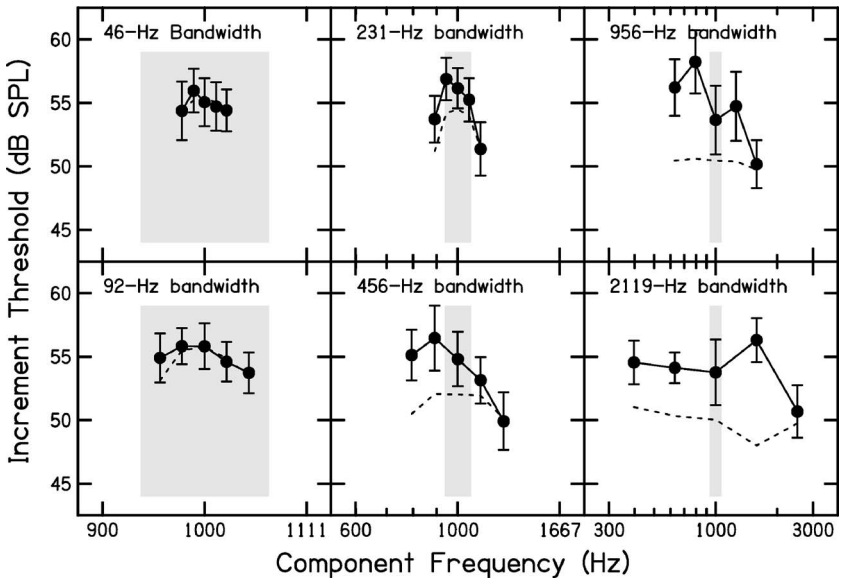

Fig. 1. Average increment thresholds for individual components across subjects for each frequency-spacing condition.

(231 and 456 Hz) for both the data and the model. In contrast, the correlation was not significant between weights and masked thresholds for the widest two conditions (956 and 2119 Hz).

3.2 Intensity discrimination for individual components

For the widest bandwidth condition, Leibold *et al.* observed a lack of agreement between the observed and predicted perceptual weight associated with individual components, between observed and predicted thresholds for individual components, and between thresholds and weights. A potential explanation for the discrepancy between the observed data and the model is that all components were too far above threshold in this condition for differences in threshold to have an effect on the weight associated with individual components or on the contribution of those components to loudness. The purpose of measuring the just-noticeable-difference (jnd) for intensity discrimination for each component was to obtain a threshold measure at the level of the components used in the loudness judgment task.

The closed circles in Fig. 1 show the mean threshold as a function of component position for each bandwidth, reported as the level of the added tone producing the intensity increment. Error bars are ±1 S.E. around the mean across subjects. The data are reported as increment thresholds because conversion to other standard measures of intensity discrimination, $10 \log (\Delta I/I)$ or $(10 \log(1+\Delta I/I))$, would require an assumption regarding the level of the standard or pedestal. Should we assume that the subjects are detecting an increment in a single component or an increment in the total complex? At the two narrowest bandwidths, where all components fall within a critical band, it is reasonable to assume that the standard is 60 dB SPL, the level of the total complex, but the appropriate assumption regarding the level of the standard becomes less clear as the bandwidth increases. By reporting increment thresholds, the need to assume a level of the standard is avoided and the data are presented in units comparable to the masked thresholds reported by Leibold *et al.* (2007). There was little overall improvement in the average increment threshold across the five components as bandwidth increased. This suggests that the subjects were unable to process the components individually in the broad bandwidth conditions, but yet performance varied as a function of component position even at the narrowest bandwidth. At broader bandwidths, performance was better for the highest than for the lowest frequency component.

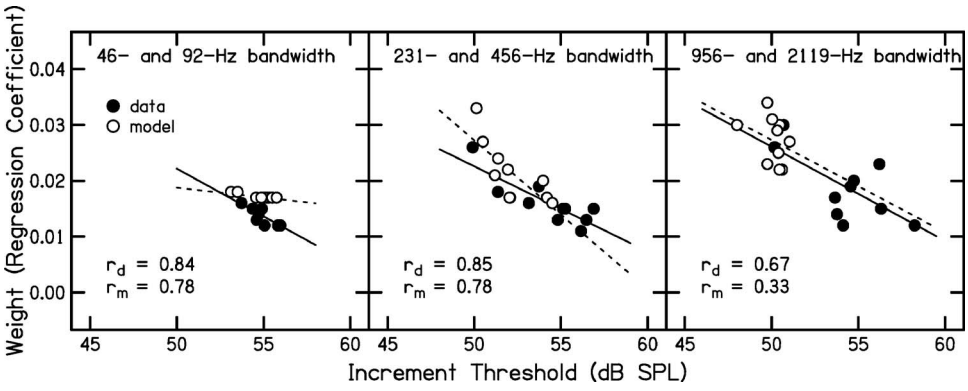

Fig. 2. Average weight as a function of increment threshold for individual components across six subjects.

Estimates of increment threshold provided by the loudness model are shown by the dashed lines in each panel. These were obtained by treating the five-tone complex as a masker and the increment tone as a signal and assuming that the partial loudness of the signal at threshold is 8 phons. This higher criterion was chosen because it resulted in equal increment thresholds for the model and the data across the five components in the narrowest bandwidth condition. The model predicts differences in increment thresholds as a function of component position that parallel the data for the three narrowest bandwidths. The model deviates from the data in predicting an orderly improvement in performance with increasing bandwidth and comparable performance for the highest and lowest frequency components.

The relation between increment threshold and weight is shown in Fig. 2. A strong correlation was found for the two narrowest bandwidth conditions (46 and 92 Hz) and for the two intermediate conditions (231 and 456 Hz). The results are similar for the model and the data. These results are comparable to the strong correlations observed for the two narrowest and two intermediate conditions in the previous study (Leibold *et al.*, 2007). In contrast, the correlation was not significant between weights and increment thresholds for the widest two conditions (956 and 2119 Hz). Note also that Leibold *et al.* reported no significant correlation between weights and masked thresholds at the widest bandwidth.

The results in Fig. 1 indicate that intensity discrimination for high and low frequency components differs by more than the model would predict at broader bandwidths. There may be a connection between this pattern of results and the increased perceptual weight associated with higher frequency components at broader bandwidths in the loudness matching task used by Leibold *et al.* The connection is not apparent, however, in Fig. 2.

The subjects' task in this experiment, detection of an increment in one tone of a multitone complex, is comparable to profile analysis (e.g., Green, 1988), but without an overall rove in level between observation intervals. Profile-analysis data generally indicate better performance for detection of an increment in the center tone of the complex than for detection of an increment in the highest or lowest tone (Green, 1988; Green and Mason, 1985). There is also an improvement with increasing bandwidth (Green *et al.*, 1984). Neither effect was apparent in the data. Although the model predicts smaller jnds with increasing bandwidth, it predicts better detection of an increment in the highest or lowest component than of an increment at the center of the complex.

4. Conclusion

The Moore *et al.* (1997) loudness model provides a good account of the increased loudness of multitone patterns with increasing bandwidth and of the perceptual weights and masked thresholds of individual components, except at the widest bandwidth. The model also provides a good account of intensity discrimination for individual components for the three narrower band-

widths, but fails to predict results at wider bandwidths. Efforts to relate differences in perceptual weight at the wider bandwidths to differences in intensity discrimination for individual components were unsuccessful.

Acknowledgments

This work was supported by funding from the NIH (R01 DC006648 and T32 DC00013). This work benefited from discussions with Douglas Keefe and Emily Buss as well as from helpful comments by Rhona Hellman and Keith Wilson.

References and links

[1]These data as well as data contained in the Leibold *et al.* (2007) published paper were presented at the 152nd Meeting of the Acoustical Society of America in Honolulu, HI. Previously unpublished intensity discrimination data were emphasized here to avoid duplication with the Leibold *et al.* (2007) paper.

Green, D. M. (**1988**). *Profile Analysis* (Oxford University Press, New York).
Green, D. M., and Mason, C. R. (**1985**). "Auditory profile analysis: Frequency, phase, and Weber's law," J. Acoust. Soc. Am. **77**, 1155–1161.
Green, D. M., Mason, C. R., and Kidd, G., Jr. (**1984**). "Profile analysis: Critical bands and duration," J. Acoust. Soc. Am. **75**, 1163–1167.
Leibold, L. J., Tan, H., Khaddam, S., and Jesteadt, W. (**2007**). "Contributions of individual components to the overall loudness of a multi-tone complex," J. Acoust. Soc. Am. **121**, 2822–2831.
Levitt, H. (**1971**). "Transformed up-down methods in psychoacoustics," J. Acoust. Soc. Am. **49**, 467–477.
Moore, B. C. J., Glasberg, B. R., and Baer, T. (**1997**). "A model for the prediction of thresholds, loudness, and partial loudness," J. Audio Eng. Soc. **45**, 224–237.
Viemeister, N. F., and Bacon, S. P. (**1988**). "Intensity discrimination, increment detection, and magnitude estimation for 1-kHz tones," J. Acoust. Soc. Am. **84**, 172–178.
Zwicker, E., Flottorp, G., and Stevens, S. S. (**1957**). "Critical bandwidth in loudness summation," J. Acoust. Soc. Am. **29**, 548–557.
Zwicker, E., and Scharf, B. (**1965**). "A model of loudness summation," Psychol. Rev. **72**, 3–26.

An introduction to induced loudness reduction

Michael Epstein
Auditory Modeling and Processing Laboratory, Department of Speech-Language Pathology and Audiology (106A FR), Communications and Digital Signal Processing Center, ECE Department, Northeastern University, 360 Huntington Avenue, Boston, Massachusetts 02115
m.epstein@neu.edu

Abstract: Induced loudness reduction (ILR) is a phenomenon by which a preceding higher-level tone (an inducer tone) reduces the loudness of a lower-level tone (a test tone). The strength of this effect depends on a number of parameters, reviewed here. Some of the implications of ILR on loudness data are presented via the analysis of several studies in which ILR likely resulted in otherwise unexplained biases in data sets. These results serve as examples of the pervasiveness of ILR in loudness measurements and indicate that it is necessary to consider ILR when designing any psychoacoustical experiment in which level varies.

PACS numbers: 43.66.Cb, 43.66.Mk [DKW]
Date Received: March 26, 2007

1. Introduction

Induced loudness reduction (ILR), previously called loudness recalibration (Mapes-Riordan and Yost, 1997; Marks, 1994; Mapes-Riordan and Yost, 1999; Arieh and Marks, 2001) or identified as a "slippery-context" effect (Marks, 1992), is a phenomenon by which the loudness of a sound is reduced when it is preceded by a higher-intensity sound (inducer) at a close frequency with an equal or longer duration. The amount of ILR depends on several factors including (1) tone levels (Mapes-Riordan and Yost, 1999); (2) frequency separation between inducer and test tones (Marks, 1994); (3) durations of inducer and test tones (Nieder *et al.*, 2003); (4) time separation between inducer and test tones (Arieh and Marks, 2003); (5) number of exposures to inducers (Arieh *et al.*, 2005); and (6) individual differences (Epstein and Gifford, 2006; Wagner and Scharf, 2006).

The purpose of the present letter is to introduce the reader to ILR, provide some insight into the pervasiveness of the effect, and remind experimenters that ILR must be considered during the experimental design phase for any methodology that includes sounds that vary in level. Perhaps the most important reason for the study of ILR is that the results of nearly all loudness experiments are affected by ILR. Many times, discrepancies between data sets have been attributed to procedural or instructional biases; in fact, many of these discrepancies can likely be explained by ILR.

Additionally, there is some evidence that ILR may be closely tied to earlier discovered loudness phenomena such as loudness enhancement and loudness decrement (Arieh and Marks, 2003; Scharf *et al.*, 2002; Oberfeld, 2007). The present letter, however, will focus primarily on ILR.

2. How is ILR measured?

Although some studies have used direct magnitude estimation to assess ILR (e.g., Wagner and Scharf, 2006), loudness matching is the most common procedure. Loudness matches are made between two sounds, one that is affected by ILR and the other carefully selected to avoid the effects of ILR. Typically, such studies have used tones of two different frequencies, often 500 and 2500 Hz. These frequencies were selected to be far enough apart that interactions could be avoided [at least 4 critical bands according to Marozeau *et al.* (2006)], but not so far apart as to result in great differences in cochlear processing or loudness growth (Suzuki and Takeshima, 2004).

The listener first performs a "baseline" match in which one tone (test tone)—typically presented at the frequency that will be affected by ILR in the subsequent "experimental" condition—is fixed in level and the other tone is varied (comparison tone) until the two tones are judged to be equally loud. After the baseline condition is completed, a similar loudness match is made in the experimental condition, which differs only by the inclusion of a high-level tone (inducer tone), usually presented at the same frequency as the test tone. General ILR experiments commonly use inducers at 80–90 dB SPL and test tones at 60–70 dB SPL as it appears that maximal ILR occurs under these conditions (Mapes-Riordan and Yost, 1999; Nieder *et al.*, 2003). The amount of ILR is defined as the final level of the comparison tone in the baseline minus the final level of the comparison tone in the experimental condition. This is based on the assumptions that the test tone is only affected by the inducer tone in the experimental condition and that the comparison tone is unaffected by ILR in either condition. In fact, if the conditions are run close together in time, the comparison tone in the baseline condition can cause ILR on the comparison tone in the experimental condition (Epstein and Gifford, 2006). Additionally, if the comparison tone begins at a level that is higher than the expected matching level, as is common in many matching procedures, it is possible that those high-level presentations may cause unintended ILR on subsequent presentations of the comparison tone.

3. ILR Studies

3.1 The effect of level

Mapes-Riordan and Yost (1999) found that an 80 dB SPL inducer caused maximal ILR on 60–70 dB SPL test tones (about 11 dB of ILR). They also found less than 5 dB of ILR for 40 and 80 dB SPL test tones and virtually no effect on threshold. These findings indicate that ILR caused by higher-level tones is maximal for tones lower, but relatively close in level. That is, high-level sounds seem to cause maximal ILR on moderate level sounds, but little ILR on very low level sounds.

It is somewhat puzzling that an 80 dB SPL inducer was found to cause some ILR on an 80 dB SPL test tone. Further examination of the procedure used in Mapes-Riordan and Yost (1999) and many other loudness-matching studies (e.g., Arieh *et al.*, 2005; Arieh and Marks, 2003; Nieder *et al.*, 2003) reveals that the starting level of the comparison tone may have been high enough to cause unintended ILR on the final loudness matches. It is possible that studies using this procedure may overestimate the amount of ILR by several decibels. This possibility requires careful further examination, but is supported by the lower overall ILR (about 8 dB) found in studies using modified procedures (Epstein and Gifford, 2006; Wagner and Scharf, 2006).

3.2 The effect of frequency

Wagner and Scharf (2006) found that ILR is fairly constant across the frequencies 0.5–8 kHz when the inducer and test tone are at the same frequency. This supports the idea that ILR is a pervasive effect and not just something that occurs within a very limited bandwidth.

Marozeau *et al.* (2006) found that an inducer at a fixed frequency caused maximal ILR at and near that frequency, but also caused significant ILR at surrounding frequencies, similar in nature to excitation patterns (Moore and Glasberg, 1987; Zwicker and Fastl, 1990). The effects were significant as far away as 4 critical bands toward higher frequencies.

3.3 The effect of duration

Nieder *et al.* (2003) found that 200 ms inducers cause as much ILR on 5 ms test tones as 5 ms inducers. However, 5 ms inducers cause less ILR on 200 ms test tones than 200 ms inducers. Additionally, a 500 ms inducer causes the same amount of ILR on a 200 ms test tone as a 200 ms inducer. These findings indicate that it is likely that ILR is maximized when the inducer is at least as long as the test tone.

3.4 The effect of time separation

Arieh and Marks (2003) examined the effect of the interval between the inducer and the test tone. They presented trials that contained an inducer (recalibrating tone), a variable interval, a test tone (target tone), a 1 s interval, and finally a comparison tone. As the duration of the variable interval increased, the amount of ILR increased. This relationship begins to asymptote at a variable interval of about 500 ms, but may continue even beyond the duration examined (3.3 s). The increase in ILR with the increase in length of the variable interval is inconsistent with the idea that ILR is a relatively long-lasting effect with a slow recovery time (Epstein and Gifford, 2006; Wagner and Scharf, 2006). Thus, it is possible that the increase in ILR with increasing length of variable interval is actually a decreasing amount of loudness enhancement overlaid upon a constant quantity of ILR. These two phenomena are, however, quite difficult to unravel experimentally. Scharf *et al.*(2002) and Oberfeld (2007) further discuss the intertwinement of ILR and loudness enhancement.

3.5 Recovery time and the effect of exposure

Upon the onset of an inducer, ILR begins rapidly (Epstein and Gifford, 2006; Mapes-Riordan and Yost, 1999). There does, however, appear to be some accumulation of effect over increased exposure (Arieh *et al.*, 2005; Wagner and Scharf, 2006). For a small number of inducers, recovery was reported by Arieh *et al.* (2005) to take anywhere from 70 s for 5 inducer exposures to about 2 min for 40 inducer exposures. Other studies with greater exposures report far longer for recovery. Mapes-Riordan and Yost (1998) suggested that recovery in some cases could take as long as 20 min. Epstein and Gifford (2006) found that recovery for most subjects was completed in under 10 min, but suggested that as long as 15 min might be necessary in some individuals after a large number of exposures.

3.6 Individual differences

The consistent presence of differences across listeners in the amount of ILR indicates that the variability is not likely to be a result of experimental variance, but rather a true reflection of the individual differences. Although most studies do not report individual results, some examples of ranges are: Wagner and Scharf (2006), −1.0–13.6 dB, and Epstein and Gifford (2006), 2.38–12.81 dB.

4. ILR and psychophysical procedures

Although ILR may seem like an esoteric effect, in fact, it is essential to consider the possible role ILR may play when making any loudness measurements using a procedure in which level varies. These examples are not special, rare cases, but rather very common cases that will arise in the measurement of any loudness-related phenomena at moderate and high levels.

4.1 ILR and trial repetition

Figure 6 from Hellman and Zwislocki (1963) shows three magnitude estimates for each test level from 5 dB–90 dB SL for a single listener. Although the first estimates are greater than the second and third estimates at all levels, there is a particularly marked difference between the first and later estimates from 50–70 dB SL. A second listener [see Fig. 7 from Hellman and Zwislocki (1963)] shows a similar pattern from 40–60 dB SL. The shape of this pattern indicates clearly that as sound exposure increases, the loudnesses of moderate sounds change more than the loudnesses of higher- and lower-level sounds. In order to clearly illustrate this effect, Fig. 1 here shows the mean of the ratios between the first and second trials and the first and third trials at each level for the listener shown in Fig. 6 of Hellman and Zwislocki (1963). When the ratio is greater than one, as it is for all levels, the loudness estimate decreased as the experiment progressed (i.e., the estimate of loudness was greater on the first trial than it was on later trials). With respect to ILR, it is most important to examine the change in ratio as a function of level. The mean ratio from 50–70 dB SL is greater than 3. At all other levels, this ratio is between 1.5 and 2.5. This relationship between level and ratio is consistent with the pattern of ILR observed

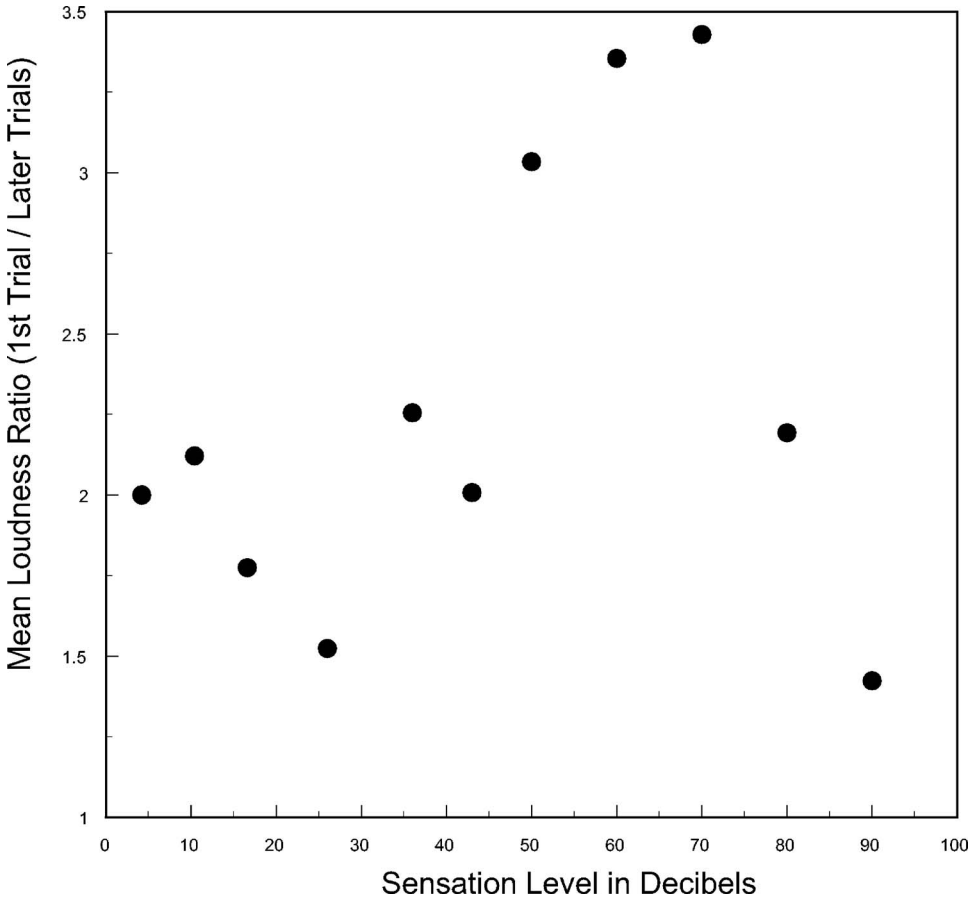

Fig. 1. The mean loudness ratio between the first and second and first and third magnitude estimation trials for the single listener shown in Fig. 6 of Hellman and Zwislocki (1963) as a function of sensation level.

by Mapes-Riordan and Yost (1999), lending support to the idea that at least some of the variation in the magnitude estimates across repetition was likely to have resulted from ILR.

4.2 ILR and frequency

In Experiment 2 from Marks and Warner (1991), tones of two frequencies were presented within a block. The lower levels (30–65 dB SPL) were presented at one frequency and the higher levels (50–85 dB SPL) at a second frequency. Tones of both frequencies were presented in an overlapping range from 50–65 dB SPL. In condition A [see Fig. 2 of Marks and Warner (1991)], the two frequencies were 1002 and 1248 Hz. When the higher-level tones were presented at 1002 Hz, the 1002 Hz tones were judged as slightly louder than the 1248 Hz tones for the same SPL at the overlapping levels. In the second case, when the higher-level tones were presented at 1248 Hz, the 1002 Hz tones were judged about the same as (or very slightly louder than) the 1248 Hz tones for the same SPL at the overlapping levels. In contrast, in condition C [see Fig. 2 of Marks and Warner (1991)], in which the frequencies were 800 and 1560 Hz, the frequency presented at higher levels was always less loud than the low-level frequency for the same SPL at the overlapping levels. (That is, when the 800 Hz tone was presented at high levels, the 1560 Hz tone was judged louder for the same SPL; when the 1560 Hz tone was presented at high levels, the 800 Hz tone was judged louder for the same SPL.) In condition A, both sets of

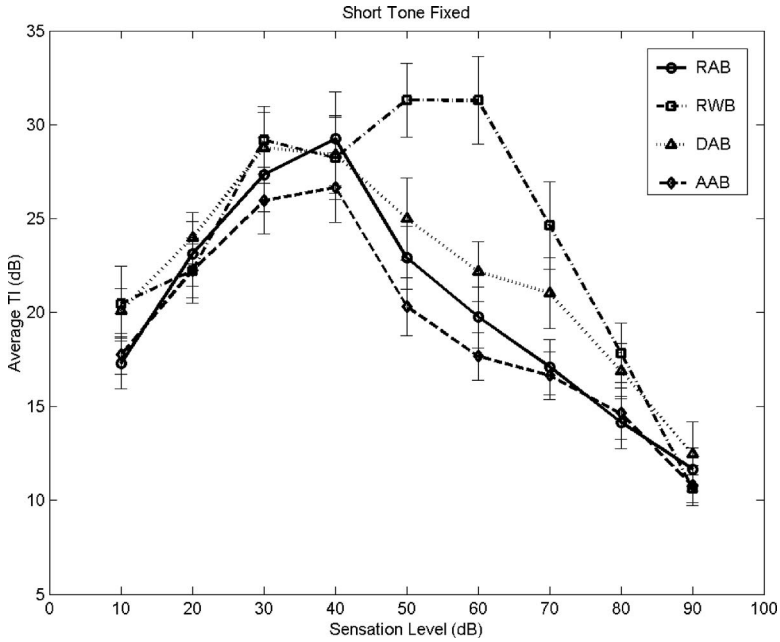

Fig. 2. Data replotted from panel 1 of Fig. 4 of Silva and Florentine (2006). The average amount of temporal integration as a function of sensation level for six listeners measured using four test paradigms: random across blocks (RAB), ascending across blocks (AAB), descending across blocks (DAB), and random within blocks (RWB).

moderate-level tones were equally affected by ILR because the frequencies were close together. In condition C, primarily the moderate-level tones at the same frequency as the high-level tones were affected by ILR.

4.3 ILR and temporal integration

Silva and Florentine (2006) examined different procedures used for measuring temporal integration in an attempt to explain discrepancies seen across a number of studies. Temporal integration—the difference in level for equally loud short and long tones—is likely to increase as a result of sound exposure. Because high-level short sounds will cause ILR primarily only on short sounds and high-level long sounds will cause ILR on both short and long sounds, the short sounds in these experiments will be affected by ILR more than their longer counterparts (Nieder *et al.*, 2003). The result is that the difference in level for equally loud short and long sounds (i.e., the amount of temporal integration) will increase for moderate sound levels if the experimental paradigm results in ILR. In Fig. 2 [data from Fig. 4 of Silva and Florentine (2006)], amounts of temporal integration are shown for four experimental paradigms. Because presentation level is randomized from trial to trial, the random-within-block (RWB) paradigm is the condition in which exposure to high-level sounds followed by immediate exposure to moderate-level sounds is most likely to occur. In fact, the RWB results are quite consistently different from the other paradigms from 50–70 dB SL. The other three paradigms show some consistent differences in the resulting amount of temporal integration; however, they were not found to be statistically different from one another. See Silva and Florentine (2006) for further discussion.

5. Conclusion

Induced loudness reduction is a pervasive effect of debated origin and needs to be carefully considered during experimental design for any loudness experiment involving the presentation of a range of levels, particularly any experiment that groups moderate- and high-level presentations. In fact, ILR is likely to be the cause of much of the procedural variability attributed to a

number of unexplained or loosely explained biases. The elucidation of the effects of ILR also raises important questions regarding the "true" nature of the loudness function, particularly the shallow, compressive region seen at moderate levels, the origin of which is still in debate (Buus *et al.*, 1999; Epstein and Florentine, 2005; Ward *et al.*, 1996; Parker and Schneider, 1994; Schneider and Parker, 1990; Braida and Durlach, 1972; Florentine and Epstein, 2006). Therefore, loudness must not only be measured and modeled by controlling stimulus parameters, but also by context parameters. Additionally, the physiological mechanisms of ILR are still up for debate, but several hypotheses have been put forth, including efferent-system involvement [see Nieder *et al.*, (2003) for further discussion] and top-down gain control (Parker and Schneider, 1994). Recent measures of the effects of a contralateral inducer indicate that, at a minimum, there is a partial central effect (Nieder *et al.*, 2007). Without further examination to find the physiological causes of ILR, it is difficult to assign to a specific region or mechanism within the auditory system.

Acknowledgment

The author would like to thank Mary Florentine for collaboration on the original presentation of this material and Jeremy Marozeau for his suggestions, particularly the inclusion of the effects of ILR in Hellman and Zwislocki (1963). The author would also like to thank editors Rhona Hellman and Yôiti Suzuki and two anonymous reviewers for their suggestions. This research was supported by NIH/NIDCD Grant No. R01DC02241.

References and links

Arieh, Y., Kelly, K., and Marks, L. E. (**2005**). "Tracking the time to recovery after induced loudness reduction (L)," J. Acoust. Soc. Am. **117**, 3381–3384.
Arieh, Y., and Marks, L. E. (**2001**). "Recalibration of loudness: Sensory vs. decisional processes," in *Fechner Day 2001*, edited by E. Sommerfeld, R. Kompass, and T. Lachmann (Pabst, Berlin).
Arieh, Y., and Marks, L. E. (**2003**). "Time course of loudness recalibration: Implications for loudness enhancement," J. Acoust. Soc. Am. **114**, 1550–1556.
Braida, L. D., and Durlach, N. I. (**1972**). "Intensity perception. II. Resolution in one-interval paradigms," J. Acoust. Soc. Am. **51**, 483–502.
Buus, S., Florentine, M., Poulsen, T., and Müsch, H. (**1999**). "On the relation between peripheral compression and the growth of loudness," J. Acoust. Soc. Am. **105**, 1022.
Epstein, M., and Florentine, M. (**2005**). "A test of the equal-loudness-ratio hypothesis using cross-modality matching functions," J. Acoust. Soc. Am. **118**, 907–913.
Epstein, M., and Gifford, E. (**2006**). "A potential carry-over effect in the measurement of induced loudness reduction," J. Acoust. Soc. Am. **120**, 305–309.
Florentine, M., and Epstein, M. (**2006**). "To honor Stevens and repeal his law (for the auditory system)," in *Fechner Day*, edited by D. E. Kornbrot, R. M. Msetfi, and A. W. MacRae (International Society for Psychophysics, St. Albans, UK).
Hellman, R. P., and Zwislocki, J. J. (**1963**). "Monaural loudness function at 1000 cps and interaural summation," J. Acoust. Soc. Am. **35**, 856–865.
Mapes-Riordan, D., and Yost, W. A. (**1997**). "Loudness recalibration as a function of recalibration and comparison tone level," J. Acoust. Soc. Am. **101**, 3170.
Mapes-Riordan, D., and Yost, W. A. (**1998**). "Temporal properties of loudness recalibration," Proc. 16th International Congress on Acoustics, Seattle, WA, pp. 2361–2362.
Mapes-Riordan, D., and Yost, W. A. (**1999**). "Loudness recalibration as a function of level," J. Acoust. Soc. Am. **106**, 3506–3511.
Marks, L. E. (**1992**). "The slippery context effect in psychophysics: Intensive, extensive, and qualitative continua," Percept. Psychophys. **51**, 187–198.
Marks, L. E. (**1994**). "'Recalibrating' the auditory system: The perception of loudness," J. Exp. Psychol. Hum. Percept. Perform. **20**, 382–396.
Marks, L. E., and Warner, E. (**1991**). "Slippery context effect and critical bands," J. Exp. Psychol. Hum. Percept. Perform. **17**, 986–996.
Marozeau, J., Epstein, M., Florentine, M., and Ioffe, S. (**2006**). "Loudness reduction caused by a tone at a different frequency," American Speech-Language-Hearing Association (ASHA), Miami, FL.
Moore, B. C., and Glasberg, B. R. (**1987**). "Formulae describing frequency selectivity as a function of frequency and level, and their use in calculating excitation patterns," Hear. Res. **28**, 209–225.
Nieder, B., Buus, S., Cazals, Y., and Scharf, B. (**2007**). "Loudness reduction induced by a contralateral tone," J. Acoust. Soc. Am. **122**, 35–37.
Nieder, B., Buus, S., Florentine, M., and Scharf, B. (**2003**). "Interactions between test- and inducer-tone durations in induced loudness reduction," J. Acoust. Soc. Am. **114**, 2846–2855.

Oberfeld, D. (**2007**). "Loudness changes induced by a proximal sound: Loudness enhancement, loudness recalibration, or both?," J. Acoust. Soc. Am. **121**, 2137–2148.
Parker, S., and Schneider, B. (**1994**). "The stimulus range effect: Evidence for top-down control of sensory intensity in audition," Percept. Psychophys. **56**, 1–11.
Scharf, B., Buus, S., and Nieder, B. (**2002**). "Loudness enhancement: Induced loudness reduction in disguise? (L)," J. Acoust. Soc. Am. **112**, 807–810.
Schneider, B., and Parker, S. (**1990**). "Does stimulus context affect loudness or only loudness judgments," Percept. Psychophys. **48**, 409–418.
Silva, I., and Florentine, M. (**2006**). "Effect of adaptive psychophysical procedure on loudness matches," J. Acoust. Soc. Am. **120**, 2124–2131.
Suzuki, Y., and Takeshima, H. (**2004**). "Equal-loudness-level contours for pure tones," J. Acoust. Soc. Am. **116**, 918–933.
Wagner, E., and Scharf, B. (**2006**). "Induced loudness reduction as a function of exposure time and signal frequency," J. Acoust. Soc. Am. **119**, 1012–1020.
Ward, L. M., Armstrong, J., and Golestani, N. (**1996**). "Intensity resolution and subjective magnitude in psychophysical scaling," Percept. Psychophys. **58**, 793–801.
Zwicker, E., and Fastl, H. (**1990**). *Psychoacoustics—Facts and Models* (Springer, Berlin).

Loudness growth in individual listeners with hearing losses: A review[a)]

Jeremy Marozeau[b)] and Mary Florentine
Communication Research Laboratory, Department of Speech-Language Pathology and Audiology (106A FR) and Institute for Hearing, Speech, & Language, Northeastern University, 360 Huntington Avenue, Boston, Massachusetts 02115
j.marozeau@neu.edu,florentine@neu.edu

Abstract: This letter reanalyzes data from the literature in order to test two loudness-growth models for listeners with hearing losses of primarily cochlear origin: rapid growth and softness imperception. Five different studies using different methods to obtain individual loudness functions were used: absolute magnitude estimation, cross-modality matching with string length, categorical loudness scaling, loudness functions derived from binaural loudness summation, and loudness functions derived from spectral summation of loudness. Results from each of the methods show large individual differences. Individual loudness-growth functions encompass a wide range of shapes from rapid growth to softness imperception.

PACS numbers: 43.66.Cb, 43.66.Ba, 43.66.Sr [DKW]
Date Received: March 15, 2007 **Date Accepted:** May 21, 2007

1. Introduction

Research indicates that there are large individual differences in how loudness grows with increasing sound pressure level for listeners with sensorineural hearing losses of primarily cochlear origin (Dix *et al.*, 1948; Knight and Margolis, 1984; Hellman and Meiselman, 1990; Brand and Hohmann, 2001; Buus and Florentine, 2002; Whilby *et al.*, 2006). In fact, listeners with similar audiograms can have different loudness-growth functions (Hellman, 1994; Florentine *et al.*, 1997). The purpose of this review is twofold: to review individual loudness functions from hearing-impaired listeners (HIL) that have been obtained by various researchers using a variety of methods and to test models of loudness growth for HIL.

Four types (or models) of common loudness-growth functions have been proposed: typical, attenuation, rapid growth, and softness imperception (Florentine, 2004). Typical is the loudness function for normal-hearing listeners (NHL), and is widely known as the power law (Stevens, 1955). It states that loudness is related to the intensity raised to the power 0.3. Although widely cited, the power law is inaccurate in its details at threshold (Richardson and Ross, 1930; Hellman and Zwislocki, 1961) and at moderate levels (Florentine *et al.*, 1996). Buus and Florentine (2001) integrated these modifications and proposed an inflected exponential function (INEX function), which is shown in Fig. 1(a). The slope of the INEX function, shown in Fig. 1(b), is steeper than the power function at low levels and shallower at moderate levels. In addition, loudness at threshold is greater than zero. [For a review, see Florentine and Epstein (2006).]

Of the three common types of loudness growth for HIL, the attenuation type applies to conductive hearing loss and is parallel to the normal loudness function on a logarithmic scale. The rapid-growth type (the same as the classical view of recruitment) described the loudness growth as follows: (1) loudness at threshold is the same for NHL and HIL, (2) loudness from threshold to midlevels of HIL grows more rapidly than for NHL,[1] and (3) loudness is the same

[a)]This work was presented at the Fourth Joint Meeting of the Acoustical Society of America and the Acoustical Society of Japan.
[b)]j.marozeau@neu.edu

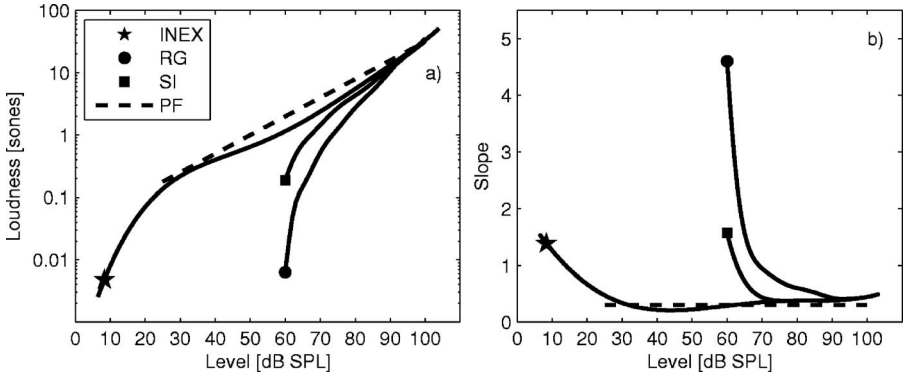

Fig. 1. Comparison of the loudness-growth models: power function (dashed line), INEX function (star); rapid growth (circle), and softness imperception (square). (a) Loudness in sones is plotted as function of sound pressure level. (b) Slopes of the functions shown in (a) are plotted as function of sound pressure level.

or approaches that of NHL at high levels (for a review see Brunt, 1994; Moore, 2003). A typical rapid-growth type of function is shown in Fig. 1(a) by the line identified by a circle. For comparison, the INEX function is represented in the same plot by a line identified by a star. Loudness at threshold is equivalent for both functions. In order to match up with the INEX function at high levels, the rapid growth loudness function must have a very steep slope at and near threshold, as well as at midlevels [see Fig. 1(b)]. The final type of loudness growth is softness imperception, so named because it refers to the inability of the listener to hear soft sounds. This model described loudness growth as follows: (1) loudness at threshold is higher for HIL than NHL, (2) loudness growth at and near threshold is similar for NHL and HIL, (3) the loudness of some HIL exhibits a loss of compression at midlevels that results in faster-than-normal loudness growth, and (4) the loudness-growth function approaches that of NHL at higher levels. A softness imperception type of loudness function is shown in Fig. 1(a) by the line identified by a square.

Because slopes of loudness-growth functions change with level and are essential to a basic understanding of loudness growth, the same data plotted in Fig. 1(a) are plotted with slope on the ordinate in Fig. 1(b). The slope of the softness imperception function starts at the same rate as the INEX function, whereas the rapid growth function starts with a steeper slope than the INEX function. All the functions approach the same slope at high levels.

The rapid loudness growth type is the most well known model. It is well accepted in the audiology community and presented in textbooks as the only model for HIL with sensorineural hearing loss of primarily cochlear origin. The recently proposed softness imperception model is still controversial. Moore (2004) tested the concept of softness imperception by asking four asymmetrical HIL to match the loudness of low SL pure tone across ears. He expected that for HIL with softness imperception, the SL of the tone in the normal ear will be significantly greater than the SL of an equally loud tone in the impaired ear near threshold. Results showed no differences in SL and, therefore, claimed to refute softness imperception. However, asymmetrical HIL have significantly steeper loudness functions than symmetrical HIL (Knight and Margolis, 1984); therefore, this conclusion should be restricted to this specific type of HIL. Buus and Florentine (2002) derived loudness at threshold from loudness matches between pure tones and four-tone complex. Their data indicate that loudness at threshold increases with hearing loss in at least some HILs, supporting the concept of softness imperception. However, according to Moore and Glasberg (2004) the same data can be fitted with a loudness model based on the idea that loudness at threshold is independent of hearing loss. In summary, it may be that neither of the two models correctly describes loudness-growth functions of all HIL. Some listeners may show rapid growth, some softness imperception, and some an intermediate behavior. In order to test these hypotheses, data from five different studies using five different methods to

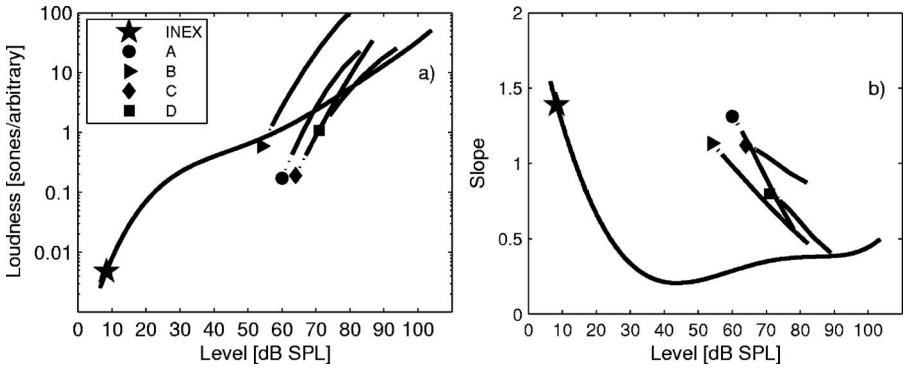

Fig. 2. (a) Individual data of four hearing-impaired listeners (see the inset) from Hellman and Meiselman (1990) are replotted compared with the INEX function in the same manner as Fig. 1(a). (b) Slopes of the loudness functions in (a) are plotted in the same manner as Fig. 1(b).

obtain individual loudness functions for HIL are compared to the models. The loudness function of a listener showing rapid growth should exhibit a steeper slope at and near threshold. A listener showing softness imperception should exhibit a loudness function similar to NHL at low levels, and loss of compression may result in a faster than normal loudness growth at moderate levels.

2. Methods

Data from five studies were reanalyzed. For three studies (cited later in Secs. 3.1, 3.3, and 3.5), the data were not directly accessible. Therefore, the data were extracted from the published figures using the software DATATHIEF (v1.0). The data were then fit with a six-order polynomial in order to reduce the extraction error. For two studies (cited later in Secs. 3.2 and 3.4) the data were directly accessible. The five studies were selected because they used different methods and they showed individual data. From each of these studies four individual listeners were selected to represent the range of responses, then their individual loudness functions were compared with averaged normal data from that study (i.e., the reference for the typical model). A symbol represents the loudness at threshold of each of the HIL in all of the following plots. If not measured, the loudness at threshold was extrapolated from the threshold SPL and the slope of the loudness function at the lowest levels measured. Extrapolated loudness functions are represented in the figures by a dashed line. The slope of every function was calculated from their derivative of the logarithm [slope$=d(\log(\text{loudness}))/d(\text{level})$].

3. Studies

3.1 Absolute magnitude estimation

Hellman and Meiselman (1990) comprehensively studied the loudness growth of 100 HIL. This review presents the data of only four representative HIL performing magnitude estimation. They were asked to judge the loudness of 1-s tones with a number. Frequencies varied from 500 to 4000 Hz. Figure 2(a) shows the results of the four typical listeners. For comparison, the INEX function is represented by a line identified by a star. The data show that there are individual differences. Figure 2(b) shows the slopes of these functions. For all listeners, the loudness growth at threshold is the same or shallower than the INEX function.

3.2 Cross-modality matching with string length

Marozeau and Florentine (unpublished) asked eight HIL to judge the loudness of 200–ms monaural and binaural tones by cutting a piece of string as long as the sound was loud. [The same procedure was used with NHL in Marozeau *et al.* (2006)]. The tones were either 1 or 2 kHz. Figure 3(a) shows the results of four of their listeners and the average data of eight NHL (from

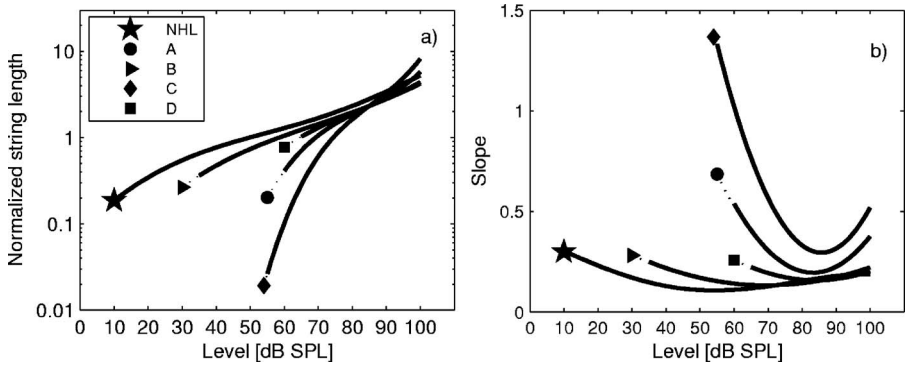

Fig. 3. (a), (b) Individual data of four hearing-impaired listeners from Marozeau and Florentine (unpublished) compared with the group average of eight NHL (Marozeau *et al.*, 2006) plotted in the same manner as Figs. 2(a) and 2(b).

Marozeau *et al.*, 2006). As expected, the slopes are shallower for the cross-modality method than for other methods [see Epstein and Florentine (2005)]. Figure 3(b) shows that listeners B and D share the same slope at threshold and high levels as NHL. Listener C shows a rapid growth of loudness at threshold and listener A shows an intermediate behavior.

3.3 Categorical loudness scaling

Brand and Hohmann (2001) asked eight NHL and eight HIL with different etiologies to rate the loudness of narrowband noises centered at 4 kHz on an 11-category scale, ranging from "very soft" to "very loud." Figure 4(a) shows the individual results in linear scale [as represented in Figs. 3 and 6 of Brand and Hohmann (2001)]. Figure 4(b) shows that listener BH has the same slope as NHL at threshold and high levels; listener BK shows a slope steeper than normal slope at threshold, and the same as normal at high levels; listener MI seems to show a loudness function parallel to the normal function as in the attenuation type of loss; and finally listener DD shows a constant, moderately steep slope at every SPL.

3.4 Binaural loudness summation

Whilby *et al.* (2006) asked eight HIL and eight NHL to adjust the level of a monaural tone to match the loudness of a binaural tone and vice versa. Stimuli were 200-ms 1-kHz tones. Individual loudness functions were extracted from these data. Figure 5(a) shows the individual results and the group average of NHL. Figure 5(b) shows that listener A has a loudness growth

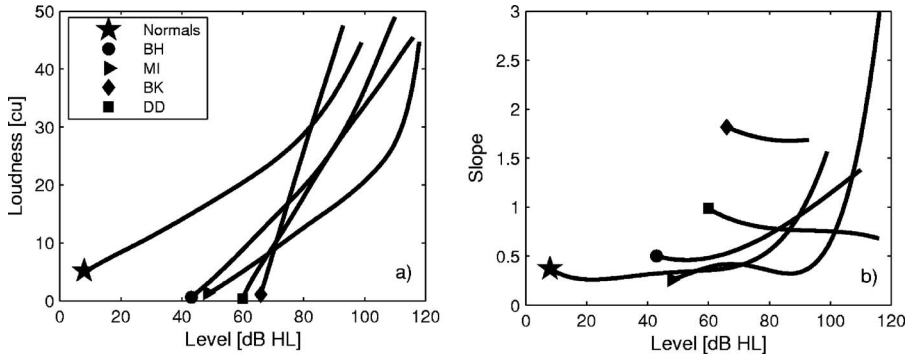

Fig. 4. (a), (b) Individual data of four hearing-impaired listeners from Brand and Hohmann (2001) compared with the group median of eight NHL from the same study plotted in the same manner as Figs. 2(a) and 2(b).

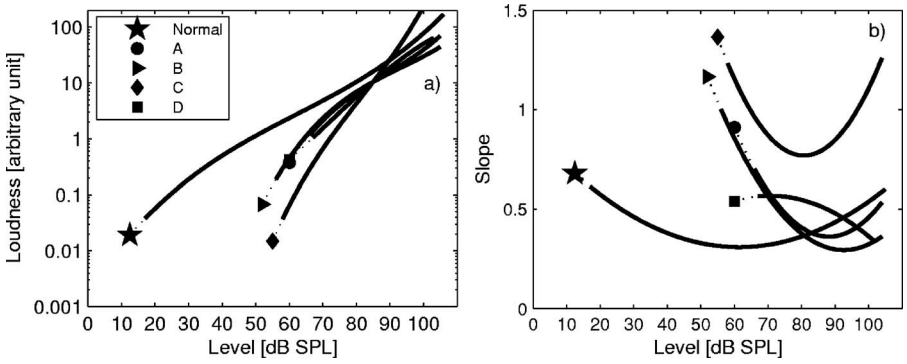

Fig. 5. (a), (b) Individual data of four hearing-impaired listeners from Whilby *et al.* (2006) compared with the group average of eight NHL from the same study plotted in the same manner as Figs. 2(a) and 2(b).

similar to NHL at threshold and high levels.[2] Listener B shows a steeper than normal slope at threshold and a slope similar at high levels. Listener C shows an overall steeper than normal slope. Listener D's function decreases with level.

3.5 Spectral integration of loudness

Buus and Florentine (2002) asked five hearing-impaired listeners to adjust the level of a 1600-Hz tone to match the level of a complex tone centered around that frequency and vice versa. The stimuli were 500 ms. They implemented a method to extract the slope of individual loudness functions from these data. This method allows estimation of the loudness function at and near threshold. Figure 6(a) shows the individual loudness functions and the INEX function. Figure 6(b) shows that loudness growth of all listeners at threshold is the same or shallower than the INEX function. At high levels, loudness growth is similar for both normal and impaired listeners.

4. Discussion

Four out of the five studies presented in this review show the average results from NHL. It is interesting that the loudness functions averaged over many NHL changed among the studies. This indicates that one should be careful when considering a loudness function out of context. It seems reasonable to state that a loudness function does not reflect only the "psychological" dimension of loudness, but this dimension transformed into a measurable quantity (number, classes, string length, etc.). Therefore, a loudness function should only be compared to another

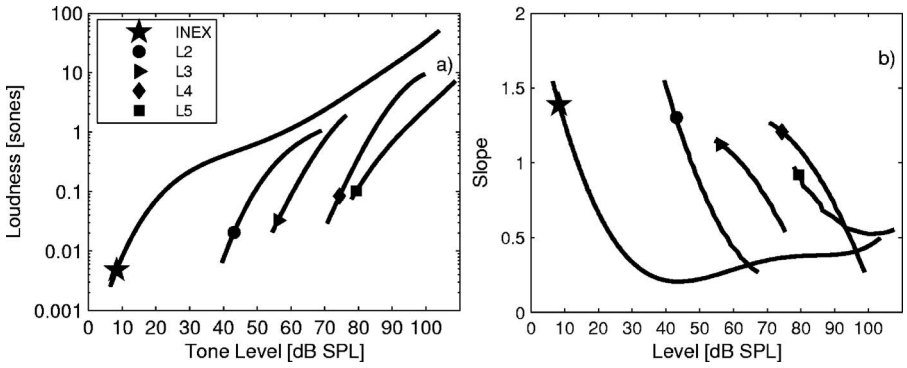

Fig. 6. (a), (b) Individual data of four hearing-impaired listeners from Buus and Florentine (2002) compared with the INEX function from the same paper plotted in the same manner as Figs. 2(a) and 2(b).

loudness function derived with the same method. Furthermore, because Hellman and Meiselman (1990) showed that slope distributions depend strongly on the procedure, it is important to consider this source of variance while analyzing the data. Results from NHL could help to estimate this procedural variability.

The data presented in this review from various published sources strongly indicate that there are large individual differences among the individual loudness functions of HIL. These important differences would be masked if the individual data were averaged. These substantial differences are present in all data sets using five different methods for obtaining loudness functions. The comparison between loudness growth of NHL and individual HIL at low levels shows which type of loudness function is most appropriate. Individual loudness functions range from the rapid growth to the recently described softness imperception. For example, listener C in study 2, listener BK in study 3, and listener C in study 4 can be modeled by rapid growth. Listener A in study 1, listener B in study 2, listener BH in study 3, and listener A in study 4 can be modeled by softness imperception. Listener A in study 2, listener DD in study 3, and listener C in study 4 cannot be modeled by either model in their present form.

These results dispel the notion that all listeners with sensorineural hearing losses of primarily cochlear origin perceive loudness in a similar way. This notion can be traced through the literature since the inception of the concept of recruitment. Textbooks that try to package and simplify information perpetuate this fallacy. Although it is useful to have conceptual models of loudness growth, it is essential that we do not allow one model to dominate our thinking. When one takes the time to examine loudness-growth functions of individual listeners, considerable variation can be found. The individual differences that are apparent in this review should be noted—and perhaps even treasured—because they are likely to reveal important mechanisms that contribute to loudness. These variations may be important for optimal rehabilitation of impaired listeners.

Whereas it is tempting to speculate what mechanisms contribute to the observable variations in loudness, it is not warranted because too little is known about the etiologies of the listeners. More data are needed from larger groups of listeners with well-diagnosed etiologies.

5. Conclusions

This review reviews five experiments using different methods to obtain individual loudness functions of hearing-impaired listeners. Results suggest that: (1) individual differences are more important for hearing-impaired listeners than for normal listeners, (2) some hearing-impaired listeners seem to show rapid growth, some softness imperception, and some a combination of both, and (3) averaging the results across hearing-impaired listeners will mask these differences.

Acknowledgments

The authors thank Dr. Rhona Hellmann, Professor Michael Epstein, Professor Brian Moore, and an anonymous reviewer for their helpful comments. This work was supported by NIH/NIDCD Grant No. R01DC02241 and the Swiss National Science Foundation.

References and links

[1]Moore (2004) describes loudness-growth functions of HIL as follows: (1) HIL and NHL have the same loudness at threshold, (2) both groups show the same loudness growth from 0 to 5dB SL, and (3) HIL show a steeper slope after 5dB SL.

[2]The parabolic shape of the slope is due to the loudness function model using a third order polynomial. In order to model a loudness function with a similar shape as the INEX function, a higher degree polynomial is needed.

Brand, T. and Hohmann, V. (**2001**). "Effect of hearing loss, centre frequency, and bandwidth on the shape of loudness functions in categorical loudness scaling," Audiology **40**, 92–103.

Brunt, M. A. (**1994**). "Tests of cochlear functions," in *Handbook of Clinical Audiology*, 4th ed., edited by J. Katz (Williams and Wilkins, Baltimore), pp. 165–175.

Buus, S., and Florentine, M. (**2001**). "Modifications to the power function for loudness," in *Fechner Day 2001*,

edited by E. Sommerfeld, R. Kompass, and T. Lachmann (Pabst, Berlin), pp. 236–241.
Buus, S., and Florentine, M. (**2002**). "Growth of loudness in listeners with cochlear hearing losses: Recruitment reconsidered," J. Assoc. Res. Otolaryngol. **3**, 120–139.
Dix, M. R., Hallpike, C. S., and Hood, J. D. (**1948**). "Observations upon the loudness recruitment phenomenon, with especial reference to the differential diagnosis of disorders of the internal ear and VIII nerve.," Proc. R. Soc. Med. **41**, 516–526.
Epstein, M., and Florentine, M. (**2005**). "A test of the Equal-Loudness-Ratio hypothesis using cross-modality matching functions," J. Acoust. Soc. Am. **118**, 907–913.
Florentine, M. (**2004**). "Softness imperception—Defining a puzzling problem," Hearing Health **20**(1), 31–34.
Florentine, M., Buus, S., and Hellman, R. P. (**1997**). "A model of loudness summation applied to high-frequency hearing loss," in *Modeling Sensorineural Hearing Loss*, edited by W. Jesteadt (Erlbaum, New York), pp. 187–198.
Florentine, M., Buus, S., and Poulsen, T. (**1996**). "Temporal integration of loudness as a function of level," J. Acoust. Soc. Am. **99**, 1633–1644.
Florentine, M., and Epstein, M. (**2006**). "To honor Stevens and repeal his law (for the auditory system)," in *Fechner Day*, edited by D. E. Kornbrot, R. M. Msetfi, and A. W. MacRae (International Society for Psychophysics, St. Albans, UK), pp. 37–42.
Hellman, R., and Zwislocki, J. J. (**1961**). "Some factors affecting the estimation of loudness," J. Acoust. Soc. Am. **33**, 687–694.
Hellman, R. P. (**1994**). "Relation between the growth of loudness and high-frequency excitation," J. Acoust. Soc. Am. **96**, 2655–2663.
Hellman, R. P., and Meiselman, C. H. (**1990**). "Loudness relations for individuals and groups in normal and impaired hearing," J. Acoust. Soc. Am. **88**, 2596–2606.
Knight, K. K., and Margolis, R. H. (**1984**). "Magnitude estimation of loudness. II. Loudness perception in presbycusic listeners," J. Speech Hear. Res. **27**, 28–32.
Marozeau, J., Epstein, M., Florentine, M., and Daley, B. (**2006**). "A test of the binaural equal-loudness-ratio hypothesis for tones," J. Acoust. Soc. Am. **120**, 3870–3877.
Moore, B. C. J. (**2003**). *An Introduction to the Psychology of Hearing*, 5th ed. (Academic, San Diego).
Moore, B. C. J. (**2004**). "Testing the concept of softness imperception: Loudness near threshold for hearing-impaired ears," J. Acoust. Soc. Am. **115**, 3103–3111.
Moore, B. C. J., and Glasberg, B. R. (**2004**). "A revised model of loudness perception applied to cochlear hearing loss," Hear. Res. **188**, 70–88.
Richardson, L. F., and Ross, J. S. (**1930**). "Loudness and telephone current," J. Gen. Psychol. **3**, 288–306.
Stevens, S. S. (**1955**). "The measurement of loudness," J. Acoust. Soc. Am. **25**, 815–829.
Whilby, S., Florentine, M., Wagner, E., and Marozeau, J. (**2006**). "Monaural and binaural loudness of 5- and 200-ms tones in normal and impaired hearing," J. Acoust. Soc. Am. **119**, 3931–3939.

Perceptual relevance of the temporal envelope to the speech signal in the 4–7 kHz band

Kyung Tae Kim, Jeung-Yoon Choi, and Hong Goo Kang
Electrical and Electronic Engineering, Yonsei University, 134 Shinchon-dong, Sudaemoon-ku, Seoul 120-749, Korea
kktae@dsp.yonsei.ac.kr, jychoi@yonsei.ac.kr, hgkang@yonsei.ac.kr

Abstract: The perceptual relevance of adopting the temporal envelope to model the frequency band of 4–7 kHz (highband) in wideband speech signal is described in this letter. Based on theoretical work in psychoacoustics, we find out that the temporal envelope can indeed be a perceptual cue for the high-band signal, i.e., a noiseless sound can be obtained if the temporal envelope is roughly preserved. Subjective listening tests verify that transparent quality can be obtained if the model is used for the 4.5–7 kHz band. The proposed model has the benefits of offering flexible scalability and reducing the cost for quantization in coding applications.

PACS numbers: 43.72.Gy, 43.71.Gv, 43.72.Ar [DO]
Date Received: April 5, 2007 **Date Accepted:** June 26, 2007

1. Introduction

Wideband speech, sampled at 16 kHz with a signal bandwidth of around 7 kHz, offers a more pleasant quality than narrow-band speech (sampled at 8 kHz) used in conventional telephony systems.[1] To reduce the number of bits required to encode wideband speech directly, bandwidth extension techniques are often introduced to speech communication systems. Bandwidth extension is a method to generate a virtual image of wideband sound from a narrow-band speech signal without utilizing additional information or with minimal information.

Speech coders using bandwidth extension methods for wideband signals generally adopt the source-filter model using linear prediction. While the source-filter model can improve coding efficiency, it cannot provide scalability at the bit-stream level. Scalability is the ability of a coder to support an ordered set of bit streams that can produce a reconstructed sequence, and this quality now has various application areas of concern as noted by the objectives of several standard coders. Since the synthesis process of the source-filter model tightly couples with the look-back memory consisting of the synthesized signal in previous frames, scalable implementation of the encoding stage cannot be unique to the decoding stage, which significantly degrades perceptual quality. In addition, the source-filter model is not effective at higher frequency bands (higher than around 4 kHz) where the spectral envelope is relatively flat compared to the spectral envelope at lower frequencies.

In contrast to the source-filter theory that represents speech by multiplying the spectral envelope and the fine structure in the frequency domain, the speech signal can also be reconstructed by multiplying the temporal envelope with the fine structure in the temporal domain, which we call the *temporal envelope model*. In other words, the *temporal envelope* represents the temporal energy contour and the *fine structure* represents rapid fluctuation. The concept of the temporal envelope model is already utilized in several coders though detailed implementing methods are different. For example, temporal noise shaping[2] used in the advanced audio codec series aims to include temporal envelope information, and ITU-T G.729.1[3] utilizes the temporal envelope information in bandwidth extension based on the source-filter model. Though the importance of the temporal envelope information has been empirically recognized as shown in the previous examples, it remains unclear as to why and how the temporal envelope affects perceptual quality.

In this letter, we find psychoacoustically related evidence to verify the importance of the temporal envelope and the fact that perceptually transparent quality can be obtained if the

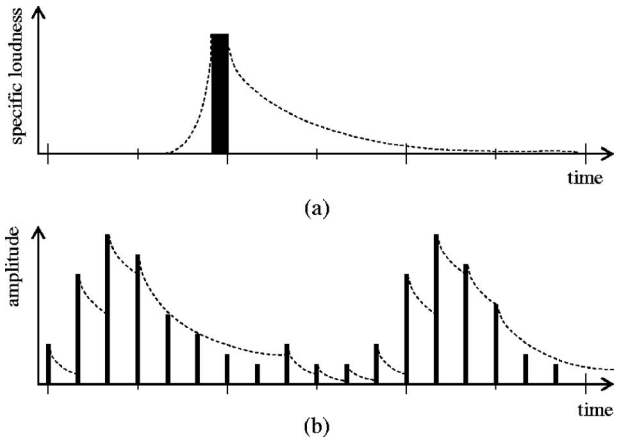

Fig. 1. Examples of temporal masking: (a) premasking and postmasking (Ref. 5) and (b) temporal masking imitating motion of neuron firings (Ref. 6).

temporal envelope information in the high band (4–7 kHz) is reasonably maintained, which is confirmed through experiments. The temporal envelope model representation of the speech signal using just the temporal envelope guarantees bit-stream level scalability because its operation is composed of simple multiplications, as opposed to convolution in the source-filter model. Moreover, some perceptual characteristics of the temporal envelope specific to the speech signal suggest the possibility of applying this method for efficient coding.

2. Theoretical foundations of the temporal envelope model in the high-band signal

It is well known that the auditory system, like all sensory systems, has limited temporal resolution and cannot perceive temporal change if it occurs too rapidly.[4] This characteristic gives us the inspiration to use a slowly varying temporal envelope as a perceptual cue of wideband speech in the high frequency band (4–7 kHz). Here we construct the *temporal envelope model* such that the band-limited signal, $x(n)$, is composed of multiplying the *temporal envelope*, $t(n)$, representing the temporal energy contour, with the *fine structure*, $f(n)$, representing rapid fluctuation as follows:

$$x(n) = t(n)f(n). \tag{1}$$

Based on the model, we can first assume that the speech signal can be synthesized to be perceptually identical to the original speech without any information about the original fine structure. Since the fine structure in the high band varies more rapidly than human listener can follow, the aberrations in the phase of the fine structure cannot be detected. Considering this characteristic, we suggest that a synthesized signal consisting of a fine structure that is obtained from random noise signals and a temporal envelope from the original gives signal quality that is comparable to the original speech.

2.1 Temporal masking and the temporal envelope

The temporal masking effect, which includes premasking and postmasking[5] the human auditory system, provides us with the motivation of the temporal envelope model. Premasking represents the masking effect that occurs even before the masker is switched on.[5] Conversely, postmasking results from the gradual retreat of the masker. That is, masking does not immediately stop when the masker is switched off, but it still lasts while no masker is actually present, as shown in Fig. 1(a).[5] Though the temporal masking effect has been shown under the assumption that both the masker and maskee exist, it can also be applied to peak points in the signal wave form itself without distinguishing a separate masker from the maskee.[6] This is reasonable if we

consider the peak point as a masker having a very short duration. It is also possible to induce positive peak points in the wave form of some auditory-filtered signal (bandpassed signal) to lead to a high rate of neuron firings psychoacoustically.[7] In the auditory model, each neuron has a state that decays exponentially with a characteristic decaying time and is reset when it fires. The reset level depends on the input level during the firing stage. The exponential decay is modeled after the postmasking effect, and therefore the temporal masking threshold can be obtained to make it decay exponentially following each peak pulse, leading to neural firing as shown in Fig. 1(b). The temporal masking threshold obtained in this way looks similar to the temporal envelope of the corresponding band signal in the high frequency band.[6] Therefore, in the high frequency band, the variation of the fine structure under the fixed temporal envelope cannot be perceptually detected. The effect may not be applied to a lower band signal where the decaying rate of a masking threshold is faster than the fluctuation of the band signal itself.

2.2 Just-noticeable amplitude variation and just-noticeable frequency variation

In psychoacoustics, just-noticeable amplitude variation (JNAV) and just-noticeable frequency variation (JNFV) can be examined in order to confirm the suitableness of the temporal envelope model. Just-noticeable variations are useful for producing scales of sensations and are important as the basis on which sensations are built.[5] JNAV is often measured by amplitude modulation. The detectability of amplitude modulation in the absence of spectral cues provides a quantitative description of temporal resolution for steady-state signals with relatively small amplitude changes. Modulation thresholds for sinusoidally amplitude-modulated wideband noise are measured as a function of modulation frequency, which results in generating the temporal modulation transfer function (TMTF).[4] Detection experiments show that human sensitivity to the modulation could be modeled by a low-pass filter whose cutoff frequency is about 50 Hz. Moreover, Viemeister[4] showed that the cutoff frequency of the TMTF increases as the center frequency increases. This means that the variation in the temporal envelope is easily detected for higher frequency bands. Meanwhile, JNFV is measured by using sinusoidal frequency modulation. The just-noticeable value is given as a function of carrier frequency.[5] According to the function, at low carrier frequencies, the just-noticeable frequency is approximately constant and has a value of about 3.6 Hz. Above about 500 Hz, it increases nearly in proportion to the carrier frequency, which is strongly correlated with the critical band rate. Considering the same amount of frequency variation caused by quantization or estimation, the human ear cannot detect the frequency variation of the fine structure well in a high frequency band compared to a low frequency band. As inferred from the characteristics of JNAV and JNFV, it is reasonable to exclude the fine structure and to preserve the temporal envelope for a high-band signal.

2.3 Temporal envelope of the speech signal

The temporal envelope has been studied in various speech processing applications because it is believed to be related to many perceptual attributes of speech, such as intelligibility and quality. For the purpose of speech quality measurement, Kim[8] previously hypothesized that the human auditory system made use of the modulation spectrum, which is related to temporal envelope information. In the paper, spectral components located at a certain modulation frequency region are said to be perceived as being more annoying than at other frequencies. This distortion-related frequency region is assumed to be around 30–50 Hz, from the observation that the speed of mechanical movement of the human articulatory system is limited to 2–30 Hz and that the human modulation detection is bounded to the cutoff frequency of about 50 Hz.[4] With the assumptions Kim sets out, it can be hypothesized that the temporal envelope with limited bandwidth could give sufficient representation of speech perceptually.

The band-limited characteristic of the temporal envelope is also shown with respect to distortion as well as speech identification. Ghitza,[9] through various experiments, showed that roughly one-half of one critical band of the envelope information for a given auditory channel is sufficient to preserve speech quality without any audible distortions.

The narrow-band characteristic guarantees efficient quantization for coding of the

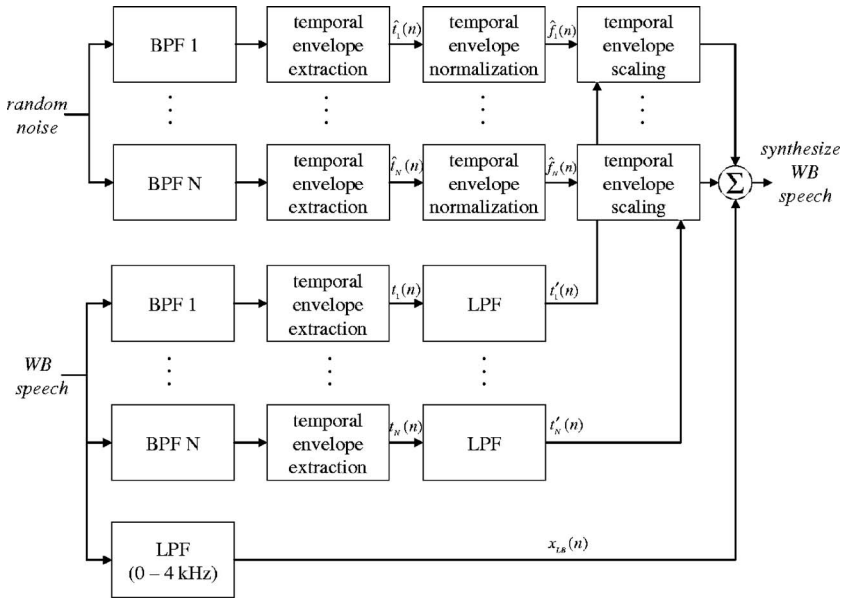

Fig. 2. Block diagram of generating test materials for verification of temporal envelope modeling.

temporal envelope. The premise that using just the temporal envelope information can determine speech quality by itself and that it has most information in a narrow band of around 2–50 Hz means that the temporal envelope is able to give perceptually summarized aspects of the speech signal.

3. Experiments and discussions

3.1 Generation of test materials

To verify the hypothesis described in Sec. 2, we perform subjective listening tests with test samples synthesized using the temporal envelope model. Detailed steps to generate test samples are depicted in Fig. 2. Under the assumption of the temporal envelope model, an arbitrary high-band signal can be expressed by summing the multiplication of temporal envelopes and fine structures of subbands:

$$x_{\mathrm{HB}}(n) = \sum_{i=1}^{N} t_i(n) f_i(n), \tag{2}$$

where $x_{\mathrm{HB}}(n)$ is the input high-band signal and $t_i(n)$ and $f_i(n)$ are the temporal envelope and the fine structure of the ith subband, respectively, N is the number of the subbands.

The test materials for the listening tests are composed of the low-pass filtered temporal envelopes, $t_i'(n)$ from the original wideband speech signal and fine structures, $\hat{f}_i(n)$ from random noise signals. To obtain the temporal envelopes of the subbands, the subband signals are extracted in advance from the original wideband signal through the bandpass filters with 64th order FIR filters. We divide the 4–7 kHz band into four subbands (whose bandwiths are 500, 700, 800, and 1000 Hz, respectively) by considering the critical-band rate approximately. The temporal envelopes, $t_i(n)$, are obtained by the subband signals, but detailed extraction methods will be explained in Sec. 3.2. In addition, in order to confirm the band-limited characteristic of the temporal envelope, the temporal envelopes are low-pass filtered with cut-off frequencies of one-half of each critical-band bandwidth, which validates efficiency when coding. For the fine structures, $\hat{f}_i(n)$, an arbitrary white noise signal is bandpass filtered by the filters, whose band-

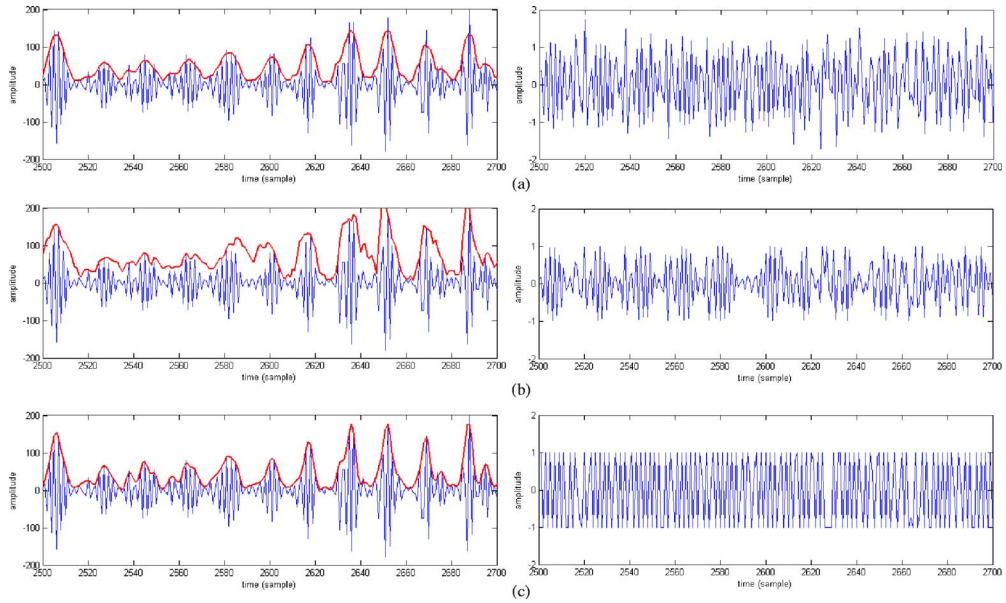

Fig. 3. (Color online) The examples of the temporal envelope extraction methods: (a) energy contour, (b) Hilbert transform, and (c) local maxima interpolation; the left part indicates the subband signal and the corresponding temporal envelopes and the right part the corresponding fine structures.

widths are the same as those used in obtaining $t_i(n)$. The temporal envelopes, $\hat{t}_i(n)$, of the subband signals of the white noise are obtained by the temporal envelope extraction method chosen in the previous process and the corresponding fine structures, $\hat{f}_i(n)$, are calculated through dividing the subband signals of the white noise by the temporal envelopes, $\hat{t}_i(n)$ ("temporal envelope normalization" process in Fig. 2). The multiplication of the low-pass filtered temporal envelopes, $t_i'(n)$, and the fine structures, $\hat{f}_i(n)$, become the synthesized subband signals. The synthesized subband signals in the $4-7$ kHz band and the original low-band signal, $x_{\mathrm{LB}}(n)$, are summed to result in the synthesized wideband signal, that is, the test materials.

Though we cannot regenerate the exact spectrum by using random noise for the fine structures as illustrated in the previous paragraph, the following experiments show that fine structure is not important perceptually, i.e., it is difficult to distinguish the synthesized signal from the original one.

3.2 Temporal envelope extraction methods

In applications where the temporal envelope is needed, we may introduce either a simple short-time energy contour or take the Hilbert transform, which are commonly used in various applications. To obtain a more accurate envelope, we also simulate a method to pick local peaks of each subband signal and to interpolate them in a sample-by-sample manner, which we call *local maxima interpolation method*. The local maxima interpolation method intuitively takes into account that temporal masking starts from the local peaks of the signal and a synthesized signal should preserve the local peak values that constitute the over-all temporal masking threshold. The reason we have tried three different approaches is to verify whether the accuracy of the extraction process results in variation in quality of the temporal envelope model. Figure 3 shows examples of temporal envelopes extracted by the three above-described methods (left part) and the corresponding fine structures (right part). Observing the examples of fine structures generated from the three methods, the Hilbert transform and the energy contour methods generate fluctuation caused by amplitude variation. If an arbitrary random noise is substituted for the

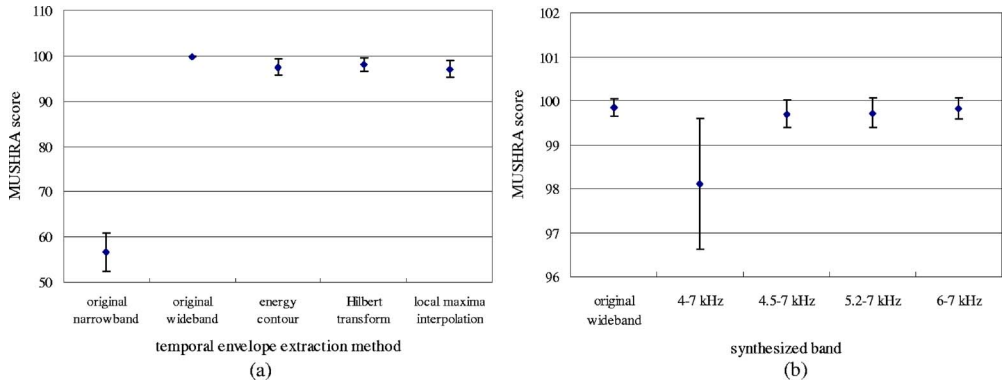

Fig. 4. (Color online) MUSHRA scores including the 95% confidential intervals: (a) for the three temporal envelope extraction methods and (b) for synthesis bandwidths.

original fine structure, the temporal envelope of the synthesized signal would not be similar to the original one. In contrast, the local maxima interpolation method can ensure wave form similarity with the original signal, although this does not necessarily mean the better quality perceptually, which is ascertained in the results of the listening tests.

3.3 Evaluation

For a subjective quality evaluation method, multistimulus test with hidden reference and anchors (MUSHRA)[10] was adopted here. In the MUSHRA test, the listener is presented with several speech stimuli. The first is the reference, which is the original wideband speech signal. The remainder are the test stimuli to which the listener must give a score between 0 and 100 depending upon their opinion of the quality. The scale given in this five-interval quality scale.is: excellent(100-80), good(80-60), fair(60-40), poor(40-20), and bad(20-0). The test stimuli include two anchors, a hidden reference and the undistorted narrow-band (0–4 kHz) speech. The listener must try to identify the hidden reference and score it as 100. The test stimuli must be randomized in order, so the listener has no clues to their identity.

The reference speech database was taken from the TIMIT[11] data set. Speech samples consist of four sentences spoken by four different male and female speakers and 20 experienced listeners are asked to make a quality judgment. Listening was carried out using headphones to give more consistent conditions than loud speakers in listening rooms. The tests were carried out with Audio-Technica ATH-A700 headphones in a quiet room where equipment noise is not audible.

Fig. 4 shows the results of subjective quality measures, the mean values of the MUSHRA scores, and the 95% confidential intervals for the tolerance. Fig. 4(a) shows the results for the cases where the three temporal envelope extraction methods are applied. The three methods give almost the same performance but the Hilbert transform method is slightly better. However, all the synthesized signals do not offer the same qualities as the original, against our expectations. Theoretical reasons for supporting the temporal envelope model are not validated when we replace subband signals starting from 4 kHz with artificial synthesized signals. The arguments we presented just confirm the trend that the temporal envelope becomes more important as frequency increases, but it does not pinpoint from what frequency we can apply the temporal envelope model. To validate the analysis with regard to quality degradation, we performed similar experiments by varying the start frequency for applying the temporal envelope model, the results of which are shown in Fig. 4(b). The synthesized signal cannot be distinguished from the original if the temporal envelope model starts around 4.5 kHz. From hypothesis tests, under significance level $\alpha=0.05$, we can also say that the qualities of the synthesized signals and the original one are equal.

As shown in Fig. 4, transparent quality can be obtained through the temporal envelope

model even if it does not include fine structure information. In the model, the speech signal in each subband is reconstructed by multiplying the temporal envelope with the fine structure. Since the fine structure does not need to be quantized, we can have additional benefits in scalability by quantizing only the temporal envelope information, in contrast to the source-filter model in which filter coefficients as well as the residual signal are needed, which also impacts the synthesis process of successive frames. Moreover, the temporal envelope is also expected to be able to be quantized effectively, considering not only its band-limited characteristics, but also the fact that it has pitch periodicity, which can be extracted by a narrow-band coder.

4. Conclusion

Based on psychoacoustic evidence, we showed that the temporal envelope of a subband with critical-band bandwidth is shown to provide a perceptual cue in the highband. Through some experiments we also confirmed that the temporal envelope model worked well in the band of 4.5–7 kHz. The temporal envelope model can be utilized in scalable wideband speech coders and speech bandwidth extension to convert narrow-band speech into wideband speech virtually. Progressive enhancement by quantizing the temporal envelope enables scalable implementation. Moreover, audio signals could also be applied if target bands are higher than our case, because the temporal envelope model is designed based on human perception. Effective quantization methods that use the band-limit characteristics and pitch-periodicity require further study.

References and links

[1]International Telecommunication Union, "Paired comparison test of wide-band and narrow-band telephony," ITU COM 12–9–E, 1993.
[2]J. Herre and J. D. Johnston, "Enhancing the performance of perceptual audio coders by using temporal noise shaping (TNS)," Audio Engineering Society (AES) 101st Conventionm, Los Angeles, 1996, p. 4384.
[3]International Telecommunication Union, "G.729 based embedded variable bit-rate coder: An 8-32 kbit/s scalable wideband coder bitstream interoperable with G.729," ITU-T G.729.1, Los Angeles, 2006.
[4]N. F. Viemeister, "Temporal modulation transfer functions based upon modulation thresholds," J. Acoust. Soc. Am. **66**, 1364–1380 (1979).
[5]E. Zwicker and H. Fastl, *Psychoacoustics, Facts and Models*, 2nd updated ed. (Springer, New York, 1998).
[6]E. Ambikairajah, J. Epps, and L. Lin, "Wideband speech and audio coding using gammatone filterbanks," *Proceedings of the ICASSP2001*, Salt Lake City, Utah, 773–776
[7]G. Kubin and W. B. Kleijn, "On speech coding in a perceptual domain," *Proceedings of the ICASSPI999*, Phoenix, Arizona, 205–208.
[8]D.-S. Kim, "A cue for objective speech quality estimation in temporal envelope representations," IEEE Signal Process. Lett. **11**, 849–852 (2004).
[9]O. Ghitza, "On the upper cutoff frequency of the auditory critical-band envelope detector in the context of speech perception," J. Acoust. Soc. Am. **110**, 1628–1640 (2001).
[10]International Telecommunication Union, "Method for the subjective assessment of intermediate quality level of coding systems," ITU-R BS.1534–1, 2003.
[11]L. F. Lamel, J. Garafolo, J. Fiscus, W. Fisher, and D. S. Pallett, "The TIMIT acoustic-phonetic continuous speech corpus," Linguistic Data Consortium, Philadelphia, 1990.

ACOUSTICAL NEWS—USA

E. Moran
Acoustical Society of America, Suite 1NO1, 2 Huntington Quadrangle, Melville, NY 11747–4502

***Editor's Note**: Readers of this journal are encouraged to submit news items on awards, appointments, and other activities about themselves or their colleagues. Deadline dates for news and notices are 2 months prior to publication.*

New Fellows of the Acoustical Society of America

Stephen I. Finette

Ronald A. Wagstaff

Lily M. Wang

Annual Reports of Technical Committees

(**See October and November issues for additional reports**)

Acoustical Oceanography

Fall 2006 Meeting, joint with the Acoustical Society of Japan (Honolulu, Hawaii). The Technical Committee on Acoustical Oceanography (AO) sponsored two special sessions: (1) "Acoustic scattering by aquatic organisms," organized by Ken Foote (Woods Hole Oceanographic Institution) and Masahiro Furusawa from the Acoustical Society of Japan; and (2) "Ocean acoustic tomography for coastal and deep water applications," organized by Jim Mercer (Applied Physical Laboratory, Seattle) and Arato Kaneko from the Acoustical Society of Japan. I want to thank Jim and Ken for their extra efforts in coordinating these sessions with their co-chairs from Japan. The Best Student Paper Awards in Acoustical Oceanography went to Paul Roberts of Scripps (first prize winner) for his paper, "Multiple-angle acoustic scattering and classification of zooplankton," and Tadanori Fujino (Fisheries Research Agency, Hasaki, Japan) who won second prize for his paper, "Target strength of a mesopelagic fish (*Maurolicus japonicus*) at 38 and 120 kHz." Andone Lavery (Woods Hole Oceanographic Institution) represented AO at the Technical Program Organizing Meeting.

Spring 2007 Meeting (Salt Lake City, Utah). The 2007 Medwin Prize in Acoustical Oceanography was awarded to Brian Dushaw of the University of Washington, Applied Physical Laboratory, Seattle, for his research on acoustic tomography to measure temperature change in the ocean. Dr. Dushaw presented the AO Prize Lecture entitled, "The recent history of our understanding of low-mode internal tides in the ocean." AO sponsored two special sessions and a memorial session for Hank Medwin. Jim Lynch (Woods Hole Oceanographic Institution) organized a special session entitled "Acoustic sensing of the ocean and seabed using gliders and AUVs." Grant Deane (Marine Physical Laboratory, UCSD) organized a special session entitled "Acoustics of bubble clouds." Mike Buckingham, David Farmer, and Van Holliday organized the memorial session for Hank Medwin. Kevin Cockrell (MIT) won first prize in the competition for the Best Student Paper Award in Acoustical Oceanography for his paper entitled. "A proposed technique for source localization using an autonomous underwater vehicle," and Jan Dettmer (University of Victoria) was awarded second prize for his paper entitled "Bayesian full-wavefield reflection coefficient inversion and uncertainty estimation." Matt Dzieciuch (UCSD) represented AO at the Technical Program Organizing Meeting.

Information on these and related matters is available on the new Acoustical Oceanography Technical Committee website. It can be reached through the ASA web page by clicking on "Committees."

This is my last report as Technical Chair of this committee. It has been a privilege to serve as chair, and I want to close by thanking all the volunteers who have helped me over the past three years.

N. ROSS CHAPMAN
Chair 2005—2007

Animal Bioacoustics

The Animal Bioacoustics (AB) Technical Committee had a productive year with good representation at the fall (Honolulu, Hawaii) and spring (Salt Lake City, Utah) meetings, and exciting plans for future meetings and events.

At the Honolulu meeting, AB sponsored or co-sponsored four special sessions that were well attended and quite successful. For a full day, we held a tribute to the late Arthur Myrberg, who was one of the founders of the field of fish bioacoustics ("Fish Bioacoustics: A Tribute to Arthur Myrberg I and II," chaired by Arthur Popper and Richard Fay). The presentations covered the history of the field, and Art Myrberg's participation in it together with recent research on acoustic communication, the effects of noise, and hearing

 0001-4966/2007/122(3)/1287/16/$23.00

by fishes. In a special session titled "Acoustic Scene Analysis and Communication in Animals," co-chaired by Cynthia Moss and Hiroshi Riquimaroux, papers were presented on the phenomenon of auditory scene analysis revealed in nonhuman animals, from bats to insects. W. Tecumseh Fitch and Kiyoshi Honda co-chaired a special session on "Vertebrate Vocal Production: Themes and Variations," covering vocal structures and mechanisms to evolutionary principles. On Friday and Saturday, AB sponsored extensive poster sessions on Marine Mammal Acoustics, and Avian Acoustics.

In Salt Lake City, Animal Bioacoustics sponsored two, well-attended special sessions. "Paleohearing" (cochaired by Richard Fay and John Rosowski) brought together those interested in estimating hearing capabilities in extinct species based on structures of living animals and the fossil record for a very exciting session. One highlight was the talk by Robert Dooling, Otto Gleich, and Geoffrey Manley estimating the hearing capabilities of dinosaurs from extant and fossil archosaurs. This presentation attracted significant media attention, with an article in the Baltimore Sun, and by Discovery.com. Our second special session, "Seismic Communication in Animals" (cochaired by Peggy Hill, and Caitlin O'Connell-Rodwell) attracted the attention of National Public Radio, which produced a feature based on the session.

At the Salt Lake City meeting, one of our young members, Dorian S. Houser, received the R. Bruce Lindsay Award as a significant contributor to the Society and to Acoustics by someone under the age of 35. Dorian has contributed new methods and data on marine mammal bioacoustics.

At the meeting of the Technical Committee, we received a planning update on the Second International Conference on Acoustic Communication by Animals by David Mellinger, who is the Chair of the Organizing Committee for the meeting. The planning for this meeting is well under way and it promises to be as successful as the previous meeting in College Park, Maryland. The conference will take place in Corvalis, Oregon on August 12–15, 2008 and will cover all aspects of animal acoustic communication, from cognition to communication in noisy environments. Peter Marler (avian communication) and Peter Tyack (whale communication) are on board as plenary speakers.

With Michel André of Barcelona, we have planned for at least eight structured sessions for the Paris meeting of the Acoustical Society of America, covering the field of animal bioacoustics.

Thank you to all the Animal Bioacoustics member volunteers who have contributed to the AB Technical Committee and its successes. Our programs and successes absolutely depend on this sort of volunteer effort. Special thanks go to Whit Au for his critical attention and interest in our TC, and to David Mellinger for his significant work organizing the Corvalis meeting on animal communication, and for keeping our web site current. Thanks also to Andrea Simmons (membership), Jim Simmons (medals and awards), Ann Bowles (ASACOS), Alison Stimpert (student representative), and to Gary Rose (TPOM rep for Salt Lake City).

RICHARD R. FAY
Chair

Architectural Acoustics

The Technical Committee on Architectural Acoustics (TCAA) had a very successful year in 2006-07. At the Fall 2006 meeting in Honolulu, held jointly with the Acoustical Society of Japan, TCAA special sessions and their organizers included "Acoustic Design for Green Buildings" (Ken Roy, Tetsuya Sakuma), "Acoustics of Large Indoor and Outdoor Performance Spaces" (Daniel Raichel, Toshiki Hanyu), "Computer Modeling of Room Acoustics" (Lily Wang, Shin-ichi Sakamoto), "Special Session in Honor of Manfred Schroeder on the Occasion of His 80th Birthday" (Ning Xiang, Juergen Schroeter, Akira Omoto), "Psychological Aspects of Sound Environment in Rooms" (John Bradley, Hiroshi Sato), "Recent Development in Acoustical Materials and Structures" (Brandon Tinianov, Kirill Horoshenkov, Kimihiro Sakagami), and "Measurement of Room Acoustics" (Boaz Rafaely, Fumiaki Satoh). David Adams served as the TCAA representative to the Technical Program Organizing Meeting for this conference.

At the Spring 2007 meeting in Salt Lake City, TCAA special sessions and their organizers included "Advancements in Speech Privacy" (Kenneth Good, Jr.), "Effects of Rooms on the Sound of Organs" (Bruce Olson), "In Situ Measurements of Absorption Coefficients (Peter D'Antonio, Christian Nocke), and "Troubleshooting in Room Acoustics" (Robin Glosemeyer-Petrone). In addition, a workshop covering the logistics on making a TCAA presentation to architects in which participants would receive continuing education credits from the American Institute of Architects was chaired by Tony Hoover and Bennett Brooks. Other special highlights included the Vern Knudsen Distinguished Lecture given by Emily Thompson, recipient of a 2005 MacArthur Fellowship, and tours of various performing arts facilities in the Salt Lake City area, organized by Tim Leishman. Bruce Olson served as TCAA representative to the Technical Program Organizing Meeting for this conference.

Many of TCAA's subcommittees were active this year. The *Newman Student Award Fund* awarded 11 medals in 2006 to students who excelled in their study of architectural acoustics. Also, two Schultz Grants were awarded in 2007 to Stephen Dance (London South Bank University) and Ralph Muehleisen (Illinois Institute of Technology), supporting their proposals to develop new educational materials on architectural acoustics. More information may be found on the website at www.newmanfund.org. The *Student Design Competition* at the Salt Lake City meeting received 20 entries this year; many thanks to Bob Coffeen and Byron Harrison for their organizational efforts and to the Wenger Foundation and Newman Student Award Fund for their sponsorship. First honors in the competition was awarded to Andrew Miller, Megan Hunziker, and Matt Pauley from the University of Kansas.

The *Third Concert Hall Research Group Summer Institute* was held in Aspen, Colorado in August 2006, organized by Bill Dohn. Nearly 60 professional attendees and 13 students participated in a variety of interesting sessions and wonderful concerts at the Aspen Music Festival (see the April issue of *Acoustics Today*, pp. 55–56, for a report on the Institute).

Achieving good classroom acoustics continues to be an important topic that TCAA members are strongly advocating. The National Research Council has endorsed the American National Standards Institute (ANSI) standard S12.60-2002 on "Acoustical Performance Criteria, Design Requirements, and Guidelines for Schools" for adoption into proposed green schools. Also the US Green Building Council has drafted a standard for LEED (Leadership in Energy and Environmental Design) school projects; many of our TCAA members have provided input on this document. We are very grateful to David Lubman and Lou Sutherland for their ongoing leadership efforts in this area.

The joint subcommittee with the Technical Committee on Noise concerning *Speech Privacy*, chaired by Greg Tocci and David Sykes, has been very active. They prepared the document "Draft Interim Sound and Vibration Design Guidelines for Hospitals and Healthcare Facilities" for the American Institute of Architects (AIA) and American Hospital Association (AHA), which is now undergoing further review. Also, members of the subcommittee influenced the "Green Guide for Health Care," which is a joint project of the Center for Maximum Potential Building Systems and Health Care Without Harm, so that the new edition of the guide (version 2.2) includes two points for acoustics. The subcommittee is also participating in ANSI working group S12 WG44 to draft measurement and performance standards regarding speech privacy. More information about this subcommittee's activities may be found on the website: www.speechprivacy.org.

Our newest subcommittee on *Green Building Acoustics* is ramping up its activities under the leadership of Ralph Muehleisen. This group can be found at the webpage: http://groups.google.com/group/asa-gba.

Work continues on two publications, based on posters presented at ASA meetings. Greg Miller and Robin Glosemeyer Petrone are editing the publication, "Another Two Decades of Drama Theaters," based on posters presented at the Spring 2004 meeting in New York City. Adam Foxwell and Rosemary Su are compiling the publication, "Another Two Decades of Worship Spaces," based on posters presented at the Spring 2006 meeting in Providence.

This year the TCAA again offered Best Student Paper Awards. Due to the large number of submissions, four awards were presented for papers given at the Honolulu meeting; First prize went to Jonathan Rathsam (University of Nebraska), while three commendation awards were given to Hisaharu Suzuki (Kyushu University), Michelle Vigeant (University of Nebraska), and Genta Yamauchi (Kyushu University). Two winners were selected for papers given at the Salt Lake City meeting: Michelle Vigeant from the University of Nebraska (first prize) and Yun Jing from Rensselaer Polytechnic Institute (second prize).

Congratulations to TCAA members who became ASA Fellows this year. New Fellows include Sergio Beristain, David Conant, Damian Doria, John Eargle, Anders Christian Gade, Lily M. Wang, and Michael Vorländer.

TCAA was especially proud that the 2006 ASA Wallace Clement Sabine Award was presented to William J. Cavanaugh for contributions to the practical application of architectural acoustics in building design and to education in architectural acoustics.

Many thanks to the following individuals for their hard work this past year in ASA on behalf of TCAA. Red Wetherill is our representative on the Medals and Awards Committee. Greg Tocci serves on the Membership Committee, and George Winzer is TCAA representative to the ASA Committee on Standards. Michelle Vigeant from the University of Nebraska served as our Student Council representative. The Associate Editors in Architectural Acoustics are Mendel Kleiner and Ning Xiang for *JASA*, Ning Xiang for *JASA-Express Letters*. Tony Hoover serves on the Editorial Board for *Acoustics Today*. Finally, thanks to Brandon Tinianov for his service as TCAA Secretary, and best wishes to him as he begins his 2007–2010 term as TCAA chair.

I have enjoyed serving as TCAA chair over the past three years, and am pleased that our technical committee continues to thrive and be energetic. I look forward to continuing my participation in this vibrant community over the years to come!

LILY M. WANG
Chair 2004—2007

Biomedical Ultrasound/Bioresponse to Vibration

Lawrence Crum kicked off the Honolulu meeting with a plenary talk entitled "Therapeutic Ultrasound." Special sessions (and organizers) at the Honolulu meeting included: "Topical Meeting on Shock Wave Therapy" (Robin Cleveland, S.H.R. Hosseini), "Acoustic Tomography in Tissue" (Jeffrey Ketterling, Iwaki Akiyama), "Interaction of Cavitation Bubbles with Cells and Tissue" (John Allen, Yoshiki Yamakoshi), "Celebration of Floyd Dunn" (William O'Brien, Junichi Kushibiki, Michael Oelze, Shin-ichiro Umemura), "Ultrasound Enhancement of Drug Activity" (Constantin Coussios, Shin-ichiro Umemura), "Elastic Imaging" (Peter Kaczkowski, Tsuyoshi Shiina), and "Biomedical Imaging and Microscopy" (Suk Wang Yoon, Yoshifumi Saijo). Contributed sessions (and chairs) included: "Ultrasound Contrast Agents" (Charles Church) and "Medical Ultrasound" (Yuri Pishchalnikov, Yoshiaki Watanabe). John Allen was the TPOM representative who was able to schedule all these sessions. ASJ TC Chair Iwaki Akiyama coordinated having an ASA and an ASJ co-chair for each session.

Special sessions (and organizers) at the Salt Lake meeting included: "Coded Signals and Compression" (Jonathan Mamou, Michael Oelze), "Biomedical Applications of Acoustic Radiation Force" (Mostafa Fatemi), and "Modeling Acoustic Cavitation *In Vivo*" (Sheryl Gracewski, Diane Dalecki). The contributed sessions were "Therapeutic Ultrasound and Bioeffect" (John Allen), "Imaging and Detection Theory" (Bruno Durning), and "Tissue Scattering and Imaging" (Carr Everbach). Michael Bailey was the TPOM representative.

Several members of the BBTC received awards and recognition. James McAteer, Michael Bailey, Paul Barbone, and T. Douglas Mast were named Fellows of the ASA. The R. Bruce Lindsay Award recipient, Dorian Houser, has worked with several in the BBTC on sonar interaction with marine mammals. Edwin Carstensen was awarded the Helmholtz-Rayleigh Interdisciplinary Silver Medal in Biomedical Ultrasound/Bioresponse to Vibration and Physical Acoustics. The citation reads succinctly, "…for contributions to the physics of biomedical ultrasound." Newly elected ASA President Mark Hamilton is a significant contributor to the BBTC in addition to other technical committees. Student award winners were Matthew Urban of the Mayo Clinic College of Medicine (first) for "Harmonic motion detection in a vibrating scattering medium" and Jose Sanchez of the University of Illinois at Urbana-Champaign (second) for "An ultrasonic imaging speckle suppression technique by means of frequency compounding and coded excitation."

Several people should be acknowledged for their work for the BBTC. Shira Broschat continues to maintain the BBTC website (http://moab.eecs.wsu.edu/ shira/asa/bubv.html). Lawrence Crum is the representative to the Medals and Awards Committee, and Carr Everbach is the representative to the Membership Committee and ASACOS. Anthony Brammer and Peter Kaczkowski ably substituted on the Membership Committee and ASACOS in Honolulu. Paul Barbone is the ASA representative to the Biomedical Imaging Research Opportunities Workshop (BIROW). Michael Canney of the University of Washington will complete his term as the BBTC representative to the ASA Student Council and become the Chair of the Student Council. In addition, thank you to those who have volunteered their time and effort to the BBTC and are not listed.

Over a dozen special sessions are already scheduled between the next two meetings. The ASA, primarily through the BBTC and the PATC, is co-sponsoring the 18th International Symposium on Nonlinear Acoustics in Stockholm almost immediately following the Paris 2008 meeting. We will be electing a new Student Council representative and TC chair this year, so please submit nominations.

MICHAEL R. BAILEY
Chair

Engineering Acoustics

The Engineering Acoustics Technical Committee (EATC) met at two meetings of the Society—in Honolulu, Hawaii, and in Salt Lake City, Utah — over the past year.

Dennis Jones, who was elected Chair to the committee prior to the Providence, Rhode Island, meeting, has stepped down from the Chairmanship for personal reasons. Daniel Warren, runner-up in that election, has taken over the Chairmanship for the remainder of the term. The committee thanks Dennis for his service, and wishes him well. Steve Thompson sat as acting chair in the interim, including the Honolulu meeting.

The Committee sponsored a student paper competition in Honolulu which yielded a tie between Junfeng Li, for "A new speech enhancement method for two-input two-output hearing aids," and Marie Nakazawa, for "Multilayered high-performance transducer using polyurethane (sic) thin films." Both papers were excellently prepared and presented.

At the Salt Lake meeting, the EATC sponsored four sessions, including one special session co-sponsored by Underwater Acoustics and Signal Processing, organized by Roger Richards, "Acoustic Technologies for Coastal Surveillance and Harbor Defense," and co-sponsored another two sessions. Thank you to Jim Powers for organizing the papers and securing the meeting spaces at the Technical Program Organizing Meeting.

The Best Student Paper recipients from the Salt Lake meeting are first prize to Brian Anderson for "Grating lobe reduction in transducer arrays through structural filtering of supercritical plates" and second prize to Brian Borowski for "Estimation of passive acoustic threat detection distances in estuarine environments." Congratulations to both for a job well done.

After six years of service, Mahlon Burkhard has decided not to renew his seat on the Medals and Awards committee, and will be replaced by Kim Benjamin. Thank you from the committee to Mahlon and Kim.

DANIEL M. WARREN
Chair

Noise

The Fall 2006 meeting of the ASA in Honolulu, Hawaii was a special occasion for the Technical Committee on Noise: It was the ASA/ASJ 4th Joint Meeting and it was followed by Internoise. It was again a time to showcase widespread aspects of noise. TC-Noise took the lead with ten special sessions: "Progress in Hearing Protection and Hearing Conservation I and II" (Elliott Berger and Hiroaki Takinami); "Active Noise Control" (Yukio Iwaya); "Noise, Architectural Acoustics, and Speech Communication: Acoustical Design Factors in Spaces where Speech Communication is Critical" (Todd R. Beiler); "Soundscape and Cultural Perception I and II" (Brigitte Schulte-Fortkamp, Bennett Brooks); "Acoustics of Sports" (Joe Pope and Kenji Kurakata); "Prediction and Propagation of Outdoor Noise I and II" (Keith Wilson and Kohei Yamamoto); and "Consumer Product Noise" (Matt Nobile and Takeshi Toi). Kerrie Standlee and Tim Noonan were the Noise representatives at the Technical Program Organizing Meeting.

The Noise Young Presenter award went to Miwako Ueda, Japan for her talk, "A questionnaire survey of the attitude of Japanese and foreign residents in Japan to sound masking devices for toilets." New Fellows of the ASA who were announced at the meeting were Marehalli G. Prasad, Joos Vos, and Sergio Beristain. Alan H. Marsh was presented with the ASA Silver Medal in Noise and William Cavanaugh with the Wallace Clement Sabine Award.

The Spring 2007 Salt Lake City ASA meeting was again an exciting array of special sessions in Noise. TC Noise was lead organizer for "Engi-

neering Noise Controls for the Mining Industry" (Mike Hankard and John Seiler); "Standardization for Soundscape Techniques I and II" (Bennett Brooks and Brigitte Schulte-Fortkamp) *Workshop session;* "Aircraft Noise and General Topics in Noise" (J. Micah Downing, Kent L. Gee); "Environmental Noise in National Parks" (Nancy Timmerman); "Recent Advances in Active Noise Control" (Scott Sommerfeldt, Ken Cunefare); "Advancements in Speech Privacy" (Kenneth W. Good) and Hot Topics in Noise with Special Focus on Classroom Acoustics, Noise in Hospitals, and Soundscapes" (Brigitte Schulte-Fortkamp). Connor Duke was the Noise representative at the Technical Program Organizing Meeting.

The contributions of several Noise people were also recognized at this meeting. For the Salt Lake City meeting, we had a winner of the Noise Young Presenter award: Ben Shafer for his talk: "Determination of optimal near field error sensor locations for active control of cooling fan noise using spherical harmonic expansions." We have a new Fellow of the ASA, Damian Doria.

The efforts of several volunteers should be recognized. Mike Stinson has been elected as new Member of the Executive Council and Bennett Brooks as Chairman of working group adopted ANSI 1255. Nancy Timmerman is our Noise representative on the Medals and Awards Committee, John Erdreich is our representative on the Membership Committee, and Richard Peppin is our representative on the ASA Committee on Standards. Connor Duke is our Student Council representative and, following the practice initiated a few meetings ago, the secretary for the TC-Noise meetings. Cole Duke has replaced Connor Duke as the new TC Noise Student Council representative.

The Noise web page ⟨http://www.nonoise.org/quietnet/tcn/⟩ is maintained by Les Blomberg. Ralph Muehleisen is coordinator for the Noise Young Presenter Awards. He would like to pass this position on to someone else. Serving as Associate Editor for *JASA Express Letters* is Mike Stinson and *JASA* Associate Editors are: Keith Attenborough, Kenneth Cunefare, Vladimir Ostashev, and Brigitte Schulte-Fortkamp.

My term as Chair of TC-Noise started after the Providence meeting. It is truly an honor and a privilege for me to chair the Technical Committee Noise following Mike Stinson, our chair from 2003 to 2006, who has provided the committee with excellent leadership. It is my hope to move forward with good leadership and with new initiatives in the challenging area of Noise.

BRIGITTE SCHULTE-FORTKAMP
Chair

Psychological and Physiological Acoustics

Although P&P policy is to de-emphasize fall meetings, the fall 2006 meeting in Hawaii was a clear exception. This was due not only to the popular location, but also due to the fact that it was the Fourth Joint Meeting with the Acoustical Society of Japan. We thank Bill Yost for organizing the sessions for this meeting. There were seven sessions sponsored by P&P, one of which was co-sponsored by Music, and another of which was co-sponsored by ASACOS. In addition, P&P co-sponsored six sessions. We thank the organizers of the three special sessions: Rhona Hellman ("New Insights on Loudness and Hearing Thresholds"), Valter Ciocca ("Auditory Grammar"), and Diana Deutsch ("Perception of Music and Speech: Evidence for Modularity and for Common Processing Mechanisms"). The TC chair did not attend the meeting, and acknowledges Bill Yost and Donna Neff for taking care of administrative duties.

P&P joined the Society in celebrating the award of the Silver Medal in Psychological and Physiological Acoustics to Bill Yost. He joins an elite group of eight previous medalists. We look forward to his continuing contributions to the field of psychological acoustics.

The spring meeting in Salt Lake City was a busy one. There were seven sessions sponsored by P&P. Of these, two were special sessions. We extend our thanks to the organizers of the special sessions: Chris Plack and Deb Hall ("The Neural Coding of Pitch: Insights from Psychophysics, Neurophysiology, and Brain Imaging") and Valeriy Shafiro and Brian Gygi ("Topics and Methods in Environmental Sound Research"). We thank Don Sinex for accomplishing the challenge of organizing the P&P sessions for the Salt Lake City meeting.

The P&P open meeting was lively. The student council representative, Suzy Carr, showed great resourcefulness in sending her report via Don Sinex when she was unexpectedly unable to attend the meeting. Bill Hartmann and Bill Yost gave an overview of the Paris meeting, Acoustics08, coming up in the summer of 2008. The TC members were concerned about the large number of special sessions. Bill Yost informed the TC about a proposal for a new online publication series for conference proceedings. The TC was largely opposed to this idea, citing concern about putting the ASA stamp of approval on something that is not peer-reviewed. The P&P Associate Editors provided an overview of their efforts. We thank the continuing P&P Associate Editors, Rich Freyman, Ruth Litovsky, Brenda L. Lonsbury-Martin, and William P. Shofner and outgoing AEs John Grose, Bob Lutfi, and Andrew Oxenham for their able service. And we welcome John Middlebrooks, Brian C. J. Moore, and Magda Wojtczak as incoming AEs. Their efforts on our behalf are greatly appreciated; the work of our associate editors is important but also time-consuming and difficult. Their willingness to contribute, and the contributions of the other associate editors, is highly valued by the community. We express our thanks to Hedwig Gockel and Jennifer Lentz for organizing the ballot for election to the Technical Committee, and to members of the P&P community who so willingly added their names to the ballot. The newly elected members of the Technical Committee are Huanping Dai, Christian Lorenzi, Christophe Micheyl, Roy Patterson, Daniel Pressnitzer, and Brian Roberts. We thank our outgoing members, David Eddins, Lawrence Feth, Hedwig Gockel, Jennifer Lentz, and Mario Ruggero.

We also thank Bill Hartmann, our representative to the Medals and Awards Committee, Lynne Werner, our representative to the Membership Committee, and Brent Edwards, our representative to ASACOS. We also appreciate the efforts of our members of the executive council, Bill Yost, Donna Neff, Judy Dubno, and Peggy Nelson.

The P&P Technical Initiatives continue unchanged. The initiatives include travel support for invited speakers, student receptions, and homepage maintenance. Suggestions for uses of funds, including innovations such as workshops, satellite meetings, etc., are welcome (estrick@purdue.edu).

ELIZABETH A. STRICKLAND
Chair

Signal Processing in Acoustics

The Signal Processing Technical Committee (SPTC) has been very active during the period of this report. We organized six sessions and cosponsored another five for the Fourth Joint Meeting of the ASA and the Acoustical Society of Japan in Honolulu in November 2006. We also organized five sessions and cosponsored another five for the 153rd ASA meeting in Salt Lake City in June 2007. We sponsored a competition for best paper by a young presenter for both meetings, the Gallery of Acoustics competition in Salt Lake City, and a student challenge problem. We also cosponsored a workshop in Cambridge, England on Nonlinear Statistical Signal Processing, organized by Jim Candy, that included plenary sessions by R. E. Kalman, N. Gordon, and J. S. Liu.

At the Honolulu meeting, special sessions were organized on "Blind Signal Processing" (Leon Sibul and Shoji Makino), "Spatial Sound Processing, Control, and Performance Evaluation" (William Martens and Kazuhiro Iida), "Sensor Array and its Applications" (Henry Cox and Masato Miyoshi), and "Adaptive Signal Processing" (Juan Arvelo and Kensaku Fujii). The Best Paper by a Young Presenter Award was given to James Gregory for his presentation "Pressure-sensitive paint as a distributed microphone array." We wish to thank John Burgess for helping put together the SP sessions during the Technical Program Organizing Meeting (TPOM).

For the Salt Lake City meeting, Max Deffenbaugh and Alan Meyer organized a special session on "Topics in Seismic Signal Processing." This is part of an ongoing effort to increase interaction between acousticians and the seismic exploration community. Another special session on "Signal Processing and Uncertainty" was organized by Lee Culver and Ning Xiang. This proved to be a very popular session with 13 invited speakers on topics ranging from Bayesian techniques, passive sonar, estimation of parameter distributions, polynomial chaos expansions, and source localization. The Best Paper by a Young Presenter Award was split between Georges Dossot, for his paper "Acoustic measurements in shallow water using and ocean glider," and Daniel Mennitt, for his paper "Coarse classification of acoustic signals using temporal and spectral characteristics." We also wish to thank Sean Lehman and Karl Fisher for representing SP at the Salt Lake City TPOM.

The Gallery of Acoustics, organized by Sean Lehman, was held at the Salt Lake City meeting. This is a competition for the best audio-visual presentation of work in acoustics. We had three entries: "A Technical Look at Swing Rhythm in Music" by Ken Lindsay and Pete Nordquist, "Acoustic Demonstrations of Vowel Production Using Vocal-tract Models" by Takayuki Arai, and "Sound Propagation through Atmospheric Turbulence: Visualizations from High-resolution Simulations" by D. Keith Wilson, Edgar Andreas, and Matthew Lewis. All three showed creative uses of both animation and audio to present their work. Meeting attendees were asked to vote on each entry. The winner of the $500 first prize went to Takayuki Arai.

Each year Signal Processing sponsors a Student Challenge problem that can be found in the SP section of the ASA web site. This year's problem asked the student to estimate the speed, altitude, and propeller blade rate of an aircraft from the sound recorded on the ground. Paul Gendron organized the contest and judging. Out of several entries, the top two entries split the $1000 prize. One entry was submitted by the team of M. Farrookhrooz and S. Mousazadeh, both students at University of Texas at Dallas. The other was submitted by Jonathan Galbraith from Fairbanks, Alaska.

We wish to thank our Associate Editors of the *Journal of the Acoustical Society of America*, Edmund J. Sullivan and William Carey, and James V. Candy, our Associate Editor for *JASA Express Letters*, for their selfless service to the Society and SP.

As the new chairman I would like to thank all the SPTC members who organize sessions, run competitions, and serve in many ways to promote the discipline of signal processing in acoustics. I also wish to thank the previous chair, Charles Gaumond, for his advice and assistance in making the transition into this new role.

DAVID H. CHAMBERS
Chair

Speech Communication

The Speech Technical Committee (TC) supports the activities, meetings, publications, etc., for the largest technical area in the Society. This report covers the meetings in Honolulu, Hawaii and Salt Lake City, Utah. The current members of the Committee are Augustine Agwuele, Jean Andruski, Norma Barroso, Fredericka Bell-Berti, Tessa Bent, Lynne Bernstein, Ocke-Schwen Bohn, Suzanne E. Boyce, Ann Bradlow, Dani Byrd, Roger Chan, Alexander Francis, Bruce Gerratt, Kenneth Grant, Helen Hanson, Paul Iverson, Diane Kewley-Port, Jody E. Kreiman, Anders Lofqvist, Benjamin Munson, Shrikanth Narayanan, Terrence Nearey, Peggy Nelson, Douglas O'Shaughnessy, Joseph Perkell, Astrid Schmidt-Nielsen, Christine Shadle, Rahul Shrivastav, Brad Story, and Gary G. Weismer. Other STC members who assisted us by serving on committees were Abeer Alwan (Membership Committee), Shrikanth Narayanan (ASACOS), Fredericka Bell-Berti (Medals and Awards Committee), and Jennell Vick (Student Representative). Brad Story maintains our web page. The continuing Associate Editors are: Speech Production—Anders Lofqvist, Christine Shadle, and Brad Story; Speech Perception—Ann Bradlow, Kenneth Grant, Paul Iverson, Mitch Sommers, and Joan Sussman; Speech Processing—Douglas O'Shaughnessy. New appointments as of June 2007 include: Jody Kreiman as representative to the Membership Committee; and Rochelle Newman and Allard Jongman as Associate Editors in Speech Perception.

The two ASA meetings went very smoothly this year because of the particular efforts of several members: First, we are grateful to our Technical Program Organizing Meeting (TPOM) representatives, who sorted papers, arranged the technical programs, and determined presentation rooms. They were: Victoria Anderson and Amy Shafer in Hawaii and Bruce Smith in Salt Lake City. Second, we greatly appreciate the effort of the coordinators for student judging at the meetings: Carol Espy-Wilson in Hawaii and Terrance Nearey in Salt Lake City. We also are very happy to welcome Jody Kreiman as a new fellow of the ASA in the Speech Communication TC.

Student Activities

In our continuing effort to promote student participation in ASA meetings, the Speech Technical Committee sponsored two student activities at each meeting, a competition with a cash award for best student presentation and an evening reception. The evening reception, which is joint with other technical committees, is intended to allow students to meet more senior ASA members informally. The receptions were well attended. The student papers were judged by STC members and the winners were awarded $300 for first prize and $200 for second prize. At the Rhode Island meeting the first place winner was Joseph Toscano, University of Iowa, for his poster entitled "A lexical locus for the integration of asynchronous cues to voicing: An investigation with natural stimuli." The second place winner was Harsha Sathyendra, University of Florida, for "Noise robust bandwidth extension of telephone speech for mobile and landline communications." In Hawaii, we awarded first and second place prizes to student members of both the ASA and the Acoustical Society of Japan (ASJ). The first place winner of the ASA was Maria Kondaurova of Purdue University for her poster entitled "Russian and Spanish listeners perception of the English tense/lax vowel contrast." The second place ASA winner was Eric Oglesbee of Indiana University for his poster entitled "Finding perceptual categories in multidimensional acoustic spaces." The first place winner of the ASJ was Tatsuya Akagawa of the Tokyo Institute of Technology for his poster entitled "Toward hidden Markov model-based spontaneous speech synthesis." The second place ASJ winner was Ito Masashi of Tohoku University for his poster entitled "Pitch determination and sinusoidal modeling for time-varying voiced speech."

Special Sessions, Special Talks, And Workshops

To create stimulating and focused sessions we sponsor special sessions every year, which focus on themes of interest to the speech community. In Honolulu special sessions addressed "Communicative Speech Synthesis and Spoken Dialogue," cochaired by Alan Black and Yoshinori Sagisaka, and "Speech Timing and Pronunciation Training for the Japanese Language," cochaired by Robert Port and Yukari Hirata. In Salt Lake City, "Frontiers of Spectrum Analysis, with Speech Applications" was chaired by Sean Fulop. Finally, this is my last report as Speech TC chair. I thank STC members for their support and cooperation in the work we do for the society. I also thank the Technical Council for being such an agreeable group to work with. My successor is Carol Espy-Wilson from the University of Maryland.

MAUREEN L. STONE
Chair 2004–2007

Underwater Acoustics

The Hawaii meeting in December 2006 was a great success for the Underwater Acoustics Technical Committee (UWTC), with 12 sessions spread over five days, including special sessions organized by Eric Thorsos and Masao Kimura on Sediment Acoustic Processes, a memorial session in Honor of Leonid Brekhovskikh chaired by Bill Kuperman and Oleg Godin, and a memorial session in honor of Frederick Fisher, also chaired by Bill Kuperman. Many thanks to our Hawaii TPOM representative Martin Siderius for organizing all the sessions together with the special and memorial session organizers. The best student papers in underwater acoustics were "Higher frequency matched field processing" by Claire Debever of Scripps Institute of Oceanography and "Adapting results in filtering theory to inverse theory, to address the statistics of non-linear geoacoustic inversion problems" by Andy Ganse of the University of Washington. New fellows named at the Hawaii meeting with primary or secondary interest in underwater acoustics included Philippe Blanc-Benon, Charles Holland, Kevin LePage, David Palmer, Peter Rona, and Mark Trevorrow. Also announced at the meeting was Aaron Thode's receipt of the 2005 A.B. Wood medal from the Institute of Acoustics. Congratulations to all.

After the Hawaii meeting Kathleen Wage, our student paper awards organizer, stepped down after several years of exemplary service to the TC. Juan Arvelo agreed to take up Kathleen's work for the next few years, starting with the Salt Lake meeting. I would like to thank Kathleen and Juan on behalf of the UWTC for agreeing to do this important work.

Also the Hawaii meeting was the last meeting at which Joseph Zalesak represented our TC on the ASA Committee on Standards (ASACOS). On behalf of the TC I would like to thank Joseph for his service.

The Hawaii meeting was followed by the Salt Lake City meeting in the Spring of 2007, with Tracianne Neilsen doing a yeoman's job at the TPOM meeting, with some timely assistance from George Ioup. There were ten sessions either sponsored or cosponsored by the UWTC, including an AO-sponsored Hank Medwin memorial session chaired by Vance Holliday and David Farmer that was very well attended, and a UW-sponsored special session on Passive Imaging using Random Wavefields chaired by Karim Sabra and Martin Siderius. New fellows named at the meeting included Karim and Claire Prada. Results are also just in on the student paper award

winners. I would like to announce that the winner is Philip Gillett of Virginia Tech with his talk "Advantages of using diffracting cylinders and spheres in acoustic arrays," and the runner up is Claire Debever with "Coherent-broadband, white noise constraint, matched-field processing." Congratulations!

KEVIN D. LE PAGE

Chair

USA MEETINGS CALENDAR

Listed below is a summary of meetings related to acoustics to be held in the U.S. in the near future. The month/year notation refers to the issue in which a complete meeting announcement appeared.

2007

5–8 Oct.	123rd Audio Engineering Society Convention, New York, NY [Audio Engineering Society, 60 E. 42 St., Rm. 2520, New York, NY 10165-2520; Tel: 212-661-8528; Fax: 212-682-0477; Web: www.aes.org]
22–24 Oct.	NOISE-CON 2007, Reno, NV [Institute of Noise Control Engineering, INCE Business Office, 210 Marston Hall, Ames, IA 50011-2153; Tel.: 515-294-6142; Fax: 515–294-3528; E-mail: ibo@inceusa.org]
27 Nov.–2 Dec.	154th Meeting of the Acoustical Society of America, New Orleans, LA (note Tuesday through Saturday) [Acoustical Society of America, Suite 1NO1, 2 Huntington Quadrangle, Melville, NY 11747-4502; Tel.: 516-576-2360; Fax: 516-576-2377; E-mail: asa@aip.org; www: http://asa.aip.org].

2008

29 June–4 July	Acoustics08, Joint Meeting of the Acoustical Society of America (ASA), European Acoustical Association (EAA), and the Acoustical Society of France (SFA), Paris, France [Acoustical Society of America, Suite 1NO1, 2 Huntington Quadrangle, Melville, NY 11747-4502; Tel.: 516-576-2360; Fax: 516-576-2377; E-mail: asa@aip.org; www: http://asa.aip.org/meetings.html].
27–30 July	NOISE-CON 2008, Dearborn, MI [Institute of Noise Control Engineering, INCE Business Office, 210 Marston Hall, Ames, IA 50011-2153; Tel.: 515- 294-6142; Fax: 515-294-3528; E-mail: ibo@inceusa.org]
28 July–1 Aug.	9th International Congress on Noise as a Public Health Problem (Quintennial Meeting of ICBEN, the International Commission on Biological Effects of Noise), Foxwoods Resort, Mashantucket, CT [Jerry V. Tobias, ICBEN 9, Post Office Box 1609, Groton, CT 06340-1609; Tel. 860-572-0680; E-mail: icben2008@att.net; Web: www.icben.org.]

Cumulative Indexes to the Journal of the Acoustical Society of America

Ordering information: Orders must be paid by check or money order in U.S. funds drawn on a U.S. bank or by Mastercard, Visa, or American Express credit cards. Send orders to Circulation and Fulfillment Division, American Institute of Physics, Suite 1NO1, 2 Huntington Quadrangle, Melville, NY 11747-4502; Tel.: 516-576-2270. Non-U.S. orders add $11 per index. Some indexes are out of print as noted below.

Volumes 1–10, 1929–1938: JASA, and Contemporary Literature, 1937–1939. Classified by subject and indexed by author. Pp. 131. Price: ASA members $5; Nonmembers $10.

Volumes 11–20, 1939–1948: JASA, Contemporary Literature and Patents. Classified by subject and indexed by author and inventor. Pp. 395. Out of Print.

Volumes 21–30, 1949–1958: JASA, Contemporary Literature and Patents. Classified by subject and indexed by author and inventor. Pp. 952. Price: ASA members $20; Nonmembers $75.

Volumes 31–35, 1959–1963: JASA, Contemporary Literature and Patents. Classified by subject and indexed by author and inventor. Pp. 1140. Price: ASA members $20; Nonmembers $90.

Volumes 36–44, 1964–1968: JASA and Patents. Classified by subject and indexed by author and inventor. Pp. 485. Out of Print.

Volumes 36–44, 1964–1968: Contemporary Literature. Classified by subject and indexed by author. Pp. 1060. Out of Print.

Volumes 45–54, 1969–1973: JASA and Patents. Classified by subject and indexed by author and inventor. Pp. 540. Price: $20 (paperbound); ASA members $25 (clothbound); Nonmembers $60 (clothbound).

Volumes 55–64, 1974–1978: JASA and Patents. Classified by subject and indexed by author and inventor. Pp. 816. Price: $20 (paperbound); ASA members $25 (clothbound); Nonmembers $60 (clothbound).

Volumes 65–74, 1979–1983: JASA and Patents. Classified by subject and indexed by author and inventor. Pp. 624. Price: ASA members $25 (paperbound); Nonmembers $75 (clothbound).

Volumes 75–84, 1984–1988: JASA and Patents. Classified by subject and indexed by author and inventor. Pp. 625. Price: ASA members $30 (paperbound); Nonmembers $80 (clothbound).

Volumes 85–94, 1989–1993: JASA and Patents. Classified by subject and indexed by author and inventor. Pp. 736. Price: ASA members $30 (paperbound); Nonmembers $80 (clothbound).

Volumes 95–104, 1994–1998: JASA and Patents. Classified by subject and indexed by author and inventor. Pp. 632. Price: ASA members $40 (paperbound); Nonmembers $90 (clothbound).

Volumes 105–114, 1999–2003: JASA and Patents. Classified by subject and indexed by author and inventor. Pp. 616. Price: ASA members $50; Nonmembers $90 (paperbound).

Members of Technical and Administrative Committees of the Acoustical Society of America

The Technical and Administrative Committees listed below have been appointed by the President with the approval of the Executive Council. These appointments, with such changes as may be made by the President from time to time, will be in effect until the Spring meeting of the Society in 2007.

Technical Committees 2007–2008

Acoustical Oceanography

James H. Miller, Chair to 2010

Term to 2010
Kyle M. Becker
N. Ross Chapman
Grant B. Deane
Brian D. Dushaw
Matt A. Dzieciuch
Peter Gerstoft
Oleg A. Godin
John K. Horne
Bruce M. Howe
James F. Lynch
Anthony P. Lyons
Ralph A. Stephen
Alexandra I. Tolstoy
Kathleen E. Wage
Peter F. Worcester

Term to 2009
Mohsen Badiey
Michael J. Buckingham
Dezhang Chu
John A. Colosi
Christian de Moustier
Stan E. Dosso
Kenneth G. Foote
D. Vance Holliday
Andone C. Lavery
Zoi-Heleni Michalopoulou
Jeffrey A. Nystuen
David R. Palmer
Simon D. Richards
Martin Siderius
Aaron M. Thode

Term to 2008
Daniela Di Iorio
Gerald L. D'Spain
Gary J. Heald
Jean-Pierre Hermand
David P. Knobles
Timothy G. Leighton
Daniel Rouseff
Emmanuel K. Skarsoulis
Jerome A. Smith
Dajun Tang

Ex officio:
Peter F. Worcester, member of Medals and Awards Committee
Kenneth G. Foote, member of Membership Committee
Anthony P. Lyons, member of ASACOS
Lora J. Van Uffelen, member of Student Council

Animal Bioacoustics

Richard R. Fay, Chair to 2009

Term to 2010
Michael L. Dent
James J. Finneran
Mardi C. Hastings
Charlotte W. Kotas
Marc O. Lammers
David A. Mann
Marie A. Roch
Gary J. Rose
Joseph A. Sisneros

Term to 2009
John R. Buck
Christopher W. Clark
William C. Cummings
Robert J. Dooling
David K. Mellinger
Arthur N. Popper
Annemarie Surlykke

Term to 2008
Whitlow W. L. Au
Kelly J. Benoit-Bird
W. Tecumseh Fitch
Dorian S. Houser
Lee A. Miller
Larry L. Pater
Hiroshi Riquimaroux
Peter M. Scheifele
James A. Simmons
Edward J. Walsh

Ex officio:
James M. Simmons, member of Medals and Awards Committee
Andrea M. Simmons, member of Membership Committee
Ann E. Bowles, member of ASACOS
Alison Stimpert, member of Student Council

Architectural Acoustics

Brandon D. Tinianov, Chair to 2010

Term to 2010
Russell L. Altermann
Russ Berger
Warren E. Blazier
Joseph F. Bridger
Norm Broner
Bennett M. Brooks
Steven M. Brown
Todd A. Busch
Richard H. Campbell
Andrew C. Carballeira
Emily L. Cross
F. M. del Solar Dorrego
Erin L. Dugan
Edward C. Duncan
Jesse J. Ehnert
Ronald T. Eligator
Michael Ermann
Ronald R. Freiheit
Klaus Genuit
Kenneth W. Good, Jr.
Lewis S. Goodfriend
Brad N. Gover
Pamela J. Harght
Mark A. Holden
K. Anthony Hoover
Jerald R. Hyde
Jodi Jacobs
Basel H. Jurdy
David W. Kahn
Brian F.G. Katz
Michael P. Kerr
Jonathan E. Kirchner
Brian J. Landsberger
Martha M. Larson
Jonathan S. Leonard
Gary S. Madaras
Benjamin E. Markham
David L. Moyer
Paul B. Ostergaard
Dennis A. Paoletti
Stephen W. Payne
Richard F. Riedel
Lauren Ronsse
Hari V. Savitala
Benjamin C. Seep
Neil A. Shaw
J. Michael Spencer
Rose Mary Su
Jeff D. Szymanski
Richard H. Talaske
Michelle Vigeant
Alicia J. Wagner
Lily M. Wang
Ewart A. Wetherill
George E. Winzer

Term to 2009
Nils-Ake Andersson
C. Walter Beamer, IV
Leo L. Beranek
Sergio Beristain
Jim X. Borzym
Erica Bowden
David T. Bradley
David Braslau
Todd L. Brooks
Courtney B. Burroughs
Paul T. Calamia
Alexander U. Case
William J. Cavanaugh
Dan Clayton
Jessica S. Clements
Elizabeth A. Cohen
David A. Conant
Damian Doria
John Erdreich
Robin S. Glosemeyer
Timothy E. Gulsrud

Byron W. Harrison
Robert D. Hellweg
Murray R. Hodgson
Ian B. Hoffman
Jin Yong Jeon
Jian Kang
Bertram Y. Kinzey, Jr.
Mendel Kleiner
Alexis D. Kurtz
Timothy W. Leishman
Jerry G. Lilly
Edward L. Logsdon
Peter A. Mapp
David E. Marsh
Gregory A. Miller
Matthew A. Nobile
Christian Nocke
Bruce C. Olson
Cornelius H. Overweg
Richard J. Peppin
Stephen D. Pettyjohn
Scott D. Pfeiffer
Norman H. Philipp
James E. Phillips
Joseph Pope
Jens Holger Rindel
Carl J. Rosenberg
Kenneth P. Roy
Hiroshi Sato
Melvin L. Saunders
Ron Sauro
Paul D. Schomer
Kevin P. Shepherd
Yasushi Shimizu
Gary W. Siebein
Abigail E. Stefaniw
Christopher A. Storch
Jason E. Summers
Louis C. Sutherland
Jiri Tichy
Nancy S. Timmerman
Gregory C. Tocci
Alfred C. C. Warnock
George P. Wilson
Ning Xiang

Term to 2008
Wolfgang Ahnert
Christopher N. Blair
John S. Bradley
Christopher N. Brooks
Angelo J. Campanella
Quinsan Ciao
Robert C. Coffeen
Peter D'Antonio
William Dohn
Timothy J. Foulkes
Richard D. Godfrey
Tyrone Hunter
Clare M. Hurtgen
J. Christopher Jaffe
Jeff P. Kwolkoski
Brad W. Lewis
Stephen J. Lind
David Lubman
Ralph T. Muehleisen
Boaz Rafaely
Jack E. Randorff
Jonathan Rathsam
H. Stanley Roller
Steven R. Ryherd
B. Schulte-Fortkamp
Noral D. Stewart
Michael Vorländer

Ex officio:
Ewart A. Wetherill, member of Medals and Awards
Ronald R. Freiheit, member of Membership Committee
George E. Winzer, member of ASACOS
Michelle Vigeant, member of Student Council

Biomedical Ultrasound/Bioresponse to Vibration

Michael R. Bailey, Chair to 2008

Term to 2010
Constantin-C. Coussios
Sheryl M. Gracewski
Ronald E. Kumon
Pascal P. Laugier
T. Douglas Mast
Thomas J. Matula
James A. McAteer
Robert J. McGough
James G. Miller
Todd W. Murray
Michael L. Oelze
Neil R. Owen
Ronald A. Roy
Preston S. Wilson
Suk Wang Yoon
Evgenia A. Zabolotskaya

Term to 2009
Emmanuel Bossy
Anthony J. Brammer
Robin O. Cleveland
Mostafa Fatemi
Yuri A. Ilinskii
Peter J. Kaczkowski
Jeffrey A. Ketterling
Vera A. Khokhlova
Oliver D. Kripfgans
James C. Lacefield
James A. McAteer
Yuri A. Pishchalnikov
Tyrone M. Porter

Term to 2008
John S. Allen
Whitlow W. L. Au
Paul E. Barbone
Charles C. Church
Gregory Clement
Floyd Dunn
E. Carr Everbach
Mark S. Hamilton
Christy K. Holland
R. Glynn Holt
Subha Maruvada
Wesley L. Nyborg
James A. Simmons
Andrew J. Szeri

Ex officio:
Lawrence A. Crum, member of the Medals and Awards Committee
E. Carr Everbach, member of the Membership Committee and member of ASACOS
Michael Canney, member of Student Council

Engineering Acoustics

Daniel M. Warren, Chair to 2009

Term to 2010
Mahlon D. Burkhard
Fernando Garcia-Osuna
Charles S. Hayden
Jan F. Lindberg
Elizabeth A. McLaughlin
Alan Powell
Roger T. Richards
Kenneth D. Rolt
Neil A. Shaw
James F. Tressler

Term to 2009
Stanley L. Ehrlich
Gary W. Elko
Robert D. Finch
Guillermo C. Gaunaurd
Thomas R. Howarth
Dehua Huang
Sung Hwan Ko
Victor Nedzelnitsky
James M. Powers
P. K. Raju
Stephen C. Thompson
James E. West
George S. K. Wong

Term to 2008
Steven R. Baker
David A. Brown
Stephen C. Butler
Robert D. Corsaro
Stephen E. Forsythe
Brian H. Houston
W. Jack Hughes
Robert M. Koch
L. Dwight Luker
Arnie L. Van Buren
Kenneth M. Walsh
Joseph F. Zalesak

Ex officio:
Kim C. Benjamin, member of Medals and Awards Committee
Thomas R. Howarth, member of Membership Committee
Mahlon D. Burkhard, member of ASACOS
Douglas Wilcox, member of Student Council

Musical Acoustics

James W. Beauchamp, Chair to 2008

Term to 2010
R. Dean Ayers
Judith C. Brown
Courtney B. Burroughs
John R. Buschert
Thomas M. Huber
Bozena Kostek
Barry Larkin
Daniel O. Ludwigsen
Thomas R. Moore
Thomas D. Rossing
David B. Sharp
Julius O. Smith
William J. Strong
Joe Wolfe

Term to 2009
Rolf Bader
Xavier Boutillon
Jonas Braasch
Murray D. Campbell
Rene E. Causse
Antoine J. Chaigne
Neville H. Fletcher
Nicholas J. Giordano
J. M. Harrison
William M. Hartmann
William L. Martens
James M. Pyne
Daniel A. Russell
Punita G. Singh
Sten O. Ternstrom
Paul A. Wheeler
Shigeru Yoshikawa

Term to 2008
George A. Bissinger
Annabel J. Cohen
James P. Cottingham
Diana Deutsch
Uwe J. Hansen
Roger J. Hanson
Peter L. Hoekje
James H. Irwin
Ian M. Lindevald
Stephen E. McAdams
Gary P. Scavone
Chris E. Waltham

Ex officio:
Uwe J. Hansen, member of Medals and Awards Committee
James P. Cottingham, member of Membership Committee
Ian M. Lindevald, member of ASACOS
Eric Dieckman, member of Student Council

Noise

Brigitte Schulte-Fortkamp, Chair to 2009

Term to 2010
Martin Alexander
Brian E. Anderson
Keith Attenborough
John P. Barry
Leo L. Beranek
Arno S. Bommer
Dick B. Botteldooren
Giovanni Brambilla
James O. Buntin
John C. Burgess
Jim R. Cummins
Kenneth A. Cunefare
Paul R. Donavan
Andre Fiebig
Ronald R. Freiheit
Klaus Genuit
David C. Haser
Gerald C. Lauchle
George C. Maling
Thomas R. Norris
John P. Seiler
Noral D. Stewart
Louis C. Sutherland
Jiri Tichy
D. Keith Wilson
Ning Xiang
Yuzhen Yang

Term to 2009
Sergio Beristain
Susan B. Blaeser

Erica E. Bowden
Bennett M. Brooks
Ilene J. Busch-Vishniac
Angelo J. Campanella
William J. Cavanaugh
Gilles A. Daigle
Patricia Davies
Damian J. Doria
Connor R. Duke
Jesse J. Ehnert
Tony F. W. Embleton
John Erdreich
David J. Evans
Bradford N. Gover
Robert D. Hellweg
Tyrone Hunter
William W. Lang
Richard H. Lyon
Alan H. Marsh
Ralph T. Muehleisen
William J. Murphy
Joseph Pope
Kenneth P. Roy
Kevin P. Shepherd
Scott D. Sommerfeldt
Kerrie G. Standlee
George S. K. Wong

Term to 2008
Elliott H. Berger
Ann E. Bowles
Frank H. Brittain
Steven M. Brown
Mahlon D. Burkhard
Robert D. Collier
Lawrence S. Finegold
Samir N. Y. Gerges
Richard D. Godfrey
Matthew V. Golden
Murray R. Hodgson
Jerry G. Lilly
Stephen J. Lind
David Lubman
George A. Luz
Matthew A. Nobile
Richard J. Peppin
Robert A. Putnam
Jack E. Randorff
Stephen I. Roth
Paul D. Schomer
Michelle E. Swearingen
Nancy S. Timmerman
Brandon D. Tinianov
Gregory C. Tocci
Lily M. Wang

Ex officio:
Nancy S. Timmerman, member of Medals and Awards Committee
John Erdreich, member of Membership Committee
Richard J. Peppin, member of ASACOS
Connor R. Duke, member of Student Council

Physical Acoustics

Murray S. Korman, Chair to 2010

Term to 2010
David T. Blackstock
David A. Brown
John A. Burkhardt
Kerry W. Commander
Bruce C. Denardo
Kent L. Gee
Logan E. Hargrove
D. Kent Lewis
Julian D. Maynard
Albert Migliori
James G. Miller
George Mozurkewich
Lev A. Ostrovsky
Andrea Prosperetti
Neil A. Shaw
Victor W. Sparrow
Richard Stern
Michelle E. Swearingen
Roger M. Waxler

Term to 2009
Anthony A. Atchley
Henry E. Bass
Yves H. Berthelot
James P. Chambers
Charles C. Church
Nico Declercq
Kenneth G. Foote
Mark F. Hamilton
David I. Havelock
Philip L. Marston
Peter H. Rogers
Ronald A. Roy
James M. Sabatier
Philip S. Spoor
Larry A. Wilen
D. Keith Wilson
Evgenia A. Zabolotskaya

Term to 2008
Robert T. Beyer
Robin O. Cleveland
Lawrence A. Crum
Kenneth E. Gilbert
Robert A. Hiller
R. Glynn Holt
Bart Lipkens
Thomas J. Matula
Ralph T. Muehleisen
Harry Simpson
John S. Stroud
Richard L. Weaver
Preston S. Wilson

Ex officio:
Thomas J. Matula, member of Medals and Awards Committee
Steven L. Garrett, member of Membership Committee
Richard Raspet, member of ASACOS
Todd A. Hay, member of Student Council

Psychological and Physiological Acoustics

Elizabeth A. Strickland, Chair to 2008

Term to 2010
Sid P. Bacon
Qian-Jie Fu
Ruth Y. Litovsky
Andrew J. Oxenham
Robert A. Lutfi
Kim S. Schairer
Christopher Shera
Edward J. Walsh
Beverly A. Wright

Term to 2009
Katherine H. Arehart

Richard Freyman
Amy R. Horwitz
Jody Kreiman
Glenis R. Long
Enrique A. Lopez-Poveda
Robert S. Schlauch
Stanley E. Sheft

Term to 2008
Michael A. Akeroyd
Alain de Cheveigne
Brent W. Edwards
John H. Grose
Michael Heinz
Brenda Lonsbury-Martin
William P. Shofner
Lynne A. Werner

Ex officio:
William M. Hartmann, member of the Medals and Awards Committee
Lynne A. Werner, member of Membership Committee
Brent W. Edwards, member of ASACOS
Suzanne P. Carr, member of Student Council

Signal Processing in Acoustics

David H. Chambers, Chair to 2009

Term to 2010
Alireza A. Dibazar
Gary W. Elko
Kassiani Kotsidou
Patrick J. Loughlin
Alan W. Meyer
Daniel J. Sinder
David C. Swanson
Robert C. Waag
Preston S. Wilson
Lixue Wu

Term to 2009
James V. Candy
William M. Carey
Leon Cohen
Geoffrey S. Edelson
Stanley L. Ehrlich
Brian Ferguson
Paul J. Gendron
Peter Gerstoft
William M. Hartmann
Kevin D. Heaney
William S. Hodgkiss
Paul D. Hursky
John M. Impagliazzo
Patrick J. Loughlin
Jens M. Meyer
Joe W. Posey
James C. Preisig
Brian Rapids
Edmund J. Sullivan

Term to 2008
Frank A. Boyle
Joe A. Clark
R. Lee Culver
David J. Evans
David M. Fromm
Howard A. Gaberson
David I. Havelock
Jean-Pierre Hermand
George E. Ioup
Juliette Ioup
Matti A. Karjalainen
Sean K. Lehman
Lance L. Locey
Zoi-Heleni Michalopoulou
Brian B. Monson
Joseph Pope
Randall W. Smith
Kyriakos Tsiappoutas
James E. West
George S. K. Wong
Ning Xiang

Ex officio:
William J. Carey, member of Medals and Awards Committee
David I. Havelock, member of Membership Committee
Charles F. Gaumond, member of ASACOS
John H. Camin, member of Student Council

Speech Communication

Carol Espy-Wilson, Chair to 2010

Term to 2010
Augustine Agwuele
Patrice S. Beddor
Tessa C. Bent
Helen M. Hanson
Diane Kewley-Port
Jody E. Kreiman
Andrew J. Lotto
Shrikanth S. Narayanan
Dwayne Paschall
Christine H. Shadle
Rahul Shrivastav

Term to 2009
Jean E. Andruski
Lynne E. Bernstein
Ocke-Schwen Bohn
Suzanne E. Boyce
Ann R. Bradlow
Bruce R. Gerratt
Kenneth W. Grant
Paul E. Iverson
Benjamin R. Munson
Peggy B. Nelson
Mitchell S. Sommers
Brad H. Story
Joan E. Sussman

Term to 2008
Fredericka Bell-Berti
Ann R. Bradlow
Dani M. Byrd
Roger W. Chan
Alexander L. Francis
Kenneth W. Grant
Anders Lofqvist
Terrance M. Nearey
Douglas D. O'Shaughnessy
Joseph S. Perkell
Astrid Schmidt-Nielsen
Joan E. Sussman
Gary G. Weismer

Ex officio:
Fredericka Bell-Berti, member of Medals and Awards Committee
Jody Kreiman, member of Membership Committee
Shrikanth S. Narayanan, member of ASACOS
Jennell Vick, member of Student Council

Structural Acoustics and Vibration

Sean F. Wu, Chair to 2009

Term to 2010
Jeffrey E. Boisvert
Stephen C. Conlon
Linda P. Franzoni
Robert C. Haberman
Rudolph Martinez
Koorosh Naghshineh
Donald G. Pray
Michael F. Shaw

Term to 2009
Joseph M. Cuschieri
David Feit
Sabih I. Hayek
Philip L. Marston
James E. Phillips
Earl G. Williams

Term to 2008
Dean E. Capone
Joel Garrelick
Peter C. Herdic
Teik C. Lim
Thomas J. Royston
Angie Sarkissian
Richard L. Weaver
Jeffrey S. Vipperman

Ex officio:
Courtney B. Burroughs, member of Membership Committee
Mauro Pierucci, member of Medals and Awards Committee
Sabih I. Hayek, member of ASACOS
Micah Shepherd, member of Student Council

Underwater Acoustics

Kevin LePage, Chair to 2009

Term to 2010
Kyle M. Becker
David C. Calvo
Jee Woong Choi
Christian P. de Moustier
Stan E. Dosso
Steven I. Finette
Kenneth G. Foote
David Fromm
Christopher H. Harrison
Zoi-Heleni Michalopoulou
Tracianne B. Neilsen
Robert I. Odom
Marshall H. Orr
Gregory J. Orris
James C. Preisig
Martin Siderius
William L. Siegmann
Jixun Zhou

Term to 2009
Ralph N. Baer
John R. Buck
Chi-Fang Chen
David R. Dowling
Roger C. Gauss
Frank S. Henyey
Paul C. Hines
Chen-Fen Huang
Marcia J. Isakson
Finn B. Jensen
Sunwoong Lee
James H. Miller
John R. Preston
Purnima Ratilal
Karim G. Sabra
John B. Schneider
Ralph A. Stephen
Alexander G. Voronovich
Kevin L. Williams
Lisa M. Zurk

Term to 2008
Juan I. Arvelo, Jr.
Pierre-Philippe Beaujean
Shira L. Broschat
Geoffrey F. Edelmann
Peter Gerstoft
John H. Glattetre
Brian T. Hefner
Jean-Pierre Hermand
Charles W. Holland
John C. Osler
Kevin B. Smith
Brian J. Sperry
Christopher T. Tindle
Alexandra I. Tolstoy

Ex officio:
Henrik Schmidt, member of Membership Committee
Eric I. Thorsos, member of Medals and Awards Committee
Robert M. Drake, member of ASACOS
Andrew Ganse, member of Student Council

Administrative Committees 2007-2008

Archives and History

Julian D. Maynard, Chair to 2010

Term to 2010
Henry E. Bass
Carol Y. Espy-Wilson
E. Carr Everbach
William W. Lang
Richard Stern
David C. Swanson

Term to 2009
Jont B. Allen
Ralph R. Goodman
David I. Havelock
Wesley L. Nyborg
Richard J. Peppin
William J. Strong

Term to 2008
Anthony A. Atchley
Leo L. Beranek
William J. Cavanaugh
Steven L. Garrett
Logan E. Hargrove
Allan D. Pierce
Victor W. Sparrow

Audit

Diane Kewley-Port, Chair to 2008

Term to 2009
Wayne M. Wright

Term to 2010
Michael R. Stinson

Books[+]

David L. Bradley, Chair to 2008

Term to 2010
Richard Stern
Brandon D. Tinianov

Term to 2009
Juan I. Arvelo
Jerry H. Ginsberg
Philip L. Marston

Term to 2008
James P. Cottingham
Nancy S. McGarr
Jeffrey A. Nystuen
Neil A. Shaw
Emily A. Tobey

Allan D. Pierce, Editor-in-Chief, ex officio

College of Fellows Steering

Janet M. Weisenberger, Chair to 2010

Term to 2007
Peter G. Cable
M. David Egan
Uwe J. Hansen
Diane Kewley-Port
Thomas D. Rossing

Term to 2009
Thomas J. Matula
Scott D. Sommerfeldt
Stephen C. Thompson
Beverly A. Wright

Term to 2008
Stanley L. Ehrlich
E. Carr Everbach

William J. Cavanaugh, ex officio as past Chair
Richard H. Lyon, ex officio as past Chair

Education in Acoustics

James M. Sabatier, Chair to 2009

Term to 2007
Henry E. Bass
George A. Bissinger
David A. Brown
Stanley A. Cheyne
Robert D. Collier
Lawrence A. Crum
Corinne M. Darvennes
Bruce C. Denardo
Margaritis S. Fourakis
Carl K. Frederickson
Carole E. Gelfer
R. Glynn Holt
Daniel O. Ludwigsen
Sharon Y. Manuel
Philip L. Marston
Ralph T. Muehleisen
Andrew A. Piacsek
Thomas D. Rossing
Ronald A. Roy
Dawn R. Schuette
Scott D. Sommerfeldt
William Thompson, Jr.
Robert A. Walkling
George S. K. Wong

Term to 2009
William A. Ahroon
Takayuki Arai
Anthony A. Atchley
Fredericka Bell-Berti
Suzanne E. Boyce
Robert D. Celmer
Annabel J. Cohen
E. Carr Everbach
Thomas B. Gabrielson
Steven L. Garrett
Kent L. Gee
Uwe J. Hansen
Katherine S. Harris
Elizabeth S. Ivey
Joie P. Jones
Amy T. Neel
P. K. Raju
Deborah M. Rekart
Daniel A. Russell
M. Roman Serbyn
Victor W. Sparrow
Emily A. Tobey

Term to 2008
David T. Blackstock
Courtney B. Burroughs
Robin O. Cleveland
Kenneth A. Cunefare
D. Michael Daly
Mary Florentine
Logan E. Hargrove
Mardi C. Hastings
Peter L. Hoekje
Darrell R. Jackson
Michel T. T. Jackson
Murray S. Korman
Luc Mongeau
Neil A. Shaw
Kevin B. Smith
Ralph A. Stephen
James E. West
Wayne M. Wright

Ethics and Grievances

Janet M. Weisenberger, Chair to 2008

Term to 2008
William J. Cavanaugh
Gerald L. D'Spain
Barbara G. Shinn-Cunningham

International Research and Education

David T. Blackstock, Chair to 2010

Term to 2010
Malcolm J. Crocker
Samir N. Y. Gerges
Konstantin A. Naugolnykh
Michael Vorländer

Term to 2009
Gilles A. Daigle
Lily M. Wang
Suk Wang Yoon

Term to 2008
Sergio Beristain
William M. Hartmann
Vera A. Khokhlova
Brigitte Schulte-Fortkamp

Investments

William A. Yost, Chair to 2010

Term to 2009
Ilene J. Busch-Vishniac

Term to 2008
Lawrence A. Crum
Richard H. Lyon
David Feit, Treasurer, ex officio

Medals and Awards

David L. Bradley, Chair to 2008

Term to 2010

Fredericka Bell-Berti	Speech Communication
Kim C. Benjamin	Engineering Acoustics
William M. Carey	Signal Processing in Acoustics
Uwe J. Hansen	Musical Acoustics
Peter F. Worcester	Acoustical Oceanography

Term to 2009

Lawrence A. Crum	Biomedical Ultrasound/Bioresponse to Vibration
William M. Hartmann	Psychological and Physiological Acoustics
Thomas J. Matula	Physical Acoustics
Nancy S. Timmerman	Noise

Term to 2008

James A. Simmons	Animal Bioacoustics
Mauro Pierucci	Structural Acoustics and Vibration
Eric I. Thorsos	Underwater Acoustics
Ewart A. Wetherill	Architectural Acoustics

Meetings—June 2007–November 2007

Clark S. Penrod, Chair to 2008
Whitlow W. L. Au, Fall 2006, Honolulu
Fred C. DeMetz, Fall 2007, New Orleans
George A. Frisk, Vice President
James H. Miller, Spring 2006, Providence
Elaine Moran, ASA Office Manager, ex officio
Charles E. Schmid, Executive Director, ex officio
Scott D. Sommerfeldt, Spring 2007, Salt Lake City
Victor W. Sparrow, Vice President-Elect
William A. Yost, Spring 2008, Paris
vacant, Fall 2008

November 2007–July 2008

Clark S. Penrod, Chair to 2008
Whitlow W. L. Au, Fall 2006, Honolulu
Fred C. DeMetz, Fall 2007, New Orleans
George V. Frisk, Vice President
Elaine Moran, ASA Office Manager, ex officio
Charles E. Schmid, Executive Director, ex officio
Scott D. Sommerfeldt, Spring 2007, Salt Lake City
Victor W. Sparrow, Vice President-Elect
William A. Yost, Spring 2008, Paris
vacant, Fall 2008
Lisa Zurk, Spring 2009

Membership

Peter H. Rogers, Chair to 2009

Term to 2010

Kenneth G. Foote	Acoustical Oceanography
Ronald R. Freiheit	Architectural Acoustics
Steven L. Garrett	Physical Acoustics
David I. Havelock	Signal Processing in Acoustics
Henrik Schmidt	Underwater Acoustics

Term to 2009

James P. Cottingham	Musical Acoustics
Thomas R. Howarth	Engineering Acoustics
Jody Kreiman	Speech Communication
Andrea M. Simmons	Animal Bioacoustics
Lynne E. Werner	Psychological and Physiological Acoustics

Term to 2008

Courtney B. Burroughs	Structural Acoustics and Vibration
E. Carr Everbach	Biomedical Ultrasound/Bioresponse to Vibration
John Erdreich	Noise

Panel on Public Policy

Edward J. Walsh, Chair to 2010

Term to 2010
Angelo J. Campanella
Lawrence A. Crum
Ellen Livingston
James H. Miller

Term to 2009
Mardi C. Hastings
David Lubman
William A. Yost

Term to 2008
William M. Hartmann
Sabih I. Hayek
Peggy B. Nelson
Victor W. Sparrow

Anthony A. Atchley, ex officio as immediate Past President
George V. Frisk, ex officio as Vice President
Charles E. Schmid, ex officio as Executive Director
Paul D. Schomer, ex officio as Standards Director

Public Relations

Geoffrey E. Edelmann, Chair to 2009

Term to 2010
Kelly J. Benoit-Bird
Diana Deutsch
E. Carr Everbach
Christy K. Holland

Brenda L. Lonsbury-Martin
James H. Miller
Joe W. Posey
Barbara Shinn-Cunningham
Stephen C. Thompson

Term to 2009
Paul A. Baxley
Ann E. Bowles
Paul D. Hursky
Jack E. Randorff
Barbara J. Sotirin
Lora J. Van Uffelen
Kathleen E. Wage

Term to 2008
Katherine H. Kim
Ellen S. Livingston
Andrew A. Piacsek
Brigitte Schulte-Fortkamp

Allan D. Pierce, Editor-in-Chief, ex officio
Elaine Moran, ASA Office Manager, ex officio
Charles E. Schmid, Executive Director, ex officio
Thomas D. Rossing, Echoes Editor, ex officio

Publication Policy

Mark F. Hamilton, Chair to 2009

Term to 2010
Charles C. Church
Mardi C. Hastings

Term to 2009
Jont B. Allen
David I. Havelock
Brenda L. Lonsbury-Martin

Term to 2008
Diane Dalecki
James F. Lynch
Mark F. Hamilton, President-Elect, ex officio
Allan D. Pierce, Editor-in-Chief, ex officio

Regional Chapters

Juan I. Arvelo, Cochair to 2008
Elizabeth A. McLaughlin, Cochair to 2008

Micah Shepherd	Brigham Young Univ. Student Chapter
Angelo J. Campanella	Central Ohio
Robert M. Keolian	Central Pennsylvania
Ernest M. Weiler	Cincinnati
Rebecca Mercuri	Delaware Valley
Gary W. Siebein	Florida
Timothy J. Foulkes	Greater Boston
Michael J. Anderson	Inland Northwest
Andy Miller	Univ. of Kansas Student Chapter
Neil A. Shaw	Los Angeles
Hari S. Paul	Madras, India
Sergio Beristain	Mexico City
Roger T. Richards	Narragansett
Michelle Vigeant	Univ. of Nebraska Student Chapter
Richard F. Riedel	New York
George A. Bissinger	North Carolina
Peter F. Assmann	North Texas
James R. Angerer	Northwest
David Lubman	Orange County
Paul A. Baxley	San Diego
David Braslau	Upper Midwest
Juan I. Arvelo	Washington, D.C.
Thomas M. Disch	Wisconsin

James M. Sabatier, Chair, Education in Acoustics, ex officio
David Feit, Treasurer, ex officio
Connor Duke, Student Council representative, ex officio

Prizes and Special Fellowships

Wayne M. Wright, Chair to 2009

Term to 2010
Anthony A. Atchley
Constantine Trahiotis

Term to 2009
Fredericka Bell-Berti
James E. West

Term to 2008
Uwe J. Hansen

Rules and Governance

William M. Hartmann, Chair to 2008

Term to 2010
William J. Cavanaugh
Floyd Dunn

Term to 2009
Elaine Moran
Charles E. Schmid

Term to 2008
Ilene J. Busch-Vishnaic
Tony F. W. Embleton
Richard H. Lyon

Standards

Executive Committee
Paul D. Schomer, Chair (Standards Director)
Robert D. Hellweg, Vice Chair
Susan B. Blaeser, Standards Manager, ex officio

S1 Representation
Philip J. Battenberg, Chair S1 and ASA rep. on S1
Richard J. Peppin, Vice Chair S1
Alan H. Marsh, ASA rep. on S1
Paul D. Schomer, ASA alternate rep. on S1

S2 Representation
Ronald L. Eshleman, Chair S2
Ali T. Herfat, Vice Chair S2
Sabih I. Hayek, ASA rep. on S2
Bruce E. Douglas, ASA alternate rep. on S2

S3 Representation
Craig A. Champlin, Chair S3 and ASA rep. on S3
David A. Preves, Vice Chair S3
Mahlon D. Burkhard, ASA alternate rep. on S3

S12 Representation
Robert D. Hellweg, Chair S12
William J. Murphy, Vice Chair S12
Bennett M. Brooks, ASA rep. on S12
David Lubman, ASA alternate rep. on S12

International TAGs (ex officio)
Paul D. Schomer, Chair, U.S. TAG for ISO/TC 43 and ISO/TC 43/SC1
David J. Evans, Chair, U.S. TAG for ISO/TC 108
David J. Evans, Chair, U.S. TAG for ISO/TC 108
Victor A. Nedzelnitsky, U.S. Technical Advisor for IEC/TC 29

ASA Technical Committee Representatives
George V. Frisk, Chair, Technical Council, ex officio
Anthony P. Lyons, Acoustical Oceanography
Ann E. Bowles, Animal Bioacoustics
George E. Winzer, Architectural Acoustics
E. Carr Everbach, BiomedicalUltrasound/Bioresponse to Vibration
Mahlon D. Burkhard, Engineering Acoustics
Ian M. Lindevald, Musical Acoustics
Richard J. Peppin, Noise
Richard Raspet, Physical Acoustics
Brent W. Edwards, Psychological and Physiological Acoustics
Charles F. Gaumond, Signal Processing in Acoustics
Shrikanth S. Narayanan, Speech Communication
Sabih I. Hayek, Structural Acoustics and Vibration
Robert M. Drake, Underwater Acoustics

ASA Officers
David Feit, Treasurer, ex officio
Charles E. Schmid, Executive Director, ex officio

Past Chair of ASACOS (ex officio)
Tony F. W. Embleton

Associate Editors Standards News–JASA (ex officio)
Susan B. Blaeser, Paul D. Schomer, George S.K. Wong

Student Council

Michael Canney	Chair and Biomedical/Bioresponse
John Camin	Signal Processing in Acoustics
Suzanne P. Carr	Psychological and Physiological Acoustics
Eric Dieckman	Musical Acoustics
Connor R. Duke	Noise and Regional Chapters Committee Liaison
Andrew Ganse	Underwater Acoustics
Todd A. Hay	Physical Acoustics
Micah Shepherd	Structural Acoustics and Vibration
Alison Stimpert	Animal Bioacoustics
Lora J. van Uffelen	Acoustical Oceanography
Jennell C. Vick	Speech Communication
Michelle Vigeant	Architectural Acoustics
Douglas Wilcox	Engineering Acoustics

Tutorials

Lily Wang, Chair to 2009

Term to 2007
Paul E. Barbone
Micheal L. Dent
Michelle E. Swearingen

Term to 2009
Ann R. Bradlow
James V. Candy
James P. Chambers

Term to 2008
Kenneth A. Cunefare
David R. Dowling
Barbara G. Shinn-Cunningham
Charles E. Schmid, Executive Director, ex officio

Women in Acoustics

Lisa M. Zurk, Chair to 2009

Term to 2010
Helen M. Hanson
Marcia J. Isakson
Jennifer L. Miksis-Olds
Peggy B. Nelson

Term to 2009
Kathryn W. Hatlestad
Carolyn J. Richie

Term to 2008
Mardi C. Hastings
Brigitte Schulte-Fortkamp
Sophie Van Parijs
Lily M. Wang
Victor W Sparrow, ex officio as Vice President-Elect

Ad-Hoc Committees and Task Forces 2007–2008

JASA-EL Editorial Advisory Committee

D. Keith Wilson, Chair
Diana Deutsch
Anders Lofqvist
Brenda L. Lonsbury-Martin
Philip L. Marston
Andrew N. Norris
Allan D. Pierce
Ronald A. Roy
Michael R. Stinson

Task Force on Education Outreach
Peggy B. Nelson and James M. Sabatier, Cochairs
Fredericka Bell Berti
Uwe J. Hansen
Victor W. Sparrow

Task Force on ASA Meetings
William A. Yost, Chair
Gilles A. Daigle
George V. Frisk
Diane Kewley-Port
Donna L. Neff
Victor W. Sparrow
Janet M. Weisenberger

Task Force on the ASA Mission
Anthony A. Atchley, Chair
Mahlon D. Burkhard
Gilles A. Daigle
Judy R. Dubno
Paul D. Schomer
Stephen C. Thompson
Wayne M. Wright

Task Force on the ASA Webpage
Stephen C. Thompson, Chair
Susan B. Blaeser
Andrew Ganse
James H. Miller
Elaine Moran
Andrew Picasek

ACOUSTICAL STANDARDS NEWS

Susan B. Blaeser, Standards Manager
ASA Standards Secretariat, Acoustical Society of America, 35 Pinelawn Rd., Suite 114E, Melville, NY 11747 [Tel.: (631) 390-0215; Fax: (631) 390-0217; e-mail: asastds@aip.org]

George S. K. Wong
Acoustical Standards, Institute for National Measurement Standards, National Research Council, Ottawa, Ontario K1A 0R6, Canada [Tel.: (613) 993-6159; Fax: (613) 990-8765; e-mail: george.wong@nrc.ca]

American National Standards (ANSI Standards) developed by Accredited Standards Committees S1, S2, S3, and S12 in the areas of acoustics, mechanical vibration and shock, bioacoustics, and noise, respectively, are published by the Acoustical Society of America (ASA). In addition to these standards, ASA publishes catalogs of Acoustical Standards, both National and International. To receive copies of the latest Standards Catalogs, please contact Susan B. Blaeser.
Comments are welcomed on all material in Acoustical Standards News.
This Acoustical Standards News section in JASA, as well as the National and International Catalogs of Acoustical Standards, and other information on the Standards Program of the Acoustical Society of America, are available via the ASA home page: http://asa.aip.org.

Standards Meetings Calendar—National

The 154th ASA meeting will take place in New Orleans, LA, at the Sheraton New Orleans Hotel, 27 November through 1 December 2007 (note: Tuesday through Saturday meeting). More information, including online registration, hotel information, and a Call for Papers, can be found on the ASA website at http://asa.aip.org/meetings.html.

• ***Tuesday, 27 November 2007***

ASACOS Steering Committee

• ***Wednesday, 28 November 2007***

7:30 a.m.—ASA Committee on Standards (ASACOS) Meeting of the Committee that directs the Standards Program of the Acoustical Society.

9:15 a.m.—Standards Plenary Group (includes U.S. TAGs to ISO/TC 43, TC 43/SC 1, ISO/TC 108 and its subcommittees, and TC 29)

10:45 a.m.—Accredited Standards Committee S12, Noise

1:30 p.m.—Accredited Standards Committee S1, Acoustics

2:30 p.m.—Accredited Standards Committee, S3, Bioacoustics

4:00 p.m.—Accredited Standards Committee, S2, Mechanical Vibration and Shock

Standards Meetings Calendar—International

• ***22–26 October 2007***

ISO/TC108/SC 4 Human exposure to mechanical vibration and shock will meet at the Hotel Intercontinental Malta, St. Julians, Malta, along with its working groups 5, 9, 12, 13, and 14 and CEN/TC 231.

• ***19–23 May 2008***

IEC/TC 29 Electroacoustics will meet in Stockholm, Sweden, along with its working groups.

• ***20–24 May 2008***

ISO/TC 108/SC 5 Condition monitoring and diagnostics of machines will meet in Kyoto, Japan, along with its working groups.

• ***26–30 May 2008***

ISO/TC 43, Acoustics, and ISO/TC 43/SC 1, Noise, will meet in Borås, Sweden, along with their working groups.

Call for Participation!

The U.S. Technical Advisory Group to ISO/TC 108/SC 6, Vibration and shock generating systems, is seeking organizational members. Members may be companies, government agencies, or other organizations with a direct and material interest in this work. Members should be willing to nominate experts to work on international working groups, including necessary international travel. Membership fees vary depending on the size of the organization. Please contact Susan Blaeser for details at 631-390-0215.

Congratulations to Alan Marsh!

Alan H. Marsh, a long-time standards volunteer, has been recognized by the International Electrotechnical Commission (IEC) for his work as convenor of IEC/TC 29/WG 4, *Sound level meters*. Mr. Marsh was one of the 2007 recipients of the IEC 1906 award which was established by the IEC to honor technical experts who have contributed in an exceptional way to the work of the IEC. The three-part sound level meter standard (IEC 61672) developed in Mr. Marsh's working group is recognizd as one of the cornerstones of IEC/TC 29.

Photos from the Salt Lake City and San Antonio Meetings

Three Accredited Standards Committees, S1, S3, and S12, held their annual administrative meetings in Salt Lake City, UT, in the beginning of June, along with ten standards working groups. Accredited Standards Committee S2 held its annual meeting in conjunction with the 31st Annual Meeting of the Vibration Institute in San Antonio, TX, approximately one week later.

There are many opportunities to participate in the development of ANSI Standards. Working group membership is open to individuals with expertise in the subject and willingness to volunteer their time and knowledge. There is no cost to participate in standards working groups. Contact the Secretariat for details about the active working groups.

In Salt Lake City, plaques were awarded to Working Group Chairs upon the publication of new standards. In addition to those shown here, Philip Battenberg, new Chair of ASC S1, Acoustics, was presented with a plaque noting the completion of ANSI S1.40-2006 *American National Standard Specifications and Verification Procedures for Sound Calibrators*.

 0001-4966/2007/122(3)/1303/6/$23.00

Philip J. Battenberg,
new Chair of ASC S1,
Acoustics

We are also pleased to welcome Mr. David A. Preves, who is beginning his first term as Vice Chair of ASC S3, replacing Robert F. Burkard.

David A. Preves,
new Vice Chair of ASC S3,
Bioacoustics

Bob Hellweg presented Bennett Brooks with a plaque noting the publication of ANSI S12.55-2006 / ISO 3745:2003 *American National Standard Acoustics—Determination of sound power levels of noise sources using sound pressure—Precision methods for anechoic and hemi-anechoic rooms*.

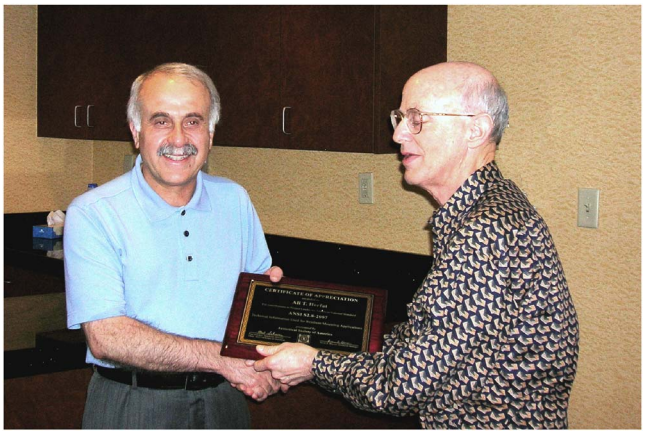

Paul Schomer presented Ali T. Herfat with a plaque noting the publication of ANSI S2.8-2007 *American National Standard Technical Information used for Resistent Mounting Applications*.

Bob Hellweg presented Richard J. Peppin with a plaque noting the publication of ANSI S12.55-2006 / ISO 3745:2003 *American National Standard Acoustics—Determination of sound power levels of noise sources using sound pressure—Precision methods for anechoic and hemi-anechoic rooms*.

S12/WG 15 Measurement and Evaluation of Outdoor Community Noise.

S12/WG 45 Measurement of Occupational Noise Exposure from Telephone Equipment.

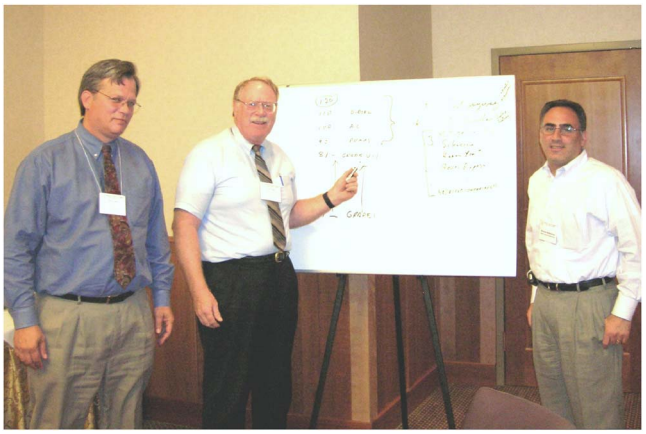

S12/WG 40 Measurement of the Noise Aboard Ships.

S1/WG 20 Measurement of Ground Impedance and Attenuation of Sound due to the Ground.

S12/WG 46 Acoustical Performance Criteria for Relocatable Classrooms.

S1/WG 26 High Frequency Calibration of the Pressure Sensitivity of Microphones.

The Salt Lake City meeting of S1 represented the final meeting chaired by John P. Seiler. Mr. Philip J. Battenberg has been appointed as the new Chair of S1. Mr. Richard J. Peppin began his term as Vice Chair of S1, replacing George S.K. Wong. Mr. Schomer also presented a plaque to Mr. Seiler thanking him for his service the last six years as both Chair and Vice Chair of S1.

Standards News from the United States

(Partially derived from *ANSI Reporter*, and *ANSI Standards Action*, with appreciation)

American National Standards Call for Comment on Proposals Listed

This section solicits comments on proposed new American National Standards and on proposals to revise, reaffirm, or withdraw approval of existing standards. The dates listed in parentheses are for information only.

ASA (ASC S12) (Acoustical Society of America)

NEW STANDARDS

BSR S12.68-200x, Methods of Estimating Effective A-Weighted Sound Pressure Levels when Hearing Protectors are Worn (New standard)

Specifies three methods, in ascending order of complexity of use and potential accuracy, for estimation of sound pressure levels that are effective when a hearing protector is worn: (1) noise level reduction statistic for use with A-weighting (NRSA), (2) noise level reduction statistic, graphical (NRSG), and (3) the octave-band method. Also specifies, in the case of NRSA and NRSG, that values will be presented for both 80th and 20th percentiles to reflect the range of attenuation that can be anticipated. (6 August 2007)

REAFFIRMATIONS

BSR S12.14-1992 (R200x), Methods for the Field Measurement of the Sound Output of Audible Public Warning Devices Installed at Fixed Locations Outdoors [Reaffirmation of ANSI S12.14-1992 (R2002)]

Describes relatively simple procedures for measuring and reporting certain properties of sounds produced by audible public warning devices. The methods described in this standard are for measurement of C-weighted sound level and for determining $\frac{1}{3}$ octave band containing fundamental frequency of tonal warning sounds produced by audible public warning devices at a distance of 100 ft from the device and at the mounted height of device. It is also used for measuring the maximum level of sound from a warning sound source at the heads of bystanders on the ground. (20 August 2007)

BSR S12.15-1992 (R200x), Acoustics—Portable Electric Power Tools, Stationary and Fixed Electric Power Tools, and Gardening Appliances—Measurement of Sound Emitted [Reaffirmation of ANSI S12.15-1992 (R2002)]

Describes relatively simple test procedures for the measurement of airborne sound from portable electric power tools, stationary and fixed electric power tools, and gardening appliances. Methods are given for the measurement of sound pressure levels and for the calculation of sound power levels. These methods may be used by manufacturers to specify, in part, the sound produced by their products. (20 August 2007)

BSR S12.16-1992 (R200x), Guidelines for the Specification of Noise of New Machinery [Reaffirmation of ANSI S12.16-1992 (R2002)]

Provides guidelines for obtaining noise level data from manufacturers of stationary equipment. The standard references existing American National Standards Institute, trade, and professional association measurement standards and techniques to request manufacturer noise level data. Appendices provide guidance for interpretation of the data received from the manufacturer. (20 August 2007)

BSR S12.43-1997 (R200x), Methods for Measurement of Sound Emitted by Machinery and Equipment at Workstations and Other Specified Positions [Reaffirmation of ANSI S12.43-1997 (R2002)]

Specifies three methods for measuring sound pressure levels from machinery and equipment, at a workstation and at other specified positions nearby, differentiated primarily by the acoustical environment in which they are made. Measurements are made by Method A: in an essentially free field over a reflecting plane, Method B: in any environment that meets certain qualification requirements specified, and Method C: in a semi-reverberant field for which the accuracy implied by measurements under Method A or B is not required. (20 August 2007)

BSR S12.44-1997 (R200x), Methods for Calculation of Sound Emitted by Machinery and Equipment at Workstations and Other Specified Positions from Sound Power Level [Reaffirmation of ANSI S12.44-1997(R2002)]

Provides a method for determining the emission sound pressure levels from the sound power level produced by all types of machinery and equipment at workstations and other specified locations. These sound pressure levels are, in general, less than those that would be measured when the machinery or equipment is operating in its normal surroundings where the environment may influence the measurement of an emission sound pressure level. (20 August 2007)

BSR S12.50-2002/ISO 3740-2000 (R200x), Acoustics—Determination of Sound Power Levels of Noise Sources—Guidelines for the Use of Basic Standards (a nationally adopted international standard) (Reaffirmation of ANSI S12.50-2002/ISO 3740-2000)

Gives guidance for the use of a series of nine International Standards describing various methods for determining sound power levels from all types of machinery and equipment. Provides brief summaries of these basic International Standards and guidance on the selection of one or more of these standards. Applies only to airborne sound. (20 August 2007)

BSR S12.51-2002/Part 1/ISO 3741:1999 (R200x), Acoustics—Determination of Sound Power Levels of Noise Sources Using Sound Pressure—Precision Method for Reverberation Rooms (a nationally adopted international standard) (Reaffirmation of ANSI S12.51-2002/Part 1/ISO 3741:1999)

Specifies a direct method and a comparison method for determining the sound power level that would be produced by a source operating in an environment at standard meteorological conditions corresponding to a characteristic impedance of $pc=400$ N3 (where p is the density of air and c is the speed of sound). Specifies: test room requirements, source location and general rules for operating conditions, and instrumentation and techniques for obtaining an estimate of mean-square sound pressure levels. (20 August 2007)

BSR S12.57-2002/ISO 3747-2000 (R200x), Acoustics—Determination of Sound Power Levels of Noise Sources Using Sound Pressure—Comparison Method *in situ* (a nationally adopted international standard) (Reaffirmation of ANSI S12.57-2002/ISO 3747-2000)

Specifies a method for determining the sound power levels of sound sources *in situ*, especially if nonmovable. A comparison method is used and all measurements are carried out in octave bands. The measurement uncertainty depends on the test environment. The measurement uncertainty is evaluated by comparing with an indicator describing the spatial sound distribution. The accuracy will either be that of an engineering method or a survey method. (20 August 2007)

BSR S12.60-2002 (R200x), Acoustical Performance Criteria, Design Requirements, and Guidelines for Schools (Reaffirmation of ANSI S12.60-2002)

Provides acoustical performance criteria, design requirements, and design guidelines for new school classrooms and other learning spaces. The standard may be applied when practicable to the major renovation of existing classrooms. These criteria, requirements, and guidelines are keyed to the acoustical qualities needed to achieve a high degree of speech intelligibility in learning spaces. Informative annexes are intended to aid in conform-

ing to the performance and design requirements, but do not guarantee conformance. Test procedures are provided. (9 July 2007)

ATIS (Alliance for Telecommunications Industry Solutions)

REVISIONS

BSR ATIS 0600315-200x, Voltage Levels for DC Powered Equipment Used in the Telecommunications Environment [Revision and redesignation of ANSI T1.315-2001 (R2006)]

Establishes requirements, and test procedures for voltage ranges and characteristics (i.e., transients and noise) associated with the input voltage of network telecommunications equipment powered from dc power systems in the telecommunications environment. (2 July 2007)

SCTE (Society of Cable Telecommunications Engineers)

REVISIONS

BSR/SCTE 62-200x, Measurement Procedure for Noise Figure (Revision of ANSI/SCTE 62-2002)

Defines a method of measurement for Noise Figure of active cable telecommunications equipment. It is intended for measurement of 75-ohm devices having type ″F″ or 5/8-24 KS connectors, and for the measurement of true broadband noise as opposed to narrowband disturbances. (13 August 2007)

Project Initiation Notification System (PINS)

ANSI Procedures require notification of ANSI by ANSI-accredited standards developers of the initiation and scope of activities expected to result in new or revised American National Standards. This information is a key element in planning and coordinating American National Standards. The following is a list of proposed new American National Standards or revisions to existing American National Standards that have been received from ANSI-accredited standards developers that utilize the periodic maintenance option in connection with their standards.

AMCA (Air Movement and Control Association)

BSR/AMCA 300-200x, Reverberant Room Method for Sound Testing of Fans (new standard)

The method of testing the sound power level of a fan employs standard sound measurement instrumentation, which is applied to rooms that are restricted to certain acoustic properties. The test setups are designed to represent the physical orientation of a fan as-installed. The test setup requirements in this standard establish the laboratory conditions necessary for a successful test. It is not recommended for field measurements. Project Need: To standardize the method for measuring the sound power level of a fan. Stakeholders: Laboratories, fan manufacturers, architects, building owners.

BSR/AMCA 320-200x, Laboratory Methods of Sound Testing of Fans Using Sound Intensity (new standard)

This standard determines sound power levels of a fan using sound intensity measurements on a measurement surface that encloses the sound source. Guidelines are provided on suitable test environment acoustical characteristics, the measurement surface, and the number of intensity measurements. Project Need: To establish a method of determining the octave band sound power levels of a fan. Stakeholders: Laboratories, fan manufacturers, architects, building owners.

Initiation of Canvasses

The following ANSI-accredited standards developers have announced their intent to conduct a canvass on the proposed American National Standard(s) listed herein in order to develop evidence of consensus for submittal to ANSI for approval as an American National Standard.

AMCA (Air Movement and Control Association)

BSR/AMCA 300-200x, Reverberant Room Method for Sound Testing of Fans (new standard)

BSR/AMCA 320-200x, Laboratory Methods of Sound Testing of Fans Using Sound Intensity (new standard)

Final actions on American National Standards

The standards actions listed below have been approved by the ANSI Board of Standards Review (BSR) or by an ANSI-Audited Designator, as applicable. Technical Reports have been registered in accordance with ANSI's *Procedures for the Registration of Technical Reports with ANSI*.

ASA (ASC S1) (Acoustical Society of America)

REAFFIRMATIONS

BSR S1.24 TR-2002 (R2007), ANSI Technical Report—Bubble Detection and Cavitation Monitoring (technical report)

This Technical Report provides descriptions of 25 techniques that have been found useful for detecting and characterizing small gas-filled cavities or bubbles, and for monitoring cavitation activity. Acoustical, optical, and electrical methods are among those employed for determining numbers, sizes, and spatial distributions of bubbles. Physical, chemical, and biological tests are used in monitoring cavitation activity. The procedures described have been applied to medicine, to oceanography, and to materials processing. Guidance is offered on the techniques that have been found suitable for specific applications. Advantages and disadvantages are discussed. References are provided for further reading. (Registered 24 June 2007)

ASA (ASC S2) (Acoustical Society of America)

REAFFIRMATIONS

ANSI S2.72-2002/Part 1 /ISO 2631-1-1997 (R2007), Mechanical vibration and shock—Evaluation of human exposure to whole-body vibration—Part 1: General requirements [Reaffirmation and redesignation of ANSI S3.18-1979 (R1999)]: 1 June 2007

ANSI S2.72-2003/Part 4 /ISO 2631-4-2001 (R2007), Mechanical vibration and shock—Evaluation of human exposure to whole-body vibration—Part 4: Guidelines for the evaluation of the effects of vibration and rotational motion on passenger and crew comfort in fixed-guideway transport systems (Reaffirmation and redesignation of ANSI S3.18-2003, Part 4 ISO 2631-4-2001): 24 May 2007

ANSI S2.73-2002/ISO 10819:1996 (R2007), Mechanical vibration and shock—Hand-arm vibration—Method for the measurement and evaluation of the vibration transmissibility of gloves at the plam of the hand (Reaffirmation and redesignation of ANSI S3.40-2002; ISO 10819:1996): 24 May 2007

ASA (ASC S3) (Acoustical Society of America)

REAFFIRMATIONS

ANSI S3.5-1997 (R2007), Methods for Calculation of the Speech Intelligibility Index [Reaffirmation of ANSI S3.5-1997 (R2002)]: 18 May 2007

ANSI S3.13-1987 (R2007), Mechanical Coupler for Measurement of Bone Vibrators [Reaffirmation of ANSI S3.13-1987 (R2002)]: 1 May 2007

ANSI S3.37-1987 (R2007), Preferred Earhook Nozzle Thread for Postauricular Hearing Aids [Reaffirmation of ANSI S3.37-1987 (R2002)]: 18 May 2007

ANSI S3.39-1987 (R2007), Specifications for Instruments to Measure Aural Acoustic Impedance and Admittance (Aural Acoustic Immittance) [Reaffirmation of ANSI S3.39-1987 (R2002)]: 18 May 2007

ANSI S3.42-1992 (R2007), Testing Hearing Aids with a Broad-Band Noise Signal [Reaffirmation of ANSI S3.42-1992 (R2002)]: 18 May 2007

REVISIONS

ANSI S3.4-2007, Procedure for the Computation of Loudness of Steady Sounds (Revision of ANSI S3.4-2005): 24 May 2007

ASTM (ASTM International)

REAFFIRMATIONS

ANSI/ASTM F2154-2001 (R2007), Specification for Sound-Absorbing Board, Fibrous Glass, Perforated Fibrous Glass Cloth Faced (Reaffirmation of ANSi/ASTM F2154-2001): 22 May 2007

Information Concerning Administrative Reaccreditations

ASC S1—Acoustics; ASC S2—Mechanical Vibration and Shock; ASC S3—Bioacoustics; ASC S12—Noise

The following Accredited Standards Committees (ASCs) have been administratively reaccredited at the direction of the Executive Standards Council, under revised operating procedures for documenting consensus on proposed American National Standards, effective 1 June 2007: ASC S1, Acoustics; ASC S2, Mechanical Vibration and Shock; ASC S3, Bioacoustics; and ASC S12, Noise.

Review of ISO Guide ISO/IEC Guide 76—Development of service standards—Recommendations for addressing consumer issues

The following is the scope of Draft ISO/IEC Guide 76. This Guide provides general guidance on the issues to be considered in standards for services. From this guidance, detailed standards may be prepared for any service. It offers a checklist (Clause 9) that may be used by consumer representatives and others participating in the process of standards development. Use of the checklist enables full consideration to be given to all matters of consumer interest, including the needs of children, older persons, persons with disabilities, and those from different ethnic and cultural heritages. This Guide is relevant to the full range of services, whether or not a formal contract is entered into or purchase price paid, but also has relevance for public or charitable services in which there is a consumer, user, or participant but not necessarily a purchase, for example, education, health, and care provision. (June 30, 2007)

Standards News from Abroad

Newly Published ISO and IEC Standards

Listed here are new and revised standards recently approved and promulgated by ISO—the International Organization for Standardization.

ISO Standards

ACOUSTICS (TC 43)

ISO 362-1:2007, Measurement of noise emitted by accelerating road vehicles—Engineering method—Part 1: M and N categories

ISO 5130:2007, Acoustics—Measurements of sound pressure level emitted by stationary road vehicles, $77.00

ISO 4869-3:2007, Acoustics—Hearing protectors—Part 3: Measurement of insertion loss of ear-muff type protectors using an acoustic test fixture

QUANTITIES, UNITS, SYMBOLS, CONVERSION FACTORS (TC 12)

ISO 80000-8:2007, Quantities and units—Part 8: Acoustics

MECHANICAL VIBRATION, SHOCK, AND CONDITION MOUNTING (TC 108)

ISO 8568:2007, Mechanical shock—Testing machines—Characteristics and performance

ISO Technical Reports

COMPRESSORS, PNEUMATIC TOOLS AND PNEUMATIC MACHINES (TC 118)

ISO/TR 27609:2007, Vibration in hand-held tools—Vibration measurement methods for grinders—Evaluation of round-robin test

ISO Draft Standards

ACOUSTICS (TC 43)

ISO/DIS 10302-1, Acoustics—Measurement of airborne noise emitted and structure-borne vibration induced by small air-moving devices—Part 1: Airborne noise measurement (12 August 2007)

ISO/DIS 389-9, Acoustics—Reference zero for the calibration of audiometric equipment—Part 9: Preferred test conditions for the determination of reference hearing threshold levels (18 August 2007)

REVIEWS OF ACOUSTICAL PATENTS

Lloyd Rice
11222 Flatiron Drive, Lafayette, Colorado 80026

The purpose of these acoustical patent reviews is to provide enough information for a Journal reader to decide whether to seek more information from the patent itself. Any opinions expressed here are those of reviewers as individuals and are not legal opinions. Printed copies of United States Patents may be ordered at $3.00 each from the Commissioner of Patents and Trademarks, Washington, DC 20231. Patents are available via the Internet at http://www.uspto.gov.

Reviewers for this issue:

ANGELO CAMPANELLA, *3201 Ridgewood Drive, Hilliard, Ohio 43026-2453*
GEOFFREY EDELMANN, *Naval Research Laboratory, Code 7145, 4555 Overlook Ave. SW, Washington, DC 20375*
JEROME A. HELFFRICH, *Southwest Research Institute, San Antonio, Texas 78228*
DAVID PREVES, *Starkey Laboratories, 6600 Washington Ave. S., Eden Prarie, Minnesota 55344*
CARL J. ROSENBERG, *Acentech Incorporated, 33 Moulton Street, Cambridge, Massachusetts 02138*
NEIL A. SHAW, *Menlo Scientific Acoustics, Inc., Post Office Box 1610, Topanga, California 90290*
ERIC E. UNGAR, *Acentech, Incorporated, 33 Moulton Street, Cambridge, Massachusetts 02138*
ROBERT C. WAAG, *Department of Electrical and Computer Engineering, University of Rochester, Rochester, New York 14627*

7,163,471

43.20.Px GOLF BALLS HAVING SOUND-ALTERED LAYERS AND METHODS FOR MAKING THEM

Hyun Jin Kim *et al.*, assignors to Taylor Made Golf Company, Incorporated
16 January 2007 (Class 473/378); filed 10 January 2003

Many golfers have reached the conclusion that their game will not improve, but that the sound they make while playing the game is still within their control. To this reviewer, this is similar to the profusion of ring tones for telephones, but, at least, most golfers use their equipment responsibly. Anyway, in this strictly prosaic patent, various formulations for the several and various covers used in a modern golf ball are described that are said to be able to alter the sound the ball makes when hit by a club. The various and sundry compounds that can be compounded to make a ball layer include nonionomeric materials (such as thermoplastic polyurethanes, polyamide nylons, 1,2-polybutadienes, and silicones), thermoplastic elastomers, and various ionomeric materials. The patent describes in detail these and other chemicals that can be used in these formulations. There is a comparison of four balls. The difference between the highest and lowest acoustic output is on the order of 1 dB.—NAS

7,201,882

43.25.Ts DEVICE FOR PRODUCING A PLASMA, IONIZATION METHOD, USE OF SAID METHOD AND PRODUCTION PROCESSES USING SAID DEVICE

Valentin Cesa, assignor to Clarq International (Societe Civile)
10 April 2007 (Class 422/186.04); filed 20 September 2001

After alluding to the works of many 19th and 20th Century physicists, and after coining the term ''harmonic evolution,'' the author provides 53 claims relating to combustion and incinerating devices comprising a resonant ''Fabry-Perot'' sound chamber **1**, which acoustically prepares the air

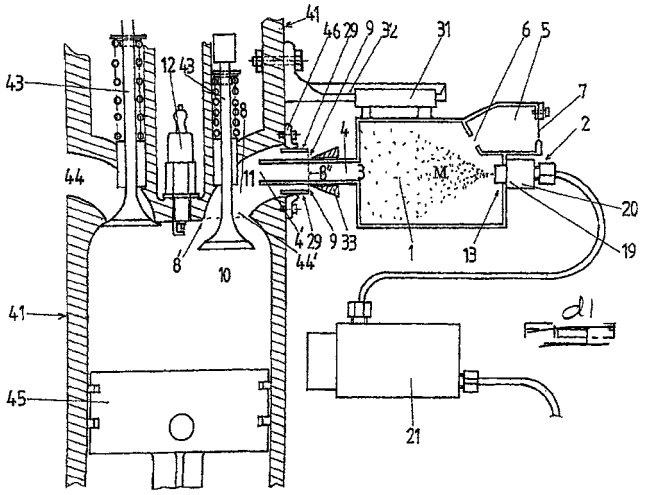

and material mixture **M**, **3** for combustion in ''soliton chamber'', **10**. Ionization is implied to occur somewhere in the system, but certainly via ignition aid **12**! Energy released is said to produce mechanical power for vehicle propulsion via a piston and cylinder (shown), or a turbine, or a ram jet, or a steam boiler. Air pollution is to be minimized by adjusting combustion aifflow.—AJC

7,190,637

43.30.Tg GUIDED UNDERWATER OBJECT

Benjamin Scott Evans and Richard John Gibson, assignors to Qinetiq Limited
13 March 2007 (Class 367/133); filed in United Kingdom 10 September 2003

An expendable/cheap unmanned undersea vehicle (UUV) is described that delivers payloads to a position guided by external means (e.g., a mother

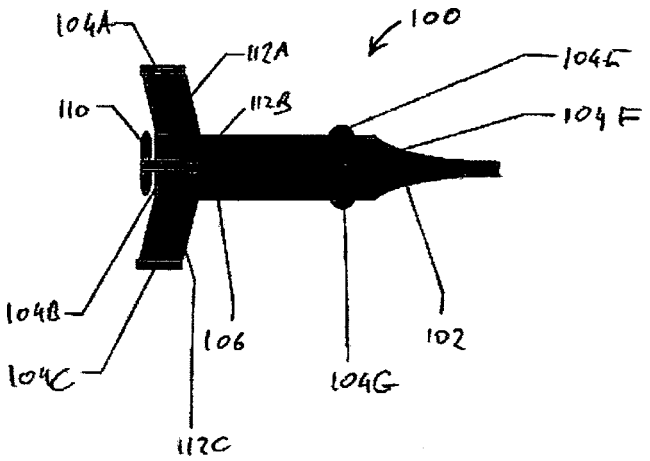

ship). In essence, four acoustic beams are shined around the desired drop zone and the UUV, which has no acoustically active navigational system of its own, attempts to remain within those four beams.—GFE

7,054,226

43.35.Yb METHOD AND APPARATUS FOR ECHOLOCATION

Robert Hickling, Huntington Woods, Michigan
30 May 2006 (Class 367/87); filed 10 May 2004

This ultrasound receiver consists of four microphones arranged in a tetrahedron. The receiver is to be packaged with a pulsed ultrasound transmitter ''for application of echolocation to robot guidance and assisting the blind.'' Recovering spatial source information from a 3D microphone array is fairly well known. Here, if the mics are thought of as located at alternate

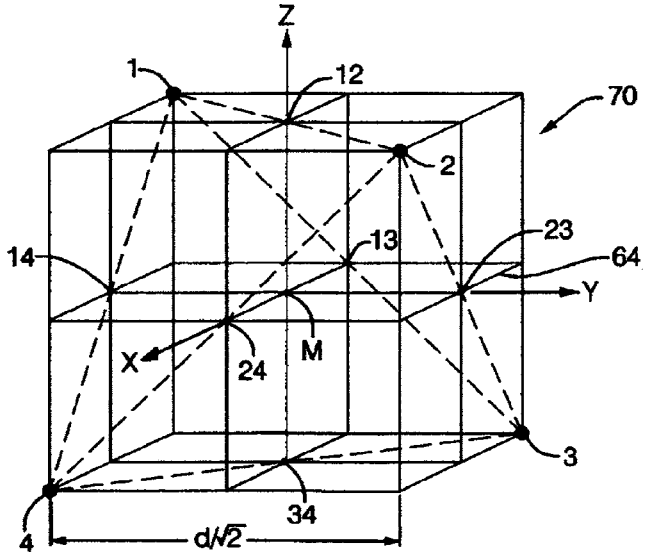

corners of a cube **1**, **2**, **3**, **4**, then the midpoints between the mics fall on the centers of the cube's six faces, **12**, **13**, **14**, **23**, **24**, **34**. In processing the microphone signals, timing and spectral signatures are recovered from the mic signals. The signals are also hetrodyned down to lower frequencies to recover precise amplitude information. The patent includes equations for the recovery of source locations based on these measurements.—DLR

7,054,228

43.35.Yb SOUND SOURCE LOCATION AND QUANTIFICATION USING ARRAYS OF VECTOR PROBES

Robert Hickling, Huntington Woods, Michigan
30 May 2006 (Class 367/124); filed 26 December 2003

This is another patent by the same author as United States Patent 7,054,226, reviewed above. Here, the same tetrahedral configuration of four ultrasound microphones is considered to be deployed in a large planar or

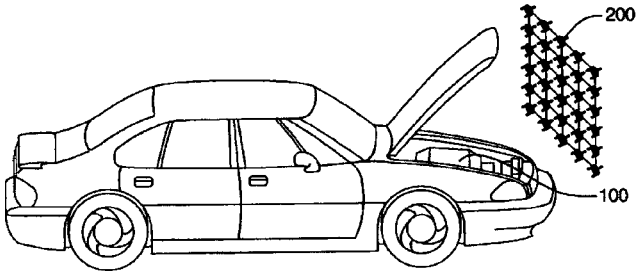

spherical array. Each element of the array at **200** is a cluster of four mics. Again, equations are provided for computing source information from the mic signals. Although issued together with the above patent, this one was actually filed five months earlier.—DLR

7,193,353

43.38.Ar OPERATING APPARATUS AND AN ELECTRIC INSTRUMENT

Osamu Miyazawa, assignor to Seiko Epson Corporation
20 March 2007 (Class 310/328); filed in Japan 3 April 2003

Those expecting a description of a new musical instrument will be disappointed by this patent, in which the authors describe a somewhat strange ''operating apparatus'' that converts linear piezoelectric oscillations of a plate **6** into rotary motion of assembly **5**. There is nothing new here save

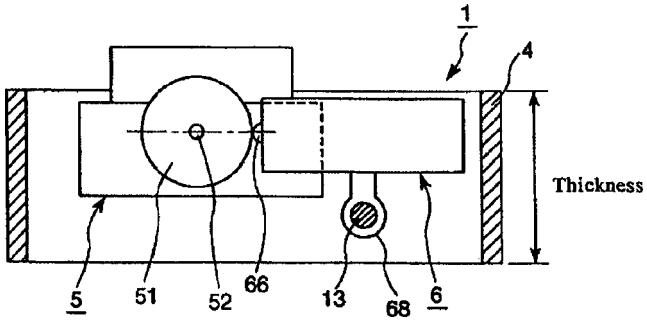

for the amount of space devoted to describing applications of this concept to various oscillating machines. The patent does describe some configurations of piezoelectric plates to generate in-plane and out-of-plane motions simultaneously that may be of interest to those in the field.—JAH

7,048,212

43.38.Fx SOUND ACTIVATED SAFETY SYSTEM FOR A REDUCTION MILL

Alan Carey, Royal Palm Beach, Florida
23 May 2006 (Class 241/34); filed 11 December 2003

During the operation of hammermill shredding equipment, such as a lawn/garden wood chipper, a serious condition can occur if nonshreddable material, such as a concrete or metal object, is fed into the chopper blades. This patent describes a system of acoustic sensors intended to detect the spectral signature of such nonshreddable material and to shut off or reverse

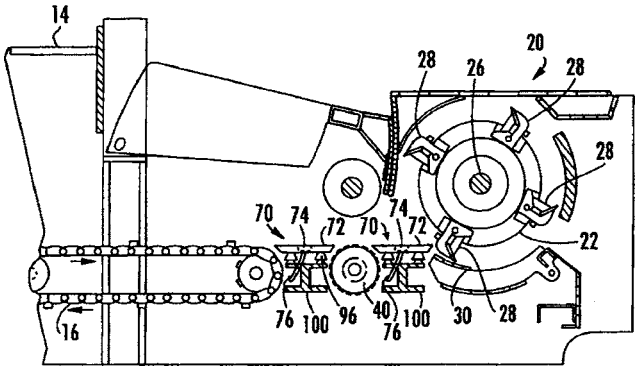

the conveyor belts feeding the chopper. One or more sensor platforms **72** include piezoelectric (PZE) pickup devices **74**. These are connected to an electronics unit, which includes a high-pass filter. The assumption is that harder materials would excite higher response frequencies in the PZE pickups. The filter passband is adjustable, as is an amplitude threshold detector, to allow the system to be tuned for maximum safety.—DLR

7,190,105

43.38.Fx SOUND OR ULTRASOUND SENSOR

Rolf Deserno and Helmut Pfeiffer, assignors to Endress + Hauser GmbH + Company KG
13 March 2007 (Class 310/322); filed in Germany 11 April 2002

This patent discloses a few innovations concerning the design of ultrasonic transducers for use in underwater ranging. The authors describe a level-sensing application that requires a narrow beam and good pulse response within a narrow bandwidth. The standard approach to backing a

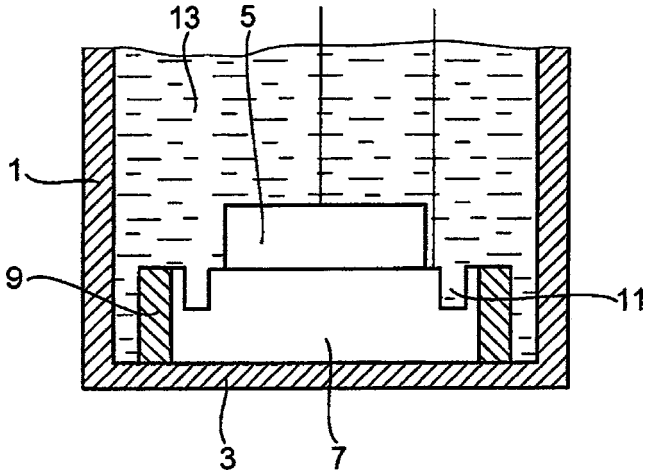

piezoelectric disc with a quarter-wave plate is improved on by using an etched plate **7** and a circumferential metal ring **9** that is said to decouple the transducer from the support and allow a narrower, more well-defined beam to be produced. The description is brief and lacking any real device measurements.—JAH

7,190,241

43.38.Rh ELASTIC WAVE APPARATUS

Yasuo Ebata and Osamu Kawachi, assignors to Fujitsu Media Devices Limited
13 March 2007 (Class 333/193); filed in Japan 2 June 2004

Cell phone protection against damage due to static-electric charges brought on by the user is achieved by a varistor layer **17** 1 – 10 μm thick on

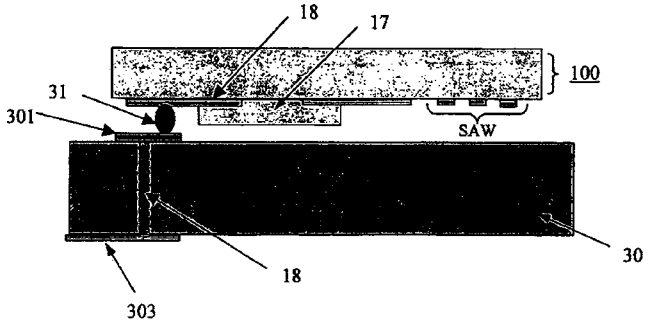

piezoelectric chip **100** between the terminal pads **18** and the package **30**.—AJC

7,193,617

43.38.Rh ACOUSTIC CONTACT DETECTING DEVICE

Shigeki Kanbara and Hiroshi Kaneda, assignors to Touch Panel Systems
20 March 2007 (Class 345/177); filed in Japan 30 June 1999

This patent discloses the techniques involved in detecting contact with an LCD screen. The glass cover of such a screen makes a good conductor of ultrasound, which can be used to detect contact (by impedance mismatch) with the glass. The authors describe some of the problems with fabricating such a device and making it user-proof. The novel concept here seems to be the use of a patterned metal diffraction grating to convert longitudinal vibrations from the transducers into surface waves that can detect a finger touch. In doing the conversion, the authors have eliminated the need for more complex and costly transducers and electrode configurations.—JAH

7,198,981

43.38.Rh VACUUM SEALED SURFACE ACOUSTIC WAVE PRESSURE SENSOR

Viorel V. Avramescu *et al.*, assignors to Honeywell International Incorporated
3 April 2007 (Class 438/107); filed 21 October 2004

Gas pressure **14** on diaphragm **11**, micromachined into quartz piezoelectric substrate **2**, changes the wave velocity of a SAW sensor placed on **2**

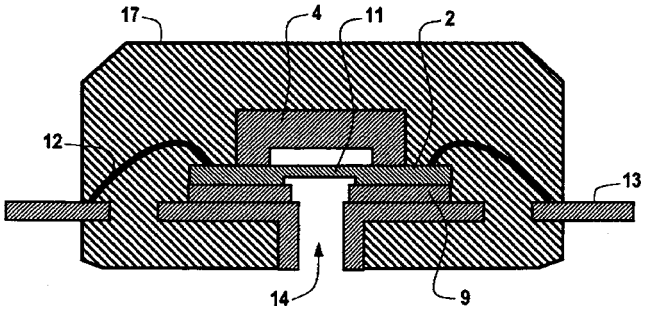

near **11**. Wafer cover **4** secures a vacuum over the sensor for absolute pressure measurement.—AJC

7,202,589

43.38.Rh TEMPERATURES STABLE SAW SENSOR WITH THIRD-ORDER ELASTIC CONSTANTS

Victor Alexandrovich Kalinin and Mark Lee, assignors to Transense Technologies PLC
10 April 2007 (Class 310/313 D); filed in United Kingdom 16 October 2001

A shaft-torque sensor is claimed with minimum error due to shaft temperature changes. It comprises two SAW devices, each aligned either 35°

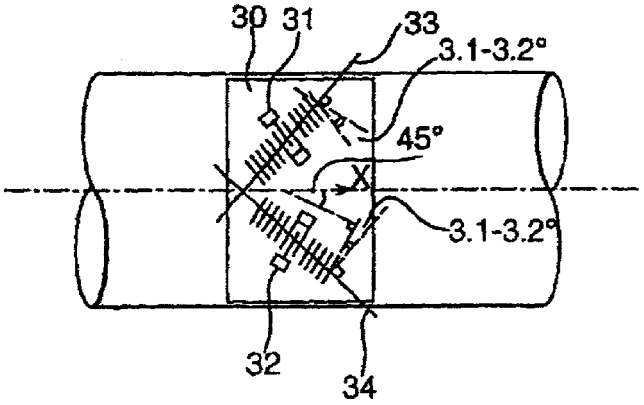

from the shaft center line or aligned 45° with an end reflector tilted a further 3.1°.—AJC

7,164,770

43.38.Tj SURROUND SOUND SPEAKER SYSTEM

Bernard Bottum, Macedonia, Ohio
16 January 2007 (Class 381/27); filed 5 September 2002

Many surround systems use small speakers to minimize visual impact. But small speakers are not suited for reproducing low frequencies. By using multicoil drivers **28**, **29** in the center channel **12** that are fed the combined low-pass signal in the range 100–200 Hz from the center, left, and right

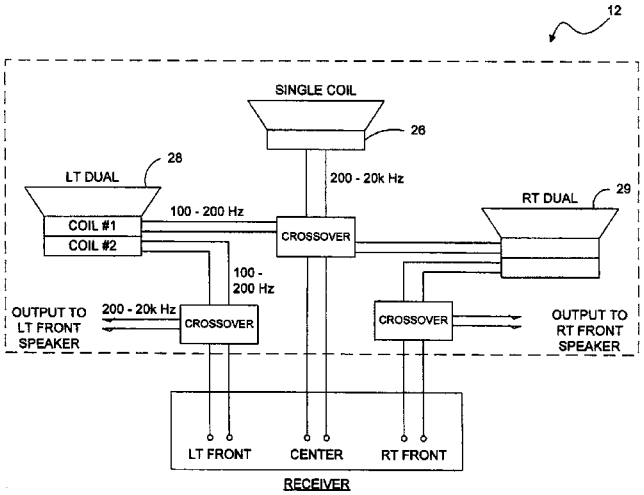

channels, only one loudspeaker unit needs to be large. This reviewer seems to recall, however, that the center channel is the one that usually is located in the most constrained space, either above or below the display device, while the left and right speakers have more room.—NAS

7,170,008

43.38.Tj AUDIO SIGNAL CABLE

Jay Victor, Redondo Beach, California
30 January 2007 (Class 174/110 R); filed 20 April 2006

For certain cable products, terms like "balanced high-, medium-, and low-frequency response" and "better sound definition" and statements like "if the conductor is too large, then high-frequency signal passage becomes difficult" and "skin effect is a challenging problem in that it commonly

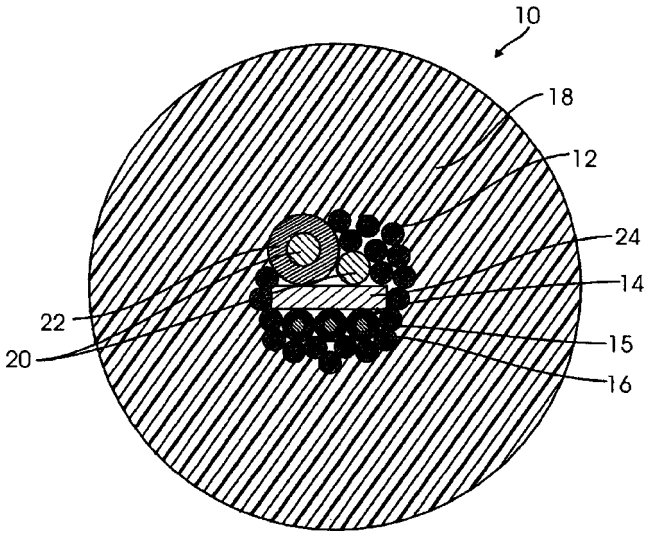

causes distortion and adversely affects signal transmission" are often seen in the literature. This patent contains these and other assertions, as well as a solution that uses different combinations of stranded **12**, circular solid **20**, tinsel **22**, and flat solid **24** wire types to mitigate problems that are said to exist in prior art cables, with no discussion of inductance and capacitance and the difference among phase, group, and signal velocity.—NAS

7,160,205

43.40.Dx GOLF CLUB HEAD

Akio Yamamoto, assignor to SRI Sports Limited
9 January 2007 (Class 473/345); filed in Japan 23 July 2002

Many golfers, it appears, have progressed to the point where, rather than concentrating on their stroke and their game, they are more concerned with the sound the club makes while striking the ball. By modifying the sole

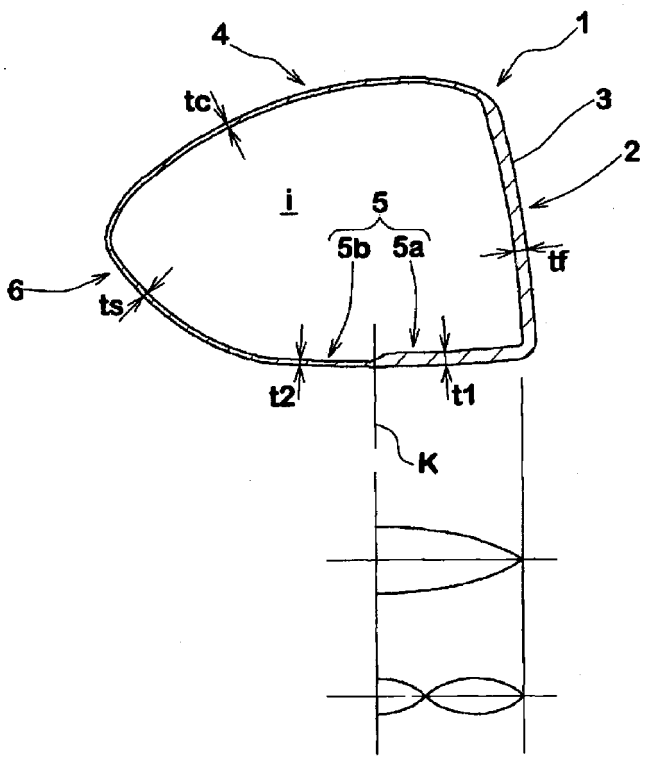

Modes of Vibration

5 of hollow club head **1**, it is possible to "produce ball hitting sounds whose maximum sound pressure level occurs at a relatively high frequency in spite of the large head volume of 355–450 cc." How this helps to make par is unclear, but the patent itself is clearly written.—NAS

7,191,073

43.40.Le BEARING ANOMALY DETECTION AND LOCATION

Kenneth Richard Astley *et al.*, assignors to Oxford Biosignals Limited
13 March 2007 (Class 702/56); filed 1 November 2005

Machinery vibrations are monitored and analyzed to identify novel tracked orders—tracked orders that are not present in machinery without defects—a "tracked order" being a vibration response associated with a specific machine component. The location of a defective bearing is determined by relating an identified novel tracked order to other tracked orders. For example, in a multishaft gas turbine, the spacing between the sidebands of a novel tracked order can be indicative of the shaft that is supported by the anomalous bearing. As a further example, the ratio between the novel tracked order and a tracked order produced by a shaft rotating in the anomalous bearing can be indicative of the part of the bearing that is faulty. The patent also describes suitable processing of data from a multitude of sensors, including neural networks that can "learn" anomaly identification.—EEU

7,191,637

43.40.Le METHOD FOR TESTING VIBRATION DAMPERS IN MOTOR VEHICLE

Reinhard Sonnenburg, assignor to ZF Friedrichshafen AG
20 March 2007 (Class 73/11.04); filed in Germany 29 April 2004

The characteristics of dampers installed in a vehicle are determined by subjecting the wheels to vibration via the road or a shaker and measuring the resulting vibrations of the wheel and vehicle body. A damper's spring constant and damping are calculated from essentially a two-degree-of-freedom model, taking account of the known wheel mass, the mass of the quarter of the vehicle near the wheel, and the known stiffness and damping of the tire. With suitable sensors installed in the vehicle the damper performance can be monitored as the vehicle travels along irregular road surfaces.—EEU

7,188,722

43.40.Tm ARTICLE CARRYING APPARATUS

Heizaburo Kato and Toshinao Kato, assignors to Sankyo Seisakusho Company
13 March 2007 (Class 198/750.8); filed in Japan 26 October 2004

This patent refers to "feeders" that line up articles in rows and transport them one at a time, with the transporting being accomplished by vibrating the surface that supports the articles in the vertical and axial directions. In order to reduce the vibration of the housing that results from its reaction to the feeding vibration, the housing is provided with a series of unbalanced rotors whose motions are phased so as to generate forces opposing the housing's motion.—EEU

7,192,014

43.40.Tm ACTIVE VIBRATION ISOLATION SUPPORT SYSTEM

Hirotomi Nemoto, assignor to Honda Motor Company, Limited
20 March 2007 (Class 267/140.14); filed in Japan 11 March 2004

Isolator **M** on axis **L** is connected to a vehicle engine via lug **20a**. The dead load and vibration are transferred by bolt **21** to elastic members **19**, **27**

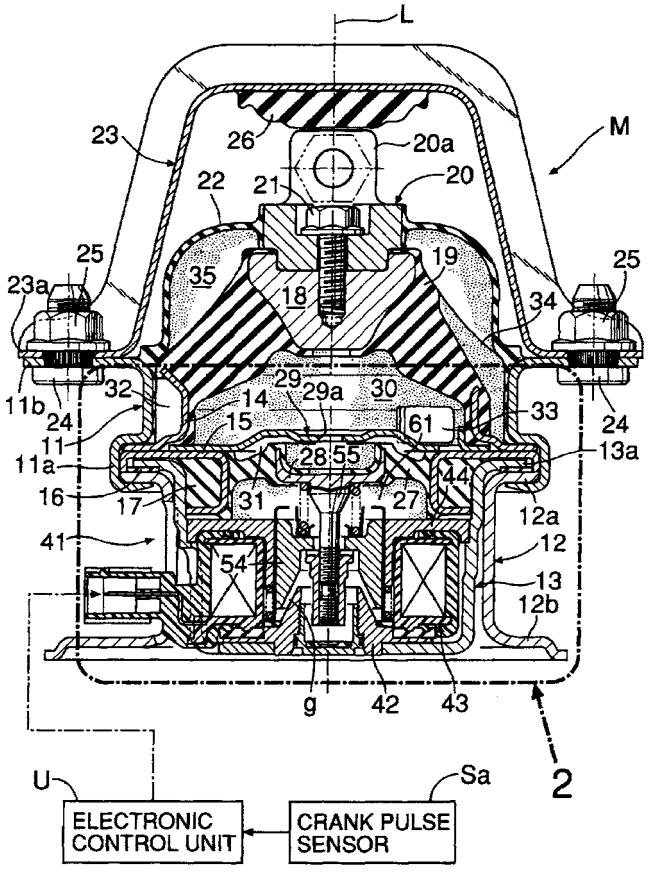

and are damped by fluid **30** and rod **55**, which is driven by coil **54** fed with current from active vibration controller **U**.—AJC

7,192,357

43.40.Tm DYNAMIC DAMPER WITH MULTIPLE DEGREE OF FREEDOM

Tetsuya Kawakami, assignor to Nissan Motor Company, Limited
20 March 2007 (Class 464/180); filed in Japan 12 February 2002

Reduction of the bending vibrations in a torque transmission tube is accomplished by mounting inside the tube a dynamic absorber that consists of an elongated mass whose two ends are supported on elastic elements. This absorber can attenuate vibrations at two frequencies: one by vibrating essentially laterally, the other by vibrating in a rocking mode.—EEU

7,194,398

43.40.Tm METHOD AND APPARATUS FOR DESIGNING AND DEVELOPING A VEHICULAR DAMPER

Takeshi Abe, assignor to Ford Global Technologies, LLC
20 March 2007 (Class 703/8); filed 13 March 2002

An apparatus, according to this patent, consists in essence of a prototype vehicular drive train, to which there is attached a controllable torque generator (in place of an engine). Between this torque generator and the drive shaft there is located a torsional assembly that has programmable frequency characteristics, representing a dynamic absorber. The torque generator can be made to simulate an internal combustion engine, and the effects of various dynamic absorber characteristics on the vibration and noise transmitted to the wheels can be observed by means of sensors attached to the wheels.—EEU

7,198,858

43.40.Tm METHOD OF VIBRATION DAMPING IN METALLIC ARTICLES

Mark H. Shipton and Sophoclis Patsias, assignors to Rolls-Royce PLC
3 April 2007 (Class 428/632); filed in United Kingdom 15 November 2002

Damping of metallic components, such as those of gas turbine engines, is accomplished by coating them with a ceramic and adding a metallic coating atop the ceramic. This results, in essence, in a constrained-layer damping arrangement, which not only can provide increased damping, but also a smooth surface and protection from erosion and particulate damage.—EEU

7,201,546

43.40.Tm MACHINE TOOL AND METHOD FOR COMPUTING ATTACHMENT POSITION OF BALANCER IN MACHINE TOOL

Kentaro Ichino *et al.*, assignors to Yamazaki Mazak Corporation
10 April 2007 (Class 409/165); filed in Japan 26 July 2004

A machine tool's rotary table on which the workpiece is supported tends to vibrate due to imbalance of the workpiece, leading to poor finish. Embodiments of this patent employ signals from vibration sensors on the rotary table for the automatic determination of where on the rotary table the machine tool operator should add counterbalance weights.—EEU

7,190,134

43.40.Vn TORSIONAL VIBRATION SUPPRESSING METHOD AND APPARATUS IN ELECTRIC MOTOR SPEED CONTROL SYSTEM

Naotake Shibata *et al.*, assignors to Kabushiki Kaisha Yaskawa Denki
13 March 2007 (Class 318/432); filed in Japan 2 December 2002

A control system is provided for suppression of the small-amplitude torsional vibrations of an electric motor due to the motor's pulsating torque or periodic load fluctuations, where the motor is connected to a machine via a flexible shaft. The deviation of the motor's speed from its mean speed is used to calculate a torque command that is applied to the motor. The control system takes account of the motor and load inertia, as well as of the rigidity of the shaft.—EEU

7,196,489

43.40.Vn ROTARY SHAFT CONTROL APPARATUS

Mitsuyuki Taniguchi and Keisuke Imai, assignors to Fanuc Limited
27 March 2007 (Class 318/652); filed in Japan 30 November 2004

This active control arrangement is intended for application to a machine tool or the like, where a rotating element is connected to a servo motor via a relatively flexible part. The output of an angular acceleration sensor that is attached to the rotating element and the signal produced by an angular velocity sensor attached to the motor are fed to a processor, which provides a control signal to the servo motor.—EEU

7,197,147

43.40.Vn COMPUTATIONALLY EFFICIENT MEANS FOR OPTIMAL CONTROL WITH CONTROL CONSTRAINTS

Thomas A. Millott *et al.*, assignors to Sikorsky Aircraft Corporation
27 March 2007 (Class 381/71.8); filed 27 February 2002

Active control of vibration and noise in the interior of a helicopter is achieved by the use of a plurality of sensors and actuators. The sensor outputs are fed via a filter to a controller, which generates control signals based on the sensor outputs and on a control weighting. The weighting is adjusted with time so that the best performance, as measured by a least-squares performance index, is always obtained, subject to actuator saturation constraints.—EEU

7,188,496

43.40.Yq METHOD FOR DETECTING THE VIBRATIONS OF A ROLL STAND

Michel Abi Karam and Emilio Lopez Sabio, assignors to Vai Clecim
13 March 2007 (Class 72/13.4); filed in France 12 November 2004

A sheet-metal rolling-mill stand **1** vibration sensor **64** is claimed that detects movements of the force adjusting piston **62** via a digital ruler within **S** and **64**. Vibrations in the 100–200 Hz range are monitored by a controller.

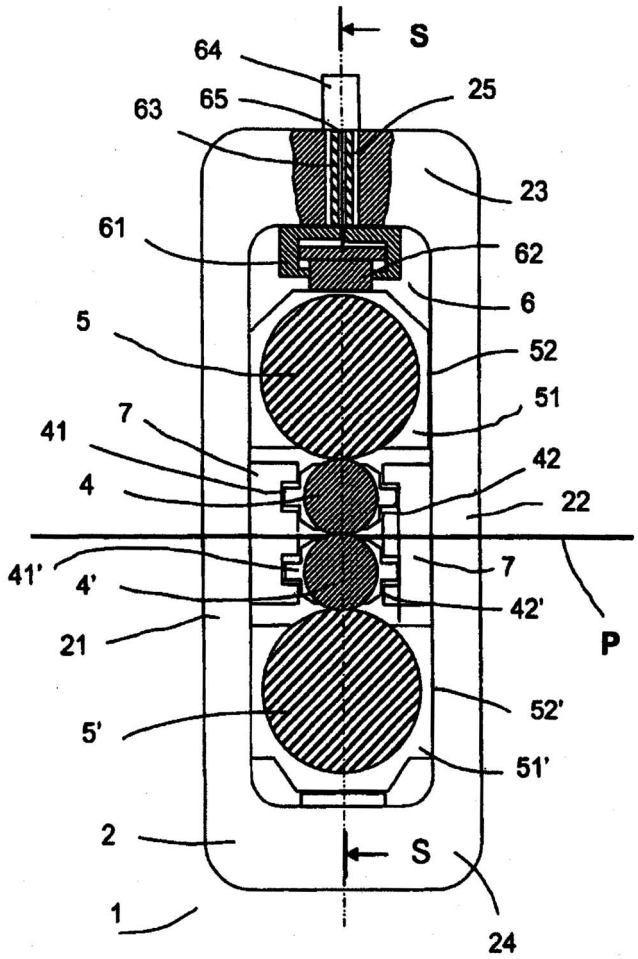

A processor counts the number of times that a predetermined displacement, known to be normal, is exceeded. When this exceeds two, corrective action is taken.—AJC

7,178,630

43.55.Ev ACOUSTIC DEVICE FOR WALL MOUNTING FOR DIFFUSION AND ABSORPTION OF SOUND

Jay Perdue, Amarillo, Texas
20 February 2007 (Class 181/290); filed 30 August 2004

This device is similar to many wall-mounted sound-absorbing panels, but in this case the front is bowed out to enhance diffusion, and the ends are capped with the same semirigid mats. This bowed configuration and the cavity that it creates allow for better low-frequency absorption.—CJR

7,179,846

43.55.Ev SOUNDPROOFING AND THERMALLY INSULATING STRUCTURAL ELEMENT

Thorsten Dreier, assignor to Bayer MaterialScience AG
20 February 2007 (Class 521/155); filed in Germany 13 March 2003

The sound-absorptive properties for a closed-cell polyurethane rigid foam are enhanced in the frequency range l000–5000 Hz if surface depressions are of different sizes.—CJR

7,192,985

43.55.Ev MORE CONTROLLABLE ACOUSTIC SPRAY PATCH

John R. Woods, assignor to Spraytex, Incorporated
20 March 2007 (Class 516/11); filed 30 October 2003

A base, a filler, an adhesive binder, an antifoaming agent, a suspension agent, and rubber particulates or polyethylene particles are mixed together with volatile propellants in a spray can for easy application to patch an acoustical ceiling surface. The patent asserts that the patch will blend right in.—CJR

7,201,253

43.55.Ev SOUNDPROOFING ASSEMBLY AND A PART COMPRISING A WALL WHICH IF COVERED WITH SAID ASSEMBLY

Arnaud Duval and Guillaume Deshayes, assignors to Faurecia Automotive Industrie
10 April 2007 (Class 181/204); filed in France 11 February 2002

A composite vehicle-interior sound-absorbing surface covering 15–50 mm thick is claimed that absorbs sound at frequencies from 400 to over 1000 Hz. Surface **12** has a resistance to airflow of 500–2000 N s/m^3

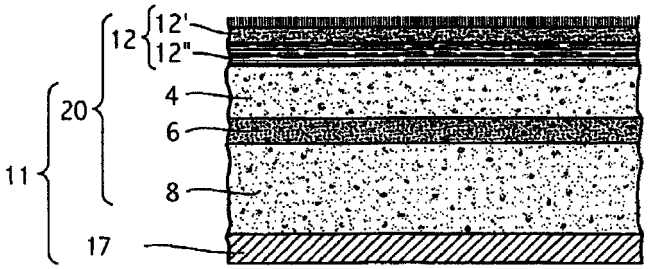

(specific acoustic impedance). Layer **4** has a resistivity of 10 000–50 000 N s/m^4 (airflow resistivity). Layer **6**, bonded to **8**, is an airtight membrane with an area mass of 0.2–9 kg/m. Layer **8** is like layer **4**.—AJC

7,181,891

43.55.Ti ACOUSTICAL SOUND PROOFING MATERIAL AND METHODS FOR MANUFACTURING SAME

Kevin J. Surace and Marc U. Porat, assignors to Quiet Solution, Incorporated
27 February 2007 (Class 52/642); filed 8 September 2003

This product incorporates a viscous interlayer (or several layers) between panels of gypsum board or plywood in order to improve sound transmission loss performance by means of damping of constrained layers. The laminations are held together by the viscous interlayer that also serves as a glue to hold the panel together.—CJR

7,178,636

43.55.Vj ELEVATOR SYSTEM

Kunio Kato and Kazuhiro Yoshikawa, assignors to Mitsubishi Denki Kabushiki Kaisha
20 February 2007 (Class 187/254); filed 25 March 2003

The elevator hoist motor is mounted on the side of the shaft, not at the top, and the patent covers appropriate vibration isolation systems for this mounting.—CJR

7,188,820

43.55.Vj VIBRATION DAMPING FLOOR STRUCTURE

Atsuhiko Kobayashi *et al.*, assignors to Hitachi Kizai, Incorporated
13 March 2007 (Class 248/636); filed in Japan 31 July 2003

A structural frame for a vibration-damping floor structure is supported on a subframe that self-adjusts to provide even loading on the ball bearings that carry the load.—CJR

7,162,913

43.58.Gn METHOD OF EVALUATING RESTITUTION CHARACTERISTIC OF GOLF CLUB, SYSTEM FOR EVALUATING RESTITUTION CHARACTERISTIC, AND GOLF CLUB

Hiroshi Saegusa and Kazunori Ono, assignors to The Yokohama Rubber Company, Limited
16 January 2007 (Class 73/11.01); filed 3 July 2002

With the profusion of golf clubs and golf balls (see United States Patents 7,160,205 and 7,163,471, reviewed in this issue) that are designed to have a signature sound, a means is needed to measure whether a design meets the design criteria in a repeatable and easy manner. For clubs, a

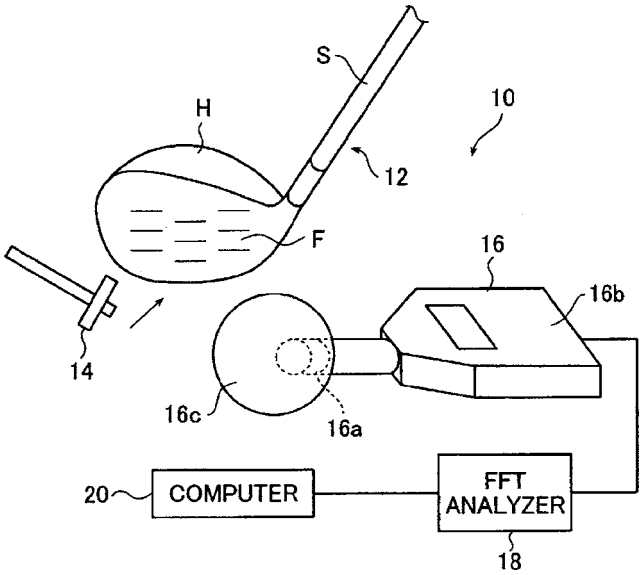

method is at hand. Input force jig **14** gives a light tap to club face **F**. Noise measuring unit **16**, analyzer **18**, and computer **20** complete the system. Another embodiment describes the use of an accelerometer and force hammer. What is novel and nonobvious here is not obvious to this reviewer.—NAS

7,193,354

43.58.Hp RESONATOR, UNIT HAVING RESONATOR, OSCILLATOR HAVING UNIT AND ELECTRONIC APPARATUS HAVING OSCILLATOR

Hirofumi Kawashima, assignor to Piedek Technical Laboratory
20 March 2007 (Class 310/370); filed in Japan 30 June 2003

This patent discloses various forms of quartz tuning forks having high quality factor Q and good suppression of second harmonics. The innovations here are unclear to this reader, but seem to involve complex combinations of electroding and support structures for the forks. It is a lengthy and not very informative patent.—JAH

7,050,591

43.60.Dh ACOUSTIC OUTPUT PROCESSING APPARATUS

Toru Marumoto, assignor to Alpine Electronics, Incorporated
23 May 2006 (Class 381/58); filed in Japan 15 March 2002

This automobile audio-output controller is connected so as to allow individual control of the gain applied to each of multiple audio sources. Such sources might include the usual audio output of the entertainment system, be that radio, CD, or other device, possibly a back-seat TV set, a navigation system, engine or vehicle warning system, or perhaps an incoming telephone call. Using a variety of preset, but adjustable, rules, a selected audio input signal would be boosted to a somewhat greater volume level, while competing signals would appear as lower-level background sounds. Although the description is for automotive application, the claims are not so limited.—DLR

7,197,135

43.60.Dh SYSTEMS AND METHODS FOR CALLER-CONTROLLED TUNE NOTIFICATION OF A CALL

Edward Michael Silver *et al.*, assignors to BellSouth Intellectual Property Corporation
27 March 2007 (Class 379/373.02); filed 24 October 2002

Yet another patent makes a claim on ring tones. This one subjects the receiver to a unique sound of the caller's choosing. The authors felt the idea was so good they put a copyright disclaimer within the patent claims.—GFE

7,200,425

43.60.Dh DEVICE AND METHOD FOR AUGMENTING CELLULAR TELEPHONE AUDIO SIGNALS

Mark Kirkpatrick, assignor to BellSouth Intellectual Property Corporation
3 April 2007 (Class 455/572); filed 21 March 2002

This patent describes a device that replaces a cellphone's battery with an acoustic device that can play ring tones. The purpose of this device is to

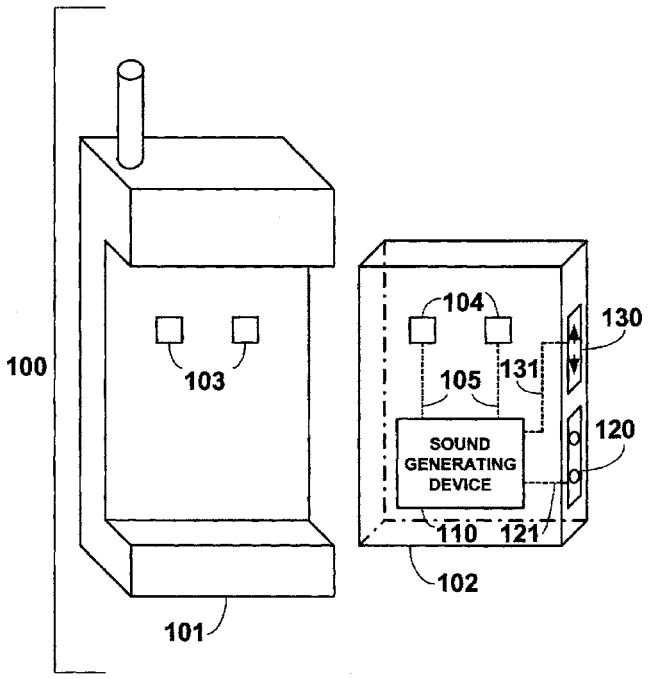

bypass the limitations and expense of purchasing ring tones through the cellular phone company.—GFE

7,203,286

43.60.Dh METHOD AND APPARATUS FOR COMBINING AMBIENT SOUND EFFECTS TO VOICE MESSAGES

Allan E. Brockenbrough *et al.*, assignors to Comverse, Incorporated
10 April 2007 (Class 379/76); filed 6 October 2000

Are you tired of leaving regular old voice mail messages? Why not augment the messages you leave on someone else's phone with music?—GFE

7,203,308

43.60.Dh ECHO CANCELLER ENSURING FURTHER REDUCTION IN RESIDUAL ECHO

Syuji Kubota, assignor to Ricoh Company, Limited
10 April 2007 (Class 379/406.05); filed in Japan 20 November 2001

Determining when and when not to clip a voice transmission to reduce echoes and doubletalk is the focus of this telephony patent. It describes a method that adapts to the environment (e.g., speaker's distance from phone and noise level).—GFE

7,203,523

43.60.Dh PORTABLE TELEPHONE WITH MUSICAL TONES PLAYBACK AND CLASS RESPONSE TO INCOMING CALL(S)

Shuhei Ito, assignor to Yamaha Corporation
10 April 2007 (Class 455/567); filed in Japan 28 December 1999

Quantify how much you like your friends with this ring-tone patent. For your good friends the phone rings completely, for your hangers-on the ring dies off quickly, and for those deadbeats the phone doesn't ring at all. Awkward social situations ensue.—GFE

7,190,635

43.60.Jn SYSTEM AND METHOD FOR MULTI-BEAM LASER VIBROMETRY TRIANGULATION MAPPING OF UNDERGROUND ACOUSTIC SOURCES

Dennis Killinger, assignor to University of South Florida
13 March 2007 (Class 367/128); filed 27 March 2006

This submission deals with the important issue of triangulating underground sources (trapped miners and oil exploration). Sadly, the claim is simply that they use LIDAR instead of a conventional microphone to receive the acoustic transmission.—GFE

7,191,090

43.60.Jn METHODS AND SYSTEMS FOR ACOUSTICALLY LOCATING COMPUTER SYSTEMS

Helen A. Cunningham, assignor to Sun Microsystems, Incorporated
13 March 2007 (Class 702/150); filed 22 March 2004

The patent describes an acoustic method for finding one broken computer amongst a server farm/cluster within a large computer center; that is, the broken computer makes a loud sound. The sound is used for localization or broadcasting identification.—GFE

7,203,132

43.60.Jn REAL TIME ACOUSTIC EVENT LOCATION AND CLASSIFICATION SYSTEM WITH CAMERA DISPLAY

Theodore W. Berger, assignor to Safety Dynamics, Incorporated
10 April 2007 (Class 367/129); filed 7 April 2006

A method for detection, classification, and video imaging of gunfire is described. As in all prior art, shots are detected acoustically and a camera is trained upon the source direction. The author claims the unique aspects that fewer/closer sensors are required and that (well-known and studied) neural network techniques are employed.—GFE

7,203,322

43.60.Rw ACOUSTIC DETECTOR WITH NOISE CANCELLATION

Peter Bostock, assignor to Metrotech Corporation
10 April 2007 (Class 381/67); filed 16 May 2003

An acoustic leak detector for buried pipe lines is claimed where pressurized fluid leakage **100** produces soil vibrations **102** in the range of 40–200 Hz that are detected by contact transducer **110**, fed by processor **160** to earphones **121**, to be heard by operator **104**. Unrelated airborne ambient

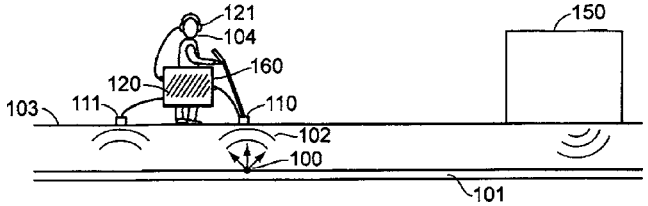

sounds are canceled by conventional active noise control via controller **120** and the ear cup speakers. Unrelated ground vibrations are also canceled by the signal from a remote sensor **111**, also processed by **120** and by the ear cup speakers.—AJC

7,048,692

43.66.Fe METHOD AND APPARATUS FOR ESTIMATING AUDITORY FILTER SHAPE

Takeshi Nakaichi *et al.*, assignors to Rion Company, Limited
23 May 2006 (Class 600/559); filed in Japan 22 January 2002

This patent describes a clinical instrument intended for use in measuring the shape of a patient's auditory response curve at a given frequency and loudness. The device would be used primarily for determining the patient's hearing impairment by making a rapid assessment of the auditory response curve. The loudness of a test tone is varied along with the width and depth of a notched masking signal in order to determine the coefficents of a roex filter used to model the auditory filter. A system for the precise control of the timing of probe and masker signals is said to allow a rapid evaluation of the auditory filter shape.—DLR

7,190,803

43.66.Ts ACOUSTIC TRANSDUCER HAVING REDUCED THICKNESS

Aart Z. van Halteren, assignor to Sonion Nederland BV
13 March 2007 (Class 381/398); filed 9 April 2002

The overall width of a hearing aid is often determined mainly by the thickness of the receiver or speaker. A receiver housing contains a magnet assembly mounted coaxially with a coil that touches one edge of a thin

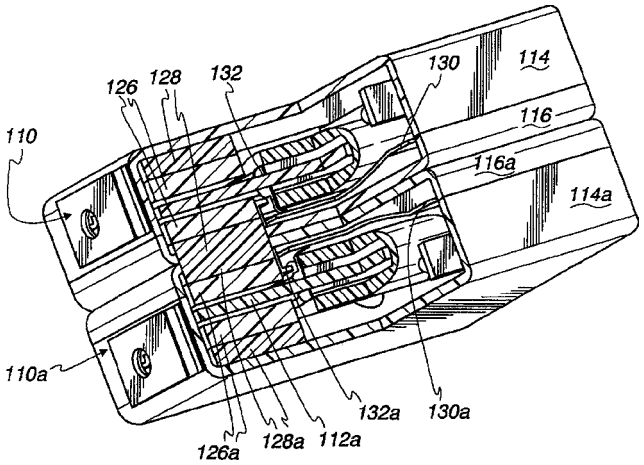

membrane **130** (**130a**), which acts as the diaphragm. The overall receiver housing may contain a pair of such transducers mounted in an abutting side-by-side manner to reduce mechanical vibration inside the hearing aid.—DAP

7,191,029

43.66.Ts RAPID PROTOTYPE FABRICATION OF A MONOLITHIC HEARING INSTRUMENT HOUSING WITH AN INTEGRALLY-FABRICATED FACEPLATE

Christopher Marxen and Martin W. Masters, assignors to Siemens Hearing Instruments, Incorporated
13 March 2007 (Class 700/118); filed 11 March 2003

In traditional custom-hearing-aid manufacturing, a separate faceplate, which provides mounting means for the battery drawer, microphone, programming contacts, volume control, switches, and circuitry, normally adheres to the earshell via an adhesive bond. The utilization of rapid prototyping with digital modeling of the external ear and hearing aid provides means

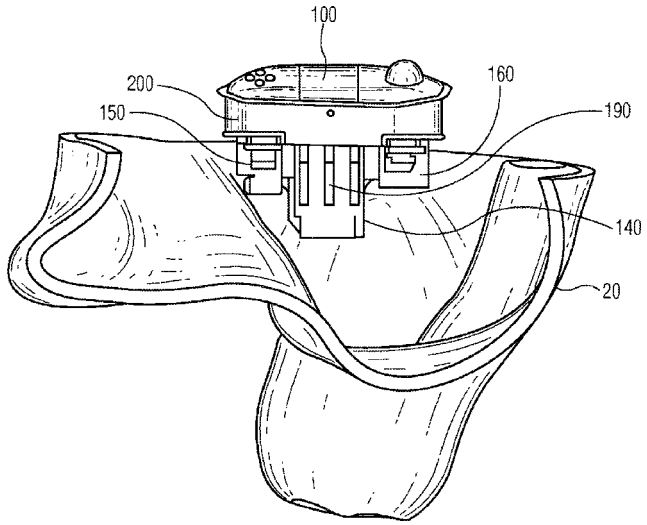

for fabricating the earshell and faceplate as one monolithic piece, thus avoiding the adhesive fastening process. An electronics module with components attached mounts into an opening in the faceplate.—DAP

7,191,867

43.66.Ts HEARING AID DEVICE THAT CAN BE WORN IN THE EAR WITH A HOUSING

Christian Schmitt, assignor to Siemens Audiologische Technik GmbH
20 March 2007 (Class 181/130); filed in the European Patent Office 25 September 2002

Frequently, wearers of custom in-the-ear hearing aids remove their hearing aids from their ears by pulling on the open battery drawers. As a result, battery drawer and faceplate breakage is a common problem for many of these hearing aid wearers, the latter being particularly true for

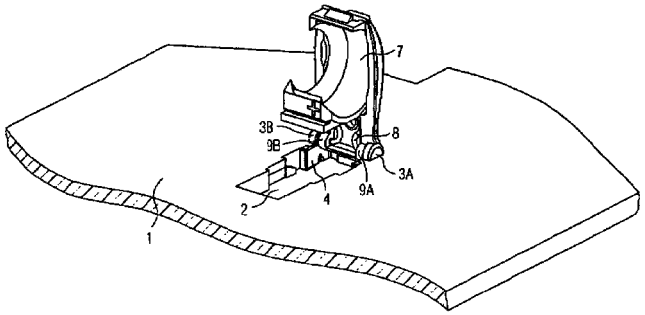

one-piece monolithic faceplate-earshells made with a rapid prototyping process. A stabilization element **4** is added to the housing in the battery drawer opening to stiffen the faceplate where the battery drawer swivels.—DAP

7,194,100

43.66.Ts METHOD FOR INDIVIDUALIZING A HEARING AID

Volker Kühnel and Andreas Von Buol, assignors to Phonak AG
20 March 2007 (Class 381/321); filed 10 April 2001

Normal loudness perception is compared to an individual's loudness perception in calculating the settings of a hearing aid. Compression and amplification parameter values are calculated as a function of frequency by

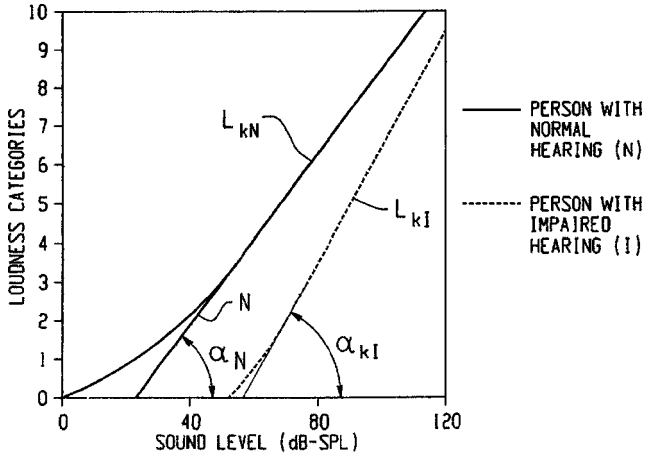

combining weighted normal loudness perception with weighted individual loudness perception. Differences between individual loudness scaling relative to average loudness scaling as a function of hearing loss are taken into account.—DAP

7,200,237

43.66.Ts METHOD AND SYSTEM FOR REMOTELY UPGRADING A HEARING AID DEVICE

Chaoying Zhang and Zezhang Hou, assignors to Apherma Corporation
3 April 2007 (Class 381/60); filed 23 October 2001

The functionality of existing hearing aids may be upgraded by downloading software to them from a remote server over a network such as the Internet. To first determine the status of a hearing aid, device information

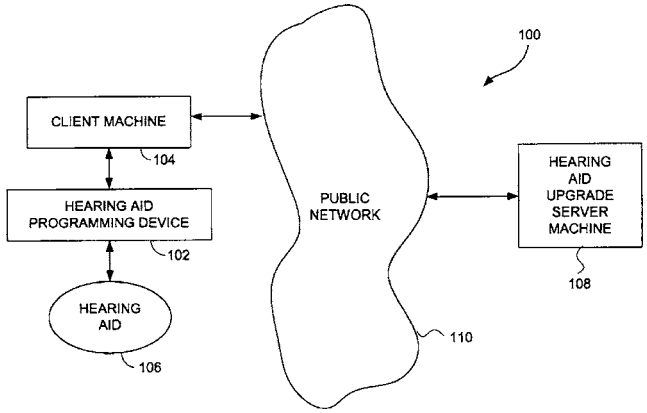

such as model and serial number is read from the hearing aid and sent to an upgrade server. After downloading, upgrade information such as a new algorithm is programmed into the hearing aid by a local programming station.—DAP

7,203,328

43.66.Ts HEARING AID, AND METHOD FOR REDUCING FEEDBACK THEREIN

Bernd Beimel and Tom Weidner, assignors to Siemens Audiologische Technik GmbH
10 April 2007 (Class 381/318); filed in Germany 27 May 2002

Hearing aids typically contain a microphone and a telecoil for converting acoustical and inductive signals, respectively, into electrical inputs. Either of these inputs can produce an oscillatory condition when high gain is combined with a feedback path with a particular phase characteristic.

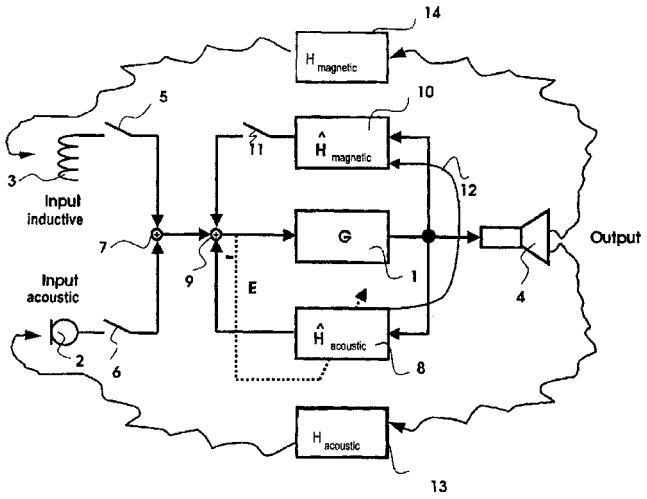

Methodology is proposed to provide two sets of filter coefficients for compensating both acoustic feedback and inductive feedback in separate feedback paths in a hearing aid. Switches disconnect the filter associated with acoustical feedback or inductive feedback from the input while the other filter is being calibrated. The filtering compensation can be either static or adaptive.—DAP

7,198,133

43.66.Yw EAR COUPLER

Jessica Ash Warring, San Carlos, California and Alfred Christian Walton, Belmont, California
3 April 2007 (Class 181/129); filed 3 June 2004

To facilitate hearing screening for infants who may move during testing and have irregular surfaces surrounding their ears, a coupler with ribbed

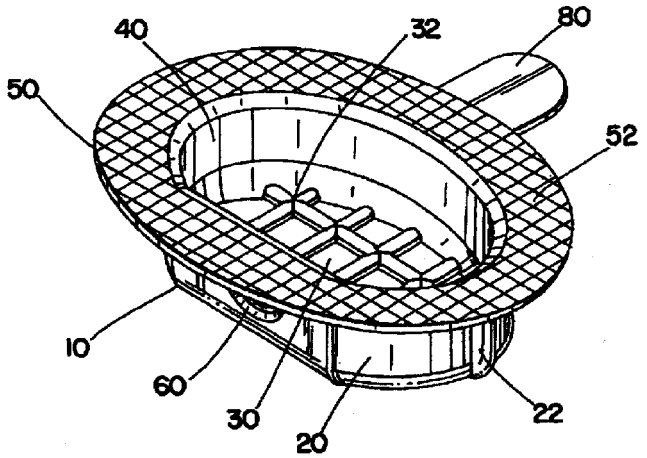

exterior wall **32** and adhesive **52** provides means to securely fasten the transducer housing into place and also to facilitate its easy removal.—DAP

7,191,126

43.72.Gy SOUND ENCODER AND SOUND DECODER PERFORMING MULTIPLEXING AND DEMULTIPLEXING ON MAIN CODES IN AN ORDER DETERMINED BY AUXILIARY CODES

Hirohisa Tasaki, assignor to Mitsubishi Denki Kabushiki Kaisha
13 March 2007 (Class 704/227); filed in Japan 3 September 2001

Deterioration in tone quality is said to be reduced by determining the order of multiplexing and demultiplexing the variable length, band-by-band,

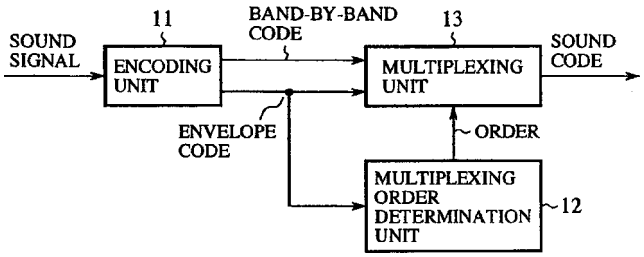

encoded and decoded data, respectively, on a frame-by-frame basis in order to minimize bit errors for high-frequency signals.—DAP

7,191,136

43.72.Gy EFFICIENT CODING OF HIGH FREQUENCY SIGNAL INFORMATION IN A SIGNAL USING A LINEAR/NON-LINEAR PREDICTION MODEL BASED ON A LOW PASS BASEBAND

Deepen Sinha *et al.*, assignors to iBiquity Digital Corporation
13 March 2007 (Class 704/500); filed 1 October 2002

To provide higher audio-signal bandwidth at lower bitrates, a coder eliminates long-term and short-term frequency domain correlation with frequency domain predictors that may utilize both linear and nonlinear models for the high frequencies. Time variations in the audio are accounted for with a compression algorithm chosen via a transmitted audio bitstream content-based header. The model can be adapted to different frequency regions.—DAP

7,193,538

43.72.Gy MATRIX IMPROVEMENTS TO LOSSLESS ENCODING AND DECODING

Peter Graham Craven *et al.*, assignors to Dolby Laboratories Licensing Corporation
20 March 2007 (Class 341/50); filed in United Kingdom 7 April 1999

To reduce decoding computational resource requirements, an audio stream is divided into two substreams: the first contains fewer channels (e.g., two) than the original multichannel signal and provides information on the downmix signal obtained by matrixing; the second provides further information, such as channel order, so that the original multichannel signal can be losslessly recovered by a decoder. Dither is used for synchronizing pseudorandom sequence generators in the decoder and encoder and for computing truncation or rounding within the matrixing.—DAP

7,200,557

43.72.Gy METHOD OF REDUCING INDEX SIZES USED TO REPRESENT SPECTRAL CONTENT VECTORS

James G. Droppo *et al.*, assignors to Microsoft Corporation
3 April 2007 (Class 704/242); filed 27 November 2002

For personal, mainframe, mini, or server computers and hand-held or laptop devices, first and second decision trees are associated with first and second types of audio sounds and code words, respectively. One of the code words is selected as the code word of the vector that describes the spectral content of the audio signal. The first and second types of audio sounds may be vowels and consonants, respectively.—DAP

7,047,194

43.72.Ja METHOD AND DEVICE FOR CO-ARTICULATED CONCATENATION OF AUDIO SEGMENTS

Christoph Buskies, Hamburg, Germany
16 May 2006 (Class 704/258); filed in Germany 19 August 1998

The patent begins by mangling the definitions of phones and phonemes, stating that both are defined in acoustic and articulatory terms without any mention of linguistic issues. The method of speech synthesis involves segment concatenation following a set of rules by which segments are combined, taking account of leading, central, and trailing portions. The rules may specify that the trailing and leading portions of adjacent segments

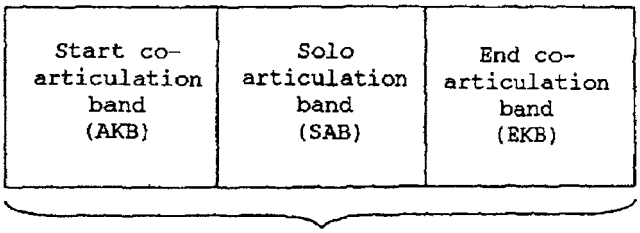

may be abutted, one may replace the other, or a cross fade may be performed, blending the two. The entire patent deals with the details of the rules. However, there are no tables, listings, or other details clarifying how the various phonemes are to be represented by these three-part segments, other than to inform us that there are two types of phonemes, static and dynamic. Curiously, diphthongs are considered to be static, as is some sort of phoneme called a ''vibrant.''—DLR

7,047,198

43.72.Ne AUDIO INPUT DEVICE AND METHOD OF CONTROLLING THE SAME

Takeshi Ono and Okihiko Nakayama, assignors to Nissan Motor Company, Limited
16 May 2006 (Class 704/275); filed in Japan 11 October 2000

An automobile computer would be equipped with a speech recognition system connected to a number of controllable installations, such as audio devices, air conditioner, etc. In order to reduce the chance of recognition errors causing the wrong device to respond to a command, an additional hand-held remote unit is provided. Before a speech command is executed, the remote would normally be used to select the intended device. However, the patent goes into lengthy detail describing a system of weights by which the device selector may be overridden. This mechanism includes additional inputs from sources such as the vehicle speed, which may indicate that greater caution should be taken before allowing a device to be controlled by voice command.—DLR

7,050,550

43.72.Ne METHOD FOR THE TRAINING OR ADAPTATION OF A SPEECH RECOGNITION DEVICE

Volker Steinbiss and Thomas Eisele, assignors to Koninklijke Philips Electronics N.V.
23 May 2006 (Class 379/88.01); filed in Germany 11 May 2001

This system takes its place among a stable of speech recognizers designed for the purpose of controlling various computer or mechanical functions. Controllable devices such as home theater components and kitchen appliances are mentioned as examples. The only factor which might serve to distinguish this instance from the stable seems to be a provision for the user to yell ''stop'' (or use some other means) to abort the execution of the

control function in the case of a faulty recognition result. Does this really qualify as a nonobvious, and therefore patentable, innovation?—DLR

7,050,971

43.72.Ne SPEECH RECOGNITION APPARATUS HAVING MULTIPLE AUDIO INPUTS TO CANCEL BACKGROUND NOISE FROM INPUT SPEECH

Paul A. P. Kaufholz, assignor to Koninklijke Philips Electronics N.V.
23 May 2006 (Class 704/226); filed in the European Patent Office 23 September 1999

The patent presents a potpourri of methods for noise cancellation using multiple microphones. The application at hand is an otherwise typical computer speech recognition system. In one arrangement, separate secondary microphones would be assigned and positioned to pick up from various individual noise sources. Each secondary mic signal would then be separately subtracted from the primary mic input signal, after adaptive delay and level adjustments. In another arrangement, several secondary microphones would be used to cancel an interfering sound from a single source. In such case, the cancellation mics may be organized as a beamformer by applying individual delay and gain settings to each secondary mic. The speech recognition system itself is a fairly straightforward, typical system.—DLR

7,053,938

43.72.Ne SPEECH-TO-TEXT CAPTIONING FOR DIGITAL CAMERAS AND ASSOCIATED METHODS

John W. Sherry, assignor to Intel Corporation
30 May 2006 (Class 348/231.4); filed 7 October 1999

This patent covers voice annotation of images taken by a digital camera. It is said here that other cameras exist which allow an audio file to be captured and stored in some way as to identify the audio file with a particular picture. However, this patent would go a step further in providing a

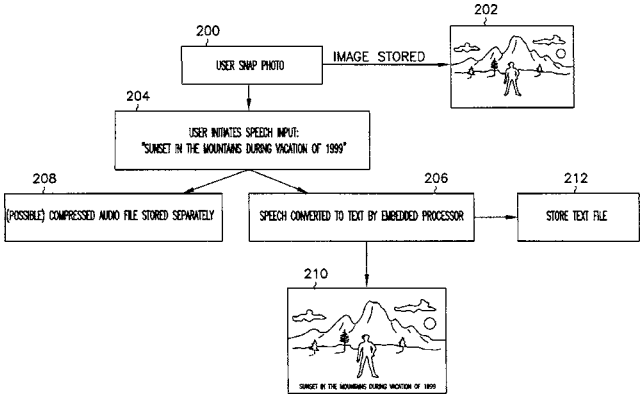

speech recognition capability in the camera. As an audio segment is collected, it is also presented to the recognition system and converted to text. The text message is then added to the stored digital image.—DLR

7,191,130

43.72.Ne METHOD AND SYSTEM FOR AUTOMATICALLY OPTIMIZING RECOGNITION CONFIGURATION PARAMETERS FOR SPEECH RECOGNITION SYSTEMS

Christopher J. Leggetter and Michael M. Hochberg, assignors to Nuance Communications
13 March 2007 (Class 704/254); filed 27 September 2002

A speech recognition system is run in a learning mode to automatically tune recognition configuration parameters in response to utterances. The

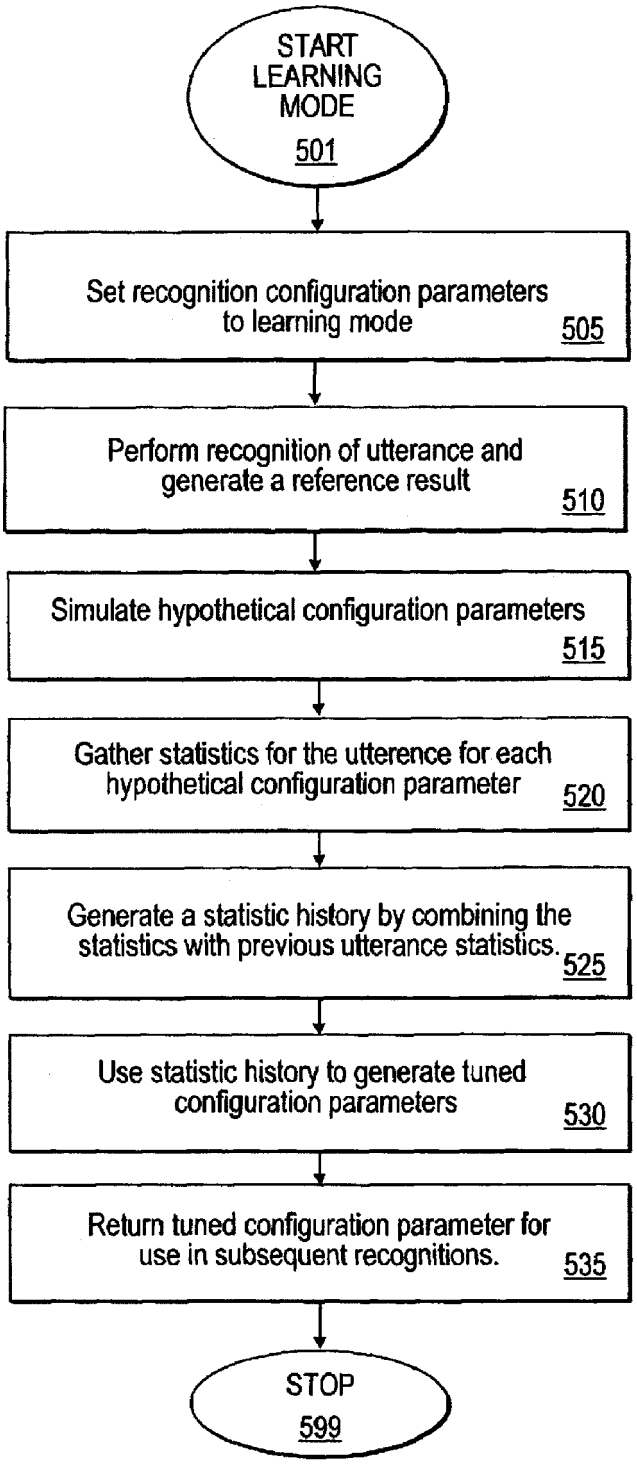

method described is said to eliminate time-consuming offline optimization simulations and configuration decisions, which ultimately reduces processing time. Statistics for utterances with several candidate configurations are gathered in generating the tuned set.—DAP

7,191,135

43.72.Ne SPEECH RECOGNITION SYSTEM AND METHOD FOR EMPLOYING THE SAME

Timothy P. O'Hagan, assignor to Symbol Technologies, Incorporated
13 March 2007 (Class 704/270.1); filed 8 April 1998

A speech recognition system performs speech decoding at a mobile terminal rather than at a host computer. The mobile terminal utilizes graphical user interface (GUI) screens that are downloaded by the host computer. To reduce processing and memory requirements, dictionary and syntax files are limited to words associated with the set of commands and data input by the user of the mobile terminal operating with a particular GUI file.—DAP

7,197,462

43.72.Ne SYSTEM AND METHOD FOR INFORMATION ACCESS

Hironobu Takagi and Chieko Asakawa, assignors to International Business Machines Corporation
27 March 2007 (Class 704/275); filed in Japan 27 April 2001

A system facilitates conversion of web pages into content suitable for easy dial-up or voice-command entry and hands-free listening with a telephone without special navigation requirements. The content of a linked

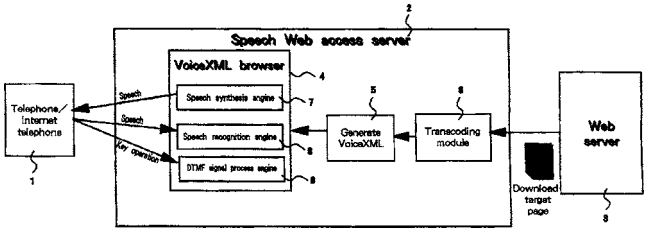

destination page that is derived from a Web server is inserted and converted into a linked location on a target page in a form appropriate for oral reading and speech output.—DAP

7,203,188

43.72.Ne VOICE-CONTROLLED DATA/ INFORMATION DISPLAY FOR INTERNET TELEPHONY AND INTEGRATED VOICE AND DATA COMMUNICATIONS USING TELEPHONES AND COMPUTING DEVICES

Joseph Siegrist and Michael Masinick, assignors to Estara, Incorporated
10 April 2007 (Class 370/352); filed 21 May 2002

A callback request from a user over a packet-switched network elicits a callback that connects the user to an automated voice processing system which requests user information. Words spoken by the user are translated to textual information that is associated with a transmitted identifier that contains dual-tone multifrequency tones. The identifier is utilized in a download request.—DAP

7,203,644

43.72.Ne AUTOMATING TUNING OF SPEECH RECOGNITION SYSTEMS

Andrew V. Anderson and Steven M. Bennett, assignors to Intel Corporation
10 April 2007 (Class 704/243); filed 31 December 2001

In dictation system applications, tuning the speech recognition process is performed automatically during usage rather than separately off-line. Feedback from the conversion of audio input signals to audio output signals is used in training to modify the speech models and grammar files to improve performance.—DAP

7,203,651

43.72.Ne VOICE CONTROL SYSTEM WITH MULTIPLE VOICE RECOGNITION ENGINES

Amit Baruch *et al.*, assignors to ART-Advanced Recognition Technologies, Limited
10 April 2007 (Class 704/270.1); filed 7 December 2001

A system that performs voice recognition of user commands for nondialing features of such devices as land-line, portable, headset, or cellular telephones, has at least two speech recognition engines to select from, each specific to one nondialing feature. Feature commands include messages, calendar, to do, memo, fax, and email.—DAP

7,193,930

43.80.Ev QUANTITATIVE ECHO SOUNDER AND METHOD OF QUANTITATIVE SOUNDING OF FISH

Takanori Satoh *et al.*, assignors to Furuno Electric Company, Limited
20 March 2007 (Class 367/12); filed in Japan 7 April 2004

The patent describes a method of estimating fish size acoustically. In order to do so accurately, the authors assert that the length of the fish must be estimated from the backscatter with knowledge of the fish's current orientation. They propose transmitting four beams and estimating the phase difference or time delay between those beams. However, to do this accurately, ship pitch and roll must be measured and removed. Not discussed is the equally innovative method of asking the fish politely to stand apart from their overlapping friends.—GFE

7,189,205

43.80.Vj SYSTEM FOR REMOTE EVALUATION OF ULTRASOUND INFORMATION OBTAINED BY A PROGRAMMED APPLICATION-SPECIFIC DATA COLLECTION DEVICE

Gerald J. McMorrow *et al.*, assignors to Diagnostic Ultrasound Corporation
13 March 2007 (Class 600/437); filed 23 May 2003

A data collection device including an ultrasound transducer and stepper motors that move the transducer is placed on a patient to image a region of interest. The data collection device is programmed to perform a specific ultrasound examination. Ultrasound data from the collection device are transmitted via a local server to a remote server that processes the data and provides application-specific information, such as a three-dimensional model, that can be used for diagnosis.—RCW

7,194,117

43.80.Vj SYSTEM AND METHOD FOR PERFORMING A THREE-DIMENSIONAL VIRTUAL EXAMINATION OF OBJECTS, SUCH AS INTERNAL ORGANS

Arie E. Kaufman *et al.*, assignors to The Research Foundation of State University of New York
20 March 2007 (Class 382/128); filed 5 February 2001

Multiple ultrasonic *b*-scans are acquired, different resolutions are used, and a skeleton of a complex three-dimensional object is created for applications that include virtual cystoscopy, virtual laryngoscopy, and virtual imaging.—RCW

7,198,601

43.80.Vj ULTRASONIC CONTRAST MEDIUM IMAGING APPARATUS AND METHOD

Hiroshi Kanda *et al.*, assignors to Hitachi Medical Corporation
3 April 2007 (Class 600/458); filed in Japan 1 February 2001

The receiving section of this apparatus contains a filter that extracts frequencies from the echo produced by a contrast agent present in the region being imaged and also contains a control section that sets the passband of the filter on the basis of the frequencies in the contrast agent response.—RCW

LETTERS TO THE EDITOR

A robust noniterative method for obtaining scattering strengths of multiply scattering point targets (L)

Xudong Chen[a] and Yu Zhong
Department of Electrical and Computer Engineering, National University of Singapore, Singapore, 117576

(Received 1 March 2007; revised 23 May 2007; accepted 25 June 2007)

A noniterative method based on the least squares technique is presented in this letter to obtain the scattering strengths of multiply scattering point targets. Benefiting from the least squares' optimization property, this new method achieves a good estimation of the scattering strengths. Compared with the noniterative method proposed in a recent paper [E. A. Marengo and F. K. Gruber "Noniterative analytical formula for inverse scattering of multiply scattering point targets," J. Acoust. Soc. Am. **120**, 3782–3788 (2006)], the new method produces more accurate results in the presence of noise. © *2007 Acoustical Society of America.* [DOI: 10.1121/1.2764464]

PACS number(s): 43.60.Pt, 43.60.Tj [LLT] Pages: 1325–1327

I. INTRODUCTION

The paper by Marengo and Gruber[1] proposes a noniterative method for solving the nonlinear inverse problem of retrieving the scattering strengths from the multi-static response matrix after the estimation of the scatterers' positions via the multiple signal classification (MUSIC) method.[2] Marengo and Gruber's noniterative method avoids the convergence problem in the iterative method proposed by Devaney *et al.*,[2] and, by using the linearly independent property of both the transmit and the receive background Green's function vector, shown in Eqs. (3) and (4) in Ref. [1], it can determine the scattering strengths exactly in the noise-free case. However, in presence of noise, the inversion equations used in Ref. [1] are somewhat inconsistent with the linear independency of the transmit and receive background Green's function vector, which may lead to the inaccuracy of the estimation of the scattering strengths, especially when the signal-to-noise ratio is low. The purpose of this letter is to present a new noniterative method which is based on the least squares technique and achieves a good estimation of the scattering strengths in the presence of noise. The new least squares retrieval method is tested through numerical simulations, and is compared with the method proposed in Ref. [1].

II. LEAST SQUARES RETRIEVAL METHOD

We first rewrite the multi-static response matrix of the scattering system in an alternative form. Assume that there are M point scatterers located at $\mathbf{X}_m, m=1,2,\ldots,M$, with scattering strength $\tau_m, m=1,2,\ldots,M$, respectively. After placing a transmitter array at $\mathbf{R}_t(i), i=1,2,\ldots,N_t$, and a receiver array at $\mathbf{R}_r(j), j=1,2,\ldots,N_r$, the multi-static response matrix generated by them could be written as

$$K = G_{r0} \cdot \tau \cdot G_t, \tag{1}$$

where $G_t=[\psi_t(\mathbf{X}_1),\psi_t(\mathbf{X}_2),\ldots,\psi_t(\mathbf{X}_M)]^T$, and $G_{r0}=[g_{0,r}(\mathbf{X}_1),g_{0,r}(\mathbf{X}_2),\ldots,g_{0,r}(\mathbf{X}_M)]$, and $\tau=diag[\tau_1,\tau_2,\ldots,\tau_M]$. Note that $\psi_t(\mathbf{X}_m)$ and $g_{0,r}(\mathbf{X}_m)$ have the same definitions as those of Ref. [1], and they are defined by

$$\psi_t(\mathbf{X}_m) = g_{0,t}(\mathbf{X}_m) + \sum_{m' \neq m} \tau_{m'} G_0(\mathbf{X}_m,\mathbf{X}_{m'}) \psi_t(\mathbf{X}_{m'}), \tag{2}$$

where $g_{0,t}(\mathbf{X}_m)=[G_0(\mathbf{X}_m,\mathbf{R}_t(1)),G_0(\mathbf{X}_m,\mathbf{R}_t(2)),\ldots,G_0(\mathbf{X}_m,\mathbf{R}_t(N_t))]^T$, and

$$g_{0,r}(\mathbf{X}_m) = [G_0(\mathbf{R}_r(1),\mathbf{X}_m), G_0(\mathbf{R}_r(2),\mathbf{X}_m), \ldots, G_0(\mathbf{R}_r(N_r),\mathbf{X}_m)]^T, \tag{3}$$

where G_0 is the background Green's function.

Note that, we in this letter make the same assumption as Ref. [1] does, i.e., $M \leqslant \min(N_t,N_r)$ and the rank of K matrix is equal to M.

Equation (2) could be written as

$$(Q_1 + Q_2) \cdot \tau \cdot G_t = G_{t0}^T, \tag{4}$$

where $G_{t0}=[g_{0,t}(\mathbf{X}_1),g_{0,t}(\mathbf{X}_2),\ldots g_{0,t}(\mathbf{X}_M)]$, $Q_1=diag[\tau_1^{-1},\tau_2^{-1},\ldots,\tau_M^{-1}]$, and

$$Q_2 = \begin{bmatrix} 0 & -G_0(\mathbf{X}_1,\mathbf{X}_2) & -G_0(\mathbf{X}_1,\mathbf{X}_3) & \ldots & -G_0(\mathbf{X}_1,\mathbf{X}_M) \\ -G_0(\mathbf{X}_2,\mathbf{X}_1) & 0 & -G_0(\mathbf{X}_2,\mathbf{X}_3) & \ldots & -G_0(\mathbf{X}_2,\mathbf{X}_M) \\ -G_0(\mathbf{X}_3,\mathbf{X}_1) & -G_0(\mathbf{X}_3,\mathbf{X}_2) & 0 & \ldots & -G_0(\mathbf{X}_3,\mathbf{X}_M) \\ & \vdots & & \ddots & \vdots \\ -G_0(\mathbf{X}_M,\mathbf{X}_1) & -G_0(\mathbf{X}_M,\mathbf{X}_2) & -G_0(\mathbf{X}_M,\mathbf{X}_3) & \ldots & 0 \end{bmatrix}. \tag{5}$$

From Eq. (4), we have $\tau \cdot G_t = (Q_1+Q_2)^{-1} \cdot G_{t0}^T$, the substitution of which into Eq. (1) yields the multi-static response matrix

$$K = G_{r0} \cdot (Q_1 + Q_2)^{-1} \cdot G_{t0}^T. \tag{6}$$

[a]Author to whom correspondence should be addressed. Electronic mail: elechenx@nus.edu.sg

After estimating the locations of the M scatterers, G_{r0}, G_{t0} and Q_2 become known matrices, and the unknown scattering strengths $\tau_m, m=1,2,\ldots,M$, are in the diagonal of Q_1.

If the singular value decomposition of an N by $M(N \geqslant M)$ matrix A is $A=U\cdot\Sigma\cdot V^*$, where * denotes the conjugate transpose, the least squares solution[3] for the overdetermined problem $A\cdot X=B$ is $X=A^{\dagger}B$, where $A^{\dagger}=V\cdot\Sigma'\cdot U^*$ is the pseudoinverse of A with $\Sigma'_{ii}=\Sigma_{ii}^{-1}$ for $\Sigma_{ii}\neq 0$ and $\Sigma'_{ii}=0$ for $\Sigma_{ii}=0, i=1,2,\ldots,M$. First, treating $(Q_1+Q_2)^{-1}\cdot G_{t0}^T$ in Eq. (6) as unknown,we obtain the least squares solution of it,

$$(Q_1+Q_2)^{-1}\cdot G_{t0}^T = G_{r0}^{\dagger}\cdot K. \tag{7}$$

Next, an equation for Q_1 could be written, from Eq. (7), as

$$\alpha\cdot Q_1^T=\beta, \tag{8}$$

where $\alpha=(G_{r0}^{\dagger}\cdot K)^T$ and $\beta=[G_{t0}^T-Q_2\cdot G_{r0}^{\dagger}\cdot K]^T$. Thus, by using the least squares method, the scattering strength for the m^{th} scatterer is given by

$$\tau_m=(\alpha_m^{\dagger}\cdot\beta_m)^{-1}, \tag{9}$$

where α_m and β_m denote the m^{th} column of matrices α and β, respectively, $m=1,2,\ldots,M$.

III. NUMERICAL SIMULATION

In order to test the least squares retrieval method and compare it with the noniterative method described in Ref. [1], we apply it to the same simulation geometry used in Refs. [1] and [2]. For the purpose of eliminating the effect of the errors in the estimation of the positions of the scatterers, we, following the second and third experiments in Ref. [1], assume that the correct positions of the scatterers are already known. Besides, we adopt the same method used in Ref. [1] to add the additive white Gaussian noises to the multiple scattering data. The accuracy of the estimates is quantified by a normalized percent error, which is also the same as that used in Ref. [1], defined by $E=100\cdot\|\hat{\tau}-\bar{\tau}\|/\|\bar{\tau}\|$, where $\|\cdot\|$ denotes the L^2 vector norm, $\bar{\tau}=[\tau_1,\tau_2,\ldots,\tau_M]^T$ is the actual value of the scattering strengths, and $\hat{\tau}$ is the estimation of the scattering strengths. All the errors in our numerical experiments are averages over 1000 repetitions. In our first experiment, we assume that all the scatterers' scattering strengths are the same, $\tau_m=1$, $m=1,2,3,4$. The retrieval result using the least squares approach is shown in Fig. 1, in which, for the convenience of comparison, we also plot the result of the second experiment in Ref. [1]. We clearly see that the least squares retrieval method gives a better estimation than the method in Ref. [1] does. The reason why the least squares method outperforms the one proposed in Ref. [1] is that one of the inversion formulas in Ref. [1], i.e., the lower equation of Eq. (6), is inconsistent to some degree with the independency of the receive background Green's function vector in the presence of noise, which can be seen upon the substitution of Eq. (2) to Eq. (6) in Ref. [1], whereas the least squares retrieval method minimizes the error in L^2 form. The retrieval result is also compared with the Cramer-Rao bound (CRB), which expresses a lower bound on the variance of estimators.[4] Using the formulas in the appendix of Ref. [5], we calculate the Fisher matrix I, and take the trace of the inverse of I as the CRB of the total variance of the four scattering strengths. In Fig. 1, we observe that the result obtained by the proposed algorithm is close to that dictated by the CRB $\left(E_{\text{CRB}}=100\sqrt{tr\{I^{-1}\}}/\|\bar{\tau}\|\right)$. In the second experiment, the scattering strengths are changed into $\tau_m=m$, $m=1,2,3,4$, and the result is shown in Fig. 2. In this experiment, we see that the least squares retrieval method also achieves a better result compared with the results shown in Fig. 3 of Ref. [1]. Furthermore, comparing with the result shown in Fig. 1, we find that, although the scattering strengths have been changed, the accuracy of the estimates almost remains the same, which indicates that the performance of the method is stable. In the third experiment, keeping $\tau_m=1$, $m=1,2,3,4$, and without moving the scatterers, we increase the number of the transceivers from 7 to 31, and the transceiver array is still centered along the x axis at

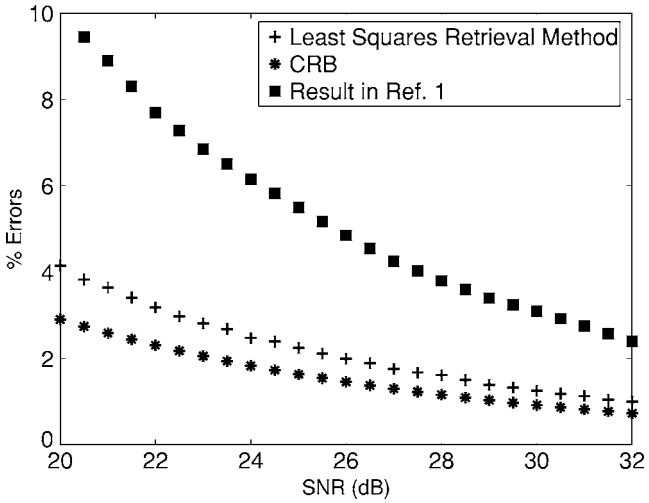

FIG. 1. Comparison of the result obtained by least squares retrieval method and that given in Ref. [1] for the case that the scatterers have same scattering strengths, $\tau_m=1$, $m=1,2,3,4$. The errors are averages of over 1000 repetitions. The CRB of the estimation is also shown.

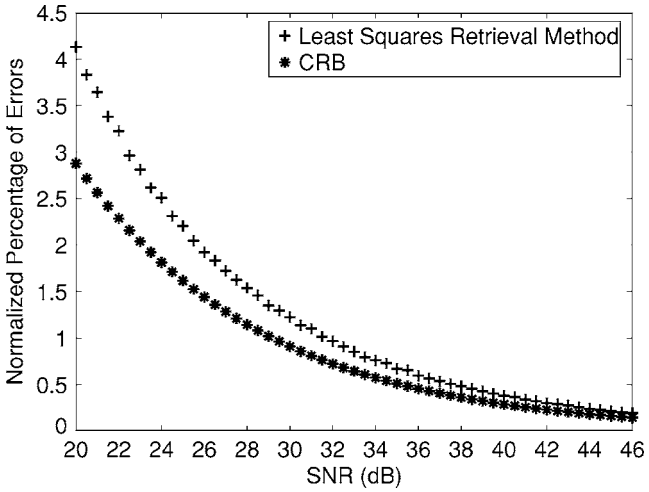

FIG. 2. Normalized percentage of the estimation errors for the case that the scatterers have different scattering strengths, $\tau_m=m$, $m=1,2,3,4$. The errors are averages of over 1000 repetitions. The CRB of the estimation is also shown.

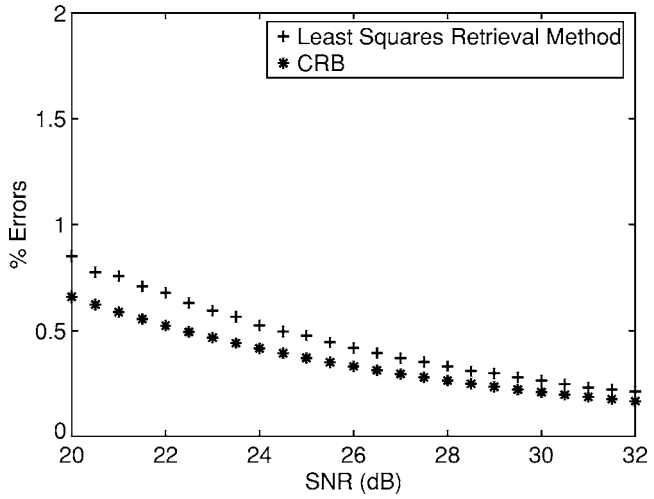

FIG. 3. Normalized percentage of the estimation errors for the case that the number of the transceivers is 31 and the scatterers have same scattering strengths, $\tau_m=1$, $m=1,2,3,4$. The errors are averages of over 1000 repetitions. The CRB of the estimation is also shown.

$z=0$ and having six wavelengths' interelement separation. The result obtained by the least squares retrieval method is shown in Fig. 3. Compared with the result in Fig. 1, we see that the performance of the least squares retrieval method is improved. In both Figs. 2 and 3, the results obtained by the proposed algorithm are close to those dictated by the CRB, respectively.

IV. CONCLUSION

Based on the least squares technique, we present a noniterative approach to solve the nonlinear inverse problem of estimating the target scattering strengths $\tau_m, m=1,2,\ldots,M$ after the target locations $\mathbf{X}_m, m=1,2,\ldots,M$ have been found. Benefiting from the error minimization property, the least squares retrieval method presented in this letter could achieve a better estimation of the scattering strengths than the one obtained by the method proposed in Ref. [1]. In addition, its performance could further be improved by increasing the number of the transceivers. Thus, the least squares retrieval method is a robust noniterative method, which could be implemented after the estimation of the positions of the scatterers by some methods, such as the time reversal MUSIC method.

ACKNOWLEDGEMENT

This work was supported by the Ministry of Education (Singapore) under Grant no. R263000357112 and R263000357133.

[1] E. A. Marengo and F. K. Gruber, "Noniterative analytical formula for inverse scattering of multiply scattering point targets," J. Acoust. Soc. Am. **120**, 3782–3788 (2006).
[2] A. J. Devaney, E. A. Marengo, and F. K. Gruber, "Time-reversal-based imaging and inverse scattering of multiply scattering point targets," J. Acoust. Soc. Am. **118**, 3129–3138 (2005).
[3] R. A. Horn and C. R. Johnson, *Matrix Analysis* (Cambridge University Press, Cambridge, UK, 1986).
[4] S. M. Kay, *Fundamentals of Statistical Signal Processing: Estimation Theory* (PTR Prentice–Hall, Englewood Cliffs, NJ, 1993).
[5] E. A. Marengo and F. K. Gruber, "Subspace-based localization and inverse scattering of multiply scattering point targets," EURASIP J. Adv. Signal Process. **2007**, 17342 (2007).

Forward-masked monaural and interaural intensity discrimination (L)

Mark A. Stellmack,[a] Neal F. Viemeister, and Andrew J. Byrne
Department of Psychology, University of Minnesota, Minneapolis, Minnesota 55455

(Received 21 March 2007; revised 12 June 2007; accepted 12 June 2007)

Intensity-discrimination thresholds were measured for a 25-ms, 6-kHz pure tone for pedestal levels from 40 to 90 dB sound pressure level (SPL) with and without a forward masker (100-ms narrowband Gaussian noise, $N_0=70$ dB). When the masker was present, the masker and probe were separated by 100 ms of silence. Unmasked and masked thresholds were measured in a two-interval monaural procedure and, separately, in a single-interval interaural procedure in which the pedestal and incremented pedestals were presented simultaneously to opposite ears. While the monaural thresholds were elevated markedly by the forward masker for mid-level pedestals, interaural thresholds were nearly unaffected by the masker across pedestal levels. The results argue against the notion that the monaural elevation in forward-masked thresholds is due to degraded encoding of intensity information at early stages of auditory processing. © *2007 Acoustical Society of America.* [DOI: 10.1121/1.2756167]

PACS number(s): 43.66.Fe, 43.66.Pn [JHG] Pages: 1328–1331

I. INTRODUCTION

Zeng *et al.* (1991) reported that intensity-discrimination thresholds (or just-noticeable differences, JNDs) could be markedly elevated for mid-level standards when thresholds were measured in the presence of an intense forward masker. Intensity-discrimination thresholds for low- and high-level standards were relatively unaffected by the forward masker. Zeng *et al.* attributed this "mid-level hump" to differences between auditory nerve fibers with high and low spontaneous firing rates (SRs) in terms of their dynamic ranges and their recovery times from prior stimulation. Auditory nerve fibers can be categorized into two populations on the basis of their spontaneous rates (Liberman, 1978). Low-SR auditory nerve fibers have higher thresholds than high-SR fibers for a criterion increase in firing rate (Liberman, 1978). In addition, low-SR fibers have a slower recovery rate from prior stimulation than high-SR fibers (Relkin and Doucet, 1991). According to Zeng *et al.* (1991), for their mid-level standards, the high-SR, low-threshold fibers were saturated while the low-SR fibers, which would ordinarily encode the intensity of a mid-level stimulus, had not recovered from the prior stimulation of the masker. This resulted in degraded encoding of the intensity of mid-level stimuli across the two populations of fibers, which in turn produced elevated JNDs.

A number of studies have called into question the interpretation that the mid-level hump in forward-masked intensity discrimination can be attributed to degraded intensity information in two populations of auditory nerve fibers. For example, Plack and Viemeister (1992) found that a comparable mid-level hump in intensity-discrimination thresholds could be produced by a masker that followed the probe to be discriminated (a backward masker), which could not possibly affect the representation of the probe at the level of the auditory nerve. However, Plack and Viemeister acknowledge that it is possible that the forward-masked and backward-masked results may be attributable to different mechanisms and that the explanation for the forward-masked results proposed by Zeng *et al.* (1991) may be tenable. Schlauch *et al.* (1997) found that a 10-ms forward masker produced a greater elevation in intensity discrimination thresholds than a 100-ms masker for a 10-ms probe. An explanation of the mid-level hump that depends on adaptation is inconsistent with the fact that auditory nerve fibers recover more slowly from adaptation with increasing duration of the adapting stimulus. Instead, Schlauch *et al.* proposed that the elevation in thresholds results from confusion caused by perceptual similarity of the masker and probe, e.g., when the masker and probe have similar durations. In support of this idea, Schlauch *et al.* also found that greater masking occurred when the masker and probe had similar spectra. While these data seem to argue against the auditory nerve as the source of mechanisms that produce the mid-level hump, Schlauch *et al.* note that their results do not rule out the cochlear nucleus as the site of origin of the effect, a possibility that was suggested by Zeng and Shannon (1995).

The present letter examines the notion that the mid-level hump in forward-masked intensity discrimination is attributable to effects occurring at levels of processing that precede the level at which binaural interaction occurs (superior olive). To this end, forward-masked intensity-discrimination thresholds were measured in a two-interval monaural task and a single-interval interaural task. Stellmack *et al.* (2004) argued that the two tasks present comparable amounts of information in each trial and they showed that monaural and interaural thresholds exhibit comparable Weber's law behavior that is attributable to mechanisms at the auditory periphery that precede binaural interaction. In the present experiment, if a degradation of mid-level intensity-discrimination thresholds is not seen in the interaural intensity-

[a]Author to whom correspondence should be addressed. Electronic mail: stell006@umn.edu

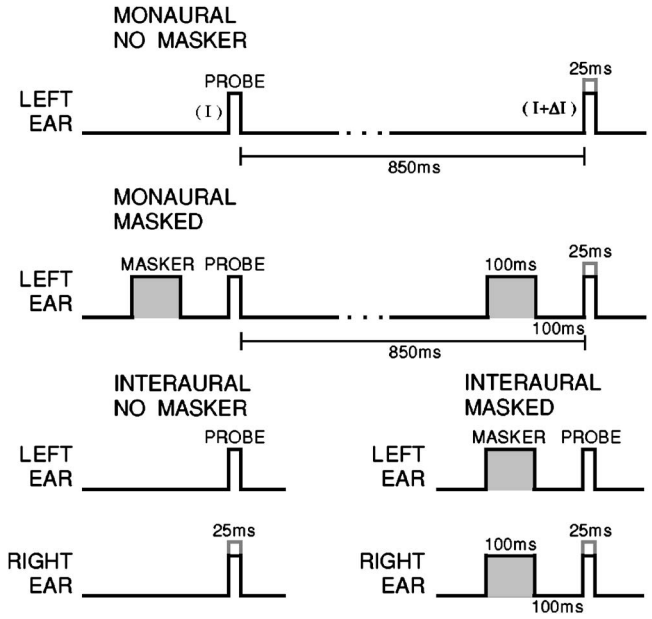

FIG. 1. A schematic illustration of the stimuli in the two-interval monaural and single-interval interaural conditions. In the two-interval monaural condition, the increment to be detected on the probe (ΔI) was presented randomly in either the first or second interval of each trial. In the single-interval interaural condition, the intensity increment was presented in either the left-ear or right-ear probe of each trial.

discrimination task, it would seem to rule out the auditory nerve and the cochlear nucleus as the sites of origin of the monaural effect.

II. METHODS

A. Stimuli

The timing of the stimuli in the two-interval monaural condition and single-interval interaural condition is illustrated in Fig. 1. The masker and probe levels and durations were similar to those of Plack and Viemeister (1992), as those parameters had been shown to produce a very large mid-level hump in monaural forward-masked intensity-discrimination thresholds. The probe (the stimulus whose intensity was to be discriminated) was a 6-kHz, 25-ms pure tone presented at a fixed (sine) starting phase. The forward masker was a narrowband of Gaussian noise (5.9–6.1 kHz) presented at a spectrum level of 70 dB and 100 ms in duration. Both the probe and masker were windowed with 5-ms raised-cosine on-off ramps.

Monaural and interaural intensity-discrimination thresholds were measured both with and without the forward masker. In the two-interval monaural task, the time between the offset of the probe in the first interval and the onset of the probe in the second interval was held constant (850 ms) across the masked and unmasked conditions as was done by Schlauch *et al.* (1997) in order to place similar demands on short-term memory across conditions. In the forward-masked conditions, the time between the offset of the masker and onset of the probe was 100 ms. Thus, the time between the offset of the probe in the first interval and the onset of the masker in the second interval was 650 ms. In the monaural conditions, the forward masker was identical in the two intervals of a trial but an independent sample of Gaussian noise was generated for each trial. The listener's task in the monaural conditions was to select the interval containing the probe plus increment. In the "masked" condition, the masker was presented only to the left ear. (A "monaural-with-diotic-masker" condition, in which the probe was presented to the left ear but the masker was presented to both ears, was added to the design later. This condition is discussed further in the Results and Discussion section.)

In the single-interval interaural intensity-discrimination conditions, the forward masker was either identical in both ears (diotic) or consisted of independent samples of noise in the two ears (dichotic). The maskers in the two ears, were gated on and off simultaneously as were the probes in the two ears. As in the monaural conditions, there was 100 ms of silence between the offset of the masker (when present) and the onset of the probe. In the interaural conditions, the listener's task was to select the ear to which the probe plus increment was presented. Given the differential effects of diotic and dichotic forward maskers in detection tasks (Kohlrausch and Fassel, 1997), it is conceivable that the different interaural configurations of the maskers (diotic or dichotic) might produce different amounts of masking in this intensity-discrimination task. However, it will be seen that no such differences were observed in the present data.

Monaural and interaural intensity-discrimination thresholds were measured for probe pedestal levels from 40 to 90 dB sound pressure level (SPL). The range was chosen based on detection thresholds for the probe (see Sec. II B below) to ensure that all probe pedestals were above detection threshold in the discrimination tasks.

All stimuli were generated digitally in MATLAB. For the maskers, a 1-s broadband noise signal was generated in the frequency domain by drawing amplitudes from a Rayleigh distribution and starting phases from a uniform distribution for all components within the desired frequency range. A time-domain signal was produced by applying an inverse fast Fourier transform to the resulting spectrum. The resulting noise wave form was truncated to the desired length and windowed with 5-ms raised-cosine on-off ramps. The digital signals were generated and converted to analog signals at a 44.1-kHz sampling rate using a PC equipped with a high-quality, 24-bit sound card (Echo Audio Gina). Stimuli were presented over Sony MDR-V6 stereo headphones to listeners seated in a sound-attenuating chamber.

B. Procedure

Prior to measuring intensity-discrimination thresholds, monaural detection thresholds were measured in each ear so that an appropriate range of probe pedestals could be determined for each listener to ensure that all probes were above detection threshold in the discrimination task. Detection thresholds were measured in a two-alternative forced-choice task and using a three-down, one-up adaptive procedure designed to estimate the 79.4 percent-correct point on the psychometric function (Levitt, 1971). The step size was set to 2 dB until four reversals occurred and then the step size was reduced to 1 dB. A block of trials was terminated after 12

reversals and the probe levels at the final eight reversals were averaged to estimate threshold. Four such thresholds were measured for the probe in each ear, with and without the forward masker.

Intensity-discrimination thresholds were measured using the same three-down, one-up adaptive procedure as in the detection conditions. The intensity of the probe plus increment was adjusted in units of dB $[10\log(\Delta I/I)]$. The intensity-discrimination procedure used the same step sizes and termination rule as in the detection conditions. The different conditions were run in the following order: monaural no masker, monaural masked, interaural no masker, interaural diotic/dichotic masker. Within each condition, each listener performed two adaptive runs at each probe pedestal level (with the probe pedestal levels presented in a random order) followed by two additional runs at each pedestal level. Blocks of trials in the interaural diotic/dichotic masker conditions were interleaved. Thus, each listener performed four adaptive runs in each condition, yielding four threshold estimates. The four threshold estimates were averaged to produce the final threshold estimate for each condition.

Each block of trials was initiated by the listener. On each trial, a "ready" light flashed on the computer screen for 250 ms followed by a 100-ms pause after which a trial was presented. The intervals were marked visually by lights on the computer monitor. Listeners entered their responses on the computer keyboard at which time the correct response was indicated on the screen. Listeners were run in 2-h sessions, during which approximately 10–12 blocks of trials were run, until all stimulus conditions were completed.

C. Subjects

The four listeners consisted of the first author and third author and two female undergraduate students from the University of Minnesota who were paid to participate in the study. All listeners had pure-tone thresholds of 15 dB hearing level (HL) or better at octave frequencies from 250–8000 Hz. All listeners had performed in intensity-discrimination experiments previously, therefore only a small number of practice trials were presented to familiarize the listeners with the stimuli prior to data collection.

III. RESULTS AND DISCUSSION

The general pattern of thresholds was similar for all listeners, therefore the thresholds were averaged across listeners and are shown in Fig. 2. In the upper panels of Fig. 2, intensity-discrimination thresholds are plotted in units of $10\log(\Delta I/I)$ as a function of the probe pedestal level. Mean monaural and interaural thresholds are plotted in separate panels. The lower panels show the amount of masking, computed as the difference between the masked and unmasked thresholds.

Comparing the monaural and interaural unmasked thresholds in Fig. 2 (open symbols), the interaural thresholds show the same pattern across probe pedestal level as the monaural thresholds, but the interaural thresholds are a few dB better than the monaural. This is consistent with the results reported by Stellmack *et al.* (2004) for unmasked monaural and interaural intensity discrimination.

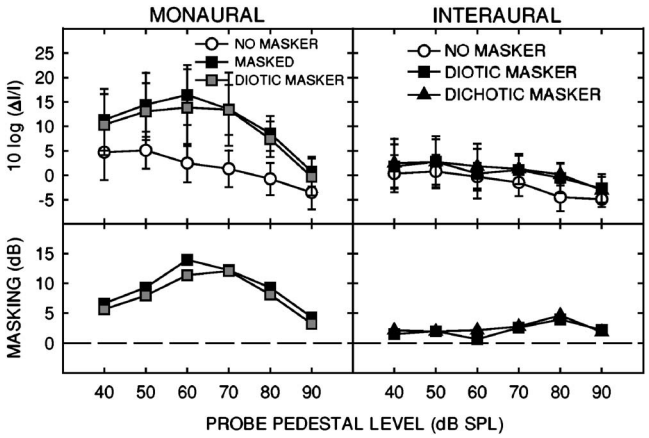

FIG. 2. Upper panels: Intensity-discrimination thresholds in dB $[10\log(\Delta I/I)]$ averaged across four listeners as a function of probe pedestal level in the monaural (left column) and interaural (right column) conditions. Open symbols show unmasked thresholds and filled symbols show masked thresholds, as indicated in the legend. Error bars represent ± one standard deviation. Lower panels: Mean amount of masking in dB, computed as the difference between the masked and unmasked thresholds in the corresponding upper panels.

In the monaural conditions, mean thresholds were higher when the forward masker was present relative to the unmasked conditions. In addition, the largest amount of masking (difference between the masked and unmasked threshold) occurred at an intermediate probe pedestal level (a mid-level hump). There were individual differences in terms of the probe pedestal level at which the greatest masking occurred, but for all listeners the greatest masking occurred at an intermediate pedestal level, such that all individual data exhibited a mid-level hump.

The mean monaural masked thresholds show the mid-level hump that has been reported in other studies (e.g., Plack and Viemeister, 1992; Schlauch *et al.*, 1997). The amount of masking across probe level in the present study is very similar to that of Plack and Viemeister (1992) for comparable stimulus parameters. A one-way repeated-measures analysis of variance (ANOVA) performed on the amount of masking in the monaural condition (lower left panel of Fig. 2) confirms that the effect of probe pedestal level was statistically significant $[F(5,15)=1.29, p=.001]$.

In contrast, the present interaural thresholds show no effect of either the diotic or dichotic masker across pedestal levels. A two-way repeated-measures ANOVA performed on the interaural data (with the factors masker configuration and probe pedestal level) confirmed that the main effect of the masker configuration (unmasked/diotic masker/dichotic masker) was not significant $[F(2,6)=4.88, p=.055]$. If the monaural mid-level hump was due to degraded intensity information at the level of the auditory nerve or cochlear nucleus, the interaural thresholds should exhibit a similar mid-level hump, but they do not. These results indicate that encoding of intensity information appears to remain nearly unaffected by forward masking across probe level at least to the level of the superior olive, the first opportunity for binaural interaction.

It is interesting that in the interaural condition the thresholds were similar with and without the masker. Assuming that the listeners were using a laterality cue to perform the task, the diotic masker might be expected to provide a strong centered reference. The listener could use this reference rather than a possibly unreliable "internal" reference to detect left-right deviations from a centered image. The similarity of the thresholds suggests that the masker was not used as a centering cue. This may be because the internal reference is sufficiently reliable to permit good performance: listeners may have a relatively noise-free representation of a centered image and do not need the reminder provided by the diotic masker.

The question remains as to the source of the mid-level hump in monaural intensity-discrimination thresholds. The idea that the effective levels or loudness of the masker and probe are combined, perhaps as a result of confusion due to perceptual similarity of the masker and probe (Schlauch *et al.*, 1997), remains a viable explanation. Perhaps the differences in perceived laterality that are introduced in the interaural condition permit the listener to perceptually segregate the masker and probe sufficiently to minimize the effects of the masker. In order to examine the effects of differential lateralization of the masker and probe, the masked monaural thresholds were measured again, but with the forward masker presented diotically ("monaural-with-diotic-masker"). All other stimulus parameters were the same as in the masked monaural conditions. In this case the masker is presumably lateralized in the center of the listener's head while the probe is lateralized at the left ear.

The data from the monaural-with-diotic-masker conditions are plotted as gray squares in Fig. 2. If the absence of the mid-level hump in the original interaural conditions of the main experiment resulted from differential lateralization of the masker and probe, we might expect the mid-level hump to be eliminated in the monaural-with-diotic-masker conditions as well. However, it can be seen that thresholds were nearly identical to those in the purely monaural conditions (represented by the black squares). A difference between the monaural-with-diotic-masker and the interaural conditions is that in the former, although the masker and probe might be lateralized differentially, lateralization does not provide a cue to performing the intensity-discrimination task. The probe and incremented probe always will be lateralized at the same intracranial position and presumably the task must be performed on the basis of changes in the loudness of the probe. In the interaural condition, differential lateralization resulting from the incremented probe being presented to either the left or right ear provides a cue that would allow listeners to perform the task; that is, it is not necessary for the listener to discriminate loudness of the probe in the interaural task. Therefore, it is plausible that the forward masker interferes with some aspect of the perceived loudness of the probe, which will interfere with performance of the monaural task but not the interaural task.

How might the forward masker interfere with the perceived loudness of the probe? Plack and Viemeister (1992) suggested a "referential coding" hypothesis, in which the masker degrades a "memory trace" for the probe, which interferes with the ability to make comparisons across temporally distinct intervals in both forward- and backward-masking situations. When a reference stimulus to which the probe can be compared is present within each interval, the system may switch to a "referential coding" mode, which does not require retention of a memory trace of the stimulus across intervals but rather encodes the stimulus on the basis of contextual relationships. Plack *et al.* (1995) showed that a fixed-level reference stimulus within each interval of a monaural forward- or backward-masked intensity-discrimination paradigm eliminates the mid-level hump. Presumably, the probe can be compared to the fixed-level reference in each interval, which facilitates encoding as a *change* in loudness within each interval. In the single-interval interaural task of the present experiment, the probe and incremented probe are presented simultaneously to opposite ears, which permits immediate comparison of the stimuli and removes any dependence on a representation in memory that might be degraded by the masker. Thus, the results of the present experiment are consistent with the referential coding hypothesis of Plack and Viemeister (1992). Although the source of the mid-level hump in monaural intensity-discrimination thresholds remains open to debate, the accumulating evidence, including that of the present letter, seems to indicate that it is not a result of processing that occurs at the auditory periphery.

ACKNOWLEDGMENTS

This work was supported by Research Grant No. R01 DC0 0683 from the National Institute on Deafness and Communication Disorders, National Institute of Health.

Kohlrausch, A., and Fassel, R. (**1997**). "Binaural masking level differences in nonsimultaneous masking," in *Binaural and Spatial Hearing in Real and Virtual Environments*, edited by R. H. Gilkey and T. R. Anderson (Lawrence Erlbaum, Mahwah, NJ), 169–190.

Levitt, H. (**1971**). "Transformed up-down methods in psychophysics," J. Acoust. Soc. Am. **49**, 467–477.

Liberman, M. C. (**1978**). "Auditory-nerve response from cats raised in a low-noise chamber," J. Acoust. Soc. Am. **63**, 442–455.

Plack, C. J., Carlyon, R. P., and Viemeister, N. F. (**1995**). "Intensity discrimination under forward and backward masking: Role of referential coding," J. Acoust. Soc. Am. **97**, 1141–1149.

Plack, C. J., and Viemeister, N. F. (**1992**). "Intensity discrimination under backward masking," J. Acoust. Soc. Am. **92**, 3097–3101.

Relkin, E. M., and Doucet, J. R. (**1991**). "Recovery from forward masking in the auditory nerve depends on spontaneous firing rate," Hear. Res. **55**, 215–222.

Schlauch, R. S., Lanthier, N., and Neve, J. (**1997**). "Forward-masked intensity discrimination: Duration effects and spectral effects," J. Acoust. Soc. Am. **102**, 461–467.

Stellmack, M. A., Viemeister, N. F., and Byrne, A. J. (**2004**). "Monaural and interaural intensity discrimination: Level effects and the 'binaural advantage,'" J. Acoust. Soc. Am. **116**, 1149–1159.

Zeng, F.-G., and Shannon, R. V. (**1995**). "Possible origins of the non-monotonic intensity discrimination function in forward masking," Hear. Res. **82**, 216–224.

Zeng, F.-G., Turner, C. W., and Relkin, E. M. (**1991**). "Recovery from prior stimulation II. Effects upon intensity discrimination," Hear. Res. **55**, 223–230.

Age-related changes in sensitivity to native phonotactics in Japanese infants (L)

Ryoko Mugitani[a)]
NTT Communication Science Laboratories, NTT Corporation, 2-4 Hikari-dai, Seika-cho, Souraku-gun, Kyoto 619-0237, Japan

Laurel Fais
Infant Studies Centre, University of British Columbia, 2136 West Mall, Vancouver, British Columbia, V6T 1Z4 Canada

Sachiyo Kajikawa
NTT Communication Science Laboratories, NTT Corporation, 2-4 Hikari-dai, Seika-cho, Souraku-gun, Kyoto 619-0237

Janet F. Werker
Infant Studies Centre, University of British Columbia, 2136 West Mall, Vancouver, British Columbia, V6T 1Z4 Canada

Shigeaki Amano
NTT Communication Science Laboratories, NTT Corporation, 2-4 Hikari-dai, Seika-cho, Souraku-gun, Kyoto 619-0237, Japan

(Received 18 October 2006; revised 13 February 2007; accepted 11 June 2007)

Japanese infants at the ages of 6, 12, and 18 months were tested on their ability to discriminate three nonsense words with different phonotactic status: canonical *keetsu*, noncanonical but possible *keets*, and noncanonical and impossible *keet*. The results showed that 12 and 18 months olds discriminate the *keets/keetsu* pair, but infants in all age groups fail to discriminate the *keets/keet* pair. Taken together with the findings in our previous study [Kajikawa *et al.*, J. Acoust. Soc. Am. **120**(4), 2278-2284 (2006)], these results suggest that Japanese infants develop the perceptual sensitivity for native phonotactics after 6 months of age, and that this sensitivity is limited to canonical patterns at this early developmental stage. © *2007 Acoustical Society of America.* [DOI: 10.1121/1.2754063]

PACS number(s): 43.71.Ft [MSS] Pages: 1332–1335

I. INTRODUCTION

Language-specific phonotactic rules influence speech perception.[1,2] Our previous study explored the development of sensitivity for native phonotactic rules by comparing discrimination of phonotactic patterns in infants from two different language backgrounds, English and Japanese.[3] The infants were tested on their discrimination of three nonsense words *neek*, *neeks* and *neekusu*. All of these words are phonotactically legal forms in English, whereas the first two are not canonical Japanese forms. Japanese is based on the "mora" as its timing unit, which consists of CV or V components. Thus, consonant clusters (CC, such as in *neeks*) and consonant pause combinations (C pause, such as in *neek*.) are not canonical phonotactic patterns in Japanese.

Although CC and C pause are illegal in Japanese phonotactics, these patterns actually occur in vowel devoicing contexts in fluent speech. High vowels (i.e., /i/ and /u/) are often devoiced when they appear between voiceless consonants or between a voiceless consonant and a pause.[4] For example, *neekusu* contains two vowels that could be devoiced: /u/ in the second syllable, positioned between voiceless consonants /k/ and /s/, and /u/ in the word-final syllable positioned between voiceless consonant /s/ and pause. Thus, *neeks* is a possible, fluent speech pronunciation of the word *neekusu*. In the same manner, *neek* is a possible, fluent speech pronunciation of the word *neeku*.

Our previous study[3] explored infants' performance from two points of view. The first involved the discrimination of a CVCC word, *neeks*, and a CVCVCV word, *neekusu*, and the second involved the discrimination of a CVCC word, *neeks*, and a CVC-pause word *neek*. For English-learning infants, all three words, *neek*, *neeks*, and *neekusu*, are different, legally formed words. When it comes to Japanese-learning infants, *neeks* and *neekusu* are closely related by vowel devoicing and thus constitute the "same" word, although *neeks* is a noncanonical form which is only possible in vowel devoicing contexts. On the other hand, *neeks* and *neek* originated from different word forms (*neekusu* vs. *neeku*), and thus, they are unrelated, although both words are noncanonical but possible forms in devoicing contexts. By comparing words with different phonotactic status in Japanese and English, cross-linguistic differences in discrimination patterns were investigated so as to reveal language-specific sensitivities for native phonotactics.

The results showed that native phonotactic congruence does affect infant discrimination. Both English and Japanese

[a)]Author to whom correspondence should be addressed. Electronic-mail: mugitani@cslab.kecl.ntt.co.jp

infants at 6, 12, and 18 months of age discriminated *neeks/neekusu*. In addition, a cross-linguistic difference was observed in the developmental trajectory of discrimination; the percentage of English infants who discriminated *neekusu* from *neeks* increased linearly with age, whereas that of Japanese infants did not change. We interpreted this finding to mean that increased experience with devoicing forms in Japanese propels infants' tendency to accept *neeks* as a devoiced form of *neekusu*. Because infants recognized the close relation between *neeks* and *neekusu*, the degree of discrimination remained the same instead of increasing as it did for English infants.

Both Japanese and English infants at 6 and 12 months of age failed to discriminate *neeks/neek*. This fact suggested that, irrespective of the native phonotactics, the phonetic differences between the two words were difficult to detect for infants younger than 12 months. At 18 months of age, English infants, but not Japanese infants, succeeded in the discrimination. Because *neeks* and *neek* are phonotactically canonical for English infants but not for Japanese infants, the phonotactic stability of the words presumably facilitated the language-experienced 18-month-old English infants' discrimination of these two legal word forms. On the other hand, even though the percentage of Japanese infants who discriminated *neeks* and *neek* increased with age, Japanese infants failed as a group to show significant discrimination of these phonotactically illegal (but possible) word forms.

These previous findings stimulated further investigation by raising several questions. The *neeks/neekusu* pair, for which Japanese infants showed robust discriminability from 6 months of age, differs not only in phonotactic acceptability but also in number of vowels (1 vs. 3). Given the fact that young infants have a perceptual sensitivity to vowels[5] and that preference for phonotactically legal over illegal words emerges not at 6, but at 9 months of age,[6] we speculated that the fine discrimination shown by Japanese infants at 6 months is accounted for by their sensitivity to the phonetic differences between the members of the stimulus pair, rather than by their phonotactic awareness. Second, *neeks* and *neek*, which Japanese infants at all ages failed to discriminate, have the same degree of phonotactic acceptability: both are noncanonical but possible forms in vowel devoicing contexts. The question we posed is that, if Japanese infants develop sensitivity for the vowel devoicing context, do they differentiate a possible vowel-devoicing word from an impossible word form according to phonotactic acceptability?

To answer these questions drawn from the previous study, we further tested discrimination in Japanese infants using new sets of word pairs: *keets/keetsu* and *keets/keet*. Just as *neeks* is the devoiced form of *neekusu*, *keets* is the devoiced form of *keetsu*. However, compared to *neekusu/neeks*, *keetsu/keets* reduces the number of syllables that cue discrimination. If discrimination by the 6-month-old infants in the previous study is guided by a sensitivity to canonical vs. noncanonical forms, then 6-month-old infants in the present study should discriminate *keetsu/keets*. On the other hand, if the degree of phonetic difference is what made discrimination of *neekusu/neeks* possible, then 6-month-olds may fail to discriminate the more phonetically similar *keetsu/keets*.

The second pair, *keets/keet* was employed to test infants' sensitivity to possible and impossible word forms in vowel devoicing contexts. Unlike *neeks*, *neek*, and *keets*, which are noncanonical but acceptable forms in Japanese phonology, *keet* is noncanonical as well as unacceptable. This is because before high vowels, /t/ has the allophonic form of either [**tʃ**] (only before /i/) or [**ts**] (only before /u/). Thus, *keets* is a possible, vowel-devoiced form of *keetsu*, whereas *keet* is an impossible pattern in any context. If Japanese infants are sensitive to phonotactic status with regard to vowel devoicing, they are expected to discriminate an impossible word form *keet* from a possible word form *keets*.

II. METHODS

A. Participants

All participants were full-term, healthy infants without a serious medical history, raised in a monolingual Japanese environment in western Japan. As in the previous study, 24 infants (12 boys and 12 girls) each at 6, 12, and 18 months made up the final sample. The makeup of each age group was as follows: 6-month group (M_{age}=6 months 21 days, SD=7.1 days), 12-month group (M_{age}=12 months 25 days, SD=8.7 days), 18-month group (M_{age}=18 months 4 days, SD=8.0 days). An additional 27 infants were tested but excluded for the following reasons: fussiness (n=15), and failure to reach the habituation criterion (n=12).

B. Stimuli

Stimuli were three nonsense words: *keet* (/ki:t/), *keets* (/ki:ts/), and *keetsu* (/ki:tsu/). All the words were accented on the first syllable. In terms of phonotactic acceptability, neither *keets* nor *keet* is phonotactically legal in Japanese, but *keets* is possible in devoicing contexts in fluent speech, and *keetsu* follows Japanese phonotactic rules perfectly. In terms of phonetics, the *keets/keetsu* pair differs in the absence/presence of a single vowel /u/, whereas the *keets/keet* pair differs in the presence/absence of a single consonant /s/.

The three words were uttered by a female speaker, and were recorded onto a computer at a sampling rate of 16 bits, 44.1 kHz. Five intonational variations for each of the words with nearly identical speaking rates were selected as final stimuli for the experiment.

C. Apparatus

The apparatus and experimental procedure were exactly the same as the previous study. The experiment involved a habituation-switch design[7] controlled by the Habit 2002 program[8] run on a Power Mac G4. The infant sat on the parent's lap, approximately 46 in. from a 19 in. monitor in a soundproof test booth. The audio stimuli were delivered at 65 dB, ±5 dB(A), over loudspeakers located below the monitor. Infants' responses were recorded by a video camera which was located 10 in. below the monitor.

The experiment comprised a habituation phase and a test phase. At the beginning of each trial, an animated, rotating blue flower was presented to draw the infant's attention to the display. During the trials in the habituation phase, audi-

TABLE I. Mean looking times (s), standard errors, and ANOVA for effects of "Same" and "Switch" trials in each age group. $^{*}p<0.05$ $^{**}p<0.01$.

Age (month)	Same-*keets*		Switch-*keet*		Switch-*keetsu*		ANOVA
	M	*SE*	*M*	*SE*	*M*	*SE*	*F* (2, 46)
6	7.33	0.49	6.64	0.32	7.24	0.81	1.14
12	6.87	0.63	7.45	0.71	9.14	0.74	4.48*
18	7.39	0.73	8.42	0.69	9.98	0.71	5.85**

tory *keets* was presented with a red-black checkerboard as the visual stimulus. Each trial was 14 s long, and seven tokens were presented randomly (five intonational variations matched across the three words with two variations repeated) with an approximately 1 s inter-stimulus interval. The habituation criterion was set to 65% of the mean looking time of the longest block of three trials. When the average looking time across a three-trial block decreased to the criterion, the habituation phase ended. The infants were expected to take part in a minimum of nine and a maximum of 27 habituation trials. Thus, those who reached the criterion at the second block with six habituation trials, and those who did not reach the criterion even at the ninth block with 27 habituation trials were excluded from the analysis.

Following the habituation phase, a test phase consisting of three trials began. One test trial was a "Same" trial in which the *keets* stimuli presented during the habituation phase were presented again. During the other two trials, the "Switch" trials, *keet* and *keetsu* were presented. It was expected that if infants detected the stimulus change from habituation trials (i.e., *keets*) to Switch trials (i.e., *keet* or *keetsu*), they would attend longer during these trials than during a Same trial. The presentation order of the test trials was counterbalanced between infants.

After the experiment, a trained coder judged infants' looking times based on frame-by-frame observation using the digitized video record (frame rate=1/30 s).

III. RESULTS

Mean looking times for the test trials were submitted to a one-way analysis of variance (ANOVA) (three word levels: [Same-*keets* vs. Switch-*keet* vs. Switch-*keetsu*]) in each age group. The main effect reached significance for the 12 and 18 month groups, but not for the 6 month group (see Table I). Post-hoc multiple comparisons (LSD) revealed that infants in both the 12 and 18 month age groups looked significantly longer during a Switch-*keetsu* trial than a Same-*keets* trial (12 months: $p=0.001$, 18 months: $p=0.003$). The difference in looking time between a Same-*keets* and a Switch-*keet* trial did not reach significance in either of the age groups ($p>0.1$, see Fig. 1).

As in the previous study, we calculated the percentage of infants who showed recovery of looking time in the Switch trials as an index of developmental change in discrimination ability. The analysis indicated that the percent of infants showing recovery was 37.5%, 54.2% and 58.3%, respectively, for the 6, 12 and 18 month groups for the Switch-*keet* trial of the *keets/keet* discrimination, and 45.8%, 79.2% and

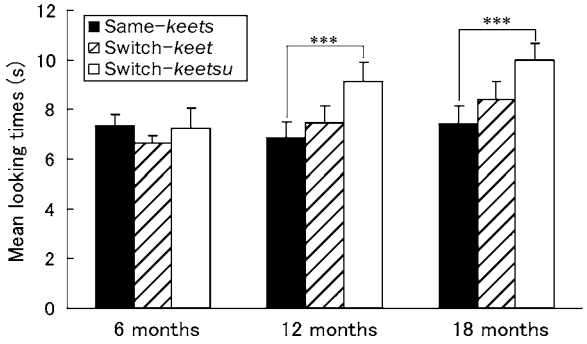

FIG. 1. Mean looking times of infants in test trials for each age group. Error bars stand for standard errors. $^{***}p<0.005$.

79.2%, respectively, for the Switch-*keetsu* trial of the *keets/keetsu* discrimination (see Fig. 2). Thus, for both *keets/keet* and *keets/keetsu* discrimination, the percentage increased from 6 to 12 months, and then remained stable after 12 months of age.

The percentage of recovery supported the results of the looking time analysis. In the 12 and 18 month groups, a nonparametric chi-square test revealed that the percentage of infants who increased looking time to the Switch-*keetsu* trial (over a Same trial) is larger than the percentage who increased looking time to the Switch-*keet* trial (12 months: $\chi^2=6.04$, $p<0.01$, 18 months: $\chi^2=4.29$, $p<0.05$). However, the 6 month group showed no such difference ($\chi^2=1.51$, $p>0.1$).

Taken together, the results suggest that Japanese 12 and 18 month olds discriminate the *keets/keetsu* pair, whereas 6 month olds fail to do so. In addition, infants in all age groups failed to discriminate the *keets/keet* pair.

IV. DISCUSSION

The present study extended the previous study by Kajikawa, Fais, Mugitani, Werker and Amano on perceptual development of native phonotactic rules to explore: 1) sensitivity to phonetic salience and phonotactic acceptability by testing *keets/keetsu* discrimination, and 2) sensitivity to phonotactic status regarding the vowel devoicing context by testing *keets/keet* discrimination in Japanese infants.

The previous study indicated that Japanese infants in all of the 6, 12, and 18 month age groups discriminated phono-

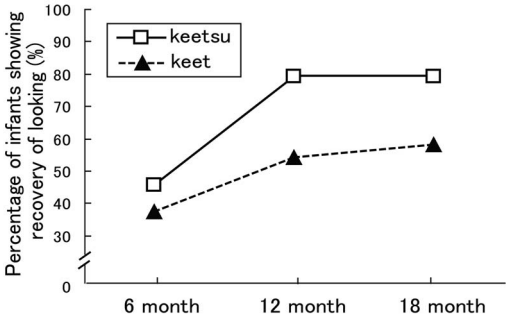

FIG. 2. Percentages of infants who showed recovery of looking in Switch trials compared to Same trial. Note that the percentage is significantly larger for the Switch-*keetsu* trial than that for the Switch-*keet* trial for the 12 and 18 month groups.

tactically canonical *neekusu* from phonotactically noncanonical but possible *neeks*. On the contrary, 6-month-old infants in the present study failed to discriminate *keetsu* from *keets* although the pair actually has the same phonotactic status (canonical vs. noncanonical but possible) as the *neekusu/neeks* pair. Given the fact that *neekusu* differs from *neeks* by the addition of two vowels, whereas *keetsu* differs from *keets* by only one vowel, we speculate that the successful discrimination of *neeks/neekusu* at 6 months of age was due to the salience of the phonetic difference, rather than phonotactic acceptability. Furthermore, the fact that the *keets/keetsu* contrast occurs in a word-final, low salience position[9] might make it especially difficult for younger infants to perceive the difference, and thus lead to a failure in discrimination.

We found that infants overcome the difficulty in differentiating *keets/keetsu* at 12 months of age. One possible phonetic account for the development of discrimination might be that infants become perceptually more sensitive to a word final vowel /u/. However, we should also consider the influence of phonotactic acceptability. By 12 months of age, infants develop not only phonetic, but also phonotactic sensitivity for the native language, and prefer listening to legal over illegal phonotactics.[6,10] Thus, the infants in the current study might have discriminated *keetsu* from *keets* based on a growing knowledge of native phonotactics.

The previous study reported that, although Japanese infants at all ages could discriminate *neekusu/neeks*, the percentage of infants who showed recovery of looking did not increase with age. On the other hand, the percentage increased linearly for English infants. We interpreted this finding as indicating that, with increased exposure to vowel devoicing, Japanese infants started to apprehend the close relationship between *neekusu* and its devoiced version *neeks*, and this suppressed infants' discrimination of these forms. This claim was further supported by the current results of the *keets/keetsu* discrimination: The percentage of infants who presented recovery of looking increased from nearly 46% at 6 months more than 33 points to above 79% at 12 months of age, and then remained the same at 18 months of age. The initial leap in recovery indicates that infants' discrimination of the word pair improved from 6 to 12 months. Then, the percentage levels off, presumably because discrimination of the pair is suppressed as infants develop a fine-grained appreciation of the relation between *keets* and *keetsu* after 12 months of age.

In Japanese phonology, CC clusters or C pause are not legitimate, but they occur sometimes in vowel devoicing contexts. Both *neeks* and *neek*, which Japanese infants at all ages failed to discriminate in the previous study, were noncanonical but possible devoiced forms of *neekusu* and *neeku*. In the present study, only *keets* is a possible word form (from *keetsu* with devoicing), and *keet* is neither canonical nor a possible word form in Japanese. If infants are aware of the different phonotactic status of *keets* and *keet*, we can expect them to discriminate the pair.

However, the results showed that infants even at 18 months of age failed to discriminate *keet* and *keets*. Taken together with our previous findings,[3] we hypothesize that at least one member of a word pair must conform to a canonical phonotactic pattern in order to guide successful discrimination at this age. According to this hypothesis, English 18-month-old infants could discriminate both *neeks/neekusu* and *neeks/neek* pairs because the paired words, *neekusu, neek, neeks*, are all legitimate surface forms in their native language. Likewise, Japanese 18-month-old infants could discriminate the *neeks/neekusu* and *keets/keetsu* pairs because one of the paired words, either *neekusu* or *keetsu*, exhibits canonical phonotactics in Japanese. However, they failed to discriminate *neeks/neek* as well as *keets/keet* probably because these pairs were made up entirely of noncanonical forms in Japanese. Although more work will be needed to fully confirm this hypothesis, infants' preference for legal phonotactic forms [6,10] supports the idea that they first develop sensitivity exclusively to phonotactically canonical patterns.

In summary, we explored the development of sensitivity to native phonotactic patterns in Japanese monolingual infants by testing discrimination of word pairs with different phonotactic status. The results revealed the following: (1) word discriminability at 6 months of age is influenced by the salience of the phonetic difference, rather than by phonotactic acceptability, (2) infants failed to detect the different phonotactic status of noncanonical words (possible in devoicing context vs. impossible) even at 18 months of age, suggesting that phonotactic sensitivity to noncanonical patterns appears later than that to canonical patterns.

[1]E. Dupoux, K. Kakehi, Y. Hirose, C. Pallier, and J. Mehler, "Epenthetic vowels in Japanese: A perceptual illusion?" J. Exp. Psychol. Hum. Percept. Perform. **25**, 1568–1578 (1999).

[2]L. Fais, S. Kajikawa, J. Werker, and S. Amano, "Japanese listeners' perceptions of phonotactic violations," Lang Speech **48**, 185–201 (2005).

[3]S. Kajikawa, L. Fais, R. Mugitani, J. Werker, and S. Amano, "Cross-language sensitivity to phonotactic patterns in infants," J. Acoust. Soc. Am. **120**(4), 2278–2284 (2006).

[4]*Voicing in Japanese*, edited by J. van de Weijer, K. Nanjo, and T. Nishihara (Mouton de Gruyter, Berlin 2005).

[5]J. Bertoncini, R. Bijeljac-Babic, P. W. Jusczyk, L. Kennedy, and J. Mehler, "An investigation of young infants' perceptual representations of speech sounds," J. Exp. Psychol. Gen. **117**, 21–33 (1988).

[6]P. W. Jusczyk, P. A. Luce, and J. Charles-Luce, "Infants' sensitivity to phonotactic patterns in the native language," J. Mem. Lang. **33**, 630–645 (1994).

[7]C. L. Stager and J. F. Werker, "Methodological issues in studying the link between speech perception and word learning," in *Advances in Infancy Research*, edited by C. Rovee-Collier, L. Lipsitt, and H. Hayne (Ablex, Stamford, CT, 1998), Vol. **12**, pp. 237–256.

[8]L. B. Cohen, D. J. Atkinson, and H. H. Chaput, "Habit 2002: A new program for obtaining and organizing data in infant perception and cognition studies (version 1.0) [Computer Software]," The University of Texas, Austin, TX (2002).

[9]P. W. Jusczyk, A. Bauman, and M. Goodman, "Sensitivity to sound similarities in different utterances by 9 month olds," J. Mem. Lang. **40**, 62–82 (1999).

[10]P. W. Jusczyk, A. D. Friederici, J. M. I. Wessels, V. Y. Svenkerud, and A. M. Jusczyk, "Infants' sensitivity to the sound patterns of native language words," J. Mem. Lang. **32**, 402–420 (1993).

Effects of periodic interruptions on the intelligibility of speech based on temporal fine-structure or envelope cues (L)

Gaëtan Gilbert,[a] Isabelle Bergeras, Dorothée Voillery, and Christian Lorenzi[b]
Laboratoire de Psychologie de la Perception, CNRS-Paris 5, DEC, Ecole Normale Supérieure, 29 rue d'Ulm, 75005 Paris, France.

(Received 1 December 2006; revised 12 June 2007; accepted 12 June 2007)

The intelligibility of speech signals processed to retain either temporal envelope (E) or fine structure (TFS) cues within 16 0.4-oct-wide frequency bands was evaluated when processed stimuli were periodically interrupted at different rates. The interrupted E- and TFS-coded stimuli were highly intelligible in all conditions. However, the different patterns of results obtained for E- and TFS-coded speech suggest that the two types of stimuli do not convey identical speech cues. When an effect of interruption rate was observed, the effect occurred at low interruption rates (<8 Hz) and was stronger for E- than TFS-coded speech, suggesting larger involvement of modulation masking with E-coded speech. © *2007 Acoustical Society of America.* [DOI: 10.1121/1.2756161]

PACS number(s): 43.71.Gv, 43.71.Es, 43.66.Mk [KWG] Pages: 1336–1339

I. INTRODUCTION

Recent studies (e.g., Shannon *et al.*, 1995; Smith *et al.*, 2002) have shown that two temporal features of filtered speech signals carry critical—and sometimes sufficient—information for identification in quiet: its temporal envelope (E) and temporal fine structure (TFS). E refers to the relatively slow modulations in amplitude over time and TFS refers to the rapid oscillations with rate close to the center frequency of the band. The roles of these components have been studied by processing speech signals via so-called E and TFS "speech processors," speech was filtered into a number of frequency bands (also called "analysis filters") with the signal from each analysis band processed using the Hilbert transform to remove either E or TFS information.

However, modeling work by Ghitza (2001) revealed that the physically removed E cues are reconstructed at the output of peripheral auditory filters and may therefore be used by listeners. As a consequence, the identification of TFS-coded speech may be "contaminated" by a contribution of reconstructed E cues. This was demonstrated by two psychoacoustical studies conducted by Zeng *et al.* (2004) and Gilbert and Lorenzi (2006), showing that TFS-coded speech items could be identified by listeners on the basis of the reconstructed E cues extracted at the output of a bank of gammachirp auditory filters. Nevertheless, the identification scores obtained by Gilbert and Lorenzi (2006) suggested that the reconstructed E cues did not play a major role in speech identification when the bandwidth of analysis filters was narrower than 4 ERBs.

The approach taken by Gilbert and Lorenzi (2006) depended upon modeling assumptions (i.e., their model of auditory periphery). Further work is therefore required to assess whether or not reconstructed E cues contribute to the intelligibility of TFS-coded speech when analysis filters are narrower than 4 ERB. Additional evidence that the identification of TFS-coded speech analyzed through narrow filters does not rely on reconstructed E cues should also be important for the interpretation of recent data showing that cochlear damage abolishes the ability to identify TFS-coded speech (Lorenzi *et al.*, 2006).

A recent study conducted by Nelson and Jin (2004) assessed the effects of periodic interruption on the intelligibility of 4- and 12-band E-coded sentences. Surprisingly, the effect of interruption on intelligibility was found to be dramatic. The results of Nelson and Jin (2004) indicate therefore that speech identification based on E cues alone is not robust to this specific type of temporal distortion. Nelson and Jin (2004) suggested that the massive drop in the intelligibility of E-coded speech was due to the fact that spectral and TFS cues are required to fuse perceptually interrupted speech signals into a coherent speech stream. This lack of robustness may also result from the drastic modifications of the speech envelope caused by stimulus interruption. Periodic interruption represents an extraneous modulation of the speech signal. This extraneous modulation may then serve as a masker of the speech signal modulation. Modulation masking and modulation detection interference (MDI) refer to the difficulty in processing specific envelope rate or pattern in the presence of a competing envelope modulation (e.g., Sheft and Yost, 2006). Kwon and Turner (2001) demonstrated modulation masking or MDI effects on speech perception, especially for speech items with a low degree of redundancy. It is thus likely that the deleterious effects of periodic interruption on the identification of E-coded speech reported by Nelson and Jin (2004) were—at least partly—due to such modulation masking and MDI effects. This is consistent with the fact that that the most dramatic effect of interruption was found at the lowest rates of interruption (below 10 Hz), given that MDI is greatest at low rates, and that rates below 16 Hz are the most important rates for speech identification (e.g., Drullman *et al.*, 1994). The effects of periodic interruption on the identification of TFS-coded speech remain un-

[a]Present address: MRC Institute of Hearing Research, Glasgow Royal Infirmary, Queen Elizabeth Building, 16 Alexandra Parade, Glasgow G31 2ER, UK. Electronic mail: gaetan@ihr.gla.ac.uk
[b]Electronic mail: christian.lorenzi@psycho.univ-paris5.fr

known. However, as an effect in the temporal-envelope domain, modulation masking or MDI are not anticipated to affect the intelligibility of TFS-coded stimuli processed using narrow (<4 ERBs) analysis filters, *unless* intelligibility is based on reconstructed E cues.

The goal of the present study was to assess the robustness of speech identification based on E and TFS cues alone when speech signals processed using narrow (<4 ERBs) analysis filters were periodically interrupted, in order to test whether or not E- and TFS-coded speech convey identical speech cues.

II. EXPERIMENT

A. Method

1. Speech material and stimuli

Bashford *et al.* (1992) demonstrated that redundancy of speech material at morphological, syntactic, or semantic levels can influence the effect of interruption on intelligibility. To keep redundancy low, meaningless vowel-consonant-vowel (VCV) logatomes were used. One set of 48 unprocessed VCV stimuli was recorded. These speech stimuli consisted of 3 exemplars of the 16/aCa/ utterances (C=/p, t, k, b, d, g, f, s, ʃ, v, z, ʒ, m, n, r, l/) read by a French female speaker in quiet (mean VCV duration=648 ms; standard deviation=46 ms). Each signal was digitized via a 16-bit analog/digital converter at a 44.1-kHz sampling frequency.

The original speech signals were submitted to three different processing schemes. In the first scheme ("intact" condition), E and TFS information was preserved within each band. A second scheme ("Envelope" condition: E) was used to measure consonant identification based on E information only. VCV stimuli were also processed using a third scheme ("temporal fine structure" condition: TFS) so that resulting stimuli contained speech information in their TFS only.

a. Speech conditions. For all speech conditions (intact, E, and TFS), each VCV signal was initially band-pass filtered using zero-phase, third-order Butterworth filters into 16 complementary, 0.4-oct (i.e., 2 ERB)-wide frequency bands (analysis bands) spanning the range of 80–8020 Hz. In the so-called "intact" condition, the signals containing both E and TFS information were summed over all frequency bands. In the E and TFS conditions, the Hilbert transform was applied in each band in order to decompose the VCV signal into its envelope (module of the analytic signal) and temporal fine structure (cosine of the argument of the analytic signal).

In the E condition, the TFS component was discarded. The E components were first downsampled to 441 Hz, and then passed through a zero-phase, sixth-order Butterworth low-pass filter (cutoff frequency=64 Hz). The resulting envelopes were upsampled back to 44.1 kHz and used to amplitude-modulate sine wave carriers with frequencies at the geometric center frequencies of the analysis bands, and with random starting phase. The modulated signals were summed over the 16 frequency bands and presented as such to the listeners.

In the TFS condition, the E component was discarded. The TFS was multiplied by the root mean square (rms) power of the band-pass filtered VCV. The "power-weighted" TFS signals were summed over the 16 frequency bands and presented as such to the listeners.

b. Periodic interruption. All previous studies used a square wave to interrupt speech signals. As an envelope modulator, the wave shape of the interruption function may be important. First, the modulation spectrum of a square modulator is more complex than that of a sine modulator. Secondly, Sheft and Yost (2006) demonstrated a greater MDI effect with a square than sine modulator. Thirdly, a square interruption introduces strong transients in the speech waveform and turns off the speech signal for a longer period than with a sinusoidal pattern. On the other hand, a square modulator preserves the original E during on-times while sinusoidal interruption modifies the entire original E of the speech signal. It is therefore not obvious which form of interruption will have the more deleterious effects. Thus, these two forms of interruption (sine and square) were tested in the present study.

Stimuli in the intact, E, and TFS conditions were submitted to sinusoidal and square (with a 50% duty cycle) interruptions. Interruption was produced by modulating the amplitude of each processed stimulus with a sine or square wave (100% depth) at rates 2, 4, 8, 16, 32, and 64 Hz. The starting phase of the modulator was randomly chosen between 0 and 360 deg across trials.

2. Listeners and procedure

All stimuli were generated using a 16-bit digital/analog converter at a sampling frequency of 44.1 kHz and delivered diotically via Sennheiser HD 565 earphones at a constant rms level of 70 dB(A). Seven native French speakers (mean age: 23 years, standard deviation: 5 years) with normal hearing participated in the experiment. They were tested individually in a sound-attenuating booth. In a typical experimental session, four complete and identical sets of the 48 VCV utterances corresponding to a given experimental condition (i.e., a given set of processed stimuli) were presented at random. Each listener was instructed to identify the presented consonant. The 16 possible choices were presented on the screen of the computer, and the listener entered his/her response by selecting a VCV on the screen with a computer mouse. No feedback was given to the listeners. The percentage of correct identification was calculated from the 192 VCV (4×48) utterances for a given set of stimuli. All sets of stimuli were presented in random order across listeners.

Prior to data collection, all listeners were given practice on E- and TFS-coded speech until performance in these conditions was stable and reached about 90% correct. No feedback was provided to listeners in these sessions. The number of sessions needed to reach stable performance was variable across listeners but was larger for TFS-coded speech (9–29 sessions) than for E-coded speech (4–11 sessions). Mean identification scores measured over the last four training sessions (98% and 94% for E- and TFS-coded speech, respectively) were not significantly different at the 0.05 level. However, it is noteworthy that, despite training, scores re-

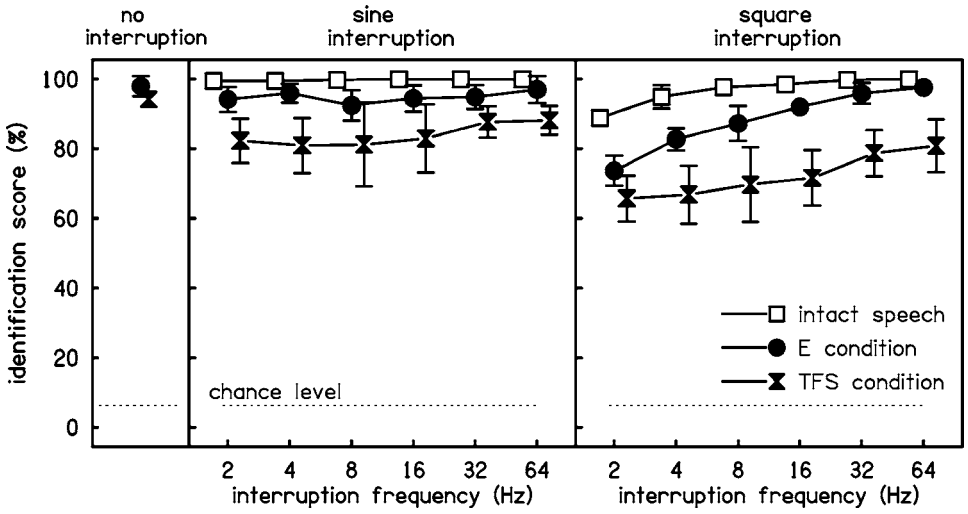

FIG. 1. Mean identification scores across listeners obtained in the intact (open squares), TFS (filled hourglasses), and E (filled circes) conditions as a function of interruption rate, for sinusoidal (left panel) and square (right panel) interruptions. For all conditions, chance level corresponded to 6.25% correct.

main slightly greater for E- than TFS-coded speech, although this difference was not significant at the 0.05 level (p =0.079).

III. RESULTS AND DISCUSSION

Figure 1 shows the mean identification scores across listeners obtained in the intact, TFS, and E conditions as a function of interruption rate, for sinusoidal and square interruptions. For all conditions, chance level corresponded to 6.25% correct. The results showed that listeners always identified consonants well above chance level (>66% correct) in the three speech processing conditions and for the two forms of interruption, demonstrating the robustness of speech perception at the acoustic/phonetic level in all experimental conditions. The high scores observed in the present study contrast with the lower scores obtained by Nelson and Jin (2004) for both intact and E-coded sentences (between 35% and 95% for intact speech, and between 10% and 50%–60% in a condition where E information was extracted within 12 frequency bands). This discrepancy seems to be primarily due to differences in frequency resolution, and possibly also to methodological differences between the two studies.[1] Nelson and Jin (2004) reported that increasing frequency resolution from 4 to 12 bands yielded a substantial increase in the intelligibility of E-coded sentences (which ranged between 10% and 50%–60% correct depending on interruption rate in a 12-band condition compared to 0%–10% in a 4-band condition). Thus, it is quite likely that an additional increase in frequency resolution (i.e., 16 bands, as in our study) should yield scores relatively similar to those reported here (>60% correct).

A three-factor repeated-measure ANOVA (with repeated measures of speech conditions, type of interruption, and interruption frequencies) on the arcsine-transformed identification scores indicated that identification scores differed significantly across the different speech conditions (intact, E-coded, and TFS-coded speech). The identification scores measured in the TFS conditions were poorer than in the E conditions by 13.5 percentage points across the interruption rates and shapes tested. However, it is important to note that performance (at the end of the training sessions) was still 4% lower for continuous (uninterrupted) speech in the TFS condition than for continuous (uninterrupted) speech in the E condition (94% versus 98%, respectively). The present data suggest therefore that, overall, both auditory features—E and TFS—show similar robustness to periodic interruption.

The three-factor repeated measures ANOVA indicated that changing the rate and shape of interruption had a significant effect on identification scores; moreover, a significant interaction between those two factors was observed. These results show that a square interruption is more disruptive than a sinusoidal one, but at the lowest interruption rates only. The effect of interruption rate is consistent with previous studies (e.g., Nelson and Jin, 2004). The three-factor repeated ANOVA also indicated a significant interaction between factors speech condition and interruption rate and a significant interaction between all three main factors (the interaction between factors speech condition and type of interruption was not significant). These results show that where an effect of interruption rate is observed (i.e., for square interruptions), the decrease in identification scores produced at the lowest interruption rates (2–4 Hz) is stronger for E- than TFS-coded speech: for square interruptions, identification of E-coded speech drops by 24 percentage points when the interruption rate is decreased from 64 to 2 Hz; by comparison, identification of TFS-coded speech drops by 15 percentage points only. As indicated above, low modulation rates (<16 Hz) are the most important rates for speech identification. This result suggests larger involvement of modulation masking in the effect of periodic interruption on E- than TFS-coded speech.

IV. SUMMARY AND CONCLUSIONS

Taken together, the results of the present study indicate the following:

(1) Periodic interruptions yield a similar and modest decrease in the identification of VCV stimuli processed in order to preserve either E or TFS information in 16 2-ERB-wide adjacent frequency bands. This shows that both E and TFS speech features are robust to periodic interruptions.

(2) When an effect of interruption rate was observed (i.e., for square interruptions), the effect occurred at low interruption rates and was stronger for E- than TFS-coded speech, suggesting larger involvement of modulation masking in E-coded speech perception. The different patterns of results obtained for E- and TFS-coded speech suggest that the two types of stimuli do not convey identical speech information.

AKNOWLEDGMENTS

This research was supported by a grant from GDR CNRS 2967 GRAEC to the first author. The authors wish to thank B. C. J. Moore and S. Sheft for valuable comments on a previous version of this manuscript.

[1]In the present study, listeners received a substantial amount of training before data collection and a closed-set format was used, whereas an open-set format was used by Nelson and Jin (2004). No indication, however, is given by Nelson and Jin (2004) about the amount of training given to their listeners. Moreover, sentences were used by Nelson and Jin (2004) whereas VCV items were used in the present study. Periodic interruption may therefore degrade specific E cues (such as segmentation cues or, in other words, speech landmarks) that are crucial for sentence processing but less important for VCV identification.

Bashford, Jr., J. A., Riener, K. R., and Warren, R. M. (**1992**). "Increasing the intelligibility of speech through multiple phonemic restorations," Percept. Psychophys. **51**, 211–217.

Drullman, R., Festen, J. M., and Plomp, R. (**1994**). "Effect of reducing slow temporal modulations on speech reception," J. Acoust. Soc. Am. **95**, 2670–2680.

Ghitza, O. (**2001**). "On the upper cutoff frequency of the auditory critical-band envelope detectors in the context of speech perception," J. Acoust. Soc. Am. **110**, 1628–1640.

Gilbert, G., and Lorenzi, C. (**2006**). "The ability of listeners to use recovered envelope cues from speech fine structure," J. Acoust. Soc. Am. **119**, 2438–2444.

Kwon, B. J., and Turner, C. W. (**2001**). "Consonant identification under maskers with sinusoidal modulation: masking release or modulation interference?" J. Acoust. Soc. Am. **110**, 1130–1140.

Lorenzi, C., Gilbert, G., Carn, H., Garnier, S., and Moore, B. C. J. (**2006**). "Speech perception problems of the hearing impaired reflect inability to use temporal fine structure," Proc. Natl. Acad. Sci. U.S.A. **103**, 18866–18869.

Nelson, P. B., and Jin, S. H. (**2004**). "Factors affecting speech understanding in gated interference: cochlear implant users and normal-hearing listeners," J. Acoust. Soc. Am. **115**, 2286–2294.

Shannon, R., Zeng, F-G., Kamath, V., Wygonski, J., and Ekelid, M. (**1995**). "Speech recognition with primarily temporal cues," Science **270**, 303–304.

Sheft, S., and Yost, W. A. (**2006**). "Modulation detection interference as informational masking," in *Hearing—from Basic Research to Applications*, edited by B. Kollmeier, G. Klump, V. Hohmann, U. Langemann, S. Uppenkamp, and J. Verhey (Springer Verlag, New York).

Smith, Z. M., Delgutte, B., and Oxenham, A. J. (**2002**). "Chimaeric sounds reveal dichotomies in auditory perception," Nature (London) **416**, 87–90.

Zeng, F. G., Nie, K., Liu, S., Stickney, G., Del Rio, E., Kong, Y. Y., and Chen, H. (**2004**). "On the dichotomy in the auditory perception between temporal envelope and fine structure cues," J. Acoust. Soc. Am. **116**, 1351–1354.

Acoustical scattering by arrays of cylinders in waveguides

Liang-Wu Cai[a)]
Department of Mechanical and Nuclear Engineering, Kansas State University, Manhattan, Kansas 66506

Dalcio K. Dacol, David C. Calvo, and Gregory J. Orris
Acoustics Division, Naval Research Laboratory, Washington DC 20375

(Received 19 December 2006; revised 11 May 2007; accepted 16 May 2007)

Multiple scattering of acoustic waves in a planar horizontal waveguide by finite-length cylinders is considered. Cylinder height equals the waveguide depth, and both are vertically constrained by the pressure-release boundaries. An analytically exact solution is obtained via normal mode expansion method in conjunction with the concept of the *T* matrix. The problem is decomposed into an infinite number of two-dimensional multiple scattering problems, modulated by waveguide mode shapes. Examples are presented for an isovelocity waveguide in which the medium is uniform and the waveguide depth is constant. It is found that, in numerical computations, including one or two evanescent modes captures the essence of the evanescent modes. Multiple scattering in the waveguide is compared with the corresponding two-dimensional case. It is concluded that, in low frequencies, the wave patterns in the two cases are very similar, with a shift in the frequency. The similarity diminishes when there are multiple propagating modes. Despite the mode mixing, some key features in the scattering as observed in the two-dimensional problem remain observable in the waveguide case. [DOI: 10.1121/1.2747207]

PACS number(s): 43.20.Mv, 43.20.Fn, 43.30.Bp [LLT] Pages: 1340–1351

I. INTRODUCTION

Waveguides are widely used in varieties of devices that are designed to control the propagations of all types of waves. Historically, scattering by obstacles in a waveguide was first studied for electromagnetic waves. Nielsen (1969) claimed to have obtained the first exact solution for scattering by a single cylindrical post in a waveguide. Similar problems were also studied by Okamoto, Snishioka, and Nakanishi (1971). Cicconi and Rosatelli (1977) and Gesche and Russenschuck (1989) studied the scattering by two columns in a waveguide. Butorin (1988), Ivanishin (1989) and Kalesinskas, Konstantinov, and Shugurov (1998) studied the scattering by cylindrical columns that do not extend to the full height of the waveguide. Kapilevich (1990), Butorin (1991) and Diamandi, Sahalos, and Vafiadis (1993) studied the resonance effects among the cylinders and between a cylinder and a waveguide wall. Kyurkchan and Manenkov (2002) studied a similar problem in a stratified medium. Huang *et al.* (2004) studied approximate solution for large-scale multiple scattering among via holes in electronic circuit boards.

In ocean acoustics, the ocean environment is a natural waveguide. The theory of scattering of an underwater sound wave by an obstacle was studied by Hackman and Sammelmann (1986) using the normal mode expansion in a spheroidal coordinate system. Their numerical study (Sammelmann and Hackman, 1987) of a spherical shell in a uniform waveguide leads to interesting findings that do not have counterparts in the scattering by the same object in free space. One is the so-called superresonance, which usually is attributed to multiple scattering in the free-space scattering problems (Tolstoy, 1986), due to the interaction between the scatterer and the waveguide surfaces in a shallow waveguide. The other is the splitting of a resonance peak in the free-space scattering into a series of spectral lines in waveguide of any depth but more appreciable when the scatterer is closer to a boundary. The scattering of an underwater sound wave by cylindrical objects has only been studied rather recently by Athanassoulis and Prospathopoulos (1996 and 2000). In the first paper, acoustic scattering by a single circular cylinder in an ocean waveguide illuminated by a point source is analyzed by the normal mode expansion method, leading to a double-series expansion solution. In the second paper, both the waveguide and the cylindrical scatterer are allowed to have layered structure, leading to the possibility of treating vertically stratified field and scatterers.

The multiple scattering of acoustic waves by an ensemble of cylindrical objects embedded in a waveguide is studied in this paper. The authors' interest in this problem stemmed from the band gap phenomenon that has been widely reported for two-dimensional acoustic scattering environments. For the latest review on this topic, see Miyashita (2005). The main interest is in understanding how a waveguide environment, which is not necessarily an ocean waveguide, would change the band gap phenomenon, and whether the mode interaction and mixing would introduce new phenomena.

In this paper, the simplest waveguide model is considered. The waveguide consists of a flat top surface and a flat bottom, which is located at a depth of h below the surface. The problem geometry is schematically shown in Fig. 1. Further simplification to the model is made by assuming a uniform and unbound medium. An analytically exact solution is

[a)]Author to whom correspondence should be addressed. Electronic mail: cai@ksu.edu

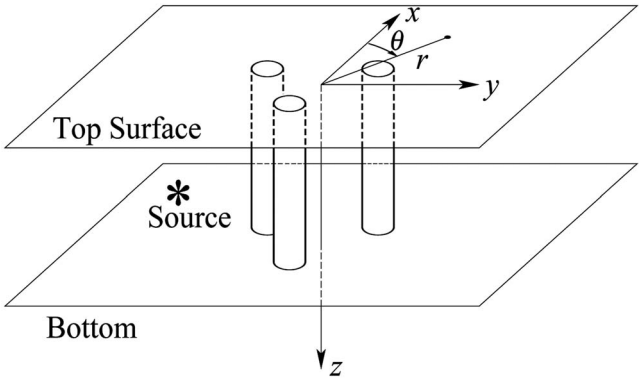

FIG. 1. Geometry and coordinate system for the waveguide.

obtained via the normal mode expansion method. It is shown that the solution is comprised of a collection of two-dimensional multiple scattering problems.

This paper is organized as the following: the general solution using the standard normal-mode expansion method is derived in Sec. II. The vertical eigenvalue problem for the simplest waveguide is discussed in Sec. III. The scattering problem in general, and scattering by common cylindrical scatterers in particular, are discussed in Sec. IV. The general solution for multiple scattering due to an ensemble of cylindrical cylinders is obtained in Sec. V. The general expression for the point wave source is discussed in Sec. VI. Numerical examples exploring both the evanescent modes and other interesting multiple scattering phenomena are presented in Sec. VII. Finally, the paper is concluded in Sec. VIII.

II. GENERAL SOLUTION FOR ACOUSTIC SCATTERING IN WAVEGUIDE

Without loss of generality, it is assumed that the medium is range independent but could be depth dependent. Using a polar coordinate system (r,θ,z), the acoustic field in the waveguide satisfies the following Helmholtz equation:

$$\left[\rho(z)\,\nabla\cdot\left(\frac{1}{\rho(z)}\,\nabla\right)+k^2(z)\right]\phi(\mathbf{r})=0, \tag{1}$$

where $\rho(z)$ is the mass density, $k(z)=\omega/c(z)$ is the wave number, ω the circular frequency, $c(z)$ is the sound speed, and $\phi(\mathbf{r})=\phi(r,\theta,z)$ is the complex amplitude of the sound pressure.

Assuming the following depth-separated solution form

$$\phi(\mathbf{r})=\Phi(r,\theta)Z(z) \tag{2}$$

and following the standard procedure of separation of variables, Eq. (1) can be separated into the following two equations:

$$\frac{d}{dz}\left(\frac{1}{\rho(z)}\frac{dZ(z)}{dz}\right)+\frac{k^2(z)-k_H^2}{\rho(z)}Z(z)=0, \tag{3}$$

$$\frac{\partial^2\Phi(r,\theta)}{\partial r^2}+\frac{1}{r}\frac{\partial\Phi(r,\theta)}{\partial r}+\frac{1}{r^2}\frac{\partial^2\Phi(r,\theta)}{\partial\theta^2}+k_H^2\Phi(r,\theta)=0, \tag{4}$$

where k_H^2 is the constant of separation.

Equation (3) is the standard form of the *Sturm-Liouville eigenvalue problem*, if the boundary conditions are linear combinations of the $Z(z)$ and $Z'(z)$, which is the case for acoustic waves in the said waveguide. In a Sturm-Liouville problem, k_V is the eigenvalue, where

$$k_V^2=k^2-k_H^2. \tag{5}$$

Furthermore, $\rho(z)$ is positive-definite over the problem domain. In such cases, the *Sturm-Liouville Theorem* states (see, e.g., Logan, 1987) that: 1) there is an infinite number of eigenvalues, denoted as $k_V^{(n)}$ with $n=1,2,\ldots,\infty$; 2) all the eigenvalues are real and non-negative, with $0\leqslant k_V^{(1)}<k_V^{(2)}<k_V^{(3)}<\cdots<k_V^{(\infty)}\to\infty$; 3) the nth eigenfunction, denoted as $Z^{(n)}(z)$, has exactly $n-1$ zeros in the entire problem domain excluding the ends; and 4) all eigenfunctions corresponding to different eigenvalues are orthogonal; that is,

$$\int_\Omega \frac{Z^{(n)}(z)Z^{(n')}(z)}{\rho(z)}dz\begin{cases}=0 & \text{if } n\neq n'\\ \neq 0 & \text{if } n=n'\end{cases}, \tag{6}$$

where Ω is the problem domain. In ocean acoustics, this set of eigenfunctions (of z) is called the *waveguide modes*.

Equation (4) is often referred to as the depth-separated Helmholtz equation, which is identical to the two-dimensional Helmholtz equation for $\Phi(r,\theta)$ with a wave number k_H, whose solution is well known (see, e.g., Pao and Mow, 1971; Cai and Williams, 1999a): the harmonics $e^{\hat{\imath}m\theta}$ as the azimuthal factor, where $\hat{\imath}=\sqrt{-1}$, and the cylindrical functions, which can be any of the following Bessel functions, $J_m(k_H^{(n)}r)$, $Y_m(k_H^{(n)}r)$, $H_m^{(1)}(k_H^{(n)}r)$, and $H_m^{(2)}(k_H^{(n)}r)$, as the radial factor. Note that $k(z)$ is the wave number in the medium, and because of Eq. (5), $k_H^{(n)}$ is called the *horizontal wave number* (in the $r-\theta$ plane) for the nth waveguide mode; and $k_V^{(n)}(z)$ is correspondingly called the *vertical wave number*.

Therefore, the general solution for Eq. (1) can be written as the following normal mode expansion:

$$\phi(\mathbf{r})=\phi(r,\theta,z)=\sum_{n=1}^{\infty}\sum_{m=-\infty}^{\infty}[A_{mn}J_m(k_H^{(n)}r)+B_{mn}H_m^{(1)}(k_H^{(n)}r)]Z^{(n)}(z)e^{\hat{\imath}m\theta}. \tag{7}$$

III. ISOVELOCITY PROBLEM

In the following, consider the simplest waveguide problem in which the medium is uniform. In such a case, the mass density ρ, the sound speed c and the wave number k are constants. This is referred to as the *isovelocity problem* in ocean acoustics. The vertical eigenvalue problem in Eq. (3) becomes

$$Z''(z)+k_V^2Z(z)=0. \tag{8}$$

Assume that both top and bottom surfaces, $z=0$ and h, respectively, are pressure-release boundaries (see, e.g., Jensen, *et al.*, 1994). Then, the eigenvalues are

$$k_V^{(n)}=\frac{n\pi}{h} \tag{9}$$

and the corresponding eigenfunctions are

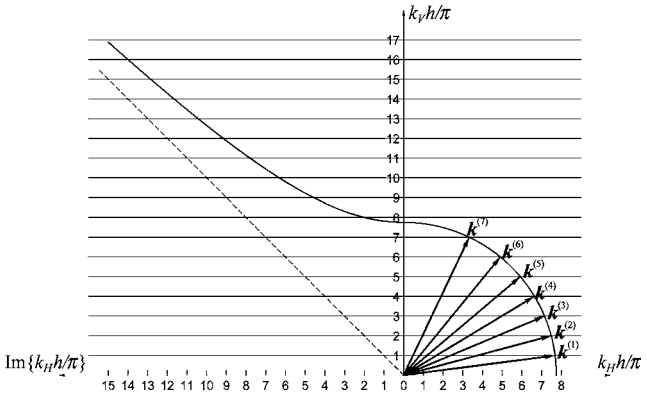

FIG. 2. Wave vectors for different propagating modes of a waveguide on the right half plane, and imaginary wave number for evanescent modes on the left half plane.

$$Z^{(n)}(z) = \sin k_V^{(n)} z = \sin \frac{n\pi z}{h}. \tag{10}$$

According to Eq. (5), $(k_H^{(n)})^2 = k^2 - (k_V^{(n)})^2$, as n increases, it is possible that $(k_H^{(n)})^2 < 0$. The waveguide modes are thus divided into two classes: when $(k_H^{(n)})^2 \geqslant 0$, or,

$$n \leqslant \left[\frac{kh}{\pi}\right], \tag{11}$$

where the square brackets denote the largest integer no larger than the enclosed argument, $k_H^{(n)}$ is real, and the mode is a *propagating mode*; and when $(k_H^{(n)})^2 < 0$ or

$$n > \left[\frac{kh}{\pi}\right] \tag{12}$$

$k_H^{(n)}$ is purely imaginary, and the mode becomes an *evanescent mode*. In such cases, the mode shape in the vertical direction is still given by Eq. (10); however, in the horizontal direction, Bessel and Hankel functions have pure imaginary arguments. Essentially, Bessel function of the first kind increases exponentially and Hankel function of the first kind decreases exponentially as the modulus of the argument increases when the argument is purely imaginary.

Physically, because of the boundary conditions, waves cannot propagate in the horizontal direction ($n=0$ results in a trivial solution). The direction of propagation must be tilted; and only a limited number of discrete tilting directions is compatible with the waveguide boundary conditions. These directions are illustrated in Fig. 2. In Fig. 2, the horizontal lines are the eigenvalues for different modes. The integer values of the normalized vertical wave number $k_V h/\pi$ gives the mode number for each line. Thus, these lines are referred to as the *modal lines*. On the right half plane, the circular arc of radius kh/π intersects with the modal lines. The vectors originating from the origin to these intersection points are the normalized wave vectors for the propagating modes. The normalized wave vector has the magnitude of the normalized wave number kh/π, and the direction of wave propagation. On the left half plane, the curve is a hyperbola that intersects with the vertical axis at the same location as the arc. The hyperbola has an asymptote of $\mathrm{Im}\{k_H h/\pi\} = k_V h/\pi$, where Im denotes the imaginary part of a complex quantity. The intersections with the modal lines give the imaginary wave numbers for the evanescent modes.

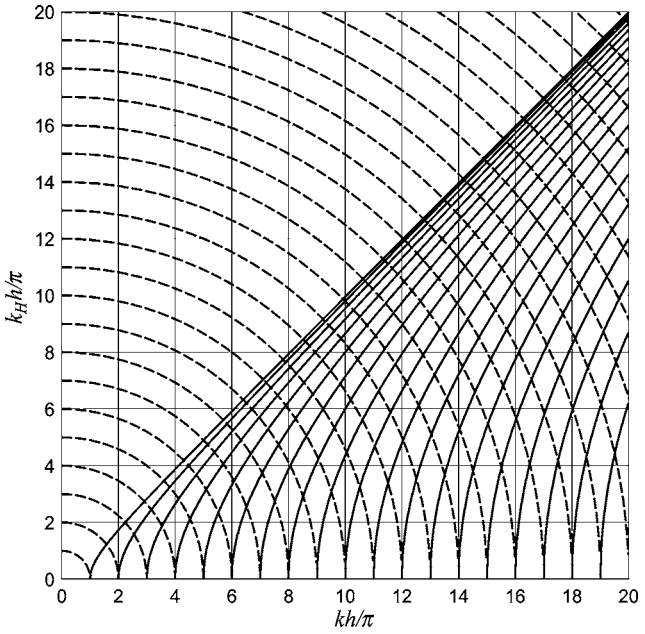

FIG. 3. Mode diagram showing the propagating modes (solid curves) and evanescent modes (dashed curves) in the horizontal direction.

Figure 3 shows the mode diagram for the waveguide. For a given wave number k, the solid curves give horizontal wave number k_H for different propagating modes, and the dashed curves give the modulus of the imaginary wave number for the evanescent modes. At any given frequency kh/π, a vertical line can be drawn, which intersects with these curves. From top to bottom, the intersections with the solid curves give the horizontal wave number in sequential order for propagating modes. After reaching the abscissa, from bottom to top, the intersections with the dashed curves give the modulus of the imaginary horizontal wave number in sequential order for the evanescent modes.

Furthermore, the series of eigenvalues starts from $n=1$. This means that there will be no propagating mode but all evanescent modes in the medium when

$$\frac{kh}{\pi} < 1 \quad \text{or} \quad k < \frac{\pi}{h} = k_{\text{cutoff}}. \tag{13}$$

This cutoff occurs when the wavelength is longer than twice the depth of the waveguide.

IV. SINGLE-SCATTERING PROBLEMS

With the presence of a single scatterer in the waveguide, the incident and the scattered waves are expressible as

$$\phi_{\text{inc}} = \sum_{n=1}^{\infty} \sum_{m=-\infty}^{\infty} \alpha_{mn} J_m(k_H^{(n)} r) Z^{(n)}(z) e^{\hat{\imath} m\theta}, \tag{14}$$

$$\phi_{\text{scr}} = \sum_{n=1}^{\infty} \sum_{m=-\infty}^{\infty} \beta_{mn} H_m^{(1)}(k_H^{(n)} r) Z^{(n)}(z) e^{\hat{\imath} m\theta}. \tag{15}$$

The total wave in the field can be written as

$$\phi_{\text{total}} = \phi_{\text{inc}} + \phi_{\text{scr}} = \sum_{n=1}^{\infty} \sum_{m=-\infty}^{\infty} [\alpha_{mn} J_m(k_H^{(n)} r) + \beta_{mn} H_m^{(1)}(k_H^{(n)} r)] Z^{(n)}(z) e^{\hat{\imath} m\theta}. \quad (16)$$

The linearity of the system requires that the expansion coefficients of the scattered wave are linearly related to those of the incident wave; thus

$$\beta_{mn} = \sum_{n'=1}^{\infty} \sum_{m'=-\infty}^{\infty} T_{n,n'}^{m,m'} \alpha_{n'm'}. \quad (17)$$

This is the well-known T-matrix relation for scattering problems although the above equation is not in a matrix form. Using this relation, the total wave can be written as

$$\phi_{\text{total}} = \sum_{n=1}^{\infty} \sum_{m=-\infty}^{\infty} \left[\alpha_{mn} J_m(k_H^{(n)} r) + \left(\sum_{n'=1}^{\infty} \sum_{m'=-\infty}^{\infty} T_{n,n'}^{m,m'} \alpha_{n'm'} \right) H_m^{(1)}(k_H^{(n)} r) \right] Z^{(n)}(z) e^{\hat{\imath} m\theta}. \quad (18)$$

Consider the cases in which there is no interaction among the waveguide modes. In such cases, the summation over n' vanishes and $T_{n,n'}^{m,m'}$ contains a Kronecker delta $\delta_{n,n'}$. In such cases, Eq. (18) can be rewritten as

$$\phi_{\text{total}} = \sum_{n=1}^{\infty} \left\{ \sum_{m=-\infty}^{\infty} \left[\alpha_{mn} J_m(k_H^{(n)} r) + \left(\sum_{m'=-\infty}^{\infty} T^{m,m'} \alpha_{nm'} \right) H_m^{(1)}(k_H^{(n)} r) \right] e^{\hat{\imath} m\theta} \right\} Z^{(n)}(z). \quad (19)$$

The assumption of no mode coupling is valid when no wave resides in the cylindrical scatterer, such as ideally soft and rigid scatterers. For penetrable cylinders, the wave inside the cylinder is still expressible by Eq. (7) with the following differences: the vertical mode shape generally is different from that of the exterior, and the z problem domain covers the length of the cylinder, which is assumed to extend at least to the entire waveguide, but may also extend beyond the top and bottom waveguide surfaces. There is one interesting case where a penetrable cylinder does not cause mode coupling: when both the waveguide and cylinder are uniform, and the cylinder length equals the waveguide depth. This special case will be discussed in greater detail in Sec. IV B. Numerical examples presented in this paper are for this case.

A. Matrix notation

Define a set of column matrices for the wave expansion coefficient $\{\boldsymbol{\alpha}^{(n)}\}$ and $\{\boldsymbol{\beta}^{(n)}\}$, one pair for each waveguide mode, such that their entries at the mth row are

$$\{\alpha^{(n)}\}_m = \alpha_{mn} \quad \{\beta^{(n)}\}_m = \beta_{mn}, \quad (20)$$

respectively, and a set of corresponding regular and singular wave expansion bases, denoted as $\{\mathbf{J}^{(n)}(\mathbf{r})\}$ and $\{\mathbf{H}^{(n)}(\mathbf{r})\}$, respectively, with

$$\{J^{(n)}(\mathbf{r})\}_m = J_m(k_H^{(n)} r) e^{\hat{\imath} m\theta} \quad \{H^{(n)}(\mathbf{r})\}_m = H_m^{(1)}(k_H^{(n)} r) e^{\hat{\imath} m\theta} \quad (21)$$

The T-matrix relation becomes, for each n,

$$\{\boldsymbol{\beta}^{(n)}\} = [\mathbf{T}^{(n)}]\{\boldsymbol{\alpha}^{(n)}\} \quad (22)$$

and

$$\phi_{\text{total}} = \sum_{n=1}^{\infty} [\{\boldsymbol{\alpha}^{(n)}\}^T (\{\mathbf{J}^{(n)}(\mathbf{r})\} + [\mathbf{T}^{(n)}]^T \{\mathbf{H}^{(n)}(\mathbf{r})\})] Z^{(n)}(z) \quad (23)$$

It is clear that a single-scatterer problem in the waveguide can be viewed as consisting of an infinite number of single-scattering problems, one for each mode, and modulated by the vertical mode shapes. However, these single-scattering problems are not identical to the two-dimensional single-scattering problems, as discussed in the following.

B. Special cases of circular cylindrical single scatterer problems

For a specific scatterer, the T matrices can be obtained by matching the boundary conditions at the scatterer boundary. Without going into details, the T matrices for a circular cylinder of radius a of three common physical properties are listed in the following. In all three cases, the T matrices are diagonal.

1. Rigid scatterer

For an ideally rigid scatterer, the boundary condition at the cylinder's surface is that the radial component of the particle velocity vanishes. This gives rise to the following T matrix

$$[T^{(n)}]_{mm} = -\frac{J_m'(k_H^{(n)} a)}{H_m^{(1)'}(k_H^{(n)} a)}. \quad (24)$$

2. Soft scatterer

For an ideally soft scatterer, the boundary condition at the cylinder's surface is that sound pressure vanishes. This gives rise to the following T matrix

$$[T^{(n)}]_{mm} = -\frac{J_m(k_H^{(n)} a)}{H_m^{(1)}(k_H^{(n)} a)}. \quad (25)$$

3. Penetrable scatterer

For a penetrable scatterer, a refracted wave resides inside the scatterer, which is expressible as

$$\phi_{\text{ref}} = \sum_{n=1}^{\infty} \sum_{m=-\infty}^{\infty} \gamma_{mn} J_m(k_{H2}^{(n)} r) Z_2^{(n)}(z) e^{\hat{\imath} m\theta}$$

$$= \sum_{n=1}^{\infty} \{\boldsymbol{\gamma}^{(n)}\}^T \{\mathbf{J}_2^{(n)}(\mathbf{r})\} Z_2^{(n)}(z), \tag{26}$$

where $\{\mathbf{J}_2^{(n)}(\mathbf{r})\}$ is the regular wave expansion basis for the interior of the scatterer, $k_{H2}^{(n)}$ is the horizontal wave number for the scatterer, which has an expression similar to Eq. (5), and $Z_2^{(n)}(z)$ is the vertical mode shape for the wave field inside the scatterer.

In an isovelocity waveguide, and assuming that the scatterer is also uniform, having the same length as the waveguide depth, and having the same boundary conditions are the top ($z=0$) and bottom ($z=h$) surfaces, the mode shapes for both interior and exterior are identical except that, when they are to be normalized, different mass densities would be used, as indicated by Eq. (6). Hence, it is advantageous to keep the same vertical mode shape for both media by using the un-normalized mode shapes.

The boundary conditions are that the pressure and the radial particle velocity are continuous across the interface. This gives rise to the following T matrix

$$[T^{(n)}]_{mm} = -\frac{\rho k_{H2}^{(n)} J_m(k_H^{(n)} a) J_m'(k_{H2}^{(n)} a) - \rho_2 k_H^{(n)} J_m'(k_H^{(n)} a) J_m(k_{H2}^{(n)} a)}{\rho k_{H2}^{(n)} H_m^{(1)}(k_H^{(n)} a) J_m(k_{H2} a) - \rho_2 k_H^{(n)} H_m^{(1)\prime}(k_H^{(n)} a) J_m(k_{H2}^{(n)} a)}, \tag{27}$$

where ρ_2 is the mass density of the scatterer, and

$$k_{H2}^{(n)} = \sqrt{k_2^2 - \left(\frac{n\pi}{h}\right)^2} = \sqrt{\left(\frac{kc}{c_2}\right)^2 - \left(\frac{n\pi}{h}\right)^2}. \tag{28}$$

This T matrix is slightly different from the T matrix for the two-dimensional scattering problem: the horizontal wave numbers are used in each medium, and they are not simply related by the wave speeds in the two media. This difference reflects the physical nature: in different modes, the waves incident upon the cylinder at different angles, and the cylinder exhibits a different apparent impedance contrast.

Again, because of the linearity of the system, γ_{mn} can be linearly related to the incident wave expansion coefficients. In light of the multiple scattering problem to be considered in the next section, it is more convenient to relate the wave expansion coefficients of the interior field to those of the scattered wave. Thus, define a new characteristic matrix $[\mathbf{U}^{(n)}]$ such that

$$\{\boldsymbol{\gamma}^{(n)}\} = [\mathbf{U}^{(n)}]\{\boldsymbol{\beta}^{(n)}\}. \tag{29}$$

Then, the boundary conditions also give

$$[U^{(n)}]_{mm} = \frac{2\hat{\imath}\rho_2}{\pi a[\rho k_{H2}^{(n)} J_m(k_H^{(n)} a) J_m'(k_{H2}^{(n)} a) - \rho_2 k_H^{(n)} J_m(k_H^{(n)} a) J_m(k_{H2}^{(n)} a)]}. \tag{30}$$

V. MULTIPLE SCATTERING PROBLEM

A. Matrix formulation

In the presence of an ensemble of N cylindrical scatterers in the waveguide, it becomes necessary to use a set of polar coordinate systems, one for each scatterer. Local coordinates are denoted as (r_i, θ_i, z) for the system local to Scatterer i. When necessary, a global coordinate system of either (x,y,z) or (r,θ,z) is used. For a given incident wave, which corresponds to a set of wave expansion coefficients $\{\boldsymbol{\alpha}_i^{(n)}\}$, the total sound field consists of the incident wave plus wave scattered by each scatterer, that is

$$\phi_{\text{total}} = \sum_{n=1}^{\infty} \left[\{\boldsymbol{\alpha}_i^{(n)}\}^T \{\mathbf{J}^{(n)}(\mathbf{r}_i)\} + \sum_{i=1}^{N} \{\boldsymbol{\beta}_i^{(n)}\}^T \{\mathbf{H}^{(n)}(\mathbf{r}_i)\} \right] \times Z^{(n)}(z), \tag{31}$$

where the expressions for wave expansion bases for the nth mode in Scatterer i's local coordinate system are the same as those in Eq. (21), except that coordinates r_i and θ_i are used in places of r and θ, respectively.

The wave that causes the scattering by scatterer i is all waves in the field except the one scattered by Scatterer i itself; that is

$$(\phi_{\text{inc}})_i = \sum_{n=1}^{\infty} \left[\{\boldsymbol{\alpha}_i^{(n)}\}^T \{\mathbf{J}^{(n)}(\mathbf{r}_i)\} + \sum_{\substack{j=1 \\ j\neq i}}^{N} \{\boldsymbol{\beta}_j^{(n)}\}^T \{\mathbf{H}^{(n)}(\mathbf{r}_j)\} \right] \times Z^{(n)}(z). \tag{32}$$

These waves are expressed in different local coordinate systems. This necessitates a coordinate transformation. The coordinate transformation is based on Graf's addition theorem for Bessel and Hankel functions, which can be written in matrix form as (Cai and Williams, 1999a)

$$\{\mathbf{H}^{(n)}(\mathbf{r}_j)\} = [\mathbf{R}_{ji}^{(n)}]\{\mathbf{J}^{(n)}(\mathbf{r}_i)\}, \tag{33}$$

where the entry for matrix $[\mathbf{R}_{ji}^{(n)}]$ at the m row and the mth column is

$$[R_{ji}^{(n)}]_{mm'} = e^{\hat{\imath}(m-m')\theta_{ji}} H_{m-m'}^{(1)}(k_H^{(n)} d_{ji}) \tag{34}$$

and (d_{ji}, θ_{ji}) are the polar coordinates of the origin of Scatterer i's local coordinate system in the Scatterer j's local coordinate system. Substituting Eq. (33) into Eq. (32) and using the T-matrix relation in Eq. (22) give

$$\{\boldsymbol{\beta}_i^{(n)}\} = [\mathbf{T}_i^{(n)}]\{\boldsymbol{\alpha}_i^{(n)}\} + \sum_{\substack{j=1 \\ j\neq i}}^{N} [\mathbf{T}_i^{(n)}][\mathbf{R}_{ji}^{(n)}]^T \{\boldsymbol{\beta}_j^{(n)}\}. \tag{35}$$

This equation can be solved by moving the $\{\boldsymbol{\beta}_j^{(n)}\}$ to the left-hand side, and constructing a super matrix in the following form:

$$\begin{bmatrix} [\mathbf{I}] & [\mathbf{T}_1^{(n)}][\mathbf{R}_{21}^{(n)}] & \cdots & -[\mathbf{T}_1^{(n)}][\mathbf{R}_{N1}^{(n)}] \\ -[\mathbf{T}_2^{(n)}][\mathbf{R}_{12}^{(n)}] & [\mathbf{I}] & \cdots & -[\mathbf{T}_1^{(n)}][\mathbf{R}_{N1}^{(n)}] \\ \vdots & \vdots & \ddots & \vdots \\ -[\mathbf{T}^{(n)}][\mathbf{R}_{1N}^{(n)}] & -[\mathbf{T}^{(n)}][\mathbf{R}_{2N}^{(n)}] & \cdots & [\mathbf{I}] \end{bmatrix} \times \begin{Bmatrix} \{\boldsymbol{\beta}_1^{(n)}\} \\ \{\boldsymbol{\beta}_2^{(n)}\} \\ \vdots \\ \{\boldsymbol{\beta}_N^{(n)}\} \end{Bmatrix} = \begin{Bmatrix} [\mathbf{T}_1^{(n)}]\{\boldsymbol{\alpha}_1^{(n)}\} \\ [\mathbf{T}_2^{(n)}]\{\boldsymbol{\alpha}_2^{(n)}\} \\ \vdots \\ [\mathbf{T}^{(n)}]\{\boldsymbol{\alpha}_N^{(n)}\} \end{Bmatrix}. \tag{36}$$

Because the diagonal blocks are identity matrices, in general, the above linear equation system will not become ill conditioned, and can be readily solved by many well-established solvers for linear equation systems.

B. Field computations

Having obtained $\{\boldsymbol{\beta}_i^{(n)}\}$ using Eq. (36), the sound pressure field can be calculated according to Eq. (31). The interior fields, if they exist, can be obtained by using the characteristic matrix $[\mathbf{U}_i^{(n)}]$ for each scatterer

$$(\phi_{\text{ref}})_i = \sum_{n=1}^{\infty} \{\boldsymbol{\beta}_i^{(n)}\}^T [\mathbf{U}_i^{(n)}]^T \{\mathbf{J}_2^{(n)}(r_i, \theta_i)\} Z^{(n)}(z). \tag{37}$$

In a scattering problem, the velocity vector has the same temporal factor as the pressure and can thus be written as $\boldsymbol{v}e^{-\hat{\imath}\omega t}$, where $\boldsymbol{v}(\mathbf{r})$ is the vectoral complex amplitude of the velocity, which can be obtained from the following fundamental relation for the acoustics:

$$\frac{\partial(\mathbf{v}e^{-\hat{\imath}\omega t})}{\partial t} = -\frac{1}{\rho}\nabla p. \tag{38}$$

The velocity field within each scatterer, if such a field exists, is relatively simple to calculate as

$$(v_{r_i})_{\text{ref}} = \sum_{n=1}^{\infty} \{\boldsymbol{\beta}_i^{(n)}\}^T [\mathbf{U}_i^{(n)}]^T \{\mathbf{J}_{2r}^{(n)}(r_i, \theta_i)\}, \tag{39}$$

$$(v_{\theta_i})_{\text{ref}} = \sum_{n=1}^{\infty} \{\boldsymbol{\beta}_i^{(n)}\}^T [\mathbf{U}_i^{(n)}]^T \{\mathbf{J}_{2\theta}^{(n)}(r_i, \theta_i)\}, \tag{40}$$

where, $\{\mathbf{J}_{2r}^{(n)}(r_i, \theta_i)\}$ and $\{\mathbf{J}_{2r}^{(n)}(r_i, \theta_i)\}$ are the *regular differential wave expansion bases* for Scatterer i's local coordinate system for the scatterer itself, with entries at the mth row

$$\{J_{2r}^{(n)}(r_i, \theta_i)\}_m = \frac{\hat{\imath}}{\rho_2 c_2} J'_m(k_{2H}^{(n)} r_i) e^{\hat{\imath} m \theta_i}, \tag{41}$$

$$\{J_{2\theta}^{(n)}(r_i, \theta_i)\}_m = -\frac{m}{\rho_2 c_2 k_{H2}^{(n)} r_i} J_m(k_{H2}^{(n)} r_i) e^{\hat{\imath} m \theta_i}. \tag{42}$$

Since velocities are vectors, velocities obtained in different coordinate systems need to be properly transformed before they can be summed together. Consider an ad hoc coordinate system whose coordinates are (r_a, θ_a, z). The velocity components in Scatterer i's local coordinate system can be calculated as

$$(v_{r_i})_{\text{scr}} = \sum_{n=1}^{\infty} \{\boldsymbol{\beta}_i^{(n)}\}^T \{\mathbf{H}_r^{(n)}(r_i, \theta_i)\}$$

$$(v_{\theta_i})_{\text{scr}} = \sum_{n=1}^{\infty} \{\boldsymbol{\beta}_i^{(n)}\}^T \{\mathbf{H}_\theta^{(n)}(r_i, \theta_i)\}, \tag{43}$$

where the definitions for the *singular differential wave expansion bases* $\{\mathbf{H}_r^{(n)}(r_i, \theta_i)\}$ and $\{\mathbf{H}_\theta^{(n)}(r_i, \theta_i)\}$ are analogous to their regular counterparts in Eqs. (41) and (42). After the coordinate transformation, in the ad hoc coordinate system, the contributions by these stress components are

$$(v_{r_a})_i^{\text{src}} = v_{r_i}^{\text{scr}} \cos(\theta_i - \theta_a) - v_{\theta_i}^{\text{scr}} \sin(\theta_i - \theta_a), \tag{44}$$

$$(v_{\theta_a})_i^{\text{src}} = v_{r_i}^{\text{scr}} \sin(\theta_i - \theta_a) + v_{\theta_i}^{\text{scr}} \cos(\theta_i - \theta_a). \tag{45}$$

VI. POINT SOURCE AS INCIDENT WAVE

A. Point source on *z* axis

First, consider a case when the source is located on the z axis at $\mathbf{r}'_1 = (0, 0, z')$. The field produced by the point source is governed by the following equation:

$$\left[\rho(z)\nabla \cdot \left(\frac{1}{\rho(z)}\nabla\right) + k^2(z)\right] P(\mathbf{r}; \mathbf{r}'_1) = \frac{\delta(r)\delta(z - z')}{2\pi r}. \tag{46}$$

The problem is axisymmetric, and hence independent of θ. The normal mode expansion solution given in terms of normalized waveguide mode shapes can be found in Jensen *et al.* (1994). Corresponding to un-normalized mode shapes, such as those in Eq. (10), the field due to the point source on the z axis is

$$P(\mathbf{r}; \mathbf{r}'_1) = \frac{1}{4\hat{\imath}\rho(z')} \sum_{n=1}^{\infty} \frac{Z^{(n)}(z')}{\int_\Omega \frac{[Z^{(n)}(z)]^2}{\rho(z)} dz} H_0^{(1)}(k_H^{(n)} r) Z^{(n)}(z), \tag{47}$$

which can be simplified for the vertical isovelocity problem as

$$P(\mathbf{r}; \mathbf{r}'_1) = \frac{1}{2\hat{\imath}h} \sum_{n=1}^{\infty} Z^{(n)}(z') H_0^{(1)}(k_H^{(n)} r) Z^{(n)}(z). \tag{48}$$

B. Point source off *z*-axis

For a multiple scattering problem, the incident wave must be expressed in each scatterer's local coordinate system in the form of wave expansion. In these coordinate systems, the point source is located off the z axis. Define a source-local coordinate system (r_s, θ_s, z) such that the source is located on its z axis at $(0, 0, z')$. Within this coordinate system, the expression for the field is the same as Eq. (47) except that coordinates r and θ carry a subscript s.

Applying the coordinate transformation in Eq. (33) between the wave expansion bases for Scatterer i's local coordinate system and the source's local coordinate system gives

$$H_0^{(1)}(r_s) = \sum_{m=-\infty}^{\infty} H_m^{(1)}(r_{is}) J_m(r_i) e^{\hat{\imath} m(\theta_i - \theta_{is})}, \quad (49)$$

where (r_{is}, θ_{is}) are the coordinates of the source in Scatterer i's local coordinate system, and the following relationships have been used: $\theta_{is} = \pi + \theta_{si}$ and $H_{-m}(\cdot) = e^{\hat{\imath}m\pi} H_m(\cdot)$. Thus, Eq. (47) becomes

$$P(\mathbf{r}_i;\mathbf{r}') = \frac{1}{4\hat{\imath}\rho(z')} \sum_{n=1}^{\infty} \sum_{m=-\infty}^{\infty} \frac{Z^{(n)}(z')}{\int_\Omega \frac{[Z^{(n)}(z)]^2}{\rho(z)} dz} \times H_m^{(1)}(k_H^{(n)} r_{is}) e^{-\hat{\imath} m \theta_{is}} J_m(k_H^{(n)} r_i) Z^{(n)}(z) e^{\hat{\imath} m \theta_i}. \quad (50)$$

In Eq. (50), $P(\mathbf{r}_i;\mathbf{r}')$ is expressed in terms of the regular wave expansion basis for Scatterer i, $\{\mathbf{J}^{(n)}(\mathbf{r}_i)\}$, with wave expansion coefficients

$$\{\alpha_i^{(n)}\}_m = \frac{1}{4\hat{\imath}\rho(z')} \frac{Z^{(n)}(z')}{\int_\Omega \frac{[Z^{(n)}(z)]^2}{\rho(z)} dz} H_m^{(1)}(k_H^{(n)} r_{is}) e^{-\hat{\imath} m \theta_{is}}. \quad (51)$$

When the density ρ is a constant, it simplifies to

$$\{\alpha_i^{(n)}\}_m = \frac{1}{2\hat{\imath}h} Z^{(n)}(z') H_m^{(1)}(k_H^{(n)} r_{is}) e^{-\hat{\imath} m \theta_{is}}. \quad (52)$$

1. Reference point source

Since the pressure due to a point source varies with both the position and the frequency, it is desirable to define a particular field point as the reference. When such a reference is needed, the field produced at $(r,z)=(a,h/2)$ by a point source located at $(r,z)=(0,h/2)$ is used as the reference, where a is a length scale chosen as the representative problem dimension. All other pressure fields will be normalized by this reference pressure. According to Eq. (48),

$$P_{\text{ref}} = \frac{1}{2\hat{\imath}h} \sum_{i=0}^{\infty} H_0^{(1)}(k_H^{(2i+1)} a), \quad (53)$$

where is it noted all the even-numbered modes vanish because of the symmetry about the mid-depth plane for this arrangement. In numerical computations, a *point source of unit strength* has the following wave expansion coefficients:

$$\{\alpha_i^{(n)}\}_m = \frac{Z^{(n)}(z') H_m^{(1)}(k_H^{(n)} r_{is}) e^{-\hat{\imath} m \theta_{is}}}{\sum_{i=0}^{\infty} H_0^{(1)}(k_H^{(2i+1)} a)}. \quad (54)$$

VII. NUMERICAL EXAMPLES

In the computer implementation of the above solutions to single and multiple scattering problems, two truncations to the double series expansion are required. One is the truncation for the multiple scattering problem in the horizontal space, for which prior experience for two-dimensional multiple scattering problems can be used as a reference. For example, based on the empirical formula in Cai and Williams (1999b), the truncation can be set at $8 + k_H^{(n)} d_{\max}$ where $d_{\max}$ is the largest distance among scatterers. Since $k_H^{(n)} < k$, the truncation can be determined by the total wave number k. The second truncation is in the number of vertical modes, which will be first explored before other numerical simulations.

For the computation of evanescent modes, since the coordinate transformation used in Eqn. (33) remains valid when the arguments for the various Bessel and Hankel functions are complex variables, the computation for the evanescent modes is straightforward if there is a unified computer interface for Bessel and Hankel functions of either real or purely imaginary arguments. For Bessel and Hankel functions of purely imaginary arguments, the following relationships are noted (Abramowitz and Stegun, 1965): for any real z,

$$J_m(\hat{\imath}z) = \hat{\imath}^m I_m(z) \quad H_m^{(1)}(\hat{\imath}z) = \frac{2}{\pi}(-\hat{\imath})^{m+1} K_m(z), \quad (55)$$

where $I_m(\cdot)$ and $K_m(\cdot)$ are the *modified Bessel functions* of the first and third kinds, respectively. They are sometimes called the *hyperbolic Bessel functions*. The following algorithms are used in the current implementation: Sookne (1975), with slight modifications by the authors, for $I_m(\cdot)$; and Temme (1976), with modifications by Campbell (1980), for $K_m(\cdot)$. Details of the implementation for these functions are omitted for brevity.

In the numerical examples that follow, the ocean water is assumed to have a mass density of 1030 kg/m^3 and a sound speed of 1450 m/s. It is assumed that the penetrable scatterers are having acoustic properties of steel, with a mass density of 7800 kg/m^3 and a sound speed of 6100 m/s. The radius of the cylinders a is used as length scale for measuring other dimensions, and the waveguide depth is $h=20a$.

A. Effects of evanescent modes

As the first example, the evanescent modes due to a point source are observed. The most significant contributions from the evanescent modes come when k_H is a very small imaginary number. According to Fig. 3, this occurs when kh/π is very close to but slightly smaller than an integer. Consider a point source of unit strength located at $z=h/5$. Figure 4 compares the resulting pressure fields at $ka=0.314$ by accounting for only the first 0, 1, 2 and 200 evanescent modes plus the propagating mode. This particular frequency is chosen because $kh/\pi=1.99897$. At this frequency, there is one propagating mode at $k_H^{(1)}h/\pi=1.73088$ (or $k_H^{(1)}a=0.27189$); and the horizontal wave numbers for the first two evanescent modes are $k_H^{(2)}h/\pi=0.06368\hat{\imath}$ and $k_H^{(3)}h/\pi=2.23697\hat{\imath}$ (or $k_H^{(2)}a=0.01002\hat{\imath}$ and $k_H^{(3)}a=0.35138\hat{\imath}$).

From Fig. 4, it is observed that the spatial spread of the evanescent modes reaches a range that is an order of magnitude larger than the depth, which is yet another order of magnitude larger than the reference dimension a. However, even in such an almost-worst scenario case, the inclusion of two evanescent modes produces a field that is almost indistinguishable from the field by including 200 evanescent modes in the region $r>2a$. Noticeable difference can be observed very close to the source. However, since the source is

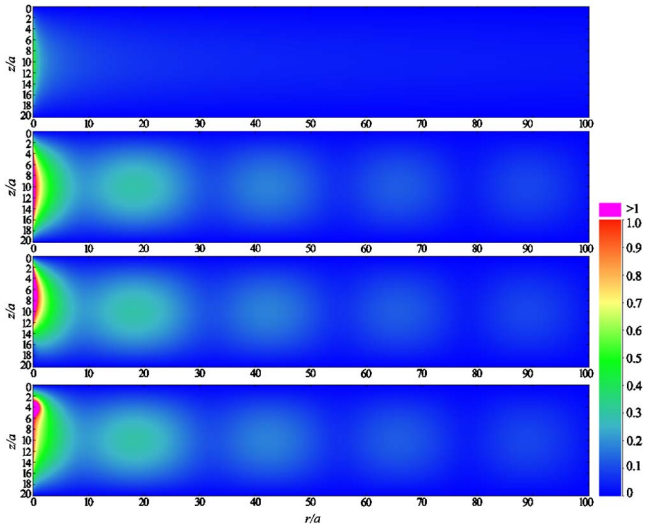

FIG. 4. (Color online) Pressure field due to a point source located at $z=h/5=4a$ in a waveguide of depth $h/a=20$ at the frequency $ka=0.314$. From top down, 0, 1, 2, and 200 evanescent modes plus the propagating mode are included.

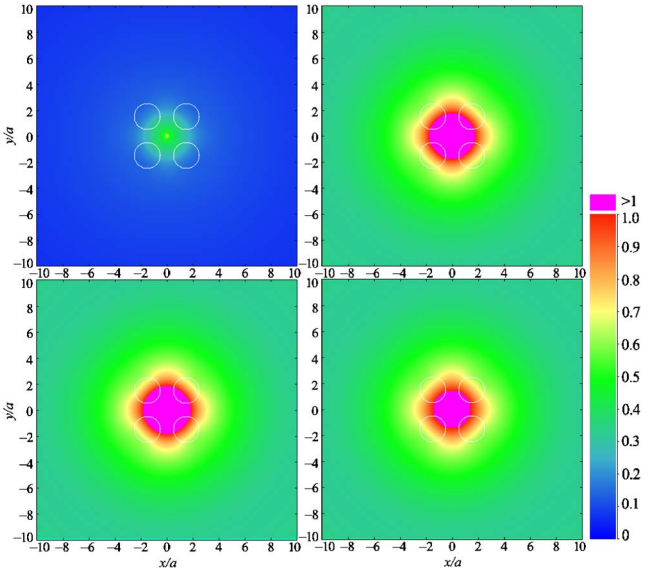

FIG. 5. (Color online) Pressure field at $z=h/4$ due to a point source located at $z=h/5$ at the center of four surrounding steel cylinders. Top left: propagating mode only; top right: one evanescent mode; bottom left: two evanescent modes; bottom right: 200 evanescent modes.

a singular point, errors are expected in the close proximity of the singular point when nonsingular terms are used to approximate the singularity.

Such an almost-worst scenario case only exists in discrete extremely narrow frequency ranges, because the curve for the evanescent modes in Fig. 3 has a slope of infinity when kh/π is an integer. When the frequency is increased slightly, to $ka=0.315$, the situation is drastically different: there are two propagating modes, and the first evanescent mode has a relatively large imaginary wave number ($k_H^{(3)}h/\pi=2.23127\hat{\imath}$ or $k_H^{(3)}a=0.35049\hat{\imath}$). Excluding all evanescent modes does not result in significant error in the computed pressure field except in the close vicinity of the source.

In the second example, the multiple scattering of the above point source by four surrounding identical cylindrical scatterers is observed. The cylinders have a radius a. The four cylinders are arranged such that their centers form a square with a side length of $3a$, and the point source is located at the center of the configuration. At the frequency $ka=0.314$, the pressure fields, obtained again by including the first 0, 1, 2, and 200 evanescent modes plus the propagating mode, in the vicinity of the cylinders in a depth $z=h/4$, are shown in Fig. 5. In this figure, the thin white circles represent outlines of the cylinders.

For the penetrable cylinders used in this example, a propagating mode in the exterior could correspond to an evanescent mode in the interior, and vice versa. In this example, the same number of waveguide modes are used in the computation for both exterior and interior fields. This ensures that boundary conditions are satisfied for each mode.

Observations similar to those made for the source alone can still be made for this case: the evanescent mode has significant spatial spread. In fact, the fields due to the evanescent modes have overwhelmed the field due to the propagating mode. But, including one or two evanescent modes in the computation captures the essence of all evanescent modes, with the only exception of a small region close to the source.

In all the computations that follow, all propagating modes plus the first two evanescent modes are included for the exterior field, and the same total number of modes are used for the interior.

B. Field distribution in depth direction

Figure 6 shows the distributions of the pressure fields in a vertical plane at frequencies: $ka=0.314$ (top left), 0.5 (top right), 1.0 (bottom left) and 1.5 (bottom right). The vertical

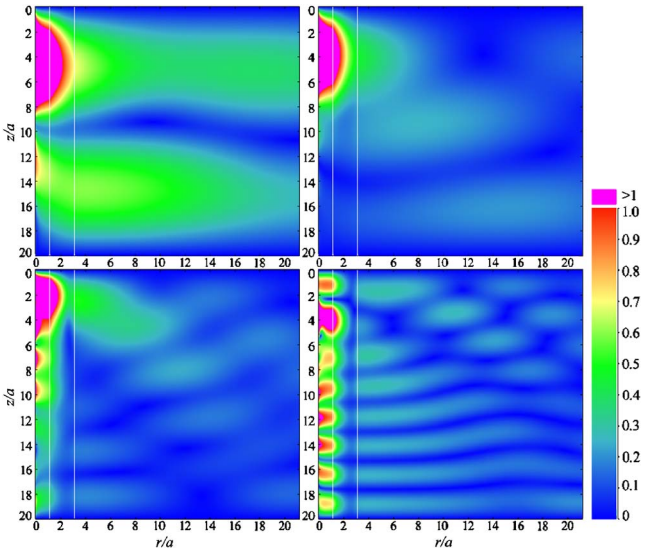

FIG. 6. (Color online) Pressure fields due to point source and four surrounding steel cylinders in vertical plane at the following four frequencies: $ka=0.314$ (top left), 0.5 (top right), 1.0 (bottom left), and 1.5 (bottom right). This is a diagonal side view, albeit at different frequencies, of region shown in Fig. 5.

plane is the diagonal cross section, through the entire depth, of the region shown in Fig. 5. Due to symmetry, only a half of the cross section is shown. The vertical thin white lines represent the outlines of the cylinders. At these frequencies, there are one, three, six and nine propagating modes, respectively.

From Fig. 6, it can be observed that the number of lumps in the vertical direction, especially near the center, equals the number of propagating modes at all frequencies except $ka=0.314$. This agrees with the fact that the nth propagating mode has $n-1$ zeros in the mode shape in the range $(0,h)$. As seen in Fig. 3, the propagating modes of the highest mode number have the smallest horizontal wave number among the propagating modes. According to Eq. (48), the smallest horizontal wave number corresponds to the largest modulus of the wave expansion coefficients, since the modulus of the Hankel function decreases monotonically as the argument increases. For the case $ka=0.314$, there is only one propagating mode but there are two lumps in the central portion of the wave field. This is a frequency at which the contribution from evanescent modes is significant or even overwhelming, and the two lumps suggest that the evanescent modes have overwhelmed the propagating mode in the region shown, which is rather close to the source.

C. Comparison with two-dimensional scattering

It is of great interest to compare the multiple scattering by an ensemble of cylinders in a waveguide with the corresponding two-dimensional multiple scattering by a similar ensemble of long cylinders, because of the close mathematical resemblance. In the two-dimensional problem, the cylindrical scatterers are infinitely long and may be subjected to planar or line incident waves. However, because of the difference in the dimensionality, exact replication is not possible. In the following, consider both waveguide and two-dimensional cases involving 80 scatterers arranged in a square grid of 20 rows (in x direction) in four columns (y direction). In the two-dimensional case, a line source is located at the $(x,y)=(-12,0)$. In the waveguide case, a line source is simulated using 20 equally spaced point sources lying along the true line source length. Each point source has a strength of 0.2.

Formulations for the corresponding single and multiple scattering problems in two-dimensional space are almost identical to those for the waveguide cases for individual propagating modes. For brevity, the formulations for the two-dimensional problems are not repeated here. The expression of the line source, using the coordinate system local to the line source, and normalized by the amplitude of the line source itself at a distance a from the source, can be written as

$$P_{LS}(r,\theta)=\frac{H_0^{(1)}(kr)}{H_0^{(1)}(ka)}.$$

Figure 7 compares pressure fields in the vicinity of the cylinder cluster for frequencies from $ka=0.1$, 0.2, 0.3, 0.4 and 0.5. The area shown in bounded by $-50\leqslant x/a\leqslant 50$ and $-50\leqslant y/a\leqslant 50$. In the waveguide case, only the pressure field at middepth is shown. Similarly, Fig. 8 compares the fields at frequencies $ka=1$, 1.5, 2, 2.5, and 3.

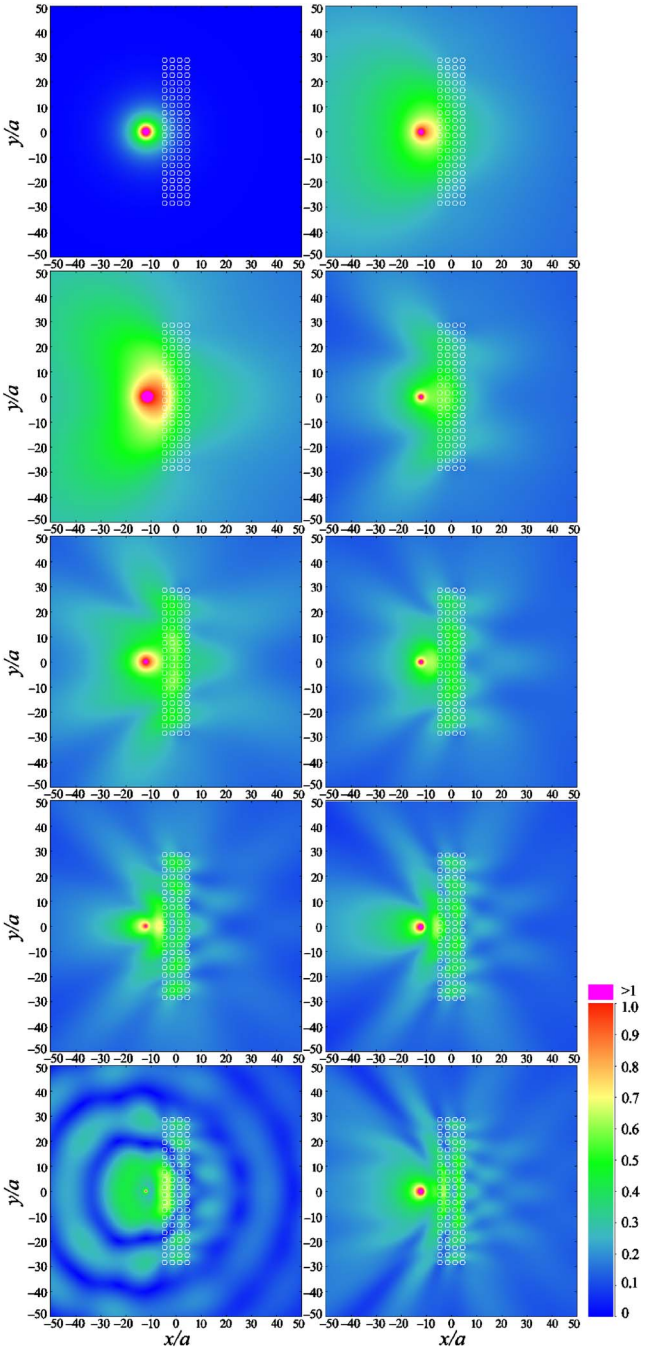

FIG. 7. (Color online) Comparison of pressure field in the waveguide (left column) and the corresponding field for the two-dimensional infinite medium (right column). From top down, $ka=0.1$, 0.2, 0.3, 0.4 and 0.5.

In Figs. 7 and 8, according to Fig. 3 and Eq. (11), the number of propagating modes $n_p=[20ka/\pi]$. However, due to the symmetry about the mid-depth plane, even-numbered modes are suppressed. For frequencies shown, from $ka=0.2$ up to 0.4, there is only one propagating mode; and for $ka=0.5,1,1.5,2,2.5$, and 3, there are 2, 3, 5, 6, 8 and 10 propagating modes, respectively. Each propagating mode has a horizontal pattern determined by the two-dimensional scatterer problem, and a modulation in the vertical direction determined by the waveguide mode shape.

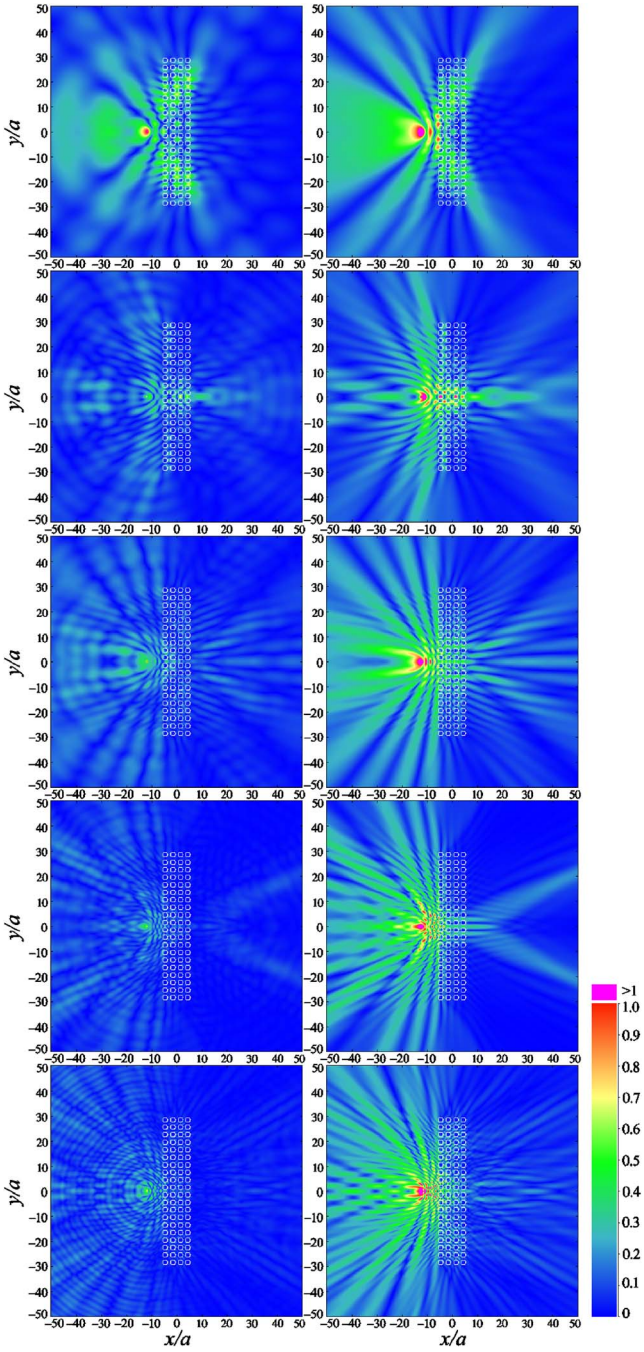

FIG. 8. (Color online) Comparison of pressure field in the waveguide (left column) and the corresponding field for the two-dimensional infinite medium (right column). From top down, $ka=1$, 1.5, 2, 2.5 and 3.

From Figs. 7 and 8, it is observed that, below the cutoff frequency ($ka=0.1$), the field for the waveguide case is quiescent because there are no propagating modes, except in the region close to the source. Between $ka=0.2$ and $ka=0.4$, the field pattern in the waveguide case is similar to that in the two-dimensional case. For example, at $ka=0.2$ the pattern in the waveguide case is similar to the two-dimensional case at $ka=0.1$. This is because $k_H<k$ and it is k_H that governs the multiple scattering in the waveguide case.

However, as the frequency increases beyond $ka=0.5$, the field patterns in the two cases start to depart. The departure of the wave patterns in the two cases can be attributed to the simultaneous presences of more than one propagating mode. As discussed earlier, the propagating mode with the highest mode number plays the most significant role in the waveguide case. The wave number in this mode can be very different from the wave number in the corresponding two-dimensional case.

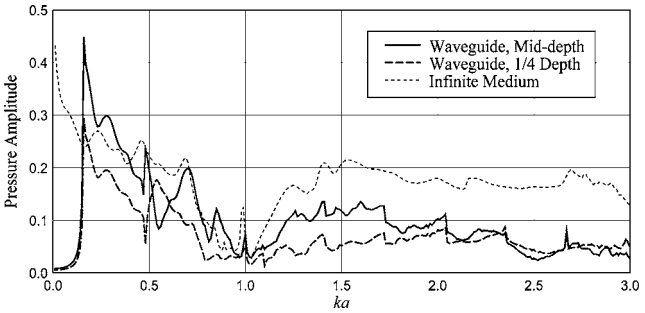

FIG. 9. Comparison of wave transmission spectra for the cases of waveguide at depth of $z=h/2$ (solid curve) and $z=h/4$ (dashed curve) compared with the two-dimensional case (dotted curve).

As the frequency continues to increase, there is lesser and lesser resemblance in the field patterns in the two cases because more propagating modes contribute to the pattern for the waveguide case. It is interesting to note that, in the waveguide case, the pressure distribution pattern is dominantly circular; whereas in the two-dimensional case, the patter is dominantly radial.

Despite the differences, some distinctive features in the wave pattern remain very similar in both cases. For instance, at $ka=1$, the waves appear to be prevented from propagating in the forward direction; at $ka=1.5$, there is a narrow beam at the center in forward direction where the wave passes through the cylinder ensemble; and at $ka=2$ and 2.5, waves split into a few beams.

Figure 9 compares the forward transmission spectra for the two cases. The spectra are the averaged pressure amplitude measured in the forward direction at $x=10a$ and over the range $0\leqslant y\leqslant 10a$. For the waveguide case, the spectra at two depths, at middepth $z=10a$ and $z=4a$, are shown.

Several observations can be made from these spectra. First, the cutoff frequencies in the waveguide are apparent, as the pressure experiences a sudden surge at the cutoff frequency. Second, in the frequency range of $k_{\text{cutoff}}a\approx 0.157 \leqslant ka\leqslant 0.471$, the curves for the waveguide case are similar to the corresponding two-dimensional case in the frequency range of $0<ka<0.471$. This is the frequency range in which there is only one propagating mode in the waveguide, and the similarity essentially reflects the relationship between the horizontal wave number and the total wave number for the waveguide case. Third, for the two-dimensional case, there is an apparent band gap in the frequency range $0.7\leqslant ka\leqslant 1.2$. The band gap is not fully developed, partially due to the limited number of cylinders in the ensemble, especially the number in the x direction, and partially due to the nature of line source, which contains wave components that propagate in all directions. In the waveguide case, the gap appears to have been shifted very slightly to higher frequencies, due to the fact that $k_H<k$, and becomes slightly narrower.

D. Modal power transmission due to scatterer array

One of the measures for the acoustic energy is the acoustic power. For a planar wave, the acoustic power P is proportional to the square of pressure (see, e.g., Pierce, 1989) as

$$P = \frac{p^2}{\rho c^2}, \tag{56}$$

where p is the (real) sound pressure. For simplicity, this is taken as the approximate measure of the acoustic power in the waveguide. For the scattering problem under consideration,

$$p = \mathrm{Re}\{\phi e^{\hat{\imath}\omega t}\} = \frac{1}{2}(\phi e^{\hat{\imath}\omega t} + \bar{\phi} e^{-\hat{\imath}\omega t}), \tag{57}$$

where Re denotes the real part of a complex quantity. Averaging the acoustic power over one period of wave motion gives the *time-averaged acoustic power* as

$$\langle P \rangle = \frac{\phi\bar{\phi}}{2\rho c^2}. \tag{58}$$

In the waveguide, the general expression for the pressure field, as show in Eqn. (7), can be written as

$$\phi = \sum_{n=1}^{\infty} \Phi^{(n)}(r,\theta) Z^{(n)}(z), \tag{59}$$

where it is noted that the $Z^{(n)}(z)$ is always real and orthogonal. Substituting Eq. (59) into Eq. (58) and integrating over the entire z range give

$$\int_{\Omega} \langle P \rangle c^2 dz = \frac{1}{2}\sum_{n=1}^{\infty} \int_{\Omega} \frac{Z^{(n)}(z)^2}{\rho(z)} dz |\Phi^{(n)}(r,\theta)|^2. \tag{60}$$

For the case of constant sound speed

$$\int_0^h \langle P \rangle dz = \frac{h}{4\rho c^2}\sum_{n=1}^{\infty} |\Phi^{(n)}(r,\theta)|^2. \tag{61}$$

Equation (61) means that the time-averaged acoustic power over the entire depth of the waveguide is the summation of those of individual modes. Therefore, the power transmission from one field point to another can be observed and analyzed for each mode. For a scattering problem, define the *modal power transmission ratio* as the ratio of time-averaged acoustic power in the total wave at a certain field point to that of the incident wave at the same field point; that is

$$\mathrm{TR}^{(n)} = \frac{|\Phi^{(n)}_{\mathrm{total}}|^2}{|\Phi^{(n)}_{\mathrm{inc}}|^2}. \tag{62}$$

Figure 10 shows the modal power transmission ratios for the first three nonzero modes: modes 1, 3 and 5. The transmission ratio is nonzero when the mode is an evanescent mode, such as $ka < 0.157$ for mode 1, $ka < 0.471$ for mode 3, and $ka < 0.875$ for mode 5. This is because the measurement point is still located at $(x,y) = (10a, 0)$, which is not a far-field point. However, the most striking feature in Fig. 10 is the similarity of all the curves: they appear to be the same

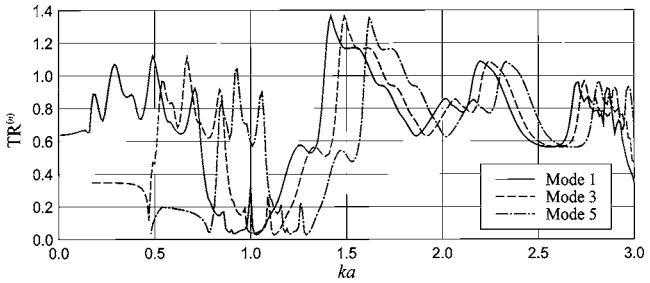

FIG. 10. Modal power transmission ratio for the first three nonzero modes.

curve shifted to higher frequencies and slightly compressed in the horizontal direction for a higher mode. This should not be a surprise since the multiple scattering process is governed by the horizontal wave number k_H.

The curves shown in Fig. 10 are replotted against the horizontal wave number k_H in Fig. 11. At lower frequencies, the curves are similar but have noticeably different transmission ratios. At higher frequencies, all curves coincide. Recall that, in different modes, the incident wave impinges onto the cylinders at different angles, giving different apparent impedances. As the frequency increases, the direction at which a mode propagates approaches to horizontal, k_H approaches to the total wave number k, and the scattering in the wave guide at each mode approaches to the two-dimensional scattering.

The band gap in the frequency range of $0.7 < k_H a < 1.2$ is rather apparent in Fig. 11. However, in Fig. 10, the band gap is located at different frequency ka ranges for different modes. The implication is that a complete band gap, which blocks all modes, may not be possible, as the stop band in one mode could be in the range of a pass band in another mode. This would be especially true for deeper waveguides, as more modes exist at the same frequency. However, comparing to Fig. 9, it is reasonable to expect that, as different modes contribute to the total wave field differently, an effective band gap, albeit not a complete band gap, is still achievable, as demonstrated in Fig. 8 for the case $ka = 1$, which is inside the band gap.

VIII. CONCLUSIONS

Scattering of acoustic waves by an ensemble of cylindrical scatterers in a planar horizontal waveguide is studied. The waveguide consists of flat top and bottom surfaces, which are both assumed to be pressure-release boundaries, filled with uniform sea water. Scatterers are penetrable circu-

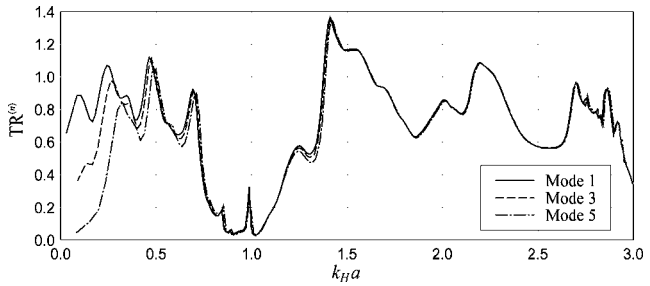

FIG. 11. The same as Fig. 10, except that the data are replotted against the horizontal wave number k_H for each mode.

lar steel cylinders that extend to the entire depth of the waveguide, and also have pressure-release top and bottom surfaces. An analytically exact solution is obtained via the normal mode expansion method. The solution is comprised of an infinite number of modes whose horizontal components are identical to those of two-dimensional multiple scattering problems, and in the vertical direction are modulated by waveguide mode shapes. Each mode has a distinctive horizontal and vertical wave number. At any given frequency above the cutoff frequency, there is only a limited number of propagating modes, while the remainder are evanescent modes. All propagating modes have the same power transmission spectrum if the power is measured through the entire depth and plotted against the horizontal wave number.

Numerical examples show that the evanescent modes are important, and could even become dominant, at certain frequencies. Including one or two evanescent modes, however, captures the essence of all evanescent modes. When compared with a case in which the same scatterer ensemble is placed in a two-dimensional infinite space, when there is only one propagating mode, the wave propagation pattern in the waveguide case at a given horizontal plane shows great similarity to the two-dimensional case at a lower frequency, due to the difference in the horizontal wave number and the total wave number. When there are more than one propagating modes in the waveguide, the mixing of the modes could destroy the similarity in the wave propagation patterns. With point sources producing the incident field, it is found that, among all propagating modes, the mode with the highest mode number, which is also the mode whose horizontal wave number differs from the total wave number the most, makes the most contribution to the scattering pattern.

Note that the studied case is a rather special case with penetrable cylinders in which the vertical mode shapes for both the waveguide and the obstacles are the same and do not depend explicitly on the frequencies. In other cases, either when the obstacles could create leakage of wave energy out of the waveguide, such as when the cylinders are longer than the waveguide depth, or when the waveguide mode shape is frequency dependent, such as more realistic models for ocean waveguide, mode coupling will generally occur. Such problems will be the subjects of future investigations of the authors.

ACKNOWLEDGMENTS

One of the authors (L.W.C.) gratefully acknowledges the support by the National Science Foundation for this research through Grant No. CMS-0510940. L.W.C. also wishes to express his sincere appreciation for the hospitality of the colleagues and staff members at the Acoustics Division of the Naval Research Laboratory when some of the work was performed there. The computer implementation for the two-dimensional multiple scattering solution was assisted by Ms. Congrui Jin, currently of the Department of Mechanical Engineering of the University of Alberta, Canada.

Abramowitz, M., and Stegun, I. A. (**1965**). *Handbook of Mathematical Functions* (Dover, New York).

Athanassoulis, G. A., and Prospathopoulos, A. M. (**1996**). "Three-dimensional acoustic scattering of a source-generated field from a cylindrical island," J. Acoust. Soc. Am. **100**(1), 206–218.

Athanassoulis, G. A., and Prospathopoulos, A. M. (**2000**). "Three-dimensional acoustic scattering from a penetrable layered cylindrical obstacle in a horizontally stratified ocean waveguide," J. Acoust. Soc. Am. **107**(5), 2406–2417.

Butorin, V. M. (**1988**). "Three-dimensional boundary-value problem of a dielectric cylinder in a rectangular waveguide," Sov. J. Commun. Technol. Electron. **33**(8), 75–79.

Butorin, V. M. (**1991**). "Resonance properties of two metal cylinders in a rectangular waveguide," Sov. J. Commun. Technol. Electron. **36**(11), 22–27.

Cai, L.-W., and Williams, J. H., Jr. (**1999a**). "Large scale multiple scattering problems," Ultrasonics **37**(7), 453–462.

Cai, L.-W., and Williams, J. H., Jr. (**1999b**). "Full-scale simulations of elastic wave scattering in fiber reinforced composites," Ultrasonics **37**(7), 463–482.

Campbell, J. B. (**1980**). "On Temme's algorithm for the modified Bessel function of the third kind," ACM Trans. Math. Softw. **6**(4), 581–586.

Cicconi, G., and Rosatelli, C. (**1977**). "Solutions of the vector wave equation for inhomogeneous dielectric in waveguide," IEEE Trans. Microwave Theory Tech. **MTT-25**(11), 885–892.

Diamandi, I., Sahalos, J. N., and Vafiadis, E. (**1993**). "Characteristics of a rectangular waveguide containing a magnetized cylindrical ferrite post," Int. J. Numer. Model. **6**(2), 99–108.

Gesche, R., and Russenschuck, S. (**1989**). "Improving the characteristics of rectangular waveguide branchings by cylindrical obstacles," IEEE Trans. Microwave Theory Tech. **37**(19), 1579–1584.

Hackman, R. H., and Sammelmann, G. S. (**1986**). "Acoustic scattering in an inhomogeneous waveguide: Theory," J. Acoust. Soc. Am. **80**(5), 1447–1458.

Huang, C.-C., Tsang, L., Chan, C. H., and Ding, K.-H. (**2004**). "Multiple scattering among vias in planar waveguides using preconditioned SMCG method," IEEE Trans. Microwave Theory Tech. **52**(1), 20–28.

Ivanishin, M. M. (**1989**). "Solution to the scattering problem of a conducting cylinder placed in a rectangular waveguide," Sov. J. Commun. Technol. Electron. **34**(11), 67–75.

Jensen, F. B., Kuperman, W. A., Porter, M. B., and Schmidt, H. (**1994**). *Computational Ocean Acoustics* (American Institute of Physics, New York).

Kalesinskas, V., Konstantinov, A., and Shugurov, A. (**1998**). "Analysis of electromagnetic waves scattering by a finite size dielectric and metal cylinder in a rectangular waveguide," Int. J. Infrared Millim. Waves **19**(12), 1773–1781.

Kapilevich, B. Y. (**1990**). "Resonance scattering by a dielectric cylinder in a rectangular waveguide below cut-off," Int. J. Electron. **69**(6), 819–825.

Kyurkchan, A. G., and Manenkov, S. A. (**2002**). "Wave scattering from a group of bodies located in a planar stratified medium," J. Commun. Technol. Electron. **47**(11), 1322–1328.

Logan, J. D. (**1987**). *Applied Mathematics: A Contemporary Approach* (Wiley, New York).

Miyashita, T. (**2005**). "Sonic crystals and sonic wave-guides," Meas. Sci. Technol. **16**(5), R47–R63.

Nielsen, E. D. (**1969**). "Scattering by a cylindrical post of complex permittivity in a waveguide," IEEE Trans. Microwave Theory Tech. **MTT-17**(3), 148–153.

Okamoto, N., Snishioka, I., and Nakanishi, Y. (**1971**). "Scattering by a ferrimagnetic circular cylinder in a rectangular waveguide," IEEE Trans. Microwave Theory Tech. **MTT-19**(6), 521–527.

Pao, Y.-H., and Mow, C.-C. (**1971**). *Diffraction of Elastic Waves and Dynamic Stress Concentrations* (Crane Russak, Melville, NY).

Pierce, A. D. (**1989**). *Acoustics: An Introduction to Its Physical Principles and Applications* (Acoustical Society of America, Melville, NY).

Sammelmann, G. S., and Hackman, R. H. (**1987**). "Acoustic scattering in a homogeneous waveguide," J. Acoust. Soc. Am. **82**(1), 324–336.

Sookne, D. J. (**1975**). "Bessel functions of real argument and integer order," J. Res. Natl. Bur. Stand., Sect. B **77A**(3/4), 125–132.

Temme, N. M. (**1976**). *On the Numerical Evaluation of the Modified Bessel Function of the Third Kind*, 2nd ed. (Department of Applied Mathematics, the Mathematical Center, Amsterdam). (Also, earlier version: J. Comput. Phys. **19**, 324–337 (**1975**).)

Tolstoy, I. (**1986**). "Super resonant systems of scatterers," J. Acoust. Soc. Am. **80**(1), 282–294.

Modeling the propagation of nonlinear three-dimensional acoustic beams in inhomogeneous media

Yuan Jing and Robin O. Cleveland[a)]
Department of Aerospace and Mechanical Engineering, Boston University, Boston, Massachusetts 02215

(Received 22 January 2007; revised 29 June 2007; accepted 9 July 2007)

A three-dimensional model of the forward propagation of nonlinear sound beams in inhomogeneous media, a generalized Khokhlov-Zabolotskaya-Kuznetsov equation, is described. The Texas time-domain code (which accounts for paraxial diffraction, nonlinearity, thermoviscous absorption, and absorption and dispersion associated with multiple relaxation processes) was extended to solve for the propagation of nonlinear beams for the case where all medium properties vary in space. The code was validated with measurements of the nonlinear acoustic field generated by a phased array transducer operating at 2.5 MHz in water. A nonuniform layer of gel was employed to create an inhomogeneous medium. There was good agreement between the code and measurements in capturing the shift in the pressure distribution of both the fundamental and second harmonic due to the gel layer. The results indicate that the numerical tool described here is appropriate for propagation of nonlinear sound beams through weakly inhomogeneous media. © *2007 Acoustical Society of America.* [DOI: 10.1121/1.2767420]

PACS number(s): 43.25.Cb, 43.35.Bf, 43.80.Qf [MFH] Pages: 1352–1364

I. INTRODUCTION

Realistic simulations of the propagation of finite-amplitude acoustic waves are applicable to many problems, including: blast waves underwater,[1] sonic boom and noise propagation in the atmosphere,[2] and diagnostic and therapeutic applications of biomedical ultrasound.[3,4] Various computational models have been developed to model the nonlinear propagation process.

A popular model for nonlinear sound beams is the Khokhlov-Zabolotskaya-Kuznetsov (KZK) equation.[5,6] This equation accounts for diffraction (in the parabolic approximation), nonlinearity, and thermoviscous absorption. Numerical solutions of the axissymmetric version (two spatial dimensions) of the KZK equation and its extended form (sound speed inhomogeneities and arbitrary absorption) for a circular source have been widely investigated.[7–11] Numerical solutions for nonlinear sound beams that have no restrictions on beam direction or focusing, but are currently limited to two dimensions, have also been reported.[12–17] Three-dimensional (3D) simulations use the KZK equation for square- and rectangular-shaped transducers[18–24] but have focused on propagation in homogeneous media.

The main purpose of the present article is to describe a 3D time-domain numerical code capable of simulating the propagation of acoustic beams of finite amplitude in inhomogeneous media where acoustic properties can vary in space. The 3D code was adapted from the "Texas code" a time-domain algorithm that was originally derived for axisymmetric sound fields[8] but has since been extended to model rectangular sources.[23] In this work the new terms associated with variations in spatial properties are incorporated into the numerical simulation along with the effects of diffraction (in the paraxial approximation), nonlinearity, thermoviscous absorption and multiple relaxation phenomena.

II. MODEL EQUATION AND NUMERICAL METHOD

The derivation of the generalized KZK equation followed the method described by Naze Tjotta and Tjotta[25] and summarized in Hamilton and Morfey.[26] Briefly, the acoustic wave is assumed to induce small perturbation to the field variables in the underlying fluid equations. The perturbations are taken to be of order ε which may be defined as $|p_0|/\rho_0 c_0{}^3$ where p_0 is a characteristic pressure, ρ_0 the density, and c_0 the small-signal sound speed. The equations of linear acoustics are obtained by retaining all terms of order ε and "finite-amplitude" acoustics result from also keeping terms of order ε^2. Following the conventions of finite-amplitude acoustics all loss terms are taken to be of order ε^2 as well. In this work, where the fluid is allowed to be inhomogeneous, it was further assumed that the spatial derivatives of the material properties are small, e.g., $(\nabla\rho_0/\rho_0)\ell$, are order ε where ℓ is a characteristic length scale, e.g., the wavelength. For an inhomogeneous, thermoviscous, relaxing fluid the wave equation, correct to second order (that is terms of order $\varepsilon^3$and smaller are neglected) is[27]

$$\nabla^2 p' - \frac{1}{c_0{}^2}\frac{\partial^2 p'}{\partial t^2} = -\left(\frac{1}{c_0{}^3}\sum_\nu \frac{2c'_\nu\tau_\nu}{1+\tau_\nu\frac{\partial}{\partial t}} + \frac{\delta}{c_0{}^4}\right)\frac{\partial^3 p'}{\partial t^3} - \frac{\beta}{\rho_0 c_0{}^4}\frac{\partial^2 p'^2}{\partial t^2} + \nabla p'\cdot\frac{\nabla\rho_0}{\rho_0} - \left(\nabla^2 + \frac{1}{c_0{}^2}\frac{\partial^2}{\partial t^2}\right)\left(\frac{\rho_0 u^2}{2} - \frac{p'^2}{2\rho_0 c_0{}^2}\right). \quad (1)$$

Here p' is the sound pressure, u^2 is the magnitude of the

a)Author to whom correspondence should be addressed. Electronic mail: robinc@bu.edu

particle velocity squared, β the coefficient of nonlinearity, δ the diffusivity of sound, τ_v the relaxation time and c_v' the small-signal sound speed increment for each of the relaxation processes ν where ν ranges from 1 up to the number of relaxation processes. In this equation all material properties can vary in space.

For many acoustic problems the last term in the Eq. (1), which contains the Lagrangian density, becomes negligible,[25] and a generalized Westervelt equation arises.[17,28] Further for a "sound beam," where the propagation is primarily in one direction (taken to be the z axis in this work) and diffraction is weak, the partial derivatives in the lateral coordinates (x and y axes in this case) can be taken to be of order $\sqrt{\varepsilon}$ and the KZK equation, generalized for propagation in relaxing inhomogeneous media, results

$$\frac{\partial p'}{\partial z} = \frac{c_{00}}{2}\int_{-\infty}^{\tau}\left(\frac{\partial^2 p'}{\partial x^2}+\frac{\partial^2 p'}{\partial y^2}\right)d\tau' + \frac{\beta}{2\rho_0 c_0{}^3}\frac{\partial p'^2}{\partial \tau} + \frac{\delta}{2c_0{}^3}\frac{\partial^2 p'}{\partial \tau^2} + \sum_{\nu}\frac{c_\nu'}{c_0{}^2}\int_{-\infty}^{\tau}\frac{\partial^2 p'}{\partial \tau'^2}e^{-(\tau-\tau')/\tau_\nu}d\tau' + \frac{c_0-c_{00}}{c_0{}^2}\frac{\partial p'}{\partial \tau} + \frac{p'}{2\rho_0}\frac{\partial \rho_0}{\partial z} - \frac{c_{00}}{2\rho_0}\int_{-\infty}^{\tau} \times\left(\frac{\partial p'}{\partial x}\frac{\partial \rho_0}{\partial x}+\frac{\partial p'}{\partial y}\frac{\partial \rho_0}{\partial y}\right)d\tau'. \quad (2)$$

Here $\tau=t-z/c_{00}$ is the retarded time in the direction of the beam, and c_{00} a constant reference value of the small-signal sound speed, e.g., the sound speed at the source. In the transition from Eq. (1) to Eq. (2) it was necessary to assume that $|c_0-c_{00}|/c_{00}$ was order ε. This restriction on the sound speed is different from that of the density and is discussed below. We note that all terms in Eq. (2), except the last one, are of second order, i.e., $O(\varepsilon^2)$. The last term, which accounts for lateral variations in density, is $O(\varepsilon^{2.5})$ which is smaller than the second order terms that were retained in the derivation of Eq. (2), but not as small as the third order terms that were neglected. There is, therefore, some ambiguity as to whether the term should be retained as it falls in between the order of the retained and neglected terms. Because the last term is the only one that carries information on variations in the density perpendicular to the primary direction of propagation, the term was included in the calculations reported here.

A numerical solution to Eq. (2) was obtained following the method of the Texas code which has been described for two-dimensional and 3D problems.[8,23] First, Eq. (2) was transformed into dimensionless form on a Cartesian grid and the following dimensionless variables introduced $\sigma=z/d$, $X=x/a$, $Y=y/b$, $\tau=\omega_0\tau'$, $P=p'/p_0$, where d is a characteristic length of the source (in this work, the focal length), the quantities a and b are the characteristic lengths in the x and y direction (e.g., the size of the source aperture), and ω_0 is a characteristic angular frequency (e.g., working frequency of the source pulse). Substitution into Eq. (2) yields

$$\frac{\partial P}{\partial \sigma} = \frac{\varphi_C}{4}\int_{-\infty}^{\tau}\left(\frac{1}{G_x}\frac{\partial^2 P}{\partial X^2}+\frac{1}{G_y}\frac{\partial^2 P}{\partial Y^2}\right)d\tau' + \varphi_N N P\frac{\partial P}{\partial \tau} + \varphi_A A\frac{\partial^2 P}{\partial \tau^2} + \sum_{\nu}\varphi_{RD}D_\nu\int_{-\infty}^{\tau}\frac{\partial^2 P}{\partial \tau'^2}e^{-(\tau-\tau')/(\theta_\nu\varphi_{RT})}d\tau' + k_{00}d(\varphi_C-1)\frac{\partial P}{\partial \tau} + \frac{1}{2\varphi_\rho}P\frac{\partial \varphi_\rho}{\partial \sigma} - \frac{\varphi_C}{4}\int_{-\infty}^{\tau}\frac{1}{G_x}\frac{1}{\varphi_\rho}\frac{\partial \varphi_\rho}{\partial X}\frac{\partial P}{\partial X}d\tau' - \frac{\varphi_C}{4}\int_{-\infty}^{\tau}\frac{1}{G_y}\frac{1}{\varphi_\rho}\frac{\partial \varphi_\rho}{\partial Y}\frac{\partial P}{\partial Y}d\tau', \quad (3)$$

where the dimensionless coefficients are:

$$G_x = k_{00}a^2/2d$$

$$G_y = k_{00}b^2/2d$$

$$N = d/\bar{z}_0$$

$$A = \alpha_{00}d$$

$$D_\nu = k_{00}dc_{\nu 0}'/c_{00}$$

$$\theta_\nu = \omega_0 t_{\nu 0}.$$

Because all the properties can vary in space, the dimensionless coefficients above were defined in terms of reference or representative values for the medium, e.g., values at the source or average values through the medium, and are indicated by the addition of a "0" to the subscript. Here $k_{00}=\omega_0/c_{00}$ is the wave number based on a reference sound speed, $\bar{z}_0=\rho_{00}c_{00}^3/\beta\omega_0 p_0$ is the plane wave shock formation distance based on reference medium properties, $\alpha_{00}=\delta_0\omega_0^2/2c_{00}^3$ is the reference thermoviscous absorption coefficient (Np/m) at the characteristic frequency. The dimensionless properties may be interpreted as follows: G_x and G_y are related to diffraction in the x and y axes, N to nonlinearity, A to thermoviscous absorption and D_ν and θ_ν are reference dispersion and relaxation time parameters for the ν^{th} relaxation process.

The spatial variations in medium properties were taken into account through the following dimensionless $\varphi(X,Y,Z)$ functions:

$$\varphi_C = c_0/c_{00}$$

$$\varphi_\rho = \rho_0/\rho_{00}$$

$$\varphi_N = \beta\rho_{00}c_{00}^3/(\beta_0\rho_0c_0^3)$$

$$\varphi_A = \alpha_0/\alpha_{00}$$

$$\phi_{RT} = t_v/t_{v0}$$

$$\varphi_{RD} = (c_v'/c_{v0})(c_0/c_{00})^2.$$

Physically, φ_C accounts for spatial variation in sound speed, φ_ρ density, φ_N nonlinearity, φ_A absorption, φ_{RT} relaxation time and φ_{RD} relaxation dispersion. For the simulations the coefficients for these inhomogeneities at each point in space were pre-calculated and stored in a file. As the code marched forward, the φ data were read from the file and the properties of the point nearest to the calculation point were used, without interpolation, to avoid smoothing the boundary of different media.

Equation (3) is an evolution equation, therefore although the pressure is a function of four variables $P(\sigma,\tau,X,Y)$, for the simulations it was only necessary to retain the pressure as a function of time and the lateral coordinates, that is τ, X, and Y. The time window was truncated using the guidelines described in Ref. 8 and discretized with a temporal grid step of $\Delta\tau$. The lateral dimensions were also truncated at 2–4 times the source dimensions and were discretized with spatial grid steps of ΔX and ΔY, respectively.

Equation (3) was solved using the operator-splitting paradigm which allows each effect to be calculated separately at each step.[29] The equations for absorption and relaxation are identical in form to the homogeneous Texas code and the same method was employed here.[8,23] The inhomogeneous terms in Eq. (3) are new and needed to be included into the numerical scheme. The transverse density fluctuation term was incorporated into the diffraction term, that is, the subequations to be solved in the operating splitting paradigm were

$$\frac{\partial P}{\partial \sigma} = \frac{\varphi_C}{4G_X}\int_{-\infty}^{\tau}\left(\frac{\partial^2 P}{\partial X^2} - \frac{1}{\varphi_\rho}\frac{\partial \varphi_\rho}{\partial X}\frac{\partial P}{\partial X}\right)d\tau' \tag{4}$$

$$\frac{\partial P}{\partial \sigma} = \frac{\varphi_C}{4G_Y}\int_{-\infty}^{\tau}\left(\frac{\partial^2 P}{\partial Y^2} - \frac{1}{\varphi_\rho}\frac{\partial \varphi_\rho}{\partial Y}\frac{\partial P}{\partial Y}\right)d\tau'. \tag{5}$$

The first order lateral derivatives of P and φ_ρ (which correspond to derivatives of ρ_0 in dimensional space) are not present in the homogeneous code and were evaluated with centered finite differences which are accurate to second order. The integrals were evaluated using Simpson's rule as is done in the Texas code algorithm.

The term associated with spatial variation in the sound speed can be combined with the nonlinear term to produce the following differential equation:

$$\frac{\partial P}{\partial \sigma} = [\varphi_N N P + k_{00} d(\varphi_C - 1)]\frac{\partial P}{\partial \tau}. \tag{6}$$

This can be solved exactly using the Poisson solution.[30]

The equation that accounts for density fluctuations in the axial direction

$$\frac{\partial P}{\partial \sigma} = \frac{1}{2\varphi_\rho}\frac{\partial \varphi_\rho}{\partial \sigma}P \tag{7}$$

was solved by using the following first-order finite difference approximation:

$$\frac{P(\sigma+\Delta\sigma)-P(\sigma)}{\Delta\sigma} = \frac{P(\sigma)}{\varphi_\rho(\sigma)+\varphi_\rho(\sigma+\Delta\sigma)} \times \frac{\varphi_\rho(\sigma+\Delta\sigma)-\varphi_\rho(\sigma)}{\Delta\sigma},$$

where the τ, x, y dependence has been suppressed in the notation and $2\varphi_\rho$ was taken to be $\varphi_\rho(\sigma+\Delta\sigma)+\varphi_\rho(\sigma)$. This finite difference equation, which accounts for the effects of density fluctuations in the axial direction, can be expressed as

$$P(\sigma+\Delta\sigma) = \frac{2\varphi_\rho(\sigma+\Delta\sigma)}{\varphi_\rho(\sigma+\Delta\sigma)+\varphi_\rho(\sigma)}P(\sigma), \tag{8}$$

which corresponds to the result for plane wave transmission across a discontinuity in density. We comment that one might expect Eq. (8) to be expressed in terms of the pressure transmission coefficient for a discontinuity, that is, the coefficient should be in terms of the specific acoustic impedance rather than the density. Indeed for the case of nonlinear sound propagation along a ray tube the evolution equation depends on the change in specific acoustic impedance (see, e.g., Ref. 31). However, the change in sound speed has two effects on wave propagation: one is to change the impedance, the second is to induce a phase shift to the wave. Because the propagation along ray tubes is quasi 1 dimensional, the phase shift associated with the change in sound speed can be accounted for in the transformation to retarded time and, the effect of sound speed on impedance is retained at second order. However, in the case of diffracting beams the phase may vary across the beam and so the phase shift associated with sound-speed inhomogeneity cannot be incorporated into the retarded time—one exception would be a layered medium where each layer was homogeneous and normal to the axis of propagation. The sound-speed induced phase shift therefore needs to be calculated explicitly, which is the role of Eq. (6). Recall that in the derivation of the generalized KZK equation (Eq. (2)) the requirement on the variations on sound speed was that $|c_0 - c_{00}| \ll c_{00}$, in which case the effect of the changes in the impedance is negligible. In contrast, the restriction on the density was that $\rho_0/|d\rho_0/dz|$ be much longer than the characteristic length scale in the problem.

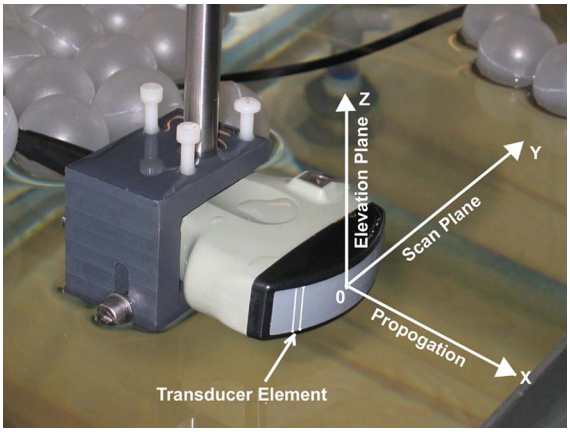

FIG. 1. (Color online) Picture of the phased array with the coordinate system overlaid.

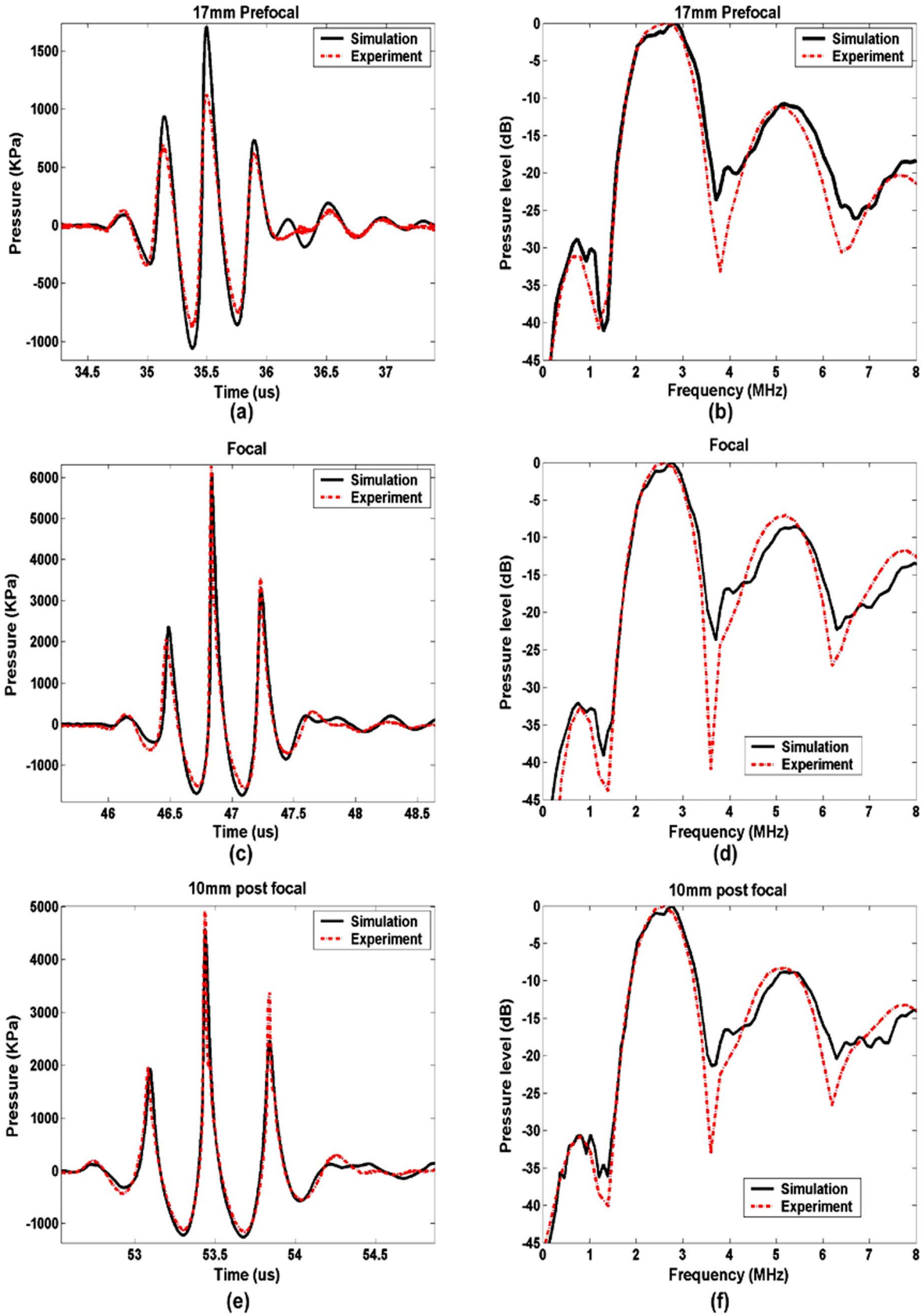

FIG. 2. (Color online) Comparison of simulated and measured wave forms and their spectra for three positions along the acoustic axis. Upper: 17 mm pre-focal (z=53 mm); middle: at the focus (z=70 mm); lower: 10 mm postfocal (z=80 mm).

The later is a weaker restriction than that imposed on the sound speed and it allows ρ_0 to become significantly different from ρ_{00} and hence effect the evolution of the pressure through Eq. (7).

The marching algorithm employs the same two methods using by the Texas code for the diffraction and absorption terms. An implicit backward finite difference method is used for the first 100 marching steps with $\Delta\sigma$=0.001, which is

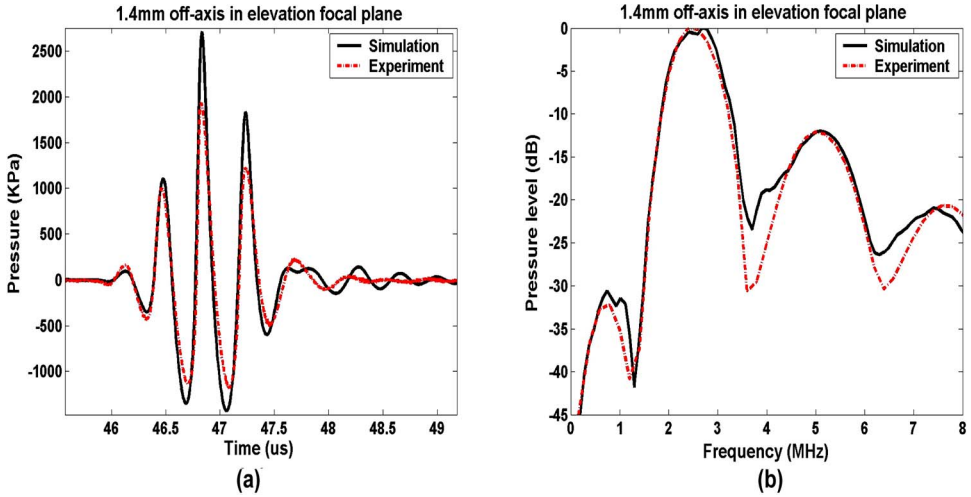

FIG. 3. (Color online) Comparison of simulated and measured wave forms and their spectra for a location 1.4 mm off axis in the elevation focal plane (x=1.4 mm, y=0 mm, z=70 mm).

effective in damping oscillations near the source. The rest of the marching is carried out using the Crank-Nicolson finite difference method, which allows larger steps in the marching direction $\Delta\sigma$=0.005.

III. EXPERIMENTAL METHOD

The experiments were carried out in a clear acrylic tank (1.50 m long, 0.91 m wide and 0.76 m high) with water that was regularly filtered, de-ionized and degassed. Filtering was accomplished with a 0.2 μm filter and de-ionizing using a resin bed. Degassing was achieved with a pinhole degasser.[32] Ingassing of the water was minimized by covering the surface of the water with 36-mm-diam "ping-pong" balls to reduce the surface area of the air-water interface. The dissolved oxygen content in the tank was kept below 40% of saturation.

The acoustic source in our experiments was a wideband curved ultrasonic array with 128 elements (Model 8665, B-K Medical, Wilmington, MA). The center frequency was 3.5 MHz and the nominal −6 dB bandwidth was from 2.2 to 5.2 MHz. Each element was rectangular in shape, 13 mm high and 0.5 mm wide with a pitch of 0.525 mm. The radius of curvature of the convex surface was 60 mm. The array was driven by an Analogic ultrasound engine (AN2300, Analogic Corp., Peabody, MA), which is the core technology employed by the Viking 2400 (BK Medical, Herlev, Denmark) clinical ultrasound scanner. The Analogic ultrasound engine has a 64 channel digital transmit beam former to excite the array. The coordinates for the transducer used in these experiments are shown in Fig. 1. The origin was defined to be the center of the array, the z axis the propagation direction of the beam, the x axis the elevation direction of the array and the y axis the scan direction of the array, that is, the axis in which electronic steering can be effected. In the elevation plane ($x-z$), the elements have a fixed focal length of 70 mm. In the scan plane ($y-z$), the electronic focusing of the Analogic ultrasound engine can be used to adjust the focus up to 1 m. The transducer was suspended from a stainless steel rod which was rigidly mounted to the tank.

The acoustic field was measured using a 15-μm-thick gold polymer polyvinylidene fluoride membrane hydrophone (Model 1502-031, Precision Acoustics, UK) with an effective active area 0.2 mm in diameter. The hydrophone was mounted to the positioning system and scanned over the acoustic field. Positioning was accomplished using a three axis motorized positioning system (VP9000, Velmex, NY) which spanned the entire tank with a nominal step size of 5 μm. At each location, the measured wave form was recorded by a digital oscilloscope (LC334A, LeCroy) and the data were transferred to a computer for later analysis. The

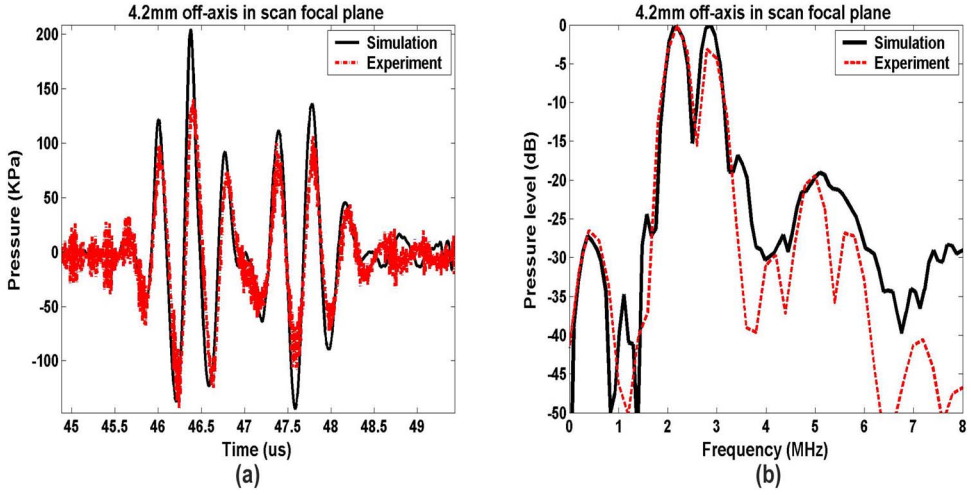

FIG. 4. (Color online) Comparison of simulation and measured wave forms and their spectra for a location 4.2 mm off axis in the scan focal plane (x =0 mm, y=4.2 mm, z=70 mm).

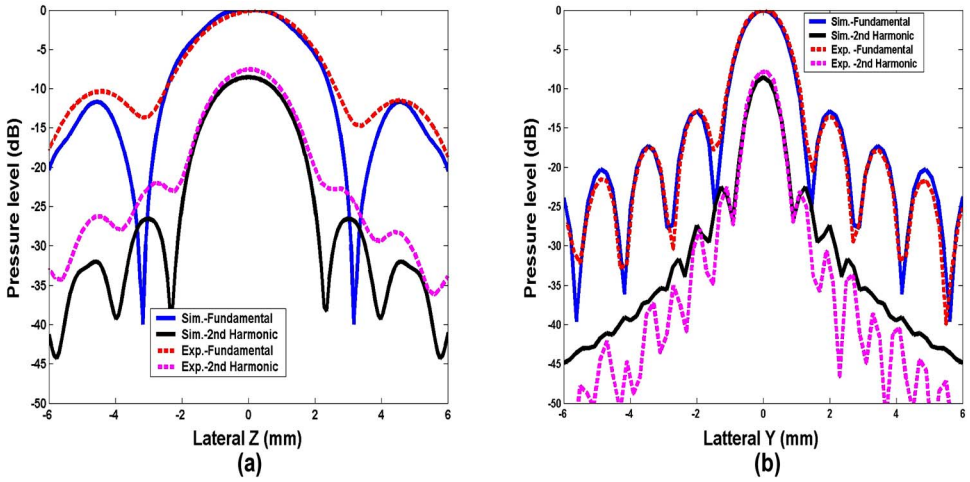

FIG. 5. (Color online) Comparison of simulated and measured focal beam patterns. Left: Beam pattern in the elevation plane. Right: Beam pattern in the scan plane.

oscilloscope was triggered by a hardware signal from the Analogic ultrasound engine and the data were averaged for 200 sweeps to improve the signal-to-noise ratio.

An inhomogeneous medium was formed by placing a layer of gel in between the transducer and the hydrophone. An agar-based recipe[33] was used to fabricate the gel layer. Briefly it consisted of 18 g agar, 54 g graphite, 0.75 g methyl paraben, 600 ml water and 50 ml 1-propanol that was prepared as a warm slurry which could be poured into a mold where it was allowed to set at room temperature. The sound speed, attenuation and the parameter of nonlinearity B/A were measured using techniques outlined in the Appendix.[33,34] The mean and standard deviations for the measured acoustic properties for three samples were $c_0=1550\pm10$ m/s, $\rho=1045\pm15$ kg/m^3, $\alpha(1\text{ MHz})=8.67\pm0.3$ Np/m, $n=1.10\pm0.03$, $B/A=5.4\pm0.2$, from which one can obtain the coefficient of nonlinearity $\beta=1+B/2A=3.7\pm0.1$. We note that all these values are in the range reported for soft tissue except for the coefficient of nonlinearity, which is lower than the typical range of 6–10.[35]

IV. RESULTS

A. Validation in water

The code was initially validated with measurements in water. The Analogic ultrasound engine was used to drive the middle 64 elements of the array with a three-cycle pulse with a center frequency of 2.5 MHz. The electronic focus of the array was set to 70 mm, that is, the scan plane focus was chosen to coincide with the fixed elevation focus. The transmit gain was set to −6 dB and no apodization was applied in the beamforming. The source wave form was obtained by measuring a wave form at the center of the array and 7 mm away from surface of the array. The peak source amplitude was $p_s=137$ kPa. The exact source condition could not be employed in the code because the array is a convex surface, whereas the KZK equation needs the source condition to be defined on a flat plane. Therefore the source was modeled as a flat rectangular element with focusing effected by a continuous change in phase in both scan and elevation directions. The height of the element in the elevation plane was the nominal element size 13 mm (that is, $b=6.5$ mm) and the focal length in both the scan and focusing planes was 70 mm. The width of the aperture in the scan plane was adjusted to get the best fit between the measured and predicted wave form at the focus. An aperture width of 29 mm ($a=14.5$ mm) resulted in the best fit and was consistent with the physical aperture size of 32 mm. The acoustic properties used for the water were $c_0=1498$ m/s, $\rho_0=998$ kg/m^3, $\alpha_0=0.1587$ Np/m at 2.5 MHz (with a frequency squared power law), and $\beta=3.5$.

Simulations were carried out on a grid that extended in the elevation plane from $x=-16.25$ mm to $x=16.25$ mm with a grid spacing of 0.08 mm (which corresponded to $X\,\text{min}=-2.5$ $X\,\text{max}=2.5$ and $\Delta X=1/80$) for a total of 400 grid points. In the scan plane the grid extended from $y=-36.25$ to 36.25 mm with a spacing of 0.18 mm which corresponded to (Y min$=-2.5$, Y max$=2.5$ and $\Delta Y=1/80$) also 400 grid points. The time window stretched from $\tau=-2.2$ μs to 3.2 μs with a sampling rate of 5 ns which in dimensionless coordinates corresponded to $\tau_{\text{MIN}}=-11\pi$ to $\tau_{\text{MAX}}=16\pi$ and $\Delta\tau=2\pi/80$ for a total of 1080 grid points. The computational grid was therefore $400\times400=160{,}000$ points in space and 1080 points in time for a total of 160 million points. These were the finest resolutions possible within the memory and calculation time limits of the computer used for these simulations.

Figure 2 compares on-axis wave forms and spectra at ranges of 53, 70 (the geometrical focus), and 80 mm. The measured and calculated wave forms and spectra are in good agreement. Figures 3 and 4 show off-axis comparisons in the elevation plane direction and scan plane respectively, with similarly good agreement.

Figure 5 shows the beam pattern of the fundamental and second harmonic in the focal plane for both the elevation and scan planes. The amplitudes of each frequency component were obtained by taking a Fourier transform of the corresponding wave forms. The numerical results show good agreement with the experimental data in particular for the locations of the null and peak positions of both the fundamental and second harmonic signals. In the elevation (Z) axis, the prediction and measurement of the main lobes of both harmonics agree well but the sidelobes are not so well captured, in particular the measured nulls are not as deep as predicted by the simulations. One likely cause is that the

model assumed a uniform excitation across the transducer in the elevation plane, however, the convex geometry of the radiating surface means that this may not have been an accurate representation of the transducer. The discrepancy in the fundamental means that the effect is exacerbated for the second harmonic. In the scan (Y) axis, the fundamental was captured very well, as well as the first few sidelobes of the second harmonic. The appearance of "fingers" in the beam pattern of the second harmonic which occur at the nulls of the fundamental beam pattern is clearly observed. We note that the good agreement in the scan plane was obtained even though the real source consisted of a finite number of element and the simulation used a continuous aperture.

Figure 6 shows the axial propagation curves of the fundamental and second harmonic. The simulations and measurements are in good agreement. There are some small discrepancies, most notably the prediction of the second harmonic does not have the same postfocal dip as the experimental data and pre-focally the second harmonic is a little higher than the experimental measurement.

B. Propagation through an inhomogeneous medium

An agar based gel was used to create a weakly inhomogeneous medium that could be used to evaluate the performance of the inhomogeneous KZK equation. Experiments were carried out by placing one of two gel layers between the transducer array and the hydrophone. The first was a "uniform layer" that had a constant thickness of 30 mm and flat surfaces on both sides. The second was an "aberatting layer" that also had a nominal thickness of 30 mm but on one side had three semicylindrical protrusions, that were 8 mm in diameter, 40 mm long and with a peak-to-peak distance of 17 mm (see Fig. 7). Both layers were placed right in front of the array and oriented to be as parallel to the transducer surface as possible. The aberatting layer was placed so that the flat surface faced the array and aligned so that the ridges were parallel with the elevation plane of the transducer. The center of the middle groove was placed to be as close to the center of the transducer as possible. In these experiments the hydrophone could only scan the region of water on the other side of the gel layer.

Simulations were carried out to model the experiment using either the flat or aberrating layers. The nominal geometry of the two layers and the acoustic parameters of agar gel were used as inputs to the simulation. The power law absorption was modeled by choosing the coefficients of two relaxation processes and a thermoviscous-like attenuation[23] so that the attenuation matched the power law attenuation over the frequency range from 100 kHz to 20 MHz. The source wave form, acoustic parameters of water and the simulation grids were the same as in Sec. IV A. The impact of the uncertainties in the properties of the agar gel were evaluated by determining the impact on the dimensionless coefficients in Eq. (2). It was found that for evaluating the ratio of the second harmonic to the fundamental, the most important properties were α, n and β. For the measurements reported here the largest uncertainty in predicted field properties was due to the 3.7% uncertainty in β.

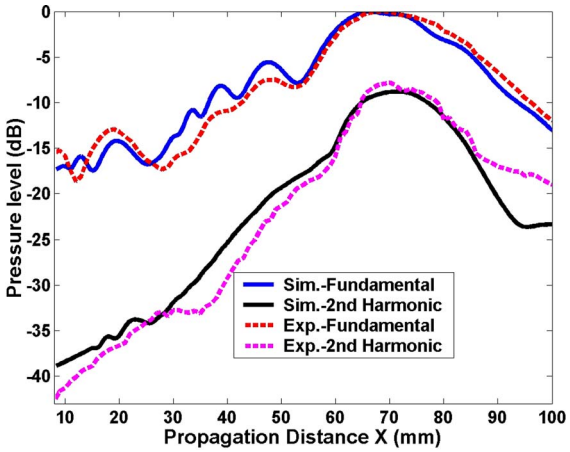

FIG. 6. (Color online) Comparison of the fundamental and second harmonic frequency components as a function of propagation distance from the transducer array.

Figure 8 compares the measured and simulated sound field of the fundamental and second harmonic in the elevation plane for the uniform layer. The agreement between the simulation and experiment is very good. The features in both images are the same and the main difference is that the nulls are not so clear in the experimental data, which is consistent with what was seen in the water measurements reported in Sec. IV A. For the fundamental, the focal spot (defined as −6 dB of the peak) was 4 mm by 33 mm in the measurements and 3.9 mm by 31 mm in the simulation. The sidelobes (the corresponding pressure levels were defined as the average value of the two symmetric sidelobes) had a peak of −11.2 dB (experiment) and −13.2 dB (simulation) at a lateral location of ±4.5 mm (experiment) and ±4.6 mm (simulation). In addition, there was a near field lobe, which in the experiments had a peak −7.9 dB at 47 mm and in the simulations had a peak of −6.1 dB at 47.6 mm. For the second harmonic, the focal spot was reduced to 2.6 by 23.5 mm (experiment) and 2.3 by 21.9 mm (simulation). The near-field lobe was a result of diffraction in the scan plane and is discussed below. The first sidelobes in the second harmonic, are fingers that appear in the null of the fundamental. The fingers result from the diffraction of the nonlinear distortion and are captured by both the experiment (±3 mm) and the

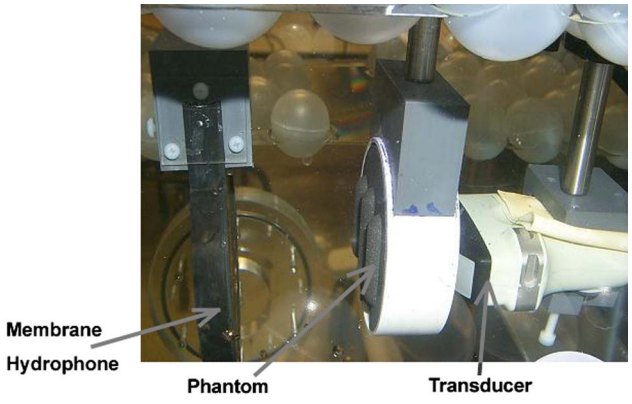

FIG. 7. (Color online) Photograph of the experimental setup for measuring the sound field after propagation through an aberrating layer.

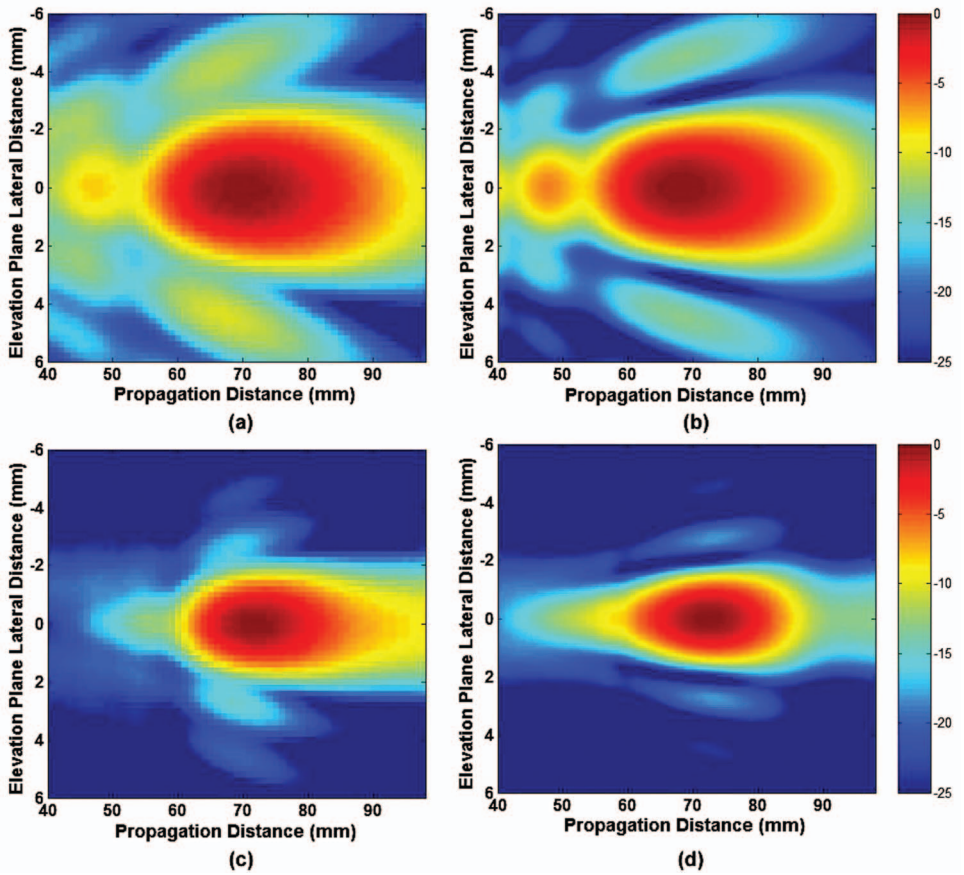

FIG. 8. Comparison of the amplitude of the fundamental and second harmonic (log scale) in the elevation plane for the flat layer: (a) experiment—fundamental, (b) simulation—fundamental, (c) experiment—second harmonic, (d) simulation—second harmonic.

simulation (±2.7 mm). The level of the first finger, −15.7 dB (experiment) and −18.4 dB (simulation), was lower than that of the fundamental sidelobe and the level of the sidelobe of the second harmonic that corresponded to that of the fundamental was −21.4 dB (experiment) and −23.9 dB (simulation). In both experiment and simulation the second harmonic did not have a distinct near-field lobe. There was both qualitative and quantitative agreement between the measured and the simulation fields.

Figure 9 compares the measured and simulated sound field of the fundamental and second harmonic in the scan plane for the flat gel layer. For the fundamental, the lateral width of the focal spot was 1.8 mm (experiment) and 1.7 mm (simulation). The first sidelobe appeared at ±2 mm in both experiment and simulation. Both experiment and simulation captured a large number of sidelobes. For the second harmonic, the width of the focal spot was reduced to 1 mm in both experiment and simulation. The sidelobes occurred at ±1.2 mm (experiment) and ±1.1 mm (simulation). The levels of the second harmonic sidelobes were lower than fundamental sidelobes (−16.6 dB vs −13.7 dB (experiment) and −15.8 dB vs −13.5 dB (simulation)). Again there is good agreement between the simulation and experiments.

Figure 10 compares the measured and simulated sound field of the fundamental and the second harmonic in the elevation plane for the aberrating layer. It can be observed that the surface of the gel layer was not perfectly parallel to the surface of the array as the acoustic axis of the experimental measurements can be observed to be slightly tilting downwards due to refraction. However, there is still good agreement between experiment and simulation. For the fundamental the aberrating layer pushed the focus back to 80 mm (experiment) and 75 mm (simulation) in both cases. Recall that the geometrical focus was 70 mm and the direction of the shift is consistent with the geometry of the aberration since the center of the beam was aligned with a ridge (with higher sound speed) and so the role of the aberrating layer should have been to defocus the beam. The focal spot size remained about the same size (experiment: 4.1 mm by 41 mm; simulation 4.1 mm by 37 mm) but the shape was slightly changed (the curve of the focal spot has much sharper edges) compared to the flat layer case (Fig. 8). The aberrating layer also pushed the focus of the second harmonic, from 72 mm for the flat layer, to 82 mm (experiment) and 81.5 mm (simulation).

Figure 11 compares the fundamental and second harmonic fields in the scan plane for the aberrating layer. The principal impact of the aberration in this plane was the enhancement of the edge-wave signals converging to the focus. This enhancement (relative to Fig. 9) was present in both the fundamental and the second harmonic and was captured by both the measurements and simulation. In the second harmonic both experiment and simulation show a second edge wave starting at the far left corners of the image. The asymmetries in both the fundamental and second harmonic appear because the center of the aberrating layer was not placed exactly on the transducer axis. In the simulation a small offset of 0.725 mm between the beam axis and the center position of aberrating layer in the scan plane direction was applied for the best fit with the experimental data.

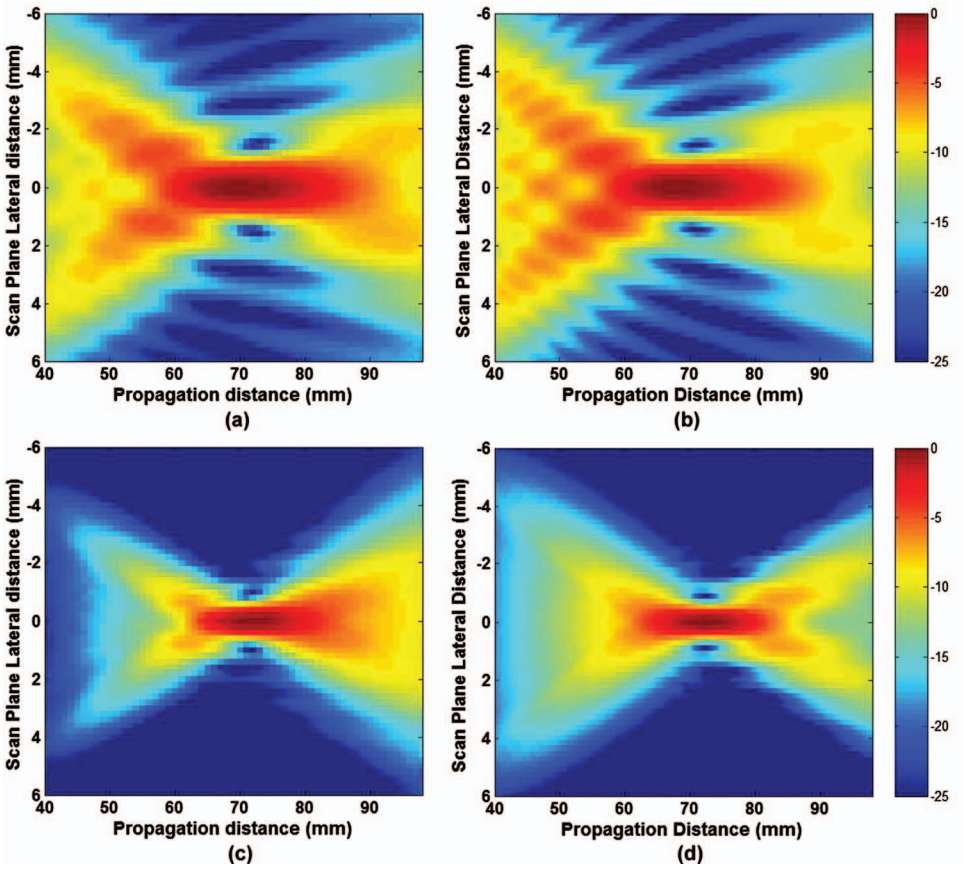

FIG. 9. Comparison of the amplitude of the fundamental and second harmonic in the scan plane (log scale) for the flat layer: (a) experiment—fundamental, (b) simulation—fundamental, (c) experiment—second harmonic, (d) simulation—second harmonic.

Figure 12 compares the measured and simulated beam patterns of the fundamental and second harmonic signals in the scan plane for both the uniform and aberrating layers. Figure 12(a) shows the results at the geometrical focus for the uniform layer. It can be seen that the simulations capture the main lobe of both the fundamental and second harmonic measurements very well and agree with the first two sidelobes of the fundamental and first sidelobe of second harmonic measurement. However, the simulation was not able to capture the details of the second harmonic signal after the first sidelobe. The discrepancy is identical to that observed in the water measurements (Fig. 5(b)) and is likely because the source condition used in the simulation was too idealized.

Figure 12(b) shows the results at the geometrical focus (70 mm) for the aberrating layer. As could be deduced from Fig. 11, it can be seen that the beam pattern of both the fundamental and the second harmonic has been significantly distorted by the presence of the aberrating layer. Notably the sidelobes of the fundamental are within 2 dB of the main lobe and the second harmonic appears to have a null on the axis. The simulations capture the structure of the experimental measurements well, in particular the asymmetry, and do a reasonable job of capturing the levels.

The beam patterns at the effective focal distance after propagation through the aberrating layer ($z=80$ mm) are shown in Fig. 12(c). In this case the fundamental does appear to have a main focal lobe—although the sidelobes are quite high (−8.4 and −12.2 dB in experiment and −8.8 and −11 dB in simulation). The second harmonic has a less distinct main focal lobe with high first sidelobes—although subsequent sidelobes drop off much more rapidly than for the fundamental. For both the fundamental and second harmonic the simulations reflect the principal structure of the experimental measurements well and were able to capture most of the levels to within a few dB.

V. CONCLUSIONS AND DISCUSSION

A time-domain algorithm that solves a generalized KZK equation in three spatial dimensions for inhomogeneous media has been described. The advance made here was to allow for the properties of the medium to vary in all three spatial dimensions. The effects of diffraction, nonlinear distortion, thermoviscous absorption, multiple relaxation processes and inhomogeneities were all accounted for in the code. We note that the 3D code is computationally intensive and memory demanding. For the simulations reported here the memory requirements were on the order of 4 GB. The code was parallelized using OpenMP and took 46 CPU h on IBM pSeries-655 SMP supercomputer using eight power4 processors running at 1.1 GHz.

The model described here is restricted to one-way propagation of sound beams in weakly inhomogeneous media. We note the restriction on the inhomogeneities is twofold. First, that reverberation is not important. Second, the inhomogeneities should not change the direction of the beam significantly as the parabolic approximation starts to break down when sound propagation is at an angle of greater than about 16°.[36] Employing more accurate models would allow for more physics to be incorporated but at higher computa-

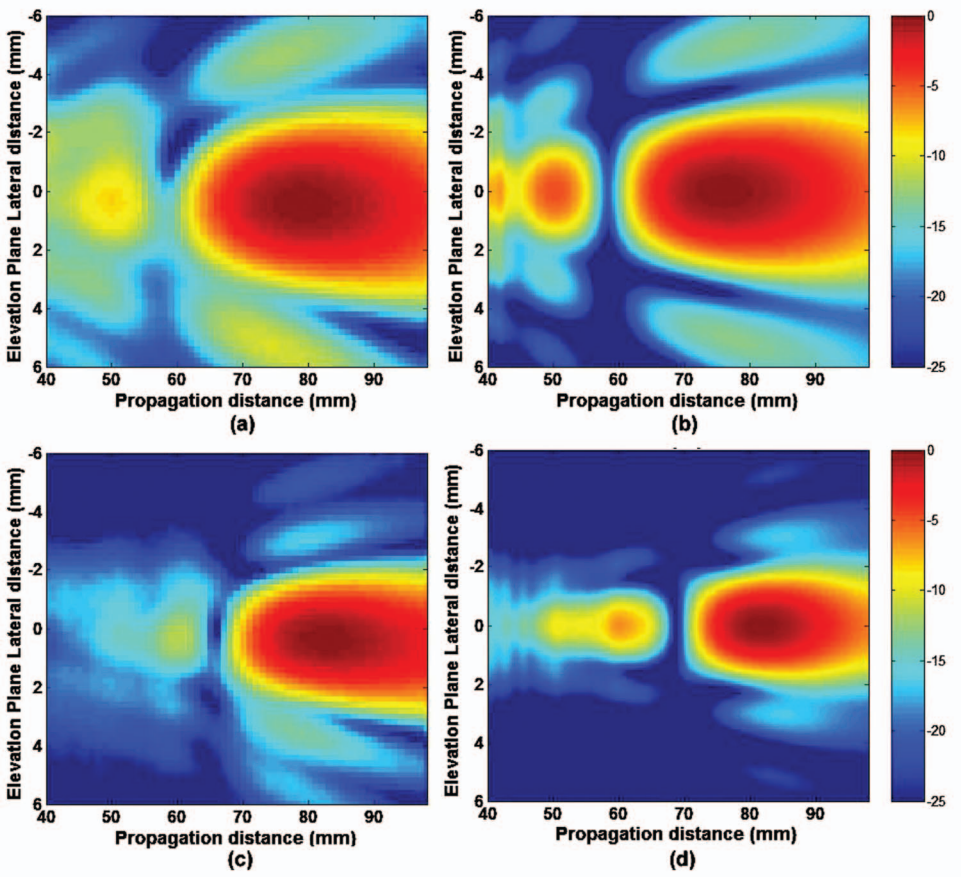

FIG. 10. Comparison of the amplitude of the fundamental and second harmonic in the elevation plane (log scale) for the aberrating layer: (a) experiment—fundamental, (b) simulation—fundamental, (c) experiment—second harmonic, (d) simulation—second harmonic.

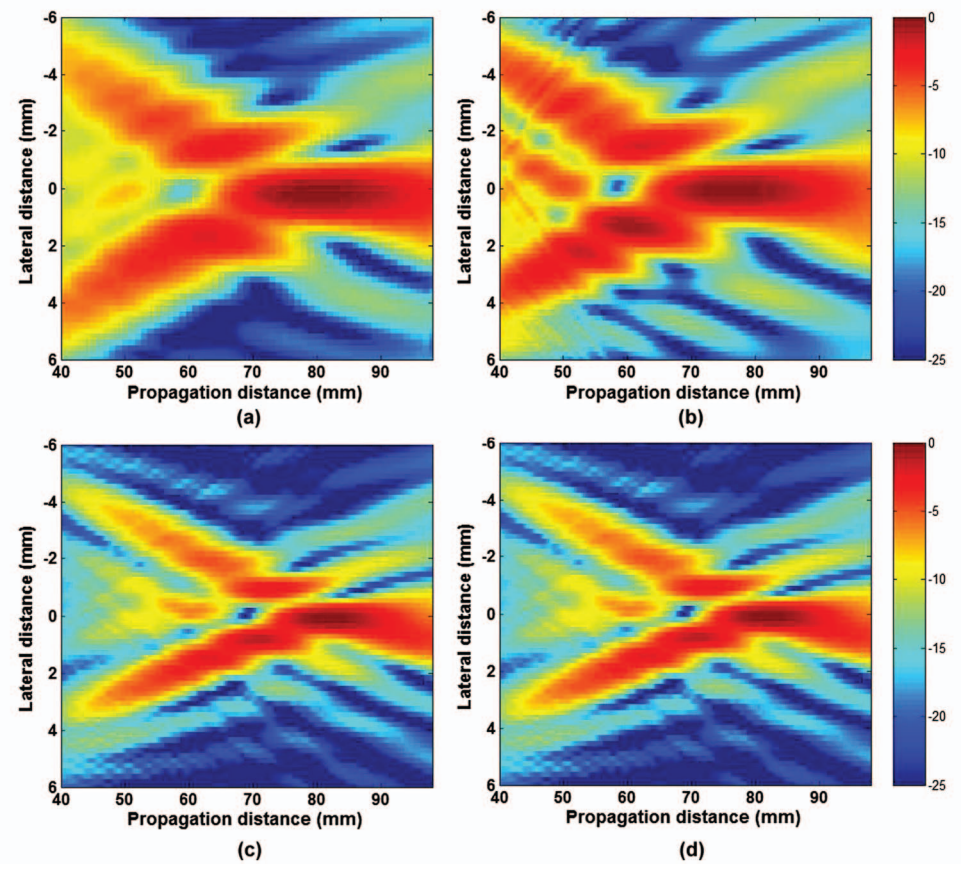

FIG. 11. Comparison of the amplitude of the fundamental and second harmonic in the scan plane (log scale) for the aberrating layer: (a) experiment—fundamental, (b) simulation—fundamental, (c) experiment—second harmonic, (d) simulation—second harmonic.

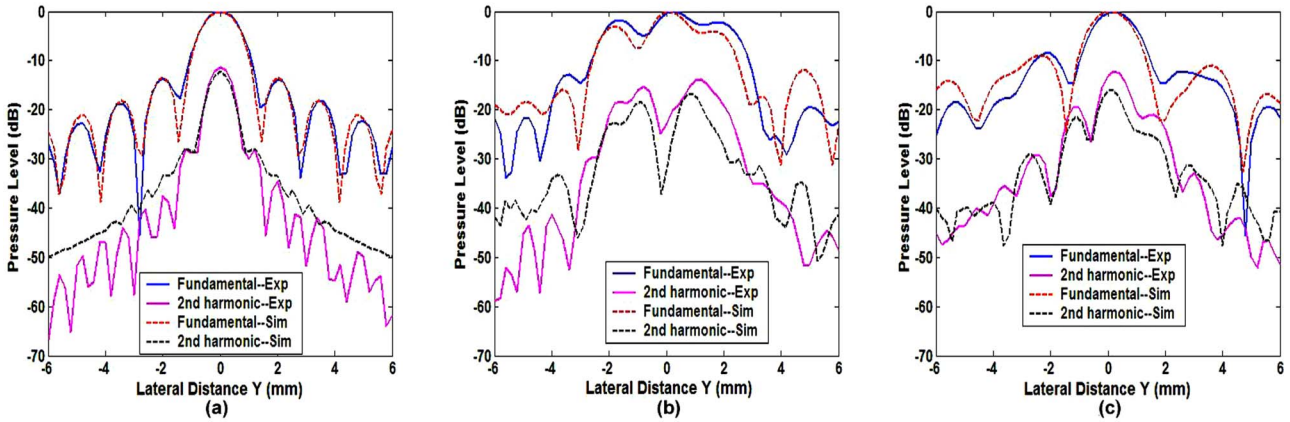

FIG. 12. (Color online) Scan plane beam pattern comparisons: (a) flat gel layer at the geometric focus (z=70 mm), (b) aberrating layer at the geometric focus (z=70 mm), (c) aberrating layer at apparent focus (z=80 mm).

tional cost. For example, using a finite-difference time-domain approach to solving the Westervelt equation one needs to employ at least 20 points per wavelength to capture the wave propagation accurately. For a simulation that is restricted to four harmonics the 10 MHz component has a wavelength of 150 μm and the grid spatial grid size would need to be 7.5 μm. For the same domain, 30 mm$\times$70 mm $\times$100 mm, this grid would result in 500×10^9 grid points which for three time steps and double floating point precision requires 36 terabytes. Further, because retarded time cannot be employed, the marching step is controlled by the Courant number which restricts the time step to 2.5 ns and more than 50,000 time steps would be required to simulate the forward propagation resulting in exaFLOPS of calculations. Even for k-space methods,[37] where the grid size can be reduced to two points per wavelength, the grid memory requirements are 36 GB. Further, in k-space methods the multiplication in the nonlinear operator results in a convolution for each spatial transform resulting in the need for a 3D convolution to be carried out at each step. Therefore, for the type of problem considered here the KZK equation is an attractive model in terms of computational feasibility.

The inhomogeneous code was validated by comparison with experimental measurements of the sound field produced by a phased array after propagation through an aberrating layer made of an agar gel. Direct comparison of wave forms and the spatial distribution of the fundamental and second harmonic were made and the results showed that there was good agreement between the experiments and the simulation. The code captured the distortion of both the fundamental and second harmonic due to the presence of the aberrating layer and correctly predicted the size of focal zones and the sidelobe levels. The main discrepancy appeared to be due to the source condition used to initialize the numerical code. In this work a single wave form was measured and then an effective source distribution estimated based on the nominal properties of the source and fitting the length of the array. A more accurate simulation could have been achieved by measuring the acoustic field in the entire source plane and using this as the source condition. However, for the phased array sources where the focus can be steered electronically it becomes impractical to measure the source plane for every possible transmit scenario. The approach here allows for and provided acceptable results for the main beam and first sidelobes.

The simulations and experiments presented here are representative of the nonlinear transmit fields employed in diagnostic ultrasound imaging—the agar gel mimicked the properties of soft tissue. One observation that can be made from the results is that the presence of the aberrating layer employed here affected the field of the second harmonic at least as much as the field of the fundamental. This may have implications in tissue harmonic imaging as the improved image quality has been ascribed to the fact that the second harmonic should be less sensitive to near-field aberrating layers than the fundamental.[38] Recent in vitro studies, where a porcine abdominal wall was used to induce aberration in the field produce by a clinical scanner,[39] indicate that in the presence of the aberrator the nonlinearly generated second harmonic (3.8 MHz) focuses more tightly than if one transmits 3.8 MHz as a fundamental. However, the data also show that when comparing the fundamental (1.9 MHz) to the nonlinear second harmonic field (3.8 MHz) both are perturbed by the aberrator about the same amount. It is the second result that is comparable to what is presented here. Recent numerical studies, using a quasi-linear solution to the 3D-KZK equation,[40] have also investigated the impact of aberration by modeling it using a series of phase screens. Their results indicate that although the second harmonic signal is weak in the near field, the development of the second harmonic signal is not independent of the fundamental signal, and therefore aberration information carried by the fundamental signal is also reflected in second harmonic. Our results are consistent with the conclusions of both of these studies. The caveat being that the results presented here are based on one experiment with a single phantom with geometry that induced a specific shift in the focus rather than a random phase across the beam.

ACKNOWLEDGMENTS

This work was supported by CenSSIS (Center for Subsurface Sensing and Imaging Systems) by NSF (Award No. EEC-9986821). Computational resources were provided by Boston University's Scientific Computing and Visualization

Group. Dr. Oleg A. Sapozhnikov, Dr. Ronald A. Roy and Dr. Emmanuel Bossy are thanked for helpful technical discussions.

APPENDIX: DETERMINATION OF ACOUSTIC PROPERTIES

The sound speed and attenuation of agar gel was measured following the method described by Huang.[33] Two different thickness gel samples were used and measurements were made of the through transmission of pulse wave forms centered at 2.25 MHz. The sound speed of the gel sample was calculated by $c_s=(d_{s2}-d_{s1})/(t_{s2}-t_{s1})$, where d_{s1} and d_{s2} are the thicknesses of the two samples, and t_{s1} and t_{s2} are the corresponding times of flight through the two samples as measured by the arrival time of first positive going zero crossing of the signal. The attenuation was calculated by $\alpha=1/(d_{s1}-d_{s2})\ln(v_{w2}/v_{w1}v_{s1}/v_{s2})$, where v_{s1} and v_{s2} are the amplitudes of received signal (for a ten cycle tone burst at the frequency of interest) in the two samples, v_{w1} and v_{w2} are the amplitudes of received signal at the equivalent propagation distances $d_{w1}=d_{s1}c_s/c_w$ and $d_{w2}=d_{s2}c_s/c_w$, respectively. The power law coefficient was obtained fitting the measured attenuation between 2.5 and 5 MHz to a power law.

The parameter of nonlinearity B/A was measured following the finite-amplitude method described by Dong.[34] A 2.25 MHz, 12.7-mm-diam unfocused transducer (Panametrics, V306) was driven with a 30-cycle sinusoidal burst with central frequency 2.25 MHz and peak-to-peak amplitude of 100 V. The receiver was a 5.0 MHz, 6.3-mm-diam unfocused transducer (Panametrics, V310), located along the beam axis and 480 mm away from the source to ensure that the wave could be approximated as a quasi-plane wave. A 160-mm-diam, 35-mm-thick cylinder filled with highly attenuating glycerol ($\alpha=10.05$ dB/cm at 4.5 MHz and 22 °C), with acoustic windows made of 100-μm-thick Mylar film was inserted in the beam path 120 mm from the receiver to reduce harmonic "contamination" associated with nonlinear distortion due to propagation in water. The gel sample of 50 mm thickness was inserted between glycerol and receiving transducer along the beam axis, and was placed as close to the receiver as possible but making sure there was no evidence of reverberation between the receiving transducer and the gel. The B/A of the sample was calculated by

$$\frac{(B/A)_s+2}{(B/A)_w+2}=\left[\frac{P_{2s}}{P_{2w}}\frac{L}{d}-\left(\frac{L}{d}-1\right)I_2^2D''D'\right]\frac{\rho_s{c_s}^3}{\rho_w{c_w}^3}\frac{d}{D''^2D'}\frac{2\alpha_{s1}-\alpha_{s2}}{I_2^2-I_1^2}, \tag{A1}$$

where the subscripts s and w refer to the gel sample and degassed water, respectively, P_{2s} and P_{2w} correspond to the amplitudes of second harmonic signal propagating through the sample and degassed water, L is the distance between the receiving transducer and the glycerol cylinder, d the thickness of the sample, α_{s1} and α_{s2} the attenuation coefficients of the sample at the fundamental and second harmonic frequencies, respectively, ρ_s and ρ_w are the density of the sample and degassed water, and c_s and c_w correspond to the sound speed of the sample and degassed water. I_1 and I_2 are defined as: $I_1=\exp(-\alpha_{s1}d)$, $I_2=\exp(-\alpha_{s2}d/2)$. D' and D'' are the amplitude transmission coefficients for sample-to-water and water-to-sample interfaces, respectively, i.e. $D'=2\rho_w c_w/(\rho_s c_s+\rho_w c_w)$, $D''=2\rho_s c_s/(\rho_s c_s+\rho_w c_w)$.

[1] T. G. Muir, "Nonlinear Acoustics: A new Dimension in Underwater Sound," in *Science, Technology and the Modern Navy*, edited by E. I. Salkovitz (Office of Naval Research, Arlington, VA, 1976), pp. 554–563.
[2] K. J. Plotkin, "State of the art of sonic boom modeling," J. Acoust. Soc. Am. **111**(1), 530–536 (2002).
[3] F. A. Duck, "Nonlinear acoustics in diagnostic ultrasound," Ultrasound Med. Biol. **28**(1), 1–18 (2002).
[4] M. R. Bailey, V. A. Khokhlova, O. A. Sapozhnikov, S. G. Kargl, and L. A. Crum, "Physical mechanisms of the therapeutic effect of ultrasound (a review)," Acoust. Phys. **49**(4), 369–388 (2003).
[5] E. A. Zabolotskaya and R. V. Khokhlov, "Quasi-plane waves in the nonlinear acoustics of confined beams," Sov. Phys. Acoust. **15**, 35–40 (1969).
[6] V. P. Kuznetsov, "Equations of nonlinear acoustics," Sov. Phys. Acoust. **16**, 467–470 (1971).
[7] S. I. Aanonsen, T. Barkve, J. N. Tjotta, and S. Tjotta, "Distortion and harmonic generation in the nearfield of a finite amplitude sound beam," J. Acoust. Soc. Am. **75**(3), 749–768 (1984).
[8] Y.-S. Lee and M. F. Hamilton, "Time-domain modeling of pulsed finite-amplitude sound beams," J. Acoust. Soc. Am. **97**, 906–917 (1995).
[9] M. A. Averkiou and M. F. Hamilton, "Nonlinear distortion of short pulses radiated by plane and focused circular pistons," J. Acoust. Soc. Am. **102**, 2539–2548 (1997).
[10] V. F. Humphrey, "Nonlinear propagation in ultrasonic fields: Measurements modeling and harmonic imaging," Ultrasonics **38**, 267–272 (2002).
[11] P. Blanc-Benon, B. Lipkens, L. Dallois, M. F. Hamilton, and D. T. Blackstock, "Propagation of finite amplitude sound through turbulence: Modeling with geometrical acoustics and the parabolic approximation," J. Acoust. Soc. Am. **111**(1), 487–498 (2002).
[12] P. T. Christopher and K. J. Parker, "New approaches to nonlinear diffractive field propagation," J. Acoust. Soc. Am. **90**(1), 488–499 (1991).
[13] J. Tavakkoli, D. Cathignol, R. Souchon, and O. A. Sapozhnikov, "Modeling of pulsed finite-amplitude focused sound beams in time domain," J. Acoust. Soc. Am. **104**(4), 2061–2072 (1998).
[14] I. M. Hallaj, R. O. Cleveland, and K. Hynynen, "Simulations of the thermo-acoustic lens effect during focused ultrasound surgery," J. Acoust. Soc. Am. **109**(5), 2245–2253 (2001).
[15] S. Ginter, M. Liebler, E. Steiger, T. Dreyer, and R. E. Riedlinger, "Full-wave modeling of therapeutic ultrasound: Nonlinear ultrasound propagation in ideal fluids," J. Acoust. Soc. Am. **111**(5), 2049–2059 (2002).
[16] G. Wojcik, J. Mould, S. Ayter, and L. Carcione, "A study of second harmonic generation by focused medical transducer pulses," Ultras. Symposium Proceedings **2**, 1583–1588 (1998).
[17] T. Varslot and G. Taraldsen, "Computer simulation of forward wave propagation in soft tissue," IEEE Trans. Ultrason. Ferroelectr. Freq. Control **52**(9), 1473–1482 (2005).
[18] A. C. Baker, A. M. Berg, A. Sahin, and J. N. Tjotta, "The nonlinear pressure field of plane, rectangular apertures: Experimental and theoretical results," J. Acoust. Soc. Am. **97**, 3510–3517 (1995).
[19] M. D. Cahill and A. C. Baker, "Numerical simulation of the acoustic field of a phased-array medical ultrasound scanner," J. Acoust. Soc. Am. **104**(3), 1274–1283 (1998).
[20] T. Nouri-Baranger, E. Closset, and D. Cathignol, "Numerical solution for nonlinear acoustic beam radiated from non-axisymmetric plane transducers using the operator splitting method," IEEE Ultrasonics Symposium Proceedings, an International Symposium **1**, 479–482 (2001).
[21] A. Bouakaz, C. T. Lancee, and N. deJong, "Harmonic ultrasonic field of medical phased arrays: Simulations and measurements," IEEE Trans. Ultrason. Ferroelectr. Freq. Control **50**(6), 730–735 (2003).
[22] R. J. Zemp, J. Tavakkoli, and R. S. C. Cobbold, "Modeling of nonlinear ultrasound propagation in tissue from array transducers," J. Acoust. Soc. Am. **113**(1), 139–152 (2003).
[23] X. Yang and R. O. Cleveland, "Time domain solution of the KZK equation for rectangular pistons with application to harmonic imaging," J. Acoust. Soc. Am. **117**(1), 113–123 (2005).
[24] V. A. Khokhlova, A. E. Ponomarey, M. A. Averkiou, and L. A. Crum, "Nonlinear pulsed ultrasound beams radiated by rectangular focused diag-

nostic transducers," Acoust. Phys. **53**(4), 481–489 (2006).
[25]J. N. Tjotta and S. Tjotta, "Nonlinear equations of acoustics, with application to parametric acoustic arrays," J. Acoust. Soc. Am. **69**, 1644–1652 (1981).
[26]M. F. Hamilton and C. L. Morfey, "Model Equations," in *Nonlinear Acoustics*, M. F. Hamilton and D. T. Blackstock, eds. (Academic Press, San Diego, 1998), pp. 41–64.
[27]Y. Jing, *Physics of Tissue Harmonic Imaging by Ultrasound* (Boston University, Boston, 2005).
[28]I. M. Hallaj, R. O. Cleveland, P. E. Barbone, S. G. Kargl, and R. A. Roy, "Amplitude degradation of time-reversed pulses in nonlinear absorbing thermoviscous fluid," Ultrasonics **38**, 885–889 (2000).
[29]W. F. Ames, *Numerical Methods for Partial Differential Equations* (Academic, New York, 1992).
[30]D. T. Blackstock, *Nonlinear Acoustics*, M. F. Hamilton and D. T. Blackstock, eds. (Academic, Austin, TX, 1997), p. 11.
[31]C. L. Morfey and F. D. Cotaras, *Nonlinear Acoustics*, M. F. Hamilton and D. T. Blackstock, eds. (Academic, New York, 1997), Chap. 12.
[32]A. R. Kaiser, C. A. Cain, E. Y. Hwang, J. B. Fowlkes, and R. J. Jeffers, "A cost effective degassing system for use in ultrasonic measurements: The multiple pinhole degassing system," J. Acoust. Soc. Am. **99**(6), 3857–3860 (1996).
[33]J. Huang, *Aerospace and Mechanical Engineering* (Boston University, Boston, 2002), pp. 65–67.
[34]F. Dong, E. L. Madsen, M. C. MacDonald, and J. A. Zagzebski, "Nonlinearity parameter for tissue-mimicking materials," Ultrasound Med. Biol. **25**(5), 831–838 (1999).
[35]R. T. Beyer, *Nonlinear Acoustics*, M. F. Hamilton and D. T. Blackstock, eds. (Academic, Austin, TX, 1997), pp. 25–37.
[36]E. H. Vefring, J. Naze-Tjotta, and S. Tjotta, "Effects of focusing on the nonlinear interaction between two collinear finite amplitude sound beams," J. Acoust. Soc. Am. **89**, 1017–1027 (1991).
[37]T. D. Mast, "Two- and three-dimensional simulations of ultrasonic propagation through human breast tissue," Acoustic Res. Lett. Online **3**(2), 53–58 (2002).
[38]P. T. Christopher, "Finite amplitude distortion-based inhomogeneous pulse echo ultrasonic imaging," IEEE Trans. Ultrason. Ferroelectr. Freq. Control **44**(1), 125–139 (1997).
[39]K. D. Wallace, M. R. Holland, B. S. Robinson, R. J. Fedewa, C. W. Lloyd, and J. G. Miller, "Impact of propagation through and aberrating medium on the linear effective apodization of a nonlinearly generated second harmonic field," IEEE Trans. Ultrason. Ferroelectr. Freq. Control **53**, 1260–1268 (2006).
[40]T. Varslot, S.-E. Måsøy, T. F. Johansen, and B. Anglesen, "Aberration in nonlinear acoustic wave propagation," IEEE Trans. Ultrason. Ferroelectr. Freq. Control **54**, 470–479 (2007).

Nonlinear phenomena in the vocalizations of North Atlantic right whales (*Eubalaena glacialis*) and killer whales (*Orcinus orca*)

Reny B. Tyson[a)]
Department of Oceanography, Florida State University, 105 N. Woodward Ave., P. O. Box 3064320, Tallahassee, Florida 32306-4320 and Department of Psychology, Florida State University, 1107 West Call Street, Tallahassee, Florida 32306-4301

Douglas P. Nowacek
Department of Oceanography, Florida State University, 105 N. Woodward Ave., P. O. Box 3064320, Tallahassee, Florida 32306-4320

Patrick J. O. Miller
School of Biology, University of St. Andrews, St. Andrews, Fife, KY16 9TS, United Kingdom

(Received 17 November 2006; revised 29 May 2007; accepted 13 June 2007)

Nonlinear phenomena or nonlinearities in animal vocalizations include features such as subharmonics, deterministic chaos, biphonation, and frequency jumps that until recently were generally ignored in acoustic analyses. Recent documentation of these phenomena in several species suggests that they may play a communicative role, though the exact function is still under investigation. Here, qualitative descriptions and quantitative analyses of nonlinearities in the vocalizations of killer whales (*Orcinus orca*) and North Atlantic right whales (*Eubalaena glacialis*) are provided. All four nonlinear features were present in both species, with at least one feature occurring in 92.4% of killer and 65.7% of right whale vocalizations analyzed. Occurrence of biphonation varied the most between species, being present in 89.0% of killer whale vocalizations and only 20.4% of right whale vocalizations. Because deterministic chaos is qualitatively and quantitatively different than random or Gaussian noise, a program (TISEAN©) designed specifically to identify deterministic chaos to confirm the presence of this nonlinearity was used. All segments tested in this software indicate that both species do indeed exhibit deterministic chaos. The results of this study provide confirmation that such features are common in the vocalizations of cetacean species and lay the groundwork for future studies. © *2007 Acoustical Society of America.* [DOI: 10.1121/1.2756263]

PACS number(s): 43.25.Ts, 43.80.Ka [WWA] Pages: 1365–1373

I. INTRODUCTION

Analyses of animal vocalizations have provided great insights into the communicative functions of many vocal signals, however, some features that may play a communicative role have been largely ignored (Tokuda *et al.*, 2002; Fitch *et al.*, 2002). One set of unexplored features, referred to as "nonlinear phenomena" or "nonlinearities" includes: subharmonics, frequency jumps, biphonation, and deterministic chaos. These complex features are produced by nonlinearities in the vocal production system, where rather simple neural commands to the system can result in highly complex and individually variable acoustic signals (Fitch *et al.*, 2002). Historically, vocalizations with these features have been either excluded from analyses (e.g. Hauser, 1993), ignored (e.g. Rendall *et al.*, 1996), or grouped together as "atonal" (e.g. Parks and Tyack, 2005) with analyses focusing primarily on harmonic signals. These phenomena have recently, however, been documented in the vocal output of humans and other primates, birds, dogs, deer, and manatees (Mende *et al.*, 1990; Herzel *et al.*, 1995; Riede *et al.*, 1997; Wilden *et al.*, 1998; Fee *et al.*, 1998; Fletcher, 2000; Riede *et al.*, 2000; Fitch *et al.*, 2002; Facchini *et al.*, 2003; Robb, 2003; Neubauer *et al.*, 2004; Riede *et al.*, 2004; Mann *et al.*, 2006; Volodina *et al.*, 2006).

The presence of such phenomena in the vocalizations of several species suggests that these features may play an important communicative role. In some cases they may form the bulk of an individual's vocalizations and/or of vocalizations of individuals within a certain age range (Fitch *et al.*, 2002). While this exact role is still under investigation, individual recognition, unpredictability, and/or indication of physical condition have been suggested as possible functions (Wilden *et al.*, 1998; Owren and Rendall, 2001; Fitch *et al.*, 2002; Mann *et al.*, 2006; Volodina *et al.*, 2006; Riede *et al.*, 2007). Before the testing of specific functions can begin, however, the occurrence and structure of these phenomena must be documented. Knowing the relative presence/prevalence of such features can indicate their level of importance and their structure may be indicative of their function.

[a)]Author to whom correspondence should be addressed. Electronic mail: tyson@ocean.fsu.edu

In this study, qualitative descriptions and quantitative analyses of nonlinear phenomena in the vocalizations of fish-eating, or "resident," killer whales and North Atlantic right whales (hereafter referred to as right whales) are provided. These two mammals are representative of the two suborders of Cetacea (whales, dolphins and porpoises); killer whales belong to the suborder Odontoceti (the toothed whales) and right whales belong to the suborder Mysticeti (the baleen whales). Power spectral analyses and visual inspection of spectrograms were used to identify subharmonics, biphonation, frequency jumps, and deterministic chaos in the vocalizations of these species, but another method was applied to determine if segments we thought were chaotic were indeed chaotic, as chaos can resemble Gaussian noise. Deterministic chaos is generated by a nonlinear process and is therefore predictable once the underlying nonlinear dynamics are determined; Gaussian noise, however, is random and thus unpredictable. To determine the underlying dynamics of suspected chaotic segments found within these species vocalizations, the software package TISEAN© (TIme SEries Analysis; Hegger *et al.*, 1999; Kantz and Schreiber, 2004) was used, which reconstructs the attractor of the underlying dynamics of the signal in the phase space and gives a measure of the unpredictability of the system. The method of surrogate data was also applied to test the null hypothesis that the signals were stationary, linear, random Gaussian signals (Schrieber and Schmitz, 2000). In addition, behavioral functions of nonlinear phenomena and/or their underlying production mechanisms are explored as these two species differ in their social structure and sound production mechanisms.

II. METHODS

Acoustic data from right whales were collected on multisensor digital acoustic recording tags (Johnson and Tyack, 2003; Nowacek *et al.*, 2004), which were attached noninvasively to animals in the Bay of Fundy, Canada in 2001, 2002, and 2005. Tags recorded sounds at sampling rates of Fs = 16 kHz (2001), Fs = 32 kHz (2002), and Fs = 96 kHz (2005) with a 12-bit resolution and received sounds from both the tagged whale and other whales in the area as well as ambient noise. Because high signal-to-noise ratio recordings are essential when investigating the occurrence of nonlinear phenomena, as significant background noise can confound the analyses, only vocalizations from the focal animal or from an animal vocalizing nearby the focal animal and those generally free of ambient noise were included in the analyses.

Recordings of northern resident killer whales in Johnstone Strait, British Columbia, were made during August and September of 1998 and 1999 using a towed array of 16 hydrophones connected to multi-channel TASCAM® recorders, which digitally recorded sounds at a sampling rate of 48 kHz. Efforts were made to obtain vocalizations only from focal whales by keeping the focal animal to one side of the array at a distance of approximately 100 m (Miller and Tyack, 1998; Nousek *et al.*, 2006). Only vocalizations recorded from identified individuals and that were generally free from ambient noise were included in the analysis. Killer whales produce calls at diverse source pressure levels, and call types known to contain biphonation are produced at higher intensities than call types without biphonation (Miller, 2006). Since we used only the highest signal-to-noise ratio calls, call types without biphonation were generally excluded from our analyses. Thus, our sample cannot be considered fully representative of the killer whale repertoire.

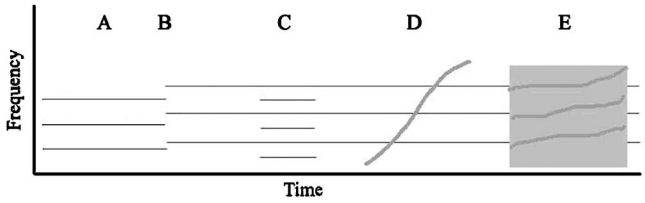

FIG. 1. Schematic narrowband spectrograms illustrating stable limit cycle (a), frequency jump (b), subharmonics (c), biphonation (d) and deterministic chaos (E) (modified after Fig. 1 from Riede *et al.*, 2004).

Analyses of nonlinear features in calls followed previously applied methods (Mann *et al.*, 2006; Riede *et al.*, 2004; Wilden *et al.*, 1998). The vocalizations were analyzed using the fast Fourier transformation (FFT), with 1024 or 2048 points FFT order, hanning windows, and a 75% overlapping of the successive windows. Spectrograms were isolated and inspected for the presence of nonlinearities using Adobe Audition® on a PC-type computer. Each vocalization was judged to include or not include each of the four nonlinear types. While all vocalizations were of generally high signal-to-noise ratio and free from ambient noise, the possibility for questionable features in signals was still present as there are limitations on recording wild animals. Thus, when a feature was in question of being scored (e.g., chaotic segment or effect of recordings) the conservative option was always taken and the feature was not scored.

The basic structures of nonlinear phenomena are displayed in Fig. 1. In the simplest case, the synchronization of vocal folds lead to periodic, regular, self-sustained oscillations that result in a purely harmonic vocalization termed a *stable limit cycle* (Fig. 1(a), a fundamental frequency, F_o, with harmonics that are integer multiples of that frequency). Because the dynamics of the larynx as a whole are "nonlinear," any and all sounds, including these harmonic signals, represent nonlinear phenomena (Riede *et al.*, 2004). For purposes of this study, however, we will contrast these harmonic, stable limit cycle signals with all other nonlinear signals.

A *frequency jump* represents a break in the F_o in which the vibration rate increases or decreases abruptly and discontinuously (Fig. 1(b)); it is qualitatively different from continuous, smooth modulation. Frequency jumps represent regime instability, i.e., the oscillation of the vocal folds may jump unpredictably (Wilden *et al.*, 1998; Riede *et al.*, 2004).

Subharmonics can occur when the natural vibratory frequencies of the two oscillators are different (Fig. 1(c); e.g., if there is more tension on one vocal fold than the other). This results in additional spectral components which appear as fractional integer values of an identifiable F_o (e.g., $F_o/2$, $F_o/3$, and so on) visible upon acoustic analysis. Energy ap-

pears on a spectrogram at evenly spaced intervals below the F_o and between adjacent harmonics (Fitch *et al.*, 2002).

Biphonation can be defined as two similar but unrelated, independent frequencies being produced simultaneously (Fig. 1(d)). On a spectrogram biphonation appears as two distinct, nonparallel autonomous fundamental frequencies (F_o and G_o) with no simple ratio relating them (e.g., 1/2 or 1/3). Biphonation can occur if the coupling between two oscillators is weak or if several oscillators are interacting (Brown and Cannito, 1995; Wilden *et al.*, 1998). Biphonation can also be found in the form of sidebands, which appear adjacent to harmonics and are associated with cyclic amplitude fluctuations in the time series waveform (Riede *et al.*, 2000; Riede *et al.*, 2004; Wilden *et al.*, 1998). Sidebands have previously been described in killer whale vocalizations, appearing off the high frequency component (Miller *et al.*, 2007).

Deterministic chaos refers to periods of nonrandom noise that are produced by desynchronized coupled oscillators (Fig. 1(e)). It is characterized by having energy across a relatively broad frequency band with some residual periodic energy related to the previous harmonic components. Deterministic chaos can often be interrupted by windows of stable limit phonation or subharmonic phonation (Neubauer *et al.*, 2004). After the initial inspection of spectrograms and power spectral analyses for deterministic chaos were completed, two segments from each species which we suspected were chaotic and which were representative across several calls of each species were cut from the original vocalizations and were analyzed in a similar manner as Facchini *et al.* (2003) and Mann *et al.* (2006) using the TISEAN© software package (Hegger *et al.*, 1999; Kantz and Schreiber, 2004).

The method of surrogate data was used to test the null hypothesis that the signals were created by a stationary, linear, random Gaussian process (Hegger *et al.*, 1999, Schrieber and Schmitz, 2000; Kantz and Schreiber, 2004). This is a Monte Carlo technique which assesses the significance of the results by comparing the original time series data to appropriate realizations of the null hypothesis (Hegger *et al.*, 1999). Surrogates were made with the TISEAN© program *surrogates*, which generates constrained realizations of the original time series data; random Fourier transforms of the original data are created that have the same power spectrum and the same single time distribution as the observed data but that differ in phase (Hegger *et al.*, 1999). The TISEAN program *predict* was then used to compare the original time series data to the surrogates to assess the significance of the results. If the value computed for the original time series data was significantly different than the values computed for the surrogate data, $P \leq 0.05$, the null hypothesis was rejected and nonlinearity was detected (Theiler *et al.*, 1992).

The method of delays was used to reconstruct the attractor of the underlying dynamics in the phase space in the four segments which we suspected were chaotic (Hegger *et al.*, 1999). Here, vectors were formed in a new space, termed the embedding space, from time delayed values of the scalar measurements: $s_n = (s_{n-(m-1)_\tau}, s_{n-(m-2)_\tau}, \ldots, s_n)$. The number m of elements is called the *embedding dimension* and the time τ is the *delay* (for a review see Kantz and Schreiber, 2004). The TISEAN© *mutual* function was used to determine the appropriate time delay τ of each segment. This delay represents a measure of correlation existing between two consecutive components of m-dimensional vectors used in the trajectory reconstruction and its value is taken as the first minimum of the average mutual information function (Facchini *et al.*, 2003). The delay is then used in the analysis of the embedding dimension m, the minimum dimension at which a reconstructed attractor can be considered completely unfolded with no overlapping in the reconstructed trajectories (Facchini *et al.*, 2003; Kantz and Schreiber, 2004). The embedding dimensions were found using the method of false nearest neighbors with the TISEAN© program *false_nearest*. When an attractor is poorly reconstructed, a false neighbor can occur at a point of trajectory intersection. As the dimension increases, the attractor is unfolded at higher fidelity and the number of false neighbors decreases to zero. The first dimension with no overlapping points is the embedding dimension (Facchini *et al.*, 2003). The *false_nearest* function allows specification of a minimal temporal separation of valid neighbors.

The delay and embedding dimensions were used in the analysis of the Lyapunov exponents, which quantify the strength of chaos (Hegger *et al.*, 1999; Kantz and Schreiber, 2004). Chaotic systems display a sensitive dependence on the initial conditions of a trajectory. The Lyapunov exponents are a measure of the time it takes for the trajectories to diverge starting from infinitesimally close initial conditions and therefore give a coordinate-independent measure of the local stability properties of a trajectory (Facchini *et al.*, 2003; Kantz and Schreiber, 2004).

Since a trajectory evolves in an N-dimensional state space, there are N exponents that are arranged in the spectrum of Lyapunov exponents, which was generated by the TISEAN© *lyap_spec* function (Hegger *et al.*, 1999; Facchini *et al.*, 2003). A trajectory was considered chaotic if it had at least one positive exponent in the Lyapunov Spectrum since chaotic segments are identified as having a maximal Lyapunov exponent (MLE) between zero and infinity (noise has a MLE of infinity and a stable limit cycle has a MLE of zero; Kantz and Schreiber, 2004). The exact value of the MLE was found by taking the maximum linear regression of the curves generated by the TISEAN© *lyap_k* function in the region between 0 and 20 iterations (Hegger *et al.*, 1999; Facchini *et al.*, 2003; Kantz and Schreiber, 2004). The MLE is a measure of the unpredictability of the system and it gives a good characterization of the underlying dynamics (note: there is some uncertainty in the estimation of the MLE; Kantz and Schreiber, 2004).

To verify that TISEAN© was correctly identifying segments as deterministic chaos, we also tested a generated harmonic and a generated random signal to compare with our suspected chaotic segments. The harmonic segment resulted in zero positive exponents in the Lyapunov spectrum indicating that it was a stable limit cycle; the random noise signal had embedding dimensions that were greater than expected for a chaotic signal (>20). Thus, the program could correctly distinguish between chaotic, harmonic, and random segments.

TABLE I. Frequency of occurrence of nonlinear phenomena in the analyzed right whale (RW) and killer whale (KW) vocalizations: frequency jumps (FJ), subharmonics (SH), biphonation (BP), and deterministic chaos (DC).

	Total	Limit cycles only (%)	Total with at least one nonlinearity (%)	Total with more than one nonlinearity (%)	FJ (%)	SH (%)	BP (%)	DC (%)
RW	172	59 (34.3)	113 (65.7)	36 (20.9)	32 (18.6)	8 (4.7)	35 (20.4)	87 (50.6)
KW	173	13 (7.6)	160 (92.4)	98 (56.6)	42 (24.3)	11 (6.4)	154 (89.0)	68 (39.3)

Generated segments were utilized here because the TISEAN© software is sensitive to factors such as duration of segment, width of frequency band, and background noise.

III. RESULTS

Nonlinear phenomena were present in the vocalizations analyzed of both species, with 92.4% of the killer whale and 65.7% of the right whale vocalizations displaying at least one nonlinear feature and 56.6% and 20.9%, respectively, displaying more than one feature (Table I; Figs. 2 and 3). Additionally, all four types of nonlinear phenomena occurred in the vocalizations of both whales albeit at different rates. The most drastic difference between the two species was the appearance of biphonation. While biphonation was found in 20.4% of right whale vocalizations, it was found in 89.0% of killer whale vocalization. This difference can partially be explained because the killer whale calls we analyzed do not necessarily represent a random sample of the total repertoire (only call types *N*1, *N*2, *N*3, *N*4, *N*5, *N*7, *N*8, *N*9, *N*12, *N*13, *N*32, and *N*33 were analyzed in this study).

Frequency jumps occurred in 24.3% of killer and 18.6% of right whale vocalizations analyzed. They could be found in both upward and downward directions and multiple frequency jumps could occur within a single vocalization. Additionally in killer whales frequency jumps could be found on either the F_o and/or G_o.

Subharmonics occurred at low rates in both species occurring in 6.4% of killer and 4.7% of right whale vocalizations analyzed and were only found in the $F_o/2$ pattern. While it appears to be common for subharmonics to be precursors to deterministic chaos in many species (e.g., Wilden *et al.*, 1998; Riede *et al.*, 2004) in the present study subharmonics were generally found alone. Subharmonics preceded deterministic chaos in only one killer whale vocalization and zero right whale vocalizations and succeeded chaos only once in both species.

Biphonation occurred in 89.0% of killer and 20.4% of right whale vocalizations analyzed. In both species, biphonation occurred either in the form of sidebands or unrelated nonparallel bands that occurred without evidence of linear combination (Wilden *et al.*, 1998; Riede *et al.*, 2004). In killer whales the unrelated nonparallel bands occurred in every *N*1, *N*2, *N*4, *N*5, *N*9, *N*13, *N*32, and *N*33 call type analyzed ($N=147$) and were always initiated at the beginning of the signal, often following a characteristic introductory buzz. The unrelated nonparallel bands were also found in the *N*7 call type, but in only 40% of vocalizations of this call type analyzed ($N=20$). Here biphonation appeared as heightened energy in the introductory buzz that then swept up to overlap one of the harmonics of the low-frequency component. Biphonations in call type *N*7 were not as intense as those found in call types *N*1, *N*2, *N*4, *N*5, *N*9, *N*13, *N*32 and *N*33. Biphonation was not found in the *N*3, *N*8 or *N*12 vocalizations analyzed.

Sidebands occurred less frequently in killer whale vocalizations (63.0%; $N_{\mathrm{kwsb}}=109$) than nonparallel bands and only occurred in call types displaying nonparallel bands (although not in every vocalization with nonparallel bands). No sidebands were present in the analyzed vocalizations of call types *N*3, *N*7, *N*8, *N*12 or *N*13. Sidebands appeared primarily around the G_o (97.2% of N_{kwsb}), which most likely resulted from the harmonically sparse G_o being amplitude modulated by the harmonically rich F_o (Wilden *et al.*, 1998; Neubauer *et al.*, 2004; Miller *et al.*, 2007). Sidebands could also be found, however, around the F_o (19.3% of N_{kwsb}) or both the F_o and G_o (15.6% of N_{kwsb}).

In right whales biphonation occurred as unrelated nonparallel bands in 62.9% of total cases ($N_{\mathrm{rwub}}=35$) and as sidebands in 37.1%. Every instance of biphonation as an unrelated parallel band occurred at the beginning of a signal and occurred in the form of a downsweep (Fig. 2(d)). Additionally 90.1% of these downsweep biphonations occurred simultaneously with deterministic chaos. Hence, it is possible that we have underestimated the percentage of vocalizations containing biphonation due to possible masking effects of chaos.

Deterministic chaos was present in both species and was the most frequently occurring nonlinearity in right whales (50.6%; $N_{\mathrm{rwch}}=87$) and second most frequently occurring nonlinearity in killer whales (39.3%; $N_{\mathrm{kwch}}=68$). In right whales chaos occurred most frequently at the initiation of the signal (78.2% of N_{rwch}) but it could also be found at the end of the signal or in multiple locations throughout the signal. In addition, one vocalization was entirely chaotic. In killer whales chaos also appeared most frequently at the initiation of a vocalization (89.7% of N_{kwch}), which generally followed an introductory buzz (Fig. 3(d)). The prevalence of chaos in this transition state may be the result of the sound production system mechanically transitioning from the stable limit cycle of the introductory buzz (which is lower in frequency) to the biphonic regime in killer whales or in both species the system transitioning from an inactive to an active state.

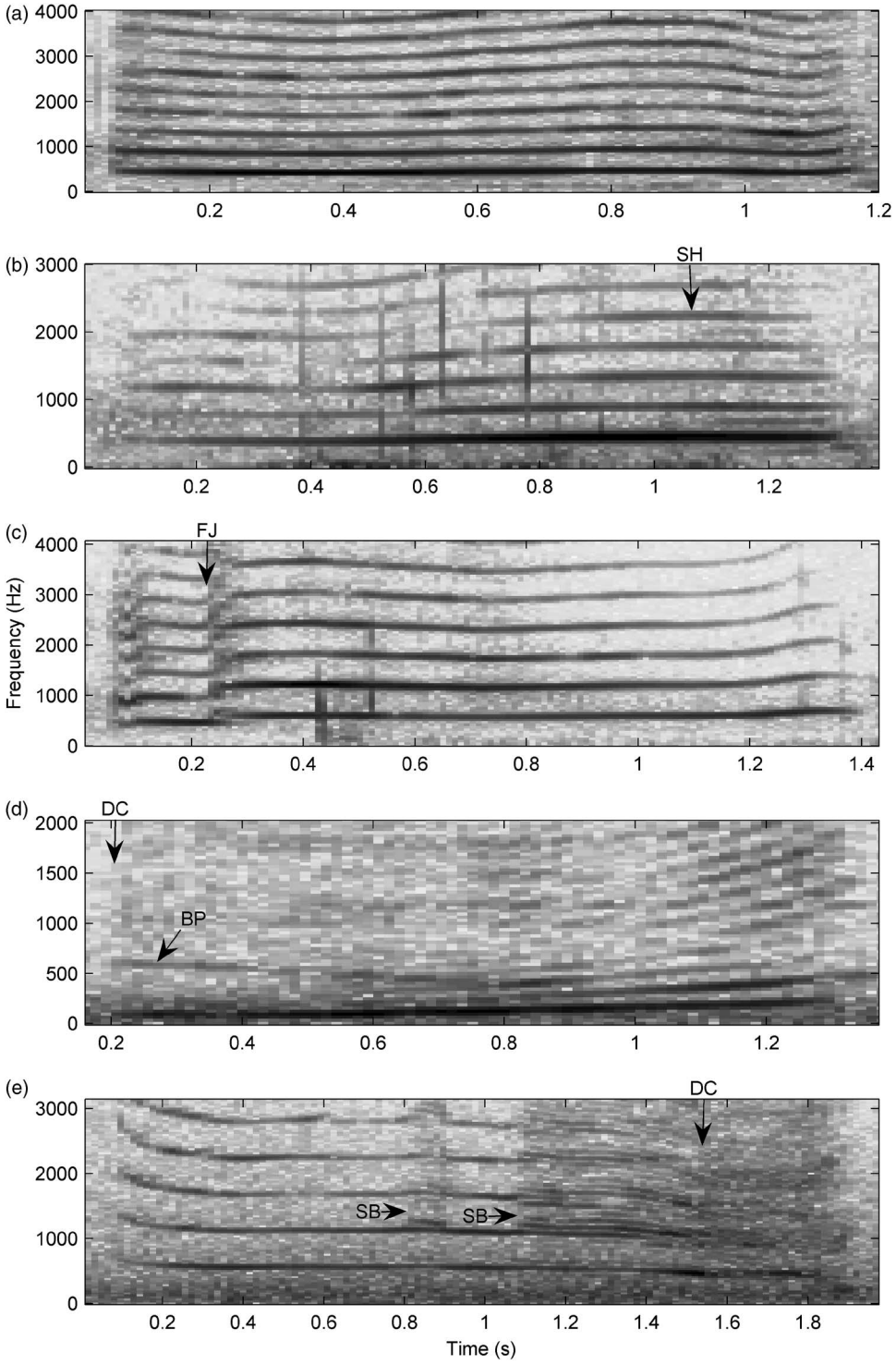

FIG. 2. Spectrograms of representative right whale vocalizations exhibiting nonlinear phenomena (note: spectrograms are zoomed in on for better resolution). (a) Stable limit cycle (SLC). (b) SLC then initiation of subharmonics (SH) indicated by arrow. (c) SLC then a frequency jump (FJ) to a higher frequency. (d) Deterministic chaos (DC, initiation indicated by arrow) with an embedded nonparallel biphonation (BP), then a transition to a SLC. (e) SLC then BP in the form of sidebands (SB) being produced twice, the second time transitioning into DC.

Of the four segments that we suspected were chaotic (two from each species) and of which we tested, only one (from a right whale, Fig. 4(a)) rejected the null hypothesis that the signal was a stationary, linear, random Gaussian signal ($P \leq 0.026$) after the method of surrogate data was applied. This may be due in part to excessive background noise in the other tested segments, which was often the result of the sound recording equipment and/or of the challenges of recording underwater sounds in the wild. In fact, Hegger *et al.* (1999) warned that as soon as more than a small or moderate amount of additive noise if present, scaling behavior will be broken and predictability of the signal will be limited. Therefore, because of our lack of segments that were entirely free of ambient noise, the method of surrogate data may not have accurately predicted the significance of the results. In addition, it was difficult for us to find segments from our sample that were of long enough duration and/or that had a large enough bandwidth to test in the TISEAN© software package and therefore we were limited in the amount of segments we could test. We still analyzed the segments that did not reject the null hypothesis to gain a better understanding of their underlying dynamics. All four segments tested had a

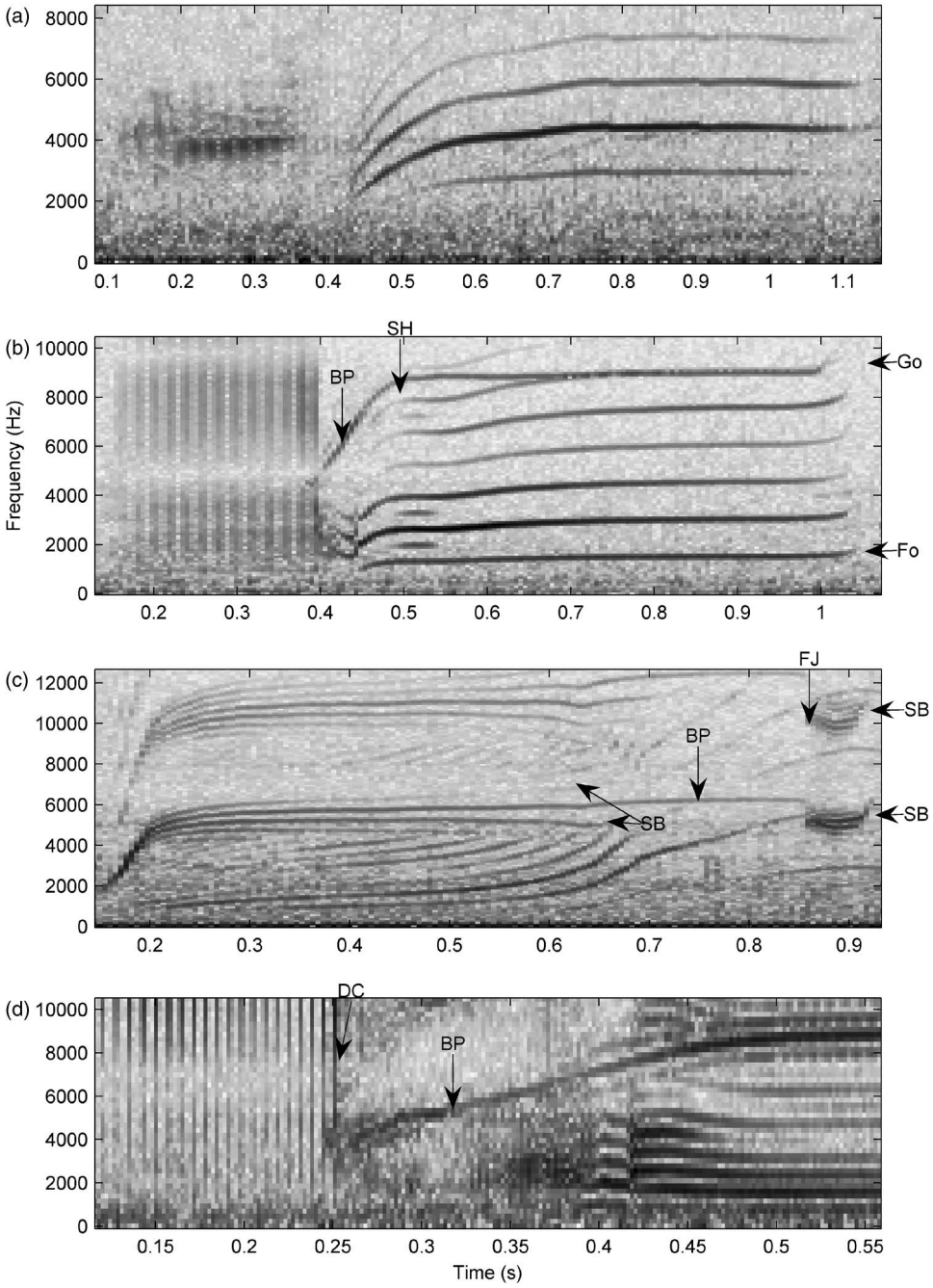

FIG. 3. Spectrograms of representative killer whale vocalizations exhibiting nonlinear phenomena (note: spectrograms are zoomed in on for better resolution). (a) Stable limit cycle (SLC) following the characteristic introductory buzz. (b) Introductory buzz then biphonation (BP) in the form of a nonparallel band and subharmonics (SH); G_o is the high frequency component, F_o is the low frequency component. (c) Nonparallel BP with sidebands (SB) appearing around the G_o and a frequency jump (FJ) to a lower frequency with SB's being produced at a new lower rate. (d) Introductory buzz followed by deterministic chaos (DC, initiation indicated by arrow) and then a transition into a nonparallel BP and a SLC.

positive Lyapunov exponent in the Lyapunov spectrum, indicating they were chaotic signals and not Gaussian noise (Fig. 4(e)). In addition, the embedding dimensions ranged from 5 to 6, whereas the embedding dimension of purely random noise is very high, e.g., 10^2, 10^3 (Table II, Fig. 4(c)).

This sensitivity of the TISEAN© software may have caused us to overestimate the occurrence of chaos to a degree because we could not test segments that were of particular interest (e.g., segments in which biphonation and potential chaos occurred simultaneously). In such cases we argue these cases are likely to be chaotic as they were similar spectrographically to segments which were run in the TISEAN© software and which had Lyapunov spectra consistent with them being in fact chaotic. The likely chaotic segments not run in TISEAN© were band limited and had bandwidths similar to the harmonic sections of the signals, but the energy was spread across the band instead of being in discrete frequencies.

IV. DISCUSSION

The presence of nonlinear phenomena in the analyzed vocalizations of both right and killer whales suggests that these features are important and could play an integral role in the communication of these species. Fitch *et al.* (2002) hypothesized that these features function to increase auditory impact on listeners by providing cues as to signaler fitness, mate quality, and overall health and may assist in communicating individual identification, animal size, and urgency. It

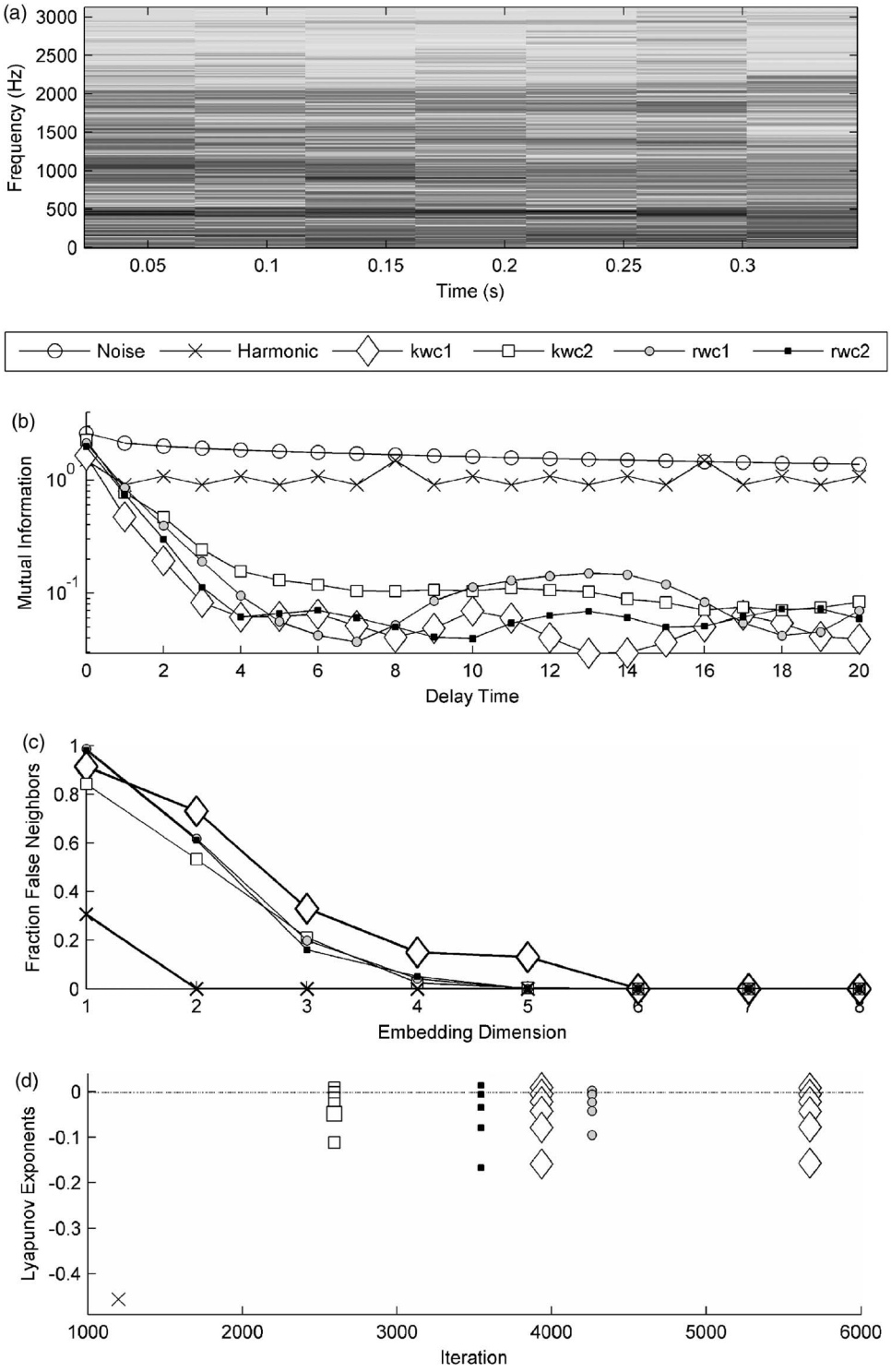

FIG. 4. Deterministic chaos analysis using the TISEAN© software program. (a) Spectrogram of a segment analyzed by the TISEAN© software program (rwc2 in Table II). This segment was cut from the vocalization seen in Fig. 2(e) at approximately 0:01.532 s and was the only segment which rejected the null hypothesis that the signal was a stationary, linear, random Gaussian signal. (b) Mutual information analysis to determine the appropriate time delay of each signal tested; taken as the first minimum (the noise segment was not further analyzed because its first minimum was >20). Note: mutual information scale is logarithmic to better display results. Legend labels follow Table II. (c) False nearest neighbor analysis to determine the appropriate embedding dimensions; taken as point where the number of false neighbors decreases to zero. (d) The spectrum of Lyapunov exponents. All signals suspected of being chaotic exhibited one positive exponent indicating they are indeed non-Gaussian signals. Note: kwc1 had results at two iterations while all other segments had results at only one iteration; an iteration is a repetition process used by TISEAN©. Also, the exponent for the harmonic signal is the maximum exponent found; an additional exponent was found at −1.13.

should be noted that the rates of nonlinear phenomena within the high signal-to-noise ratio vocalizations analyzed here cannot be considered typical of the species because the sound recording system may obtain a sample which is biased in some way in relation to nonlinear properties of signals (e.g., killer whale calls containing biphonation are produced at higher intensities than calls that do not contain biphonation; Miller, 2006). Also, rates of nonlinear signal production may be sensitive to the behavioral state of the caller, and our samples cannot be assumed to be representative. Thus, the rates discussed here only apply to our sample.

Subharmonics and frequency jumps have been found in relatively low rates in the vocalization of several species, including manatees (*Trichechus spp.*) and common chimpanzees (*Pan troglodytes*) (Mann *et al.*, 2006; Riede *et al.*, 2004). In the present study, comparable low rates were found in the analyzed vocalizations of both species. While these rates cannot necessarily be considered representative of each species' vocal repertoire, subharmonics and frequency jumps did not appear to dominate any of the call types analyzed in either species. Thus, it is possible that these features, while not prevalent, may in fact play some communicative role.

TABLE II. Analysis of four signals exhibiting deterministic chaos and the generated harmonic and random signals.

Segment analyzed	Delay time	Embedding dimension	Maximal Lyapunov exponent	Number of points sampled	Sampling rate (Hz)	Sample length
kwc1	4	6	0.093	5694	48,000	0:00.118
kwc2	8	6	0.079	2636	48,000	0:00.054
rwc1	7	5	0.089	4192	11,025	0:00.380
rwc2	4	5	0.135	3563	10,800	0:00.329
Harmonic	1	2	−0.013	1200	1200	0:01.000
Noise	>20	⋯	⋯	12,323	48,000	0:00.256

The increased prevalence of biphonation in killer whales reported here is partly due to the fact that calls known to contain biphonation are produced at more intense levels (Miller, 2006) and are therefore more commonly received at high signal-to-noise ratios required for this study. Biphonation may be less common in less intense calls not included in the sample of calls analyzed here. Still, the mechanism by which biphonation is produced may be different in killer whales compared with right whales and other mammals due to differences in the sound production mechanism of this species.

The cetacean sound production system differs from that of other mammals as they lack vocal cords typical of noncetacean species, and the precise mechanisms even differ between odontocetes (killer whales) and mysticetes (right whales). In odontocetes, the exact location of sound production and generation occurs in tissues located above the superior bony nares, termed the monkey lips/dorsal bursae (MLDB) or phonic lips (Cranford, 2000; Cranford, 1997). Excluding sperm whales (*Physeteridae*), all odontocetes have a bilateral though asymmetrical skull configuration, in that they have two MLDB complexes, one associated with each of the two nasal passages, with the right side generally larger than the left (Cranford and Amundin, 2004). These two complexes (left and right) act as two signal generators as both pairs of phonic lips, and possibly multiple locations along each of them, can produce sound (Cranford, 2000). In addition, it is possible that these sounds can be produced independently or simultaneously providing the opportunity of multiple sounds being produced at the same time (Cranford, 2000). While this has only been documented in sonar signals, it is likely that the same is true for nonsonar signals, such as the vocalizations being examined in this study (Cranford, 2000; Cranford and Amundin, 2004). Thus the source of biphonation in killer whales and other odontocetes may be the result of air being pushed across these two sets of phonic lips, though other mechanisms are also possible (Cranford, 2000). If this is the case, then biphonation in killer whales, in the form of nonparallel bands, may be viewed as a linear and not a nonlinear phenomenon as the two independent frequency contours are being produced by separate and independent sound production mechanisms. However, sidebands were commonly observed in association with the biphonations of killer whale calls, and never in calls without biphonation. Therefore, even though the production of two independent frequency contours may itself not be a nonlinear phenomenon, the mechanism by which biphonation sounds are produced by killer whales appears to commonly include a nonlinear interaction between the two independent contours (Miller *et al.*, 2007).

Little is known about the sound production system of mysticetes, but it is known that they lack such structures as phonic lips and instead have a larynx with vocal folds which may vibrate under the passage of airflow (Reidenberg and Laitman, 1988, 1992; Matthews *et al.*, 1999). This lack of phonic lips may partially explain the comparably lower rates of biphonation found in the right whale repertoire in this study. Biphonation in right whales may then result from weak couplings between other oscillators located within the larynx, such as in humans (Wilden *et al.*, 1998) and other species lacking such structures (e.g., common chimpanzees (*Pan troglodytes*) (Riede *et al.*, 2004), but our current lack of understanding of their sound production system precludes further conclusion or discussion. Any further anatomical understandings of sound production mechanisms in right whales or other mysticetes would provide useful insights.

While deterministic chaos occurs in both species, in killer whales it was primarily found as part of an otherwise harmonically rich signal (except call-type *N*3 where it could be found throughout the signal; $N_{N3}=3$). In right whales, however, chaos could be found throughout signals and in greater duration. It has been hypothesized that deterministic chaos may be used as an unpredictable signal thereby making them harder to habituate to and ignore (Fitch *et al.*, 2002). It may be possible that these species are using chaos in this way, however, in killer whales it seems more likely that chaos is generally a by-product of the sound production system transitioning from a stationary to active state.

Though few studies have reported the presence of nonlinearities, their prevalence in both right and killer whales indicates that they may play an integral role in the vocal communication of these species, and possibly across all the cetacea. The lack of correlating detailed behavioral information in this study and the lack of information on the individual whales that produced each vocalization (particularly for the right whales), however, did not allow us to address any of the proposed functional hypotheses but their prevalence indicates that they are likely more than an artifact of production and may serve communicative function(s). In future studies, collecting concurrent behavioral data would greatly increase our understanding of nonlinearities in these and perhaps other species and would bring us closer to addressing many of the functional hypotheses. Here we have provided qualitative descriptions and quantitative analyses of

nonlinearities in the vocal repertoire of North Atlantic right whales and killer whales in hopes of providing more insight into the potential functions and underlying mechanisms of these phenomena.

ACKNOWLEDGMENTS

We would like to thank the following people for their assistance with this study: David Mann, Michael Owren, Anna Nousek, Susan Parks, Rainer Hegger, Mike Kashack, and Frank Johnson. Right whale recordings in 2001 and 2002 were made under a NOAA National Marine Fisheries permit No. 1040 issued to Scott Kraus and Canadian Department of Fisheries and Oceans permits 2001-599 and 2002-258. Right whale recordings in 2005 were made under a Canadian Department of Fisheries and Oceans permit, MARSA-2005-03. Killer whale recordings were also made under research permits from the Canadian Department of Fisheries and Oceans following Canadian law.

Brown, C. H., and Cannito, M. P. (**1995**). "Modes of vocal variation in sykes's monkey (*Cercopithecus albogularis*) squeals," J. Opt. Soc. Am. A **109**, 398–415.

Cranford, T. W. (**1997**). "Visualizing dolphin sonar signal generation using high-speed video endoscopy," J. Acoust. Soc. Am. **102**, 3123.

Cranford, T. W. (**2000**). "In search of impulse sound sources in odontocetes," in *Hearing by Whales and Dolphins*, edited by W. W. L. Au, A. N. Popper, and R. R. Fay (Springer-Verlag, New York, 2000), pp. 109–155.

Cranford, T. W., and Amundin, M. (**2004**). "Biosonar pulse production in odontocetes: The state of our knowledge," in *Echolocation in Bats and Dolphins*, edited by J. A. Thomas, C. F. Moss, and M. Vater (The University of Chicago Press, Chicago), pp. 27–35.

Facchini, A., Bastianoni, S., Marchettini, N., and Rustici, M. (**2003**). "Characterization of chaotic dynamics in the vocalization of *Cervus elaphus corsicanus* (L)," J. Acoust. Soc. Am. **114**, 3040–3043.

Fee, M. S., Shraiman, B., Pesaran, B., and Mitra, P. P. (**1998**). "The role of nonlinear dynamics of the syrinx in the vocalizations of a songbird," Nature (London) **395**, 67–71.

Fitch, W. T., Neubauer, J., and Herzel, H. (**2002**). "Calls out of chaos: The adaptive significance of nonlinear phenomena in mammalian vocal production," Anim. Behav. **63**, 407–418.

Fletcher, N. H. (**2000**). "A class of chaotic bird calls?" J. Acoust. Soc. Am. **108**, 821–826.

Hauser, M. D. (**1993**). "The evolution of nonhuman primate vocalizations: Effects of phylogeny, body weight, and social context," Am. Nat. **142**, 528–542.

Hegger, R., Kantz, H., and Schreiber, T. (**1999**). "Practical implementation of nonlinear time series methods: The TISEAN package," Chaos **9**, 413–435.

Herzel, H., Berry, D., and Titze, I. *et al.* (**1995**). "Nonlinear dynamics of the voice: Signal analysis and biomechanical modeling," Chaos **5**, 30–34.

Johnson, M. P., and Tyack, P. L. (**2003**). "A digital acoustic recording tag for measuring the response of wild marine mammals to sound," IEEE J. Ocean. Eng. **28**, 3–12.

Kantz, H., and Schreiber, T. (**2004**). *Nonlinear Time Series Analysis*, 2nd ed. (Cambridge University Press, Cambridge), p. 369.

Mann, D. A., O'Shea, T. J., and Nowacek, D. P. (**2006**). "Nonlinear dynamics in manatee vocalizations," Marine Mammal Sci. **22**, 548–555.

Matthews, J. N., Rendell, L. E., Gordon, J. C. D., and MacDonald, D. W. (**1999**). "A review of frequency and time parameters of cetacean tonal calls," Bioacoustics **10**, 47–71.

Mende, W., Herzel, H., and Wermke, K. (**1990**). "Bifurcations and chaos in newborn infant cries," Phys. Lett. A **145**, 418–424.

Miller, P. J., and Tyack, P. L. (**1998**). "A small towed beamforming array to identify vocalizing *resident* killer whales (*Orcinus orca*) concurrent with focal behavioral observations," Deep-Sea Res., Part II **45**, 1389–1405.

Miller, P. J. O. (**2006**). "Diversity in sound pressure levels and estimated active space of resident killer whale vocalizations," J. Comp. Physiol., A **192**, 449–149.

Miller, P. J. O., Samarra, F. I. P., and Perthuison, A. (**2007**). "Caller sex and orientation influence spectra of two-voice' stereotyped calls produced by free-ranging killer whales (*Orcinus orca*)," J. Acoust. Soc. Am. **121**(6), pp. 3932–3937.

Neubauer, J., Edgerton, M., and Herzel, H. (**2004**). "Nonlinear phenomena in contempory vocal music," J. Voice **18**, 1–12.

Nousek, A. E., Slater, P. J. B., Wang, C., and Miller, P. J. O. (**2006**). "The influence of social affiliation on individual signatures of northern resident killer whales (*Orcinus orca*)." Biology Lett. **2**(4), pp. 481–484.

Nowacek, D. P., Johnson, M. P., and Tyack, P. L. (**2004**). "North Atlantic right whales (*Eubalaena glacialis*) ignore ships but respond to alerting stimuli," Proc. R. Soc. London **271**, 227–231.

Owren, M. J., and Rendall, D. (**2001**). "Sound on the rebound: Bringing form and function back to the forefront in understanding nonhuman primate vocal signaling," Evo. Anthro. **10**, 58–71.

Parks, S. E., and Tyack, P. L. (**2005**). "Sound production by North Atlantic right whales (*Eubalaena glacialis*) in surface active groups," J. Acoust. Soc. Am. **117**, 3297–3306.

Reidenberg, S. J., and Laitman, J. T. (**1988**). "Existence of vocal folds in the larynx of Odontoceti (toothed whales)." Anat. Rec. **221**, 884–891.

Reidenberg, S. J., and Laitman, J. T. (**1992**). "Anatomy of the vocal apparatus of the humpback whale (*Megaptera novaeangliae*)," Anat. Rec. **323**, 73A.

Rendall, D., Rodman, P. S., and Emond, R. E. (**1996**). "Vocal recognition of individuals and kin in free-ranging rhesus monkeys," Anim. Behav. **51**, 1007–1015.

Riede, R., Arcadi, A. C., and Owren, M. J. (**2007**). "Nonlinear acoustics in the pant hoots of common chimpanzees (*Pan troglodytes*): Vocalizing at the edge," J. Acoust. Soc. Am. **121**, 1758–1767.

Riede, T., Herzel, H., Mehwald, D., Seidner, W., Trumler, E., Böhme, G., and Tembrock, G. (**2000**). "Nonlinear phenomena in the natural howling of a dog-wolf mix," J. Acoust. Soc. Am. **108**, 1435–1442.

Riede, T., Owren, M. J., and Arcadi, A. C. (**2004**). "Nonlinear acoustics in pant hoots of common chimpanzees (*Pan troglodytes*): Frequency jumps, subharmonics, biphonation, and deterministic chaos," Am. J. Primatol **64**, 277–291.

Riede, T., Wilden, I., and Tembrock, G. (**1997**). "Subharmonics, biphonations, and frequency jumps—common components of mammalian vocalization or indicators for disorders?" Z. fur Säugetierkunde **62**, (Suppl. 2) 198–203.

Robb, M. P. (**2003**). "Bifurcations and chaos in the cries of full-term and preterm infants," Folia Phoniatr Logop **55**, 233–240.

Schreiber, T., and Schmitz, A. (**2000**). "Surrogate time series," Physica D **142**, 346–382.

Tokuda, I., Riede, T., Neubauer, J., Owren, M. J., and Herzel, H. (**2002**). "Nonlinear analysis of irregular animal vocalizations," J. Acoust. Soc. Am. **111**, 2908–2919.

Theiler, J., Eubank, S., Longtin, A., Galdrikian, B., and Farmer, J. D. (**1992**). "Testing for nonlinearity in time series: The method of surrogate data," Physica D **58**, 77–94.

Volodina, E. V., Volodin, I. A., Isaeva, I. V., and Unck, C. (**2006**). "Biphonation may function to enhance individual recognition in the dhole, *Cuon alpinus*," Ethology **112**, 815–825.

Wilden, I., Herzel, H., Peters, G., and Tembrock, G. (**1998**). "Subharmonics, biphonation, and deterministic chaos in mammal vocalization," Bioacoustics **9**, 171–196.

Proper orthogonal decomposition and cluster weighted modeling for sensitivity analysis of sound propagation in the atmospheric surface layer

Chris L. Pettit[a)]
Aerospace Engineering Department, United States Naval Academy, 590 Holloway Road, MS 11-B, Annapolis, Maryland 21402, USA

D. Keith Wilson
U.S. Army Cold Regions Research and Engineering Laboratory, 72 Lyme Road, Hanover, New Hampshire 03755-1290, USA

(Received 16 January 2007; revised 4 June 2007; accepted 13 June 2007)

Outdoor sound propagation predictions are compromised by uncertainty and error in the atmosphere and terrain representations, and sometimes also by simplified or incorrect physics. A model's predictive power, i.e., its accurate representation of the sound propagation, cannot be assessed without first quantifying the ensemble sound pressure variability and sensitivity to uncertainties in the model's governing parameters. This paper describes fundamental steps toward this goal for a single-frequency point source. The atmospheric surface layer is represented through Monin-Obukhov similarity theory and the acoustic ground properties with a relaxation model. Sound propagation is predicted with the parabolic equation method. Governing parameters are modeled as independent random variables across physically reasonable ranges. Latin hypercube sampling and proper orthogonal decomposition (POD) are employed in conjunction with cluster-weighted models to develop compact representations of the sound pressure random field. Full-field sensitivity of the sound pressure field is computed via the sensitivities of the POD mode coefficients to the system parameters. Ensemble statistics of the full-field sensitivities are computed to illustrate their relative importance at every down range location. The central role of sensitivity analysis in uncertainty quantification of outdoor sound propagation is discussed and pitfalls of sampling-based sensitivity analysis for outdoor sound propagation are described.
[DOI: 10.1121/1.2756176]

PACS number(s): 43.28.Gq, 43.28.Lv [VEO] Pages: 1374–1390

I. INTRODUCTION

A. Uncertainty quantification and validation of computational acoustics models

Predictions of outdoor sound propagation near the ground are compromised by statistical uncertainty and model errors in the atmosphere and terrain characterizations. Although high quality physical and numerical representations are available, imprecise knowledge of the heterogeneous propagation environment impedes attempts to achieve spatial and temporal accuracy in sound field predictions.[1] Embleton[2] summarizes many of these environmental factors, which include (i) the topography and acoustic impedance of the ground or lower boundary of the propagation domain, (ii) the interaction of the wind and radiative exchanges with this surface, as reflected in the velocity and thermal gradients in the atmospheric surface layer (ASL), and (iii) spatio-temporal variability in atmospheric turbulence. This paper describes a simulation-based method for full-field sensitivity analysis of near-ground sound propagation. The method and results described here are meant to support future efforts to obtain information about the propagation environment sufficient to ensure high confidence in the predicted sound field. A comprehensive estimate of the full-field sensitivities can help to ensure that measurements are made and used in their most productive manner as well to help the analyst understand how predictions are compromised by limited data.

To bridge the gap between making predictions and justifying confidence in those predictions, the challenge of accounting for the multiple sources of uncertainty described above and their interactions must be addressed. This concern is common to all disciplines that involve the use of complex predictive models. The field of verification and validation (V&V) of computational mechanics models is evolving to help bridge this gap, or to at least meaningfully assess its dimensions. Efforts to codify V&V concepts and methods include the monograph by Roache,[3] a standard by the American Institute of Aeronautics and Astronautics[4] for computational fluid dynamics, and more recent plans by the American Society of Mechanical Engineers for published standards in computational solid mechanics and heat transfer.

These documents cite uncertainty quantification (UQ) as a crucial step in the larger problem of verifying and validating predictive models. UQ is defined in this paper as constructing probabilistic models for forcing functions and system parameters, and transforming these models through a

[a)]Author to whom correspondence should be addressed. Electronic mail: pettitcl@usna.edu

network of computational mechanics models to predict statistics or the full distribution of a response process. Nonprobabilistic or generalized probabilistic methods, which commonly involve the introduction of fuzzy or nonadditive measures, are not considered. The broad goal of assessing model validity, i.e., physical fidelity, also is not addressed. Physics models will be called deterministic when they do not depend directly on the recognition of uncertainty.

Wave propagation in random environments has been studied for many years (e.g., see Ishimaru[5]), but the applicability of the resulting methods has been limited by the constraints placed on the underlying statistical models to produce tractable analyses. A broadened interest in accommodating random propagation environments has developed recently owing to the continuing evolution of high-resolution atmospheric simulations and pressing needs to extend acoustics predictions to increasingly complex and poorly characterized environments.

UQ for computational underwater acoustics has been studied recently by James and Dowling[6] and Finette.[7] James and Dowling developed a method to predict the evolution of the sound field probability density function (PDF) given the PDF of the source amplitude. Finette used the polynomial chaos expansion to develop a system of equations for computing the sound pressure as a stochastic process dependent upon a polynomial chaos expansion of the sound speed. Both approaches are attractive but possibly limited in practice by the difficulties of including multiple sources of parametric uncertainty and the need to develop specialized computer programs to solve the resulting equations. Finette's formulation as well as James' and Dowling's also assumes the uncertainty enters indirectly through the randomness in the sound speed or wave number; in effect, the refractive index is taken to be the injection point for parametric uncertainty. This approach could complicate follow on efforts to assess the validity of the probabilistic model because uncertainty has been inserted through a quantity more naturally viewed as an intermediate or composite source of uncertainty instead of a primary source. The distinction here is twofold in that it has both deterministic and probabilistic aspects:

1. In the underlying deterministic model, a possibly primary source of uncertainty can be considered as an independent variable or parameter when the physical conditions are completely specified; examples include the fluid temperature or salinity. The intermediate quantity may then be computed from an appropriate theoretical relationship or equation of state, such as the adiabatic sound speed, $c = \sqrt{\gamma RT}$, in an ideal gas. This approach should be preferred because it highlights the assumptions and links in the model that affect the output; it also aids comparison of competing models that depend on the same primary parameters.
2. A composite source of uncertainty typically can be represented as a function of primary sources of uncertainty. If the physics that connect the primary and composite uncertainties are bypassed; a probabilistic model can misrepresent statistical dependence in the full set of input parameters, i.e., both primary and intermediate, when the primary sources actually influence multiple intermediate sources. Primary inputs should be kept statistically independent when possible and the deterministic physics model should be allowed to induce statistical dependence between primary and intermediate parameters in the problem. This both clarifies the modeling process and simplifies the use of sampling schemes.

The principal conclusion is that model validation is facilitated by enforcing transparency and directness in both the deterministic and probabilistic parts of the model to ensure that parametric uncertainty and observed effects are attributed to primary, experimentally observable quantities when possible.

James and Dowling[6] note the importance and possible difficulty of determining *a priori* input-parameter PDFs, but they do not pursue this goal. Before this is attempted, it ought to be emphasized that introducing probabilistic modeling choices into the already complex modeling applications requires concerted efforts to ensure that the probabilistic model balances the need for capturing the statistics of each uncertain quantity with the availability of sufficient high-quality information to populate the probabilistic model. In the present context, this first requires documenting the full-field parametric sensitivity of reputable computational atmospheric acoustics models.

This paper develops full-field representations of the sensitivity of the parabolic approximation of Helmholtz's equation (see Sec. II A) to several parameters that define the propagation environment, including the acoustic impedance of the ground and the wind and temperature profiles in the ASL. These sensitivities should provide a quantitative foundation for the development of probabilistic parameter models to support high resolution simulations of outdoor sound propagation. The method developed here should be readily extendable to other computational acoustics applications. Two primary benefits are anticipated: (*i*) the resulting full-field sensitivity models should enable the informed gathering of data to support estimation of parameter PDFs, and (*ii*) they should promote the effective allocation of computational resources by ensuring that probabilistic simulations are limited to representing uncertainty only in those parameters most crucial to uncertainty in the predicted sound pressure.

B. Sensitivity analysis of sound propagation

Sensitivity analysis (SA) is broadly defined as the determination of the change in a system's response due to changes in the model's parameters. SA is the first step in uncertainty quantification for any complex, multiple parameter model because it aids in identifying the main contributors to imprecision and thereby determining which parameters require accurate probabilistic models. Sampling-based parametric SA methods, as described by Helton and others,[8,9] commonly are used in conjunction with regression or reduced order models for computationally expensive models that depend on several parameters. Sections II B and IV describe how sampling methods are used herein to facilitate SA for sound pressure fields in the ASL.

TABLE I. Parameters in the Monin-Obukhov similarity model for wind speed and temperature profiles and the relaxation model for ground acoustic impedance.

Parameter	Symbol	Units	Lower value	Upper value
Porosity	Ω	n/a	0.4	0.65
Flow resistivity	σ	kPa s m^{-2}	150×10^3	600×10^3
Surface heat flux	Q_s	W/m^2	−50	600
Friction velocity	u_*	m/s	0.05	0.50
Wind direction	α	deg	0	180
Roughness length	z_0	m	0.001	0.100

Compact representations of the sensitivity of the sound pressure field are achieved through the proper orthogonal decomposition (POD) and cluster weighted modeling (CWM), which are described in Secs. II C and II D, respectively. We are unaware of any previous studies that have combined POD and CWM to produce full-field sensitivity estimates. CWM could be replaced here by more common nonlinear function approximation methods, e.g., the neural networks used recently by Mungiole and Wilson;[10] however, preliminary comparison with their neural network results suggests that the combination of CWM and POD interpolates more accurately and robustly in this application than a neural network when given only a sparse sample of training cases. A detailed comparison has not been attempted, but we suspect that CWM provides a more flexible approach than neural network models to localized regularization in the parameter space. POD by itself also injects an unknown amount of smoothing of the training data, so combining it with CWM appears to produce an effective method for regularized approximation based on sparse data. Combining POD with Mungiole's and Wilson's neural network model might also have improved their approximation accuracy with fewer training data, but this has not been attempted. CWM also provides the additional ability to estimate the sampling-induced uncertainty in the resulting function approximation, but this capability is not employed here.

II. CONSTRUCTION OF REDUCED ORDER MODELS FOR SOUND PRESSURE FIELDS

A. Physics model

Our study is based on a simplified, six-parameter model for sound propagation in the ASL. Two-dimensional sound propagation for a single frequency point source 1.0 m above the ground is modeled with a wide-angle parabolic equation (PE) approximation,[11,12] which is solved with the Crank-Nicholson scheme. The propagation domain extends 1000 m down range of the source and 400 m above the ground. Turbulence is not included in the calculations and the ground is assumed to be flat. The ground impedance is represented by a relaxation model[10,13] and is parameterized by the flow resistivity, σ, and porosity, Ω, of the material. The mean wind and temperature profile in the ASL are represented by Monin-Obukhov similarity theory,[14,15] which is parameterized by the friction velocity, u_*, surface heat flux, Q_s, wind direction, α, and roughness length, z_0.

Because the objective is to estimate the sensitivity of the sound pressure field to variations in the system parameters, the pressure is written as an explicit function of these parameters, $p(x;\zeta)$, where p is sound pressure in dB; i.e., 20 times the logarithm of the complex sound pressure amplitude relative to the free-field sound pressure amplitude; $x\in\mathcal{D}_x\subset\mathbb{R}^2$ is the position vector; and $\zeta\in\mathcal{D}_\zeta\subset\mathbb{R}^M$ is the vector of M parameter that define the ground and flow properties of interest in the sensitivity study. The six parameters ($M=6$) listed above are distributed as defined in Table I. The ranges in Table I are not implied to cover every condition that might be encountered during sound propagation outdoors; for example, the static flow resistivity values are limited to moderately absorptive surfaces such as soil. The intent is to cover a broad enough range to get a reasonable picture of the global sensitivities without allowing samples that produce extremely unlikely or physically unrealistic combinations of parameters.

Latin hypercube sampling (see Sec. II B) was used to select specific samples of ζ. For each sample vector, the ground acoustic impedance and wind and temperature profiles were computed. The PE model then was solved to estimate the associated sound pressure field. One hundred Latin hypercube samples were selected from the parameter ranges listed in Table I. The parameter samples were normalized for the purposes of analysis and function approximation to fall within the interval $[-0.5,0.5]$; i.e., each dimensional parameter ζ_m was scaled to produce the nondimensional parameter

$$\hat{\zeta}=\frac{\zeta_m-\mu_{\zeta_m}}{d_{\zeta_m}}, \tag{1}$$

where μ_{ζ_m} and $d_{\zeta_m}=\max(\zeta_m)-\min(\zeta_m)$ are the mean value and assumed range of ζ_m.

B. Latin hypercube sampling

The sound pressure field is viewed as a stochastic process, $p(x;\zeta(\omega))$, where $\omega\in\Omega$ is an element of the sample space or universal set and $\zeta(\omega)$ is the M-dimensional random vector of system parameters. Latin hypercube sampling (LHS)[16–18] is used to choose N random realizations of the normalized parameter vector, $\hat{\zeta}$, that are distributed throughout the Cartesian product space $\times_{m=1}^{6}[-0.5,0.5]\subset\mathbb{R}^6$, the goal being to ensure every portion of each parameter's range is sampled. The parameters are assumed to be independent; this simplifies the sampling process but should not compromise the conclusions of the first-order sensitivity analysis employed here.

In LHS, each parameter is divided into N intervals of probability equal to $1/N$ and each variable is randomly sampled once within each interval. The N samples of each variable are assigned to N sample vectors by randomly permuting the order of the samples, which helps to ensure that the samples represent the range of possible combinations of the parameter values. As noted by Iman and Helton[16] and McKay,[17] the permutation step sometimes produces sample vectors that exhibit pairwise correlation between the sampled variables. This was mitigated here by computing a sample correlation matrix from the chosen vectors and repeating the LHS process if the absolute value of the maximum off-diagonal element in this matrix exceeded 0.5. Other approaches are described in the references just cited.

Careful consideration of the actual interdependence of the parameters might be needed to ensure the accuracy of predictions of the probability distribution of the sound pressure, but its relative importance cannot be known a priori. Such interdependence is not included here because it should not seriously affect the conclusions of our sensitivity study, but the following comments are offered to support future studies. Statistical dependence of two quantities usually implies that they have one or more independent determining factors in common, but a quantitative expression of this relation might not be available because of limited knowledge or data. If an explicit function can be employed, sampling should be used for the underlying common parameters and the dependent parameters should instead be included as intermediate response variables in the system model. If no practical expression is available, dependence must instead be accommodated through sampling the joint probability model of the parameters. Iman and Conover[19] describe the best-known method of enforcing a rank correlation structure in Latin hypercube samples, and Helton and Davis[8] provide additional guidance.

For near-ground sound propagation, it seems reasonable to assume that randomness in the ASL parameters is independent of randomness in the ground acoustic impedance parameters, at least away from the air-ground interface, but the individual ASL and ground parameters might not be independent of the other air and ground parameters, respectively. More will be said about this point in Sec. IV D 5.

C. Proper orthogonal decomposition of the sound pressure field

For the sake of generality, allow time to also be an independent variable, so the sound pressure is $p(t,x;\zeta(\omega))$; for a given ω, $p(t,x)$ is a single realization of the process that varies over time and space. Proper orthogonal decomposition (POD), as described by Holmes *et al.*[20] and Kirby,[21] is used herein to compute a mean-square optimal representation of the ensemble of sound pressure fields produced by LHS. POD shares its theoretical foundation with a variety of methods from several disciplines, including empirical orthogonal functions, principal component analysis, and the Karhunen-Loève decomposition.

POD is not an inherently probabilistic technique in that it often is applied in deterministic applications, e.g., Hall, *et al.*[22] and Pettit and Beran,[23] but its practical implementation requires the computation of many *snapshots* of the process. Here snapshots are realizations of a spatially distributed process with randomly sampled parameters, i.e., $\{p(x;\zeta(\omega_n))\}_{n=1}^{N}$; they also could be the field from a single realization of a time-dependent process (i.e., a single set of parameter values) at several points in time, $\{p(t_j,x)\}_{j=1}^{J}$, as they were in Pettit and Beran,[23] or some combination of both cases. In any application snapshots must be chosen that exhibit the most common system states. Snapshots in practice will be finite dimensional because they are samples of the response computed at a set of N_g grid or mesh points. If the process has a nonzero ensemble average, it should be subtracted from the snapshots before the POD computation is performed.

Let $n=\{1,2,\ldots,N\}$ be the snapshot index and $S=[s_1|s_2|\ldots|s_N]$ be the $N_g\times N$ collection of snapshots arranged as column vectors. For $x\in\mathbb{R}^2$ or higher dimensions, the POD computation is facilitated by rearranging each multidimensional snapshot as a column vector to fit this structure. POD represents the energy of the snapshots in terms of a mean-square optimal set of orthonormal vectors or modes, $\Phi^{N_g\times N}=[\varphi_1|\varphi_2|\ldots|\varphi_N]$, which are computed as linear combinations of the snapshots; i.e.,

$$\Phi = SV \tag{2}$$

and $\Phi^T\Phi=I^{N\times N}$, where $V^{N\times N}=[v_1|v_2|\ldots|v_N]$ must be computed to maximize the energy of the projection of the snapshots onto the vectors in Φ. It can be proved through an energy argument[20] or via the singular value decomposition[23] that V must satisfy the eigenvalue problem

$$S^TS\hat{V} = \hat{V}\Lambda, \tag{3}$$

where each $\lambda_m\geqslant 0$ because S^TS is symmetric and nonnegative definite. The normalization condition $\Phi^T\Phi=I$ and Eq. (2) require that the eigenvectors $\hat{V}$ be normalized such that $\hat{V}^T\hat{V}=I$ and $v_n=\hat{v}_n/\sqrt{\lambda_n}$. The eigenvalue problem in Eq. (3) typically is not computationally costly because S^TS is an $N\times N$ matrix and $N\ll N_g$ in most applications.

Because each POD mode has unit norm, its relative importance in a given snapshot is reflected in the size of the corresponding generalized Fourier coefficient, i.e.,

$$a_q^{(n)} = \varphi_q^T S_n, \quad q=1,2,\ldots,N \quad \text{or} \quad A=\Phi^T S. \tag{4}$$

Individual snapshots can be recovered by inverting the transform, i.e., $s_n=\Phi a^{(n)}$. If distributions are estimated for the modal coefficients, snapshots can also be simulated by sampling from these distributions; this is a form of reduced order modeling enabled by POD for time-independent fields like those studied herein, but it is somewhat nonphysical unless a connection is enforced between the modal coefficient distributions and the process's physics. This connection is achieved here by building models that map the parameter samples to the POD coefficients of the associated snapshots; see Sec. II D for details. The reduced order model is made even more efficient by truncating the modal approximation so that only the highest energy modes are retained, i.e., q

$=1,2,\ldots,N_r$, where $N_r<N$. Often no more than the strongest 10%–20% of the modes are needed to retain over 99% of the process's energy.

D. Reduced order models from cluster weighted approximations

Given realizations scattered throughout the parameter space, analytical sensitivities can be approximated by fitting regularized (i.e., smooth) functions to the finite ensemble. Cluster weighted modeling[24,25] is employed here to meet this need. A brief description of CWM is given here, but the complete analysis is somewhat involved and the reader is encouraged to consult the above references for details. Details of how CWM is used here for estimating sensitivity throughout the parameter space are deferred until Sec. IV.

CWM builds a smooth approximation by using local functions that are scaled and relocated iteratively to occupy the most sample-rich areas, i.e., clusters, of the normalized parameter space. The method produces an estimate of the joint probability density function, $f(a^{(n)},\hat{\zeta})$, of the parameters and their consequent responses, where $a^{(n)}$ is the generalized Fourier coefficient of the nth POD mode. Function approximation at a specific parameter location, $\hat{\zeta}_0$, is achieved by evaluating the conditional expected valued

$$E(a^{(n)}|\hat{\zeta}_0)=\int a^{(n)}f(a^{(n)},\hat{\zeta}_0)da^{(n)}. \tag{5}$$

The algorithm requires specifying the number of clusters, each of which is assigned an initial location as described below and a local Gaussian density function with an assumed function type (e.g., constant or linear in $\hat{\zeta}$) for its mean value. The Gaussian density functions are used to smooth interpolation between the assumed form of the function near each cluster's center. Random initial locations selected through LHS were used to test the CWM's ability to fit a generic data set. Better approximations might be obtained by placing clusters initially at a subset of the LHS parameter sample vectors already used in generating the realizations of the sound field, but this is not examined here. The location and strength of each cluster are iteratively updated until the approximation converges or a set number of update cycles are completed; the latter approach was used here for simplicity.

III. SOUND PRESSURE REALIZATIONS

This section first describes the computation of sound pressure fields for various realizations of the governing parameters. Next the POD modes are described to provide a foundation for sensitivity analysis in the following section.

A. Sampling the sound pressure in parameter space

Latin hypercube sampling (see Sec. II B) was used to select specific samples of the normalized parameter vector $\hat{\zeta}$. For each sample, the ground acoustic impedance and surface layer wind and temperature profiles were computed, and the PE model was solved to estimate the associated sound pressure field for a single-frequency source at a height of 1.0 m.

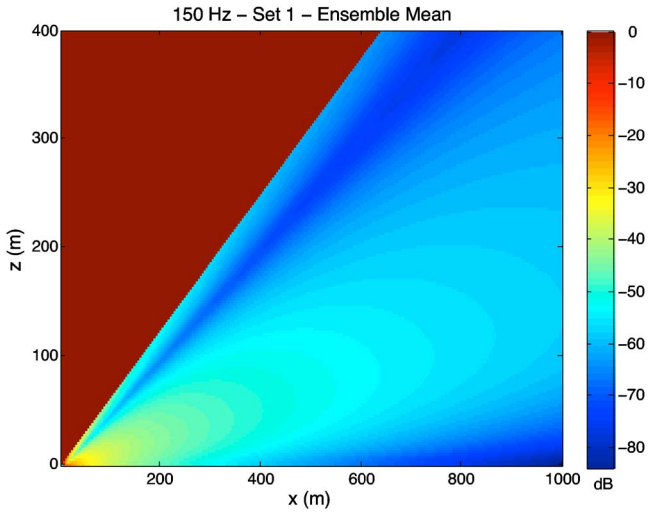

FIG. 1. (Color online) Ensemble mean of the 150 Hz sound pressure (dB) realizations

One hundred LHS samples ($N=100$) of the parameter vector were generated and sound pressure realizations were computed with these parameters for a 150 Hz source. To help validate the CWMs, the resulting realizations were separated initially into two sets of 50 realizations, which will henceforth be referred to as Set 1 and Set 2. Results presented initially are from Set 1, but later results emphasize the full 100 realization ensemble for reasons discussed below.

Whether 100 samples are sufficient depends on the application and the analyst's aims. Experience indicates that 100 samples are sufficient for global SA because high accuracy is not required in predicting the quantiles in the tails of the response's probability density function.[8] Confidence intervals on mean values computed through purely random sampling scale as $N^{-1/2}$ and LHS often produces lower variance in estimated statistics than random sampling does, so increasing N by a factor of 10 likely would only narrow the confidence intervals around the estimated mean sensitivities by a factor of 3 or less. Furthermore, our SA method is expected to be applied in the future to three-dimensional simulations of sound propagation through turbulent boundary layers. Although the two-dimensional simulations employed here are computed quickly enough that many more simulations could have been completed, the expectation that future applications will be more costly means that the practicality of the proposed SA method must be demonstrated under conditions similar to its intended use.

Each realization exhibits a characteristic, fan-like artifact emanating from the source. This is an artifact of the parabolic approximation and is not considered to be physical, but its details vary across the ensemble. This presents a challenge to using POD, which will be employed to represent the realizations in terms of a few high energy modes. To avoid having the modes contaminated by these artifacts, the spatial domain was truncated to eliminate that portion of the sound field. Figure 1 shows the ensemble mean of the truncated realizations from Set 1. The relatively low sound levels near the ground result from a combination of upward refraction,

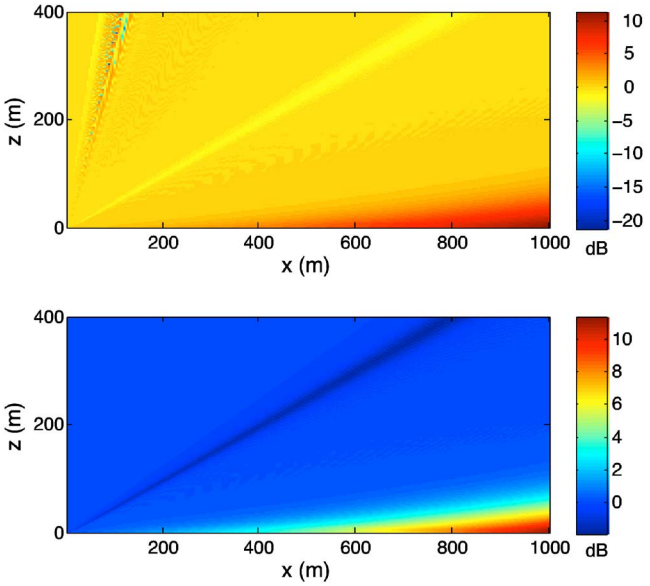

FIG. 2. (Color online) Comparison of a relative sound pressure snapshot before and after truncation of the spatial domain.

which predominates because most realizations have positive surface heat flux, and destructive interference with the ground reflections.

B. POD modes of the sound pressure

As described in Sec. II C, POD is applied to process snapshots. Each is taken to be one realization of the truncated sound pressure field from the LHS but with the ensemble average of all the realizations removed so that the POD modes optimally decompose the energy of variations about the ensemble average. The ensemble average employed here must be computed from the truncated realizations, not the full domain. The need to truncate the domain is clear in Fig. 2, which shows a single snapshot both before and after truncation of the domain. Failing to remove the fan-shaped artifact from each realization would pollute the POD modes by forcing them to incorporate the spurious high spatial frequency energy in the artifacts. Truncated snapshots like that depicted in the bottom frame of Fig. 2 will produce POD modes that represent the desired portion of the sound pressure field with many fewer modes than those from the raw snapshots. Better physical interpretation of the modes also should be possible.

Sensitivity results are discussed in Sec. IV only for the nine dominant POD modes. This group contains approximately 99.95% of the energy in the 50 snapshots that compose Set 1 of the 150 Hz realizations. The eigenvalues of the POD modes are left in the rank order produced by MATLAB, so the strongest mode in Set 1 is Mode 50 and the weakest is Mode 1. Modes 43–50 are shown in Fig. 3. Although Mode 43 contains much less energy than Mode 50, the values shown by the legends are similar because these modes have been scaled to have unit Euclidean norms. As the mode number decreases from 50 to 43, local features appear; the strongest modes contain the dominant features in the pressure field and progressively weaker modes add details at smaller scales.

In many computational mechanics applications, the strongest POD modes can be associated with physical traits and parameter sensitivities. In drawing this type of conclusion, it must be remembered that the POD modes represent variations about the mean condition, which was shown in Fig. 1 for the Set 1 realizations. It must also be understood that the modes in the present application were computed from snapshots based on simultaneous variations in six parameters, so some modes likely include coupled effects. This can lead to misattributing observed modal properties, so an attempt to connect the modes with physical behaviors will be delayed until Sec. IV.

At this juncture, only two preliminary observations will be made. First, the dominant contours and gradients in Mode 50 appear to be associated with downward refraction, most likely due to negative heat flux cases. This would account for the increased sound pressure, relative to the ensemble mean case, at down range locations near the ground. Second, Mode 49, which shows high sound pressure confined in a low-height channel along the ground, seems to contain variations from the mean upward refracting conditions associated with the ground impedance properties. These observations will be considered further in Sec. IV.

IV. SENSITIVITY ANALYSIS OF REDUCED ORDER MODELS FOR SOUND PRESSURE FIELDS

The broad field of SA, as described in Cacuci,[26] Saltelli *et al.*,[27] and Ronen,[28] includes a myriad of methods designed to address application-dependent goals and complications. Importance of the parameters is assessed here through the observation of both broad and localized effects in the sound pressure field, with some emphasis on variation in the sensitivity across the full range of the model parameters, i.e., the initial interest is in the output more than the details of the input. McKay[29,30] refers to this as a global perspective on sensitivity and uncertainty analysis.

A. Sensitivities from Latin hypercube samples

In applications that involve computationally expensive models that depend nonlinearly on the model parameters, Latin hypercube sampling often is used because it is implemented easily and in most cases explores the full range of each model parameter more efficiently than simple Monte Carlo sampling.[8,9,17,31] The equal probability partitioning of each parameter's domain in LHS has the virtues of providing a simple sampling process and unbiased estimates of response statistics. LHS is used here for two purposes: (*i*) to provide a broad view of the importance of the individual parameters and their interactions, and (*ii*) to supply data for building function approximations for estimating local sensitivities at interior points in the parameter space where samples are not available. For these purposes, the exact form of the true parameter joint distribution is not needed, but the parameter ranges must cover a physically reasonable region in the parameter space. The parameters in this study and their sampled ranges were listed previously in Table I.

Sound pressure sensitivities are estimated by employing the POD models as intermediaries. The orthonormal POD

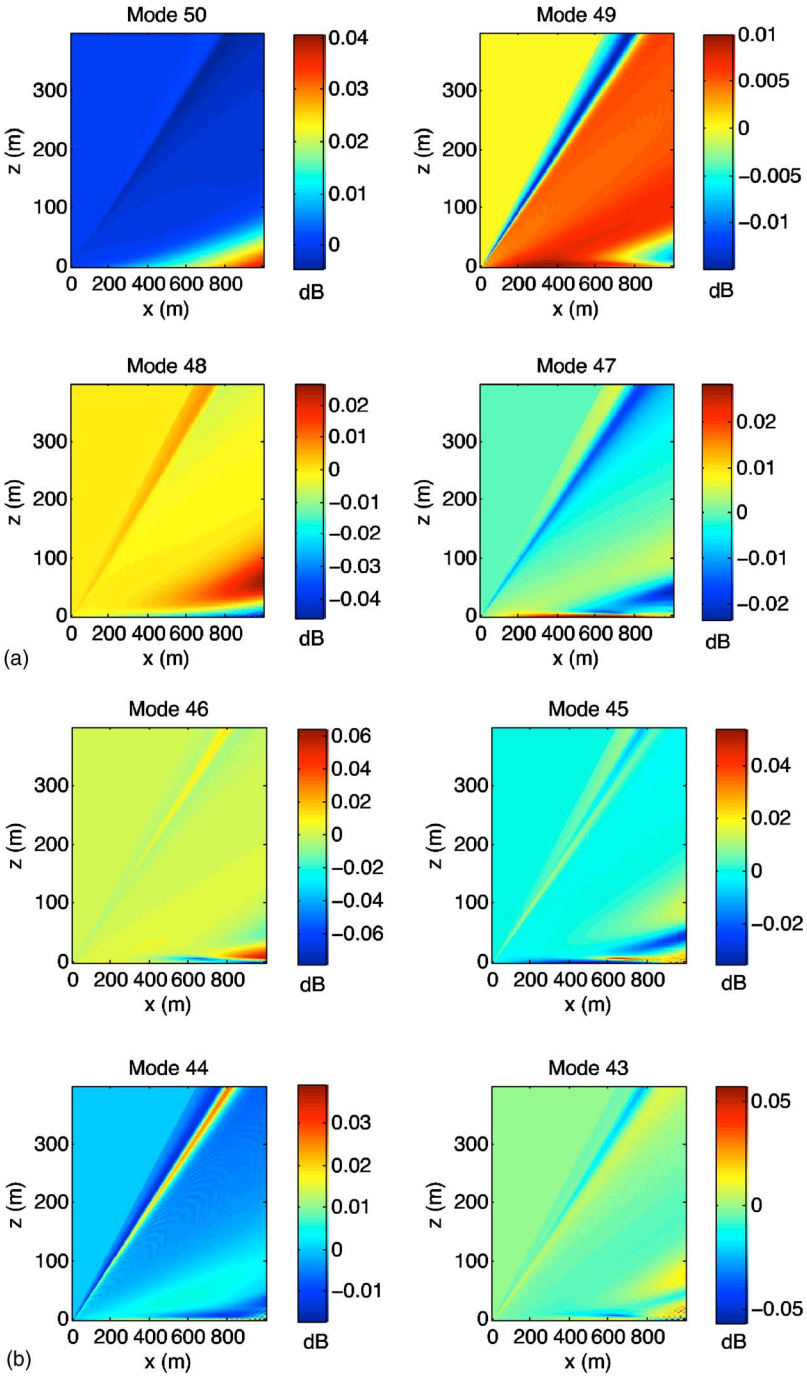

FIG. 3. (Color online) POD modes of the 150 Hz realizations from Set 1. Mode 50 is the most prominent mode and each successively lower mode has less energy, (a) Modes 50–47. (b) Modes 46–43.

basis provides the efficiency desired in a reduced order model and also simplifies the sensitivity computation by allowing a shift in focus from the sensitivity of the pressure field to that of the individual POD coefficients. Sensitivities are estimated at a given point, $\hat{\zeta}_0$, in the normalized parameter space as follows:

1. A POD model is computed from a given set of sound pressure realizations, i.e., the snapshots, for a specific source frequency. The sound pressure field may then be simulated at $\hat{\zeta}_0$ via the CWMs described in Sec. II D, i.e., $p(\hat{\zeta}_0)-\bar{p}=\Sigma_p a_q(\hat{\zeta}_0)\varphi_q$, where $\bar{p}$ is the ensemble mean, which was subtracted before the POD was performed, $q=1,2,\ldots,N_r$, and each $a_q(\hat{\zeta}_0)$ is estimated from its CWM.
2. The sensitivity of each POD coefficient to each of the six normalized parameters, i.e., $S_m^q(\hat{\zeta}_0)=(\partial a_q/\partial\widehat{\zeta_m})|_{\hat{\zeta}_0}$, where $m=1,\ldots,M(=6)$, is estimated by fitting a linear regression model to a five-level full factorial sample (see, e.g., Saltelli[27] or Montgomery[32]) of the CWM in a small M-dimensional hypercube, $D_{\hat{\zeta}}(\hat{\zeta}_0)$, around $\hat{\zeta}_0$, i.e., $\widehat{\zeta_m}\in[\widehat{\zeta_{m0}}-\Delta\widehat{\zeta_m},\widehat{\zeta_{m0}}+\Delta\widehat{\zeta_m}]$,where $|\Delta\widehat{\zeta_m}/\widehat{\zeta_m}|=0.001$ was found by experimentation to achieve an excellent fit, with coefficient of determination $R^2>0.99$ in most cases. The slopes of the linear regression functions are the estimated sensitivities of the POD coefficients to the normalized parameters. The five-level full factorial sample begins with five evenly spaced values within each parameter's

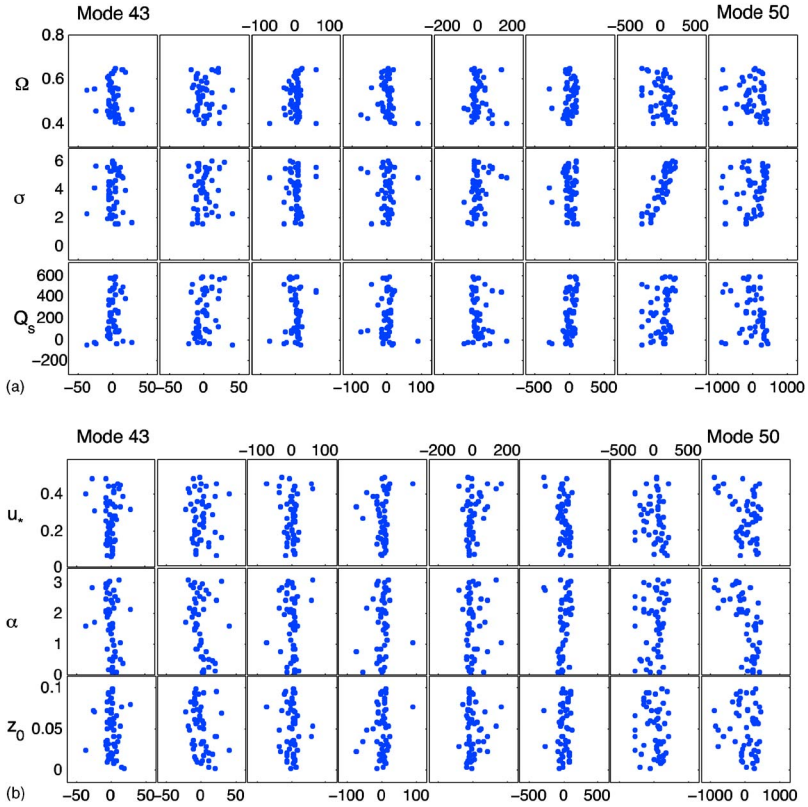

FIG. 4. (Color online) Scatter plots of POD coefficients for Set 1 of the 150 Hz realizations. Coefficients for the eight highest energy POD modes are plotted versus the six governing parameters: (a) porosity, Ω; flow resistivity, σ(kPa s m^{-2}); and surface heat flux, Q_s(W/m^2); (b) friction velocity, u_* (m/s); wind direction, α (deg); and roughness length, z_0 (m).

interval, $[\widehat{\zeta_{m0}}-\Delta\widehat{\zeta_m}, \widehat{\zeta_{m0}}+\Delta\widehat{\zeta_m}]$, and then forms an ensemble of sample vectors from every possible combination of the individual parameter samples. Full factorial sampling commonly is avoided in computational mechanics because of its high computational cost when high fidelity models are used, but this is not a concern here because each CWM evaluation is fast. It will be seen below that poor fits, e.g., $R^2<0.6$, occur around some parameter vectors at the boundary of the sampled domain. This seems unavoidable when an estimated function constructed from a relatively small sample population is used to extrapolate, as it necessarily must do to evaluate the full-factorial design in the neighborhood of a boundary point in the sampled parameter space. The justifiable precision and accuracy of the estimated sensitivities also may be in question when the CWM is used to interpolate within the parameter at locations relatively far from the closest training points, but as noted above, obtaining high precision and accuracy is less important in this application than building a broad picture on the relative importance of the parameters to support future probabilistic modeling and model validation goals.

3. The pressure field sensitivities are estimated from the POD coefficient sensitivities by differentiating the POD model

$$\left(\frac{\partial(p(\hat{\zeta})-\bar{p})}{\partial\widehat{\zeta_m}}\right)\Bigg|_{\hat{\zeta}_0} = \sum_q S_m^q(\hat{\zeta}_0)\varphi_m \tag{6}$$

and scaling the pressure through division by a representative value, which here is defined as the absolute value of the mean pressure deviation observed in the entire ensemble of truncated realizations. As is common in sensitivity analysis, scaling is performed to allow easy interpretation of sensitivities as percentage changes with respect to characteristic values of the parameters and the response variables. This procedure estimates the sensitivity of the normalized sound pressure field at each point in the computational domain to small changes in $\widehat{\zeta_m}$ as the sum of the modes weighted by the sensitivities of their coefficients. Every sensitivity value displayed below is normalized in this way. Sensitivities to the dimensional parameters are found by reversing the normalization, i.e., by dividing Eq. (6) by d_{ζ_m} and multiplying by the pressure scale factor.

B. Empirical observations from scatter plots of POD coefficients

Because the sound pressure varies in space and has high dimensionality in its discretized form, comprehensive SA requires evaluating both local and global effects. This will be of particular importance in future studies that attempt to address sensitivity to random spatial variations in acoustic impedance, topography, the atmosphere, and other relevant factors. No single sensitivity metric meets this need, but the difficulty can be overcome partly by reducing the dimensionality of the discretized pressure data. POD is used in this role herein: Sensitivity is assessed by projecting the snapshots onto the POD modes to compute the associated generalized Fourier coefficients of each snapshot and then computing the sensitivities of these coefficients to the six parameters in Table I.

The influence of the parameters on the POD coefficients for Set 1 of the 150 Hz realizations is summarized by the

scatter plots in Fig. 4. Each row of plots shows the sampled values of one of the six parameters and each column shows the coefficient of the corresponding POD mode, with the strongest mode, Mode 50, in the right-most column. The scatter plots exhibit several traits and corroborate some cause-and-effect relationships between parametric variations and the characteristics of the stronger modes. Some dominant traits are itemized here:

- Because each POD mode was scaled to have unit norm, the size of each mode coefficient reflects its relative importance in the snapshot.
- Some modes are featured in many realizations, e.g., Mode 50, whereas others contribute significantly only to a minority of realizations, e.g., Mode 43. This decrease in importance from the stronger mode through the progressively weaker modes should be expected owing to the optimal energy decomposition inherent to the POD formulation. This trend is also reflected in the increase in the spatial frequency of the modal contours in going from Mode 50 to 43, as shown in Fig. 3.
- A wide range of correlations are exhibited. Some scatter plots display little correlation between a given pair of parameter and mode number, e.g., z_0 and Mode 50. This indicates that $0.001 < z_0 < 0.1$ does not drive dominant full-field variations from the mean process. Others plots exhibit clear correlation, e.g., σ and Mode 49, which indicates strong sensitivity of the sound pressure variations in Mode 49 to flow resistivity. Some plots, such as Ω and Mode 50, are less definitive because they show wide scatter mixed with a noticeable correlation. The scatter indicates that these modes contain behaviors influenced by two or more parameters. These behaviors are detected naturally by LHS owing to its simultaneous parameter variations.
- Nonlinear correlation also is evident in some plots, particularly in the Mode 50 plots for α, u_*, and Q_s. The correlation in each case is partially obscured by scatter, which confounds the attribution of an affected POD mode to the variation of a single parameter. Permitting combined changes in parameters that individually have competing effects can lead to unexpected or seemingly contradictory behavior, such as negative values of Q_s associated with negative values of the Mode 50 coefficient, $a^{(50)}$. As noted in Sec. III B, Mode 50 appears to reflect in part the relative prominence of downward refraction as a primary variation from the mean, upward refracting, conditions; hence, given that $Q_s < 0$ promotes downward refraction, one might expect to find $a^{(50)} > 0$ if Q_s were the only parameter being varied. However, Q_s is not varied individually and the (Q_s, Mode 50) plot shows substantial scatter in the $a^{(50)}$ realizations for low Q_s, so the negative values of $a^{(50)}$ at low Q_s must be associated with parameter combinations whose net effect is to induce upward refraction by overwhelming the effect of low surface heat flux. Results described in Sec. IV D 2 further show that the direction of propagation with respect to the mean wind, i.e., whether the propagation is upwind or downwind, is responsible for this effect. This is consistent with the (α, Mode 50) and (u_*, Mode 50) scatter plots, which show that strongly upwind propagation cases are associated with negative values of $a^{(50)}$. Mode 50 thus is multipurpose in that its additive inverse is associated with shadow zone formation.
- Some parameters influence the presence of certain POD modes only in a limited range; this can be interpreted as a type of nonlinear correlation. The (Q_s, Mode 43) plot exemplifies this trait in that Mode 43 participates most strongly in realizations with low surface heat flux. Similarly, high u_* is correlated with the presence of Mode 45, which also correlates moderately with high α (i.e., upwind propagation) when the Mode 45 coefficient is positive and low α (i.e., downwind propagation) when this coefficient is negative. This makes sense because Mode 45 shows a deficit near the ground, a trait which would be promoted by upward refraction. Mode 45 also figures somewhat prominently in realizations with high ground impedance, i.e., low values of porosity and high values of flow resistivity, and is mildly correlated with Q_s. However, the wide scatter in the Mode 45 coefficients for cases with high ground impedance suggests that Mode 45 is primarily driven by the interaction between wind direction and friction velocity, which happens to be promoted by higher ground impedance values.

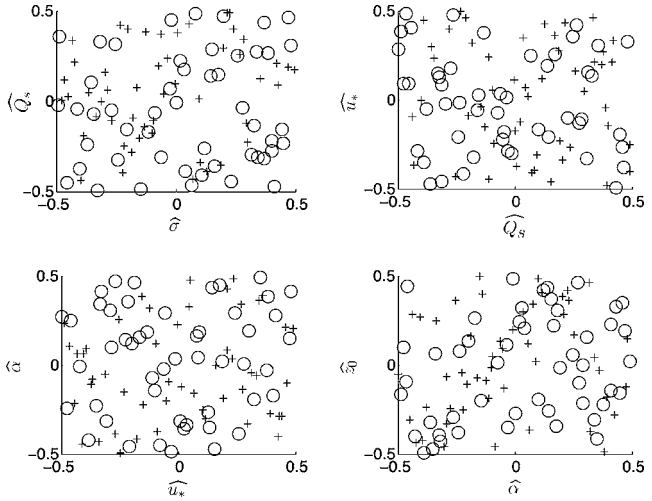

FIG. 5. Scatterplots of four pairs of normalized parameters from Set 1, the circular symbols, and Set 2, the plus symbols. Parameters are normalized as defined in Eq. (1).

C. Models for interpolating POD coefficients

Cluster weighted models will be used to estimate the sensitivity of the POD coefficients to variations throughout the parameter space. This section provides insight into how well CWMs represent the POD coefficients both in the neighborhood of the training realizations and at points relatively far from the training realizations. The benefits and shortcomings of using the Set 2 data to assess the accuracy of the Set 1 CWMs also will be examined. Figure 5 shows scatter plots of various parameters to demonstrate that the Set 2 realizations tend to be separated from the Set 1 realizations and therefore should challenge the ability of a CWM to approximate the fitted function at points between the training points in Set 1.

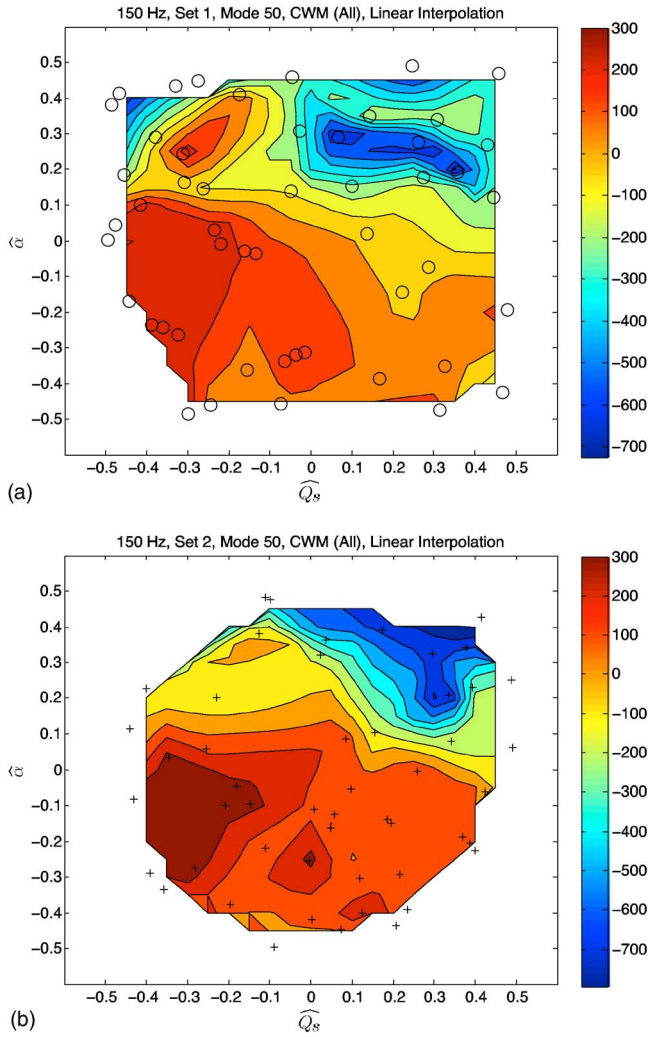

FIG. 6. (Color online) Contour plots of CWMs constructed for $a^{(50)}$, the Mode 50 generalized Fourier coefficient. In each plot, normalized values of the surface heat flux, Q_s, are on the horizontal axis and normalized values of the wind direction, α, are on the vertical axis. (a) CWM for Set 1 realizations built with all six parameters as independent variables and projected on the (Q_s, α) plane, (b) Same as (a) but for Set 2.

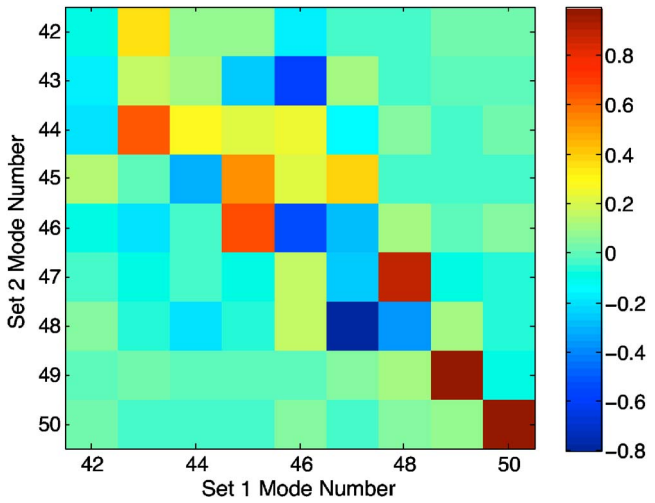

FIG. 7. (Color online) Inner product of the nine strongest POD modes from Set 1 and Set 2 of the 150 Hz realizations.

The number of dimensions in the parameter space precludes any attempt to graph a comprehensive relation between sound pressure and every parameter. This partly is mitigated by examining projections of CWMs as contour plots for specific pairs of parameters. For the sake of illustration, CWMs of the Mode 50 realizations from Set 1 are examined in detail here.

Figure 6 shows contour plots of CWMs for $a^{(50)}$, the Mode 50 generalized Fourier coefficient. The CWMs first are constructed in the six-dimensional parameter space and projected onto the normalized (Q_s, α) plane. The black circles in Fig. 6(a) show points from the Set 1 realizations in the (Q_s, α) plane where sound pressure fields were computed with the Crank-Nicholson parabolic equation method. The black plus symbols in Fig. 6(b) show the same information as the black circles but from Set 2 to facilitate cross validation of the Set 1 models. To generate these figures, the CWMs were evaluated only at the sample points in each plot. MATLAB's *griddata* function was used to linearly interpolate values onto a regular grid and contours were drawn through the resulting interpolated data. The irregular boundaries of the contour plots are caused by the inability of the *griddata* function to interpolate near the boundary of each data set.

Although not shown here, the CWM contours near each sample point in Fig. 6 are close to those formed by skipping the CWM model step and interpolating linearly throughout the (Q_s, α) domain; hence, the CWM accurately captures the training data. The spatial variations in Fig. 6 suggest that CWM or another localized nonlinear approximation could be crucial to accurate approximation away from the training data. As noted in Sec. I B, informal comparison with recent neural network results indicates that CWM might provide higher accuracy for a given number of training realizations, but more research is needed to confirm this.

In examining the use of POD modes from different data sets for cross validation of reduced order models, it must be emphasized that because these modes are based on the characteristics of the individual data sets, there is no a priori reason for a given rank-ordered mode from one set to match the same rank-ordered mode from another set, i.e., each POD mode is orthonormal to the modes from its own set, but need not be orthonormal to those from a validation set. This is clear in Fig. 7, which shows an image plot of the inner product of the nine strongest Set 1 and Set 2 POD modes. Recall that these modes have unit magnitude, so values near +1 and −1 indicate either parallel or anti-parallel modes, respectively. Comparing plots for specific modes, like those in Fig. 6(a) and Fig. 6(b), which must already be complicated by the effects of limited sampling, would therefore be meaningless unless these projection values are near ±1.

Figure 7 shows that only the two strongest modes from each set are nearly parallel and are therefore likely to exhibit similar sensitivities in the generalized Fourier coefficients. Modes 47 and 48 have fairly high projections between the two sets but appear to be switched, i.e., Mode 48 from Set 1 is similar to Mode 47 from Set 2 because their inner product is approximately 0.8; similarly, Mode 48 from Set 2 is similar to Mode 47 from Set 1, but switched in sign because their inner product is approximately −0.8. For these reasons, the

CWM is shown here only for the Mode 50 coefficient to examine the properties of the CWM approximation.

Significant modes in Set 1 and Set 2 differ because these sets were formed as random samples from a single, larger set of Latin hypercube samples, so it is almost certain that each subset will have some samples in portions of the parameter space that are not adequately sampled in the other subset. The primary consequence is that the Set 1 and Set 2 CWMs for Mode 50 are very similar in regions where they share samples, but the details are sensitive to local sample density, especially near the boundaries of the parameter space. Details also can be missed where few samples are available. This is obvious in the upper left corner of the Set 2 plot in Fig. 6, which lacks the peak near $(Q_s=-0.3, \alpha=0.25)$ in the Set 1 plot. The effect of uneven local sampling on sensitivity predictions will be examined in Sec. IV D 4.

These observations show that responses and their sensitivities estimated from a limited Latin hypercube sample population in conjunction with approximation methods must be interpreted carefully and should be counted on more for their global characteristics than local precision. This observation is consistent with trends seen in the iterative optimization of nonlinear systems through localized response surface models. It is also in line with a main goal of this study: to provide information for more refined probabilistic modeling based on the up-front identification of critical sensitivities. If limited sampling indicates high sensitivity to a given parameter, subsequent uncertainty modeling must emphasize the details of that parameter's uncertainty model and its possible dependence on other parameters.

D. Sensitivity of the sound pressure field

As noted in Sec. IV A, joining POD with CWM provides an efficient method for using sparse samples from the parameter space to estimate the mean value and other statistical moments of the first-order parameter sensitivities (i.e., normalized first derivatives) at each point in the spatial domain. This is achieved by generating a new ensemble of N_S Latin hypercube parameter samples, $\{\hat{\zeta}_0\}_{n=1}^{N_s}$, and evaluating the CWM of each of the retained POD modes in a small neighborhood around each of these samples. A local linear regression model is fitted within each sample neighborhood to the results from each CWM, and the sensitivities at each LH sample are computed from the coefficients in the corresponding linear regression model. The computational cost of this process grows substantially as the dimensionality of the parameter space is increased, so it would be impractical here without the use of efficient function approximations. Sensitivities might also be estimated more directly and quickly as finite differences of the CWMs, but this is not recommended because of the potential dependence of the finite differences on step size. The regression-based SA method is more robust and, as described below, provides diagnostic information about the quality of the estimated first-order sensitivities.

For the results presented here, the nine strongest POD modes are retained and a CWM is constructed for each mode coefficient in terms of all six parameters in Table I. Each local model around a given parameter vector is developed by fitting a hyperplane to a five-level full factorial sample of the CWM for each POD mode coefficient. For the six-dimension parameter space, this requires 15,625 evaluations of each mode's CWM for each of the Latin hypercube sample vectors. The large number of CWM evaluations is compensated for by the speed of each evaluation. A three-level factorial design would decrease this to only 729 evaluations of each POD mode's CWM for each $\hat{\zeta}_0$, but the five-level design provides better diagnosis of the quality of the linear fit, which helps to ensure that errors in the estimated sensitivities are limited to errors in the underlying CWMs.

The sensitivity at each point in the spatial domain is estimated for each Latin hypercube sample by combining the coefficient sensitivities with the POD modes as described above. The net result is an ensemble of N_S spatially varying sensitivities, i.e., $\{(\partial p(x,\hat{\zeta})/\partial\hat{\zeta})|_{\hat{\zeta}_0}\}_{n=1}^{N_s}$. Statistics are estimated by averaging across this ensemble at each spatial grid point.

Figure 8 shows the estimated mean sensitivity of the sound pressure field from the 150 Hz source simulations based on the full set of 100 realizations rather than those from Set 1 or Set 2 separately. Important items to understand when interpreting these plots include:

- As suggested in Sec. IV C, using only Set 1 or Set 2 produced questionable results due to inadequate sampling in certain portions of the parameter domain. This will be elucidated further in Sec. IV D 4.
- Each of the six parameters has been restricted to the inner 70% of its full domain to compute the sensitivities, the purpose being to avoid extrapolating with CWMs near the sampled parameter envelope. Although LHS was developed for global sampling, no guarantee exists that each parameter combination will be fully sampled in the tails of the joint distribution. Extrapolation therefore is almost unavoidable near the edges of a multidimensional domain; it is a natural consequence of using a small sample set to interrogate several parameters over a wide domain. The R^2 values computed in the linear regressions indicated whether a given CWM varied smoothly in the neighborhood of each sample point, so they were used to assess the justifiable confidence in the resulting sensitivities. Limiting the sampling range to 70% nearly always produced an R^2 of 0.98 or better, so the estimated sensitivities should not be contaminated by poor local regression models. However, the sensitivity ranges presented here might underestimate the true ranges by factors that cannot be known definitively without sampling a wider range of each parameter, which might push the parameters into unlikely physical combinations.
- The estimated mean values were computed as the 10% trimmed means to eliminate the few outliers that were not avoided by the 70% domain restriction discussed in the previous bullet item. Each outlier was clearly identifiable by its low R^2 value, usually 0.6 or less, which indicated that the CWM predicted locally high curvatures. Unless the physics of the process indicates the existence of a jump point or bifurcation, high curvatures in the parameter space of a regularized model typically indicate dropouts due to poor local sampling density. The trimmed mean therefore

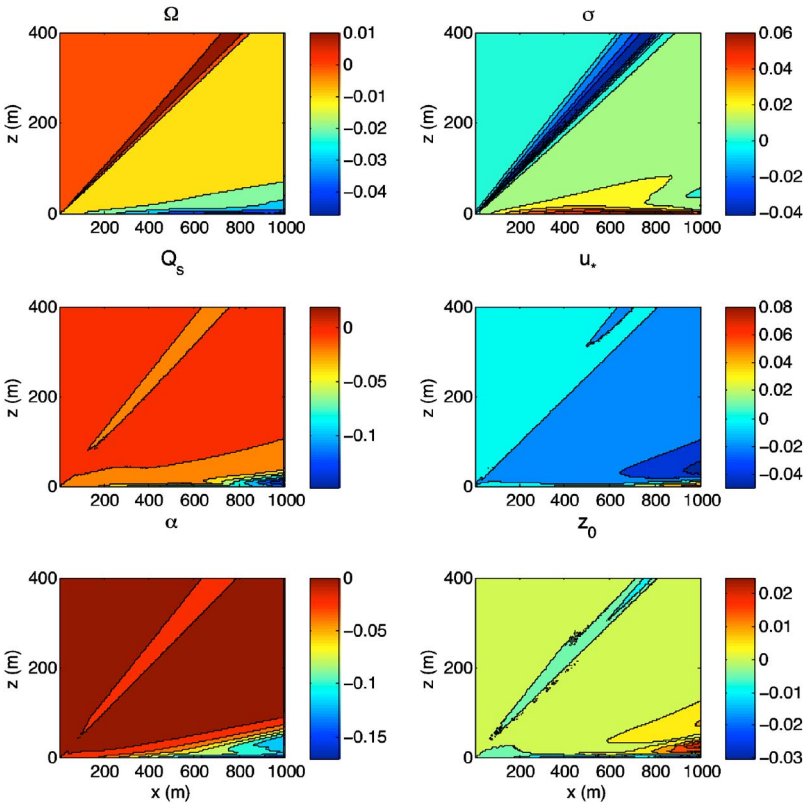

FIG. 8. (Color online) Estimated mean sensitivity to each model parameter of sound pressure from a 150 Hz source. Values in each sensitivity contour plot are normalized by the mean sound pressure and the full range of the respective parameter to facilitate equitable comparisons, and are based on the full original ensemble of 100 realizations.

provides a more robust estimate of the true mean in these conditions. Given that the 70% domain restriction clearly truncated the edges of the original domain, the remaining outliers are believed to result from small interior voids in the six-dimension parameter domain that were not sampled by the LHS algorithm when it selected the 100 sample points in the ensemble used to construct the CWMs. For example, the (σ, Q_s) scatter plot in Fig. 5 has a void centered near $(0.1, -0.1)$. Similar but smaller interior voids appear in the (Q_s, u_*) scatter plot near (0.2, 0.0) and in the (u_*, α) plot near $(-0.2, 0.0)$. These voids are endemic to sparse sampling and likely produce erroneous valleys in the CWMs of the POD coefficients, the result being locally high curvatures similar to those described in the previous paragraph.

- As described in Sec. IV A, each sensitivity value for a given dimensional parameter is normalized to facilitate comparison with sensitivities to other parameters. The normalization factors were chosen to indicate the typical percentage change in the pressure at a given location as a parameter ranges from its lowest value to its highest.

1. General observations

The top two plots in Fig. 8 show the mean sensitivity to the porosity and flow resistivity, i.e., the ground parameters, and the bottom four show the sensitivity to the surface heat flux, friction velocity, wind direction, and roughness length, i.e., the atmosphere parameters. Some clear trends seen in these plots can be explained through physical intuition. Principal observations include:

- Increasing the porosity and decreasing the flow resistivity lower the ground impedance and should therefore lower the ground reflection. The negative contours near the ground in the Ω plot and the corresponding positive contours in the σ plot follow this trend.
- Increasing surface heat flux promotes upward refraction and should therefore induce lower sound pressure near the ground at downstream locations. The Q_s plot follows this trend.
- Increasing the wind angle from 0 to 180° implies going from downwind to upwind propagation, which should produce lower near-ground sound levels as upward refraction is induced by the consequent alterations in the effective sound speed profile. The α plot follows this trend.
- Despite the qualitative agreement of these sensitivity plots with expected trends, the u_*, Q_s, and z_0 plots must be interpreted carefully because they average out the interaction between these parameters and the wind direction. This point is crucial to the correct interpretation of the sensitivities and to future modeling decisions based on these sensitivities, so it is examined carefully in Sec. IV D 2.

The contour plots in Fig. 9 show the estimated standard deviation of the normalized sensitivities at each point in the computational domain. Larger standard deviations are predicted near the ground and at down range locations. Parameters with the largest sensitivities in Fig. 8 also tend to have the largest standard deviations. Down range growth of the sensitivity standard deviation is similar to the result described recently by James and Dowling[6] for sound propagation in an underwater sound channel. They observed that the field uncertainty, as measured by the width of their predicted probability density function, increases with increasing range.

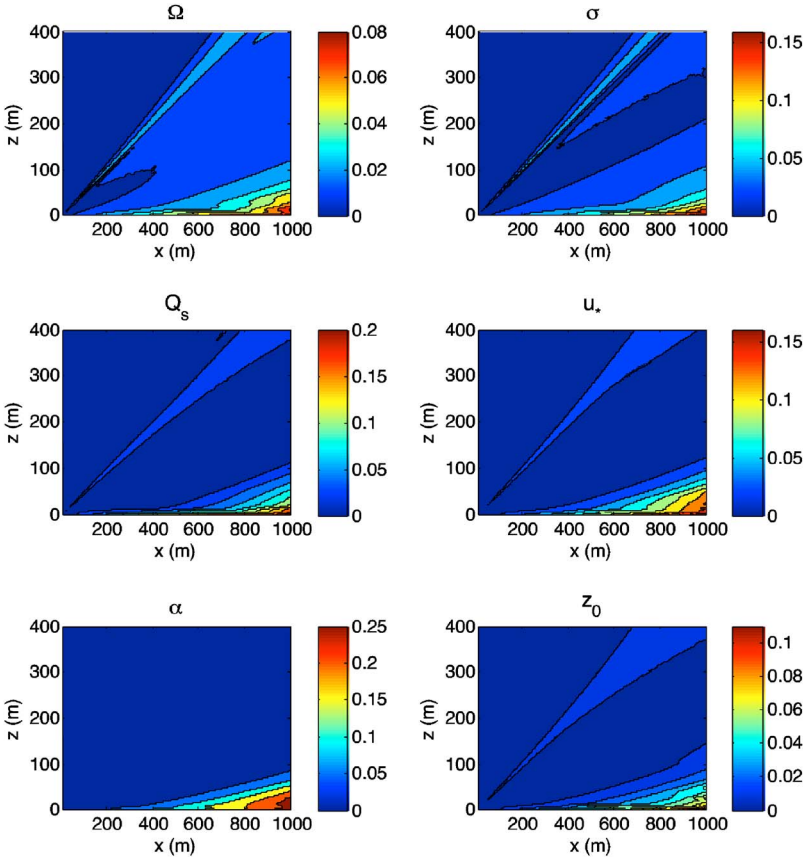

FIG. 9. (Color online) Estimated standard deviation of the normalized sensitivity to each model parameter of sound pressure from a 150 Hz source.

2. Effects of upwind and downwind propagation on sensitivities

The normalized sensitivity realizations were separated into upwind and downwind propagation cases so that their conditional statistics could be studied. For increasing friction velocity, near-ground sound levels would be expected to increase at downstream locations in downwind propagation and decrease in upwind propagation owing to the influence of u_* on the effective sound speed profile. The conditional sensitivity plots in Fig. 10 agree with this expectation, and the near symmetry of their combined range of values suggests that strong cancellation will occur when the combined average is computed. Similar but less pronounced trends were observed in the sensitivities to the other atmosphere parameters. The practical consequence is that the mean sensitivity levels in Fig. 8 underestimate the sensitivities conditioned on whether the propagation is upwind or downwind. Figure 10 and similar plots for the other parameters therefore enable assessment of the relative importance of accurately modeling both random and epistemic uncertainty in these parameters.

Much of the effect of wind direction on propagation sensitivities can be eliminated if the analyst is willing to forego knowing the sign of the sensitivity and focus instead on the mean of its magnitude. This is reasonable to do when the primary goal is to quantify the relative sensitivity levels for developing a more refined sampling strategy. Figure 11 shows the mean absolute values of the sensitivity ensemble that was used to generate the mean sensitivities in Fig. 8. The ranges of Fig. 11 contour values for the mean sensitivities to the atmospheric parameters include almost all of the absolute values of the direction-conditional contours, e.g., Fig. 10.

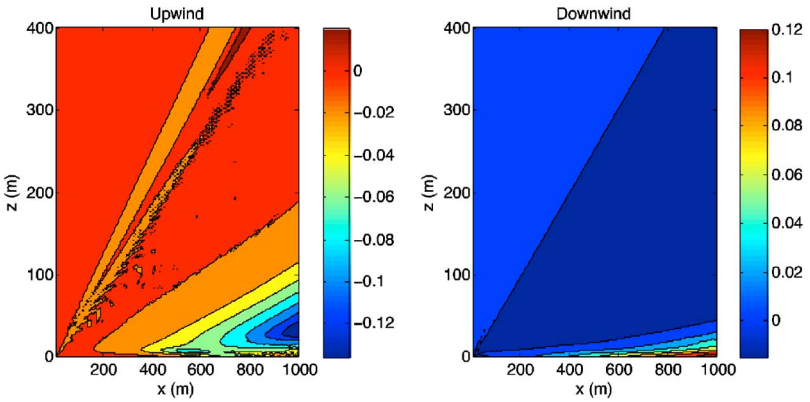

FIG. 10. (Color online) Estimated mean normalized sensitivity to friction velocity of sound pressure from a 150 Hz source. Upwind plot is for $90° \leqslant \alpha \leqslant 180°$; downwind is for $0° \leqslant \alpha < 90°$.

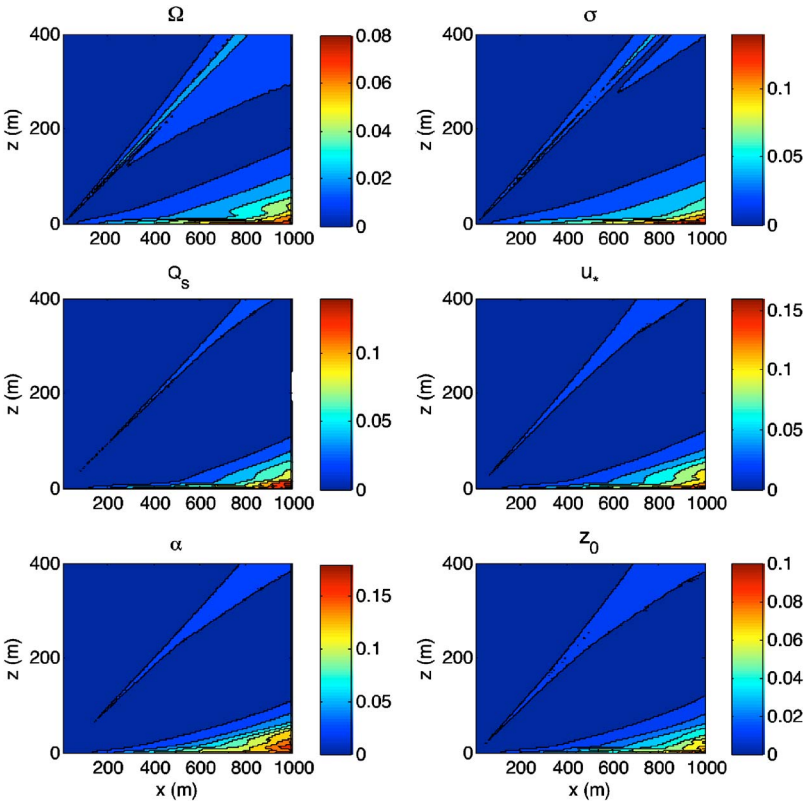

FIG. 11. (Color online) Estimated mean of the absolute value of the normalized sensitivity of sound pressure from a 150 Hz source to each model parameter. Values in each sensitivity contour plot are normalized by the mean sound pressure and the full range of the respective parameter to facilitate equitable comparisons.

The maximum absolute values of the Q_s and α contours are slightly underestimated because the absolute value operator decreases the effective range of the data.

3. Estimation of extreme sensitivities

Based on the sensitivity mean absolute values and the standard deviations, the highest likely sensitivity at each point in the computational domain can be estimated with a Gaussian assumption. This is illustrated in Fig. 12 for the mean plus three standard deviation contours. If the sensitivities were truly Gaussian and the mean absolute values were the true mean values, these contours would have a 0.00135 probability of being exceeded. These assumptions are not strictly true here, but this does not decrease the utility of the estimated extreme sensitivities as a basis for modeling decisions.

These plots suggest that, although the sound pressure is more sensitive to some parameters than to others, substantial uncertainty in any of the parameters ought to be modeled explicitly. For example, suppose LHS is to be performed with the 150 Hz source specified above, the porosity is known within a precision of 5%, and the friction velocity and roughness length are only known to within 25%. The extreme sensitivity values indicate that, if computational resources are limited, probabilistic simulations would be most effectively used if porosity were assumed to be deterministic and samples were concentrated in the other parameters.

Another use of these extreme sensitivity contours would be in an application when the sound at a specific height and down range location is the primary variable of interest. Suppose for the sake of discussion that the location is 50 m above the ground and 500 m down range of the 150 Hz source. The extreme sensitivity contours indicate that an uncertainty model of this problem need not incorporate uncertainty in z_0 because the maximum sensitivity to z_0 at this location is nearly zero. In contrast, the same height at 900 m down range shows some sensitivity to z_0, which therefore ought to be included in the uncertainty model to obtain a full picture of the range of possible responses.

4. Errors caused by poor local sampling of parameters in the original ensemble

The scatter plots of four parameter pairs in Fig. 5 show the separate locations of Set 1 and Set 2 samples. Section IV C shows that prediction details are sensitive to local sample density, especially near the boundaries of the parameter space. Consider the plot of (u_*, α) pairs in Fig. 5. The lower right corner is devoid of Set 1 samples, and the upper left corner and much of the upper right corner lack Set 2 samples. Set 1 therefore is deficient in cases of high friction velocity and strongly upwind propagation, and Set 2 is deficient in both low and high friction velocities combined with strongly downwind propagation.

Figure 13 shows the associated sensitivity to friction velocity from Set 1 and Set 2 with the upwind and downwind sensitivities plotted separately. The effect of partitioning the original set of 100 realizations into two sets is clear from comparison with Fig. 10. The Set 1-Upwind plot in Fig. 13 almost exactly reproduces the contour shapes in the upwind part of Fig. 10, and the Set 2-Downwind plot in Fig. 13 does the same for the downwind plot in Fig. 10. In contrast, the Set 1-Downwind and Set 2-Upwind plots do poorer jobs of reproducing the sensitivity characteristics of the full ensemble. The mean sensitivity levels also are larger in abso-

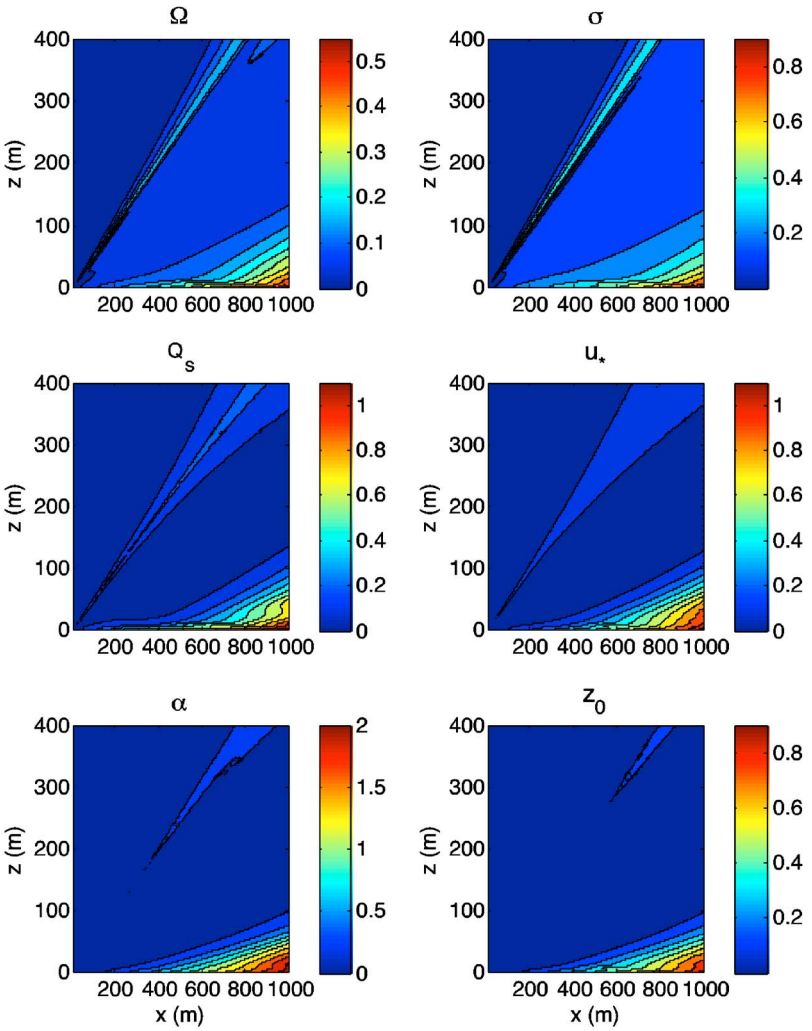

FIG. 12. (Color online) Estimated extreme normalized sensitivities based on a combination of the mean absolute value of the normalized sensitivities and three times the standard deviation of the normalized sensitivities.

lute value in the Set 1-Upwind and Set 2-Downwind plots than in the corresponding full ensemble plots. Randomly sampling the original LHS ensemble thus introduces bias into the resulting sensitivity statistics because the parameter domain no longer is decomposed into equal probability intervals. Validation of a function approximation constructed from a LHS ensemble must therefore involve the generation of an independent LHS ensemble and nonparametric model to avoid injecting additional statistical bias in either model.

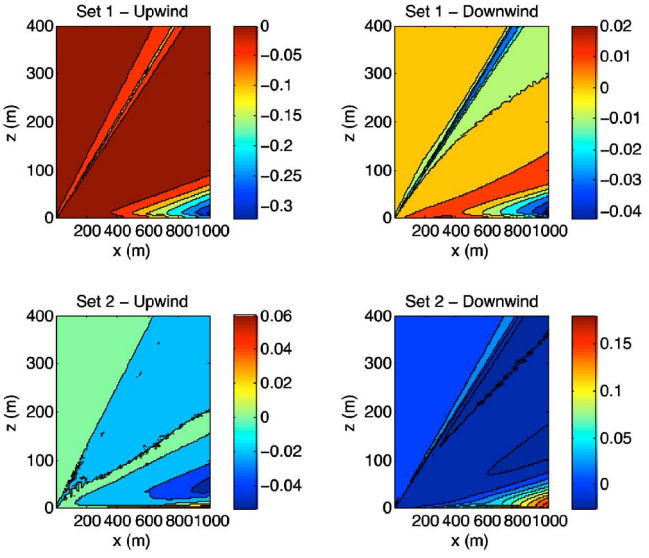

FIG. 13. (Color online) Estimated mean normalized sensitivity of sound pressure from a 150 Hz source to friction velocity from Set 1 and Set 2 samples. Upwind and downwind propagation cases are shown separately.

5. Possible importance of parameter correlation

It was observed in Section II B that for near-ground sound propagation, random variations in the ASL parameters seem likely to be independent of variations in the ground acoustic impedance parameters, at least away from the air-ground interface, but the individual air and ground parameters might not be independent of the other air and ground parameters, respectively. Some examples are cited here. Physical intuition suggests an inverse relationship and therefore a negative correlation between soil porosity, Ω, and flow resistivity, σ. Over large bodies of water, roughness length, z_0, and friction velocity, u_*, are related through Charnock's relationship.[15] Their correlation over ground is less clear but sensitive to local conditions, e.g., Clifton *et al.*[33] found z_0 was independent of u_* over snow until the drift threshold was reached. Stormy, cloudy conditions might tend to simultaneously lower the heat flux and increase the friction velocity. Certain wind directions, such as from the NW, are associated in many parts of the United States with stronger winds.

A vague sense of the relative importance of any correlation between parameters can be gained from the sensitivity results described above. For a near-ground source, maximum expected sensitivities of the sound level to the various parameters were found (see Fig. 12) to increase with down range distance from the source, x, and decrease with height above the ground, z. It seems fair to hypothesize that parameter correlation therefore will be of greater importance for large values of x and small values of z. Sound pressure was also found to be 25%–50% less sensitive to Ω than to the other parameters, so correlation between, e.g., Ω and σ likely is of less importance than correlation between u_* and z_0. A more authoritative and precise set of conclusions regarding the importance of parameter dependence would require an extensive survey of the available physical data as well as a thorough set of simulations based on samples from appropriate joint parameter distributions.

V. SUMMARY AND CONCLUSIONS

High-fidelity methods for predicting atmospheric acoustics can support important decisions in military and civilian applications. This high level of fidelity also means that a growing fraction of the total prediction error is due to the impossibility of acquiring full knowledge of the propagation environment. Rigorous validation of predictions therefore cannot be attempted without first understanding their sensitivities to reasonable variations in the governing parameters.

Sensitivity analysis of complex models often depends on the development of efficient representations of the response. Latin hypercube sampling (LHS) and proper orthogonal decomposition (POD) were employed to this end in conjunction with cluster-weighted models (CWMs). CWMs based on separate training and test ensembles were found to be locally consistent in regions of the parameter space where the training and test ensembles strongly intersected, but unavoidable discrepancies occurred in regions not adequately sampled in both the training and test sets. For ensemble sizes of 50 or greater like those used here, these local CWM differences likely do not cause large errors in the estimated lower-order statistics, but more work is required to quantify the effect of sample size and assumptions about the form of the CWM.

Ensemble statistics of the pressure sensitivities were computed to generate full-field contour plots of the mean and standard deviation of sensitivity to each parameter. The sensitivities were found to depend strongly on whether upwind or downwind propagation conditions prevailed. Pitfalls of sampling-based sensitivity analysis were also described, the primary concern being the existence of voids in an ensemble due to sparse sampling of the parameter space. These voids can produce inconsistencies between the training and test ensembles and thus complicate comparisons. Reliable mitigation of these difficulties is possible only through increasing the sampling density. Other global sampling schemes might perform better than LHS in a given application, but no global sampling method is universally superior and LHS usually is among the best.

Relative values of the estimated maximum sensitivities indicated that uncertainty in any of the six parameters considered here should be included in an uncertainty model if randomness or measurement imprecision are expected to affect the parameter. The importance of both randomness and measurement imprecision are too dependent on the details of a given application to permit further generality in this conclusion. Full-field contour plots of the sensitivities like those included here should help to guide future research and applications.

Although propagation parameters were modeled in this paper as independent random variables for sampling purposes, future efforts could extend this formulation to include random field models of the parameters with varying levels of correlation. A more complete sensitivity study would also include uncertainty in the source height and frequency, but not considering them in this study does not decrease the worth of the sensitivity results presented here, which are focused on identifying the relative importance of the parameters at every point in the spatial domain.

ACKNOWLEDGMENTS

Funding for this project was provided by the U.S. Army Engineer Research and Development Center. The constructive comments by the anonymous reviewers were valuable in revising the manuscript. The authors thank the reviewers for contributing their time and effort.

[1]D. K. Wilson, E. L. Andreas, C. L. Pettit, E. G. Patton, P. P. Sullivan, and J. W. Weatherly, "Characterization of uncertainty in outdoor sound propagation predictions," J. Acoust. Soc. Am. **121**, EL177–EL183 (2007).
[2]T. F. W. Embleton, "Tutorial on sound propagation outdoors," J. Acoust. Soc. Am. **100**, 31–48 (1996).
[3]P. J. Roache, *Verification and Validation in Computational Science and Engineering* (Hermosa, Albuquerque, NM, 1998).
[4]"Guide for the verification and validation of computational fluid dynamics simulations," Technical Report No. AIAA G-077-1998, American Institute of Aeronautics and Astronautics (1998).
[5]A. Ishimaru, *Wave Propagation and Scattering in Random Media* (IEEE Press and Oxford University Press, New York, 1997).
[6]K. R. James and D. R. Dowling, "A probability density function method for acoustic field uncertainty analysis," J. Acoust. Soc. Am. **118**, 2802–2810 (2005).
[7]S. Finette, "Embedding uncertainty into ocean acoustic propagation models," J. Acoust. Soc. Am. **117**, 997–1000 (2005).
[8]J. C. Helton and F. J. Davis, "Sampling-based methods," in *Sensitivity Analysis*, edited by A. Saltelli, K. Chan, and E. M. Scott, (Wiley, New York, 2000), Chap. 6, pp. 101–154.
[9]J. C. Helton, J. D. Johnson, C. J. Sallaberry, and C. B. Storlie, "Survey of sampling-based methods for uncertainty and sensitivity analysis," Technical Report No. SAND2006-2901, Sandia National Laboratories, Albuquerque, NM and Livermore, CA (2006).
[10]M. Mungiole and D. K. Wilson, "Prediction of outdoor sound transmission loss with an artificial neural network," Appl. Acoust. **67**, 324–345 (2006).
[11]M. West, K. Gilbert, and R. A. Sack, "A tutorial on the parabolic equation (PE) model used for long range sound propagation in the atmosphere," Appl. Acoust. **37**, 31–49 (1992).
[12]E. M. Salomons, *Computational Atmospheric Acoustics* (Kluwer, Dordrecht, The Netherlands, 2001).
[13]D. K. Wilson, "Simple, relaxational models for the acoustical properties of porous media," Appl. Acoust. **50**, 171–188 (1997).
[14]H. A. Panofsky and J. A. Dutton, *Atmospheric Turbulence: Models and Methods for Engineering Applications* (Wiley, New York, 1983).
[15]R. B. Stull, *An Introduction to Boundary Layer Meteorology* (Kluwer, Dordrecht, Germany, 1998).
[16]R. L. Iman and J. C. Helton, "A comparison of uncertainty and sensitivity analysis techniques for computer models," Tech. Report No. SAND84-1461, Sandia National Laboratories, Albuquerque, NM (1984).
[17]M. D. McKay, "Sensitivity and uncertainty analysis using a statistical

sample of input values," in *Uncertainty Analysis*, edited by Y. Ronen, (CRC, Boca Raton, FL, 1988), Chap. 4, pp. 445–186.
[18]M. Evans and T. Swartz, *Approximating Integrals via Monte Carlo and Deterministic Methods* (Oxford University Press, Oxford, 2000).
[19]R. L. Iman and W. J. Conover, "A distribution-free approach to inducing rank correlation among input variables," Commun. Stat.-Simul. Comput. **B11**, 311–334 (1982).
[20]P. Holmes, J. L. Lumley, and G. Berkooz, *Turbulence, Coherence Structures, Dynamical Systems and Symmetry* (Cambridge University Press, Cambridge, 1996).
[21]M. Kirby, *Geometric Data Analysis* (Wiley-Interscience, New York, 2001).
[22]K. C. Hall, J. P. Thomas, and E. H. Dowell, "Proper orthogonal decomposition technique for transonic unsteady aerodynamic flows," AIAA J. **38**, 1853–1862 (2000).
[23]C. L. Pettit and P. S. Beran, "Application of proper orthogonal decomposition to the discrete Euler equations," Int. J. Numer. Methods Eng. **55**, 479–497 (2002).
[24]N. Gershenfeld, *The Nature of Mathematical Modeling* (Cambridge University Press, Cambridge, 1998).
[25]N. A. Gershenfeld, B. Schoner, and E. Metois, "Cluster-weighted modeling for time series prediction and characterization," Nature (London) **397**, 329–332 (1999).
[26]D. G. Cacuci, *Sensitivity and Uncertainty Analysis*, (Chapman and Hall, London, CRC, Boca Raton, FL, 2003), Vols. **1 and 2**.
[27]A. Saltelli, K. Chan, and E. M. Scott, editors, *Sensitivity Analysis* (Wiley, New York, 2000).
[28]Y. Ronen, editor, *Uncertainty Analysis* (CRC, Boca Raton, FL, 1988).
[29]M. D. McKay, "Latin hypercube sampling as a tool in uncertainty analysis of computer models," in *Winter Simulation Conference*, Arlington, VA, 1992), (also available as a Los Alamos National Laboratory Report No. LAUR 92-2338.
[30]M. D. McKay, "Evaluating prediction uncertainty," Tech. Report No. LA-12915-MS, Los Alamos National Laboratory, Albuquerque, NM (1995).
[31]J. C. Helton and F. J. Davis, "Latin hypercube sampling and the propagation of uncertainty in analyses of complex systems," Reliab. Eng. Syst. Saf. **81**, 23–69 (2003).
[32]D. C. Montgomery, *Design and Analysis of Experiments*, 6th ed. (Wiley, New York, 2004).
[33]A. Clifton, J. Ruedi, and M. Lehning, "Wind tunnel measurements of saltation threshold for snow," in *American Geophysical Union Fall Meeting*, C21A-1053, San Francisco. (2005).

Determination of equivalent sound speed profiles for ray tracing in near-ground sound propagation

John M. Prospathopoulos[a] and Spyros G. Voutsinas
National Technical University of Athens, 9 Heroon Polytechniou Street, 15773 Zografou, Athens, Greece

(Received 4 December 2006; revised 28 June 2006; accepted 3 July 2007)

The determination of appropriate sound speed profiles in the modeling of near-ground propagation using a ray tracing method is investigated using a ray tracing model which is capable of performing axisymmetric calculations of the sound field around an isolated source. Eigenrays are traced using an iterative procedure which integrates the trajectory equations for each ray launched from the source at a specific direction. The calculation of sound energy losses is made by introducing appropriate coefficients to the equations representing the effect of ground and atmospheric absorption and the interaction with the atmospheric turbulence. The model is validated against analytical and numerical predictions of other methodologies for simple cases, as well as against measurements for nonrefractive atmospheric environments. A systematic investigation for near-ground propagation in downward and upward refractive atmosphere is made using experimental data. Guidelines for the suitable simulation of the wind velocity profile are derived by correlating predictions with measurements. © *2007 Acoustical Society of America.*
[DOI: 10.1121/1.2764476]

PACS number(s): 43.28.Js, 43.28.En, 43.28.Fp [RMW] Pages: 1391–1403

I. INTRODUCTION

Sound propagation in the atmosphere is a complex problem involving a number of physical phenomena such as geometrical spreading, molecular absorption, reflection from the ground, refraction by wind velocity, scattering by atmospheric turbulence and diffraction by obstacles. During the last decades a variety of methods, originally developed for applications in underwater acoustics, have been used to predict the sound propagation loss in the atmospheric environment. These methods can be classified as ray tracing, analytic (normal modes models), spectral integration techniques usually formulated as variations of the fast field program (FFP), parabolic equation (PE) and linearized Euler finite-difference time-domain (FDTD) models.

From the mathematical point of view, FFP[1–5] and normal modes[6,7] methods are more accurate, but they are applicable to range independent environments while at high frequencies they have heavy computational demands. The normal modes method can be extended to range dependent environments (coupled modes)[8] by significantly surcharging the computational cost. PE[9–11] and ray tracing[12,13] models are less accurate but best suited for fast calculations. In cases of high variations of the terrain or of the medium properties, however, the parabolic approximation in PE is not valid. In recent years, FDTD[14–16] models have drawn substantial interest due to their ability to handle complex topography, meteorology and complicated phenomena such as scattering from buildings and trees or dynamic turbulence fields. The treatment of finite ground impedance and the time-consuming calculations—in order to get accurate results—are the main drawbacks of these models.

The geometrical approximation of ray theory, in spite of being formulated as a high frequency approach, has given reliable predictions at long distances, even in the low frequency range.[17] L'Esperance *et al.*[18,19] developed a simple geometrical model based on the fact that the ray trajectories are circles for a linear sound speed profile. They took into account most of the sound energy attenuating mechanisms: the ground effect, the atmospheric absorption, the effect of turbulence and the refraction of rays by the wind. A major drawback of ray tracing models is that they fail to predict sound pressure levels in the so-called "shadow zones." To overcome this weakness, L'Esperance *et al.* included the analytical solution proposed by Berry and Daigle[20] for the prediction of sound pressure levels in shadow zones formed in the case of an upward refractive atmosphere. A more advanced ray tracing model was developed by Lamancusa and Daroux,[21] applicable to moving medium over complex terrain. They integrated the axisymmetric ray trajectory equations to produce the ray paths and then calculated the propagation losses due to the ground, the molecular absorption and the refraction along each ray. The shape of the complex terrain as well as the variation of the velocity, were incorporated into the discretized trajectory equations using a numerical grid procedure.

The present paper applies a ray tracing model in near-ground propagation aiming at providing guidelines for introducing the appropriate sound speed profiles in refractive atmosphere. The discretization procedure described by Lamancusa and Daroux[21] is used in order to include the velocity-temperature variations. Section II formulates the propagation problem and models the physical parameters. For the sake of completeness material from cited references is briefly outlined. In Section III, the model is validated against experimental data in nonrefractive atmosphere and numerical predictions of other methods. In Sec. IV, the effect

[a]Author to whom correspondence should be addressed. Electronic mail: jprosp@fluid.mech.ntua.gr

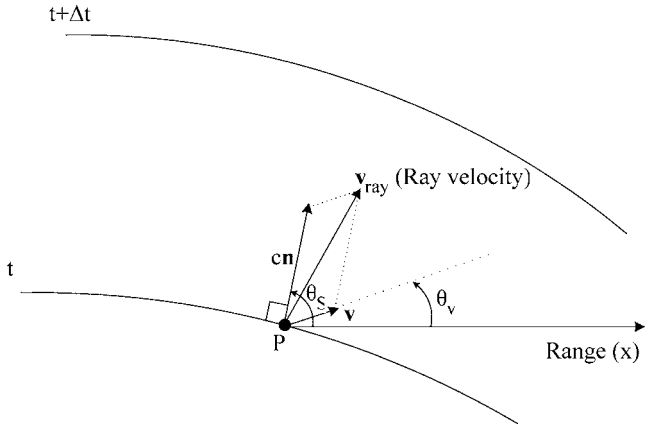

FIG. 1. Wave propagation in a moving medium. The ray velocity $\mathbf{v}_{\text{ray}}$ is the sum of the sound speed $c\cdot\mathbf{n}$ and the wind velocity $\mathbf{v}$.

of wind velocity and temperature profile is examined in detail. For a source height between 30 and 100 m, as in the case of a wind turbine, the mean wind velocity and temperature profiles estimated by the similarity theory produce satisfactory results.[22] However, in near-ground propagation (source height up to 5 m), the use of mean velocity profiles may not well simulate the high temporal fluctuations of the steep gradients which significantly affect the number of eigenrays. L'Esperance *et al.*[18] used an equivalent linear sound speed profile in their simple geometrical model, the gradient of which is derived from the mean logarithmic profiles according to the theory of the first Fresnel zone. This point is revised in Sec. IV which provides guidelines for determining the wind velocity profile in ray tracing models. Finally, Sec. V gives a summary and conclusions.

II. DESCRIPTION OF THE MODEL

A. Mathematical formulation of the axisymmetric problem

A point source of specified power spectrum, placed at $(0,0,z_S)$ with respect to a cylindrical system (x,r,z), is propagating sound in all directions above a given terrain. Assuming cylindrical symmetry for the medium properties and the terrain, and within the framework of ray theory, the calculation of the sound pressure level spectrum at the receiver point (x_R,z_R) consists of:

(1) Finding the eigenrays (resolve the ray tracing equations),
(2) Calculating the energy losses along the eigenrays, and
(3) Synthesizing the sound pressure level by superposing the contributions of the eigenrays for the entire frequency spectrum.

For a medium moving with velocity $\mathbf{v}$, the ray tracing equations are formulated with respect to the "wave slowness vector" $\mathbf{S}(\mathbf{r})=\nabla\tau(\mathbf{r})$, with $\mathbf{r}=(x,z)$. The equation $t=\tau(\mathbf{r})$ defines the wave front moving with $\mathbf{v}_{\text{ray}}=\mathbf{v}+c\cdot\mathbf{n}$, where $\mathbf{n}$ is the normal unit vector and c is the speed of sound (Fig. 1), so[23]

$$\frac{d\mathbf{r}}{dt}=c^2\frac{\mathbf{S}}{\Omega}+\mathbf{v},\quad \frac{d\mathbf{S}}{dt}=-\frac{\Omega}{c}\nabla c-(\mathbf{S}\cdot\nabla)\mathbf{v}. \tag{1}$$

$$\Omega=\frac{c}{c+\mathbf{v}\cdot\mathbf{n}}=\frac{c}{c+|\mathbf{v}|\cos(\theta-\theta_v)}, \tag{2}$$

$$\theta=\tan^{-1}(S_z/S_x),\quad \theta_v=\tan^{-1}(v_z/v_x).$$

In Eq. (2), v_x,v_z and S_x,S_z are the horizontal and the vertical components of the wind velocity and the wave slowness vector, respectively.

The amplitude of the sound pressure along a ray is given from the Blokhintzev invariant[24,25]

$$\frac{P^2A|\mathbf{v}_{\text{ray}}|}{\rho\Omega c^2}=\text{const}, \tag{3}$$

where A is the cross-sectional area of the ray tube and ρ is the density of the medium so that the flow power along a ray tube is constant. The speed of sound is given as

$$c=\sqrt{\gamma R_d T_v}, \tag{4}$$

where $\gamma=c_p/c_v$ is the ratio of the specific heats, R_d is the gas constant of dry air and T_v is the virtual temperature which accounts for humidity. In most cases the humidity effects are neglected, so T_v is approximated by the absolute temperature T.

B. Estimation of the wind velocity profile

In complex terrain, the wind velocity can vary spatially and range-dependent profiles should be taken into account. However, in a variety of cases the terrain between the source and the receiver is flat or fairly smooth, so that the mean wind velocity profile can be considered range independent.

For neutral atmospheric conditions the mean wind velocity profile follows the logarithmic law of a fully developed boundary layer[26]

$$v(z)=\frac{u_\star}{K}\ln\left(\frac{\Delta z}{z_0}\right), \tag{5}$$

where Δz is the height above ground, K is the von-Karmann constant, z_0 is the roughness length and $u_\star$ is the friction velocity.

In stratified atmospheric conditions, the logarithmic wind velocity profile is modified as follows[27]:

$$v_x(z,u_\star,T_\star)=\frac{u_\star}{K}\left[\ln\left(\frac{\Delta z}{z_0}\right)-\Psi_1\left(\frac{\Delta z}{L_{\text{mo}}}\right)\right]. \tag{6}$$

The Monin-Obukhov length L_{mo} is positive or negative for stable or unstable conditions, respectively. A similar equation applies for the potential temperature variation

$$\theta(z,u_\star,T_\star)-\theta_0=\frac{0.74T_\star}{K}\left[\ln\left(\frac{\Delta z}{z_0}\right)-\Psi_2\left(\frac{\Delta z}{L_{\text{mo}}}\right)\right], \tag{7}$$

where $T_\star$ is the temperature scale and θ_0 is the potential temperature at z_0. The Ψ_1,Ψ_2 functions are called the diabatic momentum and heat profile correction functions, respectively. Their expression depends on the stratification conditions (see Ref. 27). The temperature scale and the Monin-Obukhov length are defined as

$$T_\star=-\overline{v_z'\theta'}/u_\star \tag{8}$$

$$L_{\mathrm{mo}} = -\frac{u_\star^3 \bar{T}}{Kg\overline{v_z'\theta'}} = \frac{u_\star^2 \bar{T}}{KgT_\star}, \tag{9}$$

where $\bar{T}$ is the mean surface temperature, g is the gravity acceleration and $v_z' = v_z - \bar{v}_z$, $\theta' = \theta - \bar{\theta}$ are the turbulent fluctuations around the mean value of the vertical wind component and the potential temperature, respectively. It is noted that the potential temperature is related to the absolute temperature through the relationship $\theta = T(p_s/p_{s0})^{R_d/c_p}$, with p_s the atmospheric pressure and p_{s0} its reference value (1 atm).

Using least square fitting as Nieuwstadt[28], it is possible to determine $T_\star$ and $u_\star$ through Eqs. (6) and (7), on the basis of a set of velocity and temperature measurements. Then Eq. (9) will determine L_{mo}. By applying the Marquardt algorithm,[29] convergence is attained in about five iterations.

C. Modeling of the attenuation factors

1. Ground absorption

The resistance of the ground to the wave propagation is expressed by *impedance* which is a function of the properties of the ground materials. In the literature, several approximations for the simulation of the characteristic impedance of a material can be found, using from one up to four physical parameters.[30–33] Most commonly used is the one-parameter approach which treats the specific flow resistivity σ as a single parameter.

In the present work the semiempirical formulas proposed by Chessell[34] and Nicolas *et al.*[35] are adopted for the characteristic impedance $Z_c = R + iX$ and the wave propagation number of the material $k_b = k_1 + ik_2$

$$R = 1 + 9.08(10^{-3} f/\sigma)^{-0.75}, \tag{10}$$

$$X = 11.9(10^{-3} f/\sigma)^{-0.73}, \tag{11}$$

$$k_1/k = 1 + 10.8(10^{-3} f/\sigma)^{-0.70}, \tag{12}$$

$$k_2/k = 10.3(10^{-3} f/\sigma)^{-0.59}, \tag{13}$$

where $k = 2\pi f/c$ and σ must be given in kg/sm^3.

For large values of the specific flow resistivity ($\sigma > 3 \cdot 10^5$ kg/sm^3), the incoming sound is refracted normally to the surface and the impedance of the ground is almost independent of the angle of incidence. Under such conditions, characterized as *local reaction*,[32,34,36] simplified relationships can be used for the impedance of the ground as well as for the quantities required for the calculation of the reflection coefficient. When the specific flow resistivity is low ($\sigma \ll 3 \cdot 10^5$ kg/sm^3), which is the case for a snow layer or a moisture layer in the woods, the assumption of local reaction conditions is no longer valid. The behavior of the material is then characterized by *extended reaction*.[36]

In the subsequent analysis, local reaction conditions are assumed. For such conditions, the reflection coefficient of a plane wave R_p is given as[34]

$$R_p = \frac{\sin\phi - \beta_c}{\sin\phi + \beta_c}, \tag{14}$$

where ϕ is the angle of incidence and $\beta_c = 1/Z_c$ is the admittance of the material. When the height of the source and the receiver from the ground is large, the reflection coefficient can be satisfactorily represented by R_p. However, when the source and the receiver are close to the ground, i.e., for low angles of incidence (less than 5°), the fact that the wave front is spherical and not planar should be taken into account. This is accomplished by adding the corrective term $(1-R_p)F(w)$, known as the "ground wave," to R_p

$$Q = R_p + (1 - R_p)F(w). \tag{15}$$

Q represents the spherical reflection coefficient and $F(w)$ is the boundary loss coefficient. The so-called "numerical distance" w is given by Chien and Shoroka[37] and Ingard.[38]

If the ground is simulated by two or more layers of different materials, the equivalent impedance is given in terms of the impedances of these materials. In the case of a thin layer of an absorbent material followed by a semi-infinite layer of an acoustically hard material

$$Z = Z_c \coth(-ik_b d), \tag{16}$$

where d represents the thickness of the layer of the absorbent material.

In the case of a layer of an absorbent material lying upon a semi-infinite layer of a less absorbent material

$$Z = Z_1 \frac{Z_2 - iZ_1 \tan(k_b d)}{Z_1 - iZ_2 \tan(k_b d)}, \tag{17}$$

where Z_1 and k_b are the characteristic impedance and the wave number of the material of the upper layer, whereas Z_2 is the characteristic impedance of the material of the semi-infinite layer.

The reflection coefficients R_p and Q are calculated from Eqs. (14) and (15), by substituting Z_c with the equivalent impedance Z (Eqs. (16) and (17)).

2. Molecular absorption

Molecular absorption in the atmosphere has been systematically measured and theoretically predicted. The frequency, humidity and temperature dependent attenuation coefficient A for air absorption may be calculated using the following equation:[39,40]

$$\frac{A}{p_s} = \frac{F^2}{p_{s0}} \left\{ 1.84 \cdot 10^{-11} \left(\frac{T}{T_0}\right)^{1/2} + \left(\frac{T}{T_0}\right)^{-5/2} \left[0.01275 \frac{\exp(-2239.1/T)}{F_{r,O} + F^2/F_{r,O}} + 0.1068 \frac{\exp(-3352/T)}{F_{r,N} + F^2/F_{r,N}} \right] \right\} \frac{nepers}{m\ atm}, \tag{18}$$

where $F = f/p_s$, and $F_{r,\mathrm{O}}$, $F_{r,\mathrm{N}}$ are the relaxation frequencies for oxygen and nitrogen, respectively (see Refs. 39 and 40).

3. Interaction with the atmospheric turbulence

Atmospheric turbulence causes fluctuations of the sound waves in amplitude and phase which can significantly affect the mean sound pressure. Daigle *et al.*,[41] Clifford and Lataitis,[42] and Attenborough[43] have formulated relationships of the mean sound pressure field in the presence of turbulence, for rectilinear propagation over flat terrain. These formulations also take into account the interaction between the direct and the reflected sound wave. Experiments indicate that the distance between them is comparable to the correlation length of the meteorological fluctuations.[41] L'Esperance *et al.*[18] extended this theory to the case of more than one reflected wave reaching the receiver resulting from the interaction with the wind velocity. However, they take into account only the phase fluctuations. In the present paper, the amplitude fluctuations are added, based on the concept described by Daigle *et al.*[41] Thus, the mean time-averaged value of the squared turbulent sound pressure is taken as

$$\frac{\langle p^2\rangle}{p_0^2} = \sum_{i=1}^{N}(1+\langle a^2\rangle)C_i^2 + 2\sum_{i=2}^{N}\sum_{j=1}^{i-1} C_i C_j \times \cos\left[\omega(\tau_j-\tau_i) + Arg\left(\frac{Q_j}{Q_i}\right)\right]\Gamma_{ij}, \tag{19}$$

where p_0 is the pressure 1m away from the source and

$$C_i = \frac{A_i \cdot |Q_i|}{r_i}. \tag{20}$$

Q_i, Q_j are the spherical reflection coefficients calculated from Eq. (16), A_i, A_j are the absorption coefficients calculated from Eq. (18) and r_i, r_j are the total distances covered by the rays i, j respectively. N stands for the total number of eigenrays, $\langle a^2\rangle$ is the variance of the amplitude fluctuations and Γ_{ij} is the coherence coefficient between rays i and j. It is expressed as

$$\Gamma_{ij} = \exp[-\sigma_t^2(1-\rho_{ij})], \tag{21}$$

where σ_t^2 is the variance of the phase fluctuations and ρ_{ij} is the phase covariance of rays i and j $(0<\rho_{ij}<1)$. Daigle *et al.*[41] calculated $\langle a^2\rangle$ and σ_t^2 as functions of the distance between source and receiver, the outer scale of turbulence and the turbulent index of refraction (for their evaluation see Ref. 41).

The turbulent index of refraction is calculated in terms of the velocity and temperature variances using the relationship formulated by Wilson and Thompson[44] by neglecting the contribution of the cross wind component of the velocity. The variances of the velocity and temperature, as well as their correlation product, are approximated by semiempirical formulas in terms of $u_\star$ and $T_\star$, which are calculated as in Sec. II D. Finally, for the phase coherence ρ_{ij}

$$\rho_{ij} = \frac{L_t}{l_{ij}}\int_0^{l_{ij}/L_t} e^{-t^2}dt, \tag{22}$$

where ℓ_{ij} is the maximum distance between the eigenrays i and j. However, it has been found that the predictions of the turbulence model are improved when ℓ_{ij} equals half this value (see Ref. 41).

D. Numerical implementation

The numerical integration of the ray tracing equations is performed in a computational domain which is defined so that all possible eigenrays are contained in it. The representation of the velocity and temperature, as well as their derivatives, is made using a numerical grid which is equidistant in the horizontal direction and follows a geometrical progression in the vertical direction. In this way, any steep gradients of the velocity close to the ground are represented satisfactorily.

Ray trajectories are generated by integrating Eqs. (1) and (2) for different launching angles. At each time step, the grid cell which contains the current point of the ray trajectory is determined. Then the value of each quantity required is interpolated in the four grid points of the cell. The Bulirsch-Stoer integration algorithm with variable time step[45] has been adopted as it was found superior to the Runge-Kutta method (with constant or variable time step) in terms of accuracy and speed of convergence. To start the procedure, initial conditions $(t=0)$ are required. If x_S and z_S are the coordinates of the position of the source and θ_0 is the launching angle of the ray, initial conditions are as follows:

$$x = x_S, \tag{23}$$

$$z = z_S, \tag{24}$$

$$S_x = \frac{\cos\theta_0}{c + |\mathbf{v}|\cos(\theta_0 - \theta_v)}, \tag{25}$$

$$S_z = \frac{\sin\theta_0}{c + |\mathbf{v}|\cos(\theta_0 - \theta_v)}. \tag{26}$$

At the end of every time step, the position of the new point (x_p, z_p) of the trajectory is used in order to check whether:

- The ray intersects the ground surface or a turning point is present.
- The ray left the computational domain in the horizontal direction $(x_p > x_R)$.
- The ray left the computational domain in the vertical direction $(z_p > z_L, z_L$ is the vertical dimension of the domain).

If the second or third check is true, the next ray is launched.

When reflection occurs, the position and the direction of the ray must be properly modified before the next time step. The geometrical procedure for the specification of the ray conditions after the reflection is described in Ref. 21. The geometrical approximation error of the procedure is minimized by reducing the integration time step close to the ground. This is automatically taken care of by variable time step integration methods.

The eigenray tracing is an iterative procedure which consists of determining the proper launching angles that define the rays arriving at the receiver. As a first step, a ray fan is launched in a range of angles including all possible eigenrays. After the integration of the first ray path is completed, the initial launching angle is increased by an angle step of about 0.1°, the next ray is launched and so on until all rays have been launched. For each ray, its "history" is recorded:

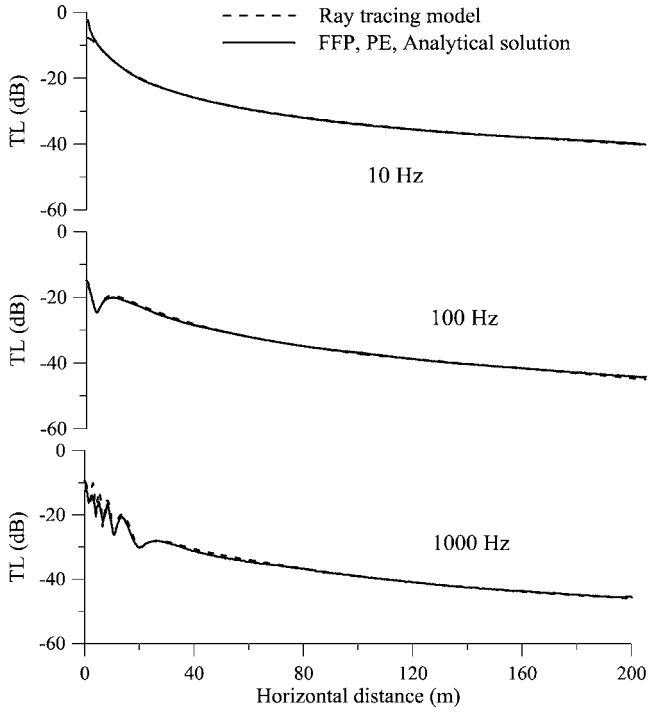

FIG. 2. Downwind propagation conditions with linear wind velocity profile of gradient 0.1 s^{-1}. Source height and receiver heights are 5 and 1 m, respectively. Comparison of the transmission loss (TL) predictions from different methodologies with increasing frequency.

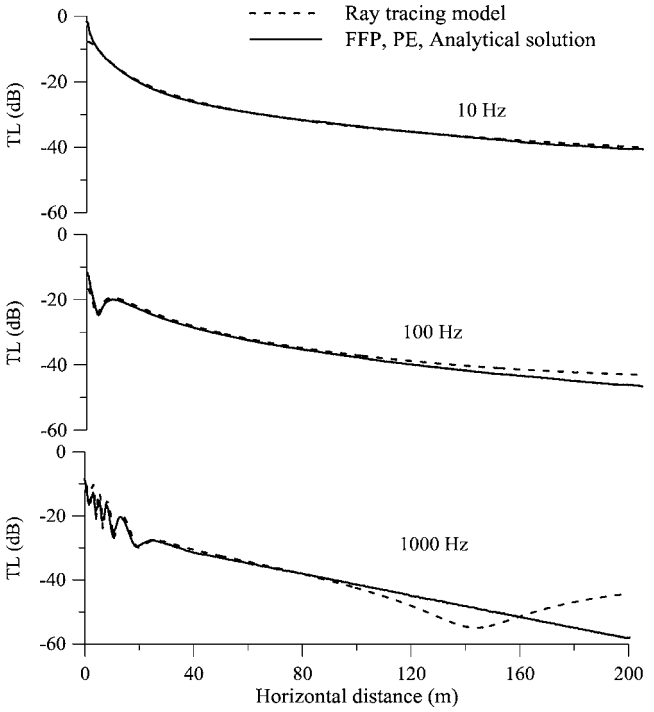

FIG. 3. Upwind propagation conditions with linear wind velocity profile of gradient −0.1 s^{-1}. Height and receiver heights are 5 and 1 m, respectively. Comparison of the transmission loss (TL) predictions from different methodologies with increasing frequency.

the total number of reflections and turning points, as well as the final z coordinate which corresponds to x_R. A pair of successive angles θ_0 and $\theta_0+\Delta\theta_0$ determines an interval for an existing eigenray if

- The rays corresponding to these angles have the same history.
- The final z coordinates of these rays lie from both sides of z_R.

Having determined the interval $[\theta_0, \theta_0+\Delta\theta_0]$, the secant[46] or golden section[47] method is used to focus on the value of the angle which corresponds to the eigenray. According to these two methods the initial interval is successively limited as the final z coordinate of the ray approaches z_R. The desired accuracy of approaching z_R is 1 cm, whereas the launching angle is specified with accuracy 10^{-4} rad (0.006°). If two successive rays fulfill only the second condition but they do not have the same history, it is still possible that an eigenray exists between them. In such a case, a fine tracing is performed in the interval $[\theta_0, \theta_0+\Delta\theta_0]$ with angle step $\Delta\theta_0'=\Delta\theta_0/20$.

III. VALIDATION

The method is validated against other known methodologies (A) and experimental data (B,C). In cases (B) and (C), atmospheric and ground parameters are estimated according to the real conditions when data are available. For the turbulent index of refraction and the ground impedance a rough estimation is made from the available data and then fine tuning best fits predictions with measurements. Such a tuning does not change the quality of the predictions significantly, but it can shift somewhat their level or frequency pattern.

A. Comparison with other methodologies

First, the method is validated against other known methodologies in some simple cases of sound propagation, presented by Attenborough *et al.*[48] Attenborough *et al.* defined four benchmark cases for which complete or at least piecewise analytical solutions are available in order to compare predictions of different numerical models. In all cases, the heights of the source and the receiver were 5 and 1 m, respectively, and the horizontal distance between them was 200 m. The terrain was considered flat with characteristic impedance $Z_c=\omega\rho_b/(k_b\rho c)$, where ω is the cyclic frequency and ρ, c are the density and the sound speed in air at 20 °C. The quantities ρ_b, k_b depend on the frequency and the ground properties.[48] A temperature of 20 °C and a relative humidity of 70% were assumed. Each case was characterized by an idealized sound speed profile. In case 1 the medium was considered isovelocity (homogeneous), in cases 2 and 3 the sound speed profile was considered as linear with constant gradient 0.1 s^{-1} and −0.1 s^{-1} respectively, and in case 4 a composite linear sound speed profile was used.

In Figs. 2 and 3 the predictions of the transmission loss (TL) by the ray tracing model are compared to the predictions of the FFP, PE and analytic (normal modes) models used in Ref. 48 for cases 2 and 3, representing downwind and upwind propagation conditions, respectively. The transmission loss at a point **r** is defined as

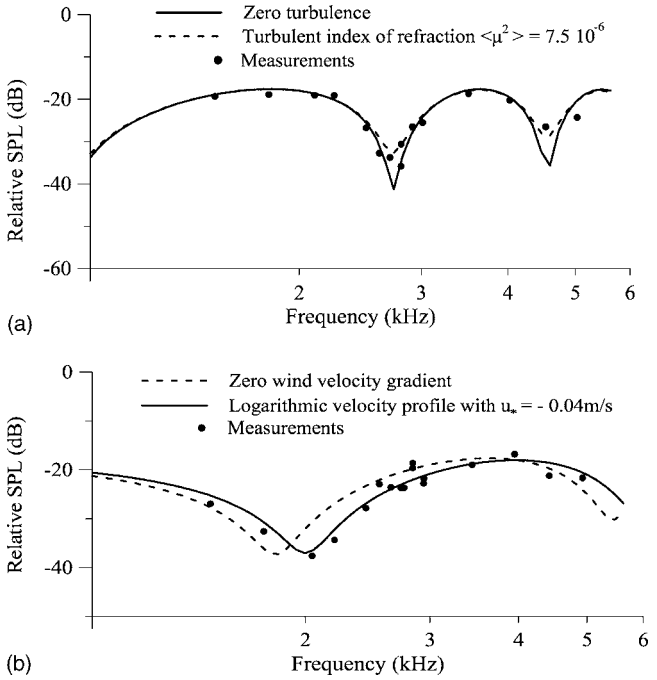

FIG. 4. Relative sound pressure level at 15 m horizontal distance from the source over an acoustically hard surface. Source height is 1.2 m. (a) Effect of turbulent index of refraction $\langle\mu^2\rangle=7.5\cdot10^{-6}$ for zero wind velocity gradient. Receiver height is 1.2 m (b) Effect of wind velocity profile with $u_\star=-0.04$ m/s. Receiver height is 0.6 m and $\langle\mu^2\rangle=7.5\cdot10^{-6}$.

$$\mathrm{TL}=-20\,\mathbf{log}\,\frac{|p(\mathbf{r})|}{p_0}, \tag{27}$$

where $p(\mathbf{r})$ is the sound pressure at the point $\mathbf{r}$ and p_0 is the sound pressure at 1 m from the source for free spherical propagation. The agreement for downwind propagation is good over the entire frequency range. For upwind propagation, the ray tracing model slightly diverges at distances greater than 100 m. This divergence is due to the reduced reliability of the geometrical approximation as the receiver approaches the shadow zone, a point also observed by L'Esperance *et al.* (Ref. 18, pp. 128–129 and Ref. 19, p. 5). Geometric models do not trace the ray trajectories well in the illuminated area (the reflection angles are not well predicted). The fact that the reflection coefficient is frequency dependent and the dominant contribution to the transmission loss up to 200 m is ground attenuation justifies the increase of error in ray tracing with frequency, as observed in Fig. 3

B. Comparison with near field measurements above an acoustically hard surface

Daigle *et al.*[41] studied the effect of atmospheric turbulence on sound propagation by measuring the near field sound pressure levels over asphalt. Asphalt can be considered an acoustically "hard" surface, reflecting sound waves perfectly. The source was positioned at 1.2 m height and the two receivers at 1.2 and 0.6 m height, respectively, and 15 m away from the source. In Fig. 4, the sound pressure level predicted relative to free spherical propagation at 1 m from the source is compared against the measurements. Figure 4(a) shows a good agreement between predictions and measurements, especially when the effect of the atmospheric turbulence is taken into account through the turbulent index of refraction. Daigle *et al.* estimated the turbulent index of refraction $\langle\mu^2\rangle=7.7\cdot10^{-6}$, using the measured standard deviations of wind velocity and temperature. Since there are no data for the wind velocity profile, the effective sound speed (sum of sound speed and wind velocity) was assumed constant with height (no wind velocity gradient).

In Fig. 4(b), the minimum of the measured spectrum has been shifted to a frequency higher than that produced by a constant effective sound speed, indicating the presence of a wind velocity profile. The shift of the spectrum is best fitted for a logarithmic wind profile with friction velocity equal to −0.04 m/s (upwind propagation conditions, weak refraction).

C. Comparison with measurements in zero mean wind speed conditions

Parkin and Scholes[49] made systematic measurements at Radlett, Hertfordshire, of the sound emitted by an aircraft engine, propagating at low height from the ground. The terrain was flat and the ground consisted of cut grass of 5–15 cm height growing in 5–7.5 cm of soil. Under this top soil there was a 1 m layer of heavy clay on top of clayey gravel for most of the range, but at 750 m from the source the subsoil changed to heavy clay and stones, about 3 m thick. The source height was 1.83 m and the receivers were eight microphones all located at 1.52 m height and at various horizontal distances from the source. The sound pressure level measured is represented relative to the sound pressure level at the first receiver (19.5 m distance from the source) in excess of atmospheric absorption and spherical spreading, namely only the ground attenuation is considered.

Parkin and Scholes report that in the analysis of their measurements no correlation could be found between turbulence and attenuation, so the turbulent index of refraction has been set to zero. Regarding the ground simulation, the options of semi-infinite, hard-backed layer and double layer were investigated by changing the parameters of layer thickness and flow resistivity. In all simulations, the basic pattern of the spectrum is well predicted, best fit with measurements found using a thin layer of 3 cm thickness and $2\cdot10^5$ kg/sm^3 flow resistivity, located above a semi-infinite hard surface.

Parkin and Scholes performed systematic measurements of the relative sound pressure level for various values of wind velocity (component in the direction of propagation) at 10 m height and separated their results in "summer" (July to October) and "winter" (November to mid-April). For each group, they provided the measurements that correspond to mean wind velocities of −4.5, 0 and 4.5 m/s. In Fig. 5, the predictions of the model from 62 up to 616 m range, using a constant effective sound speed profile (zero wind velocity gradient, no refraction), agree fairly well with the measurements carried out in winter for zero mean wind velocity. The increase of maximum attenuation and its shift to lower frequencies with increasing range is well predicted.

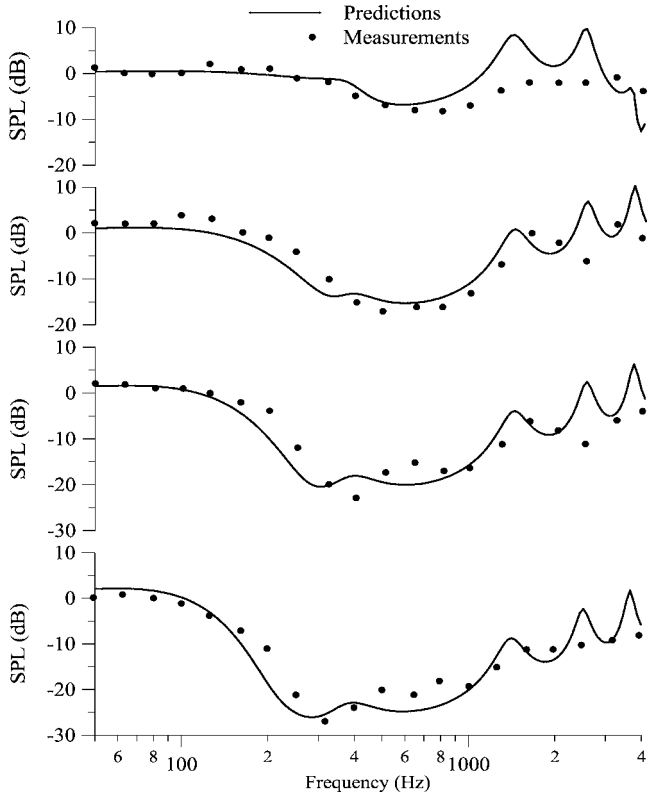

FIG. 5. Relative sound pressure level for zero wind velocity during winter. The measurements refer to the Radlett experiment, see Sec. III C. Source and receiver heights are 1.83 and 1.52 m, respectively. Thickness of absorbing material is 3 cm and flow resistivity is $2 \cdot 10^5$ kg/sm^3. Horizontal distance from the source is 62, 195, 347 and 616 m (from top to bottom).

IV. COMPARISON WITH MEASUREMENTS IN REFRACTIVE ATMOSPHERE

The previous validation tests concerned relatively simple cases of sound propagation in nonrefractive or weakly refractive atmospheric environments. In the case of strong wave refraction from the wind, the representation of the wind velocity profile plays a major role in the simulation of sound propagation and affects ray tracing substantially. In the following cases, atmospheric and ground absorption parameters are estimated according to the real conditions, whereas wind velocity profiles are sought so that predictions best fit the experimental data.

A. Comparison with Klug's measurements

Klug[50] made sound propagation measurements up to 1000 m above flat terrain in order to determine the sound speed profile in the atmospheric surface layer from the travel time difference between the direct and the ground reflected wave. The measured sound pressure level spectra are given for the long range sound propagation experiment, where both source and receiver were at 5 m height and their horizontal distance was 825 m. The ground was covered with grass, with a flow resistivity estimated 225 000 kg/sm^3. The measured temperature was 4 °C and the relative humidity 60%. Measurements were performed for two cases of downwind

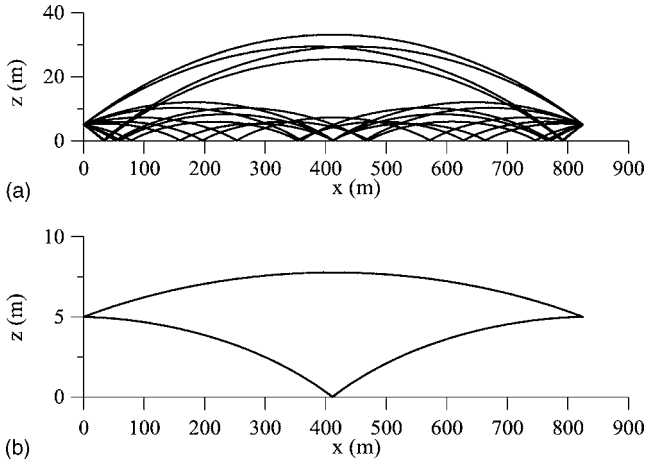

FIG. 6. Ray diagrams. (a) Stable atmospheric conditions with $u_\star$ =0.16 m/s and $T_\star$=0.07 K. (b) Unstable atmospheric conditions with $u_\star$ =0.15 m/s and $T_\star$=−0.39 K.

sound propagation, a high wind velocity gradient in stable atmospheric conditions and a low wind velocity gradient in unstable atmospheric conditions.

The mean wind velocity and temperature profiles have been derived from Eqs. (6) and (7) according to similarity theory. In each case the "effective" sound speed profile results from the superposition of the wind velocity profile and the sound speed profile. Figure 6(a) indicates that a high gradient of the wind velocity reinforced by a positive vertical gradient of the sound speed profile for stable conditions causes a strong refraction of the rays, resulting in the appearance of multiple reflections and large number of eigenrays. On the contrary, in the presence of a low gradient in unstable conditions, only two eigenrays are traced (Fig. 6(b)). In this case, the effective sound speed profile has still a positive but much lower gradient because the negative sound speed gradient (temperature decreases with height) is overcompensated by the positive gradient of the wind velocity. In Fig. 7, the comparison of the predictions with the measurements shows that the increase of the sound pressure level due to the refraction is well predicted for both stable and unstable conditions, with the exception of the low frequency part (<300 Hz) where differences exceed 10 dB (Fig. 7(a)). These differences are attributed to the high frequency approximation of ray theory resulting from the elimination of all but the first order (in frequency) transport equations. Such an approximation may result in inaccuracies of the predicted sound pressure level at the low frequency part, more pronounced for long range propagation with multiple eigenrays as in the current case of stable conditions.

B. Comparison with the measurements at Rock Springs

The experiment performed in a farm field near Rock Springs, Pennsylvania,[51] provided a complete set of acoustical and meteorological data. Measurements of sound pressure level were made at six different times of the day which correspond to different atmospheric conditions. The terrain was flat with roughness length and flow resistivity estimated at 1 cm and $1.5 \cdot 10^5$ kg/sm^3, respectively. The source height

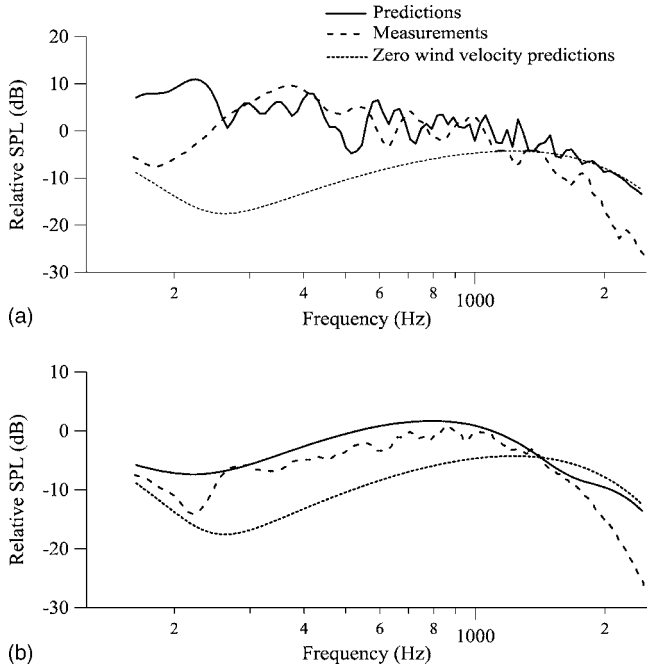

FIG. 7. Relative sound pressure level at 825 m horizontal distance from the source. Source and receiver heights are 5 m. Flow resistivity is $2.25 \cdot 10^5$ kg/sm^3. (a) Stable atmospheric conditions with $u_\star = 0.16$ m/s and $T_\star = 0.07$ K. (b) Unstable atmospheric conditions with $u_\star = 0.15$ m/s and $T_\star = -0.39$ K. Comparison is made against Klug's measurements, see Sec. IV A.

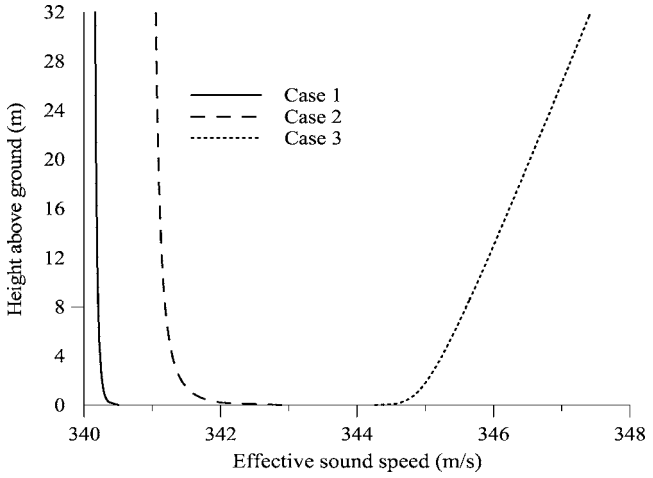

FIG. 8. The estimated mean effective sound speed profiles according to the similarity theory for three cases of sound propagation that refer to the Rock Springs experiment (Sec. IV B). Case 1: Upwind propagation conditions, weak refraction, Case 2: Upwind propagation conditions, strong refraction, Case 3: Downwind propagation conditions, strong refraction.

was 1.8 m and six microphones were placed at 1.75 m height, at horizontal distances 62, 88, 125, 175, 250 and 350 m from the source. Wind velocity was measured systematically at 10 m above ground and temperature differences were recorded between 2 and 10 m above ground. L'Esperance *et al.* derived the mean wind velocity and temperature profiles from Eqs. (6) and (7). They estimated $u_\star$ and $T_\star$ from the available measurements using an iterative procedure similar to the one described in Sec. II B.

Three sets of measurements were selected for comparison with the predictions of the ray tracing model. Two of them (Cases 1 and 2) correspond to upwind propagation (weak and strong upward refraction) and one (Case 3) corresponds to downwind propagation (strong downward refraction). The inclusion of the estimated mean logarithmic sound speed profiles, shown in Fig. 8, in the ray tracing model, provided poor results in comparison to the measurements for both upwind and downwind propagation conditions. High velocity gradients cause strong upward or downward refraction of the rays (upwind or downwind propagation) resulting in underestimation or overestimation of the sound pressure levels, respectively. A possible explanation is that for such low source heights (<2 m), the dominating refraction and turbulence effects (high temporal variation of the wind velocity and temperature gradient) are not well simulated by the ray tracing model. Such variations may be caused by eddy structures of different scales, such as convective cells, rolls and internal gravity waves, existing in both stable and unstable atmospheric boundary layer. Observations have shown that in some cases the experimental sound speed profiles show disagreement with those provided by the similarity theory, especially when the atmospheric conditions change from stable to unstable or vice versa. This results from the fact that the limited available meteorological data are not enough to predict both the turbulent index of refraction and the effective sound speed profile in complex atmospheric conditions.

In addition, it has been observed that among the instantaneous sound speed profiles, there always exist some downward profiles which produce high instantaneous sound pressure levels, even in the case of a mean upward refraction condition. Due to the logarithmic summation, these high levels have a dominant effect and significantly increase the sound pressure level in the shadow zone.[19] It is expected that the level predicted by averaging the instantaneous sound pressure levels would provide a better agreement with measurements than that predicted using the mean effective sound speed profile. If systematic measurements of the wind and temperature profile were available, the mean sound pressure level could be evaluated from a Gaussian distribution of the instantaneous sound pressure levels, with a standard deviation estimated from the turbulent index of refraction and the sound pressure level calculated using the mean sound speed profile (see Ref. 19).

1. Equivalent sound speed profile in upwind propagation conditions

In upwind propagation conditions, sound energy can be directed into areas where no eigenrays have been traced (shadow zones) by scattering at turbulent eddies. Such a turbulence effect cannot be simulated by the method of Sec. II C 3 which presupposes an interaction between the eigenrays. It is also noted that the linear effective sound speed profiles that L'Esperance *et al.*,[18] used to simulate near-ground propagation at Rock Springs correspond to significantly lower wind velocity gradients than those produced by the similarity theory at least for the lowest heights (up to 10 m). The present analysis shows that the substitution of the real vertical effective sound speed profile by a range-

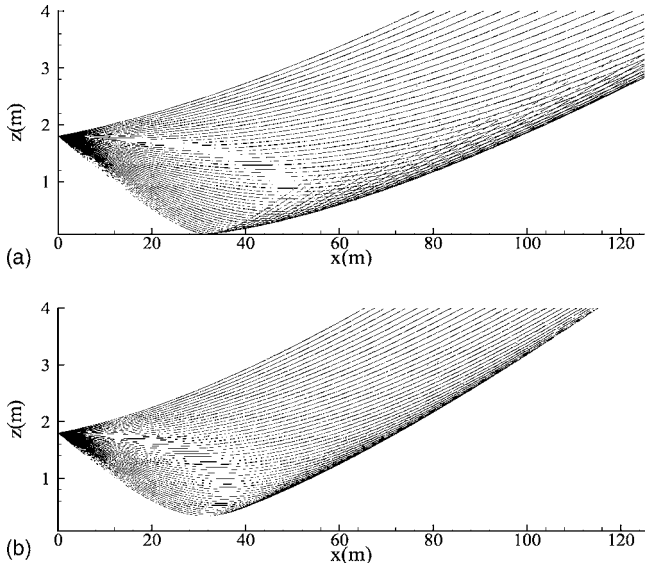

FIG. 9. Ray diagrams showing the formation of shadow zones caused by logarithmic upward wind velocity profiles: (a) weak upward refraction and (b) strong upward refraction.

dependent linear profile simulates the effect of the near-ground turbulent wind flow on sound propagation satisfactorily, providing good predictions of the sound pressure level.

In upwind propagation conditions, use of the mean logarithmic profile refracts the rays upwards resulting in the formation of shadow zones in which the receivers fall (Fig. 9). Instead of the logarithmic profile, an equivalent linear sound speed profile, $c(z)=c(0)+\lambda z$, $\lambda<0$, with $c(0)$ the sound speed on the ground, is used for the ray tracing simulation. At the lowest 10 m above ground, the gradients of the calculated sound speed profiles vary from to -0.15 to -0.004 s^{-1} in case 1 and from -0.8 to 0.01 s^{-1} in case 2. L'Esperance *et al.*[18] used the value $\lambda=-0.0034$ s^{-1} in their heuristic ray tracing model for upwind conditions and weak refraction, whereas for strong refraction they used $\lambda=-0.034$ s^{-1} or even $\lambda=-0.068$ s^{-1}. It is observed that the predictions best fit the measurements by properly reducing the absolute value of the gradient λ as the distance from the source increases. In the first case (weak refraction), $|\lambda|$ is tuned between 0.0008 and 0.15 s^{-1} for a range of distance between 62 and 350 m (Fig. 10). In the second case (strong refraction), the agreement is good when $0.012\ s^{-1}<|\lambda|<0.25\ s^{-1}$ for the same range of distance (Fig. 11). In all figures, sound pressure levels are represented relative to the free field spherical propagation level at 4 m from source. In both cases, the variation of $|\lambda|$ with range can be represented by the exponential law $|\lambda|=0.4\exp(-qx/z_S)$. The exponent q takes the values 0.035 and 0.019 (almost half) for weak and strong refraction, respectively.

2. Equivalent sound speed profile in downwind propagation conditions

"Case 3" sound speed profile corresponds to downwind propagation conditions with strong refraction. The inclusion of the mean logarithmic sound speed profile (Fig. 8) in the ray tracing model results in a number of eigenrays which are superimposed and lead to over prediction of the total sound

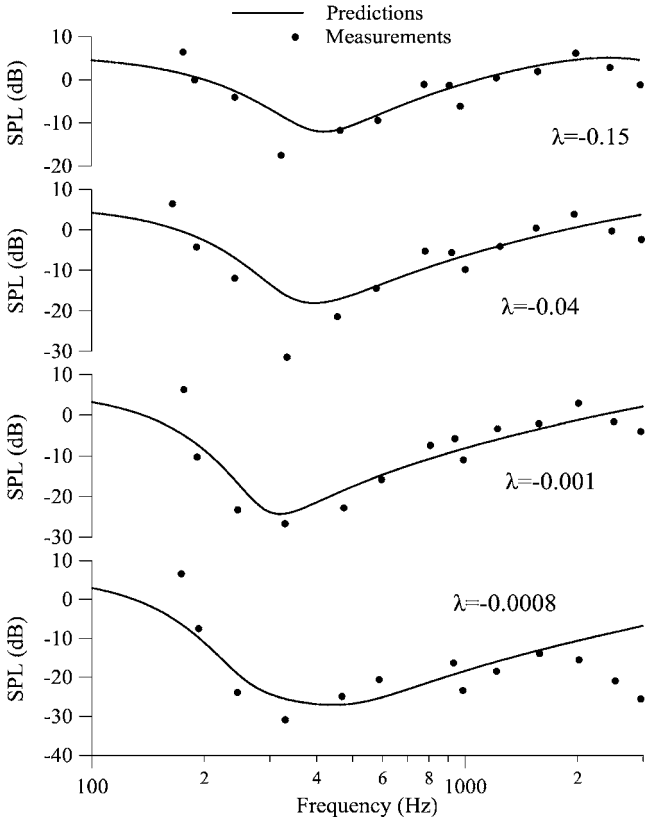

FIG. 10. Relative sound pressure level for upwind propagation, weak upward refraction. Measurements refer to the Rock Springs experiment, see Sec. IV B. Source and receiver height are 1.8 and 1.75 m, respectively. Flow resistivity is 10^5 kg/sm^3. Horizontal distance from the source is 62, 125, 250, and 350 m (from top to bottom).

pressure level, more obvious at 250 m range (Fig. 12). A possible reason for this over prediction could be the fact that the refraction loss due to the broadening of the ray tubes is not taken into account. For downward refraction and increasing range the length and the number of eigenrays increases. This factor may become important. The easiest way to calculate the pressure loss along a ray tube is by launching two neighboring rays and calculate geometrically the Blokhintzev invariant given by Eq. (3). This method is described by Lamancusa and Daroux[21] and has been applied by Prospathopoulos and Voutsinas[22] in noise propagation from wind turbines. However, it is very sensitive to numerical errors, and becomes inaccurate for long distances and multiple reflections. An alternative is to directly integrate the transport equations along the ray tube which demands the solution of three second order additional differential equations. This method is also subjected to significant numerical errors due to the complexity of the numerical calculations involved and is seldom met in bibliography.

In the present work, a reduction of the sound speed profile gradient is adopted to account for the refraction loss. At the lowest 10 m above ground, the gradient of the calculated logarithmic sound speed profile varies between 0.1 and 0.3 s^{-1}. For such conditions, L'Esperance *et al.*[18] used linear sound speed profiles with gradients $\lambda=0.034$ s^{-1} and $\lambda=0.068$ s^{-1}. Using a range-independent linear profile with gradient $\lambda=0.05$ s^{-1} the ray tracing model is found to best fit

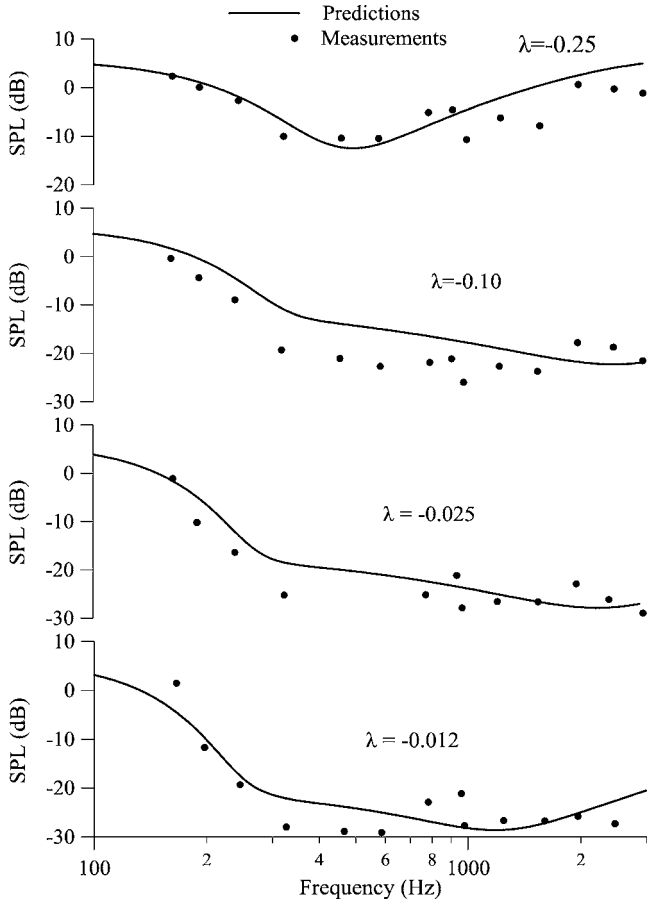

FIG. 11. Relative sound pressure level for upwind propagation, strong upward refraction. Measurements refer to the Rock Springs experiment, see Sec. IV B. Source and receiver height are 1.8 and 1.75 m, respectively. Flow resistivity is 10^5 kg/sm^3. Horizontal distance from the source is 62, 125, 250 and 350 m (from top to bottom).

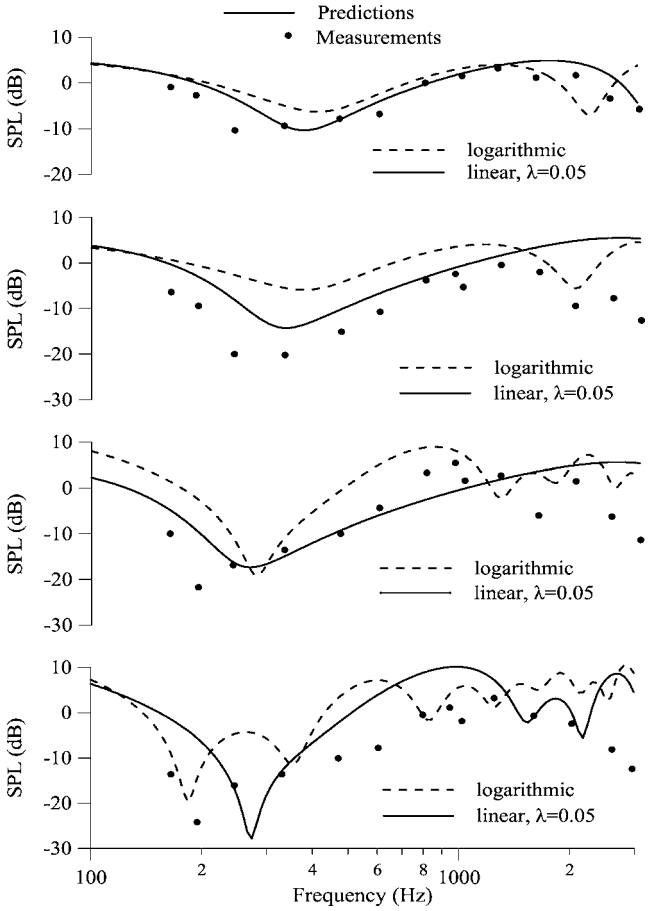

FIG. 12. Relative sound pressure level for downwind propagation, strong downward refraction. Measurements refer to the Rock Springs experiment, see Sec. IV B. Source and receiver height are 1.8 and 1.75 m, respectively. Flow resistivity is $1.5 \cdot 10^5$ kg/sm^3. Horizontal distance from the source is 62, 125, 250 and 350 m (from top to bottom).

the measurements (Fig. 12), however, the shift of the spectrum minimum to lower frequencies with increasing range is still not well reproduced. The model traces two eigenrays up to 250 m range. For the 350 m range, the minimum of the sound pressure level spectrum is generated by the superposition of two additional eigenrays.

C. Comparison with Parkin and Scholes' measurements

The configuration of the Parkin and Scholes' experiment[49] has been described in Sec. III C, where also the ground simulation parameters for winter conditions have been determined. By assuming roughness length 2 cm, a logarithmic wind velocity profile for neutral conditions is adapted to the value measured at 10 m height (4.5 m/s). At the lowest 10 m of the boundary sublayer the gradient of the calculated mean sound speed profile varies between 0.03 and 0.3 s^{-1}.

1. Equivalent sound speed profile in downwind propagation conditions

Following the line of the previous section for downwind propagation conditions (strong refraction) a linear sound speed profile with gradient $\lambda = 0.05$ s^{-1} is adopted. This provides good agreement with the measurements up to 195 m. The level of sound pressure spectrum and the shift of its minimum to lower frequencies with increasing range are well reproduced. At 347 m distance, the predictions are better correlated with the measurements by reducing λ to 0.03 s^{-1} (Fig. 13).

2. Equivalent sound speed profile in upwind propagation conditions

For upwind propagation conditions, the concept of a sound speed profile with range-decreasing gradient, as in the previous section, is applied. For ranges between 110 and 616 m predictions well fit the measurements as $|\lambda|$ decreases from 0.125 to 0.003 s^{-1} (Fig. 14). The variation of λ can be again approximated by the exponential law $|\lambda| = 0.4\ \mathbf{exp}(-0.019x/z_S)$, $\lambda < 0$, derived from the Rock Springs experiment for strong refraction. The systematic reduction of sound pressure level, occurring at high frequencies in upwind propagation conditions, is well predicted using the range-decreasing gradient, for both Rock Springs and Radlett experiments.

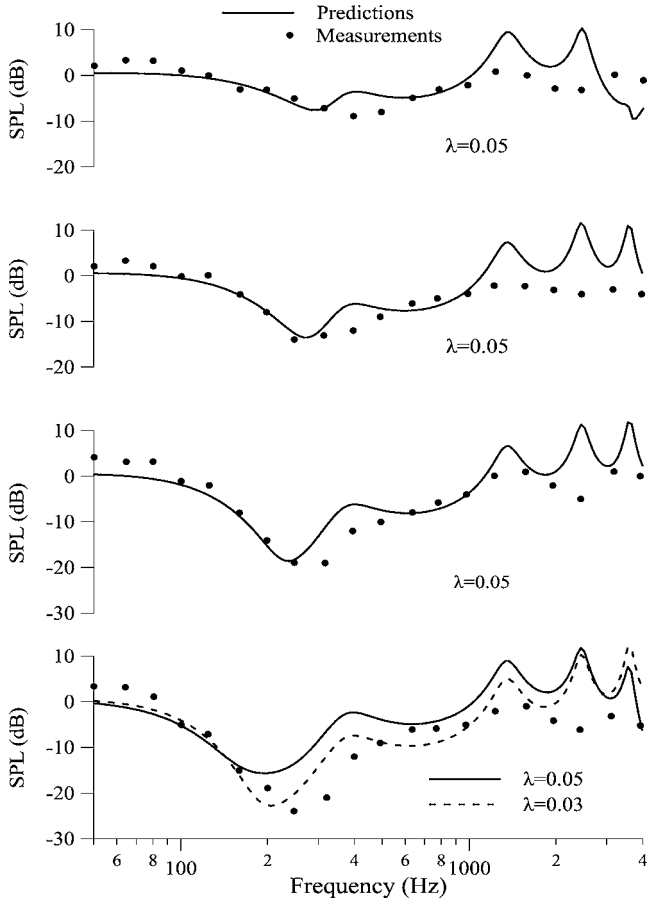

FIG. 13. Relative sound pressure level for downwind propagation, strong downward refraction. Measurements refer to the Radlett experiment, see Sec. IV C. Source and receiver heights are 1.83 and 1.52 m, respectively. Thickness of absorbing material is 3 cm and flow resistivity is $2\cdot10^5$ kg/sm^3. Horizontal distance from the source is 62, 110, 195, and 347 m (from top to bottom).

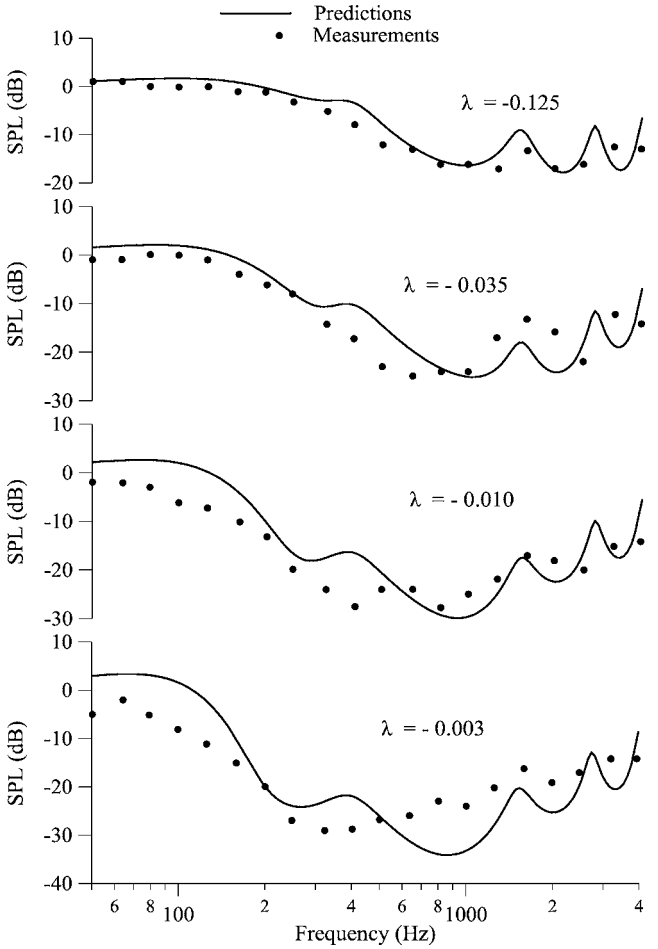

FIG. 14. Relative sound pressure level for upwind propagation, strong upward refraction. Measurements refer to the Radlett experiment, see Sec. IV C. Source and receiver heights are 1.83 and 1.52 m, respectively. Thickness of absorbing material is 3 cm and flow resistivity is $2\cdot10^5$ kg/sm^3. Horizontal distance from the source is 110, 195, 347 and 616 m (from top to bottom).

3. Equivalent sound speed profile in unstable atmospheric conditions

Parkin and Scholes repeated the same experimental configuration at another area, called Hatfield,[52] in order to investigate the effect of the atmospheric stability and the change in the nature of the ground on sound propagation. The terrain was flat, covered by cut grass of 5 cm height. The ground consisted of a top layer of silt with 0.6–1 m thickness and a second layer of silty clay with 0.6 m thickness over chalky clay. It is simulated as a semi-infinite layer with $2\cdot10^5$ kg/sm^3 flow resistivity.

In unstable atmospheric conditions, temperature decreases with height and so does the speed of sound. In the absence of wind, the negative gradient of the sound speed profile refracts the rays upwards, which is equivalent to an upwind propagation condition. In this respect, a linear sound speed profile $c(z)=c(0)+\lambda z$, $\lambda<0$, with range-decreasing gradient is utilized in the calculations. In Fig. 15, predictions show a quite satisfactory agreement with measurements when $0.0008\ \text{s}^{-1}<|\lambda|<0.2\ \text{s}^{-1}$ for ranges between 62 and 1097 m. Furthermore, the variation of λ can be still approximated by the exponential law $|\lambda|=0.4\ \mathbf{exp}(-0.019x/z_S)$.

V. SUMMARY AND CONCLUSIONS

An axisymmetric ray tracing model in moving media was developed and applied to near-ground sound propagation. The model takes into account the ground and atmospheric absorption, the wind velocity and temperature variations and the atmospheric turbulence. It was first validated against experimental and numerical data in some simple cases (constant or linear wind velocity profile). A weakness of the model, inherent to the geometrical approximation, is the prediction of sound pressure levels in the so-called shadow zones. It was observed that the reliability of the predictions decreases as the receiver approaches such areas.

In the application of real cases of atmospheric refraction, as in the experiments at Rock Springs, Radlett and Hatfield provided guidelines for the numerical simulation of the wind velocity profile in ray tracing methodologies. Although the model provided satisfactory results using the mean logarithmic wind velocity profiles estimated by similarity theory, in cases of wind turbine sound propagation[22] (source height 30–100 m), and in the experiment of Sec. IV A, where the source height is at 5 m height, it gave poor results using the respective logarithmic profiles in the experiments of Rock

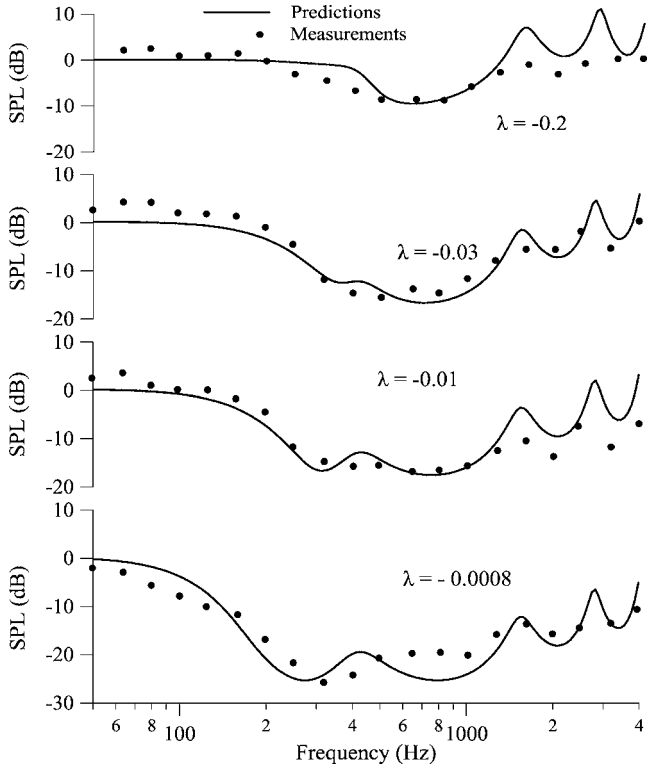

FIG. 15. Relative sound pressure level for unstable atmospheric conditions, zero wind velocity, low turbulence. Measurements refer to the Hatfield experiment, see Sec. IV C. Source and receiver heights are 1.83 and 1.52 m, respectively. Flow resistivity is $2\cdot10^5$ kg/sm^3. Horizontal distance from the source is 62, 195, 347 and 1097 m (from top to bottom).

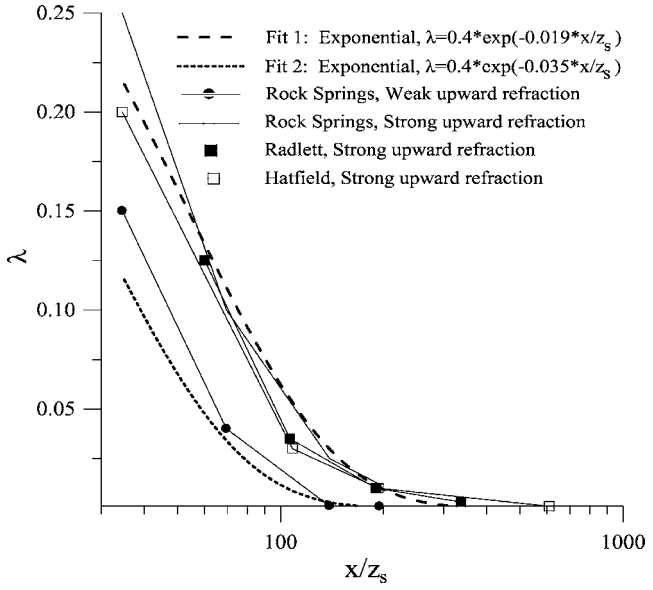

FIG. 16. Variation of the sound speed profile gradient with range for upwind propagation conditions: $|\lambda|=0.4\exp(-qx/z_S)$, $q=0.019$ and 0.035 for strong and weak upward refraction conditions, respectively.

Springs, Radlett and Hatfield, where the source height is less than 2 m. Because of that, a spatial variation of the effective sound speed profiles was sought to better simulate the high wind velocity gradients caused by turbulence at such low heights. The lack of measurements of near-ground wind speed and temperature profiles does not allow to judge how far a realistic effective sound speed profile deviates during measurement period from a constant, linear or logarithmic profile, and how such deviation affects the predicted sound pressure levels and their consistency to the measured levels.

In upwind propagation conditions, the adoption of a linear sound speed profile with diminishing gradient is suggested as the distance from the source increases. For all three cases studied in the present, the variation of the sound speed profile gradient was well approximated by the exponential law $|\lambda|=0.4\,\mathbf{exp}(-qx/z_S)$ (Fig. 16). From the comparison with the experiments it follows that this relationship is valid up to 1096 m (Figs. 14 and 15). The constant q seems to mainly depend on the wind conditions. For strong refraction $q=0.019$, whereas for weak refraction it is almost doubled ($q=0.035$). A detailed experimental database could provide a more accurate correlation between the numerical constants of the exponential law and the atmospheric conditions.

In downwind propagation conditions, the phenomenon becomes more complicated because strong downward refraction may increase the number of eigenrays significantly. In such a case the refraction loss along the ray tubes may become significant, however it cannot be easily calculated using a ray tracing model. A reduction of the real sound speed profile gradient is adopted to account for the refraction loss. In both Rock Springs and Radlett experiments, a linear sound speed profile with constant gradient $\lambda=0.05$ s^{-1} gives satisfactory predictions for distances up to 250–350 m. However, for greater distances, this factor should be reduced otherwise the appearance of a high number of eigenrays over predicts the sound pressure level.

[1]F. R. DiNapoli and R. L. Deavenport, "Theoretical and numerical Green's function solution in a plane layered medium," J. Acoust. Soc. Am. **67**, 92–105 (1980).
[2]S. W. Lee, N. Bong, W. F. Richards, and Richard Raspet, "Impedance formulation of the fast field program for acoustic wave propagation in the atmosphere," J. Acoust. Soc. Am. **79**(3), 628–634 (1986).
[3]A. Gudesen, "Application of the SAFARI model to sound propagation in the atmosphere," J. Acoust. Soc. Am. **87**(5), 1975–1986 (1990).
[4]Y. L. Li, M. J. White, and S. J. Franke, "New fast field programs for anisotropic sound propagation through an atmosphere with a wind velocity profile," J. Acoust. Soc. Am. **95**(2), 718–726 (1994).
[5]K. D. Wilson, "Sound field computations in a stratified, moving medium," J. Acoust. Soc. Am. **94**(1), 400–407 (1993).
[6]F. B. Jensen, W. A. Kupermann, M. B. Porter, and H. Schmidt, *Computational Ocean Acoustics* (American Institute of Physics, New York, 1993), Chap. 5, pp. 271–315.
[7]R. Raspet, G. Baird, and W. Wu, "Normal mode solution for low frequency sound propagation in a downward refracting atmosphere above a complex impedance plane," J. Acoust. Soc. Am. **91**(3), 1341–1352 (1992).
[8]F. B. Jensen, W. A. Kupermann, M. B. Porter, and H. Schmidt, *Computational Ocean Acoustics* (American Institute of Physics, New York, 1993), Chap. 5, pp. 315–326.
[9]K. E. Gilbert and M. J. White, "Application of the parabolic equation to sound propagation in a refracting atmosphere," J. Acoust. Soc. Am. **85**(2), 630–637 (1989).
[10]K. E. Gilbert and R. Raspet, "Calculation of turbulence effects in an upward-refracting atmosphere," J. Acoust. Soc. Am. **87**(6), 2428–2437 (1990).
[11]P. Chevrét, Ph. Blanc-Benon, and D. Juvé, "A numerical model for sound propagation through a turbulent atmosphere near the ground," J. Acoust. Soc. Am. **100**(6), 3587–3599 (1996).
[12]F. B. Jensen, W. A. Kupermann, M. B. Porter, and H. Schmidt, *Computational Ocean Acoustics* (American Institute of Physics, New York, 1993), Chap. 3.
[13]F. Walkden and M. West, "Prediction of enhancement factor for small explosive sources in a stratified moving medium," J. Acoust. Soc. Am.

84(1), 321–326 (1988).
[14]R. Blumrich and D. Heimann, "A linearized Eulerian sound propagation model for studies of complex meteorological effects," J. Acoust. Soc. Am. **112**(2), 446–455 (2002).
[15]V. Ostashev, K. Wilson, L. Liu, D. F. Aldridge, N. P. Symons, and D. Martin, "Equations for finite-difference, time-domain simulation of sound propagation in moving inhomogeneous media and numerical implementation," J. Acoust. Soc. Am. **117**(2), 503–517.
[16]D. Heimann and R. Karle, "A linearized Euler finite-difference time-domain sound propagation model with terrain-following coordinates," J. Acoust. Soc. Am. **119**(6), 3813–3821.
[17]R. Raspet, A. L'Esperance, and G. Daigle, "The effect of realistic ground impedance on the accuracy of ray tracing," J. Acoust. Soc. Am. **97**(1), 154–158 (1995).
[18]A. L'Esperance, P. Herzog, G. A. Daigle, and J. R. Nicolas, "Heuristic model for outdoor sound propagation based on an extension of the geometrical ray theory in the case of a linear sound speed profile," Appl. Acoust. **37**, 111–139 (1992).
[19]A. L'Esperance, J. Nicolas, G. Daigle, and Y. Gabillet, "Modelization of outdoor sound propagation under various meteorological conditions," in *15th AIAA Aeroacoustics Conference*, AIAA 93-4405, Long Beach, CA (1993).
[20]A. Berry and G. A. Daigle, "Controlled experiment on the diffraction of sound by a curved surface," J. Acoust. Soc. Am. **83**(6), 2059–2068 (1988).
[21]J. S. Lamancusa and P. A. Daroux, "Ray tracing in a moving medium with two-dimensional sound-speed variation and application to sound propagation over terrain discontinuities," J. Acoust. Soc. Am. **93**(4), 1716–1726 (1993).
[22]J. M. Prospathopoulos and S. G. Voutsinas, "Application of a ray theory model to the predictions of noise emissions from isolated wind turbines and wind parks," Wind Energy **10**, 103–119 (2007).
[23]A. D. Pierce, *Acoustics-An Introduction to Its Physical Principles and Applications* (McGraw–Hill, New York, 1981), Chap. 8, p. 375.
[24]L. M. Brekhovskikh and O. A. Godin, *Acoustics of Layered Media II: Point Sources and Bounded Beams* (Springer-Verlag, Berlin, 1990), Chap. 5, pp. 182–185.
[25]A. D. Pierce, *Acoustics-An Introduction to Its Physical Principles and Applications* (McGraw–Hill, New York, 1981), Chap. 8, p. 406.
[26]H. A. Panofsky and J. A. Dutton, *Atmospheric Turbulence Models and Methods for Engineering Applications* (Wiley, New York, 1984).
[27]J. A. Businger, J. C. Wyngaard, Y. Izumi, and E. F. Bradley, "Flux-profile relationships in the atmospheric surface layer," J. Atmos. Sci. **28**, 181–189 (1971).
[28]F. Nieuwstadt, "The computation of the friction velocity $u_\star$ and the temperature scale $T_\star$ from temperature and wind velocity profiles by least-square methods," Boundary-Layer Meteorol. **14**, 235–246 (1978).
[29]D. Marquardt, "An algorithm for least-squares estimation of non-linear parameters," J. Acoust. Soc. Am. **11**(2), 431–441 (1963).
[30]R. J. Donato, "Impedance models for grass-covered ground," J. Acoust. Soc. Am. **61**(6), 1449–1452 (1977).
[31]H. M. Hess, K. Attenborough, and N. W. Heap, "Ground characterization by short-range propagation," J. Acoust. Soc. Am. **87**(5), 1975–1986 (1972).
[32]K. Attenborough, S. I. Hayek, and M. Lawther, "Propagation of sound above a porous half-space," J. Acoust. Soc. Am. **68**(5), 1493–1501 (1980).
[33]J. M. Sabatier, R. Raspet, and K. Carl, "An improved procedure for the determination of ground parameters using level difference measurements," J. Acoust. Soc. Am. **94**(1), 396–399 (1993).
[34]C. I. Chessell, "Propagation of noise along a finite impedance boundary," J. Acoust. Soc. Am. **62**(4), 825–834 (1977).
[35]J. Nicolas, J. L. Berry, and G. A. Daigle, "Propagation of sound above a finite layer of snow," J. Acoust. Soc. Am. **77**(1), 67–73 (1985).
[36]K. Attenborough, "Review of ground effects on outdoor sound propagation from continuous broadband sources," Appl. Acoust. **24**, 289–319 (1988).
[37]C. F. Chien and W. W. Shoroka, "Sound propagation along an impedance plane," J. Sound Vib. **43**, 9–20 (1975).
[38]U. Ingard, "On the reflection of a spherical wave from an infinite plane," J. Acoust. Soc. Am. **23**, 329–335 (1951).
[39]ISO 9613-1, "Acoustics—Attenuation of sound during propagation outdoors—Part 1: Calculation of the absorption of sound by the atmosphere (International Organization for Standardization," Geneva, Switzerland, 1966).
[40]H. E. Bass, L. C. Sutherland, A. J. Zuckerwar, D. T. Blackstock, and D. M. Hester, "Atmospheric absorption of sound: Further developments," J. Acoust. Soc. Am. **97**(1), 680–683 (1995).
[41]G. A. Daigle, J. E. Piercy, and T. F. W. Embleton, "Effects of atmospheric turbulence on the interface of sound waves near a hard boundary," J. Acoust. Soc. Am. **64**(2), 622–630 (1978).
[42]S. F. Clifford and R. T. Lataitis, "Turbulence effects on acoustic wave propagation over a smooth surface," J. Acoust. Soc. Am. **73**, 1545–1550 (1983).
[43]K. Attenborough, "A note on short-range ground characterization," J. Acoust. Soc. Am. **95**(6), 3103–3108 (1994).
[44]K. D. Wilson and D. W. Thompson, "Acoustic propagation through anisotropic surface-layer turbulence," J. Acoust. Soc. Am. **96**(2), 1080–1095.
[45]W. H. Press, B. P. Flannery, S. A. Teukolsky, and W. T. Vetterling, *Numerical Recipes in Fortran 77* (Cambridge University Press, London, 1997), Chap. 16, pp. 718–725.
[46]W. H. Press, B. P. Flannery, S. A. Teukolsky, and W. T. Vetterling, *Numerical Recipes in Fortran 77* (Cambridge University Press, London, 1997), Chap. 9, pp. 343–347.
[47]C. Onwubiko, *Foundations of Computer-Aided Design* (West, St. Paul, MN, 1989), Chap. 7, pp. 189–196.
[48]K. Attenborough, S. Taherzadeh, H. E. Bass, X. Di, R. Raspet, G. R. Becker, A. Gudesen, A. Chrestman, G. A. Daigle, A. L'Esperance, Y. Gabillet, K. E. Gilbert, Y. L. Li, M. J. White, P. Naz, J. M. Noble, and H. A. J. M. van Hoof, "Benchmark cases for outdoor sound propagation models," J. Acoust. Soc. Am. **97**(1), 173–191 (1995).
[49]P. H. Parkin and W. E. Scholes, "The horizontal propagation of sound from a jet engine close to the ground, at Radlett," J. Sound Vib. **1**, 1–13 (1964).
[50]H. Klug, "Sound-speed profiles determined from outdoor sound propagation measurements," J. Acoust. Soc. Am. **90**(1), 475–481 (1991).
[51]A. L'Esperance, J. Nicolas, D. K. Wilson, D. W. Thompson, Y. Gabillet, and G. Daigle, "Sound propagation in the atmospheric surface layer: Comparison of experiment with FFP predictions," Appl. Acoust. **40**, 325–346 (1993).
[52]P. H. Parkin and W. E. Scholes, "The horizontal propagation of sound from a jet engine close to the ground, at Hatfield," J. Sound Vib. **2**(4), 353–374 (1965).

A computational study of the interaction noise from a small axial-flow fan

H. Z. Lu
Department of Mechanical Engineering, The Hong Kong Polytechnic University, Kowloon, Hong Kong, China

Lixi Huang[a)]
Department of Mechanical Engineering, The University of Hong Kong, Pofulam Road, Hong Kong, China

R. M. C. So and J. Wang
Department of Mechanical Engineering, The Hong Kong Polytechnic University, Kowloon, Hong Kong, China

(Received 27 June 2006; revised 15 May 2007; accepted 1 July 2007)

Small axial-flow fans used for computer cooling and many other appliances feature a rotor driven by a downstream motor held by several cylindrical struts. This study focuses on the aerodynamic mechanism of rotor-strut interaction for an isolated fan. The three-dimensional, unsteady flow field is calculated using FLUENT®, and the sound radiation predicted by acoustic analogy is compared with measurement data. Striking differences are found between the pressure oscillations in various parts of the structural surfaces during an interaction event. The suction surface of the blade experiences a sudden increase in pressure when the blade trailing edge sweeps past a strut, while the process of pressure decrease on the pressure side of the blade is rather gradual during the interaction. The contribution of the latter towards the total thrust force on the structure is cancelled out significantly by that on the strut. In terms of the acoustic contributions from the rotor and strut, the upstream rotor dominates and this feature differs from the usual rotor-stator interaction acoustics in which the downstream part is responsible for most of the noise. It is therefore argued that the dominant interaction mechanism is potential flow in nature. © *2007 Acoustical Society of America.*
[DOI: 10.1121/1.2764474]

PACS number(s): 43.28.Ra, 43.50.Nm, 43.50.Ed [GCL] Pages: 1404–1415

I. INTRODUCTION

This study is motivated by the aeroacoustics of computer cooling fan. The problem of cooling fan noise is receiving increasing attention as more CPU chips are condensed in a smaller space demanding intense ventilation. Should the ventilation capacity double in the near future, the noise radiation would be increased by about 18 dB based on a simplistic 6th power law estimate. To prevent this problem from becoming a stumbling block of computer hardware development, a much quieter fan design has to be developed. A typical fan noise spectrum consists of two components: a broadband noise caused mainly by turbulent flow features, and tones at the blade passing frequency and its harmonics. To human ears, the emergence of tones is much more annoying than the broadband noise of equal sound energy level. Tones are mainly generated by the deterministic, unsteady loading on rotor blades and motor struts. For a cooling fan consisting of an axial-flow rotor and a set of downstream motor struts, as shown in Fig. 1(a), there are two types of interactions. The first type of interaction is between eddies in the distorted inlet flow and the rotating blades. The inlet flow is typically nonuniform in a computer chassis. Furthermore, eddies in a turbulent inlet flow may get elongated in a contracting inlet stream tube and get chopped by blades giving rise to tone noise, cf. (Trunzo *et al.*, 1981), (Majumdar and Peake, 1998), (Chiu *et al.*, 1989), and (Washburn and Lauchle, 1998). The second type of interaction is between the rotor wake and the struts in close proximity.

The first interaction mechanism is often the more powerful sound radiator than the second, but, in principle, it is possible to reduce its strength by careful geometric design for both the fan inlet and the objects surrounding the cooling fan. However, the second mechanism is unavoidable, and it is the topic of the present investigation. Most existing knowledge on this aspect of fan aeroacoustics is derived from studies of rotor-stator, or inlet guide-vane-rotor interaction in ducted turbofans (Blake, 1986), where the downstream set of blades experience most of the unsteady loading, hence sound radiation, from the interaction event. The unsteady loading is derived from both potential field interactions and viscous wake impingement. For such interactions, semiempirical models (Kemp and Sears, 1953, 1955) still serve as a good starting point. Potential field interaction dominates when the gap is less than one half of a blade chord or so (Lowson, 1965, 1970). The potential flow interaction is particularly strong when the percentage of the flow blockage by the downstream struts is large. For the cooling fan studied in this work, it is around 15%. The reason why the downstream set

a)Author to whom correspondence should be addressed. Electronic mail: lixi.huang@hku.hk

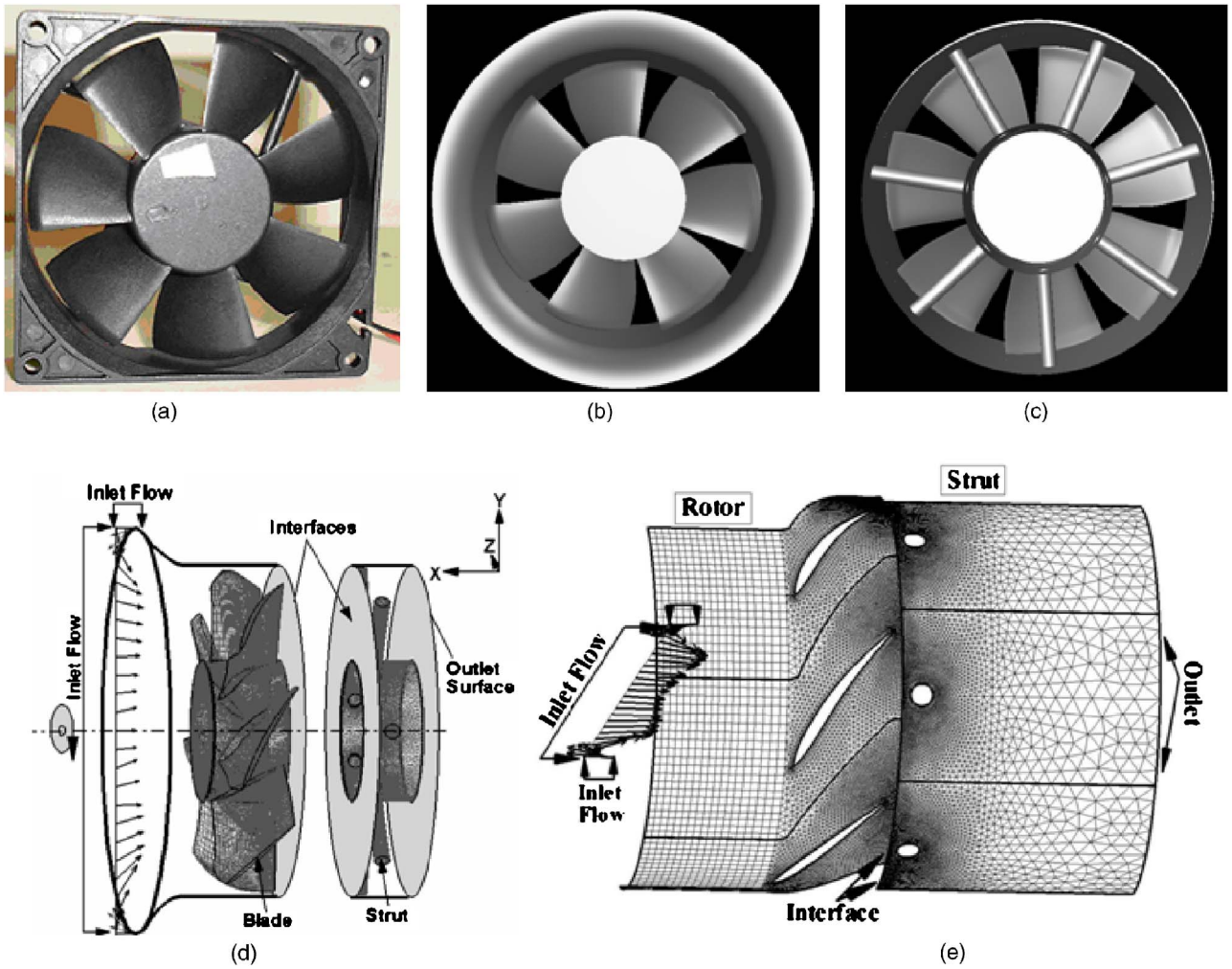

FIG. 1. The computational and experimental configuration. (a) Photo of the real cooling fan on which the computational model is based. (b) Front view of the model fan with circular bellmouth. (c) Back view of the model fan showing seven radial struts. (d) Computational model with extended inlet and exit ducts. (e) Mesh on a cylindrical cross section at 70% of the radial span.

of blades, rotor or stator, as the case may be, bears more fluctuating loading is due to the aerodynamic sensitivity of the blade leading edge. When the downstream set of blades is cylindrical struts, the forces generated might not be as large. It could be even less than that on the upstream rotor blades since, after all, most rotor blades are designed to generate lift. It is anticipated that the forces on both rotor blades and the downstream struts could be equally important. Apart from the interaction between different blade rows, interaction between the tip leakage vortex with the neighboring blades of the same blade row can also be important in terms of both broadband and tonal noise (Fukano *et al.*, 1986; Cudina, 1992; Kameier and Neise, 1997).

In terms of the unsteady fluid dynamics during the inter-blade-row interaction, there have been quite a few papers on the topic in the turbomachinery community, e.g. (Hodson, 1985), (Mayle and Dullenkopf, 1989), (Mailach and Volgeler, 2004a), which are mainly focused on the viscous effects of the upstream wake on the downstream blade. Studies on the reaction of the downstream blades on the upstream blade rows due to the potential flow effect are rare (Mailach and Volgeler, 2004b), apparently due to its much weaker strength when compared with the viscous effects from the upstream blades on the downstream blades, with the exception of Mailach *et al.*, (2003) in which the guide vane wake from the upstream is rather thin. To the best of the authors' knowledge, the interaction between an upstream blade and a downstream bluff body has not been studied apart from the preliminary effort made by the second author and his colleagues (Huang *et al.*, 2003) using a coarse, quasi-orthogonal mesh which was not adaptable enough to cope with the complex geometry. In this study, FLUENT® (version 6.3) is used to simulate the three-dimensional (3D), unsteady flow through a complete but isolated cooling fan. Admittedly, the commercial software package may not resolve all details of the unsteady flow field that could be of potential interest to acoustics, especially for such a complicated configuration with relative motion between rotor and struts. However, the focus of attention here is the rotor-strut interaction event, and it is hoped that FLUENT® can capture the large-structure flow field reasonably well. As a measure to check against possible loss of major acoustic mechanisms excluded by the current simulation, comparison with experiment is made for the time-domain pressure wave form. The specific questions asked in this study are as follows. (1) How important is the 3D flow effect in a design which seems to be based on two-

TABLE I. Geometry of the rotor blades and the incidence angle distribution.

Span (%)	Chord (m)	Stagger (deg)	Camber (deg)	Incidence (deg)
0	0.0239	41.6	13.2	25.7
18	0.0252	46.6	22.2	11.9
35	0.0270	50.4	22.5	7.3
53	0.0289	53.3	20.8	5.5
71	0.0307	55.0	19.1	4.7
89	0.0320	57.1	20.4	1.1
100	0.0307	61.3	19.1	−1.8

dimensional (2D) radial equilibrium? (2) What is the noise source distribution on the blade and strut surfaces, and how does noise from one part interfere acoustically with another? (3) What are the aerodynamic mechanisms of the surface pressure fluctuations which control the far-field noise radiation?

In what follows, Sec. II outlines the computational configuration and the calibration of the numerical scheme. The main results for the sound source are presented in Sec. III. Section IV is devoted to the comparison of the predicted sound and the acoustic measurement. Conclusions are drawn in Sec. V.

II. COMPUTATIONAL MODEL AND MESH TEST

A. Physical fan model for experiment

For simplicity, a free-delivery working condition is considered for both experimental study and numerical simulation although it is well known that the source mechanisms at other working conditions, e.g. near a surge point, can be very different. In order to focus on the rotor-strut interaction noise mechanism, a model fan was fabricated based physically on a real fan purchased from the market. The modifications essentially eliminated the noise radiated by the inlet flow distortion coming towards the rotor. The real fan is shown in Fig. 1(a). It is a typical 90-mm-diam cooling fan used in desktop computers. There are seven rotor blades rotating anti-clockwise when viewed from the front. There are four cylindrical struts of 4 mm in diameter, and the axial clearance between the cylinder and the blade trailing edge is 3 mm. The design speed for the fan is 3000 rpm. The blade span is 25.5 mm. The tip clearance is 1.5 mm, or 6% of the span. The midspan chord length is 28 mm. The main geometric features of the rotor blade are given in Table I. The struts lean towards the rotational direction and are almost tangent to the rotor hub within which the motor is located. The model fan had two modifications from the real fan shown in Fig. 1(a). The rationale for the modifications is described below. The inlet bellmouth shown in Fig. 1(a) is incomplete due to the square outer frame, and it has been shown to cause considerable extra noise (Huang and Wang, 2005). In order to focus attention on the rotor-strut interaction noise, a complete bellmouth with lip radius of 10 mm is used, as shown in Figs. 1(b) and 1(d), which have different view angles. The configuration of the four tangential struts in the real fan is highly three dimensional, and its noise pattern is a complex rotating dipole (Huang, 2003). To simplify the matter, seven radial struts are used instead. The back view of the struts is shown in Fig. 1(c). When the number of rotor blades coincides with the number of struts, the noise pattern is a simple thrust noise beaming along the rotational axis.

B. Computational domain and boundary conditions

Despite the recent advances in direct computation of flow-generated noise (Wang *et al.*, 2006), acoustic analogy (Lighthill, 1952; Ffowcs Williams and Hawkings, 1969) remains as a reliable and efficient approach. As the free-space Green's function is used in the FW-H equation, the source should be calculated by compressible flow solvers with appropriate boundary conditions when the source is noncompact; otherwise a suitable Green's function should be used when pressure from incompressible flow solvers are used for low-speed flows (Howe, 1999). However, this requirement can be relaxed if the source is acoustically compact. In the present study, the Mach number is below 0.05 and the ratio of the fan diameter to the typical wavelength is less than 0.1. Therefore, the incompressible flow solver is chosen together with a compact computational domain shown in Fig. 1(d). A cylindrical cross section view with mesh is given in Fig. 1(e). The model closely follows the physical model fan shown in Figs. 1(b) and 1(c), but there are minor modifications based on numerical needs and are expected to have minimal impact on computational results. The two minor modifications are explained as follows.

For the inlet, the only certainty is that the stagnation pressure is atmospheric and the velocity vanishes at a location very far away from the bellmouth. The actual volume flow rate of the rotor should be a result of numerical simulation with appropriate exit boundary conditions. The volume flow rate, hence the incoming flow velocity, cannot be determined a priori. Such prediction would pose a heavy demand on computational resources due to the large computational domain. In order to limit the demand on computational resources, there is a need to set an inlet computational domain boundary in the near field where the exact velocity is uncertain theoretically, but can be specified in practice if experimentally measured velocity data is available. In other words, the velocity is measured and not calculated. This is justified by the focus on the interaction dynamics of the rotor trailing edge with the struts, which are much further downstream. The exact location of such near-field inlet boundary is dictated by experimental convenience and is illustrated in Fig. 1(d) by vectors shown near the labels of "inlet flow." Laser-Doppler Anemometry was utilized to measure the flow velocity on a plane 5 mm upstream of the frontier of the inlet bellmouth, which was also 1.4 times the axial chord length from the blade leading edge. Near the outer rim of the inlet bellmouth, velocity measurement was conducted over a cylindrical surface across which the inlet flow was most likely perpendicular to the fan axis and parallel to the local bellmouth curvature. The measured flow rate for the free delivery condition for this fan was 0.0302 kg/s, and the distribution of the inlet flow velocity vector is shown in Fig. 1(d). The average axial-flow velocity at the inlet was around 5 m/s over the whole inlet plane.

At the downstream end, the circular flow passage provided by the casing is flush with the trailing edge of the struts. Since the flow just downstream of the cylinder is nonuniform, it is impossible to specify any flow quantity which can be deduced either theoretically or determined experimentally. For convenience, the casing flow passage is further extended by about 10 mm from the rear edge of the struts. On this exit plane, the atmospheric static pressure is given for the outer radius of the exit plane, and the inner parts of the exit plane are required to satisfy a radial force equilibrium, which is one type of boundary condition provided by Fluent®. Due to the swirling exit flow, the pressure near the center of the exit plane is lower than the atmospheric pressure. The boundary conditions elsewhere are straightforward. All structural surfaces are given the no-slip condition.

Since the rotor blades rotate while the struts remain stationary, the computational domain is divided into two parts separated by an artificial interface which is set midway between the blade trailing edge and the cylinder leading edge. All fluid properties are identical on the two sides of the virtual interface. The mesh is allowed to have relative sliding, and the continuity condition there is enforced by simple interpolation where nodes are not overlapped. The two computational domains are deliberately shown as being separated in Fig. 1(d) to illustrate the position of the computational interface. In Fig. 1(e), the interfaces are joined back together, and the 2D mesh on the 70% of the radial span is shown illustrating the relative positions of the rotor blades, which are shown as airfoils, and the downstream cylinders, which are shown as circles just downstream of the interface.

For the model of seven blades supported by seven struts, which is designated the "coincident" configuration (Wang and Huang, 2006), there are two ways the computation can be carried out. In the first, the whole rotor and the set of seven struts can be modeled without making any geometrical simplification. The second method is to calculate only one seventh of the flow passage through both rotor and struts in relative motion. In the second method, a periodic boundary condition is assumed in the circumferential direction. Such assumption would be invalid if unsteady flow mechanisms are not phase locked with the rotation. For example, vortex shedding from the cylindrical struts might be independent of the motion of the upstream rotor. In other words, there is a risk of losing some physical phenomena when only a single flow passage is calculated. The potential advantage, however, is that the mesh density can be much higher for the same amount of computing resources. Comparison of two computational configurations with the same mesh density shows that the single-passage calculation can be used.

C. Numerical solver, mesh and convergence test

The commercial software package of FLUENT® (version 6.3) was used to solve the unsteady, incompressible, Reynolds averaged Navier-Stokes equation. The Reynolds number based on the midspan rotor blade chord is 8700, which is too low for any "natural" transition from laminar to turbulence, i.e., that arising from Tollmien-Schlichting wave development, to take place. However, factors like inlet flow turbulence or flow separation may cause early transitions. A "rule-of-thumb" critical Reynolds number would be 350 000 (Mayle and Roberts, 1991). Therefore, the flow in the rotor region is unlikely to be turbulent although it is not impossible. The Reynolds number based on the strut diameter is 1590; therefore, the wake flow is likely to be turbulent (Zdravkovich, 1997). The cylinder is located downstream of the rotor and its inlet flow changes from a fairly uniform potential flow to the wake flow periodically. The lift and drag fluctuations induced by the changes in the incoming flow are shown to be much larger than those induced by its own vortex shedding which might well be turbulent; the data for the latter may be found from Norberg, 2001. Furthermore, numerical tests also showed that the timing of the vortex shedding from the cylinder was fully locked to the rotor-strut encounter, and the pattern of self-induced vortex shedding for an isolated cylinder no longer existed. The shedding frequency for an isolated cylinder is estimated as follows. For a cylinder of 4 mm in diameter, placed in a free cross stream of 6.4 m/s, which is the flow velocity relative to the strut, the Strouhal number for the vortex shedding frequency is around $\mathrm{St}=0.2$, hence $f=\mathrm{StU/D}=0.2\times 6.4/0.004=320$ Hz. This frequency is close to but below the blade passing frequency (350 Hz) of the rotor.

A first-order time-accurate scheme was used for the simulation, and the scaled convergence criterion for mass continuity was set at 10^{-4}. For velocities in the axial and lateral directions, a scaled momentum conservation criterion was used and the limit was set at 10^{-6}. For mass continuity, the scaled convergence is defined as the sum of the absolute mass imbalance over all cells divided by the largest such sum in the first five time steps. For the momentum conservation, the criterion is defined as the sum of the absolute momentum imbalance over all cells divided by the sum of absolute momentum fluxes across all cell boundaries. Tests with the second-order time-accurate scheme in FLUENT® showed that it was simply not robust enough for such a complex task.

Computations with three laminar/turbulence model settings were conducted for the rotor-strut interaction and the results are compared in Fig. 2(a). In the first, the laminar flow model is used in both the upstream rotor and the downstream strut domains. In the second, the flow in the rotor domain is assumed laminar, while that in the strut is turbulent. In the third model, both domains are assumed to be turbulent. For the turbulence model, the Reynolds stress model (RSM) is chosen together with the standard wall function treatment with $y^+=1$. Other turbulence models, such as *k*-epsilon and *k*-omega, were also tested but RSM was found to perform better in the sense discussed below. As a basic check on the impact of the choice of the flow models, three-dimensional cross flow through an isolated strut is studied for the diameter based Reynolds number of 1600. The mesh density near the cylinder surface is basically the same as that used in the rotor-strut interaction study, cf. Fig. 1(e). The mean drag, root-mean-square lift and the vortex shedding frequencies are given in Table II where they are also compared with experimental results from literature. It is found that both laminar solver and RSM give reasonable approximation for the shedding frequency and the mean drag, but

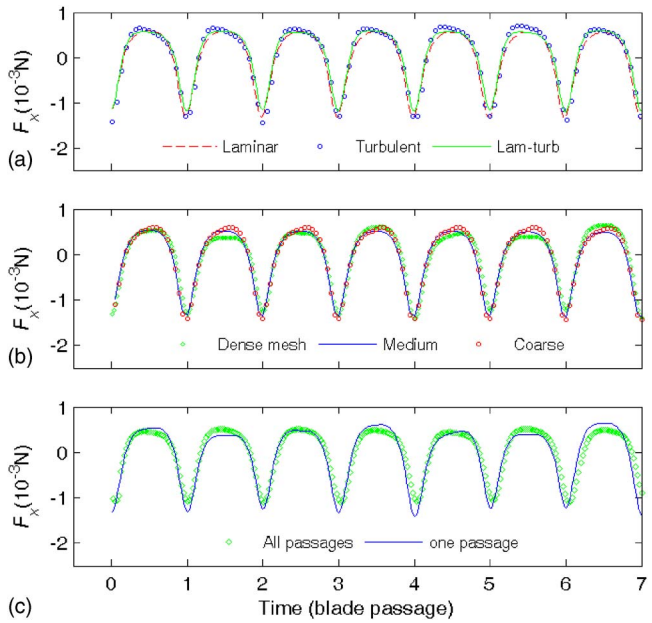

FIG. 2. Flow model and mesh test. (a) Total thrust F_x calculated by three laminar/turbulent flow model settings for the rotor and strut domains. (b) Total thrust F_x calculated by three levels of mesh density: dense mesh with 1.8×10^5 cells, medium mesh with 10^5 cells and coarse mesh with 0.5×10^5 cells. (c) Comparison of the single-passage calculation with the seven-passage calculation, both with high mesh density.

both overestimate the fluctuating lift. In this test, the RSM performs better than the laminar model, but the latter is also retained in this study to examine whether an overestimated wake fluctuation would have serious impact on the final sound radiation. No attempt is made to fine tune the turbulence model to match with the experimental data, which is well known to be a difficult task for certain ranges of Reynolds numbers (Cox *et al.*, 1998; Norberg, 2001) and is beyond the scope of the present investigation. Coming back to the rotor-strut interaction, it is found that different models produce different details of pressure distributions over the strut surface as well as over the rotor pressure side. However, the pressure on the suction side of the rotor blade is relatively insensitive to the laminar/turbulent flow models adopted. The total axial force experienced by the rotor and strut, which is here defined as the thrust, F_x, and shown below to be crucial for the sound radiation, is given as a function of time in Fig. 2(a) for the three settings of flow models for the two domains. The difference of F_x among the three predictions is minimal considering the differences found in the flow details, especially on the strut. It is observed that the force experienced by the strut is basically

TABLE II. Tests of laminar and turbulent flow models for 3D flow across an isolated strut at Re_d=1600.

Method→	Laminar flow	Reynolds stress	Experimental data
Strouhal number	0.19	0.19	0.21 (Norberg, 2001)
Mean drag coefficient	1.1	0.94	1.0 (Zdravkovich, 1997)
RSM lift coefficient	0.53	0.23	0.045 (Norberg, 2001)

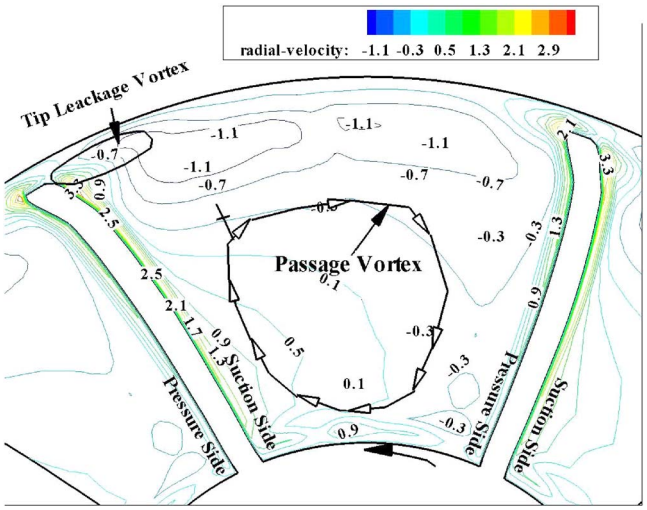

FIG. 3. Radial velocity contour in the rear region with the passage vortex and the tip leakage vortex illustrated.

cancelled out by that on the pressure side of the rotor blades, a phenomenon which is discussed in more detail in Fig. 5. Based on the earlier discussions on the likelihood of flow turbulence, the subsequent flow field analysis is based on the results obtained by the laminar flow for the rotor domain and the RSM for the strut domain.

Apart from these basic tests, tests using the single-passage, laminar-flow model were also conducted to see what level of mesh density would be sufficient. The results are shown in Figs. 2(b) and 2(c). Figure 2(b) shows that the results for three mesh density levels, 5×10^4 cells (open circle), 1×10^5 cells (solid line) and 1.8×10^5 cells (diamond), are rather close. Note that the far-field sound is, in this case, essentially derived from the time derivative of the axial thrust force, dF_x/dt. Details are given in later sections. In addition to the mesh test, tests were also conducted to see if there was any difference between the single-passage model, for which a periodic boundary condition was imposed in the circumferential direction, and the complete model without imposing any circumferential boundary condition. The mesh density, or the number of cells per flow passage, used in the complete model was the same as that used in the single-passage flow model, the latter having 1.8×10^5 cells. The comparison is shown in Fig. 2(c). Given the moderate ratio of mesh cell counts, the convergence of results is satisfactory. In all these calculations, a total of at least 140 time steps were used for one rotational cycle for the unsteady flow computation.

III. ANALYSIS OF THE INTERACTION MECHANISM

A. Features of three-dimensional flow

Before analyzing the unsteady fluid dynamics of the rotor-strut interaction, the overall features of the three-dimensional flow are studied by conducting a steady flow computation using the mixing-plane model at the interface between the rotor and struts. The steady flow field is shown in Fig. 3 for a cross section located at 85% of the axial blade chord from the plane of the leading edge. Despite the small

size of the fan, the flow in the fan rotor is strongly three dimensional, mainly due to (a) the intrinsic fluid dynamics of boundary layers and, (b) large percentage of tip clearance. Shown in Fig. 3 is the contour of the radial velocity, superimposed by sketches of the tip leakage vortex and the passage vortex. The radial transport near the blade suction (convex) side, and the transport from the pressure (concave) side to the suction side on the hub, combined with the tip leakage flow from the suction side to the pressure side in the passage form the passage vortex. The tip leakage flow forms the leakage vortex in the midpassage region of the blade tip. Although the strut is installed in the radial direction and the blade span is also nearly radial, the rotor-strut interaction is a very three-dimensional phenomenon due to the 3D flow structure.

B. Overall sound source distribution

The interaction mechanism is first analyzed in terms of the overall sound source intensity distribution on the blade and strut surfaces. Here, the sound source is characterized essentially by the time derivative of the thrust force or the time derivative of the blade surface pressure, $\partial p/\partial \tau$. The analysis is then focused on the critical moments when the blade sweeps past the struts and strong lift fluctuation occurs. Other moments of weak interaction are also analyzed together with the overall phase angle relations for pressure fluctuations in all parts of the interacting surfaces.

Figure 4 shows the contours of $\partial p/\partial \tau$, with suction and pressure sides of the blades separated. Since the final radiated sound derives from a particular spectral component of $\partial p/\partial \tau$, the contour of the selected spectral component is also shown. Figures 4(a)–4(c) are contours of the root-mean-square values of $\partial p/\partial \tau$. Figure 4(c) is for strut surfaces in unwrapped view.

Locally, the sound source is found to be high in four regions.

(1) The pressure side surface near the trailing edge and 70% of the radial span.
(2) The corresponding trailing edge region on the suction side surface in a less concentrated manner.
(3) The midchord, blade tip region on the suction side where the leakage flow is strong.
(4) The region of strut surface between the front stagnation line and the expansion line, where alternating flow separation occurs.

The relation between the phase angle of the unsteady pressure on the two sides of the rotor blade is such that the sound radiated by the two sides basically adds to each other.

C. Events surrounding the peak lift fluctuation

Sound radiation is a result of acoustic interference among all surfaces. The phase relation between pressure fluctuations on the suction, pressure and strut surfaces is crucial for the final sound radiation. The relation is shown in Fig. 5(a) where the contributions to the integrated lift are decomposed for the time worth of two blade passages. For this particular example, the total thrust (simple solid line) is almost the same as the contribution from the blade suction surface (dashed line) since the contributions from the pressure side (solid line with downward triangle) are found to be almost completely cancelled out by that from the strut (solid line with open circles). It may be said that the pressure side of the blade is always "seen" by the strut and the two behave very much like two cylinders in tandem at a separation distance sufficiently large to allow this effect to cancel out. This observation is only true for the geometric parameters chosen; changing them could alter the results. Notice, however, that the cancellation may not be so complete when the working parameters are changed.

Figure 5(b) shows the time derivative of the total thrust. Three moments, labeled as A, B and C, are identified for further analysis of the flow field. The pressure contours for the three moments are shown in Fig. 6 for the revolution surface on the 70% of the radial span. The event near the peak, labeled as A, occurs when the center of the strut is immediately downstream of the blade trailing edge. Figure 6(a) shows that, due to the relative motion, the flow towards the cylinder hits the upper left side of the cylinder, where the stagnation point is located. The high pressure here essentially blocks the flow passing over the suction side of the blade, leading to a sudden increase of pressure on the suction surface. The opposite event occurs for the pressure side of the blade. The expansion point on the lower-right quadrant provides a low pressure condition for the flow over the pressure side leading to a decrease of pressure there compared with if the stagnation point were on the lower left without rotor-strut relative motion.

An interesting feature is found for times B and C and, to a lesser extent, also for time A. For the pressure side of the blade, pressure contour lines intercept the surface curve, meaning that the pressure increases from the leading edge towards the trailing edge. On the suction surface, however, the contour lines are almost parallel with the surface. In other words, the pressure response on the upper surface is almost uniform.

D. Weak interactions

During much of the time period from A to C in Fig. 5(b), the total thrust force is almost constant, cf. solid line in Fig. 5(a). In this period, the strut is passing through the "potential core" region of the blade passage and the blade-strut interaction is weak. The pressure contours of B and C are shown in Figs. 6(b) and 6(c). Two observations are made.

(a) As time advances from B to C, the pressures on the pressure side of the blade and on the strut change in a smooth manner, and the two almost cancel each other out in terms of their contributions towards the integrated thrust. However, the suction surface of the blade maintains almost constant pressure, as shown in Figs. 5(b) and 5(c). This could be a result of a shielding effect of the suction surface from the downstream cylinder. In other words, the cylinder can only be seen by the pressure side of the blade during this period of time.
(b) Moving from time B to time C, again as shown in Figs. 5(b) and 5(c), the front stagnation point of the cylinder

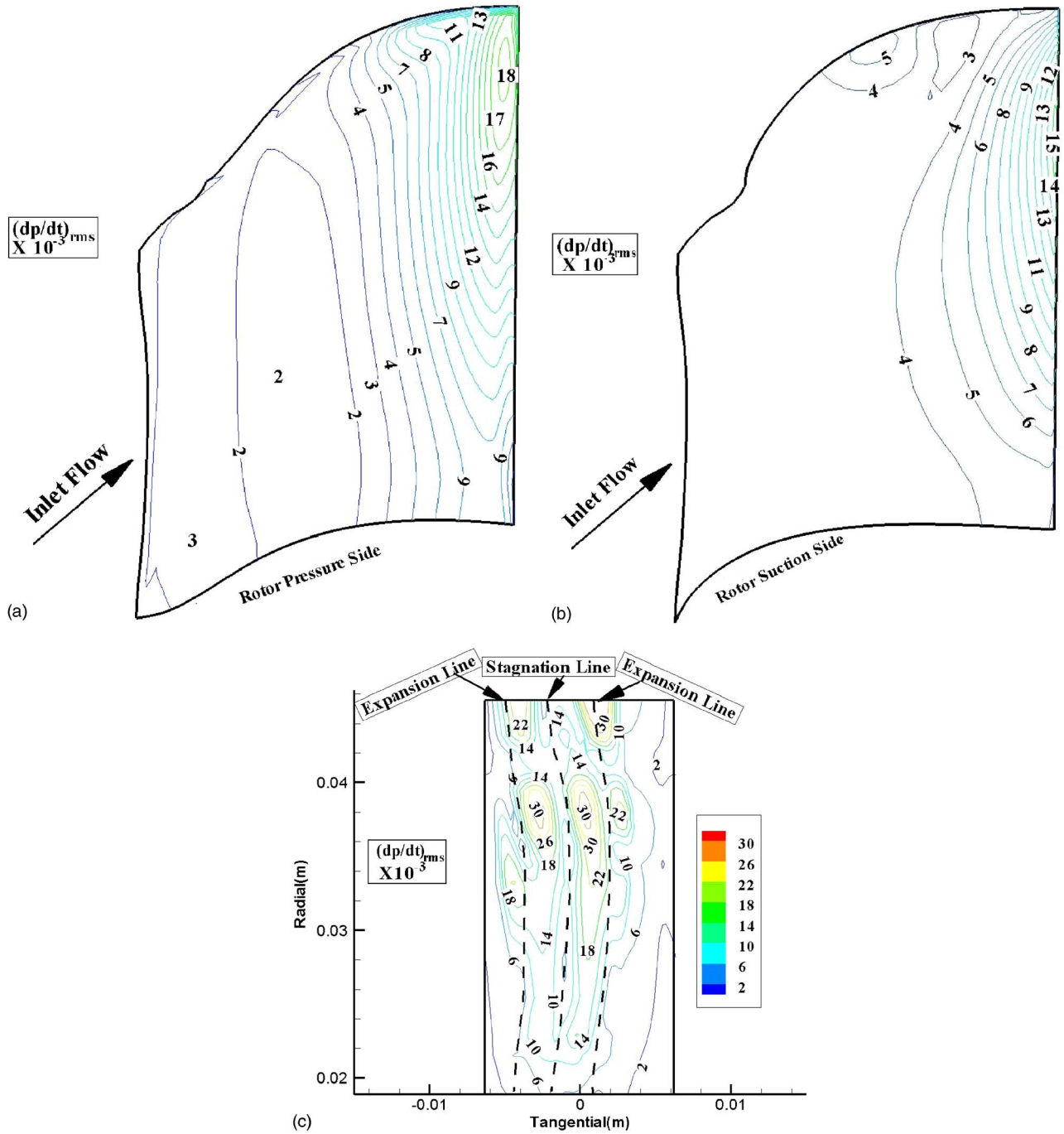

FIG. 4. Contours of the sound source term $\partial p/\partial \tau|_{rms}$ on (a) the rotor pressure side, (b) the rotor suction side, and (c) the strut suction and pressure sides in unwrapped view.

projects a "column" of high pressure region which is connected to the trailing edge of the blade, leading to a maximum pressure on the pressure side of the blade. Since the thrust force F_x described here is the force acting on the fluid from the blade, high pressure on the blade pressure side means a high thrust in the positive x direction. For the strut, the thrust acting on the fluid is directed towards upstream, hence the negative value.

IV. PREDICTION OF SOUND AND EXPERIMENTAL VALIDATION

It is difficult to measure the unsteady flow field experimentally on the rotating blades. The comparison between the computation described above and the experiment is conducted at the acoustic level. The sound radiation predicted by integrating the Ffowcs Williams-Hawkings' acoustic equation is compared with the measured sound in terms of (a) the acoustic directivity of sound intensity, and (b) the time-domain sound pressure signature.

A. Computation of the radiated sound

The prediction of the radiated sound follows the well established Ffowcs Williams-Hawkings' equation (1969), which is the extension of the Lighthill acoustic analogy. With

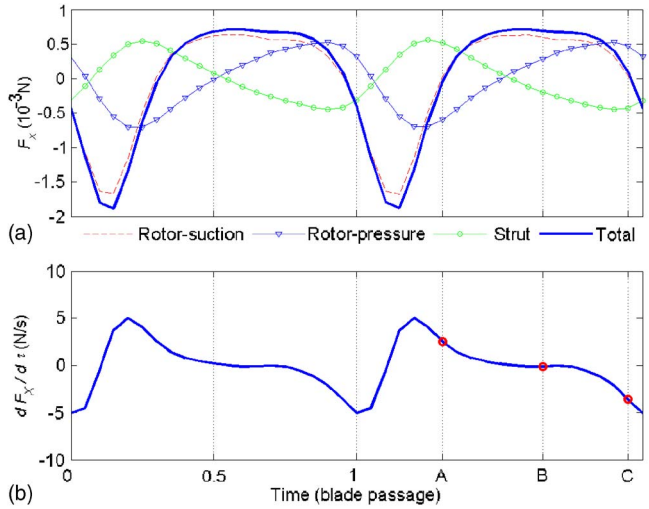

FIG. 5. Strong and weak interaction periods. (a) Decomposition of the thrust forces into contributions from the two blade surfaces and the strut. (b) The time derivative of the total thrust.

the quadrupole term neglected for the low-speed applications, the equation is written in its integral form as

$$p(\mathbf{x},t) = \frac{\partial}{\partial t}\int_S \left[\frac{\rho_0 v_n}{4\pi r|1-M_r|}\right]_{\text{ret}} dS - \frac{\partial}{\partial x_i}\int_S \left[\frac{F_i}{4\pi r|1-M_r|}\right]_{\text{ret}} dS, \quad (1)$$

where $x=(x_1,x_2,x_3)$ is the position of the observer, t is the reception time, ρ_0 is the undisturbed fluid density, c_0 is the speed of sound, S is the source (blade) surface which moves at an outward normal velocity of v_n, $r=|x-y|$ is the source-to-observer distance, M_r is the Mach number of the source movement velocity projected to the r direction, F_i is the pressure force acting on the surface projected to the x_i direction, and subscript "ret" implies evaluation at the retarded time

$$\tau = t - \frac{r}{c_0} \quad (2)$$

when the sound is radiated. Note that the square brackets in Eq. (1) are evaluated at this retarded time. The actual implementation of Eq. (1) is easier if the time and space derivatives are absorbed into the integrands which depend on x_i and t through the retarded time τ and the factor of r. The result is the so-called Formulation 1A derived by Farassat and Succi (1983)

$$p = p'_T + p'_L,$$

$$4\pi p'_T = \rho_0 \int_S \left[\frac{(\dot{v}_n + v_{\dot{n}})}{r|1-M_r|^2} + \frac{v_n(r\dot{M}_r + c_0(M_r - M^2))}{r^2|1-M_r|^3}\right]_{\text{ret}} dS,$$

$$4\pi p'_L = \frac{1}{c_0}\int_S \left[\frac{\dot{F}_r}{r|1-M_r|^2} + \frac{c_0(F_r - F_M M)}{r^2|1-M_r|^2} + \frac{F_r(r\dot{M}_r + c_0(M_r - M^2))}{r^2|1-M_r|^3}\right]_{\text{ret}} dS, \quad (3)$$

where the sound pressure is divided into thickness (subscript T) and loading (subscript L) contributions, the dot over variables is the retarded time derivative, F_M is the force projected to the source movement direction. For the current problem, the time derivative for the Mach number is essentially the centripetal acceleration

$$\dot{M}_r = \frac{\partial \mathbf{M}}{\partial \tau}\cdot\frac{\mathbf{r}}{r} = -\omega M \frac{\mathbf{r}_s\cdot\mathbf{r}}{r_s r}, \quad \frac{\mathbf{r}_s\cdot\mathbf{r}}{r_s r} = \sin\alpha, \quad (4)$$

where r_s is the cylindrical radius of the source element dS with respect to the rotational axis, and α is the latitudinal angle of the observer measured from the rotational axis.

Notice that the terms with a distance dependence of r^{-1} is the far-field sound, while those with r^{-2} are the near-field sound. Since the computed sound is to be compared with experimental measurement at a distance of $r_0=0.5$ m from the fan center, and the wavelength of the blade passing frequency is $c_0/f=340/350=0.97$ m, there is a certain near-field effect. The effect of the near field on the measured sound pressure signature is discussed later.

In the third group of the third expression of Eq. (3), there are both far-field and near-field terms, the one associated with $F_r\dot{M}_r$ being the far-field term. This term joins the first term of $\dot{F}_r$ and form the far-field loading noise

$$p'_{L\infty}(\mathbf{x},t) = \frac{1}{4\pi c_0}\int_S \left[\frac{\dot{F}_r}{r(1-M_r)} - \frac{F_r\omega M\sin\alpha}{r|1-M_r|^3}\right]_{\text{ret}} dS. \quad (5)$$

When the loading measured in the rotating reference frame is a constant, $F_r(\tau)=$const, the second term in the above equation makes far-field noise by the changing radiation distance due to the source movement. This is part of the so-called Gutin noise, which also includes the far-field terms of p'_T in Eq. (3). Gutin noise is only significant when the rotating speed is reasonably high. Using the formulations of (Lowson, 1970) and the approximation for small tip Mach number, $M=0.037$ in this case, it can be shown that the ratio of the sound pressure radiated by the Gutin noise to that of the interaction noise is proportional to $L_0(BM)^B/L_1$, where L_0 is the amplitude of the steady flow loading, L_1 is the amplitude of the blade passing frequency (BPF) component of the loading caused by the interaction, and B is the number of blades, seven in this case. A detailed estimate for the present fan working in free delivery condition indicates that the integrated sound power from the Gutin noise is about 70 dB below that of the interaction noise. Back to Eq. (5), the rotor-stator interaction noise derives from the unsteady loading $\dot{F}_r$. The dominant far-field noise in this case is approximated by neglecting the factor of $1-M_r$ in Eq. (5) and the Gutin noise

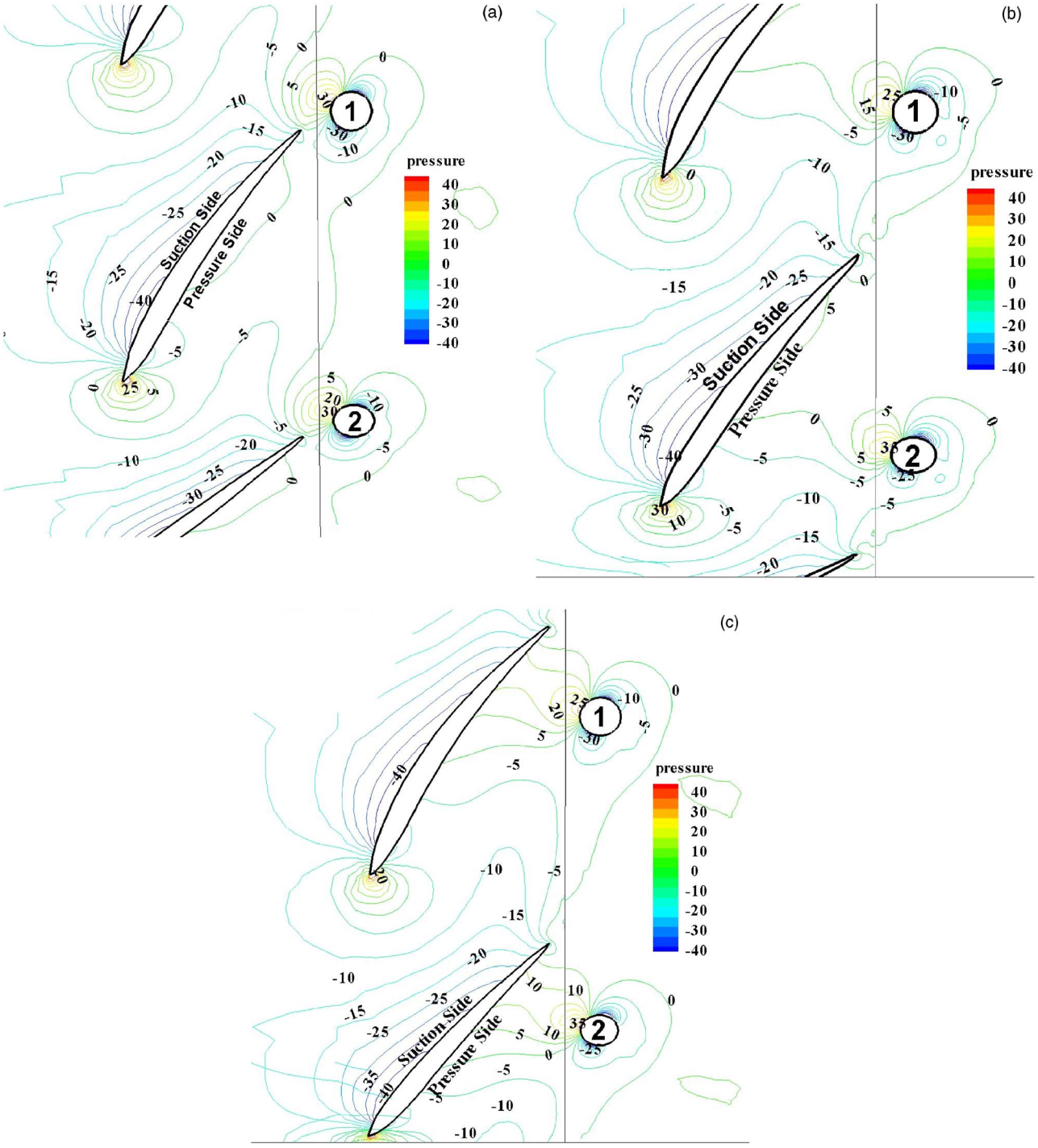

FIG. 6. The pressure contours on the revolution surface of 70% radial span at three moments A, B, and C marked in Fig. 5(b).

$$p_\infty(\mathbf{x},t) \approx \left[\frac{\partial}{\partial\tau}\int_S F_r dS\right]_{\text{ret}} \Big/ (4\pi r_0 c_0), \tag{6}$$

where r_0 is the distance of the observer to the center of the fan. Also, when the forces do change with time, the second term of Eq. (5) should be computed as part of the non-Gutin noise. Besides, all loading noise terms associated with F_r and F_M in Eq. (3) should also be computed for the purpose of comparison with the experimentally measured sound in the near field.

Equation (6) is a point-source approximation for small and slow axial-flow fans, and its deviation from the full integration of Eq. (5) represents a measure of source noncompactness, which is apparently small for the present study. Having said that, it does not mean that there is no acoustic interference between sound waves radiated at different parts of the fan. The interference arises mainly through different phase angle distributions on the blades, which determines the outcome of $[\int_S F_r dS]_{\text{ret}}$ in Eq. (6). As shown earlier, the suction surface of the rotor blade seems to have rather uniform phase angle, as evidenced by the pressure contours parallel to the surface in Fig. 6, but the pressure surface has a diverse

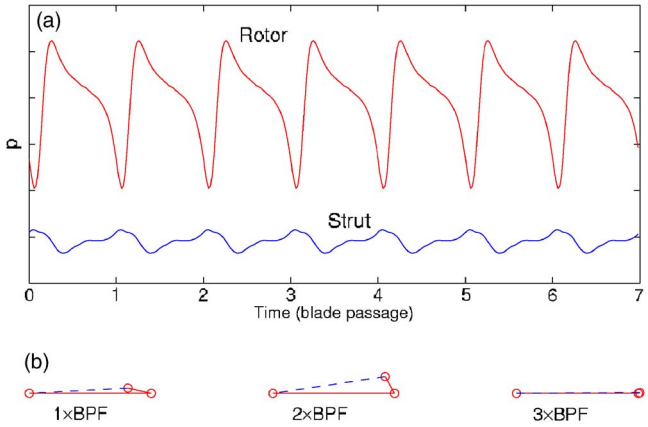

FIG. 7. Rotor-strut acoustic interference. (a) Sound pressure decomposition into rotor (upper curve) and strut (lower curve) contributions. (b) Vectorial representation of complex sound amplitudes for the first three blade passing frequencies. The broken lines are the total sound amplitude consisting of the rotor (horizontal line) and strut (oblique line) contributions.

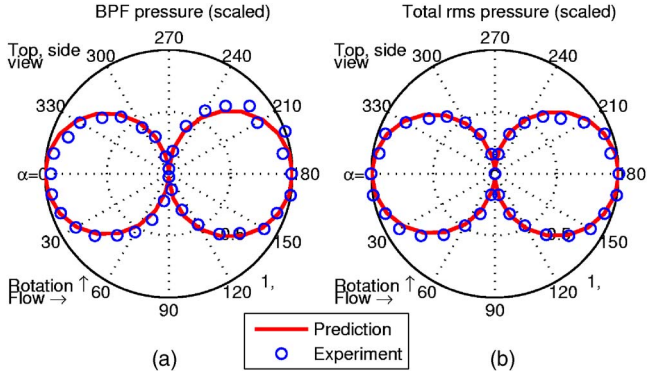

FIG. 8. Comparison of the acoustic directivity of sound pressure (rms) between experiment (○) and prediction (−) for the (a) BPF and (b) all frequencies. Both are scaled by the values on the pressure on the rotational axis. The directivity is taken on the horizontal plane while the fan stands in its upright position with flow from left to right.

phase distribution. Nevertheless, it is physically more straightforward to study the acoustic interference between the sound waves radiated by the rotor blades and those by the struts, instead of waves from the two surfaces of the rotor blades. The result of the rotor-strut acoustic interference is shown in Fig. 7 for sound received at r_0=0.5 m upstream of the fan center along the rotational axis.

Figure 7(a) decomposes the sound radiated by the rotor blades (upper curve) and struts (lower curve) in a waterfall format with the same vertical scale. Overall, the ratio of the linear pressure amplitudes is 5.8 in favor of the rotor blades. Considering the fact that the strut is downstream of the rotor, this result reveals that the aeroacoustic mechanism in a small fan like this differs from the familiar interaction mechanism between a rotor and profiled stator blades. In the current configuration, the rotor experiences periodic change in the blockage by the downstream strut. This is mainly a potential flow interaction. The struts, on the other hand, experience drastic changes in the incoming flow due to the rotor wakes periodically hitting the struts. The interaction has both viscous and inviscid contributions. Due to the nature of the bluff body, the oscillating force occurring on the strut is not as impulsive as that which occurs on the rotor blades.

Figure 7(b) analyzes the acoustic interference in terms of the first three BPF harmonics. First, Fourier transform is applied to both sound waves shown in Fig. 7(a). The complex amplitude of the strut sound is then divided by that of the rotor sound. The complex ratio is shown in vector form. The horizontal line has a length of unity and it represents the rotor noise. The connecting oblique solid line represents the strut noise and the broken line is the total noise. The phase angle differences between the rotor and strut sounds are 167.1°, 119.5°, and 26.2°, for the (1–3) BPF frequencies, respectively. The length of the strut noise is seen to decrease with the harmonic index of the BPF. In other words, the strut noise features more at low frequencies. The interference is destructive for the first two frequency components. The strut noise for the third BPF is insignificant, so is its interference with the rotor noise. If the strut is considered to produce cancellation noise, its timing is found to lag behind the rotor by 12.9°, 60.5° for the first two BPFs, respectively.

B. Experiment and comparison

Experimentally, it is only possible to measure the total sound radiated by the fan and this is compared with the prediction as follows. The acoustic measurement was conducted in the full anechoic chamber. Details of the general setup are given in (Huang and Wang, 2005). The measurement microphone was placed at r_0=0.5 m from the fan center. The reason why the measurement was not taken at a much longer distance from the fan center was that higher frequency components became, as shown in Fig. 9(b), rather faint for the microphone to capture, higher frequency component being crucial for the detailed wave signature during the event of rapid rotor-strut encounter. The sampling rate is 16 kHz, and the BPF is 350 Hz. A special feature in this measurement is that sound waves are averaged over many rotational cycles determined by the tachometer signals. The time period for the rotational cycle varies as the fan speed varies from one cycle to the next. Typically, the rpm varies by ±10 with a mean of 3000 in one test lasting 10 s. This variation is corrected and the synchronous average of the sound signal thus derived has a sharp peak on the BPF and its higher order harmonics. Without such time-base correction, spectral leak or broadening would occur.

The comparison of acoustic directivity is shown in Figs. 8(a) and 8(b) for the BPF component and the total rotary noise, respectively. Experimental results are shown in open circles and the numerical predictions in solid curves. In order to focus on the distribution pattern, both experimental results and the predictions are normalized by the rms sound pressure on the rotational axis. The orientation of the fan is such that the flow goes from 0° to 180°(left to right), and the axis formed between 90° and 270° represents the rotational plane. Very close agreement is found in terms of the spatial distribution. The pattern is a clear thrust dipole (Huang, 2003) as no drag noise can be radiated in this coincident design in which the number of rotor blades is equal to the number of struts. When sound intensity is integrated over the measurement sphere, sound power is obtained. For the BPF, the pre-

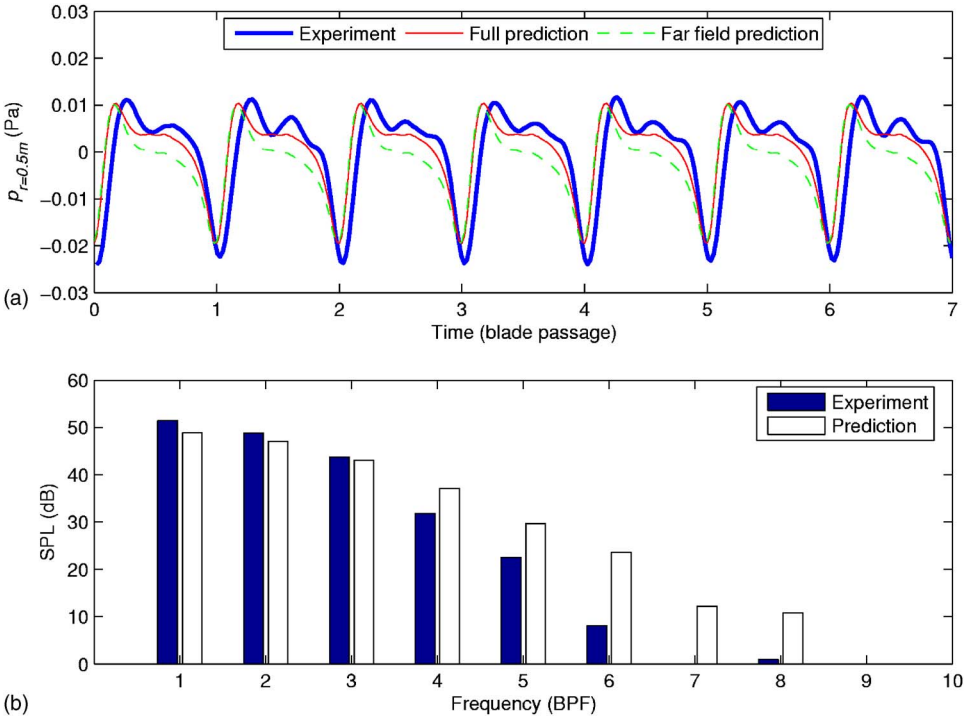

FIG. 9. Comparison of experimental measurement and numerical prediction of sound at 0.5 m upstream of the fan center on the rotational axis. (a) Pressure wave forms. (b) Spectra.

diction is 48.9 dB (re 10^{-12} W) while the experiment is 51.7 dB. When all BPF harmonics are added, the prediction has 51.8 dB while the experiment has 53.8 dB. The noise is under predicted by about 2.8 and 2.0 dB for the BPF and all frequencies, respectively.

Since the radiation of sound peaks on the rotational axis, the comparison of prediction and experiment is conducted for the upstream axial point. The result is shown in Fig. 9. Figure 9(a) shows that there is a general agreement of wave form between the measured sound pressure (thick solid line) and the predicted one (thin solid line). Both show a rather sharp impulse for each blade passage in front of struts, but there are several differences. First, the falling curve and the rising edge of the impulse are rather symmetrical with respect to the trough in the experimental data while the computational results are not. Second, the measured sound pressure features some ringing ripples, while the computation gives a smooth curve in the region between two consecutive impulses. Having said this, the overall signatures agree with each other very closely.

When the near-field terms are neglected in the prediction, the radiated sound is given by Eq. (5) and the result is shown as the dashed line in Fig. 9(a). The major difference between the near-field sound (thin solid line) and the far-field sound (dashed line) lies in the pressure level during the weak-interaction period illustrated by Figs. 6(b) and 6(c). The near-field effect maintains the pressure at a high level following the strong interaction, while the far-field radiation features more symmetrical impulses before and after the rotor-strut encounter.

Figure 9(b) compares the spectra of the experiment (filled bar) and the near-field prediction (open bar). The sound pressure level for the fundamental blade passing frequency (BPF) is very close, the prediction being 2.5 dB lower than the experiment. Over prediction occurs when the order of harmonics is greater than 3. These over predictions are obvious manifestations of the sharp rise of sound pressure following the rotor-strut encounter. The discrepancy of the total sound pressure level is mainly controlled by the first few peaks, and the prediction is 1.9 dB below the experiment. This difference could be attributed to many factors: such as the difference between the real flow conditions and the boundary conditions imposed in the numerical simulation for the sake of numerical convenience, possible inlet flow distortions occurring in the experiment.

V. CONCLUSIONS

This study is motivated by the understanding of the aeroacoustic mechanism of the tonal noise radiated by a well-designed fan. The study is based on the numerical simulation of incompressible flow through a rotor and a set of downstream struts. The physical construction of the fan is such that a two-dimensional aerodynamic design procedure might suffice as both the blades and the struts are almost aligned in the radial direction. However, the flow field is found to be highly three-dimensional due to the existence of strong tip leakage flow, passage vortex, and radial transport of boundary layer flow, or the secondary flow. Three-dimensional, unsteady flow is simulated by FLUENT® 6.3 for which the convergence test for mesh density and benchmark tests are conducted. The simulated thrust fluctuation is compared with the acoustic measurement, and the overall discrepancy in terms of the total sound power is around 2.0 dB. The numerical results are analyzed to reveal a few interesting phenomena of the rotor-strut interaction. The following conclusions are drawn.

(1) When compared with the acoustic measurement, the 3D simulation method adopted in the current study seems to under predict the lift deficit and recovery immediately

following the passing of the blade trailing edge in front of the strut. Nevertheless, it is argued that the main character of the thrust fluctuations is captured satisfactorily.

(2) The fluctuating forces are derived from contributions from three parts: the blade suction (convex) surface, the blade pressure (concave) surface, and the strut. The two latter factors seem to cancel each other out fairly completely, and the overall signature resembles closely the response of the suction surface.

(3) The suction surface experiences sudden pressure increase, hence lift deficit, when the cylinder (strut) first emerges from the pressure side of the flow passage. The response on the whole chord length is rather uniform, unlike the pressure side response which is more concentrated near the trailing edge. In terms of the radial distribution of the sound source, highest response is found at around 70% of the blade span.

(4) The mechanism of the suction surface pressure increase is explained by the blockage of the flow past the suction surface when the front stagnation point provides a high back pressure for the suction surface.

(5) The sound radiated by the coincident design of $B=S$ features thrust dipole along the rotational axis. The acoustic interference between the rotor and the strut is destructive and the strut sound lags behind the rotor sound.

ACKNOWLEDGMENT

The project is supported by the Central Allocation Scheme of the Research Grants Council of the Hong Kong SAR Government (PolyU1/02C).

Blake, W. K. (**1986**). *Mechanics of Flow-Induced Sound and Vibration* (Academic, Orlando, FL).

Chiu, W. S., Lauchle, G. C., and Thompson, D. E. (**1989**). "Subsonic axial-flow fan noise and unsteady rotor force," J. Acoust. Soc. Am. **85**, 641–647.

Cox, J. S., Brentner, K. S., and Rumsey, C. L. (**1998**). "Computation of vortex shedding and radiated sound for a circular cylinder: Subcritical to transcritical Reynolds numbers," Theor. Comput. Fluid Dyn. **12**, 233–253.

Cudina, M. (**1992**). "Noise generated by a vane-axial fan with inlet guide vanes," Noise Control Eng. J. **39**, 21–30.

Farassat, F., and Succi, G. P. (**1983**). "The prediction of helicopter discrete frequency noise," Vertica **7**, 309–320.

Ffowcs Williams, J. E., and Hawkings, D. L. (**1969**). "Sound generation by turbulence and surfaces in arbitrary motion," Philos. Trans. R. Soc. London, Ser. A **264**, 321–342.

Fukano, T., Takamatsu, Y., and Kodama, Y. (**1986**). "The effects of tip clearance on the noise of low pressure axial and mixed flow fans," J. Sound Vib. **105**, 291–308.

Kameier, F., and Neise, W. (**1997**). "Rotating blade flow instability as a source of noise in axial turbomachines," J. Sound Vib. **203**, 833–853.

Kemp, N. H., and Sears, W. R. (**1953**). "Aerodynamic interference between moving blade rows," J. Aeronaut. Sci. **20**, 583–598.

Kemp, N. H., and Sears, W. R. (**1955**). "Unsteady forces due to viscous wakes in turbomachines," J. Aeronaut. Sci. **22**, 478–483.

Hodson, H. P. (**1985**). "Measurements of wake-generated unsteadiness in the rotor passages of axial flow turbines," J. Eng. Gas Turbines Power **107**, 467–476.

Howe, M. S. (**1999**). "Trailing edge noise at low Mach numbers," J. Sound Vib. **225**, 211–238.

Huang, L. (**2003**). "Characterizing computer cooling fan noise," J. Acoust. Soc. Am. **114**, 3189–3200.

Huang, L., and Wang, J. (**2005**). "Acoustic analysis of a computer cooling fan," J. Acoust. Soc. Am. **118**, 2190–2200.

Huang, L., Zou, Z. P., and Xu, L. (**2003**). "Prediction of computer cooling fan noise using a 3D unsteady flow solver," *Noise-Con 2003*, Cleveland, Ohio, 23–25 June.

Lighthill, M. J. (**1952**). "On sound generated aerodynamically: I. General theory," Proc. R. Soc. London, Ser. A **211**, 564–587.

Lowson, M. V. (**1965**). "The sound field for singularities in motion," Proc. R. Soc. London, Ser. A **286**, 559–572.

Lowson, M. V. (**1970**) "Theoretical analysis of compressor noise," J. Acoust. Soc. Am. **47**, 371–385.

Mailach, R., Muller, L., and Vogeler, K. (**2003**). "Experimental investigation of unsteady force on rotor and stator blades of an axial compressor," *Proc. Fifth Euro. Conf. Turb.-Fluid Dyn. Thermo.* pp. 221–223, M. Stastny, C. H. Sieverding, and G. Bois, editors., March 18–21, Prague, Czech Republic.

Mailach, R., and Vogeler, K. (**2004a**). "Aerodynamic blade row interactions in an axial compressor-Part 1: Unsteady boundary layer development," J. Turbo. **126**, 35–44.

Mailach, R., and Vogeler, K. (**2004b**). "Aerodynamic blade row interactions in an axial compressor-Part 2: Unsteady profile pressure distribution and blade force," J. Turbo. **126**, 45–51.

Majumdar, S. J., and Peake, N. (**1998**). "Noise generation by the interaction between ingested turbulence and a rotating fan," J. Fluid Mech. **359**, 181–216.

Mayle, R. E., and Roberts, W. B. (**1991**). "The role of laminar-turbulent transition in gas turbine engines," ASME J. Turbomach. **113**, 509–537.

Mayle, R. E., and Dullenkopf, K. (**1989**). "A theory for wake-induced transition," J. Turbo. **111**, 188–195.

Norberg, C. (**2001**). "Flow around a circular cylinder: Aspects of fluctuating lift," J. Fluids Struct. **15**, 459–469.

Trunzo, R., Lakshminarayana, B., and Thompson, D. E. (**1981**). "Nature of inlet turbulence and strut flow disturbances and their effect on turbomachinery rotor noise," J. Sound Vib. **76**, 233–259.

Wang, J., and Huang, L. (**2006**). "Quantification and control of noise sources in a small axial-flow fan," Noise Control Eng. J. **54**, 27–32.

Wang, M., Freund, J. B., and Lele, S. K. (**2006**). "Computational prediction of flow-generated sound," Annu. Rev. Fluid Mech. **38**, 483–512.

Washburn, K. B., and Lauchle G. C., (**1998**) "Inlet flow condition and tonal sound radiation from a subsonic Fan," Noise Control Eng. J. **31**, 101–110.

Zdravkovich, M. M. (**1997**). *Flow Around Circular Cylinders Vol. 1: Fundamentals* (Oxford University Press, Oxford).

Tomographic reconstruction of atmospheric turbulence with the use of time-dependent stochastic inversion

Sergey N. Vecherin
Department of Physics, New Mexico State University, Las Cruces, New Mexico 88003

Vladimir E. Ostashev
NOAA/Earth System Research Laboratory, Boulder, Colorado 80305 and Department of Physics, New Mexico State University, Las Cruces, New Mexico 88003

A. Ziemann
University of Leipzig, Institute for Meteorology, Stephanstrasse 3, 04103 Leipzig, Germany

D. Keith Wilson
U.S. Army Engineer Research and Development Center, Hanover, New Hampshire 03755

K. Arnold
University of Leipzig, Dezernat 2, Goethestr. 6, 04109 Leipzig, Germany

M. Barth
University of Leipzig, Institute for Meteorology, Stephanstr. 3, 04103 Leipzig, Germany

(Received 16 November 2006; revised 14 June 2007; accepted 18 June 2007)

Acoustic travel-time tomography allows one to reconstruct temperature and wind velocity fields in the atmosphere. In a recently published paper [S. Vecherin *et al.*, J. Acoust. Soc. Am. **119**, 2579 (2006)], a time-dependent stochastic inversion (TDSI) was developed for the reconstruction of these fields from travel times of sound propagation between sources and receivers in a tomography array. TDSI accounts for the correlation of temperature and wind velocity fluctuations both in space and time and therefore yields more accurate reconstruction of these fields in comparison with algebraic techniques and regular stochastic inversion. To use TDSI, one needs to estimate spatial-temporal covariance functions of temperature and wind velocity fluctuations. In this paper, these spatial-temporal covariance functions are derived for locally frozen turbulence which is a more general concept than a widely used hypothesis of frozen turbulence. The developed theory is applied to reconstruction of temperature and wind velocity fields in the acoustic tomography experiment carried out by University of Leipzig, Germany. The reconstructed temperature and velocity fields are presented and errors in reconstruction of these fields are studied. © *2007 Acoustical Society of America.* [DOI: 10.1121/1.2756798]

PACS number(s): 43.28.We, 43.28.Vd, 43.20.Dk [RR] Pages: 1416–1425

I. INTRODUCTION

Knowledge about temperature and wind velocity fields is important in many disciplines, e.g. boundary layer meteorology, theories of turbulence, and studies of electromagnetic and acoustic wave propagation in the atmosphere. A conventional way to measure the temperature and wind velocity is to use *in situ* sensors. However, such measurements can provide the data only at some spatial points. To measure the temperature and velocity fields with high resolution, a very large number of sensors is required. This will not only increase the cost of measurements but also distort the original fields. This problem can be overcome by using acoustic tomography.

Acoustic travel-time tomography of the atmosphere allows one to reconstruct temperature $\tilde{T}(\mathbf{R})$ and wind velocity $\tilde{\mathbf{V}}(\mathbf{R})$ fields in a tomographic volume or area given positions of sound sources and receivers and travel times t_i^{tr} of sound propagation between them. Here, $\mathbf{R}=(x,y,z)$ is a vector in the Cartesian coordinate system and $i=1,2,\ldots,I$, where I is the number of data t_i^{tr}, i.e., the number of sound propagation paths between sources and receivers.

In the past decade, several acoustic travel-time tomography experiments have been carried out in the lowermost few meters of the atmosphere.[1–9] Further, some works were done on numerical simulation of acoustic tomography of the atmosphere.[10–13] One of the main problems in both tomography experiments and numerical simulations is to find a good inverse algorithm for reconstruction of $\tilde{T}$ and $\tilde{\mathbf{V}}$ fields. Most of the algorithms used so far employed a partition of a tomographic volume into grid cells where the values of $\tilde{T}$ and $\tilde{\mathbf{V}}$ are constant, and a subsequent solution of a set of algebraic equations.[3–9,11,12,14,15] Numerical simulations have shown[12] that these algebraic algorithms can give a good reconstruction of $\tilde{T}$ and $\tilde{\mathbf{V}}$ fields if the number of the grid cells is small enough so that a corresponding inverse problem is overdetermined (the number of equations is greater than the number of unknowns). However, in two-dimensional (2D)

tomography experiments, for example, there are three continuous fields to reconstruct (temperature and two components of velocity), whereas the number of data is limited. (A large number of sources and receivers can distort the $\tilde{T}$ and $\tilde{\mathbf{V}}$ fields inside a tomographic area.) Therefore, the number of grid cells where $\tilde{T}$ and $\tilde{\mathbf{V}}$ are reconstructed is relatively small (a few dozen or less).

To increase spatial resolution of the reconstructed temperature $\tilde{T}$ and velocity $\tilde{\mathbf{V}}$ fields, one can use a stochastic inversion (SI), which is appropriate for solutions of inverse problems involving continuous fields.[2,16] In SI, the increase in spatial resolution comes with a price: One needs to know spatial covariance functions $B_{TT}^{s}(\mathbf{R}_1,\mathbf{R}_2)$ and $B_{ij}^{s}(\mathbf{R}_1,\mathbf{R}_2)$ of temperature and velocity fluctuations at the time moment t of an experiment. Here, s stands for spatial, and i and j indicate the components of wind velocity vector. Recent studies have shown[13,17] that, in SI, the use of different covariance functions (exponential, Gaussian, von Kármán, and some others) results in the reconstructed temperature and velocity fields which are nearly identical (with a relationship between correlation lengths that provides the equality of the integral lengths of these functions, see Ref. 18 for details). Therefore, one of these covariance functions, e.g., Gaussian, can be used in SI. Note that in SI the accuracy of $\tilde{T}$ and $\tilde{\mathbf{V}}$ reconstruction increases with the increase of the number I of data.

To increase the number of data without increasing the number of sources and receivers, a time-dependent stochastic inversion (TDSI) in acoustic tomography of the atmosphere was proposed in Ref. 19. In TDSI, the travel times t_i^{tr} are measured repeatedly at the time moments $t_1,t_2,\ldots,t_n$. Then, the fields $\tilde{T}(\mathbf{R},t)$ and $\tilde{\mathbf{V}}(\mathbf{R},t)$ are reconstructed given n sets of t_i^{tr}, positions of sources and receivers, and assuming that the spatial-temporal covariance functions of temperature and wind velocity fluctuations, $B_{TT}(\mathbf{R}_1,t_1;\mathbf{R}_2,t_2)$ and $B_{ij}(\mathbf{R}_1,t_1;\mathbf{R}_2,t_2)$, are known. In Ref. 19, these spatial-temporal covariance functions were determined assuming that turbulence is frozen,[20] i.e., temperature and wind velocity fluctuations are advected with the constant wind velocity $\mathbf{V}_0$. Numerical simulation of acoustic tomography of the atmosphere showed that TDSI allows better reconstruction of temperature and velocity fields than SI does.[19]

A general idea to use spatial-temporal covariances in SI is known in the literature. For example, this idea has been successfully used in the satellite altimetry of the ocean surface level.[21–23] TDSI in acoustic tomography of the atmosphere is somewhat similar to methods used in the satellite altimetry. However, a mathematical apparatus of TDSI is different from that used in altimetry and was developed in Ref. 19.

The main goal of the present paper is further development of a mathematical apparatus of TDSI and the use of the developed theory in the reconstruction of the $\tilde{T}$ and $\tilde{\mathbf{V}}$ fields in the acoustic tomography experiment STINHO (STructure of turbulent transport under INHOmogeneous surface conditions) carried out by University of Leipzig, Germany.[9] First, we derive analytical formulas for $B_{TT}(\mathbf{R}_1,t_1;\mathbf{R}_2,t_2)$ and $B_{ij}(\mathbf{R}_1,t_1;\mathbf{R}_2,t_2)$ for the case of locally frozen turbulence which is a generalization of the hypothesis of frozen turbulence. The obtained formulas for $B_{TT}(\mathbf{R}_1,t_1;\mathbf{R}_2,t_2)$ and $B_{ij}(\mathbf{R}_1,t_1;\mathbf{R}_2,t_2)$ account for the variance of wind velocity fluctuations σ_V and, hence, are much more realistic than those for the case of frozen turbulence where σ_V is tacitly assumed 0. Second, we determine errors in the input data for TDSI. Finally using these errors and formulas for $B_{TT}(\mathbf{R}_1,t_1;\mathbf{R}_2,t_2)$ and $B_{ij}(\mathbf{R}_1,t_1;\mathbf{R}_2,t_2)$ for locally frozen turbulence, we apply TDSI for reconstruction of $\tilde{T}$ and $\tilde{\mathbf{V}}$ fields in the acoustic tomography experiment STINHO. Note that this is the first reconstruction of the temperature and wind velocity fields in an acoustic tomography of the atmosphere experiment using TDSI.

The paper is organized as follows. Section II describes starting equations for acoustic tomography and the TDSI algorithm. Formulas for spatial-temporal covariance functions of temperature and wind velocity fluctuations for locally frozen turbulence are derived in Sec. III. Using the residual analysis, the errors in the input data for TDSI are obtained in Sec. IV. In Sec. V, new methodology is applied to reconstruction of temperature and velocity fields in the acoustic tomography experiment STINHO. The conclusions are presented in Sec. VI.

II. STARTING EQUATIONS

In this section, starting equations for acoustic travel-time tomography of the atmosphere and a brief description of TDSI are presented. A detailed description of TDSI can be found in Ref. 19.

Let $\tilde{u}(\mathbf{R},t)$, $\tilde{v}(\mathbf{R},t)$, and $\tilde{w}(\mathbf{R},t)$ be x, y, and z components of the random, three-dimensional (3D) vector of wind velocity $\tilde{\mathbf{V}}(\mathbf{R},t)$:

$$\tilde{\mathbf{V}}(\mathbf{R},t)=\tilde{u}(\mathbf{R},t)\mathbf{e}_x+\tilde{v}(\mathbf{R},t)\mathbf{e}_y+\tilde{w}(\mathbf{R},t)\mathbf{e}_z. \tag{1}$$

Here $\mathbf{e}_x$, $\mathbf{e}_y$, and $\mathbf{e}_z$ are the unit vectors along the x, y, and z axes, respectively. The adiabatic sound speed c_L, temperature $\tilde{T}$, and wind velocity $\tilde{\mathbf{V}}$ within a tomographic area at the time moment t can be represented as sums of their spatially averaged values $c_0(t)$, $T_0(t)$, $\mathbf{V}_0(t)=(u_0(t),v_0(t),w_0(t))$ and their fluctuations $c(\mathbf{R},t),T(\mathbf{R},t),\mathbf{V}(\mathbf{R},t)=(u(\mathbf{R},t),v(\mathbf{R},t),w(\mathbf{R},t))$:

$$c_L(\mathbf{R},t)=c_0(t)+c(\mathbf{R},t),\tilde{T}=T_0(t)+T(\mathbf{R},t),$$
$$\tilde{\mathbf{V}}(\mathbf{R},t)=\mathbf{V}_0(t)+\mathbf{V}(\mathbf{R},t). \tag{2}$$

Note that tomography allows one to reconstruct *acoustic virtual* temperature, which we denote as $\tilde{T}$. It is related to the thermodynamic temperature T_{th} by the following relationship: $\tilde{T}\cong T_{\mathrm{th}}(1+0.511q)$, where q is the specific humidity of air.[18]

We will assume that the spatially averaged values are equal to the mathematical expectations of the random fields at each spatial point at the time moment t, i.e.,

$$\langle c_L(\mathbf{R},t)\rangle = c_0(t), \quad \langle \tilde{T}(\mathbf{R},t)\rangle = T_0(t), \quad \langle \tilde{\mathbf{V}}(\mathbf{R},t)\rangle = \mathbf{V}_0(t). \tag{3}$$

Hereinafter, the angular brackets $\langle\ \rangle$ denote averaging over an ensemble of realizations. Note that it follows from Eqs. (2) and (3) that the mathematical expectations of the fluctuations at any point $\mathbf{R}$ and time t are equal to zero.

Most acoustic tomography arrays used so far were 2D. In Ref. 19 TDSI was developed for the 2D case in which sources, receivers, and sound propagation paths are located in one plane. For concreteness, we will assume that this plane coincides with the (x,y) plane. In this case, the travel times of sound propagation between sources and receivers are given by linearized equations of the forward problem of acoustic travel-time tomography of the atmosphere[19]:

$$t_i^{\mathrm{tr}}(t) = \frac{L_i}{c_0(t)}\left(1 - \frac{u_0(t)s_{xi} + v_0(t)s_{yi}}{c_0(t)}\right) - \frac{1}{c_0^2(t)} \times \int_{L_i} dl\left\{\frac{c_0(t)}{2T_0(t)}T(\mathbf{R},t) + u(\mathbf{R},t)s_{xi} + v(\mathbf{R},t)s_{yi}\right\}. \tag{4}$$

Here L_i is the distance between a source and receiver, $s_{xi} = \cos\varphi_i$, and $s_{yi} = \sin\varphi_i$, where φ_i is the angle between $\mathbf{e}_x$ and the direction of sound propagation. Note that in the linearized forward problem the paths of sound impulses can be approximated by straight lines.

The inverse problem of 2D acoustic travel-time tomography of the atmosphere is to reconstruct the mean fields $T_0(t)$, $u_0(t)$, $v_0(t)$ and their fluctuations $T(\mathbf{R},t)$, $u(\mathbf{R},t)$, $v(\mathbf{R},t)$ given the travel times $t_i^{\mathrm{tr}}(t)$, the angles φ_i, and the distances L_i. This reconstruction consists of two steps. First, $T_0(t)$, $u_0(t)$, and $v_0(t)$ are reconstructed using the least-squares estimation. Then, the fluctuations $T(\mathbf{R},t)$, $u(\mathbf{R},t)$, and $v(\mathbf{R},t)$ are reconstructed with the help of TDSI.

When reconstructing $T_0(t)$, $u_0(t)$, and $v_0(t)$, the integral term on the right-hand side of Eq. (4) is neglected. In this case, Eq. (4) can be rewritten in a matrix notation:

$$\mathbf{Gf} = \mathbf{b}. \tag{5}$$

Here the elements of the column-vector $\mathbf{b}$ are known (can be calculated from experimentally measured values of $t_i^{\mathrm{tr}}(t)$ and L_i):

$$b_i = \frac{t_i^{\mathrm{tr}}(t)}{L_i}, \tag{6}$$

the unknown column-vector $\mathbf{f}$ has three elements

$$f_1 = \frac{1}{c_0(t)}, \quad f_2 = \frac{u_0(t)}{c_0^2(t)}, \quad f_3 = \frac{v_0(t)}{c_0^2(t)}, \tag{7}$$

and the matrix $\mathbf{G}$ is given by

$$\mathbf{G} = \begin{bmatrix} 1 & -\cos\varphi_1 & -\sin\varphi_1 \\ \vdots & \ddots & \vdots \\ 1 & -\cos\varphi_I & -\sin\varphi_I \end{bmatrix}. \tag{8}$$

Then, the overdetermined inverse problem for the elements of vector $\mathbf{f}$ (I is assumed to be greater than 3) is solved using the least-squares estimation:

$$\hat{\mathbf{f}} = (\mathbf{G}^T\mathbf{G})^{-1}\mathbf{G}^T\mathbf{b}. \tag{9}$$

Here $\hat{\mathbf{f}}$ is the optimal least-squares estimation of $\mathbf{f}$. The optimal estimations $\hat{c}_0$, $\hat{u}_0$, $\hat{v}_0$ of the mean fields c_0, u_0, v_0 can easily be calculated from $\hat{\mathbf{f}}$ using Eq. (7). The mean temperature $\hat{T}_0$ can be obtained from $\hat{c}_0$ using the following formula:

$$c_0^2 = \gamma R_a T_0, \tag{10}$$

where $\gamma \approx 1.41$ is the ratio of the specific heats and R_a is the gas constant for dry air.

The estimated values $\hat{c}_0$, $\hat{T}_0$, $\hat{u}_0$, and $\hat{v}_0$ are substituted back into Eq. (4). The resulting equation can be written in the following form:

$$q_i(t) = \int_{L_i} dl\left\{\frac{\hat{c}_0(t)}{2\hat{T}_0(t)}T(\mathbf{R},t) + u(\mathbf{R},t)s_{xi} + v(\mathbf{R},t)s_{yi}\right\}, \tag{11}$$

where $q_i(t)$ are given by

$$q_i(t) = L_i[\hat{c}_0(t) - \hat{u}_0(t)s_{xi} - \hat{v}_0(t)s_{yi}] - \hat{c}_0^2(t)t_i^{tr}(t). \tag{12}$$

After the reconstruction of the mean fields, $q_i(t)$ are known.

Equation (11) is a starting equation for TDSI whose goal is to reconstruct $T(\mathbf{R},t)$, $u(\mathbf{R},t)$ and $v(\mathbf{R},t)$ given the values of $q_i(t)$, φ_i, and L_i. The $q_i(t)$ are known at the time moments $t_1, t_2, \ldots, t_n$ of an experiment and are used to form the vector $\mathbf{d}$ of the input data for TDSI:

$$\mathbf{d} = [\mathbf{q}(t_1); \mathbf{q}(t_2); \ldots; \mathbf{q}(t_n)]. \tag{13}$$

Here $\mathbf{q}(t_k)$ are column vectors with elements given by Eq. (12), and the semicolons indicate that these $\mathbf{q}$ are arranged in the column vector $\mathbf{d}$.

Let $\mathbf{m}(t)$ be a column vector of the fluctuations being reconstructed at certain spatial points $\mathbf{R}_1, \ldots, \mathbf{R}_J$, where J is a total number of points:

$$\mathbf{m}(t) = [T(\mathbf{R}_1,t); \ldots; T(\mathbf{R}_J,t); u(\mathbf{R}_1,t); \ldots; u(\mathbf{R}_J,t); v(\mathbf{R}_1,t); \ldots; v(\mathbf{R}_J,t)]. \tag{14}$$

Note that in TDSI the fluctuations can be reconstructed at any time moment t. Of course, one can expect a good reconstruction of $T(\mathbf{R},t)$, $u(\mathbf{R},t)$, and $v(\mathbf{R},t)$ fields if t is within the time interval $[t_1,t_n]$ or close to it. In TDSI, the optimal reconstruction $\hat{\mathbf{m}}(t)$ of $\mathbf{m}(t)$ is given by the following formula:

$$\hat{\mathbf{m}}(t) = \mathbf{C}_{\mathbf{md}}\mathbf{C}_{\mathbf{dd}}^{-1}\mathbf{d}, \tag{15}$$

where $\mathbf{C}_{\mathbf{md}} = \langle \mathbf{md}^T \rangle$ is a model-data covariance matrix and $\mathbf{C}_{\mathbf{dd}} = \langle \mathbf{dd}^T \rangle$ is a data covariance matrix given by Eqs. (18)–(21) from Ref. 19. The elements of these matrices are expressed in terms of the integrals along the sound propaga-

tion paths between sources and receivers, whose integrands contain the spatial-temporal covariance functions of temperature and wind velocity fluctuations, $B_{TT}(\mathbf{R}_1,t_1;\mathbf{R}_2,t_2)$ and $B_{ij}(\mathbf{R}_1,t_1;\mathbf{R}_2,t_2)$. In an experiment, the components q_i of the vector $\mathbf{d}$ are always known with some uncertainties (observation noise) which we denote as Δ_{qi}. As a result, the matrix $\mathbf{C_{dd}}$ has additional terms on its main diagonal[19] equal to the variances of these uncertainties $\sigma_{qi}^2=\langle\Delta_{qi}^2\rangle$.

Expected squared errors of the estimation $\tilde{\mathbf{m}}(t)$ are elements on the main diagonal of the error covariance matrix $\mathbf{C}_{\boldsymbol{\epsilon\epsilon}}$, given by[19]

$$\mathbf{C}_{\boldsymbol{\epsilon\epsilon}}=\mathbf{C_{mm}}-\mathbf{C_{md}}\mathbf{C_{dd}}^{-1}\mathbf{C}_{\mathbf{md}}^{T}, \tag{16}$$

where $\mathbf{C_{mm}}=\langle\mathbf{mm}^T\rangle$ is a model covariance matrix.

Thus, in order to implement TDSI for reconstruction of temperature and wind velocity fields, one needs to know spatial-temporal covariance functions $B_{TT}(\mathbf{R}_1,t_1;\mathbf{R}_2,t_2)$ and $B_{ij}(\mathbf{R}_1,t_1;\mathbf{R}_2,t_2)$ and the variances σ_{qi}^2. These covariance functions and variance will be calculated in the next two sections.

III. LOCALLY FROZEN TURBULENCE

In this section, analytical formulas for the spatial-temporal covariance functions of temperature and wind velocity fluctuations, $B_{TT}(\mathbf{R}_1,t_1;\mathbf{R}_2,t_2)$ and $B_{ij}(\mathbf{R}_1,t_1;\mathbf{R}_2,t_2)$, are derived for the case of locally frozen turbulence.

For this derivation, we will need particular forms of the spatial covariance functions of temperature and wind velocity fluctuations $B_{TT}^s(\mathbf{R}_1,\mathbf{R}_2)$ and $B_{ij}^s(\mathbf{R}_1,\mathbf{R}_2)$. We will assume that turbulence is statistically isotropic and homogeneous, and that the spatial covariance functions of temperature and longitudinal velocity fluctuations are given by Gaussian functions. The components of the tensor $B_{ij}^s(\mathbf{R}_1,\mathbf{R}_2)$ can be calculated from the covariance function of longitudinal velocity fluctuations using Eqs. (6.34) and (6.35) in Ref. 18. As a result, we obtain the following spatial covariance functions of temperature and velocity fluctuations:

$$B_{TT}^s(\mathbf{R}_1,\mathbf{R}_2)=\sigma_T^2\exp\left(-\frac{\boldsymbol{\rho}^2}{l_T^2}\right), \tag{17}$$

$$B_{uu}^s(\mathbf{R}_1,\mathbf{R}_2)=\sigma_V^2\exp\left(-\frac{\boldsymbol{\rho}^2}{l_V^2}\right)\left(1-\frac{\rho_y^2+\rho_z^2}{l_V^2}\right), \tag{18}$$

$$B_{uv}^s(\mathbf{R}_1,\mathbf{R}_2)=\sigma_V^2\exp\left(-\frac{\boldsymbol{\rho}^2}{l_V^2}\right)\frac{\rho_x\rho_y}{l_V^2}. \tag{19}$$

Here, σ_T and σ_V are the standard deviations of temperature and velocity fluctuations, l_T and l_V are their correlation lengths, and $\boldsymbol{\rho}=\mathbf{R}_2-\mathbf{R}_1=(\rho_x,\rho_y,\rho_z)$. Other components of the tensor $B_{ij}^s(\mathbf{R}_1,\mathbf{R}_2)$ are given by formulas similar to those for $B_{uu}^s(\mathbf{R}_1,\mathbf{R}_2)$ and $B_{uv}^s(\mathbf{R}_1,\mathbf{R}_2)$.

A hypothesis of locally frozen turbulence is formulated in Ref. 24. According to this hypothesis, during a relatively small time interval τ, velocities $\tilde{\mathbf{V}}(\mathbf{R},t)$ can be considered as constant in the vicinity of each spatial point. This allows one to express the temperature field $T(\mathbf{R},t_2)$ at the time moment t_2 in terms of the temperature field at the time moment t_1:

$$T(\mathbf{R},t_2)=T(\mathbf{R}-\tilde{\mathbf{V}}(\mathbf{R},t_1)\tau,t_1), \tag{20}$$

where $\tau=t_2-t_1$. Note that in Eq. (20) the velocity $\tilde{\mathbf{V}}$ is a random function of $\mathbf{R}$ and t_1. If in Eq. (20) $\tilde{\mathbf{V}}$ were constant, this equation would become a formula for frozen turbulence which has been widely used in the literature.[20] Thus, the hypothesis of locally frozen is a generalization of that of frozen turbulence.

Equation (20) allows one to express the spatial-temporal covariance function $B_{TT}(\mathbf{R}_1,t_1;\mathbf{R}_2,t_2)$ in terms of the spatial covariance function $B_{TT}^s(\mathbf{R}_1,\mathbf{R}_2)$. Using this equation, we have:

$$\begin{aligned}B_{TT}(\mathbf{R}_1,t_1;\mathbf{R}_2,t_2)&\equiv\langle T(\mathbf{R}_1,t_1)T(\mathbf{R}_2,t_2)\rangle_{T,\tilde{\mathbf{V}}}\\&=\langle T(\mathbf{R}_1,t_1)T(\mathbf{R}_2-\tilde{\mathbf{V}}(\mathbf{R}_2,t_1)\tau,t_1)\rangle_{T,\tilde{\mathbf{V}}}.\end{aligned} \tag{21}$$

Here, $\langle\ \rangle_{T,\tilde{\mathbf{V}}}$ denotes the average over an ensemble of realizations of the random fields T and $\tilde{\mathbf{V}}$. These fields are uncorrelated in the model of homogeneous isotropic turbulence which is used in this paper.[24] Assuming Gaussian probability density distribution, these random fields are statistically independent. Therefore, in the right-hand side of Eq. (21), one can first calculate the average over an ensemble of realizations of T which yields the spatial covariance function B_{TT}^s by definition. Taking into account that $\boldsymbol{\rho}=\mathbf{R}_2-\mathbf{R}_1$, we have

$$B_{TT}(\boldsymbol{\rho},\tau)=\langle B_{TT}^s(\boldsymbol{\rho}-\tilde{\mathbf{V}}(\mathbf{R}_2,t_1)\tau)\rangle_{\tilde{\mathbf{V}}}. \tag{22}$$

The average on the right-hand side of this formula is calculated in the Appendix. The result is

$$B_{TT}(\boldsymbol{\rho},\tau)=\tilde{\sigma}_T^2\exp\left[-\frac{(\boldsymbol{\rho}-\mathbf{V}_0(t_1)\tau)^2}{\tilde{l}_T^2}\right], \tag{23}$$

where the effective variance $\tilde{\sigma}_T^2$ and the square of correlation length $\tilde{l}_T^2$ are given by

$$\tilde{\sigma}_T^2=\frac{\sigma_T^2}{\left[1+2\left(\frac{\sigma_V\tau}{l_T}\right)^2\right]^{3/2}},\quad \tilde{l}_T^2=l_T^2+2\sigma_V^2\tau^2. \tag{24}$$

Note that Eqs. (23) and (24) can also be derived from Eq. (31.29) in Ref. 24. The latter equation gives a formula for a Fourier transform of $B_{TT}(\boldsymbol{\rho},\tau)$ with respect to $\boldsymbol{\rho}$ and τ, valid for an arbitrary spatial covariance function and probability density distribution.

Similarly to the derivation of Eq. (23), one can obtain a formula for the spatial-temporal covariance function of the longitudinal velocity fluctuations and, then, formulas for $B_{uu}(\boldsymbol{\rho},t)$ and $B_{uv}(\boldsymbol{\rho},t)$:

$$\begin{aligned}B_{uu}(\boldsymbol{\rho},t)=\tilde{\sigma}_V^2\exp&\left[-\frac{(\boldsymbol{\rho}-\mathbf{V}_0(t_1)\tau)^2}{\tilde{l}_V^2}\right]\\&\times\left(1-\frac{(\rho_y-v_0(t_1)\tau)^2+(\rho_z-w_0(t_1)\tau)^2}{\tilde{l}_V^2}\right),\end{aligned} \tag{25}$$

$$B_{uv}(\boldsymbol{\rho},t)=\tilde{\sigma}_V^2\exp\left[-\frac{(\boldsymbol{\rho}-\mathbf{V}_0(t_1)\tau)^2}{\tilde{l}_V^2}\right]\times\frac{(\rho_x-u_0(t_1)\tau)(\rho_y-v_0(t_1)\tau)}{\tilde{l}_V^2},\tag{26}$$

where

$$\tilde{\sigma}_V^2=\frac{\sigma_V^2}{\left[1+2\left(\frac{\sigma_V\tau}{l_V}\right)^2\right]^{3/2}},\quad \tilde{l}_V^2=l_V^2+2\sigma_V^2\tau^2.\tag{27}$$

Equations (23)–(27) provide analytical formulas for the spatial-temporal covariance functions of temperature and velocity fluctuations for the considered case of locally frozen turbulence. In the limiting case $\sigma_V=0$ and time-independent $\mathbf{V}_0$, these formulas coincide with those for frozen turbulence.[19] It follows from Eqs. (23)–(27) that the dependence of the spatial-temporal covariance functions on τ manifests in three effects: The spatial arguments of the covariance functions are shifted by the vector $\mathbf{V}_0(t_1)\tau$, and the effective variances of the fluctuations decrease while the effective correlation lengths increase with the increase in τ.

A necessary condition of applicability of the hypothesis of locally frozen turbulence is formulated in Ref. 24:

$$\sigma_V\ll|\mathbf{V}_0|.\tag{28}$$

In this paper, we consider the case when the mean wind velocity $\mathbf{V}_0$ can slowly depend on time t. This imposes an additional necessary condition of applicability of the hypothesis of locally frozen turbulence:

$$|\mathbf{V}_0(t)-\mathbf{V}_0(t_1)|\ll|\mathbf{V}_0(t_1)|,\tag{29}$$

where $t\in[t_1,t_2]$. As far as we know sufficient conditions of applicability of the hypothesis of locally frozen turbulence have not been obtained. They should probably include a limitation on the time interval $\tau=t_2-t_1$ during which this hypothesis is valid.

IV. ESTIMATION OF THE ERRORS

In this section, the variances σ_{qi}^2 of the uncertainties Δ_{q_i} in the input data $\mathbf{d}$ are calculated. It follows from Eq. (11) that these variances depend on the variances of mean squared errors $\hat{\sigma}_c^2$, $\hat{\sigma}_T^2$, $\hat{\sigma}_u^2$, and $\hat{\sigma}_v^2$ in reconstruction of $\hat{c}_0$, $\hat{T}_0$, $\hat{u}_0$, and $\hat{v}_0$. Therefore, we first estimate these errors.

Let s_b^2 be the estimated variance of components b_i of the vector $\mathbf{b}$ which appears in the right-hand side of Eq. (5). Using a residual estimation,[16] we have

$$s_b^2=\frac{(\mathbf{b}-\mathbf{G}\hat{\mathbf{f}})^T(\mathbf{b}-\mathbf{G}\hat{\mathbf{f}})}{I-3},\tag{30}$$

where $I-3$ is a number of independent degrees of freedom in the numerator of Eq. (30). The mean squared errors $\sigma_{\hat{\mathbf{f}}}^2$ of the vector $\hat{\mathbf{f}}$ are diagonal elements of its covariance matrix[16] $\sigma_{\hat{\mathbf{f}}}^2=\mathrm{diag}[\mathbf{R}_{\hat{\mathbf{f}}\hat{\mathbf{f}}}]$. Here

$$\mathbf{R}_{\hat{\mathbf{f}}\hat{\mathbf{f}}}=s_b^2(\mathbf{G}^T\mathbf{G})^{-1}.\tag{31}$$

Using Eqs. (7) and (10) and neglecting the terms of order $(\hat{u}_0/\hat{c}_0)^2$ and $(\hat{v}_0/\hat{c}_0)^2$, the mean squared errors $\hat{\sigma}_c^2$, $\hat{\sigma}_T^2$, $\hat{\sigma}_u^2$, and $\hat{\sigma}_v^2$ can be expressed in terms of the mean squared errors $\sigma_{\hat{\mathbf{f}}}^2$:

$$\hat{\sigma}_c^2=\hat{c}_0^4\sigma_{\hat{f}_1}^2,\quad \hat{\sigma}_T^2=\frac{4\hat{c}_0^2}{(\gamma R_a)^2}\hat{\sigma}_c^2,\quad \hat{\sigma}_u^2=\hat{c}_0^4\sigma_{\hat{f}_2}^2,\quad \hat{\sigma}_v^2=\hat{c}_0^4\sigma_{\hat{f}_3}^2.\tag{32}$$

Once the errors $\hat{\sigma}_c^2$, $\hat{\sigma}_T^2$, $\hat{\sigma}_u^2$, and $\hat{\sigma}_v^2$ are known, it is possible to estimate the variances $\sigma_{q_i}^2$ of the errors in the input data $q_i(t)$ for TDSI. The errors in $q_i(t)$ are due to errors in L_i, s_{xi}, and s_{yi} caused by uncertainties in transducers positions, errors in measurements of t_i^{tr}, and errors in the reconstruction of $\hat{c}_0(t)$, $\hat{T}_0(t)$, $\hat{u}_0(t)$, and $\hat{v}_0(t)$. As $L_i^2=(x_i-x_{0i})^2+(y_i-y_{0i})^2$, where (x_i,y_i) and (x_{0i},y_{0i}) are the coordinates of the receiver and source, respectively, one can calculate the uncertainties in the sound propagation paths Δ_{L_i} taken into account that $\cos\varphi_i=(x_i-x_{0i})/L_i$ and $\sin\varphi_i=(y_i-y_{0i})/L_i$:

$$\Delta_{L_i}=[(\Delta_{x_i}-\Delta_{x_{0i}})\cos\varphi_i+(\Delta_{y_i}-\Delta_{y_{0i}})\sin\varphi_i].\tag{33}$$

Here, Δ_{x_i}, $\Delta_{x_{0i}}$, Δ_{y_i}, and $\Delta_{y_{0i}}$ are uncertainties in the transducer positions. Therefore, from Eq. (12) the uncertainty Δ_{q_i} is

$$\Delta_{q_i}=(\Delta_{x_i}-\Delta_{x_{0i}})(\hat{c}_0\cos\varphi_i-\hat{u}_0)+(\Delta_{y_i}-\Delta_{y_{0i}})\times(\hat{c}_0\sin\varphi_i-\hat{v}_0)+(L_i-2\hat{c}_0t_i^{\mathrm{tr}})\Delta_{c_0}-L_i(\Delta_{u_0}\cos\varphi_i+\Delta_{v_0}\sin\varphi_i)-\hat{c}_0^2\Delta_{t_i},\tag{34}$$

and, as $\hat{u}_0\ll\hat{c}_0$, $\hat{v}_0\ll\hat{c}_0$, and $\hat{c}_0t_i^{\mathrm{tr}}\sim L_i$, the variance $\sigma_{q_i}^2=\langle\Delta_{q_i}^2\rangle$ of the errors in q_i is

$$\sigma_{q_i}^2\approx 2\sigma_r^2\hat{c}_0^2+L_i^2(\hat{\sigma}_c^2+\hat{\sigma}_u^2\cos^2\varphi_i+\hat{\sigma}_v^2\sin^2\varphi_i)+\hat{c}_0^4\sigma_t^2,\tag{35}$$

where σ_r^2 is the variance of the errors in the transducer positions ($\sigma_r^2=\langle\Delta_{x_i}^2\rangle=\langle\Delta_{x_{0i}}^2\rangle=\langle\Delta_{y_i}^2\rangle=\langle\Delta_{y_{0i}}^2\rangle$), and σ_t^2 is the variance of an error in measurement of t_i^{tr}.

V. ACOUSTIC TOMOGRAPHY EXPERIMENT

In this section, a developed theory of TDSI is applied to reconstruction of temperature $\tilde{T}$ and wind velocity $\tilde{\mathbf{V}}$ fields in the acoustic tomography experiment STINHO carried out by scientists from the University of Leipzig.[9] The experiment was a part of a larger meteorological experiment to study turbulence, turbulent fluxes, and other meteorological parameters over heterogeneous surface.

The tomography array consisted of eight sources $S1,\ldots,S8$ and twelve receives $R1,\ldots,R12$, see Fig. 1. The size of the array was 300 m $\times$ 440 m. The sources and receivers were located above the ground at an average height of 2 m. Most of the ground within the tomography array was covered with grass except for a spot of bare soil which was in the lower left corner of the array with the size of 90 m $\times$ 300 m. This inhomogeneity might create the fluctuation of

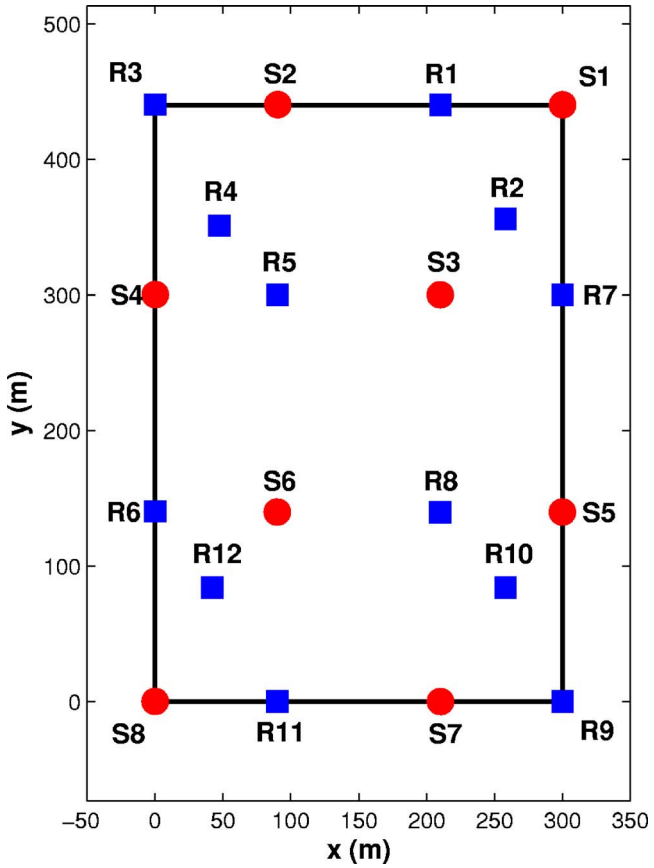

FIG. 1. (Color online) The layout of sources (S1,...,S8) and receivers (R1,...,R12) in the acoustic tomography experiment STINHO (Ref. 9).

temperature and wind velocity fields which is subject of reconstruction by TDSI. Besides, the difference between mean temperatures over different surfaces was negligible (unlike the difference in turbulent heat fluxes), and horizontal wind velocities were quite close (see Fig. 2 in the Ref. 9). The travel times t_i^{tr} of sound propagation between sources and receivers were measured every minute during 6 July 2002.

Our reconstruction of temperature $\tilde{T}$ and wind velocity $\tilde{\mathbf{V}}$ fields in this acoustic tomography experiment consisted in reconstruction of their mean values $\hat{T}_0(t)$, $\hat{u}_0(t)$, and $\hat{v}_0(t)$ and fluctuations $\hat{T}(\mathbf{R},t)$, $\hat{u}(\mathbf{R},t)$, and $\hat{v}(\mathbf{R},t)$ as described in Sec. II. The input experimental data for reconstruction of $\hat{T}_0(t)$, $\hat{u}_0(t)$, and $\hat{v}_0(t)$ were t_i^{tr}, L_i, and φ_i. The reconstructed mean values of temperature and two components of wind velocity for the 10 min time interval (5:26–5:35 a.m., Coordinated Universal Time (UTC), which is also known as Greenwich Mean Time) are plotted in Fig. 2 as solid lines. Using Eq. (32), the errors $\hat{\sigma}_T$, $\hat{\sigma}_u$, and $\hat{\sigma}_v$ in reconstruction of the mean fields were calculated. These errors are plotted in Fig. 2 as vertical bars.

Then, the obtained values of $\hat{T}_0(t)$, $\hat{u}_0(t)$, and $\hat{v}_0(t)$ and experimental values of t_i^{tr} were used to calculate the components $q_i(t)$ of the input data $\mathbf{d}$ for reconstruction of fluctuations $\hat{T}(\mathbf{R},t)$, $\hat{u}(\mathbf{R},t)$, and $\hat{v}(\mathbf{R},t)$ using TDSI. To apply TDSI, we also needed to know the variances $\sigma_{q_i}^2$ of errors in $q_i(t)$, and parameters σ_T, σ_V, l_T, and l_V of the covariance functions $B_{TT}(\boldsymbol{\rho},\tau)$ and $B_{ij}(\boldsymbol{\rho},\tau)$. The variances $\sigma_{q_i}^2$ were calculated using Eq. (35), where $\hat{\sigma}_c^2$, $\hat{\sigma}_u^2$, and $\hat{\sigma}_v^2$ were obtained from Eq. (32), whereas σ_r^2 and σ_t^2 were estimated in the tomography experiment[9] to be as follows: $\sigma_r=3$ cm and $\sigma_t=0.3$ ms. The variances of temperature and velocity fluctuations, σ_T and σ_V, were assumed to be the same as the variances measured *in situ* by a sonic thermometer-anemometer: $\sigma_T=0.27\,^{\circ}\mathrm{C}$ and $\sigma_V=0.28$ m/s. The correlation lengths l_T and l_V were chosen as follows: $l_T=l_V=75$ m. The values of l_T and l_V determine a characteristic size of fluctuations $\hat{T}(\mathbf{R},t)$, $\hat{u}(\mathbf{R},t)$, and $\hat{v}(\mathbf{R},t)$ which can be resolved in reconstruction. Note that, for the considered experiment, the values of l_T and l_V could not be chosen significantly less than 75 m since the errors in reconstruction of the fluctuations increase with decreasing l_T and l_V.[13] Finally, to apply TDSI to the reconstruction of the fluctuations $\hat{T}(\mathbf{R},t)$, $\hat{u}(\mathbf{R},t)$, $\hat{v}(\mathbf{R},t)$, three con-

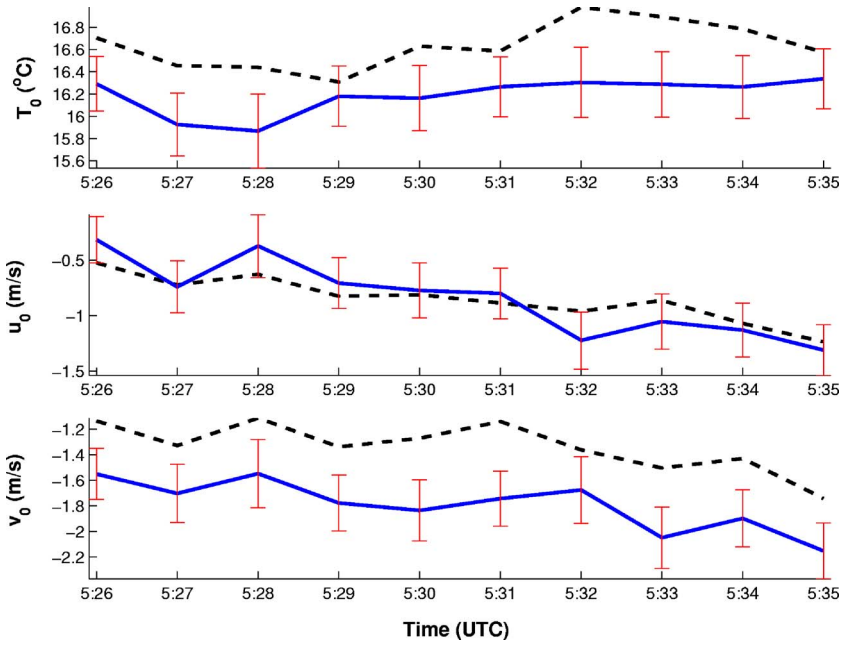

FIG. 2. (Color online) The reconstruction of the mean fields at 5:26–5:30 a.m. UTC on 6 July 2002 by TDSI (solid lines) and SIRT (dashed lines). The vertical bars indicate the estimated errors of mean field reconstruction by TDSI.

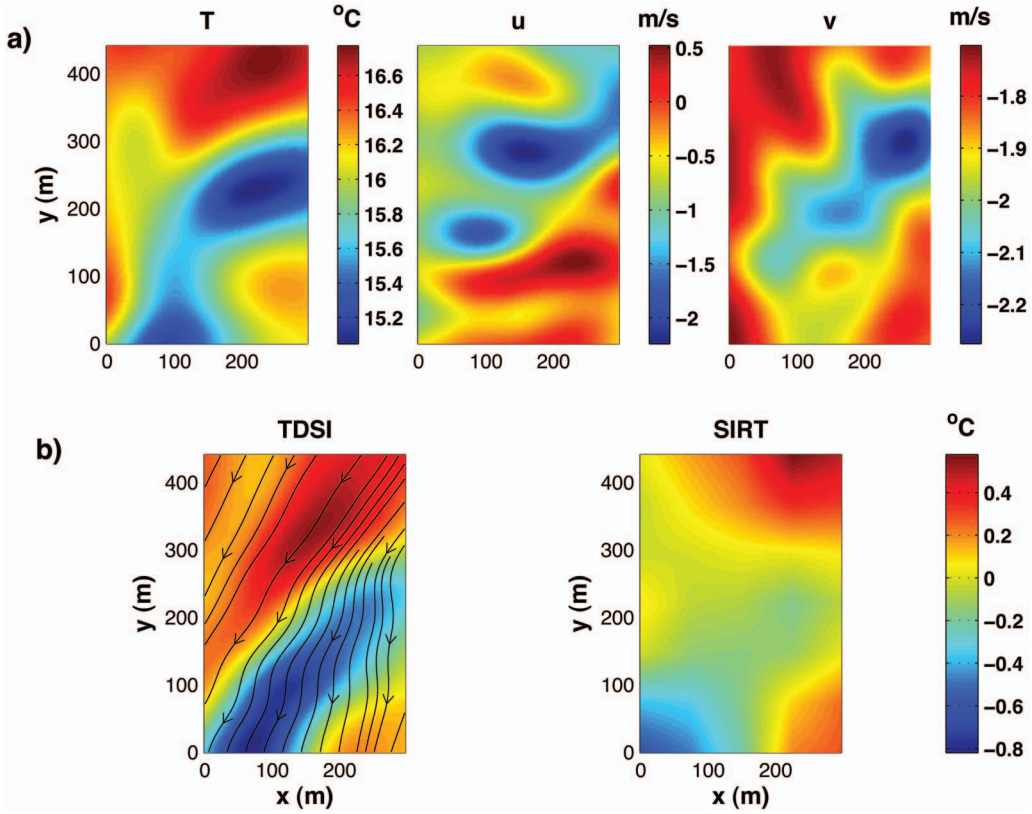

FIG. 3. (a) The TDSI reconstruction of temperature (°C) and wind velocity (m/s) fields at 5:30 a.m. UTC on 6 July 2002. (b) The 10 min averaged fields of temperature fluctuations (°C) reconstructed by (left) TDSI and (right) SIRT. The black lines in the TDSI reconstruction show the direction of reconstructed mean wind during the interval of averaging.

secutive sets of the travel times t_i^{tr} were used. (In future tomography experiments, it would be desirable to increase the number of such sets by decreasing a time interval between measurements of t_i^{tr}). After the fluctuations $\hat{T}(\mathbf{R},t)$, $\hat{u}(\mathbf{R},t)$, and $\hat{v}(\mathbf{R},t)$ were reconstructed, the total fields $\tilde{T}$, $\tilde{u}$, and $\tilde{v}$ were obtained as the sums of the mean fields and fluctuations.

Figure 3(a) shows the fields $\tilde{T}$, $\tilde{u}$, and $\tilde{v}$ reconstructed at 5:30 a.m. UTC (In the reconstruction, the travel times t_i^{tr} measured at 5:29, 5:30, and 5:31 a.m. were used.) "Cold" and "warm" temperature eddies with different scales can be seen in Fig. 3(a). High and low speed velocity eddies can also be seen. Figure 4 contains the expected root mean squared errors (RMSE) of the reconstruction of temperature and wind velocity fields shown in Fig. 3(a). These errors are calculated with the use of Eq. (16). The spatially averaged RMSE of temperature reconstruction is 0.36 °C. This error is less than the temperature differences between cold and warm eddies which can be seen in Fig. 3(a). Therefore, these cold and warm eddies are reliably reconstructed. The spatially averaged RMSE of $\tilde{u}$ and $\tilde{v}$ reconstruction are 0.35 and 0.25 m/s, respectively. These errors are also less than the velocity differences between the low and high speed eddies which can be seen in Fig. 3(a).

The reconstructed values of temperature were compared with those measured by two in-situ sensors located within the tomographic area. The results of this comparison and the coordinates of the sensors are presented in Table I. According to Table I, the reconstructed values of temperature are in a good agreement with the direct measurements: The discrepancy is 0.1 °C at the location of the first sensor and 0.01 °C at the location of the second sensor. These discrepancies are smaller than the estimated errors of the reconstruction, which are of order 0.4 °C.

For the considered tomography experiment, the temperature and wind velocity fields were also reconstructed in Ref. 9 using a Simultaneous Iterative Reconstruction Technique (SIRT) algorithm. SIRT is an algebraic algorithm which does not use *a priori* information about covariance functions of turbulent fields. It is worthwhile to compare the results presented in Ref. 9 with those obtained by TDSI. Note that the SIRT algorithm used in Ref. 9 is also a two step procedure. In the first step, the travel times t_i^{tr} are split into t_{iT}^{tr} and t_{iV}^{tr}, where t_{iT}^{tr} are affected only by the temperature field $\tilde{T}$, whereas t_{iV}^{tr} are affected only by the velocity field $\tilde{\mathbf{V}}$ (for details see Ref. 8). In the second step, the SIRT algorithm is used to reconstruct the temperature and velocity fields from t_{iT}^{tr} and t_{iV}^{tr}, respectively. In Fig. 2, the dashed lines correspond to the mean values of the temperature and two components of wind velocity reconstructed by SIRT. Comparison of these lines with the solid ones (obtained by TDSI) shows that there is an acceptable agreement in reconstruction of $\hat{T}_0(t)$, $\hat{u}_0(t)$, and $\hat{v}_0(t)$ by two algorithms. The root mean squared discrepancy between values obtained by SIRT and TDSI is 0.47 °C for the $\hat{T}_0$, 0.16 m/s for the $\hat{u}_0$, and 0.47 m/s for the $\hat{v}_0$.

TABLE I. Comparison of the reconstructed and *in situ* measured values of temperature.

Landscape type	Coordinated (m)	Humitter T (°C)	TDSI T (°C)
Bare soil	$x=28$, $y=138$	16.24	16.14
Grassland	$x=182$, $y=143$	15.78	15.77

Figure 3(b) shows the temperature fluctuations $\hat{T}$ averaged over 10 min and reconstructed with the use of TDSI and SIRT. The SIRT reconstruction of $\hat{T}$ was taken from Ref. 9 (see Fig. 4 in that reference) and then the temperature field was interpolated (2D linear interpolation) to have the same spatial grid as that used in TDSI. It follows from Fig. 3(b) that the reconstructed fields are similar on large scales of turbulent eddies. In the lower left-hand corner of Fig. 3(b), one can see a cold temperature eddy which is stretched at about 45° with respect to the x axis. Further, there are two warm eddies in the right upper and lower corners. However, there are differences in the reconstructed fields in details. According to the TDSI reconstruction, the cold eddy in the left lower corner is more distinctive, narrower and longer than that reconstructed by SIRT. The shape of the warm eddy in the upper right-hand corner is also more stretched along the diagonal and centered at a different position. It is worthwhile to note that, in TDSI, the deformation of the turbulent eddies along the diagonal coincides with the direction of reconstructed mean wind during the interval of averaging [black lines in Fig. 3(b), left plot].

The estimated RMSE for the TDSI and SIRT reconstructions are shown in Fig. 5. Note that the errors of the reconstruction by TDSI are of order 0.1 °C, and are approximately one-half the SIRT errors.

VI. CONCLUSIONS

In this paper, the TDSI methodology for acoustic tomography of the atmosphere was further developed. First, the formulas for the spatial-temporal covariance functions of temperature and wind velocity fluctuations for the case of locally frozen turbulence were derived. These formulas are more general than those for the case of frozen turbulence and account for the variance of velocity fluctuations. Second, the formulas for the variances of the errors in the input data in TDSI were derived.

The developed TDSI was, for the first time, used in the reconstruction of temperature and wind velocity fields in an acoustic tomography of the atmosphere experiment (STINHO experiment[9]). The reconstructed temperature and wind velocity fields and the errors in the reconstruction were presented. It was shown that the use of TDSI allowed us to reliably reconstruct temperature and velocity eddies within the tomographic area. The temperature field reconstructed by TDSI was compared with that reconstructed by the SIRT method. The fields reconstructed by these two approaches are similar on large scales while different in details. TDSI yields a more detailed reconstruction with the errors in about one-half those in SIRT.

Note that the STINHO experiment was not designed to take the full advantages of TDSI. In future experiments, it is worthwhile to fully exploit these advantages. For example, it would be worthwhile to reduce the time intervals between consecutive travel time measurements.

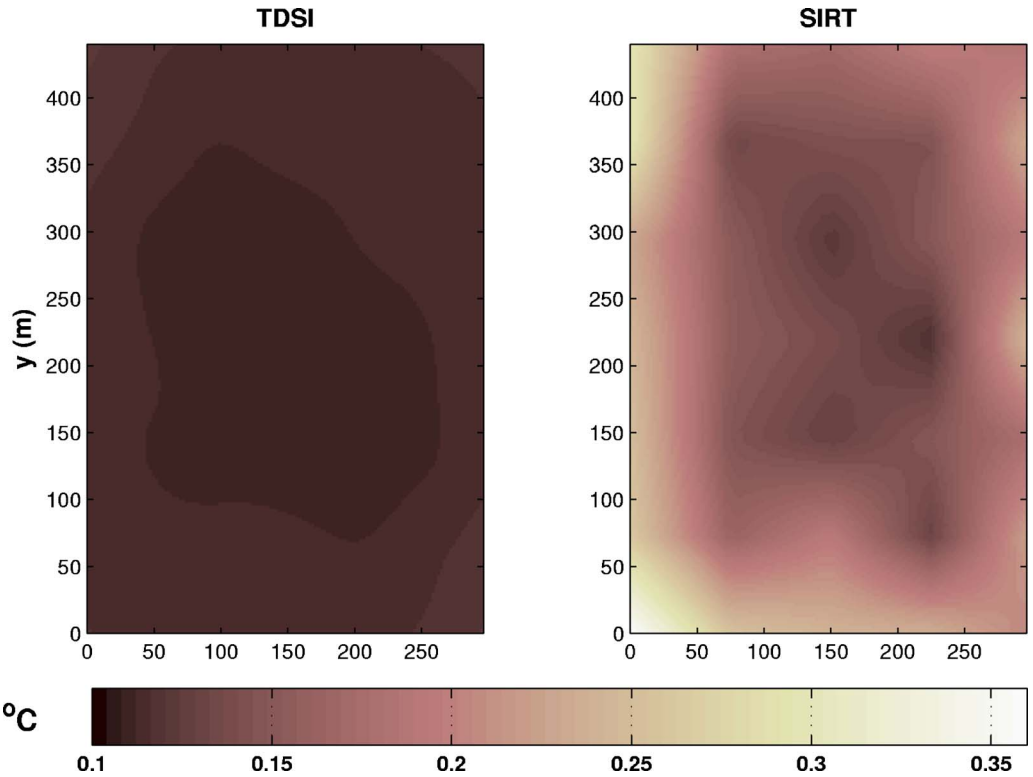

FIG. 5. (Color online) The expected root mean squared errors in the reconstructions shown in Fig. 3(b).

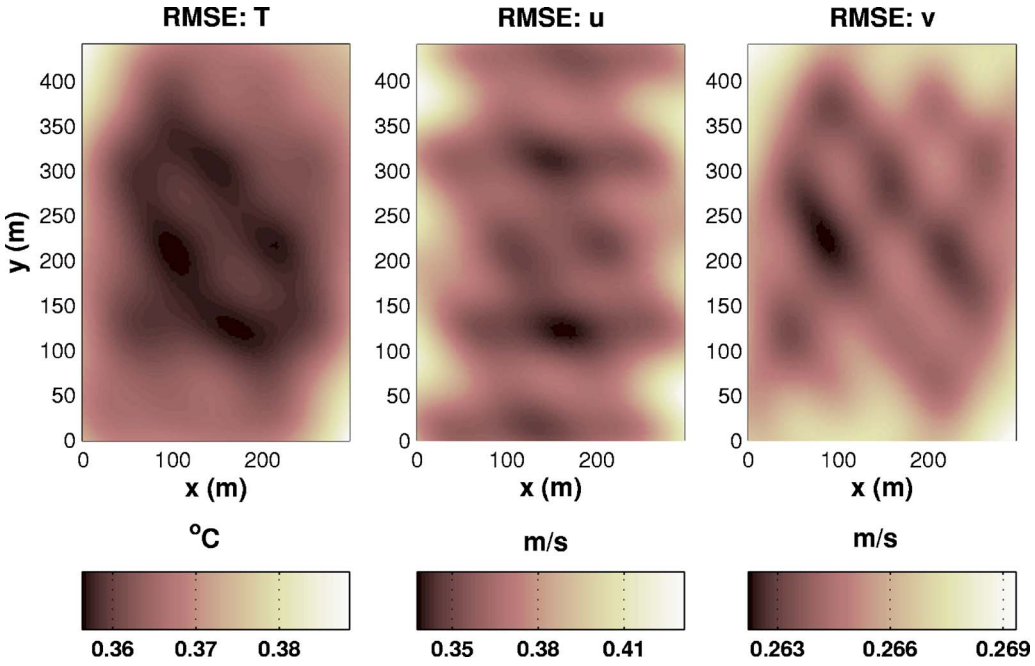

FIG. 4. (Color online) The expected root mean squared errors in the reconstructions shown in Fig. 3(a).

ACKNOWLEDGMENTS

This material is partly based upon work that was supported by the U.S. Army Research Office under Contract Nos. DAAD19-03-1-0104 and W911NF-06-1-0007. The STINHO project was performed as a part of the VERTICO (VERTIcal transports of energy and trace gases at anchor stations under COmplex natural conditions) network which was funded by the German Federal Ministry of Education and Research (BmBF) in the framework of the AFO-2000 research program (Grant No. 07ATF37).

APPENDIX: SPATIAL-TEMPORAL COVARIANCE FUNCTION FOR LOCALLY FROZEN TURBULENCE

In this appendix, we derive a formula for the spatial-temporal covariance function of temperature fluctuations for the case of locally frozen turbulence. A starting equation for this derivation is Eq. (22). Substituting the value of B_{TT}^s from Eq. (17) into Eq. (22), we have

$$B_{TT}(\boldsymbol{\rho},\tau)=\sigma_T^2\left\langle \exp\left(-\frac{(\rho_x-\tilde{u}\tau)^2}{l_T^2}-\frac{(\rho_y-\tilde{v}\tau)^2}{l_T^2}-\frac{(\rho_z-\tilde{w}\tau)^2}{l_T^2}\right)\right\rangle_{\tilde{\mathbf{V}}}. \tag{A1}$$

We will assume that the random 3D field $\tilde{\mathbf{V}}(\mathbf{R},t)$ is normally distributed with the variance $\sigma_{\tilde{\mathbf{V}}}^2$ independent of spatial coordinates and time: $\sigma_{\tilde{\mathbf{V}}}^2=\langle\tilde{\mathbf{V}}^2(\mathbf{R},t)\rangle=\langle u^2(\mathbf{R},t)\rangle+\langle v^2(\mathbf{R},t)\rangle+\langle w^2(\mathbf{R},t)\rangle=3\sigma_V^2$. Its mathematical expectation is $\mathbf{V}_0(t)=(u_0(t),v_0(t),w_0(t))$. Note that different components of $\tilde{\mathbf{V}}(\mathbf{R},t)$ are uncorrelated in the theory of homogeneous isotropic turbulence which is used in this paper. Indeed, as turbulence is stationary, at any time t the cross correlations between two different components of $\tilde{\mathbf{V}}$, e.g., $\tilde{u}$ and $\tilde{v}$, are described by B_{uv}^s given by Eq. (19). It follows from this equation that the cross correlation at a fixed point ($\rho_x=\rho_y=\rho_z=0$) is equal to zero. If components of a multidimensional normally distributed variable are uncorrelated then they are independent. Statistical independence of different components of $\tilde{\mathbf{V}}(\mathbf{R},t)$ allows one to express Eq. (A1) in the following form:

$$B_{TT}(\boldsymbol{\rho},\tau)=\sigma_T^2 I_x I_y I_z, \tag{A2}$$

where $I_x=\langle\exp[-(\rho_x-\tilde{u}\tau)^2/l_T^2]\rangle_{\tilde{u}}$, and I_y and I_z are given by similar formulas. Let $\eta=(\rho_x-\tilde{u}\tau)/l_T$. Then I_x can be written as $I_x=\langle\exp(-\eta^2)\rangle_\eta$. Note that a random function η is normally distributed as ρ_x, l_T, and τ are nonrandom quantities and $\tilde{u}$ is a normally distributed random function. Therefore, η has a Gaussian probability density

$$p_\eta(w)=\frac{1}{\sigma_\eta\sqrt{2\pi}}\exp\left[-\frac{(w-\langle\eta\rangle)^2}{2\sigma_\eta^2}\right]$$

with its mean value $\langle\eta\rangle$ and variance σ_η^2 given by

$$\langle\eta\rangle=\frac{\rho_x-u_0(t_1)\tau}{l_T},\quad \sigma_\eta^2=\frac{\sigma_V^2\tau^2}{l_T^2} \tag{A3}$$

Then

$$I_x=\int_{-\infty}^{\infty}\exp(-w^2)p_\eta(w)dw=\frac{1}{\sqrt{1+2\sigma_\eta^2}}\exp\left(\frac{\langle\eta\rangle^2}{1+2\sigma_\eta^2}\right). \tag{A4}$$

Similar results can be obtained for I_y and I_z. Substituting Eq. (A4) and similar formulas for I_y and I_z into Eq. (A2), we obtain an analytical formula for $B_{TT}(\boldsymbol{\rho},\tau)$. This formula is given by Eq. (23).

[1]J. L. Spiesberger and K. M. Fristrup, "Passive localization of calling animals and sensing of their acoustic environment using acoustic tomogra-

phy," Am. Nat. **135**, 107–153 (1990).
[2]D. K. Wilson and D. W. Thomson, "Acoustic tomographic monitoring of the atmospheric surface layer," J. Atmos. Ocean. Technol. **11**, 751–769 (1994).
[3]A. Ziemann, K. Arnold, and A. Raabe, "Acoustic tomography in the atmospheric surface layers," Ann. Geophys. **17**, 139–148 (1999).
[4]K. Arnold, A. Ziemann, and A. Raabe, "Acoustic tomography inside the atmospheric boundary layer," Phys. Chem. Earth, Part B **24**, 133–137 (1999).
[5]A. Ziemann, K. Arnold, and A. Raabe, "Acoustic travel-time tomography—a method for remote sensing of the atmospheric surface layer," Meteorol. Atmos. Phys. **71**, 43–51 (1999).
[6]A. Ziemann, K. Arnold, and A. Raabe, "Acoustic tomography as a method to identify small-scale land surface characteristic," Acta. Acust. Acust. **87**, 731–737 (2001).
[7]K. Arnold, A. Ziemann, and A. Raabe, "Tomographic monitoring of wind and temperature at different heights above the ground," Acta. Acust. Acust. **87**, 703–708 (2001).
[8]A. Ziemann, K. Arnold, and A. Raabe, "Acoustic tomography as a remote sensing method to investigate the nearsurface atmospheric boundary layer in comparison with in situ measurements," J. Atmos. Ocean. Technol. **19**, 1208–1215 (2002).
[9]A. Raabe, K. Arnold, A. Ziemann, M. Schröter, S. Raasch, J. Bange, P. Zittel, Th. Spieb, Th. Foken, M. Göckede, F. Beyrich, and J.-P. Leps, "STINHO–STructure of turbulent transport under INHOmogeneous surface conditions - a micro-α scale field experiment and LES modeling," Meteorol. Z. **14**, 315–327 (2005).
[10]D. K. Wilson, A. Ziemann, V. E. Ostashev, and A. G. Voronovich, "An overview of acoustic travel-time tomography in the atmosphere and its potential applications," Acta. Acust. Acust. **87**, 721–730 (2001).
[11]S. L. Collier, D. A. Ligon, J. M. Noble, E. Patton, P. Sullivan, and V. E. Ostashev, "Acoustic tomographic array simulation," *Proceedings of the 11th International Symposium on Long Range Sound Propagation*, Fairlee, VT, 2004.
[12]S. N. Vecherin, V. E. Ostashev, D. K. Wilson, A. G. Voronovich, G. H. Goedecke, S. L. Collier, J. M. Noble, and D. Ligon, "Forward and inverse problems of acoustic tomography of the atmosphere," *Proceedings of the 11th International Symposium on Long Range Sound Propagation*, Fairlee, VT, 2004.
[13]D. K. Wilson, V. E. Ostashev, S. N. Vecherin, A. G. Voronovich, S. L. Collier, and J. M. Noble, "Assessment of acoustic travel-time tomography of the atmospheric surface layer," *Proceedings of AMS Symposium on Boundary Layers and Turbulence*, Portland, ME, 2004.
[14]P. Holstein, A. Raabe, R. Müller, M. Barth, D. Mackenzie, and E. Starke, "Acoustic tomography on the basis of travel-time measurement," Meas. Sci. Technol. **15**, 1420–1428 (2004).
[15]M. Barth, A. Raabe, P. Holstein, R. Muller, A. Ziemann, K. Arnold, D. Mackenzie, E. Starke, and M. Seliger, "Acoustic travel-time tomography as a tool to investigate temperature distributions on different spatial scales," *12th International Symposium on Acoustic Remote Sensing and Associated Techniques of the Atmosphere and Oceans*, Cambridge, United Kingdom, 2004.
[16]K. Aki and P. G. Richards, *Quantitative Seismology. Theory and methods* (Freeman, San Francisco, 1980).
[17]V. E. Ostashev, S. N. Vecherin, D. K. Wilson, and S. L. Collier, "Correlation functions of temperature and velocity fluctuations in a turbulent atmosphere," J. Acoust. Soc. Am. **119**, 3264 (2006).
[18]V. E. Ostashev, *Acoustics in Moving Inhomogeneous Media* (E&FN SPON, London, 1997).
[19]S. N. Vecherin, V. E. Ostashev, G. H. Goedecke, D. K. Wilson, and A. G. Voronovich, "Time-dependent stochastic inversion in acoustic travel-time tomography of the atmosphere," J. Acoust. Soc. Am. **119**, 2579–2588 (2006).
[20]J. Hinze, *Turbulence* (McGraw-Hill, New York, 1975).
[21]J. Gilson, D. Roemmich, B. D. Cornuelle, and L.-L. Fu, "Relationship of TOPEX/Poseidon altimetric height to steric height and circulation in the North Pacific," J. Geophys. Res. **103**, 27947–27965 (1998).
[22]N. Ducet, P. Y. Le Traon, and G. Reverdin, "Global high-resolution mapping of ocean circulation from TOPEX/Poseidon and ERS-1 and -2," J. Geophys. Res. **105**, 19477–19498 (2000).
[23]F. P. Bretherton, R. E. Davis, and C. B. Fandry, "A technique for objective analysis and design of oceanographic experiments applied to MODE-73," Deep-Sea Res. **23**, 559–582 (1976).
[24]V. I. Tatarskii, *The Effects of the Turbulent Atmosphere on Wave Propagation* (Keter, Jerusalem, 1971).

Modal Doppler theory of an arbitrarily accelerating continuous-wave source applied to mode extraction in the oceanic waveguide

S. C. Walker[a)]
Marine Physical Laboratory, University of California, San Diego, Scripps Institution of Oceanography, La Jolla, California 92038

Philippe Roux[b)]
LGIT-Maison des Gosciences, 1381 rue de la Piscine, BP 53-38041 Grenoble Cedex 9, France

W. A. Kuperman[c)]
Marine Physical Laboratory, University of California, San Diego, Scripps Institution of Oceanography, La Jolla, California 92038

(Received 26 August 2005; revised 31 May 2007; accepted 14 June 2007)

A Doppler-based method for using a moving narrow-band source to extract the modes of acoustic propagation in a range-independent shallow ocean waveguide over a partial-water-column spanning vertical line array (VLA) is introduced. Because the modal components propagate at distinct frequencies in the case of uniform radial source motion, the modal depth functions may be isolated and extracted from a frequency decomposition of the field. Because Doppler broadening due to radial source accelerations degrades the effectiveness of the extraction method, the method incorporates a technique to compensate for Doppler broadening. As the basis for the compensation technique, a theory is introduced for describing the VLA field from an accelerating cw source. By connecting the range of the source at the time a signal feature is emitted (the retarded time) to the range of the source at the time the signal feature arrives at the receiver (the contemporary time), the theory incorporates the Doppler effects associated with the finite group velocities of the modal components. The mode extraction method and compensation technique are applied to simulation and ocean data. © *2007 Acoustical Society of America.* [DOI: 10.1121/1.2756756]

PACS number(s): 43.30.Bp, 43.60.Gk, 43.30.Es [DRD] Pages: 1426–1439

I. INTRODUCTION

It is well known that the acoustic field in a range-independent shallow ocean waveguide propagates as a set of modal components[1] (ignoring the near field). Each modal component is characterized by a unique, discrete wave number and a depth dependence that is mutually orthogonal to those of the other modes. An active area of research in recent years has been to extract information about the modes by measuring the acoustic field with an array of receivers. One of the major hurdles to overcome in the mode extraction process is the decoupling of the modes in the received field.

One class of methods that has shown some promise in extracting the modal depth functions exploits the orthogonality properties of matrix decomposition operations to decouple the modal components. Such methods require the synthesis of a well-conditioned (nonsingular) spatial cross-spectral density matrix (CSDM) from data measured over a vertical line array (VLA). Conditioning the CSDM typically involves averaging over range[2] and/or frequency.[2–4] The difficulty associated with collecting data over a sufficient range aperture in a dynamic ocean environment limits the method's effectiveness in at-sea applications. Another limitation results from the requirement that, in order to exploit the orthogonality properties of the matrix decomposition methods, the modes must be fully sampled in depth. Deploying a full-spanning VLA at-sea is costly and often prohibitive.

This paper introduces a method for extracting the modal depth functions over a partial-water-column spanning VLA using the field from a moving cw point source. As pointed out by Hawker[5] and Schmidt and Kuperman,[6] one consequence of the discreteness of the modal wave number spectrum is that the modes from a moving source are Doppler shifted relative to the source frequency in direct relation to their wave numbers and the source velocity. As a result, each mode propagates at a discrete frequency different from the other modes, thereby breaking the frequency degeneracy in the received field. Under proper conditions on the source motion, the frequency responses of the modal components are decoupled. Because the decoupling does not rely on mode orthogonality, the method may be implemented over partial-spanning VLA geometries. This paper proposes a method for isolating the modes according to their Doppler shifted discrete frequency spectrum so that they may be extracted individually. The main limitation on the method is that imposed by generating the frequency resolution needed to resolve the modal frequencies. It turns out that the resolution requirement is equivalent to the conditioning require-

[a)]Also at Physics Department, University of California, San Diego, CA; electronic mail: shane@physics.ucsd.edu
[b)]Electronic mail: philippe.roux@obs.ujf-grenoble.fr
[c)]Electronic mail: wak@mpl.ucsd.edu

ment of the CSDM discussed earlier. Similar to an earlier method proposed by the authors,[7] the method is fully self-adaptive, requiring no knowledge of the environment.

In the case of a constant radial velocity source, each modal frequency is independent of time and thus unambiguous. Performing a Fourier decomposition on the received field yields a set of peaks about the modal frequencies. In this case, decoupling the modes is merely a matter of achieving the frequency resolution needed to resolve the peaks. Associating the measured time with the source range, the frequency resolution depends on the range aperture traversed by the source. The modal frequencies are well resolved when the range aperture approaches several modal interference wavelengths. As an example, a minimum of 5 km of range aperture is required to extract modes 1 and 2 from a 100 Hz source moving in a realistic 150-m-deep ocean waveguide.

As it is unrealistic to expect to generate clean constant radial velocity data over such large distances, it is important to consider the effects of source accelerations on the mode extraction process. It is well known that source accelerations lead to Doppler broadening[5] of the modal frequencies. Even broadening associated with small source accelerations can severely degrade the effectiveness of the mode extraction method. To make the method more practical, it is extended to the case of a source under arbitrary acceleration. To this end a theory is introduced to describe the modal components of the measured time-domain VLA field from an arbitrarily accelerating cw source in a range-independent waveguide.

The difficulty in treating arbitrary acceleration in a waveguide arises from the dependence of the modal wave numbers and depth functions on the radial velocity of the source. Source accelerations result in time dependence of the modal wave numbers and depth functions. Though approximate time-domain solutions for the special cases of a slow moving constant velocity source[5,6] and a constant radial acceleration source[8] have been derived, the introduced theory is valid for arbitrary source motion. It is shown that the Doppler effect associated with the finite group velocities of the modal components results from a transformation between the source range at the time a signal feature is emitted (the retarded time) to the range of the source at the time the signal feature is measured (the contemporary time).

Applying the theory to make a connection between the source motion and the frequency response of the received field, a transformation is devised to compensate for Doppler broadening. Consequently, the mode extraction method can be effectively applied to cases of arbitrary source acceleration. Synthesizing the transformation requires knowledge of the instantaneous frequency at all sample times. Thus, a method is introduced for measuring the instantaneous frequency of the received field to high resolution using a time domain least-mean-squares fit to short duration harmonic tones.

By treating the case of accelerating sources, the proposed mode extraction method extends the scope of earlier wave number inversion procedures, such as that developed by Frisk and Lynch.[9] Indeed, the work of Frisk and Lynch can be thought of as a zero velocity limit of the mode extraction method. Though it is not the aim of this paper, combining the method with modeling can yield the wave numbers for a broad range of source motion.[10]

The field measured on a VLA due to a moving cw source is developed in Sec. II. Section III introduces the mode extraction method applied to a harmonic source traveling at a constant radial velocity. The method is illustrated with simulation results for the case of a constant radial velocity source. In Sec. IV A, the theory is expanded to include radially accelerating sources. Section IV B develops the transformation that compensates for acceleration-induced Doppler broadening and presents the frequency tracking algorithm for measuring the instantaneous frequency of the received field. The transformation and extraction methods are combined and applied to a simulated radially accelerating cw source in Sec. IV C. The mode extraction procedure is further discussed and simulated mode extraction results are presented. Section V presents the results of the mode extraction method applied to experimental data measured during the SWellEx experiment conducted in 1996. In that experiment, a source, broadcasting several cw tones, was towed along an isobath following a straight line trajectory (not radial to the VLA). Mode extraction results for one of the tones are presented. The final section provides a summary and discussion.

II. THE VLA FIELD FROM A DISTANT MOVING cw POINT SOURCE

This section derives an expression for the pressure field measured over a vertical receive array due to a distant moving cw point source. Consider the case of a cw point source moving at a constant depth, z_s, in a range-independent shallow ocean waveguide whose field is measured by a VLA at range $r=0$. The range of the source with respect to the receive array as a function of time is given as $r(t')$. The field measured at a stationary receiver at depth, z_r, due to a source that emits at angular frequency ω_s is[11]

$$P(z_r,t) = \int_{-\infty}^{\infty} dt' e^{i\omega_s t'} G(z_r,z_s,t|t'), \tag{1}$$

where $G(z_r,z_s,t|t')$ is the Green's function at $r=0$. A distinction is made between the contemporary time, t, at the VLA and the time of emission at the source, t', where t' represents the retarded time. A signal feature occurring at location $r(t')$ at time t' is measured by the VLA at some time $t>t'$. In free space, for example, the retarded time is given by $t'=t-r(t')/c$. In a dispersive medium such as the shallow ocean waveguide, the relation between t' and t is more complicated.[11]

In the case of a distant source (in the radiation zone), the pressure field measured at the VLA is dominated by the modal components and the near field contribution can be neglected. Defining the Fourier transform pair of a function $A(t)$ as

$$\tilde{A}(\omega) = \frac{1}{2\pi}\int_{-\infty}^{\infty} A(t)e^{-i\omega t}dt,$$

$$A(t) = \int_{-\infty}^{\infty} \tilde{A}(\omega) e^{i\omega t} d\omega, \tag{2}$$

where the tilde notation, $\tilde{A}$, denotes the Fourier transform, the modal portion of the Green's function is written

$$G(z_r, z_s, t|t') = \sum_{m=1}^{M} \int_{-\infty}^{\infty} d\omega e^{i\omega(t-t')} \frac{e^{i\pi/4}}{\sqrt{8\pi}\rho(z_s)} \times \phi_m(z_s,\omega)\phi_m(z_r,\omega)\frac{e^{-ik_m(\omega)r(t')}}{\sqrt{k_m(\omega)r(t')}}. \tag{3}$$

Here $\rho(z_s)$ denotes the water density at the source depth, and $\phi_m(z_s,\omega)$ and $k_m(\omega)$ represent the mode m depth function and wave number, respectively. Substituting into Eq. (1) yields where the pressure field at the VLA as a superposition of modal contributions,

$$P(z_r,t) = \sum_{m=1}^{M} P_m(z_r,t), \tag{4}$$

where the mode m component is given by

$$P_m(z_r,t) = \frac{1}{2\pi}\int_{-\infty}^{\infty} dt' e^{i\omega_s t'} \int_{-\infty}^{\infty} d\omega e^{i\omega(t-t')} \times \frac{e^{i\pi/4}}{\sqrt{8\pi}}\phi_m(z_s,\omega)\phi_m(z_r,\omega)\frac{e^{-ik_m(\omega)r(t')}}{k_m(\omega)r(t')}. \tag{5}$$

A related integral has been solved approximately via contour integration to yield an expression for the case that the receiver is in the radiation zone of (far away from) the source resulting in a solution in terms of the retarded, time t'.[11]

In the context of diagnostics applied to the received field, the retarded time solution can be quite difficult to manipulate. It is more convenient to develop a solution that depends only on the contemporary time, t, of the receiver. Redefining the retarded time corresponding to the mode m component, $t' \to t_m$, the source range at the mode m retarded time can be expanded about the range at the contemporary time,

$$r(t_m) = r(t) - \left.\frac{dr(t)}{dt}\right|_t \Delta t_m + \frac{1}{2}\left.\frac{d^2r(t)}{dt^2}\right|_t \Delta t_m^2 + \cdots = r(t) - v_s(t)\Delta t_m + \frac{1}{2}a_s(t)\Delta t_m^2 + \cdots, \tag{6}$$

where v_s and a_s denote the radial source velocity and acceleration, respectively,

$$v_s(t) \equiv \left.\frac{dr(t)}{dt}\right|_t, \quad a_s(t) \equiv \left.\frac{d^2r(t)}{dt^2}\right|_t. \tag{7}$$

The interval $\Delta t_m \equiv t - t_m$ represents the travel time of a feature of the mode m component arriving at the receiver at time t. Referring to Fig. 1, the travel time is defined in terms of the distance the feature travels from its point of origin, $r(t_m)$, to the receiver and the speed, $u_m(\omega, v_s)$, that the feature propagates,

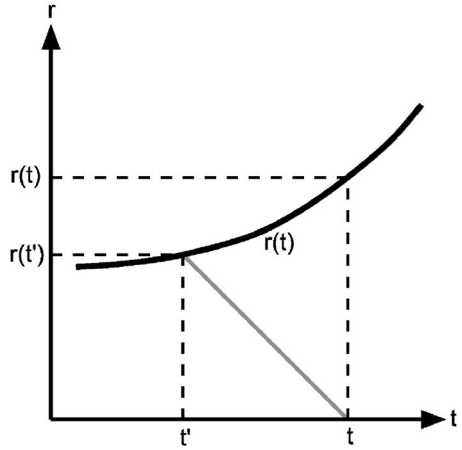

FIG. 1. Schematic for mapping the source range at the retarded time to the source range at the contemporary time. The black line represents the source trajectory. The gray line depicts the field trajectory. A field feature emitted at range $r(t')$ arrives at the receiver (at $r=0$) at time t. The travel time is $t - t'$.

$$\Delta t_m = \frac{r(t_m)}{u_m(\omega, v_s)}. \tag{8}$$

The velocity at which the feature propagates is properly the mode m group velocity at the Doppler shifted frequency,

$$u_m(\omega, v_s) = \bar{u}_m \equiv \frac{1}{\left.\frac{dk_m}{d\omega}\right|_{\bar{\omega}_m}}, \tag{9}$$

where

$$\bar{\omega}_m \equiv \omega_s - \bar{k}_m v_s \tag{10}$$

represents the mode m Doppler shifted frequency. The associated modal wave number,

$$\bar{k}_m \equiv k_m(\bar{\omega}_m), \tag{11}$$

and depth function,

$$\bar{\phi}_m(z) \equiv \phi_m(z, \bar{\omega}_m), \tag{12}$$

are also taken at the Doppler shifted frequency. Because the mode velocity depends on the source velocity at the time of emission, these quantities are implicit functions of the retarded time.

Together, Eqs. (6)–(10) yield a polynomial expression for the range at the mode m retarded time,

$$r(t_m) = r(t) - \frac{v_s(t)}{u_m(\omega, v_s)} r(t_m) + \frac{a_s(t)}{2u_m(\omega, v_s)^2} r(t_m)^2 \cdots. \tag{13}$$

To solve for $r(t_m)$ in terms of the receiver time t, the mode velocity must be made independent of the source time. Making the assumption that the mode velocity is constant, Eq. (13) can be solved for $r(t_m)$ in terms of the range, $r(t)$, and its derivatives at the receiver time t,

$$r(t_m) = \chi_m(t) r(t), \tag{14}$$

where $\chi_m(t)$ depends on the solution of Eq. (13) for the mode m component. Thus, given the full trajectory, $r(t)$, the challenge is to solve for $\chi_m(t)$, either analytically or numerically, to the desired degree of accuracy.

The constant mode velocity assumption is consistent with a source under uniform radial motion (constant v_s) and implies that the Doppler shifted modal wave number and depth function are also constant. Using this fact and substituting Eq. (14) into Eq. (5) leads straightforwardly to an expression for the time-domain pressure field at the receiver resulting from a cw source under uniform subsonic ($|v_s| < u_m$) radial motion,

$$\begin{aligned} P_m(z_r,t) &= \frac{1}{2\pi}\int_{-\infty}^{\infty} d\omega e^{i\omega t} \frac{e^{i\pi/4}}{\sqrt{8\pi}} \bar{\phi}_m(z_s)\bar{\phi}_m(z_r) \\ &\quad \times \frac{e^{-i\bar{k}_m\chi_m(t)r(t)}}{\sqrt{\bar{k}_m\chi_m(t)r(t)}} \left[\int_{-\infty}^{\infty} dt_m e^{i(\omega_s-\omega)t_m}\right] \\ &= \frac{e^{i\pi/4}}{\sqrt{8\pi}} \bar{\phi}_m(z_s)\bar{\phi}_m(z_r) \frac{e^{i(\omega_s t - \bar{k}_m\chi_m(t)r(t))}}{\sqrt{\bar{k}_m\chi_m(t)r(t)}}. \end{aligned} \tag{15}$$

The sifting property of the Dirac delta function $\delta(\omega_s-\omega)$ (the term in square brackets) has been used in arriving at the second line. In the constant radial source motion case, $\chi_m(t)$ has an analytic solution,

$$\chi_m = \frac{1}{1 + v_s/\bar{u}_m}. \tag{16}$$

This suggests a physical interpretation for χ_m. While $\bar{k}_m$ and $\bar{\phi}_m(z)$ characterize the Doppler shifted spatiotemporal properties of the mode m field contribution, χ_m is the factor that describes the Doppler shift arising from the fact that the mode propagates at a finite velocity.

Although, Eq. (15) is exact in the case of uniform radial source motion, it would be useful to extend it to cases involving arbitrary source accelerations. While $\chi_m(t)$ includes accelerations and higher derivatives of the trajectory, it is generally not possible to compute the time-varying Doppler shift for an accelerating source. Thus, the modal depth function and, more important, the modal wave number are taken at a constant value corresponding to a constant source velocity, $v_s=v_c$. Expanding $\bar{k}_m$ about velocity, v_c, the wave number varies as

$$\bar{k}_m \to k_m(\bar{\omega}_m)\left(1 - \frac{\delta v_s}{u_m(\bar{\omega}_m)} + \cdots\right), \tag{17}$$

where $\delta v_s \equiv v_s - v_c$ is the velocity deviation and where $\bar{\omega}$ is the Doppler shifted frequency corresponding to v_c. Approximating the Doppler shifted wave number by its value at v_c is valid in cases where the net deviation from uniform motion is small compared to the modal group speed, $|\delta v_s/\bar{u}_m| \ll 1$. For example, a source in uniform motion (not radial) will have a nonzero radial acceleration. When it is far from the point of closest approach, its radial velocity changes slowly. As a result, it is possible to choose a relatively long interval for which the velocity deviation (from v_c which is the average over the interval in this case) is small and the approximation $\bar{k}_m \approx k_m(\bar{\omega}_m)$ is valid.

Such an approximation has an analog in the literature. In deriving expressions for a low velocity source, Hawker[5] and Schmidt and Kuperman[6] take the modal wave numbers and depth functions in the zero Doppler shift ($v_s=0$) limit: $\bar{k}_m = k_m(\omega_s)$, and $\bar{\phi}_m(z) = \phi_m(z,\omega_s)$. Indeed, Eq. (15) reduces to these earlier expressions in the low source velocity limit, where $\chi_m(t)$ is approximately

$$\chi_m(t) = 1 - \frac{v_s(t)}{u_m}. \tag{18}$$

This low velocity approximation could be improved (over a chosen interval) in two ways:

(1) By taking the modal depth functions and wave numbers at the Doppler shifted frequency corresponding to the average velocity over the interval rather than at the unshifted source frequency.
(2) By computing $\chi_m(t)$ for the trajectory rather than using the low velocity approximation.

Though it is possible to find an analytic solution for the Doppler shifted frequency and corresponding modal wave number and depth function in certain cases (an ideal waveguide, for example), in general it must be calculated numerically. With knowledge of the modal wave number as a function of frequency for the waveguide, a solution for $\bar{k}_m$ and $\bar{\omega}$ is found through iteration of Eqs. (10) and (11) for a given source velocity, v_c. Likewise, it is not possible in general to find an analytic solution for $\chi_m(t)$ in the case of an arbitrarily accelerating source. Even in the simple case that the source trajectory is described by a regular nth order polynomial expression, it is often difficult to find an analytic expression for $n>3$. On the other hand, Eq. (15) provides a powerful and computationally tractable means of arriving at a numerical solution to a high degree of accuracy. Though the constant mode velocity assumption introduces a small error into the calculation of $\chi_m(t)$ in the case of an accelerating source, $\chi_m(t)$ becomes exact in the high frequency limit, where the modes and mode velocities become independent of frequency. Thus, Eq. (15) is most useful for the lowest order modes far from cut-off.

The remainder of the paper deals with slow-moving sources. In order to simplify the discussion, all modal wave numbers and depth functions are taken at their the source frequency (zero Doppler shift): $k_m \equiv k_m(\omega_s)$ and $\phi_m(z) \equiv \phi_m(z,\omega_s)$.

III. MODE EXTRACTION FROM A SOURCE IN UNIFORM RADIAL MOTION

In a typical at-sea scenario, only the time domain signal measured on an array of receivers is available. Assuming that some aspect of the signal results from a moving cw source, then that part of the signal can be isolated and analyzed in a number of ways. Here the signal (or some portion thereof) is Fourier analyzed to generate a frequency response. Typically,

in the matched-field context, this frequency response is matched to a model, or replica, whose parameters include not only the waveguide properties, but also the source frequency and trajectory. The aim here is to forego computational modeling and proceed self-adaptively, without knowledge of the waveguide or the source properties, to a determination of the modal depth functions. The only assumptions are that the waveguide is range independent and that the source travels at a constant depth at a velocity that is always small compared to the modal group velocities.

The scenario envisioned for the mode extraction procedure requires the field measured on a VLA of acoustic sensors from a slow moving cw source as it traverses a radial distance over the time interval, $t_0 \leqslant t \leqslant t_1$. The source must always be traveling in the same radial direction during the interval, either toward or away from the VLA. The azimuthal trajectory is irrelevant. The extraction procedure is applied to the frequency response of the measured VLA field over the interval. Applying the Fourier transform to Eqs. (4) and (15) with respect to the receiver time yields the limited time aperture frequency response of the received VLA pressure field,

$$\tilde{P}(z_r,\omega) \equiv \int_{t_0}^{t_1} dt e^{-i\omega t} P(z_r,t) = \sum_{m=1}^{M} \tilde{P}_m(z_r,\omega). \tag{19}$$

Here the mode m contribution

$$\tilde{P}_m(z_r,\omega) = \phi_m(z_r)\left(\frac{e^{i\pi/4}}{\sqrt{8\pi}}\phi_m(z_s)a_m(\omega)\right), \tag{20}$$

where all the frequency dependence is included in the factor

$$a_m(\omega) \equiv \int_{t_0}^{t_1} dt \frac{e^{-i(\omega-\omega_s t+k_m\chi_m(t)r(t))}}{\sqrt{k_m\chi_m(t)r(t)}}. \tag{21}$$

To demonstrate and develop the mode extraction procedure, it is useful to first consider the simple case of a slow moving cw source under uniform radial motion along the radial trajectory $r(t)=r_0+v_c t$, where $r_0 \equiv r(t_0)$ is defined to be the location of the source at time $t=t_0$. In this case, the χ_m Doppler factor is independent of time and is given by Eq. (16) with $v_s=v_c$. According to Eq. (21) each modal component propagates at a distinct frequency,

$$\omega_m \equiv \omega_s - k_m\chi_m v_c, \tag{22}$$

which, depending on the range aperture traversed by the source, $R \equiv |r(t_1)-r(t_0)|$, may or may not be well resolved in frequency. Interestingly, the frequency domain resolution of the modal components over the interval $T \equiv t_1 - t_0$ is an implicit function of the total range aperture,

$$\left.\begin{aligned} d\omega &= \frac{2\pi}{T} \\ R &= |v_c T| \\ d\omega &\ll |(k_m - k_{m+1})v_s| \end{aligned}\right\} \Rightarrow R \gg \frac{2\pi}{|k_m - k_{m+1}|}. \tag{23}$$

In order to resolve modal frequency component m from modal frequency $m+1$, the source must cover a distance significantly longer than the mode-m-mode-$m+1$ interference wave length, $\lambda_{m,m+1}=2\pi/|k_m-k_{m+1}|$, regardless of the time interval T. In the low source velocity limit, χ_m approaches unity so that the range at the receiver time approaches the range at the source time, $r(t) \to (t_m)$. Consequently, the range aperture, R, represents the actual physical range traversed by the source. In the long aperture limit the integral of Eq. (21) approaches a Dirac delta function about the modal frequency,

$$\lim_{R\to\infty} a_m(\omega) = 2\pi\delta(\omega-\omega_m). \tag{24}$$

In this limit the VLA field is a superposition of weighted modal depth functions

$$\tilde{P}(z_r,\omega) = \sum_{m=1}^{M} \phi_m(z_r)\left(\frac{e^{i\pi/4}}{\sqrt{2}}\phi_m(z_s)\delta(\omega-\omega_m)\right). \tag{25}$$

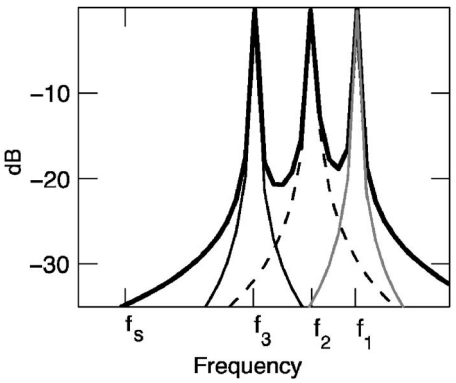

FIG. 2. Schematic of the discrete modal frequency spectrum from a constant radial velocity cw source. This environment supports three propagating modes. The thin black line, the thin, dashed black line, and the thin gray line represent the Fourier transforms of the individual modal components. The thick black line is the Fourier transform resulting from a modal superposition. For a constant radial velocity source, the modal frequencies for modes 1–3, indicated by f_1, f_2, and f_3, respectively, are unambiguously discrete. In this case, the source is moving toward the sensor, $v_s<0$, so that the modal frequencies are higher than the source frequency, f_s.

The source motion has effectively broken the frequency degeneracy of the modal components. This modal decoupling in the frequency domain VLA field serves as the basis for the mode extraction technique. To illustrate, Fig. 2 shows a schematic of the magnitude of the pressure field frequency spectrum [Eqs. (19)–(21)] for an approaching constant velocity source. Though all formalism is developed in terms of the angular frequency and phase, all figures are plotted in frequency (Hz) and *cycles*. The three propagating modes are shifted to higher frequencies (indicated by f_1, f_2, and f_3) than the source frequency (f_s). The pressure frequency spectra of the individual modal components are also plotted for the purposes of illustration. For a sufficiently large range aperture, Fig. 2 demonstrates that the mode m component dominates in the vicinity of its modal frequency. This suggests the possibility of extracting its depth dependence by selecting the appropriate frequency component of the spectrum projected over the VLA.

Figure 3 shows the absolute value of the pressure frequency response of a simulated constant velocity source projected over the VLA. Superimposed on the image (black line) is the normalized pressure response summed incoherently over the VLA elements. The resolution of the frequency response is dictated by the limited time aperture,

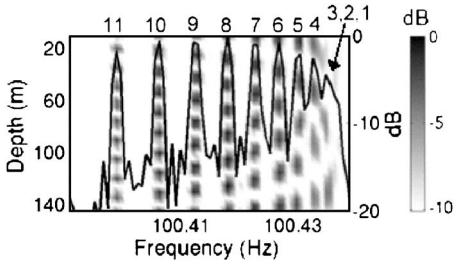

FIG. 3. Fourier transform frequency response of a simulated VLA pressure field from a constant radial velocity cw source. The absolute value of the frequency domain pressure field as a function of depth (left axis) is imaged in decibels. The solid black line represents the frequency domain pressure field summed incoherently over depth in decibels (right axis). The source (f_s=100.17 Hz) is traveling toward the VLA at a constant radial velocity. The modal components are labeled for clarity.

which in this case is T=600 s. As discussed in the following, a long time aperture is necessary to resolve the Doppler shifted modal frequencies.

The simulation was carried out using the spectral integration method of Refs. 1 and 10 for a source moving radially toward the VLA at v_c=4 m/s at a constant depth of 145 m in a 150-m deep Pekeris waveguide. The water sound speed, water density, bottom sound speed, and bottom density were c_w=1500 m/s, ρ_w=1026 kg/m^3, c_b=1800 m/s, and ρ_b=1800 kg/m^3, respectively. The VLA consisted of 28 elements evenly spaced between 10 and 145 m of depth.

The modal components, which are enumerated across the top, are clearly evident in Fig. 3. Each peak of the incoherent sum corresponds to a modal component at a unique frequency. Also evident are the modal depth functions. Because the source is moving toward the array the modes are Doppler shifted to higher frequencies than the source frequency, fs=100.17 Hz. Mode extraction is carried out by isolating the frequency component corresponding to a given mode. The frequency resolution is such that modal frequencies for modes 5–11 appear well isolated with the result that their modal depth functions are extractable. The frequency resolution is insufficient to resolve the modal frequencies of modes 1–4. As a result, these modal depth functions are not extractable.

Figure 4 shows the minimum range aperture [as defined by resolution relations (23)] needed to resolve the theoretical modes of the simulation. The range aperture of the simulation was 2400 m. Because the modal components are monochromatic and coherent in the constant velocity case, the Fourier analysis results in a coherent summation of the modal depth functions. The modal components become sharper and more intense in direct proportion to the size of the time aperture used to calculate the frequency response. Equating time to range, the peak intensity can be related to source velocity. For a given range aperture, the peak intensity, PI, increases in inverse proportion to the magnitude of the source velocity, $\mathrm{PI} \propto T = R/|v_c|$. Because the modal components sum coherently, while the ambient noise is incoherent, it is expected that, for a given range aperture traversed by the source, the signal-to-noise ratio (SNR) of the modal components should increase as source velocity decreases, i.e., as the time aperture increases. For a slow moving source, then, that covers a large range aperture, it is possible to extract the modes simply by isolating the depth dependence at a given frequency maximum. Equations (24) and (25) treat the infinite aperture limit. A finite range aperture will result in an additional complex phase that is constant over depth. A method for removing the phase and mode extraction results are discussed in Sec. IV.

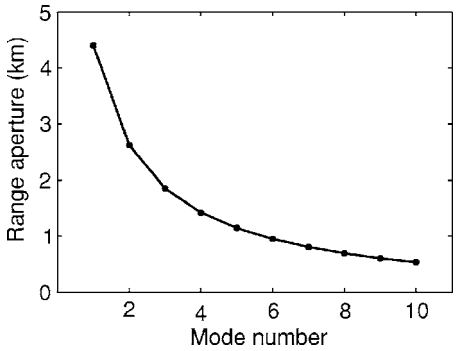

FIG. 4. Minimum range aperture required to resolve adjacent modal frequencies. This corresponds to the simulation shown in Fig. 2.

IV. MODE EXTRACTION FROM A RADIALLY ACCELERATING cw SOURCE

Considering the frequency resolution arguments outlined in Sec. III, effective mode isolation in shallow ocean applications requires several kilometers of range aperture. In the dynamic ocean environment, it is unrealistic to expect to be able to generate clean, constant radial velocity data over such large distances. For the technique to be relevant, the goal must be to extract modes using signals from sources of opportunity that follow unknown trajectories in a dynamic ocean environment with waves, wind, and currents.

Recall that in the case of uniform radial source motion, the modal phase progressions are linear in time, resulting in a frequency response that is a superposition of well-defined cw tones, one for each mode (see Fig. 2). In contrast, for a radially accelerating source, there is not a unique constant frequency for each mode throughout the duration of the time aperture. The phase does not progress linearly with time. The frequency response is a superposition of quasitonal components, or tones that waver with time, resulting in a Fourier decomposition featuring "smeared" or Doppler-broadened modal contributions. If the magnitude of the velocity change is too great, Doppler broadening can lead to the overlap of modal components and render them indistinguishable in the frequency response.

As an example, consider Fig. 5(a), which shows a schematic of the magnitude of the pressure field frequency response for an approaching source under constant acceleration. Because the source is approaching, its velocity is negative over the time aperture and positive acceleration manifests as a decrease in the magnitude of the radial speed. The modal frequencies, thus, attain their highest values at the beginning of the time aperture. As the source velocity increases, the modal frequencies decrease, resulting in a broadening of the frequency responses of the modal components. As a consequence, the modal depth functions are not be identifiable as isolated regions (compare to Fig. 3).

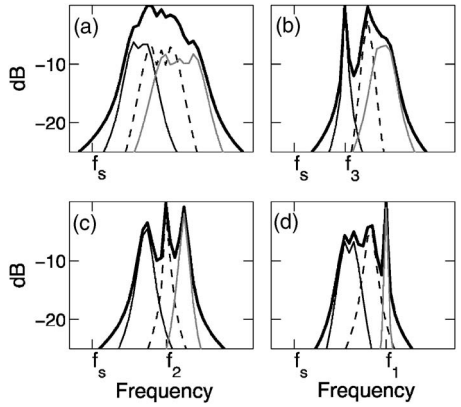

FIG. 5. Schematic of the modal frequency spectrum from a radially accelerating cw source. The thin black line, the thin, dashed black line, and the thin gray line represent the Fourier transforms of modes 1, 2, and 3, respectively (each considered individually). The thick black line is the Fourier transform of the superposition of the modes. (a) At the beginning of the source track, when the radial velocity of the source is the least, the modal frequencies are the greatest. As the radial velocity of the source increases, the modal frequencies decrease, approaching the source frequency, f_s, causing a "smearing" or Doppler broadening of the frequency responses of the modes in the received signal. By applying a transform to the received signal that compensates for the radial acceleration, it is possible to remove the Doppler broadening. In cases of extreme acceleration, this can only be done for one mode at a time. (b)–(d) The effects of the compensation procedure. Each mode is brought into coherence at a frequency related to the choice for the reference frequency, f_c.

Even modest Doppler broadening of the modal frequencies can severely degrade the performance of the mode extraction technique. In this section the mode extraction technique is adapted to deal with radially accelerating sources. The basic strategy is to develop a transformation for removing the Doppler broadening effects that result from accelerations so that the mode extraction method can be applied. The issues at hand are the following:

(1) Starting with the assumption of modal propagation, can the phase evolution of the measured signal from an accelerating source be adjusted so that one or more of the modal components becomes a pure cw tone, i.e., follows a linear phase progression?
(2) If so, can the information needed to transform the phase be extracted from the signal itself?

This section is divided into three parts. The first above-presented question is addressed in Sec. IV A, which extends the theory of Secs. II and III to the case of a radially accelerating source. The second question is addressed in Sec. IV B, which introduces a method for detecting and compensating for the time-varying Doppler effects associated with radial acceleration. Section IV C presents simulated compensation and mode extraction results and further develops the extraction procedure.

A. Modal Doppler effects from a radially accelerating source

In deriving an expression for the VLA field from an accelerating source, it is convenient to decompose the change in range into a uniform motion component at the average velocity, v_c, over the interval and a component that represents deviations from uniform motion (due to accelerations), $\hat{r}(t)$,

$$r(t) = r_0 + v_c t + \hat{r}(t). \tag{26}$$

Defining v_c to be the average velocity on the interval ensures that the deviations satisfy the initial and final conditions, $\hat{r}(t_0)=0$ and $\hat{r}(t_1)=0$, respectively. Substituting Eq. (26) into Eq. (21), the mode m component frequency response is then governed by

$$a_m(\omega) \approx \int_{t_0}^{t_1} dt \frac{e^{-i(\omega-\omega_m)t}}{\sqrt{k_m r(t)}} e^{ik_m \hat{r}(t)}. \tag{27}$$

where ω_m is given by Eq. (22) with $\chi_m=1$. Equation (27) assumes that the corrections to the wave number and χ due to source motion are negligible, i.e., the low velocity source approximation. The approximation symbol has been used to reflect the fact the modal wave number and χ_m have been taken at zero Doppler shift.

B. Detecting and compensating for time-varying Doppler effects

According to Doppler theory, source velocity deviations result in frequency deviations in the measured VLA field. The strategy is to self-adaptively track the instantaneous Doppler shifted frequency response as a function of time with enough accuracy to extract the acceleration term $k_m\hat{r}(t)$, of Eq. (27) and use this knowledge to develop a transformation that compensates for the resulting Doppler broadening.

To this end, a high resolution nonlinear frequency-tracking technique is introduced for measuring the time evolution of the instantaneous frequency response of an experimental pressure field in a modal environment. The technique is a time domain least mean squares fit to short time duration intervals of the measured signal. To implement the fit, the measured time domain pressure field is bandpass filtered to remove any strong frequency components not related to modal propagation arising from the source at frequency ω_s. The filtered field on the ith VLA element, $P_i(t) \equiv P(z_i,t)$, where z_i is the depth of the element, is decomposed into time windows of duration $\delta\tau_{\text{win}}$ at intervals of Δt_{samp}. The jth time window sampled at time $t=j\Delta t_{\text{samp}} \equiv t_j$ is denoted by $P_i(t_j;t_j+\delta t_{\text{win}})$. Each window is assigned to the array $D_{ij}(t'')=P_i(t_j;t_j+\delta t_{\text{win}})$. Here the $t''=t-t_j$ is the local time relative to the start time of each time window. Indices $i=1,2,\ldots,I$, and $j=0,1,\ldots,J$ denote the particular VLA array element and time window, respectively. Each time window is fit to a two-parameter model, $\sin(\hat{\omega}t''+\sigma)$, for each element using a least mean squares method. For high SNR in the $\delta t_{\text{win}} \to 0$ limit, this procedure is equivalent to sampling the instantaneous time derivative of the phase of the received signal at times t_j. For the fit to be valid, δt_{win} must be small enough that the frequency content is nearly monochromatic over the duration of the window.

The appropriate window duration and sampling interval are determined by the dynamics of the measured pressure field. As shown earlier, the time domain pressure field is composed of several time-varying monochromatic modal

frequency components whose instantaneous frequency distribution depends on the instantaneous wave numbers and instantaneous source velocity. Interference among these frequency components results in beating of the time domain signal. In order for the monochromatic assumption to be valid, the window duration must be smaller than the characteristic beating duration, Δt_b. The beating duration depends on the maximum frequency interval between the highest and lowest modal frequency components,

$$\Delta t_b \approx \frac{2\pi}{\left|\left(\frac{1}{c_b}-\frac{1}{c_w}\right)\omega_s v_s\right|_{\max}},$$

where c_b and c_w are sound speeds characterizing acoustic propagation in the bottom and water, respectively. The sampling interval must be small enough that it adequately samples the macroscopic frequency behavior. However, oversampling causes no error, so Δt_{samp} may be as small as computation power allows.

The minimization function is defined as

$$Q_{ij}(\hat{\omega},\sigma) = \int_0^{\Delta t_{\text{win}}} dt'' |D_{ij}(t'') - \mathcal{E}_{ij}(t'')\sin(\hat{\omega}_{ij}t'' + \sigma_{ij})|^2, \tag{28}$$

where $\hat{\omega}_{ij}$ and σ_{ij} are the fit parameters. The quantity $\mathcal{E}_{ij}(t'')$ is defined as the envelope of $D_{ij}(t'')$. Including the envelope accounts for modulations caused by the beating and thereby improves the ability of the two-parameter model to fit the data. The value of the frequency parameter, $\hat{\omega}_{ij}$, that minimizes Q_{ij} on element i for window j, is regarded to be the instantaneous frequency response of the pressure field on the ith element sampled at times t_j. The phase parameter, σ_{ij}, is ignored.

Signal minima arising from destructive interference among the modal frequency components can lead to unacceptable mismatch and poor values for the instantaneous frequency response of a given element at various times. Sampling the signal over depth ensures that, for any particular time, t_j, some elements will not experience a destructive interference minima. Such redundancy allows for a variety of schemes for determining the instantaneous frequency response at each time sample, ranging from an averaging of the individual element fits to acceptance of only the best fit. The multielement best fit frequency at time t_j is denoted by $\hat{\varpi}(t_j)$.

Figure 6 shows the results of the frequency tracking procedure applied to simulation for a source moving at a constant velocity of 4 m/s in a direction that does not coincide with the radial direction (the case studied by Hawker[5] and Schmidt and Kuperman[6]). Thus, the radial velocity of the source is not uniform, i.e., the radial acceleration of the source is nonzero. The source depth is held at a constant depth of 5 m in the same Pekeris waveguide environment from Sec. III. The VLA elements are also at the same depths. The source range and radial velocity trajectories are plotted in Figs. 6(a) and 6(b).

The frequency tracking technique was applied using a time window duration of $\delta t_{\text{win}}=2$ s and a sampling interval of $\Delta t_{\text{samp}}=1$ s. The thick black line in Fig. 6(c) is the frequency tracking result. It is plotted along with the theoretical time-dependent modal frequencies. There is one thin black curve for each of the 11 time-varying modal frequencies. The fluctuations in the frequency tracking result are physical and arise from the complex dynamics of the interference among the modal frequencies. Notice the fluctuations fall within the spread of the theoretical modal frequencies and diminish as the spread diminishes. Sampling the field over depth minimizes these fluctuations.

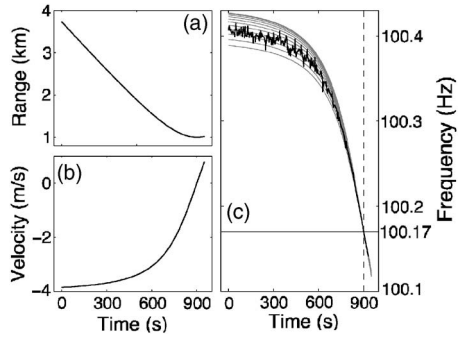

FIG. 6. Time-dependent (a) range and (b) velocity of the simulated radially accelerating cw source. (c) The corresponding frequency tracking algorithm results. The thick black line represents the output of the algorithm. The fine black lines indicate the expected frequencies of each propagating mode over the source trajectory. The dashed line marks the time of closest approach, and the solid medium black line marks the source frequency.

Interpolating the frequency track result to the sampling rate of the received field, $\hat{\varpi}(t_j)\rightarrow\hat{\varpi}(t)$, yields the desired instantaneous frequency as a function of time needed to perform the transformation. Identifying the instantaneous frequency with the time derivative of the signal phase progression, a model for relating the interpolated measured frequency track to the results of Sec. IV A is introduced,

$$\hat{\varpi}(t) = \omega_s + \alpha(v_c + \dot{\hat{r}}(t)). \tag{29}$$

Here and throughout, the notation $\dot{A}=(d/dt)A$ denotes the time derivative of quantity A. Equation (29) is assumed to represent the instantaneous Doppler shifted frequency at the contemporary time measured on the VLA due to source motion at time at the retarded time. As discussed in Sec. II, because the modal components travel at different group speeds, the modal features arriving at the array at time t originate from different ranges. In the low source velocity, mild acceleration limit, the range differences are negligible. The unknown constant α ($\alpha>0$) has been introduced to account for the fact that the measured instantaneous frequency is an average over the weighted modal frequencies.

The time-dependent frequency deviation is defined as $\hat{\delta\omega}(t)=\hat{\varpi}(t)-\omega_c$, where

$$\omega_c \equiv \frac{1}{T}\int_{t_0}^{t_1} dt\hat{\varpi}(t) \tag{30}$$

is the average frequency over the measured interval $t_0\leqslant t \leqslant t_1$. Introducing the dummy variable of integration, t'', and substituting Eq. (29), the deviation in phase from the uniform phase progression of a monochromatic component at ω_c as a function of time is given by

$$\hat{\Theta}(t) \equiv \int_{t_0}^{t} dt'' \delta\hat{\omega}(t'') = (\omega_s - \omega_c + \alpha v_c)(t - t_0) + \alpha \hat{r}(t). \tag{31}$$

The condition $\hat{r}(t_0)=0$ (see Sec. IV A) has been used in the second line of Eq. (31). The transformation function is defined

$$\mathcal{F}(\gamma,t) = e^{-i\gamma\hat{\Theta}(t)}, \tag{32}$$

where γ is a free parameter whose meaning will become clear shortly.

Applying this transformation to the time-domain pressure field of Eq. (19) yields the transformed frequency response,

$$\hat{\tilde{P}}(z_r,\omega,\gamma) \equiv \int_{t_0}^{t_1} dt e^{-i\omega t} P(z_r,t)\mathcal{F}(\gamma,t) = \sum_{m=1}^{M} \hat{\tilde{P}}_m(z_r,\omega,\gamma) \tag{33}$$

where the transformed mode m contribution is given by

$$\hat{\tilde{P}}_m(z_r,\omega,\gamma) = \phi_m(z_r)\left(\frac{e^{i\pi/4}}{\sqrt{8\pi}}\phi_m(z_s)a_m(\omega,\gamma)\right). \tag{34}$$

Returning to Eq. (27) and using Eqs. (31) and (32), the factor $a_m(\omega,\gamma)$ is transformed according to

$$\begin{aligned} a_m(\omega,\gamma) &= \int_{t_0}^{t_1} dt \frac{e^{-i(\omega-\omega_m)t}}{\sqrt{k_m r(t)}} e^{ik_m\hat{r}(t)} e^{-i\gamma\hat{\Theta}(t)} \\ &= e^{i\hat{\omega}_m t_0} \int_{t_0}^{t_1} dt \frac{e^{-i(\omega-\hat{\omega}_m(\gamma))t}}{\sqrt{k_m r(t)}} e^{i(k_m-\gamma\alpha)\hat{r}(t)}, \end{aligned} \tag{35}$$

with $\hat{\omega}_m$ given by

$$\begin{aligned} \hat{\omega}_m(\gamma) &= \omega_m - \gamma(\omega_s - \omega_c + \alpha v_c) \\ &= (1-\gamma)\omega_s + \gamma\omega_c - (k_m + \gamma\alpha)v_c. \end{aligned} \tag{36}$$

At the value $\gamma=\Gamma_m \equiv k_m/\alpha$ the equation $(k_m-\gamma\alpha)\hat{r}(t)=0$ is satisfied for all t. At this value the function $a_m(\omega,\Gamma_m)$ approaches a delta function in the long aperture limit,

$$\lim_{R\to\infty} a_m(\omega,\Gamma_m) = 2\pi\delta(\omega - \hat{\omega}_m), \tag{37}$$

about the frequency

$$\hat{\omega}_m \equiv \hat{\omega}_m(\Gamma_m) = (1-\Gamma_m)\omega_s + \Gamma_m\omega_c. \tag{38}$$

Thus by searching over a range of the parameter γ it is possible to bring the modes into coherence one mode at a time. Noting that the receiver signal is brought into coherence at the same frequency for the same value of $\gamma=\Gamma_m$ over all elements, the modal depth functions can be extracted one at a time using the mode extraction technique of Sec. III. Additionally, using Eq. (38), the source frequency, ω_s, can be determined with knowledge of ω_c, $\hat{\omega}_m$, and Γ_m. Taking the derivative of Eq. (38) with respect to Γ_m, it is clear that the set of points $(\hat{\omega}_m,\Gamma_m)$ fall along a straight line of slope $\omega_c - \omega_s$. A positive (negative) slope corresponds to an approaching (a receding) source.

The process is represented schematically in Fig. 5, which shows a series of transformed fields corresponding to selected values of the continuous transformation parameter, γ. Figure 5(a) shows the frequency response of the received field from a cw source under constant radial acceleration emitting at frequency f_s in a three-mode environment. Doppler broadening leads to an overlap of modal components. With knowledge of the instantaneous frequency behavior of the received field, the transformation of Eq. (32) is constructed and applied to the received field. Figure 5(b) shows the transformed field, $\hat{\tilde{P}}(z_r,\omega,\gamma)$, of Eq. (33) at the value $\gamma=\Gamma_3$, where the mode 3 component is brought into coherence at the frequency $\hat{\omega}_3$ (f_3 in Fig. 5). The transformed field at values $\gamma=\Gamma_2$ and $\gamma=\Gamma_1$ for which modes 2 and 1, respectively, are brought into coherence are depicted in Figs. 5(c) and 5(d).

In theory, the parameter γ represents a normalized wave number with the set of values Γ_m equal to the modal wave numbers normalized by α, the average of the weighted modal frequencies. The modal frequency weightings are assumed to be proportional to the modal excitations, $|\phi_m(z)|$, so that α is a function of depth. Under the constant source depth assumption α is expected to be constant. Due to the nonlinear nature of the frequency tracking algorithm, the precise formulation of α is ill-defined, though it is reasonable to assume that the average falls somewhere within the range of modal wave numbers, i.e., between k_M and k_1. Assuming α to be an unknown constant, the set of Γ_m can be used to determine the ratios between the modal wave numbers, $k_m/k_n=\Gamma_m/\Gamma_n$.

C. Phase compensation and mode extraction from a simulated radially accelerating source

Having developed the formalism of the phase compensation, the transformation is applied to the simulated pressure field of the radially accelerating source discussed in Sec. IV B. The time aperture corresponding to the first 750 s of the simulation (see Fig. 6) is chosen. The frequency tracking results (solid dark curve), $\hat{\varpi}(t)$, over the time aperture are shown in Fig. 7(a). The dashed line indicates the average frequency ω_c over the time aperture. The corresponding acceleration induced time-dependent phase deviation, $\hat{\Theta}(t)$, is plotted in Fig. 7(b). Notice that because the phase deviation is calculated with respect to the average frequency over the time aperture, the total phase deviation is zero at the end of the aperture. Figure 8 shows the frequency response resulting from a transformed pressure field (black curve) summed incoherently over depth, $\Sigma_q|\hat{\tilde{P}}(z_q,\omega,\gamma)|$ (for receiver depths z_q). Because the acceleration is mild, several modes have been brought into coherence simultaneously for a single value of the transformation parameter (in this case, $\gamma=0.93$). The modal components are labeled for clarity. In this case, the mode 10 response is the best for the purposes of mode extraction. The received (untransformed, $\gamma=0$) frequency response, $\Sigma_q|\tilde{P}(z_q,\omega)|$, is plotted for comparison (gray curve).

In Fig. 9 the incoherent sum over the VLA elements of the transformed pressure field frequency response,

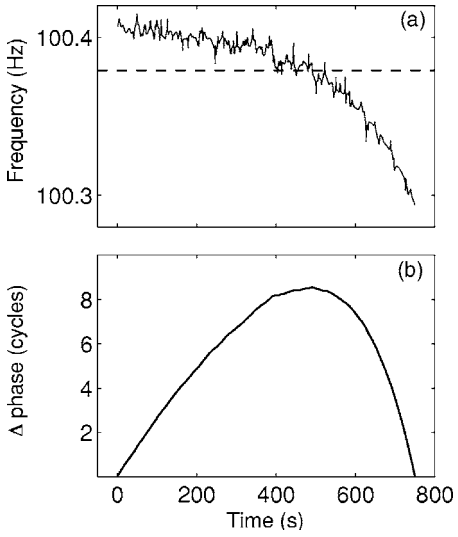

FIG. 7. (a) Frequency tracking result for the simulated radially accelerating cw source. The solid curve is the frequency track result. The dashed line indicates the average frequency over the time aperture. (b) Time-dependent phase deviation derived from the frequency tracking result shown in (a).

$\Sigma_q|\hat{\tilde{P}}(z_q,\omega,\gamma)|$, is imaged as a function of γ. As γ increases, the modal components are brought sequentially into coherence (dark regions) with corresponding modes labeled. The shallow source depth resulted in poor excitation of the low order modes. The slope of the line passing through the points $(\hat{\omega}_m,\Gamma_m)$ is positive, indicating an approaching source. Using the slope of this line, (0.240), and the known value of $\omega_c(f_c=100.385$ Hz) yields an estimate of the source frequency $\omega_s(f_s=100.145$ Hz), which compares well with the actual source frequency (100.170 Hz).

It is important to note that it is not possible in general to estimate the source frequency with high precision in this manner. Recalling that $\gamma=\Gamma_m$ is the value at which the phase deviation of the mode m component of the transformed field goes to zero, $(k_m-\Gamma_m\alpha)\hat{r}(t)=0$, it is clear that the uncertainty in Γ_m is related to the source acceleration. As the acceleration increases, the ambiguity associated with this equation decreases, reducing the uncertainty in Γ_m. However, if the acceleration is large, the usable range aperture is reduced

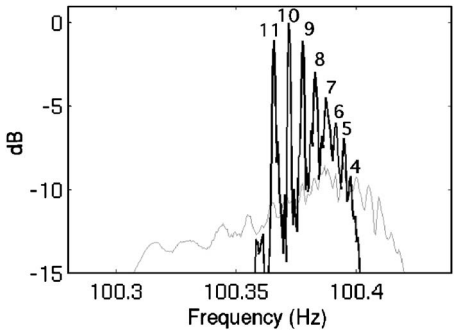

FIG. 8. Transformed vs received ($\gamma=0$) frequency spectra from a simulated radially accelerating source. The gray line represents the frequency response summed incoherently over the elements of the VLA. The black line is the frequency response that results from applying a transformation to the time domain pressure field. The transformed spectra resembles the field from a constant radial velocity source. The modal components are labeled for clarity.

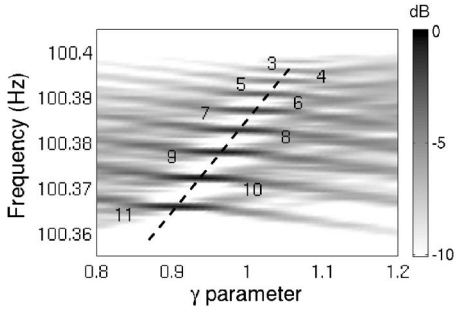

FIG. 9. Simulated transformed frequency response of the accelerating source field as a function of the transformation parameter, γ. The frequency response has been summed incoherently over depth. The dark regions indicate where the respective modal components (labeled for clarity) achieve coherence. The dashed line is a fit of Eq. (38).

(because this theory is restricted to small velocity deviations) and the ambiguity in $\hat{\omega}_m$ increases. In the constant radial velocity limit, where the range deviation goes to zero $[\hat{r}(t)\rightarrow 0]$ the uncertainty in Γ_m goes to infinity. In the simulation the source acceleration is mild, resulting in a small uncertainty in $\hat{\omega}_m$ but a relatively large uncertainty in Γ_m.

Returning to the extraction of the modal depth functions, Fig. 10 demonstrates the relationship between modal depth dependence and the frequency response for different values of γ. These images show the absolute value of the frequency response, $\hat{\tilde{P}}(z_q,\omega,\gamma)$, projected over the VLA. For each image, the normalized incoherent sum over the VLA (black line) for the given value of γ is superimposed. Figure 10(a) shows the optimal transformation $(\gamma=\Gamma_{10})$ for mode 10

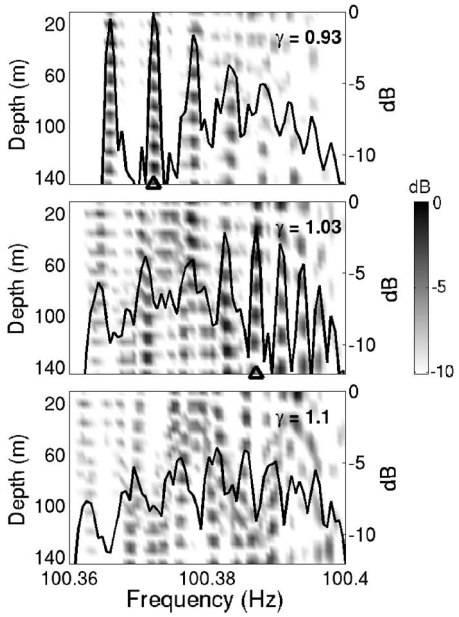

FIG. 10. Simulated frequency response as a function of depth of the transformed VLA field for the radially accelerating cw source. The results for three values of the transformation parameter, γ, are shown. The solid black line represents the frequency response of the respective fields summed incoherently over depth in decibels (right axis). As the γ is increased, different modal frequencies are resolved. Mode 10 (triangle, top panel) is best resolved at $\gamma=0.93$, while $\gamma=1.03$ results in the best resolution for mode 7 (triangle, middle panel). At $\gamma=1.1$ (bottom panel) no modes are well resolved.

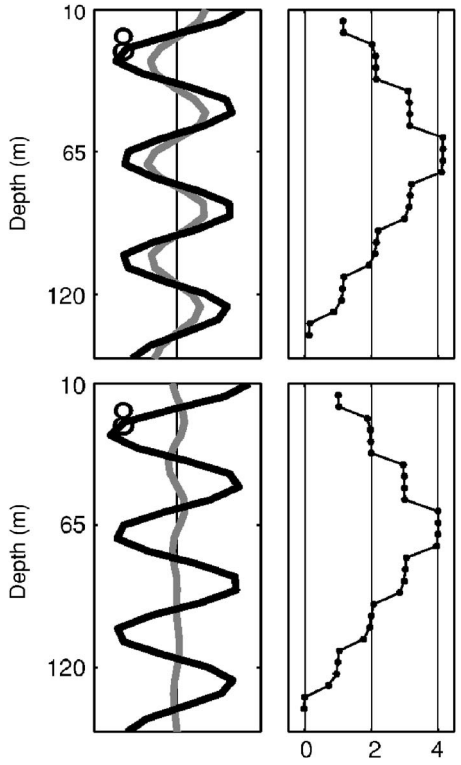

FIG. 11. Extracted mode 8 from simulated accelerating source field and its complex phase. The depth projection of the transformed pressure field at a given modal frequency is a product of the depth dependence of the mode and a complex phase. For a vertical, untilted array, of sensors the complex phase should be constant over depth. The top-left panel shows the modal depth dependence at the mode 8 modal frequency. The top-right panel shows the complex phase at each array element in units of π. The phase has been "unwrapped" so that it can assume values outside the range $[-\pi, \pi]$. The staircase structure of steps of π indicates that the phase is constant at all depths. The bottom panels show a phase translation that results in the depth dependence being purely real.

(though mode 9 and 11 modal frequencies are also well resolved). The mode 7 modal frequency and depth dependence are well resolved in the transformed field of Fig. 10(b). In Fig. 10(c), γ is too high $(\gamma > k_1/\alpha)$ to resolve any of the modes.

Mode extraction requires that the frequency response of a given modal component be resolvable from and significantly peaked above the other modes and the noise. The mode 10 depth function is extracted by isolating the frequency component corresponding to the maximum of its transformed frequency response projected over the VLA [see Fig. 10(a)]. This procedure is applied to all modes that are well resolved and isolated from the neighboring modes for some value of γ. As mentioned in Sec. III, the depth function obtained in this manner will, in general, result in a complex vector of the form $e^{i\theta}\phi_m(z_q)$ for each element of the array. The top left panel of Fig. 11 shows the real and imaginary components of the complex mode vector resulting from the mode extraction procedure. The top right panel shows the phase "unwrapped" in units of π. For a vertical array, the phase associated with the modal depth dependence of a well-resolved and isolated mode is expected to be constant. The staircase structure of the unwrapped phase indicates that the array is vertical and that the modal depth dependence is free

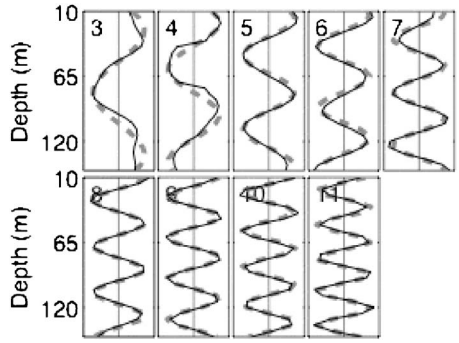

FIG. 12. Simulated mode extraction results for the radially accelerating cw source. The extracted modes (solid black lines) are compared to the theorectical modes (gray dashed lines). Each mode extraction corresponds to a different value of γ. The range aperture covered by the source was insufficient for extracting modes 1–4.

from interference from neighboring modes. Multiplying the mode vector by $e^{-i\delta\theta}$, where $\delta\theta$ is the modulus of θ with respect to π for one of the vector components, removes the complex phase. The bottom panels of Fig. 11 show the results of applying the transformation to the complex vector of the top panels. Mode extraction results for modes 3–11 are plotted in Fig. 12. The dark solid curves are the mode extraction results. The theoretical modes (dashed curves) are plotted for comparison. As mentioned in Sec. III, the range aperture was insufficient to successfully resolve, isolate, and extract modes 1–4.

V. EXPERIMENTAL MODE EXTRACTION FROM A RADIALLY ACCELERATING SOURCE

In this section the transformation and mode extraction procedure are applied to experimental data. The data were recorded during the SWellEx-96 experiment conducted near San Diego, CA in the spring of 1996. During this experiment, an acoustic cw source was towed along an isobath of a mildly sloping environment. The water depth was approximately 210 m. The data were recorded by a vertical line array composed of 64 elements evenly distributed over the bottom half of the water column, between 94 and 210 m. This analysis considers only 21 of the 64 elements at depth intervals of approximately 5 m over the extent of the VLA. In earlier work, matched field processing was successfully employed[12] using a set of normal modes calculated from the knowledge of the measured environmental parameters.[13] These modes, then, are used as a benchmark for the mode extraction results.

Figure 13(a) shows the source range as a function of time. The source-tow, indicated by the gray line, followed an approximately straight, nonradial trajectory at a speed of about 2 m/s, beginning about 8 km from the VLA and passing within a 1 km of the array at the point of closest approach. In addition to the radial acceleration introduced by the nonradial trajectory, the forward speed of the source also varied over the track. The closed circles along the source trajectory indicate 5 min intervals. The source depth was approximately 9 m. The superimposed black line indicates the portion of the track used for mode extraction. The time aperture used for the mode extraction was 25 min. During this

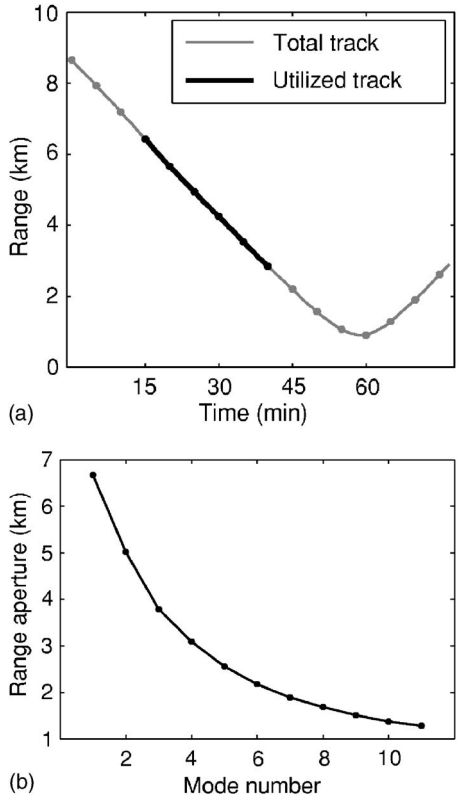

FIG. 13. (a) Source range as a function of time for the SWellEx 1996 source-tow (gray line). The dots represent 5 min intervals. The thick black line indicates the approximate range aperture used for mode extraction. (b) Minimum range aperture required to resolve adjacent modal frequencies.

time the source traversed about 3.5 km. The set of benchmark wave numbers generated from the normal mode method was used to estimate the minimum amount of range aperture needed to resolve and extract the propagating modes. Referring to Fig. 13(b), the range aperture is sufficient to extract modes 7–12 under the assumption that at least two modal interference wavelengths of aperture are required for resolution of adjacent modes.

The result of the frequency tracking technique applied to the time aperture of the experimental data is plotted in the top panel of Fig. 14. The gray curve is the frequency tracking result, $\hat{\varpi}(t)$. The dashed line marks the average frequency, ω_c over the time aperture. The fluctuations are too large to be explained merely by beating of the modal frequencies. Additionally, because the frequency tracking algorithm yielded the same results for several combinations of δt_{win} and Δt_{samp}, it must be concluded that the fluctuations are not a by-product of random errors arising from the frequency tracking algorithm. Thus, it is reasonable to speculate that the fluctuations reflect physical source accelerations. Interestingly, the magnitude of the frequency fluctuations and the dominant 8 s periodicity of the fluctuations are consistent with source velocity fluctuations of ±20 cm/s possibly resulting from surface wave action.

The bottom panel shows the resulting time-dependent phase deviation, $\hat{\Theta}(t)$. The source frequency was $\omega_s = 109.00$ Hz. The frequency response (black curve) for a selected value of γ summed incoherently over depth,

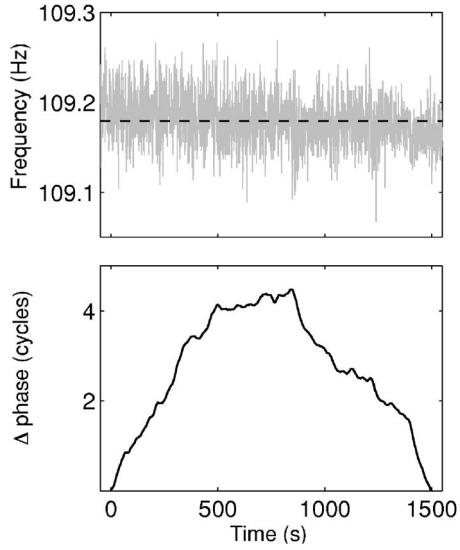

FIG. 14. Frequency tracking algorithm result (top panel) and the resulting phase transformation function (bottom panel) for the SWellEx source. The thin gray line indicates the frequency tracking result. The thick black line is the phase transformation function. The dashed line marks the average frequency over the interval used by the compensation procedure.

$\Sigma_q |\hat{\tilde{P}}(z_q, \omega, \gamma)|$, is plotted in Fig. 15 along with the frequency response of the received (untransformed, $\gamma=0$) field (gray curve). Because the radial acceleration is very mild over the time aperture, the frequency response improvement is not as drastic as in the simulation of the last section. However, the displayed transformation still results in a substantial gain in SNR for a few of the modal components. The absolute value of the frequency response projected over the VLA for the same value of γ is shown in Fig. 16. Again, the normalized incoherent sum over the VLA (black line) for the given value of γ is superimposed. The depth dependence of mode 9 is well resolved. Modes 8 and 10 on either side are also resolved.

Figure 17 shows the mode extraction results. The data derived modes projected over the VLA are indicated by black curves. They are plotted against the calculated benchmark normal modes (dashed lines) for comparison. A few data-derived mode results are plotted in each panel. Each data-derived mode was extracted for a different value of the transformation parameter. As expected, the range aperture

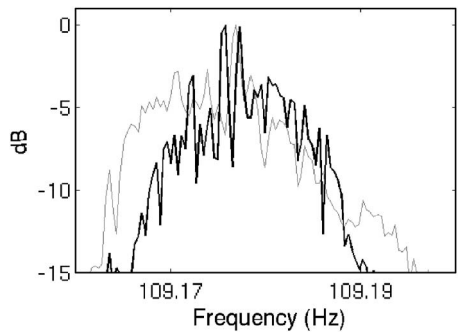

FIG. 15. Transformed vs received ($\gamma=0$) experimental frequency spectrum from the SWellEx source data. The gray line is the frequency response of the measured pressure field summed incoherently over the elements of the VLA. The black line is the frequency response of the transformed field.

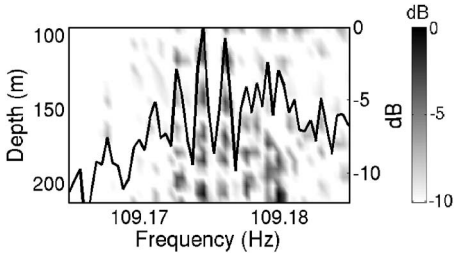

FIG. 16. Frequency response as a function of depth of the transformed VLA pressure field from the SWellEx source data. This result corresponds to a single value of γ. The solid black line represents the frequency domain pressure field summed incoherently over depth in decibels (right axis).

was insufficient to extract the low order modes. In addition to the limitations posed by the short aperture, the low order modes were not highly excited by the shallow source. Because the extracted mode functions are known only over the VLA, they have been normalized to unity over the VLA. This limitation is unavoidable in partial-spanning applications and can lead to normalization mismatch between the low order and high order modes. Estimating the source frequency from the data proved to be difficult and was not possible in this case. One possible explanation is that the environment had some range dependence. Indeed, it is an open question whether useful wave number and source frequency information can be extracted in this manner in at-sea applications, where the effective time/range aperture is limited by the errors associated with acoustic noise and measurement (which compound with the increased aperture).

VI. SUMMARY AND DISCUSSION

A theory has been introduced for calculating the time domain field measured by a stationary receiver in the radiation zone of a cw source under arbitrary acceleration in a range-independent shallow ocean waveguide. By mapping the retarded time at the source to the local time at the receiver, the theory deduces a general and exact formulation of the Doppler shift arising from the finite propagation speed of the modal components. The theory has been used to develop a method for extracting the modal depth functions over a partial-spanning VLA of acoustic sensors using the field from a radially accelerating acoustic cw point source. The mode extraction method is fully self-adaptive, using only the measured field without any knowledge of the environment. The method assumes only that the source is slow moving and that the field is dominated by modes of acoustic propagation.

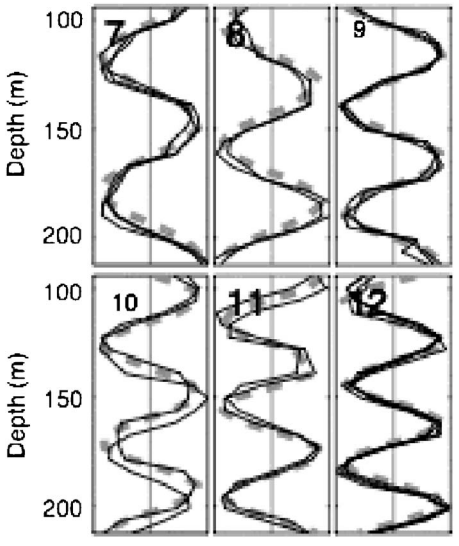

FIG. 17. Mode extraction results from the transformed SWellEx source track VLA field. The extracted modes (solid black lines) are compared to the modes modeled from knowledge of the environmental parameters (gray dashed lines). Each extraction was performed for a unique value of γ. The range aperture covered by the source was insufficient for extracting modes 1–6.

Doppler effects arising from the source motion break the degeneracy of the modal frequency response so that each mode propagates at a distinct frequency from the other modes. For a constant velocity source, the modal frequencies remain constant in time. As a result, coherent processing methods such as the Fourier transform lead to high SNR gains for the modal depth functions. Modes for which the range aperture is long enough can be resolved in the frequency domain and isolated and extracted individually.

However, radial source accelerations lead to Doppler broadening of the modal frequencies reducing the SNR and resolution. Radial accelerations become an issue in at-sea applications where the required range aperture can be on the order of kilometers. In order to make this technique practical, a method for compensating for the time-varying Doppler effects has been developed in conjunction with the mode extraction technique. The acceleration-induced Doppler dynamics are measured with a time domain least mean squares fit to short duration harmonic tones. This information makes it possible to transform the measured time domain pressure field so that one or more of the modal frequencies remain constant in time.

The technique has been successfully applied to both simulation and experimental data. The depth-dependent mode functions projected over a partial-water column spanning VLA were successfully extracted in both instances, limited only by the resolution restrictions related to the range aperture traversed by the source. In both cases, the range aperture was insufficient for extraction of the low order modes. Though this technique may only yield a subset of the modal depth functions over only a portion of the water column, there is still a potential for application to coherent matched field processing and matched mode processing[14] techniques. For example, this technique, in conjunction with the optimization scheme presented by Hursky *et al.*[15] (which assumes *a priori* knowledge of the sound speed profile of the water column), could be used to determine the full set of full-spanning modal depth functions and their corresponding wave numbers. In a similar fashion, an accurate knowledge of the modal depth functions can serve as the basis for bottom property inversion techniques. Though the frequency response analysis in this work has been developed in the context of Fourier decompositions, other methods for determining the frequency response can be used. For instance, because the compensation procedure renders one or more of the modal frequency responses constant over the time aperture, a high resolution nonlinear frequency-comb

method such as that proposed by Roux *et al.*[16] may allow for the relaxation of the range aperture requirements.

[1]F. B. Jensen, W. A. Kuperman, M. B. Porter, and H. Schmidt, *Computational Ocean Acoustics* (AIP, New York, 1994).
[2]T. B. Neilsen and E. K. Westwood, "Extraction of acoustic normal mode depth functions using vertical line data," J. Acoust. Soc. Am. **111**, 748–756 (2002).
[3]W. A. Kuperman and F. Ingenito, "Spatial correlation of surface generated noise in a stratified ocean," J. Acoust. Soc. Am. **67**, 1988–1996 (1989).
[4]P. Hursky, W. S. Hodgkiss, and W. A. Kuperman, "Extracting modal structure from vertical array ambient noise data in shallow water," J. Acoust. Soc. Am. **98**, 2791 (1995).
[5]K. E. Hawker, "A normal mode theory of acoustic Doppler effects in the oceanic waveguide," J. Acoust. Soc. Am. **65**, 675–681 (1979).
[6]H. Schmidt and W. A. Kuperman, "Spectral and modal representations of the Doppler-shifted field in ocean waveguides," J. Acoust. Soc. Am. **96**, 386 (1994).
[7]S. C. Walker, P. Roux, and W. A. Kuperman, "Data-based mode extraction with a partial-water-column spanning array," J. Acoust. Soc. Am. **118**, 1518 (2005).
[8]K. Sabra, "Broadband performance of time-reversing arrays in shallow water," Ph.D. thesis, University of Michigan, Appendix E, 2003, pp. 233–235.
[9]G. V. Frisk, and J. F. Lynch, "Shallow water waveguide characterization using the Hankel transform," J. Acoust. Soc. Am. **76**, 205–216 (1984).
[10]E. M. Giddens, "Geoacoustic inversion using sound from light aircraft," Ph.D. thesis, Scripps Institution of Oceanography, Univ. of California, San Diego, CA, 2005.
[11]P. H. Lim and J. M. Oznard, "On the underwater acoustic field of a moving point source. I. Range independent environment," J. Acoust. Soc. Am. **95**, 131 (1994).
[12]P. A. Baxley, "Matched-field replica model optimization and bottom property inversion in shallow water," Master's thesis, University of California, San Diego, CA, 1997.
[13]M. B. Porter, "The KRAKEN normal mode program," SACLANT Undersea Research Center, La Spezia, Italy, 1991.
[14]T. C. Yang, "A method of range and depth estimation by modal decomposition," J. Acoust. Soc. Am. **82**, l736–1745 (1987).
[15]P. Hursky, W. S. Hodgkiss, and W. A. Kuperman, "Matched field processing with data derived modes," J. Acoust. Soc. Am. **109**, l355–1366 (2001).
[16]P. Roux, D. Cassereau, and A. Roux, "A high-resolution algorithm for wave number estimation using holographic array processing," J. Acoust. Soc. Am. **115**, 1059 (2004).

On the width of a ray

Irina I. Rypina[a] and Michael G. Brown
RSMAS/AMP, University of Miami, 4600 Rickenbacker Causeway, Miami, Florida 33149

(Received 13 February 2007; revised 25 June 2007; accepted 25 June 2007)

Consistent with earlier work by Kravtsov and Orlov, a simple general expression for the width of a Fresnel zone δr_F in a smooth inhomogeneous environment is derived; this is the diffractive contribution to the width of a ray. In a stratified environment at long range, the general Fresnel zone width expression is shown to reduce approximately to one that is proportional to $\sqrt{|\alpha| r(R-r)/\sigma}$ where α is the ray stability parameter, σ is the acoustic frequency, r is the range from the source to the field point of interest, and R is the source to receiver range. In a stratified environment on which a weak small-scale perturbation is superimposed, deterministic rays in the background environment that connect fixed end points break up into bundles of micromultipaths at moderate to long range and a second, scattering-induced, contribution δr_s to the width of a ray must be considered. It is shown that δr_s is proportional to $|\alpha| r(R-r)$ and argued that in a micromultipathing environment the total effective width of a background ray is $\delta r_{\text{tot}} = \sqrt{\delta r_F^2 + \delta r_s^2}$. Theoretical predictions are shown to agree well with travel-time sensitivity kernel calculations. © *2007 Acoustical Society of America.*
[DOI: 10.1121/1.2764465]

PACS number(s): 43.30.Cq, 43.30.Ft, 43.20.Dk, 43.20.El [RAS] Pages: 1440–1448

I. INTRODUCTION

The work reported here was motivated by recent theoretical work[1–3] underlying the computation of full-wave-based travel-time sensitivity kernels (TSKs) for use in inverse problems. These full-wave TSKs are natural finite-frequency generalizations of ray paths. The latter are poorly suited for use as kernels in inverse problems because they have infinitesimal width. The most commonly used quantitative measure of the width of a ray is the width of the first Fresnel zone. This suggests the following question: how do TSKs compare to Fresnel zones in realistic ocean environments? The situation is complicated by the fact that in a smooth environment on which a highly structured perturbation is superimposed, what appears to be an isolated ray arrival may actually be comprised of a large number of unresolved scattered rays or micromultipaths. To account for this phenomenon, a second scattering-induced or micromultipathing contribution to the effective width of a (background) ray must be considered. In this paper, both diffractive and scattering-induced contributions to the effective width of a ray are considered and quantitative estimates of the effective width of a ray are compared to numerically computed TSKs. Throughout this paper attention is restricted to propagation in a vertical (range-depth) plane.

In the following section some relevant background material is presented. This material is used in Sec. III to derive a general expression for the width of a Fresnel zone in a smooth inhomogeneous environment. The special case of a stratified environment at long range is then considered. Theoretical predictions are compared to numerically evaluated travel-time sensitivity kernels in a stratified environment at long range. Also in this section, it is argued that, apart from an $O(1)$ constant, monochromatic wave field (or cw for continuous wave) Fresnel zone width estimates are applicable to a large class of transient wave fields. Section IV is devoted to estimating the width of a bundle of micromultipaths in a stratified environment on which a weak perturbation is superimposed. Theoretical predictions are compared to numerically evaluated TSKs in an environment with micromultipathing. In the final section a summary of the work presented is given. Also in this section we briefly discuss extensions of our two-dimensional (2D) analysis to the three-dimensional (3D) problem and full-wave-based numerical alternatives to TSKs.

II. BACKGROUND

The propagation of fixed-frequency acoustic waves is governed by the Helmholtz equation

$$[\nabla^2 + k^2(\mathbf{r})]u = 0, \tag{1}$$

where $k^2(\mathbf{r}) = \sigma^2/c(\mathbf{r})^2$. Here u is the acoustic pressure, σ is the acoustic wave frequency and $c(\mathbf{r})$ is the sound speed. For simplicity we restrict our attention to 2D problems $\mathbf{r} = (z, r)$ where z is depth and r is range. The solution to Eq. (1) in the short-wave limit can be represented as a sum of locally plane waves or rays

$$u(\mathbf{r};\sigma) = \sum_j A_j(\mathbf{r}) \exp(i\sigma T_j(\mathbf{r})). \tag{2}$$

Substitution of this expression into the Helmholtz Eq. (1) yields, after collecting terms of like powers in σ, the eikonal equation

$$(\nabla T)^2 = c^{-2} \tag{3}$$

and the transport equation

[a]Author to whom correspondence should be addressed. Electronic mail: irypina@rsmas.miami.edu

$$\nabla \cdot (A^2 \nabla T) = 0. \tag{4}$$

In Eqs. (3) and (4) we have omitted the subscript j on A and T. Here T represents the travel time, whose gradient is the ray slowness vector

$$\nabla T = \mathbf{p} = (p_z, p_r). \tag{5}$$

The solution to the eikonal equation can be constructed by solving a system of ray equations that have Hamiltonian form. For directed wave propagation, r can be treated as an independent or time-like variable, and a system of one-way Helmholtz ray equations results

$$\dot{z} = \partial H/\partial p_z, \quad \dot{p}_z = -\partial H/\partial z \quad \text{and} \quad \dot{T} = p_z \dot{z} - H. \tag{6}$$

Here the Hamiltonian $H(p_z, z, r) = -\sqrt{c^{-2}(z,r) - p_z^2} = -p_r$.

For the range-independent problem the system of one-way ray equations (6) is integrable; $z(r)$ and $p_z(r)$ are periodic functions, $H = -p_r$ is constant following the ray, and the motion is most conveniently described in terms of action-angle variables (I, θ). Like H, the action I is constant following a ray and the conjugate coordinate θ increases by 2π after each period of motion. The canonical transformation that relates implicitly the old momentum-position variables (p_z, z) to the new action-angle variables (I, θ) with $H(p_z, z) = H(I)$ requires the introduction of a generating function $G(z, I) = \int^z p_z(H(I), z')dz'$ and is given by $p_z = \partial G/\partial z$, $\theta = \partial G/\partial I$. Details of this canonical transformation are well known[4–6] and will not be given here. Below we note a few defining relationships for quantities that appear in expressions in the two sections that follow. The action variable is defined by

$$I(H) = \frac{1}{2\pi} \oint p_z(H) dz = \frac{1}{\pi} \int_{\check{z}(H)}^{\hat{z}(H)} \sqrt{c^{-2}(z) - H^2}\, dz, \tag{7}$$

where $\check{z}(H)$ and $\hat{z}(H)$ are the lower and upper turning depths, respectively, of a ray. The range of one cycle of the ray motion is

$$R_\ell(H) = 2 \int_{\check{z}(H)}^{\hat{z}(H)} \frac{dz}{\frac{dz}{dr}(H)} = -2H \int_{\check{z}(H)}^{\hat{z}(H)} \frac{dz}{\sqrt{c^{-2}(z) - H^2}} \tag{8}$$

and the spatial frequency of ray motion is

$$\omega(I) = \frac{dH}{dI}(I) = \frac{2\pi}{R_\ell(H(I))}. \tag{9}$$

Another important quantity is the ray stability parameter, which is defined as

$$\alpha(I) = \frac{I}{\omega} \frac{d\omega}{dI}. \tag{10}$$

A simple interpretation of α is a measure of shear in the phase space (θ, I); the ray stability parameter is a measure of the rate at which two initially nearby points in phase space, (θ_0, I_0) and $(\theta_0, I_0 + \mathrm{d}I)$, drift apart in θ as r increases under the influence of the background Hamiltonian $H(I)$. Many observable wave field features are controlled by α, both in range-independent and range-dependent environments.[5–7] It follows from Eqs. (9) and (10) that[7]

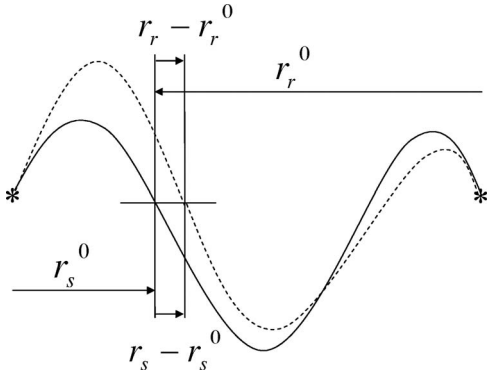

FIG. 1. Schematic diagram showing an eigenray (solid line) and a perturbed piecewise continuous ray path (dashed line) connecting a source and receiver.

$$\alpha(I) = 2\pi \frac{I}{R_\ell^2} \frac{dR_\ell}{dp_r}. \tag{11}$$

III. FRESNEL ZONES IN INHOMOGENEOUS MEDIA

In the scope of the Huygens-Fresnel-Kirchhoff approach, the Fresnel zone is defined as the volume surrounding an eigenray within which contributions from virtual secondary sources add in phase with the contribution from the eigenray. A general expression for the width of the Fresnel zone in a smooth inhomogeneous environment was derived by Kravtsov and Orlov[8,9]—see also Ref. 10. In this section an alternative derivation is presented. The arguments used in the derivation are analogous to those used to derive the width of the Fresnel zone in a homogeneous medium.

We focus in this section on the sound field generated by a compact source and measured at a specific receiver location in a smooth inhomogeneous ocean. Consider an eigenray of this problem as shown in Fig. 1. The travel time along the ray path is $T(r)$. Consider a perturbation in r to some point along the ray path and the associated continuous and piecewise smooth perturbed ray connecting the source and the receiver, as shown in Fig. 1. The travel time along this piecewise smooth path is the sum of travel times along its smooth pieces. For small deviations from the original eigenray, we can make use of Taylor series expansions to compute travel times along each smooth piece

$$T_p(r_s) \approx T(r_s^0) + \frac{\partial T}{\partial r_s}(r_s^0)(r_s - r_s^0) + \frac{1}{2}\frac{\partial^2 T}{\partial^2 r_s}(r_r^0)(r_s - r_s^0)^2,$$
$$T_p(r_r) \approx T(r_r^0) + \frac{\partial T}{\partial r_r}(r_r^0)(r_r - r_r^0) + \frac{1}{2}\frac{\partial^2 T}{\partial^2 r_r}(r_r^0)(r_r - r_r^0)^2. \tag{12}$$

Here r_s and r_r are the horizontal distances from the source and the receiver to the field point of interest, T is the travel time along the original eigenray, $T_p(r_s)$ and $T_p(r_r)$ are travel times along the two pieces of the perturbed ray path, and the superscript "0" denotes the point on the unperturbed ray that is perturbed.

It is seen from Fig. 1 that $(r_s - r_s^0) = -(r_r - r_r^0) \equiv \delta r$, while it follows from Eq. (5) that for any smooth $c(z, r)$,

$\partial T/\partial r_s(r_s^0)=\partial T/\partial r_r(r_r^0)=p_r$ on the unperturbed ray at the point being perturbed. Thus, the first-order terms in Eq. (12) cancel when these contributions are added, so the travel time along the perturbed ray path differs from the travel time along the unperturbed eigenray path by a second order correction in δr

$$T_p = T + \frac{(\delta r)^2}{2}\left[\frac{\partial p_r}{\partial r_s}(r_s^0) + \frac{\partial p_r}{\partial r_r}(r_r^0)\right]. \tag{13}$$

Within a Fresnel zone all perturbed paths interfere constructively with the unperturbed eigenray, so

$$\sigma|T_p - T| \leqslant \pi/2, \tag{14}$$

which, when combined with Eq. (13), yields a simple general expression for the width (in range) of a Fresnel zone in a smooth inhomogeneous environment

$$\delta r_F = \sqrt{\frac{\pi}{\sigma}\left|\left(\frac{\partial r_s}{\partial p_r}(r_s^0)\right)^{-1} + \left(\frac{\partial r_r}{\partial p_r}(r_r^0)\right)^{-1}\right|^{-1}}. \tag{15}$$

The partial derivatives in Eqs. (12), (13), and (15) are evaluated with ray depth z held constant. We emphasize that the derived expression (15) is quite general as our derivation requires only smoothness of the sound speed profile $c(z,r)$. Not surprisingly, the frequency dependence of δr_F in Eq. (15) is identical to that of a Fresnel zone width in a homogeneous environment. Also, Eq. (15) is consistent with earlier work by Kravtsov and Orlov[8] with two minor caveats. First, Kravtsov and Orlov assumed that the right-hand side of Eq. (14) was replaced by π, so their expression for δr_F is $\sqrt{2}$ greater than Eq. (15). Second, Kravtsov and Orlov did not express the second derivatives of T as the inverse of range derivatives. Expressing δr_F in terms of range derivatives is convenient for numerical purposes because the range derivatives can easily be evaluated after an eigenray is found. Also, the approximate expression for δr_F that will now be derived follows from approximating the range derivatives.

We consider now a special case of the general expression (15), corresponding to a stratified environment, $c=c(z)$, at long range. Assume that $r=0$ at the source, r is range from the source to an arbitrary field point, and R is the source to receiver range; then $r_s=r$ and $r_r=R-r$. Also, r_s and r_r can be written as integral multiples of R_ℓ plus correction terms. Provided r_s/R_ℓ and r_r/R_ℓ are not too small the correction terms can be neglected and we can make use of the approximate relations

$$r_s = n_s R_\ell, \quad r_r = n_r R_\ell. \tag{16}$$

Using the long-range approximation (16), the general expression, Eq. (15), reduces to

$$\delta r_F = \sqrt{\frac{\pi}{\sigma}\left|\frac{\partial R_\ell}{\partial p_r}\right|\left(\frac{1}{n_s}+\frac{1}{n_r}\right)^{-1}}. \tag{17}$$

With use of Eq. (11) this expression can be rewritten in the form

$$\delta r_F = \sqrt{\frac{|\alpha|R_\ell^2}{2\sigma I}\frac{n_s n_r}{(n_s+n_r)}}, \tag{18}$$

where $\alpha(I)$ is the ray stability parameter. Using the long range approximation (16) one more time, Eq. (18) can be further simplified to give

$$\delta r_F = \sqrt{\frac{|\alpha|R_\ell}{2\sigma I}}\sqrt{\frac{r(R-r)}{R}}. \tag{19}$$

Fractional errors associated with Eq. (19), i.e., the ratio of the magnitude of neglected to retained terms when reducing Eq. (15) to Eq. (19), are $O(R_\ell/r, R_\ell/(R-r))$. Note, however, that Eq. (19) has been constrained to correctly predict $\delta r_F=0$ at the source $r=0$ and the receiver $r=R$, so errors vanish at these points. Thus, fractional errors associated with Eq. (19) are $O(R_\ell/R)$ but are nonuniform in range, generally being smaller in the middle of the domain than near the source and receiver, but vanishing at the source and receiver. Note that Eq. (15) contains oscillations associated with the structure of the range derivatives (which may vanish) that are not present in Eq. (19).

According to the approximate expression Eq. (19) the width of the Fresnel zone in a stratified environment at long range is controlled by the ray stability parameter α. This result is not surprising because both travel-time spreads,[6] and spatial and temporal broadening of beams are controlled by α. Also, the derived approximate expression (19) exhibits the same range dependence as the expression for the Fresnel zone width in a homogeneous environment.

It has been argued[11,12] that the first Fresnel zone is inappropriate for use with transient signals because it does not account for the finite duration of a signal. Assume that the transmitted signal has center frequency f_0 and bandwidth Δf. For this class of problems it is natural to replace criterion (14) by $|T_p-T_p| \leqslant \Delta T/2$, where $\Delta T=(\Delta f)^{-1}$ is the temporal duration of a resolved multipath arrival. In this case, Eqs. (15) and (19) are still applicable after multiplying the right-hand sides by the constant $\sqrt{2Q}$, where $Q=f_0/\Delta f$ is the so-called quality factor of the signal. In many situations of interest, including the simulations shown in this paper, Q is $O(1)$ and the factor $\sqrt{2Q}$ is close to unity. (Recall also, as noted previously, that some authors prefer to define Fresnel zone widths using π- rather than $\pi/2$- on the right-hand side of Eq. (14).) This argument shows that, although Fresnel zones are normally thought of as properties of cw wave fields, essentially the same width can naturally be ascribed to multipath arrivals in transient wave fields provided Q is $O(1)$. At first sight it seems contradictory that the same effective width estimate should apply when $Q\to\infty$ (the cw limit) and when $Q=O(1)$. This is possible because different definitions of effective ray width—that lead to essentially the same result—arise naturally in the two cases.

In the remainder of this section our theoretical predictions for Fresnel zone widths will be compared to numerically calculated TSKs. The TSK K_i is the kernel of the linear integral relationship that relates changes in the travel time for a particular peak arrival ΔT_i to sound speed variations Δc, $\Delta T_i=\int\int\int_V \Delta c(\mathbf{r}')K_i(\mathbf{r}';\mathbf{r}_s,\mathbf{r}_r,c)dV(\mathbf{r}')$. The algorithm for the

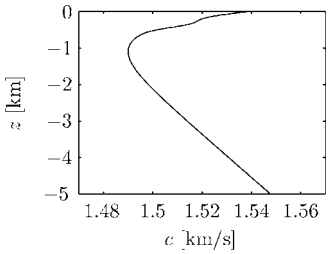

FIG. 2. Perturbed canonical sound speed profile with a small Gaussian perturbation in the upper ocean.

TSK calculation is explained in detail in Ref. 1 and will not be further discussed here except to note that the TSKs shown in Figs. 4, 5, and 7 have units time/(volume × sound speed) or $s^2\,m^{-4}$ appropriate for the description of propagation in a 3D space; the reported TSK values assume cylindrical spreading of wave fields, consistent with our neglect of cross-range (out-of-plane (z,r)) propagation effects.

The sound speed profile that was used for numerical calculations is shown in Fig. 2. This is a perturbed canonical profile,[13] $c(z)=c_M(z)+dc\,\exp\left[-\frac{1}{2}\left(\frac{z_c-z}{z_w}\right)^2\right]$, $c_M=c_a(1+\varepsilon(e^{\eta}-\eta-1))$ with $\eta=2(z-z_a)/B$. Here z increases upward, $z_a=-1.1$ km is a sound channel axis depth, $c_a=1.49$ km/s is the sound speed on the channel axis, $B=1.0$ km is a thermocline depth scale, $\varepsilon=0.0057$ is a dimensionless constant, $z_w=0.1$ km is the width of a Gaussian perturbation, $z_c=-0.35$ km is the depth of the midpoint of the Gaussian perturbation, and $dc=0.008$ km/s is the maximum amplitude of the Gaussian perturbation.

All of the simulations shown in this paper, both ray and full wave, are based on the Thomson-Chapman[14] parabolic wave equation, for which $H=-\sqrt{c_0^{-2}-p_z^2}+1/c_0-1/c(z,r)=-p_r$. With this choice of H, Eqs. (5) and (6), the first equalities in Eqs. (8) and (7), and Eqs. (9) through (26) are unchanged. (Generalizations of Eqs. (1), (3), and (4) consistent with the Thomson-Chapman approximation can be found, for example, in Ref. 15). This choice was made because it is important that the ray and full-wave simulations are consistent with each other, and because it is most natural to perform full-wave simulations in a range-dependent environment by making use of a parabolic wave equation. The practical effect of making use of the Thomson-Chapman form of H is that $R_\ell(I)$ and $\alpha(I)$ computed using this approximate H are slightly different from $R_\ell(I)$ and $\alpha(I)$ computed using the one-way Helmholtz form of H.

The upper panel of Fig. 3 shows transient finite-frequency wave fields at a range of $R=990$ km produced by an omnidirectional axial source with center frequency 100 Hz and computational bandwidth 50 Hz in the stratified

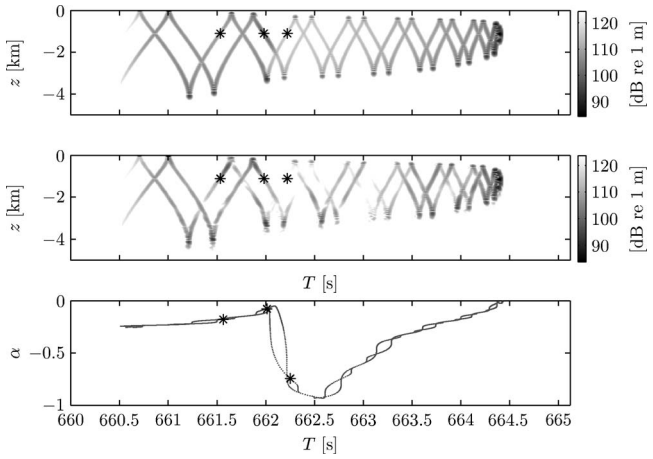

FIG. 3. (Upper panel) In the environment shown in Fig. 2, wave field intensity for a broadband ($f_0=100$ Hz, computational $\Delta f=50$ Hz) axial source is plotted in the depth-time plane at a range of 990 km. The intensity scale is logarithmic with a dynamic range of 40 dB. (middle panel) Same as upper panel, but with an internal-wave-induced sound speed perturbation superimposed on the background sound speed profile. (lower panel) The associated α structure computed in the background environment as a function of travel time. Three peak arrivals that are used for TSK calculations are indicated by asterisks, with peaks numbered 1, 2 and 3 from left to right.

environment described above. The wave field shown in the middle panel of Fig. 3 was computed using the same source-receiver geometry and background environment that were used to produce the upper panel. In the simulation shown in the middle panel, however, an internal-wave-induced perturbation to the background sound speed profile was superimposed. The algorithm described in Ref. 16 was used to construct the internal-wave-induced sound speed perturbation field using an internal wave strength parameter equal to the nominal Garrett-Munk value E_{GM}. The associated α structure as a function of travel time is shown on the lower panel of Fig. 3. We will focus on three peak arrivals, indicated by asterisks in Fig. 3, that have different α values. TSKs corresponding to the arrivals identified in the middle panel of Fig. 3 will be discussed in the following section. Regions of higher intensities in the two upper panels of Fig. 3 are seen to correspond to regions of smaller $|\alpha|$ values. This is because, as noted previously, many wave field properties, including geometric amplitudes, are controlled by the ray stability parameter α.[5–7]

For the first peak arrival shown in the upper panel of Fig. 3, with the intermediate α value, the TSK in the domain $r\in[0,R/2]$ is shown in Fig. 4. The boundary of the Fresnel zone for the corresponding ray, calculated using Eq. (19), is also shown in Fig. 4 with solid lines. The approximate Fresnel zone width estimate, Eq. (19), is seen to compare

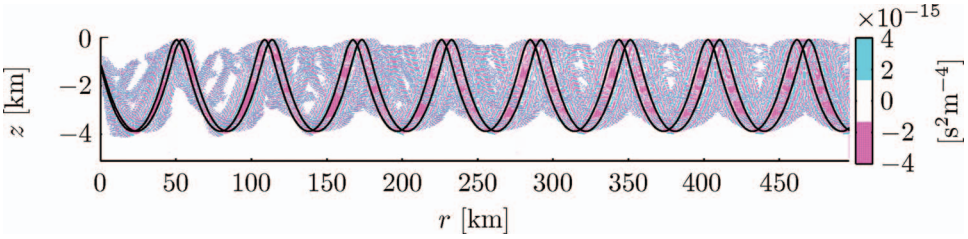

FIG. 4. TSK in the first half of the source-receiver domain, $r\in[0$ km, 495 km], for the first peak arrival in the upper panel of Fig. 3. The solid lines show displacements of the background ray by $\pm\delta r_F$, computed using Eq. (19). These lines show the left and right bounds of the Fresnel zone associated with the background ray.

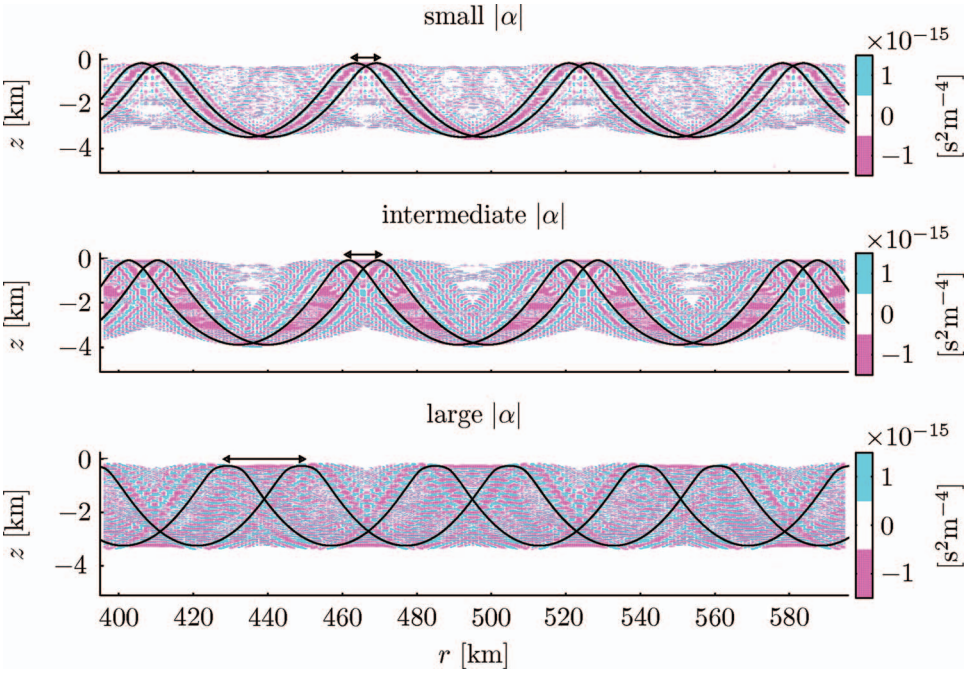

FIG. 5. TSK for each of the three peak arrivals (indicated by asterisks) in the upper panel of Fig. 3 in the 200 km domain centered at the midpoint between the source and the receiver, $r \in [395\ \text{km}, 595\ \text{km}]$ (Upper subplot - peak 2 (small $|\alpha|$); middle subplot - peak 1 (intermediate $|\alpha|$); lower subplot - peak 3 (large $|\alpha|$)). The solid lines show displacements of the corresponding background ray by $\pm\delta r_F$, computed using Eq. (19). These lines show the left and right bounds of the Fresnel zone associated with the corresponding background ray. The horizontal extent of the theoretically estimated Fresnel zone is also identified above an upper turn of the background ray in each subplot.

favorably with the TSK calculation; they exhibit similar range dependence being zero at the source, $r=0$, and having the largest value at $r=R/2$. The agreement is slightly better near $r=R/2$ because the approximate Fresnel zone width expression, Eq. (19), is a better approximation at long ranges from the source and receiver than near the source and receiver. (We have chosen to show only the left half of the propagation domain in Fig. 4 because in a range-independent background environment both TSKs and our expressions for δr_F (Eqs. (15) and (19)) in the left ($r \in [0, R/2]$) and right ($r \in [R/2, R]$) halves of the propagation domain have similar qualitative features. Our approximate result (Eqs. (19)) has exact left-right symmetry and Eq. (15) possesses this property if the corresponding ray path has this property.) After presenting more examples of comparisons between TSKs and predicted Fresnel zones, the color scheme that we have used to plot TSKs will be further discussed together with the criteria used to assess good vs. poor agreement between TSKs and predicted Fresnel zones.

Figure 5 illustrates the α dependence of the Fresnel zone width. The domain shown in Fig. 5 covers the 200 km range interval centered at the midpoint between the source and the receiver. Figure 5 shows the TSK for each of the three peak arrivals shown in the upper panel of Fig. 3. The boundary of the Fresnel zone for the corresponding ray, evaluated using Eq. (19), is also shown in Fig. 5 with solid lines. Overall, Fig. 5 shows favorable agreement between Eq. (19) and the TSK calculation, and illustrates the dependence of effective ray width on $|\alpha|$ predicted by Eq. (19).

The color scheme used to plot TSKs in Figs. 4, 5, and 7 divides the dynamical range of the TSK values $[-K_i^{\max}, K_i^{\max}]$ into three equal regions with each region shown using a different color. TSK values $K_i \in [-K_i^{\max}, -K_i^{\max}/3]$ are shown in pink; TSK values $K_i \in [-K_i^{\max}/3, K_i^{\max}/3]$ are shown in white; TSK values $K_i \in [K_i^{\max}/3, K_i^{\max}]$ are shown in blue. When the Fresnel zone width is small compared to the background ray cycle distance, acoustic energy within the Fresnel zone is all propagating in essentially the same direction. (This statement is violated close to the turning depths of the background ray. We will return to this point below.) Because the Fresnel zone is defined such that all acoustic paths contained in this region interfere constructively with the background ray, one expects that within this region using our adopted color scheme the TSK should be predominantly pink or blue. Furthermore, with the color scheme that we have chosen, one expects to see a white region near the boundaries of the Fresnel zone. The location of this white boundary region should depend only weakly on the choice of the value of K_i at which the transition from pink/white and white/blue takes place. The properties just described are clearly visible in Fig. 4 and the upper and middle panels of Fig. 5. Near the turning depths of a background ray both up- and down-going energy is present inside the Fresnel zone. Loosely speaking the Fresnel zone intersects itself in those regions. Up- and down-going energy in these regions interferes destructively at some locations producing interference fringes. Interference fringes are clearly visible near the background ray upper turning depths in the middle panel of Fig. 5. As the Fresnel zone width increases, the "intersecting" regions of the Fresnel zone near the background ray turning depths increase in size until the entire Fresnel zone contains interfering up- and down-going energy. This is what is happening in the lower panel of Fig. 5. Note (especially in the middle and lower panels of Fig. 5) that in a narrow band of depths near the turning depths of the background ray, all energy is propagating horizontally, all interference is constructive, and the TSK has a single color within a domain whose horizontal extent is in good agreement with predicted Fresnel zone widths. Finally we note that the TSKs shown in Figs. 4 and 5 do not reveal a zero crossing close to the location of the background ray; this is the "banana" portion of the "banana-doughnut" structure.[3] It

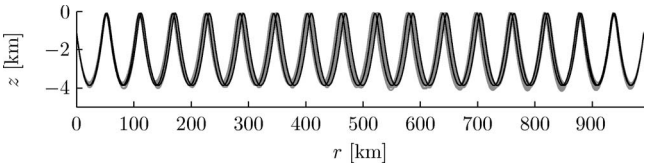

FIG. 6. An incomplete set of micromultipaths corresponding to peak number 1 in the environment used to produce the middle panel of Fig. 3. Black lines show displacements of the background ray by $\pm\delta r_s$, computed using Eq. (24). These lines show the predicted approximate bounds on the scattering-induced broadening of the background ray.

can be shown analytically that this structure is present in an unbounded homogeneous environment.[1] This structure is also a robust feature of TSKs at short ranges when the ray geometry is simple. Possible reasons that we do not see the banana structure in our computed TSKs are: (1) this structure is present only when the ray geometry is simple; (2) such structures are thin and difficult to resolve numerically at long range when the ray geometry is complicated.

IV. MICROMULTIPATHS

In deep ocean environments (where R_ℓ is typically about 50 km) at ranges of a few complete ray cycle distances or more, scattering by small-scale inhomogeneities, mostly internal waves, causes deterministic rays connecting a fixed source and receiver in the background environment to break up into a collection of generally unresolved micromultipaths, all with the same source and receiver inclination and the same turning history as the ray in the background environment, and all connecting the same fixed end points. Micromultipaths play an important role in path integral theories[17] of wave field fluctuations. Micromultipaths are also consistent with the notion of ray chaos[18] and can be found numerically.[19] An example of an incomplete set of micromultipaths is shown in Fig. 6 with gray lines. This set of micromultipaths corresponds to peak number 1 in the middle panel of Fig. 3 and was computed using the same environment that was used to produce that figure. (In practice, only the least chaotic eigenrays can be reliably found, so we refer to a set of numerically obtained micromultipaths as an incomplete set.)

In the following we derive an approximate expression for the width δr_s of a bundle of micromultipaths, which we refer to as the scattering-induced contribution to the effective width of a ray. For simplicity we assume that the sound speed structure has the form $c(z)+\delta c(z,r)$ and employ a simple scattering model to account for δc. Under typical deep ocean conditions at ranges of hundreds of km or more δr_s is greater than the diffractive contribution δr_F. It is important to keep in mind, however, that in sufficiently unstructured environments or at very short range in any environment there are no micromultipaths and δr_s makes no contribution to the effective width of a ray.

The scattering model employed makes use of the so-called apex approximation.[17] Within this approximation the ray action I and Hamiltonian H are piecewise constant, taking discrete jumps at each ray upper turn; transition regions are assumed to be negligibly thin. Between apex scattering events r advances by $R_\ell(I)$. This simple approximation is quantitatively accurate in typical midlatitude deep ocean environments for purely refracted rays with axial angles greater than about 10°, while maintaining qualitative correctness for rays with axial angles as small as a few degrees.

Consider a ray that undergoes n apex scattering events. Consider first a ray that is constrained only at the source, and, for simplicity, assume that the final partial ray loop is a complete ray loop. After n apex scattering events the deviation in range of the scattered ray relative to the unscattered ray with initial action I_0 is

$$\Delta r_n = \frac{dR_\ell(I_0)}{dI}\sum_{i=1}^{n}(I_i - I_0). \tag{20}$$

Here I_i is the ray action after the ith apex scattering event

$$I_i - I_0 = \sum_{j=1}^{i}\delta I_j, \tag{21}$$

where δI_j is the jump in I at the jth scattering event. Under typical conditions the separation in range between adjacent apex scattering events R_ℓ is large compared to the horizontal correlation length of δc, so, to an excellent approximation, δI_j is a delta-correlated zero-mean random variable

$$\langle \delta I_j\rangle = 0, \quad \langle \delta I_j \delta I_k\rangle = \langle(\delta I)^2\rangle\delta_{jk}. \tag{22}$$

It follows from Eqs. (21) and (22) that $\langle(\Delta I_n)^2\rangle=\langle(I_n-I_0)^2\rangle=\langle(\delta I)^2\rangle n\approx\langle(\delta I)^2\rangle r/R_\ell$. Also, it is straightforward to show with use of Eqs. (20)–(22) that $\langle(\Delta r_n)^2\rangle$ grows like $n^3/3$ for large n.

Now consider the constraint that the scattered ray connects the same fixed end points (the source and receiver) as the unperturbed ray. Assume that the scattered ray undergoes N apex scattering events between source and receiver, $n\leqslant N$ with N fixed and n variable, and assume that all ray cycles are complete. (An error estimate associated with these approximations is given below). With these assumptions, the problem is defined by Eqs. (20)–(22) and the additional constraint $\Delta r_N=0$. This constraint is handled by introducing the variable $\Delta r_n'=\Delta r_n-(n/N)\Delta r_N$, which satisfies the end point constraint. (This is the standard technique used to construct what is known in stochastic calculus as a Brownian bridge. The problem considered here is a generalization of the standard Brownian bridge problem; in that problem the variance of the unconstrained random variable grows like n rather than n^3 as in our problem.) It follows from Eqs. (20)–(22) that

$$\langle(\Delta r_n')^2\rangle = \left(\frac{dR_\ell}{dl}(I_0)\right)^2\langle(\delta I)^2\rangle \times\left[\frac{n^2}{3N}(N-n)^2+\frac{n}{6N}(N-n)\right]. \tag{23}$$

For large N the second term in square brackets can be neglected. With this approximation and use of the approximate relationships, $n=r/R_\ell$, $N=R/R_\ell$ and Eq. (11), this equation becomes (after replacing $\langle(\Delta r_n')^2\rangle^{1/2}$ by δr_s)

$$\delta r_s = \frac{|\alpha|}{\sqrt{3}} \frac{\langle (\delta I)^2 \rangle^{1/2}}{I} \frac{r(R-r)}{\sqrt{R_\ell R}}. \tag{24}$$

Several important points concerning our derivation of Eq. (24) are worth noting. First, consistent with the approximations made, imposition of the constraint $\Delta r_N = 0$ also leads (to first order in $I_i - I_0$) to the condition $\Delta T_N = 0$; see, e.g., Ref. 6. Thus, our derivation of Eq. (24) is consistent with the implicit assumption that all of the micromultipaths corresponding to a deterministic multipath are not temporally resolved and thus appear as a single ray arrival. Second, our use of the apex approximation to derive Eq. (24) is not essential. What is critical is the assumption, Eq. (22), that the jumps in I at scattering events have zero mean and are delta correlated. This assumption leads to the result that for an unconstrained ray the total mean square deviation in action $\langle (\Delta I)^2 \rangle(r)$ grows like $r\langle (\delta I)^2 \rangle / L$ where L is the horizontal separation between scattering events. With the apex approximation $L = R_\ell$. Note that Eq. (24) depends only on the ratio $\langle (\delta I)^2 \rangle / R_\ell$. Generalizing Eq. (24) to a slightly more general scattering model requires only that this ratio be replaced by the appropriate (constant) value of $d\langle (\Delta I)^2 \rangle / dr$. We have chosen to make use of the apex approximation because of its conceptual appeal and because it is a good lowest-order description of sound scattering by internal waves in deep ocean environments. We have numerically estimated that $\langle (\delta I)^2 \rangle \approx 10^{-5}$ s^2 for typical steep (but not surface-reflecting) rays in a deep ocean environment with an internal-wave-induced sound speed perturbation superimposed. Virovlyansky[20,21] has obtained a similar estimate and has derived an approximate analytical expression for $\langle (\delta I)^2 \rangle$. In general this quantity depends on both the background and perturbation sound speed fields and is a function of I (which is defined in the background). Finally, we note that the same comments made earlier about errors associated with Eq. (19) also apply to Eq. (24): fractional errors are $O(R_\ell / R)$ but vanish at $r=0$ and $r=R$.

The derived expression (24) is a quantitative estimate of the width of a bundle of micromultipaths or, equivalently, the scattering-induced contribution to the width of a ray in a stratified environment with a weak perturbation superimposed. Note that both diffractive Eq. (19) and scattering-induced Eq. (24) contributions to the effective width of a ray are controlled by the ray stability parameter α. Note, however, that unlike Eq. (19), expression (24) has no frequency dependence because a purely geometric argument was used in the derivation of this expression.

To investigate the validity of the micromultipathing contribution, Eq. (24), to the effective width of a ray, we turn our attention back to Fig. 6. The derived expression for the width of a bundle of micromultipaths Eq. (24) is shown in Fig. 6 with black lines. To evaluate the right-hand side of Eq. (24), values of I, $R_\ell(I)$ and $\alpha(I)$ corresponding to the background ray were used and $\langle (\delta I)^2 \rangle$ was estimated from the micromultipaths shown. The theoretical estimate for a width of a bundle of micromultipaths is seen to be in good agreement with the distribution of micromultipaths shown. A caveat is that Eq. (24) does not account for the slight vertical extension of turning depths of the micromultipaths relative to the background ray turning depth. This effect is larger in the deep ocean, where the background sound speed gradient is small, than in the upper ocean.

In environments that support micromultipathing, both diffractive and scattering effects contribute to the total effective width of a ray. Because the diffractive contribution Eq. (19) and scattering-induced contribution Eq. (24) are independent of each other, it is natural to assume that the total width of a ray can be estimated as

$$\delta r_{\text{tot}} = \sqrt{\delta r_F^2 + \delta r_s^2}. \tag{25}$$

We offer no rigorous justification of Eq. (25) but note that it is commonly assumed (see, e.g., Ref. 17) that scattering-induced and deterministic contributions to time spreads combine in quadrature. It follows from Eqs. (19), (24), and (25) that the dimensionless parameter

$$\gamma = \frac{R}{R_\ell} \sqrt{\frac{|\alpha|\sigma}{6I}} \langle (\delta I)^2 \rangle^{1/2} \tag{26}$$

controls whether the diffractive or scattering contribution to δr_{tot} is largest. When $\gamma < 1$ the diffractive contribution dominates at all $r \in [0, R]$. When $\gamma > 1$ the diffractive contribution dominates near $r=0$ and $r=R$, while the scattering contribution dominates near $r=R/2$.

In Fig. 7 theoretical predictions for the total effective width of a ray (Eqs. (19), (24), and (25)) are compared to numerically calculated TSKs in the environment (with micromultipathing) that was used to produce the middle panel of Fig. 3. The TSKs shown in Fig. 7 were computed for the three arrivals identified in the middle panel of Fig. 3. Similar to Fig. 5, each peak arrival TSK shown in Fig. 7 was calculated in a 200 km domain centered at the midpoint between the source and the receiver. Because of the range dependence of the environment, TSKs in Fig. 7, unlike Fig. 5, do not possess left-right symmetry. The color scheme used to show TSKs in Fig. 7 is identical to that used in Fig. 5. The corresponding theoretical bounds on the total effective ray width, evaluated using Eqs. (19), (24), and (25), are shown with solid lines. The corresponding values of the dimensionless parameter γ for the three rays are $\gamma = 0.60$ (small $|\alpha|$), $\gamma = 0.92$ (intermediate $|\alpha|$) and $\gamma = 1.64$ (large $|\alpha|$), respectively. Thus, in the upper subplot of Fig. 7, which is centered at $r = R/2$, the diffractive contribution to the effective width of a ray dominates. In the middle subplot both diffractive and scattering-induced contributions are important, while in the lower subplot the scattering-induced contribution dominates. As predicted by the theoretical estimate, Eq. (25), the total effective width of a ray increases with increasing $|\alpha|$. The comments made earlier about interference effects inside the first Fresnel zone (recall Fig. 5) apply to Fig. 7 as well. When the effective width of a ray is small compared to the ray cycle distance, the corresponding TSK is predominantly of one sign (or color in Fig. 7) except close to the ray turning depths. Near the ray turning depths interfering up- and down-going rays inside the bounds of the fattened effective ray path should lead to interference effects in the TSK. This behavior is seen in the middle panel of Fig. 7. Not surpris-

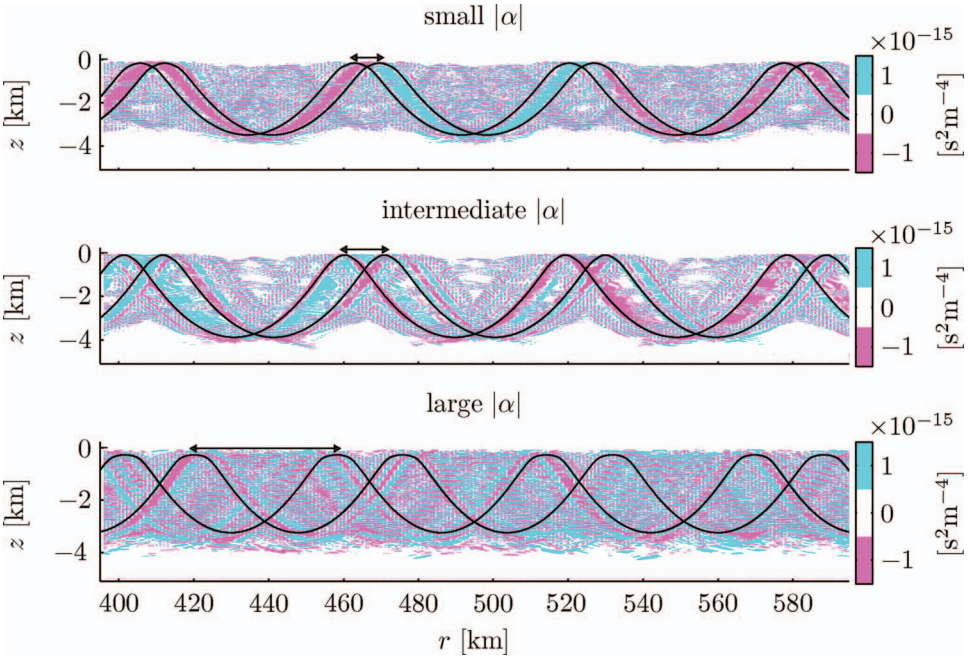

FIG. 7. Same as Fig. 5 for the environment used to produce the middle panel of Fig. 3. Note that unlike Fig. 5, in Fig. 7 both diffractive and scattering-induced contributions to the width of a ray are present. Solid lines show displacements of the background ray by $-\delta r_{\text{tot}}$ and $+\delta r_{\text{tot}}$, computed using Eqs. (19), (24), and (25). These lines show the predicted approximate bounds on the diffractive and scattering-induced broadening of the corresponding background ray. The horizontal extent of the theoretically estimated total effective ray width is also identified above an upper turn of the background ray in each subplot.

ingly, the TSK interference fringes seen in that figure lack the symmetry of the interference fringes seen in the middle panel of Fig. 5. When the effective ray width $2\delta r_{\text{tot}}$ approaches the background ray cycle distance R_ℓ, up- and down-going rays interfere with each other everywhere within the fattened effective ray path, which then covers essentially the entire column between the upper and lower turning depths of the background ray; this behavior is illustrated in the lower panel of Fig. 7. Consistent with Eqs. (19) and (24), effective TSK widths in Fig. 7 are seen to increase with increasing $|\alpha|$.

V. DISCUSSION AND SUMMARY

This paper is concerned with quantifying the effective width of a ray in an inhomogeneous environment. A general expression for the width of a Fresnel zone in a smooth inhomogeneous environment was derived. The result obtained is consistent with the earlier work by Kravtsov and Orlov.[8–10] In spite of the fact that the geometric ray formalism was used, the width of a Fresnel zone is a frequency-dependent quantity. The obtained frequency dependence agrees with that for the well-known homogeneous medium result. It was argued that a simple generalization of the derived expression also applies to broadband signals provided the Q of the transmitted signal is $O(1)$. We have argued that in range-dependent environments in which micromultipathing is present a second scattering-induced contribution δr_s to the effective width of a ray must be considered. An approximate expression for δr_s was derived. Numerical simulations of TSKs performed in environments both without and with a superimposed small-scale range-dependent perturbation were shown to be in good agreement with theoretical predictions of the effective ray width derived in this paper. Although we have confined our full-wave computations in this paper to TSKs, it should be noted that other related computational algorithms have been developed[11,12,22] to which our theoretical estimates of δr_F and δr_{tot} can—and should—be compared. We intend to make such a comparison in the near future.

As is common practice in long-range ocean acoustic applications, we have neglected out-of-plane (z,r) propagation effects. To the extent that this assumption is valid, it implies that in the cross-range plane (fixed z) the homogeneous environment Fresnel zone width estimate is an excellent approximation. More generally, the argument leading to Eqs. (12) can be generalized to a fully 3D environment. This leads to the notion of Fresnel volumes, whose transverse principal axes are found from diagonalization of a quadratic form; see Refs. 8–10 for details. In an almost stratified environment of the type we have considered, the results described in Refs. 23 and 24 provide the basis for treatment of the scattering-induced contribution in the cross-range direction to the effective width of a ray.

It is interesting to note that both the diffractive (Eq. (19)) and scattering-induced (Eq. (24)) contributions to the effective width of a ray supplement the list of the physical quantities, such as travel-time dispersion,[7] ray stability,[25] constrained and unconstrained travel-time spreads,[5,6] the spatial and temporal broadening of beams, and modal group time spreads,[7] that are controlled by the ray stability parameter α.

ACKNOWLEDGMENTS

We thank Oleg Godin and Matt Dzieciuch for their insightful comments on an early draft of this paper, and Ken Palmer, Ilya Udovydchenkov, Bruce Cornuelle, John Spiesberger, Javier Beron-Vera and Huseyin Koçak for the benefit of discussions related to the material presented. This work was supported by the Office of Naval Research, Code 321, and the National Science Foundation, Grant No. CMG0417425.

[1]E. K. Skarsoulis and B. D. Cornuelle, "Travel-time sensitivity kernels in ocean acoustic tomography," J. Acoust. Soc. Am. **116**, 227–238 (2004).
[2]H. Marquering, G. Nolet, and F. A. Dahlen, "Three-dimensional waveform sensitivity kernels," Geophys. J. Int. **132**, 521–534 (1998).
[3]H. Marquering, F. A. Dahlen, and G. Nolet, "Three-dimensional waveform sensitivity kernels for finite-frequency traveltimes: The banana-doughnut paradox," Geophys. J. Int. **137**, 805–815 (1999).
[4]L. D. Landau and E. M. Lifshitz, *Mechanics*, 3rd ed. (Pergamon, New York, 1976).
[5]A. L. Virovlyansky, "Ray travel times at long range in acoustic waveguides," J. Acoust. Soc. Am. **113**, 2523–2532 (2003).
[6]F. J. Beron-Vera and M. G. Brown, "Travel time stability in weakly range-dependent sound channels," J. Acoust. Soc. Am. **115**, 1068–1077 (2004).
[7]M. G. Brown, F. J. Beron-Vera, I. Rypina, and I. A. Udovydchenkov, "Rays, modes, wavefield structure and wavefield stability," J. Acoust. Soc. Am. **117**, 1607–1610 (2005).
[8]Yu. A. Kravtsov and Yu. I. Orlov, "Limits of applicability of the method of geometric optics and related problems," Sov. Phys. Usp. **23**, 750–762 (1980).
[9]Yu. A. Kravtsov and Yu. I. Orlov, "Boundaries of geometrical-optics applicability and related problems," Radio Sci. **16**, 975–978 (1981).
[10]Yu. A. Kravtsov and Yu. I. Orlov, *Geometrical Optics of Inhomogeneous Media* (Springer-Verlag, Berlin, 1990).
[11]J. L. Spiesberger, "Regions where transient signals are influenced between a source and receiver," Waves Random Complex Media **16**, 1–21 (2006).
[12]J. L. Spiesberger, "Regions that influence acoustic propagation in the sea at moderate frequencies, and the consequent departures from the ray-acoustic description," J. Acoust. Soc. Am. **120**, 1842–1850 (2006).
[13]W. H. Munk, "Sound channel in an exponentially stratified ocean with application to SOFAR," J. Acoust. Soc. Am. **55**, 220–226 (1974).
[14]D. J. Thomson and N. R. Chapman, "A wide-angle split step algorithm for the parabolic equation," J. Acoust. Soc. Am. **74**, 1848–1854 (1983).
[15]I. I. Rypina, I. A. Udovydchenkov, and M. G. Brown, "A transformation of the environment eliminates parabolic equation phase errors," J. Acoust. Soc. Am. **120**, 1295–1304 (2006).
[16]J. A. Colosi and M. G. Brown, "Efficient numerical simulation of stochastic internal-wave-induced sound speed perturbation fields," J. Acoust. Soc. Am. **103**, 2232–2235 (1998).
[17]S. Flatté, R. Dashen, W. Munk, K. Watson, and F. Zachariasen, *Sound Transmission Through a Fluctuating Ocean*. Cambridge Monographs on Mechanics and Applied Mathematics (Cambridge University Press, 1979).
[18]M. G. Brown, J. A. Colosi, S. Tomsovic, A. L. Virovlyansky, M. Wolfson, and G. M. Zaslavsky, "Ray dynamics in long-range deep ocean sound propagation," J. Acoust. Soc. Am. **113**, 2533–2547 (2003).
[19]F. J. Beron-Vera, M. G. Brown, J. A. Colosi, S. Tomsovic, A. L. Virovlyansky, M. A. Wolfson, and G. M. Zaslavsky, "Ray dynamics in a long-range acoustic propagation experiment," J. Acoust. Soc. Am. **114**, 1226–1242 (2003).
[20]A. L. Virovlyansky, *Ray Theory of Long-Range Sound Propagation in the Ocean* (Institute of Applied Physics of the Russian Academy of Science at Nizhny Novgorod (in Russian, 164 pages), 2006).
[21]A. L. Virovlyansky, *Ray travel times in range-dependent acoustic waveguides*. http://arxiv.org/abs/nlin/0012015. (Last viewed 25 June 2007). 2002.
[22]J. B. Bowlin, "Generating eigenray tubes from two solutions of the wave equation," J. Acoust. Soc. Am. **89**, 2663–2669 (1991).
[23]O. A. Godin, "Systematic distortions of signal propagation times in random inhomogeneous media," Dokl. Phys. **48**, 389–394 (2003).
[24]O. A. Godin, V. U. Zavorotny, A. G. Voronovich, and V. V. Goncharov, "Refraction of sound in a horizontally-inhomogeneous, time-dependent ocean," J. Oceanic Eng. **31**, 384–401 (2006).
[25]F. J. Beron-Vera and M. G. Brown, "Ray stability in weakly range-dependent sound channels," J. Acoust. Soc. Am. **114**, 123–130 (2003).

Acoustic scattering from double-diffusive microstructure

Andone C. Lavery[a)]
Department of Applied Ocean Physics and Engineering, Woods Hole Oceanographic Institution, Woods Hole, Massachusetts 02543

Tetjana Ross
Department of Oceanography, Dalhousie University, Halifax, Nova Scotia B3H 4J1, Canada

(Received 26 January 2007; revised 28 June 2007; accepted 2 July 2007)

Laboratory measurements of high-frequency broadband acoustic backscattering (200–600 kHz) from the diffusive regime of double-diffusive microstructure have been performed. This type of microstructure, which was characterized using direct microstructure and optical shadowgraph techniques, is identified by sharp density and sound speed interfaces separating well-mixed layers. Vertical acoustic backscattering measurements were performed for a range of physical parameters controlling the double-diffusive microstructure. The echoes have been analyzed in both the frequency domain, providing information on the spectral response of the scattering, and in the time domain, using pulse compression techniques. High levels of variability were observed, associated with interface oscillations and turbulent plumes, with many echoes showing significant spectral structure. Acoustic estimates of interface thickness (1–3 cm), obtained for the echoes with exactly two peaks in the compressed pulse output, were in good agreement with estimates based on direct microstructure and optical shadowgraph measurements. Predictions based on a one-dimensional weak-scattering model that includes the actual density and sound speed profiles agree reasonably with the measured scattering. A remote-sensing tool for mapping oceanic microstructure, such as high-frequency broadband acoustic scattering, could lead to a better understanding of the extent and evolution of double-diffusive layering, and to the importance of double diffusion to oceanic mixing. [DOI: 10.1121/1.2764475]

PACS number(s): 43.30.Ft, 43.20.Fn, 43.30.Gv [JAC] Pages: 1449–1462

I. INTRODUCTION

Acoustic scattering techniques make it possible to rapidly characterize oceanic microstructure and fine structure at high-resolution and on temporal and spatial scales difficult to achieve using traditional oceanographic profiling instruments. Even without a detailed understanding of the scattering physics, acoustic scattering techniques have provided high-resolution, synoptic images of physical processes occurring in the ocean interior, e.g., internal waves (Proni and Apel, 1975; Moum *et al.*, 2003), hydraulic jumps (Farmer and Armi, 1999), and oceanic thermohaline fine structure across oceanographic fronts (Holbrook *et al.*, 2003). There is the potential to obtain additional information regarding oceanic microstructure and fine structure by developing a deeper understanding of the underlying scattering processes, though confounding effects due to other sources of scattering, such as zooplankton, need to be considered (Lavery *et al.*, 2007). For example, the dissipation rate of turbulent kinetic energy has been inferred from high-frequency acoustic scattering measurements in regions of elevated turbulent microstructure (Warren *et al.*, 2003).

Microstructure, which can be broadly categorized into turbulent and double-diffusive microstructure, refers to any physical process that gives rise to small-scale temperature and salinity fluctuations, resulting in density and sound speed fluctuations, which can scatter sound. There are two types of double-diffusive microstructure (Schmitt, 1994): the diffusive regime, which occurs when temperature and salinity generally increase with increasing depth, and the salt fingers regime, which occurs when temperature and salinity generally decrease with increasing depth. In this study we concentrate on double-diffusive interfaces generated by the diffusive regime of double-diffusive microstructure. Double-diffusive microstructure is maintained since the molecular diffusion of heat is two orders of magnitude faster than the molecular diffusion of salt. For the diffusive regime of double-diffusive microstructure, salinity and temperature gradients have opposing influences on the density, with the salinity gradient acting to stabilize the density and the temperature gradient acting to destabilize the density. Rapid heat transfer (relative to salt) causes small vertical perturbations to be suppressed and results in sharp interfaces separating well-mixed layers (Fig. 1). High-latitude regions (Neal *et al.*, 1969; Muench *et al.*, 1990) are generally susceptible to this type of microstructure, which is manifested as thermohaline staircases with a series of well-mixed layers separated by relatively thin interfaces.

There have been few studies pertaining to high-frequency acoustic scattering from either salt fingers or the diffusive regime of double diffusion. A theoretical study of the influence of salt finger thermohaline structure on acoustic propagation was performed by Mellberg and colleagues (Mellberg and Johannessen, 1972; Mellberg *et al.*, 1974) using ray-tracing techniques, though no subsequent measure-

[a)]Electronic mail: alavery@whoi.edu

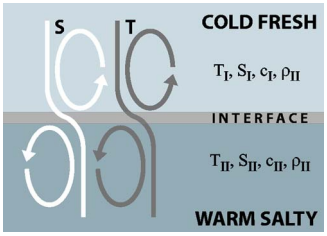

FIG. 1. (Color online) Illustration of the diffusive regime of double diffusion.

ments were performed. In contrast to double-diffusive microstructure, there have been a number of theoretical studies (Goodman, 1990; Seim, 1999; Lavery *et al.*, 2003) and band-limited field measurements (Seim *et al.*, 1995; Ross and Lueck, 2003; Warren *et al.*, 2003) of scattering from turbulent microstructure, and a series of laboratory measurements focusing on turbulent temperature microstructure (Goodman *et al.*, 1992; Stanton *et al.*, 1994; Oeschger and Goodman, 1996, 2003). A recent review (Kelley *et al.*, 2003) suggests that there are fundamental questions regarding the formation and evolution of double-diffusive microstructure, for example, the importance of layer splitting in controlling layer thickness, that would benefit from a rapid, high-resolution, remote mapping technique such as high-frequency acoustic scattering.

In order to improve our understanding of scattering from oceanic microstructure, controlled laboratory measurements of high-frequency broadband acoustic scattering from single, sharp, double-diffusive interfaces have been performed over a range of parameters controlling the double-diffusive microstructure. The experimental methods are described in Sec. II. The echoes from the double-diffusive interfaces have been analyzed in both the spectral domain (Sec. II F 1), as the spectral characteristics of the echoes provide one approach for discrimination between, and identification of, different types of microstructure, and the temporal domain (Sec. II F 2), using pulse compression techniques (Chu and Stanton, 1998) that allow individual scattering features to be resolved, such as the front and back edges of the double-diffusive interfaces. The ping-to-ping characteristics (Sec. III A), variability (Sec. III B), and coherence (Sec. III C) of the echoes are analyzed, and the dominant physical factors influencing the scattering are identified (Sec. III D). The interface thickness has been inferred acoustically (Sec. III E) and compared to measurements based on direct microstructure and optical shadowgraph techniques. A simple one-dimensional weak-scattering scattering model based on actual density and sound speed profiles has been developed (Sec. IV). The results are summarized in Sec. V.

II. EXPERIMENTAL SETUP, METHODS, AND PROCEDURES

The measurements of high-frequency broadband acoustic scattering from double-diffusive (DD) interfaces were conducted at a tank facility (Schmitt *et al.*, 2005) at the Woods Hole Oceanographic Institution (WHOI). Direct measurements of the physical properties of the DD interface were also performed. The relevant details of this facility and the instrumentation used to perform the measurements are described below. The experiments were performed a total of six times. The results presented here correspond to the experiment performed between 27 July (year day 208) and 10 August (year day 222) 2004 and are representative of the results obtained in the other experiments at the WHOI facility.

A. Double-diffusive interface tank

The double-diffusive interface tank was cylindrical in shape, 4.7 m deep, 91.4 cm in outer diameter, and with 2.54 cm thick walls (Fig. 2). The top of the tank was surrounded by a platform from which the acoustic and microstructure instruments were deployed. The bottom of the tank was heated by a resistive heating element powered by a variable transformer and controlled by a thermostat. The top of the tank was cooled by means of a heat exchanger consisting of coiled copper tubing mounted beneath foam that provided both floatation and insulation. The side-walls were insulated to minimize heat loss. It was estimated that approximately 30% of the heat supplied to lower layer was lost through the side walls (Schmitt *et al.*, 2005). Temperature differences of 10–15 °C across an interface approximately 1–3 cm thick, corresponding to temperature gradients of 300–1500 °C/m, were maintained for extended periods of time. Initially, the tank was filled to the desired location of the interface (200–230 cm below the top of the tank, co-located with the shadowgraph imaging system) with room-temperature fresh water filtered with a 5-μm filter. Chlorine was used to minimize the growth of biota in the tank. Commercially available "SeaSalt," manufactured by Lake Products Co., was added to set the salinity at approximately 15 psu. The upper layer was then slowly filled with cold fresh filtered water, resulting in initial salinity gradients of 300–1500 psu/m. The slow diffusion of salt reduces the maintainable temperature contrast across the interface, and, after 2–3 weeks, the double-diffusive system overturns and becomes fully mixed (Fig. 3).

B. Physical properties of the upper and lower mixed layers

Two fixed temperature (T) and conductivity (C) sensors (Falmouth Scientific, Inc.), collecting data every 30 s, were mounted within the top and bottom mixed layers at depths of 1 and 3 m. The 1978 Practical Salinity Scale (PSS78) (Fofonoff and Millard, 1983) was used to calculate salinity (S) from measurements of conductivity, temperature, and pressure. Density (ρ) and sound speed (c) were also derived from these measurements (Fofonoff and Millard, 1983). Throughout this study, properties of the upper and lower mixed layers are denoted by the subscripts "I" and "II," respectively (Table I).

The overall stability of the DD interface system is determined by the density ratio $R_\rho = \beta \Delta S / \alpha \Delta T$, where $\alpha = -(1/\rho)\partial\rho/\partial T$ and $\beta = (1/\rho)\partial\rho/\partial S$ are the thermal expansion and haline contraction coefficients, respectively, and $\Delta T = T_{II} - T_I$ and $\Delta S = S_{II} - S_I$ are the temperature and salinity differentials between the upper and lower mixed layers. The heating and cooling of the DD interface tank were approxi-

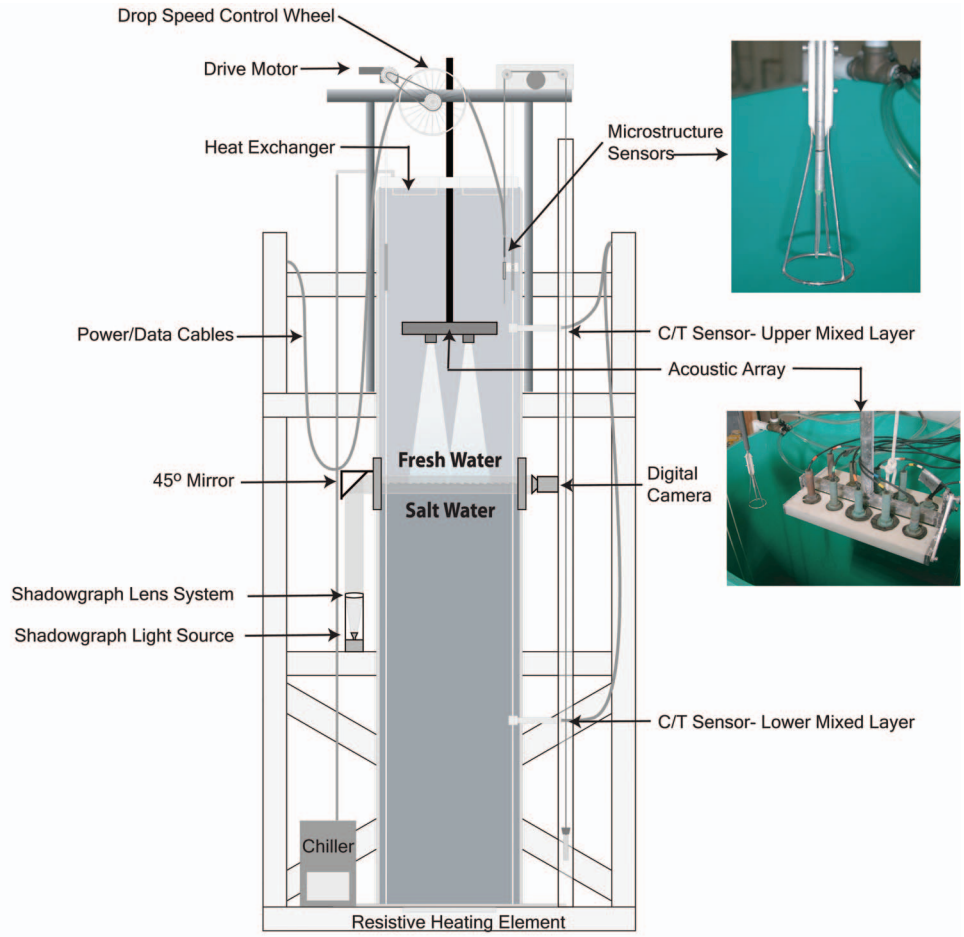

FIG. 2. Illustration of the double-diffusive interface tank.

mately constant throughout the July–August 2004 experiment, so that R_ρ was maintained at values between 4 and 5, except on year days 212 (29 July), and 216 (4 August) when the cooling was removed to maintain the salinity differential during a period of inactivity in the laboratory and to control the density ratio. Removal of the heating and cooling results in a thickening of the interface, which slows the diffusion of salt across the interface. A sharp interface can be reestablished by reapplying the heating and cooling. Towards the end of the experiment, $R_\rho \rightarrow 1$, the fluxes across the interface are largest, and the system becomes unstable and ultimately overturns.

C. Direct microstructure measurements

High-resolution microstructure probes (Precision Measurement Engineering, Inc.: Model 125 MicroScale Conductivity and Temperature Instrument), consisting of a fast-response thermistor (FP-07) closely co-located to a four-electrode conductivity cell, were used to directly measure the vertical temperature and conductivity structure across the interface. The fall rate of the sensors was controlled by a geared motor, typically set to 10 cm/s. The microstructure and depth data were digitally recorded at 1 kHz using an 8-bit 16-channel A/D converter (National Instruments Model

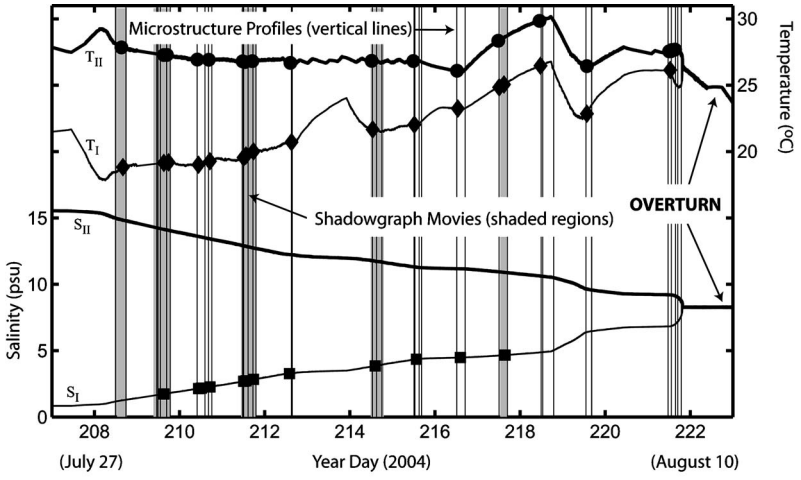

FIG. 3. Temperature and salinity evolution in the upper and lower mixed layers of the DD interface tank during the July–August 2004 experiment. The circles show the times of the 30-min, 1-Hz, 250-kHz BB data acquisition periods, the squares show the times of the 30-min, 1-Hz, 500-kHz BB data acquisition periods, and the diamonds show the times of the 3-min, 10-Hz, 250-kHz BB data acquisition periods. The vertical lines correspond to the times at which direct microstructure measurements were performed. The gray shading corresponds to times at which digital shadowgraph movies were collected.

TABLE I. Initial and final values of the physical properties of the upper and lower mixed layers of the double-diffusive interface system during the July–August 2004 experiment.

Initial upper layer	Initial lower layer	Final
T_I=18.9 °C	T_{II}=26.7 °C	$T_I=T_{II}$=23.7 °C
S_I=2.2 psu	S_{II}=13.5 psu	$S_I=S_{II}$=8.3 psu
ρ_I=1000.1 kg/m^3	ρ_{II}=1006.7 kg/m^3	$\rho_I=\rho_{II}$=1003.6 kg/m^3
c_I=1481.5 m/s	c_{II}=1515.7 m/s	$c_I=c_{II}$=1502.3 m/s

PXI-5112) with custom-written LabView data acquisition software. The microstructure data were then filtered using a Butterworth filter with a 100-Hz cutoff. Profiles of temperature and conductivity were collected several times a day throughout the duration of the experiment. The interface thickness was determined from the conductivity profiles (as the conductivity sensor has a faster response time than the temperature sensor) by looking for rapid changes in the conductivity gradient (greater than a standard deviation of the mean mixed layer values). A small number of profiles had more noise than others, in which case the interface thickness was determined manually. Density and sound speed profiles were calculated from the temperature and conductivity profiles by matching the dynamic responses of the temperature and conductivity probes (Secs. 3c and 3d of Schmitt *et al.*, 2005). A total of 37 microstructure profiles were conducted during the July–August 2004 experiment (Fig. 4).

The DD interface was visibly disrupted by the passage of the microstructure instruments. The interface was allowed to settle for 15–20 min after each microstructure profile before any acoustic data were collected. The appropriate duration for the settling time was determined by monitoring the interface both acoustically (the interface disruption manifested itself as increased variability in the backscattered echoes from various instruments mounted along the side of the tank) and visually using the shadowgraph system.

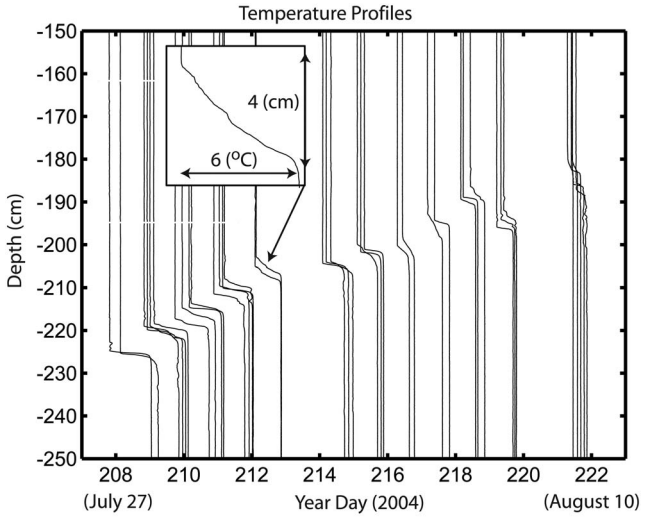

FIG. 4. Temperature profiles collected during the July–August 2004 experiment with the temperature microstructure sensors. The inset shows a close-up of the DD interface. The interface slowly migrated upwards, an effect that has been attributed to the nonlinearity of the equation of state (McDougall, 1981; Schmitt *et al.*, 2005).

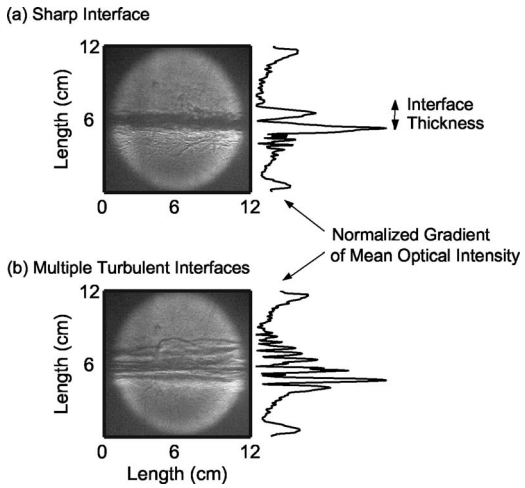

FIG. 5. Shadowgraph images collected on year day 214 (2 August), 2004: (a) A sharp double-diffusive interface and (b) a turbulent double-diffusive interface after the passage of an internal wave or seiche. The line plots to the right of the shadowgraph images show the normalized gradient of the mean optical intensity. The interface thickness for the sharp interfaces was calculated from the separation between the two primary peaks in the normalized gradient of the mean intensity.

The micro-temperature sensors were calibrated by the manufacturer various times throughout the experiments. The temperature was also verified by comparison with the fixed CT sensors in the upper and lower mixed layers. It was assumed that the response of the micro-conductivity sensor was linear and the fixed CT sensors in the upper and lower mixed layers provided a two-point calibration. The fixed CT sensors were calibrated by the manufacturer prior to installation and on two occasions in the DD interface tank by comparison to a calibrated CT instrument (Seabird SBE37).

D. Optical shadowgraph imaging

The optical shadowgraph system consisted of projecting a bright, collimated beam of monochromatic light horizontally through the DD interface, across the middle of the tank, and onto tracing paper, which was then imaged using a 5M pixel digital camera (Nikon Coolpix 5700). The light source was located near the bottom of the tank. The collimated beam was projected parallel to the tank, then reflected by a 45 deg mirror, and through two 40-cm-long rectangular windows of 1.27-cm-thick glass on diametrically opposite sides of the tank. The bottom sills of the shadowgraph windows were 230 cm below the top of the tank. Variations in temperature and salinity led to variations in the density and optical index of refraction within the interface, thus refracting light and allowing the interface to imaged (Williams, 1975). Optical shadowgraph images of the DD interface are inherently qualitative because the light beam is projected across the entire width of the tank, thus integrating horizontally over almost 1 m of the interface. One-minute digital movies of the shadowgraph imaged interface were collected periodically throughout the experiment, at a 15-Hz frame rate (900 images per minute-long movie).

Typical shadowgraph images of the DD interface exhibited two bright edges with an almost completely dark band in between [Fig. 5(a)]. The interface thickness was obtained by

TABLE II. Transducer and general experimental parameters. Unless otherwise stated, all parameters are evaluated at center frequency and at a range of r_{scat}=75 cm.

	250-kHz BB (200–300 kHz)	500-kHz BB (350–565 kHz)
Center frequency (kHz)	250	500
Transducer diameter, D (cm)	2.54	1.53
Full beamwidth, θ (degrees at −3 dB)	14.10	12.50
Directivity index (dB)	8.70	8.73
Far field, D^2/λ (cm)	10.75	6.82
First Fresnel radius, $\sqrt{\lambda r_{scat}}$ (cm)	4.75	3.35
Footprint radius, $r_{scat}\tan(\theta/2)$ (cm)	10.45	8.85
Pulse length, T (μs)	200	400 (300)
Bandwidth, B (kHz)	100	215
SNR gain, $2BT$	40	170 (130)
Inverse bandwidth, $1/B$ (μs)	10	4.65
Spatial resolution (cm): pulse compression	1.5	0.7
Spatial resolution (cm): pulse length	15	30(23)
No. of 1-Hz 30-min data acquisition periods	17	12
No. of 10-Hz 3-min data acquisition periods	17	NA

finding the separation between the two largest peaks in the gradient of the mean light intensity across each image [Fig. 5(a)]. The interface thickness was not calculated for images in which either the upper or lower edges of the dark band were not sufficiently distinct to give significant gradients above the background noise [Fig. 5(b)].

E. Acoustic scattering hardware and calibration

The acoustic scattering system, described below, consisted of a custom-built backscattering array, a programmable pulse-echo system, and custom-written data acquisition software.

1. Acoustic array and transducers

The acoustic backscattering array consisted of two pairs of identical transducers facing approximately vertically down. The transducers were mounted on two Plexiglas plates that could be rotated to focus the transducers at a particular range, that is, the orientation of each transducer relative to the horizontal (<5 degs to the horizontal at the ranges of this experiment) could be adjusted so that the acoustic footprint of each transducer pair was coincident at a particular range. Each pair of transducers, consisting of a transmitter and receiver, was as closely spaced as possible (7.5 cm center-to-center) to simulate backscattering. This configuration was chosen over a single transmit/receive transducer to minimize switching noise at close ranges. The transducers used were 250- and 500-kHz center frequency octave-bandwidth broadband (BB) (pistonlike) transducers (Table II). The transmitted signals were linearly modulated chirps with frequency sweeps from 200 to 300 kHz and from 350 to 650 kHz. In fact, for the 500-kHz BB transducers the usable band (−6 dB to −6 dB) was 350–565 kHz. The vertical position of the array in the tank could be adjusted in 1-mm increments spanning a 2.25-m range. The acoustic data presented here were collected at a range of r_{scat}=75 cm.

2. Pulse-echo system

The pulse-echo electronics (Fig. 6) was computerized and used for both the signal generation and digitization. The system consisted of a National Instruments (NI) data acquisition system (NI Model PXI-1000B) with an embedded computer controller (NI Model PXI-8175 running Windows 2000) and custom-written LabView data acquisition software. The transmitted signals were generated by a single-channel, 12-bit, 40 MHz Arbitrary Waveform Generator (NI Model PXI-5411), and then amplified by a 100-W linear power amplifier (ENI Model 2100L: 50-dB gain, 10-kHz to 12-MHz bandwidth). The received signal was amplified and filtered by an integrated preamplifier and bandpass filter (RITEC Inc., Model BR-640A: 32-dB gain, 100-kHz to 3-MHz bandwidth). A multi-channel high-speed (10 MHz per channel) simultaneously sampling DAQ module (NI

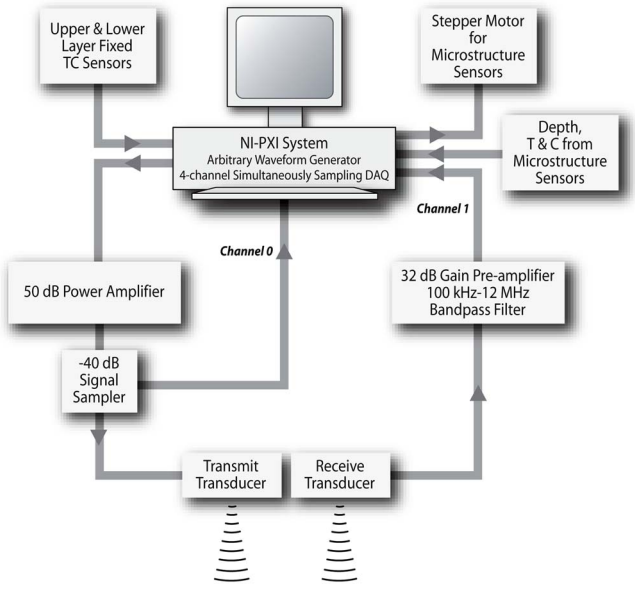

FIG. 6. (Color online) Box diagram of the pulse-echo electronics used to perform the experiments.

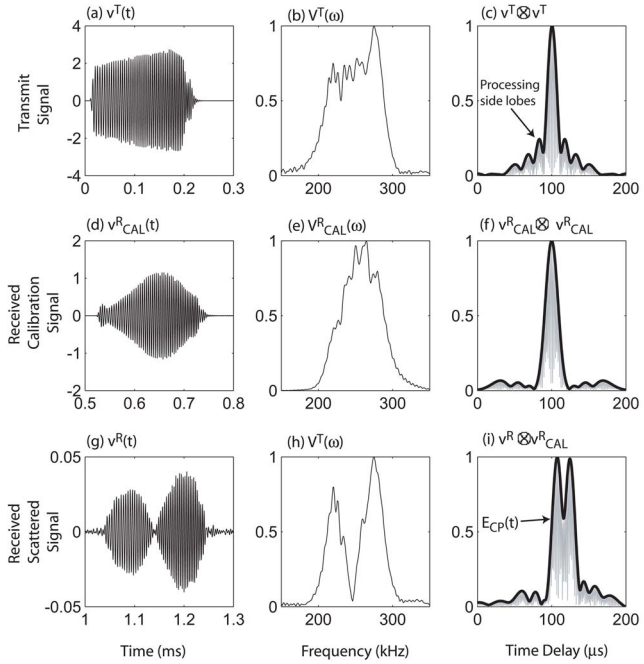

FIG. 7. (Color online) Top row: (a) Typical transmit time series, $v^T(t)$, (b) the Fourier transform, $V^T(\omega)$, of the transmit time series, and (c) the normalized autocorrelation function of the transmit time series, $v^T(t) \otimes v^T(t)$, where $\otimes$ represents cross-correlation. Center row: (d) Typical received calibration time series, $v^R_{\text{cal}}(t)$, (e) the Fourier transform, $V^R_{\text{cal}}(\omega)$, of the received calibration time series, and (f) the normalized autocorrelation function of the received calibration time series, $v^R_{\text{cal}}(t) \otimes v^R_{\text{cal}}$. Bottom row: (g) Typical received time series of scattering from the DD interface, $v^R(t)$, (h) the Fourier transform, $V^T(\omega)$, of the received time series, and (i) the normalized compressed pulse output of the received time series, $v^R(t) \otimes v^R_{\text{cal}}$. The solid black lines in (c), (f), and (i) correspond to the envelope of the compressed pulse output, E_{CP}.

Model PXI-6115) made it possible to synchronously sample up to four input signals. All transmit and receive signals were sampled at 2 MHz for the July–August 2004 experiment. All the electronics and tank water were grounded to the same ground. Both the transmit voltage time series, $v^T(t)$, as measured by a 40-dB-down signal-sampler (RITEC Inc., Model SS-40) on the output end of the power amplifier, and received voltage time series, $v^R(t)$, were digitized during each ping (Fig. 7). A third-order Butterworth bandpass filter was applied to the received voltage time series, with cutoff frequencies at 150 and 350 kHz for the 250-kHz BB data, and at 300 and 700 kHz for the 500-kHz BB data. The echoes from the DD interface were range gated to eliminate any unwanted echoes. Acoustic data were collected for 30-min periods at a 1-Hz repetition rate (1800 pings per file) and for 3-min periods at a 10-Hz repetition rate (1800 pings per file), various times a day from the time the DD interface was generated to the time it became unstable and overturned (Table II).

3. Calibration of acoustic system

The technique used for the calibration measurements is similar in principle to a self-reciprocity calibration and involves separating the transducers so that they are directly facing each other. The transmitted, $v^T_{\text{cal}}(t)$, and received, $v^R_{\text{cal}}(t)$, calibration voltage time series are measured while keeping all other system parameters identical to those for the backscattering measurements. However, the transmit amplitude was reduced by approximately a factor of 15 in order to prevent saturation of the receive transducer when the transducers were facing each other in calibration mode. This technique has been used successfully in previous laboratory scattering experiments (DiPerna and Stanton, 1991; Stanton *et al.*, 1998). The separation between the transducers during the calibration procedure was $r_{\text{cal}}=76.4$ cm. The calibration measurements were performed with the transducers well within the upper mixed layer to ensure that there was no scattering due to temperature and salinity microstructure. This calibration technique results in an estimate of the relative pressure incident on the DD interface and allows the acoustic system to be calibrated without detailed knowledge of parameters such as the transmit source level and transducer sensitivities.

Standard target calibrations were also performed using a 20-mm tungsten carbide (6% cobalt) sphere (Foote and MacLennon, 1984). There was excellent agreement between the measured and calculated target strengths, with the deep nulls reproduced across the frequency bands of interest, with particularly good agreement for the 250-kHz BB data.

4. Noise threshold and background reverberation

All echoes from the DD interface that were smaller than a threshold value for noise were discarded. The procedure followed for setting a value for the noise threshold involved digitizing data for each insonification of the DD interface that included a period of time that did not contain any echoes from any of the auxiliary instruments mounted on the tank or from the DD interface. This window of data was used to set the noise threshold for each ping. To maximize the data quality, a conservative noise threshold was set, and it was required that the mean voltage of each echo from the DD interface be larger than the maximum noise value recorded for that particular insonification.

Scattering from the tank without the DD interface present was measured to ensure that there were no unwanted returns, for example from the surface or side-lobe reflections from the tank walls, in the range-gate window that was used when the DD interface was present. Coherent subtraction of unwanted reverberation could not be performed as it was not possible to measure the scattering from the tank without the DD interface present at the exact same ranges (within a fraction of the acoustic wavelength) used to perform the backscattering measurements. The reason for this was that the position of the interface was slowly, but continuously, changing, and so the position of the acoustic array was gradually changed throughout the experiment so that the range to the interface was always 75 cm.

F. Acoustic data analysis

The far-field scattered pressure for a single scattering realization from the DD interface is given by p_{scat} and can be expressed in terms of the spherically divergent incident sound field at the DD interface, $p_{\text{inc}}=P_0 r_0 e^{ikr_{\text{scat}}}/r_{\text{scat}}$, where k is the acoustic wavenumber ($k=2\pi/\lambda$, where λ is the acous-

tic wavelength) and P_0 is the incident wave amplitude at a reference distance r_0. However, there is some uncertainty in the range dependence of p_{scat}. The problem of scattering of spherically diverging waves from rough surfaces has received much attention in the literature over the years (e.g., Eckart, 1953; Beckmann and Spizzichino, 1963; Horton *et al.*, 1967; Medwin and Novarini, 1981; Pace *et al.*, 1985). There are two limiting cases that can be considered. If the characteristic surface roughness, or root-mean-square (rms) surface height, h_{rms}, is small compared to the wavelength ($h_{rms} \ll \lambda$), then the interface will appear as an infinite, smooth interface. In this case, the well-known image solution can be arrived at by decomposing the incident spherically diverging wave into a sum of incident plane waves, resulting in a $1/2r_{scat}$ range dependence for the scattered pressure (Sec. 4.3 in Brekhovskikh and Lysanov, 2001). At the other extreme, if the interface roughness is larger than the wavelength ($h_{rms} > \lambda$), then the interface will appear to be a distribution of point scatterers and the scattered pressure will have an $1/r_{scat}^2$ range dependence.

As the range dependence of the scattered pressure from the DD interface is not known, scattering experiments were performed over a range of distances from the interface (r_{scat}=50, 75, 100, and 125 m), with the maximum range dictated by the size of tank. However, this restricted range was not sufficient to allow the range dependence to be established above the strong variability that was observed in the scattering.

1. Spectral domain

As a consequence of the uncertainty in the range dependence of the scattering, the frequency dependence of the scattered pressure is presented using the following equation (modified form of Eq. (10) in DiPerna and Stanton, 1991):

$$\frac{P_{scat}}{P_{inc}} = G(\omega)\frac{V^R(\omega)}{V^R_{cal}(\omega)}\frac{r_{scat}}{r_{cal}}, \tag{1}$$

where ω is the angular frequency ($\omega = 2\pi c/\lambda$ and c is the speed of sound), P_{scat} is the amplitude of the scattered pressure, and P_{inc} is the amplitude of the pressure incident at the DD interface. $V^R(\omega)$ is the absolute value of the Fourier transform of the received voltage time series, and $V^R_{cal}(\omega)$ is the absolute value of the Fourier transform of the received calibration voltage time series. $G(\omega) = V^T_{cal}(\omega)/V^T(\omega)$ is the ratio of absolute value of the Fourier transform of the transmit calibration voltage time series to the absolute value of the Fourier transform of the transmit voltage time series. This slightly frequency-dependent factor accounts for the fact that the transmit amplitude during calibration was smaller than the transmit amplitude during the actual scattering experiments. This equation accounts for the spherical spreading of the wave incident on the DD interface and also for the spherical spreading of the calibration wave, but does not account for the range dependence of the wave scattered from the interface. Thus, P_{scat}/P_{inc} at one range cannot necessarily be compared directly to another range as there is an implicit range dependence still embedded in the equation. However, if the characteristic surface roughness of the DD interface is small compared to the wavelength, and the scattered pressure has a $1/2r_{scat}$ range dependence, then P_{scat}/P_{inc} will be range independent. Losses due to attenuation are ignored in this analysis, which is a reasonable assumption given the short ranges used.

The high signal-to-noise (SNR) levels for the 250-kHz BB transducers allowed the spectral response of the echoes from the DD interface to be analyzed on a ping-by-ping basis in this frequency band throughout the duration of the July–August 2004 experiment. Low transducer sensitivity resulting in low SNR levels for the 500-kHz BB transducers precluded the analysis of the echoes in this frequency range towards the end of the experiment when the echoes from the DD interface were smaller as a result of the smaller temperature and salinity differentials across the interface.

2. Temporal domain: Pulse compression techniques

Increased signal-to-noise levels (proportional to $2BT$, where B is the bandwidth and T is the pulse length of the applied signal) and temporal resolution (proportional to $1/B$) can be achieved by applying pulse compression to the received voltage time series (Chu and Stanton, 1998). The compressed pulse output is given by cross-correlating the received voltage time series from the DD interface to the received calibration time series [Eq. (14) in Stanton *et al.*, 1998]:

$$CP(t) = k_{CP}^{-1} v^R(t) \otimes v^R_{cal}(t), \tag{2}$$

where $\otimes$ represents cross-correlation and k_{CP} is the autocorrelation function of v^R_{cal} evaluated at zero time lag. The envelope of the compressed pulse output is denoted $E_{CP}(t)$ (Fig. 7).

Peaks in the CP output corresponding to arrivals that are separated by greater than $1/B$ can be individually resolved. The interface thickness was calculated on a ping-by-ping basis for all broadband acoustic data that exhibited exactly two peaks in E_{CP}. The interface thickness is given by: $h = (c_I/2)|t_1 - t_2|$, where $t_i (i = 1, 2)$ are the delay times corresponding to the two peaks in E_{CP} and c_I is the sound speed in the upper mixed layer. All peaks in E_{CP} smaller than the signal processing side lobes of the autocorrelation function of v^R_{cal}, or smaller than 25% of the primary interface return, were discarded.

III. RESULTS

A. Individual echoes

The majority of the echoes from the DD interface did not exhibit significant spectral structure and had exactly one peak in the CP output. These "featureless" echoes were associated to larger mean scattering levels. However, a significant number of the echoes from the DD interface did show considerable spectral structure (Fig. 8). Many echoes exhibited a pattern in the spectral response that was consistent with the constructive and destructive interference pattern that would be expected from a layer with at least two primary interfaces, with nulls that were 10–15 dB below peak values

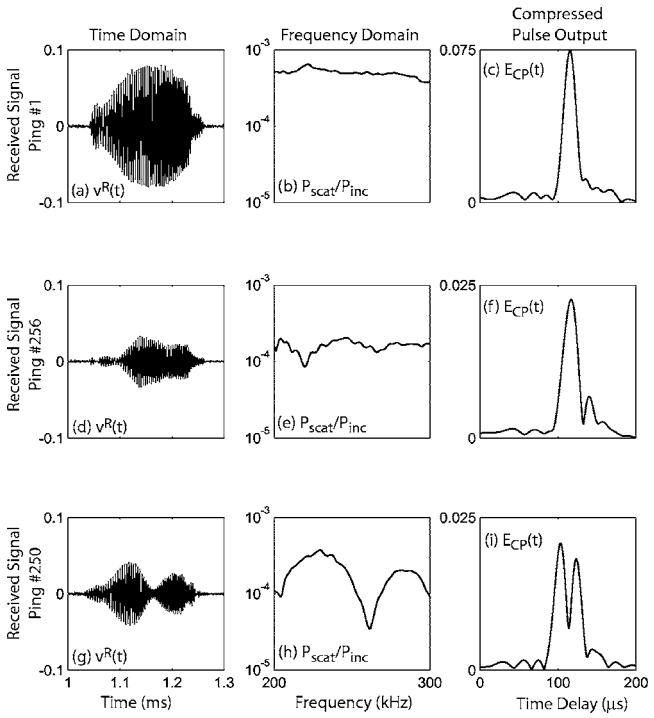

FIG. 8. Three typical received voltage time series in the 250-kHz BB frequency range on year day 214 (2 August), 2004. Ping 1 (top row) showing little spectral structure and a single peak in the CP output: (a) $v^R(t)$, (b) $P_{\text{scat}}/P_{\text{inc}}$, and (c) E_{CP}. Ping 256 (center row) showing little spectral structure but two peaks in the CP output: (d) $v^R(t)$, (e) $P_{\text{scat}}/P_{\text{inc}}$, and (f) E_{CP}. Ping 250 (bottom row) showing significant spectral structure and two peaks in the CP output: (g) $v^R(t)$, (h) $P_{\text{scat}}/P_{\text{inc}}$, and (i) E_{CP}.

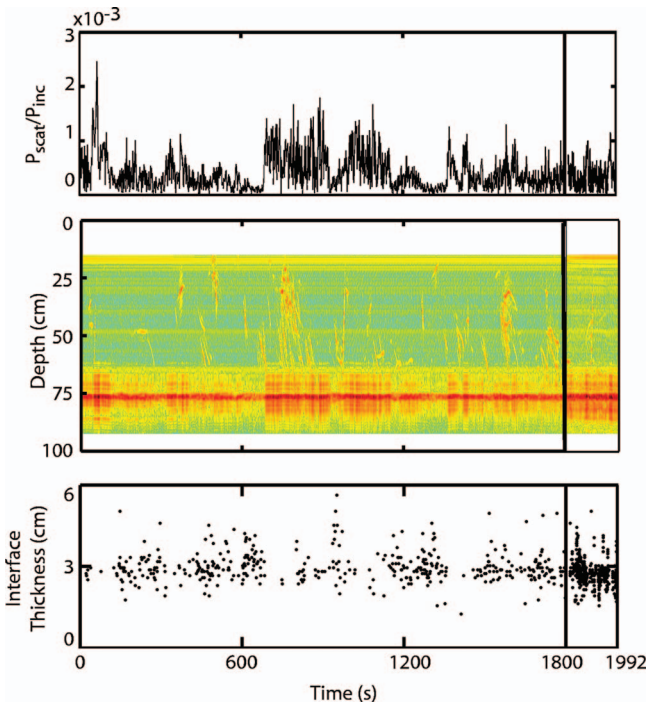

FIG. 10. (a) $P_{\text{scat}}/P_{\text{inc}}$, (b) the envelope of the CP output, E_{CP}, as function of time and depth, and (c) the interface thickness inferred from echoes exhibiting exactly two peaks in the CP output, for the 30-min 250-kHz BB data (1800 pings at 1 Hz) followed by the 3-min 250-kHz BB data (1800 pings at 10 Hz) acquired on year day 214 (2 August), 2004. There was a 12-s delay separating the two data collection periods. Each ping in (b) has been normalized to its largest value.

for a given echo. For exactly two primary scattering interfaces, the nulls in the interference pattern occur when $\lambda(n+1/2)=h$ (for $n=0,1,2,\ldots$).

Pulse compression analysis of the echoes exhibiting significant spectral structure revealed that there were usually at least two clear peaks in the CP output. Due to the increased temporal resolution achieved through pulse compression, echoes that appeared relatively featureless in the frequency domain sometimes had separable peaks in the compressed pulse output (Fig. 8).

Based on the 30-min data acquisition periods, approximately 24% of the echoes from the DD interface in the 250-kHz BB frequency band showed exactly two peaks in the CP output, while approximately 31.5% of the echoes in the 500-kHz BB frequency band showed exactly two peaks in the CP output (Fig. 9). The number of echoes that had greater than two peaks in the CP output in the 250-kHz BB frequency range was small, approximately 3% on the average, while the number of echoes that had more than two peaks in the CP output in the 500-kHz BB frequency range was larger, which is attributed in part to lower SNR in this frequency range. There was little correlation between the number of echoes that showed exactly two peaks in the CP output and the temperature (ΔT) or salinity (ΔS) differential between the upper and lower mixed layers.

The number of echoes showing exactly two peaks in the CP output based on the 3-min data acquisition periods was highly variable as intermittent high-scattering events (described in more detail in the next section), which are highly correlated to echoes that show little spectral structure, were not always fully captured in the 3-min data acquisition periods.

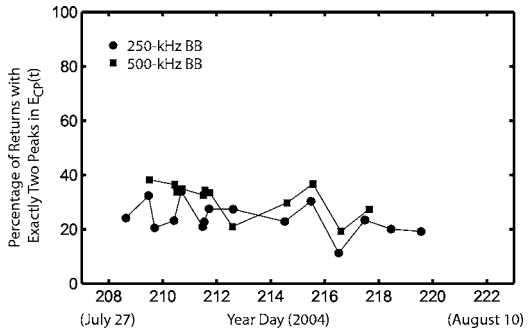

FIG. 9. Percentage of echoes with exactly two peaks in the CP output.

B. Variability of echoes

Significant ping-to-ping variability was observed for the echoes from the DD interface. For any given data acquisition period, the amplitude of the scattered pressure normalized by the incident pressure at the interface, $P_{\text{scat}}/P_{\text{inc}}$, fluctuated by more than an order of magnitude at all frequencies [Fig. 10(a)].

Intermittent events with scattering levels elevated by more than an order of magnitude occurred every few minutes. The duration of these intermittent events varied from tens of seconds to a couple of minutes. During these events, distinct returns could be seen in the water column above the

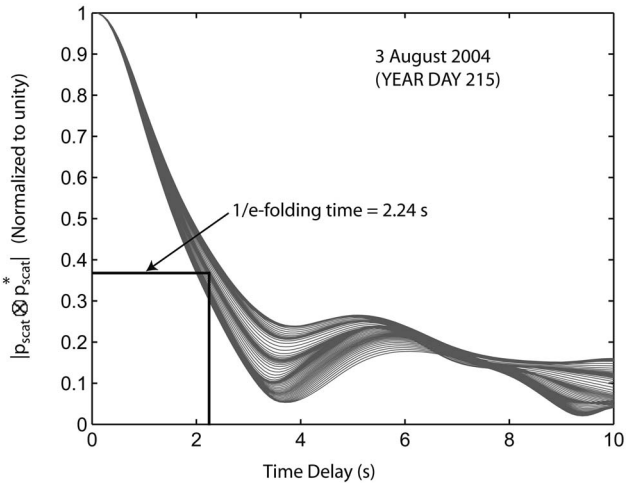

FIG. 11. The amplitude of the autocorrelation function of the scattered pressure, $|p_{\mathrm{scat}} \otimes p^{*}_{\mathrm{scat}}|$, for all frequencies (in 1-kHz increments) for the 3-min, 10-Hz, 250-kHz BB data, collected on year day 215 (3 August), 2004. The e-folding time for these data is 2.24 s, representative of entire July–August 2004 experiment.

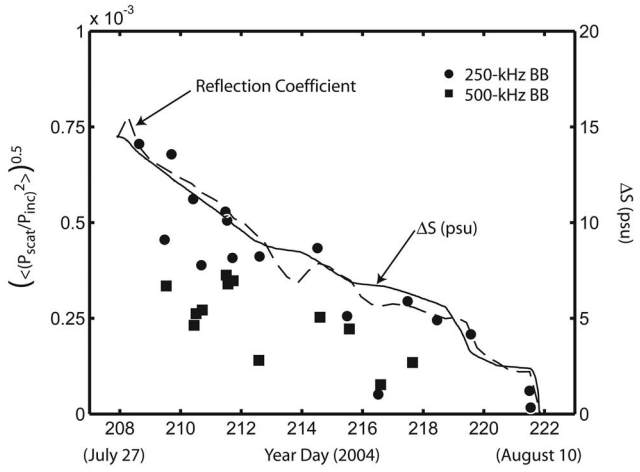

FIG. 12. Root-mean-square scattered pressure, $\langle (P_{\mathrm{scat}}/P_{\mathrm{inc}})^2 \rangle^{0.5}$, at 250 kHz for the 30-min 250-kHz BB data (solid circles) and at 500 kHz for the 30-min 500-kHz BB data (solid squares). The solid line, corresponding to the scale on the right-hand axis, shows the salinity contrast, ΔS, between the upper and lower mixed layers. The dashed line shows the reflection coefficient, arbitrarily scaled to fit the axes shown.

interface. These returns appeared to be due to physical structures that were generally moving upwards from the interface [Fig. 10(b)]. It is speculated that these structures are related to turbulent thermal plumes breaking away from the interface and traveling through the upper mixed layer, trapped by convection cells driven by the strong heating and cooling applied to the DD system. There were a larger number of echoes from the DD interface exhibiting either strong nulls in the frequency domain or multiple peaks in the CP output when the mean value of $P_{\mathrm{scat}}/P_{\mathrm{inc}}$ across the frequency band was low and when less returns were observed in the water column above the interface.

The observed variability in the scattered echoes was related to the degree of heating and cooling applied to the DD system, which was held constant and high during the July–August 2004 experiment, but systematically modified in later experiments. When it was completely removed, the variability in the echoes quickly decreased, there were more echoes that had exactly two peaks in the CP output, and the mean scattered levels decreased. In addition, the scattering from physical structures above the DD interface disappeared.

C. Coherence of echoes

The temporal correlation between individual backscattered echoes (the decorrelation time scale) (Fig. 11) from the DD interface decreased significantly in approximately 2–3 s, due to changes in the position, thickness, and roughness of the DD interface resulting from processes such as waves on the interface and turbulent plumes. The decorrelation time scale was determined by calculating the amplitude of the autocorrelation of the scattered pressure, $|p_{\mathrm{scat}} \otimes p^{*}_{\mathrm{scat}}|$, at each frequency for all pings in a given data collection period. The 3-min data acquisition periods (10-Hz repetition rate) were used for this analysis to ensure that the shortest time scales were adequately sampled. However, the longer 30-min data collection periods we sampled sufficiently fast (1 Hz) that the Nyquist sampling criterion was satisfied. The decorrelation time scale was relatively uniform across all frequencies, and throughout the duration of the experiment. As a result of the short decorrelation time scale, over any given 30-min data collection period, the echoes from the DD interface were almost completely incoherent, that is $\langle p_{\mathrm{scat}} \rangle^2 \approx 0$.

The decorrelation time scale is in good agreement with the time scale dictated by interface waves, in which the layer moves up and down, or oscillates, at the buoyancy frequency scaled appropriately for a DD interface (Turner, 1973):

$$N_{DD} = [(1 - 1/\mathrm{Le})/3(\mathrm{Pr} + 1)]^{1/2} N, \tag{3}$$

where N is the buoyancy frequency ($N^2 = -g/\rho \partial\rho/\partial z$ and g is the acceleration due to gravity), $\mathrm{Le} = \kappa/\kappa_S (\approx 1.5)$ is the Lewis number (κ and κ_S are the molecular diffusivity of heat and salt, respectively), and $\mathrm{Pr} = \nu/\kappa (\approx 6.32)$ is the Prandtl number (ν is the kinematic viscosity). For typical parameters of the DD interface experiment, $1/N_{DD} \approx 1/(1.55N) \approx 3$ s. It was not possible to probe the DD interface on relevant time scales using the direct microstructure sensors as the interface was significantly disturbed for 15–20 min after each of these measurements.

D. Dependence of echoes on the physical parameters controlling the double-diffusive interface

Over the duration of the experiment, the root-mean-square scattered pressure, $(P_{\mathrm{scat}}/P_{\mathrm{inc}})_{\mathrm{rms}} = \langle (P_{\mathrm{scat}}/P_{\mathrm{inc}})^2 \rangle^{0.5}$, where the average is over all echoes from the DD interface in a 30-min data collection period, decreased as the temperature and salinity differentials across the DD interface decreased. The trend generally followed the trend observed in the salinity differential across the interface (ΔS) (Fig. 12) but not temperature differential (ΔT) (results not shown). Though this was generally also the case for the 3-min data collection periods, incomplete sampling of the strong but intermittent events resulted in significantly increased variability. The density contrast was more important than the sound speed contrast in determining the trend in root-mean-square scattered

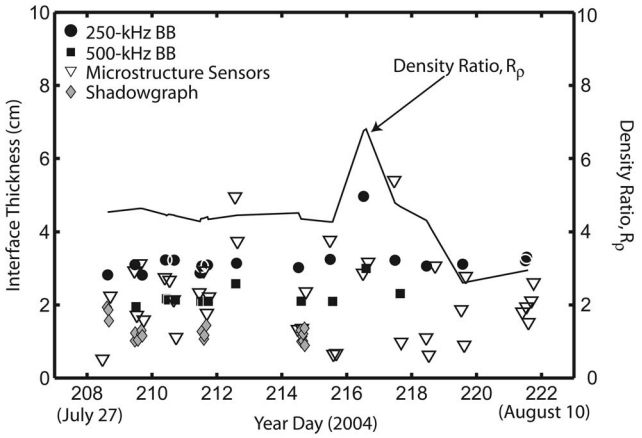

FIG. 13. Mean interface thickness based on the 30-min data acquisition periods for the 250-kHz BB (solid circles) and the 500-kHz BB (solid squares) acoustic data. The interface thickness was determined on a ping-by-ping basis from the separation between the peaks in the CP outputs that exhibited exactly two peaks, and then averaged over the 30-min data acquisition periods. The interface thickness as determined from the direct microstructure sensors (open triangles), and from 1-min averages of optical shadowgraph images (solid gray diamonds), are also shown.

pressure, which is not surprising as temperature plays a more important role than salinity in determining sound speed. The root-mean-square scattered pressure was slightly smaller in the 500-kHz BB frequency range than in the 250-kHz BB frequency range.

E. Interface thickness

The interface thickness was relatively uniform throughout the duration of the experiment (Fig. 13) until the DD system was close to overturning, independent of changes in the temperature and salinity differential across the DD interface. However, as the applied heating and cooling was maintained relatively constant throughout the experiment, the density ratio, R_ρ, which in later experiments was found to be important in controlling the interface thickness, was also relatively constant. R_ρ was briefly elevated above its nominal value of 4.5 on 4 August, and the interface thickness was seen to increase (Fig. 13). The acoustically inferred estimates of interface thickness based on the 500-kHz BB data were in better agreement with the direct micrsotructure and optical shadowgraph estimates, potentially due to the larger bandwidth and increased spatial resolution of the 500-kHz BB transducers.

IV. COMPARISON OF SCATTERING DATA WITH A SIMPLE MODEL

In this section, the scattered echoes from the double-diffusive interface are compared to a one-dimensional weak-scattering model that includes both the actual and idealized representations of the density and sound speed profiles [Fig. 14(a)]. This simple model consists of dividing the density and sound speed profiles into a finite number of sublayers, each with homogeneous density and sound speed (Gupta, 1966). The upper and lower mixed layers are modeled as homogeneous half-spaces. The scattered pressure at each interface is then calculated and added coherently. The scattering from the DD interface falls into the weak-scattering regime as the density and sound speed contrasts across the interface, based on measurement of temperature and conductivity, were small (reflection coefficient $<19.5\times10^{-3}$). Using this simple model, the scattered pressure can be calculated for both incident plane and spherical waves.

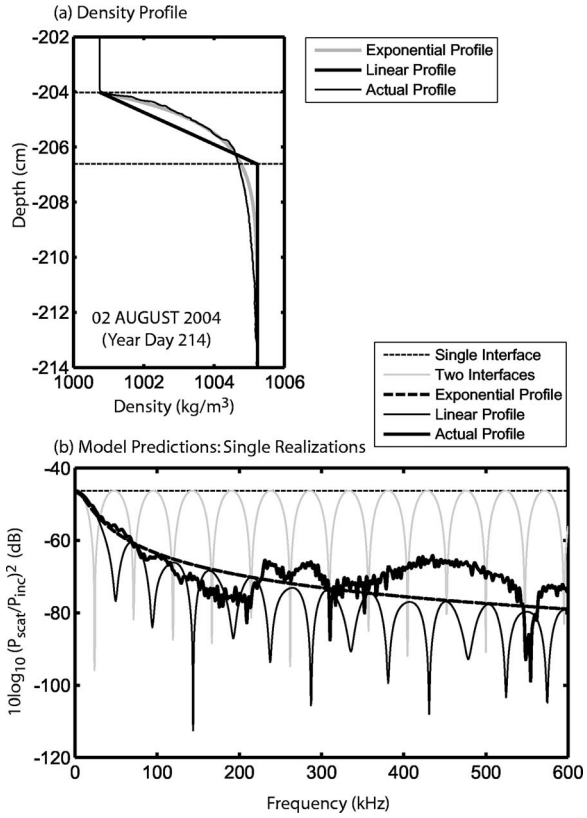

FIG. 14. (a) Measured density profile (thin black line) through the DD interface on year day 214 (2 August), 2004. The measured density profile was fit to a linear profile (thick black line) and an exponential profile (thick gray line). (b) Predicted scattering $10\log_{10}(P_{scat}/P_{inc})^2$ versus frequency for a spherically diverging wave incident on the DD interface on year day 214 (2 August), 2004 assuming a single interface (thin dashed black line), a two-interface layer (thin gray line), exponential density and sound speed profiles (thick dashed black line), linear density and sound speed profiles (thin black line), and the actual density and sound speed profiles (thick black line).

A. A one-dimensional weak-scattering model for the double-diffusive interface

1. Single interface

For an incident plane wave scattering from a single, infinite, smooth, interface, the magnitude of the scattered pressure normalized by the magnitude of the pressure incident at the interface is given by

$$\frac{P_{\text{scat}}}{P_{\text{inc}}^{PW}} = R_{I,II} = \frac{\rho_{II}c_{II} - \rho_I c_I}{\rho_{II}c_{II} + \rho_I c_I}, \tag{4}$$

where $P_{\text{inc}}^{PW} = P_0$ and $R_{I,II}$ is the traditional reflection coefficient. For a spherically spreading incident wave, the magnitude of the backscattered pressure is given by the image solution: $P_{\text{scat}} = R_{I,II}P_0 r_0/2r_{\text{scat}} = P_{\text{inc}}R_{I,II}/2$. However, this single-interface model cannot explain the echoes from the DD interface that exhibit constructive and destructive inter-

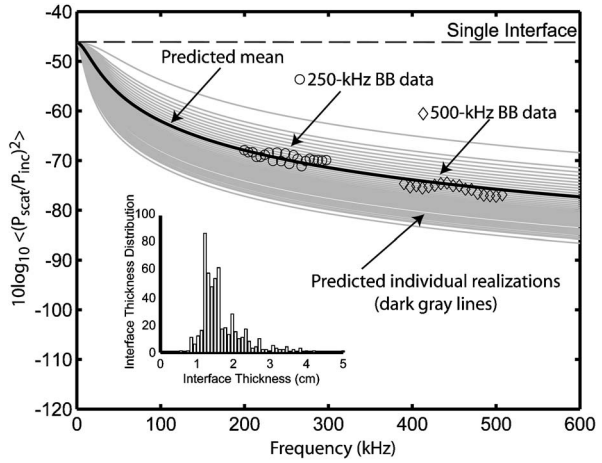

FIG. 15. Comparison of measured and predicted scattering using a one-dimensional weak-scattering model with no adjustable parameters for spherically diverging acoustic waves incident on the DD interface on year day 214 (2 August), 2004. The predicted scattering is based on exponential density and sound speed profiles and on the distribution of interface thicknesses acoustically inferred from the 500-kHz BB data (inset). The exponential decay parameters h_c and h_c were related to the acoustically derived interface thickness, h, by $h_c=1.93h$ and $h_\rho=2.3h$. Individual realizations are shown in light gray and the model average is shown in black. The symbols show the 30-min incoherently averaged data, $10\log_{10}\langle(P_{\text{scat}}/P_{\text{inc}})^2\rangle$, for the 250-kHz BB data (circles) and 500-kHz BB data (diamonds).

ference patterns (or multiple peaks in the CP output) and significantly overpredicts the observed scattering from the DD interface (Figs. 14 and 15).

2. Single homogeneous layer (two interfaces)

A model that consists of two, infinite, smooth interfaces separated by a homogenous fluid layer with intermediate properties between the upper and lower mixed layers can, in general terms, explain the echoes with exactly two peaks in the CP returns (Fig. 14). For an incident plane wave, the magnitude of the scattered pressure normalized by the magnitude of the pressure incident at the interface is given by (Sec. 3.3 in Brekhovskikh and Lysanov, 2001)

$$\frac{P_{\text{scat}}}{P_{\text{inc}}^{PW}}=\frac{R_{I,L}+R_{L,II}e^{2ik_Lh}}{1+R_{I,L}R_{L,II}e^{2ik_Lh}}, \tag{5}$$

where k_L is the wavenumber within the homogeneous fluid layer, $R_{I,L}$ is the reflection coefficient between the upper mixed layer and the intermediate layer, $R_{L,II}$ is the reflection coefficient between the intermediate layer and the lower mixed layer, and h is the interface thickness. Since the scattering from each interface is weak, so that $R_{I,L}\ll 1$ and $R_{L,II}\ll 1$, and the transmission coefficient across each interface is approximately unity, then $P_{\text{scat}}/P_{\text{inc}}^{PW}\approx R_{I,L}+R_{L,II}e^{2ik_Lh}$. This is the same expression that is obtained if only the first echo from each interface is coherently added.

Following similar arguments for an incident spherical wave, assuming weak scattering, the image solution at each interface, and coherently adding the first echo from each interface, the magnitude of the scattered pressure is given by

$$P_{\text{scat}}=P_0r_0\left(\frac{R_{I,L}}{2r_{\text{scat}}}+\frac{R_{L,II}}{2(r_{\text{scat}}+h)}e^{2ik_Lh}\right). \tag{6}$$

The far-field approximation is valid since the interface thickness is much smaller than the range to the DD interface, thus $(r_{\text{scat}}+h)\approx r_{\text{scat}}$. Substituting $P_{\text{inc}}=P_0r_0/r_{\text{scat}}$, the magnitude of the scattered pressure normalized by the magnitude of the pressure incident at the interface is given by

$$\frac{P_{\text{scat}}}{P_{\text{inc}}}\approx\frac{1}{2}(R_{I,L}+R_{L,II}e^{2ik_Lh}). \tag{7}$$

Though this two-interface model can account for the constructive and destructive interference patterns of echoes from the DD interface with exactly two peaks in the CP output, it significantly overpredicts the observed scattering from the DD interface (Figs. 14 and 15).

3. Inhomogeneous multi-layered medium (multiple interfaces)

Following the procedure outlined above, the actual density and sound speed profiles can be used to calculate the scattering from the DD interface by dividing the profiles into N finely spaced homogenous sublayers of thickness Δ_n, where n runs from 1 to N. The thickness of each sublayer was set to be $\lambda_{600}/20$, where λ_{600} is the wavelength corresponding to the highest frequency of interest, namely 600 kHz. Assuming an incident spherical wave, weak scattering at each interface, the image solution at each interface, including only the first echo from each interface, and correctly accounting for the phase at each interface, then the magnitude of scattered pressure is approximately given by

$$P_{\text{scat}}\approx P_0r_0\left(\frac{R_{I,1}}{2r_{\text{scat}}}+\sum_{n=1}^{N}\frac{R_{n,n+1}e^{2i\Sigma_{m=1}^{n}k_m\Delta_m}}{2(r_{\text{scat}}+\sum_{m=1}^{n}\Delta_m)}\right), \tag{8}$$

where the reflection coefficient between each sublayer is given by $R_{n,n+1}$, $R_{I,1}$ is the reflection coefficient between the upper mixed layer and the first sublayer, and $R_{N,N+1}=R_{N,II}$. Again, the far-field approximation is valid since the interface thickness is much smaller than the range to the DD interface, thus $(r_{\text{scat}}+\Sigma_{m=1}^{N}\Delta_m)\approx r_{\text{scat}}$. The magnitude of the scattered pressure normalized by the magnitude of the pressure incident at the interface is given by

$$\frac{P_{\text{scat}}}{P_{\text{inc}}}\approx\frac{1}{2}\left(R_{I,1}+\sum_{n=1}^{N}R_{n,n+1}e^{2i\Sigma_{m=1}^{n}k_m\Delta_m}\right), \tag{9}$$

which is half the magnitude that would be obtained if the incident waves had been plane instead of spherical waves. The assumptions made in arriving at this expression are similar in principle to the assumptions of the distorted wave Born approximation, in which it is assumed that the incident wave is unaffected by the scattering from the preceding sublayers, but correctly accounts for the change in the phase of the incident wave as it traverses through each sublayer. This expression assumes normal incidence as the experiment was performed in the backscattering configuration. It is straightforward to generalize the formulation to other angles of incidence, at least for incident plane waves, by replacing k_n

with $k_n \cos \gamma_n$, where γ_n is the angle of incidence, measured from the normal, at the front interface of each sublayer, and γ_n is related to γ_{n+1} by Snell's law, namely $k_n \sin \gamma_n = k_{n+1} \sin \gamma_{n+1}$.

The reflection coefficient of a plane acoustic wave incident on an arbitrary number of layers, each of which has constant density and sound speed, but is not necessarily weakly scattering, can be easily calculated numerically (Sec. 3.3 in Brekhovskikh and Lysanov, 2001). The weak scattering assumption made here was tested against this numerical approach for actual density and sound speed profiles for incident plane waves. In addition, the reflection of a plane acoustic wave incident on a layered medium with density and sound speed that vary continuously with depth can be calculated analytically for a restricted number of idealized profiles (Robins, 1990, 1991). The accuracy of Eq. (9) was tested by comparison to a number of these analytical solutions.

B. Density and sound speed profiles

The scattering from the DD interface was calculated using Eq. (9) with the actual density and sound speed profiles as well with idealized profiles [Fig. 14(a)]. Idealized profiles provide insight into the important scattering processes as well as allowing predictions to be made when the actual density and sound speed profiles are not known. Exponential profiles are typically used by physical oceanographers to address the mismatch in the time response of microstructure temperature and conductivity sensors (Schmitt *et al.*, 2005). Thus, exponential density and sound speed profiles were used, given by

$$\rho(d) = \rho_I + (\rho_{II} - \rho_I)(1 - e^{-d/d_\rho}), \tag{10}$$

$$c(d) = c_I + (c_{II} - c_I)(1 - e^{-d/d_c}), \tag{11}$$

where d is the depth, $d=0$ is defined as the top of the interface, and the density and sound speed are set to ρ_I and c_I, respectively, for $d<0$. d_ρ and d_c are constants that determine how fast the profiles asymptote to the lower-layer homogeneous values of density (ρ_{II}) and sound speed (c_{II}). d_ρ and d_c were determined by performing a least-squares fit of the measured profiles to the predicted profiles, namely $\Sigma_{n=1}^{N}[\rho_{\text{measured}}(d_n) - \rho(d_n)]^2$ and $\Sigma_{n=1}^{N}[(c_{\text{measured}}(d_n) - c(d_n)]^2$ were minimized. Linear density and sound speed profiles were also used, given by

$$\rho(d) = \begin{cases} \rho_I + (\rho_{II} - \rho_I)d/h_\rho & \text{for } d < h_\rho, \\ \rho_{II} & \text{for } d \geq h_\rho, \end{cases} \tag{12}$$

$$c(d) = \begin{cases} c_I + (c_{II} - c_I)d/h_c & \text{for } d < h_c, \\ c_{II} & \text{for } d \geq h_c. \end{cases} \tag{13}$$

h_ρ and h_c were determined by performing a least-squares fit of the actual density and sound speed profiles to the linear profiles. As with the exponential profiles, $d=0$ is defined as the top of the interface, and the density and sound speed are set to ρ_I and c_I, respectively, for $d<0$. Only data for which $(c-c_I)/(c_{II}-c_I)$ and $(\rho-\rho_I)(\rho_{II}-\rho_I) < 0.95$ were included in the linear fits. The error in the least squares fit was smaller when exponential profiles were used to represent the actual density and sound speed profiles rather than linear profiles. For the direct microstructure profiles of density and sound speed obtained on year day 214 (2 August), 2004 in between the 250- and 500-kHz BB data acquisition periods, it was found that $h_c = 1.93 d_c$ and $h_\rho = 2.3 d_\rho$.

C. Model predictions

Modeling the DD interface with linear density and sound speed gradients results in a constructive and destructive interference pattern, with the positions of the nulls dictated by the interface thickness. There is a significant phase-shift (almost completely out of phase) in the position of the nulls [Fig. 14(b)] relative to a single layer with two interfaces. The value of $P_{\text{scat}}/P_{\text{inc}}$ is similar to that of a single interface at low frequencies (long wavelengths relative to the interface thickness), however, the peak values are almost 25 dB smaller at the frequencies relevant to this study (200–600 kHz).

The constructive and destructive interference pattern is completely eliminated when the DD interface is modeled with exponential density and sound speed profiles [Fig. 14(b)]. $P_{\text{scat}}/P_{\text{inc}}$ is again approximately 25 dB smaller than a single sharp interface at the frequencies relevant to this study.

When the actual density and sound speed profiles are used to model the DD interface, the clear constructive and destructive interference pattern that is observed when the DD interface is modeled by linear sound speed and density profiles is significantly reduced, though there is increased fine-scale spectral structure. $P_{\text{scat}}/P_{\text{inc}}$ is again reduced by approximately 25 dB over the frequency range of interest, relative to a single interface [Fig. 14(b)].

D. Comparison of model predictions to data

It was not possible to perform coincident acoustic scattering and direct microstructure measurements of the DD interface. As a consequence it is not possible to compare scattered spectra on a ping-by-ping basis to predictions based on actual density and sound speed profiles. However, it is possible to compare the incoherently averaged echoes, $\langle (P_{\text{scat}}/P_{\text{inc}})^2 \rangle$, where the average is over all echoes in a 30-min data acquisition period, to model averages, where the averages are over the acoustically inferred distribution of interface thicknesses. This comparison is shown in Fig. 15 for the data collected on year day 214 (2 August), 2004. The acoustically inferred distribution of interface thicknesses based on the 500-kHz BB data was used as this agreed better than the inferences based on 250-kHz BB data with both the direct microstructure and optical shadowgraph estimates of the interface thickness performed on this day, and throughout the experiment (Fig. 13 and Table III). Both exponential and linear profiles in density and sound speed were used to perform the model averages. Averaging the model predictions based on the linear profiles resulted in the smoothing of the nulls and the predicted trend closely followed the averaged predictions based on the exponential profiles, but shifted down by approximately 4 dB (results not shown).

TABLE III. Mean interface thickness throughout the duration of the July–August 2004 experiment. Data from year day 216 (4 August) have not been included in this mean as the density ratio was elevated on this day.

Method of measurement	Mean interface thickness (cm)	Standard deviation (cm)
Acoustically inferred (250-kHz BB)	3.2	1.2
Acoustically inferred (500-kHz BB)	1.8	0.7
Direct microstructure	2.2	1.1
Optically inferred	1.3	0.4

The remarkable agreement between the averaged model prediction, which contains no adjustable parameters, and the incoherently averaged broadband data strongly suggests that the range dependence of the scattered pressure is $1/2r_{\mathrm{scat}}$, as this is an inherent assumption of the model.

E. Considerations for further modeling

The simple one-dimensional weak-scattering model developed here includes two important components of the problem of scattering of acoustic waves from DD interfaces, that is, incident spherical waves and gradients in the density and sound speed profiles. However, to more accurately model the scattering, both volume and surface roughness effects (Ivakin, 1997) should be included, for which knowledge of both the acoustic sampling volume (Foote, 1991) and the interface roughness is necessary.

Another important modeling consideration is the effect of small beamwidth transducers, resulting in an insonified area that is range dependent and only includes a finite number of Fresnel zones (Horton and Melton, 1970). The simple model described above assumes that an infinite number of Fresnel zones contribute to the scattering, while in fact the measurements are in the transition region with 2.5 to 6 Fresnel zones encompassed by the insonified region, depending on the frequency and transducer pair employed (Table II). To incorporate these effects, one approach is to decompose the incident spherical waves into a sum of incident plane waves (Sec. 4.3 in Brekhovskikh and Lysanov, 2001) before integrating over the size of the acoustic footprint at the DD interface. The importance of the size of the acoustic footprint relative to the size of the Fresnel zones could be investigated experimentally by performing scattering measurements with transducers operating in the same frequency band but with different beamwidths.

V. SUMMARY AND CONCLUSIONS

In this study, controlled laboratory measurements of high-frequency broadband acoustic backscattering from the diffusive regime of double-diffusive microstructure have been performed. The diffusive regime of double-diffusive microstructure is characterized by sharp density and sound speed interfaces. Acoustic backscattering has been measured for a range of physical parameters driving the double-diffusive microstructure. It has been demonstrated that double-diffusive microstructure can be investigated acoustically on spatial and temporal scales that are difficult to achieve using techniques that are more commonly used to study oceanic microstructure, namely, free-falling direct microstructure sensors and optical shadowgraph techniques. The acoustic echoes from the double-diffusive interface have been analyzed in both the frequency domain, providing information on the spectral response of the scattering, and in the time domain, through pulse compression techniques that result in improved spatial resolution and increased signal-to-noise ratios. Exploiting broadband pulse compression techniques, the interface thickness has been remotely measured and found to be in reasonable agreement with the almost-coincident optical and direct microstructure measurements of interface thickness (Table III).

A simple one-dimensional weak-scattering model for spherically diverging acoustic waves incident on the double-diffusive interface, which includes realistic representations of the measured density and sound speed profiles, has been developed. Predictions based on this model, which has no adjustable parameters, are in significantly better agreement with the measured scattering than predictions based on a one-layer model in which the scattering is due to two smooth interfaces separated by a homogeneous, weakly scattering, fluid layer. Over the frequency range of interest, inclusion of the actual density and sound speed profiles decreases the predicted scattering by approximately 25 dB compared to a one-layer scattering model. The model developed here has illustrated that the scattering from the double-diffusive interface is sensitive to both the interface thickness and the exact shape of the density and sound speed profiles, for individual realizations.

A remote-sensing technique that could be used to map the extent of oceanic double diffusion, the evolution of multiple double-diffusive layers, and the thickness of such layers could lead to an increased understanding of the importance of double diffusion to oceanic mixing. However, it is unclear from the results of this study if the measurements of broadband acoustic scattering from laboratory generated double-diffusive microstructure can be extended to realistic oceanic double diffusion. Though the density ratio used in this study is typical of that found in oceanic double diffusion (almost by definition), the temperature and salinity gradients in the laboratory are significantly larger than those seen in typical oceanic double-diffusive thermohaline staircases. Thus, though the measurements performed in this study show promise, further work is needed to determine if high-frequency broadband acoustic scattering techniques are a viable remote sensing tool for studying the diffusive regime of oceanic double diffusion.

ACKNOWLEDGMENTS

The authors gratefully acknowledge the help received from Ray Schmitt throughout the experiments and from Gonzaloo Feijoo for conversations regarding the development of the scattering model for double diffusion. The authors also thank Joe Warren for initiating this project, and David Wellwood and David Stuebe for assistance with the development of the shadowgraph system and the setup of the

double-diffusive interfaces. Funding for this project was provided by the Ocean Acoustics program at the Office of Naval Research and by the Woods Hole Oceanographic Institution Cecil and Ida Greene Technology Award. Tetjana Ross was supported by the WHOI Postdoctoral Scholarship through the generous support of the Doherty Foundation.

Beckmann, P., and Spizzichino, A. (**1963**). *The Scattering of Electromagnetic Waves from Rough Surfaces* (MacMillan, New York).

Brekhovskikh, L. M., and Lysanov, Y. P. (**2001**). *Fundamentals of Ocean Acoustics*, AIP Series in Modern Acoustics and Signal Processing (AIP, Springer-Verlag, New York).

Chu, D., and Stanton, T. K. (**1998**). "Application of pulse compression techniques to broadband acoustic scattering by live individual zooplankton," J. Acoust. Soc. Am. **104**, 39–55.

DiPerna, D. T., and Stanton, T. K. (**1991**). "Fresnel zone effects in the scattering of sound by cylinders of various lengths," J. Acoust. Soc. Am. **90**, 3348–3355.

Eckart, C. (**1953**). "The scattering of sound from the sea surface," J. Acoust. Soc. Am. **25**, 566–570.

Farmer, D. M., and Armi, L. (**1999**). "Stratified flow over topography: the role of small scale entrainment and mixing in flow establishment," Proc. R. Soc. London, Ser. A **455**, 3221–3258.

Fofonoff, P., and Millard, R. C., Jr. (**1983**). "Algorithms for computation of fundamental properties of seawater, 1983," UNESCO Tech. Pap. in Mar. Sci. **44**, 53.

Foote, K. G. (**1991**). "Acoustic sampling volume," J. Acoust. Soc. Am. **90**, 959–964.

Foote, K. G., and MacLennan, D. N. (**1984**). "Comparison of copper and tungsten carbiude calibration spheres," J. Acoust. Soc. Am. **75**, 612–616.

Goodman, L. (**1990**). "Acoustic scattering from oceanic microstructure," J. Geophys. Res. **95**, 11557–11573.

Goodman, L., Oeschger, J., and Szargowicz, D. (**1992**). "Ocean acoustics turbulence study: acoustic scattering from an axisymmetric plume," J. Acoust. Soc. Am. **91**, 3212–3227.

Gupta, R. N. (**1966**). "Reflection of sound waves from transition layers," J. Acoust. Soc. Am. **39**, 255–260.

Holbrook, S. W., Paramo, P., Pearse, S., and Schmitt, R. W. (**2003**). "Thermohaline fine structure in an oceanographic front from seismic reflection profiling," Science **301**, 821–824.

Horton, C. W., Mitchell, S. K., and Barnard, G. R. (**1967**). "Model studies of the scattering of acoustic waves from a rough surface," J. Acoust. Soc. Am. **41**, 635–643.

Horton, C. W., and Melton, D. R. (**1970**). "Importance of the Fresnel correction in scattering from a rough surface. II. Scattering coefficient," J. Acoust. Soc. Am. **47**, 299–303.

Ivakin, A. N. (**1997**). "A unified approach to volume and roughness scattering," J. Acoust. Soc. Am. **103**, 827–837.

Kelley, D. E., Fernando, H. J. S., Gargett, A. E., Tanny, J., and Ozsoy, E. (**2003**). "The diffusive regime of double-diffusive convection," Prog. Oceanogr. **56**, 461–481.

Lavery, A. C., Schmitt, R. W., and Stanton, T. K. (**2003**). "High-frequency acoustic scattering from turbulent oceanic microstructure: the importance of density fluctuations," J. Acoust. Soc. Am. **114**, 2685–2697.

Lavery, A. C., Wiebe, P. H., Stanton, T. K., Lawson, G. L., Benfield, M. C., and Copley, N. (**2007**). "Determining dominant scatterers of sound in mixed zooplankton populations," J. Acoust. Soc. Am. (accepted).

McDougall, T. J. (**1981**). "Double-diffusive convection with a nonlinear equation of state. II. Laboratory experiments and their interpretation," Prog. Oceanogr. **10**, 91–121.

Medwin, H., and Novarini, J. C. (**1981**). "Backscattering strength and the range dependence of sound scattered from the ocean surface," J. Acoust. Soc. Am. **69**, 108–111.

Mellberg, L. E., Johannessen, O. M., and Lee, O. S. (**1974**). "Acoustic effect caused by a deep thermohaline stepped structure in the Mediterranean Sea," J. Acoust. Soc. Am. **55**, 1081–1083.

Mellberg, L. E., and Johannessen, O. M. (**1972**). "Layered oceanic microstructure—it's effect on sound propagation," J. Acoust. Soc. Am. **53**, 571–580.

Moum, J. N., Farmer, D. M., Smyth, W. D., Armi, L., and Vagle, S. (**2003**). "Structure and generation of turbulence at interfaces strained by internal solitary waves propagating shoreward over the continental shelf," J. Phys. Oceanogr. **33**, 2093–2112.

Muench, R. D., Fernando, H. J. S., and Stegen, G. R. (**1990**). "Temperature and salinity staircases in the northwestern Weddell sea," J. Phys. Oceanogr. **20**, 295–306.

Neal, V. T., Neshyba, S., and Denner, W. (**1969**). "Thermal stratification in the Arctic Ocean," Science **166**, 373–374.

Oeschger, J., and Goodman, L. (**1996**). "Acoustic scattering from a thermally driven buoyant plume," J. Acoust. Soc. Am. **100**, 1451–1462.

Oeschger, J., and Goodman, L. (**2003**). "Acoustic scattering from a thermally driven buoyant plume revisited," J. Acoust. Soc. Am. **100**, 1451–1462.

Pace, N. G., Al-Hamdani, Z. K. S., and Thorne, P. D. (**1985**). "The range dependence of normal incidence acoustic backscatter from a rough interface," J. Acoust. Soc. Am. **77**, 101–112.

Proni, J. R., and Apel, J. R. (**1975**). "On the use of high-frequency acoustics for the study of internal waves and microstructure," J. Geophys. Res. **80**, 1147–1151.

Robins, A. J. (**1990**). "Reflection of plane acoustic waves from a layer of varying density." J. Acoust. Soc. Am. **89**, 1546–1552.

Robins, A. J. (**1991**). "Reflection of a plane wave from a fluid layer with continuously varying density and sound speed." J. Acoust. Soc. Am. **89**, 1686–1696.

Ross, T., and Lueck, R. (**2003**). "Sound scattering from oceanic turbulence," Geophys. Res. Lett. **30**, 1344.

Schmitt, R. W., Millard, R. C., Toole, J. M., and Wellwood, W. D. (**2005**). "A doubly-diffusive interface tank for dynamic-response studies," J. Mar. Res. **63**, 263–289.

Schmitt, R. W. (**1994**). "Double diffusion in oceanography," Annu. Rev. Fluid Mech. **26**, 255–285.

Seim, H. E., Gregg, M. C., and Miyamoto, R. T. (**1995**). "Acoustic backscatter from turbulent microstructure," J. Atmos. Ocean. Technol. **12**, 367–380.

Seim, H. E. (**1999**). "Acoustic backscatter from salinity microstructure," J. Atmos. Ocean. Technol. **16**, 1491–1498.

Stanton, T. K., Chu, D., Wiebe, P. H., Martin, L. V., and Eastwood, R. L. (**1998**). "Sound scattering by several zooplankton groups. I. Experimental determination of dominant scattering mechanisms," J. Acoust. Soc. Am. **103**, 225–235.

Stanton, T. K., Wiebe, P. H., Chu, D., and Goodman, L. (**1994**). "Acoustic characterization and discrimination of marine zooplankton and turbulence," ICES J. Mar. Sci. **51**, 469–479.

Turner, J. S. (**1973**). *Buoyancy Effects in Fluids* (Cambridge Univ. Press, Cambridge, UK).

Warren, J. D., Stanton, T. K., Wiebe, P. H., and Seim, H. E. (**2003**). "Inference of biological and physical parameters in an internal wave using multiple-frequency acoustic scattering data," ICES J. Mar. Sci. **60**, 1033–1046.

Williams, A. J. (**1975**). "Images of ocean microstructure," Deep-Sea Res. **22**, 811–829.

High-frequency diffraction corrections to backscattering cross sections from a rough three-dimensional surface

Iosif Fuks[a)]
Zel Technologies, LLC and NOAA/Earth System Research Laboratory, 325 Broadway, R/PSD-99, Boulder, Colorado 80305

(Received 2 March 2007; revised 12 June 2007; accepted 15 June 2007)

Diffraction corrections to scalar wave fields at perfectly free and rigid rough surfaces were derived by two iterations of the corresponding integral equations. These diffraction corrections to the pressure or normal velocity (which, in the geometrical optics limit, are doubled at perfectly rigid and free surfaces, respectively) were obtained with an accuracy of $\sim 1/k^2$, where k is the wave number of incidence radiation. Based on these corrections to the surface fields, the backscattering cross sections at normal incidence from the statistically rough Gaussian surfaces were derived. It was found that for the gentle roughness, diffraction results in effective "smoothing" of roughness for rigid and free surfaces and increasing of the backscattering cross sections, but for a rigid surface with steep roughness, the "fictitious" surface can be more rough than the real one, and the diffraction corrections become negative. © *2007 Acoustical Society of America.* [DOI: 10.1121/1.2756794]

PACS number(s): 43.30.Hw, 43.20.El, 43.20.Fn, 43.60.Cg [SLB] Pages: 1463–1471

I. INTRODUCTION

The problem of wave diffraction has an important place in general acoustics and its numerous applications, e.g., Pierce[1] and Brekhovskikh and Lysanov.[2] Progress in the application of numerical methods and computer simulation for solving the diffraction problem (e.g., Jensen *et al.*,[3] Tsang *et al.*,[4] and Warnic and Chew[5]) does not diminish the actuality of obtaining results in analytical form: At higher frequencies, more discretization points are needed, and the cost of computing increases dramatically. The analytical results play a valuable role as tests for existing and developing computer codes, and for on-line analysis and predictions of the role of diffraction effects in various physical phenomena as well as in operative problem solving in engineering.

For simply shaped bodies, when the separation of variables in the Helmholtz equation is possible, the exact solution of the diffraction problem can be represented as an expansion on the infinite series of eigenfunctions of the Helmholtz equation (see, e.g., Morse and Feshbach[6]). However, the number of body shapes for which the exact solutions are known is limited only by a few cases (see, e.g., Bowman *et al.*[7]), and in a general case, only some approximate methods can be used for this problem solving.

One of the most powerful methods (Geometrical Theory of Diffraction) of high-frequency asymptotic solving of the general diffraction problem was suggested and developed in the set of fundamental papers by Keller *et al.*[8,9] (see also Refs. 10–12 and references cited therein). In the framework of this method, the asymptotic solution for the diffracted wave can be found by solving the set of so called, "transport equations" for the coefficients of expansion of the wave amplitude and phase in an asymptotic series of inverse powers of the wave number k. In principle, having the set of the recursive equations, it is possible to obtain the coefficients of terms $\sim 1/k^n$ of any order of n. But in practice, this program can be realized in full only in a few simple cases: The resulting equations in a general case are so cumbersome that it is impossible to obtain any result in the explicit form, even for the first corrections $\sim 1/k$ to the geometrical optics (GO) formulas. Only for a relatively simple case of body of revolution and only the first correction $(\sim 1/k)$ to the GO result was obtained by Schensted[13] in the explicit analytical form. It had such a cumbersome appearance [see also Eq. (I.122) in Ref. 7] that the next coefficient for the term of order of $\sim 1/k^2$ was not obtained until now. Moreover, it has taken 20 years (see Ref. 14) to discover some errors in Ref. 13, where this result was first published.

In application to the high-frequency scattering problems, the most utilized and productive analytical method is the so-called Kirchhoff approximation, or tangent plane method (see details in Refs. 15–17). In this method, the wave field and its normal derivative on the surface are assumed to be the same as at the tangent plane to the surface at every point. Strictly speaking, it is true only in the GO limit for the infinitesimal wavelength of a diffracted field, and only in the case when shadowing and multiple scattering effects can be neglected. For the decades that have passed since this method was primarily introduced by Brekhovskikh,[18] and was extended to the statistically rough surfaces by Isakovich,[19] there were several attempts made to improve this method, and in particular, to obtain corrections to the surface fields due to the local surface curvature (the history of these efforts can be found in the review of Elfouhaily and Guérin[20]). Apparently, Lynch[21] was the first to obtain the first-order corrections $(\sim 1/k)$ to the surface fields caused by local surface curvature in the special case of a two-dimensional 2D (cylindrical) acoustically perfectly soft surface of a general shape. Note that to obtain the diffraction corrections to the wave amplitude at the surface, it is necessary to obtain terms of the order of $1/k^2$ in the field asymptotic expansion: The first term $(\sim 1/k)$ is orthogonal to

[a)]Electronic mail: iosif.fuks@noaa.gov

the zero-order (GO) field and gives diffraction correction only to the field phase. More general results for a three-dimensional (3D) surface were obtained by Rodrígues[22,23] in the framework of the small momentum transfer equation method, which is applicable only for rough surfaces with extremely small slopes.

In Elfouhaily *et al.*[24–27] an approach based on the approximate solutions of an integral equation for surface fields and their derivatives is developed, which has the main goal of connecting the classical low- and high-frequency asymptotic methods. It was shown that the low-frequency results of the small perturbation method (and its numerous modifications, including the small-slope approximation,[17] the tilt-invariant approximation,[28] etc.) as well as the high-frequency equations given by the Kirchhoff approximation, can be obtained as iterations of the unified general integral equation, if one takes into account not only the local surface slopes but also the surface curvature. In the framework of this approach, the Kirchhoff approximation for the surface field is the result of the first iteration of the integral equation. The second and higher iterations give the diffraction corrections to the tangent plane method results, which are limited only by the case of small momentum transfer, i.e., they are applicable to rough surfaces with extremely small slopes.

In this paper, we obtain the diffraction corrections up to terms of $\sim 1/k^2$ to the GO values of wave fields directly at 3D arbitrarily shaped smooth curved surfaces of two limiting types: perfectly rigid (hard) and perfectly free (soft). The paper is organized as follows. In Sec. II, we introduce notations and integral equations for the surface pressure and its normal derivative (at rigid and free surfaces, respectively). In Sec. III, the general form of diffraction corrections to the GO results was obtained by successive iterations of the corresponding integral equations with accuracy of up to $1/k^2$. These expansions are used in Sec. IV to derive the diffraction corrections to GO backscattering cross sections from a statistically rough Gaussian surface using the Huygens-Kirchhoff principle. In Sec. V, a summary of the most significant results is presented.

II. INTEGRAL EQUATIONS FOR SURFACE FIELDS

Hereinafter, we consider scattering of the monochromatic scalar wave (potential of velocity in acoustics) of frequency ω, with the phase factor $\exp(-i\omega t)$ omitted. We represent the incident plane wave in the form $U=U_0\exp(i\mathbf{kR})$, where U is the potential of velocity, $\mathbf{k}$ is the wave vector, $k=\omega/c$ is the wave number, $\mathbf{R}$ is the radius vector in 3D space, and c is the wave propagation velocity.

The potentials of velocities, U_f^{sc} and U_r^{sc}, in an arbitrary point $\mathbf{R}$ for wave fields scattered by a perfectly free or perfectly rigid surface S, respectively, can be represented as surface integrals according to the Huygens-Kirchhoff principle:

$$U_f^{\mathrm{sc}}(\mathbf{R}) = -\int_S \frac{\partial U_f(\mathbf{r})}{\partial n} G_0(\mathbf{R},\mathbf{r})d\mathbf{r}, \tag{1}$$

$$U_r^{\mathrm{sc}}(\mathbf{R}) = \int_S U_r(\mathbf{r}) \frac{\partial}{\partial n} G_0(\mathbf{R},\mathbf{r})d\mathbf{r}, \tag{2}$$

where $G_0(\mathbf{R},\mathbf{r})$ is the Green function of the Helmholtz equation for a free space,

$$G_0(\mathbf{R},\mathbf{r}) = \frac{1}{4\pi|\mathbf{R}-\mathbf{r}|} = e^{ik|\mathbf{R}-\mathbf{r}|}, \tag{3}$$

and $\partial/\partial n$ implies the derivative along the normal $\mathbf{n}$ to the surface S at the point of integration $\mathbf{r}\subset S$. The potential $U_r(\mathbf{r})$ and its normal derivative $\partial U_f(\mathbf{r})/\partial n$ at a perfectly rigid or perfectly free surface $\mathbf{r}\subset S$, respectively, satisfy the integral equations:

$$\frac{\partial U_f(\mathbf{r})}{\partial n} = 2\frac{\partial U_0(\mathbf{r})}{\partial n} - 2\int_S \frac{\partial U_f(\mathbf{r}')}{\partial n'} \frac{\partial}{\partial n} G_0(\mathbf{r},\mathbf{r}')d\mathbf{r}', \tag{4}$$

$$U_r(\mathbf{r}) = 2U_0(\mathbf{r}) + 2\int_S U_r(\mathbf{r}') \frac{\partial}{\partial n'} G_0(\mathbf{r},\mathbf{r}')d\mathbf{r}'. \tag{5}$$

Instead of $\partial U_f(\mathbf{r})/\partial n$ and $U_r(\mathbf{r})$, let us introduce two new functions, u_f and u_r, such that

$$\frac{\partial U_f(\mathbf{r})}{\partial n} = i(\mathbf{k}\cdot\mathbf{n})u_f(\mathbf{r})e^{i\mathbf{kr}}, \tag{6}$$

$$U_r(\mathbf{r}) = u_r(\mathbf{r})e^{i\mathbf{kr}}, \tag{7}$$

and the new variable of integration $\boldsymbol{\rho}=\mathbf{r}'-\mathbf{r}$ in Eqs. (4) and (5). Assuming that the incident wave U has the unit amplitude, i.e., $U=\exp(i\mathbf{kR})$, we obtain, instead of Eqs. (4) and (5):

$$u_f(\mathbf{r}) = 2 + \frac{1}{2\pi}\int_S u_f(\mathbf{r}+\boldsymbol{\rho}) \frac{(\boldsymbol{\rho}\cdot\mathbf{n})}{\rho^3} \frac{(\mathbf{k}\cdot\mathbf{n}')}{(\mathbf{k}\cdot\mathbf{n})} \times (ik\rho - 1)e^{i(k\rho+\mathbf{k}\boldsymbol{\rho})}d\boldsymbol{\rho}, \tag{8}$$

$$u_r(\mathbf{r}) = 2 + \frac{1}{2\pi}\int_S u_r(\mathbf{r}+\boldsymbol{\rho}) \frac{(\boldsymbol{\rho}\cdot\mathbf{n}')}{\rho^3} \times (ik\rho - 1)e^{i(k\rho+\mathbf{k}\boldsymbol{\rho})}d\boldsymbol{\rho}, \tag{9}$$

where $\mathbf{n}=\mathbf{n}(\mathbf{r})$ and $\mathbf{n}'=\mathbf{n}(\mathbf{r}+\boldsymbol{\rho})$ are the unit vectors normal to the surface at points $\mathbf{r}$ and $\mathbf{r}'=\mathbf{r}+\boldsymbol{\rho}$, respectively.

We introduce the local Cartesian frame of reference $(\xi\eta\zeta)$ in every point $\mathbf{r}$ of surface S, with the point of origin O in $\mathbf{r}\subset S$, axis $O\zeta$ directed along the normal $\mathbf{n}=\mathbf{n}(\mathbf{r})$, and axis $O\xi$ located in the plane of incidence, generated by vectors $\mathbf{k}$ and $\mathbf{n}$ (Fig. 1). In the vicinity of point $\mathbf{r}$, the surface S equation can be written in the form $\zeta=s(\boldsymbol{\rho}_\perp)$, where $\boldsymbol{\rho}_\perp=(\xi\eta)$ is the projection of $\boldsymbol{\rho}$ at the plane $\zeta=0$. In this frame of reference, we have

$$\mathbf{n}=\mathbf{e}_\zeta, \quad \mathbf{n}'=n'_\zeta(\mathbf{e}_\zeta-\mathbf{g}), \quad g=\boldsymbol{\nabla}s(\boldsymbol{\rho}_\perp), \quad n'_\zeta=1/\sqrt{1+\mathbf{g}^2}, \tag{10}$$

$$\rho=\sqrt{\boldsymbol{\rho}_\perp^2+s^2(\boldsymbol{\rho}_\perp)}, \quad \mathbf{k}=(k\sin\vartheta,0,-k\cos\vartheta), \tag{11}$$

where ϑ is a local angle of incidence. When $s(\boldsymbol{\rho}_\perp)=0$, the integral terms in Eqs. (8) and (9) vanish, and surface fields

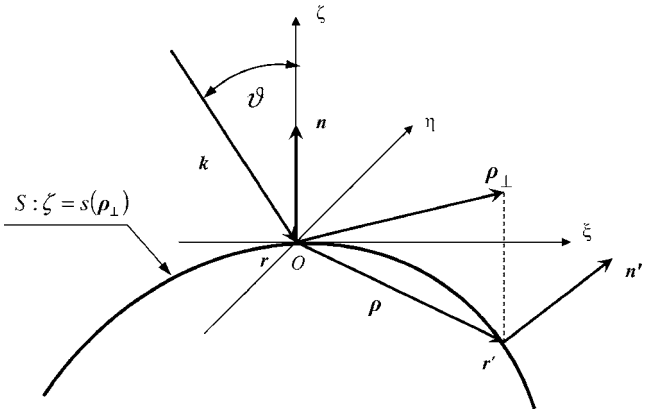

FIG. 1. Geometry of the problem in the local frame of reference (ξ, η, ζ).

take their GO values $u_f(\mathbf{r})=u_r(\mathbf{r})=2$. For a rough surface, these solutions correspond to the "local" GO limit, when all multiple reflections or shadowing can be neglected. To obtain the diffraction corrections to the local GO values $u_f(\mathbf{r})=2$ and $u_r(\mathbf{r})=2$ up to terms of $\sim 1/k^2$, caused only by the surface curvature in the vicinity of every point $\mathbf{r}\subset S$ (but not by multiple reflections or shadowing), we can use the following expansions:

$$\rho \approx \rho_\perp + \frac{s^2(\boldsymbol{\rho}_\perp)}{2\rho_\perp}, \quad e^{i\mathbf{k}\boldsymbol{\rho}} \approx e^{i\mathbf{k}_\perp\boldsymbol{\rho}_\perp}(1 - iks(\boldsymbol{\rho}_\perp)\cos\vartheta), \tag{12}$$

and confine ourselves to terms proportional to $s^2(\boldsymbol{\rho}_\perp)$ in the integral terms in Eqs. (8) and (9). This local expansion is limited by distances $\rho_\perp \lesssim a(ak)^{-1/3}$, where a is a characteristic curvature radius of the surface at the point $\mathbf{r}\subset S$ (e.g., Fok[29]). Substituting Eq. (12) into Eqs. (8) and (9), we obtain

$$u_f(\mathbf{r}) = 2 + \frac{1}{2\pi}\int u_f(\mathbf{r}+\boldsymbol{\rho})\exp[i(k_\perp\rho_\perp + \mathbf{k}_\perp\boldsymbol{\rho}_\perp)] \times \frac{(ik\rho_\perp - 1)}{\rho_\perp^3}\left[1 - iks(\boldsymbol{\rho}_\perp)\cos\vartheta + \tan\vartheta\frac{\partial s(\boldsymbol{\rho}_\perp)}{\partial\xi}\right]s(\boldsymbol{\rho}_\perp)d\xi d\eta, \tag{13}$$

$$u_r(\mathbf{r}) = 2 + \frac{1}{2\pi}\int u_r(\mathbf{r}+\boldsymbol{\rho})\exp[i(k_\perp\rho_\perp + \mathbf{k}_\perp\boldsymbol{\rho}_\perp)] \times \frac{(ik\rho_\perp - 1)}{\rho_\perp^3}[1 - iks(\boldsymbol{\rho}_\perp)\cos\vartheta] \times [s(\boldsymbol{\rho}_\perp) - \boldsymbol{\rho}_\perp\mathbf{g}(\boldsymbol{\rho}_\perp)]d\xi d\eta, \tag{14}$$

where $\rho_\perp=\sqrt{\xi^2+\eta^2}$, and integration is implied in the infinite limits over variables ξ and η.

III. FIELDS AT A ROUGH SURFACE

In the general case, we can represent $s(\boldsymbol{\rho}_\perp)$ in the vicinity of every point $\mathbf{r}\subset S$ as an expansion in double Taylor series on local coordinates ξ and η, and to obtain the corrections up to $\sim 1/k^2$, it is enough to confine this expansion only to the third-order terms:

$$s(\boldsymbol{\rho}_\perp) \approx \tfrac{1}{2}(s_{\xi\xi}\xi^2 + 2s_{\xi\eta}\xi\eta + s_{\eta\eta}\eta^2) + \tfrac{1}{6}(s_{\xi\xi\xi}\xi^3 + 3s_{\xi\xi\eta}\xi^2\eta + 3s_{\xi\eta\eta}\xi\eta^2 + s_{\eta\eta\eta}\eta^3), \tag{15}$$

where the evident notations are used: $s_{\xi\xi}\equiv\partial^2 s/\partial\xi^2$, $s_{\xi\eta}\equiv\partial^2 s/\partial\xi\partial\eta$, $s_{\xi\eta\eta}\equiv\partial^2 s/\partial\xi\partial\eta^2$, etc.

In dimensionless variables $\mathbf{p}=k\mathbf{r}$, $\mathbf{t}=k\boldsymbol{\rho}$, after transition to integration over the polar coordinates $t=|\mathbf{t}|$ and φ, where φ is the angle between the vector $\mathbf{t}$ and axis $O\xi$, integral equation (13) can be written in the following form:

$$u_f(\mathbf{p}) = 2 + \frac{1}{4\pi}\int_0^\infty dt\int_0^{2\pi} d\varphi u_f(\mathbf{p}+\mathbf{t}) \times [Y_{f1}(t,\varphi) + Y_{f2}(t,\varphi) + Y_{f3}(t,\varphi)], \tag{16}$$

where kernels $Y_{fm}(t,\varphi)$, $m=1, 2, 3$ have the following appearance:

$$Y_{f1}(t,\varphi) = \frac{1}{k}(s_{\xi\xi}\cos^2\varphi + 2s_{\xi\eta}\cos\varphi\sin\varphi + s_{\eta\eta}\sin^2\varphi) \times (it-1)e^{it(1+\sin\vartheta\cos\varphi)}, \tag{17}$$

$$Y_{f2}(t,\varphi) = \frac{1}{k}Y_{f1}(t,\varphi)\left[t\tan\vartheta(s_{\xi\xi}\cos\varphi + s_{\xi\eta}\sin\varphi) - \frac{i}{2}t^2\cos\vartheta(s_{\xi\xi}\cos^2\varphi + 2s_{\xi\eta}\cos\varphi\sin\varphi + s_{\eta\eta}\sin^2\varphi)\right], \tag{18}$$

$$Y_{f3}(t,\varphi) = \frac{t\cos\varphi}{3k^2}(s_{\xi\xi\xi}\cos^2\varphi + 3s_{\xi\eta\eta}\sin^2\varphi)t(it-1) \times e^{it(1+\sin\vartheta\cos\varphi)}. \tag{19}$$

For $u_r(\mathbf{p})$, integral equation (14) acquires the same structure as Eq. (16), but with slightly different kernels:

$$Y_{r1}(t,\varphi) = Y_{f1}(t,\varphi), \quad Y_{r3}(t,\varphi) = 2Y_{f3}(t,\varphi), \tag{20}$$

$$Y_{r2}(t,\varphi) = -\frac{i}{2k}Y_{r1}(t,\varphi)t^2\cos\vartheta \times (s_{\xi\xi\xi}\cos^2\varphi + 2s_{\xi\eta}\cos\varphi\sin\varphi + s_{\eta\eta}\sin^2\varphi). \tag{21}$$

After two successive iterations of the integral equations (16) [and a similar equation for $u_r(\mathbf{r})$], we obtain

$$\begin{matrix} u_f(\mathbf{r}) \\ u_r(\mathbf{r}) \end{matrix} = 2\left\{1 \mp \frac{i}{2k\cos^3\vartheta}(2\mathcal{H}\cos^2\vartheta + s_{\xi\xi}\sin^2\vartheta) \mp \frac{1}{k^2\cos^4\vartheta}\mathcal{K} \pm \frac{\delta_{f,r}}{k^2\cos^6\vartheta} \times \left[2\mathcal{H}^2\cos^4\vartheta + (5\mathcal{H}-\mathcal{K})\cos^2\vartheta\sin^2\vartheta - \frac{1}{4}\sin 2\vartheta\frac{\partial}{\partial\xi}(2\mathcal{H}\cos^2\vartheta + s_{\xi\xi}\sin^2\vartheta)\right]\right\}. \tag{22}$$

Here, $\delta_f=1$, $\delta_r=2$, $\mathcal{H}$ is a mean curvature:

$$\mathcal{H} = \tfrac{1}{2}(s_{\xi\xi} + s_{\eta\eta}), \tag{23}$$

and $\mathcal{K}$ is a Gaussian (total) surface curvature at the point $\mathbf{r} \subset S$:

$$\mathcal{K} = s_{\xi\xi}s_{\eta\eta} - s_{\xi\eta}^2. \tag{24}$$

The first term in Eq. (22) corresponds to the GO solution, and the second term $(\sim 1/k)$ coincides with the result obtained by Rodrígues[22] [see Eq. (31) there]. As was mentioned earlier, taking into account the second-order terms $(\sim 1/k^2)$, along with the first-order ones, is necessary to obtain the first nonvanishing diffraction corrections to amplitude of the scattered fields, which have the order of magnitude $\sim 1/k^2$.

Note that in Eq. (22) the diffraction corrections to the local GO values $(u_f = u_r = 2)$ of the surface fields are expressed through the invariant surface parameters: $\mathcal{H}$, $\mathcal{K}$ and the curvature $s_{\xi\xi}$ of the normal cross section of the surface S by the plane of incidence $\xi O\zeta$.

In the limiting case of a 2D surface $\zeta = s(\xi)$ (i.e., for a cylindrical surface with a generatrix along the axis $O\eta$), from Eq. (22) it follows that

$$\begin{matrix} u_f(\mathbf{r}) \\ u_r(\mathbf{r}) \end{matrix} = 2\left\{1 \mp \frac{i}{2k\cos^3\vartheta}s_{\xi\xi} \pm \frac{\delta_{f,r}}{2k^2\cos^6\vartheta} \times\left[(1+3\sin^2\vartheta)s_{\xi\xi}^2 - \tfrac{1}{2}\sin 2\vartheta s_{\xi\xi\xi}\right]\right\}. \tag{25}$$

This result coincides with Eq. (21) obtained by Fuks.[30] Note that in Eq. (21) in Ref. 30, the last term proportional to $\sin\vartheta/bk^2$ erroneously contains the extra factor "2." At normal incidence, when $\vartheta = 0$, Eq. (22) takes the simple form:

$$\begin{matrix} u_f(\mathbf{r}) \\ u_r(\mathbf{r}) \end{matrix} = 2\left[1 \mp \frac{i}{k}\mathcal{H} \mp \frac{1}{k^2}(\mathcal{K} - 2\delta_{f,r}\mathcal{H}^2)\right]. \tag{26}$$

The second (imaginary) terms in Eqs. (22), (25), and (26) correspond to diffraction corrections to surface field phases. It is seen that they have the opposite signs for pressure-free (f) and rigid (r) surfaces. In particular, from Eq. (26) it follows that at normal incidence, the diffraction correction to the field phase at a free surface is positive for "convex" surface points (where $\mathcal{H} < 0$) and negative for "concave" points (where $\mathcal{H} > 0$), and vice versa for a rigid surface. Because the field phase shift from its GO value can be interpreted as the displacement of the position of surface point $\mathbf{r} \subset S$, we can conclude that for a free surface, diffraction results in displacement of the real convex points $\mathbf{r} \subset S$ to the fictitious ones *inside* the surface, and for concave points, *outside* the surface. For a perfectly rigid surface, these displacements have opposite signs in comparison with a free surface. For 2D surfaces, these facts were mentioned in Ref. 31 (see Fig. 2 therein). It is easy to conclude that when generated in this way, the fictitious surface is gentler than the real free surface, and it is steeper than the real rigid surface. In particular, this can result in increasing the backscattering cross section at normal incidence for the free surface and decreasing it for the rigid one, when the main contribution to backscattering is given by reflection from surface extrema.

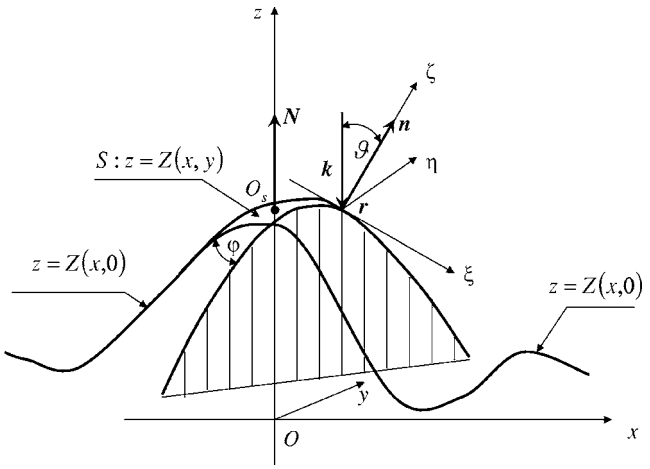

FIG. 2. Geometry of the problem in the main frame of reference (x,y,z).

IV. BACKSCATTERING CROSS SECTIONS AT NORMAL INCIDENCE

The general equations obtained [Eq. (22)] provide the diffraction corrections caused by surface local curvatures to the wave fields immediately at surface points $\mathbf{r} \subset S$. Substitution of Eqs. (6) and (7) into the surface integrals (1) and (2), with $u_f(\mathbf{r})$ and $u_r(\mathbf{r})$ given by Eq. (22), allows us to solve a wide range of problems concerning diffraction by smooth surfaces when multiple scattering and shadowing can be neglected and the main contribution to the scattered wave is given by the specular reflecting points. In particular, it is possible to obtain the diffraction corrections to the GO fields scattered by a solitary specular point, as was done in Refs. 30–33 for 2D (i.e., cylindrical) surfaces.

In this section, we apply the result (22) to the problem of sound backscattering from a statistically rough surface at normal incidence. In the main ("laboratory") frame of reference (x,y,z), the surface S is given by the equation $z = Z(x,y)$, and the incident wave propagating in the negative direction of the axis Oz with wave vector $\mathbf{k} = (0,0,-k)$ (see Fig. 2) has the form $U = e^{-ikz}$. Taking into account the definitions of $u_f(\mathbf{r})$ and $u_r(\mathbf{r})$ introduced in Eqs. (6) and (7), for fields backscattered in the far zone (at distance R from the surface satisfying the inequality $R \gg \sqrt{L/k}$, where L is the maximum linear size of the surface S in the plane $z = 0$), from Eqs. (1) and (2) we obtain

$$U_{f,r}^{\mathrm{sc}}(\mathbf{R}) = \frac{ik}{4\pi R}e^{ikR}\int_{s_0} u_{f,r}(\mathbf{r})e^{-2ikZ(\mathbf{r})}d\mathbf{r}, \tag{27}$$

where integration is performed over the projection S_0 of surface S onto plane $z = 0$, i.e., $d\mathbf{r} = dxdy$. Surface fields $u_f(\mathbf{r})$ and $u_r(\mathbf{r})$ given by Eq. (22) must be placed into the integrand in Eq. (27), written through the variables in the main frame of reference (x,y,z), where surface curvature invariants $\mathcal{H}$ and $\mathcal{K}$ have the following form:

$$\mathcal{H} = \frac{1}{2(1+\Gamma^2)^{3/2}}[Z_{xx}(1+\Gamma_y^2) - 2Z_{xy}\Gamma_x\Gamma_y + Z_{yy}(1+\Gamma_x^2)], \tag{28}$$

$$\mathcal{K} = \frac{1}{(1+\Gamma^2)^2}(Z_{xx}Z_{yy} - Z_{xy}^2). \tag{29}$$

Here, $\boldsymbol{\Gamma} = \nabla Z(\mathbf{r}) = (Z_x, Z_y)$ is the vector of surface slopes, and the following notations for partial derivatives are introduced: $Z_x = \partial Z/\partial x$, $Z_y = \partial Z/\partial y$, $Z_{xx} = \partial^2 Z/\partial x^2$, $Z_{xy} = \partial^2 Z/\partial x\,\partial y$, and $Z_{yy} = \partial^2 Z/\partial y^2$. The local incident angle ϑ in Eq. (22) is defined by the equation $\cos\vartheta = -\mathbf{k}\cdot\mathbf{n}/k$, where $\mathbf{k} = (0,0,-k)$ and $\mathbf{n}$ is a normal to the surface unit vector at the point of integration in Eq. (27):

$$\mathbf{n} = \frac{\mathbf{e}_z - \boldsymbol{\Gamma}}{\sqrt{1+\Gamma^2}}, \tag{30}$$

where $\mathbf{e}_z$ is a unit vector in the direction of the axis Oz. As to the curvature $s_{\xi\xi}$ of the normal section of surface S by the local plane of incidence generated by wave vector $\mathbf{k}$ and normal $\mathbf{n}$ (in Fig. 2 this plane is depicted by hatching), it must be expressed through derivatives of function $z = Z(x,y)$ over variables x and y, rather than through derivatives of function $\zeta = s(\xi,\eta)$ in the local frame of reference $(\xi\eta\zeta)$ at every point of the surface S, where axis $O\zeta$ is directed along the local normal $\mathbf{n}$, and axis $O\xi$ is tangent to the surface S in the local plane of incidence, and it belongs to the local plane of incidence.

Transition from the partial derivatives in the local frame of reference $(\xi\eta\zeta)$ to the main frame of reference (x,y,z) can be performed using

$$\xi = x\cos\vartheta\cos\varphi + y\cos\vartheta\sin\varphi - z\sin\vartheta, \tag{31}$$

$$\eta = -x\sin\varphi + y\cos\varphi, \tag{32}$$

$$\zeta = x\sin\vartheta\cos\varphi + y\sin\vartheta\sin\varphi + z\cos\vartheta, \tag{33}$$

where ϑ and φ are the angles that determine the direction of the normal $\mathbf{n}$:

$$n_x = \sin\vartheta\cos\varphi, \quad n_y = \sin\vartheta\sin\varphi, \quad n_z = \cos\vartheta. \tag{34}$$

Using Eqs. (31)–(33) and equations inverse to them:

$$x = \xi\cos\vartheta\cos\varphi - \eta\sin\varphi + \zeta\sin\vartheta\cos\varphi, \tag{35}$$

$$y = \xi\cos\vartheta\sin\varphi + \eta\cos\varphi + \zeta\sin\vartheta\sin\varphi, \tag{36}$$

$$z = -\xi\sin\vartheta + \zeta\cos\vartheta, \tag{37}$$

and taking into account that plane $(\xi\eta)$ is tangent to the surface S at every point $\mathbf{R}\subset S$, i.e., $s_\xi = s_\eta = 0$ at $\xi = \eta = 0$, which follows directly from Eq. (15), for $s_{\xi\xi}$ we obtain

$$s_{\xi\xi} = \cos^3\vartheta(Z_{xx}\cos^2\varphi + Z_{xy}\sin 2\varphi + Z_{yy}\sin^2\varphi). \tag{38}$$

From a comparison of Eqs. (34) and (30), the components of vector $\boldsymbol{\Gamma}$, it follows that

$$\Gamma_x = -\tan\vartheta\cos\varphi, \quad \Gamma_y = -\tan\vartheta\sin\varphi, \tag{39}$$

$$\cos\vartheta = 1/\sqrt{1+\Gamma^2}.$$

These equations allow us to express the trigonometric functions of angles ϑ and φ in Eq. (38) through surface slopes Γ_x and Γ_y and to rewrite Eq. (38) in the following form:

$$s_{\xi\xi} = \frac{1}{\Gamma^2(1+\Gamma^2)^{3/2}}(Z_{xx}\Gamma_x^2 + 2Z_{xy}\Gamma_x\Gamma_y + Z_{yy}\Gamma_y^2). \tag{40}$$

In the geometrical optics limit, backscattering (retroreflection) from a smooth surface S is caused only by the small vicinity of the specular points O_s (Fig. 2), where the direction $\mathbf{N}$ of normal-to-the-surface S is opposite to the direction of the wave vector $\mathbf{k}$ of the incident wave, i.e., $\vartheta = 0$. It allows us to put $\vartheta = 0$ in the second-order terms of $\sim 1/k^2$ in Eq. (22), and after substitution of the explicit expressions (28), (29), and (40) for curvatures $\mathcal{H}$, $\mathcal{K}$, and $s_{\xi\xi}$, respectively, we obtain the surface fields $u_f(\mathbf{r})$ and $u_r(\mathbf{r})$:

$$u_f(\mathbf{r}) = 2\left[1 - \frac{i}{2k}(Z_{xx}+Z_{yy}) + \frac{1}{2k^2}(Z_{xx}^2 + 2Z_{xy}^2 + Z_{yy}^2)\right], \tag{41}$$

$$u_r(\mathbf{r}) = 2\left[1 + \frac{i}{2k}(Z_{xx}+Z_{yy}) - \frac{1}{k^2}(Z_{xx}^2 + Z_{xy}^2 + Z_{xx}Z_{yy} + Z_{yy}^2)\right]. \tag{42}$$

For statistically rough surface $z = Z(\mathbf{r})$, the specific (from the unit area at plane $z=0$) backscattering cross sections $\sigma_{f,r}$ are introduced by

$$\sigma_{f,r} = 4\pi\frac{R^2}{S_0}\langle|U_{f,r}^{\mathrm{sc}}(\mathbf{R})|^2\rangle = \frac{k^2}{4\pi S_0}\int_{S_0} d\mathbf{r}\int_{S_0} d\mathbf{r}' \times \langle e^{2ik[Z(\mathbf{r}')-Z(\mathbf{r})]}u_{f,r}(\mathbf{r})u_{f,r}^*(\mathbf{r}')\rangle, \tag{43}$$

where $\langle\cdots\rangle$ means the statistical averaging over the ensemble of realizations of the random function $z = Z(\mathbf{r})$ of two variables $\mathbf{r} = (x,y)$. In the GO limit, when $u_r(\mathbf{r}) = u_f(\mathbf{r}) = 2$, from Eqs. (27) and (43) we obtain the following expression for the backscattering cross section σ_0, which is the same for both surfaces, perfectly free and perfectly rigid:

$$\sigma_0 = \frac{k_2}{\pi S_0}\int_{S_0} d\mathbf{r}\int_{S_0} d\mathbf{r}'\langle e^{2ik[Z(\mathbf{r}')-Z(\mathbf{r})]}\rangle. \tag{44}$$

Because in the GO limit $(k\to\infty)$, the fields scattered by spatially separated surface points $\mathbf{r}$ and $\mathbf{r}'$ are incoherent, only the small vicinity $\mathbf{r}'$ around point $\mathbf{r}$ is significant for integration in Eq. (44). For this reason, the difference $Z(\mathbf{r}') - Z(\mathbf{r})$ can be replaced by its expansion over $\boldsymbol{\rho} = \mathbf{r}' - \mathbf{r}$, and only the first term $Z(\mathbf{r}') - Z(\mathbf{r}) \approx \boldsymbol{\Gamma}(\mathbf{r})\boldsymbol{\rho}$ of this expansion can hold. After this, the integration over new variable $\boldsymbol{\rho}$ within infinite limits gives the δ function:

$$\int e^{2ik\boldsymbol{\Gamma}(\mathbf{r})\boldsymbol{\rho}}d\boldsymbol{\rho} = \frac{\pi^2}{k^2}\delta[\boldsymbol{\Gamma}(\mathbf{r})]. \tag{45}$$

Integration of Eq. (45) over the remaining variable $\mathbf{r}$ in Eq. (44) results in representation of σ_0 as a sum of contributions of separated specular points located at $\mathbf{r}_i$, where $\mathbf{r}_i$ is the full set of solutions of the equation $\boldsymbol{\Gamma}(\mathbf{r}) = 0$. The final result can be obtained by subsequent statistical averaging over the surface curvature parameters at the specular points

$\mathbf{r}_i$. The derivations can be significantly simplified if we change the order of integration over $\mathbf{r}$ and the statistical averaging.

For the statistically homogeneous surface $z=Z(\mathbf{r})$, the result of statistical averaging of $\delta[\mathbf{\Gamma}(\mathbf{r})]$ with the probability density function (PDF) of surface slopes $w(\mathbf{\Gamma})$ does not depend on the variable $\mathbf{r}$, and therefore the consequent elementary integration over $\mathbf{r}$ gives the value of area S_0. Thus, from Eq. (44) it results in the well-known expression (e.g., Eq. (20.38b) in Ref. 16) for a backscattering cross section from a statistically rough surface at normal incidence as follows:

$$\sigma_0 = \pi w(\mathbf{\Gamma})|_{\mathbf{\Gamma}=\mathbf{0}}. \tag{46}$$

To obtain the diffraction corrections to the GO backscattering cross section σ_0, it is necessary to keep more terms in the series expansion of $Z(\mathbf{r}')-Z(\mathbf{r})$ over the powers of the difference $\boldsymbol{\rho}=\mathbf{r}'-\mathbf{r}=(x,y)$ in Eq. (44):

$$e^{2ik[Z(\mathbf{r}')-Z(\mathbf{r})]} \approx e^{2ik\mathbf{\Gamma}(\mathbf{r})\boldsymbol{\rho}} \times \left[1 + ik(Z_{xx}x^2 + 2Z_{xy}xy + Z_{yy}y^2) + \frac{ik}{3}(Z_{xxx}x^3 + 3Z_{xxy}x^2y + 3Z_{xyy}xy^2 + Z_{yyy}y^3) - \frac{k^2}{2}(Z_{xx}x^2 + 2Z_{xy}xy + Z_{yy}y^2)^2\right], \tag{47}$$

implying that additional terms in square brackets are small in comparison with unity. This condition is equivalent to the inequality

$$|Z_iZ_j| \gg |Z_{ij}|/k, \quad i,j=x,y. \tag{48}$$

In the similar expansions of products $u_{f,r}(\mathbf{r})u^*_{f,r}(\mathbf{r}')$ in Eq. (43) in the series of powers of difference $\boldsymbol{\rho}=\mathbf{r}'-\mathbf{r}$, it is enough to confine ourselves to linear terms only:

$$u_f(\mathbf{r})u^*_f(\mathbf{r}') \approx 4\left\{1 + \frac{i}{2k}[(Z_{xxx}+Z_{xxy})x + (z_{xyy}+Z_{yyy})y] + \frac{1}{4k^2}[5(Z_{xx}^2+Z_{yy}^2) + 2Z_{xx}Z_{yy} + 8Z_{xy}^2]\right\}, \tag{49}$$

$$u_r(\mathbf{r})u^*_r(\mathbf{r}') \approx 4\left\{1 - \frac{i}{2k}[(Z_{xxx}+Z_{xxy})x + (Z_{xyy}+Z_{yyy})y] - \frac{1}{4k^2}[7(Z_{xx}^2+Z_{yy}^2) + 6Z_{xx}Z_{yy} + 8Z_{xy}^2]\right\}. \tag{50}$$

After substituting Eqs. (47)–(50) in Eq. (43), we obtain the expression for the integrand, which is a function of all partial derivatives of $Z(x,y)$ with respect to both variables x and y up to the third order.

Further derivations will be performed for a statistically homogeneous roughness $z=Z(\mathbf{r})$ with an autocorrelation function $C(\boldsymbol{\rho})=\langle Z(\mathbf{r})Z(\mathbf{r}+\boldsymbol{\rho})\rangle$ and Gaussian statistics. Because $C(\boldsymbol{\rho})$ is the even function, $C(-\boldsymbol{\rho})=C(\boldsymbol{\rho})$, the second derivatives Z_{pq}, $(p,q=x,y)$ do not correlate with slopes Z_x, Z_y and with the third derivatives Z_{pqm}, $(p,q,m=x,y)$ as well. Moreover, for the Gaussian surfaces they are statistically independent. It allows us to perform the statistical averaging over second derivatives Z_{pq} $(p,q=x,y)$ in Eq. (43) in an explicit form. The second statistical moments (variances) of Z_{pq} can be expressed through the fourth derivatives of $C(\boldsymbol{\rho})$ (e.g., Feller[34]):

$$\langle Z_{xx}^2\rangle \equiv h_{xx}^2 = C^{(4,0)}, \quad \langle Z_{yy}^2\rangle \equiv h_{yy}^2 = C^{(0,4)}, \tag{51}$$

$$\langle Z_{xy}^2\rangle = \langle Z_{xx}Z_{yy}\rangle \equiv h_{xy}^2 = C^{(2,2)}, \tag{52}$$

$$C^{(n,m)} \equiv \left.\frac{\partial^{n+m}}{\partial x^n\,\partial y^m}C(x,y)\right|_{x,y=0}. \tag{53}$$

The third derivatives Z_{pqm}, $(p,q,m=x,y)$ appear in the integrand in Eq. (43) only linearly, and averaging them with corresponding Gaussian conditional (with respect to slopes Γ_x, Γ_y) PDFs $W(Z_{pqm}|\Gamma_x,\Gamma_y)$ also can be easily performed:

$$\langle Z_{xxx}\rangle = -\Gamma_x\frac{h_{xx}^2}{h_x^2} - \Gamma_y\frac{C^{(3,1)}}{h_y^2}, \tag{54}$$

$$\langle Z_{yyy}\rangle = -\Gamma_x\frac{C^{(1,3)}}{h_y^2} - \Gamma_y\frac{h_{yy}^2}{h_y^2},$$

$$\langle Z_{xxy}\rangle = -\Gamma_x\frac{C^{(3,1)}}{h_x^2} - \Gamma_y\frac{h_{xy}^2}{h_y^2}, \tag{55}$$

$$\langle Z_{yyx}\rangle = -\Gamma_x\frac{h_{xy}^2}{h_x^2} - \Gamma_y\frac{C^{(1,3)}}{h_y^2},$$

where $h_x^2\equiv\langle\Gamma_x^2\rangle$ and $h_x^2\equiv\langle\Gamma_y^2\rangle$ are the surface slope variances. These equations are the particular cases of the general equation (6.10) in Ref. 34.

Integration in Eq. (43) over the difference $\boldsymbol{\rho}=\mathbf{r}'-\mathbf{r}$ is possible to perform within infinite limits, if the following inequalities hold:

$$h_x \gg \frac{1}{kL_x}, \quad h_y \gg \frac{1}{kL_y}, \tag{56}$$

where L_x and L_y are the linear sizes of the surface patch S_0 in Ox and Oy directions, respectively. These inequalities (56) have a simple geometrical meaning: The angular widths of the backscattering pattern (which are of the order of surface slope rms h_x and h_y) must exceed the angles of diffraction by the plane patch with linear sizes L_x and L_y: $1/kL_x$ and $1/kL_y$, respectively. Integration over $\boldsymbol{\rho}$ in Eq. (43) results in the appearance of δ functions and their derivatives $\delta^{(n)}$:

$$\int\int_{-\infty}^{\infty} e^{2ik(x\Gamma_x+y\Gamma_y)}x^ny^m\,dx\,dy = \frac{\pi^2}{k^2(2ik)^{n+m}}\delta^{(n)}(\Gamma_x)\delta^{(m)}(\Gamma_y). \tag{57}$$

The final statistical averaging can be performed by multiplying the integrand in Eq. (43) by the slope PDF $w(\Gamma_x,\Gamma_y)$

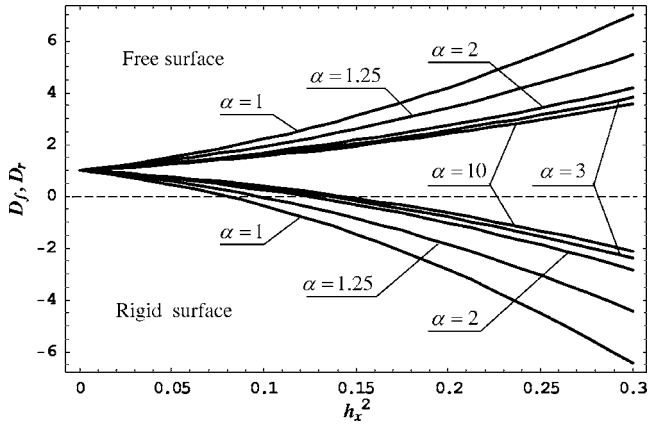

FIG. 3. Dependence of the diffraction correction factors on the roughness slope variance h_x^2 for the set of anisotropy coefficient α: D_f for a perfectly free surface (upper curves), and D_r for a perfectly rigid surface (lower curves). Plots for $\alpha=1$ correspond to the isotropic roughness.

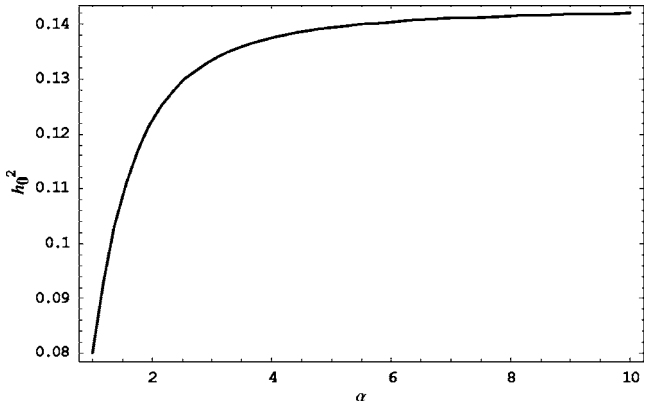

FIG. 4. Dependence of the critical slope variance h_0^2 (at which the diffraction correction to the backscattering cross section from a perfectly rigid surface changes its sign) on the value of the anisotropy coefficient α.

and by integrating over the random slopes Γ_x, Γ_y, which can be completed easily because of the presence of δ functions and their derivatives $\delta^{(n)}$ in the integrand:

$$\frac{\sigma_f}{\sigma_r}=\sigma_0\left\{1+\frac{1}{4k^2}\left[\frac{1}{8}\left(\frac{h_{xx}^2}{h_x^4}+2\frac{h_{xy}^2}{h_x^2h_y^2}+\frac{h_{yy}^2}{h_y^4}\right)\pm\left(\frac{h_{xx}^2+h_{xy}^2}{h_x^2}+\frac{h_{yy}^2+h_{xy}^2}{h_y^2}\right)\pm(6\mp1)(h_{xx}^2+2h_{xy}^2+h_{yy}^2)\right]\right\}. \tag{58}$$

Here, we took into account that at normal incidence, we can choose the reference frame xOy in such a way that slopes Γ_x and Γ_y do not correlate: $\langle\Gamma_x\Gamma_y\rangle=-C^{(1,1)}=0$. Note that the diffraction correction to σ_f is always positive, in contrast to the correction to σ_r, which is positive only for gentle roughness with small enough slope variances h_x^2, h_y^2, when the first term in the square brackets in Eq. (58) exceeds the second and the third terms.

For the specific case of a Gaussian autocorrelation function

$$C(\boldsymbol{\rho})=h^2\exp\left(-\frac{x^2}{l_x^2}-\frac{y^2}{l_y^2}\right), \tag{59}$$

backscattering cross sections (58) can be represented in the following form:

$$\sigma_{f,r}=\sigma_0\left[1+\frac{1}{4(kh)^2}D_{f,r}(\alpha,h_x)\right], \tag{60}$$

$$\frac{D_f(\alpha,h_x)}{D_r(\alpha,h_x)}=1\pm4\frac{1+\alpha^2}{\alpha^2}h_x^2\pm(6\mp1)\frac{3+2\alpha^2+3\alpha^4}{\alpha^4}h_x^4, \tag{61}$$

where $\alpha=l_y/l_x\geqslant1$ is the coefficient of anisotropy, and $h_x^2=2h^2/l_x^2$ is the variance of roughness slopes along the Ox direction. The dependence of functions D_f and D_r on the slope variance h_x^2 is depicted in Fig. 3 for the set of coefficients α. Actually, at $h=$const., the plots in Fig. 3 represent the dependence of diffraction corrections D_f and D_r on the maximal curvature variance $k_m^2\equiv h_{xx}^2=3h_x^4/h^2$ at surface extrema, rather than on the surface slope variance h_x^2. Diffraction correction to the backscattering cross-section σ_r from the rigid surface changes sign and becomes negative for steep roughness with $h_x^2\geqslant h_0^2$, where

$$h_0^2=\frac{\alpha^2}{2(1+\alpha^2)+\sqrt{25(1+\alpha^4)+22\alpha^2}}. \tag{62}$$

The dependence of the critical slope h_0^2 on the coefficient of anisotropy α is depicted in Fig. 4. For a statistically isotropic surface ($\alpha=1$), from Eq. (62) it follows that $h_0^2=(4+6\sqrt{2})^{-1}\simeq0.08$, and $h_0^2\approx1/7\simeq0.14$ for $\alpha>5$.

For 2D rough surface $z=Z(x)$, all terms in Eq. (58) containing y in their subscript turn to zero, and backscattering cross sections take the simple forms:

$$\frac{\sigma_f}{\sigma_r}=\sigma_0\left\{1+\frac{h_{xx}^2}{4k^2}\left[\frac{1}{8h_x^4}\pm\frac{1}{h_x^2}\pm(6\mp1)\right]\right\}. \tag{63}$$

Note that in the 2D case, σ_f corresponds to the backscattering cross section from a perfectly conducting surface of TE-polarized electromagnetic wave (HH—"horizontal" polarization in radio wave propagation applications, or s polarization in optics), and σ_r corresponds to TM-polarized wave (VV—"vertical" polarization in radio wave propagation applications, or p polarization in optics). The first term in the square brackets in Eq. (63), which is dominant for small slopes $h_x^2\ll1$, coincides with the correction to the GO result obtained in Lynch.[21]

In the opposite limiting case of statistically isotropic roughness, when $C(\boldsymbol{\rho})=C(\rho)$, from Eq. (58) it follows that

$$\frac{\sigma_f}{\sigma_r}=\sigma_0\left\{1+\frac{\Delta^2C}{4k^2}\left[\frac{1}{2(\Delta C)^2}\mp\frac{2}{\Delta C}\pm(6\mp1)\right]\right\}_{\rho=0}, \tag{64}$$

where Δ is the radial part of the Laplace operator in the cylindrical variables in plane (x,y):

$$\Delta=\frac{1}{\rho}\frac{\partial}{\partial\rho}\left(\rho\frac{\partial}{\partial\rho}\right), \tag{65}$$

and all derivatives in Eq. (64) refer to the point $\rho=0$. Note that $\Delta C|_{\rho=0}$ is negative, because $C(\rho)$ has the maximum in $\rho=0$, and its absolute value is equal to the surface roughness slope variance:

$$\langle(\nabla Z)^2\rangle = -\Delta C|_{\rho=0} \equiv \Gamma_0^2. \tag{66}$$

By substituting Eq. (66) into Eq. (64) and taking into account that $\Delta^2 C$ is positive (it is proportional to the variances of the surface second derivatives and in the Cartesian frame of reference has the form $\Delta^2 C = h_{xx}^2 + 2h_{xy}^2 + h_{yy}^2$), we find that the diffraction correction to σ_f is always positive, in contrast to the correction to σ_r, which is positive only for gentle roughness with small enough slope variance $\Gamma_0^2 < (2+3\sqrt{2})^{-1} \simeq 0.16$, and it is negative for more steep roughness.

For a specific form of the Gaussian autocorrelation function

$$C(\rho) = h^2 e^{-\rho^2/l^2}, \tag{67}$$

where $h^2 = \langle Z^2\rangle$ is the roughness height variance (with the assumption that $\langle Z\rangle = 0$) and l is a correlation radius (an effective roughness "horizontal length"), we can represent Eq. (64) in the following form:

$$\frac{\sigma_f}{\sigma_r} = \sigma_0 \left\{ 1 + \left[\frac{1}{4(kh)^2} \pm \frac{4}{(kl)^2} \pm \frac{(6 \mp 1)}{4(ka)^2} \right] \right\}. \tag{68}$$

Here, the characteristic roughness curvature radius a at the surface extrema, where specular points responsible for the backscattering at normal incidence are located, is introduced:

$$\frac{1}{a^2} \equiv \Delta^2 C = \frac{32h^2}{l^4}. \tag{69}$$

The first term in the square brackets in Eqs. (58), (64), and (68) is the same for both surfaces (free and rigid), because it is generated by the expansion (47) of the "propagation" exponent in the Huygens-Kirchhoff equation (27). It is not affected by the diffraction corrections to the surface fields $u_{f,r}(\mathbf{r})$, and therefore it can be interpreted as a result of the *interference* of scattered waves in the process of their propagation in space. The next two terms in corrections to GO backscattering cross sections have the opposite signs for free and rigid surfaces, and, as seen from Eq. (68), they are caused by *diffraction* at roughness characteristic length l and curvature a. It is necessary to emphasize that this qualitative consideration relates only to the specific form (67) of the autocorrelation function, when the ratio $\Delta^2 C/(\Delta C)^2_{\rho=0} = 2/h^2$ does not depend on the roughness correlation lengths and is determined only by the roughness height variance h^2.

V. CONCLUSIONS

By iteration of integral equations for wave fields at smooth perfectly free or rigid surfaces, we have derived explicit equations for high-frequency corrections (up to $\sim 1/k^2$) to GO surface values of fields caused by diffraction at *local* surface curvature, rather than by multiple scattering or shadowing. These corrections depend on four independent invariant parameters: the local incident angle ϑ, the mean, $\mathcal{H}$, and the Gaussian (total), $\mathcal{K}$ surface curvatures, and the curvature $s_{\xi\xi}$ of the surface cross section by the local plane of incidence. It was shown that diffraction corrections to surface field phases are functions of the mean surface curvature and the curvature of the normal surface cross section by the local plane of incidence. They do not depend on the Gaussian curvature and are of the first order of small parameter $1/k$; their absolute values are equal to each other, and they have the opposite signs for free and rigid surfaces.

As an application of these general results to the specific case, we obtained the diffraction corrections to GO backscattering cross sections from Gaussian statistically rough free and rigid surfaces at normal incidence ($\vartheta = 0$). The explicit expressions of these corrections depend on the variances of the first and second derivatives (i.e., slopes and curvatures) of the surface equation, which, for a statistically homogeneous surface, can be expressed through the second and fourth derivatives of the roughness autocorrelation function, respectively.

For the Gaussian PDF $w(\boldsymbol{\Gamma})$ of surface slopes $\boldsymbol{\Gamma} = \boldsymbol{\nabla} Z(\mathbf{r})$, the GO backscattering cross-section σ_0 from a statistically isotropic rough surface at normal incidence takes the form $\sigma_0 = 1/\Gamma_0^2$, where Γ_0^2 is the surface slope variance. The positive diffraction corrections to σ_0 can be interpreted as a decrease in slope variance, i.e., as "smoothing" of the surface roughness. It is seen that for a free surface, when the diffraction corrections are positive, diffraction results in effective smoothing of surface roughness. For a rigid surface and steep roughness $\Gamma_0^2 > 0.16$, diffraction results in the effective sharpening of surface roughness. The fact that diffraction corrections to GO backscattering cross section σ_r from a perfectly rigid surface turn to zero for some "critical" value $\Gamma_0^2 = 0.16$ of the roughness slope variance means that in this case, diffraction corrections are proportional to the higher than $1/k^2$ order of $1/k$, and the GO results are valid in a wider range of wavelengths and surface roughness parameters than they are in a general case.

ACKNOWLEDGMENTS

The author would like to thank Dr. Valery Zavorotny and Dr. Vladimir Irisov for fruitful discussions. The reviewers' and the associate editor's professional comments and suggestions are greatly appreciated.

[1] A. D. Pierce, *Acoustics* (Acoustical Society of America, New York, 1994).
[2] L. M. Brekhovskikh and Yu. P. Lysanov, *Fundamentals of Ocean Acoustics* (Springer, Berlin, 2003).
[3] F. B. Jensen, W. A. Kuperman, M. B. Porter, and H. Schmidt, *Computational Ocean Acoustics* (Springer, New York, 2000).
[4] L. Tsang, J. A. Kong, K. H. Ding, and C. O. Ao, *Scattering of Electromagnetic Waves: Numerical Simulations* (Wiley, New York, 2001).
[5] K. E. Warnick and W. C. Chew, "Numerical simulation methods for rough surface scattering," Waves Random Media **11**, R1–R29 (2001).
[6] P. M. Morse and H. Feshbach, *Methods of Theoretical Physics, Part I* (McGraw-Hill, New York, 1953).
[7] J. J. Bowman, T. B. A. Senior, and P. L. E. Uslenghi, *Electromagnetic and Acoustic Scattering by Simple Shapes* (Hemisphere, New York, 1987).
[8] J. B. Keller, R. M. Lewis, and B. D. Seckler, "Asymptotic solution of some diffraction problems," Commun. Pure Appl. Math. **9**, 207–265 (1956).
[9] J. B. Keller, "Geometrical theory of diffraction," J. Opt. Soc. Am. **52**, 116–130 (1962).
[10] V. M. Babič and V. S. Buldyrev, *Short-Wavelength Diffraction Theory* (Springer, Berlin, 1991).
[11] V. A. Borovikov and B. Ye. Kinber, *Geometrical Theory of Diffraction* (The Institution of Electrical Engineers, London, 1994).
[12] Yu. A. Kravtsov and Yu. I. Orlov, *Geometrical Optics of Inhomogeneous Media* (Springer, Berlin, 1990).
[13] C. E. Schensted, "Electromagnetic and acoustical scattering by a semi-infinite body of revolution," J. Appl. Phys. **26**, 306–308 (1955).

[14]S. W. Lee, "Electromagnetic reflection from a conducting surface: Geometrical optics solution," IEEE Trans. Antennas Propag. **AP-23**, 184–191 (1975).
[15]P. Beckmann and W. K. Spizzichino, *The Scattering of Electromagnetic Waves from Rough Surfaces* (Pergamon, Oxford, 1963).
[16]F. G. Bass and I. M. Fuks, *Wave Scattering from Statistically Rough Surfaces* (Nauka, Moscow, 1972, in Russian); English translation: International Series in Natural Philosophy, edited by C. B. Vesecky and J. F. Vesecky (Pergamon, Oxford, 1978), Vol. **93**.
[17]A. G. Voronovich, *Wave Scattering from Rough Surfaces*, 2nd ed. (Springer, Berlin, 1999).
[18]L. M. Brekhovskikh, "Wave diffraction by rough surface," Zh. Eksp. Teor. Fiz. **23**, 275–278 (1952); **23**, 289–304 (1952).
[19]M. A. Isakovich, "Wave scattering from a statistically rough surface," Zh. Eksp. Teor. Fiz. **23**, 305–314 (1952).
[20]T. M. Elfouhaily and C. A. Guérin, "A critical survey of approximate scattering wave theories from random rough surfaces," Waves Random Media **14**, R1–R40 (2004).
[21]P. J. Lynch, "Curvature corrections to rough-surface scattering at high frequencies," J. Acoust. Soc. Am. **47**, 804–815 (1970).
[22]E. Rodrígues, "Beyond the Kirchhoff approximation," Radio Sci. **24**, 681–693 (1989).
[23]E. Rodrígues, "Beyond the Kirchhoff approximation II. Electromagnetic scattering," Radio Sci. **26**, 121–132 (1991).
[24]T. Elfouhaily, M. Joelson, S. Guingnard, and D. R. Tompson, "Analytical comparison between the surface current integral equation and the second-order small-slope approximation," Waves Random Media **13**, 165–176 (2003).
[25]T. Elfouhaily, S. Guingnard, R. Awadallah, and D. R. Tompson, "Local and non-local curvature approximation: A new asymptotic theory for wave scattering," Waves Random Media **13**, 321–3338 (2003).
[26]T. Elfouhaily, S. Guingnard, and D. R. Tompson, "Formal tilt invariance of the local curvature approximation," Waves Random Media **13**, L7–L11 (2003).
[27]T. M. Elfouhaily and J. T. Johnson, "Extension of the local curvature approximation to third order and improved tilt invariance," Waves Random Complex Media **16**, 97–119 (2006).
[28]M. I. Charnotskii and V. I. Tatarskii, "Tilt-invariant theory of scattering by rough surface," Waves Random Media **5**, 361–380 (1995).
[29]V. A. Fok, *Electromagnetic Diffraction and Propagation Problems* (Pergamon, Oxford, 1965).
[30]I. M. Fuks, "High-frequency asymptotic expansions of a backscattered cross section and *HH*/*VV* polarization ratio for smooth two-dimensional surfaces," Waves Random Media **14**, 143–156 (2004).
[31]I. M. Fuks, "Asymptotic solutions for backscattering by smooth 2-D surfaces," Prog. Electromagn. Res. **53**, 189–226 (2005).
[32]I. M. Fuks, "High-frequency asymptotic solutions for backscattering by cylinders with conic section directrices," IEEE Trans. Antennas Propag. **53**, 1653–1662 (2005).
[33]I. Fuks, "Diffraction corrections to fields specularly reflected by a smooth 2-D surface," IEEE Trans. Antennas Propag. **54**, 2703–2712 (2006).
[34]W. Feller, *An Introduction to Probability Theory and its Applications* (Wiley, New York, 1966).

A computationally efficient finite element model with perfectly matched layers applied to scattering from axially symmetric objects

Mario Zampolli,[a] Alessandra Tesei, and Finn B. Jensen
NATO Undersea Research Centre, Viale San Bartolomeo 400, 19138 La Spezia, Italy

Nils Malm
COMSOL AB, Tegnérgatan 23, SE-111 40 Stockholm, Sweden

John B. Blottman III
Naval Undersea Warfare Center, Code 1516, 1176 Howell Street, Newport, Rhode Island 02841-1708

(Received 4 March 2007; revised 25 June 2007; accepted 28 June 2007)

A frequency-domain finite-element (FE) technique for computing the radiation and scattering from axially symmetric fluid-loaded structures subject to a nonsymmetric forcing field is presented. The Bérenger perfectly matched layer (PML), applied directly at the fluid-structure interface, makes it possible to emulate the Sommerfeld radiation condition using FE meshes of minimal size. For those cases where the acoustic field is computed over a band of frequencies, the meshing process is simplified by the use of a wavelength-dependent rescaling of the PML coordinates. Quantitative geometry discretization guidelines are obtained from *a priori* estimates of small-scale structural wavelengths, which dominate the acoustic field at low to mid frequencies. One particularly useful feature of the PML is that it can be applied across the interface between different fluids. This makes it possible to use the present tool to solve problems where the radiating or scattering objects are located inside a layered fluid medium. The proposed technique is verified by comparison with analytical solutions and with validated numerical models. The solutions presented show close agreement for a set of test problems ranging from scattering to underwater propagation. © *2007 Acoustical Society of America.* [DOI: 10.1121/1.2764471]

PACS number(s): 43.30.Jx, 43.20.Fn, 43.58.Ta [JGM] Pages: 1472–1485

I. INTRODUCTION

The technique of choice with which many researchers study structurally and geometrically complex problems is the finite element (FE) method.[1] The numerical solution of structural acoustics problems with the FE method remains a computational challenge even in the low- to mid-frequency regime, where the structure of interest is not larger than a few tens of acoustic wavelengths. This article describes a FE modeling scheme for solving acoustic-structure interaction problems in the presence of a surrounding homogeneous or layered fluid medium of infinite extent. By restricting the attention to axially symmetric geometries subject to nonsymmetric forcing functions, solutions are computed well into the mid-frequency regime.

The solutions of exterior Helmholtz problems must satisfy the Sommerfeld radiation condition[2] at infinity, which implies that all sources of radiation or scattering can be circumscribed by a surface, beyond which all waves are outgoing. Such a surface can be defined within numerical models by applying boundary conditions or external layers, so that the reflection of the outgoing waves at the boundary is minimized. An exhaustive discussion of numerical radiation conditions can be found in the review article by Thompson[1] and in the work of Shirron and Babuska.[3] The computationally most efficient technique is the unconjugated infinite element (UIE) method.[3–5] The main disadvantages associated with the UIE are the need for nonstandard basis functions and the integration of highly oscillatory integrands over infinite intervals, which can cause difficulties when implementing the technique in generic FE tools. A viable and readily available alternative is the perfectly matched layer (PML) technique, introduced originally by Bérenger.[6,7] The PML can be implemented easily either by introducing anisotropic material damping parameters or by a complex coordinate scaling.[8–11] In the past, the PML has been applied in the presence of interfaces between heterogeneous media using the finite difference time domain technique (FDTD).[12] Shirron and Giddings[13] and some of the authors of this paper[14,15] have recently applied the technique to heterogeneous interfaces using the FE method.

Section II reviews briefly the basic definitions and the three-dimensional variational equations, which serve as a basis for the azimuthal modal variational technique outlined in Sec. III. The modal superposition technique breaks the three-dimensional (3D) FE problem into a series of independent smaller two-dimensional (2D) problems, which can be solved more efficiently than the original 3D problem.[16–19]

[a]Author to whom correspondence should be addressed. Electronic mail: zampolli@nurc.nato.int

The technique has been applied to structural acoustics by Shirron and co-workers[5,11,20] using unconjugated infinite elements as numerical radiation condition.

The PML is applied to the azimuthal modal superposition technique in Sec. IV. Some of the open questions regarding the placement of the interface and the layer thickness[1] are addressed here, with particular attention to structural acoustics applications. A wavelength-dependent coordinate stretching parameter introduced in this paper makes it possible to define PML's of constant thickness throughout the entire frequency band of the computations. This has clear advantages in terms of the FE mesh design, since one can define a frequency-independent geometry and discretization for the PML in the outgoing direction. In earlier FDTD methods, similar coordinate stretching parameters have been used to improve the performance of PML's.[12,21–23] Because of the broadband nature of many time-domain problems of interest, any choice of the stretching parameter is necessarily optimized with respect to certain frequency components of the analyzed time-domain pulse. This is not the case in the frequency domain, since each frequency is analyzed independently of the others. Therefore, a wavelength-dependent coordinate stretching, such as the one presented in Sec. IV, appears to be the most reasonable choice for the frequency-domain PML.

The analysis of the PML reflection presented in Sec. IV A suggests that PML's can be applied in direct contact with a radiating or vibrating convex structure. This property, together with the adaptability of PML's to various geometries,[8,10] makes the technique particularly desirable in structural acoustics applications. The limitations in the usability of the PML near coincidence frequency, discussed in Sec. IV A, are reminiscent of the complex layer resonance effect found by DiPerna and Feit[24] in the analytical approximation of the Green's function of a flat plate.

In various applications, the quantity of interest is the acoustic far field, which can be obtained from the near field FE solution via the Helmholtz-Kirchhoff integral. In the case where the far field is required in the presence of a layered background medium, the computation of the layered medium Green's functions causes the evaluation of the Helmholtz-Kirchhoff integral to become computationally expensive. A convenient method for computing the far field via approximate Green's functions is described in Sec. VI. The decomposition of the Helmholtz-Kirchhoff far field integral in cylindrical harmonics is briefly illustrated.

Section VII contains numerical results for a number of problems with which the proposed model has been verified. Particular attention is dedicated to criteria for the design of FE meshes in structural acoustics. The convergence of structural acoustic models is significantly affected by short-wavelength subsonic waves[25–27] generated in layered elastic structures, which couple to the surrounding fluid and radiate into the far field. Physics-based meshing guidelines, obtained from pre-asymptotic convergence criteria derived by Ihlenburg,[11] are discussed in Sec. VII B in relation to the subsonic structure-borne waves. The discretization criteria, which apply to general 2D and 3D structural acoustics problems, are verified via a set of examples in which the structural complexity is progressively increased. The numerical solutions are compared to converged solutions from a validated reference model.[5,11,20]

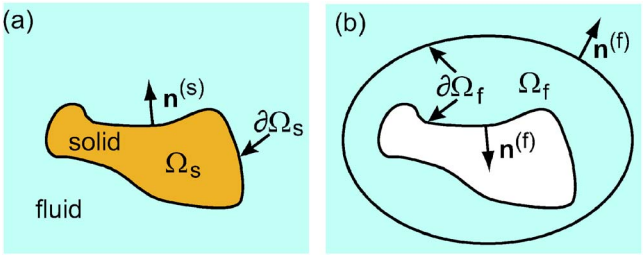

FIG. 1. (Color online) Elastic structure Ω_s embedded in a fluid domain of infinite extent (a). In the numerical model (b), the fluid domain is truncated, and approximate radiation conditions are applied on the outer part of the fluid boundary $\partial\Omega_f$.

In Sec. VII C an underwater propagation benchmarking problem is solved, illustrating an application of the frequency domain PML in the presence of heterogeneous interfaces between different fluids. The scattering from an object located on the interface between two different fluids is studied in Sec. VII D, where the far field is computed using the approximate Green's function based method presented in Sec. VI.

II. VARIATIONAL FORMULATION OF THREE-DIMENSIONAL LINEAR STRUCTURAL ACOUSTICS

Throughout the entire paper the attention is restricted to harmonic oscillations of constant frequency f. The complex time dependence $e^{i\omega t}$, with t representing time, and with $\omega = 2\pi f$, is factored out of the equations.

A. The elastic domain

The time-harmonic linear oscillations in an isotropic elastic medium occupying the volume Ω_s (Fig. 1) are described by the wave equation[28]

$$(C_{ijkl}u_{k,l})_{,j} + \omega^2\rho_s u_i = 0, \tag{1}$$

where ρ_s is the density of the solid. The indices are in the range $i,j,k,l=1,2,3$. The summation convention is assumed for repeated indices. The notation "$_{,j}$" indicates differentiation with respect to the jth coordinate, i.e., "$\partial/\partial x_j$." The vector $\mathbf{u}$ describes the displacement of the solid particles

$$\mathbf{u}(x_1,x_2,x_3) = u_i\mathbf{e}_i, \tag{2}$$

where $\mathbf{e}_i$ denotes the unit vector of the ith coordinate, such as, for example, $\mathbf{e}_x$, $\mathbf{e}_y$, $\mathbf{e}_z$ in Cartesian coordinates, or $\mathbf{e}_r$, $\mathbf{e}_\theta$, and $\mathbf{e}_z$ in cylindrical coordinates. The deformation of the medium is described by the symmetric small strain tensor

$$\varepsilon_{ij} = \frac{1}{2}\left(\frac{\partial u_i}{\partial x_j} + \frac{\partial u_j}{\partial x_i}\right). \tag{3}$$

The stress tensor σ_{ij} is related linearly to the strain tensor ε_{ij} via the stress-strain equation

$$\sigma_{ij} = C_{ijkl}\varepsilon_{kl}, \tag{4}$$

where, for an *elastically isotropic* material, the tensor of elastic constants C_{ijkl} obeys the relation[28]

$$C_{ijkl} = \lambda \delta_{ij}\delta_{kl} + \mu(\delta_{ik}\delta_{jl} + \delta_{il}\delta_{jk}), \tag{5}$$

with λ, μ representing the Lamé elastic constants, and δ_{ij} being the symmetric Kronecker delta tensor. This yields the Hooke's law

$$\sigma_{ij} = \lambda \varepsilon_{kk}\delta_{ij} + 2\mu\varepsilon_{ij}. \tag{6}$$

The longitudinal and transverse sound speeds c_L and c_T are related to the Lamé constants via

$$c_L = \sqrt{\frac{\lambda + 2\mu}{\rho_s}}, \quad c_T = \sqrt{\frac{\mu}{\rho_s}}. \tag{7}$$

The principle of virtual work for the elastic medium yields the variational equation[11,28]

$$\int_{\Omega_s} (-\omega^2 \rho_s u_i \delta u_i + \sigma_{ij}\delta\varepsilon_{ij}) d\Omega - \int_{\partial\Omega_s} t_i \delta u_i dS = 0, \tag{8}$$

where, $i,j=1,2,3$, δu_i and $\delta\varepsilon_{ij}$ represent admissible variations of the unknown displacement vector and of the unknown strain tensor, respectively. The surface traction vector is given by Cauchy's stress formula

$$t_i = \sigma_{ij} n_j, \tag{9}$$

with n_j being the components of the outward pointing unit vector normal to $\partial\Omega_s$. Boundary conditions for the elastic domain can be applied as Neumann boundary conditions via the surface traction t_i, as Dirichlet boundary conditions by constraining u_i to conform to some known displacements, or as combinations of Neumann and Dirichlet conditions for the different components of the unknowns.

B. The fluid domain

In the part of the domain occupied by a fluid, Ω_f, the unknown fluid pressure $p(\mathbf{x})$ is modeled by the familiar Helmholtz wave equation in the form admitting a position dependent fluid density $\rho_f(\mathbf{x})$ and sound speed $c_f(\mathbf{x})$[29,30]

$$\nabla \cdot \left(\frac{1}{\rho_f(\mathbf{x})} \nabla p(\mathbf{x}) \right) + \frac{k^2}{\rho_f(\mathbf{x})} p(\mathbf{x}) = 0, \quad \mathbf{x} \in \Omega_f, \tag{10}$$

where $k=\omega/c_f(\mathbf{x})$ is the wave number.

For the unbounded fluid domain, the Sommerfeld radiation condition must hold at infinity[2]

$$\lim_{R\to\infty} \left[R\left(\frac{\partial p(R)}{\partial R} + ikp(R) \right) \right] = 0 \tag{11}$$

with R being the spherical radial coordinate, originating at a nominal center of the computational domain. Other boundary conditions for the pressure may be of Dirichlet, Neumann, or mixed Dirichlet/Neumann type.

Following the derivations presented in the literature[11,31] one obtains the variational equation for the pressure in the fluid domain

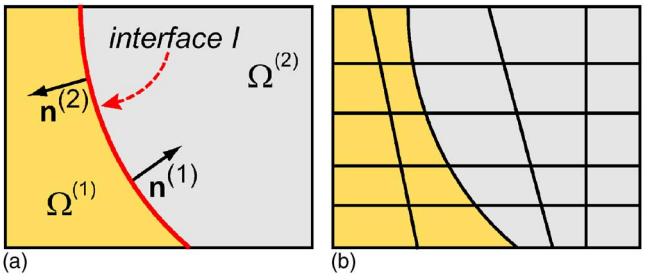

FIG. 2. (Color online) (a) Two generic components of the computational domain, $\Omega^{(1)}$ and $\Omega^{(2)}$, separated by a common interface I. (b) Schematic representation of the subdivision of the two domain components into finite elements.

$$\int_{\Omega_f} \left(-\frac{1}{\omega^2\rho_f} \nabla p \cdot \delta(\nabla p) + \frac{1}{\rho_f c_f^2} p\delta p \right) d\Omega + \int_{\partial\Omega_f} \frac{1}{\omega^2\rho_f} \nabla p \cdot \mathbf{n}\delta p dS = 0. \tag{12}$$

The quantity

$$\frac{1}{\omega^2\rho_f} \nabla p \cdot \mathbf{n} = u_n \tag{13}$$

represents the normal component of the particle displacement, applied at the surface of the boundary $\partial\Omega_f$. Using Eq. (13), Neumann boundary conditions and mixed boundary conditions can be applied via the boundary integral term in Eq. (12). In accordance with the symmetric potential formulation introduced by Everstine,[32,33] the scaling $1/\omega^2$ is applied in Eq. (12) with the purpose of obtaining a symmetric coupled fluid-solid FE equation system.[29] This makes it possible to use a symmetric sparse solver in the numerical scheme, which is generally a more efficient option compared to nonsymmetric solvers.

If the quantity of interest in the fluid domain is the acoustic field scattered by an obstacle, and the incident acoustic pressure p^{inc} and its normal derivative ∇p^{inc} are known *a priori*, then one has

$$p = p^{scat} + p^{inc}, \quad \nabla p = \nabla p^{scat} + \nabla p^{inc}, \tag{14}$$

where p^{scat} is the unknown scattered field component, and p represents the total acoustic pressure. Consequently substitution of Eq. (14) into the weak Eq. (12) yields

$$\int_{\Omega_f} \left(-\frac{1}{\omega^2\rho_f} \nabla p^{scat} \delta(\nabla p^{scat}) + \frac{1}{\rho_f c_f^2} p^{scat} \delta p^{scat} \right) d\Omega + \int_{\partial\Omega_f} \frac{1}{\omega^2\rho_f} (\nabla p - \nabla p^{inc}) \cdot \mathbf{n}\delta p^{scat} dS = 0. \tag{15}$$

The incident field may be given via some direct analytical expression, or by some other numerical method (such as, for example, a waveguide propagation model), or it may have been determined experimentally.

C. Interface boundary conditions

Any two adjacent elastic domain components, say $\Omega^{(1)}$ and $\Omega^{(2)}$ (see Fig. 2), are assumed to be perfectly bonded,

which implies that the continuity of displacement u_i and stress t_i must be satisfied across the interface I. The finite element method, which partitions the computational domain into a finite number of nonoverlapping finite-sized elements, would, for example, yield two elements like $\Omega^{(1)}$ and $\Omega^{(2)}$. In particular, the continuity of t_i across the interface between two adjacent solid volumes implies that the boundary integral contributions over the interface I from $\Omega^{(1)}$ and $\Omega^{(2)}$ in Eq. (8) vanish

$$\int_I \underbrace{(t_i^{(1)} + t_i^{(2)})}_{\sigma_{ij}^{(1)} n_j^{(1)} - \sigma_{ij}^{(2)} n_j^{(1)}} \delta u_i dS = 0, \tag{16}$$

where the normal $n_j^{(1)}$ is chosen to point from $\Omega^{(1)}$ into $\Omega^{(2)}$. The continuity of the primary variables u_i in the solid is guaranteed by the inter-element continuity condition.

Similarly, the pressure and the normal displacement, Eq. (13), both must be continuous across the interface separating two adjacent portions of the fluid domain. The latter condition in particular implies that, if $\Omega^{(1)}$ and $\Omega^{(2)}$ belong to the fluid domain, the boundary integral contribution from the two subdomains in Eq. (12) becomes

$$\int_I \left(\frac{1}{\omega^2 \rho_f^{(1)}} \nabla p \cdot \mathbf{n}^{(1)} - \frac{1}{\omega^2 \rho_f^{(2)}} \nabla p \cdot \mathbf{n}^{(1)} \right) \delta p dS = 0. \tag{17}$$

This is true also if the two volumes are occupied by two heterogeneous fluids. The continuity of the primary variable p is ensured also in this case by the inter-element continuity condition.

If one of the two subdomains, say $\Omega^{(1)}$, is a solid and the other one, say $\Omega^{(2)}$, is a fluid, then the normal displacement across the interface and the normal stress, which is related to the acoustic pressure by $\sigma_{ij} = -p\delta_{ij}$, must both be continuous across I. Equations (8), (12), and (15) imply in this case that

$$\int_I t_i \delta u_i dS = -\int_I \begin{Bmatrix} p \\ p^{\text{scat}} + p^{\text{inc}} \end{Bmatrix} n_i \delta u_i dS, \tag{18}$$

$$\int_I \frac{1}{\omega^2 \rho_f} \begin{Bmatrix} \nabla p \\ \nabla p - \nabla p^{\text{inc}} \end{Bmatrix} \cdot \mathbf{n} \delta p dS = -\int_I \begin{Bmatrix} \mathbf{u} \\ \mathbf{u} - \frac{1}{\omega^2 \rho_f} \nabla p^{\text{inc}} \end{Bmatrix} \cdot \mathbf{n} \delta p dS, \tag{19}$$

respectively. The upper or the lower expression in the brackets is chosen depending on whether the unknown is p or p^{scat}. In what follows the attention is restricted to the scattered field equations in the fluid, knowing that the total field case can always be recovered by the substitutions $p^{\text{inc}} \to 0$ and $p^{\text{scat}} \to p$.

III. VARIATIONAL FORMULATION FOR AXIALLY SYMMETRIC GEOMETRIES WITH NONSYMMETRIC LOADING

In the case where the geometry of the problem is axisymmetric (Fig. 3), but the loading is not necessarily axially symmetric, the variational equations for the 3D problem presented in Sec. II are rewritten in cylindrical coordinates $\mathbf{r} = r\mathbf{e}_r + \theta\mathbf{e}_\theta + z\mathbf{e}_z$, with $0 \leqslant \theta < 2\pi$. A generic incident acoustic field p^{inc} can be decomposed in a Fourier series

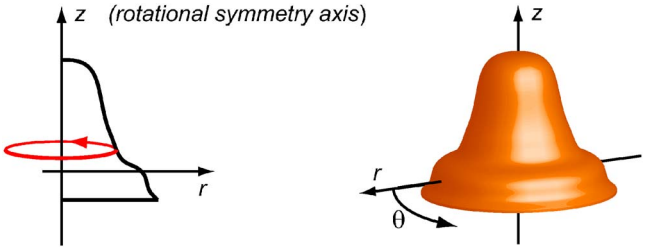

FIG. 3. (Color online) A 3D axisymmetric geometry is obtained by rotating a generating line around the symmetry axis.

$$p^{\text{inc}}(r,\theta,z) = p_m^{\text{inc}}(r,z) e^{im\theta}, \quad -\infty < m < +\infty. \tag{20}$$

Of particular interest to the examples presented below is the expansion of a plane wave having the wave number vector parallel to the rz plane and forming an angle ϕ with the r axis:[34]

$$p^{\text{inc}}(r,\theta,z) = \epsilon_m p_m^{\text{inc}}(r,z)\cos(m\theta), \quad 0 \leqslant m < +\infty, \tag{21}$$

$$p_m^{\text{inc}}(r,z) = i^m e^{(ikz \sin \phi)} J_m(kr \cos \phi), \tag{22}$$

with $\epsilon_0 = 1$ and $\epsilon_m = 2$, $m = 1, \ldots, +\infty$, and with J_m representing the Bessel function of order m.

Consistently with the chosen decomposition of the applied load, the solid displacement $(u_1, u_2, u_3) = (u, v, w)$ and the pressure p are decomposed in the same way

$$\begin{pmatrix} u(r,\theta,z) \\ v(r,\theta,z) \\ w(r,\theta,z) \\ p(r,\theta,z) \end{pmatrix} = \begin{pmatrix} u_m(r,z) \{e^{im\theta}; \cos(m\theta)\} \\ v_m(r,z) \{e^{im\theta}; \sin(m\theta)\} \\ w_m(r,z) \{e^{im\theta}; \cos(m\theta)\} \\ p_m(r,z) \{e^{im\theta}; \cos(m\theta)\} \end{pmatrix}. \tag{23}$$

The complex exponential or the trigonometric functions in the brackets are chosen depending on whether the forcing is decomposed according to Eq. (20) or Eq. (21). Applying the substitutions to the variational Eqs. (8) and (15) written in cylindrical coordinates, with $d\Omega = r dr d\theta dz$, $\Omega_{s/f}^0 = \{(r,\theta,z) \in \Omega_{s/f} : \theta = 0\}$, carrying out the integration over θ explicitly, and making use of the orthogonality property of the Fourier basis, yields

$$\begin{aligned} \int_{\Omega_s^0} \Bigg[& -\omega^2 \rho_S \left((u_m \delta u_m + w_m \delta w_m) \begin{Bmatrix} 2\pi \\ I_{cc} \end{Bmatrix} + v_m \delta v_m \begin{Bmatrix} 2\pi \\ I_{ss} \end{Bmatrix} \right) \\ & + (\sigma_r^m \delta(\varepsilon_r^m) + \sigma_\theta^m \delta(\varepsilon_\theta^m) + \sigma_z^m \delta(\varepsilon_z^m)) \begin{Bmatrix} 2\pi \\ I_{cc} \end{Bmatrix} \\ & + (2\sigma_{r\theta}^m \delta(\varepsilon_{r\theta}^m) + 2\sigma_{\theta z}^m \delta(\varepsilon_{\theta z}^m)) \begin{Bmatrix} 2\pi \\ I_{ss} \end{Bmatrix} + 2\sigma_{rz}^m \delta(\varepsilon_{rs}^m) \\ & \times \begin{Bmatrix} 2\pi \\ I_{cc} \end{Bmatrix} \Bigg] r dr dz + I_{\partial\Omega_s^0} = 0, \end{aligned} \tag{24}$$

$$\int_{\Omega_f^0}\left[-\frac{1}{\omega^2\rho_f}\left(\frac{\partial p_m^{\text{scat}}}{\partial r}\delta\left(\frac{\partial p_m^{\text{scat}}}{\partial r}\right)\begin{Bmatrix}2\pi\\ I_{cc}\end{Bmatrix}+\frac{m^2}{r^2}p_m^{\text{scat}}\delta(p_m^{\text{scat}})\right.\right.$$
$$\times\begin{Bmatrix}2\pi\\ I_{ss}\end{Bmatrix}+\frac{\partial p_m^{\text{scat}}}{\partial z}\delta\left(\frac{\partial p_m^{\text{scat}}}{\partial z}\right)\begin{Bmatrix}2\pi\\ I_{cc}\end{Bmatrix}\Bigg)$$
$$\left.+\frac{1}{\rho_f c_f^2}p_m^{\text{scat}}\delta(p_m^{\text{scat}})\begin{Bmatrix}2\pi\\ I_{cc}\end{Bmatrix}\right]rdrdz+I_{\partial\Omega_f^0}=0. \quad (25)$$

The factors for the case of a loading decomposed in a cosine series are

$$I_{ss}=\begin{cases}\pi, & m\neq 0\\ 0, & m=0\end{cases},\quad I_{cc}=\begin{cases}\pi, & m\neq 0\\ 2\pi, & m=0.\end{cases} \quad (26)$$

The boundary terms $I_{\partial\Omega_s^0}$ and $I_{\partial\Omega_f^0}$ can be split into contributions from the free faces $\Gamma_{s\backslash fsi}$ and $\Gamma_{f\backslash fsi}$, and the contributions from the fluid-solid interfaces Γ_{fsi}. This yields the contour integral terms

$$I_{\partial\Omega_s^0}=\int_{\Gamma_{fsi}}(p_m^{\text{scat}}+p_m^{\text{inc}})(n_r\delta u_m+n_z\delta w_m)\begin{Bmatrix}2\pi\\ I_{cc}\end{Bmatrix}rd\ell$$
$$+\int_{\Gamma_{s\backslash fsi}}\left[(t_r^m\delta u_m+t_z^m\delta w_m)\begin{Bmatrix}2\pi\\ I_{cc}\end{Bmatrix}\right.$$
$$\left.+t_\theta^m\delta v_m\begin{Bmatrix}2\pi\\ I_{ss}\end{Bmatrix}\right]rd\ell, \quad (27)$$

$$I_{\partial\Omega_f^0}=\int_{\Gamma_{fsi}}\left[u_m n_r+w_m n_z-\frac{1}{\omega^2\rho_f}\left(\frac{\partial p_m^{\text{inc}}}{\partial r}n_r+\frac{\partial p_m^{\text{inc}}}{\partial z}n_z\right)\right]$$
$$\times\begin{Bmatrix}2\pi\\ I_{cc}\end{Bmatrix}\delta p_m^{\text{scat}}rd\ell+\int_{\Gamma_{f\backslash fsi}}\frac{1}{\omega^2\rho_f}\left[\frac{\partial}{\partial r}(p_m-p_m^{\text{inc}})n_r\right.$$
$$\left.+\frac{\partial}{\partial z}(p_m-p_m^{\text{inc}})n_z\right]\begin{Bmatrix}2\pi\\ I_{cc}\end{Bmatrix}\delta p_m^{\text{scat}}rd\ell. \quad (28)$$

In Eq. (27) t_r^m, t_θ^m, and t_z^m represent the modal components of the applied traction vector t_i in cylindrical coordinates. The summation convention for repeated indices does not apply to the index m in Eqs. (24), (25), (27), and (28).

IV. PERFECTLY MATCHED LAYERS

One method for converting a fluid layer into a Bérenger[6,7] perfectly matched layer (PML), consists of applying a transformation to the coordinates.[8,11] The transformation is a scaling to complex coordinates such that the new medium becomes selectively dissipative in the direction perpendicular to the interface between the PML and the physical domain.

This work focuses on the application of PML's specifically in the context of structural acoustics problems. For this purpose, the PML scaling and the PML reflection properties are analyzed here in a planar 2D geometry, with the underlying assumption that the conclusions on the applicability of the method can be extended to other curvilinear geometries in the same way as one can extend the coordinate scaling functions.[8–10] Considering the planar Cartesian coordinate system $\mathbf{x}=x\mathbf{e}_x+z\mathbf{e}_z$, with the interface between PML and fluid being the z axis (inset in Fig. 4), the coordinate scaling is defined as:

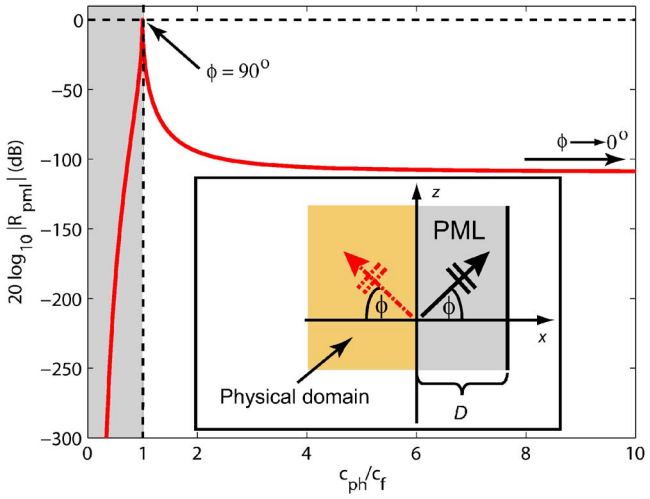

FIG. 4. (Color online) PML reflection coefficient for fluid-borne structural waves. At coincidence frequency $c_{ph}/c_f=1$, and the waves transition from the evanescent regime (shaded area) to the propagating regime. The inset shows the PML in the domain $x>0$, the plane wave launched into the PML at an angle ϕ (solid) and the PML-reflected plane wave (dashed) reflected back into the physical domain. In general the physical domain can be a structure or a fluid.

$$\tilde{x}(x)=\frac{\lambda}{D}x-\frac{i}{\omega}\int_0^{\lambda/Dx}\sigma(\xi)d\xi, \quad (29)$$

$$\frac{d\tilde{x}}{dx}=\frac{\lambda}{D}\cdot\frac{i\omega+\sigma(x)}{i\omega}, \quad (30)$$

for $x>0$. D is the thickness of the PML, and $\lambda=c_f/f$ is the acoustic wavelength. The scaling satisfies the continuity property $\sigma(0)=0$.[6–8] It is also required that $\tilde{x}(D)=(1-i)\lambda$ and $\mathrm{Im}(\tilde{x})<0$. The latter property implies that the PML is capable of absorbing evanescent plane waves as well as propagating ones, with the well known limitations for angles near grazing incidence.[13,21,35] The coordinate stretching introduced in FDTD implementations of the PML[12,21–23] can be chosen in a particularly convenient manner in frequency domain models, such as the one presented here. By introducing the λ/D stretching in Eqs. (29) and (30) the scaled coordinate is normalized with respect to λ. In the finite element model, this has the advantage that one can define one single PML geometry for a given multi-frequency problem, with one fixed discretization of $\tilde{x}$ applicable throughout the frequency band of interest.

A. Applicability in structural acoustics

If the medium in the domain $x\leqslant 0$ is a radiating or scattering vibrating structure, the fluid waves in $x>0$ generated by the fluid-structure interaction can be represented by the homogeneous plane-wave spectrum[30,36]

$$p(x,z) = e^{-k\beta x} e^{-ik\sqrt{\beta^2+1}z}, \tag{31}$$

with $\beta = \sqrt{(c_f/c_{ph})^2 - 1}$, and where c_{ph} is the phase speed at which the horizontal displacement component propagates along z (inset in Fig. 4). The evanescent spectrum of the homogeneous plane wave is in the range $0 < c_{ph}/c_f < 1$. Identifying the coupling angle of the wave as $\phi = \cos^{-1}(-i\beta)$, $\mathrm{Re}(\phi) = 90°$ and $\mathrm{Im}(\phi) \geqslant 0$ is monotonically increasing to infinity as $c_{ph}/c_f \to 0^+$. In the propagating spectrum $\phi = 90°$ for $c_{ph}/c_f = 1$, and $\phi \to 0°$ as $c_{ph}/c_f \to \infty$. The condition $c_{ph}/c_f = 1$ is reached at the coincidence frequency f_c.[30,36]

Placing the planar PML in contact with the physical domain, as shown in Fig. 4, considering waves in the form of Eq. (31) incident from the $x < 0$ domain, and requiring the pressure and the normal displacement, respectively, to be continuous at the interface $x = 0$, yields the reflection coefficient

$$R_{pml} = e^{-4\pi\beta(1-i)}. \tag{32}$$

The logarithmic plot of R_{pml} in Fig. 4 exhibits a strong decay of the plane waves away from the coincidence frequency. The steep decay of the evanescent waves makes it necessary to discretize the PML through the thickness with a sufficient number of degrees of freedom. When setting up a numerical model for a given frequency band of interest, one can *a priori* estimate the minimum phase speed c_{ph} of the structural waves using analytical methods, and discretize the PML accordingly.

Close to the coincidence frequency, the PML can exhibit significant reflections in both the evanescent and the propagating regime. This can in principle lead to inaccurate numerical solutions. Nevertheless, for a large number of cases of interest the structures have a curvature, so that the coupling angle of the structural waves is never above the threshold value beyond which numerical reflections become significant. This makes the PML widely applicable to problems of scattering and radiation from localized structures surrounded by fluids. As an example to substantiate this claim, scattering from a spherical shell is studied in Sec. VII A.

Reflection effects around the coincidence frequency, similar in nature to the one found here for the PML, have been encountered by DiPerna and Feit[24] in the context of complex layer analysis (CLA). In the CLA method a semi-infinite fluid layer is replaced by a generic acoustic layer of finite complex thickness. Using the CLA, DiPerna and Feit derive an analytic approximation to the frequency-domain Green's function for a fluid loaded plate driven by a line source. Around coincidence frequency, a rational function approximation of the spectral acoustic impedance of the fluid breaks down and a nonphysical standing wave is generated in the layer. These observations substantiate the analysis presented here for PML's applied in contact with elastic structures.

B. Applicability to interfaces between different fluids

The PML technique can be employed also in those cases where the numerical radiation condition is applied across the interface between different fluids. This useful feature has been used by others in the past, who have developed FDTD models in the presence of planar sloping and nonsloping fluid-fluid boundaries.[12] In frequency domain FE models, PML's have been applied across interfaces between different fluids independently by some of the authors of this paper[14] and by Shirron and Giddings.[13] The applicability of heterogeneous perfectly matched layers is made possible by the extension of the continuity property for the normal displacement, Eq. (17), to the complex scaled PML coordinates. Examples are presented below in Sec. VII for an upslope underwater wedge propagation problem and for scattering from a sphere lying on the interface between two different fluids.

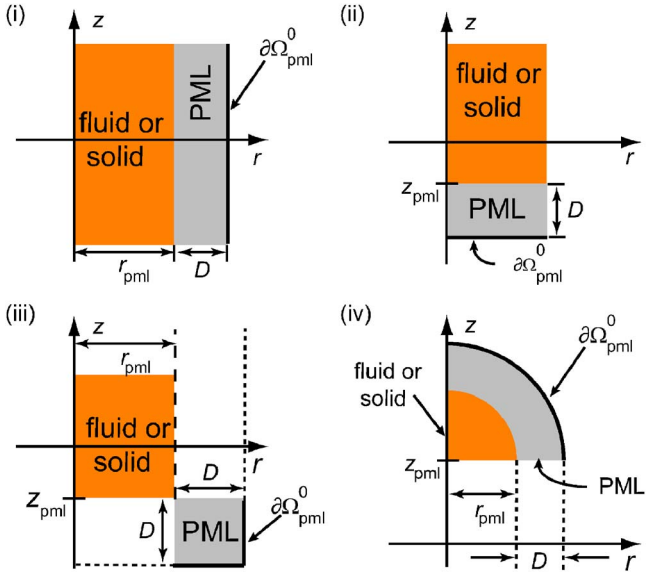

FIG. 5. (Color online) Definition of PML geometries in cylindrical coordinates. The z axis is the axis of rotational symmetry.

C. PML in cylindrical coordinates

The PML is applied in cylindrical coordinates following the approach outlined by Collino and Monk.[8] The chosen scalings yield $\tilde{r}(r,z)$ and $\tilde{z}(r,z)$ coordinates which satisfy the counterpart of Eq. (30) in the curved coordinate system. To obtain the results presented in Sec. VII, quadratic PML's are defined for four different geometries (Fig. 5): (i) a cylindrical boundary generated by a line parallel to the z axis, (ii) the base of a circular cylinder, (iii) a corner where the dissipation is required in both r and z and (iv) a hemisphere. For each of the four cases depicted in Fig. 5, the coordinate scalings are, respectively

$$\text{(i)} \quad \begin{cases} \tilde{r} = r_{pml} + \left(1 - \dfrac{i}{D}(r - r_{pml})\right)\dfrac{\lambda}{D}(r - r_{pml}) \\ \tilde{z} = z \end{cases} \tag{33}$$

$$\text{(ii)} \quad \begin{cases} \tilde{r} = r \\ \tilde{z} = z_{pml} + \left(1 + \dfrac{i}{D}(z - z_{pml})\right)\dfrac{\lambda}{D}(z - z_{pml}) \end{cases} \tag{34}$$

(iii)
$$\begin{cases} \tilde{r} = r_{\text{pml}} + \left(1 - \dfrac{i}{D}(r - r_{\text{pml}})\right)\dfrac{\lambda}{D}(r - r_{\text{pml}}) \\ \tilde{z} = z_{\text{pml}} + \left(1 + \dfrac{i}{D}(z - z_{\text{pml}})\right)\dfrac{\lambda}{D}(z - z_{\text{pml}}) \end{cases} \tag{35}$$

(iv)
$$\begin{cases} \tilde{r} = R_{\text{scaled}}(r,z)/R(r,z)r \\ \tilde{z} = R_{\text{scaled}}(r,z)/R(r,z)(z - z_{\text{pml}}) + z_{\text{pml}}, \end{cases} \tag{36}$$

where $R(r,z) = \sqrt{r^2 + (z - z_{\text{pml}})^2}$ is a spherical radial coordinate centered at the origin of the hemisphere, and $R_{\text{scaled}}(r,z) = r_{\text{pml}} + (1 - i/D(R(r,z) - r_{\text{pml}}))\lambda/D(R(r,z) - r_{\text{pml}})$. In Eq. (34) the signs are chosen to account for the negative z_{pml}.

Using the Jacobian determinant

$$|J(r,z)| = \frac{\partial \tilde{r}}{\partial r} \cdot \frac{\partial \tilde{z}}{\partial z} - \frac{\partial \tilde{r}}{\partial z} \cdot \frac{\partial \tilde{z}}{\partial r}, \tag{37}$$

the variational Eq. (25) for the PML domain Ω_{pml} becomes

$$\int_{\Omega^0_{\text{pml}}} \left[-\frac{1}{\omega^2 \rho_f} \left(\frac{\partial p_m^{\text{scat}}}{\partial \tilde{r}} \delta\left(\frac{\partial p_m^{\text{scat}}}{\partial \tilde{r}} \right) \begin{Bmatrix} 2\pi \\ I_{cc} \end{Bmatrix} + \frac{m^2}{\tilde{r}^2} p_m^{\text{scat}} \delta(p_m^{\text{scat}}) \right.$$
$$\times \begin{Bmatrix} 2\pi \\ I_{ss} \end{Bmatrix} + \frac{\partial p_m^{\text{scat}}}{\partial \tilde{z}} \delta\left(\frac{\partial p_m^{\text{scat}}}{\partial \tilde{z}} \right) \begin{Bmatrix} 2\pi \\ I_{cc} \end{Bmatrix} \Bigg)$$
$$\left. + \frac{1}{\rho_f c_f^2} p_m^{\text{scat}} \delta(p_m^{\text{scat}}) \begin{Bmatrix} 2\pi \\ I_{cc} \end{Bmatrix} \right] \tilde{r} |J(r,z)| dr dz + I_{\partial \Omega^0_{\text{pml}}} = 0. \tag{38}$$

At the interface between the PML and the fluid or solid domain, the integral $I_{\partial \Omega^0_{\text{pml}}}$ coincides with the integral over Γ_{fsi} given in Eq. (28). The boundary conditions at the outer end of the PML are chosen to be homogeneous Neumann boundary conditions, which implies that the boundary integral $I_{\partial \Omega^0_{\text{pml}}} = 0$ on the outer PML boundary. Other boundary conditions, such as Dirichlet or Bayliss-Turkel,[37] could be applied at the outer PML boundary. Researchers who have addressed this issue[8] identify the Bayliss-Turkel condition as being the one which yields the best accuracy. On the other hand, the Bayliss-Turkel condition gives rise to numerical reflections at the interface between different fluids. For this reason the homogeneous Neumann condition, which is also straightforward to implement in the FE method, was chosen for the outer PML boundary. This choice does not appear to have any adverse effect on the numerical results reported in Sec. VII.

V. FINITE ELEMENT METHOD

The variational method outlined in Secs. III and IV C has been implemented by modifying the weak equations in the 2D acoustics and the 2D axial symmetry stress-strain application modes of a commercially available general-purpose finite-element modeling tool.[14,38] The procedure for the azimuthal modal superposition has been implemented via a script driver for the built-in direct sparse linear equation solver. The computational domains are discretized using structured quadrilateral element meshes or unstructured triangular element meshes, with Lagrange polynomial basis functions.

VI. FAR FIELD COMPUTATIONS

In Cartesian coordinates, the pressure field at a point $\mathbf{r}$ exterior to a surface S_0 enclosing a finite volume V_0 can be computed from the pressure p and the normal displacement u_n sampled on S_0 using the Helmholtz-Kirchhoff integral theorem[30]

$$p(\mathbf{r}) = \int_{S_0} \left[\frac{\partial G(\mathbf{r},\mathbf{r}_0)}{\partial n(\mathbf{r}_0)} p(\mathbf{r}_0) - \rho_f \omega^2 G(\mathbf{r},\mathbf{r}_0) u_n(\mathbf{r}_0) \right] dS. \tag{39}$$

If the quantity of interest is the scattered field, one simply needs to replace p by p^{scat} and u_n by the scattered field normal displacement u_n^{scat}. If S_0 is the interface between the elastic scatterer, on which u_n can be sampled from the solution in the elastic domain, and the fluid, one has $u_n^{\text{scat}} = u_n - u_n^{\text{inc}}$ where u_n^{inc} is computed from the incident field gradient via Eq. (13). The Green's function $G(\mathbf{r},\mathbf{r}_0)$ is the solution of

$$(\nabla^2 + k^2) G(\mathbf{r},\mathbf{r}_0) = \delta(\mathbf{r} - \mathbf{r}_0), \quad \mathbf{r},\mathbf{r}_0 \in V, \quad \mathbf{r} \neq \mathbf{r}_0, \tag{40}$$

where the volume $V \supset V_0$ can be the free space, a multilayered medium, an underwater waveguide or any other suitable background configuration. To compute the results of Sec. VII the cases of interest are where V is a free space, and where V is a two layered fluid medium, with $\mathbf{r},\mathbf{r}_0$ both contained in the upper medium (see, for example, Fig. 16). The free space Green's function is

$$G(\mathbf{r},\mathbf{r}_0) = \frac{e^{-ik|\mathbf{r} - \mathbf{r}_0|}}{4\pi |\mathbf{r} - \mathbf{r}_0|}. \tag{41}$$

Using the cylindrical coordinates $\mathbf{r} = (r,\theta,z)$ and $\mathbf{r}_0 = (r_0,\theta_0,z_0)$, the solution of Eq. (40) for the two layered medium is represented by the plane wave spectral integral in cylindrical coordinates[39]

$$G^{(12)}(\mathbf{r},\mathbf{r}_0) = \frac{\epsilon_m}{4\pi} \cos(m(\theta - \theta_0)) \int_0^\infty J_m(k_r r) J_m(k_r r_0)$$
$$\times \left[e^{-ik_{z1}|z - z_0|} + R(k_r) e^{-ik_{z1}(z + z_0)} \right] \frac{k_r}{k_{z1}} dk_r, \tag{42}$$

where $z > 0$, the boundary coincides with the plane $z = 0$, $k_{z1} = \sqrt{k_1^2 - k_r^2}$ and $k_1 = \omega / c_f^{(1)}$. The density and the sound speed in the upper and lower fluid are represented, respectively, by $\rho_f^{(1)}$ and $\rho_f^{(2)}$ and by $c_f^{(1)}$ and $c_f^{(2)}$. The reflection coefficient of each individual plane wave component in the spectral integral is

$$R(k_r) = \frac{\rho_f^{(2)} k_{z1} - \rho_f^{(1)} k_{z2}}{\rho_f^{(2)} k_{z1} + \rho_f^{(1)} k_{z2}}, \tag{43}$$

with $k_{z2} = \sqrt{k_2^2 - k_r^2}$ and $k_2 = \omega / c_f^{(2)}$. A convenient approximation of Eq. (42), valid if $\mathbf{r}$ is not closer than $\lambda/2$ to the two medium interface, is the free space point source-image point source superposition[39]

$$G^{(12)}(\mathbf{r},\mathbf{r}_0) \approx G(\mathbf{r},\mathbf{r}_0) + R(k_2 \cos\alpha) G(\mathbf{r},\mathbf{r}_0') \tag{44}$$

with $k = k_1$. The image point source is located at $\mathbf{r}_0' = (r_0, \theta_0, -z_0)$ and $R(k_2 \cos\alpha)$ is the plane wave reflection coefficient at the interface $z = 0$ for a ray connecting $\mathbf{r}_0'$ and $\mathbf{r}$, which has

an angle of incidence $\alpha=\sin^{-1}((z+z_0)/|\mathbf{r}-\mathbf{r}_0'|)$. The approximation (44) is convenient since it allows to speed up the far field calculations in the presence of a fluid-fluid interface by avoiding the integration of the full wave number spectrum in Eq. (42).

Decomposition of the far field Helmholtz-Kirchhoff integral in cylindrical harmonics

In the far field limit, where $|\mathbf{r}|\gg|\mathbf{r}_0|$, one has:

$$G(\mathbf{r},\mathbf{r}_0)\approx\frac{e^{-ik|\mathbf{r}|}}{|\mathbf{r}|}e^{ik\langle\mathbf{r},\mathbf{r}_0\rangle/|\mathbf{r}|}, \tag{45}$$

where $\langle\mathbf{r},\mathbf{r}_0\rangle$ is the inner product between the two vectors. Using Eq. (45), the far field pressure in a homogeneous medium is approximated by

$$p^{\infty}(\mathbf{r})=\frac{1}{4\pi}\frac{e^{-ik|\mathbf{r}|}}{|\mathbf{r}|}I_{\infty} \tag{46}$$

with

$$I_{\infty}=\int_{S_0}e^{ik\langle\mathbf{r},\mathbf{r}_0\rangle/|\mathbf{r}|}\left[ikp(\mathbf{r}_0)\frac{\langle\mathbf{r},\mathbf{n}(\mathbf{r}_0)\rangle}{|\mathbf{r}|}-\rho_f\omega^2\langle\mathbf{u}(\mathbf{r}_0),\mathbf{n}(\mathbf{r}_0)\rangle\right]dS. \tag{47}$$

At the point $\mathbf{r}_0\in S_0$ the outward pointing unit vector perpendicular to S_0 is $\mathbf{n}(\mathbf{r}_0)$, and the acoustic particle displacement is $\mathbf{u}(\mathbf{r}_0)$.

For an axially symmetric surface S_0 the normal is $\mathbf{n}(\mathbf{r}_0)=n_r\mathbf{e_r}+n_z\mathbf{e_z}$. Substitution of the expansion (23) into Eq. (47), and denoting with $\Gamma=\{(r_0,\theta_0,z_0)\in S_0:\theta_0=0\}$ yields

$$I_{\infty}=\int_{\Gamma}\int_0^{2\pi}e^{ikrr_0/|\mathbf{r}|\cos(\theta_0-\theta)}r_0e^{ikzz_0/|\mathbf{r}|}\begin{Bmatrix}e^{im\theta_0}\\ \cos(m\theta_0)\end{Bmatrix}\times\left[ik\frac{p_m}{|\mathbf{r}|}(rn_r\cos(\theta_0-\theta)+zn_z)-\rho_f\omega^2(u_mn_r+w_mn_z)\right]d\theta_0d\ell, \tag{48}$$

where the complex exponential or the cosine in the brackets is taken consistently with the choice adopted for Eq. (23). Applying the change of variables $\psi=\theta_0-\theta$ in the integral over θ_0 and defining $\zeta=krr_0/|\mathbf{r}|$ yields

$$I_{\infty}=\int_{\Gamma}r_0e^{ikzz_0/|\mathbf{r}|}\times\left[ik\frac{p_m}{|\mathbf{r}|}(rn_rC_m(\zeta)+zn_zE_m(\zeta))-\rho_f\omega^2E_m(\zeta)(u_mn_r+w_mn_z)\right]d\ell, \tag{49}$$

with

$$E_m(\zeta)=\begin{Bmatrix}e^{im\theta}\\ \cos(m\theta)\end{Bmatrix}I_m^{\mathrm{e}}(\zeta) \tag{50}$$

$$C_m(\zeta)=\begin{Bmatrix}e^{im\theta}\\ \cos(m\theta)\end{Bmatrix}I_m^{\mathrm{ec}}(\zeta). \tag{51}$$

The integrals

$$I_m^{\mathrm{e}}(\zeta)=\int_0^{2\pi}e^{i(\zeta\cos\psi+m\psi)}d\psi=2\pi i^mJ_m(\zeta) \tag{52}$$

$$I_m^{\mathrm{ec}}(\zeta)=\int_0^{2\pi}e^{i(\zeta\cos\psi+m\psi)}\cos\psi d\psi=-2\pi i^{m+1}J_m'(\zeta), \tag{53}$$

appearing in Eqs. (50) and (51), are obtained from standard representations of the Bessel function.[40] J_m' is the derivative of J_m.

VII. RESULTS

The results reported here were obtained on a AMD64 Opteron 285 2.6 GHz workstation running the 64 bit Linux operating system. Generally, the interest is in computing results for a frequency sweep consisting of a large number of frequency samples. The number of complex degrees of freedom of the modal linear algebraic equation system solved by the numerical code at each jth frequency and for each mode is represented by N_j^{DOF}, and the CPU time for the solution of each linear system is denoted by T_j^{CPU}. The number of Fourier modes used to represent the unknowns via Eq. (23) is M_j. The total computation time for the solution of a given problem is the sum $T^{\mathrm{CPU}}=T_j^{\mathrm{CPU}}M_j$.

In the scattering problems presented here the incident field consists of plane waves described by Eq. (21). Generalizing a truncation criterion for $\phi=0$ proved by Ihlenburg,[11] the series expansion is truncated at a modal order $m=M_j$, with M_j being the nearest integer to $1.6\,kr_{\max}|\cos\phi|$. If $\phi\neq90°$ and $M_j<10$, the default $M_j=10$ is used. For the case $\phi=90°$ it is possible to set $M_j=0$. The radius $r_{\max}$ corresponds to the largest radial coordinate at which the incident field is evaluated, which for the computations presented in Secs. VII A, VII B, and VII D corresponds to the largest radial coordinate of the interface between the scatterer and the fluid. The quantity of interest computed in the scattering examples is the far field target strength

$$TS(\mathbf{r})=20\log_{10}(|\mathbf{r}|p^{\mathrm{scat},\infty}(\mathbf{r})|/|p^{\mathrm{inc}}|). \tag{54}$$

In Secs. VII A and VII B, $p^{\mathrm{scat},\infty}$ is computed from Eqs. (46) and (49), where the curve Γ coincides with the interface between the scatterer and the surrounding fluid.

A. Applicability of the PML at coincidence frequency

To illustrate the applicability of the PML on the wet surface of convex targets, the backscattering from a submerged steel spherical shell is studied analytically and with the proposed numerical tool, referred to as "AxiScat" for convenience. The outer radius of the empty spherical shell is $a=0.5$ m, and the wall thickness is 4 cm. The properties of the steel are $\rho_S=7700\ \mathrm{kg/m^3}$, $c_L=5950$ m/s and $c_T=3240$ m/s. For the surrounding water, $\rho=1000\ \mathrm{kg/m^3}$, and $c_f=1500$ m/s. Figure 6 shows a schematic representation of the computational domain drawn to scale. The PML is ap-

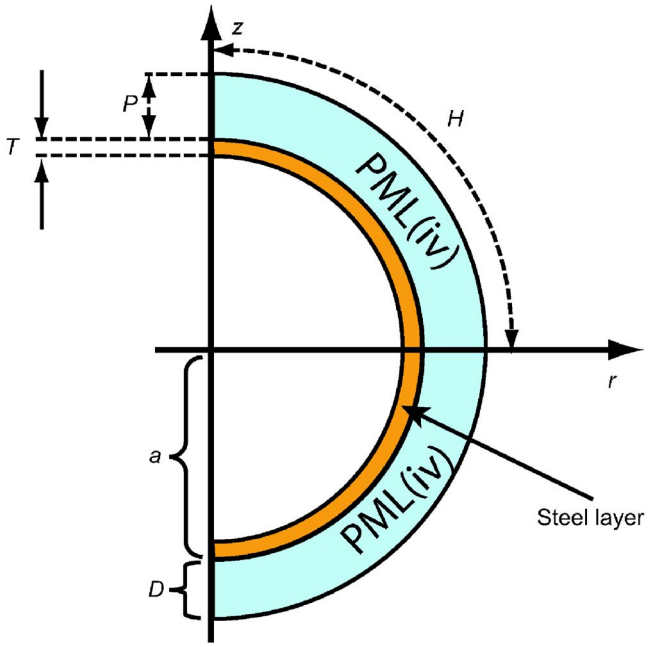

FIG. 6. (Color online) Finite element computational domain for scattering from the submerged void steel spherical shell.

plied in direct contact with the scatterer. The structured mesh consists of quadrilateral cubic Lagrange finite elements with $H=80$ elements along the arc depicted in the figure, $P=16$ elements through the thickness of the PML and $T=6$ elements through the thickness of the elastic layer. The same mesh is used throughout the entire frequency band. In particular, the PML thickness D can be chosen arbitrarily, and it can remain constant for all frequencies, since the scaling defined in Eq. (29) is normalized with respect to the wavelength λ.

The frequency band 10 Hz–15 kHz is discretized in 10 Hz intervals, and it includes the coincidence frequency f_c in the vicinity of 6.5 kHz. The incident plane wave is evaluated at $r_{\max}=a$. $N_j^{\mathrm{DOF}}=51\,000$ and $T_j^{\mathrm{CPU}}=4.7$ s. The plane wave is incident along the z axis, so that $\phi=90°$ and one can retain only the first Fourier mode. The solution for the entire frequency sweep is computed in $T^{\mathrm{CPU}}=7050$ s. The axisymmetric finite element solution, labeled "AxiScat PML" in Fig. 7 is compared to an analytical solution based on the representation of the acoustic field in a series of spherical harmonic basis functions.[34] The agreement between the two results demonstrates the applicability of the PML in contact with the elastic structure at coincidence frequency. To verify the applicability of the PML also for higher order azimuthal modes, the same result has been obtained using a plane wave incidence angle $\phi=90°$, with $M_{15\ \mathrm{kHz}}=51$.

B. Convergence in the presence of structure borne resonances

The pre-asymptotic relative error of a high order FE solution of the Helmholtz equation can be written with respect to the H^1 norm in the form[1,11]

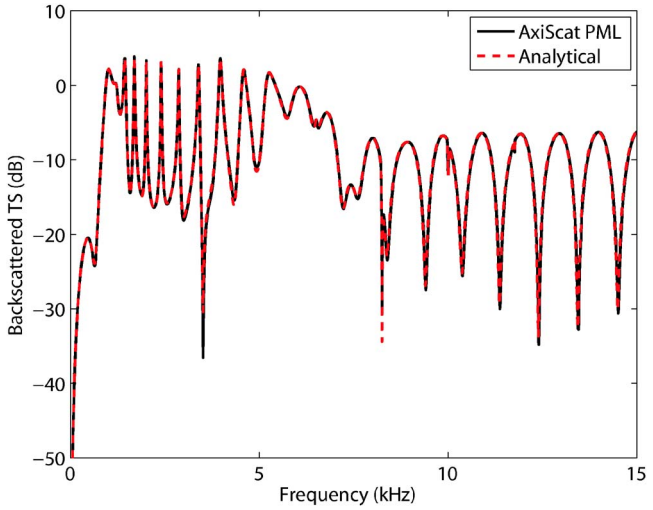

FIG. 7. (Color online) Backscattered far field for the submerged void steel spherical shell. The coincidence frequency is approximately at 6.5 kHz.

$$\tilde{e}=\mathrm{O}(\theta_{\mathrm{ph}}+k_{\mathrm{ph}}\theta_{\mathrm{ph}}^2),\quad \theta_{\mathrm{ph}}=\left(\frac{k_{\mathrm{ph}}h}{p}\right)^p<1, \tag{55}$$

where $k_{\mathrm{ph}}=2\pi f/c_{\mathrm{ph}}=2\pi/\lambda_{\mathrm{ph}}$ is the wave number, h is the size of the elements in the FE mesh, and p is the order of the polynomials. In structural acoustics applications, physics based meshing guidelines can be obtained by analyzing the critical parameter θ_{ph} in relation to the phase speeds c_{ph} of short-scale structure-borne waves, such as asymmetric Lamb waves. The approach is illustrated here using the void elastic cylindrical shell of Fig. 8 as an example. Analytical methods presented in the literature[25–27] are used to estimate the phase speeds c_{ph} of the asymmetric A_0^- Lamb waves supported by the end-capped cylinder. The phase speeds of the A_0^- waves generated in the hemispherical end cap are roughly equal to the corresponding phase speeds supported by a sphere of the same material, radius and thickness as the hemispherical end cap, and similarly the phase speeds for the cylindrical por-

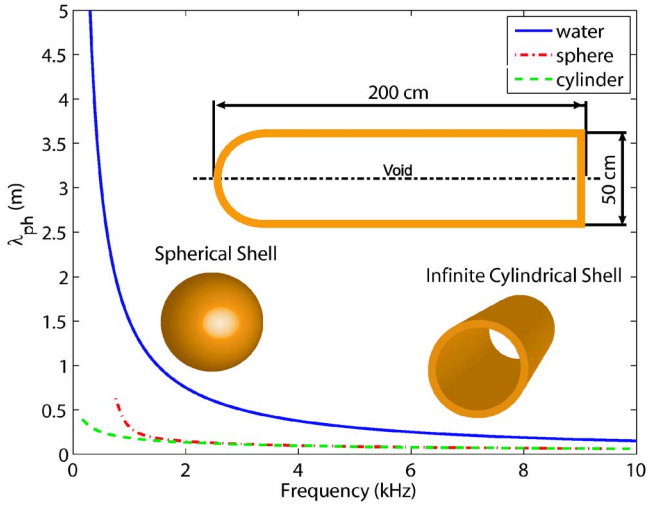

FIG. 8. (Color online) Wavelength associated with the phase speed of the structure-borne waves for the spherical and the cylindrical component of the end-capped cylinder compared to the wavelength associated with the sound speed in the water. The wall thickness is 1 cm.

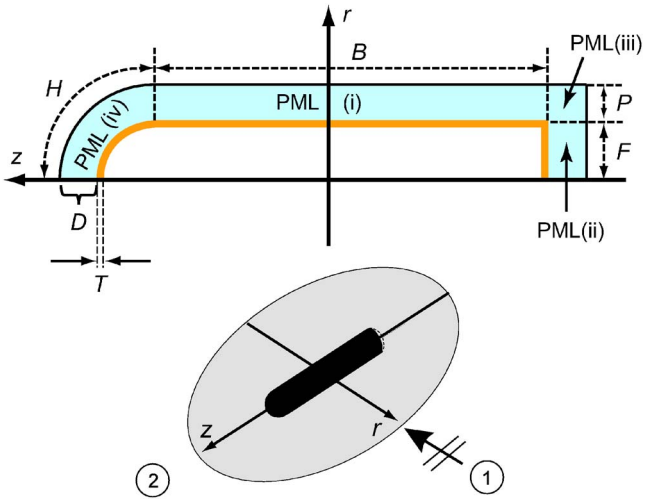

FIG. 9. (Color online) Finite element computational domain for scattering from the submerged cylinder, and definition of the incident plane wave and far field receiver points.

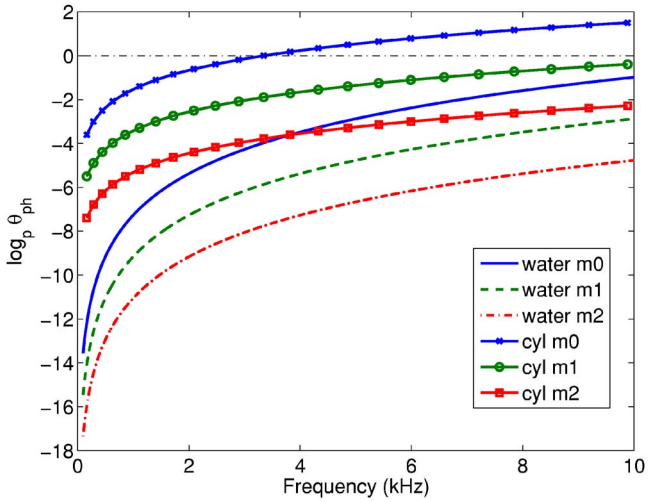

FIG. 10. (Color online) Logarithmic plot of the convergence parameter θ_{ph} computed relative to $c_{\mathrm{ph}}=c_f$ and $c_{\mathrm{ph}}=c_{A0-}^{\mathrm{cyl}}$ with mesh $m0$, $m1$, and $m2$, respectively.

tion of the scatterer are estimated using an infinite cylinder. The cylinder has $\rho_{\mathrm{s}}^{\mathrm{shell}}=3000\ \mathrm{kg/m^3}$, $c_{\mathrm{L}}^{\mathrm{shell}}=3500\ \mathrm{m/s}$ and $c_{\mathrm{T}}^{\mathrm{shell}}=1400\ \mathrm{m/s}$ and is surrounded by water. A plane wave is incident from broadside.

The geometry is discretized using the structured mesh of cubic $p=3$ quadrilateral elements described in Fig. 9, with $T=1$ representing the number of elements through the shell thickness, H the number of elements around the hemispherical end cap, B the number of elements along the cylinder body, F the number of elements along the flat end cap and P the number of elements through the PML of thickness D. Table I shows the parameters defining the three meshes used. The reference solutions used here for comparison are converged solutions obtained with the SONAX tool, which is a validated high order FE structural acoustic modeling tool for axisymmetric elastic bodies.[5,11,20] The radiation condition in SONAX is satisfied using an axisymmetric version of the unconjugated prolate spheroidal infinite element (UIE).[3,4]

As a first test, the elastic structure is neglected and homogeneous Neumann boundary conditions are applied to the total pressure p at the surface of cylinder. In this case the relevant wavelength is $\lambda=c_{\mathrm{f}}/f$, which is represented by the curve labeled "water" in Fig. 8. The curve labeled "water $m0$" in Fig. 10 shows that $\theta_{\mathrm{ph}}\ll 1$ for the entire frequency band, which results in the good agreement between the AxiScat result and the reference solution shown in Fig. 11. For this example, $N_j^{\mathrm{DOF}}=9600$, $T_j^{\mathrm{CPU}}=0.8$ s and $T^{\mathrm{CPU}}=4.9$ h. The frequency band 100 Hz–10 kHz is divided in 5 Hz intervals.

As the elastic cylinder is considered, the situation changes dramatically because of the presence of the short Lamb waves shown in Fig. 8. The structural wavelengths $\lambda_{\mathrm{cylinder}}$ and $\lambda_{\mathrm{sphere}}$ are shorter than λ_{water} by more than one order of magnitude in the low-frequency band, and they exhibit a slow decay with increasing frequency. This suggests that the mesh density should remain constant across the entire frequency band considered. Mesh $m0$ is not sufficient to guarantee convergence in the structural acoustics problem, as shown in Fig. 12 and substantiated by the curve "cyl $m0$" in Fig. 10 which shows in particular that $\theta_{\mathrm{ph}}>1$ for $f>3.3$ kHz. The disagreement with the reference solution is much less evident at the far field receiver located in front of the hemispherical end cap because the Lamb waves mainly reradiate tangentially along the circular cross section of the cylinder at broadside insonification. The convergence improves with mesh $m1$ (Fig. 13), with some minor disagreements in the higher end of the frequency band, where $\theta_{\mathrm{ph}}\to 1$ (Fig. 10). For mesh $m2$ $\theta_{\mathrm{ph}}\ll 1$ throughout the entire frequency band, and the AxiScat solution is virtually indis-

TABLE I. Meshes used for the void cylindrical shell; h is the length of the longest element edge.

Mesh	h (cm)	H	B	F	P
m0	5	8	35	5	16
m1	2.5	16	70	10	16
m2	1.25	32	140	20	16

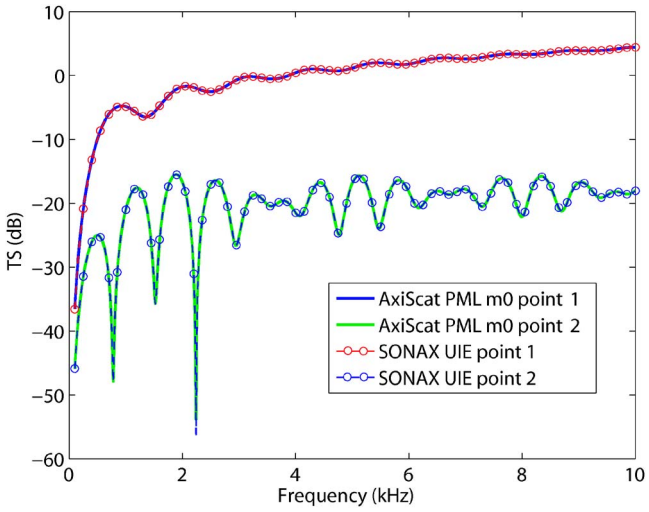

FIG. 11. (Color online) Scattered field target strength for the perfectly rigid cylinder.

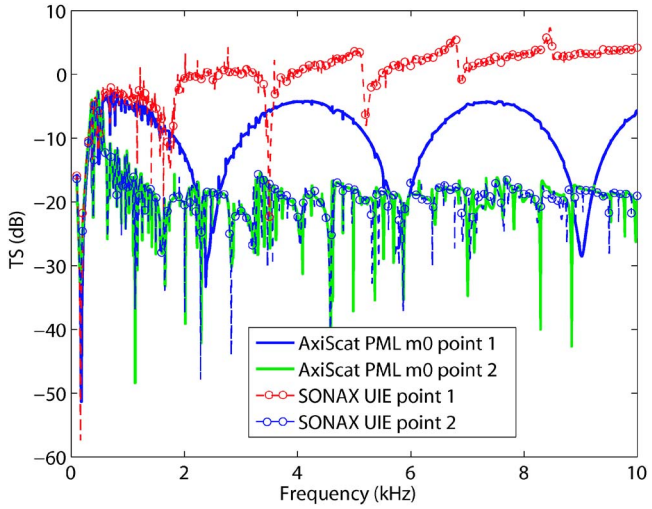

FIG. 12. (Color online) Scattered field target strength for the void elastic cylindrical shell. The disagreement with the reference solution, caused by the insufficient discretization of the shell borne Lamb waves, is particularly evident in the backscatter direction (point 1).

tinguishable from the SONAX solution. The FE problem size and solution times for the cylindrical shell scattering example are reported in Table II.

A further level of structural complexity is added to the problem by considering the cylinder partially filled with a solid having $\rho_s^{\text{fill}}=2000\ \text{kg/m}^3$, $c_L^{\text{fill}}=2500\ \text{m/s}$ and $c_T^{\text{fill}}=1200\ \text{m/s}$. Using mesh $m2$ yields the agreement with the reference solution shown in Fig. 14. In this case, $N_j^{\text{DOF}}=113\,500$, $T_j^{\text{CPU}}=15$ s and $T^{\text{CPU}}=$four days.

Similar effects of structure borne waves on the convergence of FE methods as the ones reported here have been observed by the authors[41] also using a fully 3D FE code[29] with unconjugated infinite elements.[4] As a practical meshing guideline for structural acoustics FE applications, one can envision using standard analytical methods to estimate the shortest wavelength supported by the structure and subsequently designing the mesh such that $\theta_{\text{ph}}\ll 1$.

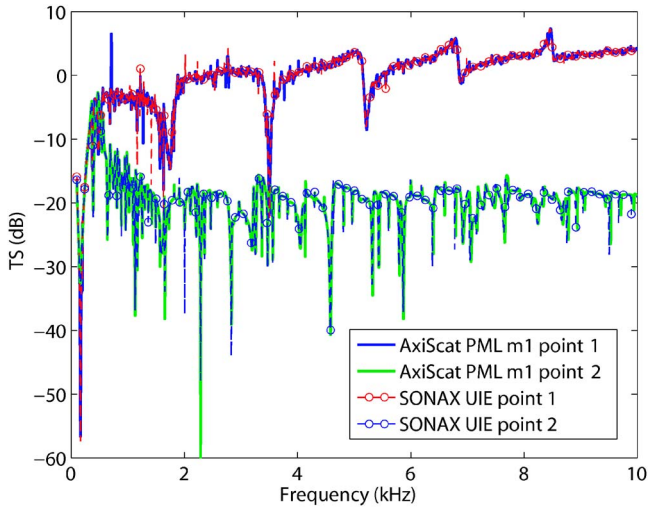

FIG. 13. (Color online) Scattered field target strength for the void elastic cylindrical shell. Discretization of the Lamb waves with mesh $m1$ improves the agreement with the reference solution.

TABLE II. Number of complex DOF and CPU times for the empty cylindrical shell computations.

Mesh	N_j^{DOF}	T_j^{CPU} (s)	T^{CPU} (h)
m0	11 500	1	6.4
m1	20 100	1.6	9.7
m2	37 700	3.1	19.6

C. Upslope ocean wedge propagation

The applicability of the PML in the presence of interfaces separating different fluid domains, mentioned in Sec. IV B, is illustrated here via the axisymmetric low-frequency ocean propagation problem[15] depicted in Fig. 15(a). The 15 Hz point source is located at $(r,z)=(0,100)$. The ocean surface, at which homogeneous Dirichlet conditions are applied to the total pressure, coincides with the plane $z=0$. The bottom is supposed to extend out to infinity in r and z, and the water column extends to infinity in r. The properties of the water are $\rho_f^{(1)}=1000\ \text{kg/m}^3$, $c_f^{(1)}=1500\ \text{m/s}$. The bottom is described as a fluid with $\rho_f^{(2)}=2000\ \text{kg/m}^3$ and $c_f^{(2)}=2400\ \text{m/s}$ having an attenuation of $\alpha=0.2\ \text{dB}/\lambda$, which is modeled by making $c_f^{(2)}$ complex. The domain is discretized with an unstructured mesh of quadratic Lagrange triangular elements. Convergence is reached with approximately 4 quadratic elements per acoustic wavelength, for which the convergence parameter $\theta_{\text{ph}}\approx 0.6<1$. The corresponding number of degrees of freedom is $N=290\,000$, and the solution time is $T^{\text{CPU}}=20$ s.

The PML's are applied according to Fig. 15(b), which

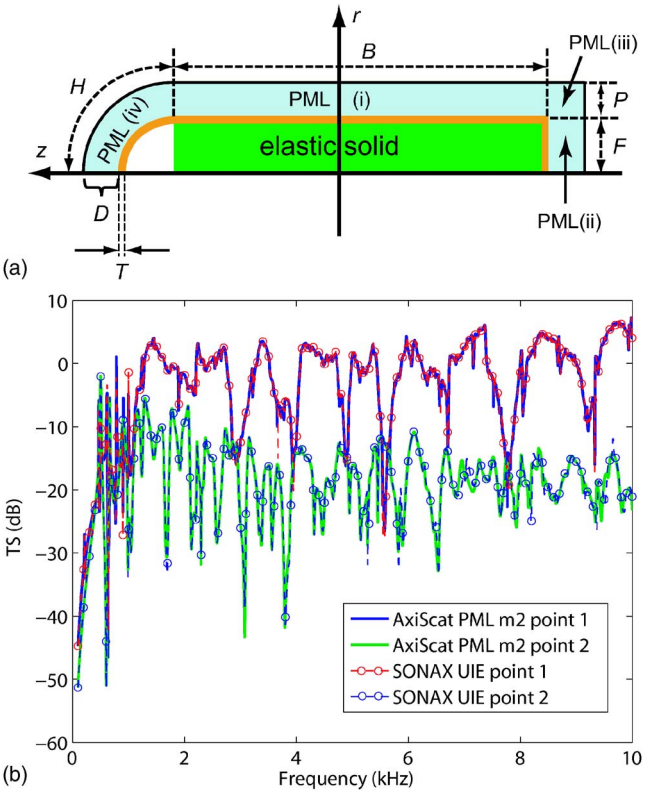

FIG. 14. (Color online) Scattered field target strength for the partially solid-filled elastic cylindrical shell compared to the reference solution.

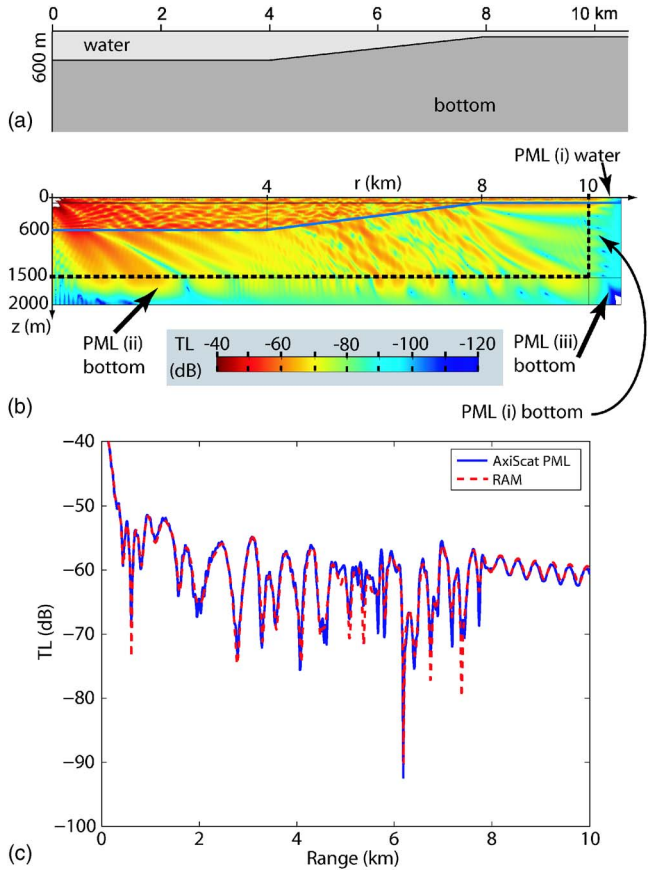

FIG. 15. (Color online) Propagation from a 15 Hz point source located at 100 m depth in an upslope ocean wedge (a, b). Transmission loss sampled at a constant depth of 30 m compared to the reference result from the parabolic equation model RAM (c).

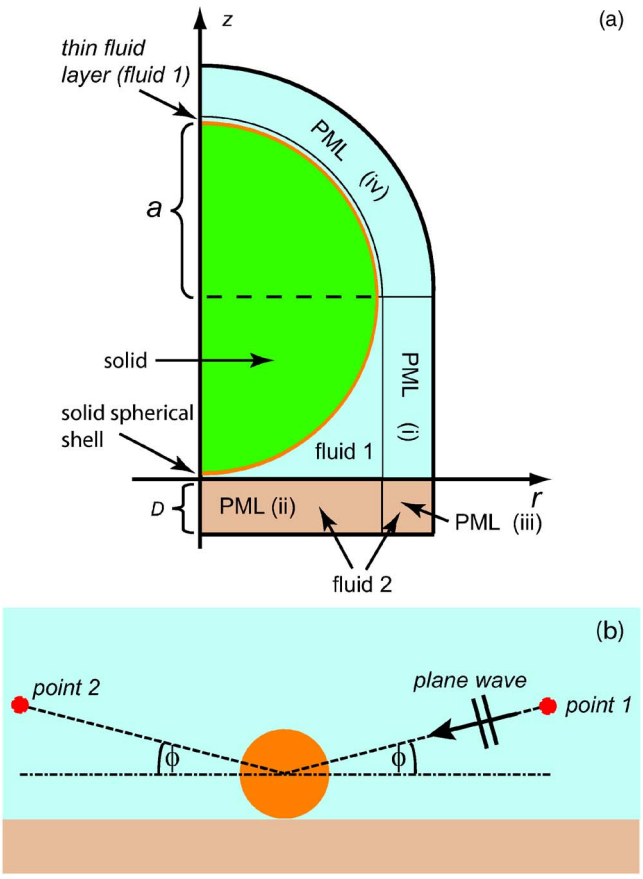

FIG. 16. (Color online) Finite element computational domain for scattering from an elastic layered sphere lying on the interface between two different fluid half spaces (a), and definition of the problem geometry (b).

shows in particular that the water PML is in direct contact with the bottom PML. The transmission loss, defined as $TL = -20\log_{10}|p(r,z)/p_0|$, where p_0 is the pressure at 1 m from the source, is plotted in Fig. 15(b). The graph of TL sampled at a constant depth of 30 m shown in Fig. 15(c) agrees well with the reference solution obtained from a parabolic equation model.[42,43]

D. Sphere proud on the interface between two different fluids

The PML is particularly attractive for computing the field scattered or radiated by an object located within a layered medium. As an example the far field scattering from a layered elastic sphere lying on the interface between two different fluids is considered in Fig. 16. The upper fluid has the properties $\rho_f^{(1)}=1000$ kg/m^3, $c_f^{(1)}=1500$ m/s and the lower fluid has $\rho_f^{(2)}=1800$ kg/m^3, $c_f^{(2)}=1600$ m/s with a dissipation of $\alpha=0.5$ dB/λ. The critical angle of reflection is around 20°. The outer radius of the sphere is $a=0.5$ m, and the shell is 1 cm thick. The shell material has $\rho_s^{\text{shell}}=3000$ kg/m^3, $c_L^{\text{shell}}=3500$ m/s and $c_T^{\text{shell}}=1400$ m/s, and the solid filling has $\rho_s^{\text{fill}}=2000$ kg/m^3, $c_L^{\text{fill}}=2500$ m/s and $c_T^{\text{fill}}=1200$ m/s. Two different insonification angles are considered: supercritical insonification at $\phi=25°$ and subcritical insonification at $\phi=15°$. The far field is sought at the two points shown in the figure and located 50 m from the center of the sphere.

The computational domain is described in Fig. 16(a), where the PML for the upper fluid is in direct contact with the PML for the lower fluid at the interface $z=0$. The sphere is lifted by a distance of 0.25 cm along z from the bottom interface to circumvent meshing difficulties arising from the presence of degenerate corners at $(r,z)=(0,0)$ and at $(r,z)=(a,a)$. This makes it also necessary to introduce the 0.25-cm-thick layer of fluid between the upper hemisphere and the PML depicted in the figure. The domain is discretized using an unstructured mesh of triangular cubic Lagrange elements. The A_0^- phase speed estimated analytically for the spherical shell[25,27] varies between a minimum of 167 m/s at approximately 550 Hz and a maximum of 600 m/s at 10 kHz. The shell and its surroundings are meshed with elements having a maximum edge length of 0.5 cm, which corresponds to $\theta_{\text{ph}}(550\text{ Hz})=4\times10^{-5}$ and $\theta_{\text{ph}}(10\text{ kHz})=5\times10^{-3}$. The element size away from the shell increases up to 1.5 cm. This results in $N_j^{\text{DOF}}=205\,000$ and $T_j^{\text{CPU}}=35$ s, which for the sweep from 100 Hz to 10 kHz in 5 Hz intervals amounts to a total computation time of 14.5 days.

The incident field applied on the interface between the elastic sphere and the fluid domain is

$$p^{\text{inc}}(r,\theta,z) = p^{\text{inc}}_{\phi}(r,\theta,z) + R(k_2 \cos\phi) p^{\text{inc}}_{-\phi}(r,\theta,z), \qquad (56)$$

where p^{inc}_{ϕ} is defined in Eqs. (21) and (22), the reflection coefficient R is given in Eq. (43) and the incidence angle ϕ is defined in Fig. 16. The far field target strength, Eq. (54), at the ith receiver is computed by approximating the 3D Helmholtz-Kirchhoff integral for the scattered field, Eq. (39), via the discrete sum

$$p^{\text{scat}}(\mathbf{r}_i) = \left(\frac{\partial G^{(12)}_{ij}}{\partial n_j} p^{\text{scat}}_j - \rho^{(1)}_{\text{f}} \omega^2 G^{(12)}_{ij} (u^{\text{scat}}_n)_j \right) dA_j, \qquad (57)$$

where the scattered pressure $p^{\text{scat}}_j = p^{\text{scat}}(\mathbf{r}_j)$ and the normal displacement of the scattered field $(u^{\text{scat}}_n)_j = u^{\text{scat}}_n(\mathbf{r}_j)$ are obtained using the Fourier sum (23). The 2188 sampling points $\mathbf{r}_j$ used here are approximately equidistributed on the surface of the sphere, and dA_j is the area associated with each point. The Green's function for the two-layered medium $G^{(12)}_{ij} = G^{(12)}(\mathbf{r}_i, \mathbf{r}_j)$ is used in the approximate form given in Eq. (44).

The solution computed with the present method is compared to a solution obtained with the scattering module of the wave number propagation tool OASES,[44,45] which uses an analytical model to compute scattering from the layered elastic sphere and the full wave number integral for the two layered medium Green's function $G^{(12)}$. Another difference between the present solution and the OASES solution is that the latter neglects multiple scattering between the scatterer and the fluid-fluid interface beyond the first bounce. Figure 17 shows that the solutions agree well for both incidence angles, with some differences between the AxiScat and the OASES solutions being more evident in the subcritical case for backscattering (Fig. 17(b)). These differences may be attributed to the approximation of the Green's function in the AxiScat solution, Eq. (44), which degrades as the receiver angle moves closer to grazing, and to the neglection of the higher order scattering between the fluid-fluid interface and the scatterer in the OASES solution. Nevertheless, the results demonstrate the applicability of the PML in complex geometries, such as the one studied here.

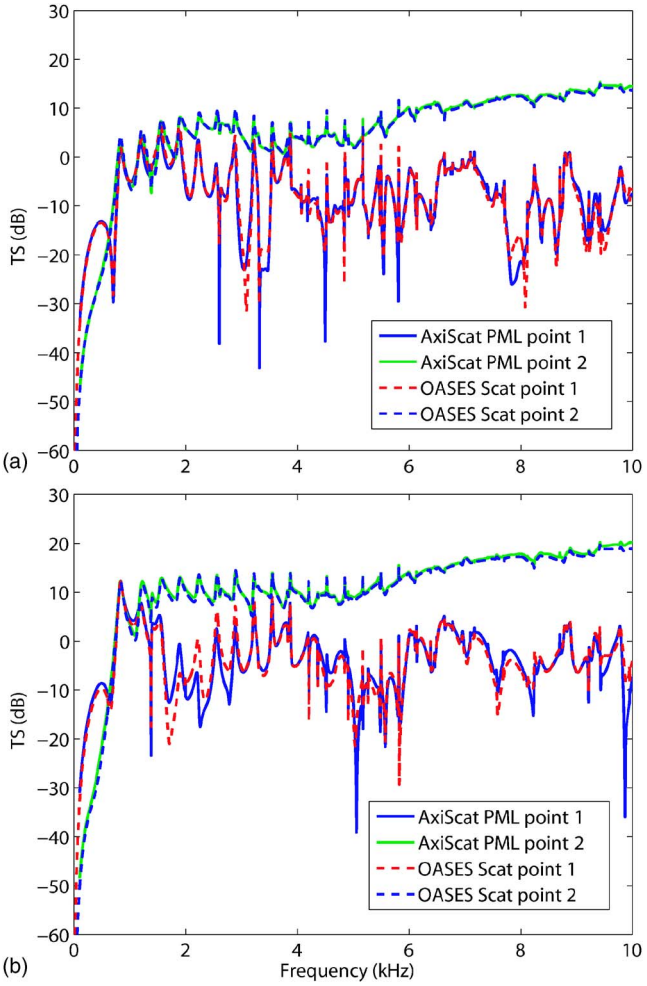

FIG. 17. (Color online) Far field target strength for the spherical target (a) at supercritical incidence $\phi = 25°$ and (b) at subcritical incidence $\phi = 15°$.

VIII. CONCLUSIONS

The finite-element structural-acoustic modeling technique presented can be applied to the analysis of axially symmetric geometries subject to nonsymmetric loading, at frequencies which reach into the mid-frequency regime. The main feature of the model is the Bérenger perfectly matched layer, implemented here in the azimuthal modal decomposition FE scheme, which makes it possible to study radiation or scattering from complex structures in the presence of layered background media. The flexibility with which the PML can be adapted to a variety of convex geometries makes it possible to construct efficient meshes for a number of cases of practical interest. An analytical study of the reflection from fluid PML's in direct contact with elastic structures shows that the PML can be placed on the wet surface of convex objects. This is particularly advantageous in the study of elongated elastic structures. The wavelength-dependent scaling introduced in Sec. IV facilitates the use of the PML by making it possible to define absorbing layers of fixed thickness throughout the entire frequency band. The applicability of PML's across heterogeneous fluid interfaces makes the tool useful in a range of cases of practical interest.

The computation times reported in this paper suggest that further improvements to the computational efficiency of the numerical model are desirable. One immediate approach would be to break a frequency sweep computation into a number of subbands, each of which can be dispatched to the individual nodes of a parallel computer system. The computational efficiency of the tool is also affected by the fact that the FE matrices are recomputed for each frequency. Inspection of the variational equations in Sec. II and in Sec. III suggests that one could identify a number of matrices which would not need to be recomputed for each frequency, but simply multiplied by the frequency and reassembled using a set of coefficients which are computed only once for a given geometry. Such an approach would improve the CPU times of the computations with the present model, but its implementation within the FE framework used by the authors is not straightforward. For this reason, it could not be presented here, but it certainly deserves further attention. To improve the tool further, one can also consider techniques such as the Padé-based interpolation method, introduced recently by

Avery *et al.*,[46] which increases the computational efficiency by reducing the number of frequency samples required to solve broadband problems.

A physics-based meshing guideline for structural acoustics problems, which takes into account the effect of subsonic structure-borne waves on the convergence of the model, is presented and verified by numerical results. The agreement with solutions from a validated axisymmetric FE infinite-element model[5,11,20] establishes a confidence basis for the applicability of the PML on the wet surface of the scattering or radiating structure.

The technique for the evaluation of the far field in a layered medium via the approximation of the Green's function, presented in Sec. VII D, is a useful tool for treating a number of practical problems. In general, one can envision a variety of different background medium configurations for which the Helmholtz-Kirchhoff integral can be evaluated using the appropriate Green's functions. The investigation of approximate Green's functions for such cases is the subject of ongoing research.

[1]L. L. Thompson, "A review of finite-element methods for time-harmonic acoustics," J. Acoust. Soc. Am. **119**, 1315–1330 (2006).
[2]A. Sommerfeld, "Die Greensche Funktion der Schwingungsgleichung" ("The Green's function of the oscillation equation"), Jahresber. Deutsch. Math. Ver. **21**, 309–353 (1912).
[3]J. J. Shirron and I. Babuska, "A comparison of approximate boundary conditions and infinite element methods for exterior Helmholtz problems," Comput. Methods Appl. Mech. Eng. **164**, 121–139 (1998).
[4]D. S. Burnett, "A three-dimensional acoustic infinite element based on a prolate spheroidal multipole expansion," J. Acoust. Soc. Am. **96**, 2798–2816 (1994).
[5]J. J. Shirron, "Solution of exterior Helmholtz problems using finite and infinite elements," Ph.D. dissertation, University of Maryland (1995).
[6]J. P. Bérenger, "A perfectly matched layer for the absorption of electromagnetic waves," J. Comput. Phys. **114**, 185–200 (1994).
[7]J. P. Bérenger, "Perfectly matched layer for the FDTD solution of wave-structure interaction problems," IEEE Trans. Antennas Propag. **44**, 110–117 (1996).
[8]F. Collino and P. Monk, "The perfectly matched layer in curvilinear coordinates," SIAM J. Sci. Comput. (USA) **19**, 2061–2090 (1998).
[9]E. Turkel and A. Yefet, "Absorbing PML boundary layers for wave-like equations," Appl. Numer. Math. **27**, 533–557 (1998).
[10]Q. H. Liu, "Perfectly matched layers for elastic waves in cylindrical and spherical coordinates," J. Acoust. Soc. Am. **105**, 2075–2084 (1999).
[11]F. Ihlenburg, *Finite Element Analysis of Acoustic Scattering* (Springer-Verlag, New York, 1998).
[12]Q. H. Liu and J. Tao, "The perfectly matched layer for acoustic waves in absorptive media," J. Acoust. Soc. Am. **102**, 2072–2082 (1997).
[13]J. J. Shirron and T. E. Giddings, "A finite element model for acoustic scattering from objects near a fluid-fluid interface," Comput. Methods Appl. Mech. Eng. **196**, 279–288 (2006).
[14]M. Zampolli, A. Tesei, and J. B. Blottman, "Scattering from axially symmetric objects: Theory, FEMLAB model implementation and results," Technical Report No. NURC-FR-2006-010, NATO Undersea Res. Ctr. (2006).
[15]F. B. Jensen, P. L. Nielsen, M. Zampolli, M. D. Collins, and W. L. Siegmann, "Benchmarking range-dependent seismo-acoustic propagation problems," in *Proceedings of the 8th European Conference on Underwater Acoustics*, Carvoeiro, Portugal (2006).
[16]E. L. Wilson, "Structural analysis of axisymmetric solids," AIAA J. **3**, 2269–2274 (1965).
[17]O. C. Zienkiewicz and R. L. Taylor, *The Finite Element Method*, 4th ed. (McGraw–Hill, London, 1994), Vols. I and II.
[18]R. D. Cook, *Concepts and Applications of Finite Element Analysis*, 2nd ed. (Wiley, New York, 1981).
[19]D. S. Burnett, *Finite Element Analysis-from Concepts to Applications* (Addison-Wesley, Reading, MA, 1988).
[20]S. Dey, J. J. Shirron, and L. S. Couchman, "Mid-frequency structural acoustic and vibration analysis in arbitrary, curved three-dimensional domains," Comput. Struct. **79**, 617–629 (2001).
[21]J. P. Bérenger, "Application of the CFS PML to the absorption of evanescent waves in waveguides," IEEE Microw. Wirel. Compon. Lett. **12**, 218–220 (2002).
[22]Y. Q. Zeng and Q. H. Liu, "A staggered-grid finite-difference method with perfectly matched layers for poroelastic wave equations," J. Acoust. Soc. Am. **109**, 2571–2580 (2001).
[23]O. B. Matar, V. Preobrazhensky, and P. Pernod, "Two-dimensional axisymmetric numerical simulation of supercritical phase conjugation of ultrasound in active solid media," J. Acoust. Soc. Am. **118**, 2880–2890 (2005).
[24]D. T. DiPerna and D. Feit, "An approximate analytic solution for the radiation from a line-driven fluid-loaded plate," J. Acoust. Soc. Am. **110**, 3018–3024 (2001).
[25]S. G. Kargl and P. L. Marston, "Observations and modeling of the backscattering of short tone bursts from a spherical shell: Lamb wave echoes, glory, and axial reverberations," J. Acoust. Soc. Am. **85**, 1014–1028 (1989).
[26]G. S. Sammelmann, D. H. Trivett, and R. H. Hackman, "The acoustic scattering by a submerged spherical shell. I: The bifurcation of the dispersion curve for the spherical axisymmetric Lamb wave," J. Acoust. Soc. Am. **85**, 114–124 (1989).
[27]J. D. Kaplunov, L. Y. Kossovich, and E. V. Nolde, *Dynamics of Thin Walled Elastic Bodies* (Academic, San Diego, 1998).
[28]J. D. Achenbach, *Wave Propagation in Elastic Solids* (North-Holland, Amsterdam, 1993).
[29]D. S. Burnett and M. Zampolli, "FESTA: A 3-D finite element program for acoustic scattering from undersea targets," Technical Report No. SR-394, NATO Undersea Res. Ctr. (2004).
[30]A. D. Pierce, *Acoustics-An Introduction to its Physical Principles and Applications* (Acoustical Society of America, Melville, NY, 1991).
[31]A. D. Pierce, "Variational formulations in acoustic radiation and scattering," *Physical Acoustics* (Academic, San Diego, 1993), Vol. XXII.
[32]G. C. Everstine, "A symmetric potential formulation for fluid-structure interaction," J. Sound Vib. **79**, 157–160 (1981).
[33]G. C. Everstine, "Finite element formulations of structural acoustics problems," Comput. Struct. **65**, 307–321 (1997).
[34]N. D. Veksler, *Resonance Acoustic Spectroscopy* (Springer-Verlag, Berlin, 1993).
[35]J. P. Bérenger, "Evanescent waves in PML's: Origin of the numerical reflection in wave-structure interaction problems," IEEE Trans. Antennas Propag. **47**, 1497–1503 (1999).
[36]M. C. Junger and D. Feit, *Sound, Structures, and Their Interaction* (MIT Press, Cambridge, 1972).
[37]A. Bayliss, M. Gunzberger, and E. Turkel, "Boundary conditions for the numerical solution of elliptic equations in exterior regions," SIAM J. Appl. Math. **42**, 430–451 (1982).
[38]COMSOL AB, Stockholm, *COMSOL Multiphysics 3.2—User's Guide* (2005), http://www.comsol.com. Last viewed 8/13/07.
[39]P. M. Morse and K. U. Ingard, *Theoretical Acoustics* (McGraw-Hill, New York, 1968).
[40]M. Abramowitz and I. A. Stegun, *Handbook of Mathematical Functions* (National Bureau of Standards, Washington D.C., 1968).
[41]M. Zampolli, A. Tesei, F. B. Jensen, and J. B. Blottman, "Finite element and hybrid modeling tools for the detection and classification of buried objects in shallow water," in *Proc. Conf. on Boundary Influences in High Frequency Shallow Water Acoustics*, edited by N. Pace and P. Blondel (University of Bath, UK, 2005), pp. 349–356.
[42]F. B. Jensen, W. A. Kuperman, M. B. Porter, and H. Schmidt, *Computational Ocean Acoustics* (Springer-Verlag, New York, 2000).
[43]M. D. Collins, "A split-step Padé solution for the parabolic equation method," J. Acoust. Soc. Am. **93**, 1736–1742 (1993).
[44]H. Schmidt and J. Glattetre, "A fast field model for the three-dimensional wave propagation in stratified environments based on the global matrix method," J. Acoust. Soc. Am. **78**, 2105–2114 (1985).
[45]I. Lucifredi and H. Schmidt, "Subcritical scattering from buried elastic shells," J. Acoust. Soc. Am. **120**, 3566–3583 (2006).
[46]P. Avery, C. Farhat, and G. Reese, "Fast frequency sweep computations using a multipoint Padé-based reconstruction method and an efficient iterative solver," Int. J. Numer. Methods Eng. **69**, 2848–2875, (2007).

On pore-fluid viscosity and the wave properties of saturated granular materials including marine sediments

Michael J. Buckingham[a)]
Marine Physical Laboratory, Scripps Institution of Oceanography, University of California, San Diego, 9500 Gilman Drive, La Jolla, California 92093-0238

(Received 6 April 2007; revised 20 June 2007; accepted 22 June 2007)

The grain-shearing (GS) theory of wave propagation in a saturated granular material, such as a marine sediment, is extended to include the effects of the viscosity of the molecularly thin layer of pore fluid separating contiguous grains. An equivalent mechanical system consisting of a saturating, strain-hardening dashpot in series with a Hookean spring represents the intergranular interactions. Designated the VGS theory, the new model returns dispersion curves that differ mildly from those of the GS theory at lower frequencies, below 10 kHz, where effects due to the viscosity of the pore fluid may be non-negligible. At higher frequencies, the VGS dispersion curves approach those of the GS theory asymptotically. The VGS theory is shown to match the SAX99 dispersion curves reasonably well over the broad frequency band of the measurements, from 1 to 400 kHz. This includes the frequency regime between 1 and 10 kHz occupied by Schock's chirp sonar data, where the viscosity of the pore fluid appears to have a discernible effect on the dispersion curves.
 [DOI: 10.1121/1.2759167]

PACS number(s): 43.30.Ma, 43.20.Bi [AIT] Pages: 1486–1501

I. INTRODUCTION

In the grain-shearing (GS) theory[1,2] of wave propagation in a saturated, unconsolidated granular material such as a marine sediment, two types of wave are predicted, a longitudinal or compressional (sound) wave and a much slower transverse (shear) wave. Each of these waves is characterized by a pair of dispersion relations, which express the phase speed and the attenuation as functions of the frequency as well as the physical properties (e.g., the porosity) of the granular medium. Both dispersion pairs are causal, representing propagating waves with finite phase speeds. Four important wave properties are predicted by the GS dispersion relations: (1) logarithmic dispersion of the compressional wave, of the order of 1% per decade of frequency for water-saturated granular materials; (2) attenuation of the compressional wave that scales essentially as the first power of frequency; (3) logarithmic dispersion of the shear wave; and (4) attenuation of the shear wave that scales essentially as the first power of frequency. The two dispersion pairs, along with the full set of auxiliary equations necessary to characterize the granular medium, have been summarized by Buckingham.[2]

Numerous measurements of the speed and attenuation of the compressional wave in water-saturated granular materials have been reported over the past few decades, many of which are referenced in Buckingham.[2] Most of these measurements were taken at high frequencies, above 10 kHz, and for the most part are in accord with the predictions of the GS theory. This agreement between the GS theory and the data is not confined to the frequency dependencies of the wave speed and attenuation: the observed relationships between wave properties (e.g., the compressional wave speed) and the physical properties of the medium (e.g., the porosity) are also faithfully reproduced by the theory, as demonstrated in Buckingham's comparative analysis.[2]

In an effort to extend the dispersion measurements to lower frequencies, below 10 kHz, the ONR-supported sediment acoustics experiment, SAX99, was conducted in the northern Gulf of Mexico off Fort Walton Beach in 1999. The sediment at the experiment site is a medium sand, which was investigated using a variety of measurement techniques[3] that between them spanned frequencies ranging from 0.125 to 400 kHz. Thus, the SAX99 dispersion curves are composites of data sets obtained using different instrumentation in slightly different locations over a time span of several days.

In a separate experiment, Simpson *et al.*[4] also investigated the wave properties of a medium sand sediment over a band that extended to lower frequencies, below 10 kHz. Their measurements were taken in St. Andrews Bay, Florida with a synthetic aperture array, which returned data at frequencies between 3 and 80 kHz. Although this bandwidth is not as broad as that covered in SAX99, the St. Andrews Bay data set is of interest because it is not a composite but was taken with the same instrumentation at a single location in a relatively brief time window.

At-sea measurements, such as those performed during SAX99 and the St. Andrews Bay experiment, return a wealth of information about the wave properties of sediments saturated with sea water. Of course, if the seawater were replaced with a pore fluid of different viscosity, the wave properties of the granular medium might be expected to change significantly, which suggests a potential check on the available theories of wave propagation in saturated granular materials. With this in mind, Hefner and Williams[5] conducted laboratory experiments on the wave properties of glass beads satu-

[a)]Also affiliated with the Institute of Sound and Vibration Research, The University, Southampton, SO17 1BJ, UK; Electronic mail: mjb@mpl.ucsd.edu

rated with (1) water and (2) a silicone oil with viscosity some 100 times greater than that of water. Their measurements of the sound speed and attenuation in both types of granular medium were made in the high-frequency band from well above 10 kHz to as high as 260 kHz, the exact range depending on the measurement in question. With both types of pore fluid, the attenuation was found to scale essentially linearly with the frequency and the dispersion was approximately logarithmic in frequency. At any given frequency, the effects of the higher-viscosity silicone oil were to increase the attenuation by a factor close to 10, to reduce the sound speed by a factor of about 2/3, and to increase the dispersion (i.e., the gradient of the sound speed versus frequency) by a factor of about 3 relative to the corresponding values observed with water.

In addition to reporting the results from their glass bead experiments, Hefner and Williams[5] also discuss the GS[1] and Biot[6,7] theories of wave propagation in saturated granular materials. As they demonstrate, the GS theory satisfactorily accommodates the difference of two orders of magnitude in the viscosity of the pore fluid, returning sound speed and attenuation curves that provide an excellent match to both sets of glass-bead data. They also show that the Biot theory fails to fit both data sets (see Figs. 2c and 2d in Hefner and Williams[5]), in that it does not return an attenuation that scales linearly with the frequency: Biot's attenuation scales as the square of the frequency below some threshold frequency, above which it transitions to the square root of the frequency.[8] This functional form is identical to that for the attenuation of sound in a viscous fluid.[9]

Returning now to the sound speed and attenuation data from SAX99,[3] there is some evidence to suggest that, at lower frequencies, between 1 and 10 kHz, the viscosity of the pore fluid may be having an effect on the dispersion curves: Schock's sound speed data are low and his attenuation data slightly high relative to the dispersion curves predicted by the GS theory. Similar departures from the predictions of the GS theory could be present in the St. Andrews Bay[4] data, although in this case it is more difficult to tell since the effects, if present at all, are quite small.

In the original GS theory, the viscosity of the pore fluid was neglected, since it has little effect over the higher frequency ranges, above 10 kHz, where most measurements of the wave properties of sediments have been taken. The main purpose of this article is to extend the GS theory by including the effects of pore-fluid viscosity on the grain-shearing process. The mechanism in question concerns lubrication due to the molecularly thin layer of pore fluid separating contiguous grains. Such lubrication, it should be appreciated, constitutes a different physical phenomenon from the motion of the pore fluid relative to the mineral "frame" that is a central element of the Biot theory.[6,7]

For convenience, the extended version of the GS theory will be designated the VGS theory, where the first initial serves as a reminder that the viscosity of the pore fluid is included in the physical model of the grain-shearing process. The generalization leading to the VGS theory represents a lower-frequency effect, which manifests itself in the dispersion curves below about 10 kHz, at least for water-saturated granular materials. At higher frequencies, the VGS dispersion relations reduce identically to those of the GS theory.

To begin the discussion, the GS model is summarized, and some clarification is offered as to why the values of the material exponent, n, are restricted to the interval $0<n<1$. This is followed by a brief review of four sound speed and attenuation data sets that have appeared in the literature: glass beads saturated with water,[5] glass beads saturated with silicone oil,[5] SAX99,[3] and St. Andrews Bay.[4] The VGS theory is then developed and shown to yield dispersion curves that match all four data sets, including the lower-frequency SAX99 data between 1 and 10 kHz, where the effects of viscosity seem to be most pronounced.

II. THE GS DISPERSION RELATIONS

A. Summary of the GS theory

The GS dispersion relations for the compressional and the shear wave are stated here without proof, since the derivation of these expressions may be found in Buckingham.[1] Adopting a similar nomenclature to that of Buckingham,[2] the compressional-wave speed, c_p, and attenuation, α_p, are

$$c_p = \frac{c_0}{\mathrm{Re}[1+\chi(j\omega T)^n]^{-1/2}}, \quad 0<n<1 \tag{1}$$

and

$$\alpha_p = -\frac{\omega}{c_0}\,\mathrm{Im}[1+\chi(j\omega T)^n]^{-1/2}, \quad 0<n<1, \tag{2}$$

where $j=\sqrt{-1}$. The corresponding expressions for the shear-wave speed, c_s, and attenuation, α_s, are

$$c_s = \sqrt{\frac{\gamma_s}{\rho_0}}\frac{(\omega T)^{n/2}}{\cos\left(\frac{n\pi}{4}\right)}, \quad 0<n<1 \tag{3}$$

and

$$\alpha_s = \omega\sqrt{\frac{\rho_0}{\gamma_s}}(\omega T)^{-n/2}\sin\left(\frac{n\pi}{4}\right), \quad 0<n<1. \tag{4}$$

(Note: The units of the attenuations, α_p and α_s, in these expressions are Np/m). In Eqs. (1) and (2), the dimensionless grain-shearing coefficient, χ, is

$$\chi = \frac{\gamma_p + (4/3)\gamma_s}{\rho_0 c_0^2}, \tag{5}$$

where γ_p and γ_s are the compressional and shear rigidity coefficients, respectively. The remaining variables and parameters in the dispersion relations are as follows: the material exponent, n, which is constrained to lie in the interval $0<n<1$; the sound speed, c_0, in the granular medium in the absence of grain-to-grain interactions, as given by Wood's equation for the equivalent suspension;[10] the bulk density of the material, ρ_0; the angular frequency, ω; and an arbitrary time $T=1$ s, introduced to avoid awkward units in those terms that are raised to a fractional power. Note that in Eq. (1) the compressional wave speed is always greater than or equal to the sound speed in the equivalent suspension, that is, $c_p \geqslant c_0$. As the frequency goes to zero, the GS wave proper-

ties reduce to the following: the sound speed, c_p, in Eq. (1) approaches c_0 asymptotically; the sound attenuation, α_p, in Eq. (2) goes to zero; the shear speed, c_s, in Eq. (3) goes to zero; and the shear attenuation, α_s, in Eq. (4) also goes to zero.

Three parameters in the GS theory characterize the microscopic intergranular interactions, including strain hardening, that occur at grain boundaries: the two rigidity coefficients, γ_p and γ_s, and the material exponent, n. The latter scales inversely with the strain hardening coefficient,[1] hence a higher value of n corresponds to a reduced degree of strain hardening. All three parameters, γ_p, γ_s, and n, are discussed in some detail in Buckingham,[2] where, in Table II, numerical values are presented which yield wave speeds and attenuations that match the average trends of many published data sets on the wave properties (e.g., sound speed versus porosity) of marine sediments. In particular, the material exponent takes a value $n \approx 0.1$ for many, if not all, surficial marine sediments, from coarse sands to silts and clays.

B. Evaluation of the three grain-shearing parameters

To date at least, it has not been possible to calculate the values of γ_p, γ_s and n; instead they must be determined by selecting three of the four GS dispersion relations and fitting each to a spot-frequency data point. The situation is analogous to that encountered with Coulomb friction, where the coefficient of kinetic friction, which depends on the nature of the surfaces in contact, cannot be calculated but must be evaluated experimentally from a measurement.

A straightforward procedure for evaluating γ_p, γ_s, and n from data is based on a rearrangement of the expressions for the speed and attenuation of the compressional wave in Eqs. (1) and (2):

$$\frac{c_0}{c_p} - j\frac{c_0\alpha_p}{\omega} = [1 + \chi(j\omega T)^n]^{-1/2}. \tag{6}$$

A further rearrangement yields

$$\left[1 + \chi(\omega T)^n\left\{\cos\left(\frac{n\pi}{2}\right) + j\sin\left(\frac{n\pi}{2}\right)\right\}\right] = \left(\frac{c_p}{c_0}\right)^2 \frac{[1 - X^2 + 2jX]}{[1 + X^2]^2}, \tag{7}$$

where

$$X = \frac{c_p\alpha_p}{\omega} \tag{8}$$

and the identity

$$(j)^n = \cos\left(\frac{n\pi}{2}\right) + j\sin\left(\frac{n\pi}{2}\right) \tag{9}$$

has been used. Equating real parts in Eq. (7) yields

$$\chi(\omega T)^n\cos\left(\frac{n\pi}{2}\right) = \left(\frac{c_p}{c_0}\right)^2 \frac{[1 - X^2]}{[1 + X^2]^2} - 1 \tag{10}$$

and from the imaginary parts

$$\chi(\omega T)^n\sin\left(\frac{n\pi}{2}\right) = \left(\frac{c_p}{c_0}\right)^2 \frac{2X}{[1 + X^2]^2}. \tag{11}$$

The coefficient χ may be eliminated from these expressions by division, which returns the following tangent identity for n:

$$\tan\left(\frac{n\pi}{2}\right) = \frac{2X}{[1 - X^2] - \left(\frac{c_0}{c_p}\right)^2[1 + X^2]^2}. \tag{12}$$

Assuming that c_p, α_p, and hence X, are known from measurements taken at a spot angular frequency ω, n may be evaluated directly from Eq. (12), which then allows χ to be determined from either Eq. (10) or (11). It is implicit here that the porosity of the granular medium is known, along with the density and bulk modulus of the constituent materials, since these are needed to compute Wood's sound speed, c_0. The value of γ_s may be obtained from Eq. (3), assuming that the speed of the shear wave has been measured at a spot frequency (which need not be the same as the frequency of the two compressional-wave measurements). With γ_s and χ both known, γ_p may be evaluated from Eq. (5), thus fully characterizing the GS dispersion relations for the particular granular medium under consideration.

A possible alternative technique for evaluating n is based on Eqs. (3) and (4) for the speed and attenuation of the shear wave. By forming the product of these two expressions, γ_s is eliminated and another tangent identity for n is obtained:[1]

$$\tan\left(\frac{n\pi}{4}\right) = Y, \tag{13}$$

where

$$Y = \frac{c_s\alpha_s}{\omega}. \tag{14}$$

Clearly, if spot frequency measurements of c_s and α_s were available, n could be evaluated from Eq. (13), allowing γ_s and γ_p to be determined from the GS dispersion relations. Although Eq. (13) has the advantage of simplicity, it relies on two measurements of shear wave properties, at least one of which is usually not available. Thus, the technique for evaluating the grain shearing parameters based on Eq. (12) is preferred.

C. An identity coupling the compressional and shear wave

From the elementary identity

$$\tan(2A) = \frac{2\tan(A)}{1 - \tan^2(A)} \tag{15}$$

and the expressions in Eqs. (12) and (13), it follows that

$$\frac{X(\omega_1)}{[1-X^2(\omega_1)]-\left(\frac{c_0}{c_p(\omega_1)}\right)^2[1+X^2(\omega_1)]^2}=\frac{Y(\omega_2)}{1-Y^2(\omega_2)}, \tag{16}$$

where the frequency dependencies of the compressional and shear terms have been expressed explicitly. As the terms on either side of Eq. (16) are frequency invariant, the actual values of ω_1 and ω_2 at which the measurements are made may be chosen for convenience.

Equation (16) expresses a coupling between compressional wave properties on the left and shear wave properties on the right. Moreover, it involves none of the three grain-shearing coefficients but only measured wave speeds and wave attenuations. Thus, the identity in Eq. (16) could provide a rigorous test of the GS theory once precision measurements of all four wave properties (compressional and shear wave speeds and attenuations) are known for a given granular medium. Since three wave properties are needed to evaluate the three grain-shearing coefficients, a measurement of the fourth (independent) property is needed as the check on the theory. A difficulty at the moment is that, often, no more than three of the four wave properties are available, with the shear attenuation being the usual absentee. An exception is the SAX99 sediment for which measurements of all four wave properties have been reported;[3] but even in this case the relatively large uncertainties in the shear speed (mean of 120 m/s with a range of 97–147 m/s) and the shear attenuation (mean of 30 dB/m with a range of 21–40 dB/m) preclude using Eq. (16) as a test of the GS theory.

D. Approximations for the dispersion and attenuation of the compressional wave

When $0<n\ll 1$, as is the case for many water-saturated granular materials, the compressional wave speed given by Eq. (1) increases approximately logarithmically with the frequency. To demonstrate this logarithmic frequency dependence, Eq. (1) is expanded to first order in the small parameter, n, which yields

$$c_p \approx c_0\sqrt{1+\chi}\left[1+\frac{n\chi}{2(1+\chi)}\ln(\omega T)\right]. \tag{17}$$

This expression has been obtained with the aid of Eq. (9) and the identity

$$(\omega T)^n = e^{n\ln(\omega T)}. \tag{18}$$

Similarly, the compressional wave attenuation in Eq. (2) may be expressed to first order in n as

$$\alpha_p \approx \frac{\omega}{4c_0}\frac{n\chi\pi}{(1+\chi)^{3/2}} \approx \frac{\omega}{4c_p}\frac{n\chi\pi}{(1+\chi)}. \tag{19}$$

Since the sound speed is approximately logarithmic in frequency, the dispersion, D, is conveniently defined as the change in sound speed per decade of frequency. Thus, to first order in n, D is a constant, independent of frequency and it follows from Eq. (17) that

$$D \approx c_0\sqrt{1+\chi}\frac{n\chi}{2(1+\chi)}\ln(10). \tag{20}$$

Straightforward substitutions from Eqs. (17) and (19) allow D to be expressed in terms of the compressional-wave speed and attenuation:

$$D \approx \frac{2c_p^2\alpha_p}{\pi\omega}\ln(10). \tag{21}$$

Note that in this expression, D depends only on the directly measurable quantities c_p and α_p at angular frequency ω. Equation (21) states that the dispersion, that is, the *gradient* of the semilogarithmic plot of sound speed versus frequency, is constrained by the magnitude of the sound speed and the attenuation at angular frequency ω. Thus, once broadband measurements of the sound speed and attenuation are available, Eq. (21) provides a rough check of the GS theory.

E. Allowed values of the material exponent, *n*

The reason that values of $n\geqslant 1$ are prohibited in the GS theory concerns the divergence of the Fourier integrals representing the compressional and shear rigidity coefficients, γ_p and γ_s, respectively. According to Buckingham,[1] each of these coefficients is given by an integral of the form[11]

$$\int_0^\infty t^{-n}e^{-j\omega t}dt = \frac{\Gamma(1-n)}{(j\omega)^{1-n}}, \tag{22}$$

where $\Gamma(\cdot)$ is the gamma function. Equation (22) is valid provided $0<n<1$, otherwise the integral diverges, in which case γ_p and γ_s would both become indefinitely large.

The effect of these infinities on the GS dispersion relations is easily established by evaluating Eqs. (1)–(4) in the limit as n approaches unity (from below). This may be achieved with the aid of the reflection formula for the gamma function:[12]

$$\Gamma(1-n) = \frac{\pi\csc(\pi n)}{\Gamma(n)}. \tag{23}$$

Now, bearing in mind that γ_p and γ_s are both proportional to $\Gamma(1-n)$, and recalling the identity in Eq. (9), some straightforward algebra yields the limiting values of the wave speeds and attenuations. The result is that, in the limit as n approaches unity, both the compressional speed and the shear speed become infinite, while the congressional attenuation and the shear attenuation both go to zero. To avoid such unphysical behavior, the condition $0<n<1$ must be satisfied.

III. GLASS-BEAD DATA SETS

In an effort to establish the effect of pore-fluid viscosity on the wave properties of granular materials, Hefner and Williams[5] made high-frequency (i.e., well above 10 kHz) measurements on the compressional wave in two types of medium: glass beads saturated with water, and glass beads saturated with a silicone oil whose viscosity is some 100

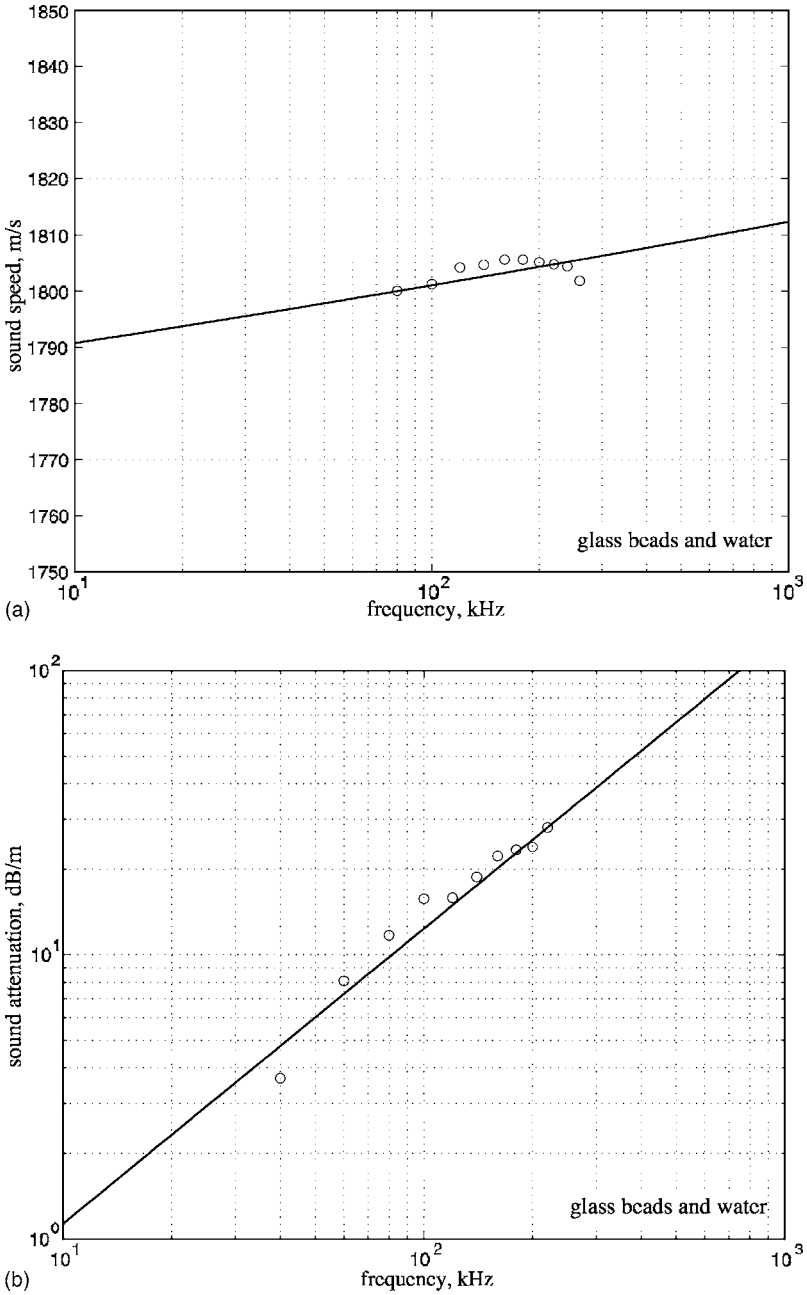

FIG. 1. Dispersion curves for glass beads saturated with water. The open circles represent data and the smooth lines are from the GS theory, evaluated using the parameters in Table I. (a) Sound speed vs frequency. (b) Sound attenuation vs frequency.

times greater than that of water. Their measurements of the sound speed and attenuation in the two materials are depicted by the open circles in Figs. 1 and 2.

With both pore fluids, the data show some dispersion and an attenuation that scales essentially linearly with the frequency. The effect of the 100-fold increase in the viscosity of the pore fluid is to reduce the sound speed and increase the attenuation by factors of approximately 2/3 and 10, respectively. In addition, the gradient of the sound speed versus frequency is higher with silicone oil than with water by a factor of about 3.

The solid curves in Figs. 1 and 2 represent the GS dispersion relations, Eqs. (1) and (2), in which n and χ were evaluated using the technique described in connection with the tangent identity in Eq. (12). All the parameters used in evaluating these expressions are listed in Table I. It is clear that the GS theory provides a very good match to the sound speed and attenuation data from both materials, a result that was also found by Hefner and Williams[5] and illustrated in their Fig. 2.

Interestingly, the value of $n \approx 0.38$ with silicone oil as the pore fluid is almost an order of magnitude higher than $n \approx 0.05$ for the water-saturated case. The fact that n increases significantly as the viscosity of the pore fluid rises could be due to the fact that silicone oil is a much better lubricant than water, having the effect of reducing friction and thus allowing grains to slide against one another more easily. This results in a reduced degree of strain hardening at grain contacts, which accounts for the higher value of n, since the latter scales inversely with the strain-hardening coefficient.[1]

It is perhaps worth noting that, since the value $n \approx 0.38$ is not very small compared with unity, the approximations in Eqs. (17) and (19), respectively, for the full GS expressions

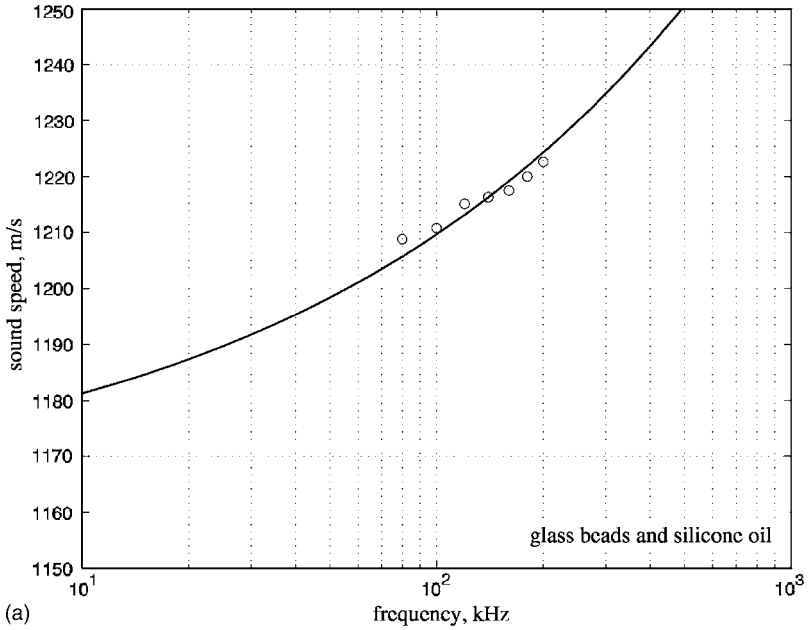

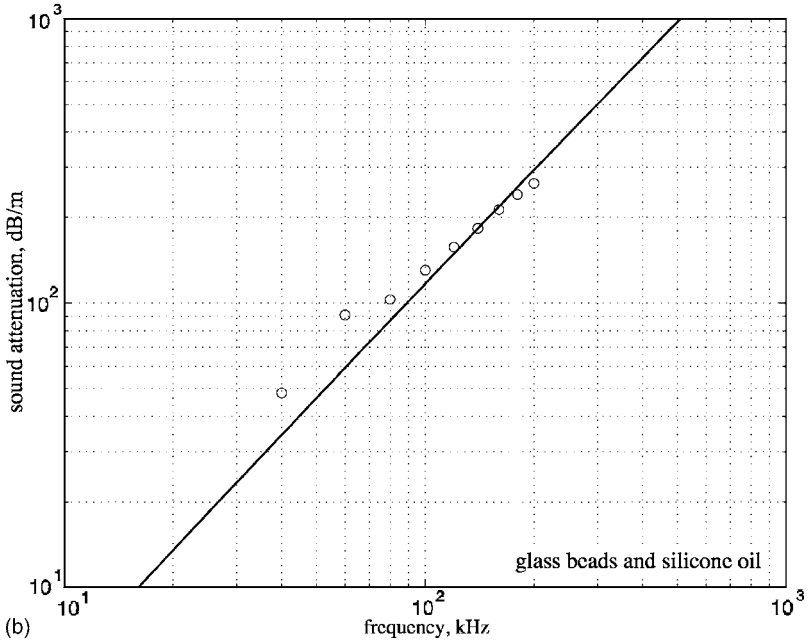

FIG. 2. Dispersion curves for glass beads saturated with silicone oil. The open circles represent data and the smooth lines are from the GS theory, evaluated using the parameters in Table I. (a) Sound speed vs frequency, (b) Sound attenuation vs frequency.

for the sound speed and attenuation are rather poor for the glass beads saturated with silicone oil. This contrasts with the glass beads in water, for which the value $n \approx 0.05$ is much smaller than unity, and Eqs. (17) and (19) represent reasonable approximations.

IV. THE SAX99 DATA SET

The dispersion curves measured during SAX99 in the medium-sand sediment off Fort Walton Beach in the northern Gulf of Mexico are depicted by the various symbols in Fig. 3. In these composite plots, each type of symbol represents a particular experimental procedure. The symbols that are common to Figs. 3(a) and 3(b) are: red diamonds, representing chirp sonar data obtained by Schock; green circles between 11 and 50 kHz, representing data returned by the APL-UW buried array;[13,14] red asterisks at 38 kHz, representing Richardson's data from ISSAMS;[3] blue circles between 100 and 260 kHz, representing data obtained from both the diver deployed attenuation array[13] and an acoustic tomography array known as the Acoustic Imager;[15] and magenta asterisks at 400 kHz, obtained from diver cores by Briggs.[15] Additional symbols appear in Fig. 3(a) showing the sound speed ratio (i.e., the ratio of the sound speed in the sediment to that in the seawater immediately above the sea bed): the blue triangle at 125 Hz represents a bottom-interface measurement by Stoll,[16] performed using geophones and an impulsive source on the sea bed; the blue asterisk at 400 Hz represents a similar type of measurement by Bibee; and the black triangles spanning the band 25–100 kHz represent Richardson's ISSAMS data.[17]

As described in Appendix B of Williams *et al.*,[3] the green circles between 11 and 50 kHz in Fig. 3(a) do not represent absolute values because of a circular argument involving, the assumed value of the sound speed necessary to

TABLE I. Parameter values used in the GS theory for four saturated granular materials. Values in parentheses were used in the VGS theory.

Material parameter	Symbol	Beads (water)	Beads (silicone oil)	SAX99	St. Andrews Bay
Density of pore fluid (kg/m^3)	ρ_w	1000	968	1023	1023
Bulk modulus of pore fluid (Pa)	K_w	2.23×10^9	9.68×10^8	2.395×10^9	2.375×10^9
Sound speed in pore fluid (m/s)	c_w	1493	1000	1530.1	1523.6
Density of grains (kg/m^3)	ρ_s	2500	2500	2690	N/A
Bulk modulus of grains (Pa)	K_g	7.0×10^{10}	7.0×10^{10}	3.2×10^{10}	3.2×10^{10}
Porosity	N	0.384	0.36	0.385	0.379
Bulk density of sediment (kg/m^3)	ρ_0	1924	1949	2048.2	2035
Bulk modulus of sediment (Pa)	κ_0	5.525×10^9	2.62×10^9	5.557×10^9	5.587×10^9
Wood's speed (m/s)	c_0	1694.6	1160.6	1647.1	1656.9
Material exponent	n	0.0452	0.3755	0.0822 (0.0617)	0.1726 (0.1559)
Grain-shearing coefficient	χ	0.0710	0.00067	0.0564 (0.0724)	0.0097 (0.0119)
Compressional coefficient (Pa)	γ_p	3.603×10^8	4.289×10^5	2.895×10^8 (3.734×10^8)	4.431×10^7 (5.492×10^7)
Shear coefficient (Pa)	γ_s	2.390×10^7	1.005×10^6	1.785×10^7 (2.172×10^7)	7.441×10^6 (8.734×10^6)
Viscoelastic time constant (ms)	τ	N/A	N/A	0.12	0.12
GS matching frequency (kHz)		220	140	38	50

locate the sensors in the APL-UW array. To overcome this problem, a common scaling factor was applied by Williams *et al.*[3] to the (relative) data set such that the green circle at 40 kHz matched the reference red asterisk at 38 kHz. In effect, this scaling procedure allowed the green-circle data set to be moved as a unit along the vertical axis in Fig. 3(a) to obtain the required match to the reference datum.

A similar scaling procedure was used by Williams *et al.*[3] on Schock's chirp sonar data in Fig. 3(a). The matching criterion in this case was continuity of the highest frequency chirp sonar data (red diamonds) with the APL-UW buried array results (green circles). Again, the whole data set was moved as a unit along the vertical axis to achieve the matching condition. Thus, in Fig. 3(a), the chirp sonar data set (red diamonds), which spans a frequency range that is crucially important in the investigation of dispersion in sediments, has been scaled to match a data set (green circles) that itself has been scaled to match the reference datum (red asterisk) at 38 kHz.

The solid blue lines in Fig. 3 are the compressional-wave dispersion curves of the GS theory, as computed from Eqs. (1) and (2). In computing these expressions, the parameters n and χ were evaluated using the above-described technique in connection with Eq. (12). The matching frequency was 38 kHz, as shown in Table I along with the values of all the other parameters used in plotting Eqs. (1) and (2). To evaluate Wood's sound speed, c_0, which is needed in the GS dispersion relations, the porosity of the sediment, the bulk densities of sand and seawater, and the bulk moduli of sand and seawater were assigned the same values as those listed in Table 1 of Williams *et al.*[3] for the SAX99 sediment. Note that the value of the material exponent found for the SAX99 data is much less than unity at $n=0.0822$.

It is clear from Fig. 3 that, at higher frequencies, from 10 to 400 kHz, the GS theory provides a very reasonable fit to the SAX99 data set. In this frequency band, the sound speed shows weak logarithmic dispersion and the attenuation scales essentially as the first power of frequency. At intermediate frequencies, between 2 and 10 kHz, Schock's chirp sonar data (red diamonds) fall below the GS sound speed and above the GS attenuation. The two low-frequency sound-speed data points, between 0.1 and 1 kHz (blue triangle and blue asterisk), fall well below the GS curve in Fig. 1(a); and it is also worth noting that these two low-frequency sound speeds are significantly less than the Wood's value, c_0, which, when expressed as a sound speed ratio for the SAX99 sediment, is equal to 1.0764.

The observation of sound speeds below the Wood's value is difficult to explain, since, under gas-free conditions, the minimum sound speed that might be expected is c_0, corresponding to the situation where the medium is a simple suspension with no intergranular interactions. The available evidence suggests that the SAX99 sediment contained a negligible concentration of gas,[15] which leaves the interpretation of the two data points between 0.1 and 1 kHz unresolved. Both data points have large error bars (see Fig. 3 in Williams *et al.*[3]), due to the nature of the experimental procedures used in making the measurements, which may account for the discrepancy between the two observations and the theoretical expectations.

V. THE ST. ANDREWS BAY DATA SET

Measurements of the sound speed and attenuation in the sediment of St. Andrews Bay, Florida were made by Simpson *et al.*[4] using a synthetic aperture array. Their data, depicted by the open circles in Fig. 4, lie in the frequency band

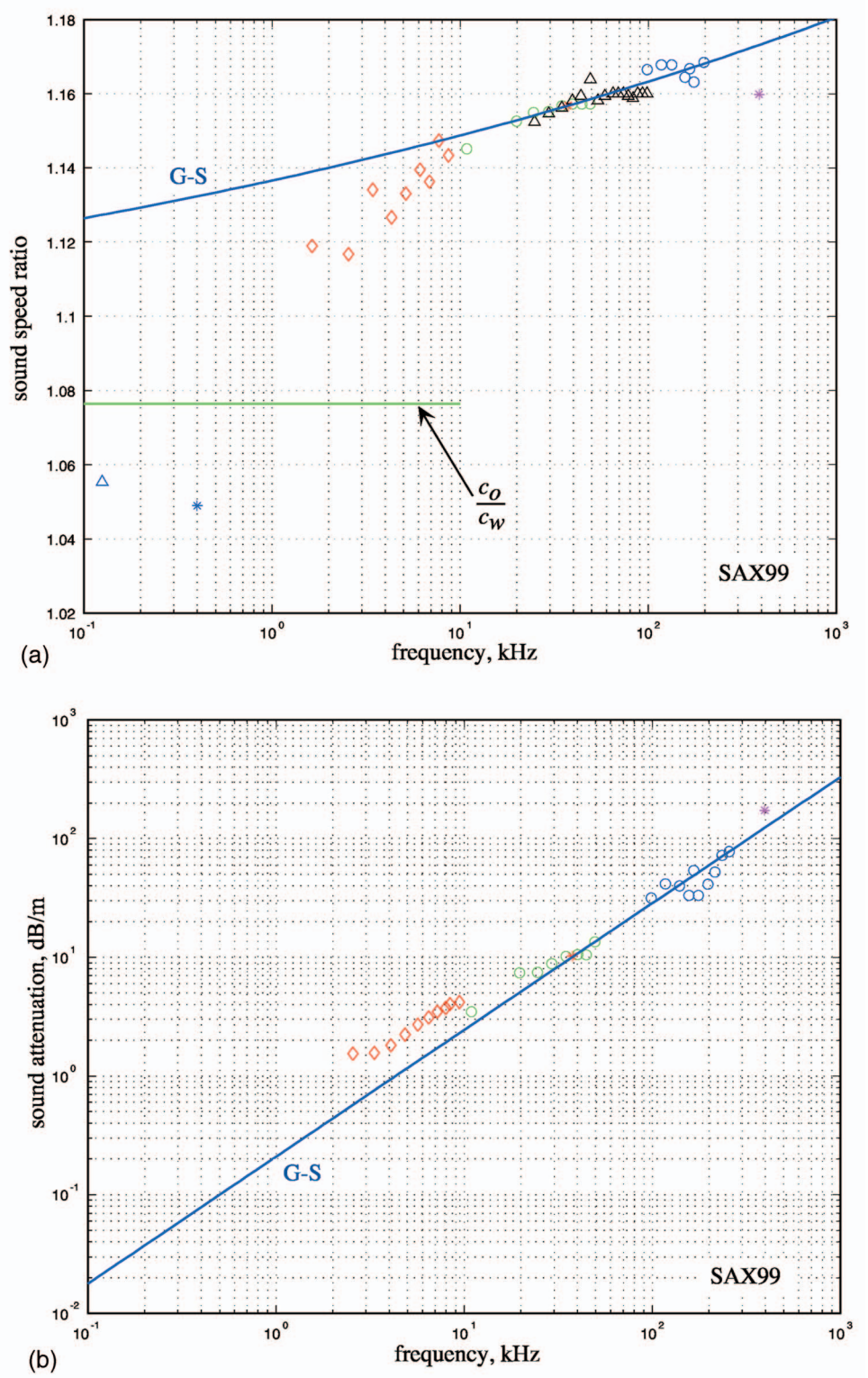

FIG. 3. The SAX99 dispersion curves for a medium sand sediment in the northern Gulf of Mexico. The symbols represent data and the blue lines are from the GS theory, evaluated using the parameters in Table I. (a) Sound speed ratio vs frequency and Wood's sound speed ratio (horizontal green line). (b) Sound attenuation vs frequency.

from 3 to 80 kHz. This is roughly the same frequency range as that covered in Fig. 3 by the SAX99 data acquired from the chirp sonar (red diamonds), the APL-UW buried array (green circles), and ISSAMS (black triangles and red asterisks). The solid curves in Fig. 4, representing the GS theory, were computed using the technique for obtaining n and χ described earlier in connection with Eq. (12). In this case, the theoretical curves were matched to sound speed and attenuation data points taken at a frequency of 50 kHz. The value of the material exponent returned by this procedure for the St. Andrews Bay sediment, although much less than unity at $n=0.1726$, is about twice the value of $n=0.0822$ for SAX99. All the parameter values used in computing the GS dispersion curves shown in Fig. 4 are listed in Table I.

The sound speed data in Fig. 4(a) exhibit weak dispersion, the trend of which is logarithmic at approximately 1.4% per decade of frequency. A small maximum is evident in the data around 30 kHz, a feature which is not present in the

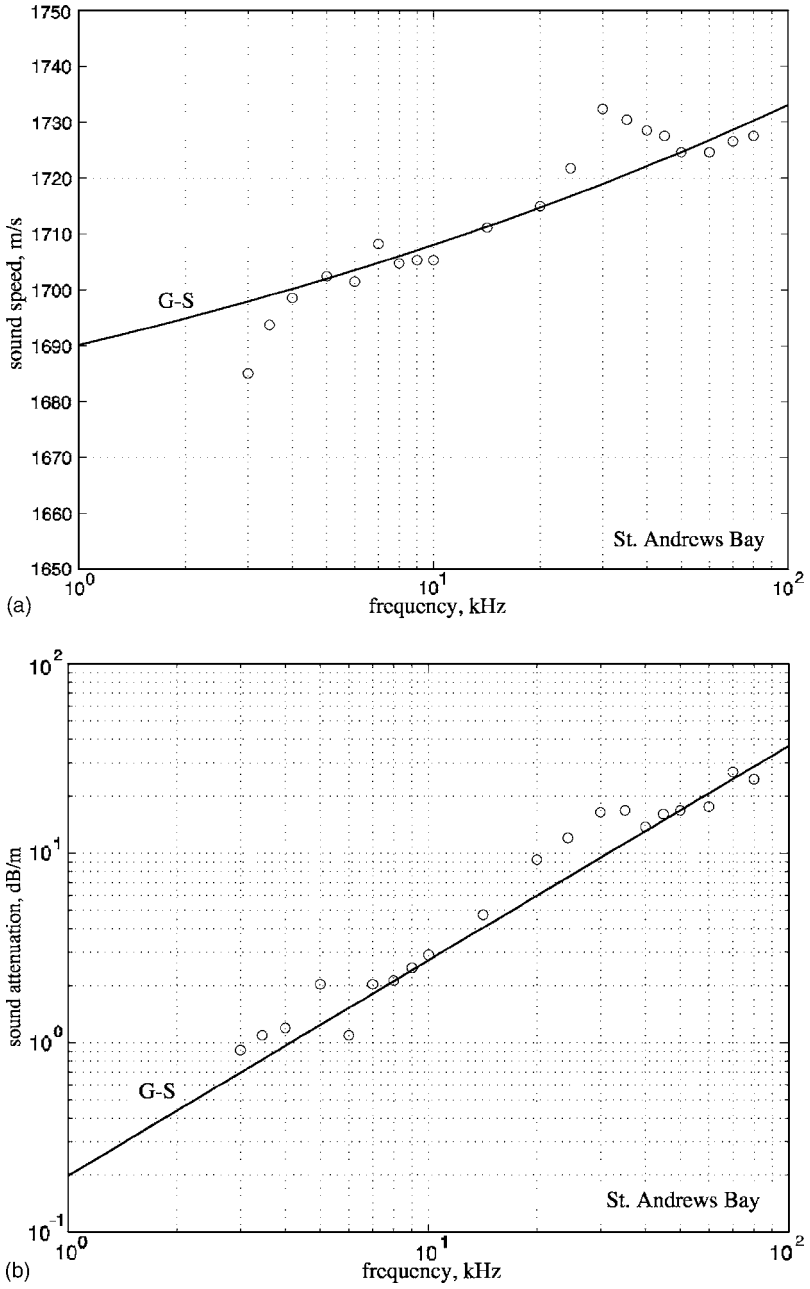

FIG. 4. Dispersion curves for a medium sand sediment in St. Andrews Bay. The open circles represent data and the smooth lines are from the GS theory, evaluated using the parameters in Table I. (a) Sound speed vs frequency. (b) Sound attenuation vs frequency.

SAX99 data [Fig. 3(a)]. The GS theory provides a satisfactory fit to the St. Andrews Bay dispersion data over most of the 3–80 kHz frequency range, although it does not reproduce the peak at 30 kHz. The two lowest-frequency data points in Fig. 4(a) fall a little below the GS curve, possibly indicating a trend toward stronger dispersion at lower frequencies, reminiscent of that exhibited by Schock's SAX99 data (red diamonds) in Fig. 3(a).

In Fig. 4(b), the St. Andrews Bay sound attenuation data show a little scatter but follow closely a linear dependence on frequency. These data are reasonably represented by the GS theory throughout the measurement frequency range, from 3 to 80 kHz.

VI. PORE-FLUID VISCOSITY AT LOW FREQUENCIES

At low frequencies, below 10 kHz, the departure of Schock's SAX99 sound speed and attenuation data sets from the predictions of the GS theory is suggestive of effects associated with the viscosity of the pore fluid. A similar observation applies to the behavior of the two lowest frequency sound speed measurements in Fig. 4(a) from St. Andrews Bay, although the deviation from the GS theory is more subtle in this data set.

If viscous dissipation does indeed influence the low-frequency (below 10 kHz) dispersion curves of saturated granular materials, then the physical mechanism responsible for the effects is a question of considerable interest. According to the Biot theory,[6,7] the motion of the viscous pore fluid relative to the mineral "frame" governs the character of the dispersion curves. However, it is well established, as exemplified in Fig. 4 of Williams *et al.*,[3] that the Biot theory cannot return the linear scaling of attenuation with frequency that is observed in the higher-frequency data, above 10 kHz.

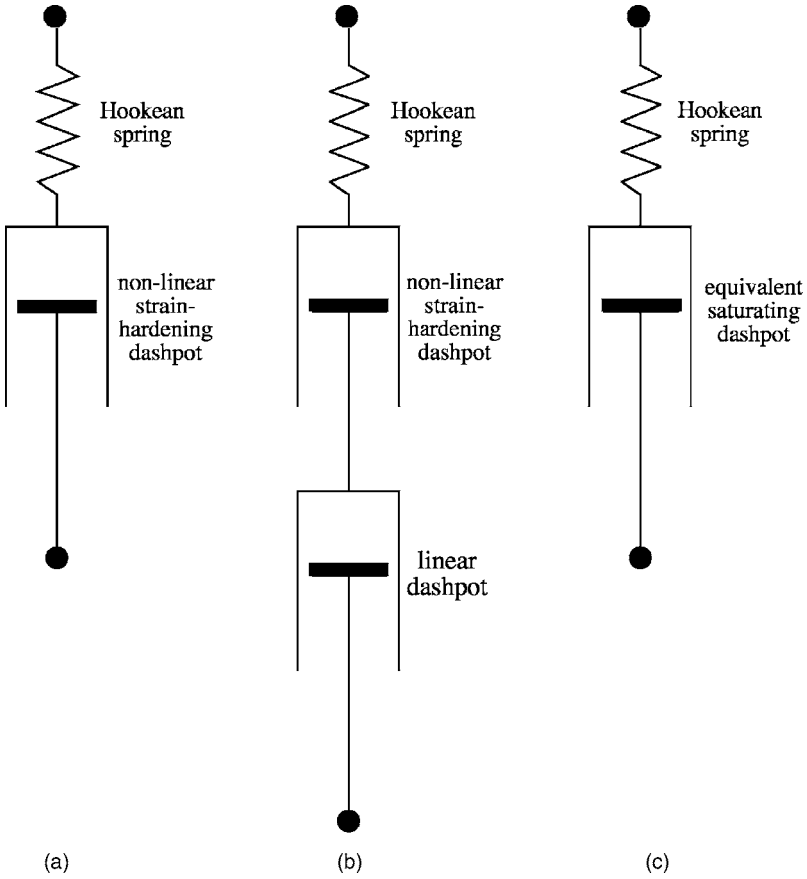

FIG. 5. (a) Maxwell element of the GS theory consisting of a Hookean spring in series with a nonlinear, strain-hardening dashpot. (b) Modified Maxwell element consisting of a spring, a nonlinear strain-hardening dashpot, and a linear dashpot, all in series. (c) The equivalent modified Maxwell element with a single nonlinear, saturating dashpot in series with the spring.

Motion of the pore fluid through the "frame" is not the only mechanism whereby viscosity of the pore fluid could influence wave propagation in a saturated, unconsolidated granular medium. In the GS theory,[1] contiguous grains are separated by a molecularly thin layer of pore fluid, which, it is postulated, exhibits strain hardening as grains slide against one another. Viscous dissipation in this thin fluid layer was not included in the original analysis of grain shearing[1] because its effects are negligible at higher frequencies, above 10 kHz, where most of the available sound speed and attenuation measurements[18,19] have been made.

At lower frequencies, below 10 kHz, it is conceivable that viscous dissipation in the very thin layer of fluid between grains could become a significant factor in the grain-shearing process. Lubricated sliding over a molecularly thin layer of fluid lies in the realm of nanotribology[20] and the detailed mechanisms involved are not only very complicated but still not fully understood. However, for the purpose of extending the GS theory to include the viscosity of the fluid layer confined between grains, it is not necessary to delve too deeply into the physics of the lubrication process: The viscous dissipation can be accommodated by a simple modification to the original nonlinear Maxwell element representing the grain-shearing process.[1]

VII. THE VISCOUS GRAIN-SHEARING (VGS) MODEL

Figure 5 in Buckingham[1] shows two contiguous grains, each with a microasperity on the circle of contact. The two microasperities are separated by a very thin layer of pore fluid, just a few molecules thick. Under grain shearing, the interaction between the two asperities is postulated to be nonlinear, as represented by an equivalent mechanical system, a form of Maxwell element shown here in Fig. 5(a), consisting of a Hookean spring in series with a strain-hardening dashpot. The spring represents the elastic deformation of the mineral asperities, while the dashpot represents the dissipation that occurs during grain sliding. Although the stress in the strain-hardening dashpot is conventional, in the sense of being proportional to the strain rate, the coefficient is time dependent, making this particular Maxwell element a nonlinear system. At the instant sliding begins, the coefficient of the dashpot is taken to be zero, subsequently increasing linearly with time as sliding progresses. Such behavior represents the strain-hardening process, which is a form of time-dependent viscous dissipation.

Under this strain-hardening model, the damping would eventually become so heavy as to extinguish the motion of the dashpot entirely. In practice, however, the damping could not increase indefinitely but must saturate at some level governed by the (time-independent) viscosity of the very thin layer of pore fluid between the grains. From studies in molecular tribology, it is known that the viscosity of a thin layer of fluid may differ markedly from that of the bulk fluid,[21] implying that the appropriate value for the "effective" viscosity may have to be found from a match to data. To accommodate the saturation phenomenon, the Maxwell element in Fig. 5(a) requires an additional component.

Figure 5(b) shows a modified strain-hardening Maxwell element, similar to the original nonlinear Maxwell element in Fig. 5(a), except for the addition of a linear dashpot in series,

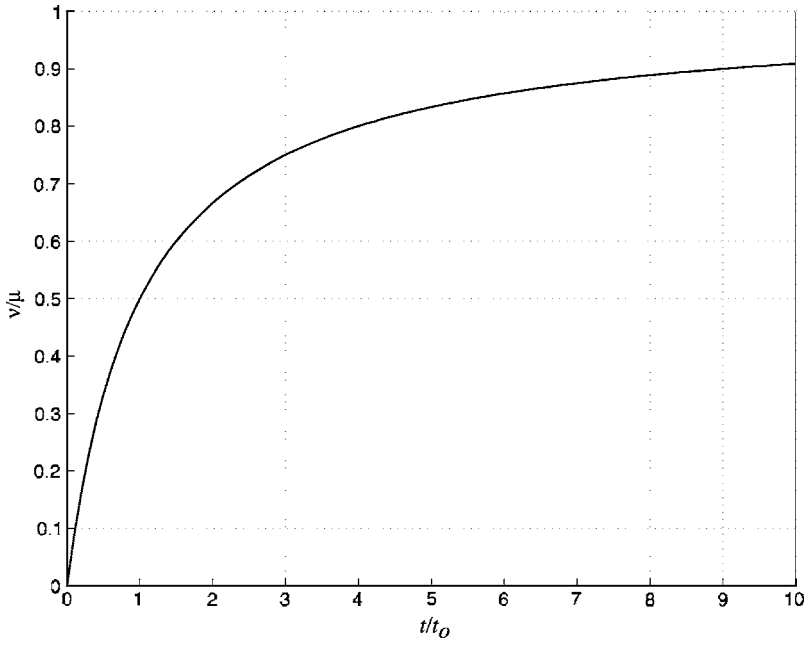

FIG. 6. Time dependence of the normalized coefficient, ν/μ, for the equivalent saturating dashpot in Fig. 5(c).

representing time-independent viscous dissipation. This new "constant viscosity" dashpot may be regarded as representing the lubrication provided by the thin layer of pore fluid between grains. Immediately after a steady strain is applied across the modified Maxwell element, the strain-hardening dashpot controls the damping, since it is much weaker than the linear dashpot. Eventually, however, the strain-hardening dashpot becomes stronger, so much so that it effectively locks up, leaving the linear dashpot as the sole damping element. Such behavior is representative of the approach to viscous saturation that might be expected in practice as lubricated sliding progresses.

The analysis of grain shearing now proceeds in much the same way as in Buckingham.[1] Assume that a constant strain, ϵ, is applied to the modified Maxwell element in Fig. 5(b) at time $t=0$. Taking the stress at time $t>0$ to be $\sigma=\sigma(t)$, then by Hooke's law the stress in the spring is

$$\sigma = E\varepsilon_s, \tag{24a}$$

where E is the spring constant and ε_s is the time-varying strain in the spring. The stress in each of the two dashpots is proportional to the rate of strain:

$$\sigma = \xi(t)\frac{d\varepsilon_d}{dt} \tag{24b}$$

and

$$\sigma = \mu\frac{d\varepsilon_\nu}{dt}, \tag{24c}$$

where ε_d is the strain across the strain-hardening dashpot and μ is the coefficient of viscosity of the thin layer of pore fluid, characterized by the linear dashpot, which supports a strain ε_ν. In Eq. (24b), the coefficient $\xi(t)$ is taken to increase linearly with time:[1]

$$\xi(t) = \theta t, \tag{25}$$

where θ is the strain-hardening coefficient.

As illustrated in Fig. 5(c), a single equivalent dashpot may be used to represent the series combination of the strain-hardening and linear dashpots in Fig. 5(b). With dashpots in series, it is readily shown that the reciprocals of the coefficients add, yielding the coefficient of the equivalent dashpot as

$$\nu = \left(\frac{1}{\mu} + \frac{1}{\theta t}\right)^{-1} = \frac{\mu\theta t}{\mu + \theta t}. \tag{26}$$

In Fig. 6, which shows the ratio ν/μ as a function of the normalized time, t/t_0, where $t_0=\mu/\theta$, it can be seen that for short times such that $t<t_0$, ν is in the strain-hardening regime, increasing approximately linearly with time; and for longer times, beyond $t=t_0$, ν saturates, approaching the constant value μ asymptotically.

Bearing in mind that the applied strain is the sum of the individual strains,

$$\varepsilon = \varepsilon_s + \varepsilon_d + \varepsilon_\nu, \tag{27}$$

the nonlinear differential equation for the stress after time $t=0$ is

$$\frac{d\sigma}{dt} + \frac{E}{\nu}\sigma = 0, \tag{28a}$$

which may be written as

$$\frac{d\sigma}{\sigma} = -\left(\frac{E}{\mu} + \frac{E}{\theta t}\right)dt. \tag{28b}$$

By integrating both sides, some elementary algebra leads to the solution

$$\sigma(t) = A\frac{e^{-t/\tau}}{t^n}, \tag{29}$$

where A is a constant of integration,

$$n = \frac{E}{\theta} \tag{30}$$

is the material exponent, and

$$\tau = \frac{\mu}{E} \tag{31}$$

will be referred to as the viscoelastic time constant. Equation (29) is the response of the modified Maxwell element in Fig. 5(c) to an impulse of strain rate (i.e., a step function strain).

Following Buckingham,[1] the material impulse response function, $h(t)$, characterizing the sliding of grains is assigned the same time dependence as that in Eq. (29) for the modified Maxwell element in Fig. 5(c):

$$h(t) = \frac{\tau^{-1+n}}{t^n} e^{-t/\tau}, \tag{32}$$

where the scaling factor in the numerator has been chosen to give $h(t)$ the dimensions of reciprocal time [the same as the delta function, $\delta(t)$]. The temporal Fourier transform of $h(t)$ is therefore dimensionless, having the form[11]

$$H(j\omega) = \tau^{-1+n} \int_0^\infty t^{-n} e^{-(1+j\omega\tau)t/\tau} dt$$

$$= \frac{\Gamma(1-n)}{(1+j\omega\tau)^{1-n}} \quad \text{for } 0 < n < 1, \tag{33}$$

where $\Gamma(\cdot)$ is the gamma function. After a minor rearrangement, the frequency response function in Eq. (33) can be written as

$$H(j\omega) = \frac{\Gamma(1-n)}{(j\omega\tau)^{1-n}} g(\omega), \tag{34}$$

where

$$g(\omega) = \left(1 + \frac{1}{j\omega\tau}\right)^{-1+n} \tag{35}$$

represents the effect of the viscous dissipation on $H(j\omega)$. At high frequencies (i.e., $\omega\tau \gg 1$), $g(\omega)$ approaches unity asymptotically and hence in this regime the frequency response function in Eq. (34) reduces to the same form as in the original GS theory. It is only at lower frequencies, where $\omega\tau \ll 1$, that the effect of viscosity becomes significant, as evident from the form of $g(\omega)$ in Eq. (35).

The derivation of the compressional and shear dispersion relations now proceeds exactly as in Buckingham,[1] but with the frequency response function replaced by the modified formulation in Eq. (34). This procedure yields the following expressions for the sound speed and attenuation:

$$c_p = \frac{c_0}{\mathrm{Re}[1 + \chi(j\omega T)^n g(\omega)]^{-1/2}}, \quad 0 < n < 1, \tag{36}$$

$$\alpha_p = -\frac{\omega}{c_0} \mathrm{Im}[1 + \chi(j\omega T)^n g(\omega)]^{-1/2}, \quad 0 < n < 1, \tag{37}$$

and similarly, for the shear wave speed and attenuation,

$$c_s = \frac{\sqrt{\gamma_s/\rho_0}}{\mathrm{Re}[(j\omega T)^n g(\omega)]^{-1/2}}, \quad 0 < n < 1, \tag{38}$$

$$\alpha_s = -\omega \sqrt{\frac{\rho_0}{\gamma_s}} \mathrm{Im}[(j\omega T)^n g(\omega)]^{-1/2}, \quad 0 < n < 1. \tag{39}$$

At higher frequencies, where $g(\omega) \approx 1$, these expressions are unchanged from those in the GS theory, and thus they return wave speeds that increase logarithmically with frequency and attenuations that scale as the first power of frequency. Only at lower frequencies does viscosity have an effect, introducing mild departures from the behavior predicted by the original GS theory.

VIII. COMPARISON OF THE VGS MODEL WITH DATA

A. Glass beads in water and in silicone oil

Hefner and Williams' sound speed and attenuation data[5] on glass beads in water and glass beads in silicone oil were taken at relatively high frequencies, where the effects of viscosity, as represented by $g(\omega)$ in Eq. (35), are minor, if not negligible. In this regime, the VGS theory is essentially the same as the GS theory and, as illustrated in Figs. 1 and 2, the latter yields dispersion curves that match the data returned by Hefner and Williams' glass-bead experiments.[5]

B. SAX99 data

Unlike the glass-bead data, the SAX99 data set extends to a lower frequency band, where, apparently, effects due to the viscosity of the pore fluid may not be negligible. Figure 7 shows the same SAX99 dispersion data as in Fig. 3, superimposed upon which are the predictions of the VGS theory (red lines), as evaluated from Eqs. (36) and (37). The value of the viscoelastic time constant in Eq. (31) was set at $\tau = 0.12$ ms on the basis of a simple visual fit to the SAX99 sound speed and attenuation data. Some such procedure is necessary because τ is a measure of the effective viscosity of the molecularly thin layer of seawater separating grains, which is not known but is likely to be significantly different from the viscosity of the bulk fluid.[21]

As shown in Table I, the values of the grain-shearing parameters used in evaluating the VGS dispersion expressions are marginally different from those used in the evaluation of the GS theory (blue lines in Figs. 3 and 7) because the effect of viscosity, on the attenuation in particular, is not entirely negligible at the matching frequency of 38 kHz. It follows that, to achieve the matching condition, slightly different values of n, γ_p, and γ_s are needed in the GS and VGS theories, which accounts for the fact that the red and blue curves in Fig. 7 do not converge in the limit of high frequency.

It is evident in Fig. 7(a) that at lower frequencies, between 1 and 10 kHz, the sound speed predicted by the VGS theory exhibits relatively strong dispersion due to the effective viscosity of the thin layer of pore fluid between contiguous grains. This behavior matches nicely Schock's chirp sonar data (red diamonds). At higher frequencies, the VGS theory is similar to the GS theory in that both show weak

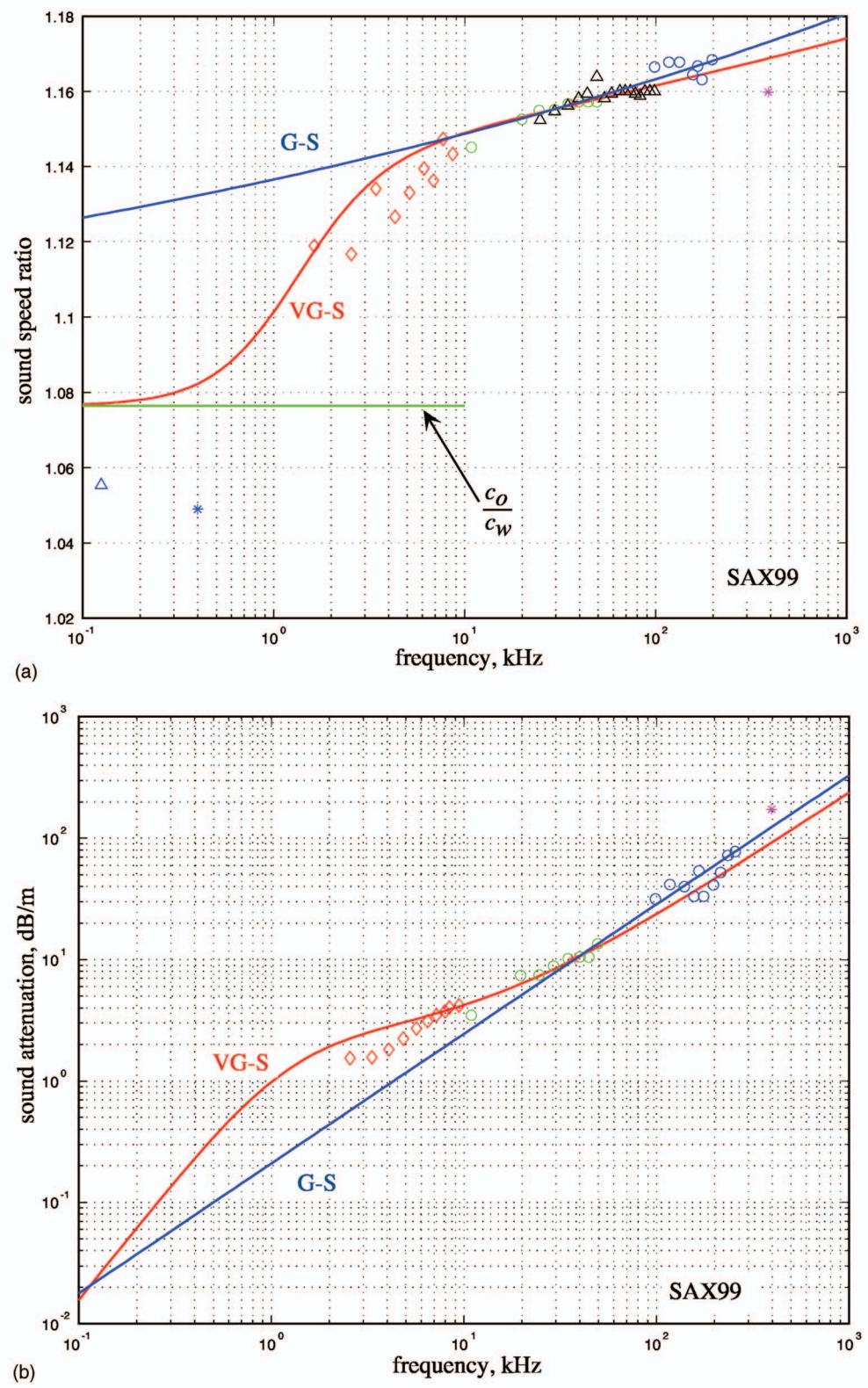

FIG. 7. The SAX99 data, represented by the symbols, with the predictions of the VGS theory, evaluated using the parameters in Table I, shown as red lines. For comparison, the blue lines of the GS theory from Fig. 3 are included, (a) Sound speed ratio vs frequency and Wood's sound speed ratio (horizontal green line). (b) Sound attenuation vs frequency.

logarithmic dispersion, in agreement with the multiplicity of SAX99 data sets above 10 kHz. Below 1 kHz, the VGS theory can be seen to approach asymptotically Wood's sound speed, c_0, for the equivalent suspension. It is evident that c_0 is higher than the two SAX99 data points in this band. As mentioned earlier, the reason for the discrepancy is not clear but three possibilities come to mind: (1) gas bubbles could have been present in the sediment, although this seems unlikely since earlier surveys showed no evidence of gas,[15] and anyway gas would probably have affected the higher fre-

quency measurements, too, which appears not to be the case; (2) some other, unknown mechanism was at work, which reduced the effective stiffness of the sediment to below that of the equivalent suspension; and (3) the error bars on the two measurements (shown in Fig. 3 of Williams *et al.*[3]) are such that they span c_0.

Figure 7(b) shows the SAX99 attenuation data and for comparison the prediction of the VGS theory (red line), which can be seen to match the measurements throughout the entire frequency range. At the higher frequencies, above 10 kHz, the VGS curve approaches asymptotically the (near) linear frequency dependence predicted by the GS theory (blue line), with similar behavior exhibited by the data. Between 1 and 10 kHz, where the effective viscosity of the thin layer of pore fluid between contiguous grains becomes significant, the VGS curve departs from a linear frequency dependence, following Schock's chirp sonar data (red diamonds) reasonably well.

C. St. Andrews Bay data

Those features in the St. Andrews Bay dispersion data[4] that may possibly be attributed to the viscosity of the pore fluid are considerably less pronounced than their counterparts in the SAX99 data set. This is apparent in Fig. 8, which shows a comparison between the St. Andrews Bay data[4] of Fig. 4 with the dispersion curves predicted by the VGS theory (red lines) in Eqs. (36) and (37). As with SAX99, the grain shearing parameters (see Table I) used in evaluating the VGS theory are slightly different from those used in the GS theory (blue lines in Figs. 4 and 8) because the effective viscosity of the pore fluid has a small effect on the predicted attenuation at the matching frequency of 50 kHz. The matching condition thus leads to slightly different values of n, γ_p, and γ_s for the GS and VGS theories, as a result of which the red and blue curves in Fig. 8 do not quite converge in the high-frequency limit.

In Fig. 8(a), it is evident that the sound speed predicted by the VGS theory matches the data throughout the frequency range of the measurements, with the exception of the small peak in the data around 30 kHz. The relatively high dispersion at the lower frequencies, below 5 kHz, is reasonably represented by the VGS theory, as is the weak logarithmic dispersion of approximately 1.4% per decade at higher frequencies.

Although the attenuation data points in Fig. 8(b) show a little spreading, it is clear that the trend is a near-linear variation with frequency over the bandwidth of the measurements. Such behavior indicates that, in this case, the effects of viscosity on the attenuation are minimal. The VGS theory for the St. Andrews Bay attenuation is consistent with this point of view, since its departure from the GS theory is quite small at lower frequencies, where viscous effects, if present, would be observed. As may be seen in Fig. 8(b), the VGS theory returns a reasonable fit to the attenuation data above 10 kHz but tends to be a little higher than the data at lower frequencies.

Overall, the evidence for the presence of viscous effects in the St Andrews Bay data set is not compelling. On comparing the red and blue lines in Fig. 8, it is arguable that the GS theory fits the data better than the VGS theory, with the exception of the measured sound speeds between 3 and 4 kHz, which fall below the GS curve. The case for viscosity rests solely on these high-dispersion sound speed data below 10 kHz but against this are the attenuation data, which show little if any sign of viscosity since they vary linearly with frequency throughout the measurement band. Apparently, the viscous effects in question, if they exist at all, are almost too small to be resolved by the St. Andrews Bay data. Moreover, the GS theory and VGS theory in this case are so similar, at least above 5 kHz, that either one returns an acceptable fit to the data.

IX. DISCREPANCIES BETWEEN THE SAX99 AND ST. ANDREWS BAY DATA

Since the physical properties of the SAX99 and St. Andrews Bay sediments are similar, though not identical, why do the respective dispersion curves, particularly the attenuations, look so different at low frequencies (below 10 kHz)? In other words, why does pore-fluid viscosity manifest itself more prominently in the SAX99 data than in the St. Andrews Bay data? And why is this behavior mirrored by the VGS dispersion curves, as computed for the SAX99 and St. Andrews Bay sediments?

To help answer these questions, it is instructive to return to the SAX99 and St. Andrews Bay attenuation data in Figs. 7(b) and 8(b), respectively. These curves may be thought of as being comprised of two components, one, broadband, due to grain shearing, and varying essentially as the first power of frequency, and the other, low frequency (below 10 kHz), associated with pore-fluid viscosity. On comparing the levels of the attenuation at some higher frequency (say, 80 kHz), where only the broadband, grain-shearing component is significant, it is evident that St. Andrews Bay exceeds SAX99 by at least 5 dB/m. The reason for this enhanced attenuation at St. Andrews Bay could be related to grain shape, which may well affect the grain shearing processes that underpin both the GS and VGS theories. Some support for this grain shape argument is found in the fact that the material exponent, n, for the St. Andrews Bay sediment is approximately twice the value of n for SAX99.

Be that as it may, since the component of attenuation due to pore-fluid viscosity is about the same in each of the two sediments (τ=0.12 ms in both cases), a plausible interpretation is that, in the St. Andrews Bay sediment, the higher-level of grain-shearing attenuation, associated with the higher value of n, masks the viscous component of attenuation. In contrast, with a lower level of grain-shearing attenuation in the SAX99 sediment, the viscous attenuation is revealed and appears relatively prominently. This somewhat loose physical argument is supported quantitatively by the good quality of the match between the VGS theory and the sound speed and attenuation data from SAX99 on the one hand and St. Andrews Bay on the other, as illustrated in Figs. 7 and 8, respectively.

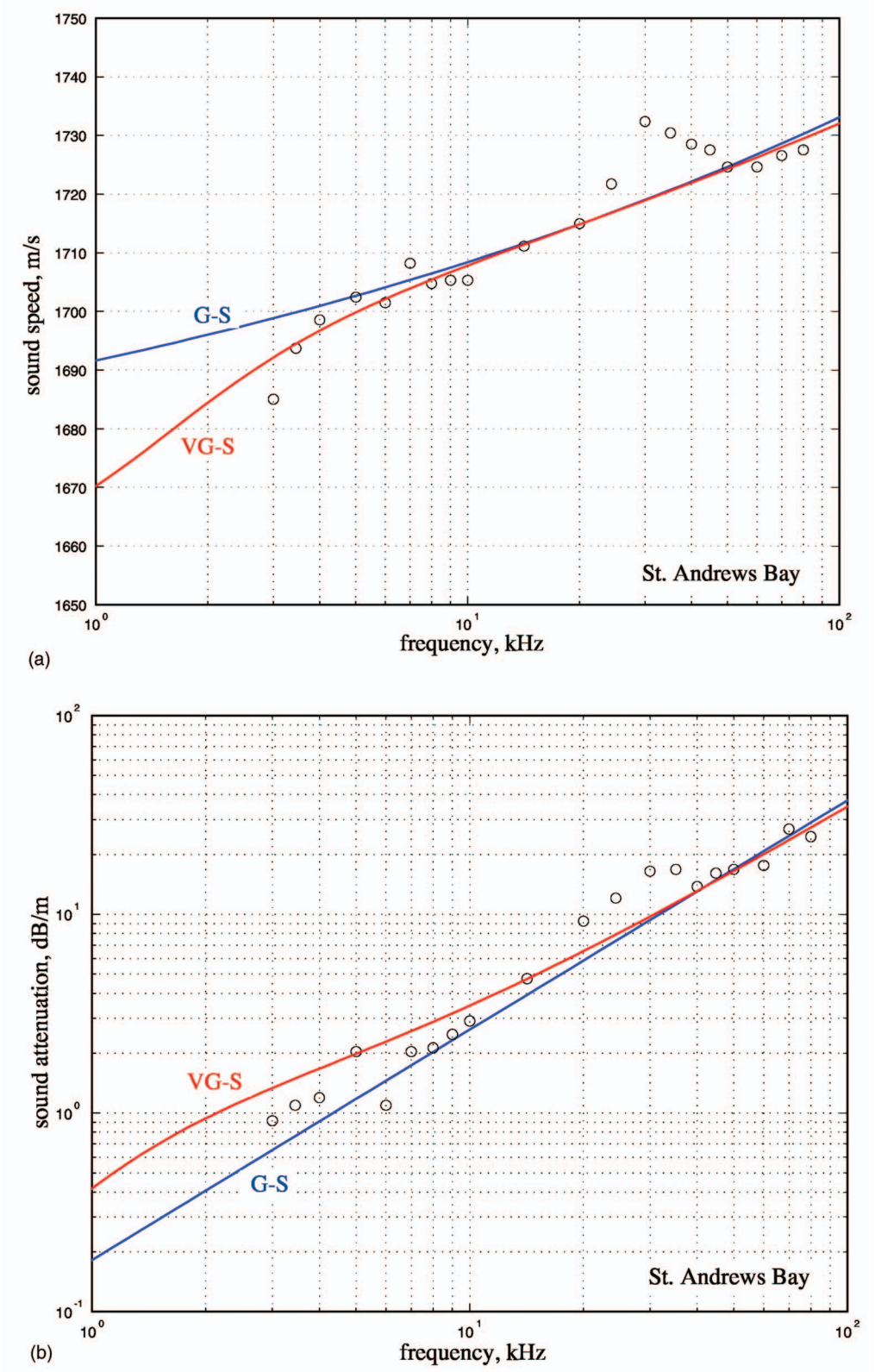

FIG. 8. The St. Andrews Bay data, represented by the circles, with the predictions of the VGS theory, evaluated using the parameters in Table I, shown as the red lines. For comparison, the blue lines of the GS theory from Fig. 4 are included. (a) Sound speed vs frequency. (b) Sound attenuation vs frequency.

X. CONCLUDING REMARKS

The GS theory[1] of wave propagation in saturated granular materials has been extended in this article to include the effects of the viscosity of the molecularly thin layer of pore fluid separating contiguous grains. In the extended analysis, designated the VGS theory, the intergranular interactions are characterized in terms of an equivalent mechanical system taking the form of a Hookean spring and a saturating, non-

linear dashpot in series. For times less than a certain critical value, the coefficient of the dashpot increases essentially linearly with time, representing strain hardening, much as in the GS theory; and after the critical time, the coefficient of the dashpot approaches a constant value, representative of lubrication associated with the effective viscosity of the thin layer of pore fluid between grains, which is expected to differ significantly from the viscosity of the bulk fluid.

In addition to the three grain-shearing parameters that appear in the GS model, the VGS theory includes a fourth, a time constant representing the transition from strain-hardening to viscous saturation. Since no theoretical treatment is available for calculating their values, all four parameters have to be determined from a fit to data. The situation is not unlike that encountered with Coulomb friction, where the coefficient of kinetic friction between two surfaces sliding against each other can only be evaluated through experimental measurement.

Several sets of data on sound speed and attenuation in saturated granular materials are examined in the article, including the composite dispersion data from SAX99. These data sets are of considerable interest because they match the GS theory at higher frequencies, above 10 kHz, but in the lower frequency band from 1 to 10 kHz, occupied by Schock's data, the sound speed (attenuation) measurements lie below (above) the predictions of the GS theory. The frequency band between 1 and 10 kHz is where the viscosity of the pore fluid could have a significant effect on the dispersion curves. A comparison of the VGS dispersion curves with the SAX99 data appears to support this interpretation: There is very reasonable agreement between the new theory and the SAX99 data, not only between 1 and 10 kHz, but over the entire frequency range from 1 to 400 kHz.

In another set of dispersion data, obtained from a synthetic aperture sonar in St. Andrews Bay, Florida,[4] the effects of pore-fluid viscosity are much less pronounced than in the SAX99 data set. In this case, the grain-shearing parameters are such that the original GS theory and the VGS theory return similar dispersion curves and both show a reasonable fit to the St Andrews Bay data over the entire measurement band from 3 to 80 kHz. It would appear that the significance of pore-fluid viscosity is an issue that remains unresolved in the St. Andrews Bay data set. A plausible explanation for this situation is that, perhaps as a result of grain shape, the dominant mechanism in the St. Andrews Bay sediment is grain shearing, which more or less masks the effects of pore-fluid viscosity on the dispersion curves.

As a final comment, the GS theory has been shown to match many published data sets on wave properties versus physical properties of saturated sediments.[1] These extensive comparisons between the GS theory and experimental data relate to wave measurements that were made almost exclusively at higher frequencies, beyond 10 kHz, where the viscosity of the pore fluid is likely to have a negligible effect. Thus, the comparisons remain valid irrespective of whether pore-fluid viscosity is significant or not at lower frequencies.

ACKNOWLEDGMENTS

The research was supported by Dr. Ellen Livingston and Dr. Robert Headrick, Ocean Acoustics Code, the Office of Naval Research, under Grant No. N00014-07-1-0109.

[1] M. J. Buckingham, "Wave propagation, stress relaxation, and grain-to-grain shearing in saturated, unconsolidated marine sediments," J. Acoust. Soc. Am. **108**, 2796–2815 (2000).
[2] M. J. Buckingham, "Compressional and shear wave properties of marine sediments: Comparisons between theory and data," J. Acoust. Soc. Am. **117**, 137–152 (2005).
[3] K. L. Williams, D. R. Jackson, E. I. Thorsos, D. Tang, and S. G. Schock, "Comparison of sound speed and attenuation measured in a sandy sediment to predictions based on the Biot theory of porous media," IEEE J. Ocean. Eng. **27**, 413–428 (2002).
[4] H. J. Simpson, B. H. Houston, S. W. Liskey, P. A. Frank, A. R. Berdoz, L. A. Kraus, C. K. Frederickson, and S. Stanic, "At-sea measurements of sound penetration into sediments using a buried vertical synthetic array," J. Acoust. Soc. Am. **114**, 1281–1290 (2003).
[5] B. T. Hefner and K. L. Williams, "Sound speed and attenuation measurements in unconsolidated glass-bead sediments saturated with viscous pore fluids," J. Acoust. Soc. Am. **120**, 2538–2549 (2006).
[6] M. A. Biot, "Theory of propagation of elastic waves in a fluid-saturated porous solid. I. Low-frequency range," J. Acoust. Soc. Am. **28**, 168–178 (1956).
[7] M. A. Biot, "Theory of propagation of elastic waves in a fluid-saturated porous solid. II. Higher frequency range," J. Acoust. Soc. Am. **28**, 179–191 (1956).
[8] M. J. Buckingham, "A three-parameter dispersion relationship for Biot's fast compressional wave in a marine sediment," J. Acoust. Soc. Am. **116**, 769–776 (2004).
[9] M. J. Buckingham, "Causality, Stokes' wave equation and acoustic pulse propagation in a viscous fluid," Phys. Rev. E **72**, 026610(9) (2005).
[10] A. B. Wood, *A Textbook of Sound*, 3rd ed. (Bell, London, 1964).
[11] I. S. Gradshteyn and I. M. Ryzhik, *Tables of Integrals, Series and Products* (Academic, New York, 1980).
[12] M. Abramowitz and I. A. Stegun, *Handbook of Mathematical Functions* (Dover, New York, 1965).
[13] E. I. Thorsos, K. L. Williams, N. P. Chotiros, J. Christoff, K, Commander, C. F. Greenlaw, D. V. Holliday, D. R. Jackson, J. L. Lopes, D. E. McGehee, J. E. Piper, M. D. Richardson, and D. Tang, "An overview of SAX99: Acoustic measurements," IEEE J. Ocean. Eng. **26**, 4–25 (2001).
[14] D. R. Jackson, K. L. Williams, E. I. Thorsos, and S. G. Kargl, "High-frequency subcritical acoustic penetration into a sandy sediment," IEEE J. Ocean. Eng. **27**, 346–361 (2002).
[15] M. D. Richardson, K. B. Briggs, D. L. Bibee, P. A. Jumars,W. B. Sawyer, D. B. Albert, T. K. Berger, M. J. Buckingham, N. P. Chotiros, P. H. Dahl, N. T. Dewitt, P. Fleischer, R. Flood, C. F. Greenlaw, D. V. Holliday, M. H. Hulbert, M. P. Hutnak, P. D. Jackson, J. S. Jaffe, H. P. Johnson, D. L. Lavoie, A. P. Lyons, C. S. Martens, D. E. McGehee, K. D. Moore, T. H. Orsi, J. N. Piper, R. I. Ray, A. H. Reed, R. F. L. Self, J. L. Schmidt, S. G. Schock, F. Simonet, R. D. Stoll, D. J. Tang, D. E. Thistle, E. I. Thorsos, D. J. Walter, and R. A. Wheatcrof, "Overview of SAX99: Environmental considerations," IEEE J. Ocean. Eng. **26**, 26–53 (2001).
[16] R. D. Stoll, "Velocity dispersion in water-saturated granular sediment," J. Acoust. Soc. Am. **111**, 785–793 (2002).
[17] M. J. Buckingham and M. D. Richardson, "On tone-burst measurements of sound speed and attenuation in sandy marine sediments," IEEE J. Ocean. Eng. **27**, 429–453 (2002).
[18] E. L. Hamilton, "Acoustic properties of sediments," in *Acoustics and the Ocean Bottom*, edited by A. Lara-Saenz, C. Ranz Cuierra, and C. Carbo-Fité (Consejo Superior de Investigacions Cientificas, Madrid, 1987), pp. 3–58.
[19] M. D. Richardson, "In-situ, shallow-water sediment geoacoustic properties," in *Shallow-Water Acoustics*, edited by R. Zhang and J. Zhou (China Ocean Press, Beijing, 1997), pp. 163–170.
[20] B. Bhushan, J. N. Israelachvili, and U. Landman, "Nanotribology: Friction, wear and lubrication at the atomic scale," Nature (London), **374**, 607–616 (1995).
[21] S. Granick, "Soft matter in a tight spot," Phys. Today **52**, 26–31 (1999).

Perception-based automatic classification of impulsive-source active sonar echoes

Victor W. Young[a] and Paul C. Hines
Defence R&D Canada – Atlantic, Box 1012, Dartmouth, Nova Scotia B2Y 3Z7, Canada

(Received 22 January 2007; revised 5 July 2007; accepted 6 July 2007)

Impulsive-source active sonar systems are often plagued by false alarm echoes resulting from the presence of naturally occurring clutter objects in the environment. Sonar performance could be improved by a technique for discriminating between echoes from true targets and echoes from clutter. Motivated by anecdotal evidence that target echoes sound very different than clutter echoes when auditioned by a human operator, this paper describes the implementation of an automatic classifier for impulsive-source active sonar echoes that is based on perceptual signal features that have been previously identified in the musical acoustics literature as underlying timbre. Perceptual signal features found in this paper to be particularly useful to the problem of active sonar classification include: the centroid and peak value of the perceptual loudness function, as well as several features based on subband attack and decay times. This paper uses subsets of these perceptual signal features to train and test an automatic classifier capable of discriminating between target and clutter echoes with an equal error rate of roughly 10%; the area under the receiver operating characteristic curve corresponding to this classifier is found to be 0.975.
[DOI: 10.1121/1.2767001]

PACS number(s): 43.30.Vh, 43.60.Bf, 43.66.Jh [RG] Pages: 1502–1517

I. INTRODUCTION

When operating in littoral environments, active sonar performance is often degraded by the presence of naturally occurring clutter objects, which lead to false alarm echoes. Sonar performance could be improved if there were a technique for reliably discriminating between echoes from clutter objects and echoes from true targets.

Typically target-clutter discrimination is carried out by a human operator using visual displays like time-frequency sonograms. There have also been attempts to develop automatic classifiers for active sonar using signal features based on parametrized representations of the echo spectra,[1] using signal features based on the statistics of the temporal and spectral echo envelopes,[2] and using signal features derived from physics-based models of specific target types.[2] These conventional approaches have met with some success but they ignore a potentially valuable tool for target-clutter discrimination: the human auditory system.

There is anecdotal evidence and mounting experimental evidence[3,4] to suggest that when auditioned (i.e., auralized or listened to) by a human operator explosive-source echoes from man-made metallic objects *sound* very different than similar echoes from naturally occurring objects. This paper describes the development of an automatic classifier for explosive-source active sonar based upon the specific aural cues or perceptual signal features employed in the human auditory system. The purpose of this paper is not to develop a new classifier architecture—indeed, the classifier employed is one of the very simplest available—but instead to describe new perceptual signal features and to demonstrate that they can be used to perform target-clutter discrimination for an explosive-source data set.

It is possible to draw an analogy between explosive-source active sonar echoes and the sounds produced by percussive musical instruments: Both types of sounds are generated by exciting a physical object with an impulse. Motivated by this analogy, this paper considers perceptual signal features that have previously been identified as important to the perception of musical timbre. The American National Standards Institute (ANSI) defines timbre as: "that attribute of auditory sensation in terms of which a subject can judge that two sounds similarly presented and having the same loudness and pitch are dissimilar."[5] Unlike loudness and pitch, which are closely related to the one-dimensional concepts of intensity and frequency, respectively, timbre is a multidimensional attribute that cannot be closely associated with a single one-dimensional quantity: There are multiple one-dimensional quantities or perceptual signal features that affect the timbre of a sound.

The musical acoustics literature includes many papers describing experiments that attempt to identify the specific perceptual signal features that underlie timbre.[6–12] These experiments typically rely on a technique called multidimensional scaling (MDS), in which human subjects are played pairs of sounds and asked to rate the perceptual distance between them. The MDS algorithm generates a multidimensional space within which the individual sounds are distributed as points, such that the distance between pairs of sounds (points) reflects the perceptual distance specified by the human subjects. The distribution of sounds along each dimension of the MDS space is correlated with perceptual signal features suspected of underlying timbre and each dimension is associated with the particular perceptual signal feature that leads to highest correlation.

[a]Electronic mail: victor.young@drdc-rddc.gc.ca

Perceptual signal features identified in the musical acoustics literature as strong timbre-correlates include: subband attack,[6–8,11–13] decay,[6–8,11] and synchronicity,[8,11] and the centroid,[8,9,11,12] roughness,[14,15] and peak value (or fundamental[9]) of the perceptual loudness spectrum. These are the perceptual signal features that will be applied to the problem of target-clutter discrimination in this paper. It should be noted that the purpose of this paper is not to suggest that these perceptual signal features are somehow superior to the parametrized spectral, statistics-based, or target model-based features conventionally applied to the problem of target-clutter discrimination; rather the hope is to demonstrate that target-clutter discrimination, at a very high level, is possible using perceptual signal features. The optimum technique for sonar classification would probably include some combination of all four types of signal features.[2,16]

The body of this paper is structured as follows. Section II contains a description of the explosive-source active sonar data set and how it was obtained; this includes discussion of the experimental sea trial during which the raw data were collected, discussion of the simple detection algorithm used to locate target and clutter echoes within the raw data, and discussion of the techniques used to condition the individual echoes once detected. Section III describes the extraction of perceptual signal feature values using a simple auditory model. Section IV provides a brief overview of the classifier architecture and describes how the full data set is divided into training and testing subsets. Section V outlines the feature selection algorithm used to identify subsets of particularly useful perceptual features. Finally, Sec. VI presents automatic classification results in the form of feature-space scatter plots and receiver operating characteristic (ROC) curves.

II. THE DATA SET

A. Experimental sea trial

The data set considered in this paper was collected in the spring of 2004 during an experimental sea trial on the Malta Plateau, a region of the Mediterranean between the islands of Sicily, to the north, and Malta, to the south. A map of this region is presented in Fig. 1. The water depth in this region is on the order of 100 m and the bottom is known to be silty. This region was selected as the experimental site because it is known to be rich in clutter objects.[17]

Nine signal underwater sound (SUS) charges were deployed during the sea trial to serve as broadband active sonar sources. The nine charges were deployed one at a time from the stern of the Canadian Forces Auxiliary Vessel (CFAV) Quest. The charges were deployed in a relatively tight cluster, over the course of about 4 h. Each charge contained 0.82 kg of trinitrotoluene (TNT) and was set to detonate at a water depth of 87.0 m. SUS charges were selected for the active sonar source in this experiment because they transmit a great deal of energy over an extremely broad bandwidth. SUS charge wave forms and spectra have been studied extensively and are well characterized in the literature.[18,19]

The active sonar receiver for the experiment was a towed array composed of 96 omnidirectional elements, with

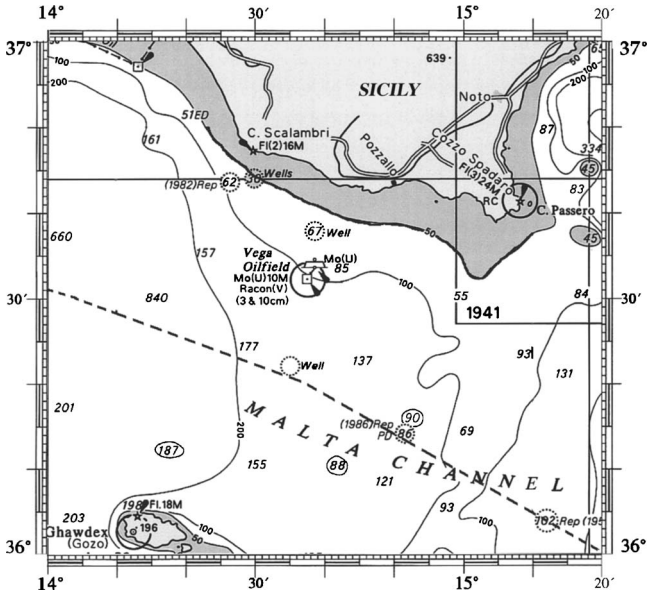

FIG. 1. The Malta Plateau: The experimental location where the data examined in this paper was collected.

0.5 m spacing between elements. The receiver array was towed behind CFAV Quest (i.e., the same ship from which the SUS charges were deployed). The receiver array was towed at a speed of roughly 6 knots and at a depth of about 40 m; it was sampled at a rate of 4096 Hz. Each element of the towed array had a nominal dynamic range of 24 bits and an effective dynamic range of 18 bits.

Conventional time delay and sum beamforming, with a Hann window for spatial shading, was applied to the towed array data in order to form 81 horizontal beams, equally spaced in cosine. Because the towed array is composed of omnidirectional elements there is an inherent left-right ambiguity in the beampattern. During the experiment, attempts were made to account for this left-right ambiguity by using three different array orientations: for the first three SUS drops the array was towed on a heading of 266°, for the second three SUS drops the array was towed on a heading of 146°, and for the final three SUS drops the array was towed on a heading of 26°.

The experimental geometry is illustrated in Fig. 2. As mentioned earlier, the nine SUS charges were deployed in a relatively tight cluster from the same ship that was towing the receiver. Therefore, the receiver array can be thought of as colocated with the SUS charge drop sites in Fig. 2. Two man-made metallic structures, the Campo Vega oil platform and the tanker ship that attends it, are located to the northwest of the drop site at a range of roughly 13.5 km. As discussed in the following, these two structures serve as target objects for the purposes of this paper. Because the range to the targets far exceeds the source-receiver separation, throughout this paper the experimental geometry will be treated as monostatic. Although propagation modeling lies outside the scope of the present paper, summaries of the environmental conditions, including the wind speed, the sound speed profile, and the ambient noise power spectrum at the time of the experiment, are presented in Fig. 3 for the interested reader.

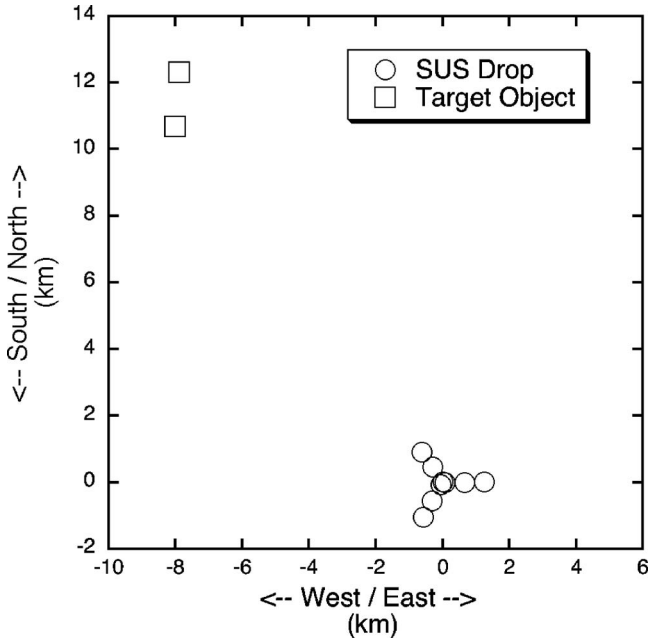

FIG. 2. Experimental geometry employed during data collection.

Not much information about the structure of the target objects is available in the open literature and details about the structure have been obtained primarily from photographs taken at the time of the experiment. Essentially, the subsurface portion of the Campo Vega oil platform consists of about eight main pipes, or support legs, running from the superstructure to the seafloor. The tending tanker ship is tethered to a vertical pipe that spans the water column.[17] This tether is a single-point mooring such that the tanker can change its orientation based on the prevailing winds and ocean currents so it is possible that the tanker ship was presenting different aspects to the source receiver during the course of the 4 h experiment. That said, it is not clear whether the echoes attributed to this target result from the pipe or from the tanker ship itself—it may be that what this paper refers to as tanker echoes are, in fact, a combination of returns from both the vertical pipe and the tanker. In any case, since this paper focuses on perception-based discrimination of the echoes, and no attempt is made to associate parts of the echo with specific target elements or components, detailed information about the structure of the targets is not necessary.

B. Echo detection, refinement, and extraction (DRE)

The active sonar data collected during the experimental sea trial consists of nine large data files of beamformed pressure time series: one for each of the nine SUS drops. Within these data files are individual echoes from target and clutter objects that must be detected and extracted. The process of echo detection, refinement, and extraction (DRE) is illustrated in Fig. 4.

The process begins by filtering each beam of the nine pressure time series data files between 512 and 1536 Hz. Filtering the data in this way makes the individual echoes more obvious by eliminating the low-frequency rumble that often dominates explosive-source active sonar data.

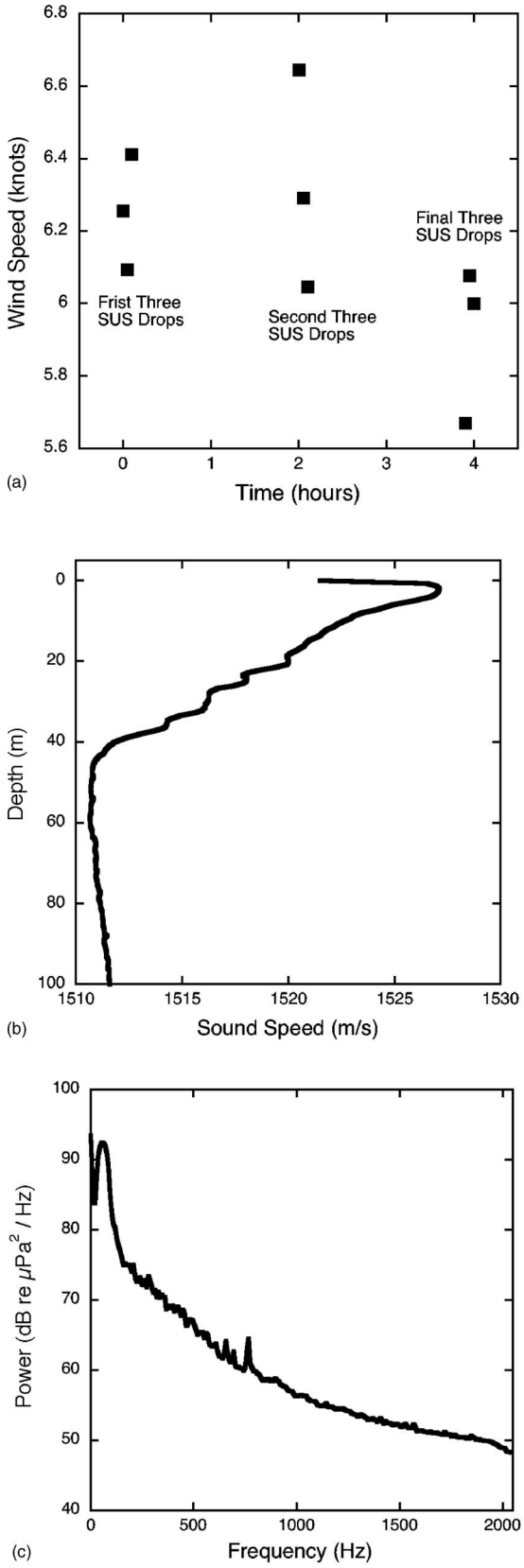

FIG. 3. Environmental conditions: (a) The wind speed at the time of each SUS drop; (b) a sound speed profile recorded very near the time of the first SUS drop—the sound speed profile remained relatively constant throughout the 4 h experiment duration; (c) ambient noise power spectrum averaged over the 4 h experiment duration—the ambient noise estimate was obtained from the towed-array elements while under way and so includes contributions from both true ambient noise and flow noise.

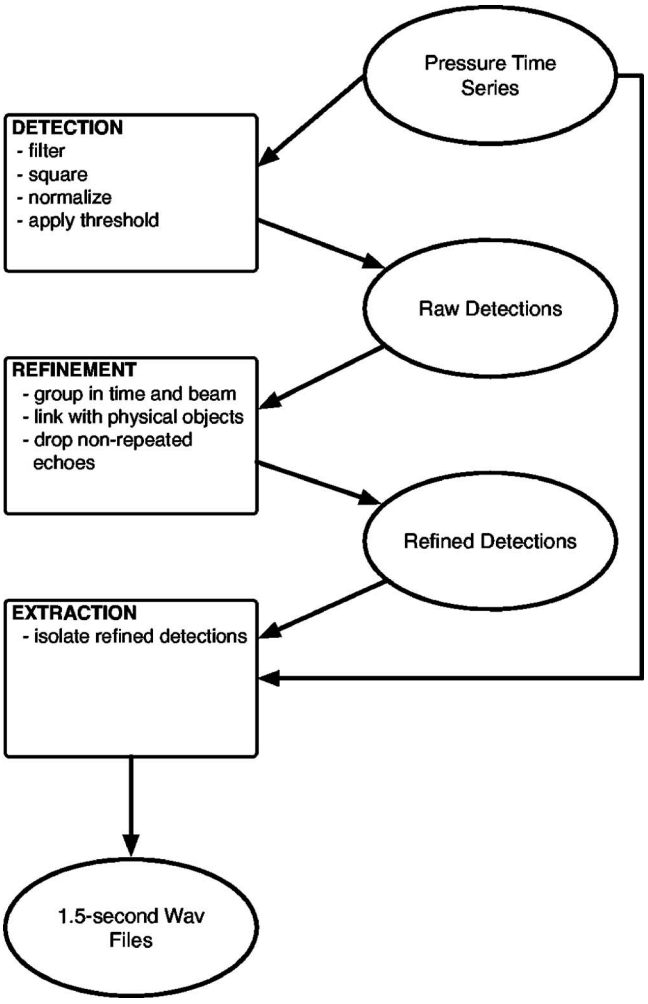

FIG. 4. The echo detection, refinement, and extraction (DRE) process.

The DRE process continues by squaring each of the filtered pressure time series to obtain data that are proportional to power. The power time series are then subjected to a two-pass mean (TPM) normalization process in order to eliminate diffuse reverberation caused by the SUS charge detonations. The specific TPM normalization algorithm employed in this paper is described in detail by Struzinski and Lowe.[20,21]

A power threshold, established so as to yield a fixed number of detections for each of the nine SUS drops, is applied to the normalized time series. Any samples that exceed the threshold are taken to be raw detections.

Because the target and clutter objects being sought have finite physical extent, their echoes must necessarily have finite temporal extent. In other words, the echo from a single target or clutter object could possibly exceed the power threshold for multiple time series samples. In addition, because the individual towed-array beams have finite width, it is possible for the echo from a single target or clutter object to appear on multiple adjacent beams. To account for the possibility of multiple superthreshold samples for a single echo, a grouping tolerance is applied to the raw detections in both time and beam. The specific grouping tolerance employed in this paper is three beams and 0.375 s: Any two raw detections located within three beams and 0.375 s of one another are assumed to be part of the same echo and are

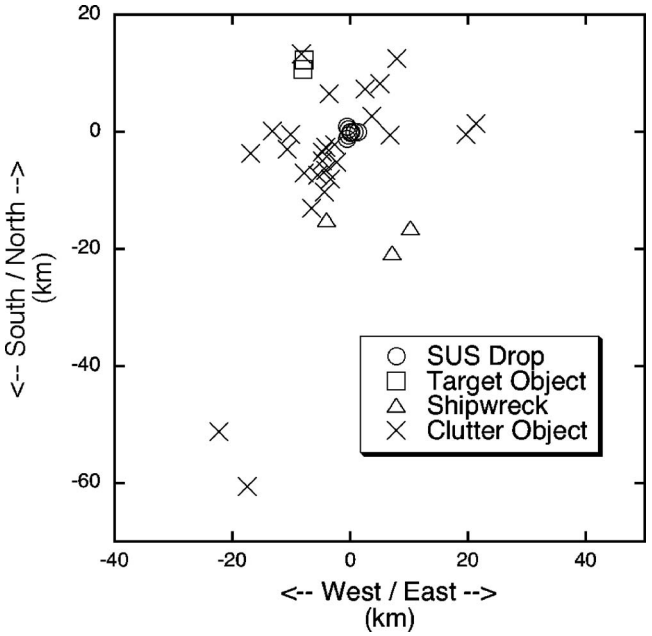

FIG. 5. Target, clutter, and shipwreck objects that lead to repeatable active sonar echoes; shipwreck echoes will not be considered in this paper.

grouped accordingly. These tolerance values were chosen because they led to all raw detections associated with the Campo Vega oil platform being grouped together and all raw detections associated with the tanker ship being grouped together. In other words, this choice of grouping tolerance ensures that, for any one SUS drop, there will be only one refined detection per target.

Using the known experimental geometry, the refined detections are associated with specific positions on the seafloor. Echoes from the nine different SUS drops are then grouped together and linked with a single physical object using a distance tolerance similar to the above-described time/beam grouping tolerance. The specific distance tolerance employed in this paper is equal to twice the width of the average beam for the range at which the detections occur.

To ensure that each refined detection is in fact an active sonar echo off a physical object in the environment and not just a spurious pressure signal unrelated to the active sonar experiment, repeatability is required for each group of detections. In other words, echoes from the same point on the seafloor are required to appear for at least two different array orientations; otherwise the detections are dropped from further consideration, since their origin cannot be confirmed.

As illustrated in Fig. 5, the process of echo detection and refinement leads to the identification of target and clutter objects that are responsible for repeatable active sonar echoes. Specifically, there are repeatable echoes from two different target objects, the Campo Vega oil platform and the tanker ship that attends it, and 26 different clutter objects. There are also echoes from three different shipwrecks, but these echoes will not be considered in this paper because they do not obviously fall into either of the target or clutter classes. In some sense, shipwrecks represent an intermediate class between targets and clutter: The shipwrecks are man-

TABLE I. Link between 23 of the 26 clutter objects considered in this paper and Prior's Malta Plateau scattering regions (Ref. 17). Note that the link is established based upon position on the seafloor and that each of Prior's scattering regions encompasses several of the clutter objects considered in this paper.

Prior scattering region No.	Prior description	Number of associated clutter objects in this paper
1	Certain rock outcrop	5
8a	Probable sediment disturbance	2
8b	Possible sediment disturbance	4
14	Probable change in sediment type	12

made objects, like targets, but they may be partially filled with sediment and buried in the seafloor, like clutter.

Information about the nature of 23 of the 26 clutter objects considered in this paper can be obtained from previously published work by Prior.[17] Table I provides a link between these 23 clutter objects and Prior's Malta Plateau scattering regions. Three of the clutter objects considered in this paper cannot be definitively associated with any of the Prior scattering regions;[17] specifically, the two clutter objects located to the extreme southwest of the experimental area and the clutter object located directly to the north of the two target objects (see Fig. 5). The proximity of the first two unidentified clutter objects to Malta suggests that they may be bathymetry, sediment, or other structural changes related to the presence of the island. The third unidentified clutter object may appear to be located in the vicinity of Prior Object 13 (i.e., "probable wellhead"), but is actually more than 2 km southwest of this object: much too far away to establish a definitive link between the two, and so for the purposes of this paper it will be treated simply as an unidentified clutter object.

The final step in the DRE process is to extract the target and clutter echoes from the main data files and store them in WAV-format audio files. A WAV file is created for each echo that comes through the detection and refinement processes. Each WAV file is 1.5 s in duration and is centered on the echo in both time and beam. Although the time series data were temporarily filtered, squared, and normalized as part of the detection and refinement process, the individual echoes are extracted from the appropriate beams of the raw pressure time series data files. In other words, the filtered, squared, and normalized data are used to identify echoes during the detection and refinement process, but during the extraction process these echoes are extracted from the appropriate beams of the raw pressure data files. As described in the following, echoes are not maintained in this raw form but are conditioned in several ways prior to feature extraction.

C. Echo conditioning

Echo conditioning is a four-step process to prepare the target and clutter echoes for feature extraction. The first step in the conditioning process is to apply a Butterworth filter to each of the echo WAV files. The Butterworth filter is high pass with a single pole at 500 Hz. In order to ensure that the filter does not introduce any phase distortion, it is applied to each WAV file twice: once in the forward direction and once in the backward direction. In this way any phase distortion introduced on the forward pass is removed on the backward pass. The purpose of the Butterworth filter is to "whiten" the spectrum of each WAV file so as to make the echoes more salient, both visually and aurally, and the Butterworth filter has been designed with this purpose in mind. In other words, the shape of the "whitening" Butterworth filter is related to the average spectrum of the received echoes. Figure 6 illustrates the effect of applying the Butterworth filter to each of the echo WAV files.

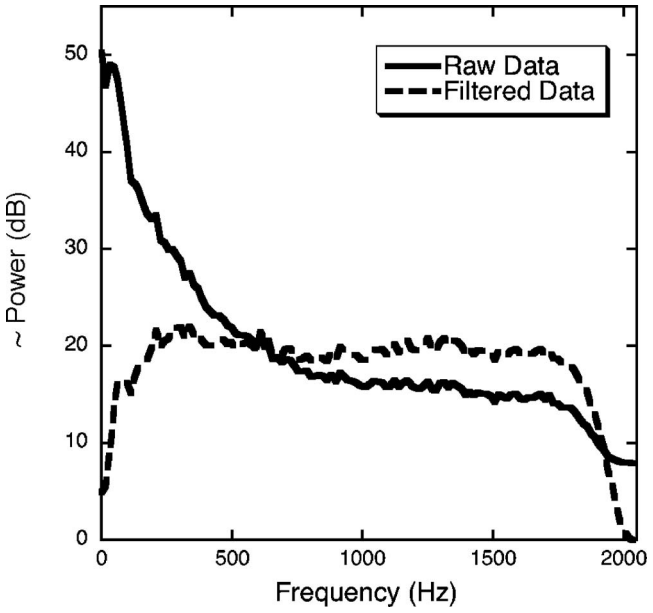

FIG. 6. Effect of applying the two-way, high-pass Butterworth filter to each of the echo WAV files; the solid line denotes the average WAV file spectrum before application of the filter and the dashed line denotes the average WAV file spectrum after application of the filter.

The target and clutter echoes are stored in WAV files 1.5 s long. However, no echo is actually 1.5 s in duration. In fact, the echoes are all substantially shorter than 1.5 s and so each WAV file necessarily contains regions of noise-only context both before the echo begins and after the echo finishes. The purpose of the second step in the conditioning process is to identify the beginning and ending of each echo relative to the WAV file in which it is stored.

The beginning and ending of each echo are identified using a technique originally developed by Kliewer and Mertins for use in audio subband coding schemes.[22] For each sample from a given WAV file, n, the Kliewer-Mertins technique estimates the energy to the left,

$$E_L(n) = \frac{1}{L}\sum_{k=n-L}^{n-1} x^2(k), \tag{1}$$

and the energy to the right,

$$E_R(n) = \frac{1}{L}\sum_{k=n+1}^{n+L} x^2(k), \tag{2}$$

where $x(k)$ represents the WAV file pressure at sample k, and L represents the length of window used in estimating the energy. In this paper $L=1024$ samples. The Kliewer-Mertins technique uses Eqs. (1) and (2) to construct the energy ratio functions

$$C_{\text{start}}(n) = \log_{10}\left(\frac{E_R(n)}{E_L(n)}\right)E_R(n) \tag{3}$$

and

$$C_{\text{end}}(n) = \log_{10}\left(\frac{E_L(n)}{E_R(n)}\right)E_L(n). \tag{4}$$

The WAV file sample for which C_{start} reaches its maximum value is taken to be the start of the echo. Similarly, the WAV file sample for which C_{end} reaches its maximum value is taken to be the end of the echo.

Once the beginning and ending of each echo has been determined via the Kliewer-Mertins technique, it is possible to estimate each echo's signal-to-noise ratio (SNR) as

$$\text{SNR} = 10\log_{10}\left(\frac{\sigma_s^2 - \sigma_n^2}{\sigma_n^2}\right), \tag{5}$$

where σ_s^2 represents the WAV file variance between the beginning and ending of the echo and σ_n^2 represents the WAV file variance in the noise-only context regions both before the echo begins and after the echo ends. SNR is not an inherent property of the target and clutter objects: SNR depends heavily on propagation range, environmental factors, and characteristics of the ambient noise field. Therefore, SNR is not a robust signal feature for target-clutter discrimination. However, because of the specific experimental geometry and relative target strengths of the target and clutter objects being considered, in this paper the target echoes tend to have substantially higher SNR than the clutter echoes. As described in the following, this paper attempts to eliminate SNR as a target-clutter discrimination cue by balancing the SNR histograms for the target and clutter classes.

The approach used to balance the SNR histograms is to work with off-beam target echoes. The towed-array beams have finite width and so it is possible for the echo from a single target to appear on multiple beams. SNR gradually decreases for beams pointing progressively further away from the target object so by selecting off-beam target echoes it is possible to match the target SNR histogram to the clutter SNR histogram.

There are many more clutter objects than target objects in the experimental area and so in order to balance the target and clutter SNR histograms it is necessary to include multiple off-beam target echoes for the same SUS drop. For example, for the second SUS drop it is necessary to include tanker echoes +5, −5, and −10 beams away from the main beam (i.e., the beam pointing directly at the tanker object). In this way, the number of target echoes can be increased to more closely match the number of clutter echoes. Clearly, additional target echoes generated in this way are not completely independent since they result from a single physical process; however, differences in the time series obtained by steering in different beam directions, coupled with differences in ambient noise on different beams should result in echoes that are aurally distinct (i.e., echoes that *sound* sufficiently different from one another to be treated as different realizations). Furthermore, because of the way that the data set is divided into training and testing subsets (see Sec. IV B), information obtained from one off-beam target echo is never used to classify an off-beam echo from the same target. Therefore, any dependence between off-beam target echoes from the same SUS drop cannot bias the automatic classifier results. Figure 7 shows the SNR histogram for the clutter class and the SNR histogram for the target class after SNR-balancing using off-beam target echoes.

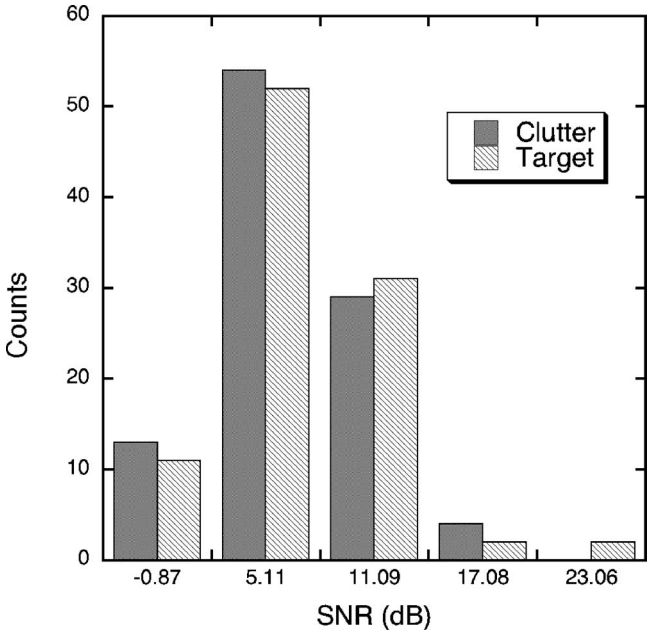

FIG. 7. Target and clutter SNR histograms after SNR-balancing using off-beam target echoes.

It should be mentioned that since towed-array beams become narrower with increasing frequency, adjusting SNR values by working with off-beam echoes slightly alters the target spectra. Specifically, low frequency components of the target echoes will persist further off-beam than high frequency components and therefore there is a small risk that the SNR adjustment process might introduce an artificial target-clutter discrimination cue. This artificial spectral cue could conceivably be eliminated by using a slightly different whitening filter on each target echo (depending on its "distance" off-beam); however, tailoring different whitening filters to specific characteristics of the individual echoes may introduce additional artificial cues that would be more problematic than those introduced by working with the off-beam echoes. Alternatively, target SNR could be reduced by adding ambient noise to the time series at the temporal locations of the target echoes. However, this procedure too presents the possibility of introducing artificial discrimination cues based on the spectral and temporal character of the ambient noise used in the process. Because of the potential problems

associated with both tailoring different whitening filters to different echoes and adding additional ambient noise, both processes were rejected in favor of the selection of off-beam target echoes, as described earlier.

The fourth and final step in the echo conditioning process is to scale each echo for complete audibility. Echo scaling relies upon the auditory model described in Sec. III and it ensures that each echo's perceptual spectrum exceeds the human hearing threshold for the entire frequency band of interest. In this paper the frequency band of interest runs from 50 Hz—near the low-frequency limit of human hearing—to 2048 Hz—the Nyquist frequency for the sampling rate used during data collection. By ensuring that each echo is completely audible, the scaling process prevents perceptual signal feature values from being calculated using portions of the echo data that are not audible to a human.

The data set that results from the echo DRE and conditioning processes consists of 198 WAV files. Each WAV file is 1.5 s in duration and contains a single active sonar echo. There are 100 WAV files that contain echoes from 26 different clutter objects and 98 WAV files that contain (off-beam) echoes from 2 different target objects. It is this collection of 198 WAV files that is examined for the purposes of automatic classification in the remainder of this paper.

III. FEATURE EXTRACTION USING AN AUDITORY MODEL

A. Auditory model

Because the signal features considered in this paper are perceptual in nature, an auditory model capable of providing a perceptual representation of each echo is required for feature extraction. The simple auditory model employed in this paper does not fully replicate the action of the human auditory system; however, it does provide a sufficient perceptual representation of each echo—a representation that is inspired by the operation of the human auditory system. There are three stages to the auditory model. First, an auditory filter bank is applied. Second, the output of the filter bank is converted into a basilar membrane excitation pattern. Finally, the basilar membrane excitation pattern is scaled to obtain a perceptual loudness spectrum.

The auditory filter bank employed in this paper is based upon Slaney's implementation of the Patterson-Holdsworth gammatone filter bank.[23] The specific version of the filter bank used in this paper consists of 100 channels with center frequencies ranging from 50 Hz to 2 kHz (i.e., spanning the frequency band of interest). Channels of the filter bank are equally spaced on the equivalent rectangular bandwidth (ERB) scale. The ERB scale—often also called the ERB rate scale—is a type of perceptual frequency scale that reflects the way in which humans perceive frequency. The relationship between ERB and conventional, linear frequency is given by[24]

$$\mathrm{ERB} = 21.4 \log_{10}(0.00437f + 1), \tag{6}$$

where f is conventional frequency expressed in units of hertz.

Each channel of the filter bank consists of an independent bandpass filter with appropriate gammatone spectral shape and impulse response. The gammatone spectral shape and impulse response were obtained by fitting results from physiological studies of the cat cochlea[25] and are thought to be a good model of the auditory filter in human beings.[26] The gain of the individual filter bank channels are scaled to reflect propagation of sound through the outer and middle ear; this amounts to decreasing the gain of the low frequency channels using an inverted version of the 100 phon equal loudness contour, where the phon is a unit defined such that a sound with loudness 1 phon is perceived as being as loud as a 1 kHz tone at 1 dB re 20 μPa.[24,27]

The auditory filter bank is applied in the time domain to each of the echoes. For each echo the output of the filter bank consists of 100 bandpass filtered versions of the original. Because the filter bank outputs are narrow band, it is possible to use the Hilbert transform to obtain a temporal envelope for each filter bank channel. The temporal envelope for a single filter bank channel is given by $|x(n)+iH\{x(n)\}|$, where $x(n)$ represents the output from one channel of the filter bank and $H\{\cdot\}$ represents the Hilbert transform. It is from these temporal envelopes that values are extracted for the time-frequency perceptual signal features subband attack, subband decay, and subband synchronicity.

The second step in the auditory model is to convert the temporal envelopes output by the filter bank into a basilar membrane excitation pattern. The basilar membrane is located inside the cochlea and functions primarily as a frequency selector, with different points on the membrane responding to different frequency stimuli. This paper considers a single, steady state basilar membrane excitation pattern for each echo and does not consider the evolution of the excitation pattern with time.[24]

It would be possible to employ a time-varying model of basilar membrane excitation[28] but this would require the calculation of "instantaneous" loudness curves that must be updated at an extremely fast rate (e.g., every 1 ms).[28] As a result, time-varying models are much more computationally intensive than the stationary model considered in this paper. In any case, extracting values for the spectral features requires a single representation of the loudness spectrum; so if a time-varying model were to be used, then feature extraction would require a conversion from a series of instantaneous loudness curves into a single perceptual loudness spectrum. The most obvious approaches to achieve this conversion would be either to select the most energetic instantaneous loudness curve or else average all of the instantaneous loudness curves—either of which would result in a perceptual loudness spectrum very similar to the output of the stationary model, at least for the echoes considered in this paper. Finally the time-frequency features that are extracted from the output of the time-domain filter bank will capture important temporal characteristics of the echoes that might later be obscured by the use of a stationary model of basilar membrane excitation.

In the stationary model employed in this paper, each point along the basilar membrane is associated with one channel of the auditory filter bank. The excitation at a given

TABLE II. Summary of the time-frequency perceptual signal features. Note that time-frequency feature values are extracted independently for each channel of the filter bank.

Perceptual signal feature	Quantitative representation	Description (i.e., how individual feature values are extracted for a given filter bank channel)
Subband attack	Time (SBAT)	Time delay between the start of the echo (as defined by Kliewer-Mertins—Ref. 22) and the peak of the temporal envelope
	Slope (SBAS)	Slope of the line joining the start of the echo and the peak of the temporal envelope
Subband decay	Time (SBDT)	Time delay between the peak of the temporal envelope and the end of the echo (as defined by Kliewer-Mertins—Ref. 22)
	Slope (SBDS)	Slope of the line joining the peak of the temporal envelope and the end of the echo
Subband synchronicity	Correlation (SBCorr)	Average correlation coefficient between the temporal envelope for the given channel, i, and the temporal envelopes for the other 99 channels: $\frac{1}{99}\sum_{j\neq i}\rho_{i,j}$

point on the basilar membrane is obtained by summing all samples of the temporal envelope from the corresponding filter bank channel. In this way the excitation for each point on the basilar membrane is obtained, and the time-frequency echo representation output by the filter bank is converted into basilar membrane excitation: a purely spectral representation.

The third and final step in the auditory model is to convert basilar membrane excitation patterns into perceptual loudness functions, which represent the perceived loudness of each echo as a function of ERB. The relationship between basilar membrane excitation and perceptual loudness is not linear; in fact, it is a relationship of nonlinear compression.[24] The specific relationship between basilar membrane excitation and perceptual loudness used in this paper was proposed by Moore and Glasberg,[24] and can be expressed as

$$N'(\mathrm{ERB}) = C(E_{\mathrm{echo}}(\mathrm{ERB})^{\alpha} - E_{\mathrm{thresh}}(\mathrm{ERB})^{\alpha}), \tag{7}$$

where N' represents perceptual loudness in units of sones/ERB, E_{echo} represents the basilar membrane excitation induced by the echo, E_{thresh} represents the background or threshold basilar membrane excitation induced by blood flow and other noises inside the head, α is the exponent that accounts for nonlinear compression, and C is a scaling factor that is set so as to ensure consistency with the standard definition of the sones scale of psychoacoustic loudness. Note that integrating N' across the frequency band of interest yields the total or complete echo loudness in units of sones.

Based on empirical results, this paper uses an α value of 0.2159[27] and a C value of 0.0702. Values for E_{echo} come from the second step of the auditory model and values for E_{thresh} are obtained from the minimal audible field standard for humans.[24,29] Because each echo has been scaled for complete audibility, E_{echo} is greater than E_{thresh} for all echoes and all ERB values and as a result N' is greater than zero for all echoes and all ERB values. In other words, each echo is indeed completely audible. As described in the following, it is from these perceptual loudness functions that values are extracted for the purely spectral perceptual signal features peak loudness, loudness centroid, and loudness roughness.

B. Feature extraction

Two major types of perceptual signal features are considered in this paper: time-frequency features and purely spectral features. Values for the time-frequency features are extracted from the temporal envelopes output by the auditory filter bank and values for the purely spectral features are extracted from the perceptual loudness functions output by the loudness model. Note that there are no purely temporal perceptual signal features because in the human auditory system the cochlea breaks incoming signals down into subbands, and so unfiltered time-domain signals are not directly available to the brain.

Table II provides a list of the time-frequency perceptual signal features considered in this paper along with a brief description of how feature values are extracted. Figure 8 illustrates the extraction of subband attack time feature values for several temporal envelopes corresponding to several channels of the auditory filter bank.

Each of the time-frequency perceptual signal features is 100-dimensional in the sense that for each echo there are 100 individual feature values, corresponding to the 100 channels of the auditory filter bank. During automatic classification the perceptual signal features are treated as axes of a multidimensional space, and so they are required to be one dimensional, i.e., one value for each echo. As illustrated in Fig. 8, the multidimensional time-frequency perceptual signal features are converted into one-dimensional perceptual signal features using summary statistics. For example, the multidimensional perceptual signal feature subband attack time (SBAT) is converted into the one-dimensional perceptual features minimum SBAT (minSBAT), mean SBAT (meanSBAT), and maximum SBAT (maxSBAT). In addition, the center frequencies of the filter bank channels corresponding to minSBAT and maxSBAT are also treated as one-dimensional perceptual features: minSBAT-F and

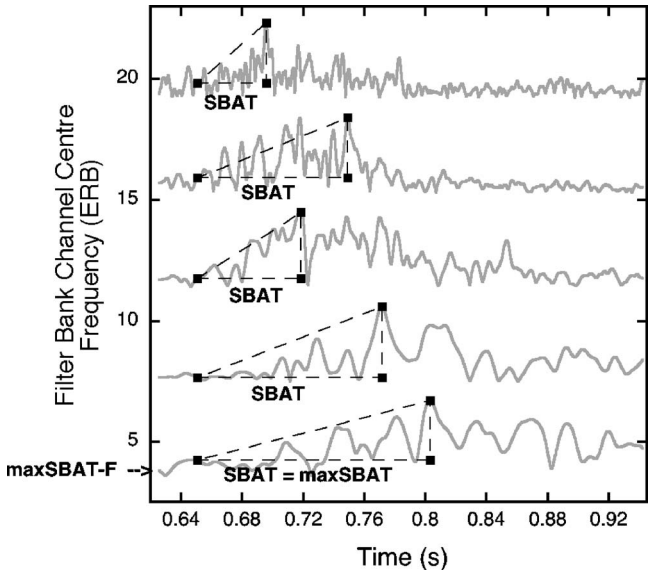

FIG. 8. Extraction of subband attack time feature values from several channels of the auditory filter bank; the lowest trace exhibits the maximum subband attack time (maxSBAT) and the frequency of this filter bank channel corresponds to maxSBAT-F.

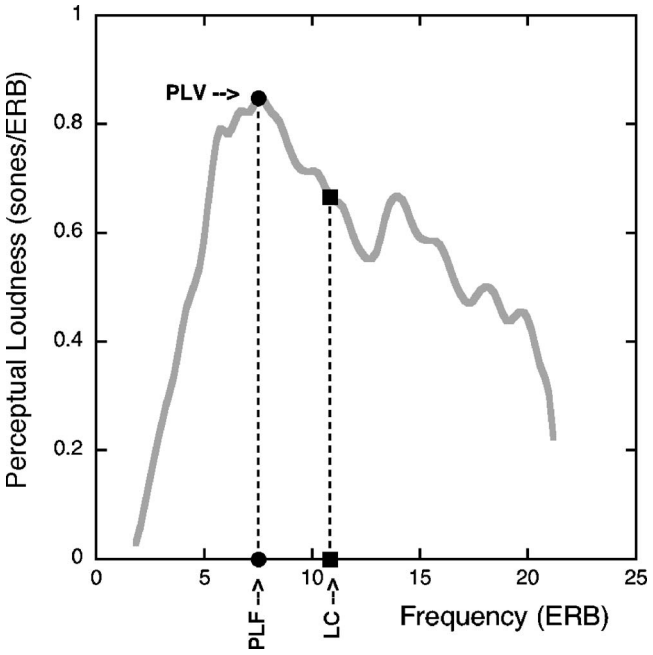

FIG. 9. Extraction of peak loudness frequency (PLF), peak loudness value (PLV), and loudness centroid (LC) feature values from a perceptual loudness function.

maxSBAT-F, respectively. In this way each multidimensional time-frequency perceptual signal feature listed in Table II is converted into 5, one-dimensional perceptual signal features for a total of 25, one-dimensional time-frequency perceptual signal features.

The use of summary statistics to simplify the time-frequency features should not be misconstrued as an attempt to parametrize the distribution of these feature values for single echoes. Although for many echoes the χ^2 "goodness of fit" test allows that time-frequency feature values may follow a Gaussian distribution (i.e., there is not enough evidence to reject the null hypothesis that the data are Gaussian distributed), this information is never really used to assist in the classification task. Instead, the sample minimum, mean, and maximum statistics are calculated directly from the echo subbands. These sample statistics are used simply as representations of single realizations (i.e., individual echoes), and they are not meant to describe an underlying ensemble.

Table III provides a list of the purely spectral signal features considered in this paper along with a brief description of how feature values are extracted. Figure 9 illustrates the extraction of peak loudness and loudness centroid feature values from a perceptual loudness function output by the auditory model.

In contrast to the time-frequency features, the purely spectral signal features are already one dimensional, i.e., they consist of one value per echo, and so there is no need to apply summary statistics.

Taken together there are a total of 30, one-dimensional perceptual signal features identified in this paper: 5 purely

TABLE III. Summary of the purely spectral perceptual signal features.

Perceptual signal feature	Quantitative representation	Description (i.e., how individual feature values are extracted)
Peak loudness	Peak loudness frequency (PLF)	Center frequency (in ERB) of the filter bank channel corresponding to the peak value of the perceptual loudness function
	Peak loudness value (PLV)	Value of the perceptual loudness function (in sones/ERB) at the filter bank channel corresponding to the PLF
Loudness roughness	Maxima to spectral bin ratio (MSBR)	The total number of local maxima in the perceptual loudness function divided by the number of filter bank channels
	Bin-to-bin difference (BBD)	The mean of the magnitude of the difference between adjacent bins (i.e., adjacent filter bank channels) of the perceptual loudness function
Loudness centroid	Loudness centroid (LC)	The frequency (in ERB) corresponding to the centroid of the perceptual loudness function

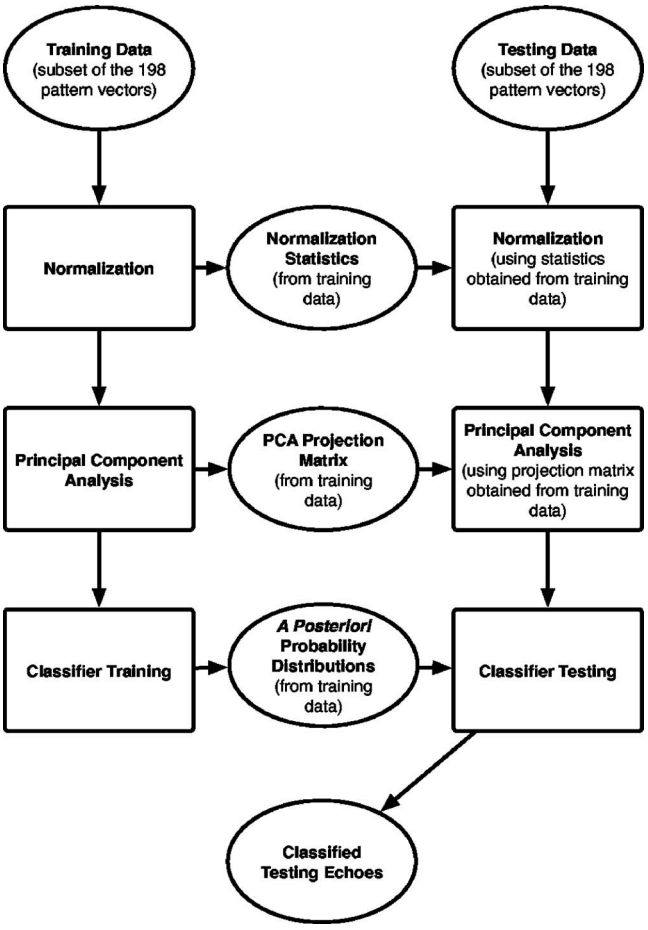

FIG. 10. Automatic classifier architecture for the Gaussian-based approach employed in this paper.

spectral features and 25 time-frequency features. For each echo, the corresponding feature values are collected into a 30-element pattern vector, where each element of the vector corresponds to a different feature. Because there are a total of 198 echoes considered in this paper, there are also a total of 198 thirty-element pattern vectors: one for each echo.

Each of the 30-element pattern vectors represents a point in 30-dimensional feature space, where the axes of the feature space correspond to the perceptual signal features. Thus, each echo is associated with a specific point in the feature space. The following sections of this paper describe the application of an automatic classifier to the distribution of target and clutter echoes within this feature space.

IV. TRAINING AND TESTING DATA

A. Classifier architecture

This paper makes use of a very simple Gaussian-based automatic classifier, which is applied to the multidimensional feature space described earlier. The classifier architecture is illustrated in Fig. 10. Each feature is treated as an axis of the feature space and the individual echoes are distributed within the feature space based on their values for the various features. The full data set is divided into training and testing subsets. Each feature is normalized such that the mean value and variance of echoes in the training subset are zero and one, respectively; normalizing the features in this way places each feature on an equal footing and ensures that the final results will not depend on the units used to measure the feature values. Note that feature normalization is carried out using sample statistics (i.e., sample mean and variance) and not by assuming an underlying statistical distribution. However, some readers may be interested to know that the χ^2 "goodness of fit" test allows that some of the perceptual signal features, including: loudness centroid (LC), peak loudness value (PLV), peak loudness frequency (PLF), frequency of the minimum subband attack time (minSBAT-F), and mean subband decay time (meanSBDT), along with several others, may follow a Gaussian distribution. Principal component analysis (PCA) is applied to the normalized training data in order to obtain a linear transformation that projects the full multidimensional feature space down onto a new two-dimensional space in which the two axes are linear combinations of the original features.

Note that the selection of two dimensions for the PCA space is somewhat arbitrary—It is possible to consider a PCA space of any number of dimensions up to and including the total number of perceptual signal features. The selection of two dimensions is justified by the fact that two-dimensional spaces are easy to represent graphically, and by the fact that, for the five perceptual features that are ultimately considered by this paper (see Sec. V and particularly the top row of Table V), more than 76% of the variance in the original feature space is associated with the first two PCA dimensions.

Within the PCA space, a Gaussian probability density function (pdf) is fit to the distribution of clutter echoes from the training subset and a separate Gaussian pdf is fit to the distribution of target echoes from the training subset. These pdfs can be thought of as the conditional or likelihood probabilities; for any point $\boldsymbol{X}=\left[\begin{smallmatrix}x\\y\end{smallmatrix}\right]$ in the PCA space the clutter pdf expresses

$$P(\boldsymbol{X}|C)=\frac{1}{2\pi|\Sigma_C|^{1/2}}\exp\left(\frac{1}{2}(\boldsymbol{X}-\boldsymbol{\mu}_C)^T\Sigma_C^{-1}(\boldsymbol{X}-\boldsymbol{\mu}_C)\right): \quad (8)$$

the probability that a clutter echo would be located at position $\boldsymbol{X}$, and the target pdf expresses

$$P(\boldsymbol{X}|T)=\frac{1}{2\pi|\Sigma_T|^{1/2}}\exp\left(-\frac{1}{2}(\boldsymbol{X}-\boldsymbol{\mu}_T)^T\Sigma_T^{-1}(\boldsymbol{X}-\boldsymbol{\mu}_T)\right): \quad (9)$$

the probability that a target echo would be located at position $\boldsymbol{X}$, where Σ_C represents the 2×2 element sample covariance matrix estimated from the clutter echoes in the training subset, Σ_T represents the 2×2 element sample covariance matrix estimated from the target echoes in the training subset, $\boldsymbol{\mu}_C$ represents the two-element sample mean vector estimated from the clutter echoes in the training subset, and $\boldsymbol{\mu}_T$ represents the two-element sample mean vector estimated from the target echoes in the training subset. The *a priori* probabilities $P(C)$ and $P(T)$ are estimated based on the relative numbers of clutter and target echoes in the training subset. Bayes' theorem is used to combine the likelihood and *a pri-*

ori probabilities into expressions for the *a posteriori* probabilities:

$$P(C|\boldsymbol{X}) = \frac{P(C) \cdot P(\boldsymbol{X}|C)}{P(\boldsymbol{X})} \tag{10}$$

and

$$P(T|\boldsymbol{X}) = \frac{P(T) \cdot P(\boldsymbol{X}|T)}{P(\boldsymbol{X})}, \tag{11}$$

where $P(\boldsymbol{X}) = P(C) \cdot P(\boldsymbol{X}|C) + P(T) \cdot P(\boldsymbol{X}|T)$.

The fitting of Gaussian pdfs to the training data is justified in three ways. First, there is an "Occam's razor"-type argument, which would suggest that in the absence of *a priori* information suggesting another statistical distribution for the training data, one should begin by fitting the simplest possible distribution: the Gaussian distribution. This principle is articulated elsewhere in the pattern classification literature as: "Gaussian classifiers… are the most common and simplest classifiers. They should always be tried first on new problems."[30] Second, using a relatively strict 1% cutoff, the χ^2 goodness of fit test does not allow for the rejection of the null hypothesis that the training data are Gaussian distributed (at least for the five features that are ultimately considered in this paper—See Sec. V). In other words, the χ^2 test suggests that there is between 1% and 2.5% chance that the training data are, in fact, Gaussian distributed. Finally, the success that is ultimately achieved when the Gaussian-based classifier is applied to the testing data (see Sec. VI) suggests that there is no reason to try fitting more complicated pdfs (e.g., Gaussian mixtures).

Returning now to the description of classifier architecture: The *a posteriori* probabilities (obtained by fitting Gaussian pdfs to the training data) are used to classify the echoes from the testing subset. The location, $\boldsymbol{X} = \left[\begin{smallmatrix} x \\ y \end{smallmatrix}\right]$, of each testing echo within the PCA space is substituted into Eqs. (10) and (11) to obtain the probability that the echo resulted from a clutter object and the probability that the echo resulted from a target object, respectively. The classification decision for each echo is then made based on the relative size of these two probabilities.

In practice the specific decision rule employed will depend on the relative costs associated with missed detections and false alarms. In the context of this paper a missed detection is a target echo that has been incorrectly classified as clutter, and a false alarm is a clutter echo that has been incorrectly classified as a target. If the cost of a missed detection is very high compared to that of a false alarm, then the appropriate decision rule would require $P(C|\boldsymbol{X})$ to be much greater than $P(T|\boldsymbol{X})$ in order for a testing echo located at $\boldsymbol{X}$ to be classified as clutter. In contrast, if the cost of a false alarm is very high compared to that of a missed detection, then the appropriate decision rule would require $P(T|\boldsymbol{X})$ to be much greater than $P(C|\boldsymbol{X})$ in order for a testing echo located at $\boldsymbol{X}$ to be classified as a target.

By varying the decision rule while keeping track of the number of missed detections and false alarms, it is possible to trace out a receiver operating characteristic (ROC) curve. ROC curves plot probability of detection, $P(D) = P(T|T)$, versus probability of false alarm, $P(\text{FA}) = P(T|C)$. In this paper, ROC curves are used to assess classifier performance: The larger the area under the ROC (AUROC) curve, the better the classifier performance.

TABLE IV. The training-testing split employed in this paper; this split was chosen to most closely approximate the operational requirement with the available data.

	Target		Clutter	
	No. objects	No. echoes/ pattern vectors	No. objects	No. echoes/ pattern vectors
Full data set	2	98	26	100
Training subset	1 (tanker)	36	13	48
Testing subset	1 (oil plat.)	62	13	52

B. Selection of training and testing subsets

There are many ways that the full data set could be split into training and testing subsets and no one approach is inherently better than any other. The only constraint on the training-testing split is that the same echo may not be included in both subsets. For example, 50% of the echoes could be randomly selected for training with the remaining 50% used for testing, or 10% of the echoes could be randomly selected for training with the remaining 90% used for testing, or 50% of the target echoes and 50% of the clutter echoes could be selected for training with the remaining target and clutter echoes used for testing. All of these approaches are valid but none accurately reflects the way in which an automatic classifier would be used operationally.

In the typical operational setting, an automatic classifier is trained on an archival database of target and clutter echoes and is then tested on novel echoes that result from totally different target and clutter objects than the ones used for training. In order to approximate the operational requirement as closely as possible using the available data, this paper considers a training subset composed of echoes from the tanker target object and 13 of 26 clutter objects, and a testing subset composed of echoes from the Campo Vega oil platform and the remaining 13 of 26 clutter objects—see Table IV. This training-testing split is not quite as challenging as would be expected operationally—where the objects in the training and testing subsets may be situated in totally different environments—but it is the best that can be achieved using the available data. At the very least the training-testing split employed here forces classification to be carried out based on inherent similarities between the echoes from the tanker and the oil platform and inherent similarities between the echoes from the different clutter objects, as opposed to simply recognizing different echoes from the same object.

V. FEATURE SELECTION

Not all of the 30 perceptual signal features being considered have equal value as target-clutter discrimination cues. Inevitably, some features are more useful than others.

This section of the paper describes the Parcel algorithm,[16,31] which is employed to select particularly effective subsets of perceptual signal features.

In practice, feature selection is carried out before training and testing the automatic classifier. However, in this paper feature selection is described only after discussing the classifier architecture because some familiarity with the classifier architecture is required to understand the Parcel algorithm. As discussed in more detail in the following, the output of the feature selection algorithm is a subset of particularly useful signal features. As discussed in Sec. VI, it is these features that are used to train and test the automatic classifier.

A. Redundancy reduction

To ensure the most efficient operation of the Parcel algorithm, redundant features must be dropped prior to its application. A feature is considered to be redundant if it expresses the same information about the relationship between echoes as another feature. Consider, for example, four features labeled A, B, C, and D. Features A and B express the same information about the relationship between echoes and therefore the feature subset consisting of features A, C, and D is equivalent to the feature subset consisting of features B, C, and D. Although both subsets are equivalent, the Parcel algorithm may consider both possibilities individually—this reduces the efficiency of the algorithm. This paper employs a correlation threshold of 0.9 to identify redundant features. In other words, if the magnitude of the correlation coefficient between two features is greater than 0.9, then one of the features is considered to be redundant and is dropped from further consideration.

Using this approach, a total of four features are identified as redundant and dropped. Features dropped from consideration include: mean subband attack slope (meanSBAS), which is highly correlated with maximum subband attack slope (maxSBAS); maximum subband decay time (maxSBDT), which is highly correlated with maximum subband attack time (maxSBAT); bin-to-bin difference (BBD), which is highly correlated with peak loudness value (PLV); and maximum subband correlation (maxSBCorr), which is highly correlated with mean subband correlation (meanSBCorr). Dropping these four features results in training and testing pattern vectors composed of 26 elements, where each element corresponds to a nonredundant perceptual signal feature.

B. Parcel algorithm

Feature selection is carried out using only the training subset, since allowing the Parcel algorithm access to the testing subset would result in it selecting features tailored specifically to the echoes in the testing subset, as opposed to features generally appropriate for the target and clutter classes.

The Parcel algorithm uses binary feature masks to represent different subsets of perceptual signal features. Each binary feature mask consists of 26 elements: one for each of the nonredundant signal features. Within these feature masks an element value of zero indicates that the corresponding feature is not included in the current subset and a value of one indicates that the corresponding feature is included in the current subset.

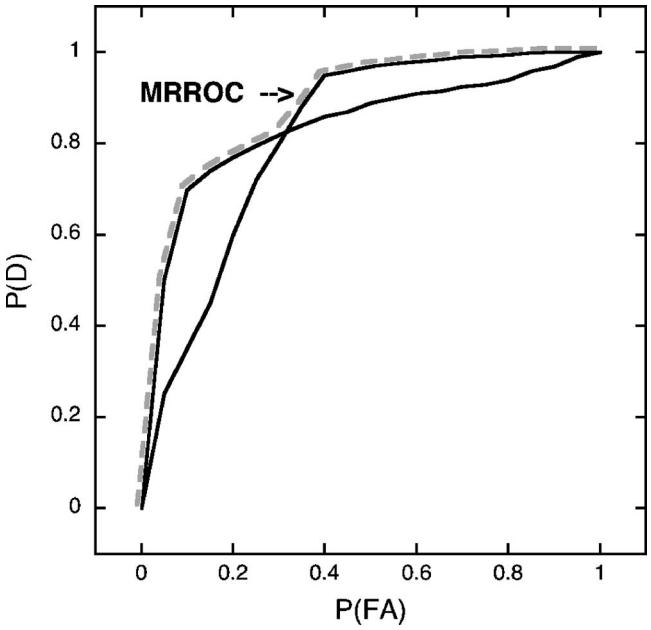

FIG. 11. Combining multiple ROC curves to obtain the maximum realizable ROC (MRROC) curve; note that individual ROC curves can cross and so multiple ROC curves can contribute to the MRROC.

The Parcel algorithm[16,31] is in an iterative process. In this paper, the Parcel algorithm is initialized with a single binary feature mask in which two randomly selected elements are set to one. Additional feature masks are constructed by successively flipping the value of each element of the initial feature mask: switching ones to zeros and zeros to ones.

For each feature mask, a fourfold cross validation process[32] is applied using only those features corresponding to ones in the binary mask. Fourfold cross validation amounts to splitting the training subset into four, mutually exclusive subgroups, training the classifier using echoes from three of the four subgroups, and then testing the classifier using echoes from the remaining subgroup, i.e., the subgroup not used for training. The cross-validation process is iterative and is run four times, each time using a different subgroup for testing. For each iteration a ROC curve is traced out by varying the classifier decision rule from the point at which $P(D)=P(\mathrm{FA})=0$ to the point at which $P(D)=P(\mathrm{FA})=1$. The ROC curves corresponding to the four iterations are averaged to obtain a single ROC curve representing classifier performance for each feature mask, i.e., the cross validation process results in one (average) ROC curve per feature mask.

As illustrated in Fig. 11, the ROC curves for the various feature masks are combined to construct the maximum realizable ROC (MRROC) curve.[16,31] At each $P(\mathrm{FA})$ value the MRROC is defined to be the maximum of the individual ROC curves. Feature masks that contribute to the MRROC are maintained for further analysis and feature masks that do not contribute to the MRROC are discarded.

This MRROC-based approach to feature selection is favored over a simpler approach based on area under the ROC (AUROC) curve because although the ROC curve with largest AUROC represents the best overall classifier performance, it does not necessarily represent the best classifier performance for all $P(\mathrm{FA})$ values. For example, it is possible for the ROC curves from two different feature masks to cross, such that one feature mask leads to better performance at small $P(\mathrm{FA})$ and the other leads to better performance at large $P(\mathrm{FA})$. As mentioned previously, in active sonar classification the operating point, i.e., the specific $P(\mathrm{FA})$ at which the sonar operates, is variable and the specific decision rule for a given operational task is chosen based on the relative costs of missed detections and false alarms. Therefore, it is important to know the specific subsets of features that perform best at each possible $P(\mathrm{FA})$ value, and hence the MRROC-based approach is employed for feature selection.

The feature masks that contribute to the MRROC on the current iteration are used to initialize the next iteration of the algorithm and the entire process is repeated. The Parcel algorithm continues to iterate in this way until the MRROC curve is no longer improving or until there are no new feature masks to be considered. The final output of the Parcel algorithm is the binary feature mask or masks that contribute to the MRROC curve on the final iteration.

It should be noted that the Parcel algorithm is a heuristic search technique. This means that it does not consider each of the 2^{26} feature masks that could be created from 26 features. Instead, the Parcel algorithm uses the MRROC-based approach to navigate through the possible feature masks, examining those feature masks that are "close" to feature masks found to contribute to the MRROC on previous iterations. Because the Parcel algorithm is nonexhaustive it may be that the feature mask or masks that it selects are not as effective as feature masks that were not examined. The feature mask or masks selected by the algorithm do, however, represent a local maximum in classifier performance in the sense that there are no close feature masks—i.e., feature masks obtained by flipping one element—that will improve classifier performance.

C. Parcel algorithm results

The Parcel algorithm is run five times using a different feature mask to initialize the algorithm on each run. The results of the five runs are summarized in Table V.

The feature masks output by the Parcel algorithm typically contain about five features. The feature LC (loudness centroid) appears in all of the feature masks, indicating that this is a particularly useful feature. Other features that appear in a relatively large number of feature masks include: maxSBDT-F (frequency of the maximum sub-band decay time), PLV (peak loudness value), PLF (peak loudness frequency), and minSBAT-F (frequency of the minimum sub-band attack time). Fifteen of the twenty-six nonredundant perceptual signal features appear at least once.

The remainder of this paper will present results obtained using the five features selected during the first run of the Parcel algorithm, i.e., the five features listed in the top row of Table V. As demonstrated in Fig. 14 in Sec. VI, these results are generally consistent with results obtained using features listed in the other rows of Table V.

TABLE V. Parcel algorithm results for five different runs. Note that on some runs the Parcel algorithm returns a single feature mask that is valid for all $P(\mathrm{FA})$ and on other runs the Parcel algorithm returns two feature masks, one of which is valid for small $P(\mathrm{FA})$ and one of which is valid for large $P(\mathrm{FA})$; the top row contains the feature mask that is considered in the remainder of this paper.

Initial feature mask	Parcel algorithm results	
	Final feature mask	Region of applicability
PLF, minSDBS-F	LC, PLF, minSBDS-F, meanSBDT, maxSBDT-F	$0 \le P(\mathrm{FA}) \le 1$
minSBAT, MSBR	LC, maxSBDT-F, PLV, minSBAT	$0.083 \le P(\mathrm{FA}) \le 1$
	LC, meanSBDT, maxSBDT-F, PLV, minSBAT	$0 \le P(\mathrm{FA}) < 0.083$
meanSBCorr, maxSBDS	LC, PLV, meanSBAT, minSBAT-F, maxSBDS	$0 \le P(\mathrm{FA}) \le 1$
meanSBCorr, maxSBAS-F	LC, PLF, meanSBCorr, maxSBDT-F, PLV	$0 \le P(\mathrm{FA}) < 0.083$
	LC, meanSBDS, maxSBDT-F, minSBAT-F, maxSBAS-F	$0.083 \le P(\mathrm{FA}) \le 1$
maxSBDT-F, maxSBAS-F	LC, meanSBDS, maxSBDT-F, minSBAT-F, maxSBAS-F	$0.083 \le P(\mathrm{FA}) \le 1$
	LC, PLF, minSBDS-F, maxSBDT-F, maxSBAT, maxSBAT-F	$0 \le P(\mathrm{FA}) < 0.083$

VI. AUTOMATIC CLASSIFIER RESULTS

The preceding sections of this paper describe processing undertaken in order to convert the original data set consisting of beamformed pressure time series data files into a format suitable for automatic classification using perceptual signal features. Each stage of this processing is summarized in Table VI. The remainder of this paper presents results obtained by applying a simple Gaussian-based automatic classifier to the data set that results from the final processing stage, i.e., the data set described in the bottom row of Table VI.

A. Training

As described in Sec. IV A, principal component analysis (PCA) is applied to the normalized training data in order to project the full five-dimensional feature-space down onto a new two-dimensional space. The result of applying PCA to the training subset is illustrated in Fig. 12.

Gaussian pdfs are fit to the distribution of training clutter and target echoes using Eqs. (8) and (9), respectively. These pdfs represent likelihood probabilities. *A priori* probabilities $P(C)$ and $P(T)$ are estimated based on the relative numbers of clutter and target echoes in the training subset—In this case, $P(C)=48/84=0.571$ and $P(T)=36/84=0.429$. The likelihood and *a priori* probabilities are combined using Eqs.

TABLE VI. Summary of the processing stages described in this paper and the data sets that result from each stage.

Processing stage	Relevant section of this paper	Resultant data set	No. perceptual features/pattern vector elements
Experimental sea trial	II A	9 raw pressure time series files with 81 beams per file	N/A
Echo DRE and conditioning	II B and II C	198 WAV files corresponding to 98 echoes from two target objects, and 100 echoes from 26 clutter objects	N/A
Feature etraction	III	198 pattern vectors	30
Training-testing split	IV B	Training subset: 36 target and 48 clutter pattern vectors	30
		Testing subset: 62 target and 52 clutter pattern vectors	30
Redundancy reduction	V A	Training subset: 84 pattern vectors	26
		Testing subset: 114 pattern vectors	
Parcel algorithm	V B and V C (specific results obtained using top row of Table V)	Training subset: 84 pattern vectors	5
		Training subset: 114 pattern vectors	

(10) and (11) to obtain the *a posteriori* probability distributions $P(C|\boldsymbol{X})$ and $P(T|\boldsymbol{X})$, respectively. As described in the following, it is these *a posteriori* probability distributions that are used to classify echoes from the testing subset.

B. Testing

PCA is applied to the testing data using exactly the same 5×2 element transformation matrix as was applied to the training data. The result is illustrated in Fig. 13.

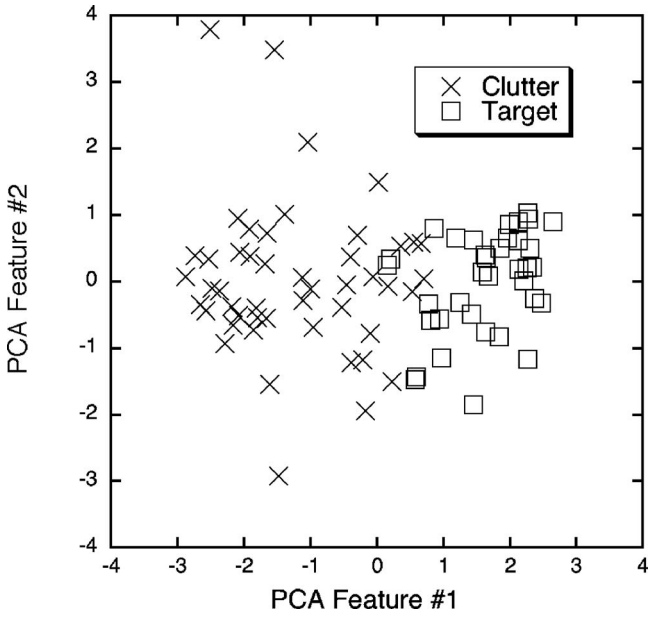

FIG. 12. Result of applying PCA to the training subset.

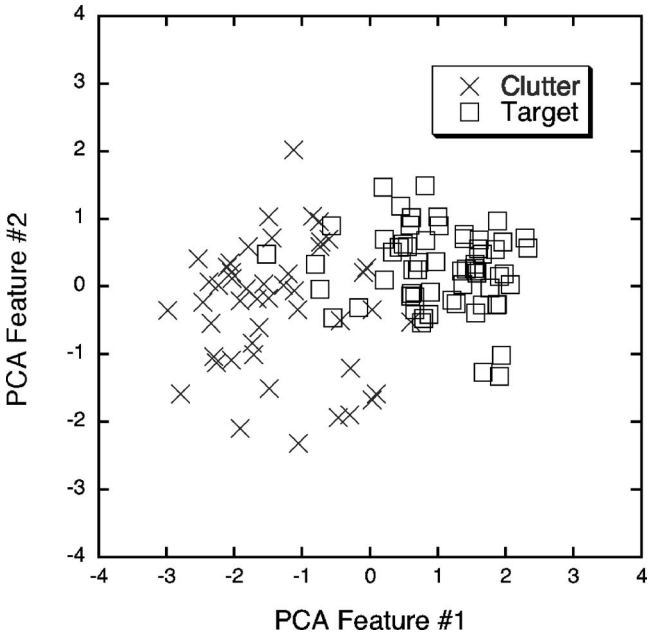

FIG. 13. Result of applying PCA to the testing subset.

Qualitatively the testing data plotted in Fig. 13 is distributed in much the same way as the training data plotted in Fig. 12. This is promising since it suggests that there is inherent similarity between echoes from the tanker ship and echoes from the oil platform, and inherent similarity between echoes from the training clutter objects and the testing clutter objects. In other words, the tanker echoes are representative of all echoes in the target class and the training clutter echoes are representative of all echoes in the clutter class—at least in terms of the five perceptual signal features selected by the Parcel algorithm.

The location of each testing echo within the PCA space, $\boldsymbol{X}=\begin{bmatrix} x \\ y \end{bmatrix}$, is substituted into the expressions for $P(C|\boldsymbol{X})$ and $P(T|\boldsymbol{X})$ that were obtained using the training data. Taking the ratio of these two probabilities: $P(C|\boldsymbol{X})/P(T|\boldsymbol{X})$, yields a single-valued quantity that can be used to classify the testing echoes. The general decision rule can be specified as: decide clutter if $P(C|\boldsymbol{X})/P(T|\boldsymbol{X})>R$ and decide target if $P(C|\boldsymbol{X})/P(T|\boldsymbol{X})<R$. As discussed in Sec. IV, the specific decision rule (i.e., the appropriate value of R) depends on the relative costs associated with missed detections and false alarms. For example, if the cost associated with a missed detection is the same as the cost associated with a false alarm then $R=1$; in other words, echoes for which $P(C|\boldsymbol{X})/P(T|\boldsymbol{X})>1$ would be classified as clutter and echoes for which $P(C|\boldsymbol{X})/P(T|\boldsymbol{X})<1$ would be classified as target.

If $R=0$ then every testing echo would be classified as clutter and therefore $P(D)=P(\mathrm{FA})=0$. In contrast, if $R=\max(P(C|\boldsymbol{X})/P(T|\boldsymbol{X}))$ then every testing echo would be classified as target and therefore $P(D)=P(\mathrm{FA})=1$. By continuously varying R between these two extreme values it is possible trace out a ROC curve for the testing data subset. Such a ROC curve is plotted in Fig. 14.

ROC curves are used to assess classifier performance in two different ways. First, the area AUROC curve is calcu-

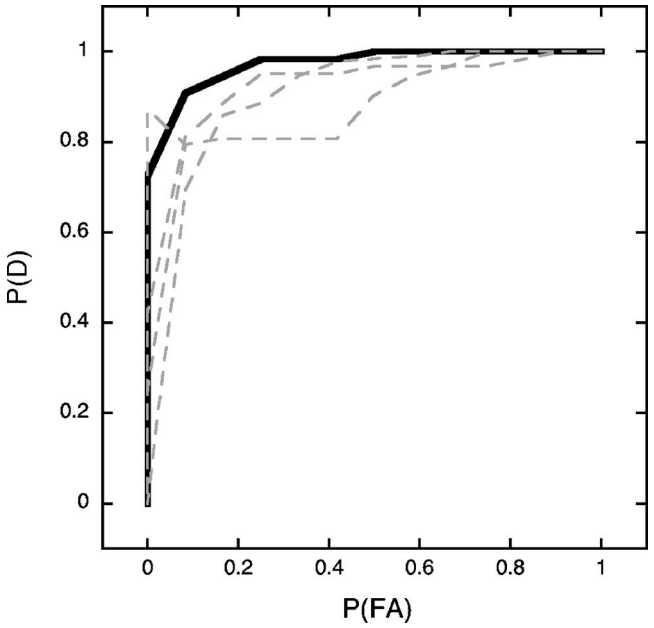

FIG. 14. ROC curve corresponding to the testing data plotted in Fig. 13 (solid line); dashed lines represent testing ROC curves for other rows of Table V (i.e., other Parcel algorithm feature subsets)—Note that these ROC curves need not be monotonically increasing because they are MRROC curves possibly composed of multiple ROC curves.

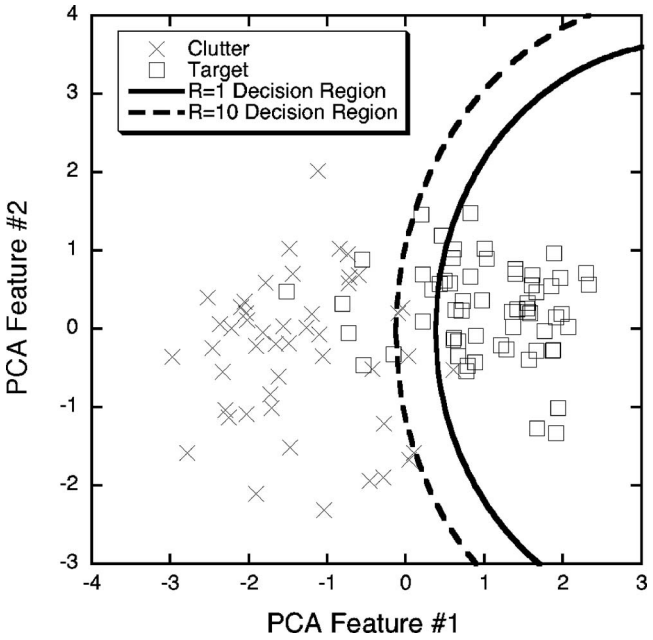

FIG. 15. Testing data and decision region corresponding to $R=1$ (solid line) and $R=10$ (dashed line); echoes inside the ellipse are classified as target and echoes outside the ellipse are classified as clutter.

lated: The larger the AUROC, the better the classifier performance. Second, the equal error rate, i.e., the point on the ROC curve at which $P(\mathrm{FA})=1-P(D)$ is identified: The smaller the equal error rate, the better the classifier performance.

The ROC curve corresponding to the testing subset has AUROC=0.975 and an equal error rate of about 0.1 or 10%. These values are generally considered to be indicative of a very successful classifier. For the purposes of comparison note that the perfect classifier, i.e., one that could achieve $P(D)=1$ for $P(\mathrm{FA})=0$, would have AUROC = 1.0 and an equal error rate of 0%. In contrast, a classifier that randomly classified testing echoes as target or clutter would have AUROC=0.5 and an equal error rate of 50%.

Selecting a specific classifier decision rule sets a specific operating point for the classifier and defines a decision surface within the PCA space. The decision surface is drawn so as to separate regions of the PCA space in which echoes are classified as clutter from regions of the PCA space in which echoes are classified as target. Figure 15 illustrates the different decision surfaces obtained by setting $R=1$ and $R=10$. Note that the specific operating points corresponding to these decision surfaces are $P(D)=\frac{51}{62}=82.3\%$, $P(\mathrm{FA})=\frac{1}{52}=1.9\%$, and $P(D)=\frac{56}{62}=90.3\%$, $P(\mathrm{FA})=\frac{4}{52}=7.7\%$, respectively. The respective total error rates are $\frac{12}{114}=10.5\%$ and $\frac{10}{114}=8.8\%$.

For completeness, note that the single false alarm associated with the $R=1$ decision region results from an echo off one of the two clutter objects that were associated with the island of Malta (see Sec. II B). The three additional false alarms associated with the $R=10$ decision region result from an additional echo off the Malta-related clutter feature, an echo off a "certain rock outcrop" (i.e., Prior clutter region 1),[17] and an echo off a "probable change in sediment type" (i.e., Prior clutter region 14).[17] Unfortunately, not enough is known about the specific nature of these clutter objects to offer any kind of explanation as to why these echoes appear more "target-like" to the automatic classifier than different echoes from the same clutter objects, or echoes from different clutter objects altogether.

VII. CONCLUSIONS

The research results presented in this paper, and specifically the automatic classifier results presented in Sec. VI, suggest that a relatively small number of timbre-based perceptual signal features can indeed be used to successfully classify an explosive-source active sonar data set. Specifically, the classifier described in this paper considers only five features and achieves an AUROC of 0.975 and an equal error rate of roughly 10%—both of these values are considered to be indicative of a very successful classifier. The Parcel algorithm results presented in Sec. V indicate that the most effective timbre-based perceptual signal feature for explosive-source active sonar classification is LC. Other features found to be particularly effective include: maxSBDT-F, PLV, PLF, and minSBAT-F.

All of the results presented in this paper are based on a single data set, which was recorded over 4 h in one environment, using one experimental geometry (monostatic), and one type of active sonar source (SUS charges). Consequently, it is not obvious how the results of this paper would generalize to data sets recorded at different times of year, in different environments, using different experimental geometries, or using different types of sonar sources. As discussed in Sec. IV, this paper attempts to account for the limitations imposed by the single data set by creating training and testing subsets in such a way that different echoes from the same object do not appear in both subsets. This training-testing

split ensures that the classifier is not simply recognizing different echoes from the same object, but it cannot account for the fact that all of the echoes were recorded at approximately the same time in the same environment, using the same experimental geometry and source type. The limitation imposed by the use of a single data set could be addressed by repeating the experimental sea trial described in Sec. II for several different environments, using different experimental geometries, and different types of sonar sources. It would be particularly interesting to apply the perceptual signal features identified in this paper to a coherent-source active sonar data set acquired using a bistatic experimental geometry.

The results presented in this paper have important potential implications in the field of active sonar processing. As mentioned in Sec. I, active sonar classification is typically carried out using visual displays. The results presented in this paper suggest that it would be worthwhile to include some type of automated aural component in this conventional classification scheme.

ACKNOWLEDGMENTS

The authors would like to gratefully acknowledge the invaluable advice and insights provided by Professor Rich Dunlap of Dalhousie University, and Dr. Sean Pecknold, Dr. John Osler, Dr. Nancy Allen, Jeff Scrutton, and Dr. Dale Ellis, all of Defence R&D Canada. The authors wish to acknowledge the technical assistance of Doug Caldwell, Paul Shouldice, Roger Arsenault, and Trevor Ponee of Defence R&D Canada. The authors gratefully acknowledge valuable interactions with Dr. Jim Pitton and Scott Philips of Applied Physics Laboratory, University of Washington, Dr. Doug Abraham of the Office of Naval Research, and Dr. Guy Brown and Mr. Robert Mill of the University of Sheffield. The authors wish to acknowledge sea trial support provided during Q282-3 by the crew and officers of CFAV QUEST. This experiment was performed as part of a joint research project involving the NATO Undersea Research Centre, the United States, and Canada and the authors wish to acknowledge the contributions by the scientists and supporting staff that participated in this collaboration. Finally, the authors wish to acknowledge financial support provided by the Natural Sciences and Engineering Research Council of Canada (NSERC) and General Dynamics Canada.

[1]P. Chestnut, H. Landsman, and R. W. Floyd, "A sonar target recognition experiment," J. Acoust. Soc. Am. **66**, 140–147 (1979).
[2]F. B. Shin, D. H. Kil, and R. F. Wayland, "Active impulse echo discrimination in shallow water by mapping target physics-derived features to classifiers," IEEE J. Ocean. Eng. **22**, 66–80 (1997).
[3]N. Allen, P. C. Hines, V. W. Young, and D. A. Caldwell, "Study on the human ability to aurally discriminate between target echoes and environmental clutter in recordings of incoherent broadband sonar," J. Acoust. Soc. Am. **119**, 3395(Abstract) (2006).
[4]J. Pitton, S. Philips, L. Atlas, J. Ballas, D. Brock, B. McClimens, and M. Miller, "Aural classification of impulsive-source active sonar echoes," J. Acoust. Soc. Am. **119**, 3394–3395(Abstract) (2006).
[5]ANSI, *Psychoacoustical Terminology S3.20* (American National Standards Institute, New York, 1973).
[6]K. W. Berger, "Some factors in the recognition of timbre," J. Acoust. Soc. Am. **36**, 1888–1891 (1964).
[7]E. L. Saldanha and J. F. Corso, "Timbre cues and the identification of musical instruments," J. Acoust. Soc. Am. **36**, 2021–2026 (1964).
[8]J. M. Grey, "Multidimensional perceptual scaling of musical timbres," J. Acoust. Soc. Am. **61**, 1270–1277 (1977).
[9]J. Marozeau, A. de Cheveigne, S. McAdams, and S. Winsberg, "The dependency of timbre on fundamental frequency," J. Acoust. Soc. Am. **114**, 2946–2957 (2003).
[10]J. M. Grey and J. A. Moorer, "Perceptual evaluations of synthesized musical instruments," J. Acoust. Soc. Am. **62**, 454–462 (1977).
[11]J. M. Grey and J. W. Gordon, "Perceptual effects of spectral modifications on musical timbres," J. Acoust. Soc. Am. **63**, 1493–1500 (1978).
[12]P. Iverson and C. L. Krumhansl, "Isolating the dynamic attributes of musical timbre," J. Acoust. Soc. Am. **94**, 2595–2603 (1993).
[13]J. E. Cutting and B. S. Rosner, "Categories and boundaries in speech and music," Percept. Psychophys. **16**, 564–570 (1974).
[14]W. M. Hartmann, S. McAdams, A. Gerzso, and P. Boulez, "Discrimination of spectral density," J. Acoust. Soc. Am. **79**, 1915–1925 (1986).
[15]J. C. Brown, O. Houix, and S. McAdams, "Feature dependence in the automatic identification of musical woodwind instruments," J. Acoust. Soc. Am. **109**, 1064–1072 (2001).
[16]S. Tucker and G. J. Brown, "Classification of transient sonar sounds using perceptually motivated features," IEEE J. Ocean. Eng. **30**, 588–600 (2005).
[17]M. K. Prior, "A scatterer map for the Malta Plateau," IEEE J. Ocean. Eng. **30**, 676–690 (2005).
[18]N. R. Chapman, "Measurement of the waveform parameters of shallow explosive charges," J. Acoust. Soc. Am. **78**, 672–681 (1985).
[19]N. R. Chapman, "Source levels of shallow explosive charges," J. Acoust. Soc. Am. **84**, 697–702 (1988).
[20]W. A. Struzinski and E. D. Lowe, "A performance comparison of four noise background normalization schemes proposed for signal detection systems," J. Acoust. Soc. Am. **76**, 1738–1742 (1984).
[21]W. A. Struzinski and E. D. Lowe, "The effect of improper normalization on the performance of an automated energy detector," J. Acoust. Soc. Am. **78**, 936–941 (1985).
[22]J. Kliewer and A. Mertins, "Audio subband coding with improved representation of transient signal segments," *Proceedings of the Ninth European Signal Processing Conference*, Rhodes, Greece, (1998), pp. 2345–2348.
[23]M. Slaney, "An efficient implementation of the Patterson-Holdsworth auditory filter bank," Apple Computer Inc., Tech. Rep. No. TR-35, 1993.
[24]B. C. J. Moore and B. R. Glasberg, "A revision of Zwicker's loudness model," Acustica **82**, 335–345 (1996).
[25]E. de Boer, "Synthetic whole-nerve action potentials for the cat," J. Acoust. Soc. Am. **58**, 1030–1045 (1975).
[26]L. Van Immerseel and S. Peeters, "Digital implementation of linear gammatone filters: Comparison of design methods," ARLO **4**, 59–64 (2003).
[27]J. E. Appel, "Loudness models for rehabilitative audiology," Ph.D. dissertation, University of Oldenburg, Oldenburg, Germany, 2002, Chap. 4.
[28]B. R. Glasberg and B. C. J. Moore, "A model of loudness applicable to time-varying sounds," J. Audio Eng. Soc. **50**, 331–342 (2002).
[29]ANSI, *Specifications for Audiometers 3.6* (American National Standards Institute, New York, 1996.
[30]L. Kukolich and R. Lippmann, *LNKnet Users's Guide: 4th Revision* (MIT Lincoln Laboratory, Lexington, MA, 2004, Chap. 3.
[31]M. J. J. Scott, M. Niranjan, and R. W. Prager, "Parcel: Feature subset selection in variable cost domains," Technical Rep. No. TR-323, Cambridge University Engineering Department, Cambridge, UK, 1998.
[32]R. O. Duda, P. E. Hart, and D. G. Stork, *Pattern Classification*, 2nd ed. (Wiley-Interscience, Toronto, 2001), pp. 483–485.

Transition term method for the analysis of the reflected and the transmitted acoustic signals from water-saturated porous plates

F. Belhocine, S. Derible,[a] and H. Franklin
Laboratoire d'Acoustique Ultrasonore et d'Electronique du Havre (LAUE), CNRS UMR 6068, Université du Havre, Place Robert Schuman, 76610 Le Havre, France

(Received 29 January 2007; revised 20 June 2007; accepted 20 June 2007)

Ultrasound reflection (R) and transmission (T) from an immersed porous plate of QF-20 (a registered trademark of Filtros®, Ferro Corporation) are investigated. Assuming open pores boundary conditions for the theoretical computations, values of the physical constants given by Johnson *et al.* [D. L. Johnson, D. L. Hemmick, and H. Kojima J. Appl. Phys. **76**(1), 115–125 (1994)] are used at first. Comparisons of R and T with experimental results show a discrepancy. It is then assumed that visco-elastic losses exist inside the solid part. When a small imaginary constant part is considered for the bulk moduli, a better fit is obtained between theoretical and experimental values of $|R|$ and $|T|$. However, the numerous and very close peaks prevent easy measures of the resonance amplitudes and widths. The transition terms built up from the linear combinations $R-T$ and $R+T$ allow these peaks to be separated. Comparisons between theory and experiments are made. This work validates, in the frequency range where the agreement is good, a method for the location of the symmetrical and antisymmetrical modes of the plate. A discrimination is also possible between modes resulting from the fluid phase motions and from the solid phase motions.
 [DOI: 10.1121/1.2757090]

PACS number(s): 43.35.Bf, 43.20.Fn, 43.20.Gp, 43.20.Ks [RR] Pages: 1518–1526

I. INTRODUCTION

The study of the reflection (R) and transmission (T) coefficients from a fluid-saturated porous plate is a way to obtain information about the medium.[1–8] A better knowledge of some properties of these coefficients seems to be important in various fields of engineering acoustics (nondestructive evaluation of porous materials, detection of surface waves propagating along submerged porous plates, ultrasonic simulations of cancellous bones, improvement of the quality of sound insulators,…). The purpose of this paper is to show that some linear combinations of the complex quantities R and T imposed by the eigenvalues of the scattering matrix of the structure, furnish more accurate results (both theoretical and experimental) than the individual coefficients.

The QF-20 porous medium considered here obeys Biot's theory[9,10] provided the frequency is less than 1 MHz.[11] With the values of the physical parameters available in Ref. 11 and whatever the value of the frequency, it is not possible to fit the theoretical and the experimental behaviors observed for the transmission coefficient T (the problem is less critical for the reflection coefficient R). The modulus $|T|$ given by the theory has a greater amplitude than the experimental ones. To diminish the discrepancies between computations and experiments, one must admit that, in the frequency range of interest [0–1 MHz], the dissipative effects in the solid part of the porous medium must be taken into account in Biot's theory. Such loss mechanisms have been extensively discussed.[12–14] In the present paper, it is simply assumed that the supplement of dissipated energy not yet accounted for is caused by the visco-elastic behavior of the consolidated frame. Therefore, the dried frame bulk modulus K_b and shear modulus μ become complex numbers[13] (the bulk modulus K_r of the individual grains remains real). If the real parts of K_b and μ may remain constants, the true problem lies in the determination of the frequency dependence of the imaginary part. The dependence can take a complicated form if the analysis is to be considered in a broad frequency band. Because the present paper is restricted to the frequency range [150–850 kHz] for the experimental study, it can be assumed that the imaginary parts are constant, without loss of generality.

To the difficulty described above, one must add a second fact. Generally, because of the intricacy of the numerous and very close peaks representing the vibrations of both the fluid and solid parts of the porous medium, the reflection and transmission coefficients do not furnish adequate information for the analysis of the porous plate. When too close peaks overlap, the result is a large bumpy peak. That is why, in place, it may be more interesting to use the transition terms[6,7,15] defined from the eigenvalues $R-T$ and $R+T$ of the scattering matrix of the structure. They allow us to distinguish, for instance, at fixed incidence angles, the frequency ranges at which the plate vibrates symmetrically or antisymmetrically. For the purpose of comparison between the theoretical and experimental transition terms, the coincidence between theory and experiments is necessary for both R and T. We are not aware of any other work which has explicitly

[a]Author to whom correspondence should be addressed. Electronic mail: serge.derible@univ-lehavre.fr

TABLE I. QF-20 and saturating water physical constants.

		Values used in the theoretical study	Values used for comparisons with experiments
Bulk modulus of grains	K_r (Pa)	$36.6\cdot10^9$	$36.6\cdot10^9$
Dried frame bulk modulus	$\bar{K}_b$ (Pa)	$(9.47+0.3i)\cdot10^9$	$(9.7+0.05i)\cdot10^9$
Dried frame shear modulus	$\bar{\mu}$ (Pa)	$(7.63+0.1i)\cdot10^9$	$(7.9+0.15i)\cdot10^9$
Solid density	ρ_s (kg m^{-3})	2760	2760
Bulk modulus of water	k_f (Pa)	$2.22\cdot10^9$	$2.22\cdot10^9$
Water density	ρ_f (kg m^{-3})	1000	1000
Water sound velocity	c_f (m s^{-1})	1478	1478
Saturating water viscosity	η (kg m^{-1} s^{-1})	$1.14\cdot10^{-3}$	$1.14\cdot10^{-3}$
Porosity	β	0.402	0.4
Permeability	K(m^2)	$1.68\cdot10^{-11}$	$1.7\cdot10^{-11}$
Pores radius	a_p (m)	$3.26\cdot10^{-5}$	$3.3\cdot10^{-5}$
Tortuosity	α	1.89	1.94

looked for the properties of plates by using the transition terms in the way described here. A very simple application to elastic plates was already done in Ref. 15.

In Section II, the definition of the transition terms is recalled. Numerical results are presented. First, the transmission coefficient calculated by using real bulk moduli is compared with the transmission coefficient calculated by using the complex bulk moduli. This justifies, together with the experimental observations, that visco-elasticity exists in the solid frame. To present a synthetic view, $|R|$, $|T|$ and the transition terms are plotted in the (fd,k_x) plane with fd the frequency-thickness product and k_x the sine of the incidence angle. Section III describes the experimental technique developed for the measure of the reflection and transmission coefficients. The transition terms are then built and the link with the Breit-Wigner resonant form discussed. Results are compared with the theoretical ones. In particular, in the frequency range where the experiments are made, both the location and the estimation of the resonance widths of the symmetrical and antisymmetrical modes of the plate are analyzed.

II. THEORY

A. Transition terms

Let us consider a water-saturated porous plate of QF-20, with a thickness d, immersed in water. All the physical constants about the media (except the imaginary parts) are given in column 3 of Table I. The water viscosity is taken into account inside the pores of the solid frame, but neglected outside the plate.

When a plane, homogeneous, time harmonic wave ($e^{-i\omega t}$ dependence) impinges the plate, it is partially reflected and transmitted into the surrounding water. The scattering matrix of the structure is a 2×2 matrix. Its diagonal elements are equal to the reflection coefficient R, while the off-diagonal elements are equal to the transmission coefficient T. Equation (A13) in the appendix give R (resp. T) as the sum (resp. difference) of symmetrical (index S) and antisymmetrical (index A) functions. The two eigenvalues of the scattering matrix then take the form

$$\mu_S = R + T = \frac{\delta_S}{\bar{\delta}_S} e^{-ik_{z0}d}, \quad \lambda_A = R - T = \frac{\delta_A}{\bar{\delta}_A} e^{-ik_{z0}d}, \tag{1}$$

allowing a separate treatment for the symmetrical and antisymmetrical vibrations of the saturated porous plate. It is recalled that in δ_S and $\bar{\delta}_S$ (resp. δ_A and $\bar{\delta}_A$), see Eqs. (A14)–(A17), C_{SFj} (resp. C_{AFj}) are functions associated with symmetrical (resp. antisymmetrical) fluid motions inside the porous plate while C_{sj} (resp. C_{aj}) are functions associated with symmetrical (resp. antisymmetrical) solid frame motions, in relation with the fast ($j=1$) or slow ($j=2$) longitudinal wave. The terms τ_j, see Eq. (A22) are due to the external fluid loading. They can be considered as perturbations to the functions C_{SFj}, C_{sj}, C_{Afj} and C_{aj}. Equations (1) show that there are no interactions between symmetrical and antisymmetrical motions.The physical meaning of the eigenvalues is contained in the transition terms T_{μ_S} and T_{λ_A} defined by

$$1 + 2iT_{\mu_S} = \mu_S, \quad 1 + 2iT_{\lambda_A} = \lambda_A. \tag{2}$$

Because of the losses due to both the saturating fluid viscosity and the visco-elasticity, one has $|\mu_S|<1$ and $|\lambda_A|<1$, i.e., the scattering matrix is not unitary. As a consequence, the amplitudes of the peaks obtained by plotting the modulus of each transition term never reach 1. The amplitudes diminish when the dissipation increases. It is shown, in the following, that the plots of $|T_{\mu_S}|$ and $|T_{\lambda_A}|$ furnish the dispersion curves of the porous plate. The use of the transition terms is actually an alternative way to obtain in a very easy way the dispersion curves of the structure.

B. Numerical results

In this section, $|R|$, $|T|$, $|T_{\mu_S}|$ and $|T_{\lambda_A}|$ are plotted *vs.* the frequency-thickness product fd (plate thickness $d=10$ mm) in the range [0 MHz mm–10 MHz mm] (f varies from 0 to 1 MHz). Two sets of values considered suitable and given in Table I are used in this paper: column 3 for the theoretical computations, column 4 for the comparisons with experiments. The constants of column 3, except the imaginary parts, are taken from Ref. 11. Next, some of the constants are assumed to be parameters: the curves obtained by varying

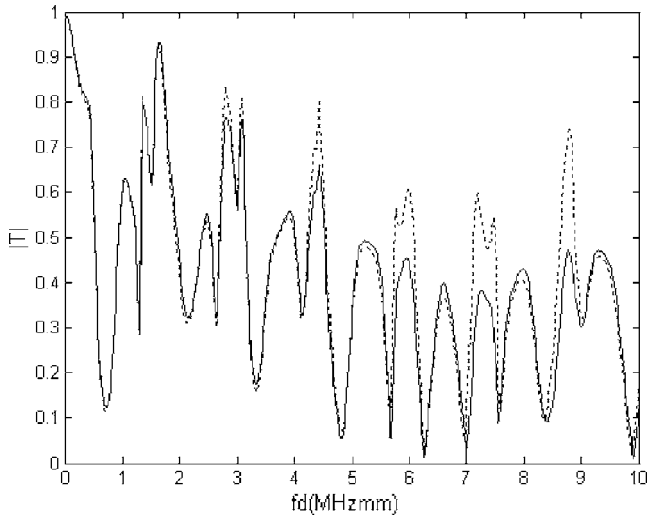

FIG. 1. Modulus of the transmission coefficient at the incidence angle $\theta = 15°$ *vs*. *fd*. Real bulk and shear moduli (dotted curve); complex bulk and shear moduli (solid curve).

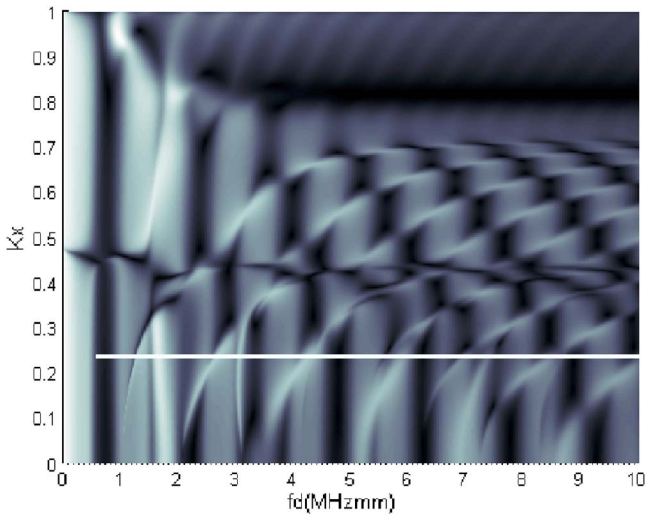

FIG. 2. (Color online) Modulus of the transmission coefficient in the (fd, k_x) plane. The white horizontal line indicates the angle $\theta = 15°$.

these parameters are compared with the experimental one until a good coincidence. Column 4 is the result of this investigation. For high frequencies, the values in Table I used for the theoretical study give the velocities $c_1 \simeq 3441$ ms^{-1} (fast wave), $c_2 \simeq 1000$ ms^{-1} (slow wave) and $c_t = 2059$ ms^{-1} (shear wave). The slow wave is diffusive at low frequencies, e.g., for $f \leqslant 10$ KHz: only the fast and the shear waves propagate. At higher frequencies, all the three waves propagate and then contribute to the guided waves in the plate.[6] It must be noticed that the curves presented here would not be the same in similar *fd* range if *d* evolved instead of *f*.

Figure 1 shows the plot of $|T|$, at the incidence angle $\theta = 15°$. The dotted curve corresponds to the case of real moduli K_r, K_b and μ (real parts in column 3 of Table I), while the solid curve corresponds to the case of complex moduli $\bar{K}_b$ and $\bar{\mu}$ (K_r remains real, complex quantities in column 3 of Table I). The effect of the complex moduli is mainly to diminish the amplitudes of the peaks of $|T|$: shifts and enlargements of peaks are negligible. The solid curve will be compared to the experimental one in the next section. One can note that the interpretation of the modal behavior of the plate is not obvious because of numerous and interfering close peaks. In addition, the peaks related to either symmetrical or antisymmetrical vibrations of the plate cannot be distinguished.

In Figs. 2–4, by using the same data as for the solid curve of Fig. 1, we have chosen to present a complete behavior of $|T|$, $|T_{\mu_S}|$ and $|T_{\lambda_A}|$ in the (fd, k_x) plane ($k_x = k_x/k_0 = \sin\theta$, θ varying from 0 to 90°). In Fig. 2, a situation of intricacy as in Fig. 1 still exists at other angles (the angle $\theta = 15°$ is materialized by the white horizontal line in Fig. 2). Two families of curves, sketched by the maxima of $|T|$ in white color, can be distinguished. One family looks like the well-known modes of an elastic (or visco-elastic) plate with longitudinal and transverse wave velocities c_1 and c_t. It intersects a second vertical family resembling the modes of an equivalent fluid plate with longitudinal wave velocity c_2. The succession of brightness and darkness, for increasing *fd*, does not contain, at this stage, a particular meaning.

In Figs. 3 and 4, the contribution of the transition terms appears clearly. First, they simplify the presentation of Fig. 2, by separating each of the abovementioned families into two sets: symmetrical (Fig. 3) and antisymmetrical (Fig. 4). Second, they improve the visualization the modes, especially those of the equivalent fluid plate (white vertical zones). To confirm the fact that the transition terms supply us with the modes of the structure and could help to find the modes, we give in Fig. 5 the dispersion curves obtained by solving the antisymmetrical characteristic equation $\bar{\delta}_A = 0$ (*fd* real, k_x complex). Only parts of curves with $\mathrm{Im}(k_x) < 0.4$ are shown. The comparison of Figs. 4 and 5 allows us to conclude that the transition terms give, globally, the same behaviors except around $\mathrm{Re}(k_x) = 0.8$ where the stair effect results probably from the interaction between the A0 mode of the equivalent solid plate and the vertical modes of the equivalent fluid plate modes. For $\mathrm{Re}(k_x) \geqslant 0.8$, e.g., far from the critical

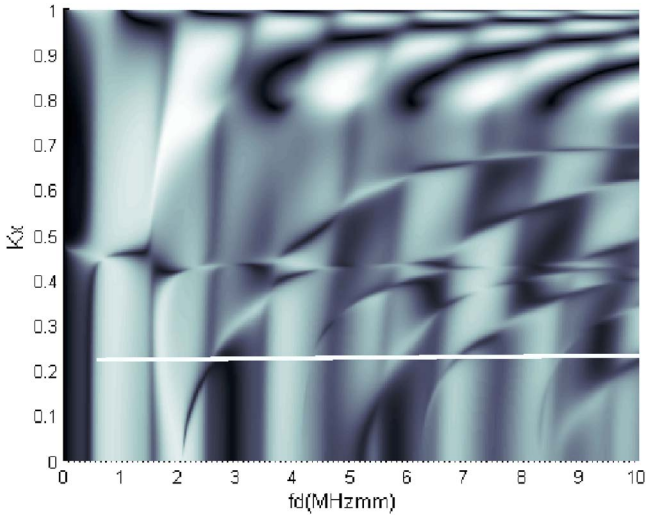

FIG. 3. (Color online) Modulus of the symmetrical transition term $|T_{\mu_S}|$ in the (fd, k_x) plane. The white horizontal line indicates the angle $\theta = 15°$.

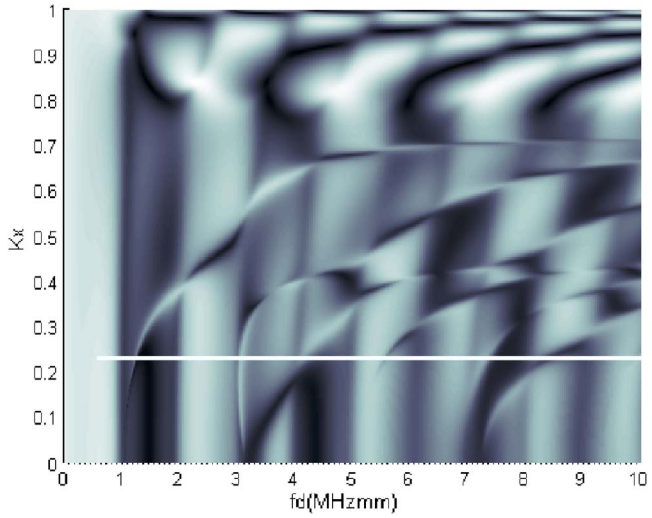

FIG. 4. (Color online) Modulus of the antisymmetrical transition term $|T_{\mu_A}|$ in the (fd, k_x) plane. The white horizontal line indicates the angle $\theta=15°$.

angles, $|R|$, $|T|$, $|T_{\mu_S}|$ and $|T_{\lambda_A}|$ exceed 1 for some values of fd. From the above comparison, and from an analysis of $\mathrm{Im}(k_x)$, one can identify in Fig. 1 the narrow peaks with the modes of the equivalent solid plate and the large peaks with the equivalent fluid plate. Observation of the vertical modes is closely linked to the thickness of the plate. The case of thicker plates, where the vertical modes vanish, can be seen in Fig. 6 of Ref. 6. For fd values ranging from 2 to 3.2 MHz mm, the transmission coefficient exhibits three peaks. By referring to the transition terms, one can deduce that the first and the second peaks represent symmetrical modes while the third represents an antisymmetrical mode. For fd values ranging from 4.8 to 5.8 MHz mm, the transmission coefficient exhibits only one peak. By referring again to the transition terms, one can see that this peak splits up into a symmetrical mode and an antisymmetrical mode. We develop these aspects in the experimental part.

III. EXPERIMENTS AND DISCUSSION

A. Experimental technique

The porous plate is obliquely insonified in order to record under the same conditions the reflected and the transmitted signals. The plate (300 mm × 200 mm × 10 mm) stands vertically in water with two transducers on one side (the emitter and the receiver of the reflected signal) and the transducer recording the transmitted signal on the other (Fig. 6). The distances between the transducers and the plate are about 50 cm; the diffraction is negligible and a plane wave model is considered. The plate is insonified with incident pulses, periodically produced by the 300 V discharge of an internal capacitor of a generator, applied to the piezoelectric slab of the emitter. The three utilized transducers are identical (Panametrics® nonfocused, diameter of the active element: 1.5 in., central frequency: 500 kHz) and can be rotated in the horizontal plane. The frequency range runs from 150 to 850 kHz (fd from 1.5 to 8.5 MHz mm). The signals are not amplified and the data are stored after the electronic perturbations have been removed thanks to an average of 300 acquisitions. The sampling frequency is 100 MHz and the recorded signals have 20,000 samples.

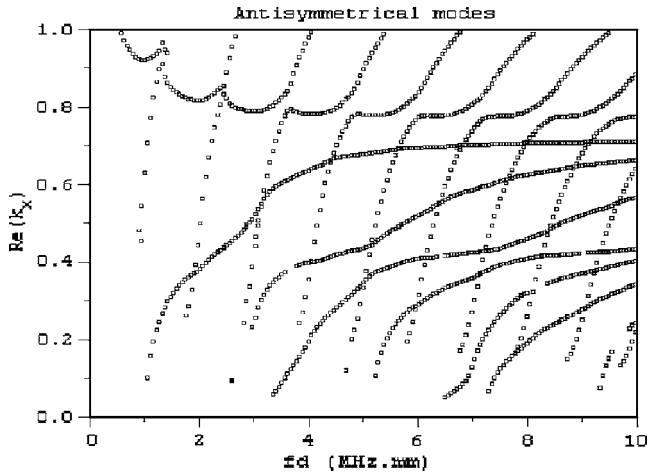

FIG. 5. Dispersion curves of the antisymmetrical modes $\mathrm{Re}(k_x)$ *vs.* fd.

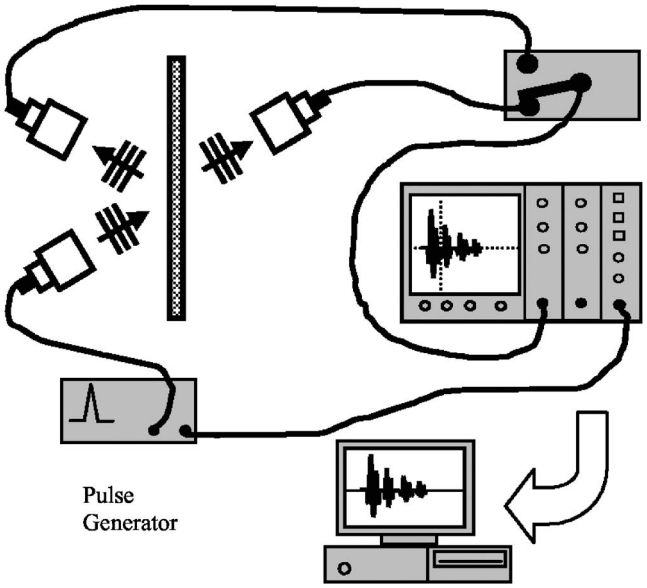

FIG. 6. Experimental setup.

The three transducers are first positioned at the same depth and each of them is successively rotated to insonify normally the plate standing vertically (the reflected signals must reach a maximal peak to peak value). From these positions, the transducers are set up in Snell-Descartes configuration for the given incidence angle. To catch the whole emerging bounded beams, the receivers are carefully translated parallel to the plate and fixed where a maximal peak to peak value is registered. The transmitted signal from the plate is normalized with the direct signal from the emitter properly aligned with the receiver, after the plate has been removed (Fig. 7). The experimental transmission coefficient is the ratio of the Fourier transform of the transmitted signal to the Fourier transform of the direct one. As proceeded in the theoretical study where the incident wave onto the plate gives the reference of the amplitude and the phase of the refraction coefficients, the direct signal has been shifted for the delay time $-d/\cos(\theta)c_f$. The normalization of the reflected signal is achieved with the reflected pulse onto the water-air interface (reflection coefficient: −1), insonified un-

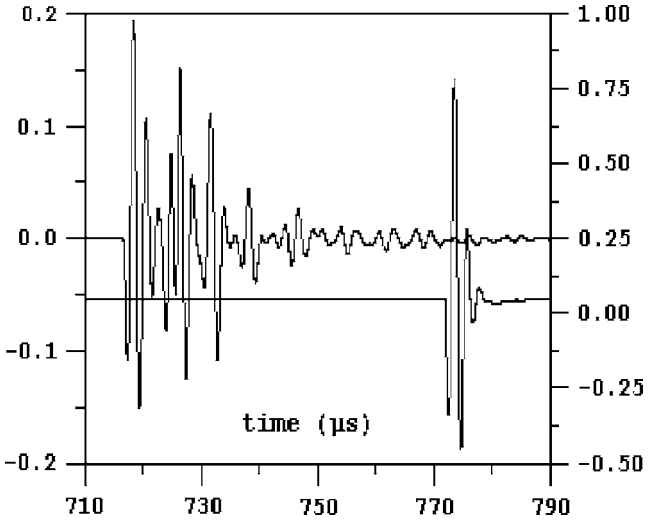

FIG. 7. Direct signal (right) and transmitted signal through the plate at the incidence angle $\theta=15°$; 500 kHz transducers. The vertical axis on the right is for the amplitude of the direct signal shifted for convenience.

der similar conditions (transducers, incidence and distances). They are plotted in Fig. 8. Via the previous experimental method, the effects of the bounded beams applied are reduced and one can consider experimental plane wave reflection and transmission coefficients. To obtain good agreements between the experimental and theoretical reflection and transmission coefficients plotted in Figs. 9 and 10, one must give to the parameters of the studied plate the values presented in Table I (last column). They are close to the mean values obtained from several plates by Johnson *et al.*[11] in 1994: the imaginary parts are not more than 2% of the real parts of the bulk moduli. It must not be forgotten that the commercially available material called QF-20 has been produced for many years and mainly used as pool water filter. Its most important characteristic is the porosity which is said to be between 0.35 and 0.45 by the manufacturer. One easily realizes that the values of the other parameters could have slightly changed sometimes. In acoustics labs, the main in-

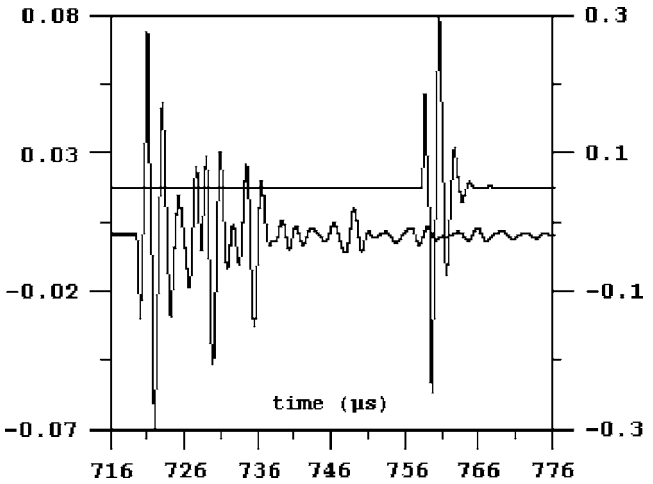

FIG. 8. Reflected signal at water/air interface (right) and reflected signal onto the plate at the incidence angle $\theta=15°$; 500 kHz transducer. The vertical axis on the right is for the amplitude of the first one shifted for convenience.

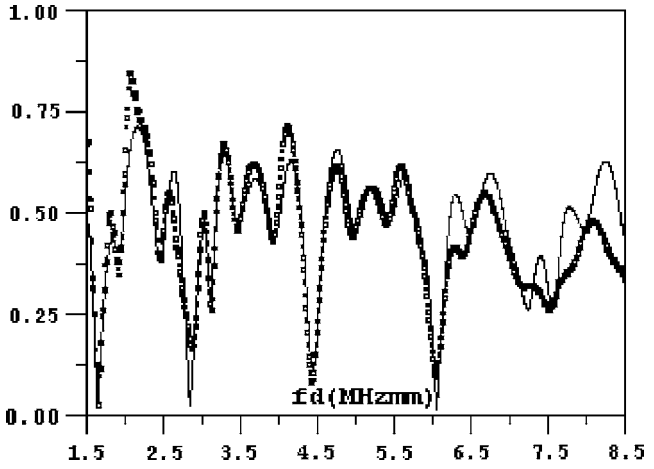

FIG. 9. Comparison between the reflection coefficients at the incidence angle $\theta=15°$. Experiments (dotted curve) and theory (solid curve).

terest of the QF-20 lies in the fact that it obeys Biot's theory. The following values of the wave velocities for high frequencies must be noticed: $c_1 \simeq 3472\ \mathrm{ms}^{-1}$ (fast wave), $c_2 \simeq 989\ \mathrm{ms}^{-1}$ (slow wave) and $c_1 \simeq 2079\ \mathrm{ms}^{-1}$ (shear wave), which do not greatly differ from those found in Sec. II B. Papers dealing with inversion of Biot parameters in water-saturated porous media were not numerous over the last 20 years. Nevertheless, a different and comprehensive approach can be found in Ref. 16. The transition terms are plotted in Fig. 11 ($|T_{\lambda_A}|$) and 12 ($|T_{\mu_S}|$). The agreement is quite good. Since each of these figures is devoted to only one kind of vibration mode (symmetrical or antisymmetrical), the resonance peaks are less numerous than in the plot of the reflection and transmission coefficients (Figs. 9 and 10) and therefore easily separated. They obey the Breit-Wigner form whose main properties are now recalled.

B. Breit-Wigner resonant form

As the resonant scattering theory has previously shown, at the vicinity of a resonance frequency, the spectra of the scattered acoustic pressure of fluid-immersed elastic- or visco-elastic targets exhibits a Breit-Wigner resonant

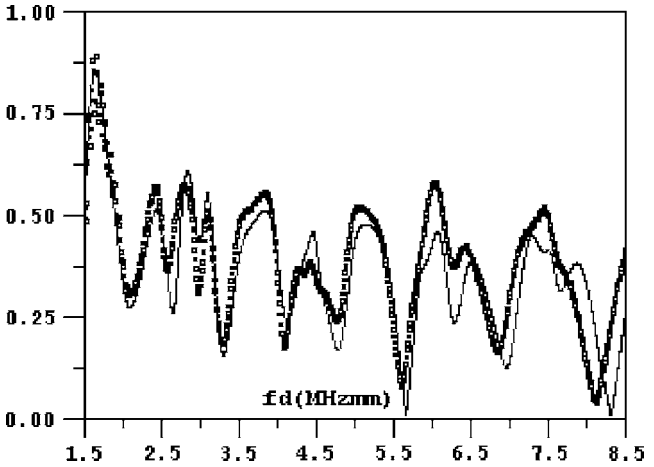

FIG. 10. Comparison between the transmission coefficients at the incidence angle $\theta=15°$. Experiments (dotted curve) and theory (solid curve).

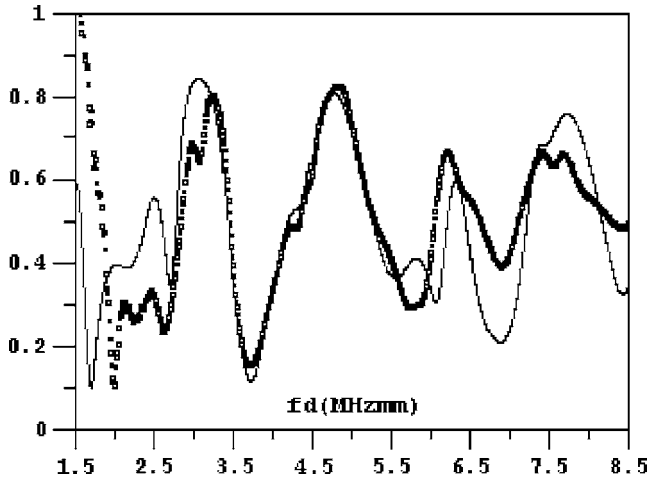

FIG. 11. Comparison between the antisymmetrical transition terms $|T_{\lambda_A}|$ at the incidence angle $\theta=15°$. Experiments (dotted curve) and theory (solid curve).

form.[17–20] The expression "vicinity of a resonance" must be understood as the frequency domain where the potential background and the other resonances play a less important role than the studied resonance characterized by its frequency ω_0, its width Γ and its amplitude K.[21] The Breit-Wigner resonant form obeys the complex formula:

$$\frac{K}{\left(1+i\left(\frac{\omega-\omega_0}{\Gamma/2}\right)\right)}. \tag{3}$$

The frequency parametric plot of the imaginary part vs. the real part of this expression is its Argand diagram[22] presented in Fig. 13. It is a circle with diameter K, described in clockwise as frequency increases and where the derivative of the curvilinear abscissa goes through a maximum at the resonance frequency. The resonance width is directly connected to the points of the circle located on the diameter making a right angle with the diameter passing through the point at the resonance frequency.

At the vicinity of a resonance, the transition terms can be written (a, b, c are complex):

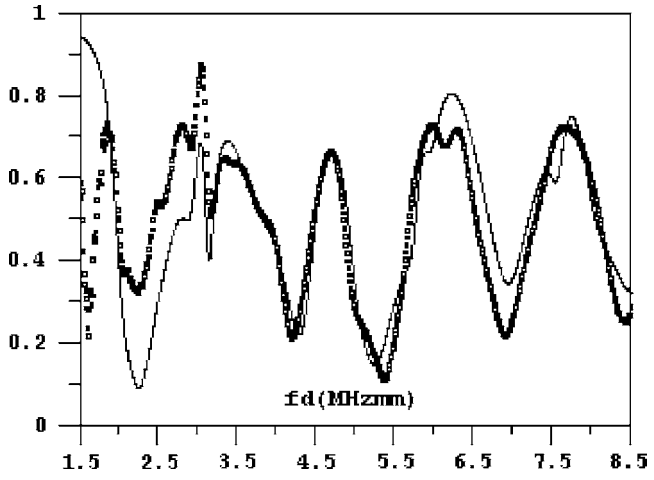

FIG. 12. Comparison between the symmetrical transition terms $|T_{\mu_S}|$ at the incidence angle $\theta=15°$. Experiments (dotted curve) and theory (solid curve).

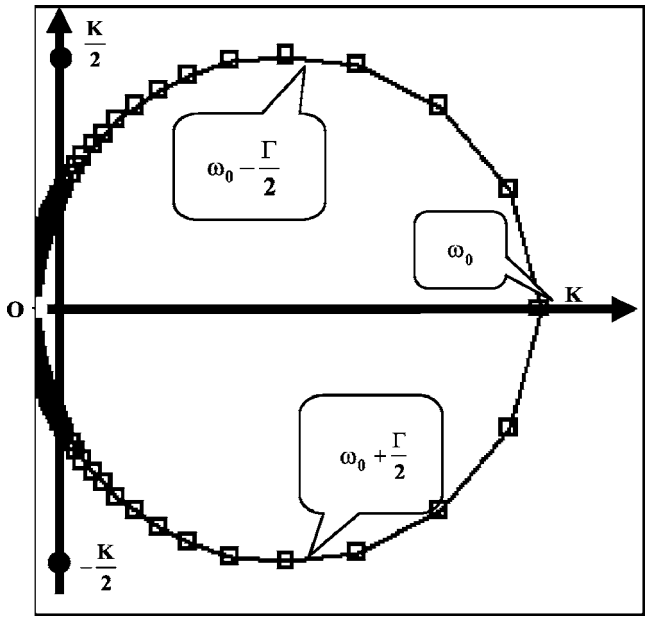

FIG. 13. Argand diagram of the Breit-Wigner resonant form.

$$\frac{K}{\left(1+i\left(\frac{\omega-\omega_0}{\Gamma/2}\right)\right)}\exp(i\varphi)+\mathrm{a}+\mathrm{b}(\omega-\omega_0)+\mathrm{c}(\omega-\omega_0)^2. \tag{4}$$

So, we assume that the Breit-Wigner resonant form is superimposed to a smooth varying polynomial expression gathering the influence of the potential background and the other resonances. A resonance will be easily located in the Argand diagram of a given frequency range of the transition terms by its circular shape; the resonance frequency is located at the peak of the derivative of the curvilinear abscissa. If the perturbations do not enable the spectra to present half a circle at the vicinity of a resonance frequency, the resonance width and the value of the diameter are simply estimated via the previous remarks. These values are the guesses of a least mean squares algorithm used to fit their calculated (or experimental) transition terms with Eq. (4). So are determined the resonance frequencies and the associated widths of the transition terms. The same method is successively performed for the calculated and the experimental spectra. As examples, some Argand diagrams are presented in Figs. 14(a), 14(b), 15(a), and 15(b). The characteristics of the resonances are given in Table II and Table III. The results are rather close for the symmetrical modes and less good for the antisymmetrical modes especially from $fd=5.4$ to 6.4 where three resonances with large width overlap each other. This overlapping already appears on Fig. 12 but the Argand diagram of this frequency range exhibits it more clearly in the accompanying Fig. 16. The discrepancies between the columns in Tables II and III also come from the fact that the acoustic beam launched by the emitter spreads a little. So in fact, only the main part of the incident energy impinges the plate under $\theta=15°$ used in the theoretical study. The other incident waves, which angles are on both sides of this value, add their own small contributions to the transmitted and reflected sig-

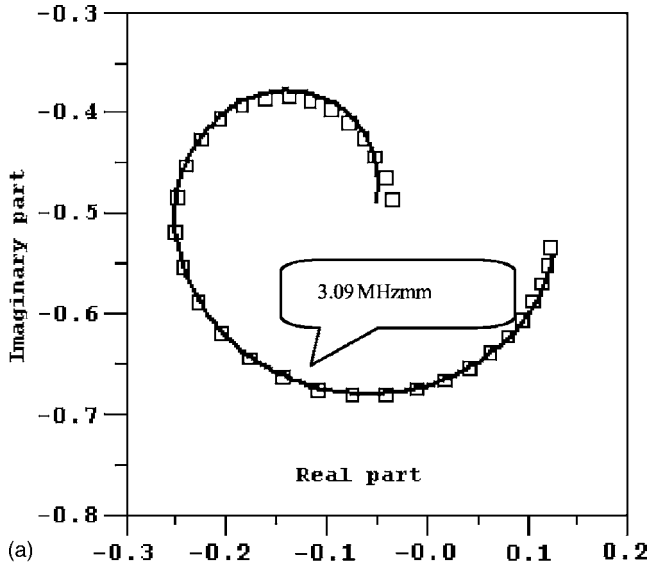

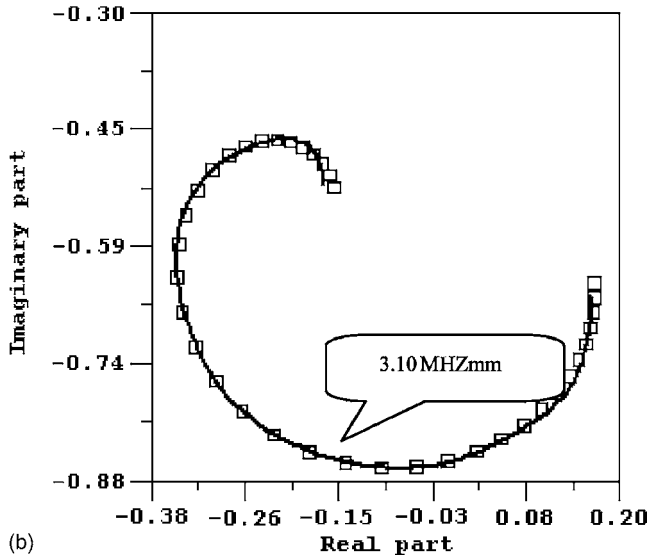

FIG. 14. a. Argand diagram of T_{λ_A} theoretical. Frequency range 2.95–3.20 MHz mm. b. Argand diagram of T_{λ_A}, experimental. Frequency range 2.95–3.23 MHz mm.

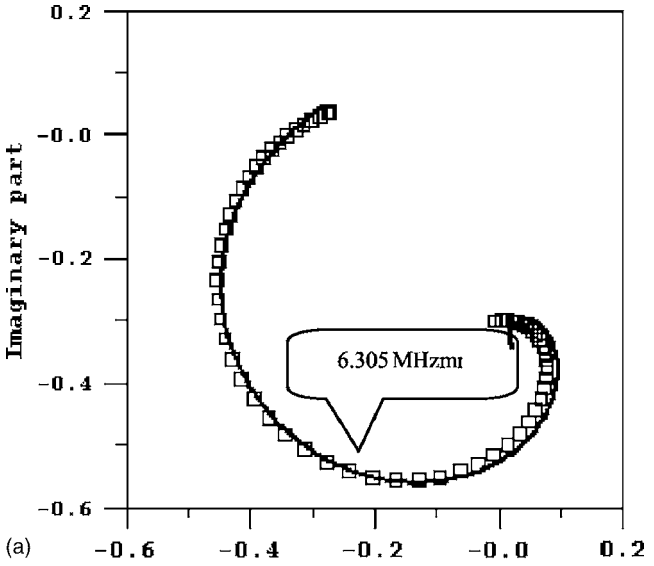

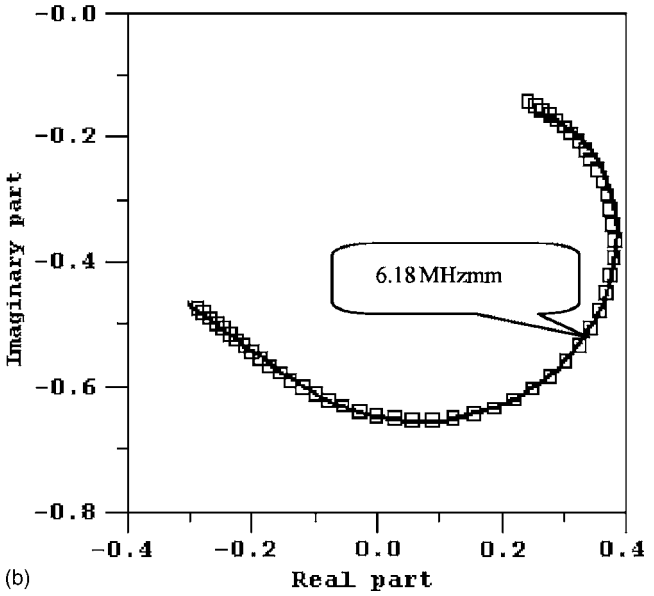

FIG. 15. a. Argand diagram of T_{μ_S}, theoretical. Frequency range 5.99–6.63 MHz mm. b. Argand diagram of T_{μ_S}, experimental. Frequency range 5.91–6.48 MHz mm.

nals. The resonance widths are more sensitive to this fact than the frequencies.

IV. CONCLUSION

We have presented the useful role the transition terms can play in the study of porous media. They exhibit only one kind (symmetrical or antisymmetrical) of the vibration modes of the plate. Their amplitudes are greater than those of the reflection and transmission coefficients used to calculate them. The experimental transition terms have been measured for a visco-elastic porous plate of QF-20 which obeys Biot's theory. Its Biot parameters have been found by fitting the theoretical transition terms to the experimental ones. The resonant behavior of the porous plate is clearly established via the properties of the Argand diagram which obeys the Breit-Wigner resonant form at the vicinity of a resonance. Carried out on the transition terms, the determination of the resonances of a porous plate could now become a means of investigation of porous media, as is already the case for elastic targets.

TABLE II. Position *fd* and width Γ of resonance. Antisymmetrical case.

Resonance of T_{λ_A}			
Theoretical (MHz mm)		Experimental (MHz mm)	
fd	Γ	*fd*	Γ
2.615	0.819	2.44	0.86
3.095	0.168	3.10	0.17
3.984	0.440	4.02	0.31
4.832	0.554		
5.405	0.696	5.51	0.15
5.827	0.196	5.73	0.88
6.199	0.733	6.38	0.387
7.004	0.758		

TABLE III. Position fd and width Γ of resonance. Symmetrical case.

Resonance of T_{μ_S}			
Theoretical (MHz mm)		Experimental (MHz mm)	
fd	Γ	fd	Γ
2.860	0.438	2.99	0.27
3.389	0.424	3.39	0.41
4.195	0.950	4.14	0.98
4.462	0.122	4.41	0.12
5.480	0.489	5.46	0.5
6.305	0.361	6.18	0.38
7.296	0.360		

APPENDIX: REFLECTION AND TRANSMISSION COEFFICIENTS FROM AN IMMERSED FLUID SATURATED POROUS PLATE

The geometry of the problem is displayed in Ref. 6: the plate interfaces are parallel to the x axis and perpendicular to the z axis. Let us consider a plane, harmonic, homogeneous wave, propagating in the external fluid (density ρ_f, sound velocity c_f). It impinges on the porous plate of thickness d (saturated by the same fluid) under an angle θ. A time dependence $e^{-i\omega t}$, with ω the angular frequency, is used in the whole paper. The associate wave vectors in the fluid are $\boldsymbol{k}^{inc}=(K_x,K_{z0})$ for the incident wave, $\boldsymbol{k}^{refl}=(K_x,-K_{z0})$ for the reflected wave and $\boldsymbol{k}^{trans}=(K_x,K_{z0})$ for the transmitted wave; they are such that

$$\boldsymbol{k}^m\boldsymbol{k}^m = K_x^2 + K_{z0}^2 = \frac{\omega^2}{c_f^2}. \quad (m = inc,\ refl\ or\ trans). \tag{A1}$$

The three waves propagating in the porous plate have complex wave vectors $\boldsymbol{k}_j=(K_x,K_{zj})$ ($j=1$: fast longitudinal wave, $j=2$: slow longitudinal wave) and $\boldsymbol{k}_t=(K_x,K_{zt})$ (transverse wave). They verify

$$K_x^2 + K_{zj}^2 = \boldsymbol{k}_j\cdot\boldsymbol{k}_j = \ell_j^2, \quad j=1,2 \tag{A2}$$

and

$$K_x^2 + K_{zt}^2 = \boldsymbol{k}_t\cdot\boldsymbol{k}_t = \ell_t^2. \tag{A3}$$

Each of the longitudinal waves is described by a compatibility coefficient[23]

$$\gamma_j = \frac{\bar{H}\ell_j^2 - \rho\omega^2}{\rho_f\omega^2 - \bar{C}\ell_j^2}, \quad j=1,2, \tag{A4}$$

allowing to define the following densities

$$\rho_j = \rho + \gamma_j\rho_f, \tag{A5}$$

$$\rho_{fj} = \rho_f\frac{\beta+\gamma_j\tilde{\alpha}}{\beta}. \tag{A6}$$

The transverse waves are described by a compatibility coefficient

$$\gamma_t = \frac{\bar{\mu}\ell_t^2 - \rho\omega^2}{\rho_f\omega^2}, \tag{A7}$$

allowing to define the density

$$\rho_t = \rho + \gamma_t\rho_f. \tag{A8}$$

In the above expressions:

— $\rho=(1-\beta)\rho_s+\beta\rho_f$ is the effective density of the porous medium, with ρ_s the density of the solid grains and β the porosity,

— $\tilde{\alpha}$ is the dynamic tortuosity,[24]

— $\bar{H}$, $\bar{M}$, $\bar{C}$ and $\bar{\mu}$ are the porous medium moduli[13] (the overbars denote complex numbers), depending on the moduli K_f (water), K_r (grains), $\bar{K}_b$ and $\bar{\mu}$ (solid frame) defined in Table I:

$$\bar{H} = \bar{K}_b + \frac{4}{3}\bar{\mu} + \frac{(K_r-\bar{K}_b)^2}{D-\bar{K}_b}, \tag{A9}$$

$$\bar{C} = \frac{K_r(K_r-\bar{K}_b)}{D-\bar{K}_b}, \tag{A10}$$

$$\bar{M} = \frac{K_r^2}{D-\bar{K}_b}, \tag{A11}$$

with

$$D = K_r[1+\beta(K_r/K_f-1)]. \tag{A12}$$

Open pores conditions are assumed at the interfaces $z=\pm d/2$: (i) continuity of normal stress ($\sigma_{zz}=-p_0$), (ii) disappearance of tangential stress ($\sigma_{xz}=0$), (iii) conservation of fluid volume ($u_{sz}+w_z=u_{0z}$), (iv) continuity of the fluid pressure ($p_f=p_0$). Here, u_{0z} and p_0 denote the z component of the displacement vector and the pressure in the external fluid; u_{sz} and w_z are the z components of the displacement vectors in the porous medium; p_f, σ_{xz} and σ_{zz} are the fluid pressure and

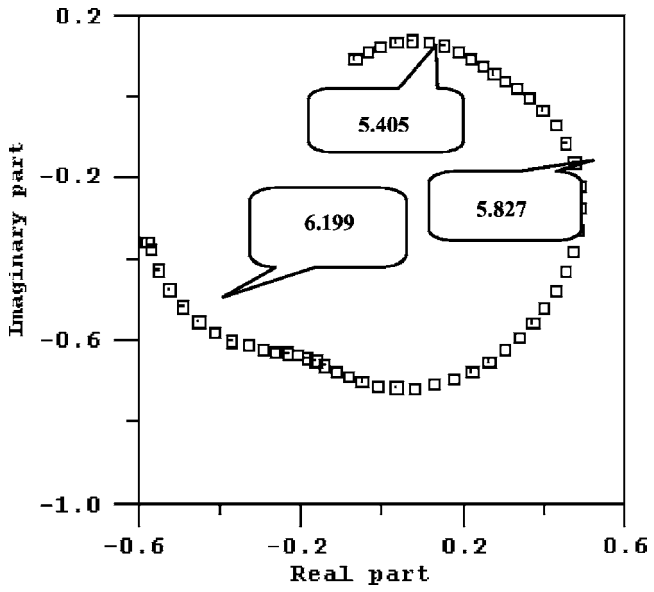

FIG. 16. Argand diagram of T_{λ_A}, theoretical. Frequency range 5.3 to 6.4 MHz mm.

stress tensor components in the porous medium. By following the procedure of Ref. 6, the reflection and transmission coefficients can be written

$$R = \frac{1}{2}\left(\frac{\delta_S}{\bar{\delta}_S} + \frac{\delta_A}{\bar{\delta}_A}\right)e^{-iK_{z0}d}, \quad T = \frac{1}{2}\left(\frac{\delta_S}{\bar{\delta}_S} - \frac{\delta_A}{\bar{\delta}_A}\right)e^{-iK_{z0}d} \quad \text{(A13)}$$

with

$$\delta_S = (C_{SF1} + i\tau_1)(C_{s2} + i\tau_2) - (C_{SF2} + i\tau_2)(C_{s1} + i\tau_1), \quad \text{(A14)}$$

$$\bar{\delta}_S = (C_{SF1} - i\tau_1)(C_{s2} - i\tau_2) - (C_{SF2} - i\tau_2)(C_{s1} - i\tau_1), \quad \text{(A15)}$$

$$\delta_A = (C_{AF1} - i\tau_1)(C_{a2} - i\tau_2) - (C_{AF2} - i\tau_2)(C_{a1} - i\tau_1), \quad \text{(A16)}$$

$$\bar{\delta}_A = (C_{AF1} + i\tau_1)(C_{a2} + i\tau_2) - (C_{AF2} + i\tau_2)(C_{a1} + i\tau_1). \quad \text{(A17)}$$

The C_{SFj}, C_{AFj}, C_{sj}, C_{aj} and τ_j terms $(j=1,2)$ are defined by

$$C_{SFj} = \frac{\rho_{fj}}{\rho_t}\ell_t^2(\ell_t^2 - 2K_x^2)\cot(K_{zj}d/2), \quad \text{(A18)}$$

$$C_{AFj} = \frac{\rho_{fj}}{\rho_t}\ell_t^2(\ell_t^2 - 2K_x^2)\tan(K_{zj}d/2), \quad \text{(A19)}$$

$$C_{sj} = (\ell_t^2\rho_j/\rho_t - 2K_x^2)(\ell_t^2 - 2K_x^2)\cot(K_{zj}d/2) + 4K_x^2K_{zj}K_{zt}\cot(K_{zt}d/2) \quad \text{(A20)}$$

$$C_{aj} = (\ell_t^2\rho_j/\rho_t - 2K_x^2)(\ell_t^2 - 2K_x^2)\tan(K_{zj}d/2) + 4K_x^2K_{zj}K_{zt}\tan(K_{zt}d/2) \quad \text{(A21)}$$

and

$$\tau_j = \frac{\rho_f}{\rho_t}\frac{K_{zj}}{K_{z0}}\ell_t^2[(\ell_t^2 - 2K_x^2)(1+\gamma_j) + 2K_x^2(1+\gamma_t)]. \quad \text{(A22)}$$

Note that in Ref. 6, we made a mistake typing about the functions C_{SFj} and C_{AFj}. It is now corrected.

[1] T. J. Plona, "Observation of a second bulk compressional wave in a porous medium at ultrasonic frequencies," Appl. Phys. Lett. **52**, 780–782 (1988).
[2] P. Rasolofosaon, "Propagation des ondes acoustiques dans les milieux poreux. Effets d'interface (théorie et expériences)." "Acoustic waves propagation in porous media. Interface effects (theory and experiments)" thesis, Université París 7, France November 1987.
[3] Q. Xue, K. Wu, L. Adler, A. Jungman, and G. Quentin, "Generalized Lamb modes in a fluid-saturated porous plate," Rev. Prog. Quant. Nondestr. Eval. **8**, 213–220 (1989).
[4] W. Lauriks, L. Kelders, and J.-F. Allard, "Surface waves and leaky waves above a porous layer," Wave Motion **28**, 59–67 (1998).
[5] P. Leclaire, K. V. Horoshenkov, and A. Cummings, "Transverse vibrations of a thin rectangular porous plate saturated by a fluid," J. Sound Vib. **247**, 1–18 (2001).
[6] G. Belloncle, H. Franklin, F. Luppé, and J. M. Conoir, "Normal modes of a poroelastic plate and their relation to the reflection and transmission coefficients," Ultrasonics **41**, 207–216 (2003).
[7] G. Belloncle, F. Luppé, H. Franklin, and J. M. Conoir, "Influence of the slow wave on the relation between the angular resonances and the leaky guided modes properties for a poroelastic plate imbedded in water," Ultrasonics **42**, 511–514 (2004).
[8] S. Derible, "Acoustical measurement of the bulk characteristics of a water saturated porous plate obeying Biot's theory," Acta. Acust. Acust. **90**, 85–90 (2004).
[9] M. A. Biot, "Theory of propagation of leastic waves in a fluid saturated porous solid: I. Low frequency range," J. Acoust. Soc. Am. **28**(2), 168–178 (1956).
[10] M. A. Biot, "Theory of elastic waves in a fluid saturated porous solid: II. How frequency range," J. Acoust. Soc. Am. **28**(2), 178–191 (1956).
[11] D. L. Johnson, D. L. Hemmick, and H. Kojima, "Probing porous media with first and second sound: II Acoustic properties of water saturated porous media," J. Appl. Phys. **76**(1), 115–125 (1994).
[12] M. A. Biot, "Mechanics of deformation and acoustic propagation in porous media," J. Appl. Phys. **33**(4), 1482–1498 (1962).
[13] R. D. Stoll, "Theoretical aspects of sound transmission in sediments," J. Acoust. Soc. Am. **68**(5), 1341–350 (1980).
[14] M. J. Buckingham, "Theory of compressional and transverse wave propagation in consolidated porous media," J. Acoust. Soc. Am. **106**(2), 575–581 (1999).
[15] H. Franklin, E. Danila, and J.-M. Conoir, "S-matrix theory applied to acoustic scattering by asymmetrically fluid-loaded elastic isotropic plates," J. Acoust. Soc. Am. **110**(1), 243–253 (2001).
[16] N. P. Chotiros, "An inversion for Biot parameters in water-saturated sand," J. Acoust. Soc. Am. **112**(5), 1853–1868 (2002).
[17] R. Fiorito, W. Madigosky, and H. Uberall, "Resonance theory of acoustic waves interacting with an elastic plate," J. Acoust. Soc. Am. **66**(6), 1857–1866 (1979).
[18] L. Flax, G. Gaunaurd, and H. Überall, "Theory of resonance scattering," *Physical Acoustics XV* (Academic, New-York, 1981), 191–293.
[19] R. Fiorito, W. Madigosky, and H. Uberall, "Theory of ultrasonic resonances in a visco-elastic layer," J. Acoust. Soc. Am. **77**(2), 489–492 (1985).
[20] R. Fiorito, W. Madigosky, and H. Uberall, "An exact resonance decomposition of the acoustic transmission and reflection coefficients of a fluid layer," J. Acoust. Soc. Am. **79**(2), 222–229 (1986).
[21] N. D. Veksler, "Resonance acoustic spectroscopy," *Springer Series on Wave Phenomena* (Springer Verlag, New-York).
[22] S. Derible, J.-L. Izbicki, and P. Rembert, "Experimental determination of acoustic resonance width via the Argand diagram," Acta Acust. (Beijing) **84** 270–279 (1998).
[23] R. D. Stoll and T.-K. Kan, "Reflection of acoustic waves at a water-sediment interface," J. Acoust. Soc. Am. **70**(1), 149–156 (1981).
[24] D. L. Johnson, J. Koplik, and R. Daschen, "Theory of dynamic permeability and tortuosity in fluid-saturated porous media," J. Fluid Mech. **176**, 379–402 (1987).

Short range scattering of the fundamental shear horizontal guided wave mode normally incident at a through-thickness crack in an isotropic plate

P. Rajagopal and M. J. S. Lowe[a)]
Department of Mechanical Engineering, Imperial College London, SW7 2AZ, United Kingdom

(Received 11 January 2007; revised 18 May 2007; accepted 29 June 2007)

Interaction of the fundamental shear horizontal mode with through-thickness cracks in an isotropic plate is studied in the context of low frequency array imaging for ultrasonic guided wave nondestructive evaluation with improved resolution. Circular wave fronts are used and the symmetric case where a line from the wave source bisects the crack face normally is considered. Finite element simulations are employed to obtain trends subject to analytical and experimental validation. The influence of the crack length and of the location of source and measurement positions on the specular reflection from the crack face is first examined. These studies show that low frequency short range scattering is strongly affected by diffraction phenomena, leading to focusing of energy by the crack in the backscatter direction. Study of the diffraction from the crack edges reveals contributions due to a direct diffraction at the edges and multiple reverberations across the crack length. A simple diffraction model is shown to adequately represent cracks up to moderate lengths, providing an easy means of estimating the far field of the waves. The presence of multiple diffraction components is quantitatively established and surface waves on the crack face are identified as equivalent to low frequency symmetric modes of rectangular ridge waveguides.
 [DOI: 10.1121/1.2764472]

PACS number(s): 43.35.Zc, 43.20.Mv, 43.20.Gp, 43.35.Cg [SFW] Pages: 1527–1538

I. INTRODUCTION

Ultrasonic guided waves are today well established in long range inspection of large structures, following a significant amount of research in recent years. Guided wave based systems are now commercially available for inspection of structures such as pipes[1] and rails.[2] Developments for using them also to inspect plate structures are now advanced.[3] But current guided wave inspection techniques are limited by their developmental context. Historically, guided waves emerged as an attractive alternative to conventional point-by-point nondestructive evaluation (NDE) for rapid inspection of large areas of structure. In applications where tens of meters of structure are to be scanned for defects, guided wave based inspection is far more efficient than the tedious and time-consuming conventional methods. Therefore, such applications use guided waves primarily as a screening tool. Sensitivity and accurate defect information are not as important as increased coverage and defect localization. The idea is that an approximate estimate of the more severe defects along with precise information about their exact location already expedites inspection. A subsequent investigation by complementary NDE methods (for example, thickness gauging[4,5] or time of flight diffraction[6,7]) can quickly be carried out if more accurate defect information is required. However, there are many applications where the areas of concern are not directly accessible, for example, regions of pipelines embedded in concrete as shown in Fig. 1. Reaching them for a secondary accurate inspection may either not be possible or involve considerable cost, rendering this two-step inspection method problematic. Therefore there is much interest in improving the resolution of guided wave NDE towards single step accurate defect sizing, and a reduction in the range of distance as compared to screening applications is acceptable in order to achieve this.

For most industrial applications, the maximum through-wall depth of the defect is the critical parameter to be known. The issue with current inspection methods is that they measure the cross-sectional area removed by defects but do not offer precise depth or width information, and this is the main stumbling block on the path to improved resolution.[8] One method of overcoming this, for instance, presently being studied at our research group, is to use array imaging methods while continuing to work at low frequencies.[9] This is illustrated in Fig. 2: the matrix of all the send-receive combinations from the transducer array will be processed by imaging algorithms, to yield defect information. Even if this can just yield information about lateral size of the defect, it can be readily used with available inspection techniques to estimate its depth. In this context, it is important to understand the interaction of cylindrical crested guided waves with defects, some key questions being how the transducer, defect location and defect extent impact the accuracy of such methods. Circular wave fronts are necessary in order to imitate the individual elements of a transducer array, which behave as point sources. Also, the direction of specular or mirror-like reflection from a defect alone cannot account for the scattered fields captured by all the array elements; since the

[a)]Author to whom correspondence should be addressed. Electronic mail: m.lowe@imperial.ac.uk

FIG. 1. Example of applications where the areas of concern are not directly accessible: regions of pipelines embedded in concrete.

range involved is relatively short, off-specular and local effects, edge or tip diffraction, would need to be considered.

General scattering studies have been carried out extensively for bulk waves, analytical methods using eigenfunction expansion for simple defect geometries (see the monograph by Pao and Mow[10] for an extensive review) and approximate and numerical methods for cracks and complex defects using the integral equation representation.[11–18] Studies in the guided elastic wave case have followed these developments, but have been more restricted because of the greater challenges involved: the possibility of existence of several propagating modes even at low frequencies, frequency dependent mode shapes and their mutual interconversion on interactions with flaws. Thus plane waves and specular reflection have mainly been studied[19–31] and numerical methods such as Finite and Boundary Elements have played an important role.[32–38] Investigation of circular crested waves[39] or the near field[40–42] and diffraction effects[43,44] is rare, especially for finite defects. Therefore ongoing research in our laboratory is focused on the general shorter range scattering of the cylindrical crested fundamental shear horizontal guided wave (SH0) mode by ideal but finite cracks in isotropic plates. The SH0 mode has features that are attractive for inspection purposes: it is nondispersive, is unaffected by fluids in contact with the structure, and it

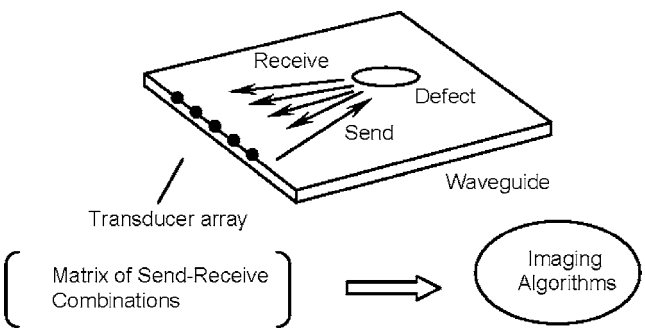

FIG. 2. The matrix of signals from the send-receive configurations from the elements of a transducer array could be used in imaging algorithms to obtain information about the dimensions of the defect.

can be exploited either as the SH0 mode in a plate or as the pipe torsional mode $T(0,1)$ used in current pipe inspection systems.

In this paper, we consider the simple case of a through-thickness crack or slit and the symmetric problem such that a line from the wave source bisects the crack face at 90°. We call this case "normal incidence" in recognition of the path of the central "ray" of the incident beam. We study the nature of scattering in terms of the specular reflection from the crack face as well as the diffraction at its tips. We begin by examining the influence on specular reflection, of the crack length, and also of the location of source and measurement positions in view of our interest in the short range. These then lead to the study of the diffraction phenomena. The finite element (FE) method is the tool used for this purpose, and the results for the reflection studies are compared with experiments. Though this is taken as general validation for our FE simulations, for the case of diffraction, known results from similar problems in literature are used to further assure us of our modeling procedure. For clarity, we use the term crack when describing FE simulations and the term slit in the context of experiments.

In the following, we first describe the problem and the general procedure for FE simulations and experiments in Sec. II. The particular strategies for the different studies and the results are described in Sec. III with specular reflection being the focus of studies in the parts A and B and validation of diffraction modeling and study of diffraction in C and D, respectively. We then discuss the results in the light of some qualitative and quantitative considerations in Sec. IV and conclude with some implications for guided wave imaging in Sec. V.

II. GENERAL METHODS

A. Studied configuration

Figure 3 shows the details of the configuration studied and also of the procedure for FE simulations described in part B of this section. A finite, fully open through crack of vanishing width (shown as "w" in Fig. 3) is located in a thin isotropic plate, its length ℓ aligned with the U2 coordinate axis. A low frequency excitation is applied in the U2 direction, at a point "P" on a line bisecting the crack at 90°. As the plate is thin, this excitation is assumed as being uniform through its thickness. Figure 4 shows the group velocity dispersion curves for modes which can exist in a free aluminium plate at low frequencies: apart from the SH0 mode only the fundamental antisymmetric (A0) and symmetric (S0) Lamb modes occur. The SH0 mode is nondispersive throughout and has constant particle vibration through the plate thickness which is entirely perpendicular to the direction of propagation and parallel to the plate surface (the U1-U2 plane in Fig. 3). At low frequencies, the S0 mode is also nondispersive with its particle vibration predominantly parallel to the direction of propagation and constant through the plate thickness, while the A0 mode is dominated by a particle vibration perpendicular to both the propagation direction and the plate surface. Thus the point excitation applied in the U2 direction generates[45] circular waves of the

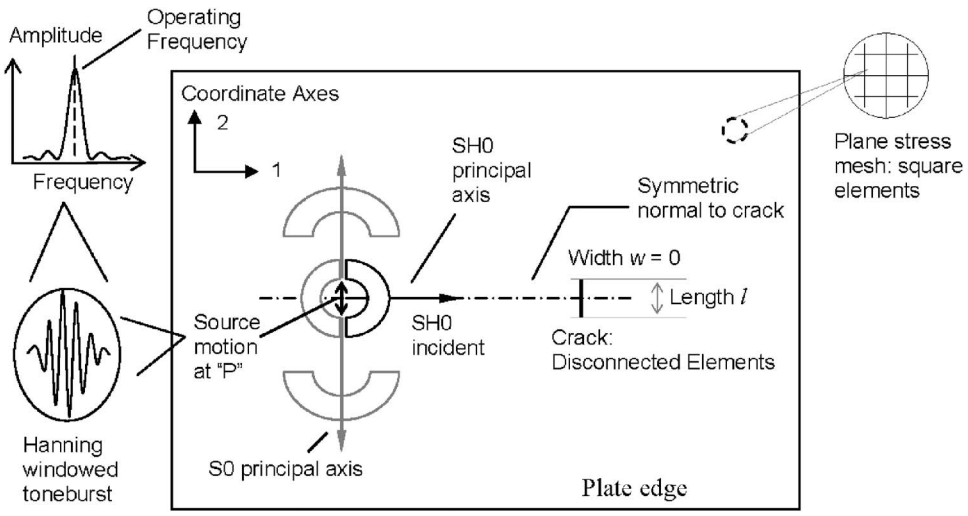

FIG. 3. Details of the configuration studied. The SH0 mode has its principal axis aligned with the symmetric normal to the crack face.

SH0 mode principally in the U1 direction and those of the S0 mode, principally in the U2 direction. The excitation is such that the principal direction of the incident SH0 waves bisects the crack face at 90°, lending symmetry to the problem. Away from their principal directions both modes exhibit a characteristic cosine angular decay of the displacement amplitude. Thus, although in general the S0 mode is also excited, we are able to study the scattering from the SH0 mode in isolation as the former does not propagate strongly towards the crack. Further, as can be seen from Fig. 4, in the low frequency-thickness regime the S0 mode travels much faster so that its effects can be time-gated out. The A0 mode is not considered in the problem as the uniform excitation parallel to the plate surface is expected to generate very little of it and the through-thickness symmetry of the crack ensures that it is not generated by the scattering.

We then study the SH0 specular reflection from the crack face and the SH0 diffraction from the crack edges. Thus we are essentially interested in the SH0 scattering phenomena happening in the U1-U2 plane parallel to the plate surface and assume uniformity through the plate thickness. If instead, we could think of this plane to be the cross section, this problem would be equivalent to that of bulk shear vertical (SV) wave scattering by internal cracks: along their sagittal planes, these two problems would share the same boundary conditions. We will touch more on this equivalence in Sec. III C.

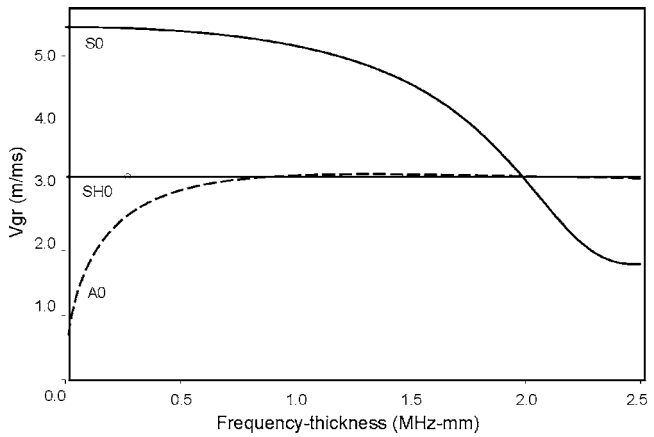

FIG. 4. Group velocity dispersion curves for low frequency Lamb and SH waves in an aluminium plate. Since the A0 mode does not occur in our problem, it is shown by a dotted line.

B. General procedure for finite element simulations

A two-dimensional domain with the assumption of plane stress was used for the FE simulations, implemented using the program ABAQUS.[46] The models so generated are representative of an arbitrarily thin plate or a section of a plate parallel to its surface and lying at its midplane; they do not support plate bending or part-through defects. Since the SH0 mode is nondispersive and its mode shape is constant through the plate thickness, such a model will represent it accurately at any given frequency-thickness value. But the S0 mode has similar properties only in the low frequency-thickness region, so the model provides reasonably accurate results for values up to 0.5 MHz mm for this mode; the FE studies were carried out at 0.1 MHz mm. For simplicity, we will assume the plate thickness to be 1 mm in the following parts of this paper, so the frequency thickness at an input frequency of say f_0 MHz would simply be f_0 MHz mm. Further, the results obtained at f_0 would be valid at any other frequency f_1 provided the dimensions are appropriately scaled by a factor of f_1/f_0 by which the wavelength is scaled: experimental verification studies have been based on this understanding and simulation results showing favorable agreement to this idea are also presented in Sec. III A. The models do not support the A0 mode but, as observed in the previous section, this mode is not expected, so this does not pose a problem.

Much of the past work in the two-dimensional domain has been done with a plane strain assumption and, consequently, focused on part depth but infinite length defects. In contrast, the plane stress study presented here helps understand the impact of the length of a finite defect on the interaction of an incident mode with the defect.

Figure 3 again shows the temporal and in-plane spatial details of the models and the coordinate system; the out-of-plane dimension (containing the U3 direction), is the direction of the plate thickness. Two strategies were used to prevent S0 reflections from the edges from arriving together

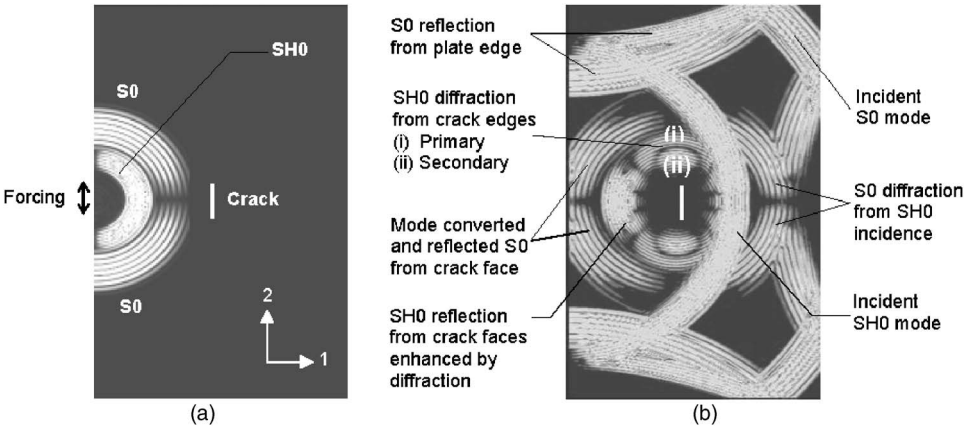

FIG. 5. Contour snapshots of the magnitude of resultant displacement from FE simulations, at different time instances (a) soon after excitation; (b) SH0 mode interaction with the crack; the S0 mode does not interact strongly with the crack as it propagates primarily away from the crack, in the U2 direction.

with the SH0 scattering from the crack at the monitored locations. For simple scattering studies, the in-plane dimensions of the model were chosen to be large and the model size was restricted by applying symmetry in the U1-U3 plane. But for the studies requiring a complete isolation of only the scattered SH0 mode, absorbing layers with increasing damping (or *ALID*, see Drozdz *et al.*[47]; see Castaings *et al.*[48,49] for more details on the use of absorbing boundaries in FE analysis) were used around the edges of the plate. The mesh consisted of perfectly square 2-mm-long elements, allowing for around 16 elements per SH0 wavelength, respecting the spatial discretization limit required for accurate modeling.[50] Cracks were created by disconnecting elements at the nodes defining the crack and were thus of zero width. Material properties of aluminium were used in all cases except for the validation of diffraction modeling (Sec. III C), where the properties of steel were chosen to match those in the literature consulted.

A 5 cycle Hanning windowed toneburst centered at 0.1 MHz was applied as a force in the U2 direction, at a single point. This generates the S0 and SH0 modes, with their principal directions parallel and perpendicular, respectively, to the applied force. Explicit time integration with a constant time step respecting the stability limit simulates the propagation of the modes. The default condition on the faces of the disconnected elements representing the crack is that of zero stress. Thus the scattering from an ideal open crack is simulated.

The reflection behavior was studied in terms of a frequency domain ratio of the resultant displacement of the reflected signal to that of the signal incident at the center of the crack face. The waves in the model decay cylindrically away from the source so the signals were compensated accordingly for beam spreading such that the ratio from a straight edge would be unity. Thus

$$\text{Reflection ratio} = \frac{R(\omega)\cdot\sqrt{D+d_M}}{I(\omega)\cdot\sqrt{d_I}}, \tag{1}$$

where $R(\omega)$ and $I(\omega)$ are the frequency spectra of the resultant displacement obtained from reflected and incident signals, respectively, D is the distance between the source and the center of the crack, d_M is the distance from the crack center to the point where the reflection is monitored and d_I is the distance from the source to the point where the incident signal is monitored.

The nature of diffraction was studied in terms of a diffraction ratio, defined as the ratio of the spectrum of the resultant displacement of the monitored diffracted signal to that of the signal incident at the center of the crack face, both compensated for beam spreading

$$\text{Diffraction ratio} = \frac{D(\omega)\cdot\sqrt{r_M}}{I(\omega)\cdot\sqrt{d_I}}, \tag{2}$$

where $D(\omega)$ and $I(\omega)$ are the frequency spectra of the resultant displacement obtained from the monitored diffracted and incident signals respectively, r_M is the distance from the tip of the crack to the point where the diffracted signal is monitored and d_I is the distance between the source and the position where the incident SH0 wave is monitored.

Figure 5 presents typical time snapshots of the contour of the magnitude of resultant displacement from FE simulations. Figure 5(a) shows an instant soon after excitation: the S0 mode travels faster and can be seen propagating mainly in the U1 direction and the SH0 mode towards the crack. Figure 5(b) shows the mode interaction with the crack: the S0 mode has little energy in this direction so it causes little scattering, while the SH0 mode reflects from the crack face and is diffracted by the crack edges. In addition to the SH0 mode, we observe that the scattered field also consists of mode-converted S0. Although in general the scattered energy is distributed between these two modes, overall it is largely and in some directions entirely concentrated in the SH0 mode. Figure 6 highlights this through the angular profile of the SH0-S0 and SH0-SH0 reflection and diffraction ratios calculated from FE simulations, for two special cases, respectively: Fig. 6(a) presents the reflection ratios according to Eq. (1) for scattering of SH0 waves by a straight edge while Fig. 6(b) shows the angular profile of the diffraction ratios according to Eq. (2) for scattering by a semi-infinite crack. In this paper, we study the reflection along the specular direction (90° to the crack face) and the diffraction along the crack line (180° to the crack face), where only the SH0 mode is present.

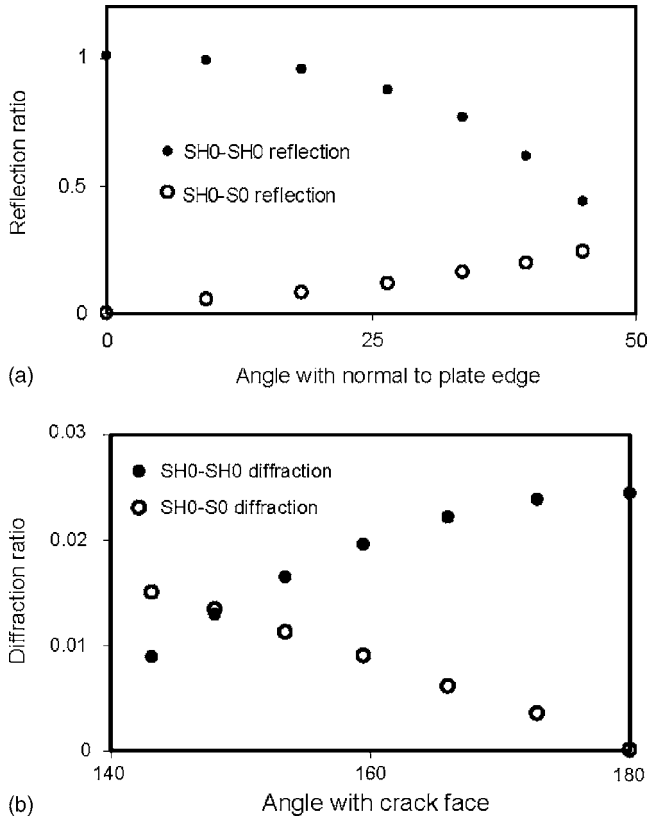

FIG. 6. (a) Shows the SH0-SH0 and SH0-S0 reflection ratios obtained for a range of angles around the incidence direction for scattering by a straight edge; (b) Shows the SH0-SH0 and SH0-S0 diffraction ratios obtained for a range of angles around the crack line for scattering by a semi-infinite crack.

C. General procedure for experiments

The experimental setup is shown in Fig. 7. A point-like source excitation was achieved by means of a plane wide-band piezoelectric shear transducer (Panametrics V301, 0.5 MHz center frequency) coupled to the plate through a thin (0.2 mm thickness) and small (3 mm diameter, roughly 1/3 that of typical wavelength) brass disk. The excited signal amplitude was measured around and away from this excitation apparatus to confirm the expected angular behavior of the excited SH0 mode amplitude and its inverse square root decay with radial distance. The excitation signal consisting of a 5 cycle Hanning windowed toneburst was generated by a Wavemaker (Macro Design Ltd., UK) instrument and centered at the required frequency.

The detection was achieved using a laser interferometer (Polytec OFV 2700, with dual differential fiber optic lines) measuring the displacement at the surface of the plate. The displacement component in the direction parallel to the surface of the plate was measured by using two laser beams each aligned at an angle of 30° to it, so that the difference between their two signals then gave the in-plane displacement. A thin reflective tape was attached to the surface of the plate to enhance the optical backscatter from the laser beam. The two optical fibers were aligned such that only the SH0 mode was picked up along the normal to the slit face. The measured signals were in general quite weak and so the quality of each displacement measurement was enhanced by applying a bandpass filter and taking an average over 500 acquisitions.

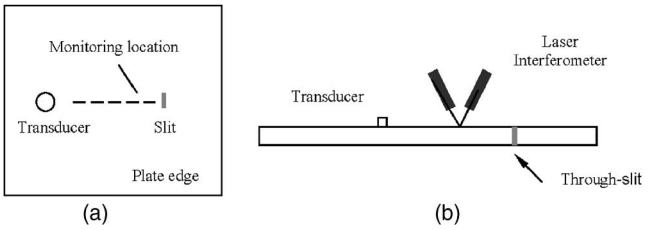

FIG. 7. The experimental setup (a) top view; (b) front view.

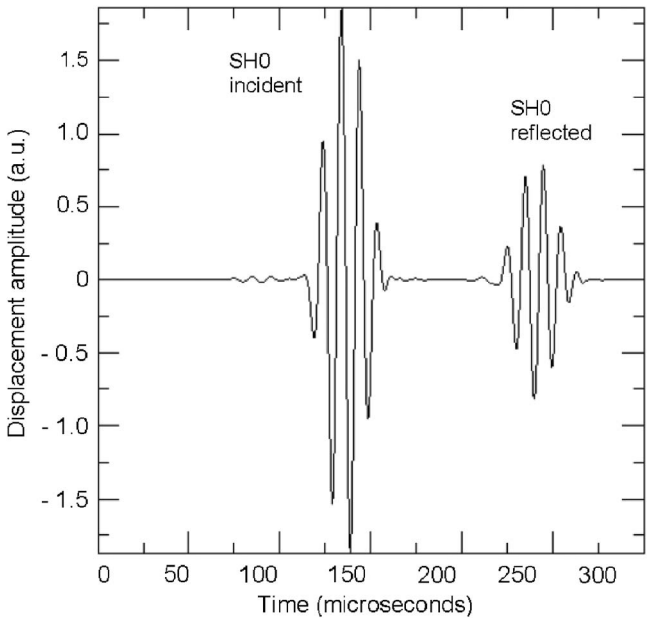

FIG. 8. Normal incidence of SH0 mode on the crack: typical time plot of displacement in the U2 direction at the monitored point from FE simulations. The tiny precursor to the SH0 mode is the S0 mode, a small amount of which is always generated.

Measurements were carried out on 0.5-mm-wide slits of lengths 8, 16, 36, and 65 mm cut in 1250 mm square standard aluminium plates of 1 mm thickness. Since the wavelength was at least 15 times that of the slit width for most of the frequencies used, these slits approximate well the cracks defined in FE. The transducer was positioned on the symmetric normal to the slit face such that the SH0 mode had its principal axis along this line; the detection was also along this line. For each slit length, the center frequency of excitation was swept from 200 to 400 kHz in order to obtain results for increasing ratios of the slit length to the wavelength. The excitation and detection positions were varied at each center frequency value, so that they were located at a certain constant number of wavelengths away from the slit.

III. SPECIFIC STUDIES AND RESULTS

A. Nature of specular reflection

A number of simple FE models with long in-plane dimensions were set up to understand the dependence of the SH0 reflection over the length of the crack. The excitation was located at a distance of 16 λ_{SH0} (SH0 wavelengths at the center frequency of the toneburst). Nodal displacements in

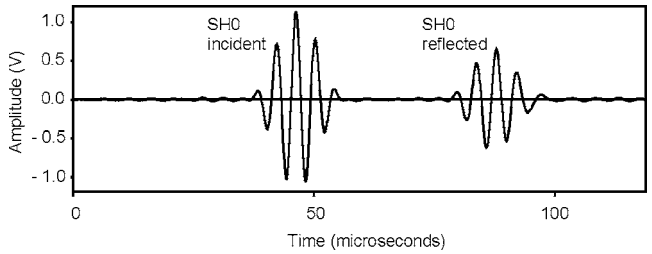

FIG. 9. Typical time plots of monitored displacement from experiments showing reflection from the slit: values measured at 250 kHz from a 65 mm slit for excitation and monitoring at 200 and 64 mm from the slit respectively.

the U2 direction were monitored 5 λ_{SH0} from the crack and along its symmetric normal. The generated S0 mode has nearly zero displacement along this line, so only the incident and reflected SH0 signals are recorded at the monitored points. Experimental measurements were taken at the appropriate excitation and monitoring distances for each frequency spanning the required slit lengths. In order to confirm that these results are equivalent to those obtained by FE at a constant frequency but for varying crack lengths, we also simulated the experimental situation in FE, sweeping the frequency from 200 to 400 kHz in steps of 50 kHz with cracks of lengths 5, 10, 36, and 65 mm to obtain various crack lengths in terms of λ_{SH0}.

Figures 8 and 9 show typical time plots of monitored displacement including reflection from the crack or slit in FE and experiments, respectively. The reflection ratio was calculated for each crack length from these monitored signals using the same procedure according to Eq. (1). Figure 10 shows measured and FE predicted values (for both single and swept frequency studies) of the reflection ratio for this monitoring location, plotted with increasing crack lengths. The crack lengths are expressed in terms of λ_{SH0}. There is a very good agreement between FE and experiments.

Coming to the reflection behavior, initially the reflection ratio rises linearly with the crack length. Although from a far-field plane wave perspective we would expect the ratio to gradually approach unity as the crack grows large, the observed anomalous overshoot is characteristic of diffraction

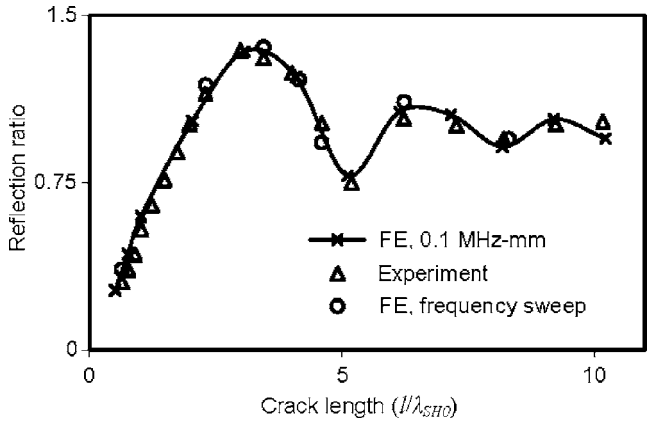

FIG. 10. Measured and FE predicted values of the reflection ratio plotted with increasing crack lengths for excitation and monitoring at 16 λ_{SH0} and 5 λ_{SH0} from the crack face, respectively.

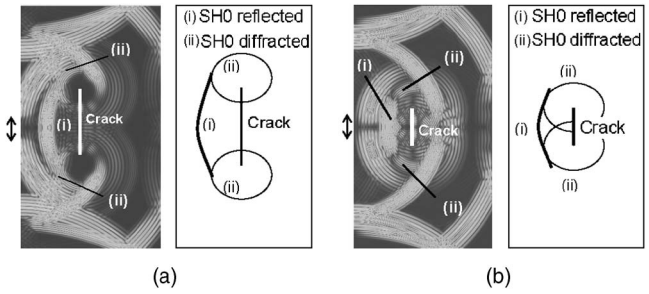

FIG. 11. Interaction of SH0 with cracks of different lengths: (a) 20 λ_{SH0} and (b) 7 λ_{SH0}. Contour of the magnitude of resultant displacement obtained from FE simulations and line diagram focusing only on reflected and diffracted SH0 due to SH0 incident are shown.

effects in the short range studied; this can be seen by examining the detailed behavior at the crack. Figure 11 shows the interaction of the SH0 mode with cracks of two different lengths: again, the contour of the magnitude of resultant displacement is plotted, along with simplified line diagrams. We observe that, for smaller cracks, the strength of the diffraction field is significant and it arrives together with the reflection, enhancing the received field. The interference between these different waves arriving together is borne out in the undulations seen in the reflection trend. These effects may be regarded as focusing of energy by the crack and we will comment on this in Sec. IV A.

B. Influence of the distance of source and measurement location on reflection behavior

The behavior of specular reflection as captured in the reflection ratio-crack length plot of Fig. 10 has important implications for imaging work. We note that this plot has been obtained for excitation and monitoring points quite close to the crack, 16 λ_{SH0} and 5 λ_{SH0} away from it, respectively. We see that in this case, for cracks longer than 3 λ_{SH0}, the reflection ratio values enter an oscillatory regime. Therefore, if our measurement location is close to the crack, in the range of a few wavelengths, we may not be able to precisely image cracks longer than 3 λ_{SH0}.

We then need to find out how the reflection behavior evolves as we vary the source and measurement positions with reference to the crack. Here we examine this issue. There are four possible combinations of source and measurement positions, depending on whether each is close to or far from the crack. But we consider only two complementary cases, to bring insight into the problem: (i) that of a measurement point close to the crack while the source position varies and (ii) that of source position far from the crack while the measurement position varies.

The FE models set up for this purpose made use of absorbing layers with increasing damping[47] around the edges of the plate. This ensured that only the SH0 reflection from the crack could be observed in preference to other unwanted reflections. For study (i), the measurement position was fixed at 5λ_{SH0} from the crack while the source position was located successively at 16 λ_{SH0}, 20 λ_{SH0} and 32 λ_{SH0}. For study (ii), the source was fixed at 32 λ_{SH0} and the reflection was monitored at distances of 5, 10, 15, 20 and 25 λ_{SH0} from the

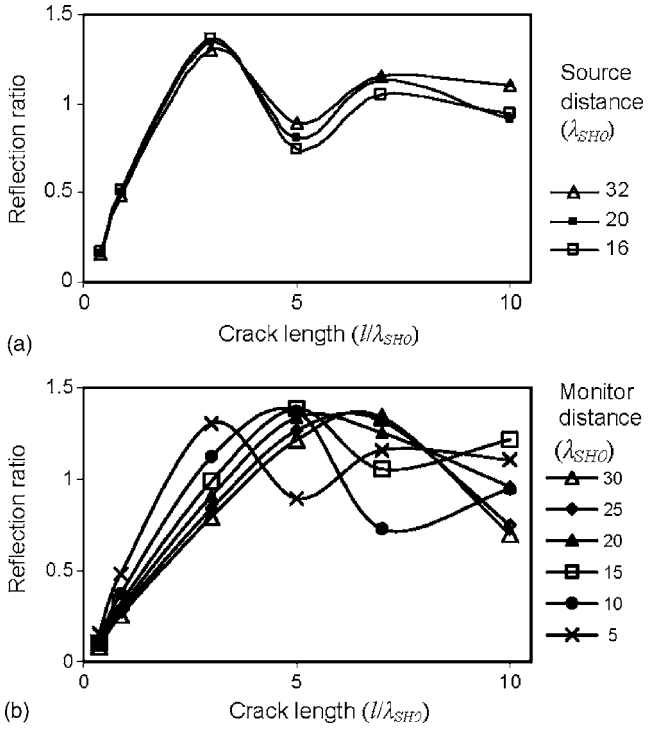

FIG. 12. Reflection ratio-crack length plot (a) monitored at 5 λ_{SH0} from the crack with range of source positions; (b) source at 32 λ_{SH0} with range of monitoring positions.

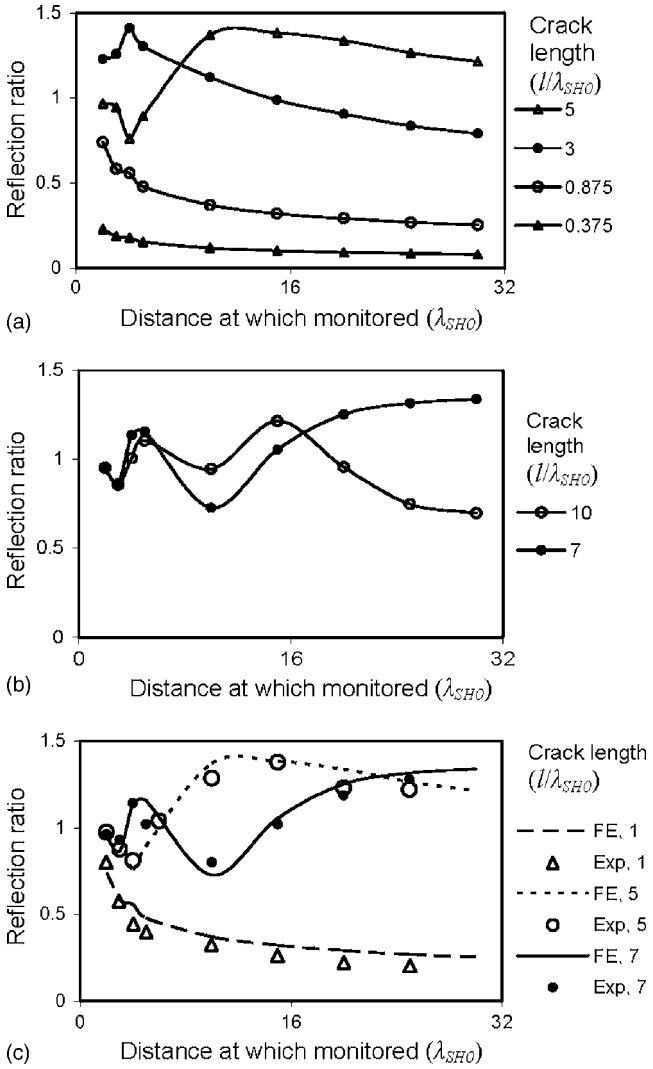

FIG. 13. The reflection ratio plotted with the monitoring distance for increasing crack lengths; (a) and (b) show FE predicted values for small and large cracks respectively; (c) comparison of FE with experimental measurements for three different slit lengths.

crack face. The crack length was again varied using a number of simulations and the reflection ratio was calculated according to Eq. (1).

Figures 12(a) and 12(b) show the plot of reflection ratio versus crack length, obtained at different source and monitoring positions from studies (i) and (ii). Figures 13(a) and 13(b) show the same information as in Fig. 12(b), but with the reflection ratio plotted with the monitoring distance instead of crack length, and 13(c) shows a comparison of these FE results with experiments for three slit length values; we see that the predictions and measurements agree very well.

From Fig. 12(a), we see that though there is a slight variation, the reflection ratio trend is nearly maintained: thus we can say, provided the source is far from the crack and beam spreading is compensated for, its position has a weak influence on specular reflection.

From Fig. 12(b) we learn that Fig. 10 represents a general trend in which reflections from finite cracks follow in the short range. The reflection ratio rises sharply with the crack length to an overshoot above unity and then gradually approaches unity with undulations due to interference phenomena. Though this behavior is different for different monitoring positions, the values converge at large monitoring distances (approximately above 15 λ_{SH0}) for even fairly long cracks. In understanding this, it would be useful to think of the crack as a secondary source and look at the similar effects observed with a piston source transducer. If we take the near field of a compressive piston source as an approximation for the near field of a crack given by the Fresnel parameter $F=\ell^2/4\lambda$ (where ℓ the length of the crack will be taken as the diameter of the piston and λ is the wavelength λ_{SH0}) we would observe that as long as the crack length is such that the monitoring distance is approximately greater than F, the reflection ratio increases linearly with the crack length. This can be seen in Figs. 14(a) and 14(b) where the reflection ratio is plotted with respect to the monitoring distance normalized to the Fresnel parameter for small and long cracks, respectively. We observe that as the monitoring distance begins to fall within what can be called the near field for the crack ($F \approx 1$) the reflection values tend to oscillate rapidly. But away from this region, the reflection values for long cracks approach unity gradually. We will consider this "crack as a source" suggestion in more detail in Sec. IV A to understand more about why the source and measurement positions have the kind of influence on reflection as observed in this section.

C. Diffraction: Validation

A number of researchers have worked on the problem of diffraction of bulk elastic waves by planar cracks.[13,51–53] One validation of the modeling procedure is comparison of the present FE results with those from comparable problems in

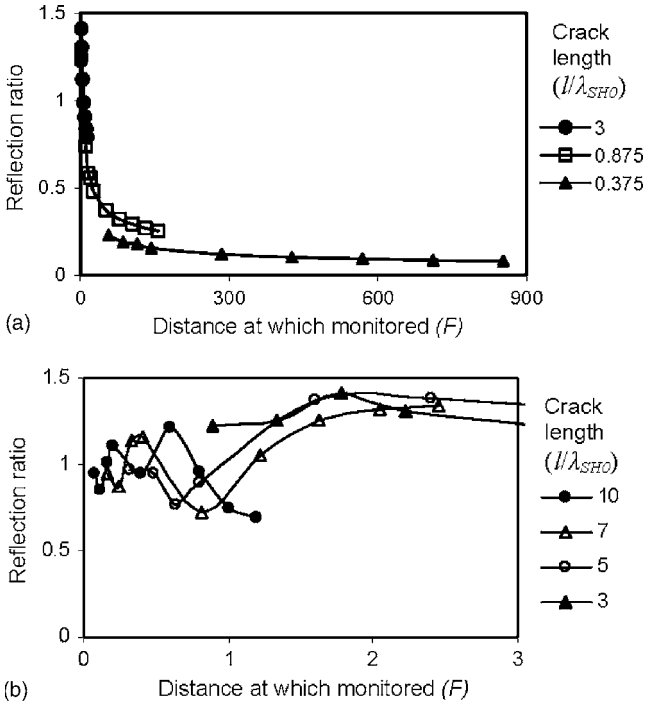

FIG. 14. The reflection ratio is plotted with the monitoring distance normalized to the Fresnel parameter F for (a) small cracks (b) long cracks.

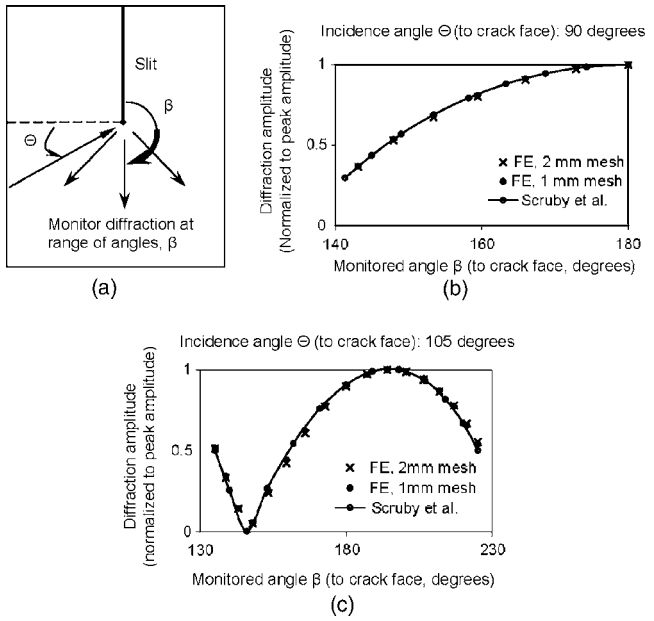

FIG. 15. (a) Representation of the model generated for validation. (b) and (c): Comparison of results from FE simulations and the theoretical calculations presented by Scruby *et al.* for incidence angle cases of 90° and 105° to the crack face.

literature. We used the theoretical calculations presented by Scruby *et al.*[54] (and confirmed with experiments by Ravenscroft *et al.*[55]), based on earlier work.[52,56] For the case of a long crack, Scruby *et al.* obtained the amplitude of a diffracted bulk shear vertical (SV) wave for incident continuous SV waves, as a function of the incident and diffracted angles. These results were obtained using a plane-strain assumption but they are valid for the guided SH0 wave with a plane-stress assumption: the latter is concerned with sections parallel to the plate surface while former deals with the plate's cross section and, as we noted in Sec. II A, these problems are equivalent. Examined with suitable coordinates in their appropriate plane, the same condition on in-plane shear stresses governs the propagation of both bulk SV and SH0 waves

$$\sigma_{12} = G\varepsilon_{12}, \tag{3}$$

where σ and ε represent the stress and strain tensor, respectively, and G is the shear modulus.

The FE model generated for this purpose is illustrated in Fig. 15(a). The tip of a long, single-tipped crack was exposed to SH0 waves incident at various angles. The diffracted signal was monitored at a range of angles around the crack. We repeated the steps with a finer mesh of 1-mm-square elements allowing around 32 elements per wavelength at 0.1 MHz mm. Following earlier work,[55,57] the amplitudes of the monitored diffracted signals are normalized to the peak value and compared with similarly normalized values from predictions by Scruby *et al.* in Figs. 15(b) and 15(c) for two different incidence angles: a very good agreement is observed. This lends confidence to our diffraction modeling.

D. Nature of diffraction

A number of simple FE models were set up to isolate the diffraction due to SH0 mode normal incidence on cracks of increasing lengths. The details of the models are shown in Fig. 16(a). We monitored the diffraction along the crack line where the S0 diffraction vanishes and the diffracted SH0 has only the U1 component. The U2 component of the incident SH0 is also monitored along a line perpendicular to the crack. The diffraction ratio is then calculated according to Eq. (2).

Figure 16(b) shows the diffraction ratio plotted with crack length, again expressed in λ_{SH0}. The observed pattern of variation of the diffraction ratio can be explained by a closer examination of the diffracted field. Figures 17(a) and 17(b) show diffraction at cracks 4 and 2 λ_{SH0} long, respectively. We observe that the diffraction field is complex and contains contributions from two interfering components: a

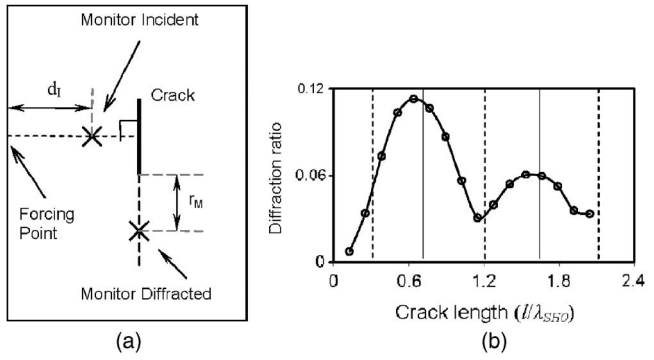

FIG. 16. (a) The positions for monitoring incident and diffracted waves, (b) the diffraction ratio calculated at 0.1 MHz for a point along the monitoring line, plotted with increasing crack length; the solid and dashed vertical lines are located at positions where the analysis in Sec. III D predicts the peaks and troughs would be located.

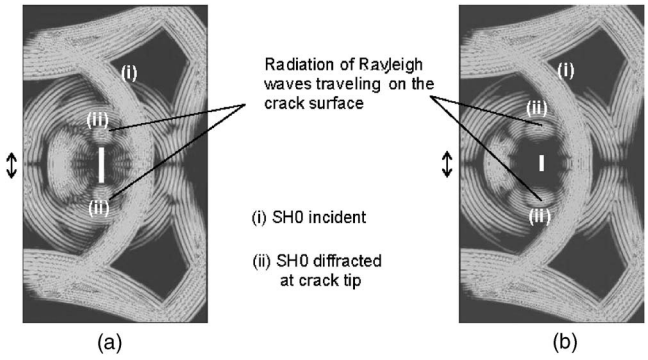

FIG. 17. Contour of magnitude of resultant displacement for diffraction study for two different crack lengths: (a) 4 λ_{SH0} (b) 2 λ_{SH0}.

"primary" diffraction from the crack tips or edges and a "secondary" diffraction due to Rayleigh-like waves traveling along the crack faces and radiating into the plate at the crack tip. We will take a quantitative look at this interference in Sec. IV B.

IV. DISCUSSION

A. Understanding reflection behavior

In Sec. III B we suggested that when the source is far away from it, the crack may be thought of as a secondary source. This is a well known idea following from the integral representation of Huygen's principle (see, for instance, Pao and Varatharajulu[58] and Achenbach[59]) for the scattered displacement in terms of sources on the surface of a scatterer

$$u_k^{sc}(r,\omega) = \int_S [u_i(s,\omega)[\Sigma_{ij;k}^0(r/s,\omega)n_j] - [\sigma_{ij}(s,\omega)n_j]G_{i;k}^0(r/s,\omega)]dS, \quad (4)$$

where $u_k^{sc}(r)$ is the component in the $\hat{e}_k$ direction of the scattered displacement observed at position $\boldsymbol{r}$ in the medium due to a flaw of surface S and outward normal n_j, $u_i(s)$ and $\sigma_{ij}(s)n_j$ are the displacement and traction induced at a position $\boldsymbol{s}$ on the flaw surface due to the incident wave, $G_{i;k}^0(r/s)$ is the Green's displacement tensor giving the displacement component in the $\hat{e}_k$ direction at $\boldsymbol{r}$ due to a point force applied at $\boldsymbol{s}$ in the $\hat{e}_i$ direction in *the free medium in the absence of a flaw*, and $\Sigma_{ij;k}^0(r/s)n_j$ is the traction due to the corresponding Green's stress tensor; steady state fields with circular frequency ω such that the displacements and stresses at time t are given by $f(r,t)=f(r,\omega)\exp(-i\omega t)$ have been assumed.

Thus the scattered displacement can be seen as arising due to a superposition of secondary sources, $u_i(s)$ and $\sigma_{ij}(s)n_j$ placed on the surface of the flaw. In the case of an ideal crack with traction-free surfaces $\sigma_{ij}(s)n_j=0$ and Eq. (4) reduces in terms of $\Delta u_i(s)=u_i(s^+)-u_i(s^-)$, the displacement jump across the crack faces s^+ and s^-, to

$$u_k^{sc}(r,\omega) = \int_{s^+} \Delta u_i(s,\omega)[\Sigma_{ij;k}^0(r/s,\omega)n_j]dS, \quad (5)$$

where the integral is now only on the insonified face s^+ of the crack.

For an exact solution to the scattering problem, Δu_i^{sc} must be accurately known along the crack face. But here we make use of a Kirchhoff-like approximation for the crack opening displacement and FE simulations, to understand how the different parameters affect scattering. Let a harmonic point excitation parallel to the crack face be located at the midplane of a thin plate at a distance R_0 from a crack of length ℓ.

Making use of cylindrical coordinates and placing the origin at the excitation point, the crack is along the line $r\cos(\theta)=R_0$ with $\hat{n}=\cos(\phi)\hat{e}_r+\sin(\phi)\hat{e}_\theta+z\hat{e}_z$ while the excitation is applied at $(0,0,0)$ along the line $\theta=\pi/2$. For points (r,ϕ) on the midplane far from the source, this generates[60]

$$u_\theta((r,\phi),\omega) = \frac{A}{\sqrt{r}}\cos(\phi)\exp(-ik_{SH0}r), \quad (6)$$

where k_{SH0} is the wave number of the SH0 wave; the time factor, $\exp(-i\omega t)$ is omitted throughout.

If ℓ is small compared to R_0, we can assume that a uniform displacement $u=u_\theta((R_0,0),\omega)\hat{e}_\theta$ impinges upon the crack face. Further, for cracks of lengths such that $k_{SH0}l \gg 1$ i.e., $l \gg \lambda_{SH0}/2\pi$, we can argue that the two faces of the crack do not interact very much because of which we can simply take $\Delta u_i^{sc}(s)=u_i^{sc}(s^+)=2u_\theta((R_0,0),\omega)$ and $\Delta u_i^{sc}(s,\omega)\times[\Sigma_{ij;k}^0(r/s,\omega)n_j]=2u_\theta((R_0,0),\omega)\Sigma_{r\theta;k}^0(r/s,\omega)\cos(\phi)$. Taking $\cos(\phi)\approx 1$ Eq. (5) now yields

$$u_k^{sc}(r,\omega) = 2u_\theta((R_0,0),\omega)\int_{S^+}\Sigma_{r\theta;k}^0(r/s,\omega)dS. \quad (7)$$

Equation (7) means that if the length of the crack is small compared to distance from the excitation, it should behave as if point shear sources of uniform strength are placed all along its insonified face: in other words, it would behave as if one face of it were a simple ideal shear transducer.

In order to test the limits of such a model, we studied the behavior of a crack with one face loaded with parallel point forces using FE simulations. Figure 18 shows the U2 amplitude monitored along the symmetric normal to the crack obtained from these simulations, for different crack lengths. In order to compare them with the earlier full-FE studies, the amplitudes have been normalized as if the crack were excited by a source located 32 λ_{SH0} from it. We observe that the shape of these amplitudes compares remarkably well with those of the actual reflection amplitudes shown in Fig. 13, for crack lengths up to 5 λ_{SH0}. This means that for small cracks, the response is indeed as if a secondary source were placed on the insonified side, but cracks that are longer than 7 λ_{SH0} cannot be represented using this simple model.

B. Understanding diffraction behavior

In Sec. III D we noted that the undulations observed in the diffraction ratio-crack length plot (Fig. 16) were due to the interference between the primary and secondary diffraction. Here we take a quantitative look at this idea, using FE simulations again. When the incident waves impinge on the crack, a direct diffraction occurs at the crack edges and surface waves are introduced along the crack faces. We can assume that these surface waves are in phase with the pri-

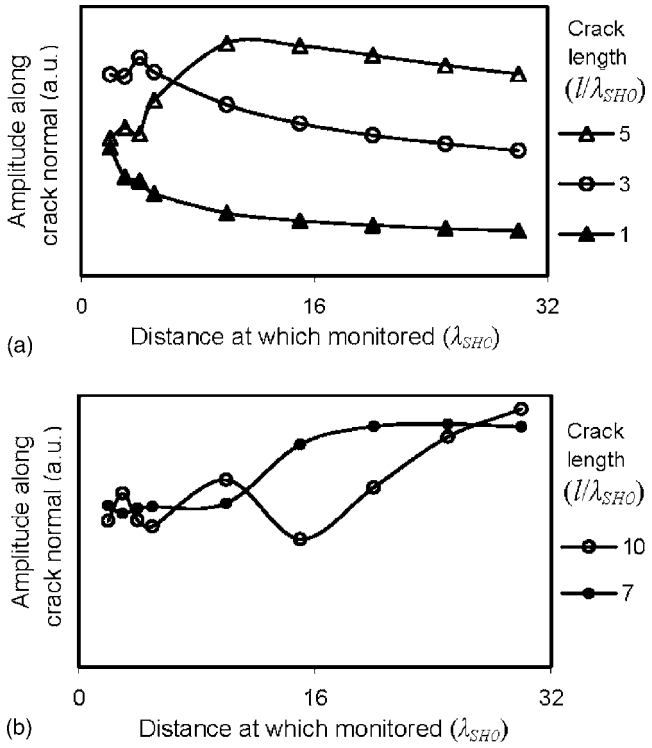

FIG. 18. U2 amplitude monitored along the symmetric normal to the crack obtained from FE simulations of cracks with one face loaded with parallel point forces; (a) Shows plots the values for cracks 1, 3 and 5 λ_{SH0} long; (b) plots those for 7 and 10 λ_{SH0} long cracks. Amplitudes have been normalized to the case in which the crack is excited by a source located 32 λ_{SH0} from it.

mary diffraction, but their phase changes as they travel along the crack face and also at the crack tip. If ϕ_P and ϕ_S represent the phase of the primary and secondary diffraction with respect to the excitation point, we can thus write at the crack tip

$$\phi_S^{\text{edge}} = \phi_P^{\text{edge}} - k_{\text{surf}}\,\ell + \Delta\phi_{P-S}^{\text{edge}}, \tag{8}$$

where k_{surf} is the wave number of the surface wave which propagates along the crack face, ℓ is the length of the crack and $\Delta\phi_{P-S}^{\text{edge}}$ is the phase change at the tip. The phase difference between primary and secondary diffraction at the crack edge should hence be

$$\phi_P^{\text{edge}} - \phi_S^{\text{edge}} = \delta\phi_{P-S}^{\text{edge}} = k_{\text{surf}}\,\lambda - \Delta\phi_{P-S}^{\text{edge}}. \tag{9}$$

We should therefore expect a plot of $\delta\phi_{P-S}^{\text{edge}}$ with ℓ to be linear with the wave number of the surface waves as its slope and the phase change at the crack edge as its intercept.

We set up FE models of SH0 wave interaction with long cracks (7–10 λ_{SH0} long) so that the primary and secondary diffraction could be separated from each other along the crack line. Absorbing boundaries using *ALID* were applied in order to study the scattering from the cracks in isolation.

For each crack length case, the U1 component of displacement was monitored at five locations along the crack line. Figure 19 shows a typical time trace: from such a signal, the primary and secondary components are extracted by time gating. The phase of the waves is then obtained as the value at center frequency of the imaginary part of the Fourier

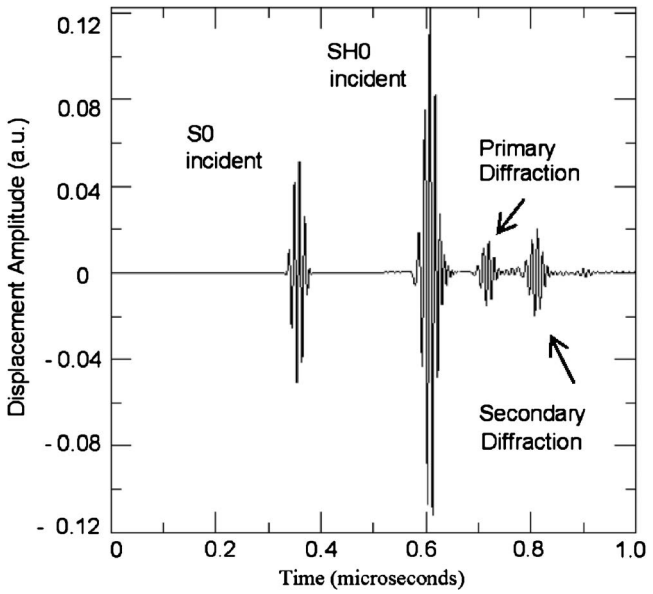

FIG. 19. Typical time trace of the U1 component of displacement monitored along the crack line. The primary and secondary diffraction components are extracted from such a signal by time gating.

transform of the respective signal. For each location at a distance "Y" from the crack edge, the phase of the signal at the crack edge is given by

$$\phi_P^Y = \phi_P^{\text{edge}} - k_{\text{SH0}}Y \quad \text{and} \quad \phi_S^Y = \phi_S^{\text{edge}} - k_{\text{SH0}}Y, \tag{10}$$

where k_{SH0} is the wave number of the SH0 wave.

Thus $\phi_P^Y - \phi_S^Y$ at any location directly gives $\delta\phi_{P-S}^{\text{edge}}$ for a given crack length and the values at the different positions will act as a cross check. $\delta\phi_{P-S}^{\text{edge}}$ obtained this way matched well for all the monitored locations and Fig. 20 shows these values plotted with crack length. We observe the expected linear variation, in this case given by $\delta\phi_{P-S}^{\text{edge}} = 7\ell + 1$ if ℓ is expressed in λ_{SH0} or equivalently, $\delta\phi_{P-S}^{\text{edge}} = 223.64\ell + 1$ if ℓ is in SI units where 223.64 would then directly give the wave number of surface waves on the crack face in radians/m.

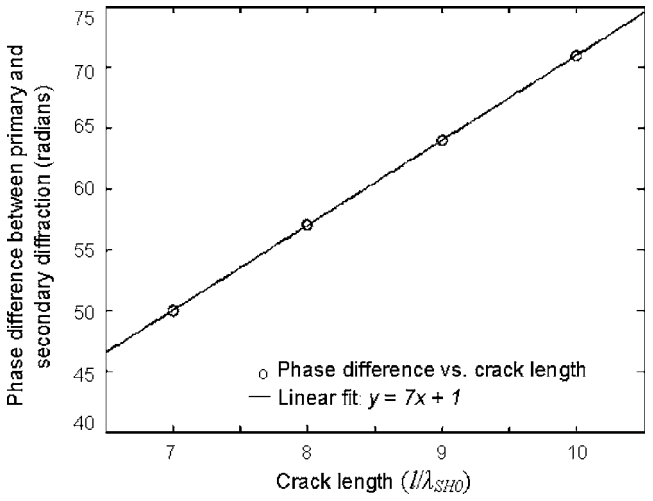

FIG. 20. $\delta\phi_{P-S}^{\text{edge}}$ from FE simulations plotted with the crack length, ℓ. A linear fit yields $\delta\phi_{P-S}^{\text{edge}} = 7\ell + 1$ if ℓ is expressed in λ_{SH0} or equivalently, $\delta\phi_{P-S}^{\text{edge}} = 223.64\ell$ if ℓ is in SI units.

For destructive interference between primary and secondary diffraction, $\delta\phi_{P-S}^{\text{edge}}=2n\pi+\pi$, $(n=0,1,2\ldots)$, and for constructive interference, $\delta\phi_{P-S}^{\text{edge}}=2n\pi+2\pi$. Thus the dips must occur at $(2n+1)\pi-1/7\lambda_{SH0}$ or 0.3 λ_{SH0}, 1.2 λ_{SH0}, 2.1 $\lambda_{SH0}\ldots$ and the peaks, at $2(n+1)\pi-1/7\lambda_{SH0}$ or 0.75 λ_{SH0}, 1.65 $\lambda_{SH0}\ldots$. These peak and dip positions are marked using solid and dashed lines, respectively, for comparison with FE results in Fig. 16: we find excellent agreement except for very small cracks whose behavior cannot be captured by our simple models. Further, for the corresponding wave number value of 223.64 rads/m for surface waves traveling along the crack face, the phase velocity at 0.1 MHz comes out to be 2809.5 m/s: this is close to the Rayleigh wave velocity of 2925 m/s for the material properties used in the FE simulations. Surface waves on the edge of thin plates have been studied in the literature on rectangular ridge waveguides[61,62] and both symmetric and antisymmetric modes are known. The symmetric surface waves on the edges of thin ridges correspond closely to Rayleigh waves (see Oliner's review,[61] for instance, for a description of the properties of these waves) and since only symmetric modes can exist in our plane stress FE models, they appear to be equivalent to the surface waves traveling on the crack face.

V. CONCLUSIONS AND FUTURE WORK

We have investigated the interaction of low frequency SH0 waves with through-thickness cracks or slits. Finite element studies confirmed by experiments show that in this frequency regime, short range scattering is strongly affected by diffraction phenomena. Studies on the influence of the crack length and source and measurement position on the measured reflection revealed the focusing of energy by the crack in the backscattered direction. A study of the influence of the crack length on the diffracted field shows that it consists of components arising from diffraction from the crack tips and radiation from Rayleigh-like waves traveling along the crack faces.

Theoretical analysis of the scattering phenomenon shows that a simple diffraction model of assuming uniform shear sources on the insonified face can yield very good results for cracks as long as seven times the wavelength considered. Investigation of the diffracted field revealed systematically the interference between the primary and secondary diffraction and showed that the waves traveling along the crack face are indeed the symmetric surface waves of rectangular ridge waveguides, which correspond closely to Rayleigh waves.

From the guided wave imaging perspective, these results provide a simple estimate for the far-field values for a given operating frequency thickness and crack length. The strong presence of diffraction means that more information may be received by a transducer array than would be contributed by specular reflection alone. An understanding of the physics of the scattering, such as the reverberation along the crack face, will aid development of imaging procedures. Future work with through-thickness cracks is directed towards understanding the nonsymmetric incidence problem.

[1]D. Alleyne, B. Pavlakovic, P. Cawley, and M. J. S. Lowe, "Rapid long range inspection of chemical plant pipework using guided wave," Insight **43**, 93–96 (2001).
[2]P. Wilcox, M. Evans, B. Pavlakovic, D. Alleyne, K. Vine, P. Cawley, and M. Lowe, "Guided wave testing of rail," Insight **45**, 413–420 (2003).
[3]P. Wilcox, "Omni-directional guided wave transducer arrays for the rapid inspection of large areas of plate structures," IEEE Trans. Ultrason. Ferroelectr. Freq. Control **50**, 699–709 (2003).
[4]J. Krautkramer and H. Krautkramer, *Ultrasonic Testing of Materials* (Springer-Verlag, Berlin, 1983).
[5]S. Dixon, C. Edwards, and S. B. Palmer, "High accuracy non-contact ultrasonic thickness gauging of aluminium sheet using electromagnetic acoustic transducers," Ultrasonics **39**, 445–453 (2001).
[6]M. G. Silk, "The use of diffraction-based time-of-flight measurements to locate and size defects," Br. J. Non-Destr. Test. **26**, 208–213 (1984).
[7]J. A. G. Temple, "Time-of-flight inspection: Theory," Ann. Nucl. Energy **22**, 335–348 (1983).
[8]A. Demma, P. Cawley, M. J. S. Lowe, A. G. Roosenbrand, and B. Pavlakovic, "The reflection of guided waves from notches in pipes: A guide for interpreting corrosion measurements," NDT & E Int. **37**, 167–180 (2004).
[9]J. Davies, F. Simonetti, M. J. S. Lowe, and P. Cawley, "Review of synthetically focused guided wave imaging techniques with application to defect sizing," in *Review of Progress in Quantitative NDE*, edited by D. O. Thompson and D. E. Chimenti (American Institute of Physics, New York, 2005), Vol. **25**, pp. 142–149.
[10]Y. H. Pao and C. C. Mow, *Diffraction of Elastic Waves and Dynamic Stress Concentrations* (Crane Russak, New York, 1973).
[11]J. D. Achenbach and A. K. Gautesen, "Geometrical theory of diffraction for three-D elastodynamics," J. Acoust. Soc. Am. **61**, 413–421 (1977).
[12]J. D. Achenbach, L. Adler, D. Kent Lewis, and H. McMaken, "Diffraction of ultrasonic waves by penny-shaped cracks in metals: Theory and experiment," J. Acoust. Soc. Am. **66**, 1848–1856 (1979).
[13]J. D. Achenbach, A. K. Gautesen, and H. Mcmaken, *Ray Methods for Waves in Elastic Solids* (Pitman Books Ltd., London, 1982).
[14]R. J. Brind, J. D. Achenbach, and J. E. Gubernatis, "High-frequency scattering of elastic waves from cylindrical cavities," Wave Motion **6**, 41–60 (1984).
[15]J. E. Gubernatis, E. Domany, J. A. Krumhansl, and M. Huberman, "The Born approximation in the theory of the scattering of elastic waves by flaws," J. Appl. Phys. **48**, 2812–2819 (1977).
[16]J. E. Gubernatis, "Long-wave approximations for the scattering of elastic waves from flaws with applications to ellipsoidal voids and inclusions," J. Appl. Phys. **50**, 4046–4058 (1979).
[17]S. K. Datta, "Diffraction of plane elastic waves by ellipsoidal inclusions," J. Acoust. Soc. Am. **61**, 1432–1437 (1977).
[18]S. Datta, "Scattering of elastic waves," Mech. Today **4**, 149–208 (1978).
[19]T. Grahn, "Lamb wave scattering from a circular partly through-thickness hole in a plate," Wave Motion **37**, 63–80 (2003).
[20]S. K. Datta, A. H. Shah, and C. M. Fortunko, "Diffraction of medium and long wavelength horizontally polarized shear waves by edge cracks," J. Appl. Phys. **53**, 2895–2903 (1982).
[21]Z. Abduljabbar, S. K. Datta, and A. H. Shah, "Diffraction of horizontally polarized shear waves by normal edge cracks in a plate," J. Appl. Phys. **54**, 461–472 (1983).
[22]J. Paffenholz, J. W. Fox, X. Gu, G. S. Jewett, S. K. Datta, and H. A. Spetzler, "Experimental and theoretical study of Rayleigh-Lamb waves in a plate containing a surface-breaking crack," Res. Nondestruct. Eval. **1**, 197–217 (1990).
[23]S. W. Liu and S. K. Datta, "Scattering of ultrasonic wave by cracks in a plate," J. Appl. Mech. **60**, 352–357 (1993).
[24]J. J. Ditri, "Utilization of guided elastic waves for the characterization of circumferential cracks in hollow cylinders," J. Acoust. Soc. Am. **96**, 3769–3775 (1994).
[25]A. N. Norris and C. Vemula, "Scattering of flexural waves on thin plates," J. Sound Vib. **181**, 115–125 (1995).
[26]C. Vemula and A. N. Norris, "Flexural wave propagation and scattering on thin plates using Mindlin theory," Wave Motion **26**, 1–12 (1997).
[27]X.-M. Wang and C. F. Ying, "Scattering of Lamb waves by a circular cylinder," J. Acoust. Soc. Am. **110**, 1752–1763 (2001).
[28]X.-M. Wang, C. F. Ying, and M.-X. Li, "Scattering of antiplane shear waves by a circular cylinder in a traction-free plate," J. Acoust. Soc. Am. **108**, 913–923 (2000).
[29]C. H. Wang and F.-K. Chang, "Scattering of plate waves by a cylindrical inhomogeneity," J. Sound Vib. **282**, 429–451 (2005).
[30]B. A. Auld, "General electromechanical reciprocity relations applied to the

calculation of elastic wave scattering coefficients," Wave Motion **1**, 3–10 (1979).
[31]M. Castaings, E. Le Clezio, and B. Hosten, "Modal decomposition method for modeling the interaction of Lamb waves with cracks," J. Acoust. Soc. Am. **112**, 2567–2582 (2002).
[32]A. Demma, P. Cawley, and M. Lowe, "Scattering of the fundamental shear horizontal mode from steps and notches in plates," J. Acoust. Soc. Am. **113**, 1880–1891 (2003).
[33]O. Diligent, T. Grahn, A. Bostrom, P. Cawley, and M. J. S. Lowe, "The low-frequency reflection and scattering of the s_0 Lamb mode from a circular through-thickness hole in a plate: Finite element, analytical and experimental studies," J. Acoust. Soc. Am. **112**, 2589–2601 (2002).
[34]M. J. S. Lowe, P. Cawley, J.-Y. Kao, and O. Diligent, "The low-frequency reflection characteristics of the fundamental anti-symmetric Lamb wave a_0 from a rectangular notch in a plate," J. Acoust. Soc. Am. **112**, 2612–2622 (2002).
[35]D. N. Alleyne, M. J. S. Lowe, and P. Cawley, "The reflection of guided waves from circumferential notches in pipes," J. Appl. Mech. **65**, 635–641 (1998).
[36]M. Lowe, D. Alleyne, and P. Cawley, "The mode conversion of a guided wave by a part-circumferential notch in a pipe," J. Appl. Mech. **65**, 649–656 (1998).
[37]Y. Cho and J. L. Rose, "An elastodynamic hybrid boundary element study for elastic guided wave interactions with a surface breaking defect," Int. J. Solids Struct. **37**, 4103–4124 (2000).
[38]Y. Cho, D. D. Hongerholt, and J. L. Rose, "Lamb wave scattering analysis for reflector characterization," IEEE Trans. Ultrason. Ferroelectr. Freq. Control **44**, 44–52 (1997).
[39]J. J. Ditri, "Phase and energy velocities of cylindrically crested guided waves," J. Acoust. Soc. Am. **97**, 98–107 (1995).
[40]V. K. Kinra and B. Q. Vu, "Diffraction of Rayleigh waves in a half-space. I. Normal edge crack," J. Acoust. Soc. Am. **77**, 1425–1430 (1985).
[41]V. K. Kinra and B. Q. Vu, "Diffraction of Rayleigh waves in a half-space. II. Inclined edge crack," J. Acoust. Soc. Am. **118**, 3585–3594 (1986).
[42]B. Masserey and E. Mazza, "Analysis of the near-field ultrasonic scattering at a surface crack," J. Acoust. Soc. Am. **118**, 3585–3594 (2005).
[43]S. Rokhlin, "Diffraction of Lamb waves by a finite crack in an elastic layer," J. Acoust. Soc. Am. **67**, 1157–1165 (1980).
[44]A. N. Norris and Z. Wang, "Bending-wave diffraction from strips and cracks on thin plates," Q. J. Mech. Appl. Math. **47**, 607–628 (1994).
[45]P. Wilcox, "Modeling the excitation of Lamb and SH waves by point and line sources," in *Review of Progress in Quantitative NDE*, edited by D. O. Thompson and D. E. Chimenti (Plenum, New York, 2003), Vol. **23**, pp. 206–213.
[46]*ABAQUS v6.5 Analysis User's Manual* (2004).
[47]M. Drozdz, M. J. S. Lowe, E. Skelton, and R. Craster, "Modeling bulk and guided wave propagation in unbounded elastic media using absorbing layers in commercial FE packages," in *Review of Progress in Quantitative NDE*, edited by D. O. Thompson and D. E. Chimenti (American Institute of Physics, New York, 2007), Vol. **894**, pp. 87–94.
[48]M. Castaings and C. Bacon, "Finite element modeling of torsional wave modes along pipes with absorbing materials," J. Acoust. Soc. Am. **119**, 3741–3751 (2006).
[49]M. Castaings, C. Bacon, B. Hosten, and M. V. Predoi, "Finite element predictions for the dynamic response of thermo-viscoelastic material structures," J. Acoust. Soc. Am. **115**, 1125–1133 (2004).
[50]D. N. Alleyne and P. Cawley, "The interaction of Lamb waves with defects," IEEE Trans. Ultrason. Ferroelectr. Freq. Control **39**, 381–397 (1992).
[51]R. K. Chapman, "A system model for the ultrasonic inspection of smooth planar cracks," J. Nondestruct. Eval. **9**, 197–210 (1990).
[52]R. K. Chapman and J. M. Coffey, "A theoretical model of ultrasonic examination of smooth flat cracks," in *Review of Progress in Quantitative NDE*, edited by D. O. Thompson and D. E. Chimenti (American Institute of Physics, New York, 1984), Vol. **3**, pp. 151–162.
[53]R. K. Chapman, "Ultrasonic reflection from smooth flat cracks: Exact solution for the semi-infinite crack," in CEGB Report NW/SSD/RR/14/81., N.D.T Applications Centre, Scientific Services Department, Central Electricity Board, U.K., North Western Region (1981).
[54]C. B. Scruby, K. R. Jones, and L. Antoniazzi, "Diffraction of elastic waves by defects in plates: Calculated arrival strengths for point force and thermoelastic sources of ultrasound," J. Nondestruct. Eval. **5**, 145–156 (1986).
[55]F. A. Ravenscroft, K. Newton, and C. B. Scruby, "Diffraction of ultrasound by cracks: Comparison of experiment with theory," Ultrasonics **29**, 29–37 (1991).
[56]J. A. Ogilvy and J. A. G. Temple, "Diffraction of elastic wave by cracks: Application to time-of-flight inspection," Ultrasonics **21**, 259–269 (1983).
[57]S. C. Her and S. Z. Lu, "The diffraction of elastic waves on the tip of slots," NDT & E Int. **20**, 133–143 (2001).
[58]Yih-Hsing. Pao and Vasundhara. Varatharajulu, "Huygens' principle radiation conditions and integral formulas for the scattering of elastic waves," J. Acoust. Soc. Am. **59**, 1361–1371 (1976).
[59]J. D. Achenbach, "Reciprocity and related topics in elastodynamics," Appl. Mech. Rev. **59**, 13–32 (2006).
[60]P. Wilcox, "Modeling the excitation of Lamb and SH waves by point and line sources," Rev. Prog. Quant. Nondestr. Eval. **23**, 206–213 (2003).
[61]A. A. Oliner, "Waveguides for acoustic surface waves: A review," Proc. IEEE **64**, 615–627 (1976).
[62]P. E. Lagasse, I. M. Mason, and E. A. Ash, "Acoustic surface waveguides—analysis and assessment," IEEE Trans. Microwave Theory Tech. **21**, 225–236 (1973).

Immiscible displacement of oil by water in consolidated porous media due to capillary imbibition under ultrasonic waves

Tarek Hamida[a] and Tayfun Babadagli[b]
University of Alberta, Department of Civil and Environmental Engineering, School of Mining and Petroleum, 3-112 Markin CNRL-NREF, Edmonton, AB, Canada T6G 2W2

(Received 10 November 2006; revised 3 June 2007; accepted 13 June 2007)

Numerous studies done in the last four decades have demonstrated that acoustic stimulation may enhance recovery in oil reservoirs. This technology is not only technically feasible, but also serves as an economical, environmentally friendly alternative to currently accepted enhanced oil recovery (EOR) method. It requires low capital expenditure, and yields almost immediate improvement without any additional EOR agents. Despite a vast body of empirical and theoretical support, this method lacks sufficient understanding to make meaningful and consistent engineering predictions. This is in part due to the complex nature of the physical processes involved, as well as due to a shortage of fundamental/experimental research. Much of what the authors believe is happening within acoustically stimulated porous media is speculative and theoretical. This paper focuses on the effects of ultrasound on the interfacial forces between immiscible fluids. Capillary (spontaneous) imbibition of an aqueous phase into oil (or air)-saturated Berea sandstone and Indiana limestone samples experiments were conducted. Solutions of water, brine (15,000 and 150,000 ppm NaCl), anionic surfactant (sodium dodecyl diphenyloxide disulfonate), nonionic surfactant (alcohol ethoxylate) and polymer (xanthan gum) were prepared as the aqueous phase. Both counter-current and co-current geometries were tested. Due to the intrinsically unforced, gentle nature of the process, and their strong dependence on wettability, interfacial tension, viscosity and density, such experiments provide valuable insight into some of the governing mechanisms behind ultrasonic stimulation.
 [DOI: 10.1121/1.2756190]

PACS number(s): 43.35.Zc, 43.35.Bf, 43.35.Cg, 43.35.Ae [TDM] Pages: 1539–1555

I. INTRODUCTION

Applications of ultrasound range from enhanced oil recovery to well stimulation, in situ upgrading of oil, wellbore cleaning, and soil remediation. Acoustic energy may be delivered into a reservoir by in situ sonication, seismic vibrations, and pressure pulsing. In the case of in situ sonication, an acoustic emitter is lowered into the well bore, generating acoustic waves at a high intensity. The acoustic waves travel through the porous media, and excite the fluids mechanically. Seismic methods are applied via explosives, earthquakes, and surface vibrators, and are generally low frequency, high intensity methods of delivering compressional waves into reservoirs. Finally, pressure pulsing is a method by which sharp pressure waves at a particular frequency are hydraulically applied to the liquid in wells. The frequency is selected based on fluid and reservoir properties.[1,2]

Despite numerous promising field trials, laboratory experiments, and patents, the exact mechanism behind ultrasonic stimulation is still poorly understood. Most of the findings have been inconclusive with limited experimental verification. The reason for this is twofold. First, the problem is very complex, involving a superposition of several competing mechanisms. Second, it is not certain how far an acoustic wave propagates into the reservoir, nor how such propagation occurs. Ultrasonic applications are limited to the near-wellbore area due to the high attenuation through the rock or fluids. When using Biot's theory, one expects that the attenuation length of ultrasound at 20 kHz ranges between 2 and 10 cm.[3–6] As a consequence, most research in recent years has shifted to low energy, low frequency waves that can propagate several kilometers into the reservoir. Nevertheless, because dispersion of low frequency waves within porous media forms high frequency harmonics (ultrasonic noise) one still expects ultrasonic waves to be present in the reservoir.[7,8] Additionally, because of its very short wavelength, ultrasound may be more influential on the capillary dynamics within a pore than large wavelength alternatives, which dominate in the bulk response of the rock.

We first provide an extensive and critical literature survey on this topic, followed by a presentation of the results and analyses on the capillary imbibition experiments conducted under ultrasonic waves.

II. LITERATURE

The potential of ultrasound as a viable method to enhance oil recovery in mature fields was first experimentally demonstrated by Duhon[9] and Duhon and Campbell.[10] They performed a series of brine flood experiments on an oil-saturated, epoxy-coated sandstone disk. After applying ultrasound at frequencies between 1 and 5.5 MHz, they observed

[a]Now with Alberta Research Council, Edmonton, AB, Canada.
[b]Author to whom correspondence should be addressed. Electronic mail: tayfun@ualberta.ca

that ultrasonic energy did have considerable effect on displacement efficiency by creating a more uniform displacement front. Such enhancement was not noticeably dependent on initial oil saturation, and seemed to yield higher recovery with decreasing viscosity and frequency. They also noted a substantial drop in permeability ratio with ultrasonically stimulated waterfloods, implying a reduced mobility ratio and an enhancement in the sweep efficiency. To explain the observed increase in recovery, and the reduction in mobility ratios, they postulated that localized pressure surges during cavitation, as well as oscillating air bubbles, may force trapped oil into adjacent pores.

Chen[11] and Fairbanks and Chen[12] investigated the influence of ultrasonic energy (20 kHz and 10 W/cm^2) on the flow of water and oil through a stainless steel filter, through porous sandstone and through a capillary. They found that in the case of porous medium, ultrasound enhanced the percolation rate by a factor of 3. Chen also showed that the observed increase is only partially due to ultrasonic heating. In a later study, Fairbanks[13] presented three systems where introduction of ultrasound resulted in enhanced liquid flow through porous media. Such systems included (1) flow of crude oil through porous sandstone, (2) flow of oil filtrate though a porous stainless steel filter, and finally (3) flow of water from a filter to an evaporation surface during drying. In all three systems, ultrasonic stimulation increased the percolation rate of liquid in the porous material. Within Biot's frequency regime, the liquid flow changes from normal viscous flow to plug-type flow, thereby reducing the friction factor within pore throats. They also showed that there exists an optimal intensity at which the liquid filtration rate is maximized. Percolation of oil in different porous rock types was also investigated by Mikhailov *et al.*,[14] Neretin and Yudin,[15] and Dyblenko *et al.*[16]

Cherskiy *et al.*[17] applied ultrasound to core samples that were saturated with fresh water, and found that the permeability sharply increased almost immediately when a pulsed ultrasonic field (26.5 kHz) was applied. However, after shutting off the ultrasound, the permeability returned to its original value. When varying the intensity, Cherskiy found that the pulsed treatment improved the permeability up to 10–15 times as compared to continuous insonication. One possible explanation for the dramatic permeability increase is traveling waves along pore walls, which may cause fluid displacement similar to "peristaltic transport." This mechanism was first proposed by Ganiev *et al.*[18] They proposed that ultrasound deforms the wall of a pore, altering the radius of the pore. This vibration causes fluctuations in capillary pressure, as well as dilation of surface films. Unfortunately, they provide only a very succinct description of their model, and a few results. They were also not particular about the acoustic power required to cause such effect, and did not elaborate on the poroelastic properties of the porous medium. Their model was later simplified by Jaffrin and Shapiro[19] and Jaffrin *et al.*,[20] Shapiro *et al.*,[21] Yin and Fung,[22] Takabatake *et al.*,[23] Aarts and Ooms,[24] and Aarts *et al.*,[25] who derived close-form analytical solutions to the problem. Tsiklauri and Beresnev[26] and Tsiklauri[27] included the influence of non-Newtonian flow behavior into the model to account for the behavior of oil and polymers. Aarts and Ooms[24] showed that the method of peristaltic transport works only at ultrasonic frequencies, and that the intensity of the ultrasonic field must exceed 104 W/cm^2. Therefore, due to the high attenuation of ultrasound, such effect is only significant near the well bore.

Gadiev[28] introduced audible sound (40 Hz–15 kHz) to oil saturated unconsolidated sand packs and observed considerable increase in oil production rate and cumulative oil production. Additionally, he observed that sound decreases the surface tension of transformer oils and the viscosity of polyacrylamid solutions. Considering the duration of excitation, these effects may have been due to a temperature increase in the fluids. He postulated that this effect was caused by a phenomenon called "sono-capillary effect," by which the liquid level within a capillary is raised due to an additional pressure generated by compressional waves. In fact, at ultrasonic frequencies, cavitation may magnify this effect and cause a dramatic increase in the level of the meniscus within a narrow capillary. Such effect was extensively studied by numerous authors from Russia and Ukraine, most notably Prokhorenko *et al.*,[29] Rozin *et al.*,[30] Rozina and Rozin,[31] Rozin *et al.*,[32] Rozina,[33] and Dezhkunov and Leighton.[34] For an excellent coverage on cavitation and bubble dynamics under ultrasound, the interested reader is referred to Gaitan *et al.*[35] Gadiev[28] also noted in his paper that ultrasound can reduce the viscosity of high-polymeric liquids by up to 22%. In fact, prolonged exposure of polymer solutions to high-intensity ultrasound permanently reduces its viscosity. Gronroos *et al.*[36] demonstrated that ultrasound preferentially degrades larger carboxymethylcellulose (CMC) molecules, and that there is an optimal concentration at which degradation is most effective. Once all the larger molecules are degraded, the process ceases and stabilizes. Similar observations were made with xanthan gum.[37]

Neretin and Yudin[15] applied a continuous ultrasonic field to lose sand saturated with water or oil, and observed that both recovery rate and final recovery were noticeably increased (65% to 85%). Simkin and Surguchev[38] and Simkin[39] observed a gradual increase in oil droplet size when continuous ultrasound was applied. They credited this improvement to ultrasonically induced coalescence due to primary Bjerknes forces. Such coalescence may assist in accelerating gravity phase separation within porous media, and improve the relative permeability of oil. Bjerknes forces acting between particles can be attractive or repulsive depending on the droplet's location relative to the wave field.[40–42] The magnitude of such force depends on the density of the continuous phase, and the radius of the droplet. Unfortunately, there are no micromodel experiments to date that visually demonstrate droplet coalescence in a porous medium due to Bjerknes forces. Simkin *et al.*[38] demonstrated in a series of experiments that during elastic vibration, ultrasound is generated within oil-saturated core blocks, which accelerates the process of capillary imbibition. Schoeppel and Howard[43] treated various samples of crude oil-water emulsions with ultrasound, and observed a considerable acceleration in coalescence.

Nikolaevskii[7,44] reviewed some possible physical processes of acoustic and seismic stimulation, and speculated

that one possible mechanism is the so-called vibrocreep effect. Such nonlinear effect associated with viscoelastic resonance restores the phase permeability of dispersed oil ganglia by either coalescing or emulsifying the oil. At the same time, such elastic wave fields may considerably reduce capillary forces by vibrating, and consequently, breaking surface films adsorbed to pore walls. When taking colloidal rotation into account, they showed that it is possible to generate bimodal waves which manifest in secondary nonlinear ultrasonic vibrations. Such ultrasonic vibrations may mobilize oil droplets into adjacent pores, or may result in coalescence due to Bjerknes forces. Ultrasonic fields may also cause additional nonlinear effects such as in-pore turbulence, acoustic streaming and cavitation. Such effects are, however, only consequential at very high intensities. Dunin and Nikolaevskii[45] and Nikolaevskii and Stepanova[8] proposed a theory on the generation of ultrasonic waves as consequence of nonlinear effects associated with seismic and low frequency acoustic action in fluid saturated porous media. They claim that the attenuation and dispersion of seismic waves in porous or fractured porous media introduces additional vibration modes at much higher frequency (dominant frequencies). The physical mechanisms responsible for such wave spectrum transformations are dry friction in contacts, instability of viscoelastic oscillations, seismic energy pumping into rotational modes, and resonance of gas bubbles and oil droplets. These mechanisms are believed to improve oil recovery. Abrashkin *et al.*[46] derived a series of analytical equations describing the motion of a drop in an axially symmetric capillary with varying cross section in high frequency and low frequency acoustic fields, taking into account wettability and hysteresis. They assumed that at high frequency, viscous forces can be ignored, while at low frequency, viscosity becomes significant.

Nikolaevskiy *et al.*[47] provided an interpretation of a vibro-seismic recovery process describing the wave requirements, wave generation and propagation in oil saturated porous media. He found that one must determine a characteristic frequency depending on reservoir lithology, fluid saturation, and layer stratification. Such frequency could alter oil and water production characteristics and enhance oil production near the residual oil saturation, while increasing water production near immobile water saturation regions. Kuznetsov *et al.*[48] studied the effect of vibro-energy on waterflood displacement rates and relative permeability ratios. They observed an increase in the oil/water relative permeability ratios when vibration is applied. In a subsequent study Kuznetsov *et al.*[49] reported significant incremental oil recovery from wells in Russia when they were stimulated by vibro-energy, and pointed out that decreased water cut was caused by the reduction of water/oil interfacial tension and increase in the relative permeability of the oil. They argued that in some cases, oscillating pressure fields induced by acoustic waves can result in reduction of local pressures below the bubble point, thereby liberating dissolved gas. In fact, even at reservoir pressures much above the bubble point, alternating pressure fields with a wavelength exceeding that of the oil droplets may mobilize the phases because of the density contrast (effective gas drive). This theory was extensively developed by Vakhitov and Simkin[50] and Kuznetsov and Simkin.[51]

Graham[52,53] and Graham and Higdon[54,55] numerically studied the motion of fluid droplets in harmonically forced capillary tubes and constricted tubes subject to a mean pressure gradient. In the case of capillary tubes, they observed a significant enhancement in mobility for large droplets, i.e., droplet diameter exceeding the diameter of the capillary, especially when oscillatory forcing is strong, and the drop capillary number is low. Such enhancement is primarily associated with increased droplet deformation, and is dependent on frequency, amplitude and type of wave form. For constricted tubes, Graham and Higdon[54] showed that oscillatory forcing effectively "unplugs" the tube by deforming the droplet. Therefore, acoustic stimulation enables oil droplets to overcome the critical threshold capillary pressure, and consequently initiates percolation. They also identified the minimum oscillatory forcing required to cause such mobilization. Later, Graham and Higdon[56,57] considered the role of oscillatory forcing on flow through porous media. Graham and Higdon,[56] considered the effects of nonzero inertial forces on steady flow, and developed a numerical model based on the steady-state Navier-Stokes equations. They used two geometries to simulate a porous structure: constricted channels and an array of cylindrical capillaries. In both cases, they observed strong nonlinear flow patterns, which may yield to enhanced mobilization under oscillatory forcing. They also observed in-pore turbulence. Graham and Higdon[57] extended their earlier model to include unsteady velocity fields. The effectiveness of the percolation rate is a strong function of dimensionless oscillation amplitude. One interesting observation was that oscillation may retard the phase mobility of the lower viscosity component, while keeping the high viscosity phase unaffected. Such process therefore enhances the permeability of higher viscosity phases, and may prove to be an effective "oscillatory filter" capable of separating two fluids with different viscosities. Recently, Beresnev[58] developed an analytical model to predict the mobilization acceleration that is required to mobilize a nonwetting oil drop within successive pores, and found that the process is most efficient at low frequencies. Successful mobilization requires accelerations of several m/s^2 in order to overcome capillary entrapment, which is not currently possible in downhole acoustic tools ($\sim 0.1\ m/s^2$). The mobilization efficiency also depends on the relative position of the oil ganglia with respect to the pore throat.

In summary, ultrasonic radiation introduces mechanical vibrations, which strongly influence interfacial forces by enhancing momentum and heat transfer across the phase interfaces. The following mechanisms are believed to be responsible for the observed improvement in percolation of oil within porous media:

- Increasing the relative permeability of the phases by promoting phase separation.
- Due to nonlinear acoustic effects such as in-pore turbulence, acoustic streaming, cavitation, and perturbation in

TABLE I. Fluid properties of oleic and aqueous phases used in spontaneous imbibition experiments. All values were measured at standard atmospheric conditions. DOWFAX 2A1=Sodium Dodecyl Diphenyloxide Disulfonate. Tergitol 15-S-7=Alcohol Ethoxylate.

Fluid	Density[a] (g/cc)	Viscosity[b] (cp)	Surface tension[c] (dynes/cm)
Water	0.9982±0.0010	1.0±0.02	71.0±1.4
Water+150,000 ppm NaCl	1.1163±0.0010	1.20±0.06	69.9±1.4
Water+150,000 ppm NaCl	1.0096±0.0010	1.20±0.06	70.5±1.4
Water+1% DOWFAX 2A1	0.9997±0.0010	2.44±0.12	33.8±0.7
Water+3%DOWFAX 2A1	1.0027±0.0010	5.32±0.27	34.1±0.7
Water+5% DOWFAX 2A1	1.0058±0.0010	8.20±0.41	34.6+0.7
Water+0.1% TERGITOL 15-S-7	0.9982±0.0010	1.05±0.05	30.1±0.6
Water+0.5% TERGITOL 15-S-7	0.9982±0.0010	1.25+0.06	27.8+0.6
Water+1.0% TERGITOL 15-S-7	0.9981±0.0010	1.50±0.08	27.5±0.6
Water+0.03% xanthan gum	0.92±0.0010	15.00+0.75	68.0+3.4
Water+0.05% xanthan gum	0.93±0.0010	25.00+1.25	66.5+3.3
Water+0.1% xanthan gum	0.94±0.0010	42.00±2.10	65.0±3.3
Light mineral oil	0.8383±0.0050	46.5+0.5	31.5±0.6
Kerosene	0.768±0.0050	2.9±0.03	27.2+0.5
Crude oil (Husky)	0.8548±0.0050	19.0±0.5	30.2+0.6

[a]Weight-volume method using a 5 cm^3 syringe.
[b]Rotational viscometer (Fann 35A).
[c]DuNouy-type tensiometer.

local pressures, ultrasound reduces the adherence of wetting films onto the rock matrix. This effect is only relevant at high ultrasonic intensities.
- Reducing surface tension, density and viscosity as a consequence of heating by ultrasonic radiation. In the case of polymers, ultrasonic degradation may reduce the viscosity as well.
- Altering of rheological properties of non-Newtonian fluids.
- Enhancing mobilization of oil blobs due to mechanical vibration of pore walls (peristaltic fluid transport), by which fluid is "squeezed" into adjacent pores.
- Strengthening the adhesion of liquid films onto vibrating pore walls.
- Microemulsification of oil in the presence of natural or introduced surfactants.
- Coalescence and dispersion of oil drops due to the Bjerknes forces.
- Increasing rock permeability and porosity due to removal of fines, clays, paraffin wax and asphaltenes.
- Oscillation and excitation of capillary trapped oil drops due to pressure perturbations generated by cavitating bubbles and mechanical vibrations of rock and fluid.

These mechanisms, which are principally governed by capillary and viscous forces, depend on the frequency and intensity of the acoustic field, as well as on rock elasticity, fluid properties, porosity, cementation, and clay content. Frequency plays an important role in wave dispersion, attenuation and heat dissipation. At higher intensity, mechanical stresses, and therefore, temperature increase. As such, the destruction of deposits and films on pore walls, as well as the reduction of viscosity and interfacial tension, may only occur with high frequency/high intensity acoustic fields. Fluid properties, such as density, viscosity and surface tension directly affect the wave propagation, compressibility, and shear response. Porosity, cementation and clay content enhance the wave dispersion, and strongly attenuate Biot's slow wave.

More recently, the authors have reported the preliminary results on the effects of ultrasonic waves on the capillary imbibition recovery for different rock and fluid samples.[59–63] They observed that the ultrasonic energy positively affects the oil recovery depending on the interaction type (co- and counter-current manner) and interfacial tension between the immiscible phases. Their subsequent visualization studies revealed that considerable changes at the interface may occur under ultrasonic waves.[62,63] This paper reports the final observations and analysis for a wide variety of oleic and aqueous phases obtained after those preliminary results.

III. EXPERIMENTAL STUDY FOR CAPILLARY IMBIBITION TESTS

In this study, a series of capillary imbibition experiments under ultrasound were conducted on sandstone and limestone plugs using a focused ultrasonic horn, as well as an ultrasonic bath. Spontaneous (capillary) imbibition is a gentle, steady process that is based on capillary suction.[64] Generally, capillary suction relies on both *rock properties* (matrix permeability, size, pore geometry, wettability, heterogeneity and boundary conditions), and *fluid properties* (viscosity of the phases and interfacial tension, and may strongly vary with aging and chemical treatment.[64–68] Unlike forced imbibition or drainage, spontaneous imbibition benefits from the absence of viscous (and gravitational forces in the case of small core samples), making it a suitable experiment for highlighting the role of interfacial forces.

A. Rock and fluid properties

A total of more than 80 cylindrical core plugs were cut from the same blocks of Berea sandstone, and Indiana lime-

stone outcrop samples, and saturated for 48 h with either mineral oil or kerosene using a vacuum desiccating chamber. Diameters and lengths of the cores were in the range of 2.5–2.52 and 6.4–7.8 cm, respectively. After cutting the core samples, they were washed with water and dried at 80 °C for at least two days, after which they were cooled at ambient conditions. The average permeability and porosity of the sandstone cores were determined to be 300 md and 21%, respectively. The average permeability of Indiana limestone was measured to be 7 md and its average porosity was 17%. Porosity values were estimated by saturating dry cores in water and oil, and measuring the change in weight.

All cores with the exception of air-water experiments were used only once to avoid undesirable alterations in wettability and grain structure due to contamination, cleaning, and matrix damage generated by ultrasonic vibrations. For air-water spontaneous imbibition, we reused the same cores to minimize the error due to clay swelling. Water saturated cores were dried in an oven at 80 °C for one day. Some of the samples were coated with epoxy from all sides except one of the ends to obtain truly counter-current imbibition. Such experiments will be labeled as "coated."

The imbibition behavior of three types of saturation fluids was studied: light mineral oil, kerosene and air. To cover a broad range of viscosity, density, interfacial tension, and wettability cases, solutions of water, brine (15,000 and 150,000 ppm NaCl), anionic surfactant (sodium dodecyl diphenyloxide disulfonate, DOWFAX 2A1), nonionic surfactant (alcohol ethoxylate, tergitol 15-S-7) and polymer (xanthan gum) were prepared as the aqueous phase. The properties of the fluids and corresponding absolute error at standard conditions (no ultrasound) are presented in Tables I and II. The interfacial tension and surface tension between aqueous and oleic phase was measured using a standard tungsten ring tensiometer (the Du Nouy method). Viscosity values were either measured using a rotational viscometer, or were obtained from the manufacturer (Canon Instruments). Density was determined by weighing a syringe filled with 5 cm^3 of fluid. To avoid ultrasonic cavitation close to the core walls, all solutions were carefully de-aerated in vacuum. We noticed that the effect of cavitation is more severe during air-water experiments, because bubbles block the pores at the outer wall of the core plug.

Reduction of interfacial tension was achieved by adding different volumes of anionic and nonionic surfactant to de-aerated water. The critical micelle concentration (CMC) of DOWFAX 2A1 (anionic), DOWFAX 3B0 (anionic) and Tergitol 15-S-7 (nonionic) was measured to occur at a concentration of about 1, 3, and 0.004 wt%, respectively. Xanthan gum polymer concentrations of 0.03, 0.05, 0.09, 0.1 and 0.15 wt% were applied to increase the viscosity of the aqueous solution. Brine solutions of de-aerated water with 15,000 and 150,000 ppm NaCl were mixed to explore the effect of alkalinity on spontaneous imbibition, especially in high clay-content Berea sandstone.

We applied an oil based coloring agent to both kerosene and mineral oil to distinguish the two phases. Such dye, although applied at very low concentrations, may change the wettability characteristics of the cores slightly. This effect is assumed to be the same for all samples, and therefore, should not contribute considerably to the observed variations.

TABLE II. Interfacial tension data for all fluid pairs used in the experiments. All values were measured at standard atmospheric conditions using a DuNouy-type tensiometer.

Aqueous phases	Air and oleic phases	Interfacial tension (dyne/cm)
Water	Air	71.0±1.4
1%DOWFAX2A1	Air	33.8±0.7
3% DOWFAX 2A1	Air	34.1±0.7
5% DOWFAX 2A1	Air	34.6±0.7
0.1%TERGITOL15-S-7	Air	30.1±0.6
0.5%TERGITOL15-S-7	Air	27.8±0.6
1.0%TERGITOL15-S-7	Air	27.5±0.6
150,000 ppm NaCl	Air	69.9±1.4
15,000 ppm NaCl	Air	70.5+1.4
Water	Light MO	61.8±1.2
150,000 ppm NaCl	Light MO	46.2±0.9
15,000 ppm NaCl	Light MO	53.2±1.1
1% DOWFAX 2A1	Light MO	10.1±0.2
3% DOWFAX 2A1	Light MO	11.2±0.2
5% DOWFAX 2A1	Light MO	12.0±0.2
0.1%TERGITOL15-S-7	Light MO	8.6±0.2
0.5%TERGITOL15-S-7	Light MO	8.2±0.2
1.0%TERGITOL15-S-7	Light MO	8.1±0.2
0.05% xanthan gum	Light MO	56.0±1.1
0.1% xanthan gum	Light MO	53.3±1.1
Water	Kerosene	40.7±0.8
5% DOWFAX 2A1	Kerosene	10.4±0.2
1.0% TERGITOL	Kerosene	6.9±0.1
3% DOWFAX 2A1	Crude Oil (Husky)	9.1±0.2
150,000 ppm NaCl	Crude Oil (Husky)	24.6±0.5

B. Experimental setup

The experimental setup is shown in Figs. 1(a) and 1(b). Cores were placed inside imbibition tubes with a graduated cylinder allowing volume measurements with a precision of ±0.1 cm^3. A homogeneous ultrasonic field was generated using a bench-top Branson ultrasonic bath (cleaner) operating at 40 kHz and 2 kW. To investigate the effect of concentrated sonication, we also employed an ultrasonic horn capable of generating a frequency of 20 kHz and power up to 250 W/cm^2. The horn was equipped with a 3/4 in. sapphire coated titanium tip. To ensure consistent insonication, we made sure that all experiments were run at the same power settings. The peak-to-peak displacement amplitude of the tip at each setting is shown in Fig. 2, and was obtained from the manufacturer. The power used during the experiments is 25 W for Setting 2 and 45 W for Setting 5.

The temperature within the ultrasonic bath increases with exposure time due to the high power output of the horn. This increase may influence the experimental results slightly by reducing the viscosity and interfacial tension of the fluids. We observed that temperature increases quasi-logarithmically with time. In a period of 750 min, the temperature within the ultrasonic bath rose by 5 °C for Setting 2 [LO], and by 8 °C for Setting 5 [HI] intensity. Expansion of

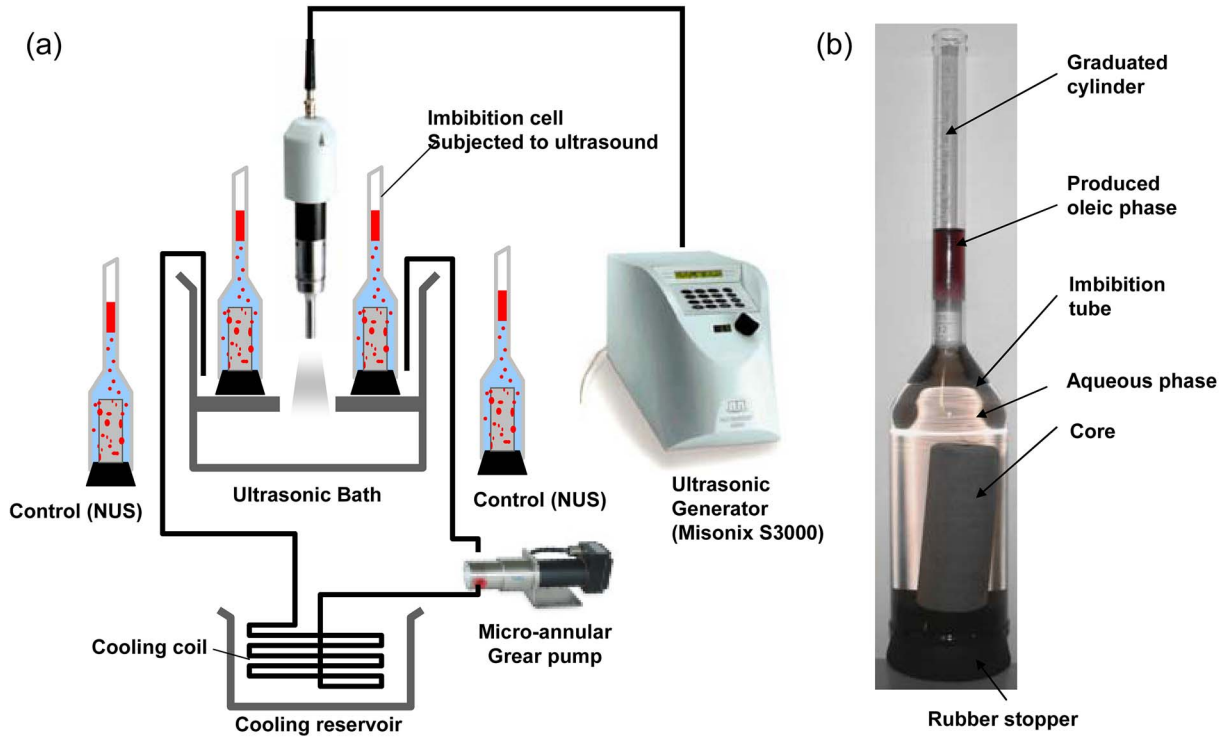

FIG. 1. (Color online) (a) Schematic of the experimental setup of imbibition experiments, (b) the glass imbibition cell used to collect oil effluent from a saturated core immersed in an aqueous phase.

the pores and alterations of fluid properties due to this temperature change is therefore negligible. Nonetheless, we decided to add a water circulation system to maintain room temperature during experiments requiring an extended period of time.

Since all samples were positioned equidistantly from the horn, and made use of the same imbibition cells, attenuation due to the carrying fluid and the imbibition cells is believed to be minor. Each experiment was repeated with and without ultrasound (control experiment using similar core from the same block). The relative performance between the ultrasonically stimulated performance and the control was then compared and analyzed.

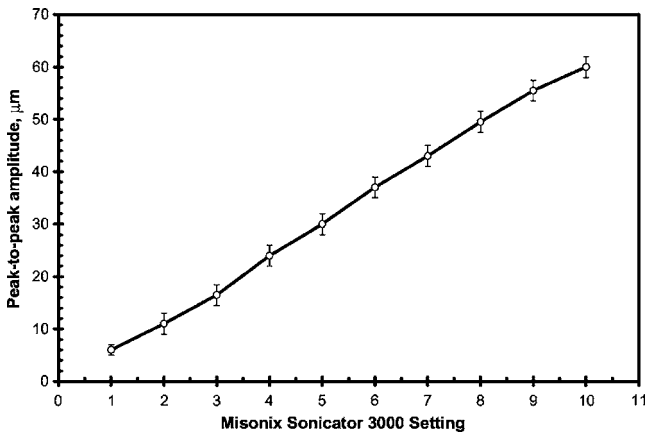

FIG. 2. Peak-to-peak amplitude of a 3/4 in. ultrasonic horn versus setting number (Misonix Sonicator 3000).

C. Procedure

Dry cores were placed within a desiccator filled with the oleic phase, and allowed to saturate under vacuum for two days. After saturation, cores were weighed and placed in the imbibition cell. After securely sealing the cell with a rubber stopper, the aqueous phase was slowly introduced via a funnel. The oil recovery was monitored versus time with and without ultrasound. Ultrasound was applied at two intensities: 25 W [Setting 2] and 48 W [Setting 5]. Occasionally, the cores were weighed using a string attached to a portable scale (via a hook) to verify that the volumes measured from the graded imbibition tube match the change in weight due to fluid influx. A flow chart of the experimental strategy is shown in Fig. 3.

In some of the surfactant experiments, we observed a stable emulsion, which slightly increased the measured volume of produced fluid. In such cases, volumes were corrected from the weight of the cores. Error in recorded volume is approximately ±2%. For every reading, the cores were carefully shaken to liberate any oil drops that remained attached to the core wall. On average, the volumes obtained by weighing the cores agree with the volumetric recording to approximately 3% accuracy.

For air-water spontaneous imbibition experiments, high precision Scout Pro scales were used to measure water influx into core samples. Core samples where suspended via a stainless wire into an ultrasonic bath, and the resulting change in weight due to water influx was measured at intervals of 5 s. The resulting data were then transferred into an Excel sheet using a LABVIEW data acquisition system. Pore

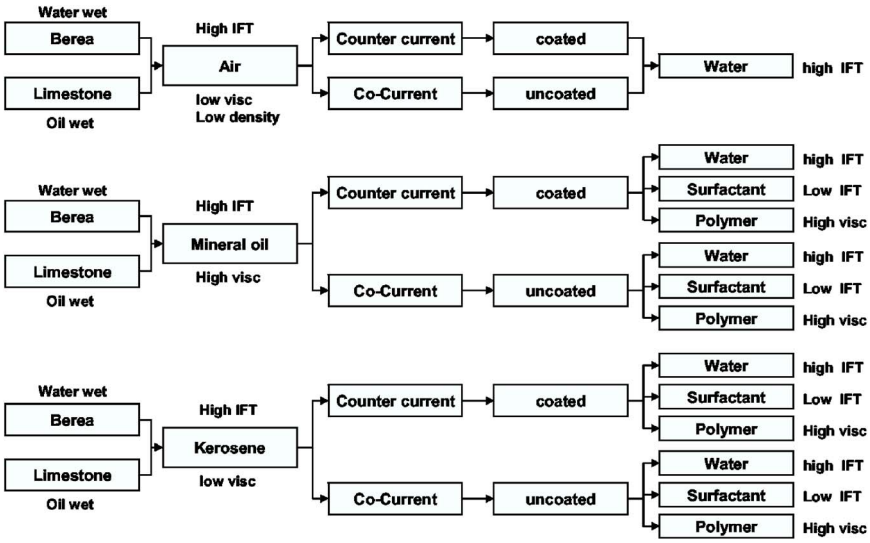

FIG. 3. (Color online) Flow chart illustrating all spontaneous imbibition experiments with different fluid pairs, rock types and boundary conditions.

volume measurements were performed by vacuum saturating all cores with water for two days.

IV. RESULTS AND DISCUSSION

A cross-correlation comparison plot of final recovery without ultrasound versus final recovery with ultrasound for all spontaneous imbibition experiments given in Fig. 3 is shown in Fig. 4. The solid 45° line represents the case when the response of capillary imbibition under ultrasound equals that of the control (No ultrasound, NUS). Dashed lines at 5% increments indicate the percent deviation from the control. It can be seen that ultrasound significantly enhanced the spontaneous imbibition recovery of oil for most fluid pairs (25 runs). Only eight experiments yielded a reduction in recovery when ultrasound was applied. Recovery changes within ±5% should be considered as unchanged, because they fall within the nominal error discussed previously. This section will present the results of each fluid pair, and discuss possible origins of the observed behavior.

A. Water into dry core samples

1. Berea sandstone

Both the recovery rate and final recovery for counter-current air-water imbibition into Berea sandstone (Fig. 5(a)) was significantly enhanced under ultrasound, yielding an additional recovery of up to 10% PV. The opposite was true for co-current imbibition, reducing the ultimate recovery by 5% PV while leaving the recovery rate unchanged.

2. Indiana limestone

A similar response was noticed with air-water imbibition into less water-wet limestone (Fig. 5(b)). The recovery from co-current spontaneous imbibition of water into dry limestone was reduced for both the ultrasonic bath and under ultrasound from the horn. It appeared that the reduction was more significant with the ultrasonic bath (40 kHz) than with the ultrasonic horn (20 kHz), implying a frequency dependence during the process. Higher frequency ultrasound may be more effective at mobilizing air bubbles within the core.

Recovery rate remained unchanged. The opposite was observed during counter-current imbibition of water into

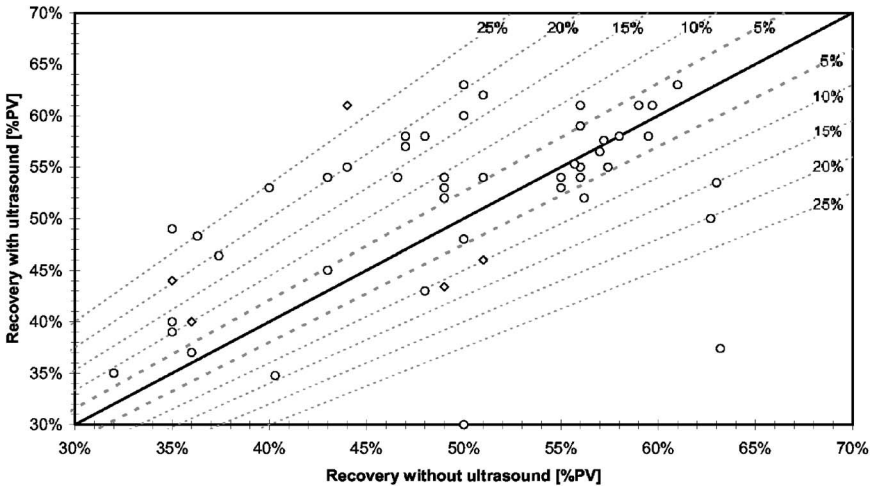

FIG. 4. Summary of final recovery with and without ultrasound for all fluid pairs. The 45° line in (b) represents the case when the response equals that of the control. Dashed lines signify the percent deviation (%) from the control case. Recovery below ±5% deviation from the 45° line is believed to be within the uncertainty range of imbibition experiments, and therefore assumed to be unaffected by ultrasound (PV=Pore Volume of the rock, equivalent to the original oil in place).

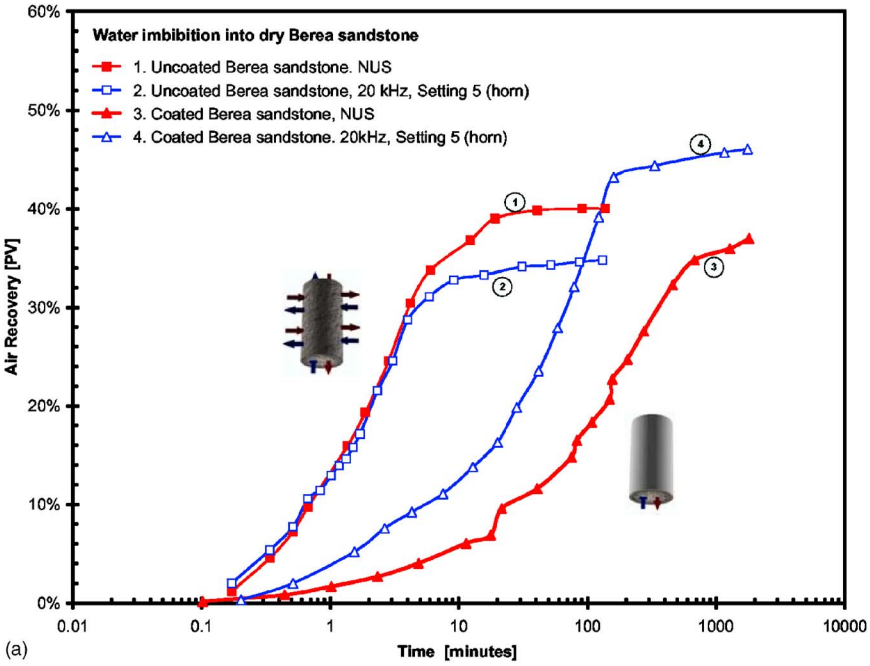

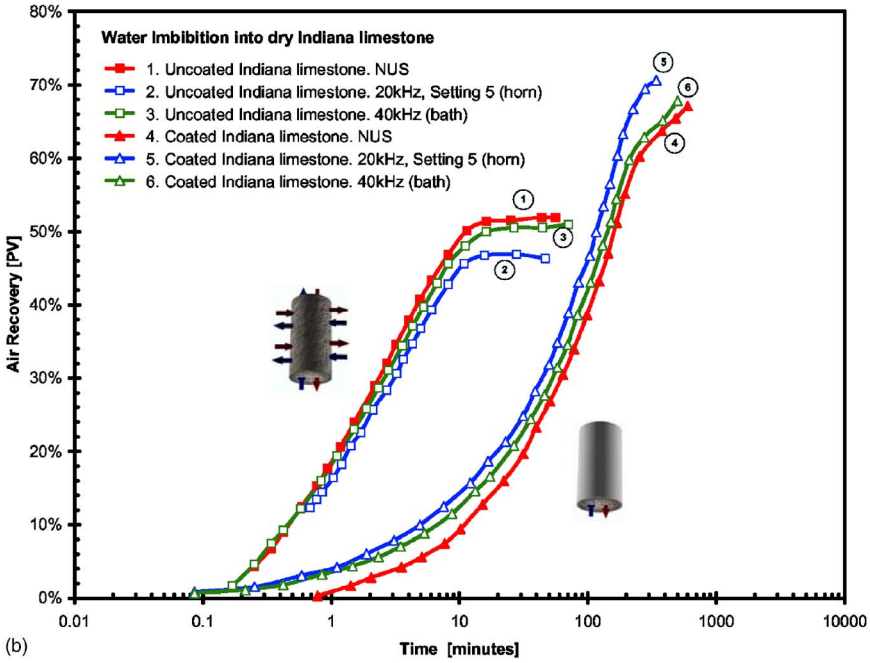

FIG. 5. (Color online) Air recovery versus imbibition time of water imbibing into dry (a) Berea sandstone and (b) Indiana limestone. Blue and green curves represent the imbibition performance under ultrasound with a horn (20 kHz, Setting 5) and ultrasonic bath (40 kHz), respectively. Red curves represent the control without the application of ultrasound. Both co-current and counter-current scenarios are shown (modified from Refs. 58 and 62).

limestone. Here, recovery is progressively improved with frequency, yielding an additional recovery of up to 7% with the ultrasonic horn. The recovery from the ultrasonic bath was comparable to the control case (NUS).

3. Discussion

The apparent dependence on the displacement process (boundary), as well as on frequency, is primarily due to the high density contrast and surface tension between air and water. In the case of co-current displacement, the absence of boundaries eases bubble migration outward from the center of the core, with a preferential upward flow due to buoyancy. Water influx occurs from all sides, and is initially fastest at the bottom end. On the other hand, during counter-current imbibition with only the bottom end open to flow, air is forced to migrate opposite to the buoyant force. Therefore, such process is predominantly capillary driven, generating a "piston-type" displacement front, in which water moves upward, and air moves downward.

The relative contribution of the dominant forces changes in the presence of ultrasonic radiation. One of the possible mechanisms behind the enhancement or reduction in recovery under co-current and counter-current spontaneous imbibition is due to air bubble vibration and streaming. Bubbles strongly affect the acoustic properties of liquids due to the large contrast in compressibility and viscosity of the gas and liquid. Predominant features in a liquid with bubbles are high dispersion and low sound speeds over a wide range of frequencies. Bubbles trapped in porous media may oscillate with ultrasound, and absorb most of the ultrasonic

energy.[69,70] For co-current spontaneous imbibition under ultrasound, bubble vibrations within the pore generate an oscillating pressure field, which is out of phase with the liquid vibration. Such process prevents bubbles from migrating into adjacent pores, and therefore reduces both the percolation rate, as well as the final recovery. On the other hand, for counter-current imbibition with only the bottom end subjected to the aqueous phase, the piston-like displacement front creates a stable interface between air and water, and only residual air trapped in pores oscillate under ultrasound. As observed by Aarts *et al.*,[25] compressibility of the fluids within porous media has a strong influence on net induced flow caused by transversal wave deformations of the pore walls. Higher density contrast yields to enhancement in induced fluid flow. Such effect is magnified with fluid pairs that have high interfacial tension, because deformations in pore walls cause fluctuations in capillary pressure. As a consequence of the counter-current nature of the displacement, the vibrational energy applied on the residual bubbles may improve air mobilization (slip effect), and accelerate the percolation process. In the case of limestone, which is less water-wet and has a more heterogeneous pore structure, the rate of water invasion is reduced and the water film along pore walls is thinner. Consequently, less air is trapped in pores, and both the effect of bubble oscillation and capillary pressure are suppressed. Although we observe the same imbibition trend, with decreasing production at different frequencies of ultrasound for co-current flow, and increasing production for counter-current flow, the overall response is not as extreme as for water-wet sandstone.

Additionally, unlike limestone, the rate of recovery for counter-current imbibition into sandstone is dramatically improved. We speculate that such recovery rate improvement is due to a positive enhancement due to water wettability. For highly water-wet sandstone, the rate of water invasion is high, resulting in more pronounced water films along pore walls. Interactions between such water films and resonating air bubbles may yield more effective air mobilization.

B. Water and brine into mineral oil and kerosene saturated rocks

1. Water

Figure 6 shows the imbibition recovery performance of water into Berea sandstone, saturated with either light mineral oil or kerosene. Both co-current (Fig. 6(a)) and counter-current (Fig. 6(b)) boundary conditions were investigated. When all sides are open to flow, we observed an improvement in recovery rate with both light mineral oil and kerosene. The final recovery for light mineral oil improved by an incremental 20% PV as compared to the control experiment, while the recovery of kerosene remained relatively unchanged. For the counter-current boundary condition, on the other hand, the recovery under ultrasound deteriorated for both light mineral oil and kerosene. In fact, while both recovery and recovery rate for light mineral oil remained unaltered under ultrasound, the recovery performance of kerosene depreciated dramatically by over 22% PV.

When the mineral oil-water control sample was introduced to the ultrasonic field, we observed an additional 4% incremental recovery (tertiary recovery), while the production from the kerosene control remained unchanged. On the other hand, after turning off the ultrasound for the counter-current kerosene sample, we observed a dramatic jump in production, which stabilized at the final recovery value obtained from the control. The differing results observed under counter-current and co-current imbibition for kerosene and light mineral oil may be due to the dissimilar wettability properties to silicates, as well as the difference in interfacial tension.

During co-current displacement, such difference manifests itself in the formation of surface films and ganglia coalescence. Light mineral oil, having an interfacial tension of 61.8 dynes/cm, does not easily coalesce in the presence of water when no ultrasound is applied. Under an ultrasonic field, however, coalescence of ganglia is enhanced due to Bjerknes forces, resulting in a higher ultimate recovery. Since kerosene has a lower interfacial tension than light mineral oil, the effect of ultrasonically induced coalescence is less pronounced, resulting in a similar ultimate recovery as with the control case. The enhancement in recovery rate for both kerosene and light mineral oil can be explained by the fact that surface films, which are preventing the mobilization of oil droplets into neighboring pores, are destroyed by ultrasound. It must be noted that the effect of clays in Berea sandstone ($>3\%$) may also influence the relative performance of the fluid pairs under ultrasound. Ultrasound may mobilize clays or reduce clay swelling, resulting in an increase in water inflow and oil expulsion.

2. Brine

In order to eliminate the effect of clay swelling, we ran a series of experiments with brine at two concentrations of NaCl; i.e., 15,000 and 150,000 ppm NaCl aqueous solutions. Figure 7 presents recovery cross-comparison curves for brine imbibition into Berea sandstone saturated with light mineral oil. In the case of 15,000 ppm NaCl brine solution, we investigated the effect of two different intensities on the imbibition process. The control experiment (nonultrasonic, NUS) recovered 35% original oil-in-place (OIIP) at a rate of 0.06%/min. Ultrasound at setting 2 did not dramatically alter the recovery rate, but increased the ultimate recovery by an additional 10% OIIP. Ultrasound at setting 5 yielded an improvement in final recovery up to and additional 9% OIIP. It can be concluded from these results that the final recovery is proportional to the ultrasonic intensity applied, while the recovery rate is relatively unaffected by ultrasonic vibrations. One possible mechanism responsible for this additional recovery is the generation of a stable displacement front due to pore vibrations and localized pressure perturbations, leaving less oil unswept during the process. On the other hand, when we swapped the cores, so that the unsonicated control cores were subjected to ultrasound and the ultrasonically stimulated cores were removed from the ultrasonic field, no considerable increase in recovery was observed. Consequently, ultrasound did not effectively mobilize oil once it was trapped in the pores. In summary, ultrasonic vibrations do assist in the dynamic process of mobilizing trapped oil blobs

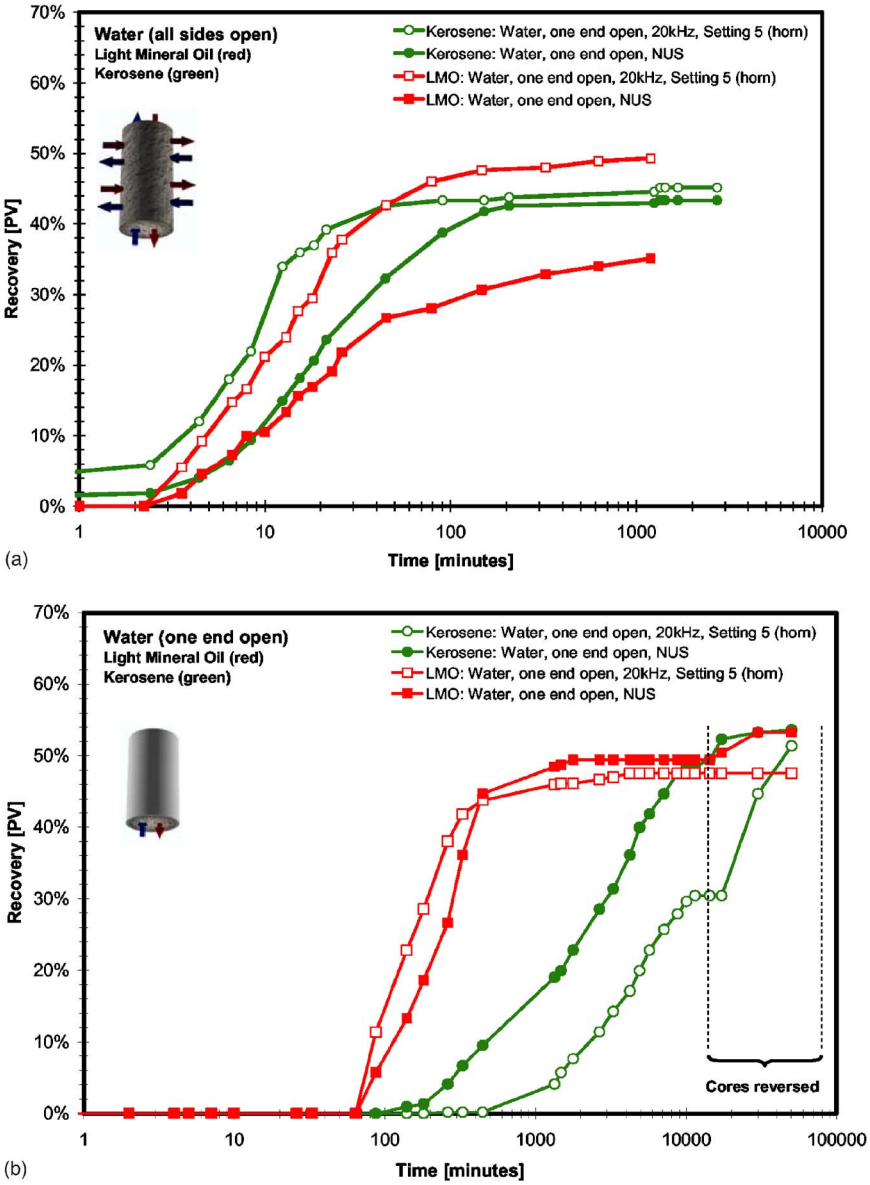

FIG. 6. (Color online) Oil recovery versus time during spontaneous imbibition of water into kerosene and light mineral oil saturated Berea sandstone at two intensities of ultrasound for two boundary conditions: (a) all sides open (uncoated) (modified from Ref. 61), (b) bottom end open (coated). The dashed interval outlines the recovery when imbibition cells are reversed (modified from Ref. 62).

during water displacement, but do not serve as an effective means to improving recovery after water flooding.

Raising the salinity of brine to 150,000 ppm NaCl had a considerable impact on the performance of ultrasonically stimulated imbibition. It can be seen that the increase in salinity improved both the recovery rate and the final recovery of the process, resulting in up to 15% PV improvement in final oil recovery, compared to 150,000 ppm NaCl brine (Fig. 7). Introducing ultrasound to highly saline brine resulted in an additional 20% recovery, leveling off at a final recovery of 63% OOIP. This improvement is primarily due to the reduction in the effect of clay within the Berea sandstone. Fine clay particles may influence the liquid-liquid interactions within pores. Clay particles absorb the imbibing water, reducing the water mobility within the pores. Lower water invasion results in reduced oil mobilization. Swollen clay may also act to considerably dissipate the ultrasound. Meanwhile, the absence of swollen clay particles at high salinity, improves water invasion into pores, resulting in better migration of oil droplets, and possibly improved coalescence. Finally, high energy acoustic fields may also resuspend fines and particles, and assist in reducing pore-throat blockage.

In fact, after aging samples in light mineral oil for one month, we observed a considerable reduction in recovery rate as well as ultimate recovery (Fig. 8). The lowered wettability to water effectively diminished the water invasion due to imbibition, causing less oil to be mobilized within pores. We observed a minor improvement of final recovery under ultrasound, but a strong enhancement of recovery rate at early stages.

C. Anionic and nonionic surfactant solutions

1. DOWFAX 3B0

Figure 9 shows a cross-comparison plot of the performance of 1% and 5% alkyldiphenyloxide disulfonic acid (DOWFAX 3B0) solutions imbibing into mineral oil saturated Berea sandstone. Continous vibrations at settings 2 and 5 were applied using an ultrasonic horn. It can be seen that for 1% DOWFAX 3B0, i.e., below the critical micelle con-

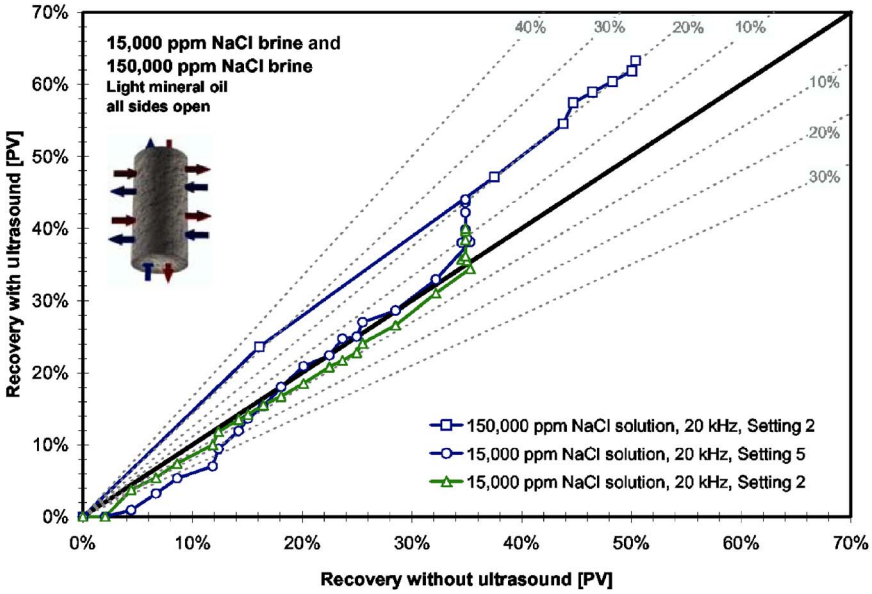

FIG. 7. (Color online) Cross-comparison plot of the spontaneous imbibition of 15,000 and 150,000 ppm NaCl aqueous solution into light mineral oil saturated Berea sandstone (all sides open) at two intensities of ultrasound, as compared to no ultrasound. The 45° line represents the condition when the response under ultrasound equals that of the control (no ultrasound). Dashed lines signify the percent (%) deviation from the control.

centration (CMC), the improvement of recovery under ultrasound is minimal, with higher recovery observed at higher intensity. Recovery of oil using 5% surfactant (above CMC) resulted in a substantial increase in ultimate recovery and production rate, compared with the control (NUS). The incremental recovery consistently improved with increasing intensity setting, yielding and incremental recovery of 20% PV at setting 2, and 28% PV at setting 5.

2. DOWFAX 2A1

Based on these results, another variant of alkyldiphenyloxide disulfonic acid, namely DOWFAX 2A1, was tested as well. Imbibition curves for concentrations of 1%, 3% and 5% DOWFAX 2A1 into light mineral oil are presented in Fig. 10. Unlike observations made with DOWFAX 3B0, changes in ultimate recovery varied by less than ±10%, which is close to the expected uncertainty margin associated with these imbibition experiments. The recovery rate, however, was raised by up to 35%, clearly surpassing the expected limit due to uncertainty.

After aging the sandstone samples for one month, we observed that for concentrations close to the CMC, the recovery rate improved by up to 60% (Fig. 11). At higher concentrations (above the CMC), however, recovery rates did not seem to alter considerably under ultrasound. At all concentrations the ultimate recovery was only marginally enhanced by up to 8% as compared to the control experiments.

3. Tergitol 15-S-7

Since both DOWFAX 3B0 and DOWFAX 2A1 are anionic surfactants which exhibit low surfactant adsorption to silicates, we decided to investigate the effect of nonionic surfactant in Berea sandstone, as well. The nonionic surfactant Tergitol 15-S-7 (Alcohol ethoxylate) was applied to light mineral oil saturated Berea sandstone samples.

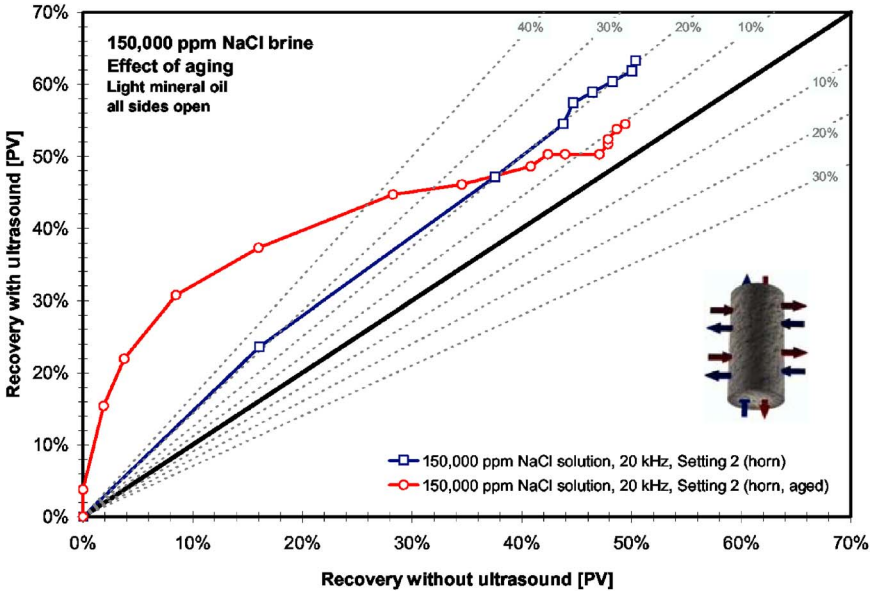

FIG. 8. (Color online) Cross-comparison plot of the spontaneous imbibition under ultrasound of 150,000 ppm NaCl brine solution into light mineral oil saturated Berea sandstone (all sides open) before and after aging for one month. The 45° line represents the condition when the response under ultrasound equals that of the control. Dashed lines signify the percent (%) deviation from the control.

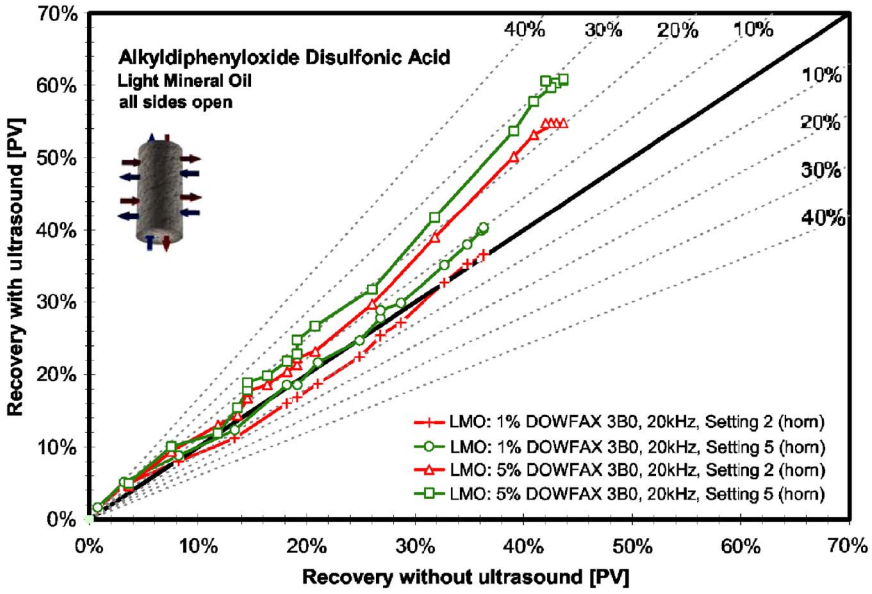

FIG. 9. (Color online) Cross-comparison plot of oil recovery during spontaneous imbibition of 1% alkyldiphenyloxide disulfonic acid (DOWFAX 3B0), and 5% alkyldiphenyloxide disulfonic acid into light mineral oil saturated Berea sandstone (all sides open) at two intensities of ultrasound. The 45° line represents the condition when the response under ultrasound equals that of the control. Dashed lines signify the percent (%) deviation from the control.

Figure 12 presents cross comparison curves of light mineral oil for a series of Tergitol 15-S-7 concentrations. For 0.1% and 1.0%, we observed a reduction in recovery under ultrasound, while for 0.5%, we witnessed an 18% improvement in recovery, implying that there exists a concentration at which the ultrasonic process is optimized. The shape of the recovery curves did not noticeably change under ultrasound.

4. Discussion

Several reasons may be responsible for the apparent improvement in recovery with surfactant under ultrasound with both light mineral oil and kerosene:

- Ultrasound may increase solubility of surfactant in water, thereby decreasing the interfacial tension. A decrease in interfacial tension will reduce the capillary pressure within pores, thus mobilizing trapped oil more effectively.
- Ultrasound may reduce the surfactant adsorption rate onto the sandstone matrix as a consequence of increasing the solubility of the surfactant, improving the wettability of the aqueous phase. This process may be more severe with anionic surfactants than with nonionic surfactants.
- Development of microemulsion (micelles) under ultrasound. Just after 100 min, we observed that the surfactant solution changed into a semitransparent, foggy microemulsion. Therefore, operating ultrasound at surfactant concentrations above CMC accelerates the generation of micelles which may enhance oil recovery.

Surfactant adsorption/desorption may be responsible for the observed variations in recovery under ultrasound for kerosene and mineral oil saturated sandstone.[71,72] The adsorption levels for both anionic and nonionic surfactants are similar in magnitude, although adsorption of nonionic surfactants on sandstone is usually higher, and is relatively insensitive to solution salinity. Negligible adsorption was ob-

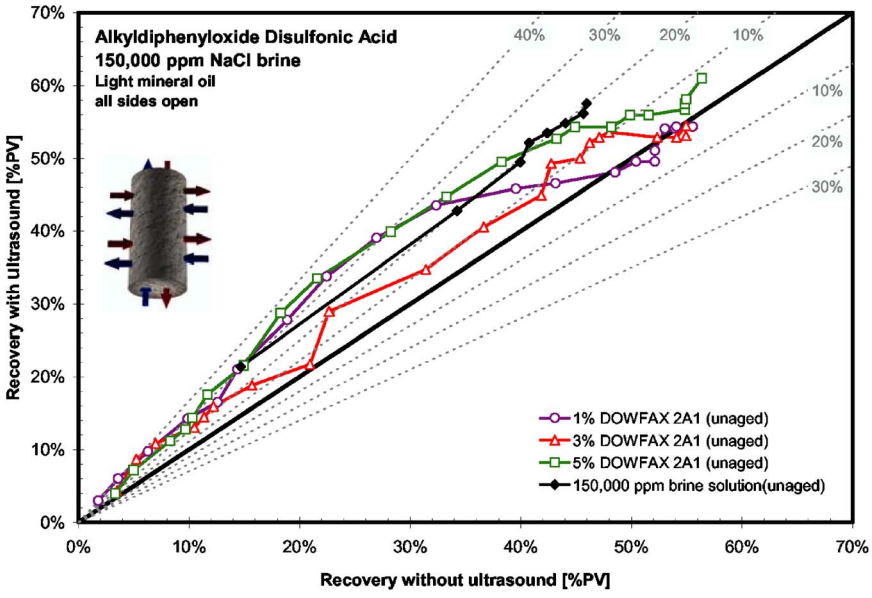

FIG. 10. (Color online) A cross-comparison plot of the spontaneous imbibition of various alkyldiphenyloxide disulfonic acid solutions (DOWFAX 2A1) into light mineral oil saturated Berea sandstone (all sides open) under ultrasound. For comparison, we also added the imbibition performance of 150,000 ppm brine solution as aqueous phase. The 45° line represents the case when the response equals that of the control. Dashed lines signify the percent deviation (%) from the control case.

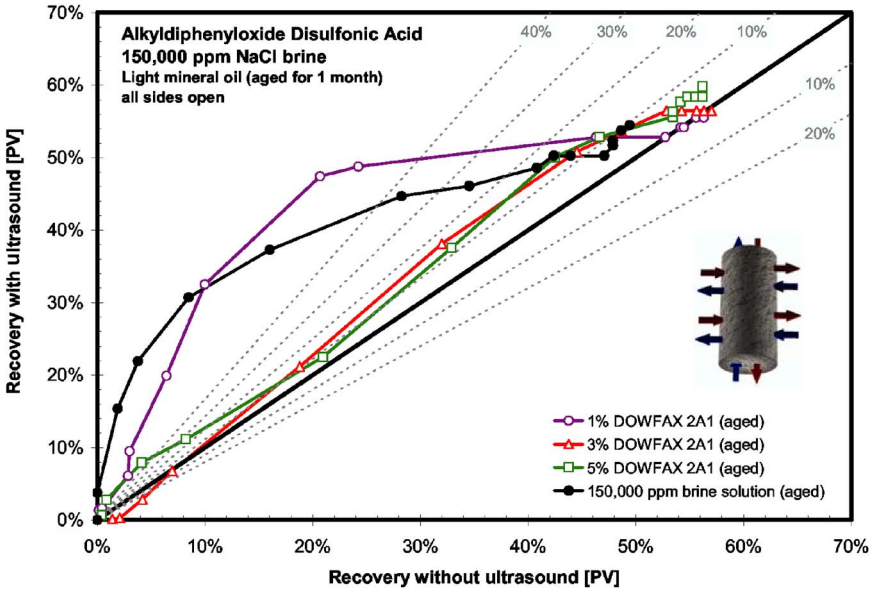

FIG. 11. (Color online) A cross-comparison plot of the spontaneous imbibition of various alkyldiphenyloxide disulfonic acid solutions into light mineral oil saturated Berea sandstone (all sides open) under ultrasound after aging samples for one month. For comparison, we also added the imbibition performance of 150,000 ppm brine solution as aqueous phase. The 45° line represents the case when the response equals to that of the control. Dashed lines signify the percent deviation (%) from the control case.

served in sulfonates containing alkyl chains shorter than nine.[73,74] Mannhardt *et al.*[75] studied the adsorption of anionic surfactants in Berea sandstone at various temperatures and salinity, and found that adsorption increases with decreasing surfactant solubility. Varadaraj *et al.*[76] investigated the wettability alteration caused by various surfactant types, and found that wetting rate is higher for ethoxylates than for sulfates, while wetting effectiveness was higher for sulfates. Although the concentration of 5% alkydiphenyloxide disulfonic acid and 1% ethoxylated alcohol are both significantly higher than the CMC, the latter demonstrated very little alteration of both recovery rate and ultimate recovery of kerosene and mineral oil when ultrasound was applied. Five percent alkydiphenyloxide disulfonic, on the other hand, resulted in significant improvement in recovery rate of mineral oil, and contrasting results in both recovery and recovery rate of kerosene at higher ultrasonic intensity.

Since interfacial tension of both sulfonates and ethoxylates is relatively similar, capillary forces cannot be the dominating factor contributing to the different behavior in recovery under ultrasound. Microemulsions were produced in both cases, as well. Therefore, micelles cannot be responsible for the significant difference either. The governing mechanism must be controlled by a sensitive interplay between the increase in surfactant solubility and decrease in adsorption due to ultrasonic mixing. We demonstrated the role of surfactant adsorption by comparing the imbibition performance of both anionic and nonionic surfactants. Depending on the level of adsorption, one expects that the wettability of Berea alters over time, severely affecting the recovery rate as well as the ultimate recovery.

D. Spontaneous imbibition of xanthan gum solution into sandstones

The effect of ultrasound on spontaneous imbibitions of polymer solutions was investigated to study the effect of viscosity. Imbibition of polymers into porous media has been

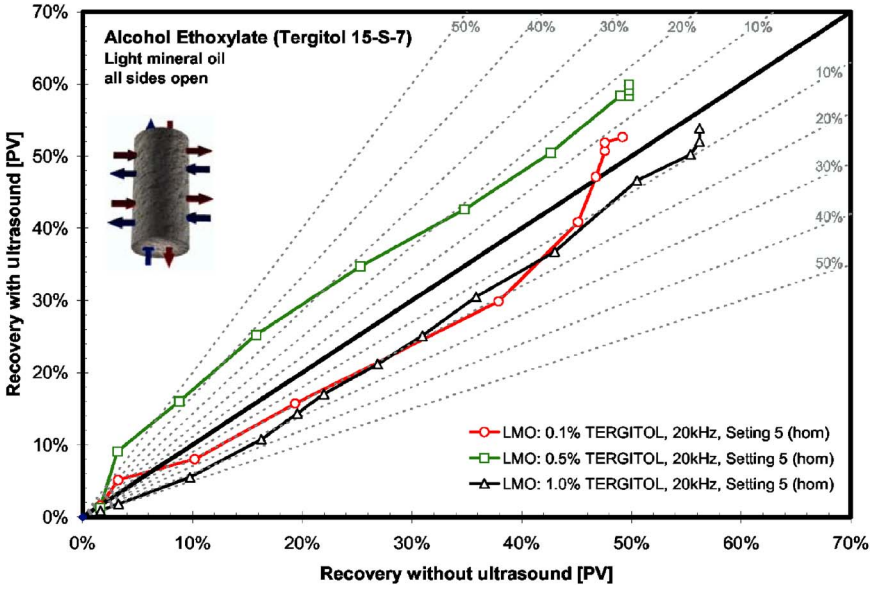

FIG. 12. (Color online) A cross-comparison plot, of the spontaneous imbibition of various alcohol ethoxylate (Tergitol 15-S-7) solutions into light mineral oil saturated Berea sandstone (all sides open) under ultrasound (Setting 5). The 45° line represents the case when the response equals that of the control. Dashed lines signify the percent deviation (%) from the control case.

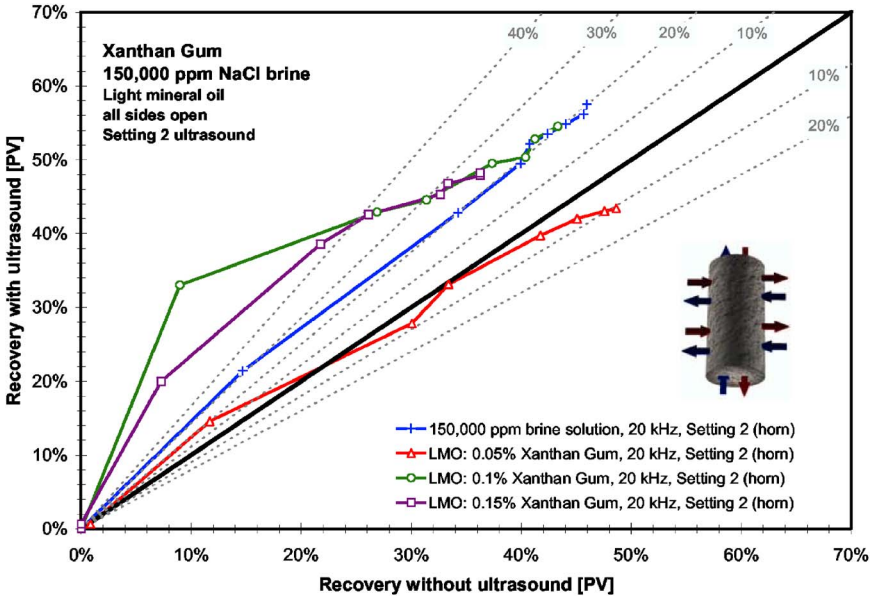

FIG. 13. (Color online) A cross-comparison plot of the spontaneous imbibition of various xanthan gum solutions into light mineral oil saturated Berea sandstone (all sides open) under ultrasound (Setting 2). For comparison, we also added the imbibition performance after using a 150,000 ppm brine solution as aqueous phase. The 45° line represents the case when the response equals that of the control. Dashed lines signify the percent deviation (%) from the control case.

investigated extensively.[77,78] Figure 13 shows recovery curves of various concentrations of xanthan gum imbibing into Berea sandstone cores saturated with mineral oil. The recovery curve of 150,000 ppm NaCl brine has been added for comparison. Without ultrasound, we observed that the recovery of oil decreases with increasing xanthan gum concentration. Introducing ultrasound at setting 2 did not follow this trend. Instead, it is apparent that ultrasonic stimulation is optimal at intermediate concentrations. Low concentrations of xanthan gum (0.05%) did not show any significant improvement in recovery under ultrasound. On the other hand, 0.1 and 0.1 wt% xanthan gum solutions favorably responded to ultrasound by significantly increasing recovery rate, and yielding up to 25% PV incremental oil as compared to the control.

E. Crude oil

Figure 14 shows the recovery curves and the cross-comparison plots for brine and surfactant imbibition into Berea sandstone cores saturated with light Husky crude oil. It can be seen that in the case of brine invasion, both the early recovery rate and the final recovery are substantially improved under ultrasound. With surfactant, however, only recovery rate is improved by 20%, while the final recovery for both ultrasound and no ultrasound remained unaltered.

V. CONCLUSIONS AND REMARKS

A series of spontaneous imbibition experiments were run to investigate the effect of ultrasound on the capillary dynamics within porous media. Various fluid pairs and boundary conditions were explored to account for a wide range of interfacial tension, wettability, density and viscosity. For most fluid pairs, we noted a considerable enhancement in recovery, and recovery rate. Altering the fluid properties of the aqueous and oleic phases had a unique response on the overall performance of the spontaneous imbibition process

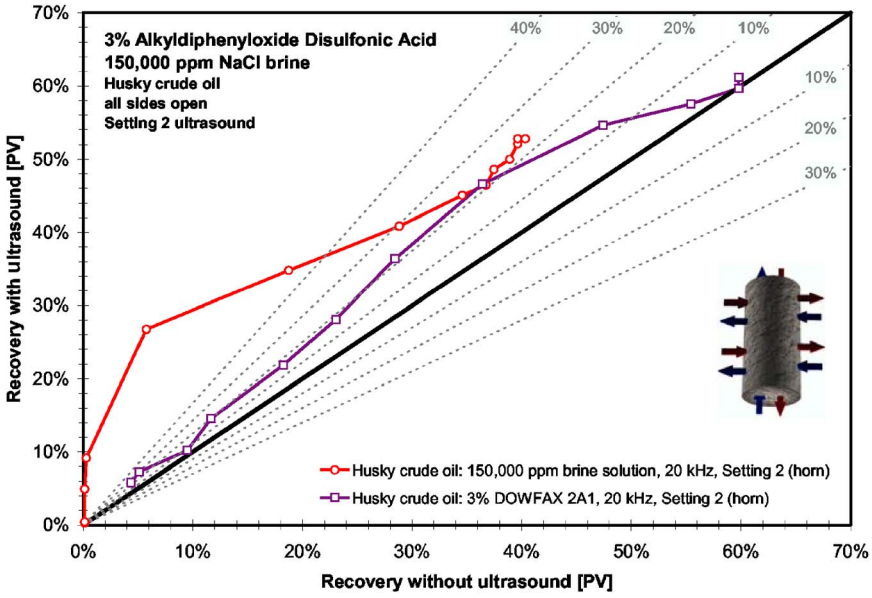

FIG. 14. (Color online) A cross-comparison plot, of the spontaneous imbibition of 150,000 ppm NaCl brine and 3% alyldiphenyloxide disulfonic acid solution into crude oil saturated Berea sandstone (all sides open) under ultrasound (Setting 2). The 45° line in (b) represents the case when the response equals that of the control. Dashed lines signify the percent deviation (%) from the control case.

under ultrasound. Furthermore, the nature of the flow, i.e., co-current or counter-current, resulted in entirely different responses for the same fluid pairs, and strongly depended on interfacial tension and density.

We investigated the spontaneous imbibition of water into dry sandstone and limestone cores under ultrasound, at two boundary conditions. It was observed that the recovery rate is relatively unchanged under ultrasound, and that for co-current flow (all sides open), the final recovery considerably decreased. The opposite is true for counter-current flow with all sides closed except the bottom end, where both the recovery rate and the final recovery were improved. A similar, but less dramatic, response was observed with limestone. For co-current imbibition, the final recovery gradually decreased with frequency, while the recovery rate remained unchanged. The opposite was noted for counter-current flow. Bubble vibration and improved acoustic streaming of air, as well as the destruction of surface films, are believed to be responsible for the observed trends.

Spontaneous imbibition of water into Berea sandstone saturated with kerosene and light mineral oil yielded opposite results as with air. For co-current flow, both the rate and the final recovery of kerosene and light mineral oil improved. The increase was observed to be higher with light mineral oil [higher viscosity, higher interfacial tension (IFT)] than with kerosene (low viscosity, intermediate IFT). For the counter-current process, we observed a minor decrease in recovery and no change in rate with light mineral oil, whereas the kerosene rate and recovery severely reduced. After discontinuing insonication, the final kerosene recovery restored to the non-ultrasonic recovery value.

When using brine as an aqueous phase, we observed a substantial increase in recovery as compared to water. In fact, both recovery rate and final recovery are proportional to salinity. Two substantial findings have been derived from these experiments. First, based on experiments with 15,000 ppm NaCl solutions, final recovery increases with increasing intensity setting. The recovery rate was unaffected. Second, for saline concentrations as high as 150,000 ppm NaCl, ultrasound improved the recovery by up to 15% PV incremental oil. Second, aging reduced the final recovery at high salinity, but still reacted favorably to ultrasonic stimulation. The curvature of the ultrasonically stimulated production rate was almost linear, compared to a more concave curvature observed with the nonultrasonic control.

Three surfactants (two anionic and one nonionic) were tested at various concentrations below and above CMC. We observed the following trends:

a. With DOWFAX 3B0, recovery is relatively insignificant at concentrations close to the CMC. At a concentration much above the CMC, recovery increases with increased ultrasonic intensity, reaching recovery improvements up to 18% PV incremental oil.

b. DOWFAX 2A1 did not exhibit the same behavior as DOWFAX 3B0. Recovery rate was substantially improved during insonication, while the improvement in final recovery remained below 10%. After aging cores for 1 month, we found that the recovery rate severely improved for concentrations close to the CMC (up to 60%), while the improvement in ultimate recovery remained below 10%. Interestingly, the recovery rate at higher concentrations seemed to be only marginally improved (below 10%). When using high concentration DOWFAX 2A1 with kerosene saturated Berea, we observed that at high intensity, ultrasound yielded unfavorable final recovery values. After discontinuing the ultrasound, however, recovery surged up, and stabilized at the recovery value obtained for low intensity ultrasound.

c. Experiments with anionic surfactant (Tergitol 15-S-7) suggest that there is an optimal concentration at which the ultrasonic process is maximized. At a concentration of 0.5%, we noted a recovery increase of up to 40%. A reduction in recovery rate was observed with both 0.1% and 1.0% Tergitol. When comparing the performance of 1% Tergitol for kerosene and mineral oil saturated samples, we observed a minor reduction in recovery ($\sim$5%) and recovery rate (20% for kerosene, and 10% for light mineral oil).

Reduction of surfactant adsorption as a consequence of improved solubility has been proposed to account for the observed behavior of both anionic and nonionic surfactant.

Results for spontaneous imbibition of xanthan gum into light mineral oil saturated Berea sandstone showed interesting results. Recovery under ultrasound is improved at higher surfactant concentrations. However, there seems to be an optimal intensity and concentration at which recovery is maximized. We determined that spontaneous imbibition of xanthan gum is maximized when using low concentrations of xanthan gum at high intensity. Ultrasonic depolymerization and deflocculation may be possible causes for this observation.

Experiments with Husky crude oil using both surfactant (DOWFAX 2A1) and brine (150,000 ppm NaCl) yielded promising results. Ultrasound improved the recovery rate with surfactant by up to 20%, but did not considerably enhance the final recovery. On the other hand, when using brine, we noted a surge in recovery rate (up to 65%), and a spectacular increase in final recovery (up to 23%).

ACKNOWLEDGMENTS

This work was partly funded by an NSERC Grant (No. G121210595). The funds for the equipment used in the experiments were obtained from the Canadian Foundation for Innovation (CFI) (Project No. 7566) and the University of Alberta. We gratefully acknowledge this support. We are also thankful to Husky Oil and Dow Chemical Canada Inc. for providing the crude oil and surfactants, respectively.

[1]T. Spanos, B. Davidson, M. Dusseault, D. Shand, and M. Samaroo, "Pressure pulsing at the reservoir scale: A new IOR approach," J. Can. Pet. Technol. **42**, 16–28 (2003).
[2]M. Dusseault, B. Davidson, and T. Spanos, "Pressure pulsing: The ups and downs of starting a new technology," J. Can. Pet. Technol. **39**, 13 (2000).
[3]M. A. Biot, "Mechanics of deformation and acoustic propagation in porous media," J. Appl. Phys. **33**, 1482 (1962).
[4]M. A. Biot, "Theory of propagation of elastic waves in a fluid-saturated porous solid. 1. Low-frequency range," J. Acoust. Soc. Am. **28**, 168–178 (1956).
[5]M. A. Biot, "Theory of propagation of elastic waves in a fluid-saturated porous solid. 2. Higher frequency range," J. Acoust. Soc. Am. **28**, 179–191

(1956).
[6]M. J. Buckingham, "Compressional and shear wave properties of marine sediments: Comparisons between theory and data," J. Acoust. Soc. Am. **117**, 137–152 (2005).
[7]V. N. Nikolaevskii, "Mechanism of vibroaction for oil recovery from reservoirs and dominant frequencies," Dokl. Akad. Nauk SSSR **307**, 570–575 (1989).
[8]V. N. Nikolaevskii and G. S. Stepanova, "Nonlinear seismics and the acoustic action on the oil recovery from an oil pool," Acoust. Phys. **51**, S131–S139 (2005).
[9]R. D. Duhon, "An investigation of the effect of ultrasonic energy on the flow of fluids in porous media," Ph.D. thesis, University of Oklahoma (1964).
[10]R. D. Duhon and J. M. Campbell, "SPE 1316 — The effect of ultrasonic energy on flow through porous media," in second *Annual Eastern Regional Meeting of SPE/AIME*, Charleston, WV. (1965).
[11]W. I. Chen, "Influence of ultrasonic energy upon the rate of flow of liquids through porous media," Ph.D. thesis, West Virginia University (1969).
[12]H. V. Fairbanks and W. I. Chen, "Ultrasonic acceleration of liquid flow through porous media," AIChE Sonochem. Eng. **67**, 105 (1971).
[13]H. V. Fairbanks, "Ultrasonic stimulation of liquid flow," in *Ultrasonics Symposium*, Annapolis, MD (1976).
[14]V. M. Mikhailov, V. D. Neretin, O. L. Kuznetsov, and S. A. Ertmova, "Study of ultrasonic effect on percolation process in porous media," *Proceedings (Trudy) All Union Research Institute of Nuclear Geophysics and Geochemistry* **24**, 78–87, Annapolis, MD (1975).
[15]V. D. Neretin and V. A. Yudin, "Results of experimental study of the influence of acoustic treatment on percolation processes in saturated porous media," Topics in Nonlinear Geophysics (Voprosi Nelineinoy Geofisiki): All Union Research Institute of Nuclear Geophysics and Geochemistry 132–137 (1981).
[16]V. P. Dyblenko L. A. Thfanov, G. A. Suleymanov, and A. P. Lysenkov, "Percolation phenomena and processes in saturated porous media under the vibro-wave action, in ways of intensification of oil production (Putu intensifikatsii dobychi nefti)," *Proceedings (Trudy) Basharki Research and Design Institute of Oil (Bashnipineft)*, 45–51 (1989).
[17]N. V. Cherskiy V. P. Tsarev, V. M. Konovalov, and O. L. Kuznetsov, "The effect of ultrasound on permeability of rocks to water," Trans. (Doklady) USSR Acad. Sci., Earth Sci. Sect. **232**, 201–204 (1977).
[18]R. F. Ganiev, L. E. Urainskii, and K. V. Frolov, "Wave mechanism for the acceleration of a liquid flowing in capillaries and porous media," Sov. Phys. Dokl. **34**, 267–283 (1989).
[19]M. Y. Jaffrin and A. H. Shapiro, "Peristaltic pumping," Annu. Rev. Fluid Mech. **3**, 13 (1971).
[20]M. Y. Jaffrin *et al.*, "Peristaltic transport," J. Appl. Mech. **36**, 379 (1969).
[21]A. H. Shapiro, M. Y. Jaffrin, and S. L. Weinberg, "Peristaltic pumping with long wavelengths at low Reynolds number," J. Fluid Mech. **37**, 799 (1969).
[22]F. Yin and Y. C. Fung, "Peristaltic waves in circular cylindrical tubes," J. Appl. Mech. **36**, 579 (1969).
[23]S. Takabatake, K. Ayukawa, and A. Mori, "Peristaltic pumping in circular cylindrical-tubes—a numerical study of fluid transport and its efficiency," J. Fluid Mech. **193**, 267–283 (1988).
[24]A. C. T. Aarts and G. Ooms, "Net flow of compressible viscous liquids induced by traveling waves in porous media," J. Eng. Math. **34**, 435–450 (1998).
[25]A. C. T. Aarts,G. Ooms ,K. J. Bil, and E. T. G. Bot, "Enhancement of liquid flow through a porous medium by ultrasonic radiation," SPEJ **4**, 321–327 (1999).
[26]D. Tsiklauri and I. Beresnev, "Non-Newtonian effects in the peristaltic flow of a Maxwell fluid," Phys. Rev. E 6403, (2001).
[27]D. Tsiklauri, "Phenomenological model of propagation of the elastic waves in a fluid-saturated porous solid with nonzero boundary slip velocity," J. Acoust. Soc. Am. **112**, 843–849 (2002).
[28]S. M. Gadiev, *Use of Vibrations in Oil Production (Ispol'zovaniye Vibratsii v Dobyche Nefti)* (Nedra, Moscow, 1977).
[29]P. P. Prokhorenko, N. P. Migun, and N. V. Dezhkunov, "Calculating the process of filling of microcapillaries with liquids under ultrasonic action," Sov. J. Nondestruct. Test. **18**, 326–331 (1982).
[30]Y. P. Rozin, E. Y. Rozina, and V. S. Tikhonova, "On the meniscus motion in a capillary under the effect of supersound," Ukr. Fiz. Zh. (Russ. Ed.) **29**, 1522–1525 (1984).
[31]E. Y. Rozina and Y. P. Rozin, "The experimental investigation of the kinetics of filling up the capillary in cavitation regime," Ukr. Fiz. Zh. **39**, 570–574 (1994).
[32]Y. P. Rozin, E. Y. Rozina, and O. N. Tistruga, "The local heating of a liquid in a capillary due to ultrasonic action," J. Mol. Liq. **93**, 55–59 (2001).
[33]E. Y. Rozina, "Effect of pulsed ultrasonic field on the filling of a capillary with a liquid," Colloid J. **64**, 359–363 (2002).
[34]N. V. Dezhkunov and T. G. Leighton, "Study into correlation between the ultrasonic capillary effect and sonoluminescence," J. Eng. Phys. Thermophys. **77**, 53–61 (2004).
[35]D. F. Gaitan, L. A. Crum, C. C. Church, and R. A. Roy, "Sonoluminescence and Bubble Dynamics for a Single, Stable, cavitation bubbles," J. Acoust. Soc. Am. **91**, 3166–3183 (1992).
[36]A. Gronroos, P. Pirkonen, and O. Ruppert, "Ultrasonic depolymerization of aqueous carboxymethylcellulose," Ultrason. Sonochem. **11**, 9–12 (2004).
[37]W. M. Kulicke, M. Otto, and A. Baar, "Improved NMR characterization of high-molecular-weight polymers and polyelectrolytes through the use of preliminary ultrasonic degradation," Makromolekulare Chemie-Macromolecular Chemistry and Physics **194**, 751–765 (1993).
[38]E. M. Simkin and M. L. Surguchev, "Advanced vibroseismic technique for water flooded reservoir stimulation, Mechanism and field tests results," in *The 6th European IOR Symposium*, Stavanger, Norway. (1991).
[39]E. M. Simkin, "A possible mechanism of vibroseismic action on an oil-bearing bed," J. Eng. Phys. Thermophys. **64**, 355–359 (1993).
[40]V. F. K. Bjerknes, *Fields of Force* (Columbia University Press, New York, 1906).
[41]F. G. Blake, "Bjerknes forces in stationary sound fields," J. Acoust. Soc. Am. **21**, 551–551 (1949).
[42]R. Mettin *et al.*, "Bjerknes forces between small cavitation bubbles in a strong acoustic field," Phys. Rev. E **56**, 2924–2931 (1997).
[43]R. J. Schoeppel and A. W. Howard, "Effect of ultrasonic irradiation on coalescense and separation of crude oil-water emulsions," *SPE 1507, 41st Annual Fall Meeting of the SPE/AIME*, Dallas, TX. (1966).
[44]V. N. Nikolaevskii, "Rock vibration and finite oil recovery," Fluid Dyn. **27**, 689–696 (1992).
[45]S. Dunin and V. N. Nikolaevskii, "Nonlinear waves in porous media saturated with live oil," Acoust. Phys. **51**, S61–S66(1) (2005).
[46]A. Abrashkin, V. S. Averbakh, S. N. Vlasov, Y. M. Zalavskii, I. A. Soustova, R. A. Sudarikov, and Y. I. Troitskaya"A possible mechanism of the acoustic action on partially fluid-saturated porous media," Acoust. Phys. **51**, S12–S22(1) (2005).
[47]V. N. Nikolaevskiy, G. P. Lopukhov, Y. Liao, and M. J. Economides, "Residual oil reservoir recovery with seismic vibrations," SPE Prod. Facil. **11**, 89–94 (1996).
[48]O. L. Kuznetsov, E. M. Simkin, G. V. Chilingar, and S. A. Katz, "Improved oil recovery by application of vibro-energy to waterflooded sandstones," J. Pet. Sci. Eng. **19**, 191–200 (1998).
[49]O. L. Kuznetsov, E. M. Simkin, G. V. Chilingar, M. V. Gorfunkel, and J. O. Robertson, "Seismic techniques of enhanced oil recovery: Experimental and field results," Energy Sources **24**, 877–889 (2002).
[50]G. G. Vakhitov and E. M. Simkin, *Use of Physical Fields in Oil Recovery (Ispol'zovaniye Fizicheskikh Poley Dlia Izvlecheniya Nefti iz Plastov)* (Nedra, Moscow, 1985).
[51]L. Kuznetsov and E. M. Simkin, *Transformation and Interaction of Geophysical Fields in Lithosphere (Preobrazovaniye i Vzaimodeystviye Geofizicheskikh Poley v Litosfere)* (Nedra, Moscow, 1990).
[52]D. R. Graham, "Acoustic stimulation of multiphase flow in porous media," Ph.D. thesis, University of Illinois 1999.
[53]D. R. Graham, "Steady and oscillatory flow through model porous media," M.Sc. thesis, University of Illinois 1997.
[54]D. R. Graham and J. J. L. Higdon, "Oscillatory flow of droplets in capillary tubes. Part 1. Straight tubes," J. Fluid Mech. **425**, 31–53 (2000).
[55]D. R. Graham and J. J. L. Higdon, "Oscillatory flow of droplets in capillary tubes. Part 2. Constricted tubes," J. Fluid Mech. **425**, 55–77 (2000).
[56]D. R. Graham and J. J. L. Higdon, "Oscillatory forcing of flow through porous media. Part 1. Steady flow," J. Fluid Mech. **465**, 213–235 (2002).
[57]D. R. Graham and J. J. L. Higdon, "Oscillatory forcing of flow through porous media. Part 2. Unsteady flow," J. Fluid Mech. **465**, 237–260 (2002).
[58]I. A. Beresnev, "Theory of vibratory mobilization on nonwetting fluids entrapped in pore constrictions," J. Scholarship Teach. Learn. **71**, N47–N56 (2006).
[59]T. Hamida and T. Babadagli, "Analysis of capillary interaction and oil recovery under ultrasonic waves," in Transp. Porous Media, in press

(2007).
[60]T. Hamida and T. Babadagli, "Investigations on the capillary interaction of different oleic and aqueous phases between matrix and fracture under ultrasonic waves," *SPE 94105, SPE EUROPEC/EAGE Annual Conference* 13–16 June, Madrid (2005).
[61]T. Hamida and T. Babadagli, "Effect of ultrasonic waves on the capillary imbibition recovery of oil," *SPE 92124, SPE Asia Pacific Oil and Gas Conference and Exhibition*, 5–7 April, Jakarta, Indonesia (2005).
[62]T. Hamida and T. Babadagli, "Effects of ultrasonic waves on immiscible and miscible displacement in porous media," *SPE 95327, 2005 SPE Annual Technical Conference and Exhibition*, Dallas, TX, 9–12 Oct. (2005).
[63]T. Hamida, and T. Babadagli, "Investigations on capillary and viscous displacement under ultrasonic waves," J. Can. Pet. Technol., 16–19 (2006).
[64]N. R. Morrow and G. Mason, "Recovery of oil by spontaneous imbibition," Curr. Opin. Colloid Interface Sci. **6**, 321–337 (2001).
[65]X. M. Zhou, N. R. Morrow, and S. X. Ma, "Interrelationship of wettability, initial water saturation, aging time, and oil recovery by spontaneous imbibition and waterflooding," SPEJ **5**, 199–207 (2000).
[66]H. Fischer and N. R. Morrow, "Spontaneous imbibition with matched liquid viscosities," in *SPE Annual Technical Conference and Exhibition*, Dallas (2005).
[67]B. G. Viksund, N. R. Marrow, G. Ma, W. Wang, and A. Graue, "Initial water saturation and oil recovery from chalk and sandstone by spontaneous imbibition," in *1998 International Symposium of the Society of Core Analysts*. The Hague, Netherlands (1998).
[68]T. Babadagli, "Scaling of co-current and counter-current capillary imbibition for surfactant and polymer injection in naturally fractured reservoirs," SPEJ 465–478 (2001).
[69]M. Herskowitz, S. Levitsky, and I. Shreiber, "Acoustic waves in a liquid-filled bed with microbubbles," Acustica **85**, 793–799 (1999).
[70]M. Herskowitz, S. Levitsky, and I. Shreiber, "Attenuation of ultrasound in porous media with dispersed microbubbles," Ultrasonics **38**, 767–769 (2000).
[71]J. Brinck, B. Jonsson, and F. Tiberg, "Kinetics of nonionic surfactant adsorption and desorption at the silica-water interface: Binary systems," Langmuir **14**, 5863–5876 (1998).
[72]J. Brinck, B. Jonsson, and F. Tiberg, "Kinetics of nonionic surfactant adsorption and desorption at the silica-water interface: One component," Langmuir **14**, 1058–1071 (1998).
[73]J. B. Lawson, "The adsorption of non-ionic surfactants on sandstone and carbonate," *SPE Symposium on Improved Methods for Oil Recovery*, (Tulsa, OK 1978).
[74]F. J. Trogus, T. Sophany, R. S. Schechter, and W. H. Wade, "Static and dynamic adsorption of anionic and nonionic surfactants," Soc. Pet. Eng. J. **17**, 337–344 (1977).
[75]K. Mannhardt, J. J. Novosad, and K. N. Jha, "Adsorption of foam-forming surfactants in berea sandstone," J. Can. Pet. Technol. **33**, 34–43 (1994).
[76]R. Varadaraj, J. Bock, N. Brons, and S. Zushma, "Influence of surfactant structure on wettability modification of hydrophobic granular surfaces," J. Colloid Interface Sci. **167**, 207–210 (1994).
[77]T. Babadagli, "Dynamics of capillary imbibition when surfactant, polymer, and hot water are used as aqueous phase for oil recovery," J. Colloid Interface Sci. **246**, 203–213 (2002).
[78]S. G. Ghedan and F. H. Poettmann, "Effect of polymers on the imbibition process: A laboratory study," SPE Reservoir Eng. 84–90 (1991).

Viscous microstructural dampers with aligned holes: Design procedure including the edge correction

Dorel Homentcovschi[a] and Ronald N. Miles
Department of Mechanical Engineering, SUNY Binghamton, New York 13902-6000

(Received 25 September 2006; revised 5 June 2007; accepted 12 June 2007)

The paper is a continuation of the works "Modelling of viscous damping of perforated planar micromechanical structures. Applications in acoustics" [Homentcovschi and Miles, J. Acoust. Soc. Am. **116**, 2939–2947 (2004)] and "Viscous Damping of Perforated Planar Micromechanical Structures" [Homentcovschi and Miles, Sensors Actuators, **A119**, 544–552 (2005)] where design formulas for the case of an offset (staggered) system of holes was provided. The present work contains design formulas for perforated planar microstructures used in MEMS devices (such as proof-masses in accelerometers, backplates in microphones, micromechanical switches, resonators, tunable microoptical interferometers, etc.) in the case of aligned (nonstaggered) holes of circular and square section. The given formulas assure a minimum total damping coefficient (including the *squeeze film damping* and the *direct* and *indirect* resistance of the holes) for an assigned open area. The paper also gives a simple edge correction, making it possible to consider real (finite) perforated planar microstructures. The proposed edge correction is validated by comparison with the results obtained by FEM simulations: the relative error is found to be smaller than 0.04%. By putting together the design formulas with the edge correction a simple integrated design procedure for obtaining viscous perforated dampers with assigned properties is obtained. © *2007 Acoustical Society of America.* [DOI: 10.1121/1.2756169]

PACS number(s): 43.38.Bs, 43.38.Kb [AJZ] Pages: 1556–1567

I. INTRODUCTION

Many microelectromechanical system (MEMS) devices include a plate that moves relative to a perforated stationary electrode, or backplate. The perforations in the backplate are often needed to reduce the time required to remove sacrificial materials between the moving structure and the backplate. In addition, the perforations are known to reduce viscous damping due to the squeezing of the air in the small space. Therefore, the study of a thin air layer being squeezed between a moving plate and a perforated backplate, referred as a planar microstructure, is important in many applications such as microphones, microaccelerometers, micromechanical switches, resonators, tunable microoptical interferometers, etc. Despite the large research effort dedicated to this subject, the elaboration of a simple design procedure for obtaining desired damping properties is still an open question. The primary aim of this paper is to describe such a design procedure including a practical approximate scheme to account for the change in damping due to the open edges of the structure.

Viscous damping is a critical factor for many MEMS transducers. Angular rate sensors require low damping in order to achieve sufficient sensitivity of the system under a given driving force in many applications. In the case of microphones (and also other sensors designed for small signal applications) the mechanical-thermal noise is often one of the limiting noise components. The magnitude of thermal noise depends only on temperature and the magnitude of mechanical damping.[1] Consequently, high viscous damping is associated also with large mechanical-thermal noise. If the damping is too low in a micromachined lateral accelerometer, the severe degree of resonance of the proof mass, upon an impact of external force, may produce a large signal that overloads the control circuitry, resulting in system failure. Many devices need to be damped for stable operation. Therefore, as was shown in Ref. 2, in designing a MEMS device, the consideration of viscous damping must be taken into account at the earliest stage. The efficient etching, the proper value of the viscous damping, and the control of the structure stiffness require a comprehensive understanding of the micromachined perforated systems and their dynamic behavior. Designers need insight into how to fine-tune the design parameters to achieve higher sensitivity and better overall performance.

The motion of the thin film of gas in a planar microstructure gives a squeezed-film damping that can adversely affect the dynamic response of the device.[3] There is an extensive literature dedicated to the study of the squeezed-film damping in MEMS (see Refs. 4–8, etc.). While the squeezed-film damping is reduced by the presence of the holes in one plate (or both plates), the vertical motion of the air within the holes gives a new viscous resistance, which adds to the squeezed-film damping. A rigorous analysis of the total damping problem requires the solution of the Navier-Stokes' system (or the simplified Stokes' approximation) in the 3-D domain composed of the space between the plates and holes. Unfortunately, as was shown in Ref. 9, the

[a]Permanent address: University Politechnica of Bucharest, Applied Science Department and Institute of Mathematical Statistics and Applied Mathematics of Romanian Academy, Calea13 Septembrie #13, RO-76100, Bucharest, Romania. Electronic mail: homentco@binghamton.edu

full 3-D simulation of the Navier-Stokes system is practically impossible due to the huge number of elements needed. To simplify the problem an "*extended*" (modified) Reynolds' equation was formulated by Veijola and Matilla,[10] by adding an additional "*leakage*" term, due to perforations to the classical Reynolds' equation. The resulting equation was solved by using finite element method (FEM) tools by a homogenization method (where the leakage due to the holes is homogenized uniformly on the plate surface) in Refs. 11 and 12 and also by a different approach where the leakage is described as a spatially variable quantity (called by the author the Perforation Profile Reynolds' method).[13] Also, Bao *et al.* in Refs. 14 and 15 wrote a "*modified*" Reynolds' equation by adding to the classical equation a term related to the flow through holes. This partial differential equation (PDE) was integrated only in the case of a very long rectangular perforated plate by reducing it to an ordinary differential equation (ODE). Both the "*extended*" and the "*modified*" Reynolds' equations have the advantage of simultaneously taking into consideration both the presence of the holes and the finite edges of the damper. The drawbacks come from the fact that they are model equations (always involving a model error) that have to be solved numerically for each particular geometry of the perforated microstructure.

The two viscous effects, squeezed-film damping and the resistance of the holes, are not independent. In order to decrease the squeeze-film damping we have to "*drill*" more and more holes but each new hole adds its resistance to the total damping. In Refs. 16 and 17 approximate analytical expressions for the squeezed-film damping and the resistance of the holes were obtained for the particular case of infinite plates containing a regular, periodic, system of holes. By using these formulas the existence of an optimum number of perforations has been proved that minimizes the total viscous damping, giving an equilibrium between the two viscous components. Also, in the cited papers design formulas were given for the case of the offset (staggered) circular holes (when the domain of influence of a hole is a regular hexagon). The use of offset holes permits a better use of material, resulting in a smaller total pressure for a given amount of open area. However, in the case of offset holes we do not know a simple method to take into consideration the effect of the edges of finite plates.

In many MEMS applications employing planar microstructures it is common to use a regular system of aligned circular or square holes. In this case the domain of influence of a hole is a square. In this paper we first give design formulas for a perforated planar microstructure, which gives the minimum total damping for a given value of the area ratio, A (the ratio of the holes' area/total area of the plate). All these formulas prove true in the case of infinite planar microstructures. The advantage of the viscous dampers containing aligned holes is that in this case a simple method to introduce edge corrections can be developed. This can be accomplished simply by taking into consideration the change in squeezed-film damping for the cells next to the sides of the structures. This permits the design procedure to account for the real (finite) geometry of the perforated microstructure. The present work completes the previous papers in Refs. 16 and 17 by providing an integrated procedure for designing perforated dampers with assigned properties.

There is some misunderstanding of the combined effects of the squeeze film damping and the resistance of the holes. The determination of the squeeze film damping assumes a zero pressure condition along the edge of the hole. On the other hand, the flow through holes assumes a p_1 (nonzero) pressure boundary condition at the rim of the hole. In order to address this apparent incompatibility we introduced a section entitled "Squeeze film damping and resistance of the holes." While the squeeze film damping is obtained by solving a boundary value problem (BVP) with homogenous boundary conditions, the resistance of the holes has two components. These consist of a direct resistance of a hole F_d^h, which results from summing the tractions along the side surface of the cylindrical hole and an indirect resistance, denoted by F_i^h, which results from the change of the boundary condition along the rim of the hole from zero to the value p_1. The total resistance of a hole is the sum of the direct and indirect components. This is exactly the value of the resistance assumed in our previous papers (Refs. 16 and 17).

The indirect resistance of a hole is larger (in absolute value) than the direct resistance F_d^h; therefore any model of the flow in a perforated microstructure which considers only the direct resistance of holes is incomplete and may produce erroneous results.

In Sec. III we analyze the case of circular holes. Since in many applications the authors consider aligned square holes, formulas are given in Sec. IV for designing perforated microplanar structures with square holes giving the smallest damping coefficient [for a fixed area ratio (A)]. Section V is dedicated to the introduction of the edge correction. The idea is to modify the dimensions of the "*side*" cells such that the new cell has the same total pressure as the "*inner*" cells. In order to test how the correction works we considered a model structure with one-dimensional periodicity modified according to the introduced edge correction. The total pressure obtained by our procedure was compared with a FEM solution for the whole structure. For the whole domain of the parameter A the error resulting by using our correction is smaller than 0.04%. This numerically validates the introduced edge correction. The result of this analysis is that in the case of domains with the sides parallel to the coordinate axes, the design problem is a simple modification of that for infinite domains, the difference being the elimination in some cases of a line and/or a column of holes.

To keep the presentation simpler and at the same time to account for special effects we added a section that discusses the limits of applicability of given formulas and indicates the modifications imposed by different special conditions.

Section VII contains an example of the design procedure for a perforated planar microstructure given in the literature.

The advantage of the new procedure over the previous design methods is that instead of writing a new model PDE (which takes into consideration somehow the presence of the holes) and integrating this equation numerically for every specified structure, we give design formulas that provide the periodic structure having the smallest damping. Afterwards,

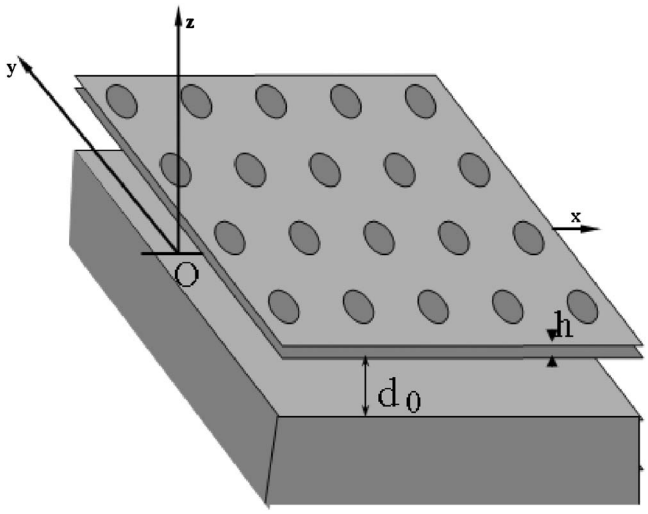

FIG. 1. A perforated planar microstructure with aligned holes.

the edge correction completes the design procedure by modifying only the dimension of the open side cells to account for the real (assigned) geometry of the damper.

II. THE SQUEEZE FILM DAMPING AND THE RESISTANCE OF HOLES

We consider the microstructure in Fig. 1 where the upper (mobile) plate has a regular system of cylindrical holes placed in the corners of a regular square web of period-d parallel to the coordinate axes Ox, Oy. Figure 2(a) shows a circular hole of radius r and domain of influence D. The union of the hole and of the domain D (called also a cell) is a square of side length d having the same center as the hole. In the cross-sectional view d_0 is the average gap between the diaphragm and counter electrode and h is the thickness of the backplate (also called the depth into the page).

A. The squeeze film damping

The Reynolds' equation, satisfied by the pressure $p(x,y)$ in the gap, yields Poisson's equation,[3–17]

$$\frac{\partial^2 p}{\partial x^2}+\frac{\partial^2 p}{\partial y^2}=\frac{12\mu}{d_0^3}w, \quad \text{in } D \tag{1}$$

where μ is the viscosity of the fluid between the plates and w is the velocity of the upper (mobile) plate. The PDE (1) has to be integrated subject to the following boundary conditions:

$$\frac{\partial p}{\partial n}=0 \quad \text{along the square sides } C_N, \tag{2}$$

$$p(x,y)=0 \quad \text{along the rim of the hole } C_0. \tag{3}$$

Once the pressure p is determined, the squeeze-film damping force F^s for the cell is defined by

$$F^s=-\int\int_D p(x,y)\,dx\,dy. \tag{4}$$

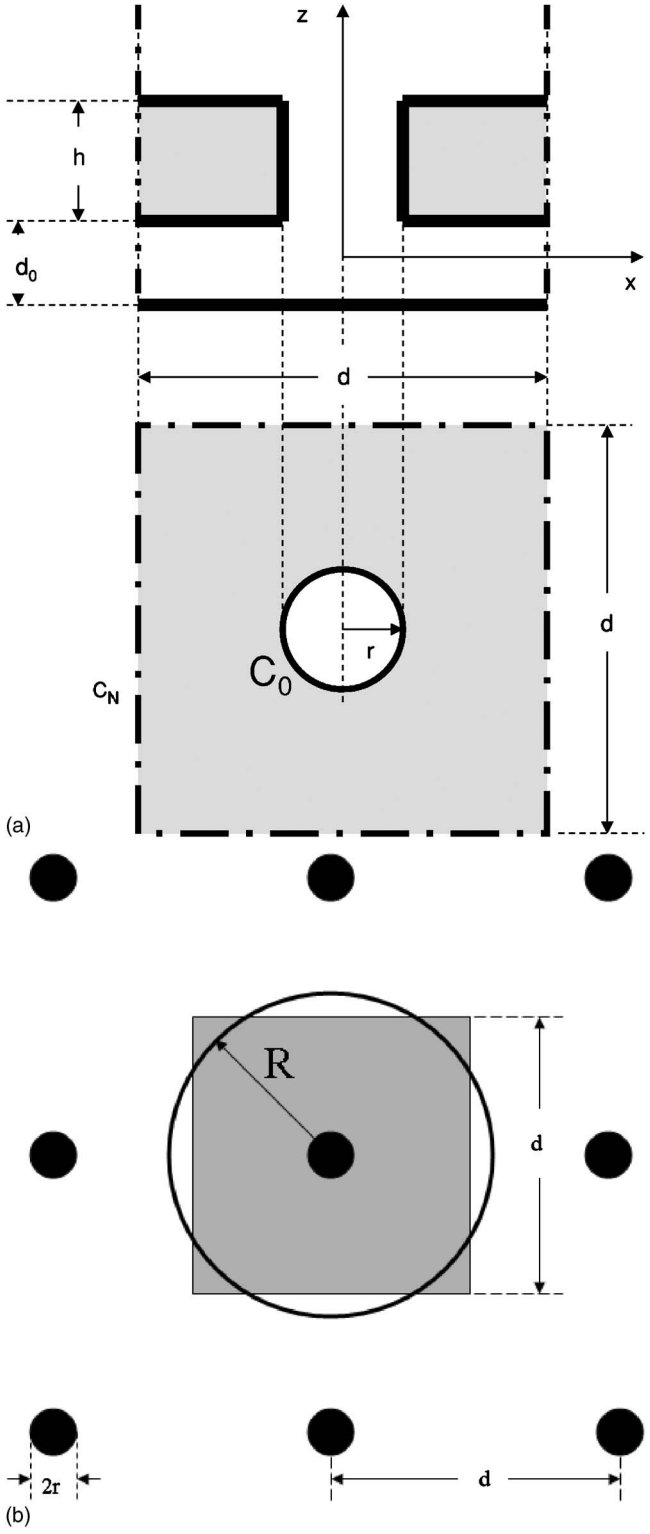

FIG. 2. (a) The cross-sectional view and the top view of a cell of the perforated microstructure with aligned circular holes. (b) The influence domain (the cell) of a circular hole and its circular approximation.

Equation (1) is valid in the case of incompressible fluids. Generally, the velocity of the mobile plate w is a function of x, y, and t. Consequently, a more rigorous approach given in Ref. 17 shows that on the left-hand side an inertial term has to be added. However, the analysis of Zuckerwar in Ref. 18

(reconsidered also in Ref. 19) shows that in the case of microphones, in the audio frequency domain the damping is practically independent of frequency.

The integration of Eqs. (1)–(3) can be performed by numerical methods using, for example, the software developed for solving steady state heat propagation problems. More analytical results can be obtained in the case where the velocity w is constant over the mobile plate (the piston problem). This is the case in many MEMS devices that employ a planar parallel-plate capacitor, in which one plate is actuated electrically and its motion is detected by capacitive changes. The pistonlike model of the moving diaphragm is applicable at sufficiently low frequencies where the amount of air displaced by the membranes rather than the exact shape of the moving surface is important in characterizing the device. Such an approximation is common in analyzing the behavior of microphones (see, for example, Ref. 19).

For obtaining a simple analytical solution, the external boundary of the cell (the square of d-side length) is substituted by a circle of radius $R=d/\sqrt{\pi}$ [Fig. 2(b)]. This way the problem becomes axially symmetric for an annulus of the same area as the domain D. In polar coordinates (ρ,θ) Eq. (1) becomes

$$\frac{1}{\rho}\frac{\partial}{\partial\rho}\left(\rho\frac{\partial p}{\partial\rho}\right)=\frac{12\mu}{d_0^3}w, \quad r<\rho<R,$$

and its solution satisfying the boundary conditions (2) and (3) is

$$p(\rho)=\frac{12\mu}{d_0^3}\left(\frac{\rho^2-r^2}{4R^2}-\ln\sqrt{\frac{\rho}{r}}\right)w. \tag{5}$$

Correspondingly, the squeeze-film damping force is given by substituting this expression for the pressure in formula (4). This leads to Švcor's formula,[20]

$$F^s=\frac{12\pi\mu R^4}{d_0^3}C(A)\omega, \tag{6}$$

where $C(A)$ is given by

$$C(A)=A/2-A^2/8-0.25\ln A-3/8,$$

and the *area ratio* A is defined as the ratio of the area of a hole to the area of a cell,

$$A=\frac{\pi r^2}{\pi R^2}=\frac{\pi r^2}{d^2}. \tag{7}$$

Remark 1: The approximation of the cell by an annulus of the same area, suggested by Švcor's approach, was performed in Refs. 3 and 16. *In Ref.* 17 *an analysis of the error involved in this approximation shows that formula* (6) *works well as long as* $A<0.4$. *A correction to this formula* (*presented in Sec.* VI C) *extends its validity until* $A=0.75$.

B. The resistance of holes

The other component of the viscous damping in a perforated microstructure, caused by the vertical motion of the fluid through the holes, is the holes' resistance denoted by F^h. For determining the resistance of holes, a hole in the lower plate is modeled as a circular pipe, of radius r and length h, and the fluid flow is assumed to be a Hagen-Poiseuille fully developed flow. The pressure along the upper edge of the hole is a constant denoted by p_1 and at the other edge is zero. The principal elements of the flow are given in Refs. 21 and 22 (specifically formulas 3-34, 3-36, and 3-38): the velocity

$$v_z=-\frac{p_1}{4\mu h}(r^2-\rho^2),$$

the rate of flow

$$Q\equiv\int\int_{\text{section}}v_z dA=-\frac{\pi r^4 p_1}{8\mu h}, \tag{8}$$

and the wall shear stress

$$\tau\equiv-\mu\frac{dv_z}{d\rho}(r)=-\frac{p_1 r}{2h}. \tag{9}$$

In these formulas, the vertical pressure gradient was taken as p_1/h.

1. The direct resistance of holes

The direct resistance of the holes F_d^h is obtained by integrating the wall shear stress (9) along the boundary of the pipe. Since τ is a constant and the side area of the pipe equals $2\pi rh$ there results

$$F_d^h=-\pi r^2 p_1. \tag{10}$$

We note that the direct resistance of holes equals the force given by the pressure p_1 over the normal section area of holes.

2. The indirect resistance of holes

The change of the rim pressure to p_1 modifies the boundary condition (3) to

$$p(x,y)=p_1, \quad \text{along the rim of the hole } C_0. \tag{11}$$

It can be shown that the function

$$\hat{p}(x,y)=p(\rho)+p_1$$

with $p(\rho)$ having the expression (5), satisfies Eq. (1) and the boundary conditions (2) and (11). Consequently, the presence of the holes increases the pressure in each point of the domain D by p_1, resulting in a supplementary damping equal to to the area of the domain times the rim pressure

$$F_i^h=-p_1(d^2-\pi r^2). \tag{12}$$

3. Determination of the pressure p_1 of the rim

The pressure p_1 is obtained by equalizing the rate of flow in the pipe (8) with the volume of the incompressible fluid wd^2 leaving (or entering) the cell per unit of time as

$$p_1 = -\frac{8\mu h d^2}{\pi r^4} w.$$

Thus, in the case where the upper plate is moving up ($w > 0$), the pressure p_1 is negative and the fluid enters the planar structure.

By adding the direct hole resistance (10) with the indirect resistance (12) the total resistance of the hole for a cell is found to be

$$F^h = 8\pi\mu h \left(\frac{R}{r}\right)^4 w. \tag{13}$$

This is exactly the expression of the resistance considered in our previous papers (Refs. 16 and 17).

Remark 2: The indirect hole resistance F_i^h is larger than the direct resistance F_d^h. Therefore the disregarding of the term F_i^h cannot be justified.

C. The optimum number of holes

The area u^2 containing N cells is

$$u^2 = N\pi R^2 = Nd^2. \tag{14}$$

The total damping force over the area u^2 defined as $F^t \equiv N(F^s + F^h)$ can be written by adding the result of Eqs. (6) and (13),

$$F^t = \left\{ \frac{12\mu u^4}{\pi d_0^3} C(A) \frac{1}{N} + \frac{8\pi\mu h}{A^2} N \right\} w. \tag{15}$$

Setting the derivative of F^t with respect to N equal to zero,

$$\frac{dF^t}{dN} = \left\{ -\frac{12\mu u^4}{\pi d_0^3} C(A) \frac{1}{N^2} + \frac{8\pi\mu h}{A^2} \right\} w = 0,$$

gives the optimum number of holes N_{opt} as

$$N_{opt} = \sqrt{\frac{3A^2 C(A)}{2\pi^2 d_0^3 h}}\, u^2. \tag{16}$$

For this number of holes the total viscous force F^t has a minimum value. The damping coefficient is defined as the ratio of the damping force to the velocity of the plate. The corresponding minimum damping coefficient $B_{\min} \equiv F^t_{\min}/w$ is

$$B_{\min} = 8\sqrt{6}\mu \frac{\sqrt{C(A)}}{A} \sqrt{\frac{h}{d_0^3}}\, u^2. \tag{17}$$

Remark 3: The above analysis considers the area ratio, A, as a constant. This parameter can be determined by imposing other restrictions related to the plate stiffness or electrical sensitivity of the structure.

III. BASIC DESIGN FORMULAS FOR A REGULAR WEB OF ALIGNED CIRCULAR HOLES

A. The optimum number of holes on u^2 area

Formula (16) can be written as

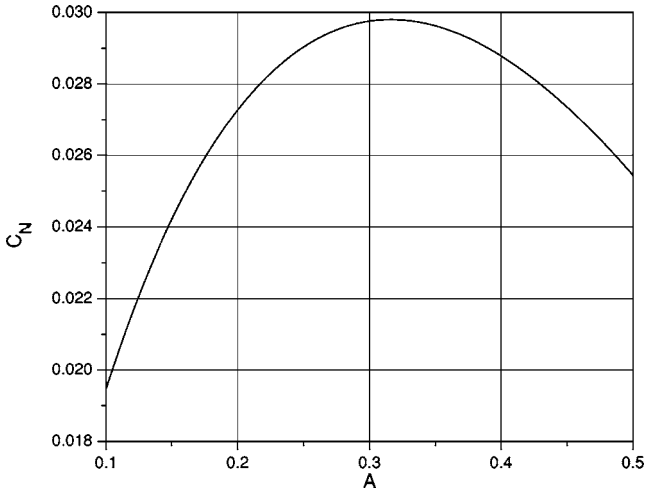

FIG. 3. The variation of the coefficient C_N with area ratio A in the case of circular holes.

$$N_{opt} = C_N \frac{u^2}{\sqrt{d_0^3 h}}, \tag{18}$$

where the coefficient C_N is

$$C_N = \sqrt{\frac{3A^2 C(A)}{2\pi^2}}. \tag{19}$$

Figure 3 gives a graph of the coefficient C_N as a function of A. The coefficient has a maximum value $C_N = 0.0298$ for $A = 0.316$. Correspondingly, the number of holes has to always be smaller than that resulting from formula (18) where the coefficient C_N has its maximum value.

B. The optimum length of the cell side

Formulas (14) and (16) give the optimum length of a side of the square cell d_{opt}

$$d_{opt} = C_d \sqrt[4]{h d_0^3}, \tag{20}$$

where the coefficient C_d has the expression

$$C_d = \sqrt[4]{\frac{2\pi^2}{3A^2 C(A)}}. \tag{21}$$

The coefficient C_d is plotted in Fig. 4. The figure shows that there is a minimum value of the cell's side length, corresponding to the same value of the area ratio $A = 0.316$, given by formula (20) where $C_d = 5.793$.

C. The optimum radius of the holes

Formulas (7), (20), and (21) provide the optimum radius of the holes as

$$r_{opt} = C_r \sqrt[4]{h d_0^3}, \tag{22}$$

where

$$C_r = \sqrt[4]{\frac{2}{3C(A)}}. \tag{23}$$

Figure 5 gives a graphical representation of the coefficient C_r as a function of A.

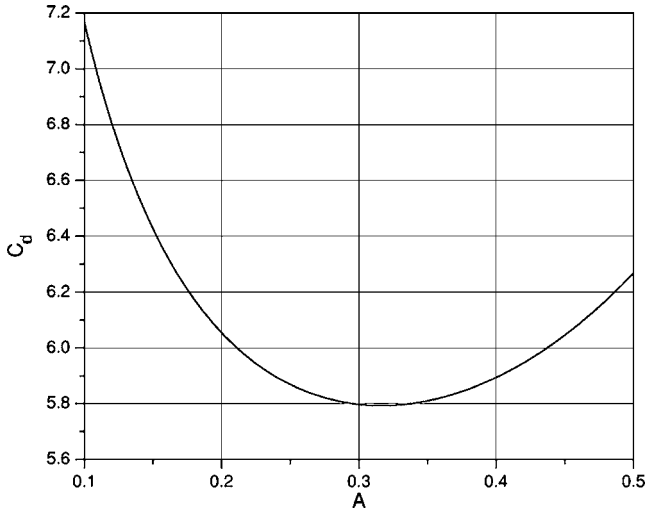

FIG. 4. The variation of the coefficient C_d with area ratio A in the case of circular holes.

D. The minimum damping coefficient

Finally, the minimum damping coefficient of Eq. (17) may be written in the form

$$B_{\min} = C_B \sqrt{\frac{h}{d_0^3}} \mu u^2, \tag{24}$$

where

$$C_B = 8\sqrt{6}\frac{\sqrt{C(A)}}{A}. \tag{25}$$

A graphical representation of the coefficient C_B is plotted in Fig. 6.

The design formulas (19), (21), (23), and (25) contain some coefficients depending only upon the area ratio. The formulas (18), (20), (22), and (24) separate the dependence on distance between the plates d_0, the thickness of the perforated plate h, and the area u^2.

Table I contains the values of these coefficients for several characteristic values of the area ratio A.

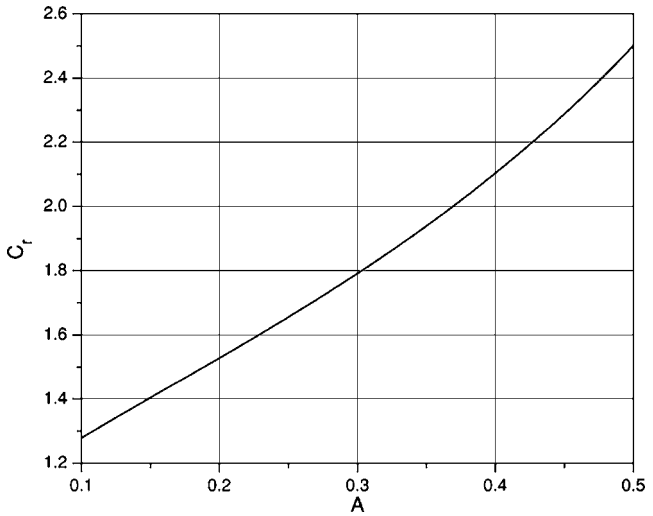

FIG. 5. The variation of the coefficient C_r with area ratio A in the case of circular holes.

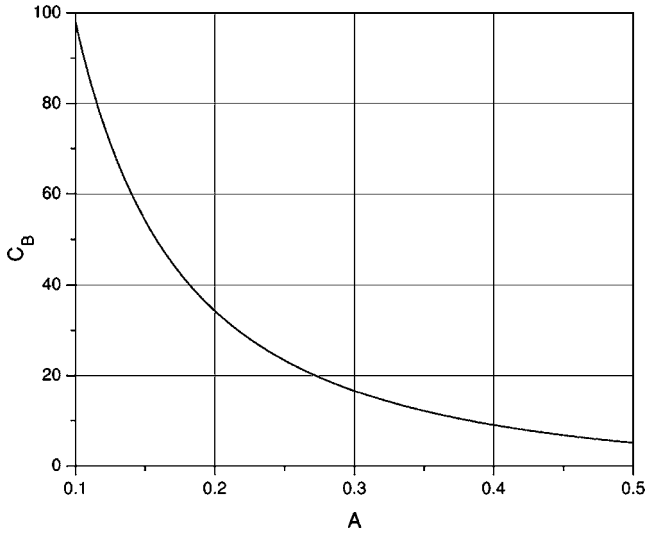

FIG. 6. The variation of the coefficient C_B with area ratio A in the case of circular holes.

Remark 4: It is possible in some cases for the value r_{opt} *to be too small to be realized technologically. If a constraint of the form*

$$r \geq r_{\min}$$

does apply, and we have $r_{\text{opt}} < r_{\min}$, *then we consider* $r_{1\text{opt}} = r_{\min}$ *and determine the other geometrical parameters by using formulas* (14) and (15). *In this case the squeeze film damping will dominate the total viscous damping.*

Remark 5: As we noted in the Introduction a certain viscous damping is needed for stabilizing the system. In the case where the minimum value of the total damping, given by formula (24), *is too low, it has to be considered again a constrained optimum value and the design parameters chosen accordingly.*

Remark 6: All the above formulas are based on modeling the squeezed film damping by Reynolds' lubrication equation. This theory applies for the viscous flow through a narrow gap between two surfaces as in Ref. 21. *In the case of less narrow gaps, the full system of Stokes equations has to be considered. Even in this case, the results obtained by applying the Reynolds' equation are conservative, the real pressure is smaller than that given by the lubrication approximation.*

IV. DESIGN FORMULAS FOR ALIGNED SQUARE HOLES

All the analysis performed in the previous section can be remade for the case where the holes are squares of $2a$ side

TABLE I. The coefficients for regular round holes.

A	$\frac{3}{4}$	$\frac{2}{3}$	$\frac{1}{2}$	$\frac{1}{3}$	$\frac{1}{4}$	$\frac{1}{5}$	$\frac{1}{6}$
C_N	0.0117	0.0167	0.0254	0.0298	0.0290	0.0273	0.0254
C_d	9.24	7.73	6.27	5.80	5.87	6.06	6.27
C_r	4.51	3.56	2.5	1.89	1.66	1.53	1.45
C_B	1.05	1.89	5.12	13.5	23.4,	34.3	46.0

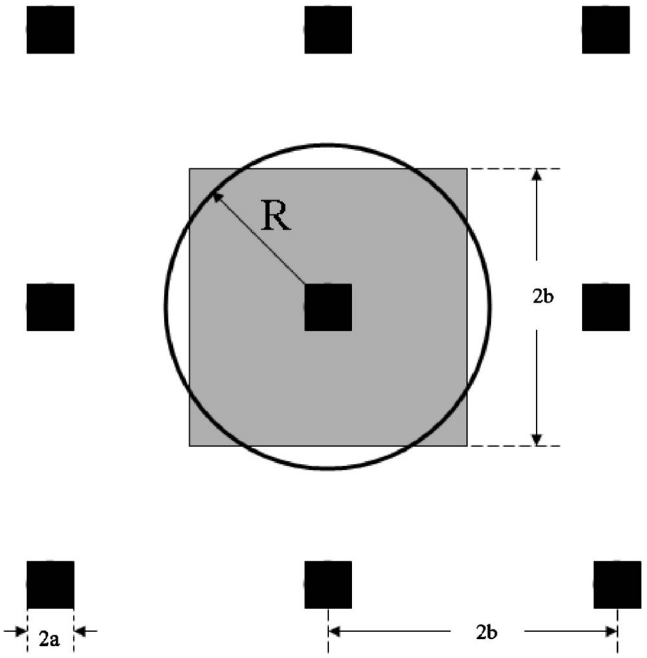

FIG. 7. The influence domain (the cell) of a square hole and its circular approximation.

lengths and the cells are also squares of $2b \equiv d$ side length (Fig. 7). We approximate the two squares with two circles of radii r and R such that

$$\pi r^2 = 4a^2, \quad \pi R^2 = 4b^2.$$

The squeezed-film damping can be written in this case as[16]

$$F^s_{\square} = \frac{192\mu b^4}{\pi d_0^3} C(A) w,$$

where now $A = a^2/b^2$.

The resistance of the holes can be obtained by using formula (24) given in Ref. 16 and the formula for the rate of flow for a square section given in Ref. 21,

$$F^h_{\square} = \frac{12}{k_1} \mu h \left(\frac{b}{a}\right)^4 w,$$

where

$$k_1 = 1 - \frac{192}{\pi^5} \sum_{j=1}^{\infty} \frac{\tanh\left((2j-1)\pi/2\right)}{(2j-1)^5} = 0.4217.$$

The total damping coefficient over area u^2 containing N cells ($u^2 = 4b^2 N$) is

$$B^T_{\square} \equiv F^T_{\square}/w = 12\mu \left[\frac{C(A)}{\pi d_0^3} \frac{u^4}{N} + \frac{1}{k_1} \frac{h}{A^2} N \right]. \tag{26}$$

This has a minimum value for

$$N_{\square opt} = \sqrt{\frac{k_1}{\pi} \frac{A^2 C(A)}{h d_0^3}} u^2. \tag{27}$$

The corresponding minimum damping coefficient is

$$B_{\square \min} = \frac{24}{\sqrt{\pi k_1}} \frac{\sqrt{C(A)}}{A} \mu \sqrt{\frac{h}{d_0^3}} u^2. \tag{28}$$

The designing formulas in this case are given in the following.

A. The optimum number of holes

We can write formula (27) as

$$N_{\square opt} = C^N_{\square} \frac{u^2}{\sqrt{h d_0^3}}, \tag{29}$$

where

$$C^N_{\square} = \sqrt{\frac{k_1}{\pi} A^2 C(A)}. \tag{30}$$

B. The optimum length of the cell side

The formula $u^2 = 4b^2 N$, combined with the relationship (27), gives the optimum cell side length as

$$d \equiv 2b_{\square \min} = C^b_{\square} \sqrt[4]{h d_0^3}, \tag{31}$$

where

$$C^b_{\square} = 1/\sqrt{C^N_{\square}}. \tag{32}$$

C. The optimum side length of the hole

Defining the coefficient $C^a_{\square}$ by the formula

$$C^a_{\square} = C^b_{\square} \sqrt{A} \tag{33}$$

and taking into account the formula $A = a^2/b^2$, the length of the side of the hole (corresponding to the minimum damping coefficient) is

$$2a_{\square \min} = C^a_{\square} \sqrt[4]{h d_0^3}. \tag{34}$$

D. The minimum damping coefficient

The minimum damping coefficient (28) can be written as

$$B_{\square \min} = C^b_{\square} \sqrt{\frac{h}{d_0^3}} \mu u^2, \tag{35}$$

where

$$C^b_{\square} = \frac{24}{\sqrt{\pi k_1}} \frac{\sqrt{C(A)}}{A}. \tag{36}$$

Remark 7: We have

$$\frac{C^b_{\square}}{C_b} = \frac{24}{8\sqrt{6}\sqrt{\pi k_1}} = 1.064.$$

Therefore the damping coefficient in the case of circular holes is smaller than that corresponding to the case of square holes, but the difference is so small that square and round holes can be considered in many cases to be practically equivalent.

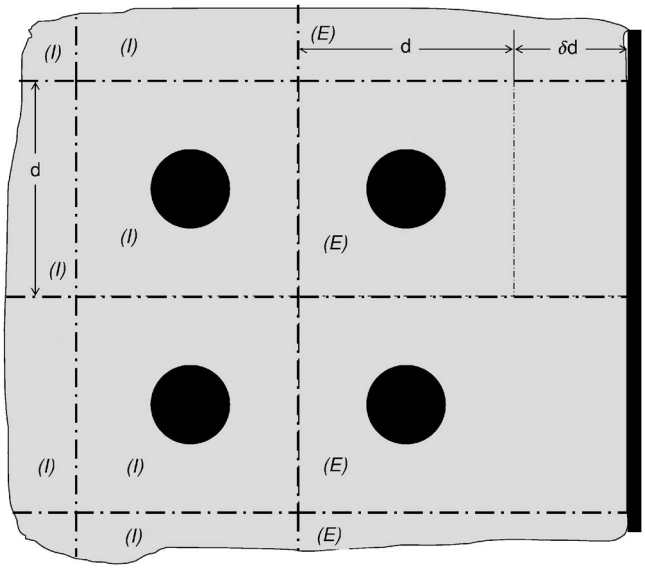

FIG. 8. The edge "*E*" and the inner "*I*" cells.

V. THE EDGE CORRECTION IN DESIGNING PERFORATED PLANAR MICROSTRUCTURES

The analysis in the previous sections assumed the perforated planar microstructure to be infinite in both the *Ox* and *Oy* directions. A real structure is, of course, finite having several edges. The Neumann boundary condition satisfied on a closed side of the domain, $\partial p/\partial n=0$, is compatible with the condition on the external curve of the cell. Consequently the closed sides of the domain boundary do not need any correction. The boundary condition on an open side of the boundary is of Dirichlet type ($p=0$), different from the Neumann condition required by the external curve of the cell. This gives a pressure change from cell to cell that breaks the periodicity of the flow and results in an additional squeezed-film flow component from the center of the microstructure towards the open edges. In order to obtain a better design of such a structure we have to include corrections due to the open structure edges.

A. The edge correction

Figure 8 shows a part of a perforated planar microstructure including some edge cells (denoted by (**E**)] and also the neighbors inside cells [denoted by (**I**)]. Correspondingly, the pressure function in an edge cell will be denoted by $p^{(E)}(x,y)$ while the same function corresponding to an inner cell will receive the superscript $(I):p^{(I)}(x,y)$. The main difference in analyzing the two types of cells is that while for (**I**)-cells the boundary condition along all rectilinear sides $\mathcal{C}_N^I$ (represented by dotted lines in Fig. 8) is of the Neumann homogenous type, for the edge cells the boundary condition along the external side of the cell, denoted by $\mathcal{C}_D^E$, requiring the canceling of the pressure, is of Dirichlet type; along the remaining external curve of the (**E**) cell's boundary $\mathcal{C}_N^E$ (dotted lines in Fig. 8) the condition is, again, of Neumann homogeneous type. Physically, this condition will give a smaller value for the total pressure of a square (**E**) cell as compared with that corresponding to an inner cell. In order

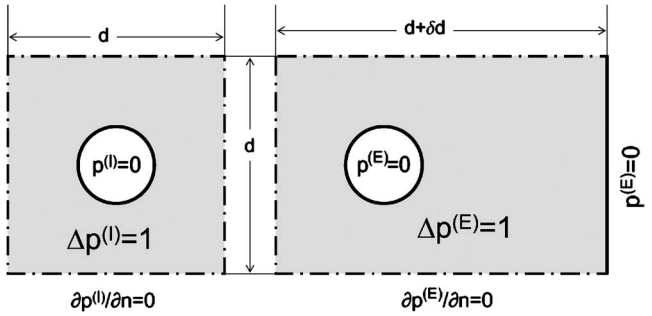

FIG. 9. The boundary-value problems corresponding to an "edge" and to an "inner" cell.

to increase the total pressure of an edge cell we increase the length of its sides perpendicular to the plate edge by a value δd. The value of this parameter is obtained from the condition that the total pressure resulting from the squeezed-film damping for the modified edge cell be equal to the total pressure corresponding to an inner cell. This increase of the total pressure of the open edge cells will result in a supplementary squeezed-film flow component, towards the center of the damper, which cancels the additional squeezed film component.

Mathematically we consider the canonical boundary-value problems (Ref. 17) for the two types of cells

$$\Delta p^{(I)}(x,y)=1 \text{ in } \mathcal{D}^{(I)}, \quad p^{(I)}|_{\mathcal{C}_0^I}=0, \quad \left.\frac{\partial p^{(I)}}{\partial n}\right|_{\mathcal{C}_N^I}=0, \tag{37}$$

$$\Delta p^{(E)}(x,y)=1 \text{ in } \mathcal{D}^{(E)}, \quad p^{(E)}|_{\mathcal{C}_0^E\cup\mathcal{C}_D^E}=0,$$

$$\left.\frac{\partial p^{(I)}}{\partial n}\right|_{\mathcal{C}_N^E}=0. \tag{38}$$

Here $\mathcal{D}^{(I)}$ and $\mathcal{D}^{(E)}$ are the domains corresponding to an inner and edge cell, respectively, and $\mathcal{C}^0$ and $\mathcal{C}_0^E$ denote the central circles in both cases (Fig. 9). The parameter δd results by solving the equation

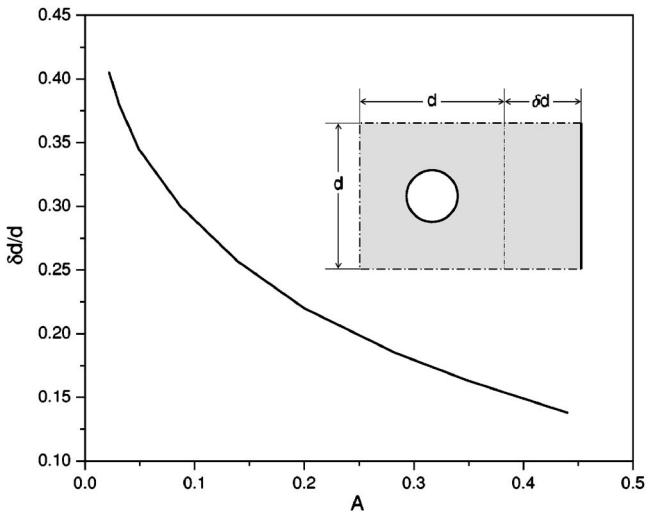

FIG. 10. The variation of the ratio $\delta d/d$ with area ratio A.

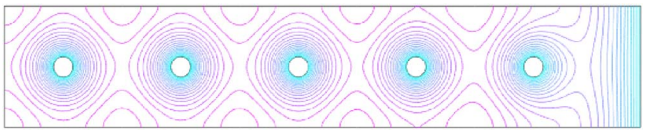

FIG. 11. (Color online) The pressure graph for a damper with five holes and with an opened right side.

$$P^{(I)} \equiv \int\int_{\mathcal{D}^I} p^{(I)}(x,y)\,dx\,dy = \int\int_{\mathcal{D}^E} p^{(E)}(x,y)\,dx\,dy \equiv P^{(E)}. \tag{39}$$

It is clear that the geometry of the problem changes with the area ratio of the domain. Consequently, the correction δd depends upon the area ratio A. This is why Eq. (39) has to be solved for each value of this parameter. We have determined the solutions of the two boundary-value problems (37) and (38), for area ratio values in the range of practical interest, by using the Partial Differential Equation (PDE) Toolbox and its associated graphical user interface (GUI) of MATLAB. Finally, we have solved Eq. (39) for each value of the area ratio by a bisection-type technique. The results are plotted in Fig. 10.

Thus the edge correction consists of increasing the sides of the edge cells (perpendicular to the edge line) by the value δd. This is the same as decreasing the domain containing uniformly spaced circular holes with the value δd for all the open sides of the physical domain parallel to the coordinate axis, and considering the design problem for the resulting domain. It can result in eliminating a line or/and a column of holes in some cases.

B. Numerical validation of the open edge correction

In order to validate the proposed correction to the open side boundaries we consider a domain with one-dimensional periodicity in the y direction, a closed side on the left, and an open side to the right. In dimensionless variables we consider the canonical boundary-value problem, which gives the Poisson' equation for the pressure

$$\Delta p(x,y) = 1$$

in the multiconnected domain consisting of a line of cells with homogeneous Neumann-type boundary conditions on the upper, lower, and left boundaries and with Dirichlet homogeneous conditions on the right (open) side and on the rim of holes. The dimensions of the open edge cell were modified according to the results in Fig. 10. Since the additional squeezed-film flow component is more important for small values of A numbers, we have chosen $d=1$, $r=0.084$.

TABLE II. The error after edge correction in the case $A=0.022$.

j	P_j	$\tilde{P}_j = j \star P_1$	ϵ_j
1	0.189 692	0.189 692	0
2	0.379 217	0.379 384	$4.\times10^{-4}$
3	0.568 906	0.569 076	$3.\times10^{-4}$
4	0.758 598	0.758 768	2.2×10^{-4}
5	0.948 291	0.948 460	1.8×10^{-4}

Hence there results $A=0.022$, $\delta d=0.405$. Due to similarity of the PDE equation and of the boundary conditions we have used the COMSOL software for the steady state heat conduction problem (which is a finite element implementation). The graph of the pressure, given in Fig. 11, shows qualitatively the periodicity of the pressure in the cells next to the end cells. We computed the total pressure P_j, $(j=1,2,\ldots,5)$ for the model domain having j cells. The total pressure given by our edge correction will be $\tilde{P}_j = j \star P_1$, $(j=1,2,\ldots,5)$. The results are given in Table II, where ε_j is the relative error.

Due to the way the boundary condition was defined, an open edge cell and the cell next to it have the same total pressure. However, ϵ_2 is not zero due to the fact that the roots of Eq. (39) were computed with several valid digits (three in this example). It is to be noticed that $\epsilon_2 > \epsilon_3 > \epsilon_4 > \epsilon_5$, indicating that the edge effect is diminishing with the distance to the microstructure edge.

For more validation of the edge correction for open boundaries we considered the simulations included in Table III covering all the range of area ratio A considered in the graph in Fig. 10.

The error in the second column is connected with the precision of the determination of the root of Eq. (39) and also the precision of the Finite Element Program for solving the corresponding BVP. The largest error introduced by our model of the edge correction is smaller than 0.04%. These simulations show that the proposed edge correction works very well validating the adopted model.

The edge correction presented here works in the case of perforated structures with unidimensional symmetry. It is clear that it is not working for the "*corner*" cells, which need separate analysis. The external geometry of a corner cell is completely determined by the geometry of the adjacent sides. This is why the only parameter that can be used for equalizing the total pressure of a corner cell with that corresponding to an inner cell is the radius of the hole. Consequently, the corner correction adjusts the radii of the corner holes. Generally, the number of corner cells is low compared with the total number of holes of a given microstructure. This is why

TABLE III. The error after edge correction for $A=0.022-0.44$.

A	r	δd	ϵ_2	ϵ_3	ϵ_4	ϵ_5
0.022	0.084	0.405	4.0×10^{-4}	3.0×10^{-4}	2.2×10^{-4}	1.8×10^{-4}
0.031	0.1	0.38	5.2×10^{-5}	3.9×10^{-5}	2.9×10^{-5}	2.3×10^{-5}
0.139	0.21	0.257	1.0×10^{-4}	7.0×10^{-5}	5.0×10^{-5}	4.0×10^{-5}
0.283	0.3	0.1855	$<10^{-6}$	$<10^{-6}$	$<10^{-6}$	$<10^{-6}$
0.44	0.374	0.138	$<10^{-6}$	$<10^{-6}$	2.5×10^{-5}	1.8×10^{-5}

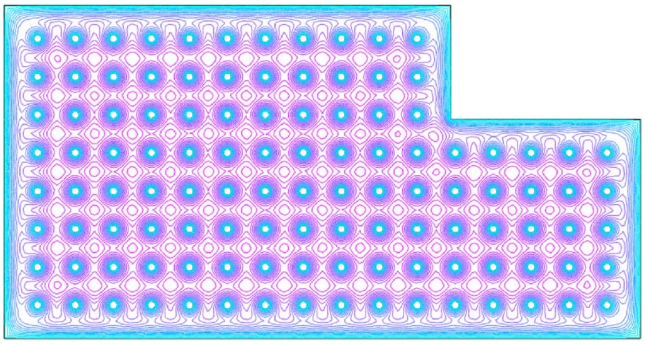

FIG. 12. (Color online) The pressure graph for a microstructural damper containing 113 holes, a reentrant corner, and five external corners.

the corner adjustments are less important than the side corrections.

The microstructure in Fig. 12 has 113 holes, five external corners, and one reentrant corner. All the sides are open such that the edge correction was applied to all of them. The total pressure obtained by using a FEM code for the whole structure equals $TP=18.460$. The total pressure for an inner cell is $TP^{(I)}=0.1629$ and hence the approximation for the whole structure equals $\widetilde{TP}=113\times TP^{(I)}=18.408$. The relative error is $\varepsilon=0.28\%$. The total pressure for the whole structure without applying the edge correction, obtained again by using a FEM code, is $TP'=15.017$. Thus, if the edge correction was not applied, the relative error for the whole structure would have been $\varepsilon'=18\%$. We also note that the smallness of the error after applying the edge correction makes it unnecessary to apply the corner corrections.

VI. SPECIAL CORRECTIONS TO THE BASIC DESIGNING FORMULAS

In this section various corrections are discussed for the design formulas, taking into consideration the rarefied gas effect, effect of the ends of the hole, compressibility of the gas, and inertia. All the corrections will be considered for the case of circular holes.

A. Corrections due to the rarefied gas effects

It has been shown in Refs. 23 and 17 that at small air gaps, when the molecular mean free path λ' is not negligible compared with the gap width d_0, which is the case in many perforated planar microstructures, the rare gas effects become important. In this case formula (6) still holds if the viscosity coefficient μ is replaced by the effective viscosity μ':

$$\mu' = \frac{\mu}{1+6\sigma_P K_n'}.$$

The Knudsen number $K_n'=\lambda/d_0$ includes the slip correction due to the flow profile for a rare gas. For a diffuse scattering model $\sigma_P=1.016$ and the molecular mean free path λ can be calculated via the pressure P, the temperature T, the shear viscosity μ, and the molecular mass m (Ref. 24),

$$\lambda = \frac{\sqrt{\pi}\mu}{2P}\left(\frac{2k_BT}{m}\right)^{1/2},$$

where $k_B=1.380658\times10^{-23}$ J/K is Boltzmann's constant.

On the other hand, if the holes are very thin (*Knudsen number* $K_n''=\lambda/r$ is large), the slip boundary condition has to be again considered in the capillaries. The resistance of the flow in holes can still be determined by using formula (13) if the effective viscosity μ''

$$\mu'' = \frac{\mu}{1+4\sigma_P K_n''},$$

is taken to be the viscosity coefficient.

Consequently, formula (16) includes a correction factor c for rarefaction

$$c = \sqrt{\frac{\mu'}{\mu''}},$$

and in formula (17) the viscosity coefficient is substituted by the geometrical average

$$\mu \to \sqrt{\mu'\mu''}.$$

Correspondingly, formula (18) has c as a factor on the right-hand side and the right-hand side terms in formulas (20) and (22) have to be divided by $\sqrt{c}$. Finally, in formula (24) $\sqrt{\mu'\mu''}$ has to be substituted for the viscosity coefficient μ.

B. The correction for the hole end effect

The fully developed Poiseuille flow, assumed in the calculations of the resistance of holes in Eq. (13), theoretically holds only for infinite ducts. In the case where the thickness of the plate h and the radius r are of comparable dimensions a correction has to be made for the effect of the finite length of holes. Shapirov and Seleznev in Ref. 24 have shown that this effect can be included in formula (13) by replacing the length of holes with

$$h_{\text{eff}} = h + \frac{3\pi r}{8}.$$

Correspondingly, in all the basic design formulas the effective length h_{eff} will be used instead of the depth into the page h.

C. Correction to Skvor's model

The derivation of the basic designing formulas was based on approximating the cell with a circular domain shown in Fig 2. The error resulting from this assumption was analyzed in Ref. 17, Sec. VII. The results show that Skvor's approximation works well for $A<0.4$. For larger values of the area ratio, A, a corrected formula

$$C^*(A) = C(A) + 10^{-4}(8.7 - 10\sqrt{A} + 26A - 27A\sqrt{A})$$

can be used instead of Skvor's function $C(A)$. This correction extends the applicability of the analytical approach up to $A=0.75$.

D. Corrections for higher frequencies

The analysis presented here holds, true in the range of audible acoustical frequencies. For higher frequencies, the effects of inertia and compressibility become important. The coefficients accounting for the combined influence of inertia and compressibility can be determined by using the formulas given in Ref. 17, Sec. IV.

VII. EXAMPLE OF APPLICATION OF GIVEN FORMULAS

As an application we consider the backplate of a high sensitivity MEMS microphone designed by Hsu *et al.* in Ref. 25 and analyzed also in Ref. 26. The backplate has a square geometry with the side length of $L=2580$ μm, the gap underneath is $d_0=4$ μm, and the thickness $h=13$ μm. The backplate has a periodic system of 441 square holes of area 60×60 μm^2. The area ratio is

$$A = (441 \times 60^2/2580^2) = 0.2385.$$

The total damping coefficient for this perforated plate can be determined by using Eq. (26) where $\mu_{\text{air}}=1.846\times 10^{-5}$ [kg/(m s)]. We obtain

$$B^{old} = 1.06 \times 10^{-2} \text{ (Ns/m)}.$$

A. Redesign the microstructure with square holes

We can redesign this planar microstructure such that the resulting device has square holes and a minimum damping coefficient. In this case formulas (29)–(36) give

$$N_{\square\text{opt}} = 6230, \quad 2b = 32.7 \ (\mu\text{m}),$$

$$2a = 16 \ (\mu\text{m}), \quad B_{\square\text{min}} = 1.48 \times 10^{-3} \text{ (Ns/m)}.$$

B. Redesign the structure with circular holes

In the case where we use circular holes instead of square perforations, the design data given by formulas (18)–(25) are

$$N_{\text{opt}} = 6630, \quad d = 31.7 \ (\mu\text{m}), \quad r = 8.7 \ (\mu\text{m}),$$

$$B_{\text{min}} = 1.4 \times 10^{-3} \text{ (Ns/m)}.$$

This way the redesign of the perforated microstructure resulted in a reduction of the damping coefficient by a factor of 7 in the case of square holes and by a factor of 7.6 when circular holes are used.

C. Application of the edge correction

In order to apply the edge correction we note that for $A=0.24$, as given above, the graph in Fig. 10 gives $\delta d/d=0.2$ and hence $\delta d=6.4$ (μm) for each side of the rectangle. Applying this correction to all sides, the reduced domain has the sides of dimensions equal to $\tilde{L}=2567$ (μm). Correspondingly, we obtain a number of $N_1=81$ cells along each side of the backplate. This gives a total of 6561 cells. The final design data are

$$d = 31.7 \ (\mu\text{m}), \quad r = 8.7 \ (\mu\text{m}), \quad N_1 = 81,$$

the central cell being in the center of the given square.

Let us now suppose that we have a technological restriction of $r \geq 20$ μm. In this case the formula (7) gives

$$d = \sqrt{\frac{\pi}{A}} r = 35.5 \ (\mu\text{m})$$

and hence

$$N_1 = \frac{\tilde{L}}{d} = 35; \quad N = N_1^2 = 1225 \text{ holes}.$$

Correspondingly, the damping coefficient, obtained by dividing the result of Eq. (15) by the velocity w, is

$$B' = 3.9 \times 10^{-3} \text{ (Ns/m)}.$$

This way we obtain a reduction of the total damping of a factor of almost 3 as compared with the initial design for the same area ratio.

D. Application of the rarefied gas and hole end effect corrections

The parameters for the air at atmospheric pressure used in the calculations are the pressure $P=101.3\times 10^3$ (N/m^2), the temperature $T=300$ K, viscosity $\mu=1.85\times 10^{-5}$ (Ns/m^2), and mean free path $\lambda=68.2\times 10^{-9}$ (m).

The results, after applying the *rarefied gas effect* correction and and the correction for the *effect of the ends of holes*, are

$$N_{\text{opt}} = 8572, \quad d = 28.3 \ (\mu\text{m}), \quad r = 6.7 \ (\mu\text{m}),$$

$$B_{\text{min}} = 1.3 \times 10^{-3} \text{ (Ns/m)}.$$

By also adding the edge correction the design data become

$$d = 28.3 \ (\mu\text{m}), \quad r = 6.7 \ (\mu\text{m}), \quad N_1 = 91.$$

VIII. CONCLUSIONS

(a) The formula for the optimal number of holes provides the smallest damping coefficient for the given area ratio.
(b) In all of the results presented here, the dependence on the area ratio is separated from the dependence on the other parameters of the problem.
(c) The effect of the side correction can be easily incorporated into analyses by reducing the domain occupied by holes by δd for each open side of the domain.
(d) It is shown (see Fig. 6) that the damping coefficient is strongly dependent on area ratio of the plate: when the area ratio is increased the damping coefficient decreases significantly. However, removing more material from the plate reduces the stiffness of the plate and also decreases its mass. Also, in some applications the (electrical) sensitivity of the system is directly correlated with the area ratio of the perforated plates. Since these elements are

basic properties it is important to find a proper balance between the removed portion (area ratio) and the damping coefficient.

(e) The analysis in Sec. II shows that the *indirect resistance of holes* is more important than the *direct resistance*.

ACKNOWLEDGMENTS

This work has been supported through NIH Grant No. R01 DC05762-1A1 to RNM.

[1]T. B. Gabrielson, "Mechanical-thermal noise in micromachined acoustic and vibration sensors," IEEE Trans. Electron Devices, **40**, 903–909 (1993).
[2]M. Gad-el-Hak (ed.), *MEMS Applications* (CRC Press, Taylor & Francis Group, Boca Raton, FL, 2006).
[3]M-H. Bao, *Micro Mechanical Transducers* (Elsevier, Amsterdam, 2000).
[4]H. M. Saad and A. K. Stiffler, "Squeeze film dampers amplitude effects at low squeeze numbers," J. Eng. Ind. **97**, 1366–1370 (1975).
[5]J. B. Starr, "Sqeeze-film damping in solid-state accelerometers," Tech. Digest IEEE Solid State Sensor and Actuator Workshop, Hilton Head Island, SC, June 1990, pp. 44–47.
[6]Y. J. Yang and S. D. Senturia, "Numerical simulation of compressible squeezed-film damping," Tech. Digest IEEE Solid State Sensor and Actuator Workshop, Hilton Head Island, SC, June 1990, pp. 76–79.
[7]A. H. Nayfeh and M. I. Younis, "A new approach to the modeling and simulation of flexible microstructures under the effect of squeeze-film damping," J. Micromech. Microeng. **14**, 170–181 (2004).
[8]T. Veijola, K. Ruokonen, and Tittonen, "Compact model for squeezed-film damping including the open border effects," in *Proceedings of MSM 2001*, Hilton Head SC, 19–21 March, 2001, pp. 76–79.
[9]T. Veijola, "Analytic Damping Model for an MEM Perforation Cell," Microfluid. Nanofluid. **2**(3), 249–260 (2006).
[10]T. Veijola and T. Mattila, "Compact squeezed-film damping model for perforated surface," in *Proc. Transducers '01*, München, Germany, 10–14 June 2001, pp. 1506–1509.
[11]P. Raback, A. Pursula, V. Junttila, and T. Veijola, "Hierarchical finite element simulation of perforated plates with arbitrary hole geometry," in *Proceedings of the 6th International Conference on Modeling and Simulation of Microsystems*, San Francisco, 2003, Vol. 1, pp. 194–197.
[12]Y.-J. Yang and C.-J. Yu, "Macromodel extraction of gas damping effects for perforated surfaces with arbitrary-shaped geometrics," in *Proceedings of the 5th International Conference on Modeling and Simulation of Microsystems*, San Juan, 2002, pp. 178–181.
[13]T. Veijola and P. Raback, "A method for solving arbitrary mems perforation problems with rare gas effects," in *Proceedings of the 8th International Conference on Modeling and Simulation of Microsystems*, NSTI-Nanotech 2005, Anaheim, Vol. 3, pp. 561–564.
[14]M. Bao, H. Yang, Y. Sun, and P. J. French, "Modified Reynolds, equation and analytical analysis of squeeze-film air damping of perforated structures," J. Micromech. Microeng. **13**, pp. 795–800 (2003).
[15]M. Bao, H. Yang, Y. Sun, and Y. Wang, "Squeeze-film air damping of thick hole-plate," Sens. Actuators, A, **A108**, 212–217 (2003).
[16]D. Homentcovschi and R. N. Miles, "Modelling of viscous damping of perforated planar micromechanical structures. Applications in acoustics," J. Acoust. Soc. Am. **116**(5), 2939–2947 (2004).
[17]D. Homentcovschi and R. N. Miles, "Viscous Damping of Perforated Planar Micromechanical Structures," Sens. Actuators, A **A119**, 544–552 (2005).
[18]A. J. Zuckerwar, "Theoretical response of condenser microphones," J. Acoust. Soc. Am. **64**, 1278–1285 (1978).
[19]C. W. Tan and J. Miao, "Analytical modeling for bulk-micromachined condenser microphones," J. Acoust. Soc. Am. **120**(2), 750–761 (2006).
[20]Z. Ščvor, "On acoustical resistance due to viscous losses in the air gap of electrostatic transducers," Acustica **19**, 295–297 (1967-1968).
[21]F. M. White, *Viscous Fluid Flow* (McGraw-Hill, New York, 1992).
[22]H. Ockendon and J. R. Ockendon, *Viscous Flow* (Cambridge U.P., Cambridge, 1995).
[23]T. Veijola, H. Kuisma, J. Lahdenperä, and T. Ryhänen, "Equivalent-circuit model of the squeezed gas film in a silicon accelerometer," Sens. Actuators, A **A48**, 239–248 (1995).
[24]M. H. Shapirov and V. Seleznev, "Data on internal rarefied gas flows," J. Phys. Chem. Ref. Data **27**, 657–706 (1997).
[25]P. C. Hsu, C. H. Mastrangelo, and K. D. Wise, "A high sensitivity polysilicon diaphragm condenser microphone," Digest Workshop on Micro-ElectroMech. Systems (MEMS), Heidelberg, January 1998, pp. 580–585.
[26]S. S. Mohite, V. H. Kesari, R. Sonti, and R. Pratap, "Analytical Solutions for the Stiffness and Damping Coefficients of Squeeze Films in MEMS Devices having Perforated Back Plates," J. Micromech. Microeng. **15**, 2083–2092 (2005).

Optimal design of resonant piezoelectric buzzer from a perspective of vibration-absorber theory

Mingsian R. Bai,[a] Rong-Liang Chen, and Chung-Yuan Chuang
Department of Mechanical Engineering, National Chiao-Tung University, 1001 Ta-Hsueh Road, Hsin-Chu 300, Taiwan

Cheng-Sheng Yu and Huey-Lin Hsieh
Ceramic Materials Section, New Materials Research & Development Department, China Steel Corporation, 1 Chung Kang Road, Hsiao Kang, Kaohsiung 812, Taiwan

(Received 24 November 2006; revised 13 June 2007; accepted 14 June 2007)

In this paper, an optimization technique is presented for the design of piezoelectric buzzers. This design technique aims at finding the optimal configuration of the coupled cavity and diaphragm structure to maximize the sound pressure output. Instead of measuring the material constants of the piezoelectric ceramic and the metal diaphragm, an "added-mass method" is developed to estimate the equivalent electromechanical parameters of the system on which an analogous circuit can be established. The electrical impedance and on-axis sound pressure level of the piezoelectric buzzer can be simulated by solving the loop equations of the electromechanoacoustical analogous circuit. An interesting finding of this research is that the nature of the piezoelectric buzzer bears remarkable resemblance to that in the dynamic vibration absorber theory. Much physical insight can be gained by exploiting this resemblance in search of the optimal configuration. According to the system characteristic equation, a design chart was devised to "lock" the critical frequency at which the system delivers the maximal output. On the basis of the analogous circuit and the vibration absorber theory, an optimal design was found with constrained optimization formalism. Experiments were conducted to justify the optimal design. The results showed that the performance was significantly improved using the optimal design over the original design. Design guidelines for the piezoelectric buzzers are summarized. © *2007 Acoustical Society of America.* [DOI: 10.1121/1.2756757]

PACS number(s): 43.38.Fx, 43.38.Ar, 43.40.Tm [AJZ] Pages: 1568–1580

I. INTRODUCTION

Piezoelectric buzzers are commonly used in many applications, such as household appliances, car security systems, medical apparatus, etc. They are essentially narrow-band devices intended to operate at the resonant frequency for large sound pressure output. In other words, the driving frequency generally coincides with the resonant frequency of the system to achieve the maximal efficiency. Although the buzzer technology is not new, this paper attempts to examine the devices in light of rigorous electroacoustic analysis. It is found from this research that interesting physical insights can be gained from these quite common devices. Useful guidelines for reaching optimal designs can also be derived from these findings.

A typical piezoelectric buzzer consisting of a piezoelectric diaphragm, a cavity with a port, and electrode terminals is shown in Figs. 1(a)–1(c). The piezoelectric diaphragm is generally made up of a piezoelectric ceramic disc attached to a slightly larger metal plate. Some studies on piezoelectric plates have been reported in the past. Caliano *et al.*[1] proposed a piezoelectric bimorph membrane sensor for pressure measurement. Tseng and Liou,[2] Dobrucki and Pruchnickli,[3] and Wang *et al.*[4] conducted theoretical and numerical investigations on the dynamic responses of bimorph piezoacoustic transducers. The dynamic behavior of a circular piezoelectric transducer was solved by numerical methods and compared to the results of the finite element method. Aronov[5,6] applied energy methods to analyze the piezoelectric transducers and established a model for simulation. A similar methodology was also applied to other piezoelectric transducers, e.g., panel speakers,[7] ultrasonic transducers,[8,9] etc. Caronti *et al.*[9] modeled a capacitive micromachined ultrasonic transducer by a two-port network. Gallas *et al.*[10] used lumped-element models to examine the frequency responses of a piezoelectric-driven synthetic jet actuator.

This paper aims at an in-depth analysis of the piezoelectric buzzer, with the emphasis on the interactions between the structural dynamics of the piezoelectric diaphragm and the acoustical response of the cavity and port. As will be demonstrated later in the paper, the physics underlying the coupled mechanical and acoustical system is surprisingly parallel to that of a *dynamic vibration absorber*.[11,12] It is this subtle mechanism that dictates the ultimate performance of the buzzer. By taking advantage of this mechanism, maximum sound pressure output can be attained. In addition, systematic search procedures can be employed to find optimal designs of the piezoelectric buzzer without time-consuming trial and error. To facilitate the design optimization, a simulation platform is established in the paper by using an experimental parameter identification method, the *added-mass*

[a]Author to whom correspondence should be addressed; electronic mail: msbai@mail.nctu.edu.tw

(a)

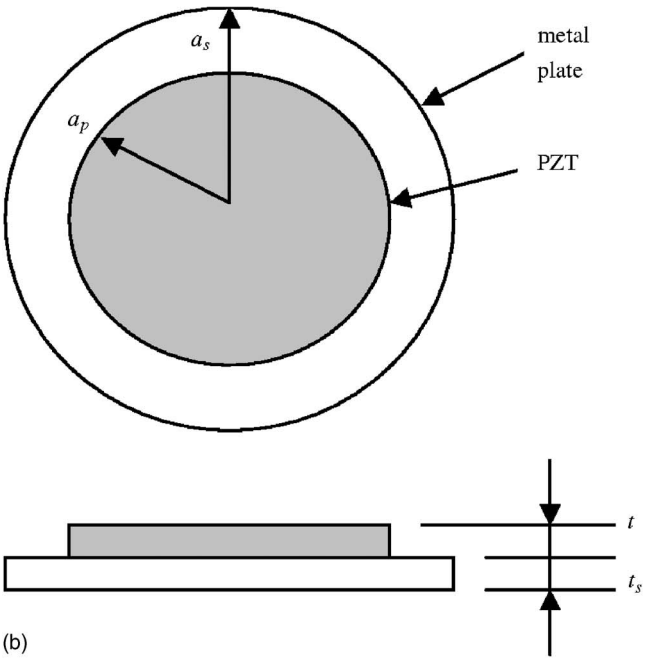

(b)

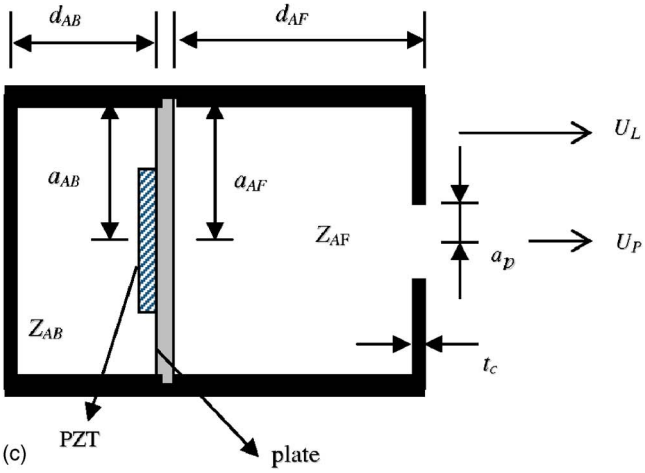

(c)

FIG. 1. (Color online) Piezoelectric buzzer, (a) Photo of the buzzer, (b) diaphragm structure, and (c) cross section of the piezoelectric buzzer.

method, similar to that used for electrodynamic loudspeakers.[13,14] With the identified parameters, the electrical impedance and the on-axis pressure response of the piezoelectric buzzer can be calculated by solving the loop equations[15] of the electromechanmacoustical (EMA) analogous circuit.[13,14] On the basis of the dynamic vibration absorber theory, a characteristic equation can be derived for predicting the resonance frequencies of the coupled mechanical and acoustical system of the piezoelectric buzzer. A design chart method was thus developed according to the characteristic equation to determine the optimal cavity and duct dimensions. The method can also be extended to a broader context in which both mechanical and acoustical parameters need to be optimized. A constrained optimization technique is developed using sequential quadratic programming (SQP)[16–18] to optimize the design parameters. On-axis pressure is selected to be the objective function for optimization, whereas the driving frequency, elctroacoustical parameters, dimensions of the cavity and port, etc., are appropriately constrained. It will be demonstrated by simulations and experiments that the optimized design significantly improves the performance of the buzzer over the original design. The physical insights as well as guidelines found in the design optimization are summarized in Sec. V.

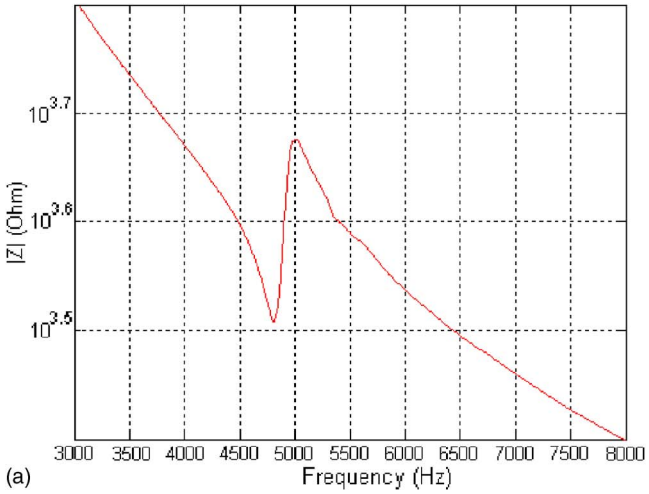

(a)

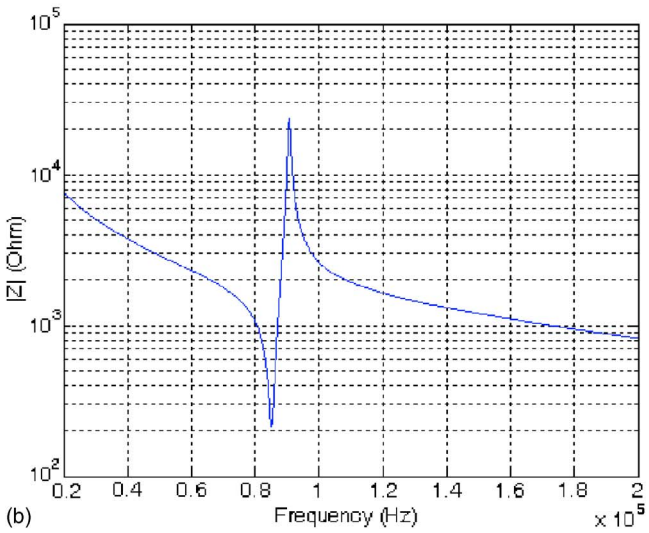

(b)

FIG. 2. (Color online) The measured electrical impedance of piezoelectric samples. (a) Rectangular plate of a standard PZT 5A and (b) piezoelectric diaphragm consisting of the PZT plate and the metal plate.

II. MODELING OF THE PIEZOELECTRIC BUZZER

A sample of a piezoelectric buzzer with a 12.7 mm diameter and 6 mm thickness is shown in Fig. 1(a). The piezo-

TABLE I. Dimensions of cavity of the piezoelectric buzzer.

Parameters	Dimension (mm)
Radius of rear cavity (a_{AB})	5.0
Height of rear cavity (d_{AB})	1.48
Radius of front cavity (a_{AF})	5.25
Height of front cavity (d_{AF})	3.08
Thickness of cavity (t_c)	0.76
Radius of port (a_p)	1.065
Radius of plate (a_s)	5.57
Thickness of plate (t_s)	0.05
Radius of PZT (a_p)	4.0
Thickness of PZT (t_p)	0.09

electric diaphragm is fitted in a plastic case. A pair of metal terminals are electrically connected to the piezoelectric diaphragm and drawn out from the back cover of the plastic case. The front portion of the buzzer consists mainly of a cavity with a circular port that serves as the sound outlet. The cross section of the piezoelectric buzzer is shown in Fig. 1(b) with dimensions indicated in Table I Figure 1(c) shows the diaphragm consisting of a circular piezoelectric ceramic (lead zirconate titanate, PZT 5A) and a circular plate (Fe-Ni alloy, Fe-60%, Ni-40%). By comparing the electrical impedance of this piezoelectric diaphragm [Fig. 2(a)] and that of a rectangular plate of standard PZT 5A sample without the metal plate [Fig. 2(b)], we found that the piezoelectric diaphragm exhibits basically similar characteristics to that of a piezoelectric ceramic alone. This suggests that the piezoelectric diaphragm can be modeled, in the low frequencies, by the same structure of the electromechanical analogous circuit in Figs. 3(a) and 3(b) as those used for a pure PZT sample. In order to determine the lumped electromechanical parameters in the circuit, a special experimental procedure was developed in this study and is detailed next.

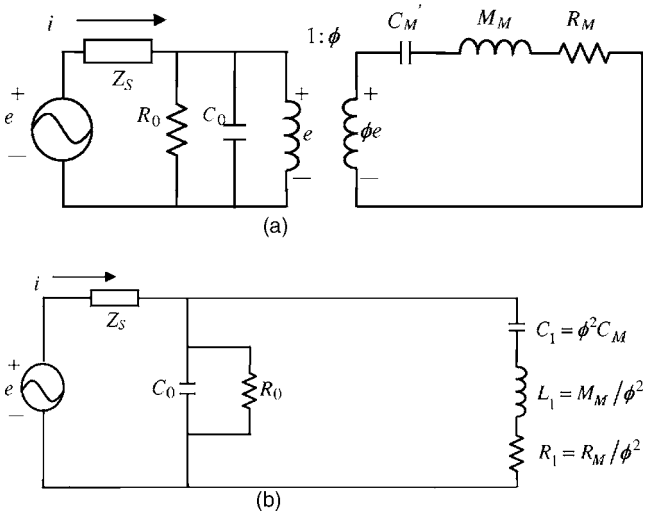

FIG. 3. Analogous circuit of the piezoelectric diaphragm. (a) The electrical and the mechanical circuits and (b) the circuit expressed in the electrical domain.

A. Parameter identification

Instead of calculating the lumped parameters using piezoelectric and other material constants, we opt to identify these parameters directly from electrical impedance measurement.[13] This approach, the *added-mass method*, was inspired by a commonly used method in identifying electrodynamic loudspeaker constants. Before the impedance measurement, the front cover of the buzzer must be removed, as shown in Fig. 4(a). Next, a 0.05 g clay patch is attached to

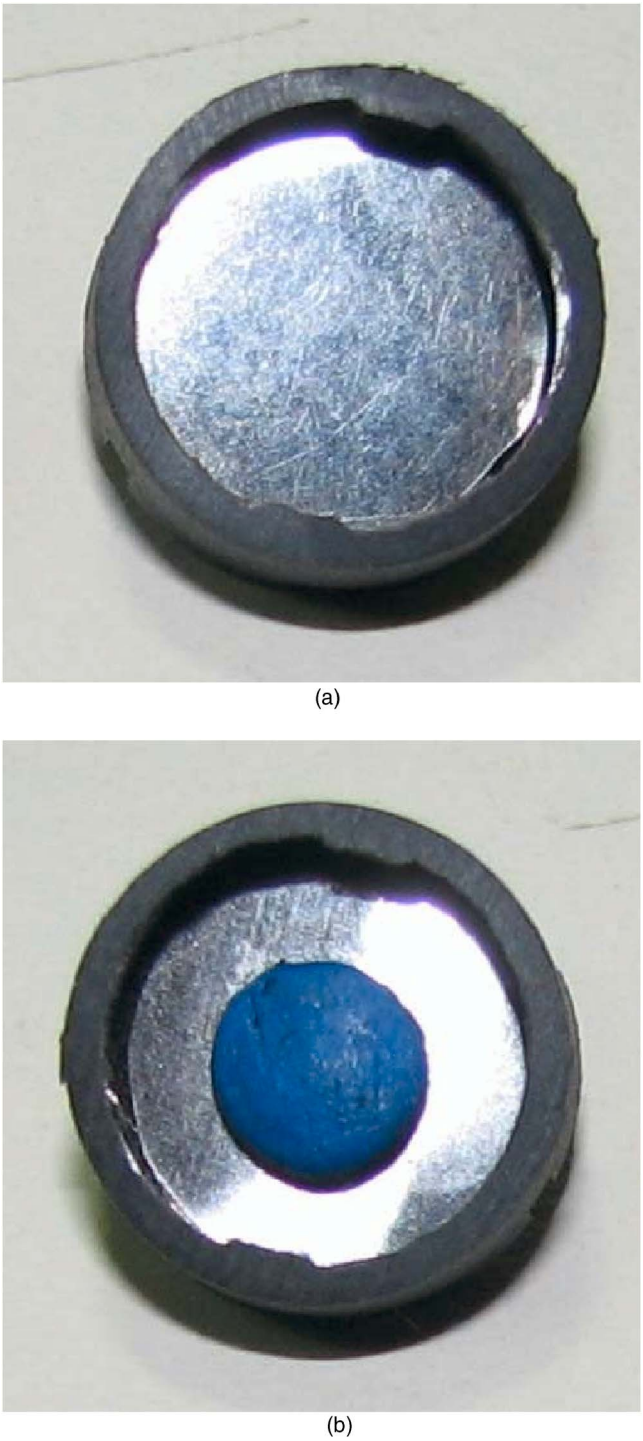

FIG. 4. (Color online) Piezoelectric buzzer without the front cover. (a) Photo of the buzzer, and (b) photo of the buzzer with the added mass on the diaphragm.

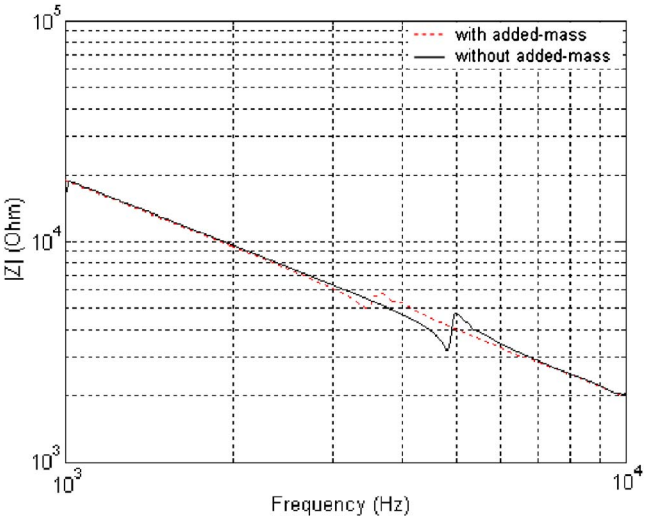

FIG. 5. (Color online) The measured electrical impedance of the buzzer, with and without the added mass.

the diaphragm, as shown in Fig. 4(b). The measured electrical impedance curves of the piezoelectric diaphragm with (solid line) and without (dashed line) the added mass are shown in Fig. 5. Clearly seen in the impedance curves, the resonant frequency (the trough in the curve) of the diaphragm has been decreased from 4875.0 to 3443.8 Hz because of the added mass.

The parameter identification procedure serves two purposes. First, the response of the buzzer, including electrical impedance, volume velocity, and sound pressure level (SPL), can be simulated and performance can be assessed on the basis of the EMA analogous circuit. Second, design optimization can be carried out on the platform of the identified model to determine the optimal loudspeaker parameters. The parameter identification procedure is outlined as follows.

1. Parameter estimation in the electrical domain

Figures 6(a) and 6(b) show a generic Nyquist plot of the electrical impedance and admittance of piezoelectric diaphragm (PZT + metal plate), respectively, from which the serial resonant frequency (f_s) and parallel resonant frequency (f_p) can be determined by locating the maxima of the real parts of the admittance ($G_{\max}$) and the impedance ($R_{\max}$), respectively. The Nyquist plot enables us to determine the parameters in Fig. 3(b). The dielectric losses (R_0) can be calculated from the minimum of the real part of admittance ($G_{\min}$),

$$R_0 = \frac{1}{G_{\min}}. \tag{1}$$

From the serial resonant frequency (f_s) and parallel resonant frequency (f_p); we may calculate the static capacitance (C_0), dynamic capacitance (C_1), inductance (L_1), and quality factor (Q) as follows:[19]

$$C_0 = (f_s/f_p)^2 C_f, \tag{2}$$

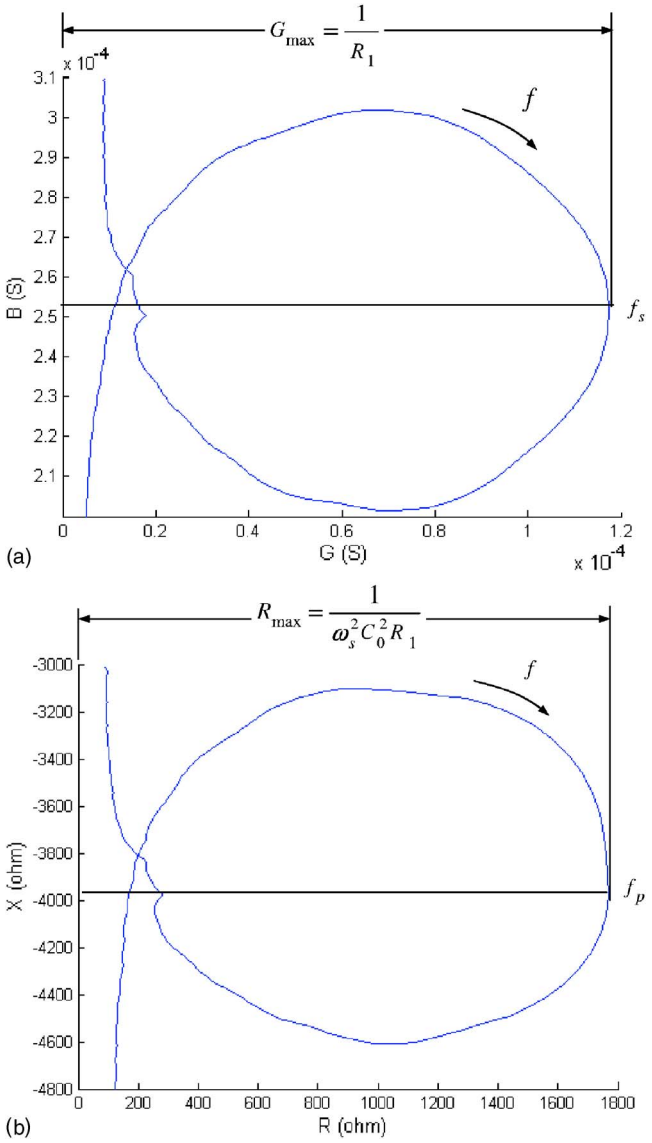

FIG. 6. (Color online) The measured Nyquist plots of the piezoelectric diaphragm without the added mass. (a) Electrical admittance $Y=G+jB$ and (b) electrical impedance $Z=R+jX$.

$$C_1 = C_f - C_0, \tag{3}$$

$$L_1 = \frac{1}{(2\pi f_s)^2 C_1}, \tag{4}$$

$$R_1 = \frac{1}{G_{\max}}, \tag{5}$$

$$Q = \frac{1}{2\pi f_s R_1 C_1}, \tag{6}$$

where C_f is the free capacitance of the PZT, which is measured as 7.167E-9 F at 1 kHz for the piezoelectric diaphragm.

2. The added-mass method

The resonance frequencies of the piezoelectric diaphragm without and with the added mass can be written as

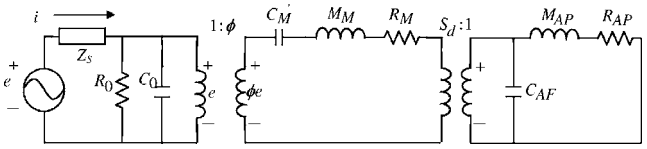

FIG. 7. The EMA analogous circuit of the piezoelectric buzzer.

$$\omega_n = \frac{1}{\sqrt{M_A C_A}}, \tag{7}$$

$$\omega_n = \frac{1}{\sqrt{(M_A + \Delta M_A) C_A}}, \tag{8}$$

where ΔM_A denotes the added mass expressed in the acoustical domain and M_A and C_A denote acoustical mass and compliance, respectively. Solving Eqs. (7) and (8) simultaneously for M_A and C_A yields

$$C_A = \frac{1}{\Delta M_A}\left(\frac{1}{\omega_n^2} - \frac{1}{\omega_n^2}\right), \tag{9}$$

$$M_A = \frac{1}{\omega_n^2 C_A}. \tag{10}$$

This corresponds to the mechanical mass and compliance,

$$M_M = M_A S_D^2, \tag{11}$$

$$C_M' = \frac{C_A}{S_D^2}, \tag{12}$$

where S_D is the effective area of the piezoelectric diaphragm (approximately 60% of the nominal area). The nonhomogeneity of the plate rather than the boundary condition leads to the large value of the effective area. Its central part is thicker than the peripheral, rendering the central part to vibrate almost as a rigid piston. Finally, the transduction factor (ϕ) and the mechanical resistance (R_M) can be estimated as follows:

$$\phi = \sqrt{\frac{C_1}{C_M}} = \sqrt{\frac{M_M}{L_1}}, \tag{13}$$

TABLE II. Lumped parameters of the piezoelectric buzzer.

Parameter	Value	Parameter	Value
f_p (Hz)	4931.3	$R_1(\Omega)$	3870.5
f_s (Hz)	4875.0	$R_0(\Omega)$	1.50E6
f_m (Hz)	4812.5	Q	40.6
f_n (HZ)	5018.8	M_M (kg)	5.25E−5
C_0 (F)	8.96E−9	C_M' (m/N)	2.08E−5
C_1 (F)	2.08E−10	R_M (N s/m)	3.86E−2
L_1 (H)	5.13	ϕ(N/V)	0.0032

$$R_M = \phi^2 R_1. \tag{14}$$

Following the preceding parameter identification procedure, lumped parameters of the piezoelectric diaphragm were calculated and summarized in Table II.

B. Frequency response simulation

After the lumped parameters of the piezoelectric diaphragm are identified, the response of the buzzer can be simulated on the basis of the EMA analogous circuit of Fig. 7. In the acoustical domain, the acoustical mass of port (M_{AP}), the acoustical resistance of port (R_{AP}), and the acoustical compliance of front cavity (C_{AF}) are calculated using the following formulas:[13]

$$M_{AP} = \frac{\rho_0}{\pi a_p^2}(t_c + 1.462 a_p), \tag{15}$$

$$R_{AP} = \frac{\rho_0}{\pi a_p^2}\sqrt{2\omega\mu}\left[\frac{t_c}{a_p} + 6.4\left(1 - \frac{\pi a_p^2}{b^2}\right)\right], \tag{16}$$

$$C_{AF} = \frac{V_{AF}}{\rho_0 c^2}, \tag{17}$$

where a_p is the radius of port, t_c is the thickness of front cavity, μ is the viscosity coefficient ($\mu = 1.56 \times 10^{-5}\mathrm{m}^2/\mathrm{s}$), b is the diameter of the piezoelectric diaphragm, V_{AF} is the volume of front cavity, c is the speed of sound ($c \approx 345$ m/s at the room temperature), and ρ_0 is the density of air ($\rho_0 = 1.21\ \mathrm{kg/m}^3$). It can be shown that the loop equations[15] corresponding to the analogous circuit of Fig. 7 are written as the following system of linear equations:

$$\begin{bmatrix} Z_S + Z_{EB} & -\phi Z_{EB} & 0 & 0 & 0 \\ Z_{EB} & -\phi Z_{EB} & -1 & 0 & 0 \\ 0 & Z_{ms} & -\phi & S_d & 0 \\ 0 & -S_d\left(M_{AP}s + \dfrac{1}{C_{AF}s}\right) & 1 & 0 & \dfrac{1}{C_{AF}s} \\ 0 & \dfrac{-S_d}{C_{AF}s} & 0 & 0 & M_{AP}s + \dfrac{1}{C_{AF}s} + R_{AP} \end{bmatrix} \begin{bmatrix} i \\ u \\ e \\ e' \\ i' \end{bmatrix} = \begin{bmatrix} V_g \\ 0 \\ 0 \\ 0 \\ 0 \end{bmatrix}, \tag{18}$$

where V_g is driving voltage, $s=j\omega$ is the Laplace variable, and

$$Z_{EB} = \frac{1}{C_0 S} \| R_0, \tag{19}$$

$$Z_{ms} = Z_M \approx M_M S + \frac{1}{C'_M S} + R_M. \tag{20}$$

Using the loop equations, the electrical impedance and the sound pressure output of the buzzer can be simulated.

C. Theory of dynamic vibration absorber

There is a common, but often overlooked, mistake in designing a resonant device of this kind. Since a piezoelectric buzzer is a narrow-band device, it is tempting to tune the resonant frequency of the acoustical system (ω_A) to coincide with that of the mechanical system (ω_M), i.e., $\omega_A=\omega_M$, such that the device would produce the maximum output when driven at this coincided frequency. Hence, instead of maximum response, the output turns out to be rather small at the driving frequency. In fact, counterintuitive phenomenon arises in the bass-reflex and bandpass designs of loudspeakers as well. Not much about its aspect has been reported in the previous research to date. It is worth exploring the physics underlying the coupled mechanical and acoustical resonators.

1. Dynamic vibration absorber

Consider a machine rotating with constant speed ω, as shown in Fig. 8(a). The displacement responses, $\bar{X}_1(\omega)$ and $\bar{X}_2(\omega)$, of this two degree-of-freedom system can be shown to be[11,12]

$$\bar{X}_1(\omega) = \frac{1}{\Delta(\omega)}(k_2 - \omega^2 m_2) F_{\text{eq}}, \tag{21}$$

$$\bar{X}_2(\omega) = \frac{1}{\Delta(\omega)} k_2 F_{\text{eq}}, \tag{22}$$

where ω is angular frequency, m_1 and k_1 are the mass and the spring constant of the rotating machine, m_2 and k_2 are the mass and the spring constant of the vibration absorber, F_{eq} is the unbalance force amplitude, and

$$\Delta(\omega) = (k_1 + k_2 - \omega^2 m_1)(k_2 - \omega^2 m_2) - k_2^2 = 0 \tag{23}$$

is the frequency-dependent characteristic equation. In general, the undamped dynamic vibration absorber is "tuned" for $k_1/m_1=k_2/m_2$ such that $\bar{X}_1(\omega)$ approaches zero at the frequency $\omega_0=\sqrt{k_1/m_1}=\sqrt{k_1/m_2}$, as shown in Fig. 8(b). This is the characteristic that is frequently exploited to suppress narrow-band vibrations of rotating machinery.

2. Design of resonant acoustical devices

The design of a resonant acoustical device, here a piezoelectric buzzer, shares quite similar electroacoustical structure with the preceding vibration absorber problem. Figure 9 shows this structure in the mechanical domain, where a serial

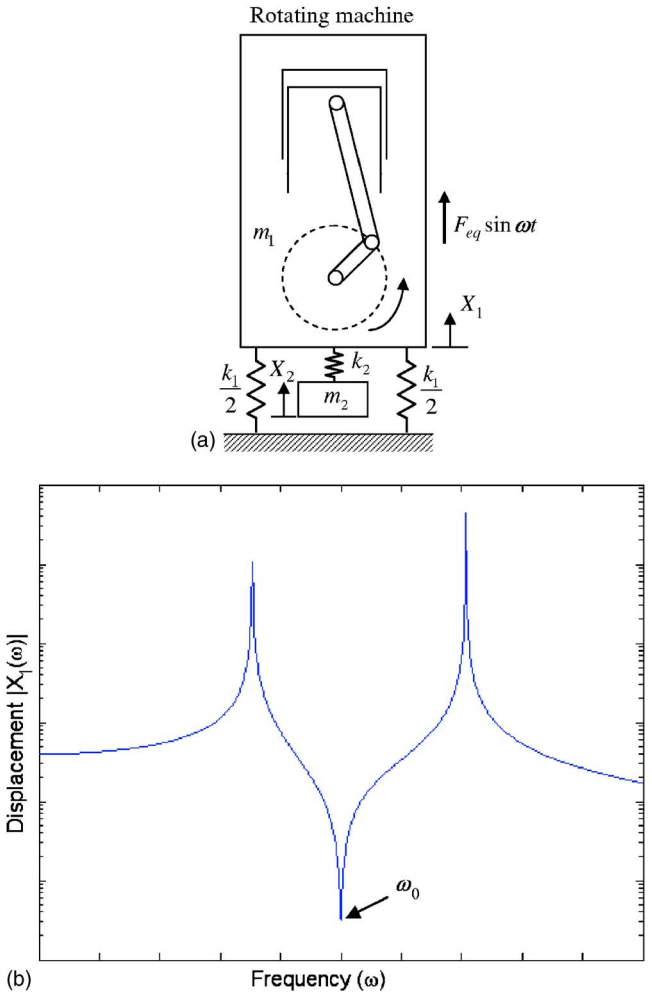

FIG. 8. (Color online) Dynamic vibration absorber. (a) A rotating machine attached with an absorber and (b) frequency response magnitude.

second-order oscillator circuit is coupled with a parallel second-order oscillator circuit. It is mathematically easier to derive the system characteristic equation by having a parallel resistance R_{AL} on the mechanical side, with R_{AP} neglected, in the circuit. Nevertheless, in deriving the design chart, only the undamped resonant frequencies are of concern. The actual position of the mechanical resistor is immaterial since both resistors are removed in the circuit of the coupled system. Note, however, that the port loss R_{AP} is considered in the constrained optimization procedures with the circuit of Fig. 3. When $\omega_A=\omega_M$, the motion of the mechanical system cancels that of the acoustical system, or alternatively viewed, the infinitely large impedance of the acoustical system

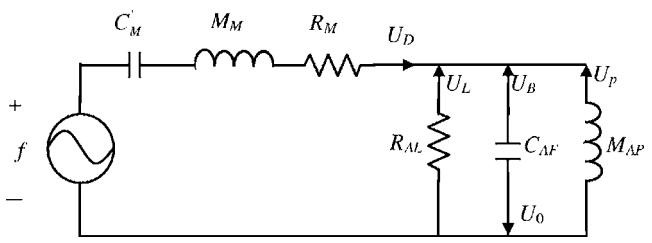

FIG. 9. A simplified analogous circuit of the piezoelectric buzzer expressed in the mechanical domain.

"blocks" the motion of the mechanical system. This is the feature that is frequently exploited to suppress vibrations, which forms the basis of vibration absorber theory. However, in the case of resonant acoustical devices, the naive approach of choosing equal resonant frequencies for both systems will result in an unexpected response null at $\omega_A = \omega_M$. This is obviously undesirable in the buzzer design. Contrary to vibration control, where one seeks to minimize the response, our purpose here in the acoustical design of buzzer is to maximize the sound pressure output, and it is the peaks of frequency response that we are after.

Let U_0 be the total velocity emitted from the diaphragm, the port, and the air leaks. From Fig. 9,

$$U_0 = U_D + U_P + U_L = -U_B, \tag{24}$$

where U_B is the net velocity entering the enclosure. The mechanical impedance and the acoustical impedance are given by

$$Z_M = M_M s + R_M + \frac{1}{C'_M s} = \frac{\frac{S^2}{\omega_M^2} + \frac{1}{Q_M}\frac{S}{\omega_M} + 1}{C'_M s}, \tag{25}$$

$$Y_A = C_{AF} s + \frac{1}{R_{AL}} + \frac{1}{M_{AP} s} = \frac{\frac{S^2}{\omega_A^2} + \frac{1}{Q_A}\frac{S}{\omega_A} + 1}{M_{AP} s}. \tag{26}$$

The total electrical impedance can be written as the sum of the mechanical impedance and the acoustical impedance:

$$Z_T = Z_M + \frac{1}{Y_A} = \frac{\Delta(s)}{C'_M s\left(\frac{S^2}{\omega_A^2} + \frac{1}{Q_A}\frac{S}{\omega_A} + 1\right)}, \tag{27}$$

where

$$\Delta(s) = \left(\frac{s^2}{\omega_M^2} + \frac{1}{Q_M^2}\frac{s}{\omega_M} + 1\right)\left(\frac{s^2}{\omega_A^2} + \frac{1}{Q_A}\frac{s}{\omega_A} + 1\right) + M_{AP} C'_M s^2 \tag{28}$$

denotes the characteristic equation, ω_M is the resonant frequency of the mechanical system (the piezoelectric diaphragm),

$$\omega_M = \sqrt{\frac{1}{M_M C'_M}}, \tag{29}$$

ω_A is the resonant frequency of the acoustical system (the cavity and port),

$$\omega_A = \sqrt{\frac{1}{M_{AP} C_{AF}}}, \tag{30}$$

and Q_M and Q_A are the quality factors of the mechanical system and the acoustical system, respectively, given by

$$Q_M = \frac{1}{R_m C'_M \omega_M}, \tag{31}$$

$$Q_A = \frac{R_{AL}}{C_{AF}\omega_A}. \tag{32}$$

It can be shown that the characteristic equation in Eq. (28) can be rewritten into an alternative form

$$\Delta = \frac{s^4}{\omega_0^4} + a_3\frac{s^3}{\omega_0^3} + a_2\frac{s^2}{\omega_0^2} + a_1\frac{s}{\omega_0} + 1 = 0, \tag{33}$$

where the frequency ω_0 and the coefficients a_1, a_2, and a_3 are defined as

$$\omega_0 = \sqrt{\omega_A \omega_M} = \frac{\omega_M}{\sqrt{\alpha}} = \omega_A\sqrt{\alpha}, \tag{34}$$

$$a_1 = \frac{1}{Q_M\sqrt{\alpha}} + \frac{\sqrt{\alpha}}{Q_A}, \tag{35}$$

$$a_2 = \frac{1}{\alpha} + \alpha + \frac{1}{Q_M Q_A} + \frac{\rho}{\alpha}, \tag{36}$$

$$a_3 = \frac{1}{Q_A\sqrt{\alpha}} + \frac{\sqrt{\alpha}}{Q_M}. \tag{37}$$

In these equations, the frequency ratio α and the mass ratio ρ are defined as

$$\alpha = \frac{\omega_M}{\omega_A} > 0, \tag{38}$$

$$\rho = \frac{M_{AP}}{M_M} > 0. \tag{39}$$

For undamped systems, where $Q_M \to \infty$ and $Q_A \to \infty$, the characteristic equation simplifies to

$$\Delta(S) = \alpha^2 r_M^4 - (1 + \alpha^2 + \rho) r_M^2 + 1 = 0 \tag{40}$$

in which the normalized frequency r_m is defined as

$$r_M = \frac{\omega}{\omega_M}. \tag{41}$$

Solving for the roots of the characteristic equation yields two undamped natural (resonance) frequencies. Note that the resonance frequencies of the coupled (mechanical and acoustical) system are generally different from, but strongly influenced by, those of the individual subsystems. According to Eq. (40), the resonance frequencies of the coupled system can be plotted versus the mass ratio ρ for various frequency ratios α. This gives the design charts shown in Fig. 10, in which the curves for mass ratio $\rho > 0$ are in used, while the curves for mass ratio $\rho \leqslant 0$ are only mathematical.

3. Acoustical design by the design chart

Assuming that the properties of the mechanical system are fixed, we now focus on the design of the acoustical

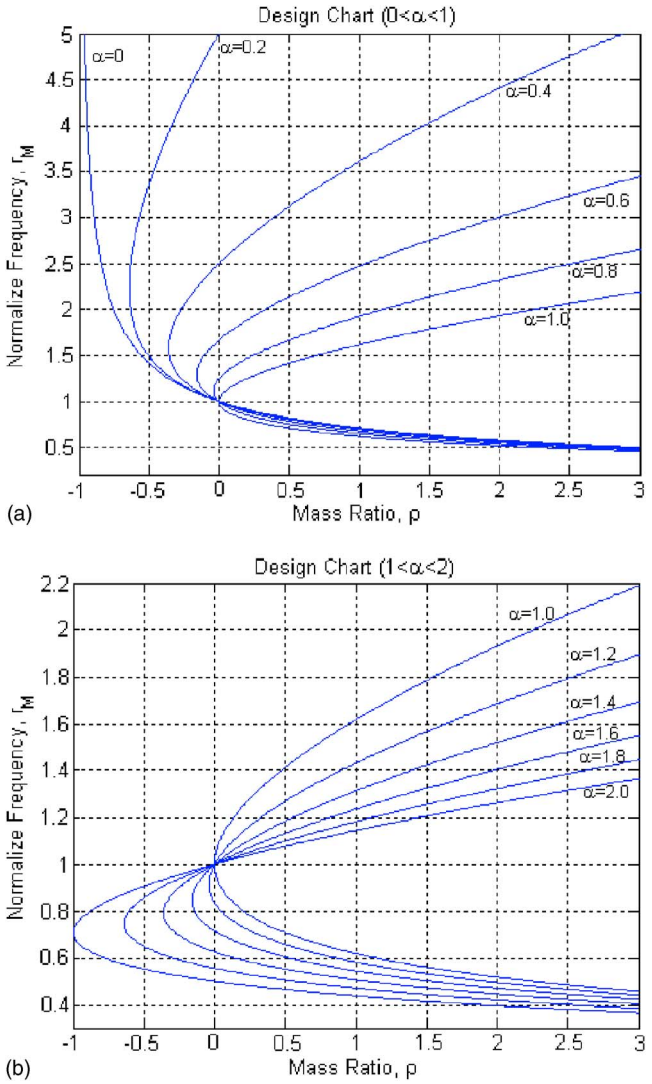

FIG. 10. (Color online) The design chart of the piezoelectric buzzer. (a) $0 \leqslant \alpha \leqslant 1$ and (b) $1 \leqslant \alpha \leqslant 2$.

system with the aid of the design chart. The design variables we wish to determine are the volume of cavity, the radius of port, and the length of duct. The design procedure is outlined as follows:

(1) Specify design constraints. Fix the mechanical resonant frequency ($f_M = \omega_M / 2\pi$) of the piezoelectric diaphragm. Assume $f_A = \omega_A / 2\pi < f_M$.
(2) Fix the first resonant frequency ($f_1 = \omega_1 / 2\pi$) of the coupled system (piezoelectric buzzer) at the driving frequency, e.g., 4 kHz.
(3) From the mechanical resonant frequency (f_M) and the first resonant frequency (f_1), calculate the normalized frequency ($r_1 = f_1 / f_M$).
(4) Choose a mass ratio (ρ) and determine the acoustical mass (M_{AP}).
(5) Assume a value for the radius of port (a_p). Determine the length of duct (t_c) according to Eq. (15).
(6) Choose the design curve (α) that corresponds to the normalize frequency and mass ratio determined previously.
(7) Determine the acoustical resonant frequency, $f_A = f_M / \alpha$.
(8) Per Eq. (30), calculate the acoustical compliance (C_A) based on M_{AP} and f_M. Also calculate the cavity volume according to Eq. (17).

III. OPTIMAL DESIGN OF THE PIEZOELECTRIC BUZZER

The optimization design procedure is based on the preceding piezoelectric buzzer model. The purpose here is to find the best mechanical and acoustical parameters of the piezoelectric buzzer to attain the maximum sound pressure output at the driving frequency under prescribed constraints. The design chart method and the Sequential Quadratic Programming (SQP) algorithm are employed to find the optimal parameters.

A. Sequential quadratic optimization theory and syntax

A brief review of a nonlinear programming technique, the SQP algorithm, is given in this section.[16–18] In the solution process of the SQP method, a nonlinear programming problem is first converted to a sequence of unconstrained minimization problems. A Quadratic Programming (QP) subproblem is then solved at each iteration. Consider the following nonlinear programming problem:[16]

$$\text{Minimize } f(\mathbf{x})$$

$$\text{subject to} \begin{cases} h_i(\mathbf{x}) = 0, & i = 1, \ldots, p \\ h_j(\mathbf{x}) \leqslant 0, & j = 1, \ldots, m, \end{cases} \tag{42}$$

where $\mathbf{x} \in R^n$ is the design variable vector, $f: R^n \to R$, being the cost function, $h_i: R^p \to R$, being the equality constraints, and $h_j: R^m \to R$, being the inequality constraints. Other types of linear constraints including matrix and bound types can all be cast into the generic form in Eq. (42). The SQP method requires a quadratic model for the objective function and a linear model for the constraint. This is done by formulating the QP subproblem based on a quadratic approximation to the Lagrangian function,[16]

$$L(\mathbf{x}, \boldsymbol{\mu}, \mathbf{v}) = f(\mathbf{x}) + \sum_{i=1}^{p} \boldsymbol{\mu}_i h_i(\mathbf{x}) + \sum_{i=1}^{m} \mathbf{v}_j [h_j(\mathbf{x}) + \mathbf{g}_j^2], \tag{43}$$

where $\boldsymbol{\mu}_i$ and $\mathbf{v}_j$ are the Lagrange multipliers, and $\mathbf{g}_j$ are termed the slack variables. By the Kuhn-Tucker conditions,[16] it suffices to solve the unconstrained optimization problem using the above-mentioned Lagrangian function. In practice, however, a simplified problem can be obtained by approximating the constraints (up to the first order) and the cost function (up to the second order) using the Taylor expansion. Thus, at the kth iteration, the SQP algorithm generates a search direction, $\mathbf{d}_k$, for the following QP subproblem:

$$\text{Minimize } \nabla f_k^T(\mathbf{x})\mathbf{d}_k + \tfrac{1}{2}\mathbf{d}_k^T\mathbf{B}_k\mathbf{d}_k$$

$$\text{subject to} \begin{cases} h_i(\mathbf{x}_k) + \nabla h_i^T(\mathbf{x}_k)\mathbf{d}_k = 0, & i = 1, \ldots, l \\ h_j(\mathbf{x}_k) + \nabla h_j^T(\mathbf{x}_k)\mathbf{d}_k \leqslant 0, & j = l+1, \ldots, m. \end{cases} \tag{44}$$

In Eq. (44), ∇f, ∇h_i, and ∇h_j denote the gradients of the cost function, the ith equality constraint, and the jth inequality constraint, respectively, $\mathbf{d}_k$ is the direction of search in the design space. The matrix $\mathbf{B}_k$ is a positive definite approximation to the Hessian matrix of the Lagrangian function $L(\mathbf{x}_k, \boldsymbol{\mu}_k, \mathbf{v}_k)$.[16–18] $\mathbf{B}_k$ is updated by using the Broyden, Fletcher, Goldfarb, and Shanon method,

$$\mathbf{B}_{k+1} = \mathbf{B}_k + \frac{\hat{\mathbf{y}}^T\hat{\mathbf{y}}}{\mathbf{s}^T\hat{\mathbf{y}}} - \frac{\mathbf{B}_k\mathbf{s}\mathbf{s}^T\mathbf{B}_k}{\mathbf{s}^T\mathbf{B}_k\mathbf{s}}, \tag{45}$$

where

$$\mathbf{s} = \mathbf{x}_{k+1} - \mathbf{x}_k, \tag{46}$$

$$\hat{\mathbf{y}} = t[\nabla_x L(\mathbf{x}_{k+1}, \boldsymbol{\mu}_{k+1}, \mathbf{v}_{k+1}) - \nabla_x L(\mathbf{x}_k, \boldsymbol{\mu}_k, \mathbf{v}_k)] + (1-t)\mathbf{B}_k\mathbf{s}. \tag{47}$$

Here, $\hat{\mathbf{y}}$ is obtained using the damping factor t in order to guarantee that $\mathbf{B}_{k+1}$ is sufficiently positive definite at the solution point. A positive definite Hessian is maintained, provided $\hat{\mathbf{y}}^T\hat{\mathbf{y}}/\mathbf{s}^T\hat{\mathbf{y}}$ is positive at each update and that $\mathbf{B}_k$ is initialized with a positive definite matrix. There are many numerical methods to solve a QP problem, e.g., the modified simplex method or the Kuhn-Tucker procedures.[17] The solution of $\mathbf{d}_k$ is used to update the estimate of $\mathbf{x}$,

$$\mathbf{x}_{k+1} = \mathbf{x}_k + \alpha_k\mathbf{d}_k. \tag{48}$$

In the update equation, the step size parameter α_k is determined by an appropriate line search procedure so that a sufficient decrease in a merit function such as the Lagrangian function is obtained.

The preceding optimization formalism was employed to solve the piezoelectric buzzer design problem on the platform of MATLAB.[20] The syntax of the constrained optimization takes the following form augmented with various linear equality and inequality constraints:

$$\min_x f(\mathbf{x}) \text{ subject to } \begin{aligned} &\mathbf{c}(\mathbf{x} \leqslant 0), \\ &\mathbf{c}_{\text{eq}}(\mathbf{x}) = 0, \\ &\mathbf{A}\mathbf{x} \leqslant \mathbf{b}, \\ &\mathbf{A}_{\text{eq}}\mathbf{x} = \mathbf{b}_{\text{eq}}, \\ &\mathbf{I}\mathbf{b} \leqslant \mathbf{x} \leqslant \mathbf{u}\mathbf{b}, \end{aligned} \tag{49}$$

where $\mathbf{x}$ is the design variable vector, $\mathbf{b}$, $\mathbf{b}_{\text{eq}}$, $\mathbf{lb}$, and $\mathbf{ub}$ are constant vectors, $\mathbf{A}$ and $\mathbf{A}_{\text{eq}}$ are constraint matrices, $\mathbf{c}(\mathbf{x})$ and $\mathbf{c}_{\text{eq}}(\mathbf{x})$ are constraint functions that return vectors, and $f(\mathbf{x})$ is the cost function that returns a scalar. $f(\mathbf{x})$, $\mathbf{c}(\mathbf{x})$, and $\mathbf{c}_{\text{eq}}(\mathbf{x})$ can be nonlinear functions. In the piezoelectric buzzer design problem considered herein, the on-axis sound pressure at the driving frequency 4 kHz of piezoelectric buzzer is defined as the cost function.

B. Constrained optimization method

In the following, two kinds of optimal design problems of piezoelectric buzzer shall be examined. The first problem focuses on the design of the acoustical system alone because of the closer acoustical resonance to the driving frequency. In this case, the volume of cavity, the port size, and the duct length are to be determined, and the parameters of the mechanical system are assumed to be fixed. The second problem focuses on the design of both mechanical and acoustical systems, where, in addition to the parameters of the first problem, the parameters of the piezoelectric diaphragm are to be determined.

1. Optimal design of the acoustical system alone

In this case, constraints are placed on design factors including acoustical mass (M_{AP}), acoustical compliance (C_{AF}), acoustical resistance (R_{AP}), the first resonant frequency of piezoelectric buzzer (f_1=4 kHz), characteristic equation of piezoelectric buzzer [$\Delta(s)$=0], radius of port (a_p) and height of front cavity (d_{AF}). Among these, a_p and t_c are selected to be the design variables for optimization. In terms of the forgoing optimal formalism,

$$\max \text{SPL}(a_p, t_c)$$

$$\text{st.} \begin{cases} 0.001 \leqslant a_p \leqslant 0.002 \\ 0.00308 \leqslant d_{AF} \leqslant 0.005 \\ 1\text{E}-7 \leqslant M_{AP} \leqslant 1\text{E}-5 \\ 2\text{E}5 \leqslant R_{AP} \leqslant 2\text{E}7 \\ 1\text{E}-4 \leqslant C_{AF} \leqslant 3\text{E}-4 \\ f_1 = 4000 \\ \Delta = 0 \end{cases} \tag{50}$$

2. Optimal design of both mechanical and the acoustical systems

The second case aims at the optimal design of the cavity and piezoelectric diaphragm. Constraints are placed on design factors including acoustical mass (M_{AP}), acoustical compliance (C_{AF}), acoustical resistance (R_{AP}), the first resonant frequency of piezoelectric buzzer (f_1=4 kHz), mechanical quality factor (Q_M), characteristic equation of piezoelectric buzzer [$\Delta(s)$=0], transduction factor (ϕ), mechanical mass (M_M), mechanical compliance (C'_M), mechanical resistance (R_M), radius of port (a_p), height of the front cavity (d_{AF}), free capacitance of piezoelectric diaphragm (C_f), and the clamped capacitance of piezoelectric diaphragm (C_0). From these parameters, M_M, C'_M, R_M, a_p, d_{AF}, C_f, and C_0 are selected to be the design variables for optimization. In terms of the forgoing optimal formalism,

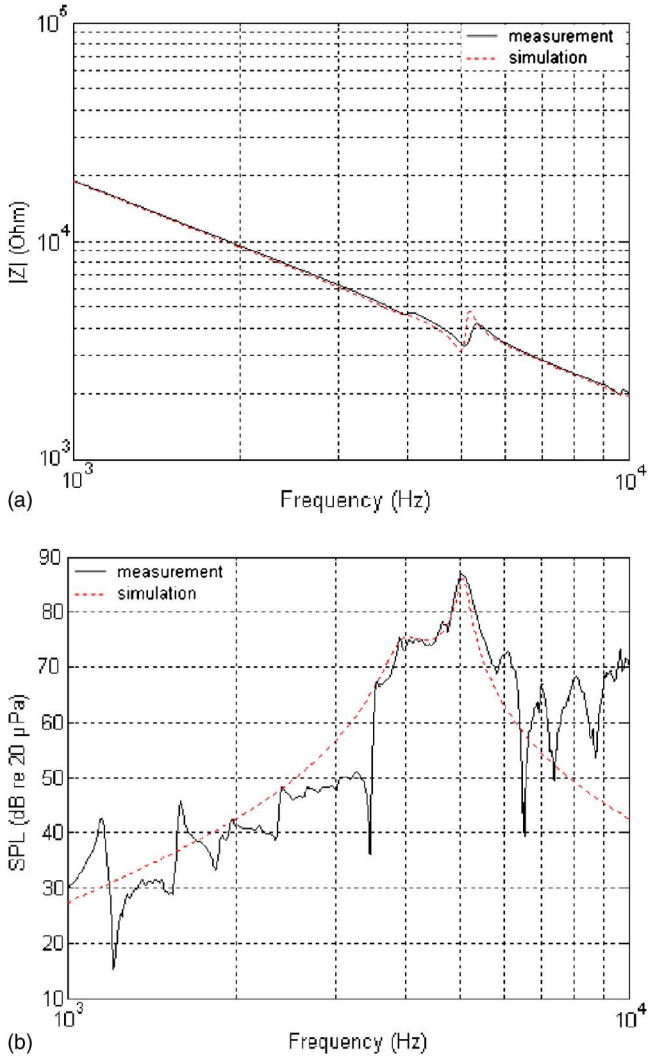

FIG. 11. (Color online) Frequency responses of piezoelectric buzzer obtained from the experiment and simulation. (a) Electrical impedance and (b) on-axis SPL.

$$\max \ \mathrm{SPL}(a_p, d_{AF}, M_M, C_M, R_M, C_f, C_0)$$

$$\text{st}\begin{cases} 0.001 \leqslant a_p \leqslant 0.002 \\ 0.0015 \leqslant d_{AF} \leqslant 0.005 \\ 4\mathrm{E}-5 \leqslant M_M \leqslant 7\mathrm{E}-5 \\ 1\mathrm{E}-5 \leqslant C_M \leqslant 5.5\mathrm{E}-5 \\ 0.01 \leqslant R_M \leqslant 0.08 \\ 8\mathrm{E}-9 \leqslant C_f \leqslant 11\mathrm{E}-9 \\ 7\mathrm{E}-9 \leqslant C_0 \leqslant 10\mathrm{E}-9 \\ 0.003 \leqslant \phi \leqslant 0.006 \\ 1\mathrm{E}-7 \leqslant M_A \leqslant 1\mathrm{E}-5 \\ 2\mathrm{E}5 \leqslant R_A \leqslant 2\mathrm{E}-7 \\ 1\mathrm{E}-4 \leqslant C_A \leqslant 9\mathrm{E}-4 \\ 30 \leqslant Q_M \leqslant 50 \\ f_1 = 4000 \\ \Delta = 0 \\ C_1 L_1 = C_M' M_M \end{cases} \tag{51}$$

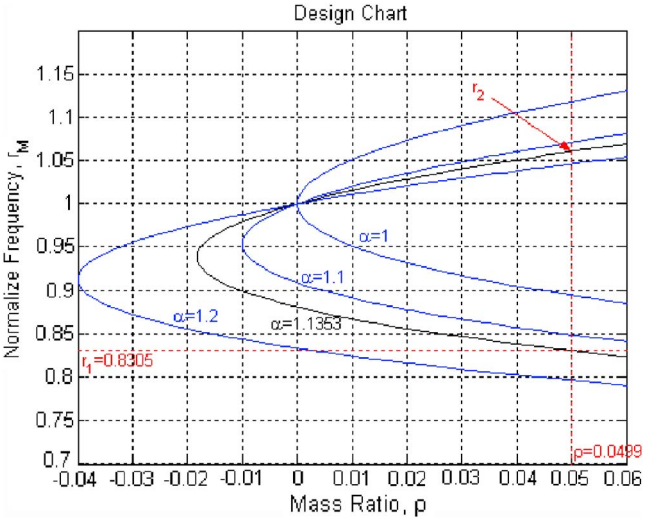

FIG. 12. (Color online) Close-up view of the design chart for the present buzzer design.

IV. NUMERICAL AND EXPERIMENTAL INVESTIGATIONS

Simulation and experimental investigations are undertaken in this paper to validate the aforementioned design optimization techniques of the piezoelectric buzzer. A 1.5 V_{rms} swept sine signal is generated to drive the piezoelectric buzzer, with the frequency ranging from 10 Hz to 20 kHz. On-axis sound pressure response was measured by a microphone positioned at 10 cm away from the piezoelectric buzzer.

A. Response simulation and experimental investigation

A simulation of the buzzer response was carried out on the basis of the lumped parameter model identified previously. Figures 11(a) and 11(b) are the electrical impedance and the on-axis SPL obtained from the simulation and experiment, respectively. The simulated electrical impedance (dashed line) is in reasonable agreement with that of the measured results (solid line). The on-axis sound pressure responses of the simulation and measurement are also in good agreement within the working range, 3.5–5.5 kHz. Except for some minor discrepancies due to unmodeled structural and acoustical modes, the main features, such as the main peaks, are well captured by the lumped parameter model.

B. Optimal design by the design chart

Suppose only acoustical design is of interest and mechanical parameters are fixed, the optimal design of the cavity and duct of the buzzer can be readily obtained from the design chart. Assume that the piezoelectric diaphragm resonant frequency is greater than the acoustical resonant frequency ($f_M > f_A$). The objective is to "lock" the first peak of the SPL of the coupled buzzer system onto the driving frequency 4 kHz. The design variables are selected to be the port radius and the duct length. According to the design chart shown in Fig. 12 and the procedure detailed in the preceding section, the optimal parameters including the port radius

TABLE III. Results obtained using the design chart method.

Parameters	Original	Optimal	Difference
t_c (mm)	0.76	2.28	–200.0%
a_p (mm)	1.065	1.5	40.8%
M_{AP} (kg/m^4)	786.81	766.01	–2.6%
R_{AP} (N s/m^5)	3.31E6	2.14E6	–35.3%
ρ	0.0513	0.0499	–2.7%
f_a(Hz)	4157.4	4242.20	2.0%
α	1.157	1.135	–1.9%
SPL (dB) at 4 kHz	73.3	79.9	6.6 dB

(a_p), the duct length (t_c), and the acoustical resistance (R_{AP}) are found and summarized in Table III. In this case, the normalized frequencies r_1=0.8305 and the mass ratio ρ =0.0499, the frequency ratio α=1.1353.

Yet another approach by incorporating a duct in the design is also a viable option that does not require an unduly increase of cavity volume. The cross section of this design is shown in Fig. 13(a). The photo of a mockup of the optimal obtained using the preceding design chart method is shown in Fig. 13(b). The results obtained using the method of design chart shown in Table III reveal that the duct length is increased by 200% to 2.28 mm, and the duct radius is increased by 40.8% to 1.5 mm. The increase of duct length and radius results in the decrease of M_{AP} and R_{AP}. Alternatively, one may opt to increase the cavity volume and the duct radius to reduce C_{AF} and R_{AP}. However, this approach by increasing the cavity volume is generally unacceptable in practical design of buzzers. As can be seen in the optimal results, a 6.6 dB increase of on-axis SPL is achieved at 4 kHz with the increased radius and length of the duct. The simulated (dashed line) and the measured (solid line) electrical impedances and SPL frequency responses of the design are verified in Figs. 14(a) and 14(b). In Fig. 14(a), the simulation and the measurement results of electrical impedance are in good agreement at the first and the second resonance frequencies. In Fig. 14(b), the on-axis sound pressure responses of the simulation and measurement are also in good agreement between the first and the second resonance peaks. Thus, the improvement of the measured SPL over nonoptimal design is approximately 6.6 dB.

The guidelines of using the design chart can be summarized as follows. Reducing the acoustical mass (M_{AP}) and acoustical resistance (R_{AP}) will increase the SPL at the peak. However, reducing M_{AP}, equivalently, the mass ratio (ρ) will shift the acoustical resonant frequency (f_A) to a higher frequency. In case of a buzzer design, the preferred strategy is to select a lower mass ratio and a design curve with smaller frequency ratio (α) in the design chart. After these search steps, a satisfactory design can generally be found.

C. Optimal design by the constrained optimization procedure

In this section, the aforementioned optimization technique is applied to two cases. First, only the acoustical parameters are to be optimized. Second, both the mechanical and the acoustical parameters are to be optimized. The SQP constrained optimization algorithms are applied to search for optimal parameters of the coupled diaphragm-cavity system. Table IV summarizes the search results for the first case, where the duct radius is increased by 45.3% to 1.547 mm and the height of front cavity is increased by 62.3% to 5.0 mm. The on-axis SPL improvement at 4 kHz achievable by the optimal design is 5.8 dB. It should be noted that an increase of duct radius will lead to reduction of the acoustical mass and, hence, the acoustical resonant frequency. In addition, increase of the height of the front cavity will lead to the increase of the cavity volume and, hence, the acoustical compliance.

Table V summarizes the search results of the cavity-diaphragm parameters for the second case. For the acoustical

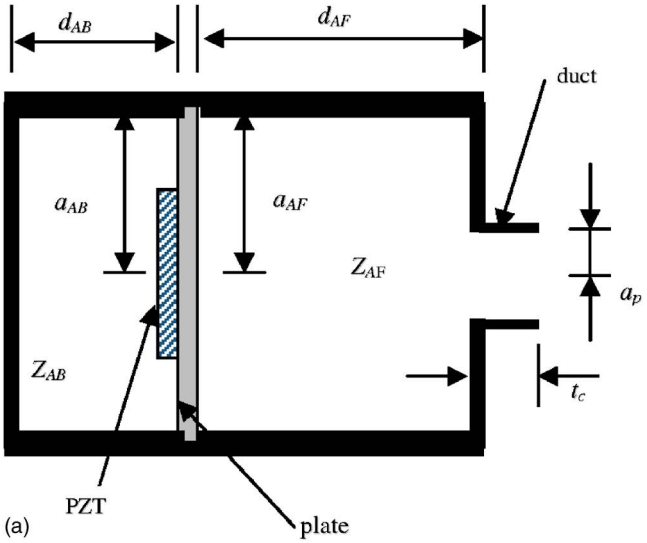

FIG. 13. (Color online) The piezoelectric buzzer with a duct resulting from the design chart method. (a) Cross-sectional diagram and (b) photo of the mockup.

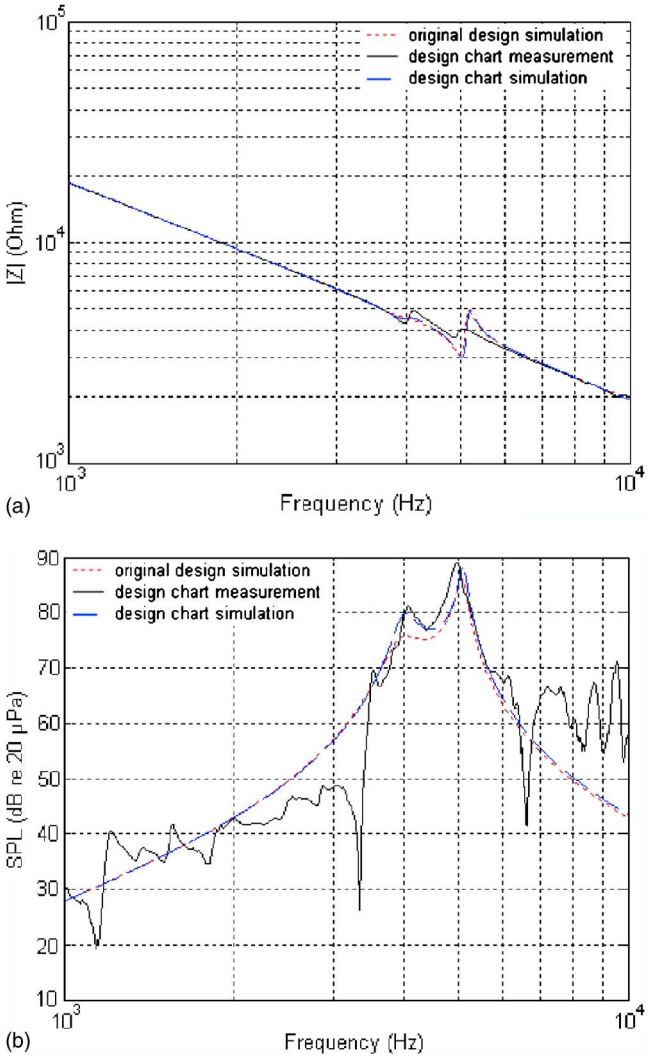

FIG. 14. (Color online) Comparison of the original design and the optimal design using the design chart method. (a) Electrical impedance and (b) on-axis SPL.

parameters, the duct radius is increased by 3.3% to 1.1 mm and the height of the front cavity is reduced by −38.3% to 1.9 mm. For the mechanical parameters, the mechanical mass is increased by 19.4% to 6.27E−2 g, whereas the mechanical compliance is increased by 10.1% to 2.29E −5 m/N. However, the electrical parameters remain almost unchanged. In addition, the resonant frequency of the structural system (f_M=4201 Hz) is lower than the resonant frequency of the acoustical system (f_A=5283 Hz). The resonant frequency of the structural system is close to the driving frequency at 4 kHz. The on-axis SPL improvement at 4 kHz achievable by this optimal design is 9.6 dB.

TABLE IV. Results obtained using the first optimal design that optimizes the acoustical system alone.

Parameters	Original	Optimal	Difference
a_p (mm)	1.065	1.547	45.3%
d_{AB} (mm)	3.08	5.0	62.3%
C_{AF} (m^5/N)	1.86E-12	3.02E-12	62.4%
M_{AP} (kg/m^4)	786.81	486.48	−38.2%
R_{AP} (N s/m^5)	3.31E6	1.48E6	−55.2%
ρ	0.0513	0.0317	−38.2%
f_a(Hz)	4157.4	4149.72	−0.2%
α	1.157	1.160	0.3%
SPL(dB) at 4 kHz	73.3	79.1	5.8 dB

TABLE V. Results obtained using the second optimal design that optimizes both mechanical and acoustical systems.

Parameters	Original	Optimal	Difference
a_p (mm)	1.065	1.1	3.3%
d_{AB} (mm)	3.08	1.9	−38.3%
M_M (kg)	5.25E-5	6.27E-5	19.4%
C'_M (m/N)	2.08E-5	2.29E-5	10.1%
R_M (N s/m)	0.0386	0.0386	0.0%
C_f (F)	9.17E-9	9.17E-9	0.0%
C_0 (F)	8.96E-9	8.96E-9	0.0%
C_{AF} (m^5/N)	1.86E-12	1.16E-12	−37.6%
M_{AP} (kg/m^4)	786.81	786.81	0.0%
R_{AP} (N s/m^5)	3.31E6	3.31E6	0.0%
ρ	0.0513	0.0482	−6.0%
f_m (Hz)	4812.4	4201	−12.7%
f_a (Hz)	4157.4	5283	27.1%
α	1.157	0.795	−31.3%
Q_M	40.6	42.9	5.7%
C_1 (F)	2.08E-10	1.82E-010	−12.5%
L_1 (H)	5.13	7.80	52.0%
R_1 (Ω)	3870.5	4874.1	25.9%
ϕ	0.0032	0.0028	−12.5%
SPL(dB) at 4 kHz	73.3	82.9	9.6 dB

For this optimal design, the electrical impedance and the SPL responses are simulated and shown in Figs. 15(a) and 15(b), respectively. The dashed line represents the original nonoptimal design. The dotted line represents the design using the first acoustical optimization approach. The solid line represents the design using the second mechanical and acoustical optimization approach. From Fig. 15(a), the electrical impedances of the original design and the first acoustic optimal designs are in reasonable agreement. However, the overall level of impedance of the original design and first optimal design are higher than the second optimal design. The response of the original design and first optimal design peak at 5 kHz (the second resonance), whereas the response of the second optimal design peaks at 4 kHz. In 15(b), the on-axis SPL responses of the second design is greater than the first design at the driving frequency 4 kHz, and both are greater than the SPL of the original nonoptimal design at 4 kHz. Specifically, the SPLs at the driving frequency 4 kHz of the first optimal design and the second optimal design are increased by approximately 5.8 and 9.6 dB, respectively, over the original nonoptimal design. The SPL response at 4 kHz of the second optimal design (82.9 dB) is higher than the first optimal design (79.1 dB) by 3.8 dB. Note that the structural resonant frequency of the second optimal design is near the driving frequency, while in the first optimal design the acoustical resonant frequency is near the driving frequency. Summarizing, a higher level of acoustic pressure appears for the resonant frequency near the original structural resonant frequency. This fact can be utilized for further im-

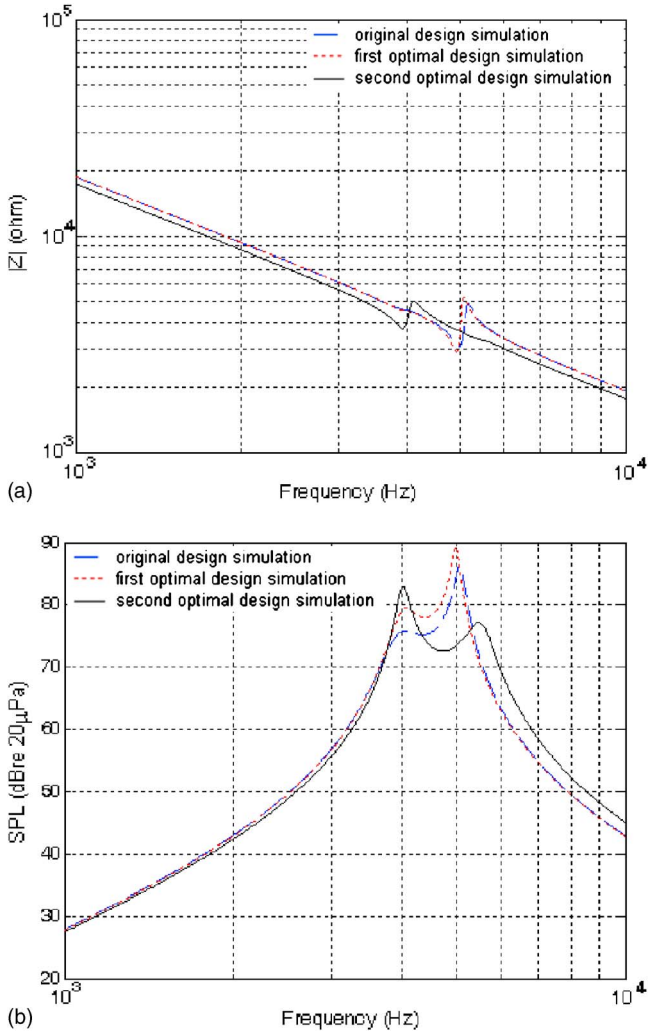

FIG. 15. (Color online) Comparison of the original design and the optimal designs using two constrained optimization approaches. (a) Electrical impedance and (b) on-axis SPL.

provement of the construction of the buzzer. The optimal result shows that the SPL attainable at the driving frequency can be significantly increased over the nonoptimal design. In addition, the resonant frequency of the structural system should be near the driving frequency of the piezoelectric buzzer. This design strategy proves effective in achieving a much improved performance, with the first resonant frequency fixed at 4 kHz.

V. CONCLUSIONS

An optimization technique has been presented in the paper for designing piezoelectric buzzers. An insightful inspection revealed that this buzzer problem can be closely related to the dynamic vibration absorber theory. A design chart was devised to design piezoelectric buzzers by exploiting the same mechanism, but opposite strategy, as the vibration absorber design. The guidelines of using the design chart were summarized in the paper. In order to establish a simulation platform for design optimization, a special kind of experimental identification procedure was also developed to estimate the lumped parameters required in the EMA analogous circuit. Using the simulation platform, electrical impedance and on-axis sound pressure response can be predicted by solving loop equations of the analogous circuit. The resonance frequencies of the coupled system are generally different from those of the individual subsystems. From the characteristic equation, the resonance frequencies of the coupled mechanical and acoustical system can be calculated. Maximum acoustical output can thus be attained by locking the resonance peak to the driving frequency.

Apart from the design chart method, constrained optimization techniques were also employed to find the design that maximizes the sound pressure output of the buzzer under practical constraints. Two approaches were applied in the optimization: acoustical-system-alone approach and mechanical-acoustical system approach. Both designs obtained using the optimization procedures provide significant performance improvement over the original design in terms of sound pressure output. However, the benefit of optimizing both mechanical and acoustical parameters is preferred over optimizing the acoustical parameters alone.

ACKNOWLEDGMENTS

The work was supported by China Steel Corporation and the National Science Council in Taiwan, Republic of China, under Project No. NSC 93-2212-E009-008.

[1]G. Caliano, N. Lamberti, A. Iula, and M. Pappalardo, "A piezoelectric bimorph static pressure sensor," Sens. Actuators, A, **46**, 176–178 (1995).
[2]C. I. Tseng and W. J. Liou, "Simulation of a bimorph transducer under acoustic excitation," Comput. Struct., **59**, 141–148 (1996).
[3]A. B. Dobrucki and P. Pruchnicki, "Theory of piezoelectric axisymmetric bimorph," Sens. Actuators, A, **58**, 203–212 (1997).
[4]Q. Wang, S. T, Quek, C. T. Sun, and X. Liu, "Analysis of piezoelectric coupled circular plate," Smart Mater. Struct., **10**, 229–239 (2001).
[5]B. Aronov, "The energy method for analyzing the piezoelectric electroacoustic transducers," J. Acoust. Soc. Am., **117**, 210–220 (2005).
[6]B. Aronov, "The energy method for analyzing the piezoelectric electroacoustic transducers. II (With the examples of the flexural plate transducer)," J. Acoust. Soc. Am. **118**, 627–637 (2005).
[7]M. R. Bai and Y. Lu, "Optimal implementation of miniature piezoelectric panel speakers using the Taguchi method and Genetic algorithm," J. Vibr. Acoust., **126**, 359–369 (2004).
[8]F. L. Wen, S. C. Mou, and M. Ouyang, "Design and construction of shaft-driving type piezoceramic ultrasonic motor," Ultrasonics **43**, 35–47 (2004).
[9]A. Caronti, G. Caliano, and M. Pappalardo, "An accurate model for capacitive micromachined ultrasonic transducers," IEEE Trans. Comput.-Aided Des., **49**, 159–168 (2002).
[10]Q. Gallas, R. Holman, T. Nishida, B. Carroll, M. Sheplak, and L. Cattafesta, "Lumped element modeling of piezoelectric-driven synthetic jet actuators." AIAA J., **41**, 240–247 (2003).
[11]F. S. Tse, I. E. Morse, and R. T. Hinke, *Mechanical Vibrations: Theory and Applications* (Allyn & Bacon, Boston, MA, 1978).
[12]L. Meirovitch, *Element of Vibration Analysis* (McGraw-Hill, New York, 1986).
[13]W. M. Leach, Jr., *Introduction to Electroacoustics and Audio Amplifier Design* (Kendall-Hunt, Dubuque, IA, 2003).
[14]L. L. Beranek, *Acoustics* (Acoustical Society of America, Melville, NY 1996).
[15]C. A. Desoer and E. S. Kuh, *Basic Circuit Theory* (McGraw-Hill, New York, 1969).
[16]P. E. Gill, W. Murry, and M. H. Wright, *Practical Optimization* (Academic, New York, 1981).
[17]J. S. Arora, *Introduction to Optimum Design* (McGraw-Hill, New York 1989).
[18]M. A. Bhatti, *Practical Optimization Methods with Mathematica Applications* (Springer, Berlin, 2000).
[19]IEEE, *IEEE Standard on Piezoelectricity* (New York, 1987).
[20]Math Works, "Matlab optimization toolbox" (http://www.mathworks.com/products/optimization/). Last viewed 7/23/2007.

Measurements of mutual radiation impedance between baffled cylindrical shell transducers[a)]

Tetsuro Oishi[b)] and David A. Brown[c)]
Acoustic Research Laboratory, Advanced Technology & Manufacturing Center and Department of Electrical and Computer Engineering, University of Massachusetts, Dartmouth, 285 Old Westport Road, North Dartmouth, Massachusetts 02747-2300

(Received 7 May 2006; revised 8 May 2007; accepted 10 July 2007)

The mutual radiation impedances between two baffled cylindrical shell transducers, made of PZT-4 piezoelectric rings with one half of the cylindrical surface covered by a compliant baffle, were determined in experiments as a function of separation distance using an experimental technique recently described [B. Aronov, J. Acoust. Soc. Am. **119**, 3822–3830 (2006)]. Two baffled cylindrical shell transducers were connected electrically in parallel and the input electrical admittance was measured at different separations when the two transducers were operated in phase and then 180° out-of-phase in both the coaxial and horizontal (side-by-side) alignments. The mutual radiation impedances were then computed using an electrical equivalent circuit to determine the significance of interaction for cylindrical elements in these array geometries. © *2007 Acoustical Society of America.* [DOI: 10.1121/1.2767611]

PACS number(s): 43.38.Hz, 43.30.Yj, 43.38.Fx [AJZ] Pages: 1581–1586

I. INTRODUCTION

Determination of the mutual radiation impedance between array elements in an underwater array is important in the design of electroacoustic transducer arrays since the acoustical load, which is nonuniformly distributed across the radiating surface as a result of acoustic interaction, often causes performance degradation on the directivity patterns and the transmit frequency response of the array. A large amount of experimental and analytical work has been reported on the mutual radiation impedances in different types transducers and arrays,[1–12] although there has been relatively little reported on interaction of cylindrical elements in the horizontal (or side-by-side) configuration or on the implementation of measurement techniques.

It is well known that piezoelectric air-backed cylindrical shell transducers without baffles can be selectively excited in different modes of vibration by corresponding division of the electrodes and electrical excitation. The most common and practical use is with selection or combinations of the first two extensional modes of vibration, the zero (breathing) and one (dipole) modes.[13,14] When a circumferential baffle is applied to one half of the cylindrical surface of the transducer, as shown in Fig. 1, the resulting radiation is made directional and the acoustic coupling due to the baffle promotes contributions from both vibration modes whether the electrodes are uniform or divided. Recent papers summarize the characteristics of these baffled transducers where directional radiation can be obtained across a frequency band containing both resonant modes and the beam patterns are relatively constant having −3 dB beamwidth of approximately $70 \pm 10°$.[15,16]

There is interest in the development of practical arrays of these baffled cylindrical transducers to exploit the broad bandwidth with relatively low cost of the transducers. An example of an array geometry is illustrated in Fig. 2. Toward this goal, the interaction of baffled cylindrical elements in both axial and horizontal array configurations is studied.

The results of measurement of the mutual radiation impedance are reported in this paper when two circumferentially (180°) baffled cylindrical shell transducers are electrically uniformly excited for transducer alignments that are coaxial and horizontal. Although the electrical excitation is uniform, the presence of the conformal acoustic baffle also promotes contributions from the mode one in addition to the zero (breathing) mode. The case of excitation of the inner electrodes halves in antiphase, which strongly excites the mode one, and to a lesser extent also excites the zero mode due to the baffle, is not treated in this paper. In practice, the vibration mode distribution is sufficiently similar that results may be generalized.

In Sec. II, the methods of measurements, experimental apparatus, and procedure are explained in detail. In Sec. III, the experimental results are presented.

II. EXPERIMENTAL INVESTIGATION

A. Measurement method

Two measurement methods were described in Ref. 17, which are referred to as the Z and V methods. The Z method is based on the measurement of input impedances of interacting transducers, while the V method is based on the measurement of the acoustomotive force generated on the surface of one of the transducers by an interacting transducer. In this

[a)]The results of this work were reported in part at the 144th and 147th Meetings of the Acoustical Society of Amnerica [J. Acoust. Soc. Am. **112**, 2407 (2002); **115**, 2526 (2004)].
[b)]Electronic mail: tetsuro@thinksound.net
[c)]Electronic mail: dbAcoustics@cox.net

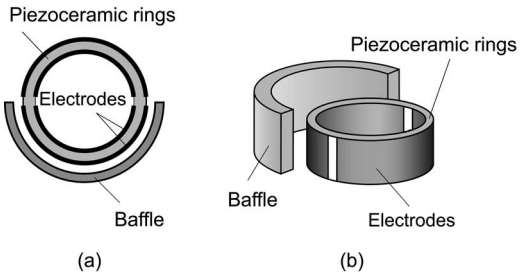

FIG. 1. Illustration of a baffled cylindrical shell transducer.

work, the Z method, which is advantageous for determining absolute values of self- and mutual radiation impedances near resonance frequencies (refer to Experiments I and II of Sec. III of Ref. 17), was implemented in a very simple experimental setup.

The acoustic coupling between transducers in an N-element array influences the net radiation impedance Z_{aci} of the ith transducer as[8]

$$Z_{\mathrm{aci}} = Z_{\mathrm{acii}} + \sum_{\ell \neq \mathrm{I}}^{N} z_{\mathrm{acI}\ell} \frac{U_\ell}{U_{\mathrm{i}}}, \tag{1}$$

where Z_{acii} and $z_{\mathrm{aci}\ell}$ are the self- and mutual radiation impedances, and U_ℓ and U_i are the surface velocities of each transducer. The influence of the neighboring transducer is considered as a coupled radiation impedance, $z_{\mathrm{aci}\ell}U_\ell/U_i$. If a two-element array is considered ($N=2$) and two identical transducers are connected in both in-phase and antiphase conditions, then $|U_2|/|U_1|=1$ due to the parallel connection and hence $Z_{\mathrm{ac}}=Z_{\mathrm{ac11}}\pm z_{\mathrm{ac12}}$ where the positive sign is for the in-phase condition and the negative sign for the antiphase condition, respectively. The corresponding equivalent circuits of the two-element array are shown in Fig. 3, where Z_e is the electric impedance, n is the electromechanical transformation coefficient, and Z_m is the mechanical impedance. The only difference in the values of the circuit components is the sign of the coupled radiation impedances between the two phase conditions. When the mechanical and acoustical parameters are transformed to the electrical domain by way of the electromechanical transformer, the electrical analogs of the self- and mutual radiation impedances are expressed as $Z_{11}=Z_{\mathrm{ac11}}/n^2$ and $z_{12}=z_{\mathrm{ac12}}/n^2$. The motional parts of the net radiation impedances are derived from the in-air and in-water input impedances measured in both phase conditions by an

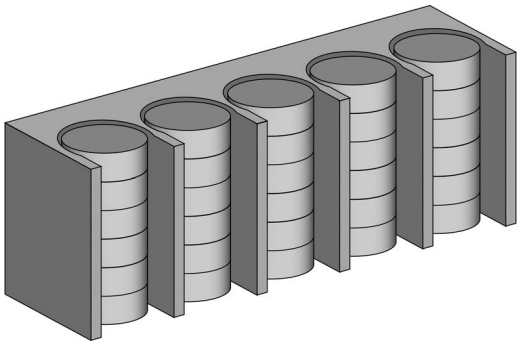

FIG. 2. Illustration of a planar array configuration of baffled cylindrical shell transducers.

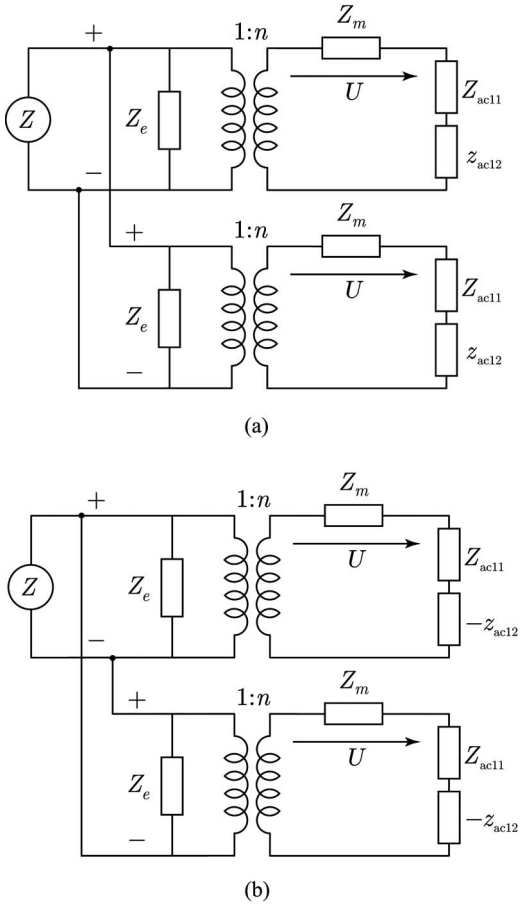

FIG. 3. Simplified equivalent circuits of the array of two transducers electrically connected in parallel: (a) in-phase and (b) antiphase.

impedance analyzer. The measured net motional impedances ($Z_{\mathrm{mot}}=R_{\mathrm{mot}}+jX_{\mathrm{mot}}$) are approximated as

$$Z_{\mathrm{mot,I}} \doteq \tfrac{1}{2}(Z_{11}+z_{12}) = \tfrac{1}{2}[(R_{11}+r_{12})+j(X_{11}+x_{12})] \tag{2}$$

and

$$Z_{\mathrm{mot,II}} \doteq \tfrac{1}{2}(Z_{11}-z_{12}) = \tfrac{1}{2}[(R_{11}-r_{12})+j(X_{11}-x_{12})], \tag{3}$$

where Z_{11} and z_{12} are the electrical analogs of the self and mutual radiation impedances. The subscripts I and II denote the in-phase and antiphase conditions of the transducers, respectively. As described in Eq. (24) of Ref. 17, the mutual radiation resistance normalized by the self-radiation resistance can be obtained based on the measurements in Eqs. (2) and (3) as

$$\frac{r_{\mathrm{ac12}}}{R_{\mathrm{ac11}}} = \frac{G_{\mathrm{mot,I}}-G_{\mathrm{mot,II}}}{G_{\mathrm{mot,I}}+G_{\mathrm{mot,II}}} \quad (f \approx f_w), \tag{4}$$

where the motional conductance is given as $G_{\mathrm{mot}}=\mathrm{Re}\{Z_{\mathrm{mot}}\}/|Z_{\mathrm{mot}}|^2$. The mutual radiation reactance normalized by the self-radiation reactance can be measured as described in Eq. (27) of Ref. 17,

$$\frac{x_{\mathrm{ac12}}}{X_{\mathrm{ac11}}} = \frac{F_{\mathrm{I}}-F_{\mathrm{II}}}{F_{\mathrm{I}}+F_{\mathrm{II}}}, \tag{5}$$

where $F=f_w(f_a^2/f_w^2-1)$, f_a is the in-air resonance frequency, and f_w is the in-water resonance frequencies of the two trans-

ducers connected in parallel. In Eq. (4), the measurement accuracy of the resistive part is dependent on the sensitivity of motional conductances to the change of radiation resistance, while in Eq. (5) the measurement accuracy of the reactive part is dependent on the sensitivity of measured resonance frequencies to the change of radiation mass.

In addition, the same approach taken in Eq. (4) can also be applied to the measurement of the reactive parts as an extension, which is not stated in Ref. 17. In the vicinity of the in-air resonance frequency, the dominant motional susceptance is the net radiation reactance as the mechanical reactance of the transducers approaches zero. The mutual radiation reactance, normalized by the self-radiation reactance, can be found from Eqs. (2) and (3) near the in-air resonance frequency as

$$\frac{x_{\mathrm{ac12}}}{X_{\mathrm{ac11}}} = \frac{B_{\mathrm{mot,I}} - B_{\mathrm{mot,II}}}{B_{\mathrm{mot,I}} + B_{\mathrm{mot,II}}} \quad (f \approx f_a), \tag{6}$$

where the motional susceptance is given as $B_{\mathrm{mot}} = \mathrm{Im}\{Z_{\mathrm{mot}}\}/|Z_{\mathrm{mot}}|^2$. In this alternative technique, the sensitivity of measured motional susceptances to the change of radiation mass was utilized instead of the sensitivity of measured resonance frequencies as shown in Eq. (5).

B. Experimental apparatus and procedure

The effect of mutual interaction between baffled cylindrical shell elements is investigated. The transducers were specifically designed and fabricated by the authors and BTech Acoustics, LLC for the measurement of radiation impedances. The photographs are shown in Fig. 4. The transducers are comprised of a piezoelectric cylinder and aluminum housing which is mechanically isolated. The internal volume between the piezoelectric ring and the aluminum housing is air-backed. The outer diameter of the encapsulated transducer is 60 mm and the height is 30 mm. The mean diameter of the piezoelectric ring is 26.5 mm and the wall thickness is approximately 3.2 mm. The height-to-mean diameter ratio is $h/2a \doteq 0.5$, where h is the height and a is the radius of a cylinder in order to reduce the effects of coupled radial and axial vibrations. The encapsulation (polyurethane coating) of the transducer was made approximately 2.0 mm thickness in order to minimize the mechanical losses. The in-air and in-water resonance frequencies of a single transducer operating in air were measured to be 19.8 and 16.9 kHz for the zero mode and 28 and 25.8 kHz for the mode one, respectively. The compliant baffle (not shown in the photograph) was applied circumferentially to cover a half of the cylindrical transducer surface. The acoustic load on the transducer changes with the application of the baffle, and the in-water resonance frequencies shift from 16.9 to 17.9 kHz for the zero mode and from 25.8 to 26.3 kHz for the mode one. Due to the similarity of the dynamic motion between the zero and one modes of a half baffled transducer, the mutual radiation impedances are also similar as a function of kd. Therefore only the results of the zero mode are presented in the following.

The measurements were done with an impedance analyzer (HP 4914A) and recorded in a computer through the GPIB port and postprocessed in MATLAB. The net input impedances of the two transducers were measured in water with the impedance analyzer in every separation distance from 30 to 250 mm by 10 mm increment for both in-phase and antiphase conditions. The net input impedances were also measured in air. Then the net motional impedance was calculated from the in-air and in-water net input impedances. Upon processing the measurement data, Eqs. (4)–(6) were computed to calculate the mutual radiation impedances.

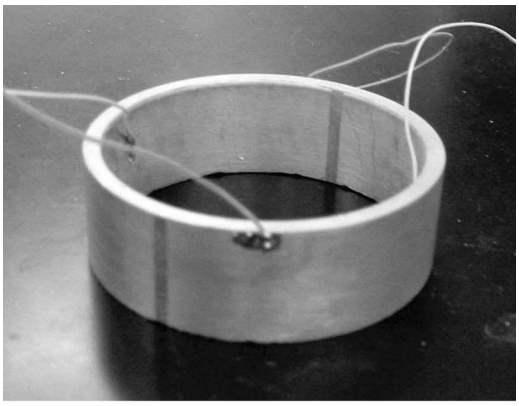

(a)

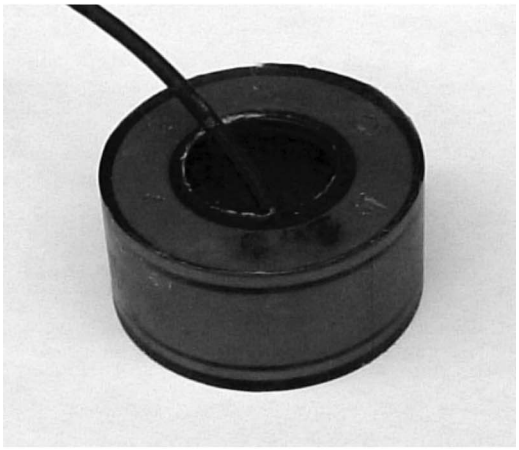

(b)

FIG. 4. Photographs of the transducer used in experiments: (a) piezoelectric ring and (b) encapsulated air-backed transducer.

An example of experimental results is shown in Fig. 5, where the motional conductances and susceptances were measured for in-phase and antiphase conditions in the separation distance $d=30$ mm for two unbaffled cylindrical shell transducers. The peak values of the motional conductances as well as the resonance frequency changes due to the effect of acoustic interactions were determined. Over the separation distance tested ($d=30-250$ mm), the measured motional conductances G_{mot} varied more than ±20% over the mean value of 0.52 mS, while the measured in-water resonance frequencies f_w varied approximately ±5% over the mean value of 17 kHz. With the alternative technique, the measured motional susceptance was observed to vary more than ±30% over the mean value of −0.2 mS. If the frequency at which the absolute value of the motional susceptance is measured is closer to the in-air resonance frequency of the trans-

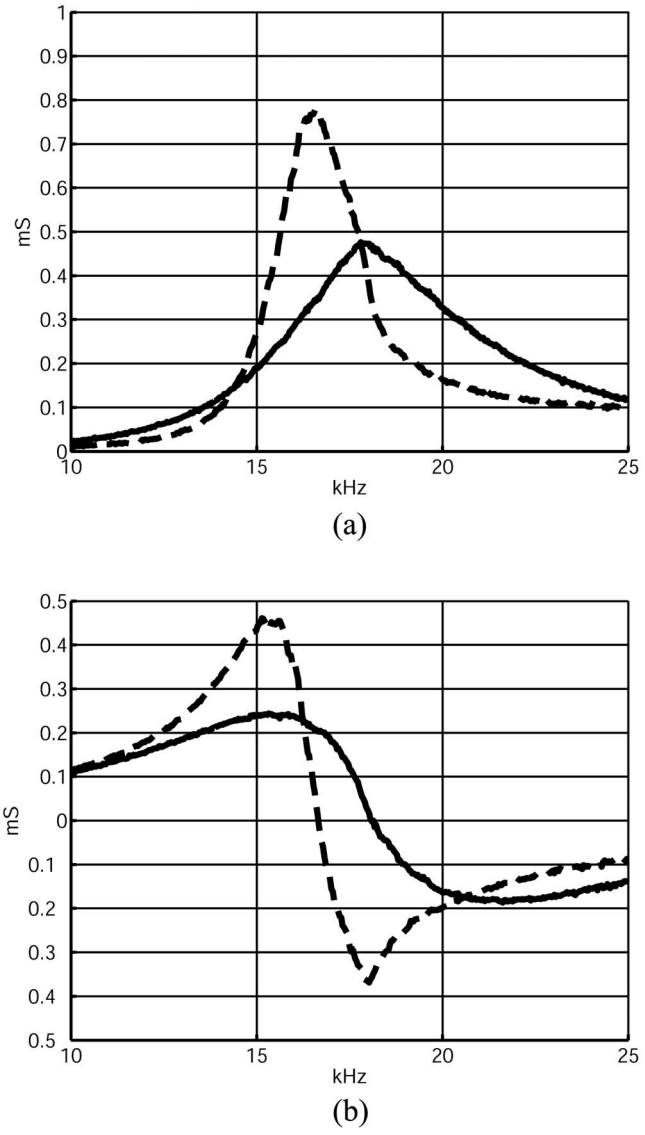

FIG. 5. Examples of measured motional impedances of two coaxially aligned unbaffled cylindrical shell transducers operating in the zero mode: (a) conductances and (b) susceptances for in-phase connection (solid line) and antiphase connection (dashed line). (The dimensions of transducers were $h=30$ mm and $a=15$ mm approximately.)

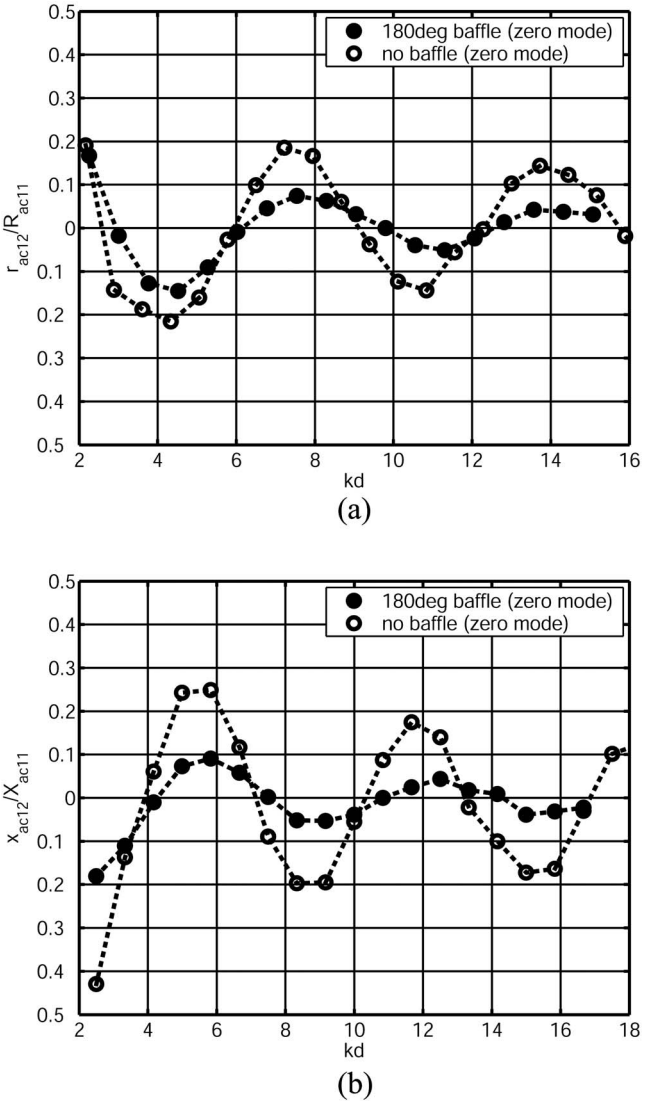

FIG. 6. Measured mutual radiation impedances for two coaxially aligned 180° corprene-baffled cylindrical shell transducers operating in the zero mode (closed circles) in comparison to the unbaffled case (open circles): (a) mutual radiation resistances normalized by self-radiation resistance, and (b) mutual radiation reactances normalized by self-radiation reactance.

ducer as shown in Fig. 5(b), the motional susceptance approaches the maximum absolute value of the motional susceptance. This condition of optimization is satisfied with the following in-water quality factor of the transducer as

$$Q_w = \frac{f_w}{2(f_a - f_w)}. \tag{7}$$

In our experiment, the unbaffled cylindrical shell transducer has approximately $Q_w \doteq 4.0$ for the zero mode operation, while the optimum value is approximately $Q_w \doteq 3.5$ with given measured frequencies of $f_w = 17.25$ kHz and $f_a = 20$ kHz. In the following experimental data, the resistive parts measured based on Eq. (4) and the reactive parts measured based on Eq. (6) are presented. The measurements were taken at 18 and 20 kHz, respectively, and the normalized mutual radiation impedances are plotted as a function of kd.

III. MEASUREMENTS OF MUTUAL RADIATION IMPEDANCE BETWEEN TWO BAFFLED CYLINDRICAL SHELL TRANSDUCERS

A. Case 1: Coaxial alignment

Figure 6 shows the experimental data for two coaxially aligned cylindrical shell transducers operating in the zero mode for both unbaffled and 180° baffled cases. The geometry of the array is illustrated in Fig. 7(a). The mutual radiation resistance and reactance are normalized by the self-radiation resistance and reactance, respectively, as a function of kd. It is observed that the variation in amplitude of the mutual radiation impedances is smaller in the case of the baffled transducers than in the case of the unbaffled transducers. Also the oscillatory phase is different between the two cases. The normalized mutual radiation impedance is almost the same between the unbaffled and baffled cases when the transducers are next to each other ($d=30$ mm). However, in the case of the baffled transducers, the mutual

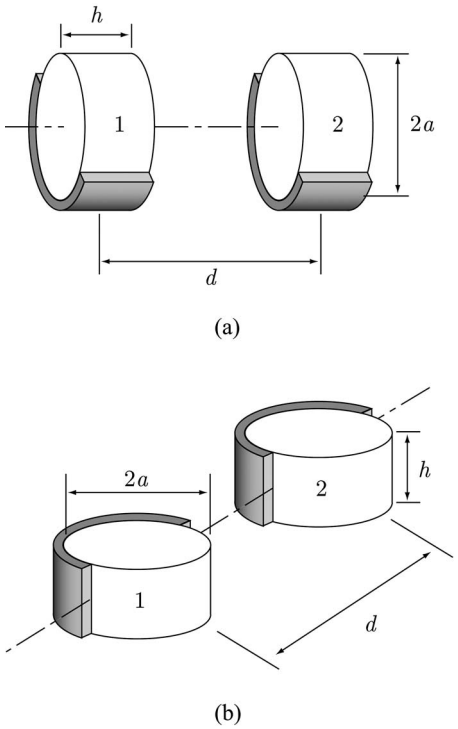

FIG. 7. Illustration of: (a) coaxially aligned baffled cylinders in free space, and (b) horizontally aligned baffled cylinders in free space.

resistance and reactance reduces more quickly with increasing kd. When the baffled transducers are more than 70 mm apart or $kd>5$, both the mutual radiation resistance and reactance are less than 10% of the self-radiation impedance.

It is also found that there exists a considerable amount (i.e., the mutual radiation resistance and reactance are more than 10% of the self-radiation impedances) of acoustic coupling between two unbaffled cylindrical shell transducers up to $kd \approx 18$. If the operation of the transducers made of PZT-4 ($c_{PZT} \doteq 3300$ ms) with aspect ratio of $h/2a \doteq 0.5$ is considered near the fundamental resonance frequency ($ka \doteq 2.2$), this corresponds to a factor of 8 of the height of the cylindrical shell transducers, $d \approx 8h$. Namely, when multiple cylindrical shell transducers are often stacked together, there exists a strong acoustic coupling between neighboring transducers. The net acoustic output of the array is not simply the addition of the array elements. The mutual radiation impedance must be taken into account since the acoustic interaction changes the phase relation between the elements. In the case of the stacked baffled transducers, this issue is less significant due to the smaller mutual radiation impedance.

B. Case 2: Horizontal alignment

Figure 8 shows the experimental data for the transducers in the horizontal alignment. For planar arrays of elements, both axial and horizontal alignment will be important. The geometry of the array is illustrated in Fig. 7(b). The minimum separation distance between two neighboring transducers is dictated by the outer diameter of the transducer. Thus, the minimum separation distance relative to the wavelength is much larger than the previous case of the coaxial alignment and is a limiting factor for optimum beam steering. The

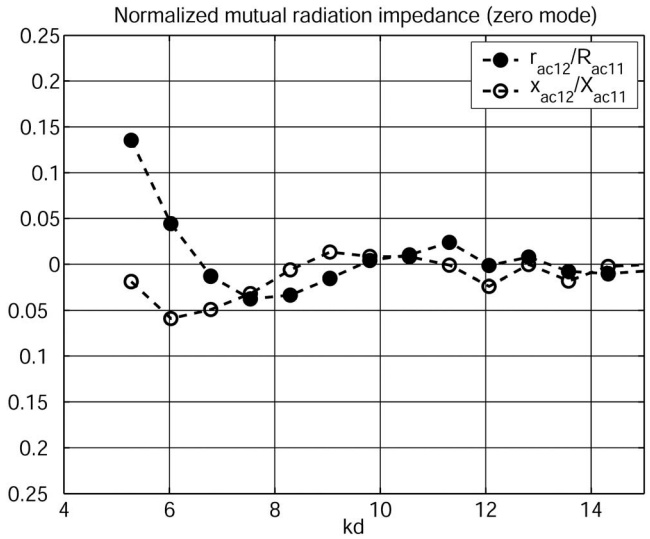

FIG. 8. Measured mutual radiation impedances for two horizontally aligned 180° corprene-baffled cylindrical shell transducers operating in the zero mode. Mutual radiation resistances normalized by self-radiation resistance (closed circles), mutual radiation reactances normalized by self-radiation reactance (open circles).

radiating surface in the direction of acoustic interaction becomes large and the mutual radiation impedance is small due to the acoustical averaging in comparison to the coaxially aligned array. The measured mutual radiation resistance was a maximum 14% of the self-resistance for the closest separation distance, but less than 5% for all the other distances tested.

The measurement results for the three different geometries tested are summarized in Fig. 9, which shows the magnitudes of the measured mutual radiation impedances normalized by the self-radiation resistance, $|z_{ac12}|/R_{ac11}$. The results of calculations obtained from the formula given by Robey[7] are also superimposed on the measured points for comparison purposes. It is observed that the values of the

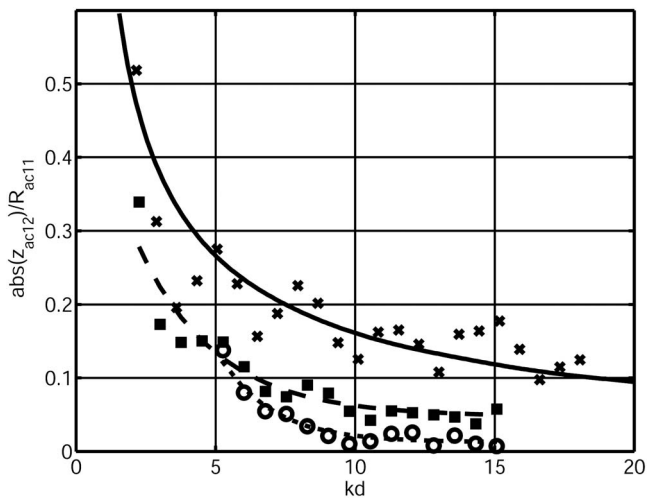

FIG. 9. Mutual radiation impedance magnitudes normalized by the self-radiation resistance of two cylindrical shell transducers operating in the zero mode: calculation of unbaffled transducers coaxially aligned (solid line), measured unbaffled transducers coaxially aligned (crosses), measured baffled transducers coaxially aligned (squares), and measured baffled transducers horizontally aligned (circles).

normalized mutual impedances are in good agreement between calculations and measurements for unbaffled transducers regardless of the difference of the geometries, i.e., the presence or absence of the infinite cylindrical baffle.

IV. SUMMARY

The application of baffled cylindrical transducers in arrays and the element-to-element interaction there within is of interest for implementing broadband sonar. The diameter of the cylindrical transducer dictates not only the operation resonance frequency, but also the element-to-element spacing in such arrays. Thus, an experimental investigation of the interaction between simple array geometries comprising two circumferentially baffled cylindrical shells was presented utilizing the experimental procedures outlined in a recent paper.[17] The results show, in general, a validation of the experimental methodology[17] and in specific, that the interaction among axially aligned elements of baffled cylinders is less than that of unbaffled elements. The interaction between horizontally oriented elements is significant between closest neighbors and was presented for 18 kHz air-backed PZT cylindrical elements having height to diameter aspect ratio of about 0.5. The measurement results of the mutual radiation impedance obtained are useful to estimate the acoustic interaction in designing arrays of baffled cylindrical shell transducers. For future work, the technique may be used with confidence for measurements of multiple elements in larger arrays.

ACKNOWLEDGMENTS

This work was supported in part by the Office of Naval Research 321MS (Lindberg). The transducer materials and fabrication were provided by BTech Acoustics, LLC. The authors would like to thank Dr. Boris Aronov for his assistance with mentoring the project. The measurements were made at the Underwater Test Facility located at School for Marine Science and Technology, at the Marine Campus of the University of Massachusetts Dartmouth.

[1]F. Pordes and C. H. Sherman, "Measurement of variation of radiation resistance with separation of pairs of underwater transducers," Proceedings of the Third International Congress on Acoustics, Stuttgart, 1959, Vol. **II**, pp. 657–677.

[2]J. S. M. Rusby, "Measurements of the total acoustic radiation impedance of rigid pistons in an array," Nature (London) **186**, 144–145 (1960).

[3]F. B. Stumpf and F. J. Lukman, "Radiation resistance of magnetostrictive-stack transducer in presence of second transducer at air-water surface," J. Acoust. Soc. Am. **32**, 1420–1422 (1960).

[4]F. B. Stumpf, "Interaction radiation resistance for a line array of two and three magnetostrictive-stack transducers at an air-water surface.," J. Acoust. Soc. Am. **36**, 174–176 (1964).

[5]F. B. Stumpf and L. A. Crum, "Interaction radiation resistance and reactance measurements for two small transducers at an air water surface," J. Acoust. Soc. Am. **40**, 1554–1555 (1966).

[6]S. J. Klapman, "Interaction impedance of a system of circular pistons," J. Acoust. Soc. Am. **11**, 289–295 (1940).

[7]D. H. Robey, "On the radiation impedance of an array of finite cylinders," J. Acoust. Soc. Am. **27**, 706—710 (1954).

[8]C. H. Sherman, "Mutual radiation impedance of sources on a sphere," J. Acoust. Soc. Am. **31**, 947–952 (1959).

[9]R. L. Pritchard, "Mutual acoustic impedance between radiators in an infinite rigid plane," J. Acoust. Soc. Am. **32**, 730–737 (1960).

[10]J. E. Greenspon and C. H. Sherman, "Mutual-radiation impedance and nearfield pressure for pistons on a cylinder," J. Acoust. Soc. Am. **36**, 149–153 (1964).

[11]E. M. Arase, "Mutual radiation impedance of square and rectangular pistons in a rigid infinite baffle," J. Acoust. Soc. Am. **36**, 1521–1525 (1964).

[12]C. Audoly, "Some aspects of acoustic interactions in sonar transducer arrays," J. Acoust. Soc. Am. **89**, 1428–1433 (1991).

[13]R. S. Gordon, L. Parad, and J. L. Butler, "Equivalent circuit of a ring transducer operated in the dipole mode," J. Acoust. Soc. Am. **58**, 1311–1314 (1975).

[14]B. S. Aronov, "Calculation of first-order cylindrical piezoelectric receivers," Sov. Phys. Acoust. **34**, 804–811 (1988).

[15]T. Oishi, B. Aronov, and D. A. Brown, "Broadband multimode baffled piezoelectric cylindrical shell transducers," J. Acoust. Soc. Am. **121**, 3465–3471 (2007).

[16]B. Aronov, D. A. Brown, and C. Bachand, "Effects of coupled vibrations on the acoustical performance of underwater cylindrical shell transducers," J. Acoust. Soc. Am. (in press), see Figs. 9 and 10.

[17]B. Aronov, "On the methods of experimental investigating of acoustical interaction between transducers," J. Acoust. Soc. Am. **119**, 3822–3830 (2006).

Global optimization of distributed output feedback controllers

Oliver Nicholas Baumann[a] and Stephen John Elliott[b]
Institute of Sound and Vibration Research, University of Southampton, University Road, Southampton, Hampshire SO17 1BJ, United Kingdom

(Received 8 September 2006; revised 24 April 2007; accepted 18 June 2007)

When the frequency range over which a reduction in vibration is desired is limited to a particular structural mode of vibration, for example, it is shown that a centralized velocity feedback controller can perform better than a decentralized controller for a given level of control effort. The decentralized controller, however, has the desirable properties of scalability and ease of implementation. A number of strategies for clustering the control locations have been proposed to exploit both the performance of the centralized controller and the scalability of decentralized controllers but these have previously been only locally optimal. This paper describes methods by which these distributed controllers may be designed to be globally optimal and gives examples of simulated results of these optimal distributed controllers. © *2007 Acoustical Society of America.* [DOI: 10.1121/1.2756796]

PACS number(s): 43.40.Vn, 43.40.Dx [KAC] Pages: 1587–1594

I. INTRODUCTION

Direct velocity feedback using multiple velocity sensors and collocated force actuators is well known for adding damping to a structure and thus, for a given disturbance excitation, reduce its vibration.[1–3] In this study, the control forces are applied to the structure at multiple control locations by means of inertial or proof mass actuators the inputs to which are described by a set of control signals as illustrated for a one dimensional structure in Fig. 1(a). In a fixed gain feedback configuration as depicted by the block diagram of Fig. 1(b) the vector of control signals **u** acting on the plant **G** is given by the product of the feedback gain matrix **H** and the vector of velocities at the control locations **y**. The primary disturbance is described by the vector **d**, and error output **e** is used to evaluate the performance of the controller. The parameters of the controller are the elements of the feedback gain matrix, and these may be optimized in order to minimize a cost function. We use a cost function in which the kinetic energy in one or more modes of vibration is moderated by the control effort. Optimizing all elements of the controller results in a centralized or fully coupled controller in which each control signal is dependent on the velocities at all control locations.

More recently, attention has been paid to systems in which the sensors and actuators are connected in individual, local loops, each control signal being dependent only on the velocity signal from the collocated sensor.[3] The corresponding gain matrix is diagonal, and an optimization for these, decentralized controllers is achieved by constraining the off-diagonal terms to be zero. It has been demonstrated in previous work that for broadband vibration control the decentralized controller performs almost identically to the centralized, and is very similar to an optimal linear quadratic Gaussian controller, regardless of any imposed control effort limit.[4] An insight is given by Elliott[5] who compares a decentralized controller with a modal controller in which each mode is given the same feedback gain. It is demonstrated that in the limit, as the number of sensors and actuators becomes large, the two controllers become identical. Designing a controller to reduce the vibration in individual modes, however, results in a feedback gain matrix in which the off-diagonal terms become significant. This implies that such a centralized controller will perform better at controlling individual modes, for a given control effort, than a decentralized controller.

Although the centralized controller has the advantage of performance, the decentralized controller has significant advantages in terms of the ease of implementation and scalability. Between the extremes of centralized and decentralized controllers lie a number of different strategies for the clustering of control locations in order to allow a robust and scalable implementation with the performance benefits of a centralized controller.[6–8] Such controllers are often referred to as distributed. Previous studies, however, have treated these distributed controllers as a set of smaller controllers, each being optimized separately, and as such, the system cannot be guaranteed to be globally optimal. This paper presents a unified approach to the global optimization of distributed controllers and therefore allows the limits of these controllers to be investigated.

We begin by discussing the model of the structure to be controlled including the dynamics of the actuators and the primary disturbance. The general method by which a controller is optimized in order to minimize the cost function is discussed in Sec. III. Sec. IV then covers the clustering strategies under study, describes how they are optimized, and presents results of the optimizations. Section V is reserved for concluding remarks.

II. MODEL

The structure to be modeled consists of a thin aluminum plate, clamped at the boundaries, upon which multiple iner-

[a]Electronic mail: onb@isvr.soton.ac.uk
[b]Electronic mail: sje@isvr.soton.ac.uk

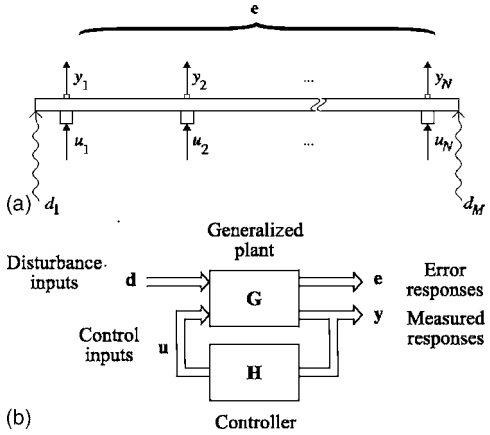

FIG. 1. Schematic of a beam with velocity sensors and inertial actuators (a) and the corresponding block diagram showing plant **G** and controller **H** with respective inputs and outputs.

tial actuators are mounted. The inertial actuators consist of a magnetic proof mass, which is suspended in a casing with a coil of wire running perpendicular the lines of magnetic flux. A schematic of an example actuator is given in Fig. 2(a). The current in the coil results in a force acting between the proof mass and the casing, which in turn, is transmitted to the structure via a fixative. Each actuator may be modeled as a simple, two degree of freedom, lumped parameter model as depicted in Fig. 2(b) where m_p and m_c represent the mass of the proof mass and the casing, k_p is the suspension stiffness, and k_c is the (large) stiffness of the attachment point between the actuator and the structure. We approximate the transverse

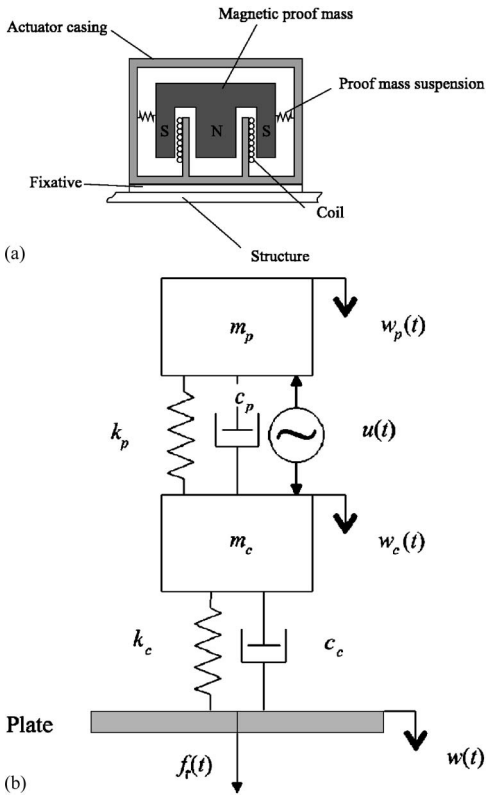

FIG. 2. (a) Schematic and (b) lumped parameter model of an inertial actuator.

displacement of the plate at N control locations described by the vector couple $\mathbf{x}_s$, $\mathbf{y}_s$ by the finite modal summation,[8] which may be expressed in vector form as

$$\mathbf{w}(\mathbf{x}_s,\mathbf{y}_s,t) \approx \mathbf{\Psi}(\mathbf{x}_s,\mathbf{y}_s)^T\mathbf{a}(t), \tag{1}$$

where $\mathbf{\Psi}$ is an N by M matrix describing the mode shape functions of M modes at the control locations and $\mathbf{a}(t)$ is the vector of modal amplitudes. The mode shape functions are those that satisfy clamped boundary conditions[9] and the modal amplitudes satisfy the second order differential equation

$$\ddot{\mathbf{a}}(t) = \mathbf{D}\dot{\mathbf{a}}(t) + \mathbf{K}\mathbf{a}(t) + \frac{4}{M_p}\mathbf{f}(t), \tag{2}$$

where M_p is the total mass of the plate and $\mathbf{D}$ and $\mathbf{K}$ are square matrices of dimensions M having the terms $-2\zeta_m\omega_m$ and $-\omega_m^2$, respectively, on the diagonal where ζ_m is the modal damping ratio and ω_m the resonance frequency of the mth mode. The coupled dynamics of the plate and actuators may be represented in state space form, the governing equations being

$$\dot{\mathbf{x}}(t) = \mathbf{A}\mathbf{x}(t) + \mathbf{B}_u\mathbf{u}(t) + \mathbf{B}_d\mathbf{d}(t), \tag{3}$$

$$\mathbf{y}(t) = \mathbf{C}\mathbf{x}(t). \tag{4}$$

The state vector $\mathbf{x}(t)$ comprises the vector of modal amplitudes $\mathbf{a}(t)$, the vector of proof mass displacements $\mathbf{w}_p(t)$, the vector of casing mass displacements $\mathbf{w}_c(t)$ and the time derivatives thereof. The matrix $\mathbf{A}$ describes the dynamics of the system, including the coupling of the plate modes and the actuator masses. The matrix $\mathbf{B}_u$ describes how the vector of control signals $\mathbf{u}(t)$ effects the system. Similarly the matrix $\mathbf{B}_d$ describes how the disturbance input $\mathbf{d}(t)$ acts on the system states. Finally $\mathbf{C}$ describes the relationship between the state vector and the vector of plate velocities at the control locations $\mathbf{y}(t)$. In the case of constant gain output feedback discussed here we may say that

$$\mathbf{u}(t) = -\mathbf{H}\mathbf{y}(t) = -\mathbf{H}\mathbf{C}\mathbf{x}(t), \tag{5}$$

such that Eq. (3) becomes

$$\dot{\mathbf{x}}(t) = \mathbf{A_0}\mathbf{x}(t) + \mathbf{B}_d\mathbf{d}(t), \tag{6}$$

where

$$\mathbf{A_0} = [\mathbf{A} - \mathbf{B}_u\mathbf{H}\mathbf{C}]. \tag{7}$$

The primary excitation vector $\mathbf{d}(t)$ and the disturbance input matrix $\mathbf{B}_d$ are chosen to represent to a "worst case scenario" in which each mode of the plate is excited by an uncorrelated white noise signal. This is equivalent to a spatially and temporally uncorrelated pressure field acting on the plate. The expectation of the state vector may be evaluated as a function of frequency by taking the Laplace transform of Eq. (7) and setting $s=j\omega$ to obtain

$$\mathbf{x}(j\omega) = [j\omega\mathbf{I} - \mathbf{A_0}]^{-1}\mathbf{B}_d\mathbf{d}(j\omega). \tag{8}$$

From which one may obtain the expectation of the kinetic energy spectrum

TABLE I. Table of plate properties.

Property	Value
l_x	0.8 m
l_y	0.5 m
h	0.002 m
ρ	2720 kg/m^3
M	53
$f_{\max}$	1100 Hz

$$E_k(j\omega) = \text{trace}[[j\omega\mathbf{I} - \mathbf{A_0}]^{-H}\mathbf{Q}[j\omega\mathbf{I} - \mathbf{A_0}]^{-1}], \tag{9}$$

where H denotes the complex conjugate transpose and $\mathbf{Q}$ is chosen such that

$$\mathbf{x}^H(j\omega)\mathbf{Q}\mathbf{x}(j\omega) = \frac{M_p}{8}\dot{\mathbf{a}}^H(j\omega)\dot{\mathbf{a}}(j\omega), \tag{10}$$

where $\dot{\mathbf{a}}(j\omega)$ is the vector of modal velocities. The spectrum of the kinetic energy for a thin aluminum plate whose properties are given in Table I with 24 inertial actuators is plotted in Fig. 3. Also plotted are the kinetic energy spectra of the plate with a decentralized, and a centralized controller optimized to minimize the kinetic energy in the third structural mode of the plate, both having a control effort of 100 N^2, which demonstrates the ability of the centralized controller to channel its effort into reducing the kinetic energy in a single mode. The decentralized controller performs slightly less well in mode three, but considerably better in all other modes. Section III describes the method by which the feedback gain matrix $\mathbf{H}$ may be optimized for these, and other control strategies.

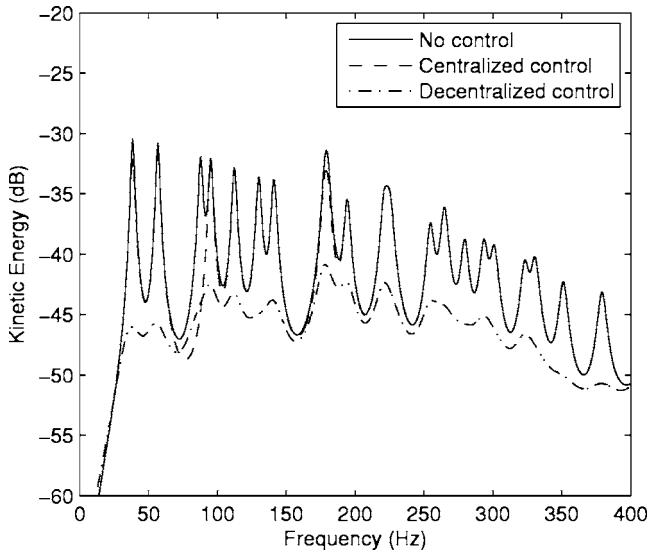

FIG. 3. The kinetic energy spectra of the plate without control (solid) and with centralized (dashed) and decentralized (dot-dashed) controllers, which are optimal for the reduction of kinetic energy in mode three with a control effort of 100 N^2.

III. CONTROLLER OPTIMIZATION

Constant gain velocity feedback controllers are designed by optimizing the elements of the feedback gain matrix $\mathbf{H}$ in order to minimize a cost function. It is convenient to express the cost function in the form

$$J = \text{E}[\mathbf{x}(t)^T\mathbf{Q}\mathbf{x}(t) + \mathbf{u}(t)^T\mathbf{R}\mathbf{u}(t)], \tag{11}$$

where E[ ] denotes the expectation operator, $\mathbf{x}(t)$ is the state vector, and $\mathbf{u}(t)$ is the control signal vector. The matrix $\mathbf{Q}$ could be defined as in Eq. (10) such that the first term of the cost function is proportional to the total kinetic energy of the plate, but if the controller is to be optimized to minimize the kinetic energy of a single mode then it can be defined by the equation

$$\mathbf{x}^H(j\omega)\mathbf{Q}\mathbf{x}(j\omega) = \frac{M_p}{8}a_m^2(j\omega), \tag{12}$$

where m denotes the mode in which the kinetic energy is to be minimized. The second term of Eq. (11) relates to the control effort. By selecting $\mathbf{R} = r\mathbf{I}$ a penalty, proportional to r, can be placed on the sum of the squared control signals. Substitution of Eq. (5) into the cost function yields[4]

$$J = \text{trace}\left(\int_0^\infty \mathbf{\Phi}(t)^T[\mathbf{Q} + \mathbf{C}^T\mathbf{H}^T\mathbf{R}\mathbf{H}\mathbf{C}]\mathbf{\Phi}(t)dt\mathbf{F}\right), \tag{13}$$

where $\mathbf{\Phi}(t)$ is the fundamental transition matrix given by

$$\mathbf{\Phi}(t) = e^{\mathbf{A_0}t}, \tag{14}$$

and $\mathbf{F}$ is a matrix relating to the primary disturbance. Levine and Athans[10] derive an expression for the gradient of this cost function with respect to the gain matrix, which we quote here

$$\frac{dJ}{d\mathbf{H}} = 2\mathbf{R}\mathbf{H}\mathbf{C}\mathbf{L}\mathbf{C}^T - 2\mathbf{B}_u^T\mathbf{K}\mathbf{L}\mathbf{C}^T, \tag{15}$$

where $\mathbf{K}$ is the positive semidefinite solution of the continuous Lyapunov equation

$$\mathbf{0} = \mathbf{K}\mathbf{A}_0 + \mathbf{A}_0^T\mathbf{K} + \mathbf{Q} + \mathbf{C}^T\mathbf{H}^T\mathbf{R}\mathbf{H}\mathbf{C} \tag{16}$$

and is not to be confused with $\mathbf{K}$ of Eq. (2), and $\mathbf{L}$ is the positive definite solution of

$$\mathbf{0} = \mathbf{L}\mathbf{A}_0^{\mathrm{T}} + \mathbf{A}_0\mathbf{L} + \mathbf{F} \tag{17}$$

The matrix gradient expression derived from Eqs. (15)–(17) may then be used in a simple multivariable gradient descent algorithm to find the elements of $\mathbf{H}$, which minimize Eq. (11) for a given control effort weighting r.

As discussed previously, the elements of the gain matrix $\mathbf{H}$, which are optimized depend on the form of the controller that is to be derived. In the case of the decentralized controller, for example, only the on-diagonal gains are optimized, all others are constrained to be zero. This is achieved by setting the elements of the gradient matrix, which correspond to those of the gain matrix, which are constrained to zero at each iteration. A complete description of the algorithm may be found in Ref. 4. Section IV discusses the form of the feedback gain matrix in terms of the clustering of control locations.

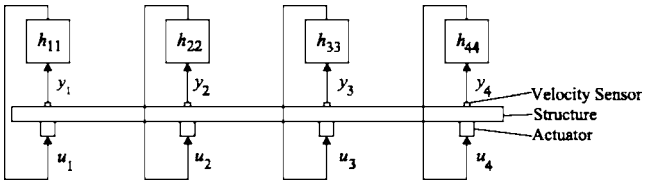

FIG. 4. A simple one-dimensional structure with velocity sensors and actuators in a decentralized control configuration.

IV. CLUSTERING STRATEGIES

The first clustering strategy we shall consider is referred to as a reach or geographical clustering strategy.[11] It is a convenient starting point as it includes both centralized and decentralized control strategies at its extremes. Figure 4 shows a schematic of a simple, one-dimensional structure with four control locations consisting of a velocity sensor and an actuator. In the decentralized case the sensors and actuators are simply connected in local loops. This system may be described as having a reach of zero as only local information is used to inform each actuator. The feedback gain matrix corresponding to this decentralized controller is a diagonal matrix and may be optimized with respect to the cost function by constraining the off-diagonal elements to be zero. Increasing the reach of the controller to one, each control signal is informed not only by the local sensor but also by neighbors within one "hop" of the forcing location. In this one-dimensional example each actuator input will comprise a weighted sum of a maximum of three velocity signals, actuators at the ends of the structure being informed by only two. This configuration is depicted for the second forcing control location in Fig. 5. The corresponding gain matrix takes the form

$$\mathbf{H} = \begin{bmatrix} h_{1,1} & h_{1,2} & 0 & 0 \\ h_{2,1} & h_{2,2} & h_{2,3} & 0 \\ 0 & h_{3,2} & h_{3,3} & h_{3,4} \\ 0 & 0 & h_{4,3} & h_{4,4} \end{bmatrix}, \tag{18}$$

and again optimization of this matrix is achieved simply by constraining the zero terms. For the four channel system under discussion, a reach of two denotes a system in which the two control signals associated with the inner control locations are derived from all velocity signals. The outer signals comprising all but the velocity signal at the opposite end. A reach of three implies that all velocity signals are used to inform each control signal and as such the controller is centralized and the feedback gain matrix is full in this example.

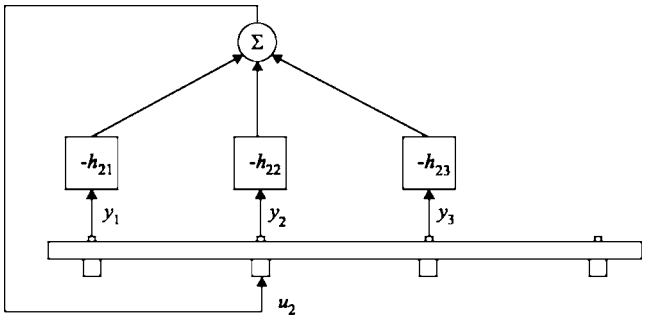

FIG. 5. A diagram depicting the derivation of the control signal at the second control location for a reach of one.

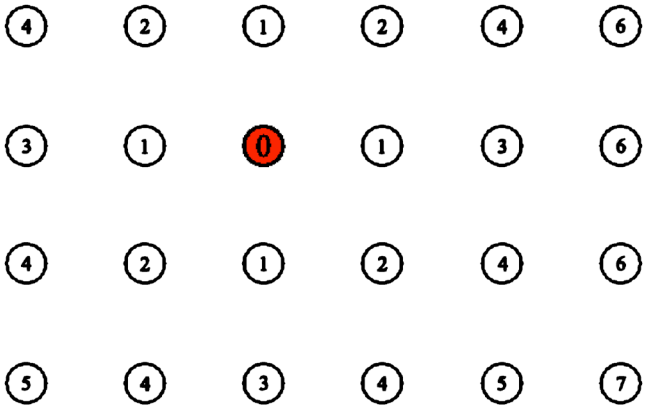

FIG. 6. (Color online) An example showing the sensors comprising the control signal at the shaded location for increasing values of reach.

The same principles may be applied in two dimensions to the control locations on the plate. The sensor signals comprising the control signal at a given location are taken to be those within a given Euclidean distance, which increases with increasing reach. Figure 6 shows a schematic of the plate with control locations. The sensors used in informing the control signal associated with the location marked with a zero are numbered according to the level of reach at which they are used. Although in the case pictured, the control signal at the location of interest is informed by all the sensors on the plate at a reach of seven, this is not the case for the control locations located nearer the edges of the plate. In order for a control signal associated with a location in the corner of the plate to include a component from the velocity signal from the opposite corner a reach of ten is required. As such a reach of ten corresponds to a fully centralized controller.

Optimizations of the nonzero elements of the gain matrix are performed for each level of reach and several values of control effort weighting r in order to minimize the kinetic energy in the third mode of the plate. The result is a set of optimal controllers each having an associated reduction in kinetic energy, control effort, and reach. These are plotted for the controllers having a reach of zero, being the decentralized controller, one, five, and ten, being the centralized controllers in Fig. 7. It is clear that for a given control effort the performance of the controller, in terms of the reduction in kinetic energy of the third structural mode, increases with increasing reach, the centralized controller offering the best performance. This is more clearly demonstrated in Fig. 8 in which the reduction in kinetic energy is plotted as a function of the reach of the controller for a fixed control effort of 100 N^2.

The reach clustering strategy provides one example of a hierarchy with a single level. Such hierarchies have been referred to as horizontal hierarchies and controllers based on these hierarchies can always be optimized in the manner described earlier. For hierarchies with more than one level, however, optimization cannot be performed in this way for reasons that we illustrate with the following example.

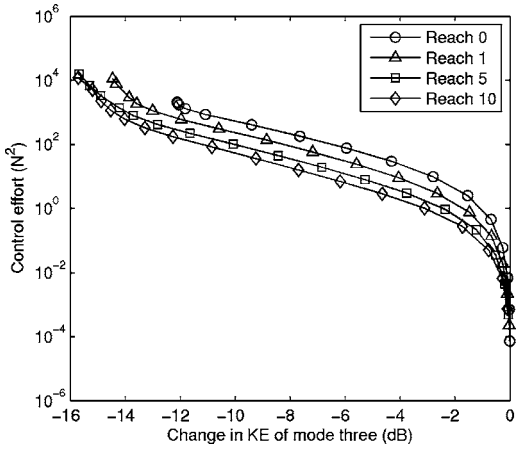

FIG. 7. Plot of the effort against the associated change in kinetic energy of mode three for optimal controllers of reach 0 (decentralized), reach 1, reach 5, and reach 10 (centralized).

A simple, four channel, two tier hierarchy is shown in Fig. 9. Each control signal comprises the velocity signal with which it is collocated weighted by a gain $h_{1,n}$, where the first subscript now denotes the level in the hierarchy and the second is a unique identifier. These gains form the first level of the hierarchy and, without the addition of subsequent layers completely describe the decentralized controller. The second layer of the hierarchy consists of two gains, which are applied to the sum of the signals below them in the tree. In this example, the gains $h_{2,1}$ and $h_{2,2}$ are applied to signals y_1+y_2 and y_3+y_4, respectively. The summation of signals at each level of a hierarchy will tend to enhance components, which are common to the child signals and as such the signals may be regarded as containing more global information. Returning to the example, the amplified signals resulting from the second level of the hierarchy are then fed back to each of the control signals below them. In general, the same principle is applied for any additional layers. The control signal at location one is therefore

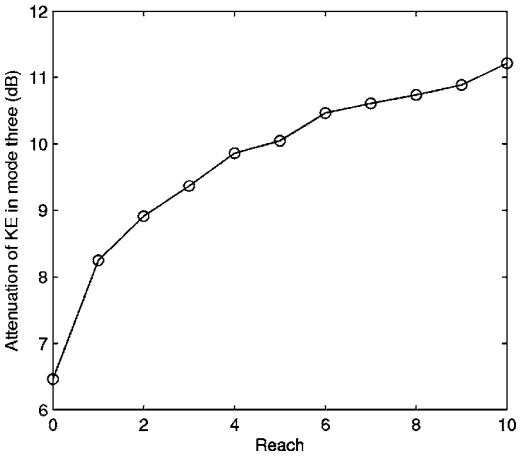

FIG. 8. Plot of the reduction in kinetic energy of mode three against the reach of the controller for a control effort of 100 N².

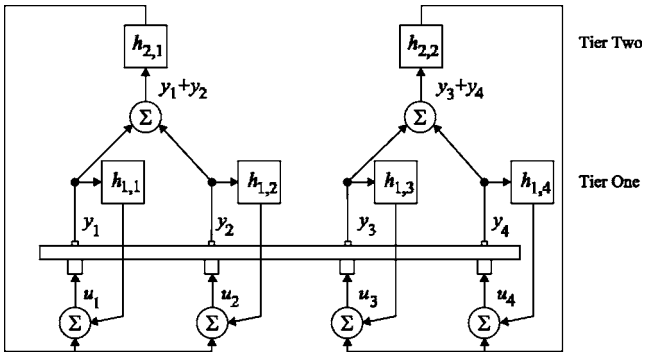

FIG. 9. A schematic of the control configuration of a four-channel, two-tier hierarchy on a one-dimensional structure.

$$u_1 = h_{1,1}y_1 + h_{2,1}(y_1 + y_2) \tag{19}$$

$$= (h_{1,1} + h_{2,1})y_1 + h_{2,1}y_2. \tag{20}$$

Similar expressions may be derived for the other control signals resulting in a feedback gain matrix of the form

$$\begin{bmatrix} h_{1,1}+h_{2,1} & h_{2,1} & 0 & 0 \\ h_{2,1} & h_{1,2}+h_{2,1} & 0 & 0 \\ 0 & 0 & h_{1,3}+h_{2,2} & h_{2,2} \\ 0 & 0 & h_{2,2} & h_{1,4}+h_{2,2} \end{bmatrix}. \tag{21}$$

Note however that the on-diagonal elements of the gain matrix consist of the sum of two gains in the hierarchy. It is therefore not possible to optimize the gains of the controller as before.

We may however transform this matrix into a form that may be readily optimized. First we define a new signal vector which includes the sum signals, i.e.,

$$\hat{\mathbf{y}} = \begin{bmatrix} y_1 \\ y_2 \\ y_3 \\ y_4 \\ y_1+y_2 \\ y_3+y_4 \end{bmatrix}. \tag{22}$$

We may thus define a transfer matrix $\mathbf{T}$ such that

$$\hat{\mathbf{y}} = \mathbf{T}\mathbf{y}. \tag{23}$$

We may then define a new gain matrix

$$\hat{\mathbf{H}} = \begin{bmatrix} h_{1,1} & 0 & 0 & 0 & 0 & 0 \\ 0 & h_{1,2} & 0 & 0 & 0 & 0 \\ 0 & 0 & h_{1,3} & 0 & 0 & 0 \\ 0 & 0 & 0 & h_{1,4} & 0 & 0 \\ 0 & 0 & 0 & 0 & h_{2,1} & 0 \\ 0 & 0 & 0 & 0 & 0 & h_{2,2} \end{bmatrix}, \tag{24}$$

and control signal vector $\hat{\mathbf{u}}$ such that

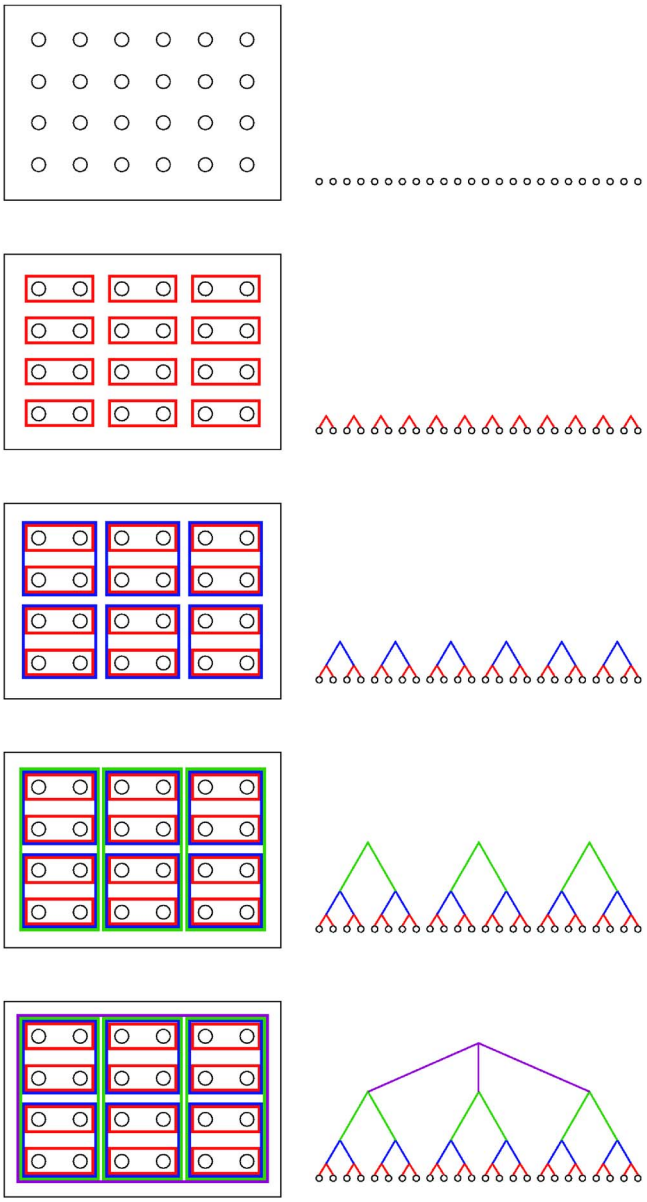

FIG. 10. (Color online) An example vertical hierarchy structure.

$$\hat{\mathbf{u}} = \hat{\mathbf{H}}\hat{\mathbf{y}}. \tag{25}$$

It can then be shown that the original control signal vector may be derived from

$$\mathbf{u} = \mathbf{T}^T\hat{\mathbf{u}} = \mathbf{T}^T\hat{\mathbf{H}}\mathbf{T}\mathbf{y}. \tag{26}$$

In terms of the optimization of the new gain matrix $\hat{\mathbf{H}}$ we may also define a new output matrix

$$\hat{\mathbf{C}} = \mathbf{T}\mathbf{C}, \tag{27}$$

and control effort weighting matrix

$$\hat{\mathbf{R}} = \mathbf{T}\mathbf{R}\mathbf{T}^T, \tag{28}$$

and substitute these into the cost function equations (13) and (15) in order to optimize the gains of the hierarchy using the method described in Sec. III.

Returning once again to the two-dimensional example of the plate with 24 control locations, the number of possibilities for clustering using vertical hierarchies is very large. In order to illustrate a set of optimal results we use the set of hierarchies depicted in Fig. 10. At the lowest level of the hierarchy, level zero, the controller corresponds to the decentralized case. The first level of the hierarchy consists of additionally feeding back signals, which are the sum of pairs of sensor signals, as illustrated in Fig. 9. These pairs are then additionally merged into fours at the second level, eights at the third, and finally at level four, the signal is the sum of all sensor signals. As for the reach clustering system, the distributed controllers associated with each hierarchy are optimized for a number of control effort weightings in order to produce a set of optimal controllers each with an associated performance measure and control effort. The reduction in kinetic energy in mode three for each optimal controller is plotted in Fig. 11.

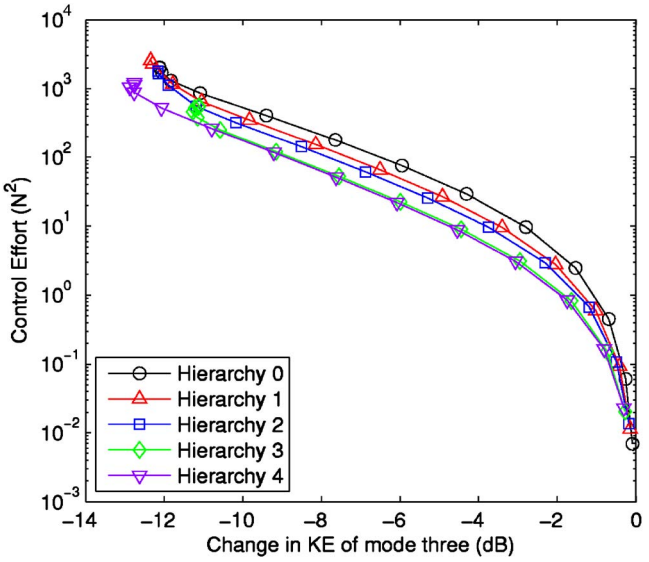

FIG. 11. (Color online) Performance versus control effort for the optimal distributed controllers based on the vertical hierarchy.

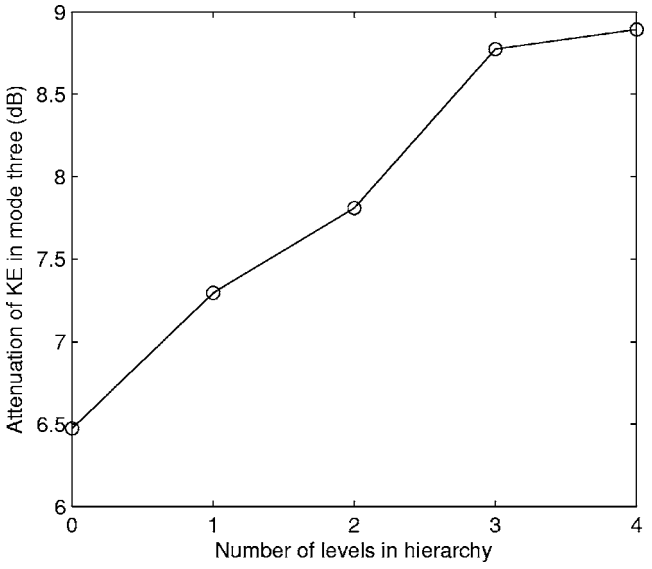

FIG. 12. Attenuation in the kinetic energy of mode three of the plate as a function of the number of levels in the hierarchy for a fixed control effort of 100 N^2.

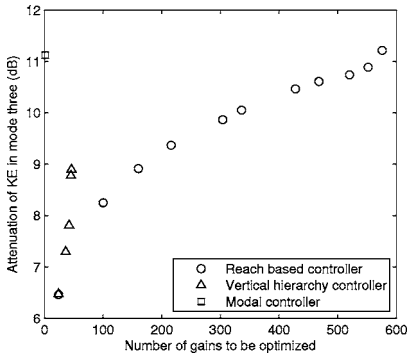

FIG. 13. Attenuation in the kinetic energy of mode three of the plate as a function of the number of gains in the hierarchy for the reach clustering and the vertical hierarchy.

It is clear from Fig. 11 that, for a given control effort, the performance of the optimal controller increases with the number of levels in the hierarchy. This is made more clear in Fig. 12 in which the performance of the optimal controllers having a control effort of 100 N^2 is plotted as a function of the number of levels in the hierarchy.

In order to compare the two clustering strategies presented here we plot the performance of the controller, for a control effort of 100 N^2 as a function of the number of gains, which are to be optimized as in Fig. 13. The result of an optimal modal controller[9,12] of the form given in Fig. 14 is also presented in Fig. 13 for a control effort of 100 N^2. In such a controller the signal vector is multiplied first by a modal analyzer, which in this case takes the form of the row vector $\mathbf{\Psi}_3$, which describes the mode shape function of the third structural mode at the control locations. The result is a scalar signal, which is multiplied by a single control gain, h, which is then fed back to the actuators via the modal synthesizer $\mathbf{\Psi}_3$. The reason for the inclusion of the modal controller is that it describes the best possible performance of a controller with only a single gain for the reduction of kinetic energy in a single structural mode of the plate. The modal controller achieves over 11 dB of attenuation by optimizing the single feedback gain. This control strategy does, however, assume that the mode shape is known perfectly, for use in the analyzer and synthesizer, which are fixed. It is also considerably less flexible than the more general clustering strategies, which could be readily tuned to control other modes or combinations of modes.

Figure 13 clearly shows that the performance of the vertical hierarchy is better than the reach clustering strategy when the number of gains to be optimized is low. The reach clustering strategy however is capable of greater reductions than the vertical hierarchy strategy, and ultimately the modal controller, albeit with considerably more gains.

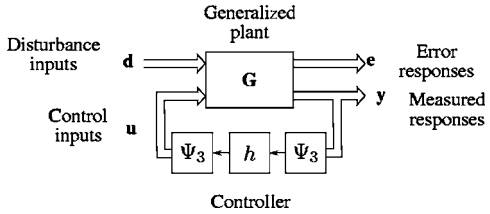

FIG. 14. Block diagram of a modal controller with modal analyzer and synthesizer for mode three.

V. CONCLUSIONS

This paper has presented a unified approach to the global optimization of clustered control strategies for distributed control. Based on a time domain model of an aluminum plate with multiple inertial actuators and collocated velocity sensors a gradient descent method was presented for the optimization of the feedback gain matrix for the minimization of kinetic energy in one or more structural modes of the plate. It was then demonstrated that for simple, so-called horizontal hierarchy clustering strategies, global optimality could be achieved simply by constraining certain terms of the gain matrix to be zero. It was then demonstrated that for hierarchies with more than one level it is not possible to use this direct optimization method as elements of the overall gain matrix contain the sum of individual gains in the hierarchy. A simple technique by which the gain matrix may be translated to a diagonal matrix of unique gains, and a transform matrix was introduced. This diagonal matrix may then be optimized with only minor changes to the technique used previously.

The results of optimizations for the distributed control of a plate with 24 inertial actuators for one horizontal hierarchy and one vertical hierarchy were presented. It is shown that for a fixed control effort the performance of both controllers increases with its complexity, be it reach, in the case of the horizontal hierarchy, or the number of levels in the vertical hierarchy. The two strategies are then compared by plotting the performance of the controller as a function of the number of gains, which require optimization. Included for comparison is the performance of the modal controller in which only a single gain requires optimization. The vertical hierarchy shows a greater performance for lower numbers of gains, but the maximum performance of the presented example is lower than that of either the horizontal hierarchy or modal controllers. The maximum performance of the horizontal hierarchy is that which corresponds to the centralised controller and in fact slightly exceeds the performance of the modal controller. It is believed that is a result of using inertial actuators and is a topic of ongoing research.

ACKNOWLEDGMENTS

The work of the first author (O.N.B.) is supported by the Data and Information Fusion Defence Technology Centre.

[1]M. J. Balas, "Feedback control of flexible systems," IEEE Trans. Autom. Control **AC-23**, 673–674 (1978).
[2]A. Preumont, *Vibration Control of Active Structures*, Solid Mechanics and it's Applications, Vol. **50**, 1st ed. (Kluwer Academic, Ontario, Canada, 1997).
[3]S. J. Elliott, P. Gardonio, T. C. Sors, and M. J. Brennan, "Active vibroacoustic control with multiple local feedback loops," J. Acoust. Soc. Am. **111**, 908–915 (2002).
[4]W. P. Engels, O. N. Baumann, S. J. Elliott, and R. Fraanje, "Centralized and decentralized control of structural vibration and sound radiation," J. Acoust. Soc. Am. **119**, 1487–1495 (2006).
[5]S. J. Elliott, "Distributed control of sound and vibration," Noise Control Eng. J. **53**, 165–180 (2005).
[6]K. D. Frampton, "Decentralized control of structual acoustic radiation," in

IMEC 2001, Noise control and acoustics division, New York, 2001.
[7]K. D. Frampton, "Distributed group-based vibration control with a networked embedded system," Smart Mater. Struct. **14**, 307–314 (2005).
[8]L. Meirovitch, *Dynamics and Control of Structures* (Wiley, New York, 1990).
[9]A. W. Leissa, *Vibration of Plates*, Vol. **NASA SP-160** (NASA, Washington, D.C., 1969).
[10]W. S. Levine and M. Athans, "On the determination of the optimal constant output feedback gains for linear multivariable systems," IEEE Trans. Autom. Control **AC-15**, 44–48 (1970).
[11]K. D. Frampton, "Vibro-acoustic control with a distributed sensor network," J. Acoust. Soc. Am. **119**, 2170–2177 (2006).
[12]C. R. Fuller, S. J. Elliott, and P. A. Nelson, *Active Control of Vibration* (Academic, New York, 1996).

The influence of sensitivity for road traffic noise on residential location: Does it trigger a process of spatial selection?

Hans A. Nijland[a)]
Netherlands Environmental Assessment Agency, Bilthoven, Utrecht 3720BA the Netherlands

Sander Hartemink
Faculty of Geographical sciences, Utrecht University, Utrecht, the Netherlands

Irene van Kamp
National Institute for Public Health and the Environment, RIVM, Bilthoven, the Netherlands

Bert van Wee
Faculty of Technology, Policy and Management, Delft University of Technology, Delft, the Netherlands

(Received 25 September 2006; revised 27 February 2007; accepted 20 June 2007)

People move to another house for different reasons. It is sometimes presumed that a process of self-selection might take place on the basis of noise sensitivity, i.e., sensitive people would either leave high noise areas or not move into these areas in the first place. Thus, a "survivor population" would remain in the high noise areas. This research aims to investigate whether such a process can be observed in the Netherlands. The study does not show evidence of a process of self-selection based on noise sensitivity. Nevertheless, the results suggest that noise-sensitive people are less satisfied with their living environment and are more willing to move than those who are not noise sensitive. Due to the limited sample size, external validity is limited. © *2007 Acoustical Society of America.* [DOI: 10.1121/1.2756970]

PACS number(s): 43.50.Qp [BSF] Pages: 1595–1601

I. INTRODUCTION

Yearly, about 10% of the Dutch population (i.e., 1.6 million people) moves to another dwelling (Ekamper and Van Huis, 2002). This percentage has been more or less constant since 1946, when Statistics Netherlands started to collect yearly figures (www.cbs.nl/nl/cijfers/statline).

This article will concentrate on the role of noise sensitivity as one of the reasons for people to move to a quiet area, or, in contrast, one of the reasons not to move into a noisy neighborhood in the first place. The outcome of the analysis should provide an answer to the question: does a process of self-selection due to road traffic noise on the basis of noise sensitivity exist? To date, very little research has focused on a self-selection process due to noise sensitivity and road traffic noise. Lako (1987) analyzed the relationship between road traffic noise and migration in a sample of 3000 dwelling units, divided in a high exposure area and a low exposure area. Unfortunately, he did not pay attention to the possible influence of noise sensitivity. This research aims to fill that gap by investigating the impact of noise sensitivity on residential location. Researchers discern a change in the household, in work, in education and dissatisfaction with the dwelling and/or the neighborhood as main reasons to move to another location. (e.g. Clark, 1982; Owen, 1992; Clark *et al.*, 1996, 1999; Mulder and Hooijmeijer, 1999; Gardner *et al.*, 2001; Housing Corporation, 2004). Literature reports relatively few environmental factors such as noise levels or concentrations of pollutants as main reason for moving (Rohrmann 1986, 1991). Leidelmeijer and Marsman (2001) found around 5% of the people in the area of Schiphol definitely wanting to move within two years mainly for environmental reasons. They mentioned noise as the most important stressor.

Noise sensitivity is often defined as a stable, personal trait, influencing one's reaction to noise, independent of the noise level (Zimmer and Ellermeier, 1999, Ellermeier *et al.*, 2001). The association between noise sensitivity and noise exposure is consistently low (Job, 1988). Research showed that noise sensitivity is a major antecedent of noise annoyance (see Taylor 1984; Stansfeld *et al.*, 1985; Stansfeld 1992, Job 1988; 1999; Staples 1996; van Kamp *et al.*, 2004). Job (1988) found noise sensitivity to explain 10.2% of the variation in noise annoyance reactions. Noise sensitivity is associated with health variables such as sleep disturbance (Ohrstrom, 1995) and psychological distress and psychiatric disorders (Stansfeld, 1992, Stansfeld *et al.*, 1985, 1993, 1996).

Figure 1 presents a conceptual model of the role of noise and noise sensitivity in the process of moving. It shows the main reasons for moving and it illustrates that the process of moving is a multi-stage decision process (as already described by Rossi, 1955). It also shows that noise sensitivity (in combination with noise level) plays a role in the different stages of that process, when moving out and when moving in.

Job (1988) and Fields (1992) hypothesized that people in high noise areas could be abnormally tolerant of high noise because of a process of self-selection, i.e., sensitive

a)Author to whom correspondence should be addressed. Electronic mail: hans.nijland@mnp.nl

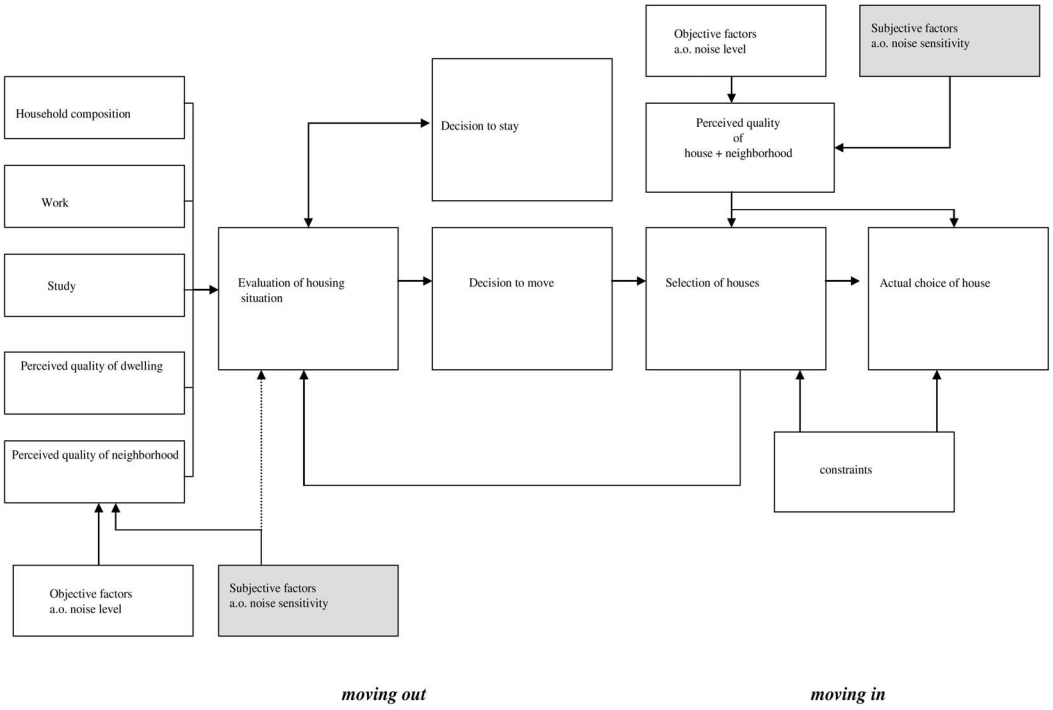

FIG. 1. Conceptual model of moving houses and the role of noise and noise sensitivity in that process.

people would either leave high noise areas or not move into the areas initially. However, in his meta-analysis, Fields did not find conclusive evidence to support this theory.

The outcome of our research might not only be of scientific interest. If such a process of self-selection exists, it might have consequences for the estimated levels of annoyance in the case of new infrastructure. It would mean that annoyance of the people affected, based on average population responses, is usually underestimated in the short and medium term, because in quiet areas an overrepresentation of noise-sensitive people might be expected. In the (very) long term, after all dwellings had new inhabitants, the new population would consist mainly of people relatively insensitive to noise. Thus, in the very long term, annoyance, again based on average population responses, would be overestimated.

II. NOISE ANNOYANCE AND NOISE SENSITIVITY

Noise is an environmental problem that has adverse effects on the daily life of many people. Exposure to noise, in combination with nonacoustical factors, determines the effects of noise on the health and well being of humans. Table I shows the effects of noise, the respective threshold levels and typical situations in which those effects occur. The values in dB(A) represent the levels above which effects occur.

It has been estimated that around 20% of the European Union's population, close to 80 million people, suffer from noise levels that scientists and health experts consider to be unacceptable. At these levels most people become annoyed, sleep is disturbed and adverse health effects are to be feared. An additional 170 million people are living in so-called "gray areas," where the noise levels are high enough to cause serious annoyance during the daytime (European Commission, 1996). Traffic, especially road traffic, is the main cause of noise.

The noise level is but one of the factors influencing people's reactions on noise. It is estimated that about a third of the individual variety of responses to noise can be explained

TABLE I. Health effects and respective threshold levels for exposure, Source: Dutch Health Council, Noise and Health, 1994.

		Noise exposure threshold level		
	Situation	Noise index	Guideline value in dB(A)	Inside/outside
- Hearing impairment	Work	L_{Aeq}, 24 h	70	Inside/outside
- High blood pressure	Work	L_{Aeq}, 8 h	<85	Inside
	Home	L_{Aeq}, 6–22 h	70	Outside
- Ischaemic heart diseases	Home			
- Serious annoyance	Home	L_{dn}	55	Outside
- Awakening	Sleep			Inside
- Sleep disturbance	Sleep	L_{Aeq}, 8 h	30	Inside
- Poor self-reported quality of sleep	Sleep			
- Negative performance at school	School	L_{Aeq}, day	35	Inside

Adjusted according to recommendations of the Dutch Health Council of 1997. This was formerly 60.

by nonacoustical factors (Guski *et al.*, 1978; Job, 1988; Guski, 1999; Höger 1999; Flindell and Stallen, 1999; Stallen, 1999). The nonacoustical factors are often categorized in personal and in situational or contextual factors (Guski 1987, Fields 1993). Situational factors may have no apparent relationship to noise, like, e.g., the visual attractiveness of the neighborhood. Research showed that people's reactions to noise are influenced by aesthetic aspects of the neighborhood (Langdon, 1976; Kastka and Noack, 1987). Other situational factors concern the overall context in which noise is perceived and assessed (Blauert 1990, Lévy-Leboyer and Moser, 1987). The personal factors can be distinguished in demographic (sex, age, household size, education, occupational status, home ownership, dependency of the source) and attitudinal factors (fear, noise sensitivity).

The largest difference in annoyance due to demographic factors is caused by age, equivalent to a difference of noise exposure of up to 5 dB(A), where the middle-aged group (30–50) is most annoyed at the same noise level (Fields 1992, Miedema 1999). The other demographic factors are less relevant and may account for differences equal to maximum 1–2 dB(A).

The main nonacoustical factors influencing the individual responses to noise are the attitudinal ones: fear of the source, sensitivity to noise and the possibility of controlling the noise (Fields, 1992). The effect of noise sensitivity is equivalent to a difference in noise exposure of 11 dB(A) (Miedema and Vos, 1999).

III. METHODS

To answer the question whether self-selection due to noise sensitivity exists, we conducted a case study at Maarssenbroek, a suburb in the western part of the Netherlands built in the 1970s and 80s. We chose that suburb for two reasons. First, the clear gradation in noise levels from road traffic gave people the choice for settling for a quieter or noisier living environment. Second, the dwellings of Maarssenbroek are more or less of the same type (fairly uniform single-family dwellings), which means that choosing a quieter environment does not automatically imply choosing a very different type of dwelling or neighborhood. The confounding influence of differences in socio-economic status was minimized as much as possible by choosing this kind of suburb.

In Maarssenbroek, dwellings are predominantly privately owned and families are typically middle class. Very high and very low incomes are rare. Maarssenbroek has approximately 9000 households and 25,000 inhabitants (CBS, 2003). The average income in Maarssenbroek (11.300 Euro/year) is slightly above Dutch average (11.000 euro/year). Average household size in Maarssenbroek (2.6) is slightly bigger and younger than Dutch average (2.3).

Maarssenbroek is located next to one of the major motorways (around 150,000 cars and lorries pass every day, AVV 2003). Noise screens were constructed simultaneously with the construction of the suburb itself. This excludes the disturbing effect of significant reductions in noise levels after the residential choice of some of the respondents. We chose two sample areas, one close to the highway, one at some distance. Noise loads at the dwellings close to the highway were around 65 dB(A) L_{den}, we will call this the high exposure area. Noise loads in the other area, further away, were 50–55 dB(A) L_{den}. We will call this the low exposure area. The noise levels were ascertained from (calculated) noise maps (Milieudienst Noord-West Nederland, 2000) as well as from our own measurements. A total of 300 households in the low (150) and in the high (150) exposure areas were randomly selected. A questionnaire was sent to the 300 households. The response rate was 67%; the most cited reasons for nonresponse were lack of time or lack of interest in the neighborhood. As compared to Maarssenbroek as a whole, single-person households were slightly underrepresented in our survey, whereas households with children were slightly overrepresented (see Table II).

The survey concentrated on noise sensitivity, noise annoyance, neighborhood (dis)satisfaction and willingness to migrate. Socio-economic and demographic variables were included as well, because they are known to be related to noise sensitivity and annoyance levels (see Sec. II).

Noise sensitivity can be measured by different questionnaires. Most broadly used are the 1-item, the 10-item (Zimmer and Ellermeier, 1998a, 1998b) and the 21-item (Weinstein 1978) questionnaire. The 10- and the 21-item questionnaires have been shown to have satisfactory predictive validity in field research (e.g., Weinstein, 1978; Topf, 1985, Zimmer and Ellermeier 1999). In this research, the 10-item version was used to measure individual noise sensitivity. We used the 1-item test only to see whether people were able to valuate their own noise sensitivity (see Discussion).

No threshold score for noise sensitivity is known from literature. Here we considered people to be sensitive to noise, if they had scored 72 points or more (of maximum 100 points) on the Noise Sensitivity Scale. We chose this value to be in line with the threshold value for noise annoyance (Miedema *et al.*, 2001). We analyzed other threshold values (the 10% and 50% most noise-sensitive ones vs. the 10% and 50% least sensitive ones). It did not really change the results of the next paragraph.

IV. RESULTS

Around 24% of the respondents were highly annoyed by roadway noise. Table II shows that significantly ($P<0.001$) more highly annoyed people live in the high exposure area as compared to the low exposure area. In our research, noise exposure therefore correlates positively with noise annoyance, as is already extensively known from the literature (e.g. Miedema *et al.*, 2001). In both the high and the low exposure areas, around 23% of the population is sensitive to noise.

There was no significant relation between noise exposure and noise sensitivity, and this remained unchanged after adjustment for potential confounders (age, gender, length of residency, size of household, education level and income). In fact, adjustment only contributes to a slight increase in variability (see Table III).

TABLE II. Survey figures compared to those for the population of Maarssenbroek.

		Survey total (N=200)	Survey low exposure (N=93)	Survey high exposure (N=107)	Maarssenbroek (source: CBS 2003)
Highly annoyed		24% (N=48)	3% (N=3)	42% (N=45)	
Noise sensitive		24% (N=47)	24% (N=22)	23% (N=25)	
Composition of household	Single person	10% (N=20)	10% (N=9)	11% (N=11)	23%
	No children	25% (N=49)	17% (N=16)	33% (N=33)	27%
	With children	64% (N=125)	73% (N=67)	57% (N=58)	50%
Age	18–24	1% (N=1)	1% (N=1)	0% (N=0)	12%
	25–44	36% (N=69)	34% (N=31)	38% (N=38)	46%
	45–64	58% (N=110)	59% (N=53)	57% (N=57)	35%
	>64	5% (N=10)_	5% (N=5)	5% (N=5)	7%
Gender	Woman	52% (N=104)	59% (N=55)	46% (N=49)	51%
	Man	48% (N=96)	41% (N=38)	54% (N=58)	49%
Length of residency (years)	0–5	11% (N=20)	14% (N=12)	8% (N=8)	
	6–10	7% (N=13)	7% (N=6)	7% (N=7)	
	>10	82% (N=155)	80% (N=70)	85% (N=85)	

Thirty-five percent of the noise-sensitive people were highly annoyed by roadway noise against only 20% of the noise-insensitive people. Similarly, 42% of the people in the high exposure area and 3% in the low exposure area were annoyed by noise. Table IV shows that relatively more noise-sensitive people are highly annoyed compared to the not noise-sensitive group. The effect on noise annoyance of the combination of the acoustical factor noise exposure and the nonacoustical factor noise sensitivity is extremely small. Whereas noise exposure alone explains 32% of the variety of individual responses, and noise sensitivity alone explains 3%, the combination of these two factors explains 36% of the variety of individual responses.

The survey contained several questions on (dis)satisfaction with the dwelling and the neighborhood and on the desire to move. Analyzing the satisfaction with the dwelling and the neighborhood by noise-sensitive and not noise-sensitive people by means of the Fisher's Exact Test showed significant differences between the two groups: i.e., the noise-sensitive group members were significantly less satisfied with their dwelling (P=0.003) and their living environment (P=0.009) than the noise-insensitive ones, in the high noise area as well as in the low noise area. The survey showed that there was no significant difference in desire to move between people in high noise and in low noise areas (P=0.44). At the same time there was a significant difference in desire to move between sensitive and not sensitive ones (P=0.008). Noise-sensitive people are nearly twice as likely to want to move than those who are not sensitive (40% against 21%). No interaction was found between noise sensitivity, noise exposure and desire to move (P=0.91)

V. CONCLUSIONS AND DISCUSSION

Our main conclusions are first that we found no relationship between noise sensitivity and noise exposure. This re-

TABLE III. Logistic regression model of the relation between noise sensitivity and noise exposure (N=200).

	Odds ratio (95% CI) high exposure, unadjusted	Odds ratio (95% CI) high exposure, adjusted for potential confounders[a]
High level on sensitivity scale	1.01 (0.49–2.08)	1.08 (0.50–2.37)

age, gender, length of residency, children at home, education level and income

TABLE IV. Percentage of people highly annoyed by road traffic noise in high and low exposure areas (Chi-square $p<0.001$).

	High exposure ($N=107$)	Low exposure ($N=93$)
Noise sensitive ($N=47$)	60% ($N=15$)	9% ($N=2$)
Not noise sensitive ($N=153$)	37% ($N=30$)	1% ($N=1$)

mained unchanged after adjustment for potential confounders. Therefore, our research did not show any evidence of a process of self-selection based upon noise sensitivity. However, it did show, secondly, that people who are noise sensitive tend to be less satisfied with their dwelling and their neighborhood than those who are not sensitive to noise. The noise-sensitive people think more often about moving elsewhere.

Our research suggests that noise sensitivity is not a major factor in the process of moving and settling down, at least not where road traffic is the major noise source. These findings are in line with the research of Babisch (presented in Prague, 2004). Other factors related to the dwelling or the neighborhood probably play a more important role, as shown by recent research on factors influencing the process of moving in the Netherlands by Van de Griendt (2004). He found that of all environmental factors, soil pollution is the major concern among potential buyers of dwellings. No doubt, this has to do with the large financial consequences of soil pollution for home owners. Noise only played a minor role in the final decision on which home to buy. These findings are confirmed by the field studies available so far (Schümer-Kohrs and Schümer, 1974; Michelson, 1980; Rohrmann, 1991). These studies indicate that significant weight is put on noise exposure among the principal considerations. Yet noise exposure has only moderate influence on actual moving or residential choice.

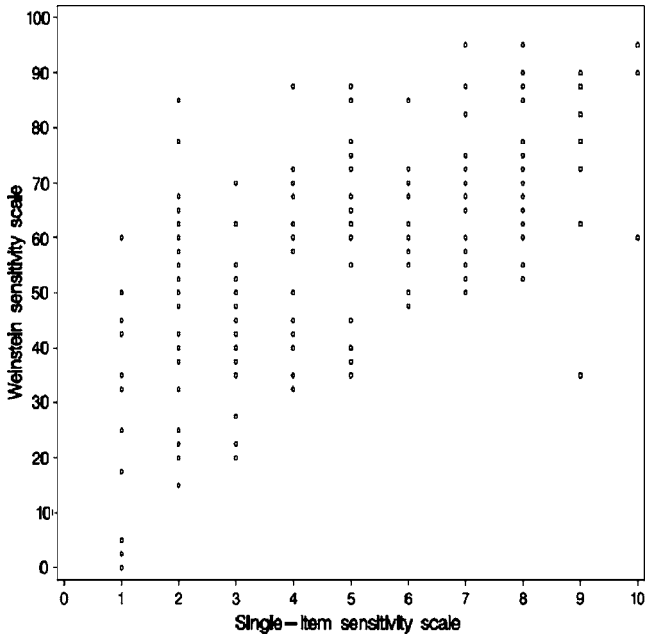

FIG. 2. Individual scores on two tests for noise sensitivity, i.e., the 1-item and 10-item tests.

Due to the cross-sectional character and the limited sample size, we could not distinguish between the role of noise sensitivity in the separate processes of moving out and moving in (see Fig. 1). To do so, either a longitudinal survey and/or a far bigger sample size is required.

In our research, we distinguished areas with high and low noise levels. We did not consider other environmental factors like odor, air pollution or vibrations that are associated with proximity to the highway as well. In future research, it may be worthwhile to pay more attention to these potential confounders.

Noise-sensitive people in our research were less satisfied with their dwelling and their living environment than those who were not noise sensitive. This is in line with research of Miedema and Vos (2003) who found indications for a general negative attitude among noise-sensitive people.

Assuming that people often act more or less rationally, one might ask: why is it (as in our case) that people who are sensitive to noise deliberately move into high exposure areas? Isn't this asking for trouble? One explanation might be that people are simply not aware that they are noise sensitive. This explanation is supported by the fact that the Weinstein 10-item test, generally regarded as a good indicator of noise sensitivity, is only weakly correlated to the 1-item test, in which people directly answer the question whether they regard themselves to be noise sensitive or not. According to the distribution-free Spearman's rank correlation test, both test results show a positive, but rather weak correlation; Spearman rho is 0.629 at 0.01 level; for a strong correlation the outcome would at least have to be above 0.8. See Fig. 2).

A second explanation, as sometimes found in literature (e.g., Zimmer and Ellermeier, 1999), could be that noise sensitivity increases with length of residency. One could hypothesize that the noise-sensitive people in the high exposure area were not noise sensitive at the time of moving in but became so during their residency. Analysis of the data in our research did not show a correlation between noise sensitivity and length of residency though.

Another explanation might lie in the tight market for dwellings, especially in the western part of the Netherlands. Potential home buyers may have a long list of criteria on which to base their decision and the noise level may be just one of those criteria. In practice, given the tight housing market, no dwelling will meet all the criteria and the final decision is usually based on a compromise in which noise levels may be traded off for other qualities of the dwelling or the neighborhood. Research including different periods with a more and a less tight housing market may give insights into the relevance of housing market characteristics at the moment of residential choice.

Yet another explanation might be that the noise-sensitive people who settled in high exposure areas did so because the higher noise levels were compensated for by lower prices for the dwellings. The (negative) correlation between house prices and noise levels is a well-known topic of study (see, for example, Nelson (1982) for one of the key studies in this area, or Navrud (2002) for a literature review). Research of Arsenio *et al.* (2006) in Lisbon yielded a correlation between income level and noise level. Noise sensitivity was not regarded in their research. Those with higher incomes and higher marginal values of noise tended to live in quieter apartments. This correlation was not further elaborated in this study due to a lack of relevant data. This may form a weakness in this research. On the other hand, one might argue that there is no reason at all why noise-sensitive people would be more willing to trade off high exposure for lower housing prices than the noise-insensitive people.

Another explanation could theoretically be that what is now a high exposure area was relatively quiet at the time of settling. However, from historical traffic data (AVV) it becomes clear that traffic intensities on the roadway passing by Maarssenbroek have increased by about 40% over a period of 20 years, the maximum residential period encountered in our research, equivalent to a rise in noise levels of about 1.5 dB. In other words, traffic growth did not account for a large change in noise loads. What is noisy now was noisy 20 years ago as well.

VI. RECOMMENDATIONS

Given the importance of noise sensitivity for the individual reactions on noise, it is recommended to pay more attention to noise sensitivity and other nonacoustical factors in future acoustical research. More questions on nonacoustical factors should be included in the national Dutch annoyance census (Franssen *et al.*, 2004), carried out every five years or so. Inclusion in that census would give insight into the prevalence and spatial distribution of nonacoustical factors.

Noise sensitivity influences residential satisfaction. More information to prospective house owners/renters on the ambient noise levels and on one's noise sensitivity might prevent disappointment and could help to better match demand and supply on the housing market. A system of labeling dwellings according to their noise loads as well as labeling potential buyers according to personal noise sensitivity might be considered.

It is highly recommended to standardize the different noise-sensitivity scales. It would enhance comparability of future research on noise sensitivity.

Finally, because of the small sample size, external validity of this research is limited. Longitudinal surveys, larger samples and surveys in other areas (preferably where housing markets are less tight) are options for future research.

ACKNOWLEDGMENTS

We would like to thank Rebecca Stellato from Utrecht University for her statistical advice. Furthermore, we are grateful for the comments made by two anonymous reviewers which helped to improve the quality of the paper.

Arsenio, E., Bristow, A. L., and Wardman, M. (**2006**). "Stated choice valuations of traffic related noise," Transp. Res., Part D (11) **1**, 15–31.

AVV (**2003**). "Verkeersgegevens, jaarrapport 2002" [Traffic data, annual report 2002], Rotterdam: Adviesdienst Verkeer en Vervoer.

Blauert, J. (**1990**). "Kognitive und ästhetische Aspekte von Lärmproblemen" [cognitive and aesthetic aspects of noise problems], Z. Lärmbekämpfung **38**, 51–54. CBS www.cbs.nl/nl/cijfers/statline.

CBS (**2003**). "Gemeente op maat 2002; Maarssen." [Municipality measured 2002; Maarssen], Voorburg: Centraal Bureau voor de Statistiek.

Clark W. A. V. (**1982**). "Recent research on migration and mobility: A review and interpretation," Prog. Planning **1**, 1–56.

Clark, W. A. V. and Dieleman, F. M. (**1996**). "Households and housing: Choice and outcomes in the housing market," New Brunswick (NJ): Center for Urban Policy Research, Rutgers the State University of New Jersey.

Clark, W. A. V., and Withers, S. (**1999**). "Changing jobs and changing houses: Mobility outcomes of employment transitions," J. Regional Sci. **39**, 653–673.

Dutch Health Council (**1994**). Noise and Health, Report No. 1994/115, Den Haag.

Ellermeier, W., Eigenstetter, M., and Zimmer, K. (**2001**). "Psychoacoustic correlates of individual noise sensitivity," J. Acoust. Soc. Am. **109**, 1464–1473.

European Commission (**1996**). "Green Paper on Future Noise Policy." Brussels: COM 96(540).

Fields, J. M. (**1992**). "Effect of personal and situational variables on noise annoyance: With special reference to implications for en route noise," Atlanta, Georgia Institute of Technology.

Fields, J. M. (**1993**). "Effects of personal and situational variables on noise annoyance in residential areas," J. Acoust. Soc. Am. **93**, 2753–2763.

Flindell, I. H., and Stallen, P. J. M. (**1999**). "Non-acoustical factors in environmental noise," Noise and Health **3**, 11–16.

Franssen, E. A. M., Dongen van, J. E. F., Ruysbroek, J. M. H., Vos, H., and Stellato, R. (**2004**). "Hinder door milieufactoren en de beoordeling van de leefomgeving in Nederland, Inventarisatie verstoringen 2003" [Noise annoyance and perceived environmental quality. Inventory 2003], RIVM-report 815120001, Bilthoven.

Gardner, J., Pierre, G., and Oswald, A. (2001). "Moving for job reasons," Mimeo, Department of Economics, University of Warwick.

Griendt, J. S. van de (**2004**). "Wonen in risicovolle situaties", [Living in risky situations], Haskoning, Utrecht.

Guski, R., Wichmann, U., Rohrmann, B., and Finke, H. (**1978**). "Konstruktion und Anwendung eines Fragebogens zur sozialwissenschaftlichen Untersuchung der Auswirkungen von Umweltlärm" [Construction and application of a questionnaire for social scientific research of the effects of ambient noise] Z. Sozialpsychologie **9**, 50–65.

Guski, R. (**1987**). *Lärm. Wirkungen unerwünschter Geräusche* [Noise. Consequences of unwanted noise]. (Hans Huber, Bern.)

Guski, R. (**1999**). "Personal and social variables as co-determinants of noise annoyance," Environ. Behav. **32**, 270–286.

Höger, R. (**1999**). "Theoretische Ansätze und Ergebnisse der psychologisch orientierten Lärmwirkungsforschung" [Theoretical principles and results of psychologically oriented research on the effects of noise], Umweltpsychologie **1**, 6–20.

Housing Corporation (**2004**). "Who moves and where? A comparison of housing association tenants in London and northern regions," sector study 40.

Job, R. F. S. (**1988**). "Community response to noise: A review of factors influencing the relationship between noise exposure and reaction," J. Acoust. Soc. Am. **83**, 991–1001.

Job, R. F. S. (**1999**). "Noise sensitivity as a factor influencing human reaction to noise," Noise Health **3**, 57–68.

Kastka, J., and Noack, R. (**1987**). "On the interaction of sensory experience, causal attributive cognitions and visual context parameters in noise annoyance," in H. S. Koelega, *Environmental Annoyance* (Elsevier, Amsterdam), pp. 245–262.

Lako, J. V. (**1987**). "Geluidbelasting en migratie: Selectie-effecten bij onderzoek naar geluidbelasting en gezondheid, "[Noise load and migration: Selection-effects in a research of noise loads and health], Interfacultaire Vakgroep Energie en Milieukunde (IVEM-rapport No. 25).

Langdon, F. J. (**1976**). "Noise nuisance caused by road traffic in residential areas," J. Sound Vib. **47**, 243–263.

Leidelmeijer, K., and Marsman, G. (**2001**). "Beleving van de leefkwaliteit: Nadere analyses nulmeting Stad en Milieu" [Perception of quality of life: Further analyses starting point city and environment], Den Haag, Ministerie van VROM.

Lévy-Leboyer, C., and Moser, G. (**1987**). "Individual differences in noise annoyance: Four explanations," in H. S. Koelega, *Environmental Annoyance* (Elsevier), Amsterdam, pp. 293–297.

Michelson, W. (**1980**). "Long and short range criteria for housing choice and environmental behavior," J. Soc. Issues1052-0643 **36**, 135–149.

Miedema, H. M. E., and Vos, H. (**1999**). "Demographic and attitudinal factors that modify annoyance from transportation noise," J. Acoust. Soc. Am. **105**, 3336–3344.

Miedema, H. M. E., and Oudshoorn, C. G. M. (**2001**). "Annoyance from transportation noise: Relationships with exposure metrics DNL and DENL and their concidence intervals and annoyance," Environ. Health Perspect. **109**, 409–416.

Miedema, H. M. E., and Vos, H. (**2003**). "Noise sensitivity and reactions to noise and other environmental conditions," J. Acoust. Soc. Am. **113**, 1492–1504.

Milieudienst Noord-West Nederland (**2000**). "Integraal geluidonderzoek Maarssenbroek" [Integral noise survey Maarssenbroek], Milieudienst Noord-West Nederland, Breukelen.

Mulder, C. H., and Hooimeijer, P. (**1999**). "Residential relocations in the life course," in *Population Issues, An interdisciplinary Focus* (Plenum, New York).

Navrud, S. (**2002**). "The state-of-the-art on economic valuation of noise," final report to European Commission DG Environment.

Nelson, J. P. (**1982**). "Highway noise and property values: A survey of recent evidence," J. Transp. Econ. Policy **16**, 117–138.

Ohrstrom, E. (**1995**). "Effects of low levels of road traffic noise during the night: A laboratory study on number of events, maximum noise levels and noise sensitivity," J. Sound Vib. **179**, 603–615.

Owen, D. (**1992**). "Migration and employment," in *Migration Processes and Patterns* (Belhaven Press, **205–224**), Vol. **2**.

Rohrmann, B. (**1986**). "Environmental stressors and housing decisions review," Darmstadt: Bericht Nr. 86-2, Institut für Psychologie der THD.

Rohrmann, B. (**1991**). "The influence of noise on housing decisions," in *Contributions to Psychological Acoustics (V)*, Oldenburg, Germany: Bibliotheks- und Informationssystem der Universität Oldenburg (BIS) pp. 75–86.

Rossi, P. H. (**1955**). *Why families move: A study in the social psychology of urban residential mobility* (Free Press, New York).

Schümer-Kohrs, A., and Schümer, R. (**1974**). "Der sozialwissenschaftliche Untersuchungsteil" [The social scientific research part] in *DFG-Forschungsbericht Fluglärmwirkungen* (Boleat, Boppart, Germany).

Stallen, P. J. M. (**1999**). "A theoretical framework for environmental noise annoyance," Noise Health **3**, 69–79.

Stansfeld, S. (**1992**). "Noise, noise sensitivity and psychiatric disorder: Epidemiological and psychophysiological studies," Psychol. Med. **15**, 243–260.

Stansfeld, S. A., Clark, C. R., Jenkins, L. M., and Tarnopolsky, A. (**1985**). "Sensitivity to noise in a community sample. I. The measurement of psychiatric disorder and personality," Psychol. Med. **15**, 243–254.

Stansfeld, S. A., Sharp, D., Gallacher, J., and Babisch, W. (**1993**). "Road traffic noise, noise sensitivity and psychological disorder," Psychol. Med. **23**, 977–985.

Stansfeld, S. A., Gallacher, J., Babisch, W., and Shipley, M. (**1996**). "Road traffic noise and psychiatric disorder: Prospective findings from the Caerphilly study," Br. Med. J. **313**, 266–267.

Staples, S. L. (**1996**). "Human response to environmental noise: Psychological research and public policy," Am. Psychol. **51**, 143–150.

Taylor, S. M. (**1984**). "A model of aircraft noise annoyance," J. Sound Vib. **96**, 243–260.

Topf, M. (**1985**). "Noise-induced stress in hospital patients: Coping and nonauditory health outcomes," J. Human Stress **11**, 125–134.

van Kamp, I., Job, R. F. Soames, Hatfield, J., Haines, M., Stellato, R. K., and Stansfeld, S. A. (**2004**). "The role of noise sensitivity in the noise-response relation: A comparison of three international airport studies," J. Acoust. Soc. Am. **116**(6), 3471–3479.

Weinstein, D. (**1978**). "Individual differences in reactions to noise: A longitudinal study in a college dormitory," J. Appl. Psychol. **63**, 458–466.

Zimmer, K., and Ellermeier, W. (**1998a**). "Konstruktion und Evaluation eines Fragebogens zur Erfassung der individuellen Lärmempfindlichkeit" [construction and evaluation of a questionnaire for the assessment of individual noise sensitivity], Diagnostica **44**, 11–20.

Zimmer, K., and Ellermeier, W. (**1998b**). "Ein Kurzfragebogen zur Erfassung der individuellen Lärmempfindlichkeit" [a short list to register one's individual noise sensitivity], Umweltpsychologie **2**, 54–63.

Zimmer, K., and Ellermeier, W. (**1999**). "Psychometric properties of four measures of noise sensitivity: A comparison," Environ. Psychol. **19**, 295–302.

Performance of artificial neural network-based classifiers to identify military impulse noise

Brian A. Bucci and Jeffrey S. Vipperman[a)]
University of Pittsburgh, Department of Mechanical Engineering, 648 Benedum Hall, Pittsburgh, Pennsylvania 15261

(Received 3 April 2007; revised 18 June 2007; accepted 20 June 2007)

Noise monitoring stations are in place around some military installations to provide records that assist in processing noise complaints and damage claims. However, they are known to produce false positives (by incorrectly attributing naturally occurring noise to military operations) and also fail to detect many impulse events. In this project, classifiers based on artificial neural networks were developed to improve the accuracy of military impulse noise identification. Two time-domain metrics—kurtosis and crest factor—and two custom frequency-domain metrics—spectral slope and weighted square error—were inputs to the artificial neural networks. The classification algorithm was able to achieve up to 100% accuracy on the training data and the validation data, while improving detection threshold by at least 40 dB. © *2007 Acoustical Society of America.*
[DOI: 10.1121/1.2756969]

PACS number(s): 43.50.Rq, 43.50.Pn, 43.50.Nm [KA] Pages: 1602–1610

I. INTRODUCTION

There is a need for an accurate method of recording impulse noise around military installations in order to monitor the impact on the surrounding communities and to corroborate noise complaints and damage claims.[1–3] As urban environments develop around military installations, these concerns have hindered military exercises that produce high levels of impulse noise. By definition, military impulse noise consists of weapons firing projectiles larger than 20 mm and all types of high explosive charges (e.g., demolitions, hand grenades, etc.). To maintain a good relationship with the surrounding community, steps have been taken to control the production of military impulse noise through computer modeling of sound propagation on ranges and changes in training procedures.[4,5]. However, sound propagation models are not perfect, and variations in terrain can further complicate sound level estimations.[6,7] It is also well known that atmospheric conditions influence the propagation of sound,[8] so exercises are scheduled to minimize the disturbance to the surrounding community.[9]

In response to the need to produce a record of noise events, monitoring stations have been installed around many installations to log events that exceed a specified threshold. These systems evolved into an online monitoring system that continuously monitored C-weighted noise levels. When levels exceeded 115 dBC, an integration unit switched on to measure sound exposure level (SEL), while the system recorded the time, duration, and peak level. Since wind noise and blast noise have predominately low-frequency content ($<$100 Hz), an unusually high amount (90%) of false-positive events were recorded, owing largely to the poor performance of windscreens at low frequency.[10,11]. An improved, second-generation of monitoring stations operate on an algorithm that expects an impulse event to have a wave form much like that of a classic Friedlander wave[12] and to comply with a set of temporal conditions. When impulse events have very high amplitude ($>$119 dBC)[13] and conditions are ideal (such as location of event and sensor[14], weather patterns, absence of multi-path propagation effects,[15] and timing of impulse events) this approach can work quite well. Unfortunately, these stations function reliably only with peak levels above 119 dBC, thus they marginally detect lower-amplitude impulse events and still suffer from occasional false positive detection of impulse noise (as high as 10%). Most false positive detections are purportedly caused by wind noise, which can pose a problem in all outdoor noise monitoring situations.

The aim of this effort is to develop a more accurate noise classifier that is able to also detect events with much lower peak levels (down to 100 dBC). Earlier efforts have proven effective in detection of snipers and other small arms fire.[16–21] These projects are different from large ordinance monitors because the spectral content and propagation characteristics of small arms are not the same as those of large ordinance. Efforts have also been made in classification for urban battlefield-type settings.[22] These cases differ from the civilian environment detection of military impulse noise in that the latter often use more complex systems, having an array of microphones, in order to precisely triangulate the location of the event while in motion. In Schomer's paper, it was shown that using windscreens and computing a correlation between two microphones could help mitigate false positives in the detection of military impulse noise.[23] Benson also suggests the use of a correlation computed between two microphones and also analyzing particular areas of the computed spectra of a wave form to identify blast noise.[24] Both of these efforts advocate the use of two microphones. In more recent work by Schomer,[25] a fuzzy logic method of evaluating blast noise is presented. The system Expert can operate off of one measurement location or multiple loca-

[a)]Author to whom correspondence should be addressed. Electronic mail: jsv@pitt.edu

tions. This system is very comprehensive but needs a large amount of input parameters. In the particular case presented in this paper, it is desirable to identify military impulse noise from measurements conducted at a single stationary location with a single microphone. The classification scheme should also be as simple as possible, with minimal hardware requirements. Ideally this algorithm could be implemented on existing monitoring stations thus eliminating the need for full hardware upgrades.

A signal classifier is a systematic approach of applying rules to a data set to identify classes of data.[26,27] Classification rules are developed either by expert analysis and intuition or by intelligent algorithms.[26,27] In its most rudimentary form, a classifier consists of raw input data, some form of data preprocessing or feature extraction, and the actual classification algorithm.[27,28] Although there are many different types of classifiers that are useful in different applications, the artificial neural network classifier[29] is the focus of this study. Given their abilities in making generalizations, strength in pattern classification, wealth of easily obtainable data, in the case of this problem, and limited requirements for prior knowledge of the problem, the artificial neural network (ANN) structure was considered the ideal method for creating noise classifiers.[26,30–33] In this classification problem, although the features are being extracted from a wave form that occurs in time, the features are not time dependent in the global sense. Classification also does not depend on the order or timing of any previous events. This classifier is merely producing decisions based on scalar metrics extracted from a specific section of a wave form where the sound pressure level exceeds a given value. Thus, this problem is most likened to a time-invariant pattern classification problem rather than problems dealing with time series classification or prediction. Accordingly, the ANN structures to be evaluated are selected from structures that have proven useful in such situations. Since this problem is truly independent of time, ANN structures containing time delay feedback or other time dependent features[34] are not applicable to this problem. Rather, the tested structures are common in the engineering field and have worked well in similar static pattern classification applications.

Three ANN structures with the desired characteristics were selected for evaluation: Radial basis function (RBF) network,[35–37] a self-organizing map[36,38–41] (SOM), and a feed-forward multilayer perceptron[35–37,42] (MLP) trained with back propagation. The performance of these three classifiers subsequently compared to that of a least squares classifier to illustrate that the nonlinear modeling capabilities of the ANN structures do indeed offer advantages over a linear classifier.

The noise classifiers consist of various artificial neural network (ANN) structures that have demonstrated good performance in similar classification problems.[30–32,43] The primary interest is in discerning impulse noise from other types of noise; however, the system can be easily extended to have more classes (e.g., impulse, wind, aircraft, and operational noise).[33] Overall accuracy is enhanced by taking into account all observed classes of noise. The major classes of noise (with L_{pk} values exceeding 80 dB) are military impulse noise, wind noise and aircraft noise (the latter two of which are nonimpulsive).[33] The inputs to the ANN structures consist of traditional acoustic metrics and new metrics tailored to the particular problem.

II. DATA COLLECTION

To develop this noise classifier, it was first necessary to collect a library of measurements containing military impulse noise and potential false positive noise sources for the classifier, as no such previous library was available. No commercially available data collection system could completely provide the functions desired to perform the data collection, so a composite system was assembled from several different components. Since the bulk of the energy for most of the measured noise sources is within the 0–100 Hz bandwidth, a B&K 4193 infrasonic microphone with bandwidth of 70 mHz–20 kHz was used. The microphone was connected to a Larson Davis 824 sound level meter (SLM). The ac output of the LD 824 SLM was in turn connected to a National Instruments (NI) DAQCard-6036E data acquisition card through a NI BNC-2110 input/output board. The DAQCard was installed into a Dell Latitude laptop with a Pentium IV processor. A virtual instrument (VI) was created to capture wave form data. The VI enables an "automatic triggering/pre-triggering mode," where data are recorded when the signal exceeds a specified threshold, in this case corresponding to a certain L_{pk} value. This feature allows impulse events to be recorded automatically. Although the threshold can be set to record at or above any desired L_{pk} level, it was typically adjusted to just above ambient noise levels in order to record as much useful data as possible. In our data collection, a 0.1–0.25 s pre-trigger was coupled with an additional 2 s of recorded data for each record. By pre-triggering, the entire event was able to be recorded. A manual (continuous) triggering mode was also possible, which was used to record longer or continuous events such as wind and aircraft noise. During multiple successive trigger events, the "automatic mode" also triggered nearly continuously. Although most of the military impulse noise energy is in the very low-frequency range (0–100 Hz), some noise sources (aircraft) have significant energy up to 2–3 kHz. Consequently, data were sampled at 10 kHz.

Approximately 1000 usable wave forms were collected (330 military impulse and 670 nonimpulse noise). The military impulse noise recordings consisted of 155 mm howitzers, 81 mm mortars, 60 mm mortars, 60 mm rockets, M67 hand grenades, and Bangalore Torpedoes (strings of 3, (27 lbs HE)). Table I shows a detailed summary of the ordinance that was recorded along with number of impulse events that occurred within the time of the recording (2.1–2.25 s). The military impulse noise records had L_{pk} values ranging from 80 to 138 dB. The nonimpulse noise records were wind noise and aircraft noise (F-16, A-10, C-130). The military impulse noise recordings were made at ranges between 1.5 and 6 km from the noise sources. Prior to entering the field measurement locations, the firing schedules for the ordinance to be recorded and geographical maps detailing the firing positions and impact areas were provided to the research team by the range control officers. This enabled

TABLE I. Summary of the recorded ordinance and number of events occurring in each recording.

Types of noise sources	Number of events during recording			
	1	**2**	**3**	**4**
155 mm howitzer firing	116	20	5	1
155 mm howitzer firing and high explosive event from 155 mm different Projectile	0	21	0	0
155 mm high explosive projectile	36	0	0	0
60 mm rockets	0	0	1	1
81 mm mortar impact	95	14	3	0
M 67 hand grenade	5	0	0	0
Bangalore Torpeo	4	0	0	0
155 mm howitzer firing with F-16 flyover	5	0	0	0
81 mm mortar impact with F-16 flyover	3	0	0	0

the research team to identify the sources of the military impulse events at all locations. Locations for the recording sessions were selected to provide the widest spectrum of different terrain types. Sessions were conducted in flat open fields, mountainous dense forest, over soft sandy soil, on top of rocky terrain, tops of ridge lines, valley bottoms, and beside large bodies of water. During the recording sessions the temperature ranged from 75 to 100 F due to the summer season in which the measurements were made. The relative humidity also varied from 44% to 100% (and raining). Because acoustic measurements can be greatly effected by terrain and weather, data collection done under these various environmental conditions is necessary to develop a robust noise classifier.

III. CLASSIFERS

In this paper, only the parameters and performance of the various classifiers' structures are presented. For a more in depth description of the operation of these classifiers, the authors suggest Haykin's text.[36] To train and validate the classifiers, 1000 sets of metrics were computed from processing each of the 1000 wave forms. Two-thirds of the data were selected in a stratified-random sample to serve as the training data, and the remaining one-third were used for evaluation. The one-third of the data used for evaluation were divided into two equal parts, half to be used for training validation and half for test data.

Five different sets of input metrics were evaluated for each classifier algorithm. The first two were initially tested with a single input of either kurtosis or crest factor to test the hypothesis of these metrics being good indicators of the presence of military impulse noise within a wave form. Next, both metrics were combined and the noise classifier performance was tested again. The complementary metrics, *WSE* and *m*, were also tested as a pair, since they were designed to work together. Finally, classifiers based on all four metrics were evaluated to investigate whether or not the combination of these metrics would produce a classifier with further improved accuracy.

A. Radial basis function network

The RBF Networks began with 1, 2, or 4 input neurons, in accordance with the above descriptions. There were 667 neurons in the hidden layer, and 2 output neurons, as the network was created as an exact fit to the training data. The network was then pruned to 28 hidden neurons. Through a heuristic optimization over a wide range of values, a Gaussian RBF spread factor of 10 was found to produce the best results. The spread factor determines the width of the Gaussian centered at each particular point of training data. A spread factor of 10 would indicate that any data point within a distance of 10 or less from a given neuron would cause the neuron to produce an activation of at least 0.5.

B. Self-organizing map

The SOM consisted of 16 neurons arranged in a 4-by-4 square lattice. The network learning parameters were set as per recommended procedures of training SOMs.[41] During the ordering phase, the initial learning rate parameter was set to 0.1 with a time constant of 1000 and the initial size of the neighborhood function was set to 2 (the approximate radius of the lattice) with a time constant of 1000/log(2). The ordering phase was conducted for 1000 iterations. During the lattice convergence phase, the learning rate parameter is held at its value at the end of the ordering phase and the neighborhood function continued to decrease. The lattice convergence phase was conducted for 20,000 iterations.

C. Multilayer perceptron

The structure of the MLP was heuristically optimized, as is the common practice when using the MLP. The networks began with 1, 2, or 4 input neurons and 2 output neurons. Additional nodes and layers were added to the network until no further performance gains could be achieved.[30] The final MLP architectures consists of 1, 2, and 4 input neurons, three hidden layers of 4 neuron with tan-sig activation functions, and 2 output neurons with log-sig activation functions. The network was trained using the reduced memory Levenberg-Marquardt algorithm with a learning rate of 0.001.[44] Training was conducted for 1000 epochs.

D. Least squares classifier

For comparison purposes, linear least squares classifiers using between 1 and 20 terms, derived from first order combination of the metrics, were tested on the data set. It was found that the classifiers performed almost identically regardless of the number of terms used. Since the hypothesis to be tested was: whether or not a neural network classifier is

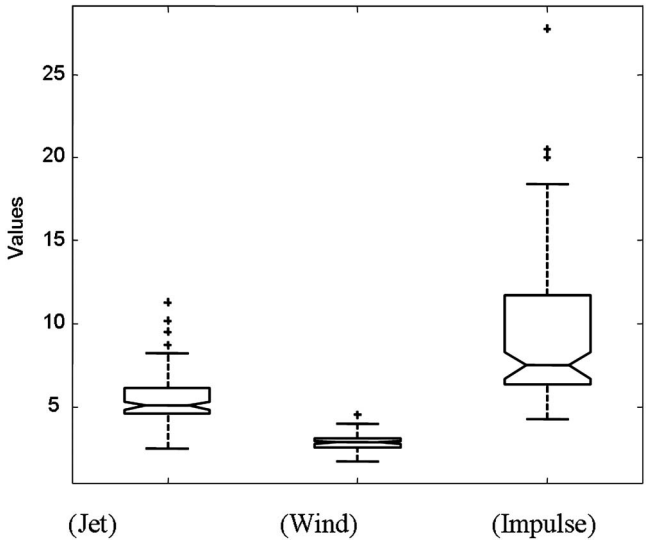

FIG. 1. Box Plot of crest factor data for all three noise classes.

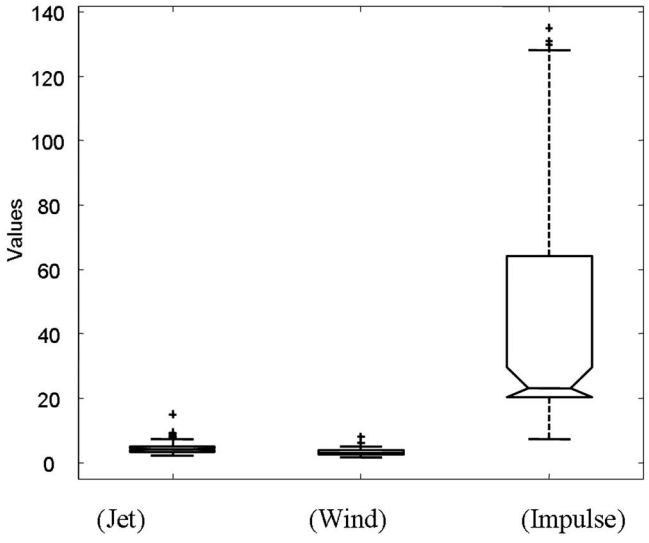

FIG. 2. Box Plot of kurtosis data for all three noise classes.

superior to a linear least squares classifier, in the case of this problem, the accuracy of the least squares classifier was taken to be the linear least squares classifier that produced the maximum accuracy, a marginal improvement over the mean accuracy evaluated over all term configurations of the linear least squares classifiers.

IV. DATA PROCESSING

Preliminary processing of the collected wave forms was done at the University of Pittsburgh using the enhanced sound level meter (ESLM) MATLAB code. The ESLM code computed the scalar metrics equivalent sound level (L_{eq}),[13] peak sound level (L_{pk}), sound exposure level (SEL),[13] crest factor, 8 h equivalent sound level (L_{8eq}),[13] kurtosis, duration (Dur), number of positive samples (Pos) and number of negative samples (Neg) and also the power spectral density (PSD).[45]

A. Time-domain metrics

Based on a preliminary examination of the collected data, kurtosis and crest factor were found to be useful for determining whether a wave form contained military impulse noise. Figures 1 and 2 show statistical box plots for crest factor and kurtosis, respectively, for the three classes of noise. The upper and lower edges of the box show the 25th and 75th percentile of the data, respectively. This is known as the interquartile range (IQR). The line in the center of the box shows the median of the data. The "whiskers" that extend from the top and bottom of the boxes show the range of the distribution of data. They are drawn to either the minimum or maximum value of the data or to a distance of 1.5 times the IQR. Data farther than 1.5 times the IQR from the box are regarded as outliers. For both metrics, the IQR for impulse noise (third column) has no overlap with that for Jet and Wind noise (columns 1 and 2, respectively). Although kurtosis (Fig. 2) has some overlap between the IQR of aircraft and wind noise, crest factor (Fig. 1) has no overlap of the IQR for all three classes, making it particularly appealing as a classification metric. For all box plots, a few mild outliers are indicated with "+" symbols. The apparent discrimination capability of impulse noise by kurtosis and crest factor is not surprising, given that they are often good indicators of impulsiveness within a signal.[45–47] These metrics have been successfully used in the past for bearing fault analysis,[45–47] which bears some similarity to military impulse noise identification. In both cases it is necessary to detect an impulse that occurs within a measured wave form. Although these metrics show great promise, it will be shown that they alone do not provide sufficient classification accuracy.

B. Frequency-domain metrics

Additional scalar metrics were also developed to improve the accuracy of the noise classifier. These metrics are based on commonalities observed in the PSD of the wave forms of similar noise sources. Spectrally based metrics offer the advantage of being less affected by multiple events that occur in a very short period of time and being less susceptible to propagation effects that can strongly influence temporal characteristics of a wave form. The PSDs were computed using a 4096 point fast Fourier transform (FFT), yielding a frequency bin width of 2.44 Hz. Figure 3 shows the PSD of a typical sample of wind noise. It is important to note the typical linear shape and negative slope of the PSD curve as plotted on a log-log scale.[10] Figure 4 shows the PSD plots for some typical military impulse noise sources (81 mm mortar (top), Bangalore torpedo (middle), and 155 m howitzer (bottom)). Although these three PSD plots may appear somewhat different, they are similar in that all three PSD functions begin with an increasing slope, peak with the greatest energy between 10 and 30 Hz, and roll off at higher frequencies.[24] These trends are denoted by the tangent lines added to Fig. 4 These three regions of the PSD are in contrast to the linear trend noted for wind noise. As previously stated, most of the signal energy of the wind noise and military impulse noise wave forms is within the 0–100 Hz bandwidth. Henceforth, the 0–100 Hz bandwidth will be referred to as the "bandwidth of interest (BWI)." Figure 5 illustrates

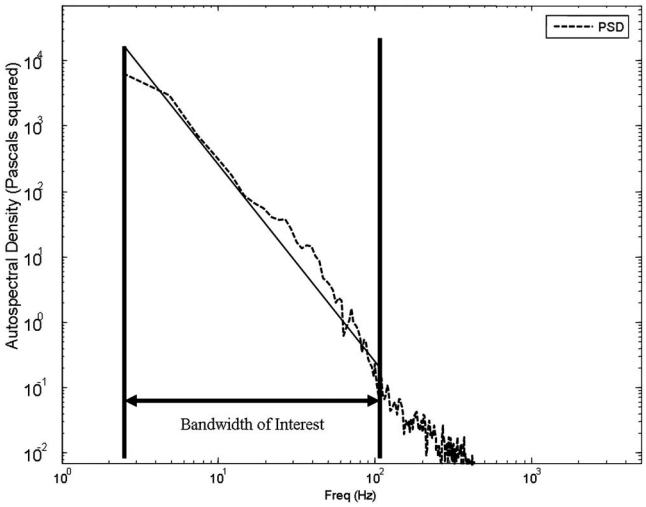

FIG. 3. PSD of wind noise.

an example of typical aircraft noise. Note that aircraft noise seems to have a relatively flat PSD within the BWI and the maximum signal energy occurs outside the BWI.

It is desirable to capture the above generalizations about the PSD for various noise sources in an efficient manner. Using all frequency bins within the BWI would add considerable complexity to the classifier. Thus, a pair of scalar metrics was designed to work in tandem. These metrics are referred to as spectral slope (m) and weighted square error (WSE).

Spectral slope (m) is computed by creating a least squares line fit,

$$\hat{y} = mx + b, \tag{1}$$

where $y=\log_{10}(\text{PSD})$ is the base-10 logarithm of the power spectral density and $x=\log_{10}(f)$ is the base-10 logarithm of frequency. The fit is conducted over the frequencies between 2.5 and 100 Hz. Although the impulse and aircraft noise sources are poorly characterized by a linear trend, the slope is still useful for differentiating from other types of noise, as will be illustrated later.

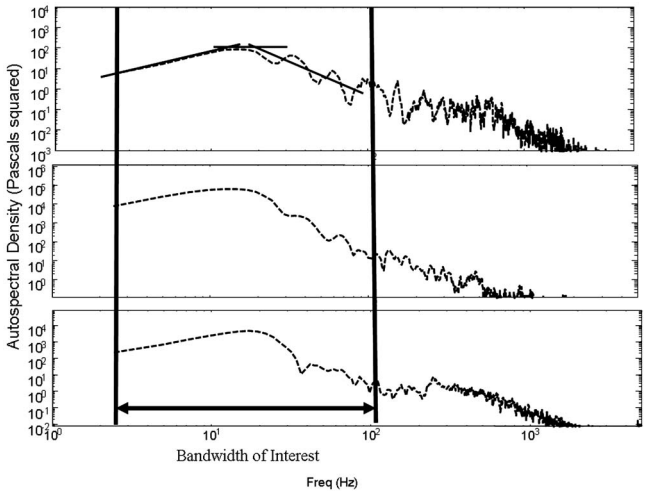

FIG. 4. (a. top) PSD for 81 mm mortar, (b. middle) PSD for bangalore torpedo, (c. bottom) PSD for 155 mm howitzer.

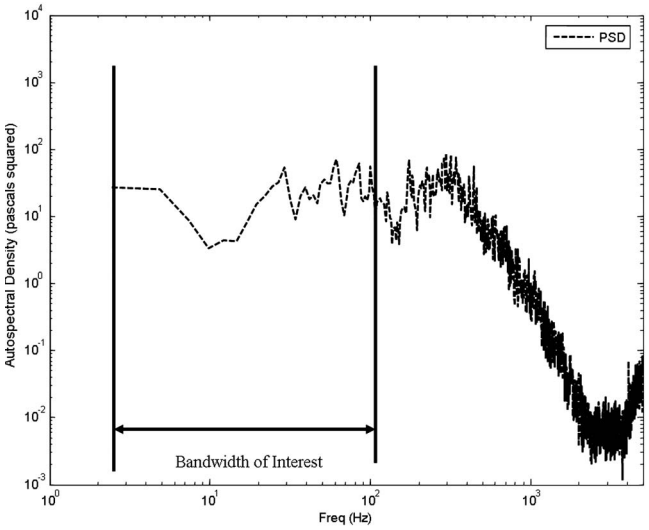

FIG. 5. PSD for typical aircraft noise (F-16 flyover).

To complement metric m, the "goodness" of the linear fit is assessed with the weighted square error (WSE), which is computed as

$$WSE = \sum_{i=1}^{41} [y_i - \hat{y}_i]^2 [\log(f_{i+1}) - \log(f_i)], \tag{2}$$

where y_i is based upon the $\log_{10}(\text{PSD}_i)$ of the ith frequency bin, $\hat{y}_i$ is the estimate of y_i from the linear curve fit, and f_i is the ith frequency. Squaring the quantity $[y_i-\hat{y}_i]$ allows WSE to remain positive and also reflects the total magnitude of the error. The term $[\log(f_{i+1})-\log(f)_i]$ serves to add greater weight to the error at the lower frequency bins. Adding greater weight to the lower frequency bins is done because the best features for identifying military impulse noise from nonimpulse noise occur at the lower reaches of the bandwidth of interest. Also, higher frequency bins within the BWI are more susceptible to contamination from other sources of environmental noise. There are 42 frequency bins from 2.5 to 100 Hz for the given spectral resolution (4096 point

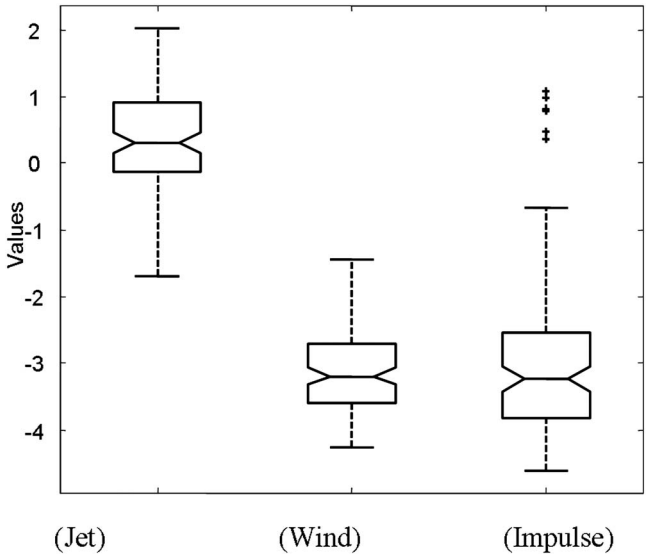

FIG. 6. Box Plot of spectral slope data, m, for all three noise classes.

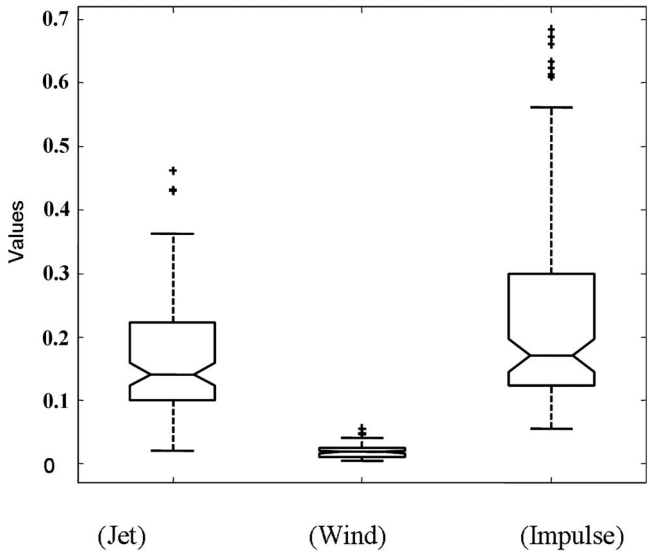

FIG. 7. Box Plot of WSE data for all three noise classes.

FFT), and the *WSE* is computed from the first 41 of these bins. In order to scale the metrics with respect to signal energy, the logarithmic PSD terms, y_i, are normalized, between [0,1], which correspond to the minimum and maximum values of $\log_{10}(\mathrm{PSD})$, respectively. Thus, y_i is computed as

$$y_i = \frac{\log_{10}(PSD_i) - \min[\log_{10}(PSD)]}{\max[\log_{10}(PSD)] - \min[\log_{10}(PSD)]}. \quad (3)$$

It is important to note to the values of $\hat{y}_i$ are not normalized. They are simply the curve fit of y_i. In summary, PSD functions that do not follow a linear trend within the bandwidth of interest will produce much larger values of *WSE* than PSD functions that exhibit a linear trend within the bandwidth of interest, namely wind.

Figures 6 and 7 show the statistical summaries for *WSE* and *m*, respectively, in the form of box plots. The relative differences provide additional means for classifying signals. In particular, while *m* (Fig. 6) differentiates aircraft noise from impulse and wind noise, *WSE* (Fig. 7) has some ability to distinguish wind noise from impulse and aircraft noise.

C. Signal metrics discussion

Although the feature space is four-dimensional, some insight can be gained by examining the relationship between pairs of metrics. Figure 8 shows the values of *m* and *WSE* plotted against each other for the entire set of collected wave forms. The military impulse and nonimpulse noise classes are observed in Fig. 8. However, there are outliers within the data set. These can occur, for example, with military impulse noise when the event is particularly short and quick to peak. These very short events, such as 60 mm rockets breaking the sound barrier, can have a PSD that is much closer to flat within the bandwidth of interest, much like what would be expected of an ideal impulse (equal energy at all frequencies). They do not share as many similarities of their PSDs with large ordinance, such as 155 mm howitzers. However, these events have a very large value for kurtosis and crest factor, making them complementary to the frequency-domain metrics. Classification algorithms, such as the ANN structures, will work well to take into account cases where some of the metrics strongly indicate the presence or absence of impulse noise while the other metrics may produce inconclusive results. A similar case can occur with the outliers in the nonimpulse noise section of the data. These events often had comparatively low L_{pk} values and less than ideal shapes for their PSDs.

The frequency-domain metrics become particularly useful in the case of multiple events occurring in a very short

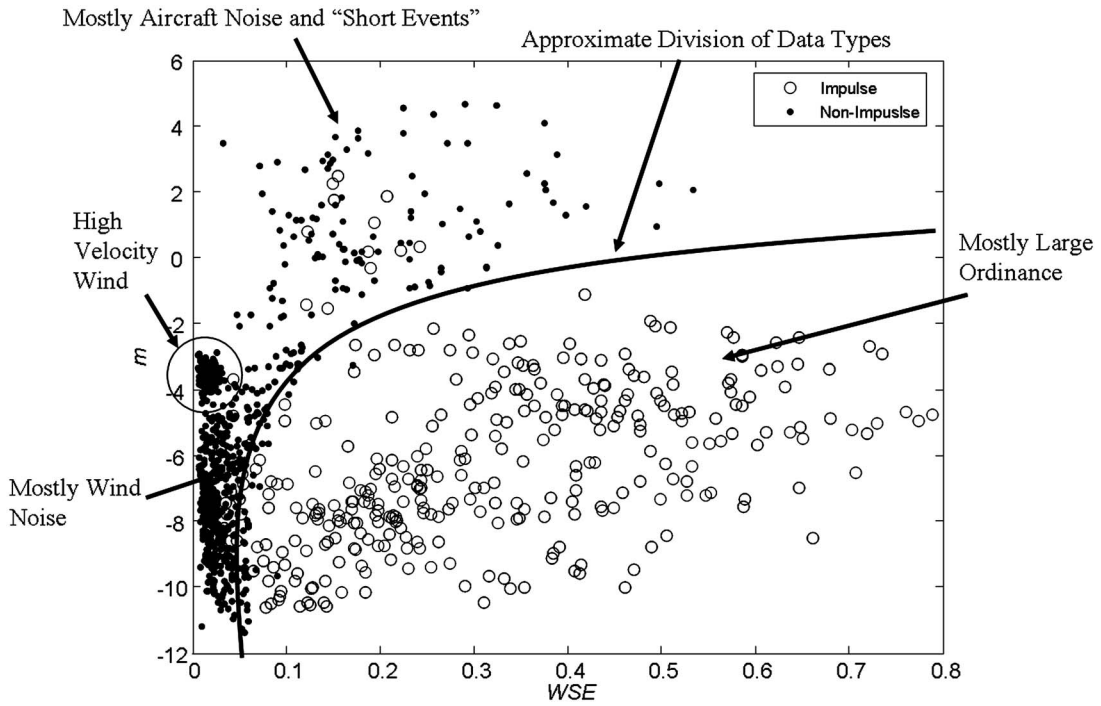

FIG. 8. *WSE* vs. *m* for impulse and nonimpulse sources.

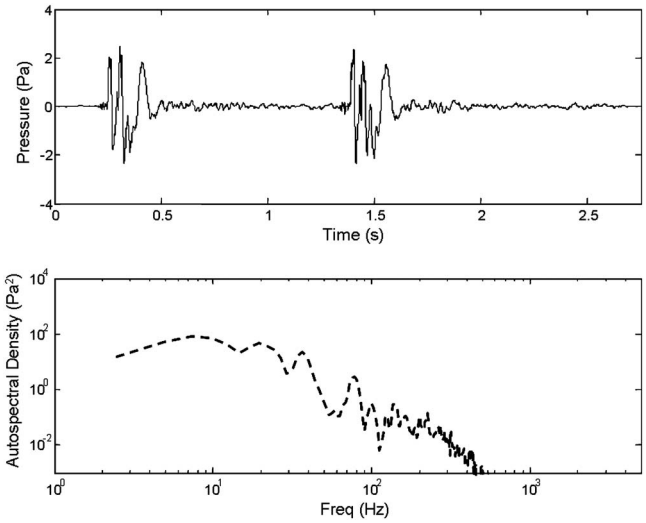

FIG. 9. Sound pressure level and PSD for multiple impulse event (two 155 mm howitzers).

period of time. Since the temporal and statistical characteristic of a wave form can change significantly for these cases, comparatively lower values for kurtosis and crest factor could be calculated for a wave form of given length. In comparison, as shown in Fig. 9, the PSD calculated over a recording containing multiple events will retain a similar shape to the PSD calculated for a single impulse event (Figure 4). Thus, by combining frequency-domain and time-domain metrics, the detection of impulse noise is improved.

V. RESULTS AND DISCUSSION

The results for the classifiers' respective accuracies are presented in Table II. The different classifying algorithms are presented in rows, while the columns represent the choice of metrics. The ANN structures (rows 3–5) performed comparably to the linear least squares classifier (row 6) for the two cases where single metrics, kurtosis or crest factor (columns 2 and 3), are used as inputs. This is expected since all of the classifiers are simply computing a threshold value for this configuration. For the three other cases consisting of pairs of metrics (kurtosis and crest factor (column 4) or *m* and *WSE* (column 5)), or all four metrics (column 6), the ANN structures outperformed the classification accuracy of the linear least squares classifier by 0.4–10.2%. It is also noticeable that all of the classifiers performed better, with respect to themselves, with the four-metric data set (column 6), as compared to the data sets with fewer metrics (columns 2–5). In fact, the SOM and MLP both achieved 100% classification accuracy on the validation and test data while the RBF network achieved very similar performance with an accuracy of 99.1% on the test data and 98.2% on the validation data. The false positive detection rate data are presented in Table III. In the case of the MLP, RBF network, and least squares classifier a threshold value of 0.5 was used to decide between the classes. When the threshold value is set at 0.5 the classifiers produce about as many false positives as they do false negatives. In an actual implementation of this system this value could be adjusted to make the detection of military impulse noise more or less sensitive, with the accompanying costs of greater chance of false positive detections and greater chance of missing events, respectively. A visual representation of the classifier outputs, using the four-metric data set, is presented in Figs. 10–12. In the figures, military impulse noise events are represented by circles and nonimpulse events (wind and aircraft) by squares. When comparing the performance of the RBF network and the MLP (Figs. 10 and 11, respectively), it is noticeable that the MLP produces a much clearer decision boundary than does the RBF network, which is consistent with the higher accuracy of the MLP. Figure 12 shows the output of the SOM. As previously stated, the SOM consisted of a 4 by 4 lattice of neurons. The junctions of the grid represent each of the neurons. The symbols placed on the junctions represent the type of noise sources that have mapped to that particular neuron. In Fig. 12, it is also noticeable how neatly the classes of data have been grouped within the SOM and to which there are no neurons that multiple classes have mapped. Thus, good performance of this classifier is also expected. Any additional classes of data could be created by increasing the number of outputs in the RBF and MLP [33] and increasing the size of the SOM.

VI. CONCLUSIONS

This paper summarizes an effort to develop a more accurate and robust method of distinguishing high-amplitude

TABLE II. Summary of the detection accuracy of the classifiers (V=validation data, T=test data).

Type of artificial neural network	Kurtosis		Crest factor		*WSE*, and *m*		Kurtosis and crest factor		Kurtosis, crest factor, *WSE*, and *m*	
	V	T	V	T	V	T	V	T	V	T
Radial basis function network	89.1%	88.9%	71.4%	70.3%	85.6%	85.3%	92.3%	93.2%	99.1%	98.2%
Multilayer perceptron	89.9%	89.9%	73.4%	72.8%	87.1%	86.3%	96%	96.2%	**100%**	**100%**
Least squares classifier	88.4%	88.8%	72.1%	71.1%	80.1%	80.4%	85.6%	85.1%	93.7%	94.1%
Self-organizing map	89.6%	89.1%	72.5%	71.9%	86.3%	86.1%	95.8%	96.2%	**100%**	**100%**

TABLE III. Summary of the false positive detections of the classifiers (V=validation data, T=test data).

Type of artificial neural network	Kurtosis		Crest factor		*WSE*, and *m*		Kurtosis and crest factor		Kurtosis, crest factor, *WSE*, and *m*	
	V	T	V	T	V	T	V	T	V	T
Radial basis function network	5.3%	6.3%	15.3%	14.6%	6.3%	6.3%	4.2%	4.0%	0%	0.3%
Multilayer perceptron	5.1%	5.1%	13.9%	14.2%	5.1%	5.3%	2.0%	1.8%	**0%**	**0%**
Least squares classifier	7.1%	7.8%	15.3%	15.5%	9.2%	9.5%	8.5%	8.9%	4.9%	5.1%
Self-organizing map	4.9%	5.1%	14.2%	13.9%	6.3%	6.7%	1.8%	2.0%	**0%**	**0%**

military impulse noise from other noise sources. Three distinct noise classes were found: military impulse, wind, and aircraft noise, the latter two of which are nonimpulsive. A library of military impulse noise and potential false-positive noise sources (wind and aircraft) was collected. The collected wave forms were then processed to extract the conventional signal metrics that were considered as signal features for the classifier. In addition, the signal power spectral density was computed. It was found that the time-domain metrics, kurtosis and crest factor, were most useful in identifying military impulse noise, as compared to the other conventional acoustic metrics: L_{eq}, L_{pk}, SEL, L_{8eq}, Dur, Pos, and Neg. Classification was first attempted with just kurtosis and crest factor as signal features to validate the assumption that kurtosis and crest factor would be good indicators of military impulse noise. To further improve detection accuracy, two frequency-domain metrics, spectral slope (m) and weighted square error (*WSE*) were developed. Finally, three ANN structures and a least squares classifier, each using various combinations of the four signal metrics as inputs, were created and trained. For the case where all four metrics were used, the ANN structures performed to 98.2–100% accuracy in identifying military impulse noise, while the least squares classifier performed to only 94.1% accuracy. These results illustrate that the nonlinear modeling capabilities of the ANN provide additional benefit over a linear classifier. When comparing the performance of classifiers based on crest factor or kurtosis alone vs. combining them, an improvement of 4.3%–24.3% in accuracy was achieved by the latter. The performances of the classifiers were further improved by 3.8%–8.5% with the addition of the complementary frequency-domain custom metrics, *WSE* and *m*. The classifiers were also able to identify impulse events with L_{pk} level down to 80 dB, where current monitors can only reliably detect events with $L_{pk} > 119$ dBC, indicating a lowering of the detection threshold by 40 dB. This algorithm was also found to work well in classifying multiple events occurring in a short span of time.

ACKNOWLEDGMENTS

This research was supported wholly by the U.S. Department of Defense, through the Strategic Environmental Research and Development Program (SERDP).

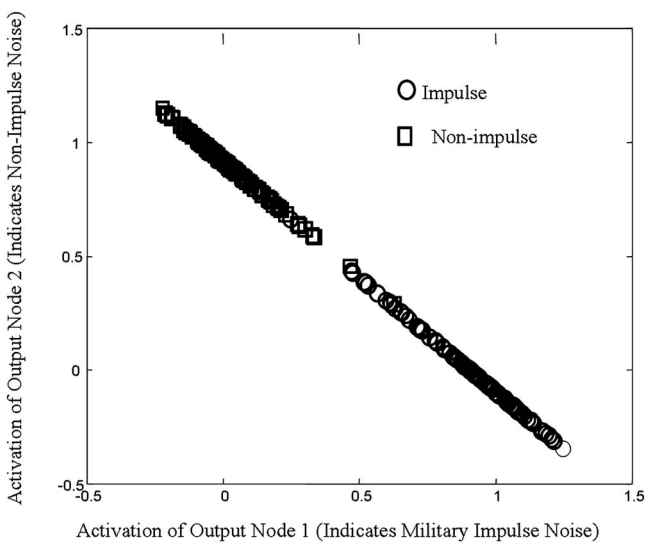

FIG. 10. Summary of performance for RBF network

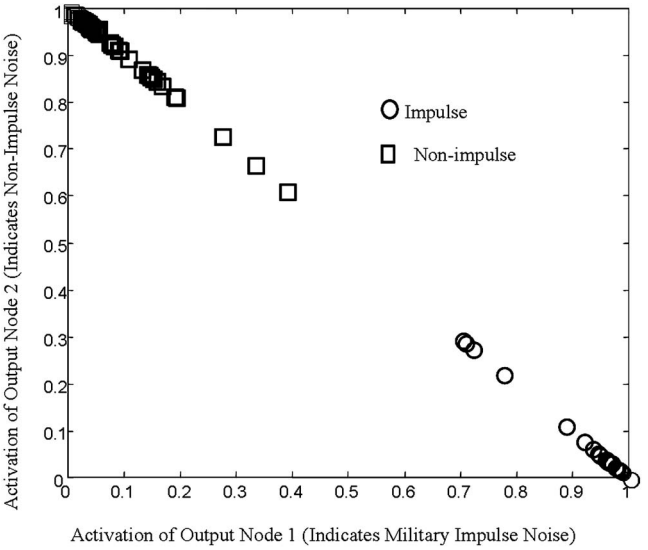

FIG. 11. Summary of performance for MLP.

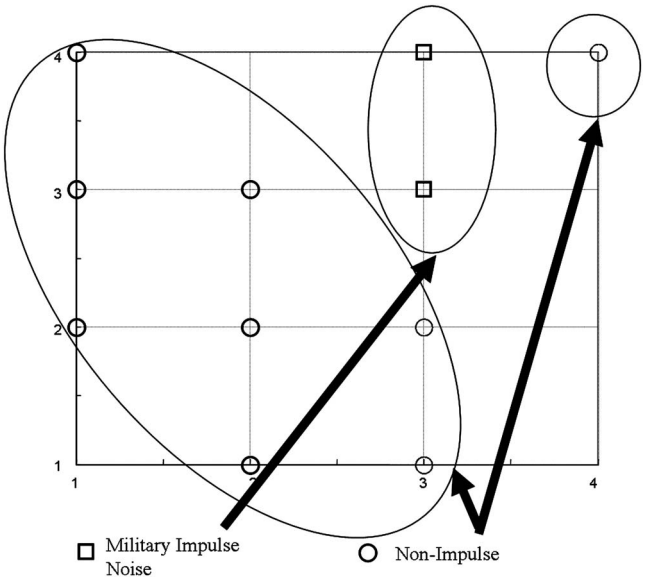

FIG. 12. Summary of performance for SOM.

[1]Anonymous. Office of Economic Adjustment, Office of Assistant Secretary of Defense, and Economic Security, "Joint Land Use Study," November 1993, Office of Economic Adjustment, DUSD(I&E), Suite 200, 400 Army Navy Drive, Arlington, VA 22202–2884 (703)604-6020.

[2]G. A. Luz, E. T. Nykaza, C. M. Stewart, and L. L. Pater, "The role of sleep disturbance in predicting community response to the noise of heavy weapons," Final Report Work Unit CNN-T352, U.S. Army Corps of Engineers Engineer Research and Development Center, ERDC/CERL TR-04-26, November (2004).

[3]G. A. Luz, "Suggested procedures for recording noise complaints at army installations," United States Army Environmental Hygiene Agency, Aberdeen Proving Ground, MD 21010-5422. HSE-08/WP Technical Guide, April 1, 1980.

[4]L. Pater, P. Woof, D. Rhoads, and M. White, "Getting started guide for the small arms range noise assessment model (SARNAM)," U.S. Army Corps of Engineers Construction Engineering Research Laboratory, CERL ADP Report No.99/48, May (1999).

[5]L. Pater and A. Krempin, "Development of a muffler for small arms range noise mitigation," U.S. Army Corps of Engineers Construction Engineering Research Laboratory, USACERL Technical Report No. 98/126, September (1998).

[6]USACHPPM, "Large arm noise," http://chppm-www.apgea.army. mil/dehe/morenoise/large_arms.aspx, (retrieved May 23, 2007).

[7]ANSI S12.17-1996. "Impulse sound propagation for environmental noise assessment," New York, NY: Acoustic Society of America.

[8]ANSI S12.17-1996. "Estimating airblast characteristics for single point explosions in air, with a guide to evaluation of atmospheric propagation and effects," New York, NY: Acoustic Society of America.

[9]W. A. Russell, Jr. and G. A. Luz *et al.* (2001), *Environmental Noise Management: An Orientation Handbook for Army Facilities*, U.S. Army Center for Health Promotion and Preventive Medicine (USACHPPM).

[10]R. D. Blevins, *Flow-Induced Vibration* (Krieger, Melbourne, FL, 2/e reprint, 2001).

[11]J. W. Benson, "A real-time blast noise detection and wind rejection system," Noise Control Eng. J. **44**(6), 306–314 (1996).

[12]ANSI (1993). "Methods for measurement of impulse noise," New York, NY: American National Standards Institute, ANSI S12.7-1986 (R1993).

[13]ISO (1996-1). "Acoustic-Description, measurement and assessment of environmental noise-Part 1: Basic quantities and procedures," ISO copyright office, Case postale 56, CH-1211 Geneva 20, ISO 1996-1:2003 (E).

[14]P. Schomer and K. Attenborough, "Basic results from full-scale tests at Fort Drum," Noise Control Eng. J. **53**(3), 94–109 (2005).

[15]I. Chunchuzov, S. Kulichov, A. Otrezov, and V. Perepelkin, "Acoustic pulse propagation through a fluctuating stably stratified atmospheric boundary layer," J. Acoust. Soc. Am. **117**(4), 1868–1879 (2005).

[16]J. Liaw and T. Berger, "Dynamic synapse for signal processing in neural networks," U.S. Patent No. 6,363,369, June 11 (1998).

[17]J. Liaw and T. Berger, "Dynamic synapse for signal processing in neural networks," U.S. Patent No. 6,643,627, March 26 (2002).

[18]E. Danicki, "The shock wave-based acoustic sniper localization," Nonlinear Anal.: Real World Appl. **65**, 956–962 (2006).

[19]M. Maroti, G. Simon, A. Ledeczi, and J. Sztipanovits, "Shooter localization in urban terrain," Computer **37**(9), 60–61 (2004).

[20]R. Stoughton, "Measurements of small-caliber ballistic shock waves in air," J. Acoust. Soc. Am. **102**(2), 781–787 (1997).

[21]Safety Dynamics Inc. Company Information, This is available online at http://www.safetydynamics.net/ (retrieved March 3, 2007).

[22]S. Young, "Robotic vehicle uses acoustic array for detection and localization in urban environments," Proc. SPIE **4364**, 264–273 (2001).

[23]P. Schomer, R. Raspet, J. Brunner, D. Marshall, M. Wagner, and D. Walker, "Reduction of wind noise for unattended blast noise monitoring," Noise Control Eng. J. **34**(2), 77–88 (1990).

[24]J. Benson, "A real-time blast noise detection and wind noise rejection system," Noise Control Eng. J. **44**(6), 307–314 (1996).

[25]P. Schomer, M. Bandy, J. Lamb, and H. Van Slooten, "Using fuzzy logic to validate blast noise monitor data," Noise Control Eng. J. **48**(6), 193–205 (2000).

[26]S. Abe, *Pattern Classification: Neuro-fuzzy Methods and Their Comparisons* (Springer-Verlag, London, 2001).

[27]M. Smith, *Neural Networks for Statistical Modeling* (Van Nostrand Reinhold, New York, 1993).

[28]R. Youssif and C. Purdy, "A multi-strategy signal pattern classifier," *Midwest Symposium on Circuits and Systems 3*, III304–III307 (2002).

[29]R. Eberhart and R. Dobbins, "Early neural network development history: The age of Camelot," IEEE Eng. Med. Biol. Mag. **9**, 15–18 (1990).

[30]R. H. Cabell, C. R. Fuller, and W. F. O'Brien, "Identification of helicopter noise using a neural network," AIAA J. **30**(3), 624–630 (1992).

[31]B. G. Kermani, S. S. Schiffman, and H. Troy Nagle, "Performance of the Levenberg-Marquardt neural network training method in electronic nose applications," Sens. Actuators B **110**(1), 13–22 (2005).

[32]R. H. Cabell, C. R. Fuller, and W. F. O'Brien, "Neural network modeling of oscillatory loads and fatigue damage estimation of helicopter components," J. Sound Vib. **209**(2), 329–342 (1998).

[33]B. Bucci and J. S. Vipperman, "Artificial neural network military impulse noise classifier," IMECE2006-14065, *Proceedings of IMECE 06: 2006 ASME International Mechanical Engineering Congress*, November 5–10, 2006, Chicago.

[34]A. Tsoi and A. Back, "Discrete time recurrent neural network architectures: A unifying review," Neurocomputing **15**, 183–223 (1997).

[35]M. Rafiq, G. Bugman, and D. Easterbrook, "Neural network design for engineering applications," Comput. Struct. **79**, 1541–1552 (2001).

[36]S. Haykin, *Neural Networks: A Comprehensive Foundation* (Prentice–Hall, Upper Saddle River, NJ, 1999).

[37]M. Arain, "Modeling and controller design of an EGR solenoid valve using neural networks," in *Neural Networks and Their Applications*, edited by J. G. Taylor (Wiley, West Sussex, England, 1996).

[38]T. Kohonen, "The self-organizing map," Proc. IEEE **78**(9), 1464–1480 (1990).

[39]B. Lavine, C. Davidson, and D. Westover, "Spectral pattern recognition using self-organizing maps," J. Chem. Inf. Comput. Sci. **44**(3), 1056–1064 (2004).

[40]O. Simula, P. Vasara, J. Vesanto, and R. Helminen, "The self-organizing map in industry analysis," *Industrial Applications of Neural Networks*, edited by L. Jain and V. Vemuri (CRC, Boca Raton, FL, 1999).

[41]S. Grossberg and G. Bradski, "A self-organizing architecture for invariant 3-D object learning and recognition from multiple 2-D views," in *Industrial Applications of Neural Networks*, edited by L. Jain and V. Vemuri (CRC, Boca Raton, FL, 1999).

[42]D. Skapura, *Building Neural Networks* (AMC, New York, 1996).

[43]N. H. Parsons, "Performance of a neural network based transient classifier at monitoring an acoustic perimeter intruder detection system," *IEEE Annual International Carnahan Conference on Security Technology, Proceedings*, Sunderstead, U.K., October 18–20, 9–13 (1995).

[44]E. Chong and S. Zak, *An Introduction to Optimization*, 2nd ed. (Wiley, New York, 2001).

[45]M. Norton and D. Karczub, *Fundamentals of Noise and Vibration Analysis for Engineers*, 2nd ed. (Cambridge University Press, New York, 2003).

[46]J. Lin and M. Zuo, "Gearbox fault diagnosis using adaptive wavelet filter," Mech. Syst. Signal Process. **17**(6), 1259–1269 (2003).

[47]J. Dron, F. Bolaers, and I. Rasolofondraibe, "Improvement of the sensitivity of the scalar indicators (crest factor, kurtosis) using a de-noising method by spectral subtraction: Application to the detection of defects in ball bearings," J. Sound Vib. **270**, 61–73 (2004).

Effects of frequency characteristics of reverberation time on listener envelopment

Masayuki Morimoto[a] and Munehiro Jinya
Environmental Acoustics Laboratory, Faculty of Engineering, Kobe University, Rokko, Nada, Kobe 657-8501, Japan

Koichi Nakagawa
Environmental Division, Nikken Sekkei Co., Ltd., Koraibashi, Chuo, Osaka 541-8528, Japan

(Received 11 December 2006; revised 12 June 2007; accepted 12 June 2007)

Spatial impression perceived in a listening space comprises at least two components: one is auditory (apparent) source width (ASW) and the other is listener envelopment (LEV). Both ASW and LEV are affected not only by temporal but also by spatial structures of reflections. It has been clarified that ASW for symphony music is significantly affected by low-frequency components of source signals and reflections, but not by their high-frequency components. The objective of this work is to investigate whether LEV is affected by the frequency characteristics of source signals and reverberation sounds, which are known to contribute to the creation of LEV. In this study, three experiments were performed to clarify the effects of reverberation time (RT) and its frequency characteristics on LEV. In contrast to the case of ASW, the experimental results show that RTs both at high and low frequencies affect LEV. © *2007 Acoustical Society of America.*
[DOI: 10.1121/1.2756164]

PACS number(s): 43.55.Fw, 43.55.Hy, 43.66.Pn [NX] Pages: 1611–1615

I. INTRODUCTION

Spatial impression is one of the important characteristics perceived in a listening space. It is widely accepted that the spatial impression comprises at least two components.[1–4] One is auditory (apparent) source width (ASW) and the other is listener envelopment (LEV). It is well known that both ASW and LEV are affected by not only temporal but also spatial structures of reflections.

In addition, ASW is also commonly affected by spectral structures of source signals and reflections. Barron and Marshall[5] discussed the effect of the reflection spectrum on ASW (they used the term "spatial impression" instead of ASW) for symphony music. They concluded that, for ASW, the frequency range covered by the 125 Hz to 1 kHz octaves is considered important, low frequencies being particularly important and desirable. Morimoto and Maekawa[6] examined the effect of low-frequency components of the source signal on ASW for a wide-band noise ranging from 100 Hz to 5.3 kHz, by changing the lower cutoff frequency and keeping the degree of interaural cross-correlation constant. The results showed that removing frequency components lower than 510 Hz decreases ASW markedly. Hidaka *et al.*[7] and Okano *et al.*[8] studied the effect of the low-frequency strength of the source signal on ASW for symphony music. The results demonstrated that the frequency components lower than 355 Hz affect ASW much more than those higher than 355 Hz. Morimoto and Iida[9] investigated the effect of high-frequency components of lateral reflections on ASW for a wide-band noise ranging from 200 Hz to 8 kHz by changing the higher cutoff frequency and keeping the degree of interaural cross-correlation constant. The experimental results indicated that the frequency components above 1 kHz do not contribute to the creation of ASW at all.

Naturally, typical physical measures of ASW for symphony music consider the low-frequency components. Barron[10] suggested LF_{E4}, which is the average value of early lateral energy fractions over the four octave bands from 125 Hz to 1 kHz, while Hidaka *et al.*[7] and Okano *et al.*[8] suggested $IACC_{E3}$, which is the average value of early interaural cross-correlation over the three octave bands from 500 Hz to 2 kHz.

On the other hand, the effect of spectral structures on LEV is not clearer than that on ASW. Beranek[11] suggested $IACC_{L3}$, which is the average value of late interaural cross-correlation over the three octave bands from 500 Hz to 2 kHz, as a physical measure of LEV, while Bradley and Soulodre[3] demonstrated that the late lateral sound level, which is the value summed for the four octave bands from 125 Hz to 1 kHz, best predicted LEV in their experiments. However, it is not clear whether the spectral structures of source signals and reflections affect the perception of LEV. In this study, three experiments are carried out to clarify the effects of the frequency characteristics of reverberation time on the perception of LEV.

II. METHOD

The same test method was used in the three experiments performed in this study. The music motif used for the experiments was a 7-s section of the first movement of Mozart's Divertimento in F major, K. 138 (125c) recorded in an anechoic chamber. The motif was reproduced with a limited frequency range from 100 Hz to 10 kHz.

[a]Electronic mail: mrmt@kobe-u.ac.jp

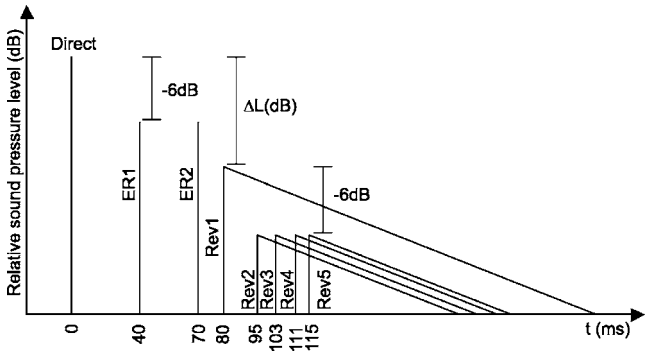

FIG. 1. Schematic diagram of impulse response of the stimulus used in the experiments.

Figure 1 shows schematically the impulse response of a stimulus. The sound field used as the stimulus consisted of a direct sound, two early discrete reflections, and five coherent reverberation sounds. The reflection delays were 40 and 70 ms and the reverberation delays were 80, 95, 103, 111, and 115 ms. The sound pressure levels of two early reflections were identical, and their relative sound pressure levels to the direct sound were −6 dB. The relative sound pressure level of the initial amplitude of the first reverberation sound was ΔL dB. The sound pressure levels of the other four reverberation sounds were identical, and their relative sound pressure levels to that of the first one were −6 dB.

Figure 2 shows the arrangement of loudspeakers. Six loudspeakers, each of which is installed in a cylindrical enclosure (diameter: 108 mm, length: 350 mm), were arranged at azimuth angles of 0 and ±45 deg from the median plane; that is, they were arranged symmetrically with respect to the aural axis, in an anechoic chamber. The distance between the center of the subject's head and the loudspeakers was 1.5 m. The direct sound was radiated from the loudspeaker at 0 deg.

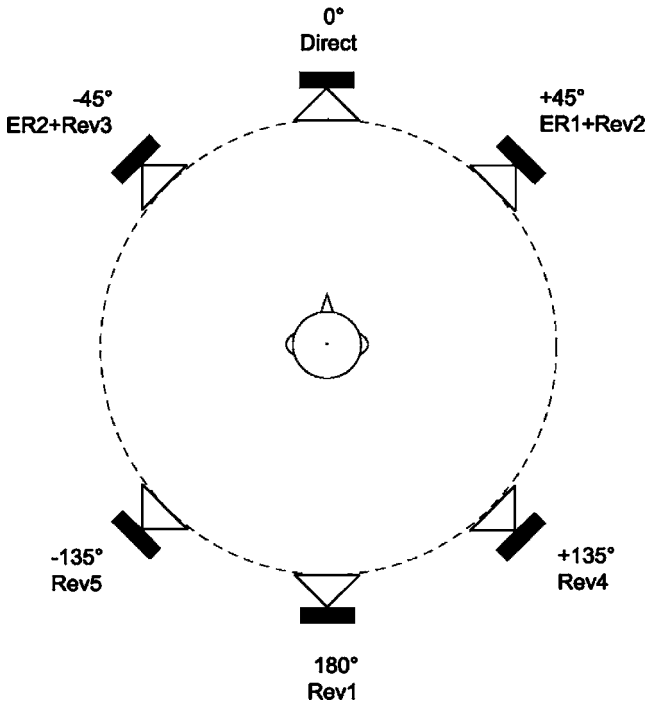

FIG. 2. Arrangement of loudspeakers in the experiments.

TABLE I. Stimuli in experiment 1.

Stimulus	Parameter		
	RT (s)	C_{80} (dB)	ΔL (dB)
1	1.0	6.0	−26.3
2	1.0	2.8	−26.3
3	1.0	0.9	−26.3
4	2.0	5.5	−26.3
5	2.0	2.7	−26.3
6	2.0	0.7	−26.3

The first and second early reflections were radiated from the loudspeakers at +45 and −45 deg, respectively. The first to fifth reverberation sounds were radiated from the loudspeakers at 180, +45, −45, +135, and −135 deg, respectively.

Paired comparison tests were performed in the experiments. The interval between the two stimuli was 2 s. Each pair of stimuli was arranged in random order and separated by an interval of 5 s. Each subject was tested individually and ten times for each pair including reversals, while seated with the head fixed in a darkened anechoic chamber. The task of the subject was to judge which LEV is greater. Before the experiments, the concept of LEV was explained to the subjects. All the subjects had sufficient experience as subjects in this kind of experiment.

The psychological scales of LEV were obtained using the Thurstone Case V model.[12,13] Gulliksen's method[13,14] was also used for incomplete data. The following must be considered in interpreting the psychological scales obtained using the Thurstone Case V model: The difference of 0.68 on the psychological scale means that the probability of discriminating the difference between two stimuli is 75%. Therefore, it is generally considered that the difference of 0.68 on the psychological scale corresponds to the just noticeable difference (jnd).

III. EXPERIMENT 1: EFFECTS OF REVERBERATION TIME ON LEV

Bradley and Soulodre[3] demonstrated that the effect of reverberation time (RT) in the range of 1.5 s on LEV was comparatively small under the condition that the early-to-late sound ratio (C_{80}) was constant. However, the effects of the amplitude of reverberation sound and RT on LEV might cancel each other out in their experiments, since the amplitudes of reverberation sounds after 80 ms were varied so that RT might be changed while keeping C_{80} constant. Here, as a preliminary experiment, it is investigated whether RT affects LEV when changing RT and C_{80} independently and keeping the relative sound pressure level of reverberation sound (ΔL) constant.

A. Experimental conditions

In this experiment, six kinds (2 RT × 3 C_{80}) of stimulus were used as shown in Table I. RT and C_{80} changed independently, keeping ΔL of all stimuli constant at −26.3 dB. The frequency characteristics of RT were flat. RT was changed using a digital reverberator (Roland SRV-3030). C_{80} was

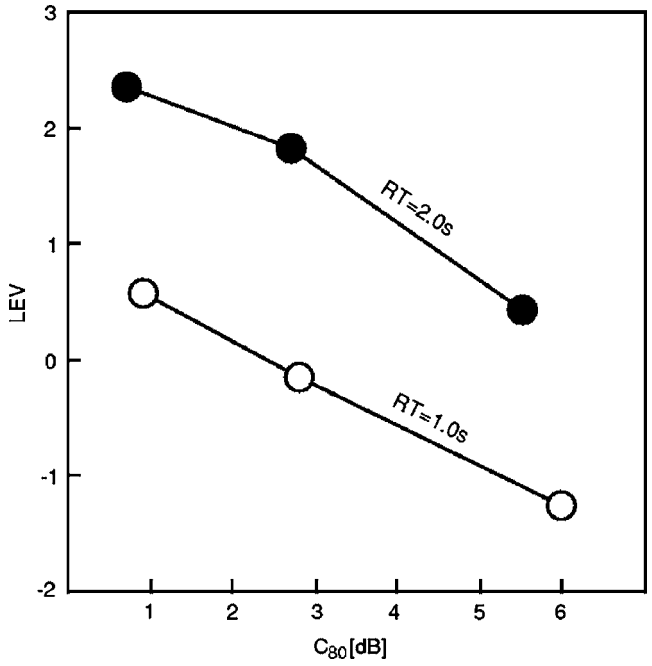

FIG. 3. Psychological scale of LEV as a function of C_{80} and as a parameter of RT in experiment 1.

controlled by changing the sound density of reverberation sound. This control technique was nothing more than an experimental one for varying C_{80}, while keeping RT, and vice versa. It included no implication about the acoustical design of real concert halls. It was verified that the change in sound density had no effect on the perception of reverberance in the experiments. Furthermore, C_{80} was measured for the overall frequency range using the music motif employed in the experiments as a measuring signal. The binaural sound pressure levels[15] of stimuli were constant at 80.0±0.1 dBA slow peak, measured at two ears of a KEMAR dummy head without an artificial ear simulator (B & K Type DB-100). The degrees of interaural cross-correlation (DICC)[16] of the reverberation sounds were constant at 0.43±0.03, as measured using a KEMAR dummy head without an artificial ear simulator. The late lateral sound level was not measured. However, it is readily understood that the late lateral sound levels of stimuli were constant as in the case of DICC since the directions of five reverberation sounds and the relative levels of lateral reverberation sounds to that from the rear direction were fixed. Seven students with normal hearing sensitivity participated as subjects for the experiment. Thirty pairs of stimuli including reversals were presented ten times to each subject.

B. Experimental results and discussion

In total, 2100 responses (30 pairs×10 times×7 subjects) were used to obtain the psychological scale of LEV. Figure 3 shows the psychological scale of LEV in experiment 1, that is, LEV with a parameter of RT and as a function of C_{80}. For each C_{80}, LEV for RT=2.0 s is greater than that for RT=1.0 s. The difference between them exceeds 0.68 for every C_{80} and is 1.68 (which means that the probability of discriminating the difference is 95.4%) at minimum when C_{80} is about 6.0. Furthermore, the differences for all three C_{80} are almost identical. This means that RT significantly affects LEV, being independent of C_{80}. Namely, LEV increases as RT becomes longer. Meanwhile, for each RT value, LEV increases as C_{80} decreases. The difference between the maximum and the minimum LEV is 1.82 (96.6%) and 1.91 (97.2%) for RT=1.0 and 2.0 s, respectively, and is far more than 0.68. This means that C_{80} also significantly affects LEV.

TABLE II. Frequency characteristics of RT for stimuli in experiment 2 (unit: s).

Stimulus	Center frequency of $\frac{1}{3}$ octave band (Hz)						
	125	250	500	1000	2000	4000	8000
	Experiment 2(a) (RT=1.0 s)						
1	0.50	0.63	0.75	0.85	0.93	1.00	1.00
2	0.66	0.77	0.77	0.91	0.94	1.00	1.01
3	1.13	1.00	1.04	1.02	0.96	1.00	1.01
4	1.82	1.28	1.19	1.06	1.01	1.06	1.99
5	2.11	1.58	1.30	1.10	1.01	1.02	1.00
6	2.34	1.82	1.41	1.10	1.03	1.02	0.99
	Experiment 2(b) (RT=2.0 s)						
1	0.49	0.92	1.21	1.61	1.81	1.91	1.93
2	1.16	1.18	1.46	1.87	1.90	1.91	1.93
3	2.20	1.93	1.91	2.03	1.96	1.92	1.94
4	2.92	2.67	2.18	2.12	1.99	1.93	1.94
5	3.33	3.22	2.45	2.17	1.98	1.91	1.94
6	3.82	3.33	2.63	2.20	2.03	1.94	1.94

IV. EXPERIMENT 2: EFFECTS OF REVERBERATION TIME AT LOW FREQUENCIES ON LEV

A. Experimental conditions

In experiment 2, the effects of RT at low frequencies on LEV were investigated for RT=1.0 and 2.0 s with flat frequency characteristics. In this experiment, six kinds of frequency characteristics of RT were used for each RT as shown in Table II. The values of RT in the table were ones measured at the point corresponding to the center of the subject's head in an anechoic chamber. RTs below around 1 kHz were changed by controlling a parameter "Low Ratio" built into the digital reverberator (YAMAHA Pro R3). This equipment can lengthen and shorten RT at low frequencies, but cannot change RT at high frequencies. For each RT, stimulus no. 3 has nearly flat frequency characteristics of RT. At low frequencies, stimuli nos. 1 and 2 have shorter RT than stimulus no. 3 and, conversely, stimuli nos. 4–6 have longer RT than stimulus no. 3.

C_{80}'s were constant at 0 dB. ΔL's were constant at −25.6±0.5 dB and −27.6±0.8 dB for RT=1.0 and 2.0 s, respectively. The binaural sound pressure levels were constant at 79.9±0.1 and 80.0 dBA for RT=1.0 and 2.0 s, respectively. DICC of the reverberation sounds were constant at 0.32±0.03. A paired comparison test was carried out separately for each RT. Six students with normal hearing sensitivity participated as subjects for the experiment. A paired

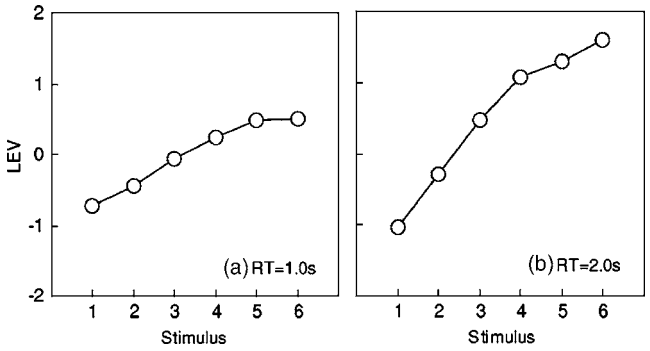

FIG. 4. Psychological scale of LEV as a function of frequency characteristics of RT for (a) RT=1.0 s and (b) 2.0 s in experiment 2. In this experiment, RT at frequencies lower than 1 kHz either shorten or lengthen. For stimulus no. 3, each RT has nearly flat frequency characteristics. As the stimulus number decreases from no. 3, RT at frequencies lower than 1 kHz shorten, and vice versa. The precise frequency characteristics of RT of each stimulus are shown in Table II.

comparison test was carried out separately for each RT. For each RT, 30 pairs of stimuli including reversals were presented ten times to each subject.

B. Experimental results and discussion

In total, 1800 responses (30 pairs×10 times×6 subjects) were used to obtain the psychological scale of LEV for each RT. Figure 4 shows the psychological scale of LEV in experiment 2, that is, the effects of RT at low frequencies on LEV. For both RT, LEV increases as RT at low frequencies becomes longer and vice versa. Here, let us compare those results with LEV for stimulus no. 3 with flat frequency characteristics of RT.

For RT=1 s, the decrease for stimulus no. 1 with the shortest RT at low frequencies is 0.672 (74.9%) and the increases for stimuli nos. 5 and 6 with longer RT at low frequencies are 0.558 (71.2%) and 0.567 (71.5%), respectively. These differences are slightly smaller than the difference of 0.68 (75%) corresponding to jnd. The decrease for stimulus no. 2 and the increase for stimulus no. 4 are 0.380 (64.8%) and 0.316 (62.4%), respectively. It cannot be considered that these differences can be discriminated.

Meanwhile, for RT=2 s, the decreases for stimuli nos. 1 and 2 with shorter RT at low frequencies are 1.501 (93.3%) and 0.750 (77.3%), respectively. These differences can be distinctly discriminated. The increase for stimulus no. 4 is 0.611 (72.9%), which is slightly smaller than the difference of 0.68 (75%) corresponding to jnd. However, the increases for stimuli nos. 5 and 6 with longer RT at low frequencies are 0.833 (79.7%) and 1.123 (86.9%), respectively. It can be considered that these differences can be discriminated distinctly.

Furthermore, for each RT, the differences in LEV between stimulus no. 1 with the shortest RT and stimulus no. 6 with the longest RT at low frequencies are 1.24 (89.3%) and 2.62 (99.6%) for RT = 1 and 2 s, respectively. The subjects could discriminate clearly the differences.

On the basis of the above experimental results, it can be concluded that RT at low frequencies affects LEV significantly when RT at low frequencies becomes longer and shorter.

TABLE III. Frequency characteristics of RT for stimuli in experiment 3 (unit: s).

Stimulus	Center frequency of $\frac{1}{3}$ octave band (Hz)						
	125	250	500	1000	2000	4000	8000
1	1.05	1.54	1.68	1.89	1.97	2.01	2.00
2	1.44	1.57	1.73	1.91	1.97	2.01	2.01
3	2.00	1.97	2.02	1.99	1.98	1.99	1.98
4	2.03	2.05	2.03	1.99	1.82	1.63	1.34
5	2.04	2.04	2.01	1.97	1.84	1.57	1.23

V. EXPERIMENT 3: EFFECTS OF SHORTENING REVERBERATION TIME AT EITHER LOW OR HIGH FREQUENCIES ON LEV

A. Experimental conditions

In experiment 3, the effects of shortening each RT at low and high frequencies on LEV were investigated for RT =2.0 s with flat frequency characteristics. In this experiment, five kinds of frequency characteristics of RT were used as shown in Table III. Table III shows the frequency characteristics of RT of the stimuli used in the experiment. RT below around 500 Hz and above around 4 kHz were shortened by controlling parameters "LF DAMP" and "HF DAMP," respectively, built into the digital reverberator (Roland SRV-3030). This equipment can shorten each RT at low and high frequencies, but cannot lengthen them. For stimulus no. 3, RT has nearly flat frequency characteristics. Stimuli nos. 1 and 2 have shorter RT at low frequencies and conversely, stimuli nos. 4 and 5 have shorter RT at high frequencies than stimulus no. 3. The values of RT on the table were ones measured at the point corresponding to the center of the subject's head in an anechoic chamber.

C_{80} were constant at 0 dB. ΔL were constant at −26.3±0.3 dB. The binaural sound pressure levels of stimuli were constant at 79.9±0.1 dBA. DICC of the reverberation sounds were constant at 0.43±0.03. Five students with normal hearing sensitivity participated as subjects for the experiment. Twenty pairs of stimuli including reversals were presented ten times to each subject.

B. Experimental results and discussion

In total, 1000 responses (20 pairs×10 times×5 subjects) were used to obtain the psychological scale of LEV. Figure 5 shows the psychological scale of LEV in experiment 3, that is, the effects of shortening RT at either low or high frequencies on LEV. LEV decreases as RT at low frequencies becomes shorter, in contrast to LEV for stimulus no. 3 with flat frequency characteristics of RT. The decreases for stimuli nos. 1 and 2 are 0.839 (79.9%) and 0.774 (78.1%), respectively, which are large enough to be discriminated. Namely, RT at low frequencies significantly affect LEV. This result coincides with those of experiment 2.

Meanwhile, LEV also decreases as RT at high frequencies becomes shorter, in contrast to LEV for stimulus no. 3

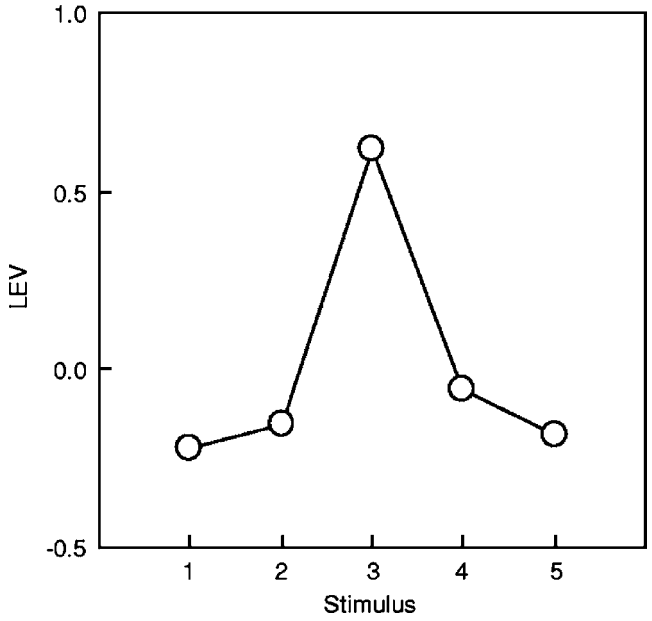

FIG. 5. Psychological scale of LEV as a function of frequency characteristics of RT in experiment 3. In this experiment, RT at frequencies either lower or higher than 1 kHz shorten. For stimulus no. 3, RT has flat frequency characteristics. As the stimulus number decreases from no. 3, RT at frequencies lower than 1 kHz shorten and, as the stimulus number increases from no. 3, RT at frequencies higher than 1 kHz shorten. The precise frequency characteristics of RT of each stimulus are shown in Table III.

with flat frequency characteristics of RT. The decreases for stimuli nos. 4 and 5 are 0.677 (75.1%) and 0.804 (80.4%), and they are almost the same as those obtained when shortening RT at low frequencies and large enough to be discriminated. This phenomenon is different from the perception of ASW that is affected by low-frequency components but not high-frequency components. In other words, high-frequency components must be considered in evaluating LEV.

VI. CONCLUSIONS

The effects of reverberation time (RT) and the frequency characteristics of RT on listener envelopment (LEV) for symphony music were investigated. Three subjective experiments were performed to clarify the effects, keeping other physical parameters, the relative sound pressure level of reverberation sound to the direct sound, the early-to-late sound energy ratio (C_{80}), and the degree of interaural cross-correlation, constant.

In the first experiment, RT was changed, keeping its frequency characteristics flat. The results indicate that RT significantly affects LEV, being independent of C_{80}. LEV increases as RT becomes longer. In the second experiment, RT at low frequencies were shortened and lengthened. The results demonstrate that LEV significantly decreases as RT at low frequencies shortened and vice versa. In the third experiment, both RT at low and high frequencies were shortened. The results show that RT at high frequencies, as well as those at low frequencies, significantly affect LEV.

In conclusion, the experimental results show that RT affects LEV, being independent of the early-to-late sound ratio (C_{80}), and that RT at high as well as low frequencies affect LEV, in contrast to the case of ASW, which is affected by the low-frequency components, but not the high-frequency ones.

In this study, the effects of lengthening RT could not be investigated owing to technical difficulties. However, it can be inferred from the results of all the experiments that lengthening RT at low as well as high frequencies increases LEV.

ACKNOWLEDGMENTS

This study was supported in part by the Twenty-First Century Center of Excellence (COE) Program "Design Strategy towards Safety and Symbiosis of Urban Space" awarded to the Graduate School of Science and Technology, Kobe University. The Ministry of Education, Culture, Sports, Science and Technology of Japan sponsored the Program.

[1]M. Morimoto and Z. Maekawa, "Auditory spaciousness and envelopment," in *Proceedings of the 13th International Congress on Acoustics*, Belgrad, (1982), Vol. 2, pp. 215–218.
[2]J. S. Bradley and G. A. Soulodre, "The influence of late arriving energy on spatial impression," J. Acoust. Soc. Am. **97**, 2263–2271 (1995).
[3]J. S. Bradley and G. A. Soulodre, "Objective measures of listener envelopment," J. Acoust. Soc. Am. **97**, 2590–2597 (1995).
[4]M. Morimoto, K. Iida, and K. Sakagami, "The role of reflections from behind the listener in spatial impression," Appl. Acoust. **62**, 109–124 (2001).
[5]M. Barron and A. H. Marshall, "Spatial impression due to early lateral reflections in concert halls: The deviation of a physical measure," J. Sound Vib. **77**, 211–232 (1981).
[6]M. Morimoto and Z. Maekawa, "Effects of low frequency components on auditory spaciousness," Acustica **66**, 190–196 (1988).
[7]T. Hidaka, L. L. Beranek, and T. Okano, "Interaural cross-correlation, lateral fraction, and low- and high-frequency sound levels as measures of acoustical quality in concert halls," J. Acoust. Soc. Am. **98**, 988–1007 (1995).
[8]T. Okano, L. L. Beranek, and T. Hidaka, "Relations among interaural cross-correlation coefficient ($IACC_E$) lateral fraction (LF_E), and apparent source width (ASW) in concert halls," J. Acoust. Soc. Am. **104**, 255–265 (1998).
[9]M. Morimoto and K. Iida, "Appropriate frequency bandwidth in measuring interaural cross-correlation as a physical measure of auditory source width," Acoust. Sci. & Tech. **26**, 179–184(2005).
[10]M. Barron, *Auditorium Acoustics and Architectural Design* (E & SPON, London, 1993).
[11]L. L. Beranek, *Concert and Opera Halls: How they Sound* (Acoustical Society of America, New York, 1996).
[12]L. L. Thurstone, "A law of comparative judgment," Psychol. Rev. **34**, 273–286 (1927).
[13]H. Gulliksen, "A least squares solution for paired comparison with incomplete data," Psychometrika **21**, 125–134 (1956).
[14]W. S. Torgerson, *Theory and Methods of Scaling* (Wiley, New York, 1958).
[15]D. W. Robinson and L. S. Whittle, "The loudness of directional sound field," Acustica **10**, 74–80 (1960).
[16]M. Morimoto and K. Iida, "A practical evaluation method of auditory source width in concert halls," J. Acoust. Soc. Jpn. (E) **16**, 59–69 (1995).

Acceptable range of speech level for both young and aged listeners in reverberant and quiet sound fields

Hayato Sato[a)]
Environmental Acoustics Laboratory, Faculty of Engineering, Kobe University, Rokko, Nada, Kobe 657-8501, Japan

Hiroshi Sato
Institute for Human Science & Biomedical Engineering, National Institute of Advanced Industrial Science and Technology, Tsukuba Central, Tsukuba, Ibaraki 305-8568, Japan

Masayuki Morimoto and Ryo Ota
Environmental Acoustics Laboratory, Faculty of Engineering, Kobe University, Rokko, Nada, Kobe 657-8501, Japan

(Received 18 November 2006; revised 3 July 2007; accepted 5 July 2007)

The speech level of verbal information in public spaces should be determined to make it acceptable to as many listeners as possible, while simultaneously maintaining maximum intelligibility and considering the variation in the hearing levels of listeners. In the present study, the universally acceptable range of speech level in reverberant and quiet sound fields for both young listeners with normal hearing and aged listeners with hearing loss due to aging was investigated. Word intelligibility scores and listening difficulty ratings as a function of speech level were obtained by listening tests. The results of the listening tests clarified that (1) the universally acceptable ranges of speech level are from 60 to 70 dBA, from 56 to 61 dBA, from 52 to 67 dBA and from 58 to 63 dBA for the test sound fields with the reverberation times of 0.0, 0.5, 1.0 and 2.0 s, respectively, and (2) there is a speech level that falls within all of the universally acceptable ranges of speech level obtained in the present study; that speech level is around 60 dBA.
 [DOI: 10.1121/1.2766780]

PACS number(s): 43.55.Hy, 43.71.Gv, 43.71.Lz [NX] Pages: 1616–1623

I. INTRODUCTION

A public address (PA) system is frequently used in public spaces, since it can supply verbal information to many people at the same time. Needless to say, verbal information should be transmitted to all listeners accurately. PA systems can amplify verbal information to transmit it accurately. However, the optimum sound pressure level of verbal information in public spaces has not been clarified. There are two reasons for this problem. First, the loudness of verbal information depends on the hearing level of individual listeners. Second, different listeners are present in public spaces, such as facilities for passengers, shopping malls, and hospitals. Furthermore, the proportions of age, sex and hearing loss of listeners depend on the type of public space. Therefore, it can be easily surmised that one listener may feel the loudness of verbal information to be comfortable while another listener may feel it to be too loud or soft, and yet another listener might not be able to understand the information presented. The fact that the number of elderly with hearing loss due to aging are increasing in such public spaces accelerates this problem. Although hearing aid systems have some potential to alleviate this problem, most listeners with mild or moderate hearing loss do not wear hearing aids unless they encounter serious difficulty in verbal communication in daily life. Common hearing aids amplify not only speech but also detrimental sounds such as noise and reverberation sounds, and they are still expensive. Therefore, the sound pressure level of verbal information presented in public spaces should be determined to make it acceptable for as many listeners as possible, while simultaneously maintaining maximum intelligibility and considering the variation of hearing levels of listeners.

The most comfortable loudness or listening level (MCL) is useful in determining the acceptable speech level of verbal information presented in public spaces. There are several studies of MCL for monaural speech a quiet condition with normal-hearing listeners, and the results of these studies demonstrate that MCL for speech in quiet fields ranges from 50 to 70 dB sound pressure level (SPL).[1–4] In addition, those studies include other important suggestions relevant to the present study. Ventry and Woods[2] and Hochberg[4] suggested that MCL would increase when the attention to intelligibility was instructed before starting listening tests. This tendency should be considered because intelligibility is essential to verbal information in public spaces. Meanwhile, Berger and Lowry[3] recommended regarding MCL as MCR: the most comfortable range, because the standard deviations of MCL were larger than those generally shown in threshold measurements. In other words, MCL is not a particular level but it has a broad range. For example, Pollack[5] reported that the difference between the upper and lower limits of MCL for

[a)]Author to whom correspondence should be addressed. Electronic mail: hayato@kobe-u.ac.jp

the pure tone of 1 kHz was more than 30 dB. Hochberg[4] reported a wider MCR variance of 40–92 dB SPL for speech.

Noise and reverberation sounds are also important factors in determining the acceptable speech level of verbal information in public spaces. While the effect of reverberation sounds on MCL is rarely studied, there are many studies of the effect of noise on MCL. The results of such studies showed that MCL increased with increasing noise level. Richards[6] measured MCLs for speech in the presence of masking noise of 55–85 dB SPL, and suggested that the slope of MCL growth as a function of noise level was 0.70 dB/dB. Heusden *et al.*[7] measured the preferred listening level of speech in a reverberant and noisy room, using a similar method and instruction to those of MCL. The results showed that the preferred listening level begins to increase from 50 dBA when the noise level exceeded 35 dBA, and that the slope of preferred listening level growth as a function of noise level was 0.31 dB/dB for noise levels of 50 dBA and higher.

From the viewpoint of the optimization of hearing aid gains, the effects of hearing level on MCL and the upper limit of MCL for speech (ULCL) have been well studied.[8–11] Generally speaking, the results of these studies demonstrated that MCL and ULCL increase with increasing hearing level or speech reception threshold. However, the slopes of MCL and ULCL as a function of hearing level or speech reception threshold varied widely from 0.18 to 0.72 dB/dB. These findings correspond to MCL measured by Nábělek and Robinette[12] who used MCL to determine the presentation level of speech stimuli.

Meanwhile, Kobayashi *et al.*[13] obtained the optimum speech level for the young by measuring listening difficulty[14] as a function of speech level. Listening difficulty is a subjective rating that is the ratio of listeners who find difficulty in listening to words. They defined the optimum speech level as the level that minimizes listening difficulty. They reported that the optimum speech level for the reverberant time of 0.5 s is around 50–55 dBA when noise level is less than 40 dBA, and that the optimum speech level is higher than the noise level by at least 15 dB when noise level is from 40 to 55 dBA. Note that they measured speech level when only the direct sound was presented. The test conditions adopted by Kobayashi *et al.* are similar to those used by of Heusden *et al.*,[7] and their results qualitatively correspond to each other.

In the present study, the acceptable speech level was obtained by the same method as used by Kobayashi *et al.*,[13] because it has several advantages for determining the acceptable speech level of verbal information in public spaces. First, listening difficulty[14] is measured using the most familiar words as the test signals. In general, the words used for verbal information in public spaces are selected to be very familiar to all listeners. Therefore, listening difficulty for the most familiar words coincides with listening difficulty in real situations. Second, listening difficulty is rated just after taking dictation of each test signal. As mentioned previously, the attention to intelligibility increases MCL.[2,4] Considering that intelligibility is essential to verbal information in public spaces, listeners' attention must be directed to intelligibility in listening tests on the optimum speech level. In the method of measuring listening difficulty, listeners' attention is directed to intelligibility by forcing listeners to take dictation of test signals. Furthermore, word intelligibility scores can be calculated from the results of the dictation. Word intelligibility scores are useful in evaluating a lower speech transmission performance that cannot be evaluated by listening difficulty ratings.[14] Finally, listening difficulty as a function of speech level is useful in investigating the upper and lower limits of the acceptable speech level.

To clarify the acceptable speech level in public spaces, it is necessary to consider speech level, background noise, reverberant sounds, and hearing loss of listeners as parameters of the listening test. However, it seems to be difficult to consider all parameters at once. Therefore, the purpose of the present study was focused on the effect of detrimental reverberant sounds on the acceptable speech level for both the young and the aged.

The acceptable range of speech level for both young listeners with normal hearing level and aged listeners with hearing loss due to aging were investigated in quiet and reverberant sound fields. The procedure of the present study is described below.

First, the acceptable ranges of speech level for the young and aged were obtained, respectively. The acceptable speech level is defined as the level that does not cause a statistically significant increase in listening difficulty relative to the minimum listening difficulty, and simultaneously maintains the maximum word intelligibility. Next, the acceptable ranges for the young and the aged were compared to clarify the overlapping range, that is, the universally acceptable range for both the young and the aged.

II. TEST I: ACCEPTABLE SPEECH LEVEL IN REVERBERATION-FREE AND QUIET SOUND FIELD

A. Method

Two groups of listeners participated in the listening test. The young group consisted of ten young adults (four males, six females) in their twenties. The aged group consisted of 20 adults (nine males, 11 females) whose age ranged from 65 to 77 years old. No listener wears a hearing aid in daily life. Hearing levels for both ears were measured using an audiometer in 5 dB steps in a sound-treated room. Figure 1 represents the mean hearing levels for the two groups and the estimated mean hearing levels for 20-, 60-, 70-, and 80-year-old listeners based on ISO 7029.[15]

The mean hearing levels for the young (open circles in Fig. 1) were close to the estimated mean hearing levels for 20-year-old listeners. This indicates that the young listeners had normal hearing levels. Meanwhile, the mean hearing levels for the aged (open triangles in Fig. 1) were almost the same as that for 70-year-old listeners at frequencies above 1 kHz. Considering that the average age of the aged group was 68.8 years old, the aged listeners used in the listening test were representative samples of typical aged people in terms of hearing levels at frequencies above 1 kHz that affect listening difficulty and word intelligibility.[16] The differences between measured and estimated hearing levels were

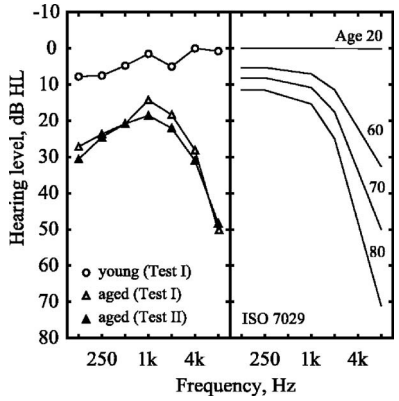

FIG. 1. Audiograms for listeners used in tests I and II. Open circles and triangles respectively represent those for the young and the aged in test I. Closed triangles represent that for the aged in test II. Solid lines in the right panel represent mean hearing levels for 20-, 60-, 70- and 80-year-old listeners estimated according to ISO 7029. The estimated hearing levels are the average of those for male and female listeners.

relatively large at frequencies from 125 to 500 Hz. This increase in hearing levels at low frequencies was common to the young and the aged. Therefore, it might be due to the background noise of the sound-treated room.

The listening tests were performed in an anechoic chamber. A total of 200 different Japanese words were used as test words. The test words were selected from the word lists by Sakamoto *et al.*[17] as most familiar words to both the young and the aged. The verbal information supplied by PA systems generally comprises sentences consisting of very familiar words that also minimize the cognitive effect of word familiarity on word intelligibility and listening difficulty. All test words have four syllables. The test words recorded in an anechoic chamber were used as the test signals. The test signals were presented from a loudspeaker (Fujitsu Ten, TD512) at a distance of 2 m in front of the listener. The frequency characteristics of the loudspeaker are flat within ±5 dB in the range from 100 to 10 kHz. The sound pressure levels of the test signals (speech level) were changed in ten steps of 5 dB from 30–75 dBA at the position of the center of the listener's head. The speech level was the A-weighted slow peak level measured using a sound level meter.

Twenty of the 200 test words were presented to each listener for each of the ten different speech levels. Thus, each listener listened to a set of 200 test signals in total (20 words × 10 speech levels) in a random order. Moreover, each word was presented to a listener only once. The interstimulus interval was 10 s. The listening test was separated into four sessions of listening to 50 test signals. A different set of 200 test signals was presented to each listener. In the whole of the listening test, 200 test signals were presented for each speech level for the young group (20 test signals ×10 listeners), and 400 test signals for each speech level for the aged group (20 test signals ×20 listeners). Each listener was tested individually. Each listener was asked to take dictation of each test signal as they listened using kana characters (Japanese phonogram) and simultaneously to rate the listening difficulty into one of the four categories shown in Table I.[14] Before the listening tests, as an exercise, each listener listened to ten test signals that consisted of ten words other than the 200 test words. The exercises for the aged listeners were repeated until they could complete the task within the interstimulus interval.

TABLE I. Categories of listening difficulty (see Ref. 14).

1	Not	difficult
2	A little	difficult
3	Fairly	difficult
4	Extremely	difficult

B. Results and discussion

Word intelligibility scores and listening difficulty ratings were obtained from the results of the listening test. The word intelligibility score is the percentage of test signals written down correctly. The listening difficulty rating is the percentage of the sum of the responses rated listening difficulty of the test signal from "2" to "4" in Table I. Note that listening difficulty ratings decrease when conditions for speech improve, contrary to word intelligibility scores.

Figure 2 represents word intelligibility scores and listening difficulty ratings as a function of speech level. Closed and open symbols respectively represent word intelligibility scores and listening difficulty ratings. Circles and triangles respectively represent the results for the young and for the aged.

A one-way repeated measures analysis of variance (ANOVA) with speech level as the within-subjects factor was used to analyze the effect of speech level on the word intelligibility scores and listening difficulty ratings. In the present study, all ANOVAs were performed in the same way.

1. Results for the young

The word intelligibility scores for the young (closed circles in Fig. 2) were close to 100% for all speech levels. The result of ANOVA revealed that the main effect of speech level was not significant ($F(9,81)=1.7, p=0.09$).

In contrast, the listening difficulty ratings for the young (open circles) were strongly affected by speech level, and varied widely from 3% to 90%. The optimum speech level that minimizes listening difficulty ratings was 60 dBA. The

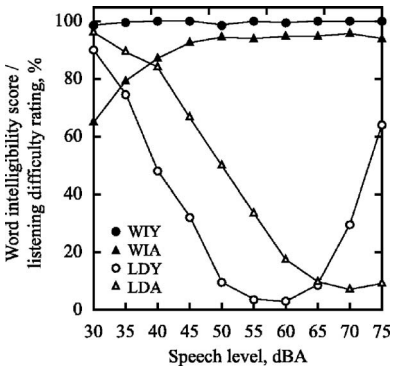

FIG. 2. Word intelligibility scores and listening difficulty ratings as a function of speech level in the reverberation-free and quiet sound field. Closed and open symbols respectively represent word intelligibility scores and listening difficulty ratings. Circles and triangles respectively represent the results for the young and the aged.

result of ANOVA revealed that the main effect of speech level was significant ($F(9,81)=25.4$, $p<0.05$). Tukey's honestly significant difference (HSD) test[18] was employed for multiple comparisons between listening difficulty ratings. HSD for the listening difficulty ratings for the young was calculated to be 28.8% ($p<0.05$). This means that differences between listening difficulty ratings greater than 28.8% would be statistically significant. The minimum listening difficulty rating was not significantly different from the listening difficulty ratings for the speech level from 50 to 70 dBA. Considering that the word intelligibility scores for the young were maximized for all speech levels, the acceptable range of speech level for the young in the reverberation-free and quiet sound field was from 50 to 70 dBA.

2. Results for the aged

The word intelligibility scores for the aged (closed triangles in Fig. 2) increased with increasing speech level, and seemed to be maximized when speech level exceeded 45 dBA. The word intelligibility scores varied from 65% to 95%. Note that the word intelligibility scores for the aged did not reach 100%, though there were not detrimental sounds such as reverberation sounds and noise. The result of ANOVA revealed that the main effect of speech level was statistically significant ($F(9,171)=25.1$, $p<0.05$). HSD for the word intelligibility scores for the aged was calculated to be 9.1% ($p<0.05$). This result revealed that there were significant differences between the maximum word intelligibility score and the word intelligibility scores for 40 dBA and lower. In other words, the minimum speech level to maximize word intelligibility scores for the aged was 45 dBA.

Similar to the young group, the listening difficulty ratings for the aged (open triangles) varied more greatly than their word intelligibility scores. The optimum speech level for the aged was 70 dBA, and it was higher than that for the young by 10 dB. The result of ANOVA revealed that the main effect of speech level was significant ($F(9,171)=94.7$, $p<0.05$). HSD for the listening difficulty ratings for the aged was calculated, to be 16.8% ($p<0.05$). The minimum listening difficulty rating was not significantly different from the listening difficulty ratings for 60 dBA and the higher speech levels, and the speech level of 60 dBA is sufficiently high to maximize word intelligibility scores for the aged. In conclusion, the acceptable speech level for the aged in the reverberation-free and quiet sound field was 60–75 dBA and higher.

III. TEST II: ACCEPTABLE SPEECH LEVELS IN REVERBERANT AND QUIET SOUND FIELDS

A. Method

Two groups of listeners participated in test II. The young group consisted of 43 young adults (23 males, 20 females) in their twenties. The young listener group did not have their hearing level tested, but none of them reported any known hearing impairment. The aged group consisted of 49 adults (24 males, 25 females) whose age ranged from 59 to 77 years old. No aged listener wears a hearing aid in daily life. All listeners were different from those in test I. Figure 1 also represents the mean hearing levels for the aged group for test II. The hearing levels for the aged for test II (closed triangles) were almost the same as those for test I. This means the aged listeners used in test II were also representative samples of typical aged people, similar to test I.

A total of 120 different Japanese words were used. All test words were also used in test I. The parameters of the test were reverberation time and sound pressure level. Test words were preliminarily convolved with artificial impulse responses using software on a computer to add reverberant sounds. The impulse responses were composed of a direct sound followed by reverberant sounds. The reverberant sounds started at 50 ms after the direct sound to simplify test sound fields by setting all reverberant sounds to be detrimental to speech perception. The sound pressure ratio of the onset component of the reverberant sounds to the direct sound (Pr/Pd) was constant at 0.1. The reverberation time was set at 0.5, 1.0 and 2.0 s. The frequency characteristic of reverberation time was flat. The reverberant sounds were generated using a digital reverberator (YAMAHA, SPX-900).

The sound pressure level of the test signal was changed in eight steps of 5 dB from 35 to 70 dBA. The sound pressure level was measured as the A-weighted slow peak level at the position of the center of the listener's head when only the direct sound was presented. The sound pressure level in the presence of reverberant sounds increased with increasing reverberation time. The sound pressure levels in the presence of reverberant sounds averaged over all test words for each of the reverberation times were higher than those without reverberant sounds by 5.6 dBA for 0.5 s, 6.7 dBA for 1.0 s, and 8.2 dBA for 2.0 s. In the present study, speech level is defined as the sound pressure level of the test signal including reverberant sounds. For example, the speech level for the reverberation time of 0.5 s changed from 40.6 to 75.6 dBA in 5 dB steps. A total of 24 sound fields (3 reverberation times $\times 8$ speech levels) were tested.

Five of the 120 test words were presented to each listener for each sound field. Thus, each listener listened to a set of 120 test signals in total (5 words $\times 24$ sound fields) in a random order. Moreover, each word was presented to a listener only once. A different set of 120 test signals was presented to each listener. The interstimulus interval was 10 s. The listening test was separated into three sessions of listening to 40 test signals. In the whole of test II, 215 and 245 test signals were presented for each sound field for the young group (5 test signals $\times 43$ listeners) and for the aged group (5 test signals $\times 49$ listeners), respectively. The test signals were presented to two listeners at a time from a loudspeaker (Technics, SBM300M2) in an anechoic room. The listening positions were located at a distance of 2 m from the loudspeaker and at $\pm 30°$ from the central axis of the loudspeaker. The frequency characteristics of the loudspeaker measured at the listening positions are flat within ±5 dB in the range from 100 to 10 kHz. The listener's task was the same as that in test I. The exercises of test II were performed in the same way as those for test I.

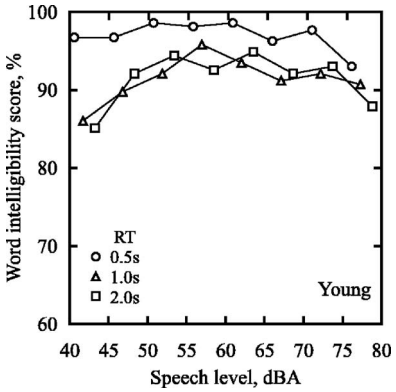

FIG. 3. The word intelligibility scores for the young in reverberant and quiet sound fields. Open circles, triangles and squares represent the word intelligibility scores for the reverberation times of 0.5, 1.0 and 2.0 s, respectively.

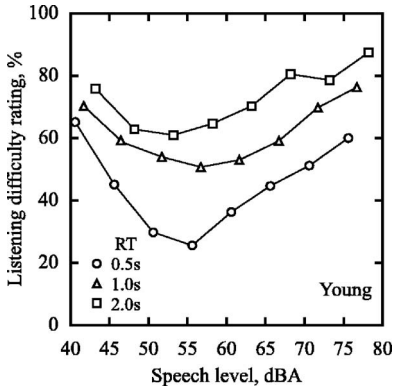

FIG. 4. The listening difficulty ratings for the young in reverberant and quiet sound fields. Open circles, triangles and squares represent the listening difficulty ratings for the reverberation times of 0.5, 1.0 and 2.0 s, respectively.

B. Results and discussion

Also in test II, a one-way repeated measures analysis of variance (ANOVA) with speech level as the within-subjects factor was used to analyze the effect of speech level on word intelligibility scores and listening difficulty ratings. The analyses were separately performed for each test sound field.

1. Results for the young

Figure 3 represents the word intelligibility scores for the young as a function of speech level. Although the word intelligibility scores for the young were 85% or higher for all sound fields and speech levels, reverberation time and speech level seemed to affect word intelligibility scores. The word intelligibility scores for 1.0 s (open triangles) and 2.0 s (open squares) were lower than those for 0.5 s (open circles), particularly for lower speech levels. The word intelligibility scores for the highest speech levels seemed to be lower than those for other speech levels for all reverberation times, except those for the lowest speech level for the reverberation times of 1.0 and 2.0 s, which also seemed to be lower than those for other speech levels. The results of ANOVA revealed that the main effect of speech level was significant for all reverberation times ($F(7,294)=2.6$, $F(7,294)=2.3$, and $F(7,294)=3.1$ for the reverberation times of 0.5, 1.0, and 2.0 s, respectively) at the 5% significant level. Tukey's honestly significant differences (HSDs) for the word intelligibility scores for the young were calculated to be 4.9, 8.1 and 8.2% ($p<0.05$) for the reverberation times of 0.5, 1.0 and 2.0 s, respectively. For the reverberation time of 0.5 s, the word intelligibility score for the highest speech level of 75.6 dBA was significantly lower than the maximum word intelligibility score. The scores for the lowest speech levels of 41.7 and 43.2 dBA for the reverberation times of 1.0 and 2.0 s, respectively, were significantly lower than the maximum word intelligibility score for each reverberation time. Therefore, the minimum speech levels to maximize word intelligibility scores for the young are 46.7 and 48.2 dBA for the reverberation times of 1.0 and 2.0 s, respectively.

Figure 4 represents the listening difficulty ratings for the young. The listening difficulty ratings for the young were affected by speech level and reverberation time, while word intelligibility scores for the young were almost never affected. The optimum speech levels that minimize listening difficulty ratings were 55.6, 56.7, and 53.2 dBA for the reverberation times of 0.5, 1.0, and 2.0 s, respectively. The minimum listening difficulty ratings increased with increasing reverberation time, and they were 26, 51 and 61% for the reverberation times of 0.5, 1.0, and 2.0 s, respectively. The results of ANOVA revealed that the main effect of speech level was significant for all reverberation times ($F(7,294)=17.2$, $F(7,294)=8.5$, and $F(7,294)=13.2$ for the reverberation times of 0.5, 1.0, and 2.0 s, respectively) at the 5% significant level. HSDs for the listening difficulty ratings for the young were calculated to be 14.4, 14.0 and 11.3% ($p<0.05$) for the reverberation times of 0.5, 1.0 and 2.0 s, respectively. The minimum listening difficulty ratings were not significantly different from the listening difficulty ratings for the speech levels from 50.6 to 60.6 dBA, from 46.7 to 66.7 dBA, and from 48.2 to 63.2 dBA for the reverberation times of 0.5, 1.0, and 2.0 s, respectively.

The word intelligibility scores for the ranges of speech level described above were maximized for all reverberation times. Therefore, in conclusion, the acceptable ranges of speech level for the young are from 50.6 to 60.6 dBA, from 46.7 to 66.7 dBA, and from 48.2 to 63.2 dBA for the reverberation times of 0.5, 1.0, and 2.0 s, respectively.

Although the optimum speech level for 2.0 s was rather smaller than those for 0.5 and 1.0 s, the optimum speech levels for reverberant and quiet sound fields were not very different from each other, or from the optimum speech level of 60 dBA for the reverberation-free and quiet sound field. The optimum speech level averaged over all sound fields used in the present study is 56.4 dBA. Kobayashi *et al.*[13] reported that the optimum speech level of direct sound was around 50–55 dBA in the sound field with the reverberation time of 0.5 s and the noise level less than 40 dBA. The reverberant sounds used by Kobayashi *et al.* are the same as those used in the present study. This means that the optimum speech level obtained by Kobayashi *et al.* would increase to around 55–60 dBA in the presence of the reverberant sounds. Therefore, the optimum speech level averaged over all sound fields used in the present study corresponds to the optimum speech level obtained by Kobayashi *et al.*[13] These

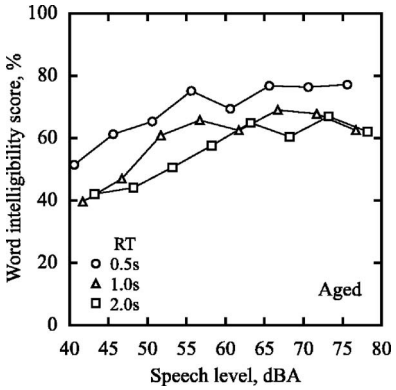

FIG. 5. The word intelligibility scores for the aged in reverberant and quiet sound fields. Open circles, triangles and squares represent the word intelligibility scores for the reverberation times of 0.5, 1.0 and 2.0 s, respectively.

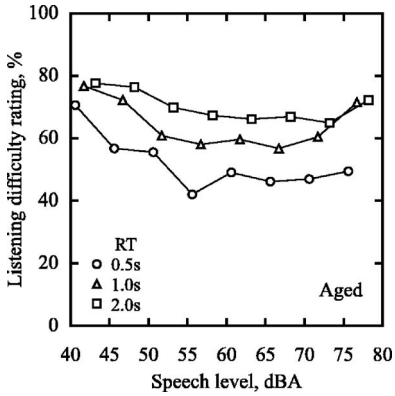

FIG. 6. The listening difficulty ratings for the aged in reverberant and quiet sound fields. Open circles, triangles and squares represent the listening difficulty ratings for the reverberation times of 0.5, 1.0 and 2.0 s, respectively.

results indicate that, for the young, the optimum speech level including reverberant sounds is not affected by reverberation time.

These results also indicate that the effect of reverberant sounds on the optimum speech level is different from that of noise. In general, MCL for noisy sound fields increases with increasing noise level.[6,7] Kobayashi *et al.*[13] also reported that the optimum speech level increased with increasing noise level, possibly because the detrimental energy of reverberant sounds also increases with increasing speech level. In other words, the speech-to-detrimental energy ratio is not improved by increasing the speech level in reverberant sound fields, while the ratio is improved in noisy sound fields.

2. Results for the aged

Figure 5 represents the word intelligibility scores for the aged. The word intelligibility scores for the aged increased with increasing speech level and seemed to be maximum at around 60 dBA. However, the word intelligibility scores for the aged did not exceed 80%, and the maximum scores were 77, 69, and 67% for 0.5, 1.0 and 2.0 s, respectively. The results of ANOVA revealed that the main effect of speech level was significant for all reverberation times ($F(7,336)=12.7$, $F(7,336)=12.5$, and $F(7,336)=12.7$, for reverberation times of 0.5, 1.0, and 2.0 s, respectively) at the 5% significant level. HSDs were calculated to be 11.2, 12.8 and 11.4% for the reverberation times of 0.5, 1.0 and 2.0 s, respectively. The results of multiple comparisons based on HSD revealed that the word intelligibility scores for the aged were not significantly different from the maximum scores for the speech levels above 55.6, 51.7 and 58.2 dBA for the reverberation times of 0.5, 1.0 and 2.0 s, respectively.

According to results of both tests I and II, the minimum speech level that maximizes word intelligibility seems to increase with increasing reverberation time. However, the minimum speech levels correspond to the speech levels of direct sound of 45, 50, 45, and 50 dBA for the reverberation times of 0.0 (reverberation-free), 0.5, 1.0 and 2.0 s, respectively. This suggests that the speech level of direct sound, or perhaps that of direct sound plus early reflections,[19] might determine the speech level that maximizes word intelligibility scores for the aged in reverberant and quiet sound fields, and also that the speech level of direct sound of at most 50 dBA is required to maximize the word intelligibility scores for the aged, regardless of reverberation time.

Figure 6 represents the listening difficulty for the aged. The listening difficulty ratings for the aged increased with increasing reverberation time. The minimum listening difficulty ratings were 42, 57, and 65% for the reverberation times of 0.5, 1.0, and 2.0 s, respectively. Although these increases in listening difficulty ratings by reverberant sounds seemed to limit the effect of speech level, the listening difficulty ratings for the aged decreased with increasing speech level, and seemed to be minimized when speech level exceeded around 50 or 55 dBA for all reverberation times. However, the optimum speech levels were unclear, because the curves of listening difficulty rating as a function of speech level for all reverberation times were too shallow and rough to visually determine a local minimum point. The results of ANOVA revealed that the main effect of speech level was significant for all reverberation times ($F(7,336)=9.9$, $F(7,336)=6.5$ and $F(7,336)=2.8$, for reverberation times of 0.5, 1.0, and 2.0 s, respectively) at the 5% significant level. HSDs for the listening difficulty ratings for the aged were calculated to be 12.2, 13.0, and 12.4% ($p<0.05$) for the reverberation times of 0.5, 1.0 and 2.0 s, respectively. The minimum listening difficulty rating was not significantly different from the listening difficulty ratings for the speech levels from 55.6 to 75.6 dBA, from 51.7 to 71.7 dBA, and from 48.2 to 78.2 dBA for the reverberation times of 0.5, 1.0, and 2.0 s, respectively.

The word intelligibility scores in the ranges of speech level described above were maximized, except for the reverberation time of 2.0 s. For the reverberation time of 2.0 s, the lower limit of the acceptable speech level that maximizes word intelligibility scores should be 58.2 dBA. In conclusion, the acceptable ranges of speech level for the aged are from 55.6 to 75.6 dBA and higher, from 51.7 to 71.7 dBA, and from 58.2 to 78.2 dBA and higher for the reverberation times of 0.5, 1.0, and 2.0 s, respectively.

IV. ACCEPTABLE SPEECH LEVEL FOR BOTH THE YOUNG AND THE AGED

Figure 7 represents the acceptable ranges of speech level for the young and the aged for the sound fields used in the

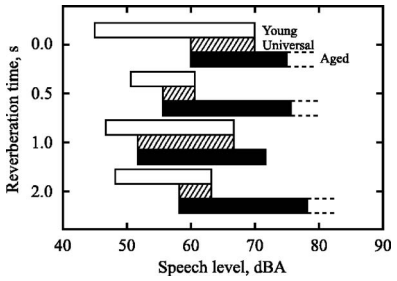

FIG. 7. The acceptable ranges of speech level for each of the sound fields. Open and closed bars represent the acceptable ranges for the young and the aged, respectively. The hatched bars represent the universally acceptable range.

present study. The acceptable ranges of speech level for the young and the aged overlap. This indicates that there is a universally acceptable range of speech level for both the young and the aged for each sound field. The universally acceptable ranges of speech level (the hatched range in Fig. 7) are from 60.0 to 70.0 dBA, from 55.6 to 60.6 dBA, from 51.7 to 66.7 dBA and from 58.2 to 63.2 dBA, for the reverberation times of 0.0, 0.5, 1.0, and 2.0 s, respectively. It is worth noting is a speech level that falls within all of the universally acceptable ranges of speech level obtained in the present study; the speech level is around 60 dBA.

Note that the acceptable speech level in the present study was obtained under quiet conditions. Considering the results reported by Heusden *et al.*[7] and Kobayashi *et al.*,[13] the acceptable speech level should be constant when the background noise level is less than 35 or 40 dBA. When the background noise level exceeds 40 dBA, the acceptable speech level increases with increasing background noise level.[6,7,13]

In the present study, the acceptable speech level was obtained only for three reverberant sound fields. The temporal, spectral, and spatial characteristics of reverberant sounds in public spaces are more complex than those of the three test sound fields. Further investigations are needed to clarify the effects of the characteristics of reverberant sounds on the upper and lower limits of the acceptable speech level.

The optimum speech level for the young might not be greatly affected by the characteristics of reverberant sounds. As described in the previous section, the results of the present study showed that the optimum speech level for the young was almost the same for the three test sound fields, and this might be because the speech-to-detrimental energy ratio under reverberant and quiet conditions was stable regardless of speech level. This indicates that the optimum speech level for the young might be determined by the loudness of speech sounds rather than the speech-to-detrimental energy ratio in reverberant and quiet conditions. Considering that loudness is determined solely by the sound pressures at the left and right ears,[20] the characteristics of reverberant sounds might not affect the optimum speech level for the young.

In the present study, single words controlled by word familiarity were used as test materials. However, the verbal information supplied by PA systems is generally in the form of sentences. It is important to discuss the difference between the acceptable speech level for single words and that for sentences to clarify the applicability of the present study. In the present study, the acceptable speech level is determined from both intelligibility scores and listening difficulty ratings. The results of the present study indicate that intelligibility scores are related to the lower limit of the acceptable speech level. Generally speaking, sentence intelligibility scores are higher than word intelligibility scores.[21] This means that a lower limit determined using word intelligibility scores would be on the safe side in real situations. Meanwhile, the results of the present study indicate that listening difficulty ratings are related to both the upper and lower limits of the acceptable speech level. It is surmised that the evaluation of listening difficulty would depend on discomfort due to loudness rather than audibility when the speech level is near the limits of the acceptable speech level. Because the minimum speech level to maximize word intelligibility scores was equal to or less than the lower limit of the acceptable speech level for almost all cases in the present study. It is expected that discomfort due to loudness for sentences would be similar to that for single words, if the peak levels in the two cases are equal. In conclusion, the acceptable range of speech level obtained using single words would be practically applicable to PA systems in public spaces.

V. CONCLUSION

The acceptable range of speech level for both the young with normal hearing level and the aged with age-appropriate hearing loss were investigated using word intelligibility scores and listening difficulty ratings in the reverberation-free and quiet sound field and three reverberant and quiet sound fields.

The acceptable ranges of speech level were obtained for each group of listeners and each sound field using ANOVA and Tukey's multiple comparison tests. The results indicated the following. (1) The acceptable ranges of speech level for the young are from 50 to 70 dBA, from 51 to 61 dBA, from 47 to 67 dBA and from 48 to 63 dBA for the test sound fields with reverberation times of 0.0 (reverberation-free), 0.5, 1.0, and 2.0 s, respectively. (2) The acceptable ranges of speech level for the aged are from 60 to 75 dBA and higher, from 56 to 76 dBA and higher, from 52 to 72 dBA and from 58 to 78 dBA and higher for the test sound fields with the reverberation times of 0.0, 0.5, 1.0, and 2.0 s, respectively.

The comparisons between the acceptable ranges of speech level for the young and the aged revealed that (1) the universally acceptable ranges of speech level are from 60 to 70 dBA, from 56 to 61 dBA, from 52 to 67 dBA and from 58 to 63 dBA for the test sound fields with the reverberation times of 0.0, 0.5, 1.0, and 2.0 s, respectively, and that (2) there is a speech level that falls within all of the universally acceptable ranges of speech level obtained in the present study; the speech level is around 60 dBA.

ACKNOWLEDGMENTS

The research project was partially supported by the research and development grant of Japan Institute of Construc-

tion and Engineering, 03011, 2004, and by Japan Society for the Promotion of Science, Grant-in-Aid for Scientific Research (B), 16360292, 2004–2006.

[1]L. L. Kopra and D. Blosser, "Effects of method of measurement on most comfortable loudness level for speech," J. Speech Hear. Res. **11**, 497–508 (1968).
[2]I. M. Ventry and R. W. Woods, "Most comfortable loudness for pure tones, noise, and speech," J. Acoust. Soc. Am. **49**, 1805–1813 (1971).
[3]K. W. Berger and J. F. Lowry, "Relationships between various stimuli for MCL," Sound **5**, 11–14 (1971).
[4]I. Hochberg, "Most comfortable listening for the loudness and intelligibility of speech," Audiology **14**, 27–33 (1975).
[5]I. Pollack, "Comfortable listening levels for pure tones in quiet and noise," J. Acoust. Soc. Am. **24**, 158–162 (1952).
[6]A. M. Richards, "Most comfortable loudness for pure tones and speech in the presence of masking noise," J. Speech Hear. Res. **18**, 498–505 (1975).
[7]E. V. Heusden, R. Plomp, and L. C. W. Pols, "Effects of ambient noise on the vocal output and the preferred listening level of conversational speech," Appl. Acoust. **12**, 31–43 (1979).
[8]C. A. Kamm, D. D. Dirks, and M. R. Mickey, "Effect of sensorineural hearing loss on loudness discomfort level and most comfortable loudness judgments," J. Speech Hear. Res. **21**, 668–681 (1978).
[9]I. M. Ventry and J. I. Johnson, "Evaluation of a clinical method for measuring comfortable loudness for speech," J. Speech Hear Disord. **43**, 149–159 (1978).
[10]B. J. Edgerton, R. C. Beattie, and J. W. Wides, "Loudness discomfort levels of hearing-impaired listeners using speech material," Ear Hear. **1**, 206–210 (1980).
[11]R. C. Beattie and V. G. Warren, "Relationships among speech threshold loudness discomfort, comfortable loudness, and PB max in the elderly hearing impaired," Am. J. Otol. **3**, 353–358 (1982).
[12]A. K. Nábělek and L. Robinette, "Influence of the precedence effect on word identification by normally hearing and hearing-impaired subjects," J. Acoust. Soc. Am. **63**, 187–194 (1978).
[13]M. Kobayashi, M. Morimoto, Hi. Sato, and Ha. Sato, "Optimum speech level to minimize listening difficulty in public spaces," J. Acoust. Soc. Am. **121**, 251–256 (2007).
[14]M. Morimoto, Hi. Sato, and M. Kobayashi, "Listening difficulty as a subjective measure for evaluation of speech transmission performance in public spaces," J. Acoust. Soc. Am. **116**, 1607–1613 (2004).
[15]ISO 7029:2000 *Acoustics-Statistical distribution of hearing threshold as a function of age* (International Organization for Standardization, Geneva, 2000).
[16]Ha. Sato, Hi. Sato, and M. Morimoto, "Effects of aging on word intelligibility and listening difficulty in various reverberant fields," J. Acoust. Soc. Am. **121**, 2915–2922 (2007).
[17]S. Sakamoto, Y. Suzuki, S. Amano, K. Ozawa, T. Kondo, and T. Sone, "New lists for word intelligibility test based on word familiarity and phonetic balance (in Japanese)," J. Acoust. Soc. Jpn. **54**, 842–849 (1998).
[18]J. W. Tukey, "The problem of multiple comparisons, Mimeographed Monograph (1953)," appears in full in *Collected Work of J.W Tukey*, edited by H. Braun (Chapman and Hall, New York, 1994), Vol. VII.
[19]J. Bradley, Hi. Sato, and M. Picard, "The importance of early reflections for speech intelligibility in rooms," J. Acoust. Soc. Am. **113**, 3233–3244 (2003).
[20]D. W. Robinson and L. S. Whittle, "The loudness of directional sound fields," Intell. Data Anal. **10**, 74–80 (1960).
[21]G. A. Miller, G. A. Heise, and W. Lichten, "The intelligibility of speech as a function of the context of the test materials," J. Exp. Psychol. **41**, 329–335 (1951).

The room acoustic rendering equation

Samuel Siltanen,[a] Tapio Lokki, Sami Kiminki, and Lauri Savioja
Telecommunications Software and Multimedia Laboratory, Helsinki University of Technology, P.O. Box 5400, FIN-02015 HUT, Finland

(Received 3 October 2006; revised 4 July 2007; accepted 5 July 2007)

An integral equation generalizing a variety of known geometrical room acoustics modeling algorithms is presented. The formulation of the room acoustic rendering equation is adopted from computer graphics. Based on the room acoustic rendering equation, an acoustic radiance transfer method, which can handle both diffuse and nondiffuse reflections, is derived. In a case study, the method is used to predict several acoustic parameters of a room model. The results are compared to measured data of the actual room and to the results given by other acoustics prediction software. It is concluded that the method can predict most acoustic parameters reliably and provides results as accurate as current commercial room acoustic prediction software. Although the presented acoustic radiance transfer method relies on geometrical acoustics, it can be extended to model diffraction and transmission through materials in future. © *2007 Acoustical Society of America.*
[DOI: 10.1121/1.2766781]

PACS number(s): 43.55.Ka, 43.55.Br, 43.20.Dk [NX] Pages: 1624–1635

I. INTRODUCTION

There are various methods for geometrical room acoustics modeling, such as the image source,[1,2] ray tracing,[3] beam tracing,[4] and acoustic radiosity[5–9] methods. Although they have certain similarities, their theoretical foundations are often derived for each method separately. These techniques rely heavily on ray optics and methods borrowed from computer graphics.

In this paper a proper foundation for geometrical room acoustics modeling is introduced. An integral equation, which generalizes a variety of known geometrical room acoustics modeling methods, is constructed. In addition, a novel modeling method, based on the radiosity method, is derived by utilizing the presented theoretical basis. This acoustic radiance transfer solution is shown to be applicable to model sound propagation in realistic, complex environments having surfaces of various materials. A comparison with actual measurement data and data predicted by other acoustics modeling software is given.

In the following, the related work to motivate the proposed room acoustic rendering equation is overviewed. After this, the equation is constructed piece by piece. Next, the widely used geometrical room acoustics modeling methods are shown to be specializations of the proposed general model. The acoustic radiance transfer is introduced with the algorithm description and experimental validation. Finally, possible extensions and future work are discussed.

II. RELATED WORK

Computer graphics models the propagation of light in an environment. The speed of light is, in most cases, assumed to be infinite, which is, in practice, a safe assumption since no information can travel faster than light. Sound, however, has to be modeled as waves propagating at finite speed. In room acoustics, the time dependence, due to propagation delays, also has to be modeled. Thus, the room acoustic rendering equation proposed here can be seen as a time-dependent extension of Kajiya's "rendering equation".[10] The formulation used by Kajiya is rarely seen, and in the modern form the rendering equation can be written as[11]

$$L(x \to \Theta) = L_e(x \to \Theta) + \int_A f_r(x, \Psi \to \Theta) \times L(y \to -\Psi) V(x,y) G(x,y) \mathrm{d}A_y, \quad (1)$$

where $L(x \to \Theta)$ is the outgoing radiance from x in the direction Θ. $L_e(x \to \Theta)$ is the emitted radiance from point x in the direction Θ, $G(x,y)$ is a geometry term, $V(x,y)$ is a visibility term, and $f_r(x, \Psi \to \Theta)$ is a bidirectional reflectance distribution function. The meaning of the corresponding terms is explained in the context of the time-dependent form presented in the next section.

Since the goal of the presented room acoustics modeling method is to model arbitrary reflections, a flexible representation is required for the reflections. In computer graphics, bidirectional reflectance distribution functions (BRDFs) are widely used to accurately describe the reflections from different types of materials.[12] Figure 1 shows an example of a BRDF representing nontrivial reflection properties of a material. Combining BRDFs with the radiosity method has been discussed, and the radiosity solution has been extended to handle some nondiffuse reflections in time-independent form.[13,14] The directional resolution of the solution greatly affects the quality of the final image, and because the memory requirements set serious restrictions on the resolution, these techniques have not been applied to computer graphics to a great extent.

Usually, in sound rendering, either scattering coefficients or diffusion coefficients, in addition to the absorption coefficients, are used to describe the properties of the reflec-

[a]Author to whom correspondence should be addressed. Electronic mail: samuel.siltanen@tml.hut.fi

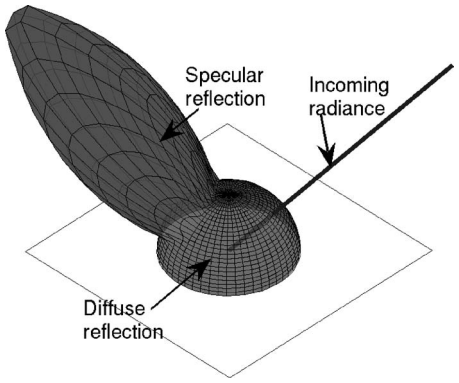

FIG. 1. A BRDF represents the directional distribution of the reflected energy for each incoming angle. Here the distribution for one angle is shown.

tions from acoustic materials.[15] However, although there is measurement data of the directional distribution of acoustic reflections, the data are paradoxically used to construct random-incident scattering coefficients thus losing the directional information.[16] There is no clear reason why the complete data of acoustic BRDFs could not be utilized. In this paper BRDFs are applied and it is shown how the BRDF models are constructed from the absorption and scattering coefficients given at each frequency band.

The time-dependent directional extension of the radiosity method is similar to the directional extensions in computer graphics,[13,14] but because the chosen BRDF representation and the application area are different from the previous work, the extension is derived from the presented theoretical basis. Due to the time dependence, one additional dimension is required, which increases computational requirements. To compensate this, the resolution of the directional data can be reduced since human hearing cannot localize the direction of sounds as accurately as vision can detect the direction of light.

III. ROOM ACOUSTIC RENDERING EQUATION

The acoustic energy propagation model presented here models the propagation of acoustic energy in an enclosure. The model is derived by beginning from the reflectance function and concluding with the room acoustic rendering equation. The detection of the acoustic energy by a receiver is presented. Then the issue of frequency dependence is covered, and limitations of the energy-based approach are discussed. The construction of equations is based on a MSc thesis by Kiminki (http://www.niksula.hut.fi/~skiminki/D-skiminki.pdf).

A. Terminology

In this paper, the terminology established in optics and computer graphics is used, because this way the analogy between those disciplines and room acoustics can be readily utilized. *Intensity* I is the intensity of energy flux. *Irradiance* $E(x,\Omega)$ is the incident power on point x on a surface from direction Ω, and *radiance* $L(x,\Omega)$ is the radiant power per unit projected area per unit solid angle. Symbols $E(x,\Omega,t)$ and $\ell(x,\Omega,t)$ are used for time-dependent irradiance and radiance, respectively, to emphasize the time dependence. For clarity, some of the parameters may be omitted in the construction below.

B. Reflectance distribution function

The reflectance function describes the directional distribution of the energy arriving at a surface point from a specified incident angle. This can be written in the form of an acoustic BRDF $\rho(\Omega_i,\Omega_e;x')$ at point x' for incident angle Ω_i and outgoing angle Ω_e. Analogously to the BRDF in optics,[12] this six-dimensional function can be defined at point x' as the ratio of the differential radiance reflected in an outgoing direction, and the differential irradiance incident through a differential solid angle

$$\rho(\Omega_i,\Omega_e;x') = \frac{dL(\Omega_e)}{dE(\Omega_i)}. \tag{2}$$

It is essential to note that the BRDF describes the acoustic material of the surface. By utilizing various BRDFs, modeling different types of reflections is possible. In this paper the BRDFs are assumed time invariant. The BRDF can be written in polar form as $\rho''(\theta_i,\phi_i,\theta_e,\phi_e;x')$ where the θ's are the azimuth angles and the ϕ's are the elevation angles.

C. Propagation operator

The operator $\hat{S}_r$ represents propagation effects on sound radiation over distance r. For an absorptive linear medium it is defined as

$$\hat{S}_r I(t) = e^{-\alpha r} S_r I(t) = e^{-\alpha r} I\left(t - \frac{r}{c}\right), \tag{3}$$

where c is the speed of sound and α is the absorption coefficient. For a nonabsorptive medium, $\alpha=0$, in which case the operator is denoted as S_r.

It is assumed that the sound is emitted as an impulse at $t=0$ and is denoted by the Dirac delta function $\delta(t)$. Thus, the following properties hold:

$$\hat{S}_r[\lambda\delta(t) + \mu\delta(t)] = [\lambda\hat{S}_r + \mu\hat{S}_r]\delta(t), \tag{4}$$

$$\hat{S}_{r_1}\hat{S}_{r_2}\delta(t) = \hat{S}_{r_1+r_2}\delta(t), \tag{5}$$

$$\hat{S}_r\delta(t) = e^{-\alpha t c} S_r\delta(t). \tag{6}$$

Equations (4) and (5) justify combining the propagation operators when all the reflections are specular. The intensity at any point is essentially the sum of intensities transmitted through the direct path and the reflections reaching that point. Further, the linearity property enables differentiation, and, therefore, S_r may be used on irradiance and radiance as well.

By using Eq. (6), considering only the response of the impulse energy in the reflection calculation and applying later the effects of air absorption and treatment of an arbitrary source signal is allowed:

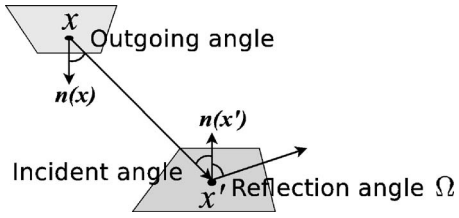

FIG. 2. The geometry term calculation between points x and x'. Surface normals at these points are $\mathbf{n}(x)$ and $\mathbf{n}(x')$ correspondingly. Thus the cosine of the incident angle at point x' equals $\mathbf{n}(x')\cdot(x-x')|x-x'|^{-1}$ and the cosine of the outgoing angle at point x equals $\mathbf{n}(x)\cdot(x'-x)|x'-x|^{-1}$. These factors, in addition to the propagation operator $S_{|x-x'|}$ and the quadratic falloff, determine the geometry term.

$$I(t)=\left[\sum_n \beta_n S_{r_n}\delta(t)\right]*e^{-\alpha tc}I_0(t)=\mathcal{H}\sum_n \beta_n S_{r_n}\delta(t), \tag{7}$$

where $I_0(t)$ is the emission intensity varied over time, β_ns are the reflection coefficients, r_ns are the lengths of reflection paths, and $I(t)$ is the detected intensity. $\mathcal{H}$ is defined for convenience to incorporate the effects of air absorption and the arbitrary source.

D. Reflected radiance and geometry term

A geometry term g, similar to that in Eq. (1), is also required in acoustics to describe the effects of the geometry on the acoustic energy flow. It can be derived from the situation depicted in Fig. 2. The differential solid angle $\mathrm{d}\omega_\Theta$, in which the differential irradiance is arriving from point x at point x', can be expressed using the differential area $\mathrm{d}A_x$ in the neighborhood of x as[17]

$$\mathrm{d}\omega_\Theta=\left|\mathbf{n}(x)\cdot\frac{x'-x}{|x'-x|}\right|\frac{\mathrm{d}A_x}{|x-x'|^2}. \tag{8}$$

The differential radiance reflected from x' to direction Ω is

$$\mathrm{d}\,\ell\,(x',\Omega)=\rho(\mathrm{d}\omega_\Theta,\Omega;x')\mathrm{d}\varepsilon(x',\mathrm{d}\omega_\Theta). \tag{9}$$

The differential incident irradiance $\mathrm{d}\varepsilon(x',\mathrm{d}\omega_\Theta)$ may be substituted with $S_{|x'-x|}\ell\,(x,-\mathrm{d}\omega_\Theta)[\mathbf{n}(x')\cdot(x-x')|x-x'|^{-1}]\mathrm{d}\omega_\Theta$, thus yielding

$$\mathrm{d}\,\ell\,(x',\Omega)=\rho(\mathrm{d}\omega_\Theta,\Omega;x')S_{|x-x'|}\,\ell\,(x,-\mathrm{d}\omega_\Theta)\times\left|\mathbf{n}(x')\cdot\frac{x-x'}{|x-x'|}\right|\left|\mathbf{n}(x)\cdot\frac{x'-x}{|x'-x|}\right|\frac{\mathrm{d}A_x}{|x-x'|^2} \tag{10}$$

By defining the *acoustic geometry term* as

$$g(x,x')=\left|\mathbf{n}(x)\cdot\frac{x'-x}{|x'-x|}\right|\left|\mathbf{n}(x')\cdot\frac{x-x'}{|x-x'|}\right|\frac{S_{|x-x'|}}{|x-x'|^2}, \tag{11}$$

the differential reflected radiance can be written as

$$\mathrm{d}\,\ell\,(x',\Omega)=\rho(\mathrm{d}\omega_\Theta,\Omega;x')g(x,x')\,\ell\,(x,-\mathrm{d}\omega_\Theta)\mathrm{d}A_x. \tag{12}$$

Thus, the acoustic geometry term g is the geometry term used in computer graphics[10] combined with the propagation operator.

E. Visibility term

To make the model applicable to nonconvex geometries, it is necessary to include a visibility term. The visibility term $\mathcal{V}(x,x')$ is defined as follows:

$$\mathcal{V}(x,x')=\begin{cases}1, & \text{when the line between } x \text{ and } x' \\ & \text{is unobstructed} \\ 0, & \text{otherwise.}\end{cases} \tag{13}$$

F. Reflection kernel

The reflectance function, the geometry term, and the visibility term together can be used to describe the reflection from point x via point x' into direction Ω (see Fig. 2) as

$$R(x,x',\Omega)=\mathcal{V}(x,x')\rho\left(\frac{x-x'}{|x-x'|},\Omega;x'\right)g(x,x'). \tag{14}$$

This is the *reflection kernel* of the room acoustic rendering equation defined in the next section. Note that the propagation operator $S_{|x-x'|}$ is contained in the acoustic geometry term.

G. Room acoustic rendering equation

Since the outgoing time-dependent radiance at any point is a combination of the reflected time-dependent radiance, as defined by Eq. (12), and the emitted time-dependent radiance, the acoustic radiance propagation in an enclosure can be written in the form of the *room acoustic rendering equation*

$$\ell\,(x',\Omega)=\ell_0(x',\Omega)+\int_{\mathcal{G}}R(x,x',\Omega)\,\ell\left(x,\frac{x'-x}{|x'-x|}\right)\mathrm{d}x, \tag{15}$$

where $\mathcal{G}\subset\mathbb{R}^3$ is the set of all surface points in the enclosure and $\ell(x',\Omega)$ is the outgoing time-dependent radiance from point x' in direction Ω. The equation has the Neumann series solution[10]

$$\ell_{n+1}(x',\Omega)=\int_{\mathcal{G}}R(x,x',\Omega)\ell_n\left(x,\frac{x'-x}{|x'-x|}\right)\mathrm{d}x,$$

$$\ell\,(x',\Omega)=\sum_{n=0}^{\infty}\ell_n(x',\Omega). \tag{16}$$

In the case of an area source, ℓ_0 represents the radiance emitted by the surface. For point sources, ℓ_0 is considered as the primary reflected radiance instead of defining the source as a part of the surface geometry to make the analysis more convenient. By denoting the position of the source by x_s and the time-dependent intensity of outgoing energy at angle Ω by $P_s(\Omega,t)$, the time-dependent irradiance from the source to point x can be calculated to be

$$\varepsilon(x)=\mathcal{V}(x,x_s)\frac{S_{|x-x_s|}P_s\left(\frac{x-x_s}{|x-x_s|},t\right)}{4\pi|x-x_s|^2}\left|\mathbf{n}(x)\cdot\frac{x_s-x}{|x_s-x|}\right|, \tag{17}$$

giving the point the primary reflected radiance

$$\ell_0(x,\Omega) = \rho\left(\frac{x_s - x}{|x_s - x|}, \Omega, x\right)\mathcal{V}(x_s,x)g_0(x_s,x)P_s\left(\frac{x - x_s}{|x - x_s|}, t\right), \tag{18}$$

where g_0 is defined as

$$g_0(x_s,x) = \left|\mathbf{n}(x) \cdot \frac{x_s - x}{|x_s - x|}\right| \frac{S_{|x_s - x|}}{4\pi|x_s - x|^2}. \tag{19}$$

For an omnidirectional point source emitting a unit impulse, the outgoing energy is defined as $P_s(\Omega,t) = \delta(t)$.

H. Detection

For a point receiver, the detection is straightforward. Conceptually, the receiver can be considered as an infinitesimally small sphere, the surface of the sphere detecting only the energy incident from the direction of the surface normal. Additionally, the receiver has a detection transfer function $\Delta(\Omega, I)$ which maps the incident energy arriving from a specific direction to detection, thus taking the possible directional sensitivity pattern into consideration. Since the room acoustic rendering equation models the interaction between surface points only, the direct and indirect sound energy detection have to be handled separately for a receiver that is not part of the geometry. The detection is the sum of the detection of the direct and reflected sound energy

$$d(t) = d_{\mathrm{D}}(t) + d_\ell(t), \tag{20}$$

where $d_{\mathrm{D}}(t)$ is the detection of the directly detected point source and $d_\ell(t)$ is the detection of the reflected radiance

$$d_{\mathrm{D}}(t) = \Delta\left(\frac{x_{\mathrm{r}} - x_s}{|x_{\mathrm{r}} - x_s|}, \mathcal{H}\mathcal{V}(x_s,x_r)\frac{S_{|x_r - x_s|}}{4\pi|x_r - x_s|^2}P_s\left(\frac{x_r - x_s}{|x_r - x_s|}\right)\right), \tag{21}$$

$$d_\ell(t) = \int_{\mathcal{G}} \Delta\left(\frac{x_r - x}{|x_r - x|}, \mathcal{H}\mathcal{V}(x,x_r)\frac{S_{|x_r - x|}}{|x_r - x|^2}\,\ell\left(x, \frac{x_r - x}{|x_r - x|}\right) \times \left|\mathbf{n}(x) \cdot \frac{x_r - x}{|x_r - x|}\right|\right) \mathrm{d}x, \tag{22}$$

where x_r is the position of the receiver, x_s is the position of the point source.

I. Frequency dependence

Until now, the frequency dependence in reflections and detection has not been considered. A widely applied technique in room acoustics modeling is to divide the analysis into subbands and consider each subband separately. This technique is valid as long as the subbands can be considered orthogonal, i.e., having no mutual interaction as is the case in typical room acoustics. Thus, the reflections and medium must be linear, as nonlinearity causes harmonics in the signal.

J. Fundamental limitations

The presented model uses energies instead of pressure disturbances as in the wave field analysis. Therefore, phase information is not included in the model. The energy field approach was chosen since there are difficulties in modeling a general reflection for wave fields. In the case of ideal specular reflections, it is possible to construct a reflection model for a wave field, which has been used in, e.g., the image source method.[1] However, the task is nontrivial in the case of arbitrary reflections presented as BRDFs.

IV. SPECIALIZATIONS OF THE MODEL

In this section the different geometrical room acoustics modeling methods are shown to be specializations of the general model given in the previous section. The visibility and acoustic geometry terms remain mostly unchanged while the reflectance function varies from method to method. Most of the commercially available acoustics prediction software are hybrids of the techniques presented below.[18,19]

A. Image source method

In the basic image source method only the specular reflections are modeled. It can be extended to handle diffraction and scattering,[20] but, for simplicity, only the basic method is covered in the following discussion. The phase information can be taken into account, although, in practice, the calculations are often done only with energies. For a rectangular room there exists an exact solution.[21] That solution can also be derived from the presented model by using the Neumann series formulation in Eq. (16). With more complex geometries the solution can be approximated by using the first n terms of the Neumann series, thus modeling the specular reflections up to the nth order.

The ideal specular reflectance function used in the image source method is

$$\rho_{\mathrm{spec}}(\Omega_{\mathrm{i}}, \Omega_{\mathrm{e}}; x) = \frac{\beta(x)}{\Omega_{\mathrm{i}} \cdot \mathbf{n}(x)}\delta(\Omega_{\mathrm{i}} - M(\Omega_{\mathrm{e}})), \tag{23}$$

where δ is the Dirac delta function, M is the mirror reflection transformation $M(\theta,\phi) = (\theta, \pi - \phi)$, and the reflectivity coefficient $\beta = 1 - \alpha$ for the absorption coefficient α. The inverse of the dot product is added to compensate the Lambertian cosine term included in the geometry term.

The beam tracing method[4] falls into the same category of acoustics modeling methods because it is used to find specular reflections also. Basically, it is simply an optimization of the visibility function computation, which is the same as in the general case.

B. Ray tracing method

There are several types of ray tracing methods which can be used in room acoustics modeling. Some methods model only specular reflections.[3] The reflection kernel is then similar to that of the image source method. One approach to improve the accuracy is to include nonspecular reflections in ray tracing.[22] This way ray tracing is essentially a numerical solving method for the reflection-iterative construction of the room acoustic rendering equation. A large number of rays is required to accurately model the sound field. Each ray can be thought of as carrying a small portion of the energy emitted

by the source. The current energies of the rays hitting the receiver are then collected to construct the energy response for the emitted impulse. From this point of view, ρ defines the reflection probability distribution so that a reflection from a ray incident with angle Ω_i is reflected into direction Ω_e with probability $\xi(\omega_i, \omega_e)$, which is the biconical reflectance factor

$$\xi(\omega_i, \omega_e) = \left(\int_{\omega_i} \cos\,\theta_i d\omega_i \right)^{-1} \times \int_{\omega_e} \int_{\omega_i} \rho(\Omega_i, \Omega_e) \cos\,\theta_i \cos\,\theta_e d\omega_e d\omega_i, \quad (24)$$

where θ_i and θ_e are the elevation angles of Ω_i and Ω_e, respectively. This evaluates the average reflectance when the incident radiation comes from a set of directions ω_i and is reflected in a set of directions ω_e. The solid angles covered by the sets of incoming and outgoing radiance are dependent on the implementation. Because integrating ρ over a hemisphere of outgoing angles gives $1-\alpha$ the ray is terminated with probability α thus correctly modeling absorption.

C. Radiosity method

The radiosity method can be derived from the room acoustic rendering equation by using the diffuse reflectance function

$$\rho_{\text{diff}}(x) = \beta(x)/\pi, \quad (25)$$

where β is the reflectivity coefficient of the material at point x. This simplifies the room acoustic rendering equation by omitting the directional dependence. Then, discretizing the geometry $\mathcal{G}$ into patches transforms the room acoustic rendering equation into the matrix form discussed in the next section.

D. Sonel mapping

Sonel mapping technique[23] uses the same framework as the photon mapping technique[24] in computer graphics. The BRDFs are assumed to be combinations of specular and diffuse reflections. A stochastic approach is used where a large number of "sonels" are used for carrying a portion of the acoustic energy sent by the sound source through their reflection paths which consist of ideal specular and diffuse reflections. The reflection paths ending in a diffuse reflection are modeled by the sonel map constructed in the first phase of the algorithm. The specular reflections from the sound source or from the diffuse surfaces are modeled by using distributed ray tracing. It is possible to split the integral in the room acoustics rendering equation in two parts based on whether the last reflection is diffuse or specular, and thus the sonel mapping algorithm can also be seen as a special case of it. Only the diffraction modeling requires special treatment.

V. ACOUSTIC RADIANCE TRANSFER METHOD

In this section, the progressive radiosity solution[25] of the rendering equation in computer graphics is extended to solve the room acoustic rendering equation. In addition, the radiosity algorithm is further extended to handle arbitrary materials represented by BRDFs, thus extending the radiosity method to model the general acoustic radiance transfer. The reflection models and their construction are discussed in the context of the directional extension.

A. Temporal extension

The derivation of the theoretical framework for the method can be started with discretizing the geometry $\mathcal{G}$ into a finite number of *patches*, N. The surface of the patch i is denoted by A_i. Rewriting Eq. (16) using patches yields

$$\ell_{n+1}(x', \Omega) = \sum_{i=1}^{N} \int_{A_i} R(x, x', \Omega) \ell_n \left(x, \frac{x'-x}{|x'-x|} \right) dx. \quad (26)$$

By assuming planar patches, the average time-dependent reflected radiance of patch i can be written as

$$\ell_n^i(\Omega) = A_i^{-1} \int_{A_i} \ell_n(x, \Omega) dx \quad (27)$$

Using this approximation, Eq. (26) can be written as

$$\ell_{n+1}^j(\Omega) = A_j^{-1} \sum_{i=1}^{N} \int_{A_j} \left[\int_{A_i} R(x, x', \Omega) \ell_n^i \left(\frac{x'-x}{|x'-x|} \right) dx \right] dx', \quad (28)$$

where point x' is located on patch j. The next step is to discretize the reflection kernel. For this, the surface-side hemisphere of a reflection point is divided into a finite number of segments. The segments are denoted as $\vartheta_j(k)$. A discretizing projection operator $\hat{\Gamma}_j(\Omega)=k$ maps direction Ω into segment index k. Using this discretization, the reflection operator is written as

$$\hat{R}(i,j,k) = \frac{\int_{A_i} \left[\int_{A_j} \left[\int_{\vartheta_j(k)} R(x, x', \Omega) d\Omega \right] dx' \right] dx}{\int_{A_i} dx \int_{A_j} dx' \int_{\vartheta_j(k)} d\Omega} \quad (29)$$

and the emitted radiance as $\hat{\ell}_n^i(k)$. The discretized reflection operator $\hat{R}$ can be approximated using, e.g., Monte Carlo methods. Using the discretized reflection operator and radiance, Eq. (28) can be written as

$$\hat{\ell}_{n+1}^j(k) = A_j^{-1} \sum_{i=1}^{N} \int_{A_j} \left[\int_{A_i} \hat{R}(i,j,k) \hat{\ell}_n^i \left(\hat{\Gamma}_i \left(\frac{x'-x}{|x'-x|} \right) \right) dx \right] dx' = \sum_{i=1}^{N} F_{i,j} \hat{\ell}_n^i. \quad (30)$$

The operator $F_{i,j}$ is a linear mapping that maps the emitted or reflected energy from patch i into reflected energy from patch j with appropriate time shifting and temporal spreading. If the patches are assumed small compared to the distance between them, temporal spreading may be ignored and the average distance may be used as an approximation for the distance between points in the patches. $F_{i,j}$ may now be represented by a time-shifting operator combined with a dis-

cretized energy distribution mapping. If $\hat{\ell}_n^j$:s are collected into vector ϕ_n and $F_{i,j}$:s into matrix F,

$$\phi_n = \begin{pmatrix} \hat{\ell}_n^1 \\ \vdots \\ \hat{\ell}_n^N \end{pmatrix}, \quad F = \begin{pmatrix} F_{1,1} & \cdots & F_{1,N} \\ \vdots & \ddots & \vdots \\ F_{N,1} & \cdots & F_{N,N} \end{pmatrix}, \quad F_{j,j} = 0, \tag{31}$$

then the nth order reflected energy can be mapped into the reflected energy of order $n+1$ as

$$\phi_{n+1} = F\phi_n. \tag{32}$$

Finally, after discretizing time in F and ϕ, the acoustic rendering equation is completely discretized for computation

$$\phi = \sum_{i=0}^{\infty} F^i \phi_0 = \phi_0 + \sum_{i=1}^{\infty} F^i \phi_0. \tag{33}$$

The sum with infinite number of terms in Eq. (33) can be rewritten by utilizing the properties of geometric series

$$\phi = \phi_0 + (I - F)^{-1} \phi_0. \tag{34}$$

If the elements of matrix F contained only real numbers, it could be possible to use standard mathematical methods which are guaranteed to converge, such as Gauss-Seidel or Jacobi methods, for computing the numerical solution. Now, the delay operator in the acoustic geometry term complicates the situation since the elements of matrix F are not real numbers and the elements of vector ϕ are time-dependent responses. The delay operator, however, does not prevent utilizing other techniques, such as progressive refinement.[25] Instead of single energy values, time-dependent energy responses, representing the outgoing energy, are stored for each patch. The responses can be discretized by using an appropriate sampling rate for the convolution required in the detection to be efficient enough. Since the sound energy left in an enclosure asymptotically approaches zero as a function of time, it is practical to cut the tail of the response when the energy is likely to stay below some threshold value.

Equation (30) would yield the accurate form factor $F_{i,j}$, but in practice the analytical solution is too difficult to calculate. To keep the numerical solution simple and efficient, it is assumed that the integrand in Eq. (30) varies very little over patch i. Then, the area-to-area form factor can be approximated by the differential-to-finite-area form factor.[26] The accuracy which is required by the target application and the computational complexity which can be afforded determine the choice of the approach. In this case, Monte Carlo integration is used since it is simple and, in most cases, accurate enough.

B. Directional extension

The reflectance function ρ can be an arbitrary BRDF. The directional information is discretized using a hemisphere divided into solid angles, as shown in Fig. 5. The BRDFs are thus approximated by the discretized reflectance functions $\hat{\rho}(i,j,k,l;x)$, where i and k are integers in the range $[0,n-1]$ and j and l are integers in the range $[0,m-1]$ when the hemisphere is divided into n azimuth angles and m elevation angles. The discretized values are computed as integrals over the outgoing directional segment with the average angle of the incoming segment. The results approach the accurate values when the discretization resolutions n and m approach infinity. The discretizations of the BRDFs are precalculated to make the evaluation of the reflection kernel fast at run time.

The patches do not contain only one energy response but $m \times n$ energy responses, one for each solid angle. When a patch receives energy from direction (i,j) the distribution values of the reflectance function $\hat{\rho}(i,j,\cdot,\cdot;x)$ are scaled by the received energy and added to the directional responses. Thus, only the outgoing energies have to be saved.

Because there is no measured acoustic BRDF data available, the BRDFs can be constructed using the absorption and scattering coefficients given to the materials. The idea is to blend the ideal diffuse BRDF and the ideal specular BRDF

$$\rho(\Omega_i,\Omega_e;x) = (1-s)\rho_{\text{spec}}(\Omega_i,\Omega_e;x) + s\rho_{\text{diff}}(x), \tag{35}$$

where ρ_{spec} and ρ_{diff} are as in Eqs. (23) and (25), weighted with the scattering coefficient s. When this is discretized as explained above, the specular direction spreads into the whole solid angle. Thus it is called "pseudospecular" reflection in the rest of the paper. Modeling the specular reflection explicitly could be done as in computer graphics,[14] but this is likely to cause an explosion in the computational requirements since most of the surfaces have the specular component. When using isotropic BRDFs which do not vary over the surface, only three dimensions are needed since the surface coordinates and the incoming azimuth angle can be omitted.

C. Algorithm description

The algorithm follows the structure of the progressive radiosity algorithm.[25] Figure 3 gives the pseudocode of the algorithm. At the main level (see section A in Fig. 3), the algorithm consists of three phases: initial shooting, iterative energy propagation, and final gathering. Figure 4 shows a visual representation of the algorithm in progress.

The first step is to distribute the energy from each sound source to all visible patches. In this case the differential-to-finite-area form factor is accurate if the sources are assumed to be point-like. However, the proposed method easily allows modeling area sound sources with patches emitting sound. In addition, volumetric sound sources can be modeled by handling their bounding surfaces as area sound sources. Sound source directivity can be taken into account at this phase by weighting the outgoing energy flow according to the sound source directivity pattern.

The energy is propagated between the patches until the solution converges, i.e., the total unshot energy drops below a desired threshold value. Assuming that at least one of the patches absorbs energy, the energy will approach zero. In addition, since in the implementation the response length is limited, the speed of sound is finite, and the distances between the patches are nonzero, it follows that after some time no energy is propagated between the patches anymore.

At every iteration, patch P with the highest unshot energy is chosen. This can be done in constant time by using an

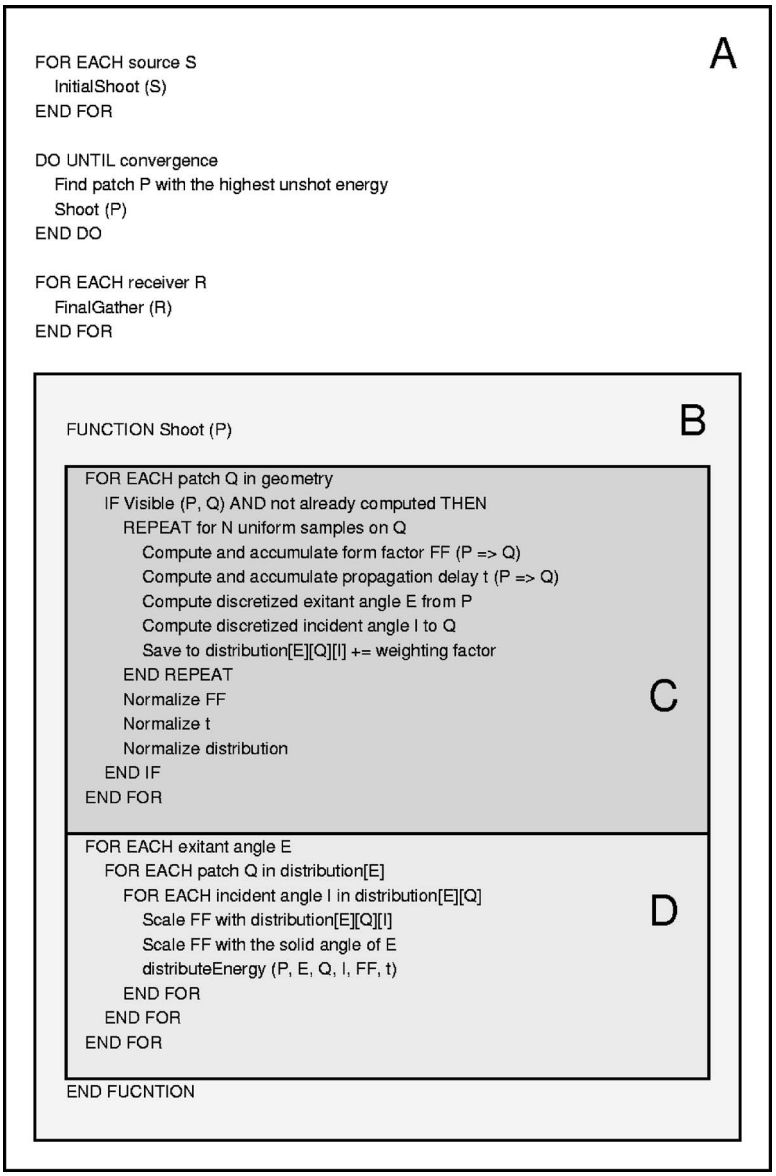

FIG. 3. Pseudocode describing the algorithm.

ordered data structure. The unshot energy of patch P is then distributed (see section B in Fig. 3). If there exists previously computed data for that patch they can be used directly. Otherwise, each patch Q, that is even partially visible to patch P, is sampled uniformly for the Monte Carlo integration (see section C in Fig. 3). The weighted form factors and propagation delays from the centroid of patch P to each sample on patch Q are accumulated and normalized to get the final results. During this process the information about the discretized outgoing angles at patch P and the incoming angles at patch Q is computed and stored into a structure indexed by the outgoing angle, target patch, and the incoming angle. Then, it is straightforward to go through each outgoing direction at patch P and find the corresponding incident direction for each outgoing direction at patch Q, and weight the form factors according to the outgoing solid angle and the proportion of it covered by the incident solid angle at the receiving patch (see section D in Fig. 3). The energy responses are then combined, which is the most time-consuming part of the algorithm when the responses consist of thousands of samples. To better simulate high frequencies, air absorption is introduced.[27] It is embedded in the calculation by weighting the accumulated responses according to the absorption factors for the distance between the patches.

The final gathering phase can be seen as the opposite of the initial shooting. The energy responses from all visible patches are accumulated for each listener. The Monte Carlo integration is different, however. The form factor and propagation delay values are not accumulated and normalized, but used in convolving the responses from individual samples directly. The directional information is thus better preserved in the accumulated response. In addition, the directional information can be saved explicitly, or it can be used to weight the incoming energy to emulate microphones with different directivities or head related transfer functions.

The number of sound sources affects only the complexity of the initial shooting. Since the initial shooting is a fast operation, modeling multiple sound sources with the same emitted signal at once takes practically the same total time as modeling only one sound source.

It is worth noting that the solution stored in patches is view independent, and thus only the final gathering operation

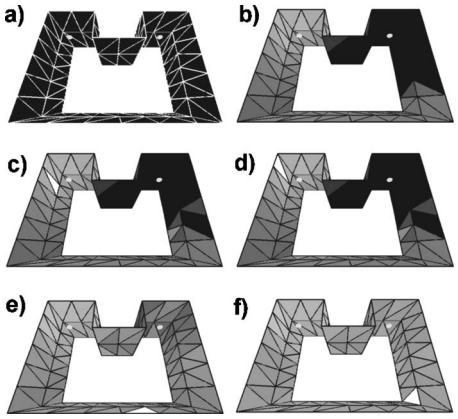

FIG. 4. The progressive radiance transfer solution. (a) The model without floor and ceiling before the initial shooting, where the source is the light dot on the left and the receiver is the dot on the right. (b) The model after the initial shooting, where the lightness of the patch is proportional to the amount of energy it has received. (c) The patch with the highest energy is emphasized, and the energy reflected from it has been added to the patches visible to that patch. This patch now no longer has the highest energy. (d) The next patch with the highest unshot energy is shown, and the energy is propagated similarly to (d). (e) The situation several steps later, and (f) the energy distribution in the model when the solution has converged. The energy from patches visible to the receiver is collected into it in the final gathering phase.

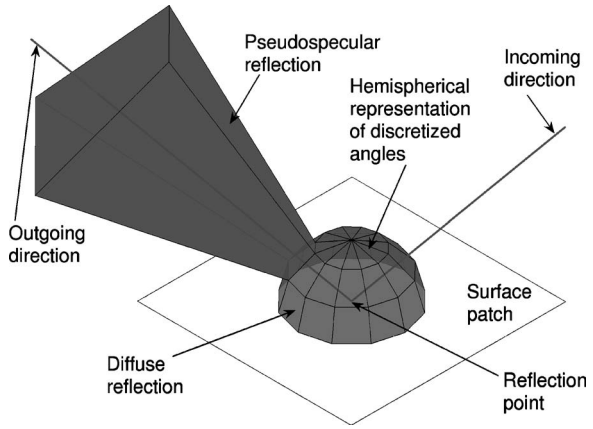

FIG. 5. Hemisphere is divided into solid angles to discretize the directional information. Here, both the azimuth angle resolution and the elevation angle resolution are 30° yielding 36 directional segments. Thus, the incoming and outgoing directions of the reflections, defined by an azimuth angle θ and an elevation angle ϕ, can be mapped onto a pair of corresponding integer values i and j. Constructed BRDFs are weighted sums of specular and diffuse reflections. The discretized distribution of the reflected energy for one incident angle is shown. Compare this to the undiscretized BRDF in Fig. 1.

is required for different receiver positions. Since the final gathering operation takes only a few milliseconds in typical models, the receiver position can be changed in real time. When combined with an efficient audio renderer, this solution would allow interactive walk-through auralizations in scenes with stationary sound sources and geometry.

VI. RESULTS

The algorithm is evaluated with the geometry given in the third round robin test on room acoustical computer simulation by Bork.[28,29] This geometry is chosen because it is a model of a room for which there is available public acoustic measurement data, in addition to the data produced by other room acoustics prediction software. Three levels of detail for the same model are given. Phase 2 geometry, consisting of 378 patches, is chosen for evaluating the acoustic parameters. It has enough details to produce unique responses at different receiver and source positions, but, on the other hand, the diffusing surfaces are not modeled too accurately to demonstrate the effects of both highly diffuse and highly specular BRDFs. The simulations are run separately for each frequency band with curtains open and closed. In addition, some results for the phase 3 geometry, consisting of 986 patches, are given to assess the algorithm performance with a higher number of patches.

A. Materials

The materials are given as absorption and scattering coefficients for six octave bands from 125 Hz to 4 kHz. The BRDFs, with a 30° elevation and azimuth angle resolution, are constructed as explained in the previous section. Figure 5 shows a discretized BRDF for one incident angle.

B. Acoustic parameters

Eight acoustic parameters are compared, namely reverberation time (T_{30}), early decay time (EDT), definition (D_{50}), clarity (C_{80}), center time (TS), strength (G), and lateral energy fractions (LF and LFC). These parameters give good insight into the advantages and disadvantages of the suggested method. The energy responses, from which the parameters are to be extracted, are simulated for two source and three receiver positions and for six octave bands with curtains open and closed. The data in the figures correspond to that shown by Bork for the other room acoustics prediction software.[29] To emphasize the positional dependency, the Tables I–III contain average values of the four middle frequencies with curtains open for varying positions.

In general, the estimates of T_{30} are very good. The values averaged over four middle octave bands remain within 0.04 s of the measured values. Figure 6(a) shows the values for each octave band at position S2R2. The values seem to be higher at low frequencies and lower at higher frequencies than the measured data with open curtains. However, the

TABLE I. The measured and simulated T_{30} and EDT values averaged for the 250 Hz, 500 Hz, 1 kHz, and 2 kHz octave bands. Each of the six combinations of source and receiver positions are given.

		T_{30}			EDT		
Src	Rcv	Meas. (s)	Sim. (s)	Err. (%)	Meas. (s)	Sim. (s)	Err. (%)
S1	R1	1.12	1.11	−0.9	1.16	1.15	−1.4
S1	R2	1.15	1.11	−2.8	1.07	1.08	1,8
S1	R3	1.13	1.11	−1.4	1.21	1.19	−1.4
S2	R1	1.13	1.11	−1.2	1.11	1.07	−2.8
S2	R2	1.13	1.11	−1.6	1.12	1.19	5.6
S2	R3	1.11	1.11	0.4	1.11	1.10	−0.5

TABLE II. The measured and simulated D_{50}, C_{80}, and TS values averaged for the 250 Hz, 500 Hz, 1 kHz, and 2 kHz octave bands. Each of the six combinations of source and receiver positions are given.

		D_{50}			C_{80}			TS		
S	R	Meas. (%)	Sim. (%)	Err. (%)	Meas. (dB)	Sim. (dB)	Err. (dB)	Meas. (ms)	Sim. (ms)	Err. (%)
S1	R1	49.19	48.94	−0.5	2.85	2.59	−0.26	78.79	83.12	5.5
S1	R2	56.61	54.68	−3.4	3.51	3.55	0.04	68.19	72.73	6.7
S1	R3	46.13	45.04	−2.4	1.90	2.16	0.26	84.52	90.56	7.2
S2	R1	53.87	55.53	3.1	3.09	3.51	0.41	71.25	72.72	2.1
S2	R2	43.49	44.33	2.0	1.94	2.20	0.25	82.69	90.81	9.8
S2	R3	53.23	51.22	−2.0	3.08	3.10	0.02	71.68	77.02	7.4

shape of the curve is similar to those shown for other prediction software.[29] Averaged T_{30} values for each listener and source positions are given in Table I.

The EDT values, presented in Table I, also follow the measured values quite accurately. The averaged values do not differ more than 0.07 s in the worst case, and these errors can also be partly explained by errors in the room model. However, the variation in individual values is larger than in T_{30}. Figure 6(b) shows the values for each position in the 1 kHz octave band. Although there are some deviations from the measured data, the positional dependency in the EDT can be seen clearly. In contrast, according to Bork some room acoustics prediction programs have difficulties in modeling it properly.[29]

The D_{50} values with curtains open are mostly near to the measured data, see Table II. Results are slightly more inaccurate with closed curtains. This can be seen in Fig. 6(c) where the D_{50} values in the 1 kHz octave band for each position are shown. In the lowest octave band (125 Hz), shown in Fig. 6(d), there are noticeable differences. However, compared to the values given by the other room acoustics prediction software,[29] the results are good. The C_{80} values show similar behavior, although the relative errors are larger. Figure 6(e) shows the C_{80} values at position S1R1 for each octave band. Since these parameters depend on the direct sound and the early reflections, based on these results it is reasonable to believe the energy of the early part of the response is properly constructed.

The TS values shown in Table II are within the subjective error difference limen (±10 ms),[28] although the simulated values are a little higher than the measured values in general. Because the integral evaluated in calculating the TS values is over the whole response, the late reflections are also taken into account. Thus it can be concluded that the late reflections are modeled properly by the acoustic radiance transfer method. Figure 6(f) shows the values for each octave band at position S1R1.

The simulated LF values are somewhat lower than the measured values while the LFC values are closer to the measured values. Otherwise, their behavior is similar. Figure 6(g) shows the LF values for each octave band at position S1R1. The simulated values do not vary much in relation to the frequency, unlike the measured values. The same phenomenon can be seen in the data produced by the other room acoustics prediction software,[29] which might indicate that the room model does not properly capture some aspects of the real room. On the other hand, since these parameters consider the directional distribution of the early reflections, especially the LF values are prone to small changes in their incident direction at some locations. It has been shown that the prediction of parameters such as LF and C_{80} are sensitive to the diffusion modeling scheme used,[30] which could explain some of the errors. The results for both LF and LFC averaged over four middle octave bands with open curtains can be seen in Table III. Figure 6(h) shows the LF values for each position in the 1 kHz octave band. Although the simulated values are lower than the measured values, the positional dependence can be seen.

The simulated G values do not differ much from the measured values. The local dependence, characterized by the direct sound and early reflections, is strong, as can be seen in the measured values in Table III. The behavior of the simulated values is similar in relation to the position of the sound sources and receivers. Figure 6(i) shows G values for each position in the 1 kHz octave band.

Most parameter values extracted from the simulated data

TABLE III. The measured and simulated LF, LFC, and G values averaged for the 250 Hz, 500 Hz, 1 kHz, and 2 kHz octave bands. Each of the six combinations of source and receiver positions are given.

		LF			LFC			G		
S	R	Meas. (%)	Sim. (%)	Err. (%)	Meas. (%)	Sim. (%)	Err. (%)	Meas. (dB)	Sim. (dB)	Err. (%)
S1	R1	25.55	20.21	−20.9	32.31	31.18	−3.5	19.33	18.86	−2.5
S1	R2	20.52	18.77	−8.5	28.07	28.25	0.7	20.48	20.06	−2.5
S1	R3	26.86	19.53	−27.3	32.00	32.49	1.6	18.94	18.72	−1.2
S2	R1	21.00	16.69	−20.5	26.33	27.61	4.9	20.01	20.91	4.5
S2	R2	24.61	20.41	−17.1	30.11	32.55	8.1	19.36	20.31	4.9
S2	R3	21.92	18.25	−16.7	27.88	28.55	2.4	19.98	20.73	3.8

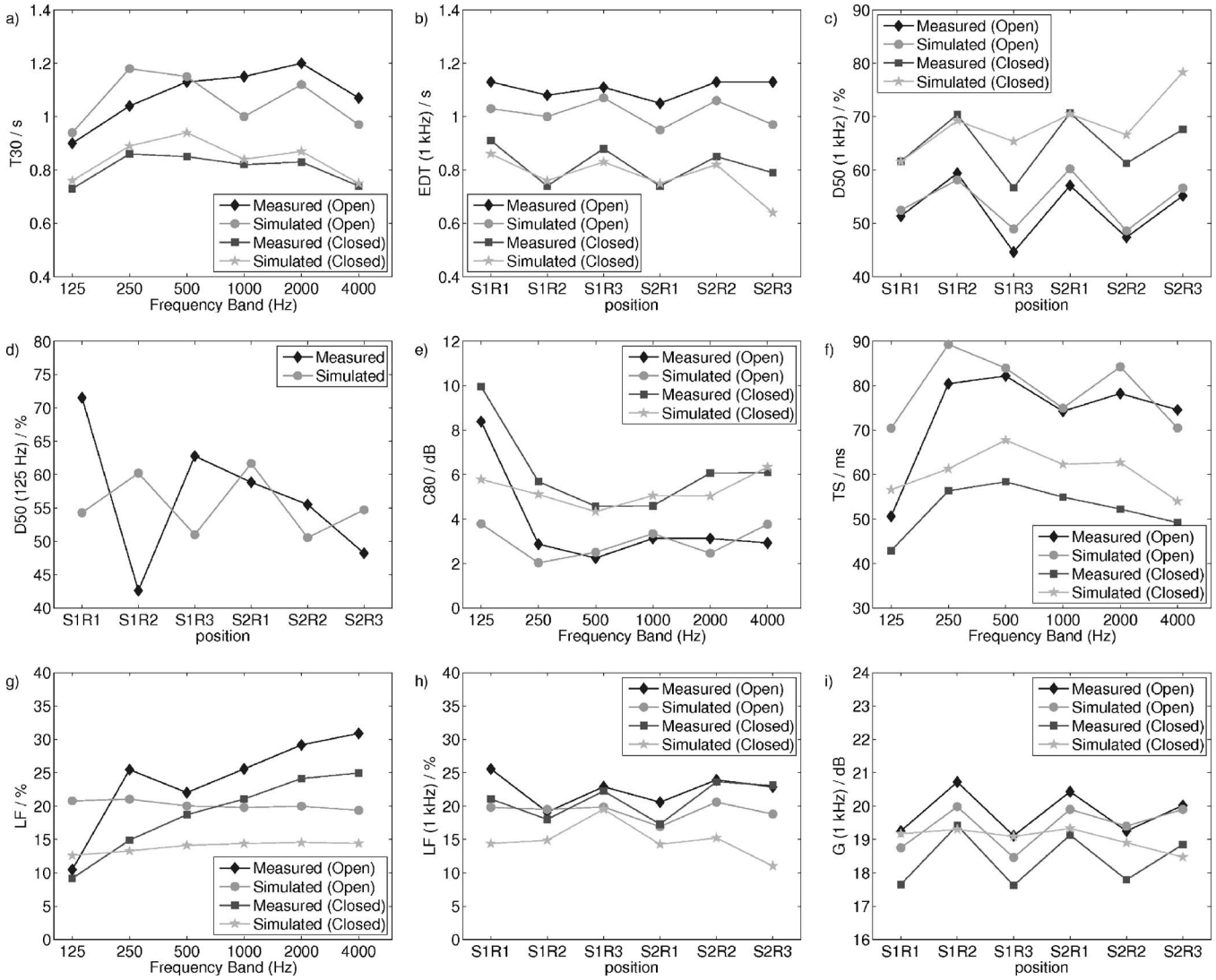

FIG. 6. The charts show (a) T_{30} values at position S2R2 (cf. Fig. 6 in Ref. 30), (b) EDT values in the 1 kHz octave band (cf. Fig. 8 in Ref. 30), (c) D_{50} values in the 1 kHz and (d) 125 Hz octave bands (cf. Figs. 10 and 11 in Ref. 30 respectively), (e) C_{80}, (f) TS, and (g) LF values at position S1R1 (cf. Figs. 13, 14, and 19 in Ref. 30, respectively), and (h) LF and (i) G in the 1 kHz octave band (cf. Figs. 20 and 17 in Ref. 30, respectively).

are close to the measured values. In some cases, the computer model of the room sets limitations on the accuracy of the results since the geometry is simplified and some of the material data is only approximate.[29] Comparing the results produced by the acoustic radiance transfer method to the results of the other acoustics prediction software with the same room model, the frequency dependent behavior of the parameters is very similar, although the results differ from the measured data. This can be explained by both the errors in the room model and the common limitations of the geometrical room acoustics modeling methods. Errors at the lower frequencies can be expected because the wave effects are not properly taken into account.[28]

C. Computational performance

The memory consumption of the algorithm is high, in typical cases hundreds of megabytes, because each patch has an energy response for each discretized hemisphere direction. The amount of memory required is directly proportional to the number of patches, number of directional segments, sampling frequency, and the length of the energy response.

The computation times are also quite long with high spatial and temporal resolutions. In addition to the factors mentioned above, the Monte Carlo sampling density and the convergence threshold value also affect the computation time. Table IV contains some computation times on a PC with a Pentium 42.8 GHz processor and 1024 MB random access memory. It is obvious that the running times of the unoptimized version of the acoustic radiance transfer method are longer than with commercial acoustics prediction software, but they are still feasible for practical applications and research purposes.

VII. POSSIBLE EXTENSIONS AND FUTURE WORK

There are several possible error sources in the acoustic radiance transfer method. Wave effects are not modeled since there is no phase information when calculating with energies. For example, the edge diffraction is not taken into account in

TABLE IV. Computation times for each octave band with phase 1, phase 2, and phase 3 geometries consisting of 90, 378, and 986 patches, respectively, using angular resolution of 30° for both azimuth and elevation angles, and a time resolution of 1 ms. The length of the response is 1.0 s, and the energy level for convergence is set to 10^{-4} of the initial energy which corresponds to 40 dB attenuation. Double precision is used for floating points.

Octave Band	Phase 1	Phase 2	Phase 3
125 Hz	5 min 33 s	24 min 42 s	1 h 41 min 43 s
250 Hz	5 min 28 s	31 min 13 s	2 h 13 min 5 s
500 Hz	5 min 28 s	28 min 57 s	2 h 26 min 25 s
1 kHz	5 min 27 s	24 min 7 s	2 h 10 min 25 s
2 kHz	5 min 14 s	27 min 32 s	2 h 26 min56 s
4 kHz	4 min 36 s	23 min 50 s	2 h 7 min 58 s

the implementation. The acoustic energy propagation model could be extended to use diffraction models[31] by modifying only the reflection kernel.

The reflection model could be improved. The relationship of the directional description to scattering and diffusion coefficients should be studied more carefully to assure their proper use.[15] The discretization of the BRDFs could be replaced by the use of spherical harmonics[14] so that in the energy response, each sample would consist of spherical harmonics coefficients. In addition, the material representation could possibly be extended to cover nonlocally reacting surfaces by applying bidirectional subsurface radiance distribution functions[12] which also model subsurface scattering. This would allow transmission through materials, although one temporal and two spatial dimensions must be added to the reflectance model.

VIII. CONCLUSIONS

A model for acoustic energy propagation is presented in the form of the room acoustic rendering equation. Several widely used geometrical room acoustics modeling methods are shown to be specializations of this model. It provides foundations for even more general methods for modeling the propagation of acoustic energy. Thus, a more accurate prediction of room acoustics is made possible.

A new method is proposed to solve the room acoustic rendering equation. The method, called acoustic radiance transfer method, is an extension of the previous work on the acoustic radiosity method, because the time-dependent acoustic radiance transfer method can handle arbitrary reflections, represented by acoustic BRDFs, in addition to the diffuse reflections. The simulated results indicate that the acoustic radiance transfer method is at least as reliable a method for room acoustics prediction as most of the methods used today. In addition, it offers flexibility in modeling arbitrary reflections and handling complex sound sources. This allows the method to be extended to handle diffracting edges and transmission through materials in the future.

ACKNOWLEDGMENTS

The authors would like to thank D.Sc. Janne Kontkanen for insightful comments on the paper, and Professor Karjalainen, Professor Sulonen, and Professor Takala for the early discussions on the subject. This research has been financially supported by the EU's FP6 IST project Uni-Verse.

[1] J. B. Allen and D. A. Berkley, "Image method for efficiently simulating small-room acoustics," J. Acoust. Soc. Am. **65**, 943–950 (1979).
[2] J. Borish, "Extension of the image model to arbitrary polyhedra," J. Acoust. Soc. Am. **75**, 1827–1836 (1984).
[3] A. Krokstad, S. Strom, and S. Sorsdal, "Calculating the acoustical room response by the use of a ray tracing technique," J. Sound Vib. **8**, 118–125 (1968).
[4] T. Funkhouser, N. Tsingos, I. Carlbom, G. Elko, M. Sondhi, J. West, G. Pingali, P. Min, and A. Ngan, "A beam tracking method for interactive architectural acoustics," J. Acoust. Soc. Am. **115**, 739–756 (2004).
[5] M. Hodgson and E.-M. Nosal, "Experimental evaluation of radiosity for room sound-field prediction," J. Acoust. Soc. Am. **120**, 808–819 (1996).
[6] E.-M. Nosal, M. Hodgson, and I. Ashdown, "Investigation of the validity of radiosity for sound-field prediction in cubic rooms," J. Acoust. Soc. Am. **116**, 3505–3514 (2004).
[7] E.-M. Nosal, M. Hodgson, and I. Ashdown, "Improved algorithms and methods for room sound-field prediction by acoustical radiosity in arbitrary polyhedral rooms," J. Acoust. Soc. Am. **116**, 970–980 (2004).
[8] T. Lewers, "A combined beam tracing and radiant exchange computer model of room acoustics," Appl. Acoust. **38**, 161–178 (1993).
[9] N. Tsingos and J.-D. Gascuel, "Acoustic simulation using hierarchical time-varying radiant exchanges," URL citeseer.ist.psu.edu/721526.html, [viewed 2007-06-27].
[10] J. T. Kajiya, "The rendering equation," Comput. Graph. **20**, 143–150 (1986).
[11] P. Dutré, P. Bekaert, and K. Bala, *Advanced Global Illumination* (A. K. Peters, Wellesley, MA, 2003).
[12] F. E. Nicodemus, J. C. Richmond, J. J. Hsia, I. W. Gingberg, and T. Limperis, "Geometric considerations and nomenclature for reflectance," Monograph 161, National Bureau of Standards (U.S.) (1977).
[13] D. S. Immel, M. F. Cohen, and D. P. Greenberg, "A radiosity solution for non-diffuse environments," Comput. Graph. **20**, 133–142 (1986).
[14] F. X. Sillion, J. R. Arvo, S. H. Westin, and D. P. Greenberg, "A global illumination solution for general reflectance distributions," Comput. Graph. **25**, 187–196 (1991).
[15] T. J. Cox, B.-I. L. Dalenback, P. D'Antonio, J. J. Embrechts, J. Y. Jeon, E. Mommertz, and M. Vorländer, "A tutorial on scattering and diffusion coefficients for room acoustic surfaces," Acta. Acust. Acust. **92**, 1–15 (2006).
[16] M. Vorländer and E. Mommertz, "Definition and measurement of random-incident scattering coefficients," Appl. Acoust. **60**, 187–199 (2000).
[17] Here, the following notation is used: $\lfloor a \rfloor = \begin{cases} a, a \geq 0 \\ 0, a < 0 \end{cases}$.
[18] G. M. Naylor, "ODEON–another hybrid room acoustical model," Appl. Acoust. **38**, 131–143 (1993).
[19] B.-I. Dalenbäck, "Room acoustic prediction based on a unified treatment of diffuse and specular reflection," J. Acoust. Soc. Am. **100**, 899–909 (1996).
[20] U. Svensson and U. Kristiansen, "Computational modeling and simulation of acoustic spaces," in *AES 22nd International Conference on Virtual, Synthetic and Entertainment Audio*, 11–30 (Espoo, Finland) (2002).
[21] H. Kuttruff, *Room Acoustics*, 4th ed. (Spon, London, 2000).
[22] H. Lehnert and J. Blauert, "Principles of binaural room simulation," Appl. Acoust. **36**, 259–291 (1992).
[23] B. Kapralos, "The sonel mapping acoustical modeling method," Ph.D. thesis, York University, Toronto, Ontario, Canada (2006).
[24] H. W. Jensen, *Realistic Image Synthesis Using Photon Mapping* (A. K. Peters, Natick, MA, 2001).
[25] M. F. Cohen, S. E. Chen, J. R. Wallace, and D. P. Greenberg, "A progressive refinement approach to fast radiosity image creation," Comput. Graph. **22**, 75–84 (1988).
[26] M. F. Cohen and D. P. Greenberg, "A radiosity solution for complex environments," Comput. Graph. **19**, 31–40 (1985).
[27] H. Bass and H.-J. Bauer, "Atmospheric absorption of sound: Analytical expressions," J. Acoust. Soc. Am. **52**, 821–825 (1972).
[28] I. Bork, "Report on the 3rd round robin on room acoustical computer simulation - Part I: Measurements," Acta. Acust. Acust. **91**, 740–752 (2005).
[29] I. Bork, "Report on the 3rd round robin on room acoustical computer

simulation - Part II: Calculations," Acta. Acust. Acust. **91**, 753–763 (2005).
[30]Y. W. Lam, "A comparison of three diffuse reflection modeling methods used in room acoustics computer models," J. Acoust. Soc. Am. **100**, 2181–2192 (1996).
[31]U. P. Svensson, R. I. Fred, and J. Vanderkooy, "Analytic secondary source model of edge diffraction impulse responses," J. Acoust. Soc. Am. **106**, 2331–2344 (1999).

Dynamic measurement of room impulse responses using a moving microphone

Thibaut Ajdler,[a] Luciano Sbaiz, and Martin Vetterli[b]
Audiovisual Communications Laboratory, Ecole Polytechnique Fédérale de Lausanne (EPFL), 1015 Lausanne, Switzerland

(Received 10 October 2006; revised 24 March 2007; accepted 3 July 2007)

A technique for the recording of large sets of room impulse responses or head-related transfer functions is presented. The technique uses a microphone moving with constant speed. Given a setup (e.g., length of the room impulse response), a careful choice of the recording parameters (excitation signal, speed of movement) leads to the reconstruction of all impulse responses along the trajectory. In the case of a moving microphone along a circle, the maximal angular speed is given as a function of the length of the impulse response, its maximal temporal frequency, the speed of sound propagation, and the radius of the circle. As a result of the presented algorithm, head-related transfer functions sampled at 44.1 kHz can be measured at all angular positions along the horizontal plane in less than 1 s. The presented theory is compared with a real system implementation using a precision moving microphone holder. The practical setup is discussed together with its limitations. © *2007 Acoustical Society of America.* [DOI: 10.1121/1.2766776]

PACS number(s): 43.55.Mc, 43.20.Ye, 43.20.Bi, 43.60.Ac [WMC] Pages: 1636–1645

I. INTRODUCTION

One of the key elements in the success of multimedia communication systems is the capability of reproducing virtual environments to be perceived by the listener as naturally as possible. To achieve realism, either real measurements need to be introduced in the system, or the environment needs to be modeled and synthetically generated.[1,2] In both cases, room impulse responses (RIRs) are used to give listeners the impression of being in a real environment and enveloped by the sound. In the case of headphone playback, head-related transfer functions (HRTFs) are usually added to achieve externalization and more realistic impressions.[3] The RIRs and HRTFs to be used need to be either measured at a large number of positions in the considered space or modeled using different techniques such as the ones described in Ref. 4 or 5. The RIRs are then provided to the playback system. This is typically the case in wave field synthesis (WFS) systems where measured RIRs at a large number of positions[6,7] are used to increase the realism of the reproduced field. Therefore, one would like to find a way to easily and rapidly measure large sets of RIRs. The usual technique is to use a single microphone or a microphone array. Nevertheless, to capture hundreds of RIRs, the array of microphones needs to be displaced to several positions. The intrusion of a person to modify the setup (e.g., displace the array) changes greatly the characteristics of the room and the temperature field inside of the room[8] and makes the measurement very time consuming. In this paper, a technique is introduced that achieves a fast recording of a large number of RIRs. It considers a fixed loudspeaker with a moving microphone. The moving element follows a trajectory (e.g., circular trajectory) with constant speed. Also, the acquisition of the data is not done position after position but happens continuously along the trajectory. The movement is uniform and does not stop during the acquisition. Thanks to this setup, one avoids problems linked to abrupt stops leading to oscillations and waiting time for the microphone to get to its next position. From the one-dimensional signal gathered by the microphone, the two-dimensional (2D) dataset (spatial and temporal) containing the RIRs at all the different spatial positions along the trajectory is reconstructed. The algorithm takes into account the Doppler shift inherent to the moving element and cancels its effect in the reconstructed RIRs. An analysis is performed to study the influence of the different parameters to be chosen so as to achieve the reconstruction of the RIRs (e.g., length and period of the excitation signal, frequencies contained in the excitation signal, speed of movement of the microphone, temporal and spatial frequencies of the reconstructed dataset). The trade-off existing between the speed of the moving element and the spacing between the frequencies contained in the excitation signal is discussed.[9] The presented theory is shown together with real measurements. These measurements are obtained using a moving microphone holder that achieves a precision of a few hundredths of a degree when rotating in the horizontal plane. An interesting application of this setup can be found in the measurement of HRTFs. These measurements are typically done in anechoic chambers to describe the influence of our body on the sound measured at the entrance of our ears.[3] For these specific filters, the impulse responses to be measured are very short (on the order of a few milliseconds) since no room reflections need to be captured. The whole dataset of azimuthal angles can then be recorded in a very fast manner. In this paper, it is shown that with the presented technique, measurement of all HRTFs in the horizontal plane can be achieved in less than 1 s.

[a]Electronic mail: ajdler@gmail.com
[b]Also at Department of EECS, University of California at Berkeley, Berkeley, CA 94720.

A. Related work

Different methods exist for the measurement of RIRs and HRTFs. To measure a RIR, the typical setup considers a calibrated loudspeaker and microphone. By measuring the signal recorded by the microphone, it is possible to obtain the room impulse response. Different excitation signals can be provided to the loudspeaker such as logarithmic sweeps[10] or maximum length sequences.[11] The simplest and most common technique for HRTF measurement consists in putting a microphone at the entrance of the ear canal and recording the sound emitted by a source located at a certain azimuth and elevation angle. By comparing the recorded signal and the emitted one, it is possible to extract the influence of the listener. This procedure needs to be repeated for every desired direction as shown in Fig. 1. Different stimuli can be used for the purpose of measuring HRTFs. White Gaussian noises, MLS, or Golay codes[12] are often used. Comparison of these signals can be found in Ref. 13. To reduce the time needed for the acquisition of large datasets of HRTFs, an interesting method has been presented by Zotkin *et al.*[14] By putting a loudspeaker emitting sound near the ear entrance, the sound pressure field is recorded with receivers located on a circular or on a spherical array of microphones. Like this, all HRTFs can be measured simultaneously. A third technique is described in this paper where a fixed source and a moving person are considered. In the proposed algorithm, it can be shown that the measurement of all possible HRTFs along the horizontal plane can be achieved in less than 1 s. Note that a similar approach was followed in Refs. 7 and 15 where room impulse response measurements were carried out using a microphone moving along a circular trajectory. Nevertheless, the assumption was made that at low angular speed, the RIRs can be obtained without taking the Doppler effect into account. This is not the case in our study where the RIRs are theoretically perfectly reconstructed. Other methods using moving microphones have been presented for improving wave field extrapolation techniques. As is described in Ref. 16, the first step is to measure the field along a certain trajectory, and, from the gathered information, extrapolation can be performed using the Kirchhoff-Helmholtz integral.[17] Considering the field to be extrapolated as stationary, the different measurements do not need to be performed simultaneously. In Refs. 18 and 19 it is explained that using a moving microphone allows for measurement of the field in more positions and therefore better extrapolation can be achieved.

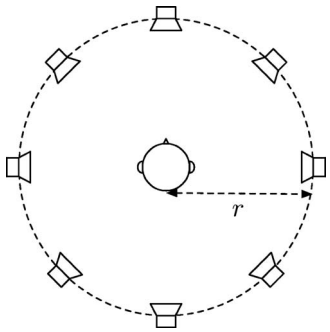

FIG. 1. Setup for the recording of HRTFs.

B. Contributions

The contributions of this work are the following:

(i) The Doppler effect is put in evidence in the two-dimensional spectrum representation of the sound pressure field when a moving receiver is used in the setup.
(ii) An algorithm for the reconstruction of the static RIRs or HRTFs is presented by removing the Doppler effect present in the recording.
(iii) A formula describing the maximal rotation speed is given as a function of the different parameters of the system.
(iv) The measurement of HRTFs at every azimuthal angle along the horizontal plane can be achieved in less than 1 s at a sampling frequency of 44.1 kHz.
(v) Experimental measurements using a moving microphone demonstrate the applicability of the algorithm and confirm the presented theory.

C. Outline

The outline of the paper is as follows. Section II describes some existing results on the study of the sound pressure field gathered along a line and a circle. The two-dimensional Fourier transform (2D-FT) of the considered sound pressure field is described for the two setups in Secs. II A and II B. Further, Sec. II C briefly recalls the Doppler effect. Section III considers the setup with a microphone moving along a trajectory with a uniform speed. In this scenario, the Doppler effect needs to be considered. It is shown in Sec. III A that, using the 2D spectrum representation of the sound pressure field along a line, the Doppler effect can be put in evidence. The signal recorded by a microphone moving along a circle is then described in Sec. III B. Section IV presents the main result of this work. It develops an algorithm to reconstruct the RIRs at every possible position, from the gathered signal by the microphone. The technique to achieve this reconstruction is presented in Sec. IV A. Some further remarks are given in Sec. IV B. A performance analysis comparing the signal to noise ratio of both the dynamic and the static measurement setups is described in Sec. V. The theory is then compared with experimental measurements in Sec. VI. The conclusions are drawn in Sec. VII.

II. SPATIO-TEMPORAL IMPULSE RESPONSES

In this section, existing results are recalled on the study of the 2D-FT of the sound pressure field along different geometries. First, the spectrum of the sound pressure field along a line in the room is presented in Sec. II A followed by the sound pressure field along a circle in Sec. II B. Finally, Sec. II C briefly reviews the Doppler effect widely used in the rest of the paper.

A. Sound field along a line

Consider the sound pressure field studied along a line in a room. As a first example, consider a plane wave of temporal frequency ω_0 arriving on the line with an angle α,

$$p(x,t) = e^{j(\omega_0 t + k_0 x \cos \alpha)}, \tag{1}$$

with $k_0 = \omega_0 / c$ and c the speed of sound propagation as shown in Fig. 2. The 2D-FT of a function $p(x,t)$ is defined as follows

$$\hat{p}(\phi,\omega) = \int_{-\infty}^{\infty} \int_{-\infty}^{\infty} p(x,t) e^{-j(\omega t + \phi x)} \, dt \, dx, \tag{2}$$

with ϕ and ω the spatial and temporal frequencies respectively.

In the case of Eq. (1), its 2D-FT is[17]

$$\hat{p}(\phi,\omega) = 4\pi^2 \delta(\omega - \omega_0) \delta\left(\phi - \frac{\omega_0 \cos \alpha}{c}\right). \tag{3}$$

We therefore see that the 2D-FT of a plane wave of temporal frequency ω_0 only has energy in one single point in the spectral domain.

Considering a plane wave emitting all possible frequencies, Eq. (1) becomes

$$p(x,t) = \delta\left(t + \frac{x \cos \alpha}{c}\right). \tag{4}$$

The 2D-FT of Eq. (4) is then

$$\hat{p}(\phi,\omega) = 2\pi \delta\left(\phi - \frac{\omega \cos \alpha}{c}\right). \tag{5}$$

This 2D spectrum is shown in Fig. 3(a). When plane waves arrive from all possible angles, the support of the spectrum is represented in Fig. 3(b) and satisfies the rule

$$|\phi| \leq \frac{|\omega|}{c}. \tag{6}$$

As can be seen, the support has a butterfly spectrum, which can intuitively be explained as follows. At low temporal frequencies, the sound wavelength is very large and therefore, spatially, the wave is varying slowly, which explains the small spatial support. For higher temporal frequencies, the sound wavelength is smaller, which makes the spatial variation larger. The spatial support for higher temporal frequencies is therefore larger. As a result, when sampling the sound

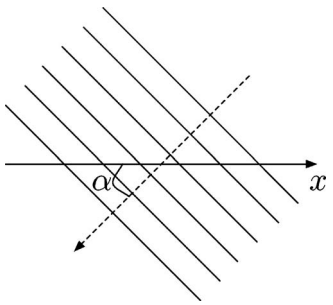

FIG. 2. A plane wave arrives on a line of microphone along the x axis with an angle of arrival of α.

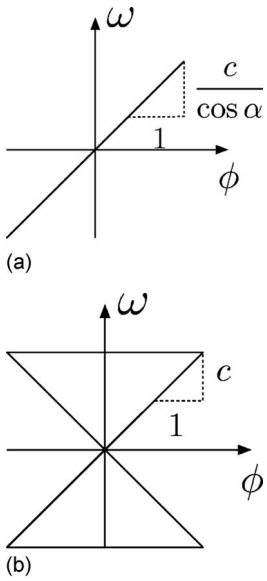

FIG. 3. Two-dimensional spectrum of the sound pressure field, (a) In case of a single plane wave, (b) In case of plane waves arriving from all possible angles.

field up to a temporal frequency of $\omega_{\max}$, the necessary spacing between the microphones needed to interpolate the field at any position along a line is of D, with

$$D < \frac{\pi c}{\omega_{\max}}. \tag{7}$$

Further work on the sampling and interpolation of the sound field has been done when considering not only the plane wave assumption but the real solution of the wave equation. More details can be found in Refs. 20 and 21.

B. Sound field along a circle

For the study of the sound pressure field along a circle, consider the scheme presented in Fig. 4(a). Consider a circular microphone array of radius r. The coordinates of the different microphones are (m_x, m_y, m_z), with $m_x = r \cos \theta$, $m_y = r \sin \theta$, and m_z constant. The sound source has coordinates (s_x, s_y, s_z). The time of arrival from the source to the receiver is given by the following expression:

$$h(\theta) = \frac{\sqrt{(s_x - r\cos\theta)^2 + (s_y - r\sin\theta)^2 + (s_z - m_z)^2}}{c}. \tag{8}$$

The free field pressure recorded on the circle of microphones due to the emission of a Dirac by the source is given by[22]

$$p(\theta,t) = \frac{\delta(t - h(\theta))}{4\pi c h(\theta)}. \tag{9}$$

Remark that $p(\theta,t)$ is 2π periodic with respect to θ. The 2D-FT of Eq. (9) is denoted as $\hat{p}(l_\theta, \omega)$. Note that l_θ is the index of the Fourier series with respect to the θ axis. In Refs. 23 and 24, it has been shown that most of the energy of the spectrum is located into a butterfly region spectrum satisfying

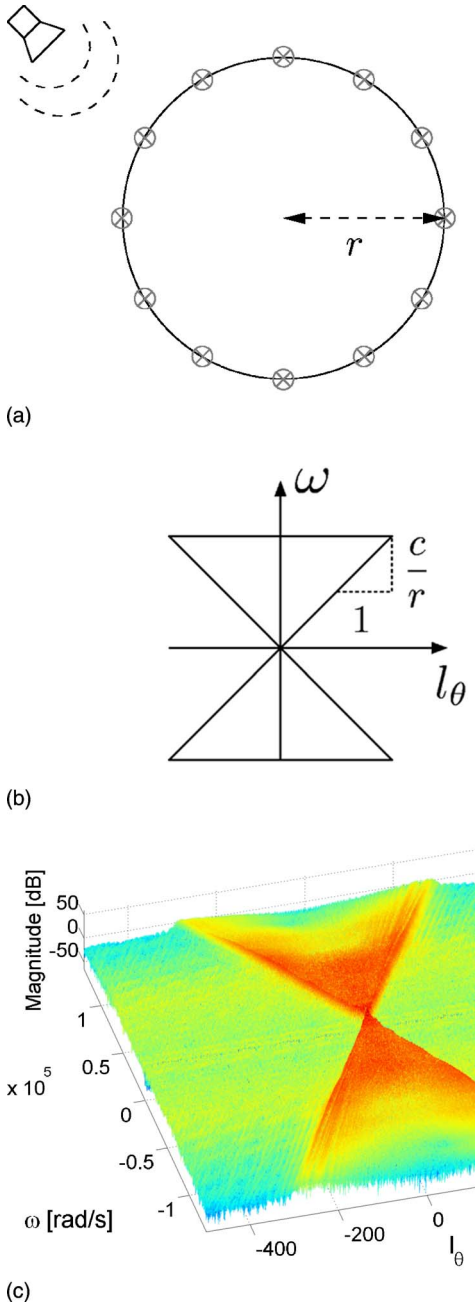

FIG. 4. (Color online) Sound field along a circle, (a) Schematic view of the setup, (b) Support of the 2D-FT of the sound pressure field analyzed on a circle. (c) 2D-FT of room impulse responses measured on a circle.

$$|l_\theta| \leq |\omega| \frac{r}{c}. \tag{10}$$

The support of the spectrum is schematized in Fig. 4(b). The intuition behind the butterfly spectrum is exactly the same as the one discussed in Sec. II A. Considering that no energy is present outside of the butterfly region, the angular spacing $\Delta\theta$ necessary to interpolate the sound field up to $\omega_{\max}$ at any azimuthal angular position is given by

$$\Delta\theta < \frac{\pi c}{r\omega_{\max}}. \tag{11}$$

Figure 4(c) shows an example of the 2D-FT of RIRs measured on a circle. These measurements were taken every 0.36 deg along a circle of radius 0.55 m. The details of the measurements as well as the database are available online.[25]

C. Doppler effect

In Secs. II A and II B the sound pressure field is considered to be measured at every positions along a line or a circle. In this paper, these measurements are obtained by using a moving microphone. When considering a moving element, a frequency shift is observed on the recorded signal. This is known as the Doppler effect and can be expressed by the following formula:[26]

$$\omega = \omega_0 \left(\frac{c + v_r}{c + v_s} \right), \tag{12}$$

with c the speed of sound propagation, ω the observed frequency, ω_0 the emitted frequency, v_s the speed of movement of the source, and v_r the speed of movement of the receiver. A convention for the sign of the speeds in Eq. (12) needs to be adopted. The positive direction is considered as the direction "listener towards source." The setup considering a moving microphone is discussed in Sec. III. There, using this convention, the sign of the speed of the receiver is considered as positive when the source and the receiver are coming towards each other as shown in Fig. 5(a), The sign of the received speed is negative when source and receiver are moving apart as in Fig. 5(b).

III. RECORDED SIGNAL FOR A MOVING MICROPHONE

In Sec. II, the sound pressure field has been described along a line and a circle. For both cases, the sound pressure field has been shown to have a butterfly spectrum. This specific shape of the spectrum will be used to study the sound field gathered by a microphone in the presence of a moving microphone.

Note that in the rest of this paper, we consider the loudspeaker and microphone to be omnidirectional devices and to present flat frequency responses. In a more realistic setup, the loudspeaker and microphone should be calibrated to be able to remove their influence on the impulse responses.

In this section, the moving microphone signal is studied when the microphone is moved along a line in Sec. III A and along a circle in Sec. III B.

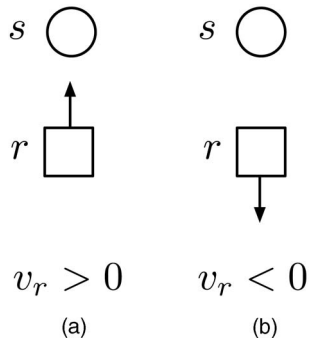

FIG. 5. Different setups for the study of the Doppler effect.

A. Microphone moving along a line

Consider a setup with a fixed loudspeaker and a microphone moving with a constant speed of v m/s along a line. Due to the constant speed of the microphone movement, the position x along the line is proportional to the time t as

$$x = vt. \tag{13}$$

The sound pressure at all positions along a line trajectory is denoted as $p(x,t)$. The 2D-FT of this signal is $\hat{p}(\phi,\omega)$. At each position the sound recorded by the microphone is the convolution of the source signal denoted as $s(t)$ with the corresponding RIR to be found in the RIRs database denoted as $h(x,t)$. Therefore,

$$p(x,t) = \int_{-\infty}^{\infty} s(i)h(x,t-i)\,\mathrm{d}i. \tag{14}$$

The sound recorded by the moving microphone is denoted as $r(t)$ with

$$r(t) = p(vt,t). \tag{15}$$

Note that Eq. (15) corresponds to a slice of the function $p(x,t)$ along the line given by Eq. (13). The spectrum of this recorded sound can be calculated as follows

$$\hat{r}(\gamma) = \int_{-\infty}^{\infty} p(vt,t)e^{-j\gamma t}\,\mathrm{d}t. \tag{16}$$

Also remark that

$$p(vt,t) = \frac{1}{4\pi^2}\int_{-\infty}^{\infty}\int_{-\infty}^{\infty} \hat{p}(\phi,\omega)e^{j(\omega t+\phi vt)}\,\mathrm{d}\phi\,\mathrm{d}\omega. \tag{17}$$

Using Eq. (17), Eq. (16) can be rewritten as

$$\begin{aligned}\hat{r}(\gamma) &= \frac{1}{4\pi^2}\int_{-\infty}^{\infty}\int_{-\infty}^{\infty}\int_{-\infty}^{\infty} \hat{p}(\phi,\omega)e^{-jt(\gamma-v\phi-\omega)}\,\mathrm{d}t\,\mathrm{d}\phi\,\mathrm{d}\omega \\ &= \frac{1}{2\pi}\int_{-\infty}^{\infty}\int_{-\infty}^{\infty} \hat{p}(\phi,\omega)\delta(\gamma-v\phi-\omega)\,\mathrm{d}\phi\,\mathrm{d}\omega \\ &= \frac{1}{2\pi}\int_{-\infty}^{\infty} \hat{p}(\phi,-v\phi+\gamma)\,\mathrm{d}\phi. \end{aligned} \tag{18}$$

For each frequency γ, the value of the spectrum of the recorded signal is obtained by projection of the 2D spectrum $\hat{p}(\phi,\omega)$ following the direction $\mathbf{v}=(1,-v)$ onto the ω axis. This result is known as the *projection-slice theorem*: a slice in the time domain corresponds to a projection in the frequency domain.[27] This theorem can be used in this scenario since the moving microphone signal corresponds to a slice of the spatio-temporal sound field as shown in Eq. (15). With an appropriate choice of the excitation signal emitted by the loudspeaker, the projection will be shown to be possibly inverted and the spatio-temporal signal reconstructed. The projection-slice theorem construction is presented in Figs. 6 and 7 where the Doppler effect is also put in evidence. Consider a plane source emitting a plane wave arriving on one microphone line with angle $\alpha=180$ deg as shown in Fig. 6(a). Consider further a moving microphone along the infinite line. The microphone is moving with a constant speed

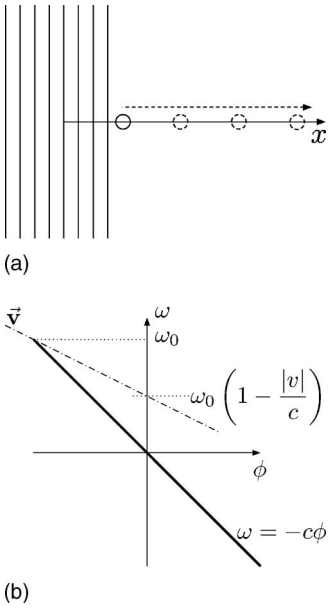

FIG. 6. Doppler effect with a receiver moving away from the source, (a) Schematic view of the situation, (b) Analysis of the situation in the 2D-FT domain.

$|v|$ away from the plane source in the positive x direction. As seen in Sec. II C, the movement leads to a frequency shift that lowers the perceived frequency at the microphone. The receiver signal can be obtained by projection of $\hat{p}(\phi,\omega)$ along the direction $\mathbf{v}$. As the sound pressure field is a plane wave with an arriving angle of $\alpha=180$ deg, it has been shown in Sec. II that its 2D spectrum lies on the line of equation

$$\omega = -c\phi. \tag{19}$$

This spectrum is shown in bold in Fig. 6(b). The component of $\hat{p}(\phi,\omega)$ at frequency ω_0 is simply the point $(-\omega_0/c,\omega_0)$ in

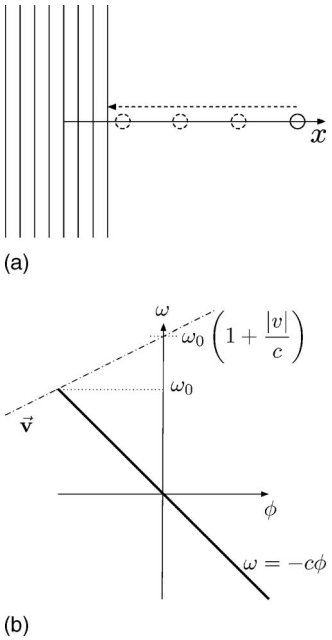

FIG. 7. Doppler effect with a receiver moving towards the source. (a) Schematic view of the situation. (b) Analysis of the situation in the 2D-FT domain.

Fig. 6(b). The projection of this point on the ω axis happens at

$$\omega = \omega_0\left(1 - \frac{|v|}{c}\right). \tag{20}$$

This is exactly the result obtained when considering the Doppler effect for a receiver moving away from the source as previously described in Eq. (12). The speed of the receiver is $v_r = -|v|$ since the case of Fig. 5(b) is considered.

Similarly, Fig. 7(a) presents the situation where the receiver is moving towards the source along the negative x direction. As can be seen in Fig. 7(b), the projection of the point $(-\omega_0/c, \omega_0)$ on the ω axis is now

$$\omega = \omega_0\left(1 + \frac{|v|}{c}\right). \tag{21}$$

This corresponds to the Doppler effect for a receiver moving towards the source.

B. Microphone moving along a circle

In this section, a source emits sound and a receiver is moving along a circle. The pressure measured at the different positions along the circle is given by $p(\theta,t)$. The sound recorded by the receiver moving with an angular speed[28] of v rad/s is $r(t)=p(vt,t)$. Similarly to Eq. (18), it can be derived that

$$\hat{r}(\gamma) = \sum_{l_\theta=-\infty}^{\infty} \hat{p}(l_\theta, -vl_\theta + \gamma). \tag{22}$$

For completeness, note that when the source emits a periodic signal $s(t)$ with period $2\pi/v$, $r(t)$ becomes also periodic with the same period. In that case, $r(l_\gamma)$ is the Fourier series of $r(t)$ with

$$\hat{r}(l_\gamma) = \sum_{l_\theta=-\infty}^{\infty} \hat{p}(l_\theta, -vl_\theta + l_\gamma). \tag{23}$$

The results presented in this section will further be used in Sec. IV.

IV. SPATIO-TEMPORAL RECONSTRUCTION OF ROOM IMPULSE RESPONSES

This section presents the main result of this work. Considering a moving microphone in the setup, the purpose is to recover the different RIRs at any position along the trajectory from the recording of the microphone. The different aspects of the technique are explored in Sec. IV A for a moving microphone. The relation between the speed of movement and the spacing between the frequency components of the excitation signal is specified. Section IV B discusses different remarks related to the presented techniques and compares both setups. Application of the technique to HRTF measurements is described. Note that in the present paper, the technique is presented for the case of a movement along a circle but can easily be applied for the linear trajectory or other trajectories.

A. Reconstruction algorithm for a moving microphone

With the knowledge of the emitted sound, the purpose of this technique is to reconstruct the different RIRs at any angle from the recording of the moving microphone. The speed of the moving microphone will be shown to be the key factor in the possible reconstruction of the RIRs at any possible angle. For this purpose, the 2D Fourier representation is used. Figure 8 shows the magnitude of $\hat{p}(l_\theta,\omega)$ representing the spectrum of the different static signals gathered at the different angular positions along the circle. To apply our algorithm of reconstruction, one needs to impose that not all temporal frequencies are present in the emitted signal. Energy is present only for the temporal frequencies shown as dashed lines in the spectrum $\hat{p}(l_\theta,\omega)$. The signal that is recorded by the microphone is given by Eq. (22). As described in Sec. III, the 2D spectrum is projected following the direction $\mathbf{v}$ on the ω axis. To be able to reconstruct the different RIRs, the emitted signal by the source has to be such that all the lines containing energy in the spectrum $\hat{p}(l_\theta,\omega)$ do not overlap once projected on the ω axis. Consider the maximal frequency emitted by the source to be ω_1. In the 2D spectrum, this frequency component corresponds to the segment $|p_1p_2|$. When projected on the ω axis, new frequency components appear in the range $\omega \in [\omega_1 - \Delta\omega_p/2, \omega_1 + \Delta\omega_p/2]$ due to the Doppler shift. To avoid any overlapping in the projections, the next frequency component emitted by the source has to be chosen carefully. Denote by i the intersection point of the projection of the point p_1 with the butterfly spectrum. To obtain the ordinate of i, denoted as ω_2, recall that the minimal slope of the triangular spectrum is given by

$$\omega = \frac{c}{r} l_\theta. \tag{24}$$

The frequency ω_2 is obtained by solving a system representing the intersection between the segment $|p_1 i|$ and one side of the butterfly spectrum:

$$\begin{cases} \omega = -vl_\theta + \omega_1\left(1 - \dfrac{rv}{c}\right), \\ \omega = \dfrac{c}{r} l_\theta. \end{cases} \tag{25}$$

The solution of this system leads to the value $\omega_2 = \omega_1((c-rv)/(c+rv))$. Defining $\Delta\omega$ as the frequency spacing between the two consecutive temporal frequency components ω_1 and ω_2 emitted by the source, it can be shown

$$\Delta\omega = \omega_1 \frac{2vr}{c+rv}. \tag{26}$$

As can be seen in Fig. 8, the spacing allowed between successive temporal frequencies is diminishing for smaller temporal frequencies. Therefore, the excitation signal could be very dense at low frequencies. It can be shown that the frequencies emitted by the sources need to satisfy the following relation:

$$\omega_{i+1} = \omega_1\left(\frac{c-rv}{c+rv}\right)^i. \tag{27}$$

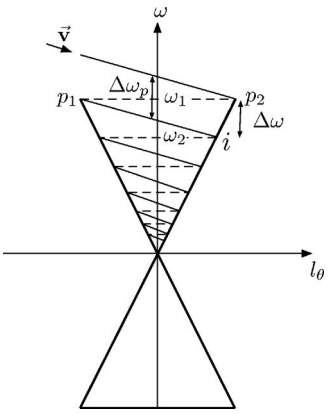

FIG. 8. Projection of the sound pressure field for an emitting sound containing frequencies spaced following Eq. (27).

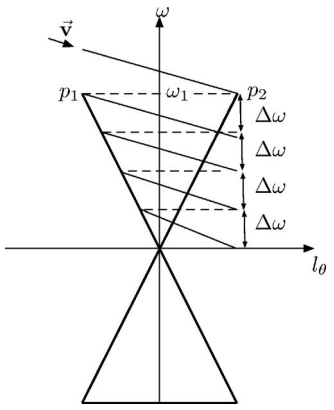

FIG. 9. Projection of the sound pressure field with an emitting signal containing frequencies spaced every $\Delta\omega$.

Nevertheless, to ease the calculation and make the processing simpler, a constant spacing $\Delta\omega$ between the temporal frequencies of the excitation signal is chosen as in Eq. (26). This new setup is presented in Fig. 9. The excitation signal is therefore a periodic signal with period $T_S=2\pi/\Delta\omega$. Remark that although the excitation signal only contains discrete frequencies, it is possible to determine the RIRs at every frequency thanks to the sampling theorem in the frequency domain.[29] Reconstruction at all frequencies is possible when considering the RIR to be of finite length. The duration of the RIR to be recorded, denoted as T, has to be smaller than the sampling period T_S to avoid any temporal aliasing, i.e.,

$$T < \frac{\pi(c+rv)}{rv\omega_1}. \tag{28}$$

To record RIRs of length T, the maximal speed at which the rotation can be applied is obtained using Eq. (28):

$$v_{\max} = \frac{\pi c}{r(\omega_1 T - \pi)}. \tag{29}$$

B. Discussion

To summarize, a description of the presented technique is given here. An excitation signal is transmitted to a loudspeaker. The emitted signal cannot contain every frequency but has to be designed carefully as discussed in Sec. IV A. The maximal speed of the moving element follows the rule given in Eq. (29). Note that, in order to keep the periodic character of the excitation signal, one will need to adapt the speed such that the time to make a full rotation corresponds to a multiple of the period of the excitation signal. After recording, the Fourier transform of the microphone signal is taken. In the case of the moving microphone this spectrum corresponds to $\hat{r}(l_\gamma)$ in Eq. (23). As discussed in Sec. IV A, it corresponds to a projection of $\hat{p}(l_\theta,\omega)$ on the ω axis. This projection needs to be undone to recreate the 2D spectrum. This can be achieved at the condition that no overlapping was present in Fig. 8. This is assured when Eq. (29) is satisfied. To obtain the different RIRs, one simply needs to divide the obtained spectrum by the spectrum of one period of the excitation signal and take the inverse Fourier transform of the dataset to obtain the RIRs at the different spatial locations. As the obtained 2D spectrum is almost bandlimited along the angular frequency dimension as was described in Sec. II, interpolation of the RIRs at any angle can be achieved.

A numerical example is given.

Using Eq. (29), to record RIRs of 100 ms on a circular array of radius of 1 m up to a frequency of 20 kHz, the rotation needs to be achieved at a maximal speed of $v=4.9$ deg/s. The duration of one full rotation is approximatively 74 s.

As was shown in Sec. IV A, due to the Doppler effect, the recorded sound can contain higher frequencies than the original emitted sound. Therefore, to avoid aliasing due to the creation of these new frequencies, one has to choose a temporal sampling frequency slightly higher than twice the largest emitted frequency component.

C. Individualized HRTF measurement

The presented technique is very suitable for the recording of very short impulse responses as is the case for HRTFs. A typical length of interest for HRTF measurement is of the order of 10 ms. Also, as was shown in Ref. 23, the support of the 2D spectrum of HRTFs along the horizontal plane has most of its energy in the region satisfying

$$|l_\theta| \leq |\omega|\frac{d}{2c}, \tag{30}$$

with d the diameter of the head (typically of the order of 18 cm). With this modification Eq. (29) becomes

$$v_{\max} = \frac{2\pi c}{d(\omega_1 T - \pi)}. \tag{31}$$

The maximal speed to reconstruct all HRTFs up to 20 kHz is therefore of 542 deg/s. In only 0.66 s, the measurement of HRTFs for all angles in the horizontal plane can be achieved. This interesting result finds application in the fast measurement of HRTFs. This technique could be further developed to allow every person to measure his own set of HRTFs and be able to use them when listening during headphone playback. Obviously, the content of the audio playback has to be adapted to support the use of HRTFs. This is precisely the goal of the new MPEG standard[30] that will allow the use of

individualized HRTFs for optimal audio rendering using headphones.

V. SIGNAL TO NOISE RATIO ANALYSIS

In this section, the performance of the proposed method with respect to a set of static measurements is studied. The goal is to determine, for the two methods, the signal to noise ratio (SNR) as a function of the measurement time and compare the results.

To simplify the analysis, it is assumed that for both the static and the dynamic measurements, a periodic signal of period T_S and duration T_P is used: moreover, the measurement noise is considered to be white on the bandwidth of interest and with spectral density W.

For the static case, a measure has to be performed at each sampling position on the circle. The minimum number of measurements N is obtained by imposing that there is no superposition on the spectral replicas of the spatio-temporal room impulse response. From Eq. (10), the value

$$N = \frac{2r}{c}\omega_1 \tag{32}$$

is obtained, where ω_1 corresponds to the maximal frequency present in the excitation signal. Each measurement consists of a repetition of the same period. In the frequency domain, the spectrum consists in a set of lines in the range $[-\omega_1, \omega_1]$ spaced at angular frequency $2\pi/T_S$ and approximate width $2\pi/T_P$. The measurement noise influences the result only for the contributions corresponding to the lines. As in the considered interval, $\omega_1 T_S/\pi$ lines are present; the noise variance σ_s^2 is given by

$$\sigma_s^2 = \frac{\omega_1 T_S}{\pi}\frac{W}{T_P}. \tag{33}$$

If e_S is the energy associated to one period of the recorded signal, the SNR for the static measurement, denoted as SNR_s, can be defined as the ratio between the power of the recorded signal e_S/T_S and the noise variance σ_s^2, namely

$$\mathrm{SNR}_s = \frac{e_S}{W}\frac{\pi}{\omega_1 T_S^2}T_P. \tag{34}$$

As one could have expected, the SNR increases linearly with the time taken by each measure. The total measurement time T_m is given by

$$T_m = N(T_P + T_t), \tag{35}$$

where the additional term T_t is added to take into account the transient between consecutive measurements. By combining Eqs. (32), (34), and (35), the relation between SNR_s and the measurement time is

$$\mathrm{SNR}_s = \frac{e_S}{W}\left(\frac{\pi c}{2r\omega_1^2 T_S^2}T_m - \frac{\pi T_t}{\omega_1 T_S^2}\right). \tag{36}$$

In the case of dynamic measurements, a single measurement is sufficient to recover the information needed to reconstruct any impulse response along the circle. In this case the variable T_p represents the duration of the full measurement rather than the duration of a single measurement. However, the Doppler shift will increase the width of the spectral lines of the recorded signal, which will imply a higher noise variance on the reconstructed room impulse responses. The ith line of the recorded signal will present an angular frequency $2\pi i/T_S$ and a width of[31]

$$|i|\frac{2\pi}{T_S}\frac{2r\upsilon}{c}, \tag{37}$$

where the index i is in the range $\pm\omega_1 T_S/2\pi$ (for simplicity, the quantity $\omega_1 T_S/\pi$ is assumed to be an even integer). To compute the noise variance, σ_d^2, the spectral density has to be integrated on the support, of the lines; this gives approximately

$$\sigma_d^2 = W\frac{r\omega_1^2\upsilon T_S}{2\pi^2 c}. \tag{38}$$

The SNR for the dynamic measurement, SNR_d, is obtained by dividing the power of one period of the recorded signal (this is assumed to be approximately constant for the different positions of the microphone) by the noise variance σ_d^2. By using the relation $\upsilon = 2\pi/T_P$, the resulting expression for SNR_d is

$$\mathrm{SNR}_d = \frac{e_S}{W}\frac{\pi c}{r\omega_1^2 T_S^2}T_P. \tag{39}$$

In the case of the dynamic measurement, the measurement time, T_m, is given by

$$T_m = T_P + T_t, \tag{40}$$

where the additive term T_t takes into account the time needed to reach the steady state at the beginning of the measurement. Combining Eqs. (39) and (40), the relation between SNR_d and measurement time is determined by

$$\mathrm{SNR}_d = \frac{e_S}{W}\frac{\pi c}{r\omega_1^2 T_S^2}(T_m - T_t). \tag{41}$$

By comparing this last relation with Eq. (36), it can be observed that the two methods deliver similar SNR. The main difference is given by the additional time T_t, which is N times larger for the static case. This extra time can be used in the dynamic case to obtain a larger SNR. Furthermore, the component of the SNR related to the measurement time T_m is essentially twice smaller for the static method than for the dynamic one. In the dynamic case, one takes advantage of the butterfly shaped spectrum, which allows an average reduction of the width of the spectral lines by a factor of 2.

The increase of SNR obtained using the dynamic compared to the static measurement setup can be quantified as follows. From Eqs. (36) and (41), it can be obtained that

$$\frac{\mathrm{SNR}_d}{\mathrm{SNR}_s} = \frac{2(T_m - T_t)}{T_m - NT_t}. \tag{42}$$

Therefore, for large RIRs ($T_m \gg NT_t$), the dynamic SNR will be about 3 dB higher than the static SNR. Nevertheless, for very short RIR measurements ($T_m \approx NT_t$), the dynamic SNR increases indefinitely compared to the static one. It can therefore be concluded that the dynamic setup leads to the highest SNR gain when small RIRs need to be measured.

VI. EXPERIMENTS

Experiments have been carried out in a sound insulated room. A loudspeaker (Genelec 1029*A*) was used to generate an excitation signal, recorded by a microphone Beyerdynamic *MC*-740. Rotation of the microphone was performed using a Pan/Tilt Unit *PTU-D*46-70. This device allows the rotation of the microphone with a precision of 0.03 deg and with a maximal rotation speed of 60 deg/s. The room, where the measurements were performed, was so that the RIRs have very small energy after 250 ms. The excitation signal was made of the sum of sinusoids spaced with 4 Hz. Each sinusoid component was given a random phase. The frequencies covered by the excitation signal ranged from 20 Hz to 22 kHz. The period of the excitation signal was of length 250 ms. To reconstruct the signal up to 22 kHz on a circular array of radius 60 cm, the maximal rotation speed is of 3 deg/s, as follows from Eq. (29). We chose to apply a rotation of 1.8 deg/s. Therefore, the full rotation was achieved in 200 s. Considering the analysis described in Sec. V, the difference between the two SNRs using either the static or dynamic method can be calculated. In the current scenario, the transient time satisfies $T_t \geq 250$ ms. Then, using Eq. (42), the dynamic SNR is shown to gain 7.8 dB compared to the static SNR. The Fourier transform of the recorded signal (in blue full lines) and of the emitted signal (in black dotted lines) are shown for low frequencies in Fig. 10(a) and for high frequencies in Fig. 10(b). As discussed in Sec. IV A, it can be observed that for the low frequencies, the projection of the triangular spectrum is very narrow while it becomes wider for larger frequencies. From the spectrum of the recorded signal, the original 2D spectrum needs to be reconstructed. This is achieved by undoing the effect of the projection appearing because of the movement of the microphone. The obtained reconstructed 2D spectrum is shown in Fig. 11. This spectrum is then further divided by the spectrum of one period of the excitation signal. Taking the 2D inverse Fourier transform of the result leads to the RIRs at the different angular positions. A typical RIR obtained by the algorithm is shown in Fig. 12. The RIR is not exactly zero at its beginning because of time aliasing. Aliasing happens since the RIR is not exactly zero after 250 ms but still contains some energy.

Estimating the correctness of the reconstructed RIRs is not a straightforward task. This is mainly due to different limitations related to the setup of the experiment. First of all, the hardware used did not allow a perfect synchronization between the moving motor and the emitted sound. Another limitation of the material was the presence of noise emitted by the motor when the Pan/Tilt unit moves. Adaptively removing the noise or putting around the motor some sound absorbing material could be considered to attenuate this noise source. Nevertheless, the reconstructed RIRs were compared with statically measured RIRs, and the mean squared error (MSE) between them was of the order of −10 to −15 dB. Note that the measurement conditions were not exactly similar for the measurement of the two sets of RIRs (one set obtained with the moving microphone and the other set using a static microphone). The temperature variation as

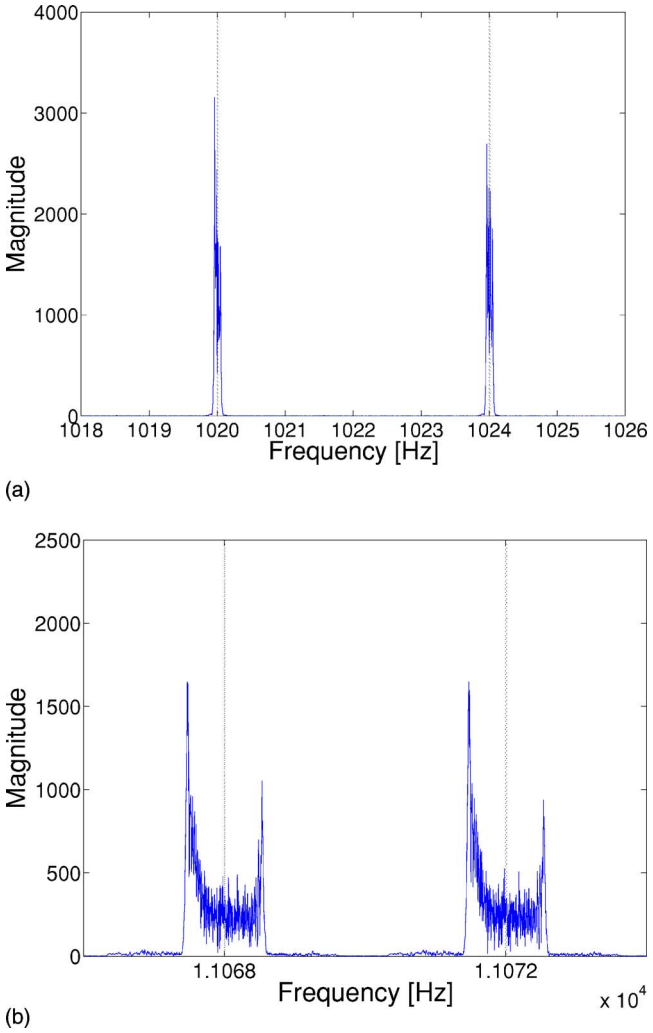

FIG. 10. (Color online) Spectrum of the moving microphone signal (a) at low frequencies (between 1018 and 1026 Hz) and (b) at high frequencies (between 11 066 and 11 074 Hz).

well as the intrusion of a person in the room can lead to variations in the speed of the sound as was shown in Refs. 8 and 20. It is shown in Ref. 8 that a variation of 0.1 deg can create a misalignment between RIRs of more than 25 dB. These different aspects make the comparison in the MSE

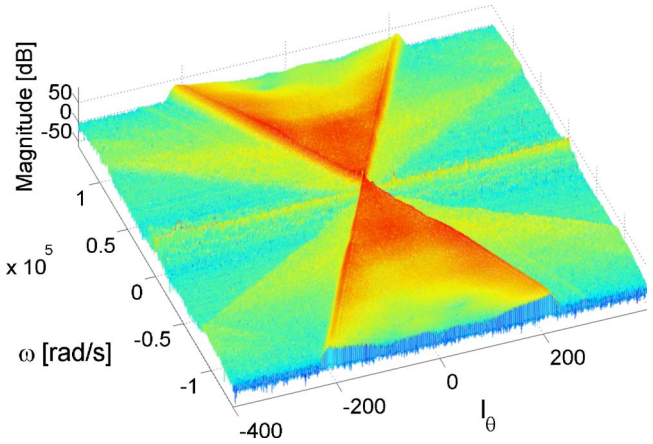

FIG. 11. (Color online) 2D-FT of the recorded data obtained after undoing the effect of the projection due to the recording by the moving microphone.

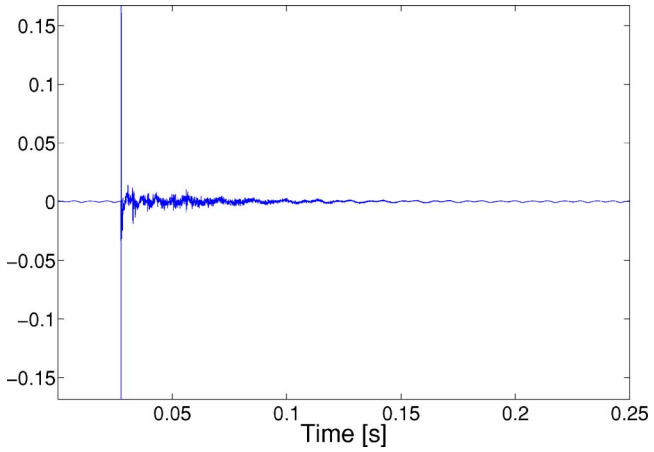

FIG. 12. (Color online) Example of a reconstructed RIR using the presented algorithm.

sense difficult. Nevertheless, the relative time difference and attenuation between the reconstructed RIRs is coherent and similar to the theoretical results obtained in Sec. II or found using a standard static technique.

This section has presented experimental results obtained using hardware showing certain limitations. The purpose of the experiments was to show the possible applicability of the presented algorithm. Further work involving the design of a system using dedicated hardware could be considered. Better attenuation of the motor noise and a better synchronization of the system would lead to better MSE between the static and dynamically reconstructed room impulse responses. The engineering effort to devise a better system is beyond the scope of this paper, since the aim of the experiments was mainly to validate the theory. The obtained MSE is sufficient for this purpose.

VII. CONCLUSION

In this paper, a technique was presented to record large sets of room impulse responses using a microphone moving along a trajectory. The technique reconstructs the room impulse responses at any position along a linear or a circular array. The speed of movement of the microphone has been shown to be the key factor for the reconstruction. The theoretical aspects of the presented algorithm have been compared with experimental results.

[1]D. Zotkin, R. Duraiswami, and L. Davis, "Rendering localized spatial audio in a virtual auditory space," IEEE Trans. Multimedia **6**, 553–564 (2004).
[2]J. Miller, "SLAB: A software-based real-time virtual acoustic environment rendering system," in *International Conference on Auditory Display*, Espoo, Finland (2001).
[3]J. Blauert, *Spatial Hearing* (MIT, Cambridge, MA, 2001).
[4]L. Savioja, "Modeling Techniques or Virtual Acoustics," Doctaral thesis, Helsinki University of Technology, Telecommunications Software and Multimedia Laboratory, Report TML-A3, 1999.
[5]T. Ajdler, "The plenacoustic function and its applications," Ph.D. thesis, Ecole Polytechnique Fédérale de Lausanne, 2006.
[6]A. J. Berkhout, D. de Vries, and P. Vogel, "Acoustic control by wave field synthesis," J. Acoust. Soc. Am. **93**, 2764–2778 (1993).
[7]D. de Vries, S. Brix, and E. Hulsebos, "Measurements of church impulse responses using a circular microphone array for natural spatial reproduction of a choir concert recording," in *21th Audio Engineering Society Conference* (2002).
[8]G. Elko, E. Diethorn, and T. Gänsler, "Room impulse response variation due to thermal fluctuation and its impact on acoustic echo cancellation," in *IWAENC*, Kyoto, Japan (2003), pp. 67–70.
[9]Remark that in this work, the turbulence of air due to the moving element is not taken into account in the analysis.
[10]S. Müller and P. Massarani, "Transfer function measurement with sweeps," J. Audio Eng. Soc. **49**, 443–471 (2001).
[11]J. Borish and J. Angell, "An efficient algorithm for measuring the impulse response using pseudorandom noise," J. Audio Eng. Soc. **31**, 478–488 (1983).
[12]B. Zhou, D. M. Green, and J. C. Middlebrooks, "Characterization of external ear impulse responses using golay codes," J. Acoust. Soc. Am. **92**, 1169–1171 (1992).
[13]C. Cheng and G. H. Wakefield, "Introduction to Head-Related Transfer Functions (HRTFs): Representations of HRTFs in time, frequency and space," J. Audio Eng. Soc., **49**, 231–249 (2001).
[14]D. Zotkin, R. Duraiswami, E. Grassi, and N. Gumerov, "Fast head-related transfer function measurement via reciprocity," J. Acoust. Soc. Am. **120**, 2202–2215 (2006).
[15]E. Hulsebos and D. de Vries, "Parametrization and reproduction of concert hall acoustics measured with a circular microphone array," in *112th Audio Engineering Society Convention* (2002).
[16]E. G. Williams, *Fourier Acoustics* (Academic New York, 1999).
[17]A. Berkhout, *Applied Seismic Wave Theory* (Elsevier Science, Amsterdam, 1987).
[18]Y.-H. Kim, "Can we hear the shape of a noise source?" in *The 18th International Congress on Acoustics* (2004).
[19]H.-S. Kwon and Y.-H. Kim, "Moving frame technique for planar acoustic holography," J. Acoust. Soc. Am. **103**, 1734–1741 (1998).
[20]T. Ajdler, L. Sbaiz, and M. Vetterli, "The plenacoustic function and its samplings," IEEE Trans. Signal Process. **54**, 3790–3804 (2006).
[21]T. Ajdler and M. Vetterli, "The plenacoustic function, sampling and reconstruction," in *IEEE Int. Conf. Acoust., Speech, Signal Processing (ICASSP)*, (2003), Vol. **5**, pp. 616–619.
[22]P. Morse and K. Ingard, *Theoretical Acoustics* (McGraw-Hill, New York, 1968).
[23]T. Ajdler, C. Faller, L. Sbaiz, and M. Vetterli, "Head-related transfer functions interpolation considering acoustics," 118th Conv. of the Audio Engineering Society (2005).
[24]T. Ajdler, L. Sbaiz, and M. Vetterli, "The plenacoustic function on the circle with application to HRTF interpolation," in *IEEE Int. Conf. Acoust., Speech, Signal Processing (ICASSP)* (2005), pp. 273–276.
[25]http://lcavwww.epfl.ch/~thibaut/Measurements/Last viewed on 23 March 2007.
[26]The formula is valid for the case of a movement along the same direction as the source-receiver axis.
[27]R. N. Bracewell, *The Fourier Transform and its Applications* (McGraw-Hill, New York, 2000).
[28]Note that in the case of a circular trajectory the speed is an angular speed and has units rad/s while along a line the speed "v" has units m/s. We chose to keep the same letter for simplicity of notation.
[29]A. V. Oppenheim and R. W. Schafer, *Digital Signal Processing* (Prentice-Hall, Englewood Cliffs, NJ, 1999).
[30]J. Breebaart, J. Herre, L. Villemoes, C. Jin, K. Kjöring; and J. Plogsties, "Multichannel goes mobile: Mpeg surround binaural rendering," in *29th Audio Engineering Society Conference* (2006).
[31]In Eq. (37), the width of $2\pi/T_p$ due to the finite duration of the emitted signal is not considered.

Effects of electrodes on performance figures of thin film bulk acoustic resonators

Tao Zhang, Hui Zhang, Zuo-qing Wang, and Shu-yi Zhang[a)]
Laboratory of Modern Acoustics, Institute of Acoustics, Nanjing University, Nanjing, Jiangsu 210093, China

(Received 20 December 2006; revised 18 June 2007; accepted 29 June 2007)

The effects of mechanical losses and elastic properties of the electrodes on the performance figures of a thin film bulk acoustic resonator (FBAR) are analyzed by numerical simulation. Results indicate that the material loss of the electrode has no visible effect on the characterization of the effective electromechanical coupling factor, k_{eff}^2. The acoustic impedance ratio of the electrode to the piezo-film dominantly determines the behaviors of the k_{eff}^2 variation with the electrode thickness. The resonance Q value, Q_s, of the FBAR closely relies on the material Q values of film and of electrodes as expected. Besides, the variation of Q_s versus the thickness of the electrodes crucially depends on the acoustic impedance ratio as well. Especially, three characteristic parameters, i.e., the maximum value of k_{eff}^2, the sectional mass ratio of the electrode to the piezo film corresponding to the maximum k_{eff}^2, and the tolerance range of the ratio to keep k_{eff}^2 near the maximum, are calculated for some typical samples. These results would be useful for optimizing FBAR designs and performances. © *2007 Acoustical Society of America.* [DOI: 10.1121/1.2764473]

PACS number(s): 43.58.Wc, 43.35.Ns, 43.20.Ks [PEB] Pages: 1646–1651

I. INTRODUCTION

Filters used in 1.9 GHz for personal communication system handsets based on thin film bulk acoustic resonators (FBARs) were first realized by micromachined thin film AlN devices,[1–4] and then various FBAR samples with much higher frequencies (even 6–8 GHz) and for different applications were reported.[5–9] In September, 2005, Agilent announced that their FBAR had been used in most of the biggest handset fabricators in the world. Because FBAR is a widely used and rapidly developing technology, better understanding of its physics is very important and so some theoretical research is still active.[6,10–15]

A key issue in engineering research and development of FBAR is the effect of electrodes, and quite a lot of research has been done by taking the effects of electrodes into consideration.[6,10–17] Many requirements and restrictions[5] on the electrodes in the FBAR are posed: (1) low acoustic attenuation, (2) high electric conductivity, (3) process compatibility, (4) better temperature compensation[4,10] and (5) to enhance the coupling coefficient of FBAR.[6,10,12–15] To satisfy these demands, thickness of the electrodes is not very thin and so its elastic properties and mechanical loss will significantly affect the performance of the FBAR.

As a kind of bulk acoustic resonator (BAR), the figure of merit of a FBAR[18] is defined as $M=k_{\text{eff}}^2 \cdot Q_s/(1-k_{\text{eff}}^2)$, where k_{eff}^2 is the effective electromechanical coupling factor,[13,18] and Q_s is the resonance quality factor. For the BAR used as oscillators, Q_s is the most crucial parameter, but FBARs are mostly used to construct ultrahigh frequency filters (at least around 1 GHz), and so k_{eff}^2 is also very important. It was demonstrated in IEEE Standard[18] that the mechanical losses in the piezoelectric materials had no effect on the piezoelectric coupling factor when the effects of the electrodes were ignored. For FBARs, however, the electrodes play an important role, and quite a bit of research[6,10–17] was reported recently. But in this research, very few papers[13] discussed the material loss effects on the FBAR performance.

In this paper, we will systematically investigate the effects of the material losses and the elastic properties of the electrodes on both the Q_s and the k_{eff}^2 of FBAR by numerical simulation for samples comprised of two usually used piezoelectric films, i.e., ZnO and AlN, and four typical electrode materials (Au, Ag, Al, and Mo). These samples represent most of the possible combinations of the piezoelectric films and electrodes.

In this paper, four research aspects and corresponding simulation results are presented: (1) the effects of mechanical losses of piezo films and electrodes on k_{eff}^2; (2) the effects of the elastic properties of electrodes on k_{eff}^2; (3) the effects of mechanical losses of piezo films and electrodes on Q_s; (4) the effects of the elastic properties of electrodes on Q_s. The discussions and conclusions are given in the final part.

II. SIMULATION METHOD AND PROCEDURE

For any kind of BAR, the k_{eff}^2 and Q_s are defined, respectively, by

$$k_{\text{eff}}^2 = (f_p^2 - f_s^2)/f_p^2 \cong 2 \cdot (f_p - f_s)/f_p, \tag{1}$$

$$Q_s = f_s/(\Delta f)_{-3dB}, \tag{2}$$

where f_p and f_s are the parallel and series resonance frequencies of the BAR, respectively. It should be kept in mind that k_{eff}^2 and Q_s are the important performance parameters of a

[a)]Author to whom correspondence should be addressed. Electronic mail: zhangsy@nju.edu.cn

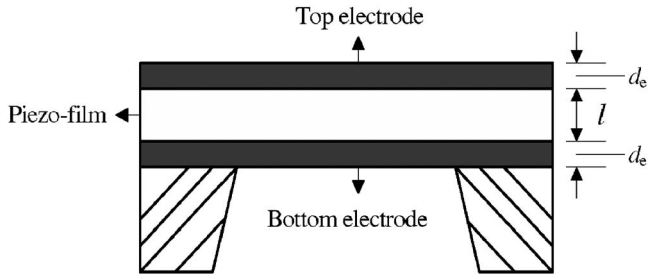

FIG. 1. A typical FBAR structure.

BAR, and, on the other hand, there are two corresponding parameters, k_t^2 and Q_m, which describe the corresponding properties of the piezoelectric film material. For a single piezoelectric resonator operating in a pure thickness extensional mode (it is the case of FBAR operating), ignoring its mechanical effects of the electrodes, the electromechanical coupling factor, k_t^2 is given by[13,18]

$$k_t^2 = \left(\frac{\pi}{2} \cdot \frac{f_s}{f_p}\right) \cdot \tan\left(\frac{\pi}{2} \cdot \frac{f_p - f_s}{f_p}\right). \quad (3)$$

The mechanical quality factor of the film and the electrode, Q_m, is defined by

$$Q_m = C'/C'', \quad (4)$$

where C' and C'' are the real part and the imaginary part of the elastic constant, respectively, and the imaginary part is responsible for the mechanical losses. In theory, k_t^2 and Q_m are only determined by the material property while k_{eff}^2 and Q_s are not only determined by k_t^2 and Q_m, but also closely related with the electrode and the resonator structure.

Now, let us discuss the calculation equations in simulation. It is shown in Eq. (1) that the k_{eff}^2 is given by, and only given by, the f_p and f_s of a FBAR. As a routine, f_p and f_s are determined by its input impedance equation. Another performance figure, the Q_s as given in Eq. (2), is merely determined by the resonance spectrum, which is determined by the input impedance of the FBAR as well. For a FBAR with two same electrodes as shown in Fig. 1, its input impedance equation can be given by[12,13]

$$Z_{in} = \frac{1}{j\omega C_0}\left[1 - \frac{k_t^2}{\gamma}\frac{z\sin\gamma + j(1-\cos\gamma)}{z\cos\gamma + (j/2)(1+z^2)\sin\gamma}\right], \quad (5)$$

where $C_0 = A\varepsilon_{33}^s/\ell$ is the clamped capacitor, A is the area of the electrodes, ε_{33}^s is the permittivity; γ is the phase shift, $\gamma = \omega\ell/V$, $V = \sqrt{C_{33}/\rho}$, ρ, V, and ℓ are the density, acoustic velocity and thickness of the piezo film, respectively. The equation $z = Z/Z_0$ is the characteristic impedance ratio of the electrodes to the piezo films. $Z = j \cdot Z_e \cdot \tan\gamma_e$, where $\gamma_e = \omega d_e/V_e$ is the phase shift in the electrode, $Z_e = \rho_e A V_e$, ρ_e, V_e, and d_e are the density, the acoustic velocity and thickness of the electrode, respectively. $Z_0 = \rho A V$ is the acoustic impedance of the piezoelectric layer.

In calculating the resonance frequencies, C_0 is excluded and so the permittivity ε_{33}^s and the area A are unnecessary. In general, all the dielectric, piezoelectric and elastic constants of the piezoelectric film and the elastic constants of the electrodes are complex. But in the following simulation we only consider the elastic constants of the piezo films and the electrodes as complex and take others as real values because we mainly investigate the effects of the electrodes on the performance of FBAR. As a result, only the acoustic velocity in piezo films and in electrodes implied in the above equations should be given by the complex,

$$V = \sqrt{C_{33}/\rho} = [(C' + j \cdot C'')/\rho]^{1/2} \approx V' \cdot [1 + j/2Q_m]; \quad (6)$$

$V' = \sqrt{C'/\rho}$ is the real part of acoustic velocity, and $V'' = \sqrt{C''/\rho}$ is the imaginary part, and then $Q_m = C'/C'' \cong V'/2V''$.[13,15] All the necessary parameters in the calculations, except the Q_m, are listed in Table I.

TABLE I. Data of material properties.

Material	Density (kg/m^3)	Velocity (m/s)	Impedance (10^6 kg/(m^2 s))	k_t^2 (%)
ZnO	5606	6350	35.6	7.50
AlN	3300	11 050	36.5	6.25
Al	2700	6418	17.3	Na
Au	19 320	3200	61.8	Na
Mo	10 000	6300	63.0	Na
Ag	10 600	3600	38.2	Na

For a designed FBAR, by substituting all those parameters into Eq. (5), the parallel and series frequencies, and the −3 dB bandwidth, i.e., f_p, f_s, and $(\Delta f)_{-3\text{ dB}}$, can be obtained by using the IEEE Standard[18] as mentioned, and then the effective coupling factor, k_{eff}^2, can be also obtained directly from Eqs. (1) and (2).

III. EFFECTS OF Q_m ON k_{eff}^2

In all the following calculations, the effects of mechanical losses in materials are expressed by the mechanical quality factors, $Q_m^{(f)}$ and $Q_m^{(E)}$, for the piezo films and the electrodes, respectively.

It is indicated in the IEEE Standard[18] that the mechanical loss in piezoelectric films has no significant effect on k_{eff}^2 if $Q_m^{(f)}$ is not very small. This conclusion was verified by HBARs with very high frequency (high overtone bulk acoustic resonators).[14,15] It can be easily found by the k_{eff}^2 definition that the mechanical losses in piezo films should have no obvious effects on the k_{eff}^2 as well. However, some simulation results reported recently showed that the k_{eff}^2 value significantly increases when $Q_m^{(f)}$ decreases at the low Q-value region.[13] We believe the result is wrong because the resonance frequency definition was misused.

The IEEE Standard[18] mentioned above is only for the cases where the effects of mechanical losses are ignored. What is the effect of the mechanical losses in electrodes on the k_{eff}^2?

Now, we will discuss the effects of mechanical losses both in piezo film and in electrodes on k_{eff}^2 of the FBARs. The k_{eff}^2 variation versus $Q_m^{(f)}$ for AlN piezo film with four different kinds of electrodes, i.e., Al, Mo, Ag, and Au, are calculated, and the results are shown in Fig. 2(a), in which the thickness $d_e = 0.2$ μm and $\ell = 1.78$ μm. Figure 2(b) shows the effects of $Q_m^{(E)}$ on k_{eff}^2, calculated for AlN piezo film with $\ell = 1.78$ μm and keeping $Q_m^{(f)} = 10\,000$ as a con-

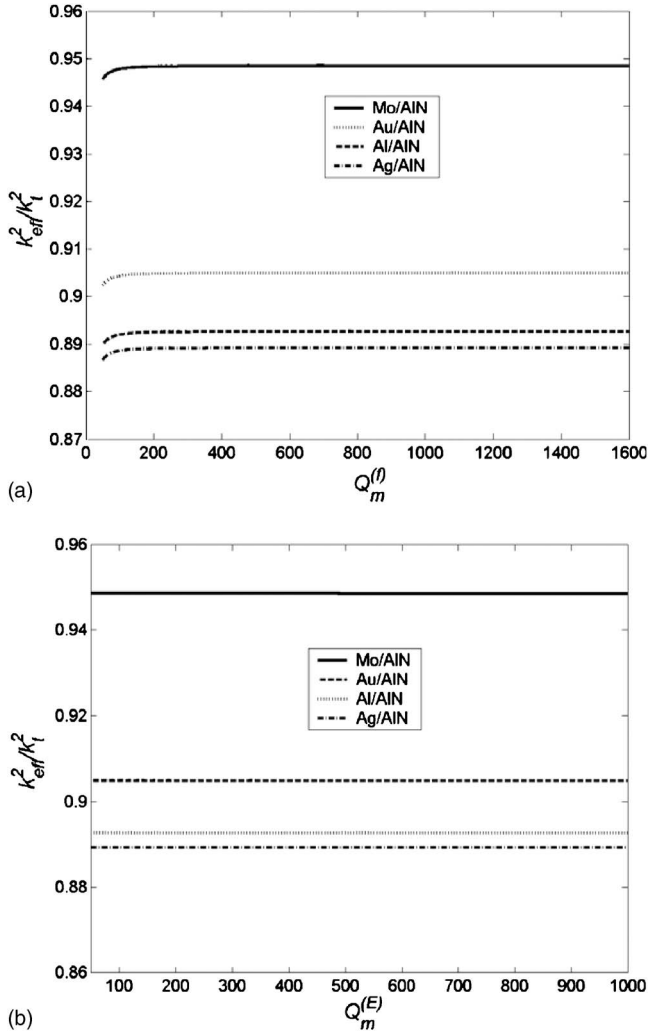

FIG. 2. AlN film with four different electrodes combinations, $\ell=1.78$ μm, $d_e=0.2$ μm, and other parameters listed in Table I: (a) k^2_{eff} vs $Q^{(f)}_m$, $Q^{(E)}_m=500$; (b) k^2_{eff} vs $Q^{(E)}_m$, $Q^{(f)}_m=10\,000$.

stant. Besides, we carried out similar calculations for Mo electrode with different thickness, i.e., $d_e=0$, 0.1, 0.2, and 0.4 μm, instead of different kinds of electrodes. The results are similar with Figs. 2(a) and 2(b), respectively, but the related figure is ignored for reducing the content.

The results shown in Fig. 2 indicate that (1) the mechanical losses both in piezo films and in electrodes have no visible effects on the k^2_{eff}; (2) the thickness and the property of the electrodes significantly affect the k^2_{eff}.

IV. EFFECTS OF ELASTIC PROPERTIES OF ELECTRODES ON k^2_{eff}

It is well recognized that the k^2_{eff} of FBAR is significantly affected by the electrodes. A modified Butterworth Van Dyke (BVD)-equivalent circuit had been developed to describe the k^2_{eff} and the resonance behaviors of FBAR by taking the electrode as an independent acoustic element.[12–15] Now, more comprehensive calculations for FBARs comprised of two kinds of piezo films, ZnO and AlN, combined with four kinds of electrodes, aluminum (Al), molybdenum (Mo), silver (Ag), and gold (Au) are carried out. As shown by Table I, both piezo films have very different density and

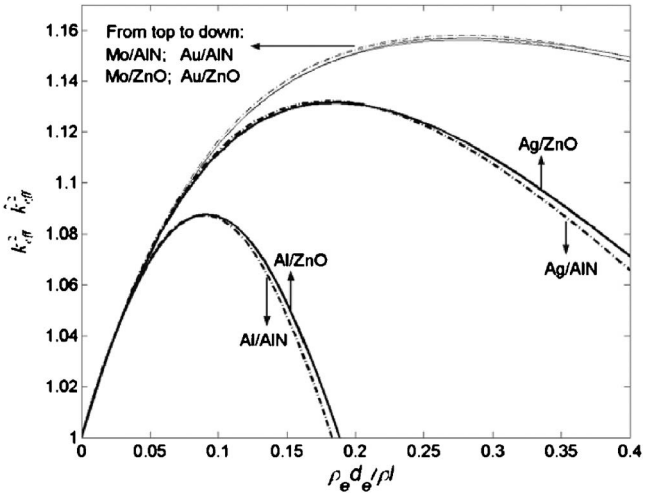

FIG. 3. $k^2_{\text{eff}}/\hat{k}^2_{\text{eff}}$ vs $\rho_e d_e/\rho l$ for two kinds of piezo films with four kinds of electrode combinations, $Q^{(f)}_m=10\,000$, and other parameters listed in Table I: for AlN film, $l=1.78$ μm; for ZnO film, $l=1.01$ μm.

acoustic velocity, but the acoustic impedances are almost the same. For the four kinds of electrodes, Mo and Au have much larger (three times) acoustic impedances than that of Al, and Mo has much higher velocity (two times) than Au but has similar acoustic impedance as Au. Comparing with the piezo films, Mo and Au have much larger (two times) acoustic impedance than that of the films, Al has much smaller acoustic impedance than that of the films, and Ag has similar impedance with the films. Therefore, these combinations of piezo films with electrodes represent most of the combinations of the practical materials from a physical point of view.

Figure 3 shows a set of typical results of the simulation. For clarity, we use $k^2_{\text{eff}}/\hat{k}^2_{\text{eff}}$ as the ordinate coordinate, where $\hat{k}^2_{\text{eff}}$ is the value ignoring the electrodes, and the abscissa is the sectional mass ratio, $(\rho_e d_e/\rho\ell)$, of electrode to film. It is shown in Fig. 3 that the curves of $k^2_{\text{eff}}/\hat{k}^2_{\text{eff}}$ versus $m'=\rho_e d_e/\rho\ell$ have definite and specific variation regulations. The curves start from $k^2_{\text{eff}}(0)$ and increase with the same slope, but reach to the maximum values at different abscissa, and then decrease gradually with different slopes. The behaviors of the curves could be described by three parameters: (1) the maximum $k^2_{\text{eff}}(m')$, (2) the abscissa $m'_c=(\rho_e d_e/\rho\ell)_c$ corresponding to the maximum $k^2_{\text{eff}}(m')$, and (3) the tolerance range of $(\rho_e d_e/\rho\ell)_{-0.1\text{ dB}}$ in which the k^2_{eff} decreases 0.1 dB from the maximum. Those parameters are evaluated and listed in Table II for the eight combinations corresponding to Fig. 3.

It is clearly shown in Fig. 3 and Table II that the acoustic impedance ratio of electrode to piezo film dominantly determines the variation of $k^2_{\text{eff}}(m')$ versus m', which include the maximum k^2_{eff} and the corresponding abscissa. The piezo films have similar acoustic impedance (although they have very different densities and velocities), and it is clearly shown that the acoustic impedance of the electrodes, i.e., (1) aluminum electrode, (2) Au and Mo electrodes (they have similar acoustic impedance), and (3) silver electrode, determine the behaviors of the curves.

TABLE II. Characteristic data for eight different combinations.

Piezo-film/ Electrode	$\frac{\rho_e V_e}{\rho V}$	$\left(\frac{k_{\text{eff}}^2}{k_{\text{eff}}^2}\right)_{\max}$	$\left(\frac{\rho_e d_e}{\rho l}\right)_c$	$\frac{d_e}{l}$	$\left(\frac{\rho_e d_e}{\rho l}\right)_{-0.1\ \text{dB}}$
ZnO/Al	0.49	1.09	0.09	0.19	0.06–0.12
AlN/Al	0.47	1.09	0.09	0.11	0.06–0.12
ZnO/An	1.80	1.16	0.28	0.08	0.17–0.43
AlN/An	1.76	1.16	0.28	0.05	0.17–0.41
ZnO/Mo	1.77	1.16	0.28	0.16	0.17–0.43
AlN/Mo	1.73	1.16	0.27	0.09	0.17–0.42
ZnO/Ag	1.07	1.13	0.19	0.10	0.12–0.26
AlN/Ag	1.05	1.13	0.18	0.06	0.12–0.26

The data given in column 4 of Table II could be used to estimate the thickness of the film and the electrodes of an FBAR for the FBAR operating near the maximum k_{eff}^2. For example, for an FBAR consisting of AlN film and Mo electrode, and operating at the resonance frequency $f_p = 1.9$ GHz, we can use the following formula (7)[12] to estimate the thicknesses of the film and of the electrode.

$$f_p \cong \frac{V}{2l} \cdot \left(1 + 2 \cdot \frac{\rho_e d_e}{\rho \ell}\right)^{-1}. \tag{7}$$

For obtaining the maximum k_{eff}^2, it is given in Table II that $\rho_e d_e / \rho \ell = 0.27$, and from Eq. (7) the thickness of the film should be around $l = 1.89$ μm based on the data in Table I, then we can find $d_e = 0.17$ μm.

It is easy in technologies to fabricate piezo-film thickness around 1–5 μm and to deposit electrode thickness around a few tens to hundreds nm. But high k_{eff}^2 is not the only factor to be considered. In fact, there are other requirements and restrictions posed on the electrodes,[5] including low acoustic wave attenuation, high electric conductivity, process compatibility, and temperature compensation,[4,10] etc. The data shown in column 5 of Table II give some guidance to modify the thickness of the piezo film and of the electrode. If it is necessary to decrease the thickness of electrode by keeping $f_p = 1.9$ GHz, one can use smaller $\rho_e d_e / \rho \ell$, for example, use $\rho_e d_e / \rho \ell = 0.17$, which is the minimum value to keep k_{eff}^2 near the maximum (only decreases 0.1 dB from the maximum). Then it can be obtained from Eq. (7) that the thickness of the piezo film should be around 2.17 μm, and the thickness of electrodes is around 0.12 μm. Contrarily, for increasing the thickness of the electrode, one can use the larger $\rho_e d_e / \rho \ell$. For example, one can take $\rho_e d_e / \rho \ell = 0.42$ which is the maximum to keep k_{eff}^2 near maximum (only decreases 0.1 dB from the maximum), and it can be found that the corresponding thicknesses are around $l = 1.58$ μm and $d_e = 0.22$ μm. Anyway, the thickness of the piezo films and the electrodes can be modified based on the requirements.

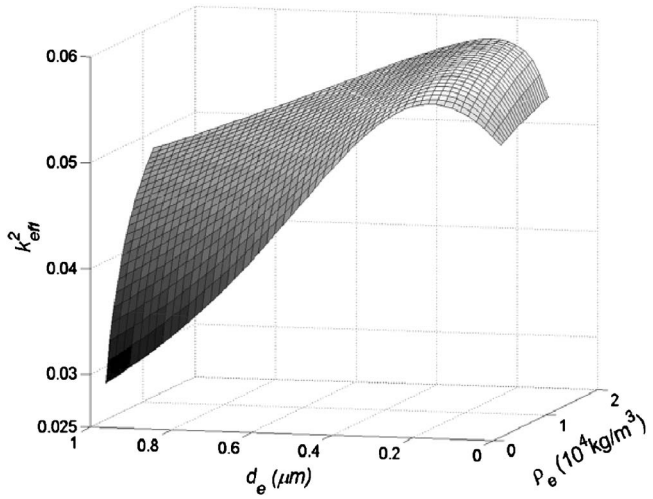

FIG. 4. Three-dimensional curve of k_{eff}^2 vs ρ_e and d_e for AlN film, $l = 1.78$ μm, $Q_m^{(f)} = 10\,000$, $v_e = 6300$ m/s.

On the other hand, the three dimensions variation of k_{eff}^2 versus ρ_e and d_e is given by Fig. 4, in which some results may be effective for the fabrication of FBAR.

Generally, the results given in this section could offer some physical insights into better understanding and some guidance in device designs and manufacture.

V. EFFECTS OF Q_m ON Q_s

The resonance quality factor, Q_s, which is defined in Eq. (2), is another important performance figure of the FBAR, especially for the devices used in frequency control systems. It is predictable qualitatively that the Q value of the piezo film and of the electrode materials will affect Q_s. But the quantitative relationship between Q_m and Q_s is interesting for the FBAR operation.

Figure 5(a) indicates the variation of $R_q = Q_s / Q_m^{(f)}$ versus $Q_m^{(f)}$, for AlN film with different electrodes, where $l = 1.78$ μm, $d_e = 0.2$ μm, and $Q_m^{(E)} = 500$. Figure 5(b) indicates the variation of $R_q = Q_s / Q_m^{(f)}$ versus $Q_m^{(f)}$ for the AlN film and Mo electrode with different thickness, $d_e = 0, 0.1, 0.2, 0.4$ μm where the piezo-film thickness l and the $Q_m^{(E)}$ are the same as in Fig. 5(a). Figure 5(c) shows R_q variation versus $Q_m^{(E)}$ for the combinations of AlN film with four kinds of electrodes, where $l = 1.78$ μm and $d_e = 0.2$ μm, by taking $Q_m^{(f)} = 10\,000$. Figure 5(d) demonstrates the variation of R_q versus $Q_m^{(E)}$ for AlN film and Mo electrode with different thicknesses $d_e = 0, 0.1, 0.2, 0.4$ μm.

It can be found in Fig. 5(b) that Q_s is always equal to the $Q_m^{(f)}$ when ignoring the electrode. The thicker the electrode, the larger decrease of the R_q is. There is a cross point for the four curves both in Figs. 5(a) and 5(b) which corresponds to $Q_m^{(f)} = Q_m^{(E)} = 500$ and $R_q = 1$. All the results are predictable and reasonable for the curves in Figs. 5(b) and 5(d). The results shown in Figs. 5(a) and 5(c) indicate that the elastic property of electrodes affects the Q_s significantly. It seems that the acoustic velocities in electrodes play an important role. The higher the velocity in electrode, the less the decrease of the

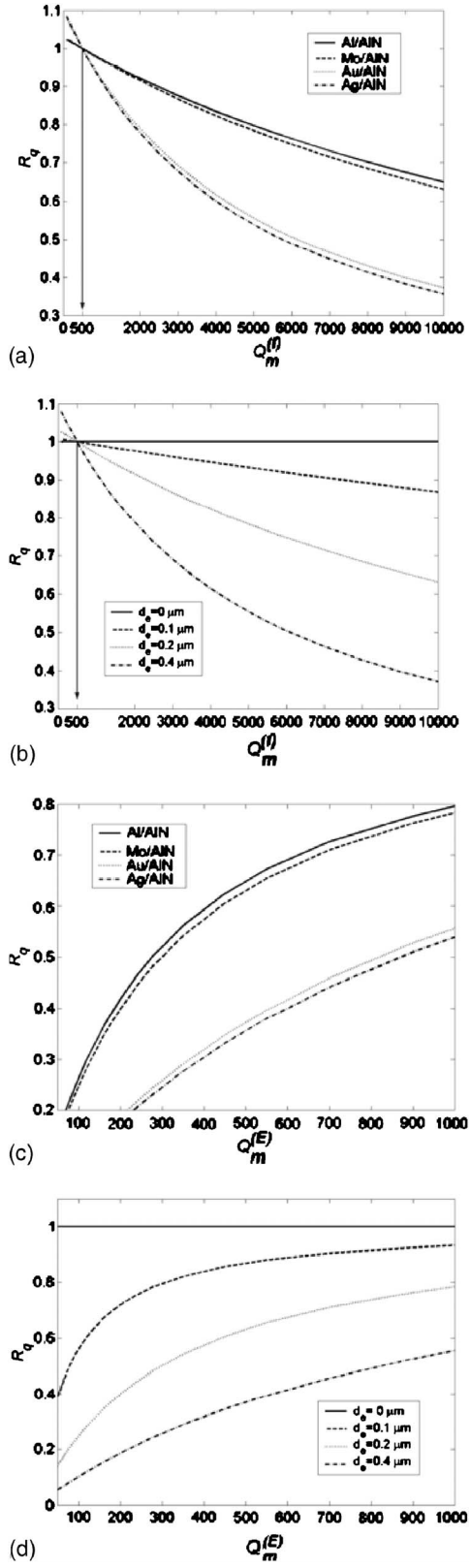

FIG. 5. AlN film with parameters as in Fig. 2: (a) $R_q(=Q_s/Q_m^{(f)})$ vs $Q_m^{(f)}$ with different electrodes, $d_e=0.2$ μm; (b) $R_q(=Q_s/Q_m^{(f)})$ vs $Q_m^{(f)}$ with Mo electrode in different thickness; (c) $R_q(=Q_s/Q_m^{(f)})$ vs $Q_m^{(E)}$ with different electrodes, $d_e=0.2$ μm; (d) $R_q(=Q_s/Q_m^{(f)})$ vs $Q_m^{(E)}$ with Mo electrode in different thickness.

R_q is, and then the four curves can be divided into two groups, because Al and Mo have similar and much higher velocity, and Ag and Au have similar but lower velocity.

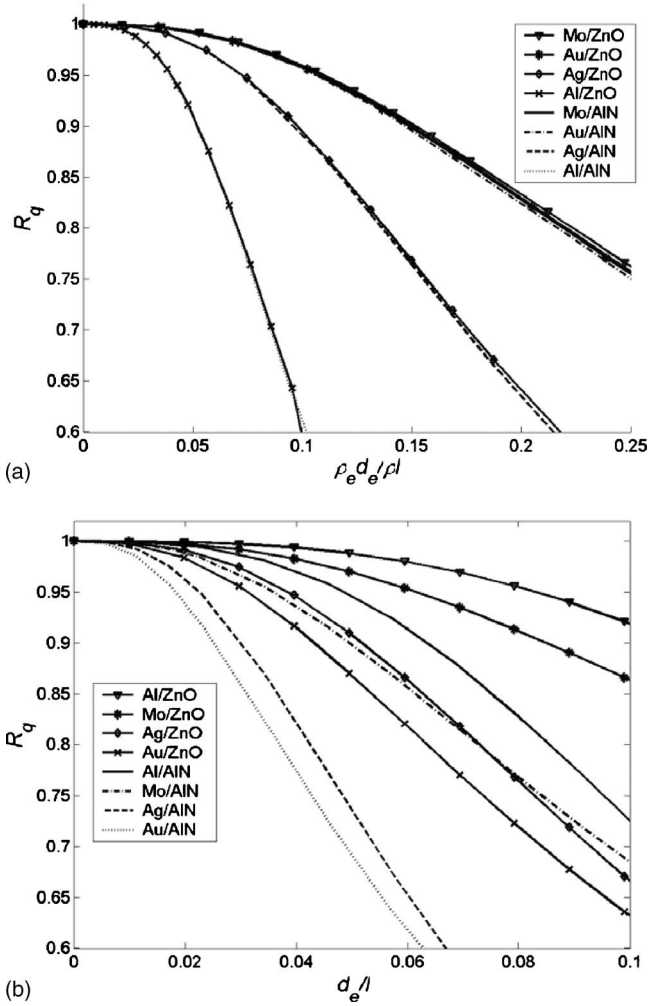

FIG. 6. Eight different combinations as in Fig. 3, $Q_m^{(E)}=500$, the piezo films with the same parameters as in Fig. 3: (a) R_q vs $\rho_e d_e/\rho l$; (b) R_q vs d_e/l.

VI. EFFECTS OF ELASTIC PROPERTIES OF ELECTRODES ON Q_s

For investigating the quantitative effects of the electrodes on the Q_s of the FBAR, some calculations have been made, and the results are shown in Fig. 6. Figures 6(a) and 6(b) are the variations of R_q versus $\rho_e d_e/\rho\ell$ and d_e/ℓ respectively, which are calculated by assuming both the piezo films having the same $Q_m^{(f)}=10\,000$. In each figure there are eight curves representing eight different combinations; and their elastic data are shown in Table II. For obtaining the same resonance frequency around 1.9 GHz, we choose the cases of $\ell=1.78$ μm for AlN film and $\ell=1.01$ μm for ZnO film, and both with Mo electrodes. The electrodes have the same $Q_m^{(E)}=500$.

It can be found from Fig. 6(a) that the $\rho_e V_e/\rho V$ definitely determines the variation of $R_q=Q_s/Q_m^{(f)}$ versus $\rho_e d_e/\rho\ell$. Comparing the data given in Table II, the four curves as the first group, i.e., Mo/ZnO, Au/ZnO, Mo/AlN, and Au/AlN, have a similar impedance ratio (1.77, 1.80, 1.73, and 1.76, respectively) and the four curves are so close that one cannot distinguish them. The second group, ZnO/Ag and AlN/Ag, have a similar impedance ratio of around 1.05. The third group, ZnO/Al and AlN/Al, have a similar impedance ratio of 0.49 and 0.47.

The variation curves of $R_q = Q_s/Q_m^{(f)}$ versus d_e/ℓ shown in Fig. 6(b) demonstrate a definite order for the curves. Taking the velocity ratio V_e/V are 1.01, 0.99, 0.58, 0.570, 0.567, 0.50, 0.33, and 0.29 corresponding to the combinations of Al/ZnO, Mo/ZnO, Al/AlN, Mo/AlN, Ag/ZnO, Au/ZnO, Ag/AlN, and Au/AlN, respectively. The order of the curves is same as the order of V_e/V, except for the curves of Mo/AlN and of Ag/ZnO, and the last two curves almost superpose with each other in the range of $d_e/\ell < 0.1$ because of their very approximate V_e/V, i.e., 0.570 and 0.567, and the other parameters such as the density should be responsible for this microdifference. In general, the higher the velocity ratio, the less decrease of the R_q there is. This phenomenon can be attributed to the relatively less attenuation in the electrode for the higher velocity ratio cases. For example, for the Al/ZnO case, where $V_e/V = 1.01$, and for relative thickness of $d_e/\ell = 0.10$, the acoustic wave in electrode only occupies about 9% of the half wavelength, and for the case of Au/AlN, where $V_e/V = 0.29$, and for the same relative thickness of $d_e/\ell = 0.10$, the acoustic wave in electrode occupies about 28% of the half wavelength. The material loss in electrode is much higher than that in piezo-film (20 times in our data), as a result, the decrease of Q_s will be more significant for the low velocity ratio cases.

VII. DISCUSSIONS AND CONCLUSIONS

In this paper, a comprehensive simulation for the effects of the electrodes on FBAR performance figures is given.

At first, it was demonstrated in IEEE Standard[18] that the mechanical loss in the piezoelectric materials can be ignored in characterizing the electromechanical coupling factor k_{eff}^2 if the effects of the electrodes are ignored. Now it is demonstrated that the effects of mechanical losses in electrodes on k_{eff}^2 of FBAR can be ignored as well; even the electrodes are not ignored, which is very different from the result, i.e., "a high mechanical Q factor leads to a low effective electromechanical coupling coefficient."[13]

Second, a definite and clear quantitative relationship between k_{eff}^2 and sectional mass ratio $\rho_e d_e/\rho\ell$ is obtained. The acoustic impedance ratio of the electrode to the piezo film dominantly determines the variation behaviors of the k_{eff}^2. Three characteristic parameters, i.e., the maximum k_{eff}^2, the corresponding sectional mass ratio, and the tolerance range to keep k_{eff}^2 near the maximum, are evaluated, which can be used as the guidance for FBAR designs and manufacture.

Third, the effects of the elastic property of electrodes on the resonance Q value are demonstrated definitely and clearly. The variation curves of the resonance Q value versus the sectional mass ratio ($R_q = Q_s/Q_m^{(f)}$ versus $\rho_e d_e/\rho\ell$) indicate that the acoustic impedance ratio determines their behaviors. The higher impedance ratio, the less degradation of the resonance Q value will be. On the other hand, the variation curves of $R_q = Q_s/Q_m^{(f)}$ versus the relative thickness, d_e/ℓ, demonstrate that the acoustic velocity ratio in electrode to that in film determines the resonance Q-value variation behaviors. The higher velocity in electrode, the less decrease of the resonance Q-value there will be. This phenomenon can be attributed to relatively less attenuation in the electrode for the higher velocity ratio cases.

Finally, we tried to find some quantitative relationship between the material Q_m and the Q_s value of FBAR, but it seems very difficult. Only some qualitative conclusions can be obtained from the simulation results and they can be predicted from physical principles actually.

ACKNOWLEDGMENT

This work is supported by National Natural Science Foundation of China, Grant No. 10374051.

[1] R. Ruby, P. Bradley, J. D. Larson III, and Y. Oshmyansky, "PCS 1900 MHz duplexers using thin film bulk acoustic resonators (FBARs)," Electron. Lett. **35**, 794–796 (1999).
[2] J. D. Larson III, R. Ruby, P. Bradley, and Y. Oshmyansky, "A BAW antenna duplexer for the 1900 MHz PCS band," *Proc. IEEE Ultrason. Symp.*, Caesars Tahoe, Nevada, 887–890 (1999).
[3] J. D. Larson III, P. D. Bradley, S. Wartenberg, and R. C. Ruby, "Modified Butterworth-Van Dyke circuit for FBAR resonators and automated measurement system," *Proc. IEEE Ultrason. Symp.*, San Juan, Puerto Rico, 863–868 (2000).
[4] J. D. Larson III, R. C. Ruby, Paul D. Bradley, J. Wen, S. L. Kok, and A. Chien, "Power handling and temperature coefficient studies in FBAR duplexers for the 1900 MHz PCS band," *Proc. IEEE Ultrason. Symp.*, Atlanta, Georgia, 869–874 (2000).
[5] R. C. Ruby, P. Bradley, Y. Oshmyansky, and A. Chien, "Thin film bulk wave acoustic resonators (FBAR) for wireless applications," *Proc. IEEE Ultrason. Symp.*, 813–821 (2001).
[6] K. M. Lakin, J. Belsick, J. F. McDonald, and K. T. McCarron, "Improved bulk wave resonator coupling coefficient for wide bandwidth filters," *Proc. IEEE Ultrason. Symp.*, 827–831 (2001).
[7] H. P. Lobl, M. Klee, C. Metzmacher, W. Brand, R. Milsom, P. Lok, and F. V. Straten, "Piezoelectric materials for baw resonators and filters," *Proc. IEEE Ultrason. Symp.*, 807–811 (2001).
[8] R. Lanz, M. A. Dubois, and P. Muralt, "Solidly mounted baw filters for the 6–8 GHz range based on AlN thin films," *Proc. IEEE Ultrason. Symp.*, 843–846 (2001).
[9] H. Campanella, J. Esteve, J. Montserrat, A. Uranga, G. Abadal, N. Barniol, and A. Romano, "Possibilities of thin-film bulk acoustic resonators as punctual mass sensors," J. Acoust. Soc. Am. **119**, 3414 (2006).
[10] J. D. Larson III and Y. Oshmyansky, "Measurement of effective k_t^2, Q, R_p, R_s vs temperature for Mo/AlN FBAR resonators," *Proc. IEEE Ultrason. Symp.*, 939–943 (2002).
[11] P. C. Y. Lee, N. H. Liu, and A. Ballato, "Thickness vibrations of a piezoelectric plate with dissipation," IEEE Trans. Ultrason. Ferroelectr. Freq. Control **51**, 52–62 (2004).
[12] M. C. Chao, Z. N. Huang, S. Y. Pao, Z. Wang, and C. S. Lam, "Modified bvd-equivalent circuit of FBAR by taking electrodes into account," *Proc. IEEE Ultrason. Symp.*, Munich, Germany, 973–976 (2002).
[13] Q. Chen and Q. Wang, "The effective electromechanical coupling coefficient of piezoelectric thin-film resonators," Appl. Phys. Lett. **86**(022904), 1–3 (2005).
[14] Y. Zhang, Z. Wang, and J. D. N. Cheeke, "Resonant spectrum method to characterize piezoelectric films in composite resonators," IEEE Trans. Ultrason. Ferroelectr. Freq. Control **50**, 321–333 (2003).
[15] H. Zhang, S. Y. Zhang, and K. Zheng, "Parameters characterization of high-overtone bulk acoustic resonators by resonant spectrum method," Ultrasonics **43**, 635–642 (2005).
[16] J. S. Yang, *Analysis of Piezoelectric Devices* (World Scientific, 2006), pp. 49–72.
[17] P. C. Y. Lee and R. Huang, "Mechanical effects of electrodes on the vibrations of quartz crystal plates," IEEE Trans. Ultrason. Ferroelectr. Freq. Control **49**, 612–625 (2002).
[18] IEEE Standard on Piezoelectricity 1760–1987, IEEE Trans. Ultrason. Ferroelectr. Freq. Control **43**, 717 (1996).

Single- and multi-channel underwater acoustic communication channel capacity: A computational study[a)]

Thomas J. Hayward[b)] and T. C. Yang
Naval Research Laboratory, Washington, DC 20375

(Received 5 October 2006; revised 24 May 2007; accepted 25 May 2007)

Acoustic communication channel capacity determines the maximum data rate that can be supported by an acoustic channel for a given source power and source/receiver configuration. In this paper, broadband acoustic propagation modeling is applied to estimate the channel capacity for a time-invariant shallow-water waveguide for a single source-receiver pair and for vertical source and receiver arrays. Without bandwidth constraints, estimated single-input, single-output (SISO) capacities approach 10 megabits/s at 1 km range, but beyond 2 km range they decay at a rate consistent with previous estimates by Peloquin and Leinhos (unpublished, 1997), which were based on a sonar equation calculation. Channel capacities subject to source bandwidth constraints are approximately 30–90% lower than for the unconstrained case, and exhibit a significant wind speed dependence. Channel capacity is investigated for single-input, multi-output (SIMO) and multi-input, multi-output (MIMO) systems, both for finite arrays and in the limit of a dense array spanning the entire water column. The limiting values of the SIMO and MIMO channel capacities for the modeled environment are found to be about four times higher and up to 200–400 times higher, respectively, than for the SISO case. Implications for underwater acoustic communication systems are discussed. [DOI: 10.1121/1.2749709]

PACS number(s): 43.60.Ac [EJS] Pages: 1652–1661

I. INTRODUCTION

One of the basic issues for underwater acoustic communications is the channel capacity. The channel capacity expresses the maximum data rate that can be supported by an acoustic channel for a given source power and source/receiver configuration. For underwater acoustic communication system design, it is imperative that the total acoustic traffic does not exceed the channel capacity.

In early work in communication theory, the problem of determining the capacity of a linear time-invariant communication channel with Gaussian source and known channel impulse response function was formulated as an extremal problem, leading to the explicit "waterfill" solution found by Shannon.[1] The Shannon result assumes that the channel is time invariant and is perfectly known to both the source and the receiver. In theory, mean data rates approaching the channel capacity arbitrarily closely, with arbitrarily low error rates, can be achieved in the limit of infinite code block lengths. Since the time invariance assumption does not hold in practice, Shannon's channel capacity result gives an upper bound on achievable data rates that may not be closely approached in practice. Nevertheless, channel capacity results for time-invariant channels provide an important benchmark for acoustic communication research.

In radio frequency communications, the noise spectrum level is often nearly constant over the frequency band of interest, while the transmission loss is often sufficiently low to permit signal reception above the noise level throughout the frequency band. As a consequence, for transmissions between a single source and a single receiver, often referred to as single-input, single-output (SISO) communications, the channel capacity is proportional to the signal bandwidth and to the logarithm of the source spectrum level. Put another way, the channel capacity is limited only by the source power. For single-input, multiple-output (SIMO) systems, assuming that the noise is uncorrelated across the receivers, the channel capacity increases theoretically as the logarithm of the number of receivers. For multiple sources and multiple receivers, or multiple-input, multiple-output (MIMO) communications,[2] the channel capacity can be significantly higher than for SISO or SIMO systems, and, in the high signal-to-noise ratio limit, is proportional to the minimum of the number of sources and the number of receivers.

For an underwater acoustic channel, the received signal and noise levels for a given source spectrum and source-receiver range are highly frequency dependent and vary significantly with the source and receiver depths and with the ocean acoustic environment. As a result, the SISO channel capacity is not a simple function of the source power, and will depend on the source bandwidth, the source and receiver depths and the propagation conditions. The MIMO channel capacity will not always increase significantly with the number of sources/receivers due to sound attenuation in the ocean, which limits the number of independent paths that can be used for communications. Determining the relationship of the channel capacity to the above-mentioned variables in an underwater channel requires a computation incorporating the

[a)] Portions of Secs. I–III have appeared previously in "High Frequency Ocean Acoustics Conference (AIP Conference Proceedings)," American Institute of Physics, New York, 2004.

[b)] Author to whom correspondence should be addressed. Electronic mail: hayward@wave.nrl.navy.mil

physics of signal and noise propagation. (Reference 3 reports channel capacity computations incorporating modeled signal propagation).

In this paper, we compute channel capacity for SISO, MIMO and SIMO, communications using a numerical model for signal propagation and ambient noise, incorporating a realistic sound speed and bottom profile measured at sea in a shallow-water experiment. While these computations assume a time-invariant ocean waveguide, they shed light on the potential increase in channel capacity between MIMO and SISO/SIMO systems and can be used as a reference for comparing with actual communication data rates achieved at sea.

In reality, the ocean acoustic channel is time varying and the channel transfer function is not perfectly known to the source or to the receiver. For a time-varying channel, the Shannon result for known, time-invariant channels will likely substantially overestimate the channel capacity. What is required for a time-varying channel is a computation of the mutual information of the source and receiver for a given assumption about the statistical nature of the channel variations, or fading. Unfortunately, for a general time-varying channel, no closed-form expression for the mutual information has been derived except for simple channel models with, e.g., Rayleigh signal fading statistics.[4] The problem is particularly difficult for time-varying MIMO channels, for which Ref. 5 provides a survey of existing channel capacity results.

While numerical computations have been carried out for some time-varying radio-frequency channels,[6] a numerical model for the channel mutual information that incorporates the time-varying signal propagation physics of an underwater acoustic channel has not been attempted; the problem is extremely complicated and is beyond the scope of this paper.

This paper is organized as follows: Sec. II provides the formula, derived by Shannon,[1] for the channel capacity of a SISO channel. Section III presents results of SISO channel capacity computations for a range-independent medium defined by the mean (time-averaged) sound speed profile measured at a site in the 1995 experiment, Shallow Water Acoustics in a Random Medium (SWARM), conducted off the New Jersey coast. In the SISO calculation, two cases are considered. In the first case, the source spectrum is unconstrained; in the second case, the source spectrum is constrained by typical bandwidth limitations of physically realizable transducers. Section IV presents SIMO and MIMO channel capacity computations for vertical arrays of sources and receivers; we consider both finite arrays and the limiting case of a densely populated vertical array spanning the entire environment. Section V presents concluding remarks.

II. SINGLE-INPUT, SINGLE-OUTPUT (SISO) CHANNEL CAPACITY

Reference 1 derives the capacity of a known time-invariant linear channel with (complex) acoustic transfer function $H(f)$ for a Gaussian source having (random) complex spectral density $\boldsymbol{X}(f)$ and average power P, and additive

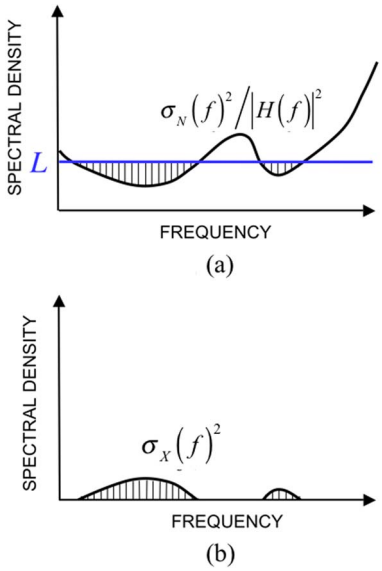

FIG. 1. (Color online) Schematic illustration of (a) spectral waterfill to a given level L; (b) optimal source spectrum defined by Eq. (3).

Gaussian noise having (random) complex spectral density $\boldsymbol{N}(f)$. In that case, the channel capacity is obtained as the maximum of the mutual information[7]

$$I = \int_0^\infty \log_2\left(1 + \frac{|H(f)|^2 \sigma_X^2(f)}{\sigma_N^2(f)}\right) df, \tag{1}$$

where $\sigma_X^2(f) = \langle |\boldsymbol{X}(f)|^2 \rangle$ and $\sigma_N^2(f) = \langle |\boldsymbol{N}(f)|^2 \rangle$, subject to the source power constraint

$$2\int_0^\infty \sigma_X^2(f) df = P_0. \tag{2}$$

(Here "$\langle \cdot \rangle$" denotes the expected value or ensemble average.) By a straightforward application of the method of Lagrange multipliers, the maximum is obtained when the source spectrum satisfies

$$\sigma_X^2(f) = \max\left\{L - \frac{\sigma_N^2(f)}{|H(f)|}, 0\right\}, \tag{3}$$

where the constant L is chosen so that Eq. (2) is satisfied. In underwater acoustic communication, the channel capacity is a function of the source-receiver range through the (implicit) dependence of the acoustic transfer function $|H(f)|^2$ on range.

The term waterfill is commonly used to express a metaphorical interpretation of Eq. (3), in which the spectral density "well" defined by the curve $\sigma_N^2(f)/|H(f)|^2$ is filled to increasingly high levels L until the source spectral density $\sigma_X^2(f)$, defined by Eq. (3), integrates over frequency to the available power P_0 (see Fig. 1.) When that level L is reached, the optimal source spectrum defined by Eq. (3) has as its spectral content the set of all frequencies f for which $L - \sigma_N^2(f)/|H(f)|^2 > 0$. The bandwidth of this optimal source may, in fact, exceed that which is physically realizable by a single source transducer. In practice, the bandwidth is often limited to a fraction of the carrier frequency. Channel capacity subject to these constraints can be found by restricting the

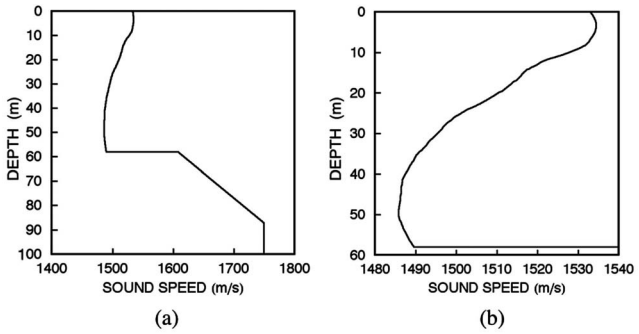

FIG. 2. Mean sound speed profiles for the SWARM yo-yo CTD site: (a) water column, sediment and subbottom; (b) detail of water column.

frequencies in Eq. (3) to the specified frequency bands.

III. SISO CHANNEL CAPACITY COMPUTATIONS

The first computations reported here are for a range-independent shallow-water environment derived from "yo-yo" (depth-cycling) conductivity/temperature/depth (CTD) measurements taken during the 1995 SWARM experiment.[8] Figure 2 shows the mean water-column and bottom sound speed profiles, based on 2 h of yo-yo CTD data and geoacoustic measurements reported in Ref. 8.

Acoustic propagation losses were computed using a Gaussian beam propagation code (Bellhop)[9] for a source at 10 m depth and a receiver at 30 m depth. Effects of bottom sound speed and attenuation were represented by reflection coefficients derived from the geoacoustic measurements. Surface scattering losses were computed using the surface loss component (SRFLOS) of the Oceanographic and Atmospheric Master Library[10] for wind speeds of 3 kn, representing the upper end of Sea State 0, and 20 kn, representing Sea State 4. Volume attenuation was represented by Thorp's Law.[11] The ambient noise spectrum was constructed based on typical shallow-water noise spectra given in Ref. 12. The acoustic fields were computed for frequencies ranging from 100 Hz to slightly less than 1 MHz in increments of 1/14 octave. This upper frequency limit was found to be sufficiently high to achieve the channel capacity in the computations for ranges greater than 1.2 km.

A. Results for unconstrained source bandwidth

Figure 3 shows the noise-to-channel function ratio $\sigma_N^2(f)/|H(f)|^2$ and the optimum source spectral density $\sigma_X^2(f)$ for the modeled SWARM environment, a source power of 193 dB μPa^2, and receiver ranges of 2, 5, 10 and 20 km. Note that, because of the high signal-to-noise ratio across the frequency band for the 193 dB source, the waterfill level L exceeds $\sigma_N^2(f)/|H(f)|^2$ by 15 dB or more over most of the available frequency band, so that the optimal spectral density in Eq. (3) is nearly flat (on a logarithmic scale), eliminating the need for a "shaped" source spectrum. The bandwidths of the optimal sources are approximately 90, 40, 23, and 20 kHz at ranges of 2, 5, 10, and 20 km, respectively. Source spectra at frequencies below 100 Hz were not included in the computations. Inclusion of these frequencies would increase the estimated channel capacity very slightly. (The capacity would increase by less than 1–2%. Note that Fig. 2 is a logarithmic plot that exaggerates the low-frequency region, while $\sigma_N^2(f)/|H(f)|^2$ will continue to rise with decreasing frequency below 100 Hz, due to the strong attenuation of the low-frequency signal in shallow water.[13]) In practice, high bandwidth systems would not likely include such low frequencies in the transmitted spectrum.

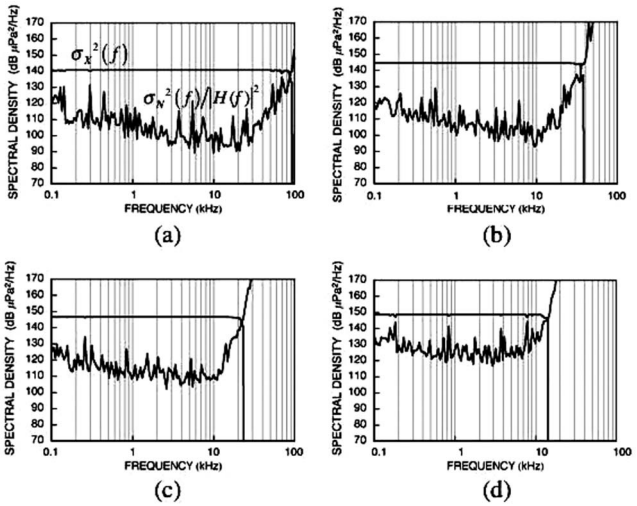

FIG. 3. Noise-to-channel function ratio $\sigma_N^2(f)/|H(f)|^2$ and optimal signal power spectral density $\sigma_X^2(f)$ for ranges of (a) 2 km, (b) 5 km, (c) 10 km, and (d) 20 km. The source power is 193 dB μPa^2, the source depth is 10 m, and the receiver depth is 30 m.

Figures 4(a) and 4(b) show the computed channel capacity for the mean sound speed profile as a function of range for wind speeds of 3 and 20 kn, respectively. The effect of the higher wind speed is to decrease the channel capacity by approximately 30–60%. These channel capacity estimates

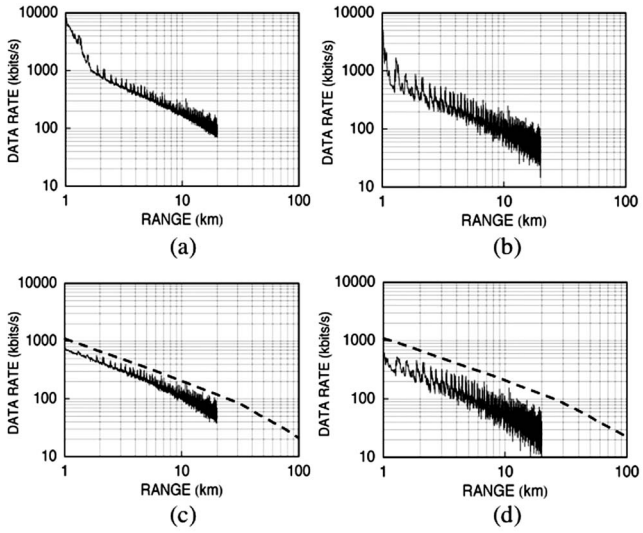

FIG. 4. Solid curves: Channel capacity estimates for the modeled SWARM environment for source power 193 dB μPa^2, source depth 10 m and receiver depth 30 m. (a) Unconstrained bandwidth, 3 kn wind speed, (b) Unconstrained bandwidth, 20 kn wind speed, (c) Constrained bandwidth, 3 kn wind speed, (d) Constrained bandwidth, 20 kn wind speed. Dashed curves: Channel capacity upper bounds for Sea State 0, subject to bandwidth equal to carrier frequency, obtained by Peloquin and Leinhos for a generic underwater channel based on sonar-equation analysis.

assume full utilization of the available bandwidth in constructing the optimal source spectrum $\sigma_X^2(f)$ given by Eqs. (2) and (3). In practice, the bandwidth of a single transducer is limited to some fraction of the carrier frequency, so that achieving the channel capacity would require multiple transducers.

B. Results for constrained source bandwidth

Considering the fact that a transducer has a limited useful bandwidth, it is of interest to determine the channel capacity for a constrained bandwidth. Channel capacities are computed in this section assuming that the source bandwidth W equals the carrier frequency, and that the carrier frequency has a range dependence of the form $f_c = a/\sqrt{r}$, where a is a constant. This functional form has been used in practice as a rule of thumb in system design (R. Peloquin and H. Leinhos, unpublished notes, 1997); it is motivated by studies of the optimal frequency for minimizing the depth-averaged transmission loss in a shallow-water waveguide.[13] The signal transmission loss increases with frequency above a certain frequency and decreases with frequency below that frequency, resulting in an optimal frequency band for maximizing the SNR; an example is shown in Ref. 14. While the optimal frequency band is waveguide dependent, in general it follows a range dependence of $r^{-1/2}$. In this section, we adapt this range dependence to the carrier frequency; specifically, we use $a=44{,}720$, determined by $f_c=20$ kHz at range $r=5$ km, a center frequency used commonly in acoustic modems.

Figures 4(c) and 4(d) show the channel capacities calculated for the modeled SWARM environment, subject to the frequency band constraints, for wind speeds of 3 and 20 knots, respectively. Also shown is the upper bound obtained by Peloquin and Leinhos for Sea State 0, based on a sonar-equation analysis for a generic underwater channel, also with the bandwidth constrained to be equal to the carrier frequency. The computed channel capacities for the modeled SWARM environment are approximately 30–90% below the sonar equation-based upper bounds, depending on wind speed and range.

Figure 4 shows an almost linear dependence of channel capacity on range in the log-log plot, suggesting that the channel capacity is approximately inversely proportional to range, i.e.,

$$C \approx \frac{\kappa}{r},$$

with the constant of proportionality κ varying from approximately 500 to 2000 km kbits/s for the two bandwidth-constrained cases (based on Figs. 4(c) and 4(d)). This may be compared with a compilation of experimental results that indicate an upper bound of approximately

$$\text{data rate} \leqslant \frac{40 \text{ km kbits/s}}{r}$$

(see Ref. 15), suggesting that limits of practically achievable data rates may be 1–2 orders of magnitude below the capacities computed for time-invariant channels. Similarly, comparisons of experimentally achieved data rates with sonar equation-based channel capacity computations (Peloquin and Leinhos, unpublished, 1997) reported a shortfall of 0.5–2 orders of magnitude.

IV. CAPACITY OF MULTI-INPUT, MULTI-OUTPUT VERTICAL ARRAY SYSTEMS AND SINGLE-INPUT, MULTI-OUTPUT SYSTEMS

This section presents channel capacity computations for the modeled SWARM shallow-water environment for multi-input, multi-output (MIMO) systems consisting of vertical source and receiver arrays, and for single-input, multi-output (SIMO) systems consisting of a single source and a vertical receiver array. We consider both arrays of finite aperture and the limiting case of a densely populated vertical array spanning the water column. As in Sec. III, the computations in this section are subject to the assumption of a time-invariant medium with perfectly known acoustic properties.

A. Capacity of MIMO systems

The appendix derives the explicit expressions for the channel capacity of a general MIMO linear system with Gaussian signal and noise. Although these expressions have been presented elsewhere,[16] a detailed derivation is given in the appendix to provide completeness and clarity of exposition and to establish notation for the application to the ocean waveguide. The optimal source cross-spectral matrix $\Sigma_{\mathbf{X}} = \Sigma_{\mathbf{X}}(f)$ is determined explicitly by specifying the source power spectral density $\bar{\rho}_j(f)$ in the jth eigenspace of the matrix

$$\mathrm{H}^{\dagger}\Sigma_{\mathbf{N}}^{-1}\mathrm{H}, \tag{4}$$

where $\mathrm{H}=\mathrm{H}(f)$ is the (matrix-valued) complex acoustic transfer function of the medium from the n sources to the n receivers and $\Sigma_{\mathbf{N}}=\Sigma_{\mathbf{N}}(f)$ is the noise cross-spectral matrix on the receiver array. This optimal source power spectral density is given by

$$\bar{\rho}_j(f) = \begin{cases} L - |q_j(f)|^{-2}, & \text{if } q_j(f) \neq 0 \\ 0, & \text{if } q_j(f) = 0, \end{cases} \tag{5}$$

where $|q_j(f)|^2$ is the jth eigenvalue of $\mathrm{H}^{\dagger}\Sigma_{\mathbf{N}}^{-1}\mathrm{H}$ and L is determined to satisfy the power constraint

$$2\int_0^{\infty} \mathrm{Tr}(\Sigma_{\mathbf{X}}(f))df = 2\int_0^{\infty} \sum_j \bar{\rho}_j(f)df = P_0. \tag{6}$$

That optimal source spectrum achieves the channel capacity, which is given by

$$C = \sum_j \int_{\{L-q_j(f)^{-2}\geqslant 0\}} \log_2(L|q_j(f)|^2)df. \tag{7}$$

B. MIMO channel capacity of range-independent waveguides with surface-generated noise

This section first derives the MIMO channel capacity for the modeled SWARM environment for the case of a noise field arising from a sheet density of uncorrelated noise sources near the ocean surface, based on the normal-mode

representation of the acoustic signal and noise fields. Then, a straightforward extension to a more realistic "slab" noise source model is applied to compute MIMO channel capacities for the same acoustic environment used in the SISO channel capacity computations.

1. MIMO channel capacity for a sheet-source noise model

Equations (4)–(7) show that computation of the MIMO channel capacity for a range-independent waveguide requires, in addition to the noise power spectrum required in the SISO case, a representation of the noise two-point cross-spectral density. One such representation is provided by the field of a sheet source of uncorrelated noise sources, originally investigated by Kuperman and Ingenito.[17] This section will derive the MIMO channel capacity in the idealized case of a sheet density of uncorrelated Gaussian noise point sources, distributed uniformly at all ranges and bearings. This noise source distribution is intended to approximate the long-term mean field of a distribution of surface-generated (e.g., breaking-wave) sources. The noise cross-spectral matrix and the medium transfer function are described explicitly in terms of the normal-mode representation of the acoustic field.

In the normal-mode representation, an approximation to the Green's function giving the acoustic field, at range 0 and depth z, of a point source at range r and depth z_0 in the water column is obtained by truncating the modal sum to M terms for sufficiently large M, viz.,

$$G(0,z;r,z_0) = \frac{i}{\sqrt{2\pi}} e^{i\pi/4} \sum_{m=1}^{M} \frac{e^{-i\lambda_m r}}{(\lambda_m r)^{1/2}} \psi_m(z_0)\psi_m(z), \tag{8}$$

where

$$\psi_m(z), \quad m = 1,2,\ldots,M$$

are the modal depth functions and λ_m, $m=1,2,\ldots,M$, are the corresponding mode eigenvalues. (M will later be taken to exceed both the number of sources and the number of receivers.)

Consider acoustic communication source and receiver arrays consisting of n_{src} sources at depths $z_1^{\mathrm{src}}, z_2^{\mathrm{src}}, \ldots, z_{n_{\mathrm{src}}}^{\mathrm{src}}$ and n_{rec} receivers at depths $z_1^{\mathrm{rec}}, z_2^{\mathrm{rec}}, \ldots, z_{n_{\mathrm{rec}}}^{\mathrm{rec}}$. Let ψ_m^{src} denote the column vector consisting of the values of the modal depth functions ψ_m at the source depths, viz.,

$$\psi_m^{\mathrm{src}} = (\psi_m(z_1^{\mathrm{src}}), \psi_m(z_2^{\mathrm{src}}), \ldots, \psi_m(z_{n_{\mathrm{src}}}^{\mathrm{src}}))^T, \tag{9}$$

$$m = 1,2,\ldots,M,$$

and let Ψ_{src} be the $n_{\mathrm{src}} \times M$ matrix formed by the column vectors ψ_m^{src}, viz.,

$$\Psi_{\mathrm{src}} = (\psi_1^{\mathrm{src}}, \psi_2^{\mathrm{src}}, \ldots, \psi_M^{\mathrm{src}}). \tag{10}$$

Similarly, let Ψ_{rec} be the matrix having as columns the values of the modal depth functions ψ_m at the receiver depths, viz.,

$$\Psi_{\mathrm{rec}} = (\psi_1^{\mathrm{rec}}, \psi_2^{\mathrm{rec}}, \ldots, \psi_M^{\mathrm{rec}}). \tag{11}$$

Now consider a uniform sheet density of uncorrelated Gaussian point sources at depth z_0 below the surface, having (random) complex noise source spectral density $N_0 = N_0(f)$ per unit of surface area (see Refs. 17 and 18). Then the two-depth noise cross-power spectrum is given by

$$\begin{aligned}\langle N(z)N(z')^* \rangle &= \langle N_0 N_0^* \rangle \int_0^\infty rG(0,z;r,z_0)G(0,z';r,z_0)^* dr \\ &= \langle |N_0|^2 \rangle \sum_{m=1}^{M} \sum_{\ell=1}^{M} \frac{i}{\lambda_m^{1/2} (\lambda_\ell^*)^{1/2} (\lambda_m - \lambda_\ell^*)} \\ &\quad \times \psi_m(z_0)\psi_\ell(z_0)\psi_m(z)\psi_\ell(z'). \end{aligned} \tag{12}$$

For an array of receivers at depths $z_1^{\mathrm{rec}}, z_2^{\mathrm{rec}}, \ldots, z_{n_{\mathrm{rec}}}^{\mathrm{rec}}$, let $\mathbf{N}$ denote the column vector of the (random) complex noise spectral values $N(z_i^{\mathrm{rec}}) = N(z_i^{\mathrm{rec}}, f)$, viz.,

$$\mathbf{N} = (N(z_1^{\mathrm{rec}}), N(z_2^{\mathrm{rec}}), \ldots, N(z_{n_{\mathrm{rec}}}^{\mathrm{rec}}))^T. \tag{13}$$

Then the noise cross-spectral matrix $\Sigma_{\mathbf{N}} = \Sigma_{\mathbf{N}}(f)$ is expressed compactly in matrix notation by

$$\begin{aligned}\Sigma_{\mathbf{N}} &= \langle \mathbf{N}\mathbf{N}^\dagger \rangle = \langle |N_0|^2 \rangle \sum_{m=1}^{M} \sum_{\ell=1}^{M} \Lambda_{ml} \psi_m(z_0)\psi_\ell(z_0) \psi_m^{\mathrm{rec}} \psi_l^{\mathrm{rec}\ T} \\ &= \langle |N_0|^2 \rangle \Psi_{\mathrm{rec}} \Psi_0 \Lambda \Psi_0 \Psi_{\mathrm{rec}}^T, \end{aligned} \tag{14}$$

where Λ is the $M \times M$ matrix whose m,ℓth entry is

$$\Lambda_{m\ell} = \frac{i}{\lambda_m^{1/2} (\lambda_\ell^*)^{1/2} (\lambda_m - \lambda_\ell^*)} \tag{15}$$

and

$$\Psi_0 = \mathrm{diag}\{\psi_1(z_0), \psi_2(z_0), \ldots, \psi_M(z_0)\}. \tag{16}$$

The acoustic transfer function from a vertical array of sources at $z_1^{\mathrm{src}}, z_2^{\mathrm{src}}, \ldots, z_{n_{\mathrm{src}}}^{\mathrm{src}}$ to a vertical array of receivers at and at range r from the sources is approximated by a complex-valued matrix $\mathrm{H}(r)$, where

$$(\mathrm{H}(r))_{jk} = \frac{i}{\sqrt{2\pi}} e^{i\pi/4} \sum_{m=1}^{M} \frac{e^{-i\lambda_m r}}{\lambda_m^{1/2} r^{1/2}} \psi_m(z_j^{\mathrm{rec}}) \psi_m(z_k^{\mathrm{src}}). \tag{17}$$

(The explicit dependence of the transfer function H on frequency f has now been omitted in favor of explicit dependence on range r.) In matrix notation, we have

$$\mathrm{H}(r) = \sum_{m=1}^{M} a_m(r) \psi_m^{\mathrm{rec}} \psi_m^{\mathrm{src}\ T} = \Psi_{\mathrm{rec}} \mathrm{A}(r) \Psi_{\mathrm{src}}^T, \tag{18}$$

where

$$\mathrm{A}(r) = \mathrm{diag}\{a_1(r), a_2(r), \ldots, a_M(r)\}, \tag{19}$$

with

$$a_m(r) = \frac{i}{\sqrt{2\pi}} e^{i\pi/4} \frac{e^{-i\lambda_m r}}{\lambda_m^{1/2} r^{1/2}}. \tag{20}$$

MIMO channel capacities were computed for the modeled SWARM environment using the procedure defined by Eqs. (4)–(7), with $\Sigma_{\mathbf{N}}$ and $\mathrm{H}(r)$ determined by Eqs. (14) and

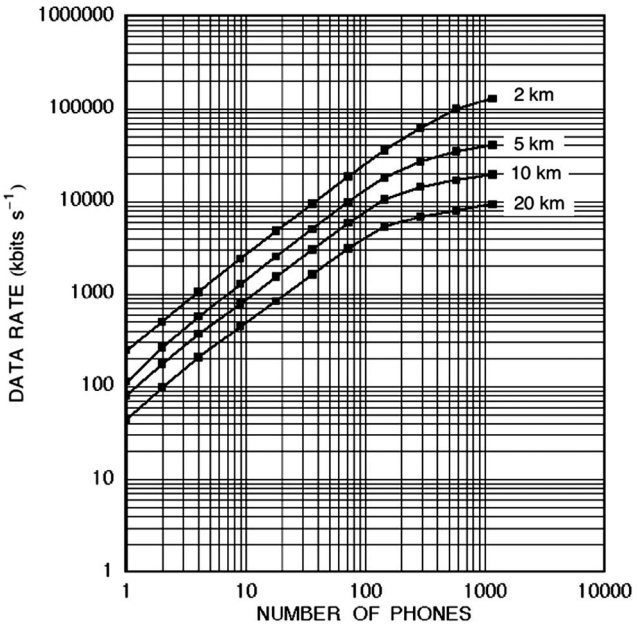

FIG. 5. MIMO channel capacity as a function of number of sources/receivers for uniformly spaced vertical arrays spanning the water column in the modeled SWARM environment. The upper frequency limit for the computation is 50 kHz. Receiver ranges from source are 2, 5, 10, and 20 km.

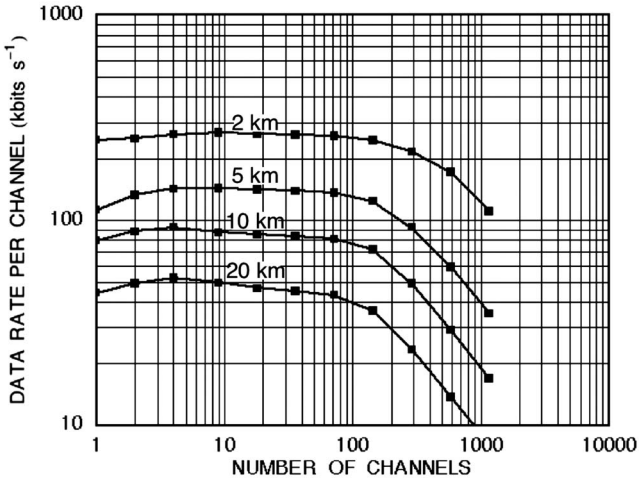

FIG. 6. MIMO channel capacity per channel as a function of number of sources/receivers for uniformly spaced vertical arrays spanning the water column in the modeled SWARM environment. Receiver ranges from source are: 2, 5, 10, and 20 km.

(18). The normal mode eigenvalues and depth functions were computed using the Kraken normal mode program.[19]

The channel capacity was computed as a function of the number of sources, equal to the number of receivers, for a source level of 193 dB (this time distributed over the entire source array as determined by the diagonal elements of $\Sigma_{\mathbf{X}}$). The source frequency was limited to 20 Hz–50 kHz because of computation time limitations. The noise covariance model was as specified by Eq. (14), except that the noise covariance was summed over five source sheets at depth intervals of 0.05–0.25 m in increments of 0.05 m, thus approximating a "slab" of uncorrelated noise sources. This noise source distribution was used in order to provide a more realistic distribution of noise (bubble) sources. The noise source spatial/spectral density $\langle|N_0|^2\rangle$ was treated as unknown, and was determined by setting the nominal noise power spectrum used in Sec. III equal to the modeled depth-averaged noise power, $1/n\ \mathrm{Tr}(\Sigma_{\mathbf{N}})$. A 30 dB down noise floor was added in order to prevent excess estimated channel capacity due to any spectral deficiency of the noise cross-spectral matrix.

Figure 5 shows the calculated MIMO channel capacities for the modeled SWARM environment as a function of the number of sources/receivers, n, for ranges of (a) 2 km, (b) 5 km, (c) 10 km, and (d) 20 km, for the 3 kn wind speed. An upper frequency limit of 50 kHz was used in the computation. For each value of n, the sources and receivers are spaced uniformly throughout the water column. For small n, the channel capacity is proportional to n. This is consistent with the observation, deducible from Eq. (A1), that, for high SNR, the channel capacity is proportional to the smaller of the number of sources and the number of receivers.[20] As n increases, the channel capacity begins to level off. This asymptotic behavior begins at smaller values of n for longer ranges, hypothetically because the number of acoustic modes contributing to the acoustic field (and hence to the spectral content of $\mathbf{H}^{\dagger}\Sigma_{\mathbf{N}}^{-1}\mathbf{H}$) is smaller at longer ranges.

Figure 6 shows the calculated MIMO channel capacity per channel as a function of the number of channels (sources/receivers) for the modeled SWARM environment. The capacity per channel is approximately constant up to about 100–300 channels, depending upon range, after which it begins to fall off rapidly. Note that this dependence on number of channels may be different for other underwater environments.

2. SIMO channel capacity

For single-input, multiple-output (SIMO) systems, the matrix-valued acoustic transfer function $\mathbf{H}(r)$ defined by Eq. (14) consists of a single column, and the matrix $\mathbf{H}^{\dagger}\Sigma_{\mathbf{N}}^{-1}\mathbf{H}$ contains a single element, equal to the sole eigenvalue $|q_1(f)|^2$. The channel capacity is determined by Eqs. (4)–(7), applied in this case to the values $|q_1(f_j)|^2$, with f_j ranging over the discrete computational frequencies.

SIMO channel capacities were computed for the modeled SWARM environment. Figure 7 shows the calculated SIMO capacity as a function of number of receivers (uniformly spaced throughout the water column) for ranges of 2, 5, 10 and 20 km (solid curves). For a small number of receivers, the capacity shows high variability associated with the sparse acoustic field sampling. For four or more receivers, the capacity shows a smooth variation and a slow growth with the number of channels. This growth, however, does not achieve the theoretical (high-SNR) dependence, given by the logarithm of the number of channels, that is a straightforward consequence of Eq. (A1). In fact, an increase from 10 to 1000 receivers results only in an approximate doubling of the channel capacity. This contrasts sharply with the linear growth of the capacity with the number of channels in the MIMO case.

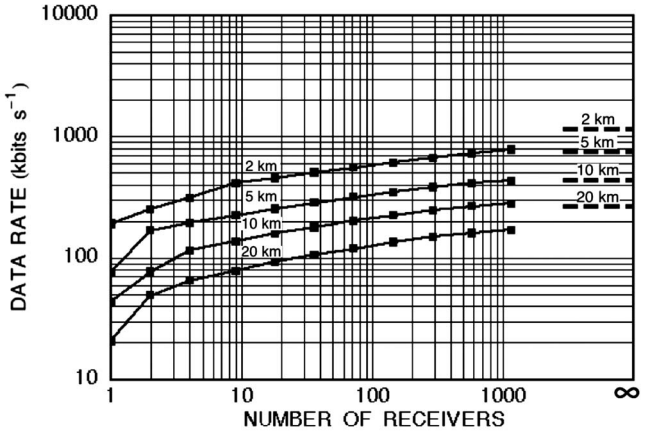

FIG. 7. Solid curves: SIMO channel capacity as a function of number of receivers for ranges of 2, 5, 10, and 20 km in the modeled SWARM environment. Dashed lines: Limit of SIMO-channel capacity as the number of receivers becomes large.

3. Limit of SIMO and MIMO channel capacities for a large number of receivers

This subsection calculates the SIMO and MIMO channel capacity of dense arrays consisting of n_{rec} receivers, in the limit as n_{rec} becomes large, for the modeled SWARM environment.

Let Ψ_{src} and Ψ_{rec} be defined by Eqs. (10) and (11). For large n_{rec} equal to the number of modes M, the matrix Ψ_{rec} is nonsingular. Equations (14) and (18) then give

$$\begin{aligned}\mathrm{H}(r)^{\dagger}\Sigma_{\mathbf{N}}^{-1}\mathrm{H}(r) &= \langle|N_0|^2\rangle^{-1}\Psi_{\mathrm{src}}\mathrm{A}(r)^{*}\Psi_{\mathrm{rec}}^{T}\cdot\Psi_{\mathrm{rec}}^{-T}\Psi_0^{-1}\Lambda^{-1}\Psi_0^{-1}\\ &\quad\times\Psi_{\mathrm{rec}}^{-1}\cdot\Psi_{\mathrm{rec}}\mathrm{A}(r)\Psi_s^{T}\\ &= \langle|N_0|^2\rangle^{-1}\Psi_{\mathrm{src}}\mathrm{A}(r)^{*}\Psi_0^{-1}\Lambda^{-1}\Psi_0^{-1}\mathrm{A}(r)\Psi_{\mathrm{src}}^{T}.\end{aligned} \tag{21}$$

For SIMO systems, this expression gives, for the row vector Ψ_{src}, the sole eigenvalue $|q_1(f_j)|^2$ for each frequency f_j, and the channel capacity is computed as before. Figure 7 shows, at the extreme right of the plot, the limiting value of the channel capacity for ranges of 2, 5, 10 and 20 km (dashed lines). These values exceed the values for ten receivers at the corresponding ranges only by a factor of approximately 2. For the 10 km range, the limiting value is about ten times higher than for the SISO ($n=1$) case.

Figure 8 shows the calculated MIMO channel capacities as a function of the number of sources/receivers, n, for ranges of (a) 2 km, (b) 5 km, (c) 10 km, and (d) 20 km, with an upper frequency limit of 33.3 kHz (solid curves). Figure 8 also shows, at the extreme right of the plot, the limiting value of the channel capacity for same ranges (dashed lines). The 33.3 kHz frequency limit was chosen for the limiting channel capacity computation because of computational difficulties for higher frequencies. The channel capacity upper bound is about twice the capacity for the 1160-receiver array. This is about 200–400 times higher than for the SISO case, depending upon range.

Figure 9 shows channel capacities as a function of range for a SISO system with source and receiver at 51.2 m depth, a SIMO system with nine receivers spaced uniformly over the water column, and a MIMO system with source and receiver arrays the same as the SIMO system receiver array. The capacity shows the same trend with range for all three classes of systems. As noted before, the capacity for the SIMO system is only slightly better than for the SISO system, while the MIMO capacity exceeds the SISO capacity by a factor approximately equal to the number of channels.

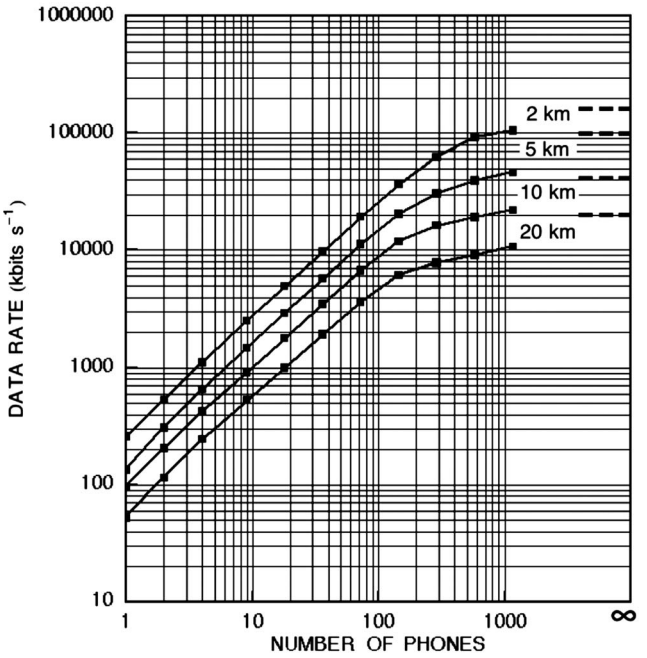

FIG. 8. Solid curves: MIMO channel capacity as a function of number of receivers for ranges of 2, 5, 10, and 20 km in the modeled SWARM environment, for an upper frequency limit of 33.3 kHz. Dashed curves: Limit of MIMO channel capacity as the number of receivers becomes large.

4. Effect of water-bottom interface scattering loss

The computations presented thus far were performed assuming a smooth (planar) interface between the water column and the sediment layer in the modeled SWARM environment. This represents the limiting case of a bottom interface that is totally reflecting below the critical angle of 22°. The energy propagating below the critical angle is attenuated only by the water-column volume attenuation determined by Thorp's Law.

In reality, some scattering loss will occur upon reflection from the water/sediment interface. As a limited initial investigation of the potential effect of such scattering loss on channel capacity, MIMO channel capacity computations were repeated using the same environment used previously, but with a small-perturbation treatment of the water/sediment interface,[21] assuming a rms roughness of 1.0 m. Figure 10 shows the computed MIMO capacities as a function of the number of sources/receivers for ranges of 2, 5, 10, and 20 km. Comparing Fig. 10 with Fig. 5 shows that, in the presence of mild interface roughness, the modeled channel capacities are diminished by factors ranging from approximately 10–15 for large numbers of receivers, with the greater effects occurring at longer ranges. These effects presumably

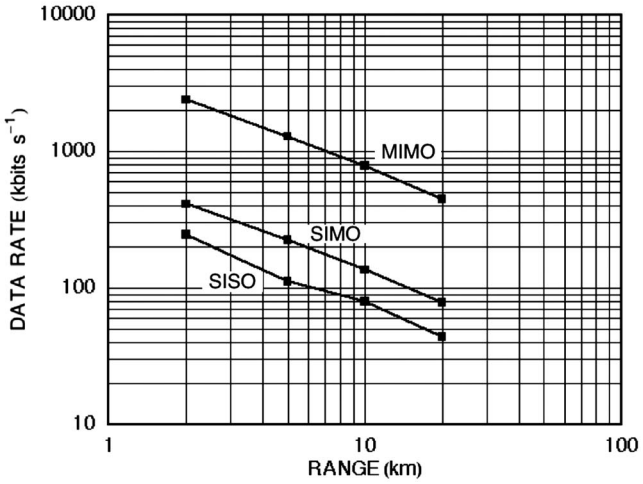

FIG. 9. Channel capacities as a function of range for: A SISO system with source and receiver at 51.2 m depth, a SIMO system with nine receivers spaced uniformly over the water column, and a MIMO system with source and receiver arrays the same as for the SISO system.

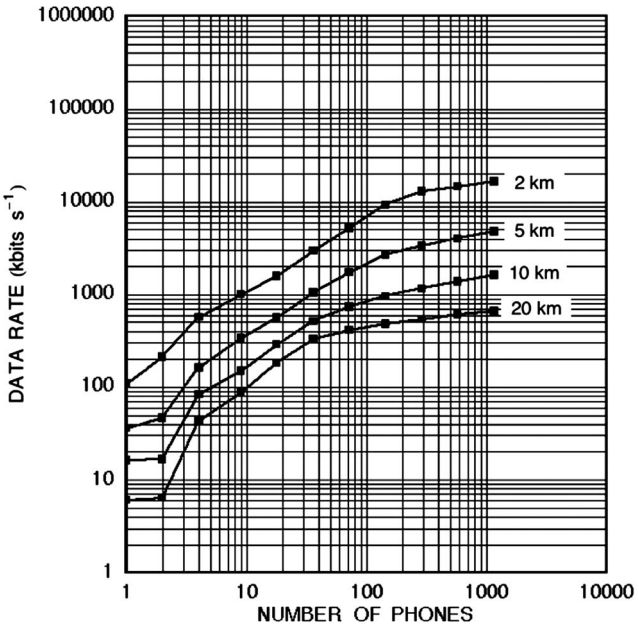

FIG. 10. MIMO channel capacity as a function of number of sources/receivers for uniformly spaced vertical arrays spanning the water column in the modeled SWARM environment with 1 m rms roughness at the bottom interface. The upper frequency limit for the computation is 50 kHz. Receiver ranges from source are 2, 5, 10, and 20 km.

result from the fact that a smaller number of modes have significant amplitude in the rough-interface case, as higher-angle modes will be attenuated by surface scattering.

V. CONCLUDING REMARKS

Acoustic communication channel capacities were computed for a single source-receiver pair for a time-invariant shallow water waveguide derived from the 1995 SWARM experiment. Without bandwidth constraints, computed SISO channel capacities for the mean environment approach 10 megabits/s at 1 km range for a source power of 193 dB μPa^2. Channel capacities subject to commonly imposed source center frequency and bandwidth constraints are up to 90% lower at ranges less than 2 km. This suggests that further study of the optimal source frequency band as a function of range for short-range communication is warranted.

MIMO channel capacities for the modeled SWARM environment were calculated as a function of number of sources/receivers. For ranges of 2, 5, 10 and 20 km, the channel capacity increases linearly with the number of users (source/receiver pairs) up to about 100–300 receivers; thus, the channel capacity per user is nearly constant. As the number of receivers increases further, the channel capacity begins to level off, so that the channel capacity per user diminishes.

SIMO channel capacities were computed as a function of number of receivers for ranges of 2, 5, 10 and 20 km. For a small number of receivers, the capacity shows high variability associated with the sparse acoustic field sampling. For four or more receivers, the capacity shows a smooth, slow growth with the number of receivers that is far less than the theoretical logarithmic dependence.

The limiting values of the SIMO and MIMO channel capacities for the modeled SWARM environment are about 4 and 200–400 times higher, respectively, than for the single-input, single-output (SISO) case.

The above numerical calculations were carried out using the acoustic environment corresponding to the 1995 SWARM experiment. Results for different shallow-water environments may differ in specific details but should agree in terms of the orders of magnitude, based on the general properties of the transmission loss. The substantial increase in the MIMO capacity over the SIMO capacity is expected to hold for typical environments as well. Channel capacity estimates more consistent with observed data rates will require an approach to calculate the channel capacity of a time-varying channel that incorporates the random-medium properties of the ocean. Factors affecting observed data rates include channel coherence time, channel estimation and tracking errors, co-channel interference, and information coding and decoding, none of which is well understood for the underwater acoustic channel at this time.

ACKNOWLEDGMENTS

This work was supported by the Office of Naval Research and by a grant of computer time from the Department of Defense High Performance Computing Modernization Program at the Army Research Laboratory Major Shared Resource Center. The authors thank Paul Gendron of NRL for helpful discussions.

APPENDIX: MIMO CHANNEL CAPACITY AND THE CAPACITY-ACHIEVING MULTI-INPUT SOURCE

This appendix determines the channel capacity and the capacity-achieving source signal cross-spectral matrix. The MIMO channel capacity has been extensively studied in radio frequency communications assuming a diagonal matrix for the noise covariance. A critical difference between underwater acoustic communications and radio frequency communications is that the noise is not white with respect to frequency and spatial (depth) correlation. For that reason,

particularly when a large-aperture vertical array is involved, it is critical to include the frequency and depth dependence of the ambient noise in the model calculation. To illustrate the role of a nondiagonal noise correlation matrix in the MIMO capacity, the expression for the channel capacity and the optimal source are briefly derived below for an underwater acoustic channel.

The MIMO capacity is the maximum of the mutual information of the source and receiver, given by

$$I(\mathbf{X},\mathbf{Y}) = \int_0^\infty \log_2 \frac{|\mathrm{H}\Sigma_\mathbf{X}\mathrm{H}^\dagger + \Sigma_\mathbf{N}|}{|\Sigma_\mathbf{N}|} df \tag{A1}$$

subject to the source power constraint

$$2\int_0^\infty \mathrm{Tr}(\Sigma_\mathbf{X}(f))df = P_0, \tag{A2}$$

where $|\mathrm{A}|$ and $\mathrm{Tr}(\mathrm{A})$ denote the determinant and the trace of a matrix A, respectively. In Eq. (A1), $\Sigma_\mathbf{X}=\Sigma_\mathbf{X}(f)=\langle \mathbf{X}(f)\mathbf{X}(f)^\dagger\rangle$ denotes the cross-spectral matrix of the source signal, assuming n sources, $\mathrm{H}=\mathrm{H}(f)$ is the acoustic transfer function (Green's function) of the ocean medium between the n source and the n receiver positions, and $\Sigma_\mathbf{N}=\Sigma_\mathbf{N}(f)=\langle \mathbf{N}(f)\mathbf{N}(f)^\dagger\rangle$ denotes the $n\times n$ noise covariance matrix. In Eq. (A1) and in most of the following, the dependencies of H, $\Sigma_\mathbf{X}$, and $\Sigma_\mathbf{N}$ on frequency f have been suppressed. Noting that $\Sigma_\mathbf{N}$ is nondiagonal, using the singular value decomposition

$$\Sigma_\mathbf{N} = \sum_{j=1}^{n} l_j \zeta_j \zeta_j^\dagger = \mathrm{ZLZ}^\dagger, \tag{A3}$$

$\Sigma_\mathbf{N}^{-1}$ can be expressed as

$$\Sigma_\mathbf{N}^{-1} = \Sigma_\mathbf{N}^{-1/2}\Sigma_\mathbf{N}^{-(1/2)\dagger}, \tag{A4}$$

where

$$\Sigma_\mathbf{N}^{-1/2} = \mathrm{ZL}^{-1/2} \quad \text{and} \quad \Sigma_\mathbf{N}^{-(1/2)\dagger} = (\Sigma_\mathbf{N}^{-1/2})^\dagger = \mathrm{L}^{-(1/2)*}\mathrm{Z}^\dagger, \tag{A5}$$

with $\mathrm{L}^{-1/2}=\mathrm{diag}\{\ell_1^{-1/2},\ell_2^{-1/2},\ldots,\ell_n^{-1/2}\}$. Equation (A1) can now be rewritten as

$$\begin{aligned} I(\mathbf{X},\mathbf{Y}) &= \int_0^\infty \log_2|\mathrm{I} + \Sigma_\mathbf{N}^{-1/2}\mathrm{H}\Sigma_\mathbf{X}\mathrm{H}^\dagger\Sigma_\mathbf{N}^{-(1/2)\dagger}|df \\ &= \int_0^\infty \log_2|\mathrm{I} + \Sigma_\mathbf{X}^{(1/2)\dagger}\mathrm{H}^\dagger\Sigma_\mathbf{N}^{-1}\mathrm{H}\Sigma_\mathbf{X}^{1/2}|df \end{aligned} \tag{A6}$$

Let

$$\mathrm{W} = \Sigma_\mathbf{N}^{-1/2}\mathrm{H} \tag{A7}$$

and let

$$\mathrm{W} = \sum_{k=1}^{n} q_k \nu_k \eta_k^\dagger = \tilde{\mathrm{N}}\mathrm{Q}\tilde{\mathrm{H}}^\dagger \tag{A8}$$

be the singular value decomposition of W, where

$$\mathrm{Q} = \mathrm{diag}\{q_1, q_2, \ldots, q_n\} \tag{A9}$$

and

$$\tilde{\mathrm{N}}^\dagger\tilde{\mathrm{N}} = \tilde{\mathrm{N}}\tilde{\mathrm{N}}^\dagger = \tilde{\mathrm{H}}^\dagger\tilde{\mathrm{H}} = \tilde{\mathrm{H}}\tilde{\mathrm{H}}^\dagger = \mathrm{I}. \tag{A10}$$

Let

$$\bar{\mathrm{Q}} = \mathrm{Q}^\dagger\mathrm{Q} = \mathrm{diag}\{|q_1|^2,|q_2|^2,\ldots,|q_n|^2\}. \tag{A11}$$

In the following, the diagonal elements of $\bar{\mathrm{Q}}$ will play a role analogous to that played by the single quantity $|q(f)|^2 = |H(f)|^2/\sigma_N(f)^2$ in the SISO case. Note that $|q_1|^2,|q_2|^2,\ldots,|q_n|^2$ are the eigenvalues of

$$\mathrm{W}^\dagger\mathrm{W} = \mathrm{H}^\dagger\Sigma_\mathbf{N}^{-1}\mathrm{H} = \tilde{\mathrm{H}}\mathrm{Q}^\dagger\mathrm{Q}\tilde{\mathrm{H}}^\dagger = \tilde{\mathrm{H}}\bar{\mathrm{Q}}\tilde{\mathrm{H}}^\dagger. \tag{A12}$$

For a given source cross-spectral matrix $\Sigma_\mathbf{X}$, the mutual information of source and receiver is given by

$$I = I(\mathbf{X},\mathbf{Y}) = \int_0^\infty \log_2|\mathrm{I} + \mathrm{S}^\dagger\bar{\mathrm{Q}}\mathrm{S}|df, \tag{A13}$$

where

$$\mathrm{S} = \tilde{\mathrm{H}}^\dagger\Sigma_\mathbf{X}^{1/2}. \tag{A14}$$

The source power P is then expressed as a function of S by

$$\begin{aligned} P(\mathrm{S}) &= 2\int_0^\infty \mathrm{Tr}(\Sigma_\mathbf{X})df = 2\int_0^\infty \mathrm{Tr}(\mathrm{SS}^\dagger)df \\ &= 2\int_0^\infty \mathrm{Tr}(\mathrm{S}^\dagger\mathrm{S})df = P_0. \end{aligned} \tag{A15}$$

As is implicit in Ref. 16, the derivative of I with respect to S can be found through the theory of the logarithm of a matrix argument.[22] For any nonsingular matrix X, the following relation between the determinant and the matrix logarithm of X can be derived:

$$\log|\mathrm{X}| = \mathrm{Tr}(\log \mathrm{X}). \tag{A16}$$

The Lagrange multiplier equations for minimizing I subject to the constraint in Eq. (A15) are then

$$\begin{aligned} 0 &= \frac{\partial I}{\partial \mathrm{S}} - \lambda\frac{\partial P}{\partial \mathrm{S}} = \frac{\partial}{\partial \mathrm{S}}(\log_2|\mathrm{I} + \mathrm{S}^\dagger\bar{\mathrm{Q}}\mathrm{S}| - 2\lambda\,\mathrm{Tr}(\mathrm{S}^\dagger\mathrm{S})) \\ &= \frac{\partial}{\partial \mathrm{S}}\left(\mathrm{Tr}\left(\frac{1}{\log 2}\cdot\log(\mathrm{I} + \mathrm{S}^\dagger\bar{\mathrm{Q}}\mathrm{S})\right) - 2\lambda\mathrm{S}^\dagger\mathrm{S}\right) \\ &= \mathrm{Tr}\left(\frac{1}{\log 2}\cdot(\mathrm{I} + \mathrm{S}^\dagger\bar{\mathrm{Q}}\mathrm{S})^{-1}\cdot 2\mathrm{S}^\dagger\bar{\mathrm{Q}} - 2\lambda\mathrm{S}^\dagger\right), \end{aligned} \tag{A17}$$

where the last equality has made use of the Chain Rule for differentiation. The last equality in Eq. (A17) will be satisfied if the matrix argument of the trace is set to the zero matrix, leading to

$$\mathrm{SS}^\dagger = \frac{1}{\bar{\lambda}}\mathrm{I} - \bar{\mathrm{Q}}^{-1}, \tag{A18}$$

where

$$\bar{\lambda} = \log 2\cdot\lambda. \tag{A19}$$

This gives the optimum source cross-spectral density as

$$\Sigma_{\mathbf{X}} = \tilde{\mathbf{H}}\mathbf{S}\mathbf{S}^{\dagger}\tilde{\mathbf{H}}^{\dagger} = \tilde{\mathbf{H}}\bar{\mathbf{S}}^{*}\bar{\mathbf{S}}\tilde{\mathbf{H}}^{\dagger} = \tilde{\mathbf{H}}\bar{\mathbf{P}}\tilde{\mathbf{H}}^{\dagger}, \tag{A20}$$

where

$$\bar{P} = \mathrm{diag}\{\bar{\rho}_1, \bar{\rho}_2, \ldots, \bar{\rho}_n\}, \tag{A21}$$

with

$$\bar{\rho}_k(f) = \begin{cases} L - |q_k(f)|^{-2}, & \text{if } q_k(f) \neq 0 \\ 0, & \text{if } q_k(f) = 0, \end{cases} \tag{A22}$$

and with $L = 1/\lambda$ to be determined by the source power constraint in Eq. (A15).

Referring to Eqs. (A12), (A21), and (A22), it is now seen that the optimal source spectrum has density $\bar{\rho}_k(f)$ at frequency f and in the jth eigenspace of $\mathrm{W}(f)^{\dagger}\mathrm{W}(f) = \mathrm{H}(f)^{\dagger}\Sigma_{\mathbf{N}}^{-1}(f)\mathrm{H}(f)$. In effect, this amounts to a "steering" of the source toward the eigenspaces of the "transfer function-to-noise" matrix $\mathrm{H}(f)^{\dagger}\Sigma_{\mathbf{N}}^{-1}(f)\mathrm{H}(f)$, with the spectral weighting of the source being stronger in those eigenspaces in which the transfer function-to-noise ratio $|q_k(f)|^2$ is larger. Note that, in the SISO case, Eq. (A22) reduces to the optimal waterfill solution given by Eq. (3).

Following Ref. 16, if the eigenvalues $|q_k(f_i)|^2$ are reordered in descending order across frequency indices i and across eigenvector indices k, i.e., if

$$|q_{k_1}(f_{i_1})|^2 \geqslant |q_{k_2}(f_{i_2})|^2 \geqslant |q_{k_3}(f_{i_3})|^2 \geqslant \cdots, \tag{A23}$$

then Eqs. (A15) and (A22) require that

$$2L\sum_{j=1}^{m} \Delta f_{i_j} - 2\sum_{j=1}^{m} |q_{k_j}(f_{i_j})|^{-2}\Delta f_{i_j} = P_0 \tag{A24}$$

for the largest value of m for which

$$|q_{k_m}(f_{i_m})|^{-2} < L. \tag{A25}$$

Put another way, the waterfill solution is determined by finding the largest value m for which

$$|q_{k_m}(f_{i_m})|^{-2}\Delta f_{i_m} < L_m = \frac{P_0 + 2\sum_{j=1}^{m} |q_{k_j}(f_{i_j})|^{-2}\Delta f_{i_j}}{2\sum_{j=1}^{m} \Delta f_{i_j}}. \tag{A26}$$

The optimal source spectrum and the channel capacity are then given, respectively, by

$$\bar{\rho}(f_{i_j}) = \max\{L_m - |q_{k_j}(f_{i_j})|^{-2}, 0\} \tag{A27}$$

and by

$$C = \sum_{\substack{j=1 \\ L_m - |q_{k_j}(f_{i_j})|^{-2} \geqslant 0}}^{m} \log_2(L_m |q_{k_j}(f_{i_j})|^2)\,\Delta f_{i_j}. \tag{A28}$$

Passing to the continuous-frequency limit and writing $L = L_m$ yields Eqs. (5) and (7).

[1] C. E. Shannon, "Communication in the presence of noise," Proc. IRE **37**, 10–21 (1949).
[2] G. J. Foschini and M. J. Gans, "On limits of wireless communications in a fading environment when using multiple antennas, Wireless Personal Communications **6**, 311–335 (1998).
[3] M. Zatman and B. Tracey, "Underwater acoustic MIMO channel capacity," *Conference Record of the Thirty-Sixth Asilomar Conference on Signals, Systems and Computers*, Pacific Grove, CA, 3–6 Nov. 2002, Vol. **2**, pp. 1364–1368.
[4] J. Li, A. Bose, and Y.Q. Zhao, "Rayleigh flat fading channels' capacity," *Proc. of the. 3rd Annual Communication Networks and Services Research Conference (CNSR'05)*, Halifax, Canada, 16–18 May, **2005**, pp. 214–217 (2005).
[5] A. J. Goldsmith, S. A. Jafar, N. Jindal, and S. Vishwanath, "Capacity limits of MIMO channels," IEEE J. Sel. Areas Commun. **21**(3), 684–702 (2003).
[6] A. J. Goldsmith and P. P. Varaiya, "Capacity of fading channels with channel side information," IEEE Trans. Inf. Theory **43**, 1986–1992 (1997).
[7] T. M. Cover and J. A. Thomas, *Elements of Information Theory* (Wiley, New York, 1991).
[8] J. R. Apel, M. Badiey, C. S. Chu, S. Finette, R. Headrick, J. Kemp, J. F. Lynch, A. Newhall, M. H. Orr, B. H. Pasewark, D. Tielburger, A. Turgut, K. vonderHeydt, and S. Wolf, "An overview of the 1995 SWARM shallow-water internal wave acoustic scattering experiment," IEEE J. Ocean. Eng. **22**, 465–500 (1997).
[9] M. B. Porter and H. P. Bucker, "Gaussian-beam tracing for computing ocean acoustic fields," J. Acoust. Soc. Am. **82**, 1349–1359 (1987).
[10] Naval Oceanographic Office, OAML-SRS-37, Stennis Space Center, Mississippi, 1992.
[11] W.H. Thorp, "Analytic description of low-frequency attenuation coefficient," J. Acoust. Soc. Am. **42**, 270 (1967).
[12] R.J. Urick, *Principles Underwater Sound*, 3rd ed. (McGraw–Hill, New York, 1983), p. 213.
[13] A. I. Eller and D. A. Gershfeld, "Low-frequency acoustic response of shallow water ducts," J. Acoust. Soc. Am. **78**, 622–631 (1985).
[14] E. M. Sozer, J. G. Proakis, M. Stojanovic, J. A. Rice, A. Benson, and M. Hatch, "Direct sequence spread spectrum based modem for underwater acoustic communication and channel measurements," *Proc. MTS/IEEE OCEANS '99*, **1**, 228–233 (1999).
[15] D. B. Kilfoyle and A. B. Baggeroer, "The state of the art in underwater acoustic telemetry," Ocean Eng. **25**, 4–27 (2000).
[16] D. W. Bliss, K. W. Forsythe, A. O. Hero, and A. F. Yegulalp, "Environmental issues for MIMO capacity," IEEE Trans. Signal Process. **50**, 2128–2142 (2002).
[17] W. Kuperman and F. Ingenito, "Spatial correlation of surface generated noise in a stratified ocean," J. Acoust. Soc. Am. **67**, 1988–1996 (1980).
[18] T. J. Hayward, "Optimization of hydrophone placement for acoustic arrays using simulated annealing," J. Acoust. Soc. Am. **95**, 201–212 (1994).
[19] M. B. Porter and E. L. Reiss, "A numerical method for bottom interacting ocean acoustic normal modes," J. Acoust. Soc. Am. **77**, 1760–1767 (1985).
[20] L. Zheng and D. N. C. Tse, "Diversity and multiplexing: A fundamental trade-off in multiple-antenna channels," IEEE Trans. Inf. Theory **49**, 1073–1096 (2003).
[21] M. B. Porter, The KRAKEN normal mode program, SACLANTCEN Memorandum No. SM-245, SACLANT Undersea Research Centre, La Spezia, Italy (1991).
[22] M. L. Curtis, *Matrix Groups*, 2nd ed. (Springer, New York, 1984), p. 49.

A one-step patch near-field acoustical holography procedure

Moohyung Lee[a)]
Ray W. Herrick Laboratories, School of Mechanical Engineering, Purdue University, 140 S. Intramural Drive, West Lafayette, Indiana 47907-2031

J. Stuart Bolton[b)]
Ray W. Herrick Laboratories, School of Mechanical Engineering, Purdue University, 140 S. Intramural Drive, West Lafayette, Indiana 47907-2031

(Received 8 September 2006; revised 23 April 2007; accepted 18 June 2007)

When performing holography measurements over a limited area of a source, the hologram pressure typically remains finite at the edge of the measurement aperture. Patch near-field acoustical holography (NAH) has been developed specifically to mitigate the effects related to that windowing. In iterative patch NAH, the source distribution is reconstructed in two steps: first, the partially measured sound field is extended iteratively, and then the extended pressure is projected onto the source surface by using conventional NAH procedures. In the present work, a one-step procedure for performing that combined task is described. In this approach, the acoustical property to be reconstructed on a surface of interest is related to the partially measured pressure on the hologram surface in terms of sampling and bandlimiting matrices, and the reconstructed result is obtained by finding the regularized least squares solution of the latter relation; a procedure for determining the cutoff wave number of the bandlimiting matrix without *a priori* knowledge of the signal bandwidth is suggested. The proposed procedure was validated by using a synthetic sound field created by a point-driven, simply supported plated. © *2007 Acoustical Society of America.*
[DOI: 10.1121/1.2756799]

PACS number(s): 43.60.Sx [EGW] Pages: 1662–1670

I. INTRODUCTION

Since near-field acoustical holography (NAH) was introduced in the 1980s,[1,2] it has been applied to various sound field visualization problems. This method allows a sound field to be reconstructed in a three-dimensional volume from data measured on a two-dimensional surface without losing the high spatial resolution information (i.e., the evanescent, high wave number components) of the source field. The earliest form of NAH, based on the use of the two-dimensional discrete Fourier transform (DFT), and thus referred to as DFT-based NAH, is efficient in terms of computation time and provides physically meaningful information about a sound field by distinguishing between propagating and evanescent wave components. However, it is required that the measurement aperture extend over a sufficiently large region to avoid inherent problems related to the use of the DFT; but it is sometimes impossible or impractical to satisfy that requirement when isolated parts of very large sources are to be visualized. Several methods that address the latter problem have since been introduced: e.g., statistically optimal NAH (SONAH),[3–5] the Helmholtz equation least-squares procedure (HELS),[6–9] the method of superposition (also referred to as the patch equivalent source method,[10–12] the patch inverse boundary element method,[12] a wavelet-based method,[13] and iterative patch NAH.[14–20] Since these methods allow measurements to be performed just over the region of interest (however, usually on a surface sufficiently close to the source surface to avoid spurious effects resulting from strong sources located outside the region of interest, if any), the effort related to measurements can be reduced.

In iterative patch NAH, in particular, the sound field measured over a finite measurement aperture is extended into the region exterior to the measurement patch based on the use of an iterative data recovery, or restoration, algorithm, thus effectively increasing the aperture size.[14] Backprojections are then performed by using the usual NAH procedures in conjunction with the extended sound field, and, as a result, the spurious windowing effect related to the use of DFT can be alleviated. This method has been further developed by incorporating a regularization procedure to implement the bandlimiting operation,[15–18] and its formulation has also been extended in terms of singular value decomposition (SVD)[16,17] which allows this method to be applied to boundary element method-based NAH. It was recently shown that the iterative patch NAH procedure can be applied to hologram pressures measured over arbitrarily chosen, discontinuous regions:[20] e.g., a source distribution can be reconstructed from hologram pressures measured over multiple, unconnected patches. Further, the spatial resolution of data measured over coarse grids can be enhanced by interpolation between measured points, thus helping to define the signal shape more accurately.

In the present work, a one-step procedure for performing patch NAH (including both data restoration and projection operations) is described. In the proposed procedure, the hologram pressure measured over a partial region is related both to the hologram pressure over a "complete" region and

a)Author to whom correspondence should be addressed. Electronic mail: leemoohy@ecn.purdue.edu
b)Electronic mail: bolton@purdue.edu

the acoustical property of interest on a reconstruction surface through sampling and bandlimiting matrices. The derivation of those signal relations shares the same theoretical basis as the iterative patch NAH procedure described in Ref. 20. However, in contrast with the iterative approach, the one-step procedure described in the present work allows various acoustical properties to be reconstructed directly from partially measured hologram pressures by finding a regularized least squares solution of the signal relation defined between them. In the present work, modified Tikhonov regularization[21] was implemented in conjunction with generalized cross validation (GCV)[22] to provide the required regularization.

The present work is organized in the following manner. In Sec. II, the theoretical derivation of the proposed method is described. In Sec. III, numerical simulation results obtained by using a sound field created by a point-driven, simply supported plate are presented. Finally, conclusions are presented in Sec. IV.

II. ONE-STEP FORMULATION FOR GENERALIZED PATCH NEAR-FIELD ACOUSTICAL HOLOGRAPHY

A. Preliminaries

Near-field acoustical holography is a method that allows an acoustical property, $\mathbf{a}$, to be reconstructed in a three-dimensional space from an acoustical property measured on a surface (usually a sound pressure, $\mathbf{p}$, referred to as the hologram pressure). Generally, $\mathbf{a}$ and $\mathbf{p}$ are related by the transfer matrix $\mathbf{T}$: i.e.,

$$\mathbf{p} = \mathbf{T}\mathbf{a}, \tag{1}$$

and the holographic reconstruction of $\mathbf{a}$ is achieved by inverting Eq. (1), which is implemented in conjunction with a regularization procedure to account for the discrete, ill-posed nature of the inverse problem.[21,22]

In the conventional, DFT-based NAH approach, $\mathbf{T}$ is decomposed as $\mathbf{T}=\mathbf{F}^{-1}\mathbf{\Sigma}\mathbf{F}$, where $\mathbf{F}$ and $\mathbf{F}^{-1}$ denote the forward and inverse two-dimensional DFT operators, respectively, $\mathbf{\Sigma}=\mathrm{diag}(\tau_1,\ldots,\tau_N)$ represents the propagation characteristics of each wave number component, and the τ_i's are determined explicitly depending both on the measurement geometry and the acoustical property to be reconstructed.[23] DFT-based NAH is known to be computationally efficient since the projection of each wave number component is performed independently based on an element-by-element multiplication rather than a full matrix calculation, but it is required that measurements be performed on a uniform grid over a sufficiently large region to avoid truncation effects related to the use of the DFT. Thus, $\mathbf{p}=[p_1,\ldots,p_N]^{\mathrm{T}}$ appearing in this article specifically represents a hologram pressure that satisfies the latter requirement (which will be referred to as the sound pressure measured over a complete region).

B. Partially sampled data set of a bandlimited signal

Consider here a case in which a sound pressure is measured at N_s ($<N$) locations arbitrarily distributed over a part of the complete hologram surface. Since the procedure in the present work is formulated based on the use of the DFT, "arbitrary" here strictly means that measurement locations are chosen selectively from a uniform grid over a complete region defined on a surface of constant coordinate in a separable geometry without being subject to any further conditions. Let $S=\{1,2,\ldots,N\}$, Γ_m represent the measured region, $\vec{r}_i$ represent the two-dimensional position vector on the hologram surface of p_i, and $S_m=\{i\in S:\vec{r}_i\in\Gamma_m\}$ (i.e., the set of the indices of the grid where measurements are performed). The elements of the partially measured (or truncated) sound pressure vector, $\mathbf{p}_m=[p_{m_1},\ldots,p_{m_N}]^{\mathrm{T}}$, can be expressed in terms of the sound pressure measured over the complete region, $\mathbf{p}$: i.e.,

$$p_{m_i}=\begin{cases} p_i & \text{when } i\in S_m \\ 0 & \text{when } i\notin S_m. \end{cases} \tag{2}$$

In matrix-vector form, Eq. (2) is equivalently expressed as

$$\mathbf{p}_m = \mathbf{D}\mathbf{p} \tag{3}$$

where $\mathbf{D}=\mathrm{diag}[D_{11},\ldots,D_{NN}]$ represents the sampling matrix whose diagonal terms are determined by

$$D_{ii}=\begin{cases} 1 & \text{when } i\in S_m \\ 0 & \text{when } i\notin S_m. \end{cases} \tag{4}$$

It is well known that "missing" data can be recovered from partially measured data when a signal satisfies a certain additional constraint.[24] In the present work, it is assumed that $\mathbf{p}$ is a signal that is bandlimited to a k-space region Ω_B, a situation frequently observed in practice. In that case, $\mathbf{p}$ can be expressed in terms of the bandlimiting matrix, $\mathbf{B}$: i.e.,

$$\mathbf{p} = \mathbf{B}\mathbf{p}. \tag{5}$$

The bandlimiting matrix can itself be decomposed in terms of the DFT operators and a k-space, low-pass filter, $\mathbf{L}=\mathrm{diag}[L_{11},\ldots,L_{NN}]$, as

$$\mathbf{B} = \mathbf{F}^{-1}\mathbf{L}\mathbf{F}. \tag{6}$$

Let the set of the indices of the wave number components that belong to the low-pass region, Ω_B, be denoted by $S_B=\{i\in S:\vec{k}_i\in\Omega_B\}$ where $\vec{k}_i$ represents the two-dimensional wave number vector corresponding to each wave number component. Then, the diagonal terms of $\mathbf{L}$ are expressed as

$$L_{ii}=\begin{cases} 1 & \text{when } i\in S_B \\ 0 & \text{when } i\notin S_B. \end{cases} \tag{7}$$

Note that signals from most real sources are not strictly bandlimited, but the sound pressure measured on the hologram surface usually (at least weakly) satisfies the bandlimitedness condition (i.e., $\mathbf{p}\approx\mathbf{B}\mathbf{p}$) since high wave number, evanescent sound field components decay quickly with distance from the source. Thus, effective bandwidths of a signal in the two k-space directions can be defined. In most practical cases, however, the latter information is not known *a priori*. Therefore, a procedure that allows the cutoff wave numbers of a low-pass filter to be determined without *a priori* knowledge of the bandwidths of a signal needs to be established: such a procedure will be described in Sec. III.B.3.

C. Signal relations—data restoration and generalized projection matrices

By combining the relations shown earlier, the hologram pressure over the complete region, $\mathbf{p}$, can be expressed in terms of the partially measured pressure, $\mathbf{p}_m$, as

$$\mathbf{p}_m = \mathbf{DBp} = \mathbf{DF}^{-1}\mathbf{LFp} = \mathbf{G}_r\mathbf{p}. \tag{8}$$

The partially measured pressure, $\mathbf{p}_m$, can also be related to the acoustical property to be reconstructed on the surface of interest, $\mathbf{a}$, by substituting Eq. (1) into Eq. (8): i.e.,

$$\mathbf{p}_m = \mathbf{DBp} = \mathbf{DBTa} = \mathbf{DF}^{-1}\mathbf{L\Sigma Fa} = \mathbf{G}_p\mathbf{a}. \tag{9}$$

By inverting Eqs. (8) and (9), $\mathbf{p}$ and $\mathbf{a}$ can finally be reconstructed from $\mathbf{p}_m$: i.e., if the inverses of $\mathbf{G}_r$ and $\mathbf{G}_p$ can be defined, then

$$\mathbf{p} = \mathbf{G}_r^+\mathbf{p}_m = \mathbf{H}_r\mathbf{p}_m, \tag{10}$$

$$\mathbf{a} = \mathbf{G}_p^+\mathbf{p}_m = \mathbf{H}_p\mathbf{p}_m, \tag{11}$$

where + denotes the regularized inverse. The terms $\mathbf{H}_r$ and $\mathbf{H}_p$ refer to the "data restoration" and "generalized projection" matrices, respectively. Here, "generalized" indicates that the distribution of measurement locations can be nonuniform even though the DFT is involved in its formulation. The regularized inverse solution can be obtained in various ways.[22] In the present work, modified Tikhonov regularization was used in conjunction with GCV for that purpose.

By comparison, in iterative patch NAH as it has been implemented previously, the extension of the partially measured hologram pressure is achieved first by using a method of successive approximations to find the fixed point that satisfies $\mathbf{p}=(\mathbf{I}-\mathbf{D})\mathbf{Bp}+\mathbf{p}_m$ where $\mathbf{I}$ represents the identity matrix:[20] i.e.,

$$\mathbf{p}^{(i+1)} = (\mathbf{I}-\mathbf{D})\mathbf{Bp}^{(i)} + \mathbf{p}_m, \quad i = 1,2,\ldots, \quad \mathbf{p}^{(1)} = \mathbf{p}_m. \tag{12}$$

The iteration is repeated until a convergence condition is satisfied, and the restored hologram pressure is then projected onto a surface of interest by using usual NAH procedures.

Note finally that since various terms involved in Eqs. (8) and (9) (i.e., $\mathbf{p}_m$, $\mathbf{D}$, and $\mathbf{L}$) include zero elements, the problems represented by those two equations can be reduced in size after proper matrix manipulations, as described in the Appendix , thus allowing the procedure to be implemented in a computationally efficient way.

III. NUMERICAL SIMULATIONS

A. Preparation of simulation data

Numerical simulations were performed by using a sound field created by a point-driven, simply supported steel plate placed within an infinite baffle. First, the velocity distribution on the plate was generated as

$$\dot{w}(x,y,\omega) = \frac{j\omega}{\rho h}\sum_{m=1}^{10}\sum_{n=1}^{10}\frac{\Phi_{mn}(x_0,y_0)\Phi_{mn}(x,y)}{\omega^2-\omega_{mn}^2} \tag{13}$$

where Φ_{mn} and ω_{mn} represent, respectively, the normal modes and natural frequencies of the plate: i.e.,

$$\Phi_{mn} = \frac{2}{\sqrt{L_xL_y}}\sin\left(\frac{m\pi x}{L_x}\right)\sin\left(\frac{n\pi y}{L_y}\right), \tag{14}$$

$$\omega_{mn} = \sqrt{\frac{Eh^2}{12\rho(1-\nu^2)}}\left[\left(\frac{m\pi}{L_x}\right)^2+\left(\frac{n\pi}{L_y}\right)^2\right]. \tag{15}$$

In this simulation, the dimension of the rectangular plate was 64 $(L_x)\times 48$ (L_y) cm with a thickness, h, of 6 mm, the force was applied was at $(x_0,y_0)=(-5.5,-4)$ cm where the center of the plate was chosen to be the origin of the coordinate system, the Young's modulus, E, was 2×10^{11} Pa, the Poisson's ratio, ν, was 0.28, and the density, ρ, was 7860 kg/m^3.

The sound pressure on a planar surface at a height of 6 cm was calculated by forward projection of the surface velocity, and random spatial noise, $\boldsymbol{\delta}$, was added to it. To ensure an accurate forward projection, the surface velocity was discretized with a 0.5-cm-lattice spacing in the x– and y–directions, and a sufficiently large number of zeros was added to simulate a baffle and to avoid wrap-around error. The simulation data were then prepared by sampling the generated surface velocities and sound pressures with a 4-cm-lattice spacing in both directions over a computational domain comprising a 40-by-40 grid.

B. Results

Simulations were performed in two cases: In the first case, the hologram pressure was measured over a single patch, and, in the second case, the hologram pressure was measured over arbitrarily distributed locations. In Fig. 1, the measurement locations in these two cases are shown. The rectangular region, comprising a 17-by-13 lattice, corresponds to a region on the hologram surface directly above the entire plate, and the circles represent the locations where sound pressures were measured. In the first case, the measurement patch comprised an 11-by-7 lattice [see Fig. 1(a)], and the sampling density, defined as the ratio of the number of measured data points to the total number of grid locations over the complete computational domain (i.e., N_s/N) was $(11\times7)/(40\times40)=0.048$. In the second case, the sampling density remained the same as in the single-patch case, but measurement locations were distributed to cover a wider region of the hologram surface [see Fig. 1(b)].

In error analysis results that will be presented later, the percentage root mean square reconstruction error was defined by $100\times\|\mathbf{a}_{\text{reconst}}-\mathbf{a}_{\text{exact}}\|/\|\mathbf{a}_{\text{exact}}\|$ (in this section, $\mathbf{a}$ is the surface normal velocity on the source plane), and was evaluated over three regions: error_1 was calculated over the entire surface of the plate (i.e., 17-by-13 grid locations), error_2 was calculated over a region directly under the measurement patch used in the single-patch case (i.e., 11-by-7 grid locations), and error_3 was calculated over a central region of the plate smaller than the region used for calculating error_2 (i.e., 7-by-5 grid locations).

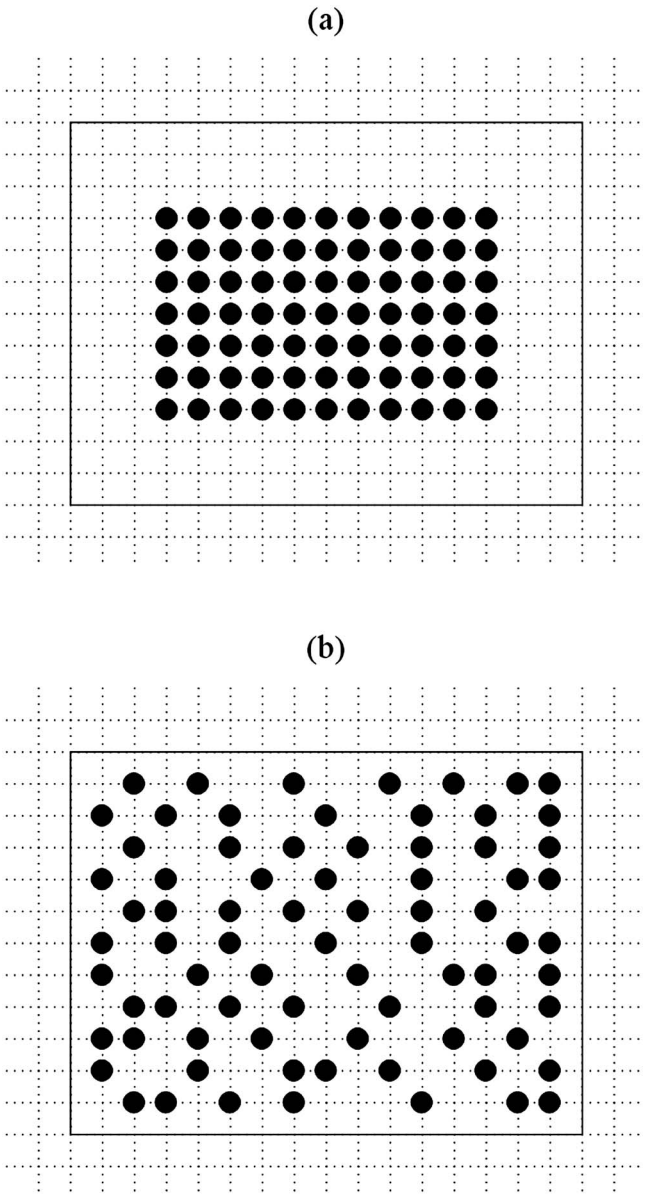

FIG. 1. Measurement arrays used in the simulation: (a) single-patch case; (b) distributed-array case. The rectangular region corresponds to a region on the hologram surface directly above the entire plate, and the circles represent the locations where sound pressures were measured. The number of the measurement points was 77 in both cases.

1. Source reconstruction

In Fig. 2, the surface velocities reconstructed by using the one-step patch NAH procedure are compared with the exact values at various frequencies. In Fig. 2, the rectangular regions depicted by solid and dashed lines represent, respectively, the entire surface of the plate and the region directly under the measurement patch used in the single-patch case. In this case, the signal-to-noise ratio (SNR) of the pressure, defined by $20\log_{10}(\|\mathbf{p}\|/\|\boldsymbol{\delta}\|)$, was 60 dB; the cutoff wave numbers of the low-pass filter in the k_x– and k_y–directions were set to values that minimized the reconstruction error (error_2), and the shape of the resulting k-space low-pass filter at each frequency was either square or rectangular depending on the k-space characteristics of the spatial signal. Since the wave number spectra of the signals used in this simulation exhibited the effect of spatial windowing (i.e., the zero normal velocity boundary condition in regions exterior to the plate), those signals were not strictly bandlimited. Even in the latter case, the effective bandwidths of a signal can be established in practical implementations so that a low-pass filter defined by their values filters out the wave number components smaller than a peak level by, say, 30 dB, and the cutoff wave numbers found to be optimal were close to those defined in that way.

In Fig. 3, error_1 and error_2 are compared with the error resulting when the pressures over the complete computational domain were used in conjunction with conventional DFT-based NAH. When the partially measured pressures were projected without further treatment by using conventional DFT-based NAH, errors were beyond the range shown in Fig. 3. Note that error_1 includes the impact of effects other than the truncation of the sound field: i.e., results in the region near the edges of the plate are likely to be less accurate since the high spatial resolution information that describes the slope discontinuity at the plate edges are filtered out by either the bandlimiting operation or regularization. Owing to this fact, the use of the complete hologram pressure also resulted in a relatively large error near that region (compare error_1 and error_2 obtained when the complete pressures were used).

From the comparison of error_1 and error_2, it can be seen that relatively better reconstruction could be achieved in the central region of the plate. The latter result was more obvious as the frequency increased. In principle, an accurate recovery of unmeasured pressures is assured over an extended region; that is, however, not always guaranteed in practical implementations due to effects such as the artificial truncation of an infinite domain, the discretization of continuous functions, and the presence of measurement noise: i.e., due to effects related to computer implementation, an accurate recovery can only be achieved to a limited degree. In patch NAH applications, the latter limitation is more apparent since the sampling density is usually very small. Thus, conservatively speaking, a "region of interest" is usually restricted to the region directly under the measurement aperture or to one slightly smaller than that region.

Of the two cases, it can be seen that the distributed-array case resulted in better reconstruction results, which follows from the fact that the effective size of the measurement aperture in the distributed-array case was larger than that used in the single-patch case: i.e., from the point-of-view of data restoration, the extrapolation of a sound field measured over a single patch is the worst case. In contrast, the interpolation of data between measured points can be achieved relatively easily with good accuracy. Thus, the effect of missing points between measured points in the distributed-array case could be suppressed effectively, and, as a result, the performance of the distributed array was equivalent or comparable to that of a single-patch array comprising 15-by-11 measurement locations.

2. Effect of additive noise

In Fig. 4, the effect of measurement noise is demonstrated. In this case, the amount of noise included in the

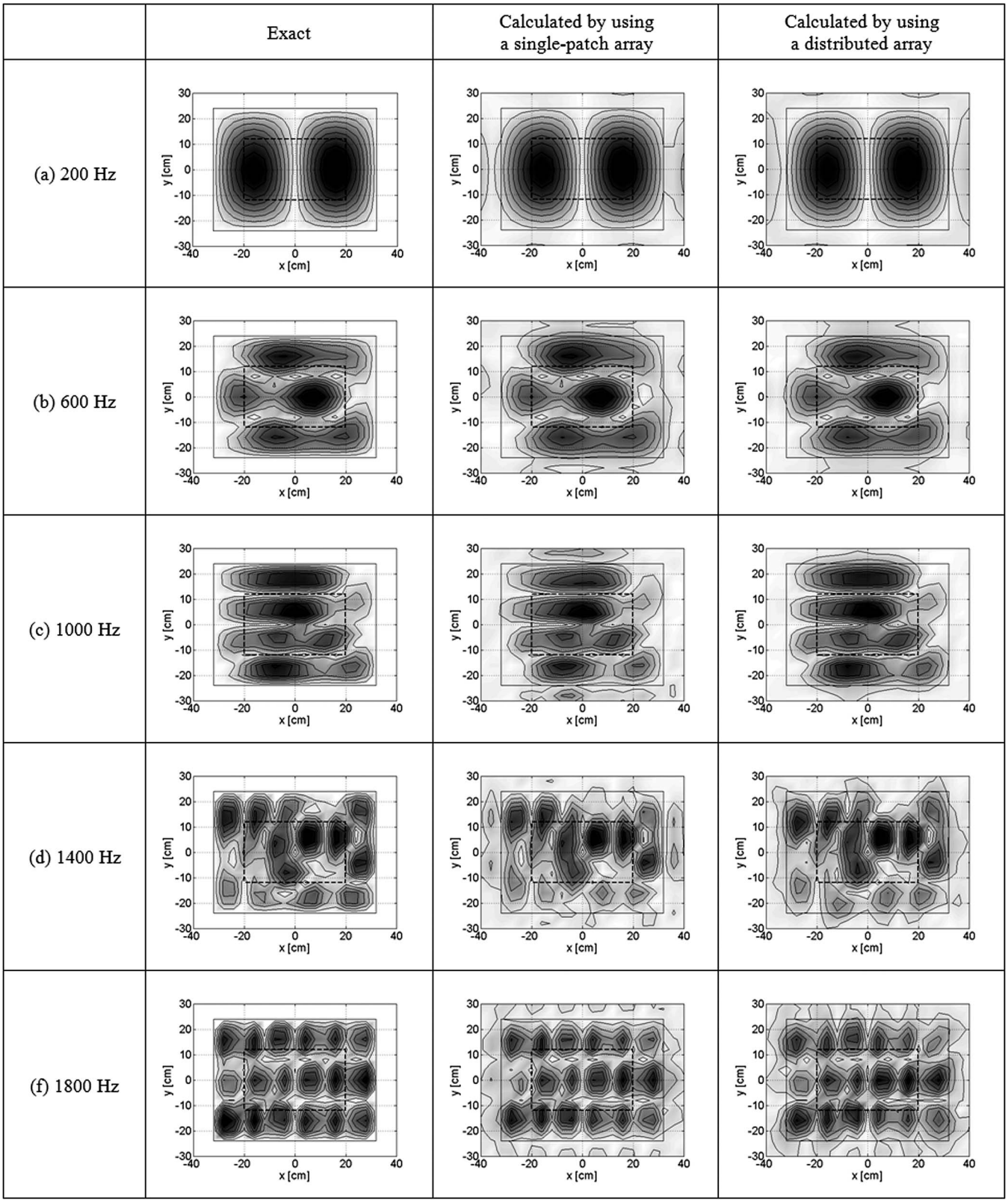

FIG. 2. Comparisons of the surface velocities reconstructed by using the proposed procedure with the exact ones at various frequencies (the SNR=60 dB, and the optimal values of the cutoff wave numbers were used).

hologram pressures was increased so that the SNR was 20 dB. It can be seen that the error evaluated over the larger region was more significantly affected by measurement noise. From the latter observation, it can be seen that the region of accurate reconstruction becomes restricted to a smaller region of the central part of the measurement aperture as the level of measurement noise increases.

The latter results can be explained by the characteristics of the singular vectors of $\mathbf{G}_p$. Since $\mathbf{G}_p$ is constructed from $\mathbf{B}$, $\mathbf{D}$, and $\mathbf{\Sigma}$, it includes information about the spatial distri-

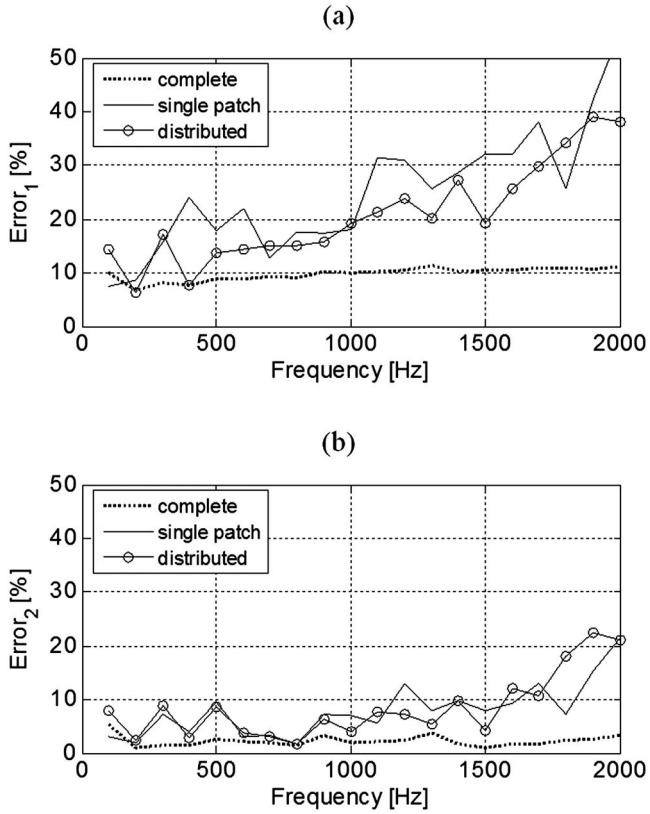

FIG. 3. The percentage root mean square reconstruction errors with respect to frequency (the SNR=60 dB, and the optimal values of the cutoff wave numbers were used): (a) error_1; (b) error_2.

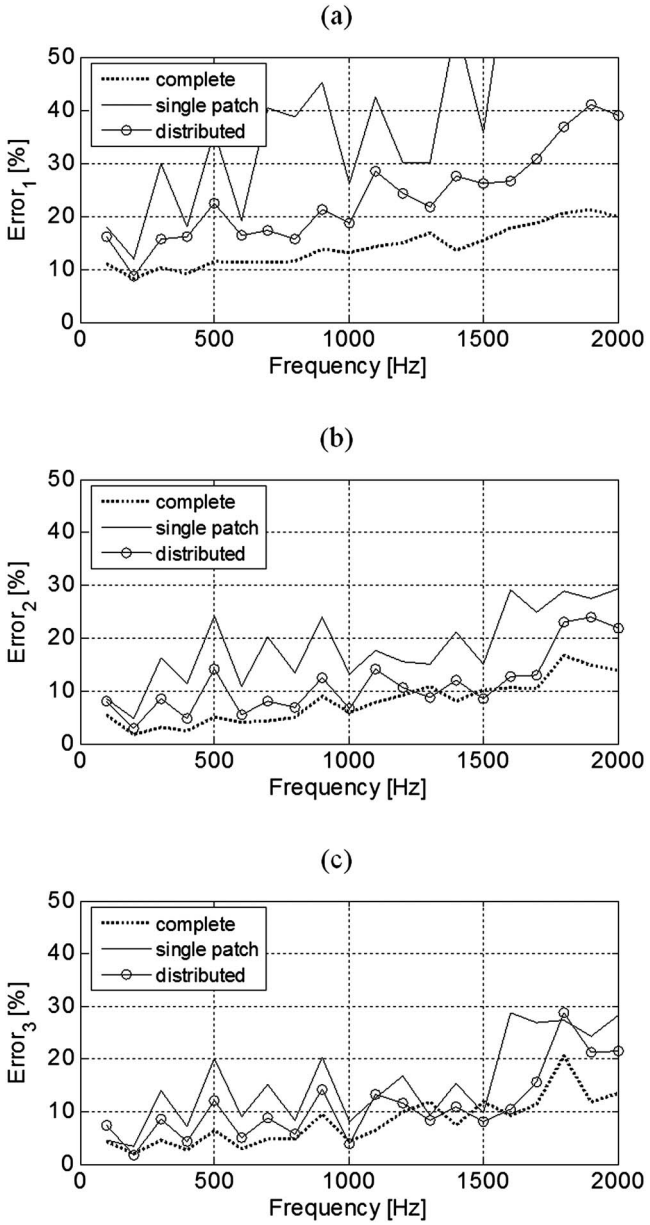

FIG. 4. The percentage root mean square reconstruction errors with respect to frequency (the SNR=20 dB, and the optimal values of the cutoff wave numbers were used): (a) error_1; (b) error_2; (c) error_3.

bution of the measurement locations and the assumed bandwidths of the signal as well as the propagation characteristics of each wave number component. The singular values are ordered by the combined effect of those factors, and information relating a measurement array and locations remote from it is usually encoded in the singular vectors corresponding to the small singular values. Since the small singular values are likely to be filtered out by regularization in the presence of noise, the region of accurate reconstruction is thus restricted to a smaller central region, as observed in this simulation results.

3. Selection of the cutoff wave numbers

In the various simulations shown above, the cutoff wave numbers of the *k*-space low-pass filter were set to their optimal values. However, the (effective) bandwidths of a signal cannot be identified from the partially measured pressure. Here, a procedure for addressing the latter concern is described.

When the cutoff wave numbers are chosen to be larger than the bandwidths of a signal, thus satisfying the condition shown in Eq. (5), the norm of the reconstructed result increases gradually as the cutoff wave numbers approach the actual bandwidths from above. When either of the cutoff wave numbers is too small, the reconstructed result typically features oscillatory fields having large amplitudes due to the effect of aliasing, thus resulting in a rapid increase in the norm. The proposed procedure for determining the cutoff wave numbers is based on the latter characteristics of a signal with respect to the choice of the cutoff wave numbers.

In Fig. 5(a), the norm of the reconstructed surface velocity obtained when various cutoff wave numbers were used is shown at 1.2 kHz in the distributed-array case. In this case, a square low-pass filter was used for demonstration purposes, and the norm represents the log amplitude of the surface velocity norm normalized to that which resulted when no bandlimiting operation was applied [i.e., $a_{\text{norm}}(k_c) = \log_{10}(\|\mathbf{a}(k_c)\| / \|\mathbf{a}(k_\infty)\|)$]. The procedure starts with the assumed bandwidth of a signal (i.e., the value depicted by the ellipse in Fig. 5), and the value that causes a rapid increase in the norm (i.e., the value depicted by the rectangle in Fig. 5) can be found by progressively decreasing the cutoff wave number. The optimal cutoff wave number is usually close to that value.

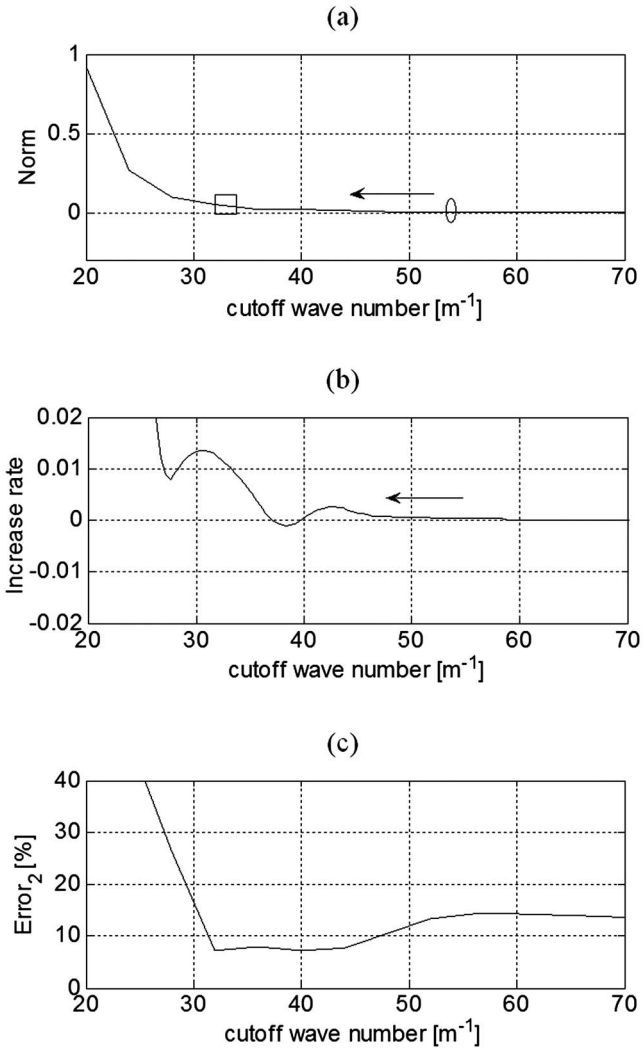

FIG. 5. Signal characteristics with respect to the choice of the cutoff wave number (the SNR=60 dB, at 1.2 kHz in the distributed-array case): (a) log amplitude of the reconstructed surface velocity norm; (b) rate of increase in the log amplitude of the norm when the cutoff wave number was decreased; (c) reconstruction error (error_2).

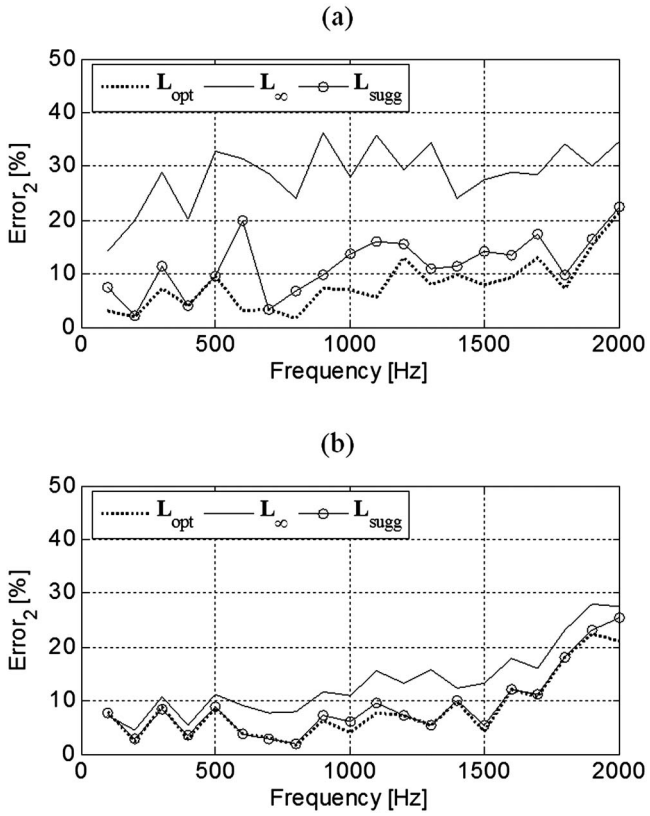

FIG. 6. The percentage root mean square reconstruction errors with respect to the various choices of the cutoff wave numbers (the SNR=60 dB): (a) error_2 in the single-patch case; (b) error_2 in the distributed-array case. $\mathbf{L}_{\text{opt}}$: with the optimal cutoff wave numbers, $\mathbf{L}_{\text{sugg}}$: with the cutoff wave numbers chosen by the proposed procedure, and $\mathbf{L}_{\infty}$: without bandlimiting operation.

In terms of numerical implementation, the proposed procedure is similar to the L-curve criterion[22] that determines the "corner" of a curve by way of monitoring the second derivative of that curve. In the present procedure, however, it is more appropriate to examine the rate of increase (i.e., the first derivative), and the final cutoff value can be fixed by limiting that rate. In Fig. 5(b), the rate of increase of the norm that resulted when the cutoff wave number was decreased (i.e., $-da_{\text{norm}}/dk_c$) is shown. In this work, the limiting value was set to 0.01 (which was determined by considering the rate when the cutoff wave numbers were large), and the cutoff wave number determined in that way was close to the optimal value [see reconstruction errors shown in Fig. 5(c)].

In Fig. 6, the reconstruction errors (error_2 in this case) are compared with respect to the various cutoff wave numbers of the low-pass filter. In this case, the SNR was 60 dB. In Fig. 6, $\mathbf{L}_{\text{opt}}$ and $\mathbf{L}_{\infty}$ indicate, respectively, that the cutoff wave numbers were set to the optimal values, and that no bandlimiting operation was applied. Therefore, $\mathbf{L}_{\text{opt}}$ and $\mathbf{L}_{\infty}$ represent, respectively, the lower and upper bounds of the reconstruction error resulting from the choice of the cutoff values when aliasing did not occur. In turn, $\mathbf{L}_{\text{sugg}}$ indicates that the cutoff wave number was chosen by the procedure described above. It can be seen that the suggested procedure yielded good results in most cases.

It should be noted that, even without the bandlimiting operation, the reconstruction errors were still smaller than those obtained when the partially measured pressures were projected in conjunction with conventional DFT-based NAH, which is to be expected since the acoustical property to be reconstructed is related explicitly to the partially measured pressure in the one-step procedure. It can also be seen that the effect of the bandlimiting operation was very small in the distributed-array case. Thus, it can be concluded that the choice of the cutoff wave numbers becomes less critical as the measurement aperture becomes larger than the region of interest, a result that can be explained by the fact that the bandlimiting operation has an effect only on the small singular values of the generalized projection matrix. The latter fact also causes the effect of the bandlimiting operation to be closely associated with the effect of measurement noise, and, as a result, the choice of the cutoff wave numbers also becomes less important as measurement noise increases.

IV. CONCLUSIONS

In the present article, a one-step procedure for reconstructing source distributions from partially known sound

fields was described. The signal relation between the sound pressure measured over arbitrarily distributed measurement locations and the acoustical property to be reconstructed was established in terms of sampling and bandlimiting matrices. The latter relation was expressed in a reduced form for the sake of computational efficiency, and the inverse solution was calculated based on a regularized least squares procedure in order to obtain reconstructed results. In the present work, modified Tikhonov regularization was used in conjunction with generalized cross validation for the latter task. It was shown that the cutoff wave number of the bandlimiting matrix can be determined without *a priori* knowledge of the bandwidth of a signal by finding the smallest wave number that does not cause a rapid increase in norm of the reconstructed result. The proposed procedure was validated by using a synthetic sound field created by a point-driven, simply supported plate, and various aspects related to a practical implementation were discussed.

APPENDIX: COMPUTER IMPLEMENTATION OF THE ONE-STEP PROCEDURE

Let $\mathbf{G}=\mathbf{F}^{-1}\mathbf{L}\boldsymbol{\Sigma}\mathbf{F}$, so that Eq. (9) represents the systems of equations:

$$\begin{cases} p_i = \sum_{j=1}^{N} G_{ij} a_j & \text{when } i \in S_m \\ 0 = 0 & \text{when } i \notin S_m. \end{cases} \tag{A1}$$

Since $(N-N_s)$ equations are self-satisfying when $i \notin S_m$, only the systems of equations comprising N_s linear equations when $i \in S_m$ need to be solved. Denote the two properties involved in the first systems of equations (i.e., a vector comprising p_i's and a matrix comprising the rows of $\mathbf{G}$), respectively, by

$$\mathbf{p}_s = [p_i]_{i \in S_m}, \quad \mathbf{G}_{sp} = [G_{ij}]_{i \in S_m}. \tag{A2}$$

Then, the first systems of equations shown in Eq. (A1) is expressed by

$$\mathbf{p}_s = \mathbf{G}_{sp}\mathbf{a}. \tag{A3}$$

As shown above, the size of the problem can be reduced from N-by-N to N_s-by-N, and the latter reduction in the size of the problem can result in a significant reduction in computation time since N_s is usually far smaller than N.

The computational effort related to constructing $\mathbf{G}_{sp}$ can also be reduced since $\mathbf{L}$ includes $(N-N_B)$ zero diagonal terms where N_B represents the number of the wave numbers that belong to Ω_B: thus only the N_B rows of $\mathbf{F}$ are involved in the calculation. Denote $\mathbf{F}_B$ and $\boldsymbol{\Sigma}_B$, the submatrices of $\mathbf{F}$ and $\boldsymbol{\Sigma}$, that are involved in the calculation by

$$\mathbf{F}_B = [F_{ij}]_{i \in S_B}, \quad \boldsymbol{\Sigma}_B = [\Sigma_{ij}]_{i \in S_B, j \in S_B}. \tag{A4}$$

Since $\mathbf{F}^{-1}=\mathbf{F}^{\mathrm{H}}$ (when $\mathbf{F}$ is defined with a unitary normalization constant, $1/\sqrt{N}$), $\mathbf{G}$ can be constructed as $\mathbf{G}=\mathbf{F}_B^{\mathrm{H}}\boldsymbol{\Sigma}_B\mathbf{F}_B$. Thus, in computer implementations, only $\mathbf{F}_B$ and $\boldsymbol{\Sigma}_B$ need be constructed, and, rather than being selected from $\mathbf{G}$, $\mathbf{G}_{sp}$ can be constructed directly as

$$\mathbf{G}_{sp} = \mathbf{F}_{sB}^{\mathrm{H}}\boldsymbol{\Sigma}_B\mathbf{F}_B \tag{A5}$$

where

$$\mathbf{F}_{sB} = [F_{ij}]_{i \in S_B, j \in S_m}. \tag{A6}$$

The same approach can be applied to Eq. (8) simply by substituting $\mathbf{B}$ in place of $\mathbf{G}$, and the signal relations shown in Eqs. (8) and (9) can finally be represented in reduced form as

$$\mathbf{p}_s = \mathbf{G}_{sr}\mathbf{p} = \mathbf{F}_{sB}^{\mathrm{H}}\mathbf{F}_B\mathbf{p}, \tag{A7}$$

$$\mathbf{p}_s = \mathbf{G}_{sp}\mathbf{a} = \mathbf{F}_{sB}^{\mathrm{H}}\boldsymbol{\Sigma}_B\mathbf{F}_B\mathbf{a}. \tag{A8}$$

The regularized least squares solution, for example, of $\mathbf{a}$ as given by Tikhonov regularization can be expressed in terms of the SVD of $\mathbf{G}_{sp}=\mathbf{U}\boldsymbol{\Lambda}\mathbf{V}^{\mathrm{H}}$ as

$$\mathbf{a} \equiv \mathbf{V}_r\mathbf{R}^{\alpha}\boldsymbol{\Lambda}_r^{-1}\mathbf{U}_r^{\mathrm{H}}\mathbf{p}_s \tag{A9}$$

where the subscript r represents the submatrices comprising, respectively, only the first R singular values and corresponding singular vectors since the rank of $\mathbf{G}_{sp}$ is $R=\min(N_s,N_B)$. In modified Tikhonov regularization, the filter factor $\mathbf{R}^{\alpha}$ has the form[21]

$$\mathbf{R}^{\alpha} = \mathrm{diag}\left(\ldots, \lambda_i^2 \Big/ \left(\lambda_i^2 + \alpha^2\left(\frac{\alpha^2}{\alpha^2+\lambda_i^2}\right)^2\right), \ldots\right), \quad i = 1,2,\ldots,R \tag{A10}$$

where λ_i's are the singular values of $\mathbf{G}_{sp}$.

The optimal value of the regularization parameter, α, can be determined by using GCV, in which the optimal value is determined by finding a value that minimizes the GCV function[22]

$$J(\alpha) = \frac{\|\mathbf{G}_{sp}\mathbf{a}-\mathbf{p}_s\|^2}{[\mathrm{trace}(\mathbf{I}-\mathbf{G}_{sp}\mathbf{G}_{sp}^{+})]^2} = \frac{\|\mathbf{R}_1^{\alpha}\mathbf{U}_r^{\mathrm{H}}\mathbf{p}_s\|^2}{[\mathrm{trace}(\mathbf{R}_1^{\alpha})]^2} \tag{A11}$$

where $\mathbf{R}_1^{\alpha}=\mathbf{I}-\mathbf{R}^{\alpha}$.

[1] E. G. Williams, J. D. Maynard, and E. J. Skudrzyk, "Sound source reconstructions using a microphone array," J. Acoust. Soc. Am. **68**, 340–344 (1980).

[2] E. G. Williams and J. D. Maynard, "Holographic imaging without the wavelength resolution limit," Phys. Rev. Lett. **45**, 554–557 (1980).

[3] R. Steiner and J. Hald, "Near-field acoustical holography without the errors and limitations caused by the use of spatial DFT," *Proceedings of 6th International Congress on Sound and Vibration*, l999.

[4] J. Hald, "Patch near-field acoustical holography using a new statistically optimal method," *Proceedings of INTER-NOISE 2003*, 2003, No. 975.

[5] Y.-T. Cho, J. S. Bolton, and J. Hald, "Source visualization by using statistically optimized nearfield acoustical holography in cylindrical coordinates," J. Acoust. Soc. Am. **118**, 2355–2364 (2005).

[6] Z. Wang and S. F. Wu, "Helmholtz equation—least-squares method for reconstructing the acoustic pressure field," J. Acoust. Soc. Am. **102**, 2020–2032 (1997).

[7] S. F. Wu and X. Zhao, "Combined Helmholtz equation—least-squares method for reconstructing acoustic radiation from arbitrarily shaped objects," J. Acoust. Soc. Am. **112**, 179–188 (2002).

[8] T. Semenova and S. F. Wu, "The Helmholtz equation least-squares method and Rayleigh hypothesis in near-field acoustical holography," J. Acoust. Soc. Am. **115**, 1632–1640 (2004).

[9] T. Semenova and S. F. Wu, "On the choice of expansion functions in the Helmholtz equation least-squares method," J. Acoust. Soc. Am. **117**, 701–710 (2005).

[10] A. Sarkissian, "Extension of measurement surface in near-field acoustic holography," J. Acoust. Soc. Am. **115**, 1593–1596 (2004).

[11] A. Sarkissian, "Method of superposition applied to patch near-field acous-

tic holography," J. Acoust. Soc. Am. **118**, 671–678 (2005).
[12]N. P. Valdivia, E. G. Williams, and J. Klos, "Reconstruction of the acoustic field using a conformal array," *Proceedings of Inter-Noise 2006*, Honolulu, HI, 2006, Paper No. 240.
[13]J.-H. Thomas and J.-C. Pascal, "Wavelet preprocessing for lessening truncation effects in nearfield acoustical holography," J. Acoust. Soc. Am. **118**, 851–860 (2005).
[14]K. Saijyou and S. Yoshikawa, "Reduction methods of the reconstruction error for large-scale implementation of near-field acoustical holography," J. Acoust. Soc. Am. **110**, 2007–2023 (2001).
[15]E. G. Williams, "Continuation of acoustic near-fields," J. Acoust. Soc. Am. **113**, 1273–1281 (2003).
[16]E. G. Williams, B. H. Houston, and P. C. Herdic, "Fast Fourier transform and singular value decomposition formulations for patch nearfield acoustical holography," J. Acoust. Soc. Am. **114**, 1322–1333 (2003).
[17]K. Saijyou and H. Uchida, "Data extrapolation method for boundary element method-based near-field acoustical holography," J. Acoust. Soc. Am. **115**, 785–796 (2004).
[18]K. Saijyou, "Regularization method for the application of K-space data extrapolation to near-field acoustical holography," J. Acoust. Soc. Am. **116**, 396–404 (2004).
[19]M. Lee and J. S. Bolton, "Patch near-field acoustical holography in cylindrical geometry," J. Acoust. Soc. Am. **118**, 3721–3732 (2005).
[20]M. Lee and J. S. Bolton, "Reconstruction of source distributions from sound pressures measured over discontinuous regions: Multipatch holography and interpolation," J. Acoust. Soc. Am. **121**, 2086–2096 (2007).
[21]E. G. Williams, "Regularization methods for near-field acoustical holography," J. Acoust. Soc. Am. **110**, 1976–1988 (2001).
[22]P. C. Hansen, *Rank-Deficient and Discrete Ill-Posed Problems* (SIAM, Philadelphia PA, 1998).
[23]E. G. Williams, *Fourier Acoustics: Sound Radiation and Nearfield Acoustical Holography* (Academic, London, 1999).
[24]D. C. Youla, "Generalized image restoration by the method of alternating orthogonal projections," IEEE Trans. Circuits Syst. **25**, 694–702 (1978).

Low-frequency and high-frequency cochlear nonlinearity in humans

Michael P. Gorga,[a] Stephen T. Neely, Darcia M. Dierking, Judy Kopun, Kristin Jolkowski, Kristin Groenenboom, Hongyang Tan, and Bettina Stiegemann
Boys Town National Research Hospital, 555 North 30th Street, Omaha, Nebraska 68131

(Received 9 April 2007; revised 29 May 2007; accepted 30 May 2007)

Low- and high-frequency cochlear nonlinearity was studied by measuring distortion product otoacoustic emission input/output (DPOAE I/O) functions at 0.5 and 4 kHz in 103 normal-hearing subjects. Behavioral thresholds at both f_2's were used to set L_2 in dB SL for each subject. Primary levels were optimized by determining the L_1 resulting in the largest L_{dp} for each L_2 for each subject and both f_2's. DPOAE I/O functions were measured using L_2 inputs from −10 dB SL (0.5 kHz) or −20 dB SL (4 kHz) to 65 dB SL (both frequencies). Mean DPOAE I/O functions, averaged across subjects, differed between the two frequencies, even when threshold was taken into account. The slopes of the I/O functions were similar at 0.5 and 4 kHz for high-level inputs, with maximum compression ratios of about 4:1. At both frequencies, the maximum slope near DPOAE threshold was approximately 1, which occurred at lower levels at 4 kHz, compared to 0.5 kHz. These results suggest that there is a wider dynamic range and perhaps greater cochlear-amplifier gain at 4 kHz, compared to 0.5 kHz. Caution is indicated, however, because of uncertainties in the interpretation of slope and because the confounding influence of differences in noise level could not be completely controlled. [DOI: 10.1121/1.2751265]

PACS number(s): 43.64.Jb, 43.64.Kc [BLM] Pages: 1671–1680

I. INTRODUCTION

In this study, we were interested in comparing nonlinear properties for high frequencies and low frequencies in responses from the normal human cochlea. Interest in this question was based on observations from both behavioral data in humans and physiological measurements in lower animals, which suggest that the question of differences in nonlinear processing for low and high frequencies is not completely resolved. In this study, distortion product otoacoustic emissions (DPOAE) were measured at 0.5 and 4 kHz in a sample of subjects with normal hearing in an effort to provide data relevant to questions regarding the frequency dependence of nonlinear processing in humans.

Several physiological studies in lower animals indicate that there may be differences in cochlear processing at the base, compared to the apex, dating back to the seminal work of Kiang *et al.* (1965). Recordings of single-fiber tuning curves [more recently referred to as frequency-threshold curves (FTCs)] showed that fibers with high characteristic frequency (CF) innervating hair cells at the cochlear base had sharper tuning, compared to low-CF fibers innervating more apically located hair cells. Kiang and Moxon (1974) noted that high-CF fibers had long low-frequency tails where threshold remained relatively constant regardless of frequency. In contrast, low-CF fibers were characterized by more symmetrical tuning, and low-frequency tails (relative to CF) were less evident. These frequency-dependent patterns of sharpness of tuning and differences in symmetry have been demonstrated in many studies since the early work of Kiang and colleagues.

Sewell (1984) recorded FTCs prior to and following administration of furosemide, which reversibly alters outer-hair cell (OHC) function through its action on the stria vascularis, which provides the driving potential for the OHCs. Soon after furosemide was administered, thresholds at CF (the tip of the FTC) were more elevated than thresholds on the tails, reflecting the frequency dependence of cochlear-amplifier gain relative to CF. Interestingly, greater threshold elevations at CF were observed for high-CF fibers, compared to fibers having lower CFs. Furosemide has also been shown to have an effect that has been interpreted as a reduction in cochlear-amplifier gain, based on direct measurements of basilar-membrane motion (Ruggero and Rich, 1991). Ruggero and Rich showed that following furosemide treatment, sensitivity was elevated at a given (basal) cochlear place to the frequency for which that place was the characteristic place (CP) prior to treatment. In contrast, the mechanical response of that same place to a frequency that was well below the best frequency for that place showed no influence from furosemide treatment. Taken together, the single-unit and basilar-membrane data indicate that cochlear-amplifier gain for any frequency is dependent on the condition of the cochlea (primarily the OHCs) at that tone's CP, and appears to be greater for high-CF regions and less for low-CF regions.

Direct measurements of basilar-membrane motion at the apical end of the cochlea, even in lower animals, is more difficult, compared to similar measurements at the cochlear base. Apparently, gaining access to cochlear structures at the apex is more traumatic. This situation might complicate the interpretation of measurements at the cochlear apex because damage to the cochlea would be expected to result in a loss of nonlinearity and a reduction in cochlear-amplifier gain. Thus, the direct observation of less nonlinearity at the

[a]Electronic mail: gorga@boystown.org

cochlear apex may be the result of damage caused by experimental procedures, and, therefore, may not reflect apical cochlear processing in the normal state. Cooper and Yates (1994) indirectly estimated cochlear nonlinearity for a wide range of frequencies, based on single-unit rate-level functions. Their work was based on the hypothesis that the response to a low-frequency tone (relative to CF) would be linear at the CF place. Their results suggested that there was less nonlinearity at the apical end of the guinea-pig cochlea, compared to its base. More recently, Cooper and Rhode have made direct measurements of cochlear mechanics at the apical end of the cochlea (Cooper and Rhode, 1995, 1997, 1998; Rhode and Cooper, 1996). In general, these data demonstrate similar nonlinearities for apical and basal cochlear regions, although the nonlinear effects appear to exist for a wider range of frequencies for apical places and perhaps are less in magnitude. Zinn *et al.* (2000) concluded that negative feedback existed for the entire cochlear length, with gain at the base but not the apex. However, Zinn *et al.* observed no evidence for compressive nonlinearity at low and medium levels in the apical region of the guinea pig cochleae. The disagreement between this observation and those made by others may be due to the difficulty of the apical preparation.

For obvious reasons, direct measurements of cochlear nonlinearity are not possible at any cochlear place in humans. As a consequence, assessment of nonlinearity in the human cochlea must rely on noninvasive, indirect measurements. There are several psychophysical studies that have examined cochlear nonlinearity in humans, but the results are not in complete agreement. For example, some studies suggest that the human cochlea is more nonlinear at its base, compared to its apex (Hicks and Bacon, 1999; Plack and Oxenham, 1998), whereas other studies report data that suggest that there are no differences in cochlear nonlinearity for low and high frequencies (Plack and Drga, 2003; Plack and O'Hanlon, 2003; Lopez-Poveda *et al.*, 2003; Schairer *et al.*, 2007). The apparent discrepancies across studies may be due to differences in the measures that were used to quantify nonlinearity, which, of necessity, must rely on indirect measurements. In some of the behavioral studies, comparisons were made for responses measured with on-frequency and low-frequency maskers, under the assumption that the response at any place along the cochlea is nonlinear only when stimulated with frequencies for which that place is the CP, and is linear in response to frequencies that are much lower than the CF for that place. However, several physiological studies (as described earlier) are consistent with the view that tuning is broader for apical cochlear places and that nonlinear response properties cover a wider range of frequencies, compared to more basal places. Behavioral studies (or any other indirect study, for that matter) that rely on comparisons between responses to CF tones and responses to tones much lower in frequency than CF might, therefore, underestimate the amount of nonlinearity for low-frequency, apical cochlear regions because the responses to the reference condition (a stimulus much lower than CF) are not entirely linear.

The present study represents an alternative effort to use noninvasive, indirect, but objective measures to determine if there are differences in cochlear nonlinearity across frequency in humans. DPOAE input/output (I/O) functions have been used as indirect measures of cochlear nonlinearity in humans (e.g., Dorn *et al.*, 2001; Neely *et al.*, 2003, 2007). These studies, as well as others, have provided estimates of compression ratio (the ratio of the change in output to the change in input) which are in the range of values observed in animal studies and in behavioral studies of humans with normal hearing. Furthermore, these ratios decrease (i.e., the response becomes less compressive) in the presence of hearing loss. Thus, DPOAE I/O functions have characteristics that are at least qualitatively similar to observations made in both normal and impaired animal preparations. In human ears with normal hearing, these functions are characterized by a linear segment as the response emerges from the noise floor, followed by a compressive region over which the output is no longer linearly related to the input. At its maximum, the compression ratio estimated from DPOAE I/O functions is approximately 4:1, at least for mid and high frequencies. In previous work, we have estimated the range of input levels over which compression takes place and the amount of compression in both normal and impaired ears (Dorn *et al.*, 2001; Neely *et al.*, 2003). Both the amount of compression and the range of input levels over which compression was observed decreased as hearing loss increased. Thus, those efforts were more concerned with changes in compression as a consequence of hearing loss, and did not focus on differences in cochlear nonlinearity between low-frequency and high-frequency primaries. In this study, we measured DPOAE I/O functions in subjects with normal hearing at two frequencies, 0.5 and 4 kHz, and then compared the I/O functions at those two frequencies to determine the extent to which they differed.

II. METHODS

A. Subjects

Data collection was completed on 103 subjects. Subjects ranged in age from 14 years to 47 years, with a mean age of 23.8 years (s.d.=8.3). Each subject had audiometric thresholds of 15 dB HL or better (re: ANSI, 1996) for all octave and interoctave frequencies from 250 to 8000 Hz and 10 dB HL or better for 250, 500, 2000, 3000, and 4000 Hz. The slightly more stringent threshold criteria were chosen to assure that hearing was well within normal limits at the frequencies related to the DPOAE measurements. In addition, each subject had normal 226-Hz tympanograms on each day on which DPOAE data were collected. For each subject, data were collected for only one ear (which was chosen as the one with the lowest thresholds; otherwise, the test ear was chosen randomly).

B. Stimuli

Experimental data were collected and analyzed for f_2 frequencies of 0.5 and 4 kHz, with $f_2/f_1=1.22$ in both cases. Thus, the distortion product (DP) frequencies were 0.32 and 2.55 kHz when $f_2=0.5$ and 4 kHz, respectively. As a practical matter, 0.5 kHz was chosen because it is perhaps the lowest frequency for which reliable DPOAE data could be collected, due to problems associated with the increase in

noise levels as frequency decreases. In general, the increase in noise level with decreasing frequency is a more significant problem for DPOAE measurements, compared to either stimulus frequency or transient evoked otoacoustic emission (TEOAE) measurements, because predictions about cochlear responses at one frequency (f_2) are based on measurements at a frequency that is about $\frac{1}{2}$ octave lower in frequency ($2f_1-f_2$). It is likely that this factor underlies differences in the accuracy with which DPOAEs and TEOAEs identify auditory status at low frequencies (Gorga *et al.*, 1993). In efforts to reduce the influence of noise level, averaging times were allowed to increase to unusually long times (see Sec. II E below) when $f_2=0.5$ kHz to reduce noise levels to sufficiently low levels for reliable DPOAE measurements at low stimulus levels. The implications of this fact and its impact on the conclusions associated with this study will be described subsequently. For comparison purposes, 4 kHz was selected because of its presumed basal characteristic place in the human cochlea. By focusing on these two frequencies, we hoped to obtain data on nonlinear processing from widely spaced regions, despite the fact that the CP for these two frequencies are probably not at the "extreme" opposite ends of the human cochlea (Greenwood, 1990). Recently, Shera *et al.* (2007) suggested that, in humans, frequencies above 1 kHz exhibit basal tuning properties whereas frequencies below 1 kHz exhibit apical characteristics. Thus, the two frequencies selected for the present study should provide information about basal and apical processing in humans.

C. Equating stimulus levels

One issue when comparing cochlear responses for low- and high-frequency stimulation relates to differences in the "internal" representation of the stimulus due to extraneous influences, such as the transfer of energy through the middle ear. Several steps were taken in an attempt to "equalize" the stimulation at 0.5 and 4 kHz. First, behavioral thresholds were measured at these two frequencies, using a two-interval, forced-choice, transformed up-down adaptive procedure that estimated the 71% correct point on the psychometric function (Levitt, 1971). Prior to behavioral threshold testing, a chirp was used to provide in-the-ear calibration of SPL for each subject. Calibration was repeated before each block of trials. Starting level was set to either 25 or 40 dB SPL, depending on f_2 (0.5 and 4 kHz). In some cases, the starting level was increased by 10 dB above these levels if the subject was experiencing difficulty with the task. For each block of trials, the initial step size was 4 dB, which was reduced to 2 dB following the first four reversals. Following each block, threshold was defined as the average level for the last six reversals at the 2-dB step size. Three or more blocks were measured at each frequency until the standard deviation of these blocks was 4.5 dB or less. The final threshold for each frequency and each subject was defined as the average of at least three blocks of trials.

The level of f_2 during DPOAE measurements (L_2) was then set in dB SL, using each subject's behavioral thresholds as the reference. This approach was followed in an attempt to equate the level of the stimuli in the cochlea, accounting for factors such as differences in forward middle-ear transmission at 0.5 and 4 kHz, which presumably influences threshold differences as a function of frequency, at least in ears with normal hearing. If these assumptions are correct, equating stimulus levels based on behavioral thresholds should control for any differences in forward transmission through the middle ear. Even if threshold differences as a function of frequency are not solely determined by middle-ear energy transfer in the forward direction, this approach should result in equivalent cochlear representation (to the extent that the factors determining threshold are independent of frequency) across frequency and across subjects. On the other hand, threshold may depend on different mechanisms at the two f_2 frequencies used in the present study. For example, phase locking may play a greater role at 0.5 kHz, compared to 4 kHz. However, there is no way this can be known and certainly no obvious approach for equating cochlear input or output. As a consequence, referencing stimulus level to the same psychophysical definition of behavioral threshold at both frequencies seems like a reasonable first approximation for equating stimulus levels at these frequencies.

D. Optimizing stimulus levels

Previously, several different approaches have been taken for setting primary levels. In some cases, L_1 was set equal to L_2 (e.g., Lonsbury-Martin *et al.*, 1990; Smurzynski and Kim, 1992). L_1 was set a constant number of decibels higher than L_2 (e.g., Stover *et al.*, 1996), the difference between L_1 and L_2 decreased as L_2 increased regardless of f_2 (e.g., Kummer *et al.*, 1998, 2000), or the difference between the two primary levels decreased as L_2 increased in a way that depended on f_2 (Neely *et al.*, 2005; Johnson *et al.*, 2006). With the exception of Neely *et al.* and Johnson *et al.*, the same primary-level conditions were applied to all subjects in these studies. That is, the levels were not customized individually for each subject. In this study, we were interested in selecting stimulus-level conditions that optimized the response for each subject and for both f_2 frequencies. We operationally defined optimal conditions as those primary levels that resulted in the largest DPOAE for each subject. The approach we took to determine these levels also obviates the need for us to take into account any differences in forward transmission for the f_1 frequencies associated with 0.5 and 4 kHz. When $f_2=4$ kHz, a procedure was used in which both L_1 and L_2 were continuously swept sinusoidally (Neely *et al.*, 2005). We refer to this as the Lissajous-path procedure. At 4 kHz, this procedure was completed in 64 s. The L_1 that resulted in the optimal (largest) DPOAE for each L_2 was identified for each subject. Following the application of an inclusion criterion based on the signal-to-noise ratio [(SNR), which we required to be $\geqslant$9 dB in order for the data point to be included], these optimal values were then fit with a linear model. The linear model was then solved to determine the L_1 that would be used for each L_2. In this way, we optimized the primary-level ratio at all L_2 levels individually for each subject when $f_2=4$ kHz.

The short averaging time associated with the Lissajous-path procedure was insufficient to identify optimal L_1 condi-

tions when f_2=0.5 kHz. Without greater averaging times, the higher noise levels at this frequency made it impossible to explore the primary-level space because reliable measurements were seldom observed when the Lissajous-path procedure was used at 0.5 kHz. As a result, an alternative procedure was used at 0.5 kHz to determine optimal L_1 levels for each L_2 for each subject. At this frequency, measurements were made for discrete stimulus-level conditions, under which averaging could continue for extended periods of time that allowed for greater noise reduction. L_2 was varied in discrete 10-dB steps from 40 to 70 dB SPL. These levels were chosen because of the increased likelihood that positive SNRs would be observed for these levels when f_2=0.5 kHz. At each L_2, L_1 was varied in 5-dB steps from 10 dB below L_2 to 20 dB above L_2 (for L_2 up to 60 dB SPL) or to 10 dB above L_2 (for L_2=70 dB SPL). For each L_2, L_1 pair, averaging continued until the noise floor was $\leqslant$−20 dB SPL, the SNR exceeded 12 dB, or artifact-free averaging time exceeded 210 s, whichever occurred first. Just as was the case at 4 kHz (where the Lissajous-path procedure was used), the L_1 at each L_2 that resulted in the largest DPOAE was fit with a linear model, following the application of same data-point inclusion criterion (SNR $\geqslant$9 dB) that was used at 4 kHz. This model was then used to select the "optimal" L_1 for each L_2 when f_2=0.5 kHz. Although this approach differs from the one used at 4 kHz, in both cases, procedures were followed that attempted to optimize stimulus-level conditions individually for each subject at both f_2 frequencies. It could be argued that L_1 could have been determined in the same manner as L_2 was selected, namely by referencing L_1 to the behavioral threshold for f_1. However, this approach would not have provided the individualized information that was needed to select relative levels between L_1 and L_2 for the wide range of L_2 levels that were used during measurements of I/O functions. Furthermore, relative level for optimal response level apparently depends on frequency (Neely *et al.*, 2005; Johnson *et al.*, 2006). By determining the optimal L_1 for each L_2 at both f_2 frequencies, we not only took into account any differences in forward middle-ear transmission at f_1, we hopefully also accounted for differences in optimal primary-level ratios across frequency.

E. Procedure for measuring DPOAE I/O functions

Prior to the collection of the DPOAE data, an in-the-ear calibration was performed with the same chirp stimulus that was used prior to behavioral-threshold measurements. While we recognize the issues associated with ear-canal SPL calibrations (Siegel and Hirohata, 1994; Siegel, 2002), we attempted to avoid problems by repositioning the probe more deeply whenever the calibration spectrum was characterized by notches near 4 kHz. This approach was favored over one in which measurements were restricted to frequencies below any observed notch in the calibration spectrum for several reasons. First, repositioning of the probe enabled us to assure that notches were not present at the frequency of interest. Second, it enabled us to collect data at the same f_2 frequencies in all subjects. Third, it allowed us to make measurements at a higher frequency than might have been possible if measurements were restricted to frequencies below any observed notch in the spectrum. As might be expected from ear-canal geometry in relation to stimulus wavelength, notches in the calibration response were never observed around 0.5 kHz. DPOAE level was estimated in the frequency bin that corresponded to the DP frequency ($2f_1-f_2$) for each f_2. Noise was estimated as the average power in the six frequency components adjacent to the DP frequency (three above and three below the DP frequency). The stimulus and response buffers were 0.25 s in duration, resulting in a 4-Hz spacing between adjacent frequency components. DPOAE I/O functions were measured for L_2 levels ranging from −20 to 65 dB SL when f_2=4 kHz, and from −10 to 65 dB SL when f_2=0.5 kHz, using each subject's previously measured behavioral threshold as the reference for 0 dB SL. At both f_2 frequencies, measurements commenced with the lowest stimulus level. L_2 was incremented in 5-dB steps (resulting in I/O functions with either 16 or 18 points, depending on frequency), and L_1 was set according to the individually optimized levels determined from either the continuously variable or discretely variable-level studies that were described earlier.

Measurement-based stopping rules were used in an effort to obtain reliable data at both f_2 frequencies over a wide range of input levels. However, in the interest of reducing time commitments on the part of individual subjects, slightly different rules were used at 0.5 and 4 kHz. When f_2 =0.5 kHz, data collection continued until any one of the following conditions were met: measurements stopped for each L_2 condition when either the noise floor was $\leqslant$−25 dB SPL, the SNR was $\geqslant$12 dB, or 210 s of artifact-free averaging time had expired, whichever occurred first. At 4 kHz, the stopping rule was also based on three conditions, although the rules varied slightly from those used at 0.5 kHz. Data collection continued when f_2=4 kHz until the noise floor was $\leqslant$−25 dB SPL, the SNR $\geqslant$20 dB, or 210 s of artifact-free averaging had taken place, whichever occurred first. The inclusion of a SNR criterion at both f_2 frequencies was intended to reduce test time for stimulus conditions in which the response was reliably measured well above the noise floor. The lower SNR stopping criterion when f_2=0.5 kHz represents an additional compromise, given the longer time it took to collect data at this frequency due to the higher noise levels. The less stringent SNR criterion was viewed as a reasonable compromise, in that response levels with a SNR $\geqslant$12 dB would be expected to vary by less than 2 dB as a result of the noise. By relaxing the SNR rule, less data-collection time was needed for high-level stimuli at 0.5 kHz, when more robust responses were observed, with little or no effect on the reliability of the measurements. When measurements were made for low-level stimuli close to DPOAE threshold, the stopping rules for 0.5 and 4 kHz were identical because the measurements at neither frequency stopped on SNR; that is, the SNR did not exceed 12 dB (0.5 kHz) or 20 dB (4 kHz) for these low-level stimulus conditions. In reality, averaging times were always short when f_2=4 kHz, typically 4–32 s, regardless of stimulus level. This occurred because it was common for the test to stop on the noise stopping criterion ($\leqslant$−25 dB SPL) at this frequency. The av-

eraging times were much longer when f_2=0.5 kHz for all stimulus levels, but especially for low-level stimuli, because of the higher noise levels at this frequency and the lower response levels at these stimulus levels. Frequently, it was the case that the measurement stopped when the (artifact-free) averaging time = 210 s at 0.5 kHz. Despite averaging times that were longer by an order of magnitude or more at 0.5 kHz, the noise floor was never as low at 0.5 kHz as it was at 4 kHz. Still, the use of slightly different measurement-based stopping rules at the two frequencies represented a compromise between total test time and reliability, thus allowing us to make measurements of DPOAE levels within reasonable amounts of time at both 0.5 and 4 kHz. Subjects were allowed to either sleep, read, or watch a DVD (captioned with sound turned off) during data collection. Subjects were provided breaks as needed.

F. Middle-ear transmission

In an effort to validate the approach in which behavioral-threshold measurements were used to "equalize" cochlear input and (presumably) remove the influence of the middle ear on the transmission of energy in the forward direction, middle-ear reflectance was also measured (Keefe, 1997) in a subset of 91 subjects from the 103 subjects who also participated in the DPOAE studies. As will be shown subsequently, these measurements revealed a similar pattern of dependence on frequency, but also suggested that behavioral threshold cannot be completely predicted from forward middle-ear transmission (at least as it is described by reflectance). The middle-ear data, however, were not viewed as central to the goals of the study, and will be described here only briefly and only in relation to the behavioral-threshold data.

The collection of a complete set of data (including screening audiometric assessments, behavioral-threshold measurements used to set L_2 in dB SL, determination of optimal primary-level for each subject at both f_2 frequencies, measurement of DPOAE I/O functions at both frequencies, and measurements of middle-ear reflectance) took 4–6 h per subject (two to three 2-h sessions). Subjects were paid an hourly rate for their participation in the study. This study was approved by the BTNRH Institutional Review Board.

III. RESULTS AND DISCUSSION

A. Behavioral thresholds and reflectance measurements

Figure 1 plots the mean behavioral thresholds in dB SPL ±1 s.d., shown as open symbols (referred to the left *y* axis), when f_2 was either 0.5 or 4 kHz. Not surprisingly, behavioral thresholds were lower (by about 8 dB) at 4 kHz, compared to 0.5 kHz. Closed symbols represent the mean reflectance converted to decibels (referred to the right *y* axis) at the same frequencies. Although the pattern is similar, there is less difference between middle-ear energy transfer in the forward direction (as estimated by reflectance) as a function of frequency, compared to the difference in behavioral threshold. The difference in reflectance between 0.5 and 4 kHz is about 5 dB. Interestingly, the variability in behavioral threshold

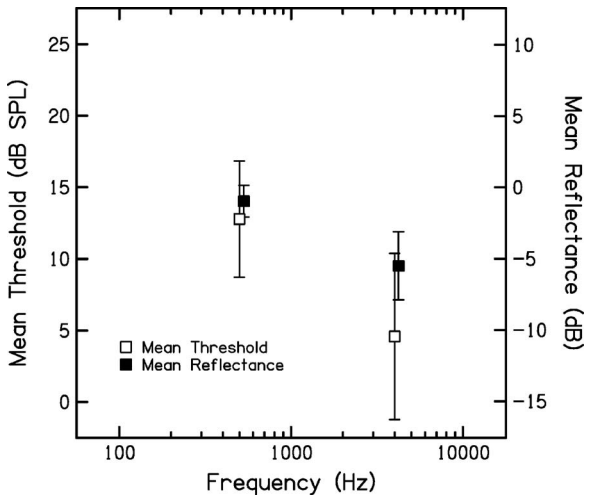

FIG. 1. Mean behavioral threshold in dB SPL (left *Y* axis) and mean middle-ear reflectance in decibels (right *Y* axis) as a function of frequency. Open symbols represent behavioral thresholds and closed symbols represent reflectance data. In both cases, error bars represent ±1 s.d. Data are shown for both f_2 frequencies (0.5 and 4 kHz). Data points representing behavioral thresholds and reflectance are offset slightly to allow for easier visualization.

was greater than the variability in reflectance. This finding also would be consistent with the view that behavioral thresholds cannot be completely explained by middle-ear transmission, although it also may be a consequence of greater inherent variability in behavioral-threshold measurements, compared to measures of energy reflectance. In any case, these data suggest that threshold is not entirely predictable from middle-ear energy reflectance. This finding does not negate the value of presenting stimuli (L_2) in dB SL for DPOAE measurements. While these data indicate that behavioral thresholds are related to reflectance, they also suggest that other factors contribute to threshold. However, the use of behavioral thresholds to normalize stimulus levels was viewed as an approach in which the output of the cochlea (not just the transfer of energy through the middle ear) is held constant at the characteristic cochlear places at which the two f_2 frequencies are represented for each subject.

B. DPOAE I/O functions-L_2 in dB SPL

Figure 2 shows mean DPOAE and noise levels (in dB SPL) as a function of L_2 (in dB SPL). The top panel shows data when f_2=0.5 kHz and the bottom panel provides the data when f_2=4 kHz. Squares represent DPOAE levels and circles represent noise levels. In all cases, error bars represent ±1 s.d. All data were included without regard to any inclusion criteria, such as SNR. We should note, however, that a reanalysis of the data restricted to those conditions for which the SNR ⩾3 dB did not change the I/O functions in any significant way. Because individually measured behavioral thresholds were used to set L_2, responses were not always measured at the exact same SPL in all subjects. For example, 0 dB SL (behavioral threshold) might have occurred at 6 dB SPL in one subject, 8 dB SPL in another subject, and 4 dB SPL in a third subject. Since L_2 was set relative to each subject's behavioral threshold and measurements were made in 5-dB steps, data were never obtained at

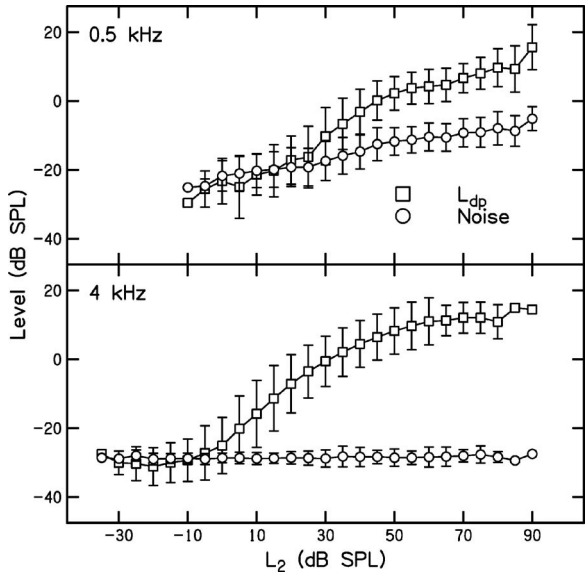

FIG. 2. Top panel: Mean DPOAE level (L_{dp}) (squares) and noise level (circles) in dB SPL as a function of L_2 in dB SPL when f_2=0.5 kHz. Bottom panel: Mean DPOAE level (L_{dp}) (squares) and noise level (circles) in dB SPL as a function of L_2 in dB SPL when f_2=4 kHz. In all cases, error bars represent ±1 s.d. Because stimuli were presented relative to each subject's threshold, L_2 was rounded to the nearest 5 dB prior to calculating the mean values shown.

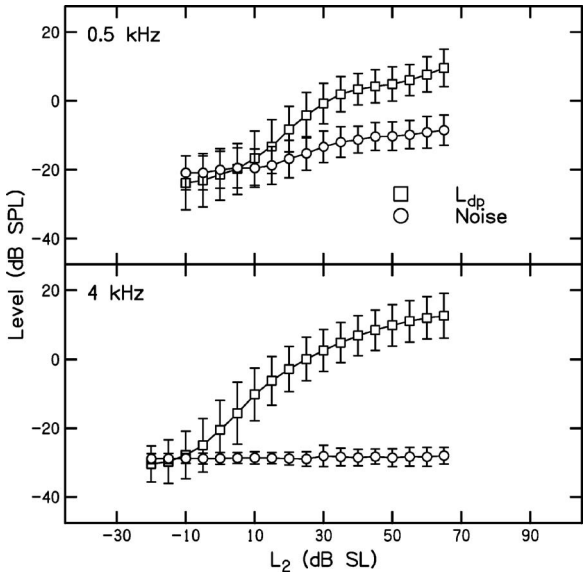

FIG. 3. Top panel: Mean DPOAE level (L_{dp}) (squares) and noise level (circles) in dB SPL as a function of L_2 in dB SL when f_2=0.5 kHz. Bottom panel: Mean DPOAE level (L_{dp}) (squares) and noise level (circles) in dB SPL as a function of L_2 in dB SL when f_2=4 kHz. In all cases, error bars represent ±1 s.d.

the exact same SPL for these three subjects. Given the goals of this study, we thought it was more important to make measurements for input stimuli that resulted in the same "cochlear output" in all subjects (as reflected in behavioral thresholds) rather than to make measurements at exactly the same input SPL in all subjects, which would ignore subtle threshold differences. However, it is more commonly the case that DPOAE I/O functions are plotted when L_2 is specified in dB SPL. In order to provide this more typical representation, L_2 was rounded to the nearest 5 dB and then averaged across subjects, which was done in the process of generating the data shown in Fig. 2. Despite this "rounding error" (which never exceeded 2.5 dB) and the fact that the measurement-based stopping rules did not result in the same noise levels at both f_2 frequencies (see the following), it can be seen that DPOAEs were measured over a wide range of input levels, perhaps as low as −5 dB SPL at 4 kHz and 20 dB SPL at 0.5 kHz. Measurements of DPOAEs extending down to these low stimulus levels are unusual, especially when f_2=0.5 kHz. Having data for such low-level inputs demonstrates that the measurement-based stopping rules were successful in reducing noise to levels that are not typically observed. The results shown in Fig. 2 indicate that there is greater output (L_{dp}) at 4 kHz, compared to the output at 0.5 kHz for virtually every input level. Across conditions in which responses were observed, DPOAE level at 4 kHz exceeded DPOAE level at 0.5 kHz by between 5 and 13 dB.

C. DPOAE I/O functions—L_2 in dB SL

Figure 3 plots mean DPOAE level and noise levels (dB SPL) as a function of L_2 (in dB SL). Thus, stimulus inputs were normalized to each subject's behavioral thresholds at the two f_2 frequencies. In all other respects, the same conventions that were used in Fig. 2 are used here. Even when behavioral thresholds were used to create more equivalent input levels, the outputs still differed, with L_{dp} being greater and measurable over a wider dynamic range for 4 kHz, compared to 0.5 kHz. This is the first indication in our data (ignoring the results shown in Fig. 2) that the responses are not identical at 0.5 and 4 kHz, even after stimulus levels were chosen in a way that we thought would help to equate cochlear inputs. DPOAEs were measured down to −5 dB SL at 4 kHz; in contrast, DPOAEs were measured down to 10 dB SL at 0.5 kHz.

Despite using a paradigm which allowed averaging time to vary in an effort to achieve similar noise levels at both 0.5 and 4 kHz, equivalent noise levels at the two frequencies were almost never achieved in individual subjects and certainly not in the mean data. Part of this effect was due to differences in the SNR stopping criteria for the two frequencies, but this factor would be expected to have no influence for low-level inputs, when the stopping rules were effectively identical, as described earlier. The noise levels were higher and more variable at all stimulus levels at 0.5 kHz, compared to 4 kHz. At 4 kHz, averaging stopped almost without exception when the noise-floor criterion (noise level $\leqslant$−25 dB SPL) was met. However, at higher primary levels, testing sometimes stopped on SNR because the L_{dp} was so large. When this occurred, it resulted in slightly higher and more variable noise levels, which is evident from an examination of the noise data in the bottom panel of Fig. 3 (circles and error bars for $L_2 \geqslant 25$ dB SL when f_2=4 kHz). At 4 kHz, it was never the case that data collection continued until the test-time criterion of 210 s was reached. At 0.5 kHz, averaging stopped more often when the SNR criterion was met at high stimulus levels, which is why the noise floor increases for $L_2 \geqslant 20$ dB SPL (circles in the top panel of Fig. 3). We are unconcerned with the higher noise levels for these higher

level stimulus conditions because the influence of the noise on the measured DPOAE level is expected to be small, given the size of the response. However, at low-stimulus levels, the average noise floor still was higher when f_2=0.5 kHz, despite the fact that data collection continued for as long as 210 s of artifact-free averaging time per measurement. In reality, the time spent collecting data at each of these lower levels at 0.5 kHz often exceeded 210 s because artifact rejection occurred frequently, thus making the effective test time greater. Theoretically, we could have increased averaging time by a factor of 4, which would presumably result in equivalent noise levels at both frequencies; however, this increase in averaging time would not have been tolerated by subjects. For this reason, increasing averaging time beyond 210 s was not considered a reasonable option for reducing the noise floor. Alternative techniques, currently unknown to us, would be needed to achieve lower noise levels at 0.5 kHz in practically feasible amounts of time. In any case, the implications of the difference in noise floors relative to our interpretation of the data will be discussed in a subsequent section.

D. Slopes of DPOAE I/O functions

One explanation for the difference in cochlear output (DPOAE level) when inputs are "equated" could be differences in reverse transmission through the middle ear as a function of frequency. While behavioral thresholds were also measured at the DP frequency ($2f_1-f_2$), which is the frequency at which reverse transmission of the DPOAE takes place, the extent to which reverse middle-ear transmission can be estimated from behavioral thresholds is not known. Previous work has shown that horizontal shifts of the DPOAE I/O function can be used to provide estimates of relative forward middle-ear transmission, while vertical shifts in the I/O function can be used as an indirect, relative measure of reverse transmission (Keefe, 2002). For both horizontal and vertical shifts, it is assumed that the form of the cochlear nonlinearity is the same at every place along the cochlea, which, in turn, is related to the assumption of cochlear scaling symmetry that has been described by others (Shera *et al.*, 2000; Zwieg, 1976). An assumption of scaling symmetry, however, would have been incompatible with the goals of the present study, which were to evaluate cochlear nonlinearity in humans for low- and high-frequency stimuli. This is one of the reasons why we referenced stimulus level to behavioral threshold as a way to equate effective excitation in the cochlea. Another reason for referencing L_2 to behavioral thresholds was to remove middle-ear influences in the forward direction, as described in Sec. II. We also needed an approach that would control or eliminate the influences of reverse middle-ear transmission on measured DPOAE level, but felt that there were too many uncertainties in using behavioral thresholds to estimate reverse transmission. As stated earlier, using vertical shifts in the I/O function was not viewed as an acceptable alternative, as it assumes the form of the nonlinearity is the same for high and low frequencies (which is the hypothesis we are attempting to test). We have opted instead to evaluate the slopes of I/O functions, which

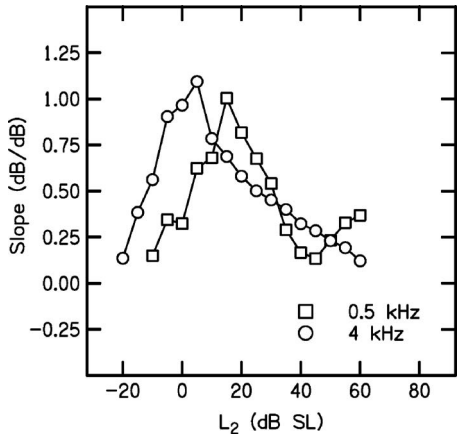

FIG. 4. Slope (dB/dB) as a function of L_2 in dB SL, calculated from the mean data shown in Fig. 3. Squares represent data for 0.5 kHz and circles represent data for 4 kHz.

are independent of the relative placement of I/O functions along the *Y* axis and, therefore, presumably independent of reverse middle-ear energy transmission. Thus, we can compare DPOAE I/O function slopes as a way of determining if the functions differ at 0.5 and 4 kHz without worrying about the influence of reverse energy transmission through the middle ear.

Figure 4 plots the slope of the I/O functions as a function of L_2 (dB SL), with circles representing data when f_2 =4 kHz and squares representing data when f_2=0.5 kHz. These slopes were derived from the data plotted in Fig. 3, calculated as the change in DPOAE level (L_{dp}) between adjacent L_2 values. At both frequencies, the slopes are close to 1 within a few decibels of DPOAE threshold (roughly defined as the level at which the DPOAE just exceeds the noise floor). More shallow slopes are observed for inputs below these levels; but, this observation may be a consequence of the fact that these estimates are dominated by the noise, which would be expected to make the slope more shallow. The slope of the DPOAE I/O functions are between 0 and 0.25 at high stimulus levels (40–60 dB SL), where the influence of noise is minimal. These slopes are consistent with previous estimates, and suggest that DPOAE I/O functions show about the same 4:1 or 5:1 compression at both frequencies for high-level inputs. Thus, there is little difference between slope estimates at the two frequencies for higher level inputs. In contrast, it appears that the maximum slope (approximately 1) is achieved for lower level inputs at 4 kHz, compared to 0.5 kHz, which represents a small deviation from scaling symmetry. This would suggest that there may be a wider dynamic range at 4 kHz, but we do not completely understand the meaning of the differences in slope, and we are cautious in our interpretation of these data because we cannot rule out the effects of differences in noise level. Recall that our efforts to reduce noise to equivalent levels were only moderately successful. This mattered little for high-level inputs, because the DPOAE level was well above the noise floor, even at 0.5 kHz. At low levels, however, the fact that the measurement-based stopping rules did not result in the same noise floor at both frequencies could have influenced the low-level differences in slope. This con-

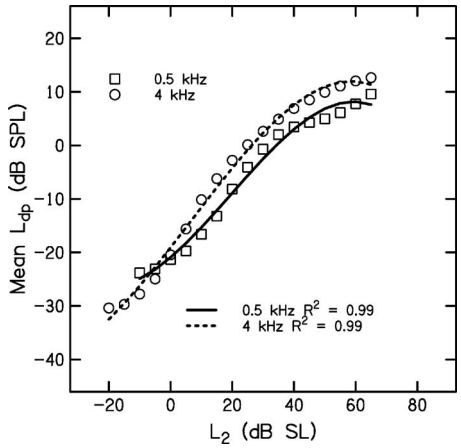

FIG. 5. Mean L_{dp} in dB SPL as a function of L_2 in dB SL, following the symbol conventions used in Fig. 4. Lines represent polynomial fits to the mean data, with the solid line representing the fit to data at 0.5 kHz and the dashed line representing the fit to data at 4 kHz. Proportion of the variance accounted for is provided as an insert.

cern is relevant for comparisons of the slope estimates for stimulus levels of 0 dB SL or less, but is of less importance for comparisons between frequencies at levels ⩾0 dB SL (4 kHz) and ⩾10 dB SL (0.5 kHz). For these stimulus conditions, the responses were above the noise floor, and yet differences in slopes of the I/O function between the two f_2 frequencies were still evident. Still, the influence of noise-floor differences at the two frequencies is a potentially important factor, and will be further discussed below.

In an effort to smooth the mean data shown in Fig. 3, data were fit with a polynomial function. The mean data are reproduced as symbols in Fig. 5, with circles representing the data at 4 kHz, squares representing the data at 0.5 kHz, and the lines representing separate polynomial fits to the data for each frequency. These polynomial equations provide good fits to the mean data, accounting for 99% of the variance.

Figure 6 plots slopes as a function of L_2 (dB SL) that were derived from polynomial fits shown in Fig. 5. As expected, these slopes follow a smoother path, compared to the

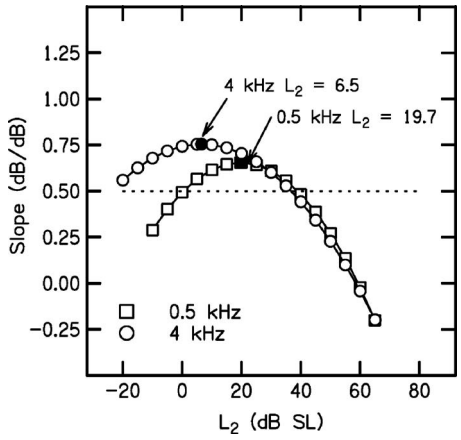

FIG. 6. Slope (dB/dB) as a function of L_2 in dB SL derived from the polynomial fits that were shown in Fig. 5. Symbol convention is the same as in previous figures. Closed symbols on each curve represent the point at which the maximum slope was achieved. Horizontal dashed line drawn at a slope of 0.5 was used as a definition of dynamic range.

data shown in Fig. 4, where the slopes were estimated from the actual mean data (as shown in Fig. 3), and not the fits to those data (shown in Fig. 5). In these smooth versions, differences in slope for inputs of 20 dB SL or greater are minimized. Slopes less than zero for inputs exceeding 55 dB SL are a consequence of the polynomial fits emphasizing nonmonotonicities at high levels. In contrast to the similarities for stimulus levels ⩾20 dB SL, there are large frequency-dependent differences in slope for lower level inputs. In an effort to quantify these differences, we estimated the level at which maximum slope was achieved from these fits. These points are represented by closed symbols on each function. At 4 kHz, this occurred for an input level of 6.5 dB SL, whereas maximum slope was observed at 19.7 dB SL when f_2=0.5 kHz. Thus, maximum slope is achieved at a level that is 13 dB lower at 4 kHz, compared to 0.5 kHz. Given the similarity in responses at high levels, the decibel difference at the low end might reflect differences in the dynamic range of response at the two test frequencies. As stated earlier, low-level stimulus conditions are particularly vulnerable to the influences of noise. For this reason, differences in slope for input levels less than about 0 dB SL at 4 kHz and less than about 10 or 15 dB SL at 0.5 kHz cannot be interpreted. For stimulus levels between these values and about 20–25 dB SL, it is difficult to see how the slope differences are due solely to frequency differences in background noise (see Figs. 3 and 4). Thus, the present data would be consistent with the view that this estimate of "dynamic range" is greater at 4 kHz, compared to 0.5 kHz.

An alternate way of estimating dynamic range, based on estimates of slope, is to define it as the range of input levels for which the slope exceeds some arbitrary value, such as the one shown by the dotted horizontal line in Fig. 6. The advantage of this approach is that it is derived from the polynomial fits to all of the data; as was seen in Fig. 5, these fits provide good descriptions of the mean data. The disadvantage of this approach is that it allows for extrapolation to extremely low-level inputs, where the influence of noise is greatest. Keeping in mind our concern that the extension toward low-level inputs based on the polynomial fits may have problems associated with it (given the potential influence of noise at these levels), we arbitrarily selected slopes of 0.5 as the inclusion criterion, mainly because the parabolas at both frequencies had slopes at or close to this value on both the low-level and high-level side of the stimulus level at which the maximum slope was observed. The range of levels between the intersections of the dashed line with each parabola was used as an estimate of the dynamic range. To the extent that this is an appropriate metric, the dynamic range at 0.5 kHz was 39 dB, while the dynamic range at 4 kHz was 61 dB.

The results shown in Fig. 6 might be consistent with the reduced differences between tip and tail thresholds as observed in frequency-threshold curves of auditory neurons (see, for example, Sewell, 1984), although we do not, as yet, have data that can be used to more directly test this hypothesis in humans. Tip-to-tail differences estimated from DPOAE suppression tuning curves have been interpreted as estimates of cochlear-amplifier gain (e.g., Pienkowski and

Kunov, 2001; Mills, 1998; Gorga *et al.*, 2002, 2003). If the interpretation of the data shown in Figs. 4 and 6 is correct, then the present results could be consistent with frequency differences in cochlear-amplifier gain, thus suggesting that nonlinear processing differs at the cochlear apex in humans, compared to its base. The present data suggest that the cochlea exhibits compressive growth at both 0.5 and 4 kHz (and, therefore, at its apex and at its base). These data would be inconsistent with the view that the human cochlea produces distortion at its base, but not its apex. Rather, the frequency differences noted here would be more a matter of the magnitude of the effect. Based on these data, we would predict that the human cochlear amplifier has less gain for low frequencies, compared to higher frequencies.

It is important to note that a level of uncertainty exists in how to interpret the differences in slope of the DPOAE I/O functions as a function of L_2. However, it remains the case that slope estimates have the advantage that they require no assumptions regarding underlying cochlear processes (such as cochlear scaling symmetry, which is what we were evaluating in humans) and are independent of reverse middle-ear energy transmission (which, in any event, may be difficult to ascertain in humans). We remain concerned by the possible confounding influence of differences in noise levels on slope estimates. It is highly impractical, if not impossible, to reduce noise to the same levels at 0.5 and 4 kHz in humans. While the results suggest that differences exist in cochlear nonlinearity as a function of frequency in humans, we remain cautious in this interpretation, based on the present data. For practical reasons, the influence of noise could not be completely controlled, and the effect of its influence might lead to the potentially incorrect conclusion that the human cochlea is less nonlinear at its apex, compared to its base. Having said this, the differences in slopes of the I/O functions for stimulus levels between about 0 and 20 dB SL are less likely to be affected by noise levels (given that positive signal-to-noise ratios were observed for these conditions). In particular, the slope data shown in Fig. 4 suggest that there are real differences between 0.5 and 4 kHz in dynamic range that cannot be entirely attributed to differences in noise level. Still, additional studies in which a paradigm is used that results in equivalent noise levels or alternative measurements less susceptible to noise may be needed to determine if nonlinearity in humans differs at the cochlear base versus its apex with greater certainty.

With current technology and noise-reduction algorithms, it is unlikely that noise can be consistently reduced to the same low levels at 0.5 kHz as is routinely possible at 4 kHz. Further refinements in measurement or analysis techniques in the future, however, might result in more equivalent noise levels at these two frequencies. The use of experimental paradigms less affected by background noise (compared to the measurement of DPOAE I/O functions) might provide insights into cochlear-processing differences between 0.5 and 4 kHz in humans. For example, measurements of the decrease in DPOAE level due to the presence of a suppressor can be used to generate DPOAE suppressing tuning curves. Estimates of "tuning" and/or cochlear-amplifier gain derived from suppression tuning curves may be less affected by noise or middle-ear transfer and could, therefore, provide a way to make base-apex comparisons that are more straightforward to interpret than I/O functions.

ACKNOWLEDGMENTS

Work supported by the NIH (NIDCD R01 2251 and P30 4662). We thank Doug Keefe for providing the software that was used for measurements of middle-ear reflectance. We are grateful for informal discussions of this study with Chris Shera, and to two anonymous reviews that provided many helpful suggestions that improved the manuscript. We would also like to thank Sandy Estee, Alberto Cervantes, and Gwen Watson for their help in recruiting subjects to participate in this study.

American National Standards Institute (**1996**). ANSI S3.6-1996, "Specifications for Audiometers," (American National Standards Institute, New York).

Cooper, N. P., and Rhode, W. S. (**1995**). "Nonlinear mechanics at the apex of the guinea-pig cochlea," Hear. Res. **82**, 225–243.

Cooper, N. P., and Rhode, W. S. (**1997**). "Mechanical responses to two-tone distortion products in the apical and basal turns of the mammalian cochlea," J. Neurophysiol. **78**, 261–270.

Cooper, N. P., and Rhode, W. S. (**1998**). "Apical cochlear mechanics: A review of recent observations," in *Proceedings of the International Symposium on Psychophysical and Physiological Advances in Hearing*, edited by A. R. Palmer, A. Rees, A. Q. Summerfield, and R. Meddis (Whurr, London), pp. 11–18.

Cooper, N. P., and Yates, G. K. (**1994**). "Nonlinear input-output functions derived from the responses of guinea-pig cochlear nerve fibers: Variations with characteristic frequency," Hear. Res. **78**, 221–234.

Dorn, P. A., Konrad-Martin, D., Neely, S. T., Keefe, D. H., Cyr, E., and Gorga, M. P. (**2001**). "Distortion-product otoacoustic emission input/output functions in normal-hearing and hearing-impaired human ears," J. Acoust. Soc. Am. **110**, 3119–3131.

Gorga, M. G., Neely, S. T., Konrad-Martin, D., and Dorn, P. A. (**2002**). "The use of DPOAE suppression as an estimate of response growth," J. Acoust. Soc. Am. **111**, 271–284.

Gorga, M. P., Neely, S. T., Bergman, B. M., Beauchaine, K. L., Kaminski, J. R., Peters, J., Schulte, L., and Jesteadt, W. (**1993**). "A comparison of transient-evoked and distortion product otoacoustic emissions in normal-hearing and hearing-impaired subjects," J. Acoust. Soc. Am. **94**, 2639–2648.

Gorga, M. P., Neely, S. T., Dierking, D. M., Dorn, P. A., Hoover, B. M., and Fitzpatrick, D. F. (**2003**). "Distortion product otoacoustic emission tuning curves in normal-hearing and hearing-impaired human ears," J. Acoust. Soc. Am. **114**, 263–278.

Greenwood, D. D. (**1990**). "A cochlear frequency-position function for several species-29 years later," J. Acoust. Soc. Am. **87**, 2592–2605.

Hicks, M. L., and Bacon, S. P. (**1999**). "Psychophysical measures of auditory nonlinearities as a function of frequency in individuals with normal hearing," J. Acoust. Soc. Am. **105**, 285–296.

Johnson, T. A., Neely, S. T., Garner, C. A., and Gorga, M. P. (**2006**). "Influence of primary-level and primary-frequency ratios on human distortion product otoacoustic emissions," J. Acoust. Soc. Am. **119**, 418–428.

Keefe, D. H. (**1997**). "Otoreflectance of the cochlear and middle ear," J. Acoust. Soc. Am. **102**, 2849–2859.

Keefe, D. H. (**2002**). "Spectral shapes of forward and reverse transfer functions between ear canal and cochlea estimated using DPOAE input/output functions," J. Acoust. Soc. Am. **111**, 249–260.

Kiang, N. Y.-S., and Moxon, E. C. (**1974**). "Tails of tuning curves of auditory-nerve fibers," J. Acoust. Soc. Am. **55**, 620–630.

Kiang, N. Y.-S., Watanabe, T., Thomas, E. C., and Clark, L. F. (**1965**). *Discharge Patterns of Single Fibers in the Cat's Auditory Nerve*, MIT Research Monograph No. 35 (MIT, Cambridge, MA).

Kummer, P., Janssen, T., and Arnold, W. (**1998**). "The level and growth behavior of the 2f1-f2 distortion product otoacoustic emission and its relationship to auditory sensitivity in normal hearing and cochlear hearing loss," J. Acoust. Soc. Am. **103**, 3431–3444.

Kummer, P., Janssen, T., Hulin, P., and Arnold, W. (**2000**). "Optimal L1–L2

primary-tone level separation remains independent of test frequency in humans," Hear. Res. **146**, 47–56.
Levitt, H. (**1971**). "Transformed up-down methods in psychoacoustics," J. Acoust. Soc. Am. **49**, 467–477.
Lonsbury-Martin, B. L., Harris, M. D., Stagner, B. B., and Martin, G. K. (**1990**). "Distortion product emissions in humans. I. Basic properties in normally hearing subjects," Ann. Otol. Rhinol. Laryngol. Suppl. **99**, 3–13.
Lopez-Poveda, E. A., Plack, C. J., and Meddis, R. (**2003**). "Cochlear nonlinearity between 500 and 8000 Hz in listeners with normal hearing," J. Acoust. Soc. Am. **113**, 951–960.
Mills, D. M. (**1998**). "Interpretation of distortion product otoacoustic emission measurements. II. Estimating tuning characteristics using three stimulus tones," J. Acoust. Soc. Am. **103**, 507–523.
Neely, S. T., Gorga, M. P., and Dorn, P. A. (**2003**). "Cochlear compression estimates from measurements of distortion-product otoacoustic emissions," J. Acoust. Soc. Am. **114**, 1499–1507.
Neely, S. T., Johnson, T. A., and Gorga, M. P. (**2005**). "Distortion-product otoacoustic emissions with continuously varying stimulus level," J. Acoust. Soc. Am. **117**, 1248–1259.
Neely, S. T., Johnson, T. A., Kopun, J. G., Converse, C., Kennedy, E., Dierking, D. M., and Gorga, M. P. (**2007**). "Quantitative estimates of DPOAE I/O functions in normal and impaired ears," 30th Midwinter Meeting of the Association for Research in Otolaryngology, Denver, CO.
Pienkowski, M., and Kunov, H. (**2001**). "Suppression of distortion product otoacoustic emissions and hearing thresholds," J. Acoust. Soc. Am. **113**, 1574–1586.
Plack, C. J., and Drga, V. (**2003**). "Psychophysical evidence for auditory compression at low characteristic frequencies," J. Acoust. Soc. Am. **113**, 1574–1586.
Plack, C. J., and O'Hanlon, C. G. (**2003**). "Forward masking additivity and compression at low and high frequencies," J. Assoc. Res. Otolaryngol. **4**, 405–415.
Plack, C. J., and Oxenham, A. J. (**1998**). "Basilar membrane nonlinearity and the growth of forward masking," J. Acoust. Soc. Am. **103**, 1598–1608.
Rhode, W. S., and Cooper, N. P. (**1996**). "Nonlinear mechanics in the apical turn of the chinchilla cochlea in vivo," Audiol. Neuro-Otol. **3**, 101–121.
Ruggero, M. A., and Rich, N. C. (**1991**). "Furosemide alters organ of corti mechanics: Evidence for feedback of outer hair cells upon the basilar membrane," J. Neurosci. **11**, 1057–1067.
Schairer, K. S. and Jesteadt, W. (**2003**). "Evidence of peripheral nonlinearity in psychometric function slopes of forward-masked tones at 250 and 4000 Hz," J. Acoust. Soc. Am. **113**, 2226. (Abstract)
Sewell, W. F. (**1984**). "The effects of furosemide on the endocochlear potential and auditory-nerve fiber tuning curves in cats," Hear. Res. **14**, 305–314.
Shera, C. A., Guinan, J. J., and Oxenham, A. J. (**2007**). "Otoacoustic estimates of cochlear tuning: Validation in the chinchilla," 30th Midwinter Meeting of the Association for Research in Otolaryngology, Denver, CO.
Shera, C. A., Talmadge, C. L., and Tubis, A. (**2000**). "Interrelations among distortion-product phase-gradient delays: Their connection to scaling symmetry and its breaking," J. Acoust. Soc. Am. **108**, 2933–2948.
Siegel, J. H. (**2002**). "Calibrating otoacoustic emission probes," in *Otoacoustic Emissions: Clinical Applications*, 2nd ed., edited by M. S. Robinette and T. J. Glattke (Thieme Medical, New York), pp. 416–441.
Siegel, J. H., and Hirohata, E. T. (**1994**). "Sound calibration and distortion product otoacoustic emissions at high frequencies," Hear. Res. **80**, 146–152.
Smurzynski, J., and Kim, D. O. (**1992**). "Distortion-product and click-evoked otoacoustic emissions of normally-hearing adults," Hear. Res. **58**, 227–240.
Stover, L. J., Gorga, M. P., Neely, S. T., and Montoya, D. (**1996**). "Toward optimizing the clinical utility of distortion product otoacoustic emission measurements," J. Acoust. Soc. Am. **100**, 956–967.
Zinn, C., Maier, H., Zenner, H. P., and Gier, A. W. (**2000**). "Evidence for active, nonlinear, negative feedback in the vibration of the apical region of the in vivo guinea-pig cochlea," Hear. Res. **142**, 159–183.
Zwieg, G. (**1976**). "Basilar membrane motion," in *Cold Spring Harbor Symposia on Quantitative Biology* (Cold Spring Harbor Laboratory, Cold Spring Harbor, NY), vol. **XL**, pp. 619–633.

Low-frequency modulation of distortion product otoacoustic emissions in humans

Lin Bian[a] and Nicole M. Scherrer
Auditory Physiology Laboratory, 3430 Coor Hall, Department of Speech and Hearing Science, Arizona State University, Tempe, Arizona 85287-0102

(Received 11 May 2007; revised 25 June 2007; accepted 26 June 2007)

Low-frequency modulation of distortion product otoacoustic emissions (DPOAEs) was measured from the human ears. In the frequency domain, increasing the bias tone level resulted in a suppression of the cubic difference tone (CDT) and an increase in the magnitudes of the modulation sidebands. Higher-frequency bias tones were more efficient in producing the suppression and modulation. Quasi-static modulation patterns were derived from measuring the CDT amplitude at the peaks and troughs of bias tones with various amplitudes. The asymmetric bell-shaped pattern resembled the absolute value of the third derivative of a nonlinear cochlear transducer function. Temporal modulation patterns were obtained from inverse FFT of the spectral contents around the DPOAE. The period modulation pattern, averaged over multiple bias tone cycles, showed two CDT peaks each correlated with the zero-crossings of the bias tone. The typical period modulation pattern varied and the two CDT peaks emerged with the reduction in bias tone level. The present study replicated the previous experimental results in gerbils. This noninvasive technique is capable of revealing the static position and dynamic motion of the cochlear partition. Moreover, the results of the present study suggest that this technique could potentially be applied in the differential diagnosis of cochlear pathologies. © *2007 Acoustical Society of America.* [DOI: 10.1121/1.2764467]

PACS number(s): 43.64.Jb, 43.64.Kc, 43.64.Bt, 43.64.Yp [BLM] Pages: 1681–1692

I. INTRODUCTION

Our ears are sensitive mechanical transducers where fluctuations of sound pressure and frequency are transformed into neural signals. The inner ear transduction demonstrates a compressive nonlinearity by which the ear can accommodate a large dynamic range and maintain a sharp sensitivity. Natural outcomes of the cochlear nonlinearity are mutual suppression and intermodulation distortion products (DPs) when the ear is stimulated by two tones [see Robles and Ruggero (2001) for a review]. In addition, cochlear hair cells are capable of a reverse transduction to facilitate a feedback mechanism to enhance hearing sensitivity. The voltage-dependent motility of either the hair bundles (Kennedy *et al.*, 2005) or the membrane proteins of the outer hair cells (OHCs) (Liberman *et al.*, 2002) can produce force that injects energy into the vibration of cochlear partition. The motion of cellular structures induced by this feedback force can escape the boundaries of inner and middle ears so that it can be detected in the ear canal as small variations of sound pressure (Kemp, 1978) or otoacoustic emissions (OAEs). Therefore, using OAEs to measure the cochlear transduction provides a powerful tool to evaluate the status of the inner ear (Lonsbury-Martin and Martin, 2003). Despite the widespread use of OAEs in hearing screening, auditory sensitivity estimation, and differential diagnosis of cochlear versus retro-cochlear dysfunctions, there is a demand for applications in quantitative evaluations of the cochlear transduction and the dynamics of hair cell function (Kemp, 2007).

One way to quantify the nonlinearity in cochlear transduction is to use the acoustic DPs measured in the ear canal or the distortion product otoacoustic emissions (DPOAEs) evoked with a two-tone stimulus (f_1, f_2, $f_1<f_2$). A low-frequency biasing technique has been used in quantifying a cochlear transducer function (F_{Tr}) from the DPOAEs measured in gerbils (Bian *et al.*, 2002; Bian, 2004). This technique fully utilizes the nonlinear effects of cochlear transduction, namely suppression and distortion, to estimate the transfer characteristics of the inner ear. By introducing a high-level low-frequency tone, this method can "slowly" shift the cochlear partition to vary the operating point (OP) of the hair cell transducer and induce an amplitude modulation (AM) of the DPOAEs. For odd-order DPs, the magnitudes are suppressed depending on the phase of the low-frequency bias tone (Bian *et al.*, 2002; Bian, 2006), whereas, for even-order DPs, the DPOAE magnitudes are enhanced at maximal displacements of the cochlear partition induced by the bias tone (Bian, 2004, 2006). These different DPOAE modulation patterns are intimately related to the cochlear transducer nonlinearity, because in principle these DP magnitudes are proportional to the appropriate derivatives of the cochlear F_{Tr}. This gives rise to the first utility to derive the cochlear F_{Tr} with inverse methods.

The second utility of the technique is perhaps a more important one, because it assesses the dynamic function of the hair cell transducer on a cycle-by-cycle basis. The temporal behavior of the DPOAE magnitude under the periodic biasing of cochlear partition reveals detailed information of the underlying dynamic system of the cochlear transducer. Not only does the variation in DP amplitudes depend on the bias tone phase, but also on the direction of change in the

[a]Electronic mail: lin.bian@asu.edu

biasing pressure. Two slightly different modulation patterns forming a hysteresis loop are observed over one biasing cycle (Bian *et al.*, 2004; Bian, 2004; Bian and Chertoff, 2006), which can be attributed to a time-dependent process within the cochlear transducer, perhaps the active force production in the OHCs that provides amplification and adaptation of the transduction process. The third utility stems from the correlation between the temporal behavior of DPOAEs and their spectral characteristics. A direct consequence of the AM of the DPOAEs is the presence of multiple sidebands around the DPs (Bian, 2006). The locations and sizes of the sidebands were closely associated with the local nonlinearity in the cochlea that generates the DPs. These sidebands are within a narrow frequency band, thus less likely can be altered by the transfer characteristics of the middle and inner ears. Furthermore, analyzing all the sidebands of a given DPOAE can provide a complete estimate of the cochlear transducer nonlinearity.

A fourth utility is that the asymmetry of the DP modulation patterns, especially those of the even-order DPs, could provide an accurate estimate of the optimal OP of the cochlear transducer where the gain is maximal (Bian, 2004). This measurement is useful in measuring the resting position of basilar membrane (BM), which is important in the understanding of cochlear mechanics and critical in the diagnosis of cochlear pathologies, including Ménière's disease or endolymphatic hydrops. Therefore, low-frequency modulation of DPOAEs could be developed into a clinical tool to estimate the function of cochlear hair cells. Towards this goal, it is necessary to quantify the effects of biasing the cochlear partition on DPOAE amplitudes in humans. It is known that two different mechanisms, namely wave-fixed nonlinearity and place-fixed reflections, are responsible for the generation of DPOAEs in humans (Shera and Guinan, 1999; Knight and Kemp, 2001). Although introducing a low-frequency tone at high levels may suppress the reflected DP from its own best frequency place on the BM (Johnson *et al.*, 2006), the feasibility and accuracy of deriving the cochlear F_{Tr} from this technique in humans remain to be tested. To date, low-frequency modulation of human DPOAEs has been reported (Scholtz *et al.*, 1999), but systematic variation and quantification of the cochlear F_{Tr} need to be further investigated.

II. METHODS

A. Experimental procedures

Data were collected in 21 ears from a total of 18 healthy subjects (mean age: 27) who were recruited from the students at the Arizona State University (ASU) under the protocol approved by the Institutional Review Board on human research subjects. All the subjects were screened for normal hearing thresholds and middle ear functions in the audiology clinic of the Department of Speech and Hearing Science at ASU. Otoscopy was performed to visually inspect the tympanic membrane to exclude diseases in the outer and middle ear. A DPOAE-gram was also measured using an 8-point/octave frequency spacing procedure (ILO92, Otodynamics) to ensure that no deep notch of DPOAEs micro-structure presented in the frequency range from 1 to 3 kHz and the DPOAE magnitude was relatively large ($\geq$5 dB SPL). In addition, presence of spontaneous OAEs was ruled out within the same frequency range to avoid interference with DPOAE measures. A standard DPOAE measurement system, including a calibrated probe microphone (Etymotic Research, ER-10B) and two coupled earphones (ER-2), was used. A coupler was inserted into the eartip to accommodate a front tube for the bias tone and the ER-10B system. The bias tone was produced from an insertion earphone with an 8.5-mm driver (HA-FX55, JVC) and the two-tone signal from the ER-2s. All earphones were connected to the recording system with three silicon front tubes (ER1-21). Two DPOAE-evoking primary tones and a bias tone were presented simultaneously and the ear-canal acoustics were recorded.

B. Signal processing and data acquisition

Signal presentation and data collection were performed with a personal computer (PC) linked to two 24-bit dynamic signal acquisition (DAQ) and generation cards (PXI-4461, National Instruments, NI) using a custom-built software written in LabVIEW (v.8, NI). The primary and bias tones with a duration of 1 s were digitally created from three sine wave generators. The two primary tones were windowed with a 5-ms $\cos^2$-shaped rise/fall ramp and the ramps of the bias tone were 10 ms long with the offset placed at 0.9 s, so that there was a 0.1-s flat tail [Fig. 1(a)]. Except the earliest three ears, the primary frequencies used were 2176 and 2688 Hz with an f_2/f_1 ratio of 1.23. Both primary and bias tones were written to three of the four output channels on both DAQ cards (eight channels total: four in, four out) housed in a PCI extension chassis (PXI-1036, NI), which was connected to an expansion slot of the host PC with a high-bandwidth serial interface card (MXI-4, NI). All three output channels for delivering stimuli and one input channel for data collection were synchronized by an onboard clock with a maximal rate of 26 MHz and digitally triggered with a minimum pulse width of 10 ns. The levels of the primary and the bias tones were adjusted with three virtual attenuators implemented in the LabVIEW software. The two primary levels (L_1 and L_2) were set at 60 dB SPL, then L_1 and L_2 were adjusted up to a 5–6-dB difference ($L_1 > L_2$) so that the amplitude of $2f_1-f_2$ (cubic difference tone, CDT) DPOAE was above 5 dB SPL. Except the earliest few subjects, five bias tone frequencies (f_{bias}) of 25, 32, 50, 75, and 100 Hz were presented in random order to modulate the DPOAEs. The sound pressure levels of the stimuli were calibrated in a 2-cc coupler with a sound level meter (SoundPro DLX, Quest Tech.). At each f_{bias}, the level was incremented so that a complete suppression of the CDT magnitude was observed. This was set as the initial bias tone level (L_{bias}) from which the peak amplitude of the bias tone was descended automatically in 41 steps to 0 Pa [Fig. 1(a)] using a cubic scaling so that the level was attenuated in smaller steps at high intensities. At each step, the ear-canal acoustic signal was amplified 20 dB by the built-in preamplifier of the ER-10B, averaged 8–16 times depending on the size of the CDT, digitized at 204.8 kHz, and saved on the hard drive.

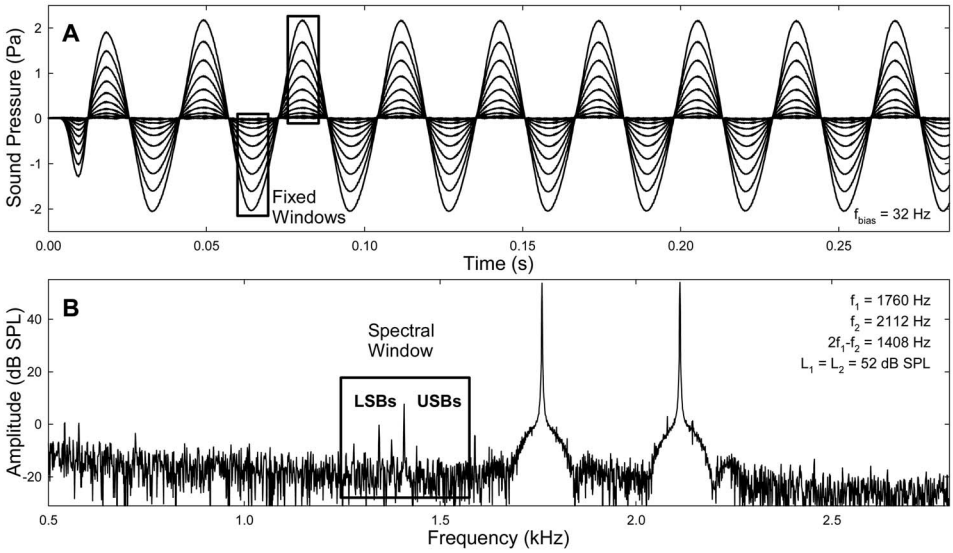

FIG. 1. Bias tones and a spectrum of the ear-canal acoustics. (a) Samples of a 32-Hz bias tone with various amplitudes. Rectangles indicate the fixed FFT windows centered at the peaks and troughs of the bias tone for extracting the quasi-static modulation pattern of CDT. Window lengths: from 3200 points (15.6 ms) for bias tones below 50 Hz to 1600 points (7.8 ms) for bias tone frequency (f_{bias}) $\geq$ 50 Hz. (b) Spectrum of an ear-canal acoustic signal. The box is a rectangular window centered at the CDT frequency covering multiple sidebands.

C. Data analysis

Data were analyzed off-line in Matlab (v.7, MathWorks). The ear-canal acoustical signals recorded at different biasing levels were high-pass filtered at 400 Hz to eliminate the bias tone and submitted to a fast Fourier transform (FFT) to obtain the frequency spectra [Fig. 1(b)]. The spectral feature of the AM of the CDT is the presence of multiple lower and upper sidebands (LSBs and USBs) on either side of the CDT component separated with integer multiples of f_{bias} (Bian, 2006). Thus, the amplitudes of two LSBs and two USBs along with the CDT were measured from the spectra. The corresponding levels of the bias tones were also measured by the peak amplitude of the low-pass filtered (at 700 Hz) ear-canal acoustic signals.

To study the effect of biasing direction on the CDT magnitude, a fixed-window method (Bian *et al.*, 2002) was used to extract the quasi-static modulation pattern [Fig. 1(a)]. Segments of 3200 or 1600 points long (15.6 or 7.8 ms) at peaks and troughs of the bias tone were windowed for FFT at f_{bias} below or above 50 Hz, respectively. The window length was selected to limit the signal inclusion within one-half biasing cycle, assuming that the BM is statically displaced in one direction within a short time window. The CDT amplitudes obtained from two adjacent biasing peaks and troughs were paired to form the positive and negative halves of a modulation pattern. The patterns obtained from a total of 22 to 88 pairs of peaks and troughs were averaged for different biasing frequencies.

Temporal features of the DP were extracted using a spectral windowing method [Fig. 1(b)]. The positive frequency half of the complex spectrum of the ear-canal acoustic signal was selected by a rectangular window centered at the CDT frequency covering four LSBs and USBs. The windowed spectrum was inverse Fourier transformed (IFFT) to yield the varying envelope of the CDT in the time domain. To examine the temporal effect more precisely, the instantaneous CDT amplitude within one biasing cycle was averaged across 20 to 86 periods to reduce noise and DPs from other sources.

III. RESULTS

A. Spectral sidebands

An important finding of the study was that the presence of LSBs and USBs around the CDT component depended on the sizes of the CDT and the bias tone. Usually, when a relatively large CDT was evoked at lower primary levels, the cochlea could easily generate sidebands with higher magnitudes when a bias tone was introduced. For primary levels about 55–65 dB SPL, if the CDT magnitude was greater than 5 dB SPL, multiple sidebands were typically observed when the L_{bias} exceeded 100 dB SPL for most frequencies below 100 Hz (Fig. 2). As the L_{bias} decreased, both the magnitudes and number of sidebands were reduced. When L_{bias} was below 75 dB SPL, hardly any sideband could be observed (bottom of Fig. 2). This indicated that the AM of the CDT occurred at high bias tone levels. The spectral locations of the sidebands were at integer multiples of the f_{bias} away from the CDT, reflecting a nonlinear AM in the time domain (Bian, 2006). When multiple sidebands presented, the relative amplitudes between the sidebands varied depending on the L_{bias}. Often at the highest biasing levels, the second sideband (sideband II), which was $2f_{bias}$ away from the CDT on each side, was greater than the first sideband or sideband I (f_{bias} from the CDT). At lower levels, sideband I exceeded sideband II, suggesting a change in the temporal modulation pattern due to lower bias tone intensity. It can be observed from Fig. 2 that the L_{bias} required to generate modulation sidebands depended on the f_{bias}. When the frequency difference between the bias tone and the CDT was small, a bias tone with relatively smaller amplitude could produce a significant number of sidebands with magnitudes up to 15 dB above noise floor (Fig. 2 left). Also noticeable was the reduction of CDT amplitude at very high L_{bias} (top panels), indicating a mixed effect of modulation and suppression.

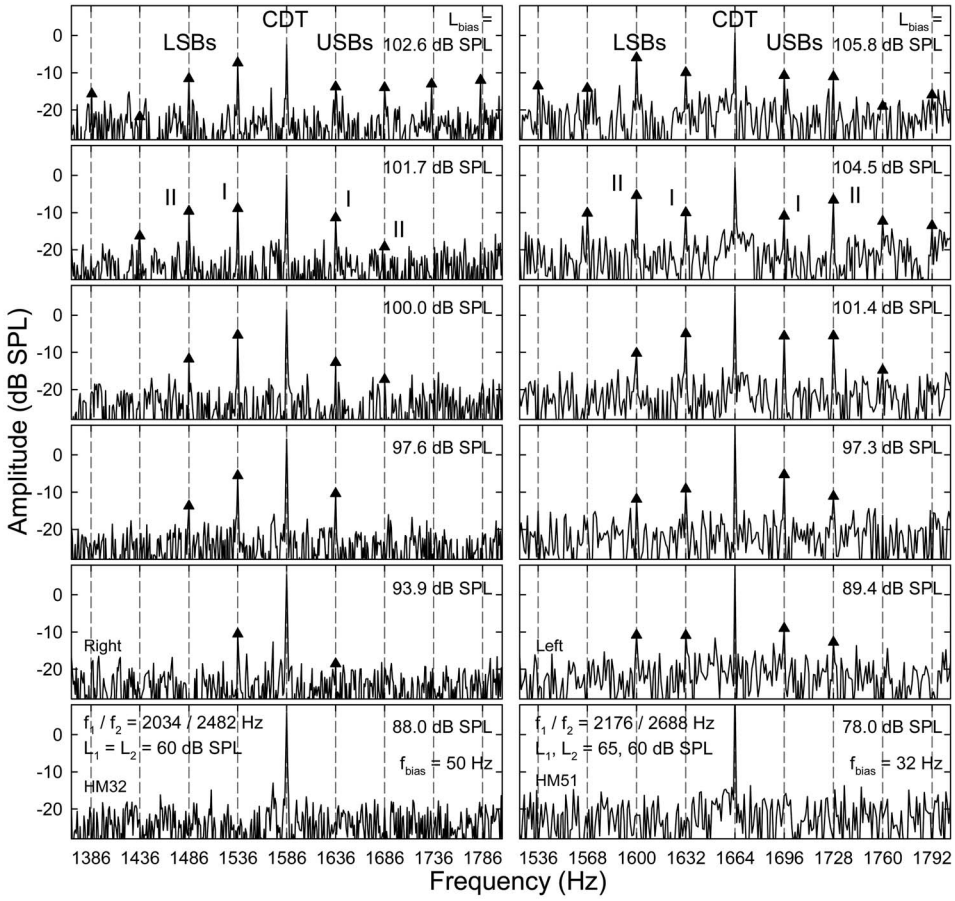

FIG. 2. Spectral sidebands: suppression and modulation. Panels in each column represent the effect of decreasing the bias tone level (L_{bias}): reduction in the spectral fine structures around the CDT. Note: the CDT magnitude increases while the number and sizes of the sidebands decrease. USB: upper sideband; LSB: lower sideband. On each side of the CDT frequency, the first and second sidebands with frequency separation of f_{bias} and $2f_{bias}$ from the CDT are termed sideband I and II, respectively.

B. Biasing effects

1. Suppression and modulation

The bias tone produced not only a modulation of the CDT, but also a suppression of the CDT. This mixed effect was studied by examining the amplitudes of the DPOAE and its closest sidebands, namely sidebands I and II on each side, as functions of the varying L_{bias} (Fig. 3). Other sidebands that were more distant from the CDT were not included in the analysis because of lower amplitudes and higher variability. Averaged across all ears, the mean amplitudes of the CDT and its two sidebands in the LSB and USB showed opposite changes as the L_{bias} increased (Fig. 3). Because the CDT magnitude was always above 0 dB SPL and the sidebands were much smaller, the mean sideband amplitudes were more variable than the CDT. For all five biasing frequencies, the CDT magnitude clearly demonstrated a suppression when the L_{bias} exceeded 90 dB SPL, while the sidebands showed a gradual increase. The rise of sidebands started at much lower biasing levels. As indicated by four consecutive symbols in the top panel of Fig. 3, the sidebands began to rise from about 70–80 dB SPL for high and low biasing frequencies. Below these biasing levels, the CDT magnitudes were stable with no sidebands (below noise floor: −20 dB SPL). For 10 to 15 dB above these levels, the sidebands increased about 5–10 dB with no noticeable reduction in CDT magnitude. When sidebands reached their maximal levels, usually about −10 to −5 dB SPL, the CDT showed a significant reduction of about 3 to 5 dB (single symbol). These effects indicated that the modulation and suppression occurred simultaneously. For 100-Hz bias tone, the L_{bias} to produce the significant CDT suppression was about 10 dB below the level of 25 Hz, suggesting that higher frequency bias tones were more effective.

The growths of different sidebands showed some variations. Sideband I started to rise at lower L_{bias} and reached a peak at about 95 to 103 dB SPL (single symbol in Fig. 3 top) depending on the f_{bias}. When the CDT was significantly suppressed above these levels, the magnitudes of sidebands I began to rollover, while sidebands II remained to increase and saturated near the highest biasing levels. Thus, below the peak levels of sidebands I, the magnitudes of sidebands I were higher than sidebands II, while above these levels sidebands II were larger (Fig. 3, lower panels). The growths of the sidebands were gradual with a rate of about 0.5 dB/dB with the rate of sidebands II being slightly higher. These differences in the relative sizes of the CDT sidebands suggest that the temporal modulation patterns of the CDT vary with the L_{bias}.

2. Effect of biasing frequency

Since the sideband amplitudes were small and variable, analysis of the effect of the f_{bias} was performed on the CDT. The maximal sideband magnitudes corresponded to a 3- to 5-dB reduction in the CDT amplitude (Fig. 3). Therefore, a 3-dB suppression of CDT was used as a criterion to evaluate the effect of the biasing frequency. The L_{bias} required to produce a 3-dB reduction in CDT magnitude across five biasing frequencies forms a 3-dB iso-suppression curve (Fig. 4),

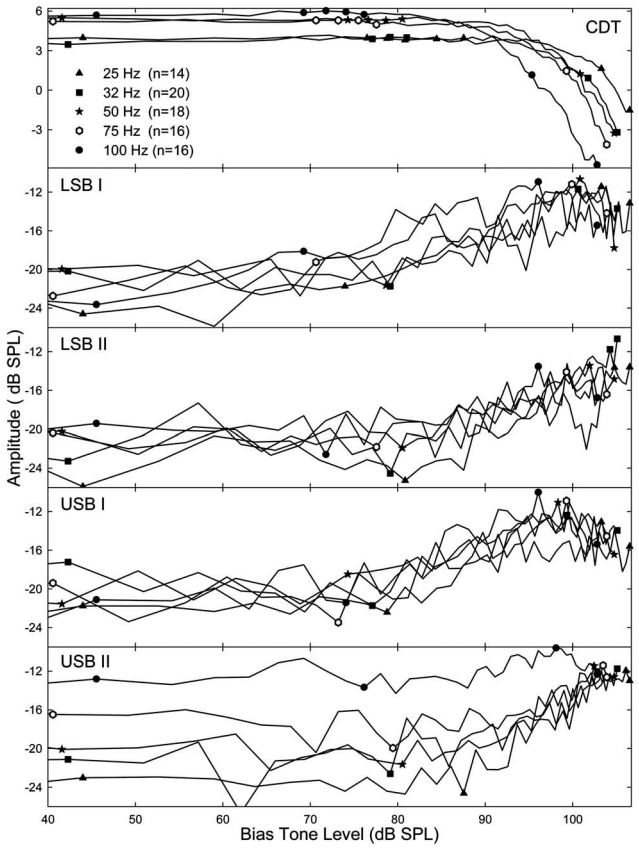

FIG. 3. Effects of L_{bias}: suppression and modulation. Each panel represents the mean CDT or a sideband magnitude as a function of the L_{bias}. Top: the CDT magnitude is suppressed when the L_{bias} reaches over 85 to 90 dB SPL. Note: the different slopes of CDT suppression at different biasing frequencies. Lower panels: the growths of four sidebands as the L_{bias} increases. The L_{bias} where the sidebands begin to rise is indicated by a group symbols that are also projected to the CDT curves in the top panel. The sidebands reach their maximal value around 100 dB SPL L_{bias} (indicated by a symbol also projected in the top panel). Sidebands I roll over above 95–100 dB SPL. Sidebands II peak at higher L_{bias}.

which represents the efficiency of biasing frequency on the modulation of CDT. The 3-dB suppression curve averaged across ears showed a general trend that higher sound pressure was required to produce the same amount CDT suppression when the f_{bias} was reduced. Moreover, the rate of increase in L_{bias} was different for higher and lower frequencies. Roughly, for biasing frequencies above 50 Hz, there is a 6-dB/oct reduction in L_{bias} when the biasing frequency was increased, whereas below 32 Hz, the rate of increase in L_{bias} approached 12 dB/oct when the f_{bias} was reduced. There was a narrow frequency range of transition between 32 and 50 Hz, where the rate of change in L_{bias} was relatively flat. This suggests that higher frequency bias tones are more efficient in suppressing and modulating the CDT, so that a lower L_{bias} can be employed.

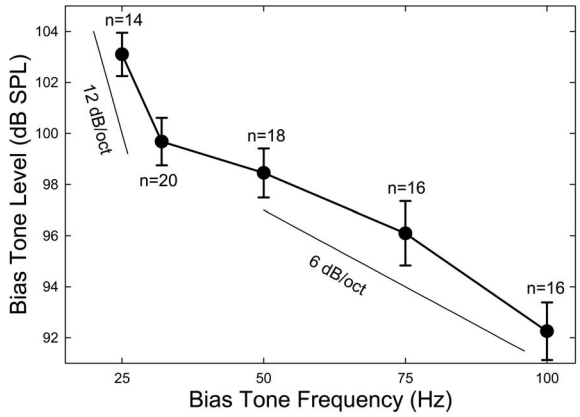

FIG. 4. The 3-dB iso-suppression curve. The means and standard errors of the L_{bias} necessary to produce a 3-dB suppression of the CTD magnitude are plotted as a function of the f_{bias}. The number of subjects (n) for each frequency is indicated. When the f_{bias} is reduced, the rates of growth in L_{bias} below and above 32 Hz are 12 and 6 dB/oct, respectively.

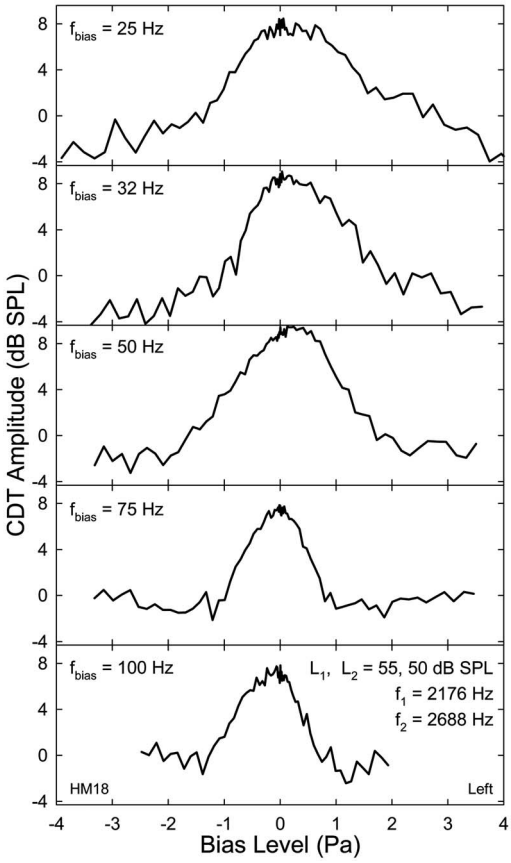

FIG. 5. Examples of quasi-static modulation patterns. The quasi-static modulation patterns show a bell-shape with notches on both sides. Note: the range of L_{bias} reduces with f_{bias}. Asymmetry in the modulation pattern is noticeable. Fluctuations on the curves indicate the variability between the steps of L_{bias} attenuation.

C. Quasi-static modulation pattern

The CDT magnitudes obtained at peaks and troughs of the bias tones with various amplitudes formed a modulation pattern representing the effect of biasing directions. It reflected the static cochlear nonlinearity over many biasing cycles where the phases were fixed at the biasing extremes. As shown by an example, the derived CDT quasi-static modulation patterns from different biasing frequencies shared similar characteristics (Fig. 5). The CDT magnitude was largest around 0 Pa and reduced when biasing pressure increased in either direction. The difference between the maximal and the minimal CDT amplitudes or the modulation

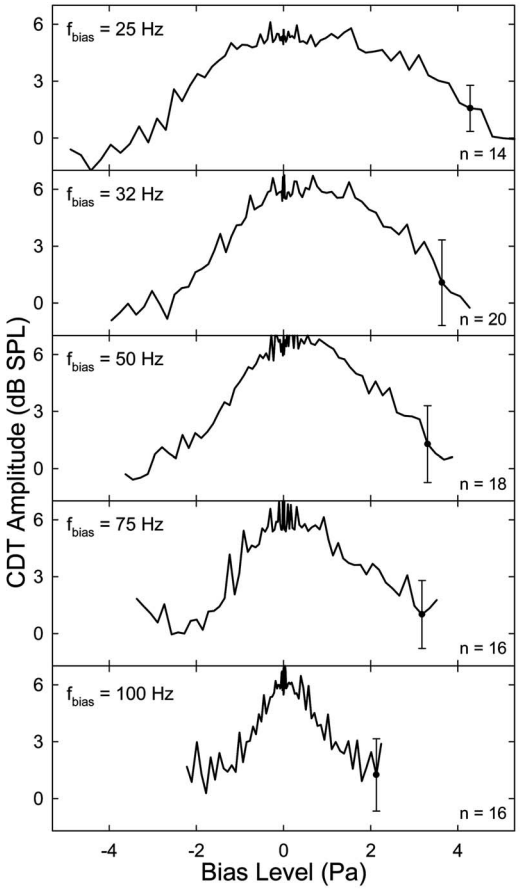

FIG. 6. Averaged quasi-static modulation patterns. The number of subjects for each f_{bias} is indicated in the panel. Error bars mark the averaged standard error across subjects and the steps of L_{bias} attenuation. Note: the asymmetry in the modulation patterns, especially at lower biasing frequencies. The peak of the pattern is shifted in the positive sound pressure direction where the slope is shallower.

depth was as large as 12 dB. This decline in CDT amplitude was gradual for a lower f_{bias} and more abrupt for higher frequencies. At the minima of the CDT magnitude, it often formed a notch on either side. The locations of the notches were farther apart for lower frequencies and closer to each other at higher f_{bias}. Thus, the modulation pattern covered different biasing pressure ranges, e.g., ±3 Pa at 25 Hz to about ±1 Pa at 100 Hz. There was also a noticeable variability or fluctuation (Fig. 5), typically less than 3 dB, on the CDT modulation patterns derived from the 22 to 88 biasing cycles depending on the f_{bias}, and the 41 presentations of bias tones at different levels. This within-subject variability was relatively small near the center of the modulation pattern and increased at higher L_{bias} on either side.

Quasi-static modulation patterns averaged across all ears (Fig. 6) showed the same characteristics as the individual case described above. The pattern was wider at lower biasing frequencies and narrower at higher frequencies with the notch locations varying from ±4 to ±2 Pa biasing pressure. This was consistent with the finding that more sound pressure was required to suppress the CDT at lower biasing frequencies (Fig. 4). Compared to the data shown in Fig. 5, the modulation depths were smaller, amounting to 6–8 dB on average, due to the variability among different ears. Apparently, there was an asymmetry in the averaged modulation patterns. The peak of the pattern was shifted away form 0 Pa in the positive sound pressure direction and the slope of the CDT reduction was steeper in the negative pressures than the positive side. For a given L_{bias}, the CDT amplitude was smaller if the cochlear partition was biased in the negative sound pressure direction. Likewise, biasing in the opposite direction could not completely suppress the CDT for lower frequency bias tones. There was a considerable variability in the mean modulation patterns among different ears. The standard errors (error bars in Fig. 4) averaged across all ears and 82 biasing pressures ranged from 2 to 3 dB for all five frequencies. This intersubject variability was highest at the center of the modulation pattern reflecting the variation of the initial CDT magnitudes among the ears.

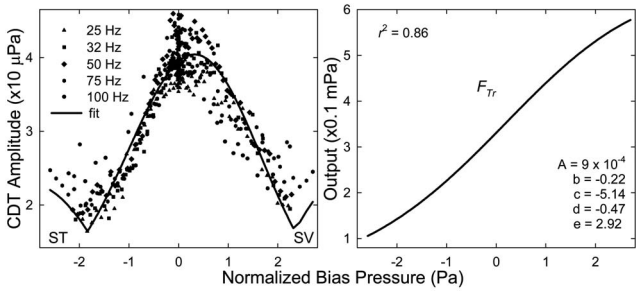

FIG. 7. Compiled quasi-static modulation pattern and cochlear F_{Tr}. Left: the mean CDT data (from Fig. 6) obtained at different f_{bias} (symbols) are normalized by scaling down the L_{bias} at lower f_{bias} to equalize the notches at 100 Hz. The normalized data then are fit with the absolute value of the third derivative of a Boltzmann function (solid line). ST: scala tympani; SV: scala vestibule. Right: the fitted Boltzmann function [Eq. (1)] representing the cochlear F_{Tr}. The correlation coefficient (r^2) and the Boltzmann parameter are given in the panel.

Although the quasi-static modulation patterns obtained at different biasing frequencies covered different pressure ranges, the cochlear nonlinearity governing the suppression and modulation of DPOAEs remained the same for fixed primary levels and frequencies. Therefore, these modulation patterns could be normalized by the input biasing pressures. One way to normalize the input was to equalize the sound pressures at the notches, because the maximal suppression occurred at a certain BM displacement that could be induced by different biasing pressures at different frequencies. Thus, the biasing pressures at frequencies from 25 to 75 Hz were normalized or scaled down to equate with the notches at 100 Hz (Fig. 7, left). The mean CDT data for each f_{bias} were left unchanged and pooled together. These CDT magnitudes lined up consistently, forming a typical CDT quasi-static modulation pattern with a center peak and two elevated tails on each side with relatively small variability (<2 dB). The pooled data from the average of all ears and all biasing frequencies were fit with the absolute value of the third derivative of a Boltzmann function

$$y = A/[1 + e^{b(x-c)} \cdot (1 + e^{d(x-e)})], \quad (1)$$

where y is the mechanical output of the cochlear transducer, x is the BM displacement represented by the normalized L_{bias}, A is a scaling factor, b and d are parameters relating to the slope of the transducer curve, and c and e are constants

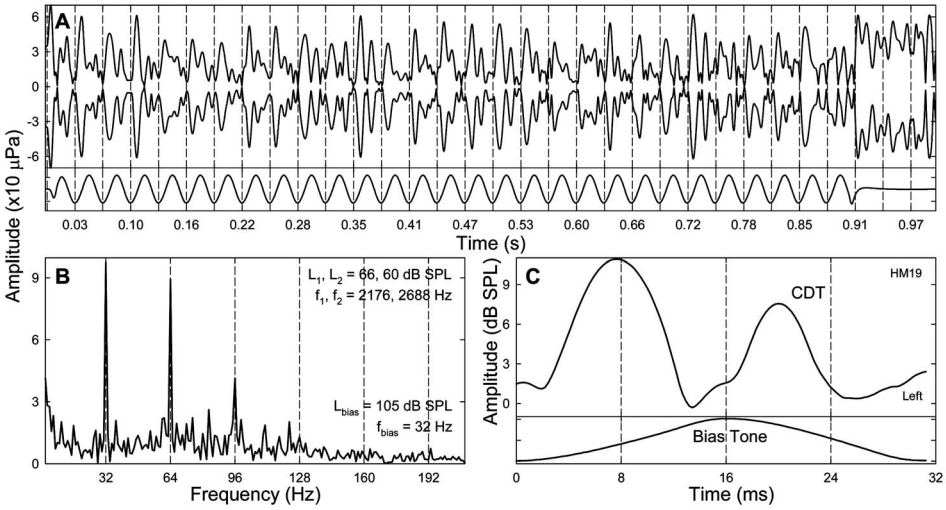

FIG. 8. Temporal modulation pattern. (a) Temporal envelope of the CDT obtained from IFFT of the spectral contents within a 250-Hz-wide window. Compared with the bias tone (lower trace), it can be observed that within one biasing cycle (between two consecutive dashed lines), there are two CDT peaks. Note: the CDT magnitude is larger but unstable in the tail of the waveform. (b) Spectrum of the envelope in panel (a). Note: two outstanding peaks present at f_{bias} (32 Hz) and $2f_{\text{bias}}$ (64 Hz) indicating that a temporal pattern repeats twice every biasing cycle. (c) Period modulation pattern derived from averaging the CDT envelope over 28 biasing cycles. The CDT amplitude peaks twice within a biasing cycle, each correlating to a zero-crossing of the bias tone (lower trace). Note: the second peak appears before the related zero-crossing and is smaller.

setting the transducer OP. The fit was relatively good with a correlation coefficient (r^2) of 0.86 (Fig. 7, right). Thus, a cochlear F_{Tr} of humans was derived with parameters given in the right panel of Fig. 7.

D. Temporal modulation pattern

The temporal envelope of the CDT was obtained from IFFT of the windowed spectral contents in the vicinity of the positive CDT frequency, including four LSBs and USBs. Because only the bias tones with highest levels produced larger sidebands (Fig. 3), for a given f_{bias}, the CDT envelopes obtained from the top 16 biasing levels (a 10-dB range) were examined to determine the most typical temporal modulation pattern. Since modulation and suppression of CDT occurred simultaneously, the nonlinearly generated CDT was weak and vulnerable to noise contamination. The CDT from other sources, e.g., multiple reflections (Shera and Guinan, 1999; Knight and Kemp, 2001), might not be synchronously modulated by the bias tone. These competing OAEs and random noise could cause irregularities in the CDT envelope [Fig. 8(a)]. This contamination can be verified by the unstable CDT amplitude at the tail portion of the waveform where there is no biasing. However, when closely examined, the apparently noisy waveform was found to possess periodicity. For each biasing cycle from one trough to the next, it was noticeable that the CDT envelope demonstrated two major peaks. One way to reveal the periodicity was to perform a FFT to the CDT envelope [Fig. 8(b)]. It was clear that there were two large peaks presented at the f_{bias} (32 Hz) and its second harmonic ($2f_{\text{bias}}$ or 64 Hz). This indicated that there was a pattern repeating in every half basing cycle. To reduce the noise and other irregularities, the CDT envelopes from 20 to 86 biasing periods beginning with a trough were averaged to yield a period modulation pattern [Fig. 8(c)], which contained two peaks each corresponding to a zero-crossing of the bias tone.

On average, a similar period modulation pattern presented in all ears at the five biasing frequencies (Fig. 9). In many cases, upward-going biasing pressure or loading of the cochlear partition yielded a larger CDT peak, while reducing pressure or unloading produced a smaller peak. The most typical modulation pattern presented at the lowest biasing frequency (25 Hz) where the CDT envelope for each half

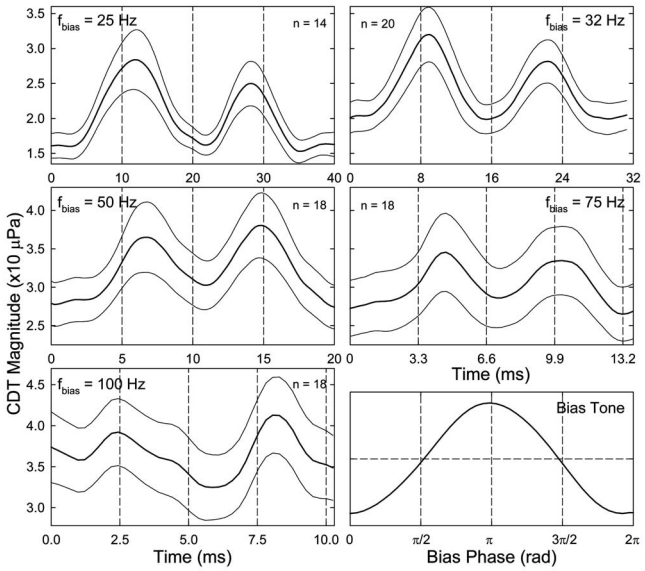

FIG. 9. Means ± standard errors of the period modulation patterns. The averaged bias tones within a period are shown in the lower right panel. Vertical grid lines indicate the phase of the bias tone with a 90-deg increment. Note: the first CDT peak is larger than the second, especially at lower f_{bias}. The first CDT peak lags the upward-going zero-crossing of the bias tone and the second peak leads the downward-going zero-crossing, except at high biasing frequencies.

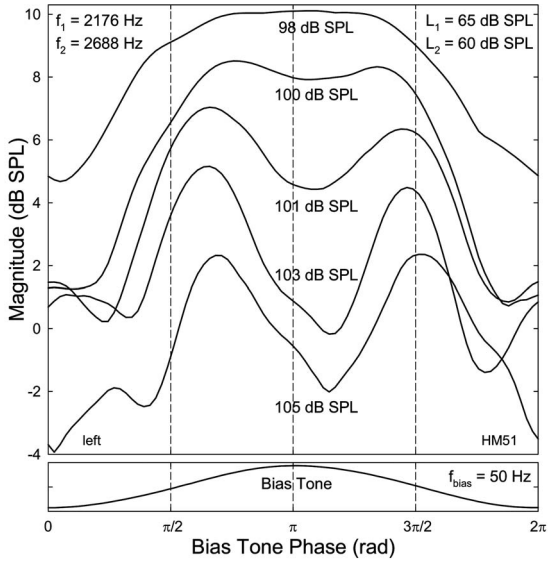

FIG. 10. Effect of the L_{bias} on the period modulation pattern of CDT. To reduce overlap, the top two traces are shifted up 2 and 1 dB and lower two traces shifted down 1 and 2 dB, respectively. When L_{bias} decreases (from bottom to top), three trends can be observed: (1) an increase in overall CDT magnitude, (2) emerging of the two CDT peaks, and (3) the second CDT peak reverses its delay to lead over the zero-cross of the bias tone (lower panel). Each half of the lowest trace resembles the absolute third derivative of the Boltzmann function. Vertical grid lines indicate the phase of the bias tone with a 90-deg increment.

cycle was similar to the absolute value of the third derivative of a Boltzmann function, consisting of a center peak and two sidelobes (Fig. 7, top). For higher biasing frequencies, the period modulation patterns were more sinusoidal with rounded minima. The presence of the CDT peaks in the period modulation pattern often followed the zero-crossings of the bias tone in both loading and unloading directions. This timing of the CDT peaks was most typical for higher frequencies (>50 Hz). However, it was commonly observed, especially at lower biasing frequencies, that the second CDT peak occurred before the zero-crossing of the biasing pressure during unloading [Figs. 8(c) and 9 top]. It seemed that cochlear partition displacement in the positive direction was less effective in suppressing the CDT. This observation is consistent with the asymmetry in the quasi-static modulation pattern, which showed a shallower slope of CDT reduction in positive sound pressures (Figs. 5–7, top).

Systematic change in the L_{bias} also revealed progressively varying period modulation patterns (Fig. 10). Higher-level bias tones induced more suppression, as demonstrated by the reduction of CDT amplitude following the peaks and troughs of the bias tone. Each half of the period modulation pattern was more similar to the shape of the absolute value of the third derivative of the F_{Tr} (bottom curve). Lowering the L_{bias} only suppressed the CDT at the negative extremes of the biasing pressure, yielding a single wide peak of the CDT envelope with a relatively smaller modulation depth (top curve). This is correlated with a simple sinusoidal AM that contains fewer sidebands (<2) on each side of the CDT as seen in the lower panels of Fig. 2. For moderately high biasing levels, the period modulation patterns showed a transition from double to single CDT peak (middle traces in Fig. 10). The modulation depth at the positive peak of the biasing pressure became progressively smaller than at the negative extremes. Moreover, due to the reduced biasing power, the second CDT peak appeared earlier than the zero-crossing of the biasing pressure in the downward swing.

IV. DISCUSSION

A. Suppression and modulation: Two sides of a coin

A chief finding of the present study is that the effects of the bias tone on DPOAEs can be expressed in both time and frequency domains. In the time domain, the CDT is amplitude modulated and suppressed (Figs. 8–10). Its spectral representation is a reduction of amplitude and generation of sidebands (Fig. 2). As the L_{bias} increases, the sideband amplitudes start to rise even before noticeable reductions in the CDT magnitude (Fig. 3). When the sidebands gradually reach their peaks, the CDT shows a significant reduction. These opposite changes in the amplitudes of DPOAE and its modulation sidebands have been observed in the acoustic modulation of electrically evoked otoacoustic emissions (EEOAEs) in lizards using an 84-Hz bias tone (Manley *et al.*, 2001). They showed a 10-dB reduction in EEOAE accompanied with a more than 20-dB increase in LSBs and USBs when the L_{bias} was raised from 70 to 100 dB SPL. These effective biasing sound levels are comparable to the present study in humans.

A derivation of the spectral contents of AM in nonlinear systems (Bian, 2006) predicts that multiple sidebands present around the carrier frequency (f_c) at $f_c \pm nf_m$, where n is an integer and f_m is the modulator frequency. In the present study, various patterns of the sidebands are observed based on the relative strength of the bias tone and the CDT. The observation that the number and sizes sidebands grow with the L_{bias} (Fig. 2) has been consistently observed in studies focusing on the reverse transduction in the inner ear. In guinea pigs, Yates and Kirk (1998) described the presence of multiple sidebands at the interaction between the EEOAE frequency (f_{E}) and the integer multiples of the acoustic f_{bias} ($f_{\text{E}} \pm nf_{\text{bias}}$). When the EEOAE was enhanced by ATP, the number and magnitudes of the sidebands were reduced (Kirk, 2002), reflecting a reduced relative strength of the bias tone (Figs. 2 and 3). The sidebands I were increased when a stimulus-frequency OAE was modulated by an electrical current injected into the gerbil cochlea (Hubbard and Mountain, 1983), or an acoustic AM signal in humans (Neely *et al.*, 2005). In low-frequency modulation of DPOAEs in gerbils (Bian, 2006), the magnitudes of the sidebands increased with both the bias tone and primary levels along with a suppression of CDT. The suppression and modulation are mostly observed below 65 dB SPL primary level, and above 106 dB SPL L_{bias}, given that CDT magnitudes in gerbils are more than 10 dB larger than in humans.

Suppression and distortion are among the essential nonlinearities of hearing universally presented in all species (Eguíluz *et al.*, 2000). All of these nonlinear phenomena have been observed by studying two-tone interactions in the cochlea, e.g., suppression tuning, two-tone suppression, and intermodulation DPs (Robles and Ruggero, 2001). Two-tone

suppression can be categorized into tonic and phasic suppressions (Geisler and Nuttall, 1997). The former refers to an overall reduction in the response at a characteristic frequency (CF, or f_{CF}) by the presence of another tone, while the latter applies to temporal modulation of the CF response amplitude when the suppressor frequency (f_s) is much lower (<2 kHz). In the phasic suppression, reductions in the CF response occur at the maximal displacement of the BM in one or two directions (Rhode, 2007). Introducing a low-frequency suppressor is shown to generate spectral sidebands at $f_{CF}-f_s$ and $f_{CF}-2f_s$ (Rhode and Cooper, 1993; Robles *et al.*, 1997) and these sidebands rise and roll over as the CF amplitude response is suppressed. In addition, the peak of $f_{CF}-2f_s$ component occurs at a higher suppressor level than the $f_{CF}-f_s$, in much the same fashion of DPOAE sidebands I and II depicted in Fig. 3. Similar behaviors of the CF and its sidebands are also observed in the auditory nerve response (Temchin *et al.*, 1997). The CDT magnitude grows and falls as the L_1 increases with fixed L_2 (Gaskill and Brown, 1990; Whitehead *et al.*, 1995; Mills, 2000), similar to the behavior of the modulation sidebands (Fig. 3). Simultaneously presented suppression and distortion are the two sides of the same coin: two-tone interference within a nonlinear cochlear transducer (Geisler *et al.*, 1990). DPs are the spectral expressions of a temporal behavior of the cochlear transducer (Brown, 1994; van der Heijden, 2005; Bian, 2006), whereas suppression is the overall consequence of the saturating characteristic of the transducer: OHCs. Therefore, results of the present study provide some human correlates of the direct observations from the inner ears of experimental animals.

B. Comparison with previous results

1. Human studies

Low-frequency modulation of DPOAE in humans has been previously reported (Scholz *et al.*, 1999) and recently measured in patients with Ménière's disease (Hirschfelder *et al.*, 2005). In both studies, the CDT amplitudes demonstrate a pattern with two maxima over one biasing cycle similar to the period modulation patterns found in the present study (Figs. 8 and 9). When the L_{bias} is reduced from 117 dB SPL at 32.8 Hz, the progressive changes of the modulation pattern are similar to Fig. 10. The smaller modulation depth at the positive biasing peaks observed in those studies is due to the higher primary frequencies adopted (from 2.5/3 to 5/6 kHz) than in the present experiment. Placing a click at various phases of a 62-Hz tone, Zwicker (1981) showed that the varying amplitude of the evoked OAE formed a suppression-period pattern, which consisted of two maxima at low click levels and a single peak at higher levels like the effect reported in Fig. 10. These results indicate that strong bias tone can shift the OP of the cochlear partition traversing twice per cycle along the transducer curve, resulting in two maximal productions of OAEs at the inflection point. However, such an effect is influenced by the asymmetry in the cochlear partition motion, such that the suppression of cochlear response is less effective at the maximal displacement in the positive sound pressure direction.

There is a strong frequency effect in the modulation and suppression of CDT. Higher frequencies are more efficient, meaning that lower L_{bias} is required to produce the same amount of effect (Fig. 4). In a comparative study using humans and guinea pigs, Marquardt *et al.* (2007) measured the levels of the bias tone required to produce an equal modulation depth in the CDT amplitude and showed that the iso-modulation function for humans changes in two distinct slopes (6 and 12 dB/dB) separated by a local maximum located around 50 Hz. Thus, the 3-dB suppression function obtained in the present study (Fig. 4) is in close agreement with the human data of theirs and others (e.g., Kummer *et al.*, 1995) given that this is essentially the very tail of a suppression tuning curve. The steeper slope of the biasing level-frequency function below 50 Hz may have potential contributions from several structures in the auditory periphery, e.g., the middle ear, the helicotrema, and the cochlear input impedance (Dallos, 1973; Cheatham and Dallos, 2001; Marquardt *et al.*, 2007). These factors significantly reduce the influence of a very low frequency tone in the relatively basal region where DPOAEs are generated. An important implication of this frequency effect is that bias tones at higher frequencies are more efficient in modulating and suppressing DPOAEs, i.e., they can be achieved at much lower signal levels. This could be useful when applying the low-frequency technique to modulate DPOAEs evoked at higher primary frequencies, where the power of the bias tone cannot reach or producing extremely high sound pressures at a very low frequency is unpractical.

2. Animal studies

The results of the present study are in agreement with those of similar investigations in animals. In an early study of OAEs, the phase-dependent modulation of transient evoked OAEs showed variations of a double peaked pattern (Zwicker and Manley, 1981) that is comparable to the period modulation patterns reported here. Frank and Kössl (1996, 1997) first described the low-frequency modulation of DPOAEs in gerbils by noting that the peak CDT amplitude coincides with the zero-crossings of the bias tone. Variations in DPOAE amplitudes depending on the bias tone phase and primary levels are found in guinea pigs (Lukashkin and Russell, 2005). In a series of studies in gerbils (Bian *et al.*, 2002, 2004; Bian, 2004, 2006), the temporal modulation patterns of DPOAEs demonstrate that the occurrence of the maximal CDT amplitudes corresponds to the zero-crossing of a 25-Hz bias tone with a small delay (<1.4 ms). Moreover, the modulation pattern in one-half biasing cycle contains a center peak and two sidelobes resembling the absolute third derivative of a sigmoid-shaped cochlear F_{Tr}. However, the period modulation patterns of CDT obtained from humans in the present study are less typical compared to the gerbil data, because the sidelobes are smaller even absent, especially at the positive biasing peaks (Fig. 10). Furthermore, the onset of the second CDT peak is often before the zero-crossing during unloading, resulting in the reduced modulation depth at the biasing peaks. These atypical variations of the modulation pattern could be attributed to the lower L_{bias} applied to larger human cochleae and the asymmetry in BM motion.

The asymmetry in low-frequency biasing can be better observed from the quasi-static modulation patterns shown in Figs. 5–7. It is apparent that the slope of the modulation pattern is shallower on the positive sound pressure side. For a given BM displacement, motion in the positive pressures yields larger CDT magnitudes than in the negative direction. Displacement of the cochlear partition towards scala tympani (ST), indicated by negative organ-of-Corti cochlear microphonic (CM) in response to a bias tone (Cheatham and Dallos, 1994) or positive round-window CM, produces a larger suppression of cochlear potentials (Nieder and Nieder, 1971; Cheatham and Dallos, 1997). Moreover, enhancement of EE-OAE and CM are found during the displacement of the BM towards scala vestibuli (SV) as marked by negative scala-media CM induced by an 86-Hz tone (Kirk and Yates, 1998) or by a force applied to the otic capsule (Zou *et al.*, 2006). Therefore, it can be inferred from these results and the current observation of asymmetry in CDT modulation patterns that positive sound pressure applied to human ears corresponds to a BM displacement towards SV, which opens the transduction channels, and vice versa. The derived cochlear transducer nonlinearity in humans is quite comparable to the results from gerbils (Bian *et al.*, 2002). The Boltzmann parameters obtained from curve fitting (Fig. 7) fall in the ranges of the values from the gerbils, except parameter d whose absolute value is considerably larger. This could indicate that the F_{Tr} is more asymmetric in the human ears.

Despite the asymmetry, the period modulation pattern obtained at the highest L_{bias} often shows equally delayed CDT peaks [Fig. 11(a)], especially for higher biasing frequencies. Under these more effective biasings, the CDT remains suppressed and the second CDT peak does not appear until the transducer OP is shifted back through the resting position of the BM. The delays of the CDT maxima are about 0.5 ms for an f_{bias} of 100 Hz [Fig. 11(a)] compared to a 1.4-ms delay observed with a 25-Hz bias tone in gerbils (Bian *et al.*, 2004). Given that the primary frequencies used in the gerbil study are higher, the delay seems to correlate with the biasing frequency, meaning shorter delay for a higher f_{bias}. When plotted as a function of the instantaneous biasing pressure, the varying CDT magnitude or the dynamic modulation pattern forms a hysteresis loop [Fig. 11(b)] similar to the double modulation pattern with separate peaks demonstrated in gerbils (Bian *et al.*, 2004; Bian and Chertoff, 2006). This indicates that the underlying cochlear transducer is a double-valued sigmoid-shaped function forming a loop with a *counter-clockwise* traversal [Fig. 11(c)]. If positive sound pressure corresponds to a BM displacement towards SV where OHC transduction channels are open, then the reduction in CDT magnitude [Fig. 11(a)] indicates decreased force production or receptor current: a sign of adaptation. Therefore, the hysteresis could be accounted for by the force generation in the stereocilia that causes a reclosure of the ion channels during the "open" state (Hudspeth *et al.*, 2000), especially during large displacements. The result of adaptation in hair cell transduction is the shift of the F_{Tr} in the direction of the displacement (Eatock, 2000) with the cost of a time delay. The CDT peak delays seem to correlate with the adaptation time constants (Ricci *et al.*, 2000).

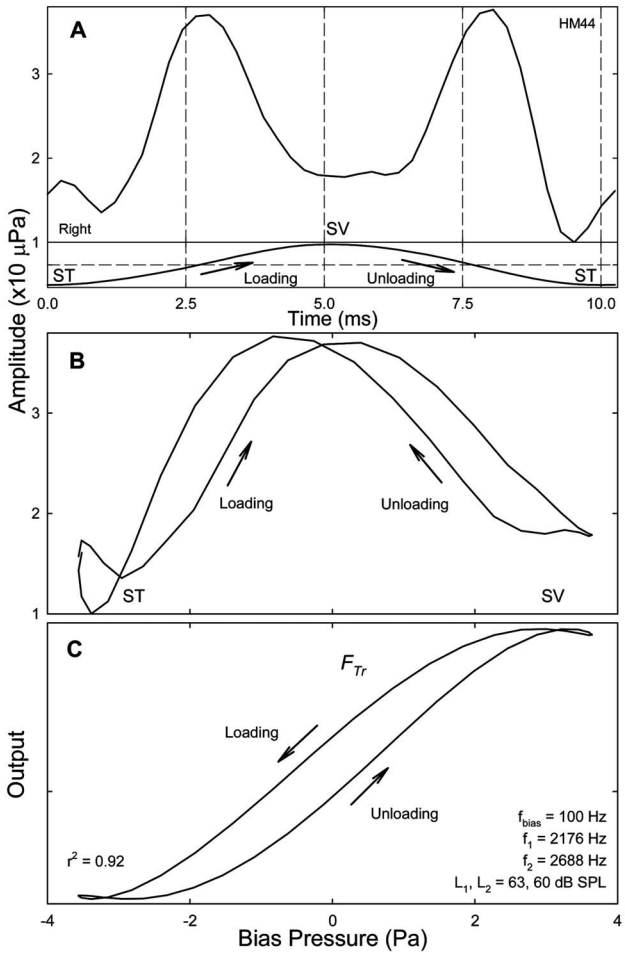

FIG. 11. Period modulation pattern and hysteresis. (a) A period modulation pattern with both CDT peaks delayed (about 0.5 ms) after the zero-crossing of the bias tone (lower trace). Note: displacement to SV (biasing peak) corresponds to a shallower notch in CDT amplitude; displacements to ST (troughs) result in deeper notches. (b) The period modulation pattern plotted against the instantaneous biasing pressure shows a double modulation pattern with hysteresis. (c) Cochlear transducer hysteresis: fitting the double modulation pattern with the third derivative model incorporating with an active force production. Loading of cochlear partition results in the shift of the transducer curve to the positive sound pressures; unloading moves the curve to the negative pressures. The traversal of the hysteresis is *counter-clockwise*.

C. Another source of $2f_1 - f_2$ DP

In a few occasions, especially at lower biasing frequencies, an exceptional quasi-static modulation pattern of CDT is observed (Fig. 12), which shows the typical pattern of even-order DPs (Bian *et al.*, 2002; Bian, 2004; Bian and Chertoff, 2006). This pattern is marked by a deep notch near zero biasing pressure that pinpoints to the inflection point of the nonlinear F_{Tr}. Biasing the cochlear partition in either direction can enhance the DP as indicated by the two peaks at roughly ±2 Pa. The modulation pattern also bears some features of the CDT, e.g., its amplitude is suppressed at both biasing extremes and the center notch is shifted in the positive sound pressure direction. Dropping in the primary levels during the experiment can be ruled out, because these levels were closely monitored during the 41 biasing steps. Therefore, the observed modulation pattern seems to reflect a mixture of odd and even DPs with the same frequency. It is

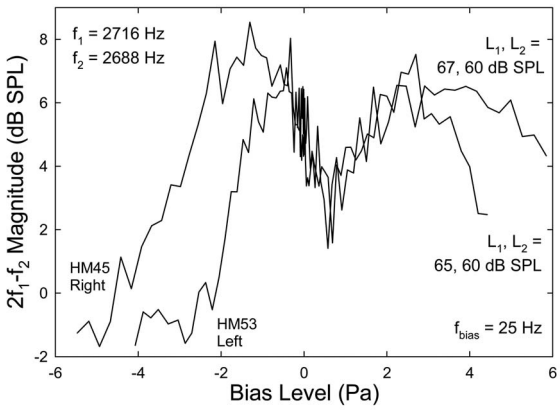

FIG. 12. Exceptional quasi-static modulation patterns of $2f_1-f_2$ DPOAE showing the characteristics of even-order DPs. Note the deep notches at the center of the modulation patterns. The position of the notch is shifted away from 0 Pa in the positive sound pressure direction. The peak in the negative sound pressures is higher than the one on the positive side in contrast to the typical pattern of CDT.

possible that the interference between the second harmonic of f_1 (i.e., $2f_1$) and the higher primary tone (f_2) can generate a quadratic difference tone (QDT), an even-order DP, at the frequency of $2f_1-f_2$ (Fahey *et al.*, 2000). The original CDT produced by the two primaries (f_1,f_2) and the QDT can be summed in the ear canal (Fahey *et al.*, 2006). If the QDT becomes dominant, the modulation pattern behaves like an even-order DP. This is especially true when L_1 is greater than L_2, since a higher L_1 can potentially produce a $2f_1$ that is strong enough to interfere with f_2. Even though the QDT was not found to affect CDT level when damaging the $2f_1$ place in guinea pigs (Whithnell and Lodde, 2006), given a larger human cochlea and lower primary frequencies in the present study, more hair cells on the BM could involve in the harmonic mechanism to produce a sizable QDT at $2f_1-f_2$. This suggests that the standard stimulus paradigm using greater L_1 to maximize the CDT magnitude should be exercised with caution to avoid unwanted contamination of catalytic DPs.

V. SUMMARY AND CONCLUSION

Low-frequency modulation of DPOAEs was measured from humans under different biasing conditions. In the frequency domain, increasing the L_{bias} resulted in a suppression of the CDT and a generation of modulation sidebands. Higher frequency bias tones were more efficient in producing the suppression and modulation. Quasi-static modulation patterns derived from measuring the CDT amplitude at the extremes of multiple bias tones showed a bell-shaped pattern with marked asymmetry. The modulation patterns correlated well with the absolute value of the third derivative of a cochlear F_{Tr}. This is important in the clinical applications to quantitatively estimate the cochlear transducer nonlinearity. In the time domain, period modulation patterns obtained from the DPOAE envelope over one biasing cycle showed two CDT amplitude peaks, each corresponding to the zero-crossings of the bias tone. Systematic variation in the L_{bias} showed progressive changes in the double-peaked modulation pattern that were consistent with cyclic shifting of the cochlear transducer OP and the asymmetry in the motion of inner ear structures. Thus far, the previous results in low-frequency modulation of CDT in gerbils (Bian *et al.*, 2002, 2004; Bian, 2006) have been replicated in humans. Results of the study shed a light on the nonlinear generating mechanisms of DPs in the cochlea by revealing the simultaneous suppression and modulation of two-tone interaction (Rhode and Cooper, 1993). Moreover, the results of the present study suggest that this technique could potentially be applied in the differential diagnosis of cochlear pathologies. The noninvasive nature and the experimental paradigm of the low-frequency biasing technique make it a valuable tool for investigation of human cochlear mechanics and development of new clinical applications.

ACKNOWLEDGMENTS

Kelly Watts is acknowledged for assisting in the pilot study of this project and help in recruiting subjects. Comments and suggestions from Terry Wiley are appreciated. The authors thank the clinical staff in the Department of Speech and Hearing Science at ASU for sharing their equipment and the subjects for participating in the study. This work was supported by a grant (R03 DC006165) from the National Institute on Deafness and Other Communication Disorders of the NIH.

Bian, L. (**2006**). "Spectral fine-structures of low-frequency modulated distortion product otoacoustic emissions," J. Acoust. Soc. Am. **119**, 3872–3885.

Bian, L. (**2004**). "Cochlear compression: Effects of low-frequency biasing on quadratic distortion product otoacoustic emission," J. Acoust. Soc. Am. **116**, 3559–3571.

Bian, L., and Chertoff, M. E. (**2006**). "Modulation patterns and hysteresis: Probing cochlear dynamics with a bias tone," in *Auditory Mechanisms: Processes and Models*, edited by A. L. Nuttall, T. Ren, P. Gillespie, K. Grosh, and E. de Boer (World Scientific, Singapore), pp. 93–100.

Bian, L., Chertoff, M. E., and Miller, E. (**2002**). "Deriving a cochlear transducer function from low-frequency modulation of distortion product otoacoustic emissions," J. Acoust. Soc. Am. **112**, 198–210.

Bian, L., Linhardt, E. E., and Chertoff, M. E. (**2004**). "Cochlear hysteresis: Observation with low-frequency modulated distortion product otoacoustic emissions," J. Acoust. Soc. Am. **115**, 2159–2172.

Brown, A. M. (**1994**). "Modulation of the hair cell motor: A possible source of odd-order distortion," J. Acoust. Soc. Am. **96**, 2210–2215.

Cheatham, M. A., and Dallos, P. (**2001**). "Inner hair cell response patterns: Implications for low-frequency hearing," J. Acoust. Soc. Am. **110**, 2034–2044.

Cheatham, M. A., and Dallos, P. (**1997**). "Low-frequency modulation of inner hair cell and organ of Corti responses in the guinea pig cochlea," Hear. Res. **108**, 191–212.

Cheatham, M. A., and Dallos, P. (**1994**). "Stimulus biasing: A comparison between cochlear hair cell and organ of corti response patterns," Hear. Res. **75**, 103–113.

Dallos, P. (**1973**). "Cochlear mechanics," in *The Auditory Periphery: Biophysics and Physiology* (Academic, New York), pp. 127–217.

Eatock, R. A. (**2000**). "Adaptation in hair cells," Annu. Rev. Neurosci. **23**, 285–314.

Eguíluz, V. M., Ospeck, M., Choe, Y., Hudspeth, A. J., and Magnasco, M. O. (**2000**). "Essential nonlinearities in hearing," Phys. Rev. Lett. **84**, 5232–5235.

Fahey, P. F., Stagner, B. B., and Martin, G. K. (**2006**). "Mechanism for bandpass frequency characteristic in distortion product otoacoustic emission generation," J. Acoust. Soc. Am. **119**, 991–996.

Fahey, P. F., Stagner, B. B., Lonsbury-Martin, B. L., and Martin, G. K. (**2000**). "Nonlinear interaction that could explain distortion product interference response areas," J. Acoust. Soc. Am. **108**, 1786–1802.

Frank, G., and Kössl, M. (**1996**). "The acoustic two-tone distortions 2f1-f2 and f2-f1 and their possible relation to changes in the operating point of

the cochlear amplifier," Hear. Res. **98**, 104–115.
Frank, G., and Kössl, M. (**1997**). "Acoustic and electrical biasing of the cochlear partition. Effects on the acoustic two tone distortions f_2-f_1 and $2f_1-f_2$," Hear. Res. **113**, 57–68.
Gaskill, S. A., and Brown, A. M. (**1990**). "The behavior of the acoustic distortion product, $2f1-f2$, from the human ear and its relation to auditory sensitivity," J. Acoust. Soc. Am. **88**, 821–839.
Geisler, C. D., and Nuttall, A. L. (**1997**). "Two-tone suppression of basilar membrane vibrations in the base of the guinea pig cochlea using 'low-side' suppressors," J. Acoust. Soc. Am. **102**, 430–440.
Geisler, C. D., Yates, G. K., Patuzzi, R. B., and Johnstone, B. M. (**1990**). "Saturation of outer hair cell receptor current causes two-tone suppression," Hear. Res. **44**, 241–256.
Hirschfelder, A, Gossow-Müller-Hohenstein, E., Hensel, J., Scholz, G., and Mrowinski, D. (**2005**). "Diagnosis of endolymphatic hydrops using low frequency modulated DPOAE," HNO **53**, 612–617.
Hubbard, A. E., and Mountain, D. C. (**1983**). "Alternating current delivered into the scala media alters sound pressure at the eardrum," Science **222**, 510–512.
Hudspeth, A. J., Choe, Y., Mehta, A. D., and Martin, P. (**2000**). "Putting ion channels to work: Mechanoelectrical transduction, adaptation, and amplification by hair cells," Proc. Natl. Acad. Sci. U.S.A. **97**, 11765–11772.
Johnson, T. A., Neely, S. T., Kopun, J. G., and Gorga, M. P. (**2006**). "Reducing reflected contributions to ear-canal distortion product otoacoustic emissions in humans," J. Acoust. Soc. Am. **119**, 3896–3907.
Kemp, D. T. (**1978**). "Stimulated acoustic emissions from within the human auditory system," J. Acoust. Soc. Am. **64**, 1386–1391.
Kemp, D. T. (**2007**). "The basics, the science, and the future potential of otoacoustic emissions," in Otoacoustic Emissions: Clinical Applications, 3rd ed., edited by M. S. Robinette and T. J. Glattke (Thieme, New York), pp. 7–42.
Kennedy, H. J., Crawford, A. C., Fettiplace, R., (**2005**). "Force generation by mammalian hair bundles supports a role in cochlear amplification," Nature **433**, 880–883
Kirk, D. L. (**2002**). "Interaction between adenosine triphosphate and mechanically induced modulation of electrically evoked otoacoustic emissions," J. Acoust. Soc. Am. **111**, 2749–2758.
Kirk, D. L., and Yates, G. K. (**1998**). "Enhancement of electrically evoked oto-acoustic emissions associated with low-frequency stimulus bias of the basilar membrane towards scala vestibuli," J. Acoust. Soc. Am. **104**, 1544–1554.
Knight, R. D., and Kemp, D. T. (**2001**). "Wave and place fixed DPOAE maps of the human ear," J. Acoust. Soc. Am. **109**, 1513–1525.
Kummer, P., Janssen, T., and Arnold, W. (**1995**). "Suppression tuning characteristics of the $2f_1-f_2$ distortion-product otoacoustic emission in humans," J. Acoust. Soc. Am. **98**, 197–210.
Liberman, M. C., Gao, J., He, D. Z. Z., Wu, X., Jia, S., and Zou, J. (**2002**). "Prestin is required for electromotility of the outer hair cell and for the cochlear amplifier," Nature (London) **419**, 300–304.
Lonsbury-Martin, B. L., and Martin, G. K. (**2003**). "Otoacoustic emissions," Curr. Opin. Otolaryngol. Head Neck Surg. **11**, 361–366.
Lukashkin, A. N., and Russell, I. J. (**2005**). "Dependence of the DPOAE amplitude pattern on acoustical biasing of the cochlear partition," Hear. Res. **203**, 45–53.
Marquardt, T., Hensel, J., Mrowinski, D., and Scholz, G. (**2007**). "Low-frequency characteristics of human and guinea pig cochleae," J. Acoust. Soc. Am. **121**, 3628–3638.
Manley, G. A., Kirk, D. L., Köppl, C., and Yates, G. K. (**2001**). "*In vivo* evidence for a cochlear amplifier in the hair-cell bundle of lizards," Proc. Natl. Acad. Sci. U.S.A. **98**, 2826–2831.
Mills, D. M. (**2000**). "Frequency responses of two- and three-tone distortion product otoacoustic emissions in Mongolia gerbils," J. Acoust. Soc. Am. **107**, 2586–2602.
Neely, S. T., Johnson, T. A., Garner, C. A., and Gorga, M. P. (**2005**). "Stimulus-frequency otoacoustic emissions measured with amplitude-modulated suppressor tones," J. Acoust. Soc. Am. **118**, 2124–2127.
Nieder, P., and Nieder, I. (**1971**). "Determination of microphonic generator transfer characteristic from modulation data," J. Acoust. Soc. Am. **49**, 478–492.
Rhode, W. S. (**2007**). "Mutual suppression in the 6 kHz region of sensitive chinchilla cochleae," J. Acoust. Soc. Am. **121**, 2805–2818.
Rhode, W. S., and Cooper, N. P. (**1993**). "Two-tone suppression and distortion product on the basilar membrane in the hook region of cat and guinea pig cochleae," Hear. Res. **66**, 31–45.
Ricci, A. J., Crawford, A. C., and Fettiplace, R. (**2000**). "Active hair bundle motion linked to fast transducer adaptation in auditory hair cells," J. Neurosci. **20**, 7131–7142.
Robles, L., and Ruggero, M. A. (**2001**). "Mechanics of the mammalian cochlea," Physiol. Rev. **81**, 1305–1352.
Robles, L., Ruggero, M. A., and Rich, N. C. (**1997**). "Two-tone distortion on the basilar membrane of the chinchilla cochlea," J. Neurophysiol. **77**, 2385–2399.
Scholz, G., Hirschfelder, A., Marquardt, T., Hensel, J., and Mrowinski, D. (**1999**). "Low-frequency modulation of the $2f_1-f_2$ distortion product otoacoustic emissions in the human ears," Hear. Res. **130**, 189–196.
Shera, C. A., and Guinan, J. J. J. Jr. (**1999**). "Evoked otoacoustic emissions arise by two fundamentally different mechanisms: A taxonomy for mammalian OAEs," J. Acoust. Soc. Am. **105**, 782–798.
Temchin, A. N., Rich, N. C., and Ruggero, M. A. (**1997**). "Low-frequency suppression of auditory nerve responses to characteristic tones," Hear. Res. **113**, 29–56.
van der Heijden, M. (**2005**). "Cochlear gain control," J. Acoust. Soc. Am. **117**, 1223–1233.
Whitehead, M. L., Stagner, B. B., McCoy, M. J., Lonsbury-Martin, B. L., and Martin, G. K. (**1995**). "Dependence of distortion-product otoacoustic emissions on primary levels in normal and impaired ears. II. Asymmetry in L_1, L_2 space," J. Acoust. Soc. Am. **97**, 2359–2377.
Withnell, R. H., and Lodde, J. (**2006**). "In search of basal distortion product generators," J. Acoust. Soc. Am. **120**, 2116–2123.
Yates, G. K., and Kirk, D. L. (**1998**). "Cochlear electrically evoked emissions modulated by mechanical transduction channels," J. Neurosci. **18**, 1996–2003.
Zou, Y., Zheng, J., Ren, T., and Nuttall, A. (**2006**). "Cochlear transducer operating point adaptation," J. Acoust. Soc. Am. **119**, 2232–2241.
Zwicker, E. (**1981**). "Masking-period patterns and cochlear acoustical responses," Hear. Res. **4**, 195–202.
Zwicker, E., and Manley, G. (**1981**). "Acoustical responses and suppression-period patterns in guinea pigs," Hear. Res. **4**, 43–52.

Effects of periodic masker interruption on the intelligibility of interrupted speech

Nandini Iyer,[a] Douglas S. Brungart, and Brian D. Simpson
Air Force Research Laboratory, Wright-Patterson AFB, Ohio, USA

(Received 19 May 2006; revised 12 June 2007; accepted 13 June 2007)

When listeners hear a target signal in the presence of competing sounds, they are quite good at extracting information at instances when the local signal-to-noise ratio of the target is most favorable. Previous research suggests that listeners can easily understand a periodically interrupted target when it is interleaved with noise. It is not clear if this ability extends to the case where an interrupted target is alternated with a speech masker rather than noise. This study examined speech intelligibility in the presence of noise or speech maskers, which were either continuous or interrupted at one of six rates between 4 and 128 Hz. Results indicated that with noise maskers, listeners performed significantly better with interrupted, rather than continuous maskers. With speech maskers, however, performance was better in continuous, rather than interrupted masker conditions. Presumably the listeners used continuity as a cue to distinguish the continuous masker from the interrupted target. Intelligibility in the interrupted masker condition was improved by introducing a pitch difference between the target and speech masker. These results highlight the role that target-masker differences in continuity and pitch play in the segregation of competing speech signals. [DOI: 10.1121/1.2756177]

PACS number(s): 43.66.Dc, 43.66.Lj, 43.66.Mk [RAL] Pages: 1693–1701

I. INTRODUCTION

Auditory scenes are easiest to process when they contain only a single source, but in the real world sounds rarely occur in isolation. Consequently, listeners are often required to integrate meaningful audio signals from the spectrotemporal "glimpses" that emerge when a target signal has a different pattern of spectrotemporal fluctuations than other, interfering sounds. Less frequently, listeners might be required to process audio signals that are "interrupted" by brief periods of silence (e.g., from a poor communications line such as a cell phone). In either case, the auditory system is faced with the somewhat daunting challenge of identifying the spectrotemporal fragments that should be grouped together as a representation of the target signal, and when interferers are present, segregating target fragments from any interfering sounds in the auditory mixture, and finally using target fragments to somehow reconstruct the original sound source.

While in many ways this might seem like a difficult or impossible task, a number of laboratory experiments have demonstrated that listeners can do it with relative ease, particularly when the target signal is speech and the masker is noise (Miller and Licklider, 1950; Howard-Jones and Rosen, 1993; Buss *et al.*, 2004). Miller and Licklider (1950) were among the first to demonstrate that intelligibility of a target sentence is only minimally affected when it is periodically interrupted by silence. When the rate of interruption is 4 Hz or less (i.e., the periods of silence are relatively long), there is some loss of information because entire syllables and words are eliminated from the stimulus. However, once the rate of interruption reaches the point where there are multiple glimpses of the target speech per phoneme (between 8 and 100 Hz), the interrupted words become just as intelligible as uninterrupted speech.

Listeners are also quite adept at integrating target information across temporal intervals that are masked by noise. For example, at 0 dB signal-to-noise ratio (SNR), word intelligibility does not change significantly when continuous speech is intermittently masked by white noise and interruption rates are varied from 1 to 100 Hz (Miller and Licklider, 1950; Dirks and Bower, 1969, 1970). In fact, at these rates of masker interruption, word intelligibility is only slightly worse than it is for speech that is interrupted by silent intervals. These results demonstrate that high levels of intelligibility can be achieved even when the listeners only have access to brief glimpses of a target speech stimulus. Indeed, numerous masking experiments (Miller, 1947; Pollack, 1955; Wilson and Carhart, 1969; Dirks and Bower, 1970) have demonstrated that target intelligibility in the presence of a steady-state noise masker can be significantly improved by interrupting or amplitude modulating the masker.

A closely related variation of the intermittent noise masking condition is the condition where the target and the masker are interrupted and temporally interleaved so the listener hears only one of the two signals at any given point in time. Listeners are so inclined to integrate speech segments across the interrupted speech intervals that they often report hearing it as a continuous speech signal masked by interrupted noise, rather than as an interrupted speech signal alternating with interrupted noise. Even when the listeners perceive the target speech as continuous, intelligibility is not improved relative to the condition where the target speech signal is interrupted by silence (Miller and Licklider, 1950). The fact that listeners perceive an auditory signal "continu-

[a]Author to whom correspondence should be addressed. Current affiliation: General Dynamics Advanced Information Systems. Electronic mail: nandini.iyer@wpafb.af.mil

ing" through a more intense burst of masking noise is related to a well-researched perceptual phenomenon known variously as the picket fence effect, the temporal induction effect, the phonemic restoration effect, or the continuity illusion (Miller and Licklider, 1950; Thurlow and Elfner, 1959; Dirks and Bower, 1970; Warren, 1970; Drake and McAdams, 1999).

Although previous experiments have thoroughly explored situations where an interrupted speech signal is masked by, or alternated with, a noise masker, virtually no information is available regarding what might occur when an interrupted speech signal is masked by, or alternated with, a speech masker. Previous experiments have shown that the impact on speech intelligibility can be very different for speech maskers compared to noise maskers in a wide variety of listening configurations. In situations where the target and masking speech signals are easily distinguished from one another, performance is generally better with a speech masker than with a noise masker presented at the same overall SNR. This occurs because listeners are able to attend to the target speech in the "dips" of the masking speech (Festen and Plomp, 1990). In other situations, where the target and masking speech utterances are perceptually similar and difficult to distinguish from one another, performance with a speech masker is often much worse than with a noise masker presented at a similar SNR value. However, in these situations large improvements in performance can occur when small perceptual differences are introduced between the two competing utterances. This often produces masking patterns that are much different than those that typically occur for speech-in-noise masking. For example, with a speech masker, performance can sometimes be better at negative SNRs because listeners can use intensity differences between two speech signals to listen to the less intense (target) talker (Brungart, 2001b; Brungart *et al.*, 2001) but they gain no benefit from intensity differences when the masker is noise. Similarly, listeners have been shown to benefit more from real or apparent spatial separation between a speech target and a speech masker than from real or apparent spatial separation from a noise masker (Freyman *et al.*, 1999; Hawley *et al.*, 2000; Arbogast *et al.*, 2002). The performance differences obtained with speech maskers (when compared with noise maskers) are fundamentally related to the listener's inability to distinguish the acoustic features of a target speech signal from those of a similar-sounding masker. The term "informational masking" (Kidd *et al.*, 1998; Freyman *et al.*, 1999; Brungart, 2001b; Brungart *et al.*, 2001) has been used to explain deficits in target identification that result from the presence of a speech masker compared to a noise masker that are not explained merely by the amount of spectral overlap. Whereas energetic masking captures the degradation in intelligibility of a target signal due to the overlapping target and masker energies in the peripheral auditory filters, informational masking has been commonly used to describe the difficulty that listeners experience when attempting to separate elements of a target signal from that of a perceptually similar masker.

Because speech-on-speech masking performance is complicated by so many factors, it is very difficult to use the prior studies that have examined speech perception with an alternating noise masker to predict what might happen when a target signal is masked by an alternating speech masker. On the one hand, one might expect listeners to benefit substantially from the dramatic increases in instantaneous SNR that result in near-ceiling performance in the alternated speech and noise conditions. On the basis of earlier speech-in-noise results, an engineer designing an enhanced multichannel speech display might consider signal alternation as a way to improve performance for a listener attending to two simultaneous speech signals. On the other hand, it is also possible that the signal interruption might somehow disrupt the cues the listeners normally use to selectively attend to a target phrase when it is masked by a perceptually similar speech competitor. The disruption of cues might offset the instantaneous SNR benefits obtained by alternating a speech target and a speech masker, or possibly even lead to reduced performance in the alternating speech-on-speech condition. The aim of this experiment was to extend Miller and Licklider's (1950) experiment on alternating speech and noise signals to conditions involving two competing speech signals, with the hope of gaining a better understanding of the processes listeners use to integrate short glimpses of information in multitalker speech perception.

II. EXPERIMENT 1: EFFECT OF MASKER TYPE, MASKER CONTINUITY AND TARGET INTERRUPTION RATE

A. Methods

1. Listeners

Eight listeners, ranging in age between 21 and 55 years, with normal hearing thresholds (audiometric thresholds $\leq$15 dB hearing level from 250 to 8000 Hz) participated. All were paid volunteers and had previous experience with the speech corpus used.

2. Signals

The speech materials were sentences from the publicly available coordinate response measure (CRM) corpus (Bolia *et al.*, 2000). The corpus contains recordings of four male and four female talkers speaking phrases of the form, "Ready [call-sign] go to [color] [number] now." A combination of eight call signs (Arrow, Baron, Charlie, Eagle, Hopper, Laker, Ringo and Tiger), four colors (red, white, blue, green) and eight numbers (1–8) resulted in 256 phrases recorded per talker for a total of 2048 phrases in the entire corpus. The sentences in the corpus were band limited to 8 kHz and sampled 40 kHz. In this experiment, the target sentence was always denoted by the call-sign "Baron." Listeners heard the target sentence in the presence of two types of maskers (noise or speech), each either continuous or interrupted. The noise masker was a Gaussian noise that was spectrally shaped so that it matched the long term average spectrum of the 2048 phrases in the CRM corpus and was presented at a root mean square (rms) level that was 8 dB more intense than the rms level of the target speech (i.e., at an SNR$=-8$ dB) *prior* to any interruption. When the masker was speech, a CRM phrase with a different call sign, color and number

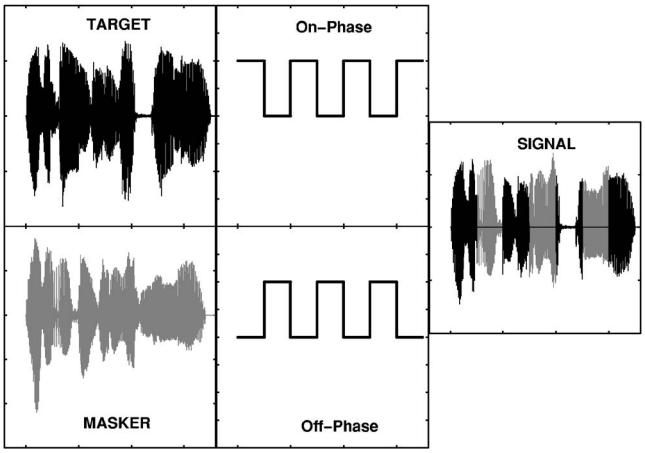

FIG. 1. Representation of the signals presented to listeners in Experiment 1 in the condition where the target and speech masker alternated with each other at the rate of 4 Hz. Two phrases from the CRM corpus (target wave form depicted in black and masker wave form in gray) are multiplied by a square wave, such that the target was multiplied by the "on" starting phase (top middle panel) and the masker, by the "off" phase (bottom middle panel). The resulting signal is segments of target phrase that alternates with those of the masker phrase.

than the target phrase was selected randomly from the corpus, set to the same rms level, and played simultaneously with the target phrase. In order to maximize similarity between the voice characteristics of the target and masking sentences, the masking talker was always the same talker as the target talker.

The target sentence was interrupted in all experimental conditions. This interruption was achieved by multiplying the target sentence by a square wave with a 50% duty cycle and a repetition rate of 4, 8, 16, 32, 64, or 128 Hz. The target sentence was always multiplied by the square wave with an "on" starting phase. When the masker was continuous, its onset was simultaneous with the interrupted target sentence. In conditions where the masker was also interrupted, it was multiplied by a square wave and switched at the same rate as the target, but with the opposite starting phase (i.e., the "off" phase). Thus, in experimental conditions where the masker was interrupted, the resulting signal consisted of alternating segments of target followed by masker segments. Figure 1 depicts one such listening condition in which the target and masker sentence were both interrupted at a rate of 4 Hz. Note that the two square waves for the target and masker have identical repetition rates but different starting phases. A control condition, where the target and masker were both continuous, was also included, and for convenience we identify that condition as the "0 Hz" condition. To summarize, there were three independent variables: target interruption rate (0, 4, 8, 16, 32, 64 and 128 Hz), masker type (speech or noise) and masker continuity (continuous or interrupted).

3. Procedure

The signals were presented diotically through Beyer DT 990 PRO headphones to listeners seated in a quiet listening room. Potential responses were displayed in a 4×8 matrix of colored digits. Listeners responded by using a cursor to select the desired color-number combination in the target sentence. Correct response feedback was provided after every trial and overall performance for each subject as well as group averages were displayed at the end of each block. In a block of trials, both the type of masker as well as masker continuity remained fixed, and four repetitions of each interruption rate were presented in a random order. The order of presentation of masker type as well as continuity of the masker was randomized across subjects. An additional block of trials was also conducted where listeners heard the target interrupted at rates of 4, 8, 16, 32, 64, and 128 Hz with no masker. A total of 20 trials were collected per masker type at each interruption rate for each subject.

B. Results and discussion

Figure 2 shows the percentage of correct color and number responses as a function of target interruption rate for the continuous and interrupted noise masker conditions (left panel) and the continuous and interrupted speech masker conditions (right panel). The data were averaged across all eight listeners and the error bars represent the 95% confidence intervals. The unfilled triangles in each panel represent performance in the control conditions, where listeners heard

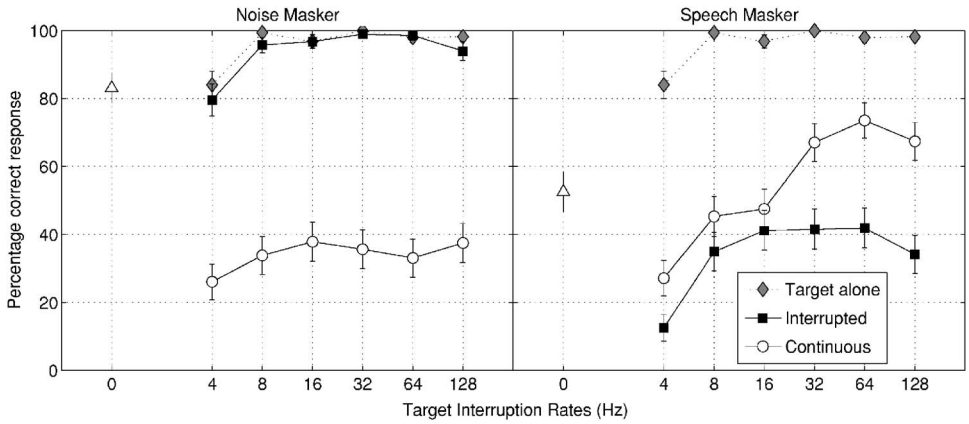

FIG. 2. Percent correct target sentence identification as a function of the target interruption rate for two masker types: noise (left panel) and speech (right panel). The circles represent performance for listeners in conditions where the masker was continuous and the squares represent performance when the maskers were alternated with the target (interrupted masker condition). The diamonds represents performance in the interrupted target condition with no masker. The unfilled triangles represent data for 0 Hz control condition. The error bars represent the 95% confidence intervals around the mean.

a continuous target in the presence of a continuous masker (the 0 Hz condition). The circles represent performance in the continuous masker condition, whereas the squares represent performance in the alternating masker condition. The diamonds represent the data from the condition where listeners heard the target alone interrupted at rates of 4, 8, 16, 32, 64, and 128 Hz.

In the control condition with noise maskers, when the target and masker were both on continuously (0 Hz point in the left panel of the figure), listeners responded with the correct color and number combination in approximately 85% of the trials. When the target was interrupted but presented with no masker (diamonds), performance was near 100% at rates of 8 Hz and above. Performance remained near perfect when the target was alternated with a noise masker, suggesting that the introduction of an alternating noise had no substantial impact on the intelligibility of an interrupted speech target. Thus, data showed that the listeners were able to obtain enough information to identify almost 100% of the color-number combinations when they heard 50% of the target signal at a SNR of ∞ dB (interrupted target alternated with interrupted noise); roughly 35% of the color-number combinations when they heard 50% of the target signal at a SNR of −8 dB (interrupted target masked by continuous noise), and 85% of the color-number combinations when they heard the entire target signal at a SNR of −8 dB (continuous target masked by continuous noise).

Performance with the speech masker showed a remarkably different trend. First, performance was about 53% in the 0 Hz control condition (continuous target, continuous speech masker) compared to 85% in the 0 Hz noise condition, despite the higher SNR (0 versus −8 dB). When the speech masker alternated with the target (squares in the right panel), listeners were able to identify 35% of the color-number combinations; in fact, performance with the interrupted speech masker was similar to that obtained with the continuous noise masker. Also, with speech maskers, target intelligibility with the continuous masker (circles in the right panel) was consistently better than with the interrupted masker. Indeed, when the target interruption rate was at least 32 Hz, performance in the continuous masker condition was actually better than it was in the 0 Hz continuous condition.

The arcsine-transformed percentage correct scores were submitted to a three-factor within-subject analysis of covariance (ANOVA) with masker type, masker continuity, and target interruption rate as factors. The analysis indicated that there were significant main effects of target interruption rate ($F_{(6,42)}=59.21$, $p<0.001$), masker type ($F_{(1,7)}=87.06$, $p<0.001$), and masker continuity ($F_{(1,7)}=34.59$, $p=0.001$). All two-way interactions were significant; masker type and masker continuity ($F_{(1,7)}=618.82$, $p<0.001$), masker type and target interruption rate ($F_{(6,42)}=7.60$, $p<0.001$), and masker continuity and target interruption rate ($F_{(6,42)}=8.35$, $p<0.001$). There was also a significant three-way interaction between masker type, masker continuity and target interruption rate ($F_{(6,42)}=32.45$, $p<0.001$).

The two-way interaction between masker type and masker continuity is apparent in Fig. 2, in that when the masker was noise, performance was consistently better in the alternating than continuous condition, whereas the converse was true with the speech masker. In order to examine the three-way interaction, two-factor within-subject ANOVA, with masker continuity and target interruption rate as factors, were conducted for both the noise and the speech masker condition. The 0 Hz control condition was not included in the analysis because it was a control condition. In addition, because the target interruption rate of 4 Hz was a special case, where performance was dominated by insufficient target information rather than the apparent continuity of the masker, only the transformed scored for target interruption rates of 8 Hz and higher were submitted to the ANOVA. Results indicated that, for noise maskers, only the main effect of masker continuity was significant ($F_{(1,7)}=574.25$, $p<0.001$). For speech maskers, both main effects were significant; target interruption rate ($F_{(4,28)}=11.51$, $p<0.001$), and masker continuity ($F_{(1,7)}=25.63$, $p<0.001$). The two-way interaction between target interruption rate and masker continuity was also significant for speech maskers ($F_{(4,28)}=6.64$, $p=0.001$). These results suggest that the two-way interaction between masker continuity and target interruption rate depended on the type of masker. Specifically, with speech maskers, there was a trend for performance to improve for the continuous masker condition, relative to the interrupted masker, as the target interruption rate increased. With noise masker, there was no trend for performance to improve with an increase in target interruption rate for either a continuous or an interrupted masker, although it must be noted that performance was near perfect with the interrupted noise masker condition.

The results from Experiment 1 indicate that the percentage of correct color-number identifications for a target sentence in the CRM corpus is substantially affected by both masker type and masker continuity. For noise maskers, the results obtained concur with those reported in prior studies; in particular, compared to the 0 Hz control condition, target word identification improves when the target alternates with the masker but deteriorates with an interrupted target and a continuous masker. The finding that an alternating noise masker is less effective than a continuous noise masker is well documented in the literature (Miller and Licklider, 1950; Dirks and Bower, 1969; Howard-Jones and Rosen, 1993). The release from masking is attributed to instances in time when the local signal-to-noise ratio is greatly improved. The auditory system is fairly adept at distinguishing the noise fragments from the speech fragments and integrating segments of the target sentence together so that performance is no different from the condition when the target sentence is interrupted by silence. In conditions when an interrupted target is heard in the presence of a continuous noise masker, three factors may be responsible for the degradation in performance relative to an interrupted noise masker. First, the listener is not afforded a glimpse of the target sentence at a favorable SNR that is sufficiently long to integrate target information. Second, the listener loses 50% of the information in the target speech due to the interruption (note that this is also true with the interrupted noise masker, where performance is near ceiling). And third, the listener faces the po-

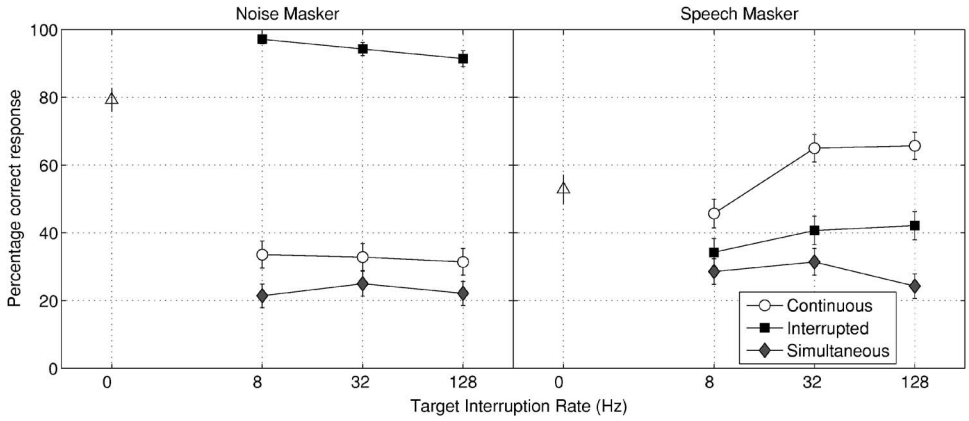

FIG. 3. The percentage of correct responses plotted as a function of the target interruption rate (Hz). The left panel depicts data from seven listeners with a noise masker, whereas the right panel depicts those with a speech masker. The circles and squares represent data for continuous and interrupted maskers, respectively, whereas the diamonds represent data in the listening condition where the maskers were simultaneously presented with the interrupted target signal. The error bars represent the 95% confidence limits around the mean.

tentially much tougher problem of extracting "noisy" speech fragments from noise (rather than extracting "clean" speech fragments from noise) in order to piece together the fragments of the interrupted target signal into a coherent stream.

The pattern of results for the speech maskers differed significantly from the noise maskers; performance in the interrupted speech masker condition was always worse than with a continuous speech masker. This result most likely occurred because the listeners had much more difficulty distinguishing the interrupted target signal from the interrupted speech masker than they did segregating it from an interrupted noise. Indeed, the interruption may have disrupted some of the cues (such as prosody) that listeners normally use to segregate multiple continuous speech signals, especially in cases when the target speaker is similar to the masking speaker. As a result, the segregation task with an interrupted speech masker was even more difficult than the control (0 Hz) segregation task, where both the signals (target and masker) were continuous. Finally, also in direct contrast to the noise condition, the improvement in performance seen in the continuous speech masker conditions over the 0 Hz condition was probably the result of the listener using continuity cues to distinguish between the target and masking voices. By intentionally listening for the interrupted speech signal and ignoring the continuous speech signal, the listeners were able to improve performance despite the lower local SNR values in the continuous masker conditions.

From the standpoint of energetic masking alone, the result with the speech masker is surprising because in the interrupted condition, the local SNR is just as favorable as in the interrupted noise masker condition. It is clear from the results that informational masking factors, related to the confusability of the target and masking voices, played a much greater role than energetic masking in determining performance in the task. Therefore, even in listening conditions where listeners could potentially utilize optimal SNR to "hear out" the target signal, the similarity between the target and masker in terms of masker continuity (i.e., both interrupted) actually disrupted performance compared to the condition where local SNR was worse, but where a continuity cue was present (i.e., continuous masker, interrupted target). This suggests that signal manipulations that decrease the perceptual similarity rather than improve the local SNR are key to improving target identification and thereby alleviate informational masking. Finally, while we are unaware of any previous results demonstrating this effect with a speech signal, it is worth noting that a number of studies have reported similar effects with tonal nonspeech signals that also tend to generate significant amounts of informational masking. For example, Kidd *et al.* (1994) reported a substantial reduction in informational masking when a 1000 Hz target was presented during every alternate instead of in every burst of a multitone masker. This reduction in masking was obtained despite the fact that the overall target energy in the alternating condition was half that present during the continuous condition. Similarly, Neff (1995) reported that informational masking was substantially reduced for an amplitude-modulated target compared to a pure-tone target presented with multicomponent maskers.

One important question left unanswered by these data is whether the listeners in the speech masking condition actually received any benefit from regions of favorable SNR that occurred in the interrupted speech condition. If energetic masking was not a factor in the speech masking conditions, then one might expect to get the same results regardless of whether the interrupted target and masking signals were presented in the same time intervals (i.e., both on, both off) or in alternating time intervals (i.e., target on, masker on). In order to address this question, a follow-up experiment was conducted that compared the interrupted condition tested in Experiment 1 with a new condition where the target and masking signals were both interrupted, but were presented simultaneously. The experimental procedures were identical to those used in Experiment 1, but data were only collected at four target interruption rates: 0 (control condition), 8, 32 and 128 MHz. Figure 3 presents the average results from seven subjects, six of whom also participated in Experiment 1. As in Fig. 2, the circles and squares represent the average percentage correct color-number responses for a continuous and interrupted masker, respectively. The diamonds represent average performance in the condition where the masker was pulsed on and off simultaneously with the target signal.

Comparing the simultaneous speech masking condition (diamonds in the right panel of the figure) to the interrupted speech masking condition (squares), it is clear that some release from energetic masking was obtained when the speech masker was interleaved with the target rather than presented simultaneously. However, the improvement in performance was small compared to that obtained with the continuous masker (circles in the figure), despite the fact that the continuous masker condition had the same local SNR value as the simultaneous masking condition. A paired sample t test with Bonferroni correction supported this conclusion; listeners' performance in the alternating and simultaneous speech masker condition was not significantly different at the three rates of interruption tested ($t=0.508$, 2.34 and 3.24, for 8, 32 and 128 Hz, respectively, $p>0.05$). Perhaps a more surprising finding is the trend for performance in the noise masking condition to be worse in the simultaneous masking condition (diamonds in the left panel of the figure) than in the continuous masking condition (circles). The trend is observed despite the possibility of additional forward or backward masking from the noise in the target-silent intervals. Although the difference is not significant at the target interruption rates tested ($t=3.29$, 1.15, 1.96, respectively, $p>0.05$), it is possible that listeners were able to use the continuity of the noise masker to help segregate the noise from the target, in the same way they were able to use the continuity cue with the speech masker.

III. EXPERIMENT 2: EFFECT OF CHANGING VOICE CHARACTERISTICS

The results from the first experiment clearly indicate that the masking obtained with a continuous or interrupted speech masker was different from a continuous or interrupted noise masker. In particular, target identification was significantly worse with an interrupted than with a continuous speech masker, whereas the opposite was true with a noise masker. In part, we hypothesized that a temporal continuity cue (continuous speech masker, interrupted target) resulted in the pattern of performance obtained with the speech maskers. However, in all listening conditions in Experiment 1, the target talker was always the same as the masking talker. So, the continuity was the only viable cue that listeners could use in the experiment. Previous experiments have demonstrated that pitch differences can also be used effectively by listeners in order to segregate a target talker in multitalker listening tasks (Brungart, 2001a; Darwin *et al.*, 2003). In the second experiment, we introduced pitch differences between the target and masking talker in the speech masking conditions. The aim of this experiment was to evaluate if listeners could use a pitch difference cue, in addition to or instead of a continuity cue, to segregate an interrupted target signal.

A. Method

The target signals in this experiment were similar to those in Experiment 1. The masker was always a speech masker and was either continuous or interrupted. In addition to masker continuity (i.e., continuous versus interrupted), the masker sentences were processed using the Praat software (Boersma and Weenink, 1996) implementation of the PSOLA algorithm (Moulines and Charpentier, 1990), so that the fundamental frequency ($F0$) and the vocal tract (v.t.) changes simulated a change from a masker that was the same sex as the target to one that was a different sex. For each male talker, individual v.t. values were multiplied by a factor of 0.96, 0.92 and 0.76 and the $F0$ were adjusted so as to correspond to semitone differences of 2.7, 5.2, and 12.4 between the original and modified voice. Effectively, the pitch of the male voice increased so that the manipulation was akin to playing a masker phrase that can be described as "quarter-female," "half-female," and "super-female" talker, respectively. Conversely, female voices were lowered in pitch by increasing the v.t. length by a factor of 1.04, 1.08, and 1.24, with associated semitone differences of −2.7, −5.2, and −12.4 between the original and altered voices. Because all changes were made with respect to the individual talkers, all absolute differences between the talkers were retained. These values and additional details about the $F0$ and v.t. manipulations are described in Darwin *et al.* (2003). Thus, there were three independent variables in this experiment: masker continuity (continuous versus interrupted speech masker), target interruption rate (4, 8, 16, 32, 64, or 128 MHz) and pitch difference between the target and masker voice (2.7, 5.2 or 12.4 semitones). Data were collected from nine listeners with hearing thresholds within normal limits. Eight of the nine listeners also participated in the previous experiment. The order of presentation of target interruption rate as well as pitch difference were randomized but only one masker continuity was tested in each block. Data from the experiment represents the average from 20 trials per condition per listener.

B. Results and Discussion

Figure 4 shows the percentage of correct color and number identifications as a function of target interruption rates in each of the three pitch difference conditions. For comparison, data with the speech maskers from Experiment 1 are also plotted, where the masking talker was the same as the target talker and hence the overall pitch difference was 0 semitones. Within each panel, the circles show performance for the continuous speech masker, whereas the squares show performance for a speech masker alternating with the target phrase. As in the previous experiment, the unfilled triangles represent data from the 0 Hz control condition. All error bars represent the 95% confidence limits.

Target identification in the control condition (0 Hz) with a continuous target and a continuous masker (leftmost point in each panel) improved when the pitch difference increased from 0 to 2.7 semitones, but differences in pitch that exceeded 2.7 semitones did not provide any additional benefit to listeners. These results are consistent with Darwin *et al.* (2003), where target identification improved by 15–25% as the pitch difference increased from 0 to 2.7 semitones but plateaued at higher pitch differences.

Except at the largest pitch separation tested, target identification in the presence of a continuous speech masker was higher than in interrupted masker conditions. A three-factor,

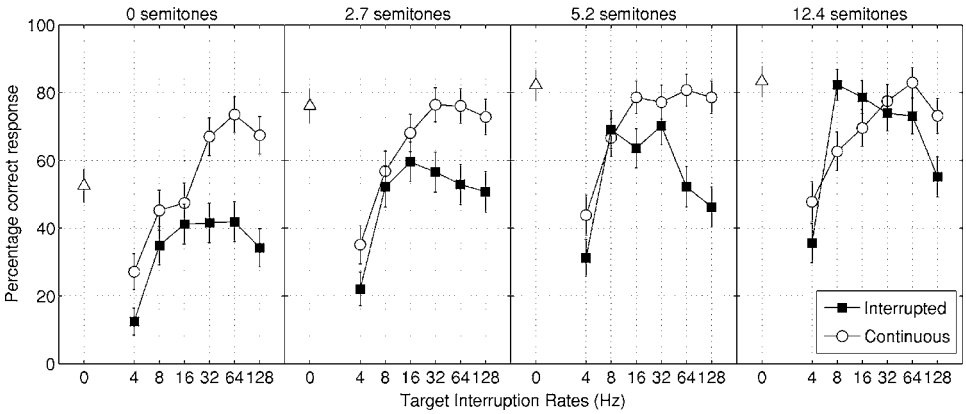

FIG. 4. The percentage of correct responses plotted as a function of the target interruption rate (Hz). The four panels represent performance of the listeners in experimental conditions where the masker and the target differed by 0, 2.7, 5.2 or 12.4 semitones. The results with continuous maskers are depicted in circles, whereas those with the interrupted maskers are depicted in squares. Data from the 0 Hz control condition are plotted as unfilled triangles. The error bars represent the 95% confidence limits around the mean.

within-subject ANOVA was performed on the arcsine-transformed mean scores. The factors were masker continuity (continuous versus interrupted), target interruption rate, and pitch separation. Results of the ANOVA indicated main effects of masker continuity ($F_{(1,7)}=53.60$, $p<0.001$), pitch separation ($F_{(3,21)}=55.63$, $p<0.001$), and target interruption rate ($F_{(6,42)}=104.20$, $p<0.001$). All two-way interactions were significant as was the three-way interaction of pitch, target interruption rate and masker continuity ($F_{(18,126)}=2.39$, $p<0.01$). In order to examine the source of the three-way interaction, a two-factor within-subject ANOVA was conducted with masker continuity and target interruption rates as factors for all four levels of pitch separation. The results of the ANOVA indicated that the main effects as well as the two way interactions were significant for all except the 12.4 semitone pitch separation. In the 12.4 semitone condition, only the main effect of target interruption rate ($F_{(4,28)}=12.17$, $p<0.001$) and the two-way interaction ($F_{(4,28)}=15.03$, $p<0.001$) was significant. The main effect of masker continuity was not significant ($F_{(1,7)}=1.01$, $p=0.349$). Thus, the observed differences between continuous and interrupted maskers at different target interruption rates depended on the pitch separation between the target and masker.

Notably, performance at the higher target interruption rates ($\geq$32 Hz) tended to plateau in all cases at the same level (80% correct responses) achieved in the continuous 0 Hz control conditions (triangles) when there was a pitch difference in the target and masker signals (Panels 2–4). One possible explanation for this result is that the pitch difference cue and the continuity cue were each equally effective at allowing the listener to distinguish the target speech from the masking speech, but that the cues were redundant rather than additive in cases where both were available to the listener. In other words, the listeners could distinguish between the target and masking speech signals on the basis of pitch or on the basis of continuity, but they gained no further advantage when both cues were available.

The introduction of a pitch difference cue had a much larger impact on performance when both the target and masker were interrupted (filled squares in Fig. 4). In these conditions, the introduction of a pitch difference had the greatest effect at intermediate interruption rates (8–32 Hz), where it systematically improved performance from roughly 40% correct responses in the 0 semitone condition to more than 80% correct responses in the 12.4 semitone condition. Indeed, performance with an interrupted masker separated by 12.4 semitones from the target was actually better than with a continuous masker at some interruption rates. The improvement in performance observed when a pitch difference was introduced in the interrupted masker condition suggests that the pitch cue was the only viable cue for segregating the target and masking speech signals. Thus, it provided a substantial benefit by allowing the listener to segregate the target and masking speech signals into two streams. At these rates of interruption (64 Hz and higher), listeners informally reported hearing two streams: a low-pitch stream, comprised of the target phrase, and a high-pitch stream comprised of the masker phrase. It is plausible that in the 12.4 semitone case at 8–16 Hz repetition rates, the pitch cue may have been so effective for segregating the target and masker into separate streams that it allowed the listeners to take advantage of the improved local SNR value in the alternating masker condition, thus explaining the higher performance obtained in that condition (though it is worth noting that performance never approached the near 100% correct level obtained for an interrupted speech signal with no masker).

At the highest interruption rates (64–128 Hz), there seemed to be a precipitous decline in performance in the interrupted speech masker condition with 5.2 and 12.4 semitone difference. The reason for this decline is not clear, but one possible explanation is that these interruption rates were high enough to directly interfere with the perception of the $F0$ values of the speech signals and that they thus disrupted the segregation of the target and masking speech signals on the basis of pitch.

Although there are clear differences between the segregation of interrupted speech signals and interrupted tones, it is perhaps worth mentioning that there are some parallels between the pitch difference effects seen in this experiment

and those observed in studies of the segregation of tones. Experiments examining the perception of alternating high and low frequency tones have also demonstrated a profound shift between the perception of a single alternating-frequency stream and two separate high and low frequency streams when the pitch difference exceeds a certain threshold for a given alternation rate (Noorden, 1977; Ciocca and Bregman, 1987). Perhaps it is surprising that listeners could not derive more benefit from the separation in pitch between the target and masker streams at these high rates of interruption in the current study. However, such performance decrements at high rates have been previously reported for noise maskers as well (Miller and Licklider, 1950; Dirks and Bower, 1970) and have been attributed to increased nonsimultaneous masking during the noise intervals or due to the introduction of sidebands (Miller and Licklider, 1950). The results from Experiment 2 suggest that increasing the pitch difference between the target and speech masker seems to improve performance when target and masker speech signals are both continuous. At a pitch difference of 12.4 semitones, listeners most effectively integrate information when the target is alternated with the masker only at slow interruption rates (between 8 and 16 Hz).

IV. GENERAL DISCUSSION

Overall, the results from these experiments support the observation that target-masker similarity can often play a dominant role in speech-on-speech masking, and they provide additional evidence that performance with a similar-sounding speech masker cannot be predicted from the results of experiments that have used noise as a masker. From a more practical standpoint, they also seem to rule out the possibility of using temporal alternation as a way to increase a listener's ability to process multiple speech signals through a monaural channel. At first glance, the results may not be surprising. Previous research has shown that, while continuous noise is more efficient than speech in terms of its ability to energetically mask the acoustic elements of a target speech signal, a perceptually similar speech masker often produces lower performance because it is much harder to segregate from the target speech. However, with speech maskers, it is often difficult to partition the effects of overlapping spectral bands between the target and masker (energetic component) from those that are caused due to similarity or uncertainty of the target and masker. In the current study, the energetic effects of a noise and speech masker were controlled by alternating the target and masker temporally. For both maskers, the nominal SNR in the alternating condition was close to infinity. While performance with the noise maskers improved due to the improvement in local SNR, the performance with the speech masker actually dropped below the control condition where both target and masker were continuous. With speech maskers, when an additional cue, continuity, was introduced that reduced the perceptual similarity of the target and masking signals, performance generally increased substantially. In most experiments that have explored these similarity-based informational masking effects in speech-on-speech masking, similarity has been operationally defined as "sameness" in pitch (Freyman *et al.*, 1999; Brungart, 2001b; Brungart *et al.*, 2001), vocal tract size (Darwin *et al.*, 2003), apparent location (Freyman *et al.*, 1999), intensity (Brungart, 2001b), or some other conventional parameter of speech. In this paper, Miller and Licklider's (1950) work in interrupted speech perception has been extended to introduce another cue that listeners can utilize to segregate the target and masker—masker continuity.

In general, the ability to segregate a target interrupted at various rates depended largely on the type and continuity of the maskers. For noise maskers, performance was worse with a continuous than an interrupted masker. Increased performance with an interrupted masker was due to a release from energetic masking, so that listeners were able to glimpse the target during epochs when there was no masker present. On the other hand, with speech maskers, performance was best when the masker was continuous instead of interrupted. Listeners were unable to hear out the target in the interrupted masker condition, despite near infinite SNR in those conditions. We believe that performance was worse in the interrupted speech masker condition because, in addition to eliminating some of the phonetic information in the target signal, this condition did nothing to make the target less "similar" to the masker. The interruption of the masker (and indeed the target signal) might also have interfered with the prosodic continuity cues that normally would have helped the listeners segregate two phrases spoken by the same talker. Conversely, in the continuous masker condition, listeners could utilize the continuity of the masker to disambiguate it from the interrupted target, leading to a marked improvement in performance at high interruption rates.

When pitch differences were introduced between the target and masker sentences, there was no improvement in performance with a continuous speech masker (compared to the baseline 0 semitone condition). Presumably, the pitch cue provided an equally salient means of segregating the target and masker as the continuity cue in these conditions. Compared to the 0 semitone condition, the greatest improvement in performance was observed in the interrupted masker condition when pitch cues were introduced, mainly because the pitch cue provided the listeners with a means to track the target sentence and/or ignore the masker. When rates of interruption increased, there was a tendency for performance to decline with both types of maskers, perhaps due to interference between the interruption rates and the $F0$ values of the talkers.

In real world listening environments, listeners are constantly required to reconstruct audio signals from a relatively sparse distribution of spectrotemporal glimpses where the target signal locally dominates the other components of a complex auditory mixture (Cooke, 2006). In this paper, we have identified a number of important attributes about this "glimpsing process." First, we have argued that the ability to extract a speech signal from an interrupted noise signal is not based on any kind of temporal "synchronization" or "entrainment" to the target signal in the glimpsing process (i.e., the ability to tie together observations that occur at fixed intervals from one another). If listeners were able to use this kind of synchronization, it should have helped them extract the

target speech from an interrupted speech masker just as easily as they were able to extract it from an interrupted noise masker. Thus, listeners must be using some acoustic properties inherent in the noise to make the distinction between speech and noise glimpses in the interrupted noise masker condition. Second, we have shown that "signal continuity" is a viable perceptual parameter that listeners can use to help segregate a continuous speech signal from an interrupted speech signal. Finally, we have shown that listeners can use *F*0 differences to help group together short alternating glimpses of speech, but that this kind of grouping falls apart when the target interruption rate exceeds 32 Hz. However, a more complete understanding of the cues listeners use to successfully piece together the sparsely distributed spectrotemporal fragments of a sound into a coherent audio image is necessary before we can begin to fully understand how human listeners are able to robustly segregate audio signals in such a wide range of listening environments.

Arbogast, T., Mason, C., and Kidd, G. (**2002**). "The effect of spatial separation on informational and energetic masking of speech," J. Acoust. Soc. Am. **112**, 2086–2098.

Boersma, P., and Weenink, D. (**1996**). "Praat, a system for doing phonetics by computer, version 3.4," Institute of Phonetic Sciences, University of Amsterdam, **134**, 1–182.

Bolia, R., Nelson, W., Ericson, M., and Simpson, B. (**2000**). "A speech corpus for multitalker communications research," J. Acoust. Soc. Am. **107**, 1065–1066.

Brungart, D. (**2001a**). "Evaluation of speech intelligibility with the coordinate response measure," J. Acoust. Soc. Am. **109**, 2276–2279.

Brungart, D. (**2001b**). "Informational and energetic masking effects in the perception of two simultaneous talkers," J. Acoust. Soc. Am. **109**, 1101–1109.

Brungart, D., Simpson, B., Ericson, M., and Scott, K. (**2001**). "Informational and energetic masking effects in the perception of multiple simultaneous talkers," J. Acoust. Soc. Am. **110**, 2527–2538.

Buss, E., Hall, J., and Grose, J. (**2004**). "Spectral integration of synchronous and asynchronous cues to consonant identification," J. Acoust. Soc. Am. **115**, 2278–2285.

Ciocca, V., and Bregman, A. (**1987**). "Perceived continuity of gliding and steady-state tones through interrupting noise," Percept. Psychophys. **42**, 476–484.

Cooke, M. (**2006**). "A glimpsing model of speech perception in noise," J. Acoust. Soc. Am. **119**, 1562–1573.

Darwin, C., Brungart, D., and Simpson, B. (**2003**). "Effects of fundamental frequency and vocal-tract length changes on attention to one of two simultaneous talkers," J. Acoust. Soc. Am. **114**, 2913–2922.

Dirks, D., and Bower, D. (**1969**). "Masking effects of speech competing messages," J. Speech Hear. Res. **12**, 229–245.

Dirks, D., and Bower, D. (**1970**). "Effect of forward and backward masking on speech intelligibility," J. Acoust. Soc. Am. **47**, 1003–1008.

Drake, C., and McAdams, S. (**1999**). "The auditory continuity phenomenon: Role of temporal sequence structure," J. Acoust. Soc. Am. **106**, 3529–3538.

Festen, J., and Plomp, R. (**1990**). "Effects of fluctuating noise and interfering speech on the speech reception threshold for impaired and normal hearing," J. Acoust. Soc. Am. **88**, 1725–1736.

Freyman, R., Helfer, K., McCall, D., and Clifton, R. (**1999**). "The role of perceived spatial separation in the unmasking of speech," J. Acoust. Soc. Am. **106**, 3578–3588.

Hawley, M., Litovsky, R., and Culling, J. (**2000**). "The 'cocktail party' effect with four kinds of maskers: Speech, time-reversed speech, speech-shaped noise, or modulated speech-shaped noise," *Proceedings of the Midwinter Meeting of the Association for Research in Otolaryngology*, **31**.

Howard-Jones, P., and Rosen, S. (**1993**). "Uncomodulated glimpsing in 'checkerboard' noise," J. Acoust. Soc. Am. **93**, 2915–2922.

Kidd, G. J., Mason, C., Deliwala, P., Woods, W., and Colburn, H. (**1994**). "Reducing informational masking by sound segregation," J. Acoust. Soc. Am. **95**, 3475–3480.

Kidd, G. J., Mason, C., Rohtla, T., and Deliwala, P. (**1998**). "Release from informational masking due to the spatial separation of sources in the identification of nonspeech auditory patterns," J. Acoust. Soc. Am. **104**, 422–431.

Miller, G. (**1947**). "Sensitivity to changes in the intensity of white Gaussian noise and its relation to masking and loudness," J. Acoust. Soc. Am. **191**, 609–619.

Miller, G., and Licklider, J. (**1950**). "The intelligibility of interrupted speech," J. Acoust. Soc. Am. **20**, 167–193.

Moulines, E., and Charpentier, F. (**1990**). "Pitch synchronous waveform processing techniques for text-to-speech synthesis using diphones," Speech Commun. **9**, 453–467.

Neff, D. (**1995**). "Signal properties that reduce masking by simultaneous random-frequency maskers," J. Acoust. Soc. Am. **96**, 1909–1921.

Noorden, L. van. (**1977**). "Minimum differences of level and frequency for perceptual fission of tone sequences abab," J. Acoust. Soc. Am. **61**, 1041–1045.

Pollack, I. (**1955**). "Masking by a periodically interrupted noise," J. Acoust. Soc. Am. **27**, 353–355.

Thurlow, W., and Elfner, L. (**1959**). "Continuity effects with alternately sounding tones," J. Acoust. Soc. Am. **31**, 1337–1339.

Warren, R. (**1970**). "Restoration of missing speech sounds," Science **167**, 392–393.

Wilson, R., and Carhart, R. (**1969**). "Influence of pulsed masking on the threshold for spondees," J. Acoust. Soc. Am. **46**, 998–1010.

Variation in spectral-shape discrimination weighting functions at different stimulus levels and signal strengths

Jennifer J. Lentz[a)]
Department of Speech and Hearing Sciences, Indiana University, Bloomington, Indiana 47405

(Received 31 July 2006; revised 18 June 2007; accepted 19 June 2007)

This study evaluated whether weights for spectral-shape discrimination depend on overall stimulus level and signal strength (the degree of spectral-shape change between two stimuli). Five listeners discriminated between standard stimuli that were the sum of six equal-amplitude tones and signal stimuli created by decreasing the amplitudes of three low-frequency components and increasing the amplitudes of three high-frequency components. Weighting functions were influenced by stimulus level in that the relative contribution of the low-frequency (decremented) components to the high-frequency (incremented) components decreased with increasing stimulus level. Although individual variability was present, a follow-up experiment suggested that the level dependence was due to greater reliance on high-frequency components rather than incremented components. Excitation-pattern analyses indicated that the level dependence is primarily, but not solely, driven by cochlear factors. In general, different signal strengths had no effect on the weighting functions (when normalized), but two of the five listeners showed variability in the shape of the weighting function across signal strengths. Results suggest that the effects of stimulus level on weighting functions and individual variability in the shapes of the weighting functions should be considered when comparing weighting functions across conditions and groups that might require different stimulus levels and signal strengths. © *2007 Acoustical Society of America.*
[DOI: 10.1121/1.2756800]

PACS number(s): 43.66.Fe, 43.66.Jh, 43.66.Ba [JHG] Pages: 1702–1712

I. INTRODUCTION

It has been argued that listeners with hearing loss adopt decision strategies that are different from normal-hearing listeners in intensity– and spectral–shape discrimination tasks, but these conclusions have been made from experiments that tested the two groups at different stimulus levels (Doherty and Lutfi, 1996, 1999) or at different signal strengths [the degree of intensity or spectral-shape change between two stimuli (Doherty and Lutfi, 1996, 1999; Lentz and Leek, 2002, 2003)]. Because the auditory system is inherently nonlinear, measurements made at different stimulus levels and at different signal strengths have the potential to influence the decision strategy adopted by an individual listener. The following experiment determines whether overall stimulus level and signal strength influence spectral-shape decision strategies for normal-hearing listeners.

For more than 25 years, controlled "profile-analysis" experiments have been used to evaluate the ability of the auditory system to distinguish between sounds with different spectral shapes [see Green (1988) for a review]. In a typical profile-analysis experiment, listeners discriminate between two multitonal stimuli that have different spectral shapes. Recent development of correlation methods applied to these experiments allows estimates of the relative importance of different frequency components to the spectral-shape discrimination decision (e.g., Berg, 1989; Richards and Zhu, 1994; Lutfi, 1995). In these methods, the levels of individual stimulus components are randomly and independently altered every time a stimulus is presented to a listener. In a two-interval, two-alternative forced-choice task, the listener's response (Interval 1 or 2) can be correlated with the level difference per component between the two intervals. A plot of the correlation coefficient versus component frequency indicates the weighting strategy, which reflects the relative importance of different components to the discrimination decision. Although spectral-shape discrimination experiments have indicated that normal-hearing listeners can adopt near-optimal decision strategies in some circumstances (Berg and Green, 1990, 1992; Dai *et al.*, 1996), listeners also commonly adopt suboptimal decision strategies, or strategies which emphasize only certain frequency components (Green and Berg, 1991; Lentz and Leek, 2003). The mechanisms underlying which components are used in the discrimination decision are unknown and are likely to be related to both cochlear and central auditory processes.

Applying a model of spectral-shape discrimination based on signal detection theory leads to specific predictions that are well-suited to being empirically tested. For a decision variable modeled as the sum of weighted, independent observations ($DV=\Sigma\alpha_i X_i$), with each observation typically referring to an auditory (frequency) channel, optimal sensitivity is given by

$$d' = \frac{\sum_{i=1}^{N} \alpha_i \Delta\mu_i}{\sqrt{\sum_{i=1}^{N} \alpha_i^2 \sigma_x^2}}, \tag{1}$$

where $\Delta\mu_i$ is the change in mean between signal and standard stimuli in decibel for channel i (and corresponds with the signal strength), α_i is the relative weight for channel i,

a)Electronic mail: jjlentz@indiana.edu

and σ_x^2 is the variance of the component-by-component level perturbation distribution needed for the estimate of decision weights (Berg, 1990). Simplification of Eq. (1) can be accomplished by using a "balanced" stimulus in which a signal stimulus is generated by increasing and decreasing all stimulus components by the same decibel amount ($\Delta\mu_i = \pm\boldsymbol{\Delta}$; Durlach *et al.*, 1986). In this case, for d' to be positive, the product $\alpha_i\Delta\mu_i$ is also positive. Then, d' simplifies to

$$d' = \frac{\Delta\sum_{i=1}^{N}|\alpha_i|}{\sigma_x\sqrt{\sum_{i=1}^{N}\alpha_i^2}}. \quad (2)$$

At least two additional predictions arise from Eq. (2). First, because there is no parameter related to overall stimulus level, overall level should not influence spectral-shape discrimination sensitivity or the estimate of decision weights (α_i). Second, because the spectral change imposed on the stimuli is the same magnitude across components, the optimal weighting strategy is one in which increased and decreased components have weights of the same magnitude but opposite sign ($\alpha_i = \pm\boldsymbol{\alpha}$). The ideal observer, then, will have sensitivity $d' = \sqrt{N}\boldsymbol{\Delta}/\sigma_x$, and deviations from the optimal weighting strategy will decrease d'. When the ideal decision strategy is adopted ($\alpha_i = \pm\boldsymbol{\alpha}$), the relationship between the weights (α_i) is not expected to change for different signal strengths, though the magnitude of those weights could vary.

The first prediction (that overall stimulus level does not influence the weighting strategy) is supported by data indicating similar spectral-shape discrimination sensitivity at different stimulus levels (Mason *et al.*, 1984; Green and Mason, 1985; Lentz, 2005). However, nonlinear auditory processes might lead to adoption of different decision weights at different stimulus levels (including but not limited to increased upward spread of masking with increasing stimulus level) and still result in similar spectral-shape discrimination sensitivity. Because listeners tend to adopt suboptimal decision strategies for spectral-shape discrimination tasks, a large number of possible decision strategies exist that would lead to similar performance. To determine whether stimulus level influences the decision strategy, this experiment measures spectral-shape weighting functions for normal-hearing listeners at different stimulus levels.

The second prediction (that signal strength does not affect the relationship among the weights) also has not been broadly tested. Dai *et al.* (1996) estimated weighting functions for a spectral-shape discrimination task at multiple signal strengths. In their experiment, listeners discriminated between a standard of five equal-amplitude components and a signal stimulus in which the central component was increased in level. Small random perturbations were imposed on all stimulus components on an interval-by-interval basis. Dai *et al.* (1996) demonstrated theoretically and experimentally that the correlation between the trial-by-trial differences in the perturbed levels of signal and standard components and the listener's responses decrease with increasing signal strength ($\Delta\mu_i$).

In light of the findings of Dai *et al.* (1996), it should be noted that the signal strength will affect the magnitude of the estimated weight (the raw correlation coefficient), but if weights are normalized in some way, then signal strength is not predicted to influence the weighting strategy. This prediction arises because when weights are normalized, the magnitude of the correlation coefficients are expressed as relative values and the absolute magnitudes are ignored. This prediction is quite important when comparing decision strategies across stimulus conditions or groups with sensitivity differences that would require different signal strengths to be used. For example, Doherty and Lutfi (1996) tested whether listeners with hearing loss adopted decision strategies similar to listeners with normal hearing for intensity discrimination of multitonal stimuli. In order to keep d' similar for both groups, the hearing-impaired listeners had to be tested at a higher stimulus level (80 dB SPL per component) and signal strength ($\Delta L = 5$ or 7.5 dB) than listeners with normal hearing, who were tested at 65 dB SPL per component and a signal strength of $\Delta L = 2.5$ dB. To compensate for the differences in signal strength between groups, Doherty and Lutfi (1996) normalized their weighting functions and showed that listeners with hearing loss adopted weighting strategies that differed from normal-hearing listeners.

In a spectral-shape discrimination experiment, Lentz and Leek (2003) estimated spectral-shape weighting functions for normal-hearing and hearing-impaired listeners by using trial-by-trial values obtained from an adaptive staircase procedure. Thus, the signal strengths used in their experiment varied across trials, across observers, and across groups. On average, hearing-impaired listeners were tested at a signal strength of about $\Delta L = 0.5$ dB higher than normal-hearing listeners. Lentz and Leek (2003) did not normalize weighting functions, but they also argued that there might be differences in the weighting strategies adopted by listeners with normal hearing and listeners with hearing loss. Because the aforementioned studies made similar conclusions using stimuli presented at different signal strengths to their listeners, the effect of signal strength on the weighting strategy should be evaluated before any definitive conclusions can be made about differences in weighting strategies across groups. Therefore, this experiment also estimates spectral-shape decision strategies for normal-hearing listeners at different signal strengths and measures weighting strategies using trials that contain no signal stimuli (e.g., catch trials) and using trials that contain signals of varied strengths.

II. METHODS

A. Stimuli

Standard stimuli were the sum of six, equal-amplitude, simultaneously presented tones ranging from 700 to 4000 Hz, spaced equidistantly on a logarithmic scale, rounded to the nearest fourth hertz, and presented at three stimulus levels in different conditions: 35, 60, and 85 dB SPL per component. Signal stimuli were generated by increasing the level of the three high-frequency components by ΔL dB (up components) and decreasing the level of the three low-frequency components by ΔL dB (down components). However, fol-

lowing convention, the signal strength is described as the mean change in amplitude of the incremented components with respect to the standard components in decibels [signal re: standard, dB; $20 \log(\Delta A/A)$; in which ΔA is the change in amplitude introduced by the increment on a standard component with amplitude A]. Each time the stimuli were presented, the starting phase of each tone was selected randomly from a uniform distribution ranging from 0 to 2π rad.

On every presentation of each stimulus, the levels of each component were altered by adding zero-mean deviates, independently drawn from a Gaussian distribution with a standard deviation of 1.5 dB. This amplitude perturbation included a new selection of component levels in each presentation interval, so that the same stimulus was not repeated within a trial. Overall levels were not randomly varied, unlike in many profile-analysis experiments.

B. Procedure

Stimuli were generated digitally and played by a 16-bit digital-to-analog converter (TDT RP2.1) at a sampling rate of 24 414 Hz. Stimuli were presented to the right earphone of a Sennheiser HD 250 II Linear headset to listeners seated in a double-walled, sound-attenuated booth. The total duration of each stimulus was 250 ms, including 30 ms cosine squared rise/decay ramps. The inter-stimulus interval duration was 450 ms. A two-alternative forced-choice procedure was used in which the signal stimulus occurred in either the first or the second interval with equal probability. Listeners responded via a button box.

Listeners were presented with trials in which signal stimuli were generated at five different signal strengths in 2.5 dB steps in an attempt to sample the psychometric function. The values of signal strengths in signal re: standard (dB) used for each listener are reported in the legend of Fig. 5. For each listener, the same signal strengths were used at each stimulus level with one exception: For Obs. 5, the lowest signal strength tested at 60 and 85 dB per component was −17 dB whereas at 35 dB per component, it was one step size higher, at −14.5 dB. On 1/6 of the trials, referred to as no-signal trials, both intervals contained standard stimuli. Listeners were presented with eight trials at each of the six signal strengths (five strengths containing signal-present trials and the one strength containing no-signal trials) in random order, for a total of 48 trials per block. When trials contained signal stimuli, four of the eight trials had the signal stimulus presented in the first interval and four had the signal stimulus presented in the second interval. On these trials listeners received correct-answer feedback. On the no-signal trials feedback was provided with a randomly chosen signal interval.

C. Observers and order of data collection

Five experienced observers, ranging in age from 19 to 48 years, participated. All observers had pure tone audiometric thresholds of 15 dB HL or less at frequencies ranging from 250 through 8000 Hz in octave intervals. The right ear was tested for four of the five listeners, as one listener's right ear (Obs. 2) did not meet the inclusion criterion, and the left ear was tested instead.

Prior to beginning experimental data collection, listeners were given two to six hours of practice to obtain familiarity with the task and to establish the signal strengths used for data collection. Once the signal strengths were selected, data collection followed a randomized block design in which a stimulus level (35, 60, or 85 dB SPL per component) first was chosen at random. Within the blocks of trials at a given stimulus level, the six signal strengths were presented in random order eight times for a total of 48 trials. Listeners were tested on ten blocks of 48 trials before a new stimulus level was chosen randomly. Thus, 80 trials at each signal strength (10 blocks × 8 replicates) were tested at one stimulus level before a new level was selected. After ten blocks were run for each of the three stimulus levels, ten more blocks at each stimulus level were run with the stimulus levels in reverse order. This process was repeated twice more such that data were collected from 60 blocks at each stimulus level (60 blocks × 48 trials = 2880 discriminations per level) for four of the listeners. Obs. 3 withdrew from the experiment early, and therefore only 54 blocks at 35 and 85 dB per component and 51 blocks at 60 dB per component were collected.

D. Weighting functions

A weighting analysis describing the relative contribution of each component to a decision statistic was carried out using the following procedure. For each trial, the level difference per component in dB (imposed by the random perturbations) between Intervals 1 and 2 was determined (not including the signal strength). Trials were sorted according to the stimulus level and signal strength tested, yielding 480 trials per condition. Following the procedure used by Lentz and Leek (2003), the 480 trials were divided randomly into 10 subgroups with 48 discriminations each. Note that because Obs. 3 withdrew from the experiment early, only 8 or 9 subgroups were obtained from her data. For each subgroup, the point biserial correlation coefficient between the level differences and the responses (interval 1 or interval 2) was computed. Weighting functions (plots of correlation versus component frequency), one per stimulus level and signal strength for a total of 18 different weighting functions per listener (3 stimulus levels × 6 signal strengths), are reported.

In the following results section, weighting functions are reported in one of two ways. When the effects of stimulus level are being evaluated and weighting functions are estimated from no-signal trials only, the functions are not normalized because these trials did not contain a spectral change that could alter the magnitude of the correlation. Thus, no-signal weighting functions contain no bias introduced by the presence of the spectral change on the signal stimulus. For the trials in which signal stimuli are present, the presence of the spectral change on the stimuli leads to a decrease in the correlation associated with an increase in the strength of the signal [see Dai *et al.* (1996) for a derivation]. To remove the confound of the decrease in correlation associated with an

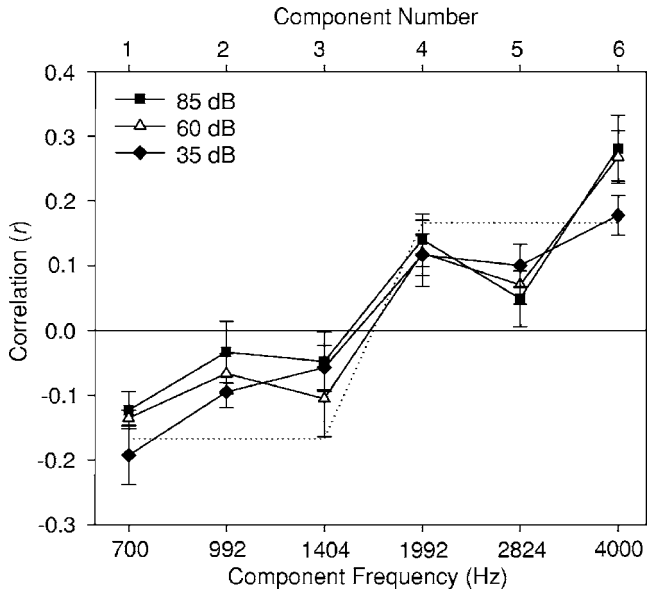

FIG. 1. Average correlations are plotted as a function of component frequency for three stimulus levels. Error bars indicate the standard errors of the mean across five listeners. The dotted line represents the optimal weighting function, within a constant of proportionality.

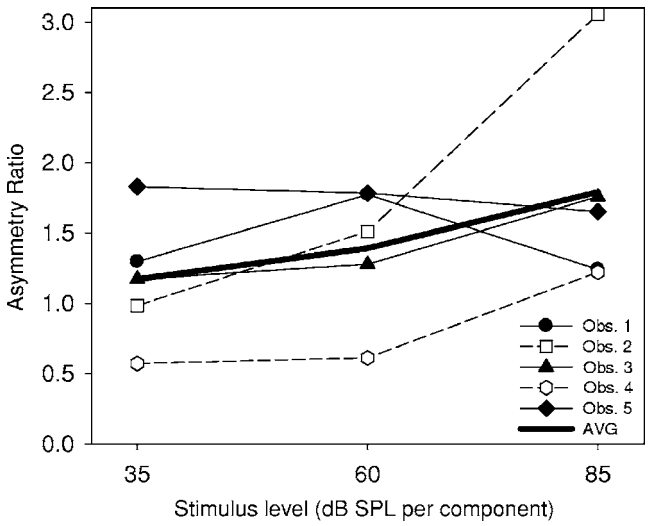

FIG. 2. Asymmetry ratios are plotted as a function of stimulus level for the five observers.

increase in signal strength, each weighting function is normalized by dividing the obtained correlation coefficient by the sum of the absolute values of the correlations obtained from all six components ($r_{i,\mathrm{norm}}=r_i/\Sigma_{i=1}^{6}|r_i|$, where $r_{i,\mathrm{norm}}$ is the normalized weight and r_i is the correlation obtained for the ith component). This normalization is equivalent to the normalization applied by Doherty and Lutfi (1996) in their intensity-discrimination task ($\Sigma\alpha_i=1$).

III. RESULTS

A. Effects of stimulus level on weighting functions

1. Main findings

Mean weighting functions (plots of correlation versus frequency) obtained from the no-signal trials and averaged across listeners are plotted in Fig. 1. Correlations obtained at 35, 60, and 85 dB per component are plotted as the filled diamonds, unfilled triangles, and filled squares, respectively. Error bars represent the standard errors of the mean across the five listeners. The optimal decision strategy (within a constant of proportionality) is also indicated on Fig. 1 as the dotted line. These no-signal functions reflect the weights obtained from no-signal trials within the context of many signal strengths.

A repeated-measures ANOVA treating component frequency and stimulus level as within-subjects measures reveals a main effect of stimulus level [$F(2,8)=7.28; p<0.02$] and component frequency [$F(5,20)=17.55; p<0.001$]. Signal strength is not included as a within-subjects measure because this ANOVA reports only effects from the no-signal subset of data. The main effect of frequency indicates that the correlations differ across frequency. The main effect of stimulus level reflects a difference in the sum of correlations across frequency with changes in stimulus level. To better observe this level-dependent asymmetry, an asymmetry ratio, in which the ratio of the mean of the absolute values of the high-frequency correlations to the mean of the absolute values of the low-frequency correlations ($|\overline{r_{\mathrm{high}}}|/|\overline{r_{\mathrm{low}}}|$), is determined. Asymmetry ratios that equal 1.0 reflect no asymmetry in the weighting function. That is, the high- and low-frequency components contribute equally to the decision variable. Values greater than 1.0 reflect high-frequency components being more heavily weighted than low-frequency components, and values less than 1.0 indicate the reverse. The asymmetry ratios are plotted in Fig. 2 for all five listeners as a function of stimulus level with the averaged asymmetry ratio indicated by the dark, solid line.

Figure 2 indicates that as a rule, the asymmetry ratio is typically greater than 1.0 (with three exceptions: Obs. 2 and 4 at 35 dB and Obs. 4 at 60 dB). The average asymmetry ratio greater than 1.0 indicates that the high-frequency (up) components play a greater role in the decision variable than the low-frequency (down) components. The asymmetry ratio of 1.17 at 35 dB reflects the smallest bias toward the high-frequency components of the three weighting functions, whereas the 85 dB function indicates the greatest bias toward the high-frequency components (asymmetry ratio=1.79). This progressive increase in the asymmetry ratio indicates a translation of the weighting functions of Fig. 1 upward on the ordinate with increasing stimulus level. This implies that increasing the stimulus level causes the low-frequency (down) components to have a diminished contribution to the discrimination decision.

No significant interaction between component frequency and stimulus level is revealed in the weighting functions of Fig. 1 [$F(10,40)=1.38; p=0.22$]. Therefore, the general pattern of weights across frequency is not influenced by stimulus level. In other words, the weighting functions are only being translated upward on the ordinate with increasing stimulus level and no changes to the shape of the weighting functions are evident across stimulus levels.

Two particular results of the current experiment are of interest. (1) On average, the weighting functions contain a bias toward the high-frequency (or incremented) compo-

nents, regardless of stimulus level. (2) The bias toward the high-frequency components in the weighting function increases with increasing stimulus level. With the current experimental design, it is unclear whether the bias in the weighting functions indicates that the high-frequency components have greater weight than low-frequency components or whether the up components have the greater weight. First, high-frequency components (the components around and above 2000 Hz) might play a greater role at all stimulus levels because equal-loudness contours indicate that they are perceived as louder than the low-frequency components (Fletcher and Munson, 1933). Perhaps listeners tend to give greater weight to the components that are perceptually more salient. Yet, equal loudness contours do not indicate that there are significant differences in the relative loudness of the frequencies tested here at different stimulus levels. Subsequently, differences in the relative loudness across frequency at various stimulus levels are unlikely to account for the observed increase in bias at high stimulus levels. Second, as observed by Ellermeier (1996), spectral-shape discrimination sensitivity to decrements is poorer than sensitivity to increments due to masking by adjacent components for frequency ratios less than 2.0. Thus, one possible explanation for asymmetry ratios greater than 1.0 is that the up components contribute more to the discrimination decision than the down components. Poorer frequency selectivity at higher stimulus levels could cause the decrements to contribute even less to the decision.

2. Source of bias in weighting functions

A follow-up experiment was conducted to establish whether the bias in the weighting functions is due to the high frequencies or to the up components. In this experiment, standard stimuli were the same as described in the main experiment, but two types of signal stimuli were used. For the down–up signal type, signal stimuli were generated by decreasing the level of the three low-frequency components and increasing the level of the three high-frequency components (i.e., the same stimulus construction in the main experiment). For the up–down signal type, the spectral-shape change was opposite that for the down–up signal type. The signal stimuli were generated by increasing the level of the three low-frequency components and decreasing the level of the three high-frequency components.

Weighting functions were estimated following the same procedure used in the main experiment. Three additional normal-hearing listeners (one being the author) were tested on the up–down and down–up signal types at two stimulus levels (40 and 80 dB SPL per component). However, only 40 blocks of 48 discriminations were collected at each stimulus level (40 blocks $\times$ 48 trials = 1920 discriminations per level). The first 10 blocks were counted as practice, while the last three blocks were used for estimating the weighting functions, yielding a total of 240 discriminations for each stimulus type, level, and signal strength combination.

No-signal weighting functions obtained from each observer exhibited large variability across the multiple estimates of the correlation coefficient. Therefore, rather than reporting weights based on no-signal stimuli, the reported weighting functions are those obtained using the full data set: 240 discriminations $\times$ 6 signal strengths (1440 total trials). To calculate these weighting functions, individual weighting functions at the different signal strengths were determined and then normalized. Final weighting functions reflect normalized weighting functions averaged across signal strength and across observers for the four conditions (2 stimulus levels $\times$ 2 signal types). As will be noted later in this paper, signal strength is not demonstrated to influence the normalized weighting function—thus, in this case, including all of the weighting functions is done to reduce within-observer variability.

The expectations for this follow-up experiment are twofold: If the general bias in the weighting functions (reflected in the asymmetry ratios greater than 1.0) is due to the high-frequency components having a greater weight than low-frequency components, asymmetry ratios [calculated as $(\overline{|r_{\text{high}}|}/\overline{|r_{\text{low}}|})$] should be greater than 1.0 for both up–down and down–up signal types. Further, if the importance of the high-frequency components relative to the low-frequency components increases with increasing stimulus level, the asymmetry ratio should increase with increasing level for both signal types. However, if the general bias in the weighting functions is due to incremented components having a greater weight than decremented components, asymmetry ratios should be greater than 1.0 for the down–up signal type but less than 1.0 for the up–down signal type. Here, weights from the down–up signal type should show an increase in the asymmetry ratio with increasing stimulus level, but weights from the up–down signal should show a further decrease away from 1.0 in the asymmetry ratio with increasing stimulus level. In both cases, the asymmetry ratio should deviate away from 1.0 with increasing stimulus level, but the direction will vary depending on whether the bias is to high-frequency components or incremented components.

Averaged normalized weighting functions for the up–down and down–up signal types are plotted in Fig. 3 in the upper and lower panels, respectively. Weighting functions obtained at 40 dB are indicated by diamonds, and weighting functions obtained at 80 dB are indicated by squares. To facilitate comparisons between the weighting functions obtained for the two signal types, the ordinate is inverted for the up–down signal type. Weighting functions for both signal types look quite similar, despite having different components incremented and decremented in the signal stimuli. At 80 dB, the up–down and down–up weighting functions indicate a large magnitude for the 4000 Hz component. On average, greater magnitude weights are assigned to the high-frequency components than to the low-frequency components with greater asymmetry for the high-frequency components at the higher stimulus level. This result is indicated in Fig. 4, which plots the asymmetry ratios as a function of stimulus level for the two signal types.

Asymmetry ratios for the up–down and down–up signals are plotted using filled symbols connected with solid lines and unfilled symbols connected with dotted lines, respectively, with different symbols indicating the asymmetry ratios obtained from each observer. Averaged asymmetry ratios are indicated by the heavy lines, with solid and dotted lines

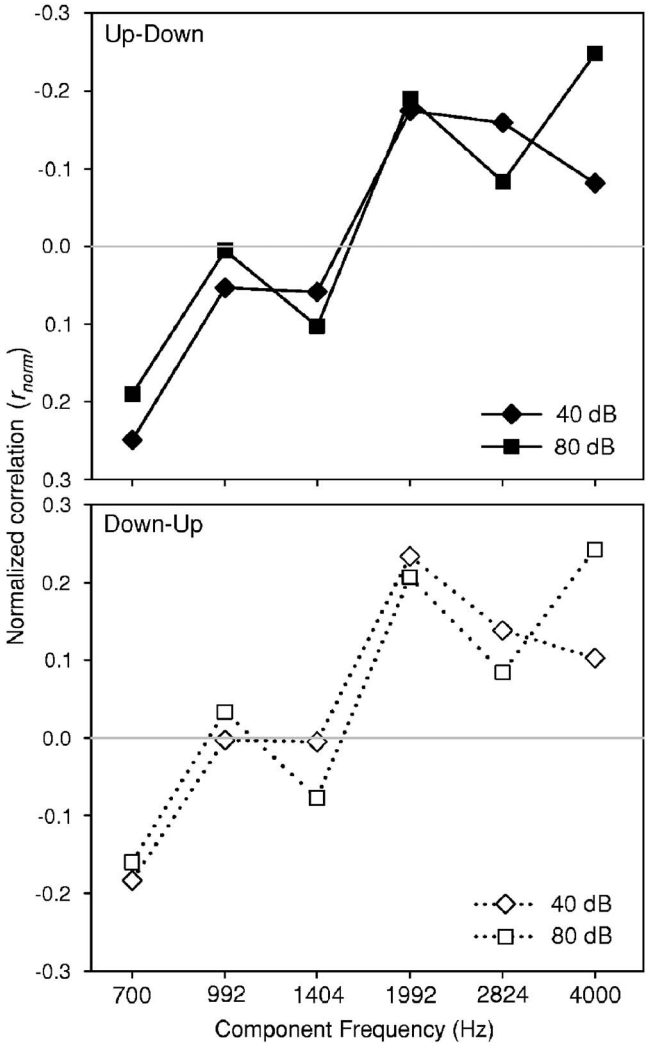

FIG. 3. Normalized weighting functions obtained for the up–down and down–up signal types, averaged across three listeners and signal strengths, are plotted in the upper and lower panels and using filled and unfilled symbols, respectively. Data obtained at 40 dB are indicated by the diamonds and data obtained at 80 dB are indicated by the squares. Note the reversal of the ordinate in the upper panel.

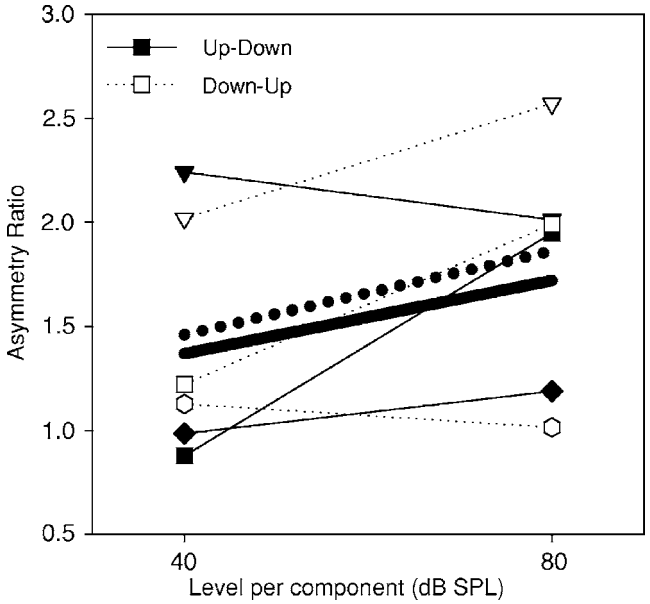

FIG. 4. Asymmetry ratios obtained from three observers for up–down and down–up signal types are plotted as a function of stimulus level. Data obtained from the up–down and down–up signal types are plotted as filled and unfilled symbols connected with solid and dotted lines, respectively. Data obtained from the different observers are indicated using different symbol shapes. Averaged asymmetry ratios are indicated by the heavy lines, with solid and dotted lines corresponding to the up–down and down–up stimulus types.

corresponding to up–down and down–up signal types. Figure 4 indicates that, generally, both signal types have weighting functions in which the high-frequency components are more heavily weighted than low-frequency components because the asymmetry ratio is typically greater than 1.0. This asymmetry is greater for the 80 dB level than for the 40 dB level (average asymmetry ratio of 1.79 at 80 dB versus 1.41 at 40 dB). However, considerable variance across listeners was observed in this experiment with one of the three subjects showing a small decrease in the asymmetry ratio with increasing stimulus level for the down–up signal type (see unfilled hexagons) and another subject showing a decrease in the asymmetry ratio for the up–down signal type (see filled inverted triangles). The variability observed in this sample of observers makes general conclusions across a population of listeners difficult, but there does appear to be a trend of an increasing relative contribution of high-frequency components to the decision variable with increasing stimulus level for both signal types.

3. Interim Summary

One main motivation of this experiment was to determine whether weighting functions were influenced by overall stimulus level. The results indicate that overall level can influence the weighting function and suggest the possibility that the different decision strategies across groups could occur when two groups are tested at different stimulus levels. These differences might be due to an increased relative contribution of the high-frequency components to the decision variable with increasing stimulus level.

To the extent that different stimulus levels lead to different weighting functions within a group, observed differences between groups could go away when the groups are tested at the same stimulus levels. Lentz and Leek (2003) tested spectral-shape discrimination in normal-hearing and hearing-impaired listeners at the same stimulus levels (equated on both sound pressure level and sensation level) and still found subtle differences in the decision strategies adopted by the two groups of listeners. Lentz and Leek (2003) also tested their listeners at different signal strengths. The following analysis evaluates whether signal strength influences spectral-shape discrimination weighting functions.

B. Effects of signal strength on weighting functions

Normalized weighting functions are averaged across stimulus level and plotted for each individual listener in Fig. 5. Individual functions are plotted because individual differences in the shape of the weighting functions are present and because the signal strengths used for each listener differ. In Fig. 5, signal strength is indicated using different symbols; the key to these symbols is indicated in the legend for each

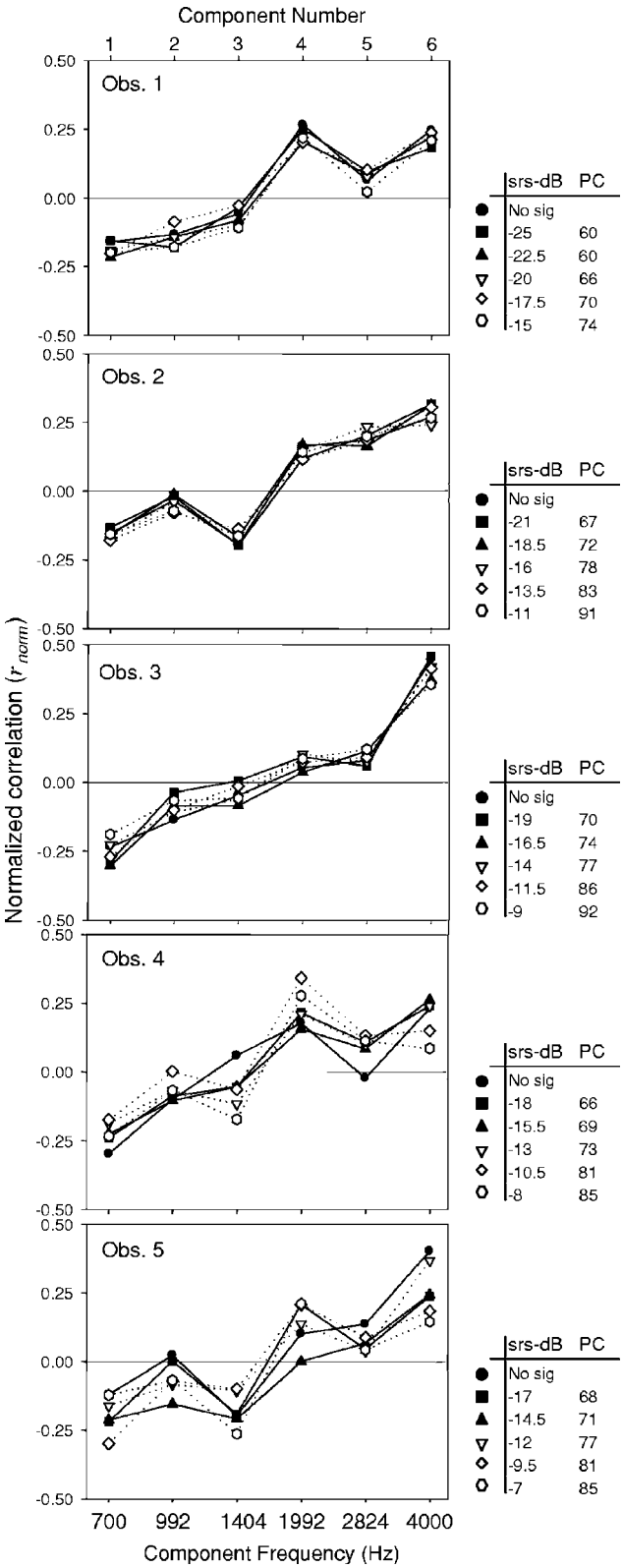

FIG. 5. Individual normalized weighting functions collapsed across stimulus level are plotted for six different signal strengths. The signal strength in signal re: standard units (indicated as srs-dB) at which each weighting function was obtained is indicated by the different symbols in the legend. For reference, the performance (in terms of percent correct) of each listener at those signal strengths is also reported.

listener. Performance (in terms of percent correct) at each of the signal strengths (in signal re: standard dB units) is also reported for reference. Recall that for Obs. 5, data obtained at the lowest signal strength (−17 dB) reflect the average of only the 60 and 85 dB weighting functions because she was not tested at that signal strength when the stimuli were presented at 35 dB per component.

In general, the signal strength tends to have only a small influence on the pattern of weights across frequency. The data obtained from Obs. 1, 2, and 3 show little change in the normalized correlation weights with changing signal strength (all symbols overlap greatly). The data obtained from Obs. 4 and 5 contain greater variability in the pattern of weights across the different signal strengths, and no consistent pattern of changing weighting functions across signal strengths is observed. A repeated-measures ANOVA treating stimulus level, component frequency, and signal strength as within-subjects measures reveals significant main effects of only level $[F(2,8)=9.1; p<0.01]$ and frequency $[F(5,20)=41.9; p<0.001]$. Measures from all variables manipulated in the experiment are included in this ANOVA so that the full data set could be evaluated. The effect of signal strength is not significant nor are any interactions involving signal strength. The absence of a main effect of signal strength or interactions involving signal strength indicates that for normalized weighting functions, signal strength does not influence the weighting functions for the group of listeners tested. Thus, the predictions of the theory of signal detection as outlined in the introduction hold and signal strength does not influence weighting strategies.

Figure 5 also shows variability across listeners in that each of the five listeners adopts a different decision strategy to solve the same task. The individual differences highlight the fact that a number of possible decision strategies could be adopted by normal-hearing listeners. These individual differences could lead to differences in sensitivity depending on whether the strategies are more or less optimal (Berg, 1990). The current data set reflects a only small subset of possible strategies that could be adopted.

IV. DISCUSSION

A. Factors influencing level-dependent weights

The effect of overall level on the weighting strategy is one compelling result of this experiment. At higher overall levels, a general bias in the weighting function is observed, in which higher-frequency components play a larger role in the spectral-shape discrimination decision than lower-frequency components. One way to characterize this bias in the weighting functions is the efficiency measure (η), which describes the degradation of sensitivity relative to the ideal observer. Berg (1990) indicates that one source of efficiency loss can be due to adoption of sub-optimal weights (η_{wgt}). Berg (1990) defines weighting efficiency as $\eta_{wgt}=(d'_{wgt}/d'_{ideal})^2$. When d'_{wgt}, the sensitivity described by the weighting pattern, is similar to the sensitivity described by the ideal weighting pattern, d'_{ideal}, the decision weights approximate the ideal, and consequently, η_{wgt} is high.

To calculate weighting efficiency, d'_{ideal} and d'_{wgt} were estimated at different stimulus levels. d'_{ideal} was obtained by assuming ideal weights ($\alpha_i=1.0$ for incremented components and $\alpha_i=-1.0$ for decremented components) and using Eq. (1)

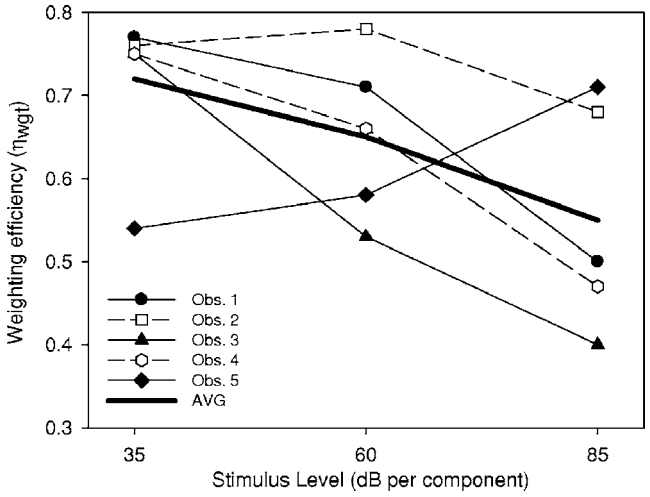

FIG. 6. Weighting efficiency (η_{wgt}) averaged across signal strengths is plotted as a function of stimulus level for each of the five listeners. Averaged weighting efficiency is illustrated by the dark, solid line.

to predict d'. $\Delta\mu_i$ and σ_x are calculated from the signal-present stimuli heard by each individual observer, with $\Delta\mu_i$ varying with signal strength. Thus, five estimates of d'_{ideal} were obtained, one for each signal strength. d'_{wgt} was calculated by using the listener's weights obtained from the signal-present trials as estimates of α_i. The same $\Delta\mu_i$ and σ_x were used as for d'_{ideal}. Weighting efficiency $[\eta_{wgt} = (d'_{wgt}/d'_{ideal})^2]$ was then estimated for each signal strength. A final estimate of weighting efficiency was calculated by averaging the efficiencies across the different signal strengths. Because signal strength ($\Delta\mu_i$) is present in both the numerator and the denominator, it is canceled and is therefore not predicted to influence η_{wgt}.

Figure 6 plots weighting efficiency for each of the original five observers as a function of stimulus level. For four of the five listeners, the weighting efficiency decreases with increasing stimulus level, indicating that increases in stimulus level lead to larger deviations of the weighting strategy from the ideal. A repeated-measures ANOVA treating stimulus level as a within-subjects variable does not show a significant effect of stimulus level on weighting efficiency $[F(2,8)=2.72; p<0.13]$; this result is likely due to a reverse trend (increasing weighting efficiency with increasing stimulus level) in Obs. 2's data. For four of five listeners, then, the bias observed in the weighting functions at increasing stimulus levels tends to lead to an increase in the deviation of the weighting functions from the optimal. Such deviations could occur due to cochlear and central auditory factors. One way to establish whether these deviations might be related to cochlear processing is to relate the weighting strategy at different stimulus levels to excitation patterns generated at different stimulus levels. The following analysis estimates weights based on the excitation pattern and compares the shape of those functions with the weights obtained at each stimulus level.

Using the level-dependent filter bank described by Glasberg and Moore (1990), excitation patterns of the stimuli presented to each observer (perturbed signal and standard stimuli) are generated. Note that only the down–up stimuli from the main experiment are used for this analysis. The filter bank consists of 22 filters with center frequencies separated by 1.2 equivalent rectangular bandwith (ERBs) ranging between 380 and 8700 Hz. Levels of excitation that do not exceed the threshold of audibility are set to the corresponding audibility threshold (dB SPL). For each trial, the change in excitation between signal and standard stimuli is calculated for each filter cf. Decision weights are estimated in the same manner as described in the methods, only the trial-by-trial changes in excitation between signal and standard stimuli are correlated with each listener's responses. In order to compare the decision weights with the change in excitation between signal and standard stimuli, a mean change in excitation is determined for each stimulus level based on only signal-present trials—generating five functions, one for each signal strength. These functions are averaged together to obtain a final mean change in excitation function. This final mean change in excitation is intended to only provide a qualitative comparison to the weighting functions based on the excitation patterns and represents an ideal weighting function based on the excitation pattern.

Averaged weighting functions based on the excitation patterns and averaged weighting functions based on the stimuli are plotted as a function of frequency in Fig. 7 as the filled circles and unfilled squares, respectively. The mean change in excitation across frequency, collapsed across observers and signal strengths, is indicated in Fig. 7 as the dotted line. The three different panels indicate data obtained at different stimulus levels.

As can be seen from Fig. 7, the weighting functions obtained using the stimuli (unfilled squares) and the excitation patterns (filled circles) are quite similar for all stimulus levels tested. Weighting functions obtained at 35 dB do not exhibit large weights at the high frequencies, in contrast to the weights obtained at 60 and 85 dB. Comparing these functions to the change in excitation (dotted lines) provides considerable insight to the high-frequency dependence at the higher stimulus levels. For the low-frequency channels, the change in excitation is relatively consistent across frequency, averaging about −1.5 dB at all stimulus levels with the lowest-frequency bands having little change in excitation due to poor audibility in the low frequencies. However, even at 35 dB, the change in excitation is greater in the high-frequency channels than in the low-frequency channels, averaging about +1.7 dB. The change in excitation in the high frequencies increases with increasing level and, for some frequency channels, approaches +3 dB at the 60 and 85 dB stimulus levels. The frequency channels that have the largest change in excitation tend to be frequency channels near or above the highest frequency in the stimulus. In these cases, the tails of auditory filters at cfs higher than the stimulus frequencies carry a large amount of information regarding the spectral-shape change. Thus, one observes a qualitative agreement between the shapes of the weighting functions (either based on the stimuli or the excitation patterns) and the shape of the function reflecting the change in excitation between signal and standard stimuli. It is likely, then, that the

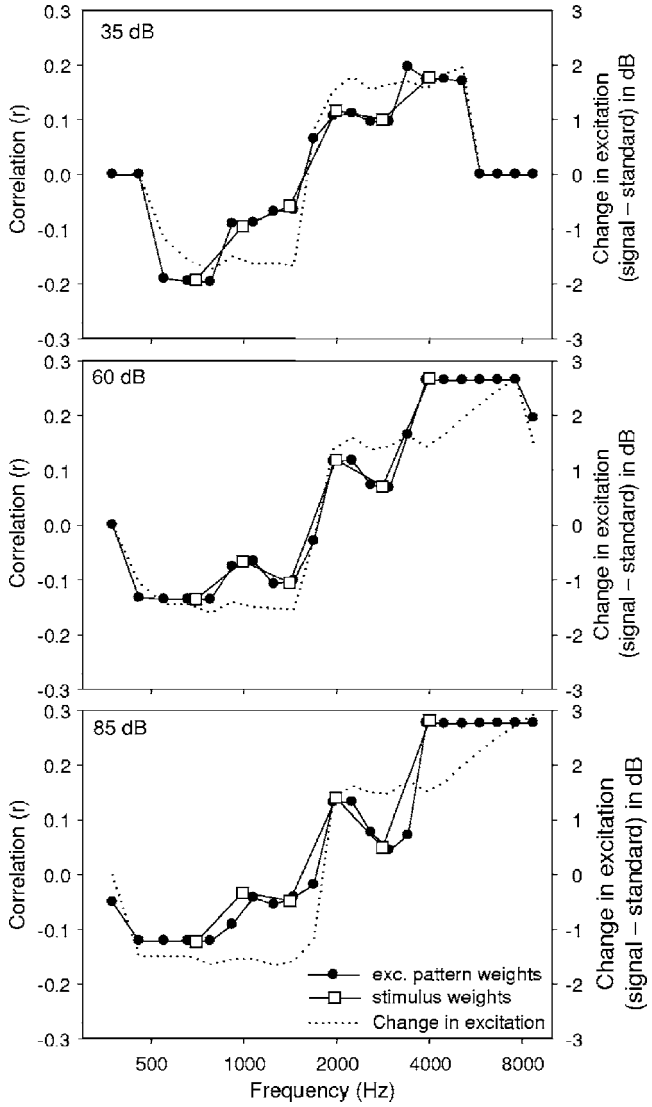

FIG. 7. Averaged weighting functions based on excitation pattern analyses (filled circles) are plotted with the weighting functions based on the stimuli of Fig. 1 (unfilled squares). The dotted lines on each panel indicate the mean change in excitation on signal-present trials between signal and standard stimuli in decibels. Data obtained at 35, 60, and 85 dB are indicted in the upper, middle, and lower panels, respectively.

bias to the high-frequencies at higher stimulus levels is due to the upward spread of excitation and is driven primarily (though not exclusively) by cochlear factors.

It is notable, however, the even though a large change in excitation is observed at 60 and 85 dB in the high-frequency channels, using this high-frequency information comes at a cost in that performance does not vary across stimulus levels. When each observer's psychometric functions (d' versus signal strength) are fitted using a straight line, spectral-shape discrimination thresholds ($d'=1$) averaged across listeners are −13.6, −14.4, and −14.2 dB at 35, 60, and 85 dB, respectively. Various profile-analysis studies have also found the same result (Mason *et al.*, 1984; Green and Mason, 1985; Lentz, 2005). Perhaps using this high-frequency information causes other frequency bands to contribute less to the decision variable. For example, the weight corresponding to the fifth stimulus component (at approximately 2800 Hz) has a smaller weight relative to the sixth component (4000 Hz) at 60 and 85 dB than at 35 dB. Although level-dependent changes in the shape of the weighting functions are not statistically significant, subtle differences in the weighting functions might be present at different stimulus levels leading to the constant spectral-shape sensitivity across stimulus levels. It is also worth noting that the weighting functions do not tend to mirror the large change in excitation in the middle of the spectrum, with the largest weights instead being assigned to the edge components (700 and 4000 Hz).

B. Factors influencing the effects of signal strength

The current experiment illustrated that signal strength did not have a large effect on the spectral-shape weighting functions for the group of listeners tested and that some listeners had much greater variability in their weighting functions than other listeners. One important aspect of this observation is that the weighting functions were normalized in order to eliminate the effects of the spectral change on the magnitude of the correlation. As pointed out by Dai *et al.* (1996) using stimuli different from those used here, the signal strength influences the magnitude of the estimated correlation coefficient. It is important to consider the effects of signal strength when estimating weights because different signal strengths are often presented to different listeners (e.g., Doherty and Lutfi, 1996, 1999; Lentz and Leek 2002, 2003).

Figure 8 illustrates the effects of the signal strength on the weighting functions when correlations are not normalized compared to weighting functions after normalization. Figure 8 plots raw and normalized weighting functions averaged across listeners and stimulus levels in the upper and lower panels, respectively, for the six different signal strengths. Note that because signal strengths varied across listeners, the weighting functions are ordered according to the relative signal strength tested (with S1 through S5 indicating signal strengths ordered from lowest to highest). The lower signal strengths are shown as filled symbols, and higher signal strengths are shown as unfilled symbols.

The upper panel of Fig. 8 shows that signal strength influences the magnitude of the correlation coefficient. Although the effect of signal strength on the correlation coefficient is somewhat small, the largest magnitude correlations tend to be associated with the lowest signal strengths (filled symbols), whereas the correlations nearest zero tend to be associated with the highest signal strengths (unfilled symbols). A repeated-measures ANOVA treating stimulus level, component frequency, and signal strength as within-subjects variables reveals a significant interaction between component frequency and signal strength $[F(25,100)=2.99; p<0.001]$ along with main effects of stimulus level $[F(5,20)=23.42; p<0.001]$ and component frequency $[F(2,8)=11.54; p<0.005]$. The influence of signal strength arises as an interaction because when correlations are negative (e.g., components 1–3), the higher signal strength leads to less negative correlations, whereas when correlations are positive (e.g., components 4–6), the higher signal strength leads to less positive correlations.

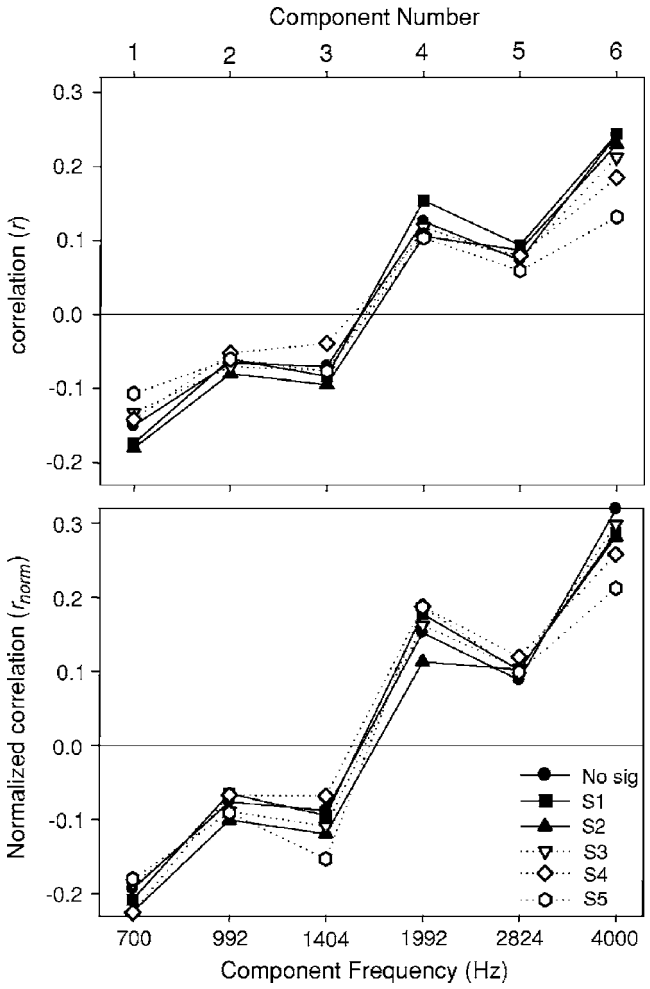

FIG. 8. Average weighting functions collapsed across stimulus level are indicated for six different signal strengths. Raw weighting functions are plotted in the upper panel whereas normalized weighting functions are plotted in the lower panel. Signal strengths are ranked from lowest to highest (from S1 to S5, respectively) and are indicated using different symbols.

The lower panel of Fig. 8 illustrates averaged weighting functions obtained from normalized correlation coefficients. Note that this panel shows data equivalent to averaging the individual data plotted in Fig. 5. The shape of the weighting functions is very similar to those in the upper panel, but there is no consistent effect of signal strength on the magnitude of the normalized correlation. A repeated-measures ANOVA conducted on the normalized data reveals no significant interaction between signal strength and frequency. It can then be argued that differences in the raw weighting functions at the different signal strengths are due to the influence of the signal strength on the estimate of correlation.

Lentz and Leek (2003) estimated spectral-shape weighting functions for normal-hearing and hearing-impaired listeners using different signal strengths between the two groups. Lentz and Leek (2003) did not normalize their weighting functions because the correlation coefficients might have led to a more sensitive measure of differences in sensitivity between the two groups that were not apparent in their threshold measures. Their experiment was similar to this one, in which a spectral-shape change was imposed by decreasing the level of three components and increasing the level of three components of a six component stimulus. Lentz and Leek (2003) noted that the weighting functions for the normal-hearing listeners tended have the largest weights at the edge of the spectral change (i.e., the third and fourth components), whereas the hearing-impaired weighting functions tended to have the largest weights at the edge of the stimulus (i.e., the first and sixth components). Whether those differences were due to the different signal strengths or to differences in the weighting strategy was not determined.

To assess whether the conclusions of Lentz and Leek (2003) could have been due to the different signal strengths across groups, their data are re-analyzed using normalized correlations. A repeated-measures ANOVA indicates that all significant effects related to group are no longer significant. This result suggests that the observed differences between the groups were due to the slightly higher signal strengths used for the hearing-impaired group compared to the strengths used for the normal-hearing group. This reanalysis of Lentz and Leek's results indicates that perhaps spectral-shape discrimination sensitivity is poorer for hearing-impaired listeners than for normal-hearing listeners, but that the pattern of weights across frequency is not altered by hearing loss.

Lentz and Leek (2003) also note that variability in weighting strategy was present across and within groups, a result that is also revealed in this experiment within a normal-hearing group. Although all listeners in this experiment adopt a decision strategy that is globally similar to the other listeners (negative weights for down components and positive weights for up components), the specific shape of the weighting function varies widely across the five individual listeners. In this experiment, decisions require only a single component for discrimination because roving levels are not present to compel comparisons of at least two spectral components. However, data obtained from all listeners indicate comparisons of at least one incremented and one decremented component, indicating that the spectral shapes of signal and standard stimuli are indeed being compared. One listener primarily uses only two of the components (Obs. 3), whereas other listeners tend to use four or five of the components.

From the current data set, it is not clear what drives the selection of the final decision strategy. Perhaps the specific amplitude perturbation values presented to a listener early in the experiment lead listeners to adopt a particular decision strategy, and listeners do not refine their strategy throughout the experiment to maximize performance. Alternative explanations could be related to limited attention of listeners—if only a limited number of across-frequency comparisons can be made, suboptimal decision strategies must always be adopted when the number of stimulus components exceeds the number of possible comparisons that can be made. This idea is supported by results of Berg and Green (1992) who demonstrate that weighting strategies tend to be closest to optimal when the discrimination is very simple. More complex spectral-shape discriminations tend to lead to weighting strategies that deviate more from the optimal strategy. Re-

gardless of the source of the across-observer variability, individual differences pose an interesting problem for comparing decision strategies across two populations of listeners.

V. SUMMARY AND CONCLUSIONS

This study suggests that differences in stimulus level and perhaps signal strength can influence weighting functions. It is recommended that further research evaluating weighting strategies between two groups of listeners be made using similar levels and signal strengths for two groups when possible. Testing multiple groups at different stimulus levels potentially poses a problem for interpreting the data, as it has been demonstrated here that weighting functions vary when collected in the same listeners at different stimulus levels. However, it is not always feasible to test two groups of listeners at the same stimulus levels. In such cases, models of auditory processing could be coupled with the weighting analysis to elucidate the mechanisms responsible for potential differences in weighting functions.

Testing two groups at different signal strengths might be less of a problem because, on the whole, signal strength does not affect weighting strategy (when weights are normalized), but variability in the estimated weighting function within an individual listener's data could be present. Thus, to ensure that signal strength cannot influence the measurement of weighting functions, better methodological alternatives for collecting weighting data might be to use a two-alternative forced choice task in which weights are estimated using catch trials interleaved among signal-present trials [described by Dai *et al.* (1996) and implemented here], or to use a yes-no task and estimate the weights using only the signal-absent trials (Richards and Tang, 2006). Weighting functions obtained using both of these methods are not influenced by signal strength, as the weights are obtained using trials in which no signal is presented.

ACKNOWLEDGMENTS

This work was supported by Grant No. DC 005825 from the National Institute on Deafness and Other Communication Disorders. The author thanks Melissa Ferrello, Deanna S. Rogers, and Melissa Woods for assistance during data collection. Dr. Larry Humes, Dr. Virginia Richards, and two anonymous reviewers provided very helpful comments on the manuscript.

Berg, B. G. (**1989**). "Analysis of weights in multiple observation tasks," J. Acoust. Soc. Am. **86**, 1743–1746.
Berg, B. G. (**1990**). "Observer efficiency and weights in a multiple observation task," J. Acoust. Soc. Am. **88**, 149–158.
Berg, B. G., and Green, D. M. (**1990**). "Spectral weights in profile listening," J. Acoust. Soc. Am. **88**, 758–766.
Berg, B. G., and Green, D. M. (**1992**). "Discrimination of complex spectra: Spectral weights and performance efficiency," *Auditory Physiology and Perception*, edited by Y. Cazals, L. Demany, and K. Horner (Pergamon, Oxford), pp. 373–379.
Dai, H., Nguyen, Q., and Green, D. M. (**1996**). "Decision rules of listeners in spectral-shape discrimination with or without signal-frequency uncertainty," J. Acoust. Soc. Am. **99**, 2298–2306.
Doherty, K. A., and Lutfi, R. A. (**1996**). "Spectral weights for overall level discrimination in listeners with sensorineural hearing loss," J. Acoust. Soc. Am. **99**, 1053–1058.
Doherty, K. A., and Lutfi, R. A. (**1999**). "Level discrimination of single tones in a multitone complex by normal-hearing and hearing-impaired listeners," J. Acoust. Soc. Am. **105**, 1831–1840.
Durlach, N. I., Braida, L. D., and Ito, Y. (**1986**). "Towards a model for discrimination of broadband signals," J. Acoust. Soc. Am. **80**, 63–72.
Ellermeier, W. (**1996**). "Detectability of increments and decrements in spectral profiles," J. Acoust. Soc. Am. **99**, 3119–3125.
Fletcher, H., and Munson, W. A. (**1933**). "Loudness, its definition, measurement and calculation," J. Acoust. Soc. Am. **5**, 82–108.
Glasberg, B. R., and Moore, B. C. (**1990**). "Derivation of auditory filter shapes from notched-noise data," Hear. Res. **47**, 103–138.
Green, D. M. (**1988**). *Profile Analysis: Auditory Intensity Discrimination* (Oxford University Press, New York).
Green, D. M., and Berg, B. G. (**1991**). "Spectral weights and the profile bowl," Q. J. Exp. Psychol. A **43**, 449–458.
Green, D. M., and Mason, C. R. (**1985**). "Auditory profile analysis: Frequency, phase, and Weber's law," J. Acoust. Soc. Am. **77**, 1155–1161.
Lentz, J. J. (**2005**). "Profile analysis: the effects of rove on sparse spectra," J. Acoust. Soc. Am. **118**, 2794–2797.
Lentz, J. J., and Leek, M. R. (**2002**). "Decision strategies of hearing-impaired listeners in spectral shape discrimination," J. Acoust. Soc. Am. **111**, 1389–1398.
Lentz, J. J., and Leek, M. R. (**2003**). "Spectral shape discrimination by hearing-impaired and normal-hearing listeners," J. Acoust. Soc. Am. **113**, 1604–1616.
Lutfi, R. A. (**1995**). "Correlation coefficients and correlation ratios as estimates of observer weights in multiple-observation tasks," J. Acoust. Soc. Am. **97**, 1333–1334.
Mason, C. R., Kidd, G., Jr., Hanna, T. E., and Green, D. M. (**1984**). "Profile analysis and level variation," Hear. Res. **13**, 269–275.
Richards, V. M., and Tang, Z. (**2006**). "Estimates of effective frequency selectivity based on the detection of a tone added to complex maskers," J. Acoust. Soc. Am. **119**, 1574–1584.
Richards, V. M., and Zhu, S. (**1994**). "Relative estimates of combination weights, decision criteria, and internal noise based on correlation coefficients," J. Acoust. Soc. Am. **95**, 423–434.

Speech segregation in rooms: Effects of reverberation on both target and interferer

Mathieu Lavandier[a] and John F. Culling
School of Psychology, Cardiff University, Tower Building, Park Place, Cardiff, CF10 SAT, United Kingdom

(Received 3 April 2007; revised 4 June 2007; accepted 27 June 2007)

Speech reception thresholds were measured to investigate the influence of a room on speech segregation between a spatially separated target and interferer. The listening tests were realized under headphones. A room simulation allowed selected positioning of the interferer and target, as well as varying the absorption coefficient of the room internal surfaces. The measurements involved target sentences and speech-shaped noise or 2-voice interferers. Four experiments revealed that speech segregation in rooms was not only dependent on the azimuth separation of sound sources, but also on their direct-to-reverberant energy ratio at the listening position. This parameter was varied for interferer and target independently. Speech intelligibility decreased as the direct-to-reverberant ratio of sources was degraded by sound reflections in the room. The influence of the direct-to-reverberant ratio of the interferer was in agreement with binaural unmasking theories, through its effect on interaural coherence. The effect on the target occurred at higher levels of reverberation and was explained by the intrinsic degradation of speech intelligibility in reverberation. © *2007 Acoustical Society of America.* [DOI: 10.1121/1.2764469]

PACS number(s): 43.66.Pn, 43.66.Dc, 43.55.Hy, 43.71.Gv [RYL] Pages: 1713–1723

I. INTRODUCTION

Studies of the cocktail party problem investigate the fact that we can understand what a person is saying when many others around are talking at the same time. A difference in fundamental frequency (Brokx and Nooteboom (1982); Culling and Darwin (1993); Darwin and Culling (1990)) and an azimuth separation of sources (Hawley *et al.* (2004); Plomp (1976)) are both well-established cues helping the segregation of competing voices. The latter effect is termed spatial release from masking or spatial unmasking: an interfering sound masks less efficiently when it is spatially separated from the target speech. Spatial unmasking in anechoic situations results from two cues (Bronkhorst and Plomp (1988)). The first cue is monaural and called head shadow. When the interferer is moved around the listener's head, its sound level is reduced at the ear which is in the acoustic shadow of the head for the given interferer position. The signal-to-noise ratio between target and interferer can be improved at this ear, and this monaural information helps the listener to better understand the target. The second cue, sometimes called binaural interaction, is caused by interaural time delays (ITDs). The azimuth separation of interferer and target induces a difference in ITDs for these two sources, thus facilitating their segregation.

Reverberation and sound reflections in rooms influence both speech intelligibility in quiet and the segregation of speech from interfering sounds. In quiet, the target intelligibility is decreased by the sound reflections mixing with the direct sound. Some objective measurements are already available to predict this intrinsic degradation of speech by reverberation, such as the Speech Transmission Index (Houtgast and Steeneken (1985)) or the useful-to-detrimental ratios (Bradley (1986); Bradley *et al.* (1999)). The room also influences the segregation of speech from interfering sounds, and many experiments have shown that spatial unmasking is reduced by reverberation. Plomp (1976) measured the intelligibility of a speech target against noise or an interfering voice, while varying the interferer's azimuth and the reverberation conditions. The experiment was realized in a room having variable acoustic characteristics, with loudspeakers surrounding the listener. The spatial unmasking observed in the anechoic condition was greatly reduced in reverberation. Bronkhorst and Plomp (1990) measured the Speech Reception Threshold (SRT)—i.e., the level of the target compared to that of the interferer for 50% intelligibility of the target—using a noise interferer and loudspeakers placed at different positions in a reverberant room. They also found that spatial unmasking was reduced in reverberation. Culling *et al.* (2003) measured SRTs under headphones with a speech interferer. They used a room simulation that allowed positioning the interferer and target at chosen positions, as well as varying the absorption coefficient of the room boundaries. The spatial unmasking observed in the anechoic condition was abolished in reverberation. Recently, Beutelmann and Brand (2006) measured SRTs under headphones with a noise interferer, creating their stimuli from binaural impulse responses measured in three different rooms: an anechoic room, a small office and a large cafeteria. Again, the spatial release from masking was reduced in the office and the cafeteria compared to the one obtained in the anechoic room. This effect was also observed in studies concerned with attentional effects and informational masking (Darwin and Hukin (2000); Kidd *et al.* (2005)). Testing the influence of individual echoes rather than full reverberation, Freyman *et al.* (2001, 1999) found that spatial unmasking from a noise interferer was reduced in the presence of an echo. This result

[a]Author to whom correspondence should be addressed. Electronic mail: lavandiermn@cardiff.ac.uk

was confirmed and extended later using different experimental protocols (Brungart *et al.* (2005); Rakerd *et al.* (2006)).

In Beutelmann and Brand (2006), the cafeteria with the largest reverberation time led to larger spatial unmasking than the office, which had only half the reverberation time. This result shows that a simple reverberation time statistic is not sufficient to predict speech segregation in a room, and that a more sophisticated measurement is needed. This measurement will require binaural information, in order to predict the spatial unmasking effects observed with directional interferers.

The aim of the present study was to investigate the influence of the direct-to-reverberant ratio of sources on the masking of speech in rooms, because reductions in direct-to-reverberant ratio result in reduced interaural coherence, which is known to affect binaural unmasking (Licklider (1948); Robinson and Jeffress (1963)). The interaural coherence of a source evaluates the similarity of the sound waveform it produces at the two ears of the listener. It is calculated through taking the maximum value from the interaural cross-correlation function. The multiple sound reflections reaching the listener in a room degrade the interaural coherence of the source. The coherence is thus related to the direct-to-reverberant energy ratio at the ears, and varies depending on the source and listener positions, and on the reverberation characteristics of the room (Hartmann *et al.* (2005)). Our interest in coherence stems from the observation by Licklider (1948) that, for speech and noise signals having different interaural phase differences, speech intelligibility in noise was reduced when the noise was less correlated at the two ears. A similar effect was observed for tone detection in noise (Robinson and Jeffress (1963)). All binaural unmasking theories predict this effect. In the following, we will consider the equalization-cancellation (E-C) mechanism of Durlach (1972) as an example to interpret our results. It predicts that a less correlated masker will be more difficult to equalize at the two ears, and then more difficult to cancel, resulting in lower speech intelligibility or poorer tone detection.

The four experiments presented in this paper considered interferer and target sources in a virtual room. They all involved SRT measurements under headphones, using target sentences and spatially separated speech-shaped noise or 2-voice interferers. The experiments were designed to investigate how the source direct-to-reverberant ratios might influence target intelligibility. Following Licklider's results, we were expecting this intelligibility to be reduced if the interferer direct-to-reverberant ratio and hence its interaural coherence were reduced by the sound reflections in the room. No binaural effect associated with the direct-to-reverberant ratio of the target was expected, but the direct-to-reverberant ratio also affects the intrinsic intelligibility of the target due to temporal and spectral distortions. The experiments enabled us to separate these two effects, and assess their relative roles in overall intelligibility. The interaural coherence/direct-to-reverberant ratio of sources was controlled independently for interferer and target, by varying the source-listener distance or the absorption coefficient of the room internal surfaces.

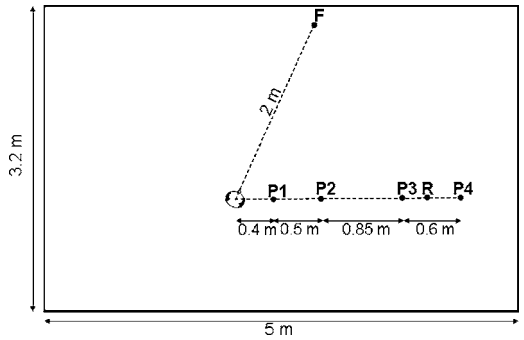

FIG. 1. Spatial configuration and virtual room considered in experiments 1 to 4.

II. GENERAL METHODS

A. Stimuli

1. Convolution by the room

The same virtual room was used in the four experiments. It was simulated using the image (ray-tracing) method presented by Allen and Berkley (1979) and Peterson (1986), as it is implemented in the |WAVE signal processing package (Culling (1996)). The room was 5 m long, 3.2 m wide and 2.5 m high (Fig. 1). The absorption coefficients of the room internal surfaces were all set to the same value, and varied all together when the reverberation condition was changed. The listener was modeled as two ears, separated by 20 cm, placed along an axis at 25° to the 5 m wall on either side of a center point located at 1.2 m from the 5 m wall and 2 m from the 3.2 m wall. The ears were modeled as omnidirectional microphones suspended in space, 1.5 m from the floor, with no head between them. The head was not modeled here, in order to avoid head shadow effects which could complicate the interpretation of the effects associated with interaural coherence. The room and listener were identical to those simulated by Culling *et al.* (2003). The interferer and target were placed 1.5 m from the floor, at different positions in the room, keeping their azimuth separation constant (65°). Binaural stimuli were produced by calculating the impulse responses between the source positions and each ear, and convolving the speech samples with these impulse responses.

The same source stimuli were involved in the four experiments. A male voice was used for the target. This same voice was used to create 2-voice interferers. As we were interested in segregation cues associated with spatial separation of interferer and target, we chose to use the same voice for both sources in order to minimize segregation cues based on between-voice differences in fundamental frequency (F0) register or voice-specific spectral characteristics (Culling *et al.* (2003); Darwin and Culling (1990)). The original corpus of sentences was from the Harvard Sentence List (IEEE (1969)). The recordings of the male voice DA, made at M.I.T. and digitized at 20 kHz with 16 bit quantization, were used as the basis of all stimuli. The sentences have low predictability, and each has five key words highlighted in capitals. For instance, one sentence was "TAKE the WINDING PATH to REACH the LAKE." Noise interferers were also used. They were speech-spectrum noises, which were obtained by filtering Gaussian noises with an finite impulse

response (FIR) filter designed to match the excitation pattern (Moore and Glasberg (1983)) of all 2-voice interferers concatenated. In each experiment, four spatial configurations or reverberation conditions and two types of interferer (noise and 2 voices) were used. Eighty target sentences were used to test the eight resulting conditions. Although only four interferers of each type were needed, eight were used with the intention of reducing the dependence of the results on the particular sentences involved. Listeners only heard four interferers of each type, different ones for different listeners. The order of the conditions was rotated for successive listeners, while sentence materials remained in the same order. Each of the 80 target sentences was thus presented to every listener in the same order and, across a group eight listeners, contributed equally to each condition. This procedure also ensured that each condition was presented in each serial position within the experimental session, counterbalancing order effects.

2. Sound level equalization

The root mean square power of source stimuli was initially equalized, but the convolution by the room impulse responses might change the signal levels differently depending on the positions used within the room and the ear considered (Bradley *et al.* (1999, 2003); Yang and Hodgson (2006)). Using stimuli equalized before the convolution by the room places control of the target-to-interferer level ratio at the emission of sound sources. The influence of the room on sound levels of interferer and target would then be included in the measured SRTs. Our experiments were intended to investigate the effect of the room-induced interaural coherence changes on SRTs. To avoid mixing the effects of sound level and interaural coherence, all stimuli were equalized in level after convolution by the room impulse responses. Left and right channels were equalized independently, removing potential interaural level differences. The target-to-interferer level ratio was then fixed at the ears.

3. Computations of direct-to-reverberant ratio and interaural coherence

The direct-to-reverberant energy ratio was calculated at each ear, for all source positions and absorption coefficients involved in our experiments. For each tested configuration, the calculation was similar to the one proposed by Zahorik (2002), using the impulse response between the source position and the considered ear. The direct-path and reverberant portions of the impulse response were separated by a time-windowing procedure. This procedure was trivial as our simulated impulse responses were not contaminated by noise. The energy of the direct-path and reverberant portions were computed, and the direct-to-reverberant energy ratio was expressed in dB.

Interaural coherence of each source at the listening position was also calculated for each experiment. It was computed as the maximum of the absolute value of the cross-correlation of the waveforms reaching the two ears from the source (Hartmann *et al.* (2005)). These waveforms were filtered between 20 and 1500 Hz prior to calculation, in order to consider only the frequency range for which binaural unmasking is most effective in broadband noise.

B. SRT measurements

SRTs were measured using a 1-up/1-down adaptive threshold method (Plomp and Mimpen (1979)). For each SRT measurement, ten target sentences were presented one after another, each one against the same interferer. For the 2-voice interferers, the sentences corresponding to the interferer were displayed on a computer screen in front of the listeners while they were listening. They were instructed to disregard these sentences, and to listen to the target sentence, not displayed on the screen. The target-to-interferer level ratio was initially very low (−32 dB). On the first trial, listeners could either enter a transcript on a computer keyboard, or replay the stimuli. If stimuli were replayed, the target level was increased by 4 dB. Stimuli could be replayed in this way until the target was loud enough to be judged partially intelligible. Listeners were instructed to attempt a transcript of this first target sentence when they believed that they could hear more than half the words of the sentence. Once the first transcript was entered, the correct transcript was displayed on the computer terminal, with the five key words in capitals. The listener self-marked the number of correct key words. Subsequent target sentences were presented only once, and self-marked in a similar manner. The target level was decreased by 2 dB if the listener correctly identified three or more of the five key words in the previous sentence, and otherwise increased by 2 dB. The SRT for a given condition was taken as the mean target-to-interferer level ratio on the last eight trials. Each SRT measurement corresponded to a different tested condition, and used a different interferer. The session began with two practice runs, using monaurally presented and unprocessed speech, in order to familiarize listeners with the task. The following eight runs measured SRTs in each of the eight different conditions.

Signals were digitally mixed, digital/analog converted, and amplified using a 24 bit Edirol UA-20 sound card and a MTR HPA-2 Headphone Amplifier. They were presented to listeners over Sennheiser HD650 headphones in a single walled IAC sound-attenuating booth within a sound-treated room. A computer terminal screen was visible outside the booth window. A keyboard was inside the booth to gather the transcripts of listeners.

C. Participants

Twenty-four listeners took part in each experiment. They were undergraduate students, paid for their participation. None of them was familiar with the sentences used during the test. All listeners reported normal hearing and English as their first language. Each listener participated in a single 50 min session, and in only one of the following experiments.

III. DISTANCE OF THE INTERFERER (EXP. 1)

SRTs were measured for spatially separated interferers and targets which always had the same azimuth separation, but with the interferer tested at different positions in the

TABLE I. Direct-to-reverberant ratio (D/R) at each ear, for the source at the positions tested in experiments 1 and 3, and an absorption coefficient of 0.5

Position[a]	P1	P2	P3	P4
D/R ratio, left ear (dB)	7.95	1.88	−2.74	−5.04
D/R ratio, right ear (dB)	11.29	3.02	−2.32	−4.79

[a]D/R ratio at position F (dB): left ear=−4.31, right ear=−4.39.

room. These positions were chosen so that they led to different values of direct-to-reverberant ratio and interaural coherence at the listener position.

A. Design

Only one reverberation condition was considered: an absorption coefficient of 0.5 was used for every room surface. Figure 1 presents the positions considered within the room. The position F was in front of the listener, at 2 m from the center of the ears. In experiment 1, the target was always at position F. The interferer was at one of the positions P1, P2, P3 or P4, all having the same azimuth. These four positions were situated along a line parallel with the 5 m wall passing through the center of the ears, at 0.4, 0.9, 1.75, and 2.35 m from this center. Table I shows that the direct-to-reverberant ratio at the listening position decreased as the source was moved from P1 to P4.

As stated above, positions P1, P2, P3 and P4 were chosen to produce different values of interaural coherence at the listening position. The coherence was calculated for the 80 target stimuli at position F and the eight interferers of each type at the four tested positions. Table II presents the mean coherence for each type of stimulus. Interaural coherence decreased as the interferer was placed further away from the listener, in the reverberant field. These sampled locations reflect the tendency for coherence to decrease with source distance, although the function is not completely monotonic (Hartmann *et al.* (2005)). The interaural coherence of a source seems to depend on its exact position relative to the listener and the room boundaries.

SRTs were measured in eight conditions: two types of interferer (noise and 2 voices) and four interferer positions (P1, P2, P3 and P4).

B. Results

Figure 2 presents the mean SRTs obtained in experiment 1, for noise or 2-voice interferers at positions P1, P2, P3 or P4; the target being always at position F (Fig. 1). For both types of interferer, SRTs increased as the interferer was moved away from the listener, from P1 to P4, with a 2 dB effect between these two extreme positions. An analysis of variance (ANOVA) showed that only the main effect of interferer position was significant [$F(3,69)=9.5, p<0.0001$]. Tukey pairwise comparisons confirmed that only SRTs involving position P1 were significantly different from SRTs involving the three other positions [$q>4.5, p<0.01$ in each case].

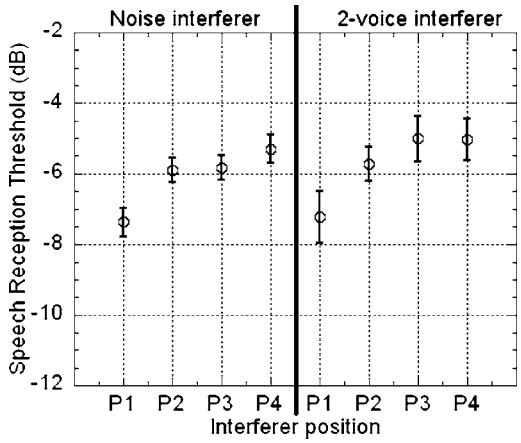

FIG. 2. Mean SRTs with standard errors measured in experiment 1 for noise or 2-voice interferers at positions P1, P2, P3 or P4; the target being always at position F (Fig. 1).

TABLE II. Mean interaural coherence with standard deviation for each type of interferer in experiment 1.

	Interferer mean coherence[a]	
Interferer position	Noise (Std dev.)	2 voices (Std dev.)
P1	0.95 (0.00)	0.95 (0.01)
P2	0.86 (0.00)	0.86 (0.00)
P3	0.77 (0.01)	0.77 (0.04)
P4	0.71 (0.00)	0.71 (0.05)

[a]Target mean coherence: 0.88 (0.03).

C. Discussion

SRTs increased with decreasing interferer coherence (Table II) as the interferer was moved from P1 to P4, in agreement with binaural unmasking theories. For instance, the E-C theory (Durlach (1972)) would predict that, for spatially separated sound sources, the less coherent interferers should be more difficult for the auditory system to cancel, producing less masking release. SRTs measured at positions P2, P3 and P4 were not significantly different. The range of coherence values sampled by our four positions might have been too limited, but these values had to be chosen among those available in the room at a fixed azimuth.

There was no significant difference between noise and 2-voice interferers in this experiment. As our sound sources were always spatially separated (Fig. 1), informational masking produced by the 2-voice interferers was probably minimal (Freyman *et al.* (2001, 1999)).

IV. ABSORPTION COEFFICIENT FOR THE INTERFERER (EXP. 2)

In order to test a broader range of interaural coherence than in experiment 1, a new experimental design was chosen for experiment 2. SRTs were measured for spatially separated interferer and target at fixed positions. The different interferer coherences were obtained by applying different reverberation conditions to this source, while the reverberation condition of the target was kept constant. This experimental design is not realistic as it implies listening simultaneously to two sources in rooms having different reverberation charac-

TABLE III. Direct-to-reverberant ratio (D/R) at each ear, for the source at position R and the absorption coefficients tested in experiments 2 and 4.

Absorption coeff.[a]	1	0.7	0.5	0.2
D/R ratio, left ear (dB)	∞	0.54	−3.70	−10.93
D/R ratio, right ear (dB)	∞	0.78	−3.47	−10.61

[a]D/R ratio at position *F* (dB): left ear=−4.31, right ear=−4.39.

teristics, but it offers the advantage of controlling interferer and target coherences individually, keeping distances and azimuth separation constant.

A. Design

Room dimensions and listener position were the same as in experiment 1, and position F was also unchanged (Fig. 1). The position R was considered. It was situated at the same azimuth as positions P1–P4 in experiment 1, on the parallel of the 5 m wall passing through the center of the ears, but at 2 m from this center, between P3 and P4. In experiment 2, the target was always at F, and the interferer at R. While computing the impulse responses between the sources and each ear, different absorption coefficients were used for the two sources. The absorption coefficient was the same for each room surface. For the target, it was set to 0.5 as in experiment 1. However, four absorption coefficients were tested for the interferer: 1, 0.7, 0.5 and 0.2. Table III shows that the direct-to-reverberant ratio at the listening position decreased with the absorption coefficient used. Interaural coherence of all stimuli was also computed. Table IV presents the mean results for each type of stimulus. The range of coherence values sampled by our four conditions was broader than in experiment 1 (Table II), with mean coherences between 1 and 0.6. As expected, the anechoic room with the absorption coefficient of 1 led to an infinite direct-to-reverberant ratio and a coherence of 1, as there was no sound reflection on the room internal surfaces.

SRTs were measured in eight conditions: two types of interferer (noise and 2 voices) and four reverberation conditions for the interferer (absorption coefficient of 1, 0.7, 0.5 and 0.2).

B. Results

Figure 3 presents the mean SRTs obtained in experiment 2, for noise or 2-voice interferers for the four levels of absorption applied to the interferer. For both types of interferer,

TABLE IV. Mean interaural coherence with standard deviation for each type of interferer in experiment 2.

	Interferer mean coherence[a]	
Interferer absorption coeff.	Noise (Std dev.)	2 voices (Std dev.)
1	1 (0.00)	1 (0.01)
0.7	0.85 (0.00)	0.85 (0.00)
0.5	0.74 (0.00)	0.74 (0.05)
0.2	0.61 (0.01)	0.61 (0.07)

[a]Target mean coherence: 0.88 (0.03).

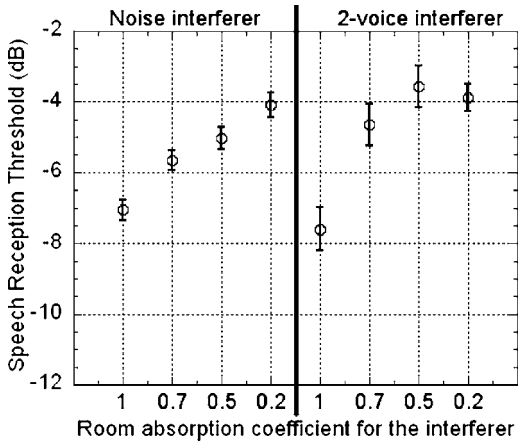

FIG. 3. Mean SRTs with standard errors measured in experiment 2, for noise or 2-voice interferers in the four tested reverberation conditions, with an absorption coefficient of 0.5 used for the target.

SRTs increased as the absorption coefficient for the interferer was decreased, making the room more reverberant for this source. A 3 dB effect was observed between the absorption coefficients 1 and 0.2 with both types of interferer. An ANOVA confirmed that the main effect of the absorption coefficient used for the interferer was significant [$F(3,69)=35.8, p<0.0001$]. Tukey pairwise comparisons showed that the absorption coefficient 1 was significantly different from the three other coefficients [$q>8, p<0.001$ in each case]. The absorption coefficient 0.7 was also significantly different from the coefficient 0.2 [$q=4.65, p<0.01$]. The other differences were not significant. SRTs measured with noise were significantly lower than those obtained with the 2-voice interferer [$F(1,23)=6.0, p<0.05$]. Interferer type and absorption coefficient did not interact significantly.

C. Discussion

As the absorption coefficient used for the interferer was decreased, this interferer produced more masking, leading to higher thresholds. This result is in agreement with the binaural E-C theory: reverberation decreased the interferer interaural coherence (Table IV), and a less coherent interferer was more difficult to cancel, producing less masking release for spatially separated sources. As the range of coherences involved was larger than in experiment 1, the effect was also larger.

The difference between noise and 2-voice interferers was significant. Some informational masking might have been involved, leading to slightly higher SRTs with the 2-voice interferers. This seems particularly so for the absorption coefficients 0.5 and 0.7, although the interaction with absorption coefficient did not reach significance. When the absorption coefficients 1 and 0.2 were used, the 2-voice interferers did not lead to higher SRTs anymore, indicating a potential reduction of informational masking in these two conditions. This reduction in informational masking may have been caused by an additional cue that helped listeners focus their attention on the target voice rather than on the interferer during the listening task. In these conditions there is a difference in the amount of reverberation between the

TABLE V. Mean interaural coherence with standard deviation for the target in experiment 3.

Target position	P1	P2	P3	P4
Target[a] mean coherence	0.95	0.86	0.78	0.72
(Std dev.)	(0.01)	(0.03)	(0.06)	(0.06)

[a]Interferer coherence: noise=0.88 (0.00), 2 voices=0.89 (0.02).

interferer—anechoic (absorption coefficient of 1) or very reverberant (absorption coefficient of 0.2)—and the target—mildly reverberant (absorption coefficient of 0.5).

After having considered the effect of reverberation on the interferer, we turned to its effect on the target. Experiments 3 and 4 used exactly the same protocol as experiments 1 and 2, respectively, but replacing the interferer by the target and vice versa. In these new experiments, the interferer coherence was fixed across conditions, whereas the target direct-to-reverberant ratio was varied. Here, we did not expect any effect of the direct-to-reverberant ratio to be mediated by interaural coherence and degraded binaural processing. Following for example the E-C theory, binaural processing cancels the interferer and not the target. Reducing the coherence of the target and so the ability to cancel it should not play any role. Instead, the Speech Transmission Index (STI) was computed for the conditions tested, to compare our listening test results with the expected intrinsic degradation of target intelligibility in reverberation.

V. DISTANCE OF THE TARGET (EXP. 3)

A. Design

Experiment 3 followed the same protocol as experiment 1. This time the interferer was always at position F, whereas the target was tested at positions P1, P2, P3 and P4 (Fig. 1). The direct-to-reverberant ratios involved are presented in Table I. Interaural coherence of all stimuli was computed. Table V presents the mean results for each type of stimulus.

SRTs were measured in eight conditions: two types of interferer (noise and 2 voices) and four target positions (P1, P2, P3 and P4).

B. Results

Figure 4 presents the mean SRTs obtained in experiment 3 for the target at positions P1, P2, P3 or P4; noise or 2-voice interferers being always at position F (Fig. 1). The results of STI calculations are also plotted along with the measured SRTs. These calculations are described and discussed in a following section of the paper. An ANOVA showed that, for both types of interferer, SRTs increased slightly as the target was moved away from the listener $[F(3,69)=9.4, p<0.0001]$. A 1 dB effect was observed with noise, when the target was moved from P1 to P3. This effect increased to 2 dB with the 2-voice interferers. Tukey pairwise comparisons showed that only position P1 was significantly different from the three other positions $[q>5, p<0.01$ in each case]. The SRT for position P1 was lower with 2-voice interferers

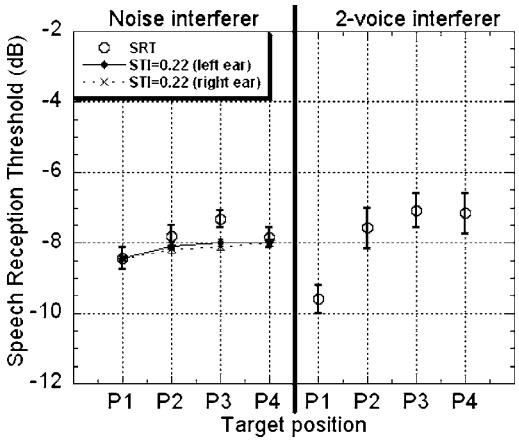

FIG. 4. Mean SRTs with standard errors measured in experiment 3 for the target at positions P1, P2, P3 or P4; the noise or 2-voice interferers being always at position F (Fig. 1). SRTs obtained with the noise interferers are compared to the target-to-interferer ratios required for the STI to be constant across the four conditions (STI=0.22 for the position P1 and a signal-to-noise ratio of −8.46 dB). The STI was computed for each ear separately.

than with noise, but neither the interferer type nor the interaction between interferer type and absorption coefficient were significant.

C. Discussion

SRTs increased with decreasing target direct-to-reverberant ratio (Table I), as the target was moved away from the listener in the reverberant field. This decrease of target intelligibility might be due to the intrinsic degradation of speech intelligibility in reverberation, occurring even when no interferer is involved, as described, for example, by the STI (Houtgast and Steeneken (1985)) or the useful-to-detrimental ratios (Bradley (1986); Bradley *et al.* (1999)). As in experiment 1, SRTs measured at positions P2, P3 and P4 were not significantly different.

Despite neither the interferer type nor the interaction between interferer type and interferer position being significant, the difference of SRTs for the target at P2 and P1 seemed larger with 2-voice interferers than with noise. This might be due to a release from informational masking when the target was moved very close to the listener. The perceived distance of the very close target might have been an attentional cue for listeners (Brungart and Simpson (2002)). Even if sound levels were equalized at the two ears, the direct-to-reverberant ratio of the target was still varying when changing its position within the room. Perceiving the target very close at position P1 could have helped listeners focus their attention on it. This effect, if present, was weak in experiment 3 and did not reach significance.

With the target in position P1, the SRT was lower with 2-voice interferers than with noise. The 2-voice interferers might produce less energetic masking than noise. Listeners could have taken advantage of some remaining silent periods in the masker to hear the target (Dusquesnoy (1983); Festen and Plomp (1990)), even though "listening into gaps" is smaller with 2-voice interferers than it would have been with 1-voice interferers (Bronkhorst and Plomp (1992)). Listeners

TABLE VI. Mean interaural coherence with standard deviation for the target in experiment 4.

Target absorption coeff.	1	0.7	0.5	0.2
Target[a] mean coherence (Std dev.)	1 (0.00)	0.86 (0.04)	0.74 (0.06)	0.62 (0.07)

[a]Interferer coherence: noise=0.88 (0.00), 2 voices=0.89 (0.02).

could have also used instantaneous F0 differences to cancel one of the interfering voices (Culling *et al.* (2005); de Cheveigné *et al.* (1995)).

VI. ABSORPTION COEFFICIENT FOR THE TARGET (EXP. 4)

A. Design

Experiment 4 followed the same protocol as experiment 2. This time the interferer was always at F, and the target at R. While calculating the impulse responses between sources and each ear, different absorption coefficients were used for the two sources. The absorption coefficient was the same for each room surface. For the interferer at F, it was set to 0.5, as in Experiment 3. However, four absorption coefficients were tested for the target at R: 1, 0.7, 0.5 and 0.2. The direct-to-reverberant ratios involved are presented in Table III. Interaural coherence of all stimuli was computed. Table VI presents the mean coherence for each type of stimulus. The range of coherence sampled by our four conditions was broader than in experiment 3 (Table V), with mean coherences between 1 and 0.6.

SRTs were measured in eight conditions: two types of interferer (noise and 2-voice) and four reverberation conditions for the target (absorption coefficient of 1, 0.7, 0.5 and 0.2).

B. Results

Figure 5 presents the mean SRTs obtained in experiment 4, for the target in the four tested reverberation conditions (absorption coefficient of 1, 0.7, 0.5 and 0.2), the reverberation condition of the noise or 2-voice interferers being fixed (absorption coefficient of 0.5). The comparison of these SRTs with STI calculations is described in the following section of the paper. For both types of interferer, SRTs increased as the absorption coefficient for the target was decreased, making the room more reverberant for this source. A 3.5 dB effect was observed between the absorption coefficients 1 and 0.2 with noise, this effect being increased to 5 dB with 2-voice interferers. An ANOVA confirmed that the main effect of the absorption coefficient used for the target was significant $[F(3,69)=44.8, p<0.0001]$. Tukey pairwise comparisons showed that SRTs were significantly higher for the absorption coefficient of 0.2 than for the three other coefficients $[q>9, p<0.001$ in each case$]$. The absorption coefficient 1 was also significantly different from the coefficient 0.5 $[q=5.14, p<0.01]$. The coefficient 0.7 did not differ significantly from the coefficients 0.5 and 1. Neither the interferer type nor the interaction between interferer type and absorption coefficient were significant.

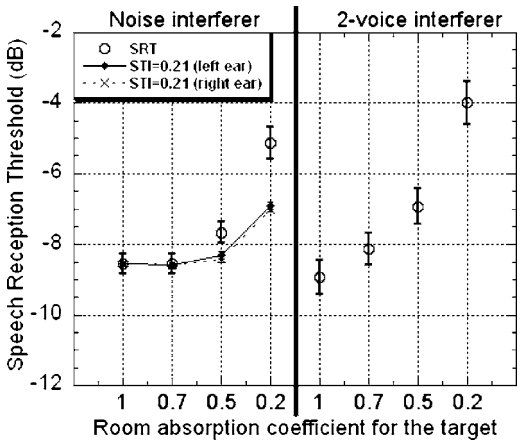

FIG. 5. Mean SRTs with standard errors measured in experiment 4, for the target in the four tested reverberation conditions, with an absorption coefficient of 0.5 used for the noise and 2-voice interferers. SRTs obtained with the noise interferers are compared to the target-to-interferer ratios required for the STI to be constant across the four conditions (STI=0.21 for the absorption coefficient of 1 and a signal-to-noise ratio of −8.50 dB). The STI was computed for each ear separately.

C. Discussion

SRTs increased with decreasing target direct-to-reverberant ratio (Table III), when the absorption coefficient used for the target was decreased. This decrease of target intelligibility might be due to the intrinsic degradation of speech intelligibility in reverberation. As the range of direct-to-reverberant ratios involved in this experiment was larger than in experiment 3, the effect was also larger.

It should be noted that SRTs from experiments 2 and 4 cannot be compared without caution, because the positions of target and interferer were switched between these experiments. The changes of coherence/direct-to-reverberant ratio introduced by the changes of absorption coefficient were limited for a source at the position F, whereas position R led to a broader range of coherence/direct-to-reverberant ratio. For this reason, for each experiment, the source with varying condition was placed at R, and the source with fixed condition was placed at F. SRTs measured in the two experiments using noise interferers and the absorption coefficient of 0.5 for both sources can be considered as an example. In experiment 2, the SRT was around −5 dB, whereas it was around −7.5 dB in experiment 4. This improvement in intelligibility could be explained by both the increase in interferer coherence—from 0.74 to 0.88 (Tables IV and VI)—and the increase in target direct-to-reverberant ratio—from −4.31/−4.39 to −3.70/−3.47 dB (Tables I and III).

VII. INTRINSIC DEGRADATION OF TARGET INTELLIGIBILITY IN REVERBERATION

In experiments 3 and 4, the increase of SRTs as the target distance increased or as the absorption coefficient used for the target decreased (Figs. 4 and 5) could result from the intrinsic degradation of target intelligibility in reverberation. To test this hypothesis, the STI was computed in the different conditions involved in the two experiments. The STI evaluates the degradation of speech by reverberation, in the pres-

ence of nondirectional background noise, from the room impulse responses between the target positions and the two ears. As the STI calculation uses only monaural information, the left and right ear were considered independently.

SRTs measured in experiments 3 and 4 corresponded to the target-to-interferer ratios required to get a fixed intelligibility of 50% of the target words. To compare STI calculations and SRTs, we assumed that the STI should be constant at this threshold. We therefore computed the target-to-interferer ratios required for the STI to correspond to the same value across all tested conditions. The reference STI value for experiment 3 was 0.22, calculated from the first SRT measured with noise interferers: impulse responses between each ear and the target position P1 (Fig. 1) were used, and the signal-to-noise ratio was set to the SRT value of −8.46 dB (Fig. 4). The signal-to-noise ratios required to get the same value of STI were computed using the room impulses responses between each ear and the target positions P2, P3 and P4. The reference STI value for experiment 4 was 0.21, again corresponding to the first SRT measured with noise interferers: impulse responses between each ear and the target position R were used, for a room absorption coefficient of 1 and a signal-to-noise ratio set to the SRT value of −8.56 dB (Fig. 5). The signal-to-noise ratios required to get the same value of STI were computed for the absorption coefficients 0.7, 0.5 and 0.2.

Figures 4 and 5 present the results obtained for each ear compared to the SRTs measured with noise interferers. For experiment 3, it seems that STI calculations and intrinsic degradation of target speech in reverberation can explain the SRTs obtained for the target at positions P2 and P4, but the SRT measured with the target at P3 was higher than the STI prediction. For experiment 4, the STI predicted correctly the observed trend: target intelligibility decreased as the absorption coefficient used for the target was decreased. However, SRTs measured with the absorption coefficients 0.5 and 0.2 were higher than the STI predictions. The difference between actual and predicted SRTs also increased as the target coherence decreased with absorption coefficient (Table VI). In both experiments the interferer coherence was kept constant. The binaural masking due to the interferer coherence was constant across conditions and could not account for the SRTs being higher than the STI predictions. As STI calculations do not take into account the interferer coherence, these higher thresholds could result from an interaction between the effects of reverberation on interferer and target. The assumption made that the STI should be constant at threshold in experiments 3 and 4 would then be wrong. A second account for the discrepancies between SRT and STI could come from the STI calculations not being completely reliable in the poor intelligibility conditions considered in our experiments.

VIII. GENERAL DISCUSSION

A. Influence of interferer coherence

Experiments 1 and 2 investigated the influence of the interferer interaural coherence by decreasing it in two different ways: the interferer was moved away from the listener into the reverberant field (experiment 1), or the room absorption coefficient used for the interferer was decreased (experiment 2). In both cases, SRTs increased with decreasing interferer coherence, with effects of 2–4 dB. This influence of the interferer coherence was in agreement with the E-C theory for binaural unmasking (Durlach (1972)): for spatially separated sound sources, a less coherent interferer would be more difficult to equalize and cancel for the auditory system, and so produce less masking release. This unmasking thus depends on the azimuth separation of sources (Beutelmann and Brand (2006); Plomp (1976)), but also on the coherence of the interferer, as shown by our experiments. This means that spatial unmasking will be influenced by the particular position of the interferer and the room characteristics.

Licklider (1948) showed that, for speech and noise having different interaural phase differences, speech intelligibility in noise was reduced when the noise was less correlated at the two ears. He used headphones with diotic target speech and a noise interferer having an interaural correlation of 0, 0.25, 0.5, 0.75 or 1. A difference of 20% word articulation was measured between the extreme correlations 0 and 1, most of the variation in intelligibility occurring between 0.75 and 1. The coherence range we have investigated in virtual rooms corresponds to the range over which he observed the greatest changes in intelligibility (Tables II and IV). Plomp and Mimpen (1979) found the same effect as Licklider while measuring SRTs, using diotic speech presented against noise which was either identical, uncorrelated or partly correlated (diffuse) at the two ears. SRTs decreased with the noise correlation, from −7.3 dB (noise identical) to −8.0 dB (diffuse noise presentation) and −9.6 dB (noise uncorrelated). Robinson and Jeffress (1963) measured the same trend and an even larger effect than Licklider for tone detection in noise. Zurek *et al.* (2004) investigated the detection of a third-octave band noise source in a virtual room, in the presence of a competing broadband noise source at a different azimuth. After having accounted for the monaural segregation cues, they found a binaural advantage very dependent on the absorption coefficient of the room internal surfaces. The detection threshold increased by up to 10 dB in a very reverberant room compared to an anechoic room. Even if they did not explicitly measure the interferer interaural coherence in their experiments, they showed that this elevation of threshold was well predicted by the E-C theory.

Beutelmann and Brand (2006) measured SRTs for a frontal target with a noise interferer, using binaural impulse responses measured in an anechoic room, a small office and a large cafeteria. As only close target sources and a limited amount of reverberation were involved, the intrinsic degradation of target intelligibility in reverberation was negligible. The thresholds for co-located sources were not significantly different in the three rooms. However, SRTs for spatially separated sources were higher in the office and cafeteria. This might be explained by a decrease of the interferer coherence in these two rooms. Other studies revealing that spatial unmasking observed in anechoic conditions was greatly reduced in reverberation might reflect the same effect (Bronkhorst and Plomp (1990); Culling *et al.* (2003); Plomp (1976)). This effect could also have influenced studies con-

cerned with attentional effects and informational masking (Darwin and Hukin (2000); Kidd *et al.* (2005)), in which spatial unmasking was also reduced in reverberation. The addition of an individual echo to the interferer might reduce its coherence, and then could account for part of the reduction of spatial unmasking observed in Freyman *et al.* (2001; 1999), Brungart *et al.* (2005) and Rakerd *et al.* (2006). Unfortunately, no interaural coherence evaluations were reported in any of these experiments. Even if these results are not directly comparable with those of experiments 1 and 2, the observed trends are the same across studies.

It should be noted that taking into account the influence of the head between the two ears of the listener might lead to larger impairments of intelligibility as reverberation increases, or at least to elevations of threshold appearing earlier. The head will lead to extra interaural decorrelation in asymmetric configurations, particularly for sources to the side, as shown by Lindevald and Benade (1986).

B. Attentional effects and informational masking

Informational masking seems to have played some role in our experiments. However, the effect of interferer type and its potential interactions with the other variables was not significant (Experiments 1, 3 and 4), or only marginally significant (Experiment 2).

The amount of informational masking depends on the task design and stimuli being used. Informational masking can be seen as an attentional effect, when listeners are presented with several voices at the same time and when there is an ambiguity as to which voice they should attend to (Kidd *et al.* (2005); Shinn-Cunningham *et al.* (2005)). On the one hand, our task design tended to minimize informational masking; for each SRT measurement, interferer sentences were kept constant and displayed on a screen in front of the listener, therefore reducing the chances of confusion and the uncertainty in the listening task (Hawley *et al.* (2004); Kidd *et al.* (2005); Watson (2005)). In addition, interferer and target were always spatially separated (Fig. 1), and a difference in perceived position is an important attentional cue reducing informational masking (Brungart and Simpson (2002); Brungart *et al.* (2005); Darwin and Hukin (2000); Freyman *et al.* (2001, 1999); Kidd *et al.* (2005); Rakerd *et al.* (2006); Shinn-Cunningham *et al.* (2005)). On the other hand, as the same voice was used for the target and the two interfering sources, and because 2-voice interferers produce more informational masking than 1-voice interferers (Freyman *et al.* (2001)), some attentional ambiguity might have remained, even if the interfering sentences were identified on the screen. After our experiments, almost all listeners reported that the task seemed more difficult with 2-voice interferers than with noise.

Even if the effects were weak and often nonsignificant, some informational masking might have occurred in experiments 2, 3 and 4. This masking should be reduced as soon as the similarity between interferer and target was reduced (Watson (2005)), as any difference between the two sources could help listeners focus their attention on the target (Shinn-Cunningham *et al.* (2005)). The difference in the amount of reverberation between target and interferer might have been used as an attentional cue by listeners in experiments 2 and 4. In experiment 3, with very close targets involved, a difference in perceived distance could have constituted such a cue, as found by Brungart and Simpson (2002).

C. Influence of target direct-to-reverberant ratio

Experiments 3 and 4 showed that the target direct-to-reverberant ratio influenced SRT measurements in rooms. In experiment 3, SRTs increased as the target was moved away from the listener in the reverberant field. The effect was small, around 1 dB, comparable to the difference of SRTs measured by Bronkhorst and Plomp (1990) while playing the target through loudspeakers that were either close or far from the listener, in a reverberant room. A larger effect was obtained in experiment 4, where SRTs increased as the absorption coefficient used for the target was decreased.

As we were expecting a monaural effect associated with the direct-to-reverberant ratio of the target rather than any binaural effect associated with the coherence of the target, our SRTs were compared to STI calculations involving only monaural information. The decrease of target intelligibility can be partially explained by the intrinsic degradation of speech intelligibility in reverberation, because STI calculations in the different configurations of our experiments were consistent with some elevation of threshold. However, the STI alone could not account for all our results, as differences between SRTs and STI predictions were observed. Experiment 4 showed that these differences increased as the target coherence decreased. As STI calculations do not take into account the interferer coherence, these differences might indicate an interaction between interferer and target coherences. Further experiments will be undertaken to investigate this question. Experiments involving diotic reverberant targets will be conducted to assess the relevance of considering the coherence of the target when describing speech segregation in rooms.

D. Towards an objective prediction of speech segregation in rooms

Some objective measurements are already available to predict speech intelligibility. The STI (Houtgast and Steeneken (1985)) or the useful-to-detrimental ratios (Bradley (1986); Bradley *et al.* (1999)) evaluate the intrinsic degradation of speech by reverberation, in the presence of nondirectional background noise. However, these measurements use only monaural information and do not consider directional interferers. Therefore, the influence of the interferer position and spatial unmasking cannot be taken into account. Zurek (1993) developed a model predicting speech intelligibility in the presence of an interfering source. It simulates head shadow and binaural interaction associated with the azimuth separation of sources, to take into account spatial unmasking. However, it applies only to noise interferers and anechoic situations.

The experiments presented in this paper revealed that, in rooms, speech intelligibility did not depend only on the azimuth separation of sound sources, but also on their inter-

aural coherence. It seems important to take this last parameter into account to predict speech intelligibility in rooms, at least when interferers and speech segregation mechanisms are involved. More experimental data are needed to describe precisely the relation between coherence and intelligibility. Zurek *et al.* (2004) proposed a model predicting the detection of a narrowband noise source in a room when a broadband noise source is also present. The model is based on room statistics and an equalization-cancellation (E-C) mechanism (Durlach (1972)). Binaural detection was quite accurately predicted, even if some discrepancies remained. These discrepancies could be linked to the approximations resulting from the use of room statistics rather than the complete room impulse responses. It is not clear how this model, designed for narrowband noise detection, could be extended to predict speech intelligibility. Beutelmann and Brand (2006) developed a model predicting the intelligibility of a speech target against a noise interferer in rooms. The model is also based on the E-C theory, and so should account for the influence of the interferer interaural coherence. However, the model only holds for near field targets, because the disturbance of the speech itself caused by reverberation is not taken into account. The model is also based on the analysis of the speech sentences spoken in the room, rather than on acoustical measurements more characteristic of the room itself.

It should be noted that we decided here to compute the interaural coherence of our signals as the maximum of the absolute value of the cross-correlation of the signals (filtered between 20 and 1500 Hz) at the two ears. While this calculation is simple and direct, it might need refinement. For example, Hartmann *et al.* (2005) measured the coherence in rooms by third octave bands, as the auditory system would not be able to use the broadband coherence, and there is evidence for the frequency channel independence of binaural unmasking (Akeroyd (2004); Culling and Summerfield (1995)). Weightings could be applied to this within-channel coherence, to take into account the spectrum of speech and the variation of the binaural masking level difference with frequency (Hirsh (1948)).

The influence of interaural coherence on intelligibility has been studied here for a fixed azimuth separation of sources. The influence of azimuth separation has been previously investigated in several studies in anechoic conditions (see Bronkhorst (2000) for a review), that is to say for sources having a fixed interaural coherence of 1. The experimental protocol we have used will allow us to investigate the interaction between coherence and azimuth separation, by varying these two parameters simultaneously.

IX. CONCLUSION

SRTs measured in a virtual room revealed that speech intelligibility in the presence of noise or speech maskers did not depend only on the azimuth separation of sound sources, but also on their interaural coherence and direct-to-reverberant ratio at the listening position. Speech intelligibility decreased as the coherence/direct-to-reverberant ratio of sources was degraded by reverberation. The influence of the interferer coherence was in agreement with binaural unmasking theories, and the effect of sound reflections on the target was partially explained by the intrinsic degradation of speech intelligibility in reverberation. It should be noted that, as the reverberation increases, speech intelligibility suffers first from the decorrelation of the interferer at the two ears, before the intrinsic loss of target intelligibility.

ACKNOWLEDGMENTS

This work was supported by the UK EPSRC. The authors are grateful to the associate editor Ruth Litovsky, to Erick Gallun and two anonymous reviewers for their helpful comments on a first version of this paper, and to all listeners who took part in the experiments.

Akeroyd, M. (**2004**). "The across frequency independence of equalization of interaural time delay in the equalization-cancellation model of binaural unmasking," J. Acoust. Soc. Am. **116**, 1135–1148.
Allen, J., and Berkley, D. (**1979**). "Image method for efficiently simulating small-room acoustics," J. Acoust. Soc. Am. **65**, 943–950.
Beutelmann, R., and Brand, T. (**2006**). "Prediction of speech intelligibility in spatial noise and reverberation for normal-hearing and hearing-impaired listeners," J. Acoust. Soc. Am. **120**, 131–342.
Bradley, J. (**1986**). "Predictors of speech intelligibility in rooms," J. Acoust. Soc. Am. **80**, 837–845.
Bradley, J., Reich, R., and Norcross, S. (**1999**). "On the combined effects of signal-to-noise ratio and room acousitcs on speech intelligibility," J. Acoust. Soc. Am. **106**, 1820–1828.
Bradley, J., Sato, H., and Picard, M. (**2003**). "On the importance of early reflections for speech in rooms," J. Acoust. Soc. Am. **113**, 3233–3244.
Brokx, J., and Nooteboom, S. (**1982**). "Intonation and the perceptual separation of simultaneous voices," J. Phonetics **10**, 23–36.
Bronkhorst, A. (**2000**). "The cocktail party phenomenon: A review of research on speech intelligibility in multiple-talker conditions," Acust. Acta Acust. **86**, 117–128.
Bronkhorst, A., and Plomp, R. (**1988**). "The effect of head-induced interaural time and level differences on speech intelligibility in noise," J. Acoust. Soc. Am. **83**, 1508–1516.
Bronkhorst, A., and Plomp, R. (**1990**). "A clinical test for the assessment of binaural speech perception in noise," Audiology **29**, 275–285.
Bronkhorst, A., and Plomp, R. (**1992**). "Effect of multiple speechlike maskers on binaural speech recognition in normal and impaired hearing," J. Acoust. Soc. Am. **92**, 3132–3139.
Brungart, D., and Simpson, B. (**2002**). "The effects of spatial separation in distance on the informational and energetic masking of a nearby speech signa," J. Acoust. Soc. Am. **112**, 664–676.
Brungart, D., Simpson, B., and Freyman, R. (**2005**). "Precedence-based speech segregation in a virtual auditory environment," J. Acoust. Soc. Am. **118**, 3241–3252.
Culling, J. (**1996**). "Signal processing software for teaching and research in psychoacoustics under UNIX and X windows," Behav. Res. Methods Instrum. Comput. **28**, 376–382.
Culling, J., and Darwin, C. (**1993**). "Perceptual separation of simultaneous vowels: Within and across-formant grouping by f0," J. Acoust. Soc. Am. **93**, 3454–3467.
Culling, J., Hodder, K., and Toh, C. (**2003**). "Effects of reverberation on perceptual segregation of competing voices," J. Acoust. Soc. Am. **114**, 2871–2876.
Culling, J., Linsmith, G. and Caller, T. (**2005**). "Evidence for a cancellation mechanism in perceptual segregation by differences in fundamental frequency," J. Acoust. Soc. Am. **117**, 2600 (A).
Culling, J., and Summerfield, Q. (**1995**). "Perceptual separation of concurrent speech sounds: Absence of across-frequency grouping by common interaural delay," J. Acoust. Soc. Am. **98**, 785–797.
Darwin, C., and Culling, J. (**1990**). "Speech perception seen through the ear," Speech Commun. **9**, 469–475.
Darwin, C., and Hukin, R. (**2000**). "Effects of reverberation on spatial, prosodic, and vocaltract size cues to selective attention," J. Acoust. Soc. Am. **108**, 335–342.
de Cheveigné, A., McAdams, S., Laroche, J., and Rosenberg, M. (**1995**).

"Identification of concurrent harmonic and inharmonic vowels: A test of the theory of harmonic cancellation and enhancement," J. Acoust. Soc. Am. **97**, 3736–3748.
Durlach, N. (**1972**). "Binaural signal detection: Equalization and cancellation theory," in *Foundations of Modern Auditory Theory*, edited by J. Tobias (Academic, New York), Vol. **II**, pp. 371–462.
Dusquesnoy, A. (**1983**). "Effect of a single interfering noise or speech source upon the binaural sentence intelligibility of aged persons," J. Acoust. Soc. Am. **74**, 739–743.
Festen, J., and Plomp, R. (**1990**). "Effects of fluctuating noise and interfering speech on the speech-reception threshold for impaired and normal hearing," J. Acoust. Soc. Am. **88**, 1725–1736.
Freyman, R., Balakrishnan, U., and Helfer, K. (**2001**). "Spatial release from informational masking in speech recognition," J. Acoust. Soc. Am. **109**, 2112–2122.
Freyman, R., Helfer, K., McCall, D., and Clifton, R. (**1999**). "The role of perceived spatial separation in the unmasking of speech," J. Acoust. Soc. Am. **106**, 3578–3588.
Hartmann, W., Rakerd, B., and Koller, A. (**2005**). "Binaural coherence in rooms," Acta. Acust. Acust. **91**, 451–462.
Hawley, M., Litovsky, R., and Culling, J. (**2004**). "The benefit of binaural hearing in a cocktail party: Effect of location and type of interferer," J. Acoust. Soc. Am. **115**, 833–843.
Hirsh, I. (**1948**). "The influence of interaural phase on interaural summation and inhibition," J. Acoust. Soc. Am. **20**, 536–544.
Houtgast, T., and Steeneken, H. (**1985**). "A review of the MTF concept in room acoustics and its use for estimating speech intelligibility in auditoria," J. Acoust. Soc. Am. **77**, 1069–1077.
IEEE (**1969**). "IEEE recommended practice for speech quality measurements," IEEE Trans. Audio Electroacoust. **17**, 227–246.
Kidd, G., Mason, C., Brughera, A., and Hartmann, W. (**2005**). "The role of reverberation in release from masking due to spatial separation of sources for speech identification," Acta. Acust. Acust. **91**, 526–535.
Licklider, J. (**1948**). "The influence of linteraural phase relations upon masking of speech by white noise," J. Acoust. Soc. Am. **20**, 150–159.
Lindevald, I., and Benade, A. (**1986**). "Two-ear correlation in the statistical sound fields of rooms," J. Acoust. Soc. Am. **80**, 661–664.
Moore, B., and Glasberg, B. (**1983**). "Suggested formulae for calculating auditory-filter bandwidths and excitation patterns," J. Acoust. Soc. Am. **74**, 750–753.
Peterson, P. (**1986**). "Simulating the response of multiple microphones to a single acoustic source in a reverberant room," J. Acoust. Soc. Am. **80**, 1527–1529.
Plomp, R. (**1976**). "Binaural and monaural speech intelligibility of connected discourse in reverberation as a function of azimuth of a single competing sound source (speech or noise)," Acustica **34**, 200–211.
Plomp, R., and Mimpen, A. (**1979**). "Improving the reliability of testing the speech-reception threshold for sentences," Audiology **18**, 43–52.
Rakerd, B., Aaronson, N., and Hartmann, W. (**2006**). "Release from speech-on-speech masking by adding a delayed masker at a different location," J. Acoust. Soc. Am. **119**, 1597–1605.
Robinson, D., and Jeffress, L. (**1963**). "Effect of varying the interaural noise correlation on the detectability of tonal signals," J. Acoust. Soc. Am. **35**, 1947–1952.
Shinn-Cunningham, B., Ihlefeld, A., Satyavarta, and Larson, E. (**2005**). "Bottom-up and top-down influences on spatial unmasking," Acta. Acust. Acust. **91**, 967–979.
Watson, C. (**2005**). "Some comments on informational masking," Acta. Acust. Acust. **91**, 502–512.
Yang, W., and Hodgson, M. (**2006**). "Auralization study of optimum reverberation times for speech intelligibility for normal and hearing-impaired listeners in classrooms with diffuse sound fields," J. Acoust. Soc. Am. **120**, 801–807.
Zahorik, P. (**2002**). "Direct-to-reverberant energy ratio sensitivity," J. Acoust. Soc. Am. **112**, 2110–2117.
Zurek, P. (**1993**). "Binaural advantages and directional effects in speech intelligibility," in *Acoustical Factors Affecting Hearing Aid Performance*, edited by G. Studebaker and I. Hochberg, (Allyn and Bacon, Needham Heights, MA), pp. 255–276.
Zurek, P., Freyman, R., and Balakrishnan, U. (**2004**). "Auditory target detection in reverberation," J. Acoust. Soc. Am. **115**, 1609–1620.

Effect of target-masker similarity on across-ear interference in a dichotic cocktail-party listening task

Douglas S. Brungart[a] and Brian D. Simpson
Air Force Research Laboratory, WPAFB, Ohio 45433

(Received 6 January 2006; revised 14 June 2007; accepted 18 June 2007)

Similarity between the target and masking voices is known to have a strong influence on performance in monaural and binaural selective attention tasks, but little is known about the role it might play in dichotic listening tasks with a target signal and one masking voice in the one ear and a second independent masking voice in the opposite ear. This experiment examined performance in a dichotic listening task with a target talker in one ear and same-talker, same-sex, or different-sex maskers in both the target and the unattended ears. The results indicate that listeners were most susceptible to across-ear interference with a different-sex within-ear masker and least susceptible with a same-talker within-ear masker, suggesting that the amount of across-ear interference cannot be predicted from the difficulty of selectively attending to the within-ear masking voice. The results also show that the amount of across-ear interference consistently increases when the across-ear masking voice is more similar to the target speech than the within-ear masking voice is, but that no corresponding decline in across-ear interference occurs when the across-ear voice is less similar to the target than the within-ear voice. These results are consistent with an "integrated strategy" model of speech perception where the listener chooses a segregation strategy based on the characteristics of the masker present in the target ear and the amount of across-ear interference is determined by the extent to which this strategy can also effectively be used to suppress the masker in the unattended ear. [DOI: 10.1121/1.2756797]

PACS number(s): 43.66.Rq, 43.71.Gv [RAL] Pages: 1724–1734

I. INTRODUCTION

Most normal-hearing listeners perform very well in dichotic speech perception tasks that require them to selectively attend to a target speech signal in one ear while ignoring an unrelated interfering speech stimulus in the other ear. Cherry (1953), for example, found that listeners could easily recite the contents of a speech message presented in their right ear without any significant interference from a second unrelated message presented in the left ear. Since Cherry's initial findings, a number of additional experiments have shown that the presence of a speech masker in one ear has little or no impact on a listener's ability to selectively attend to a target speech signal presented in the other ear (Abouchacra *et al.*, 1997; Drullman and Bronkhorst, 2000; Egan *et al.*, 1954; Moray, 1959, 1969; Wood and Cowan, 1995). Thus, on the basis of these experiments, one might conclude that listeners have little difficulty focusing their attention on the acoustic signal at one ear when a distracting or irrelevant signal is present in the other ear.

However, results from a recent study in our laboratory have shown that the ability to selectively focus attention on a single ear breaks down when a second interfering speech signal is present in the same ear as the target speech (Brungart and Simpson, 2002). In that study, listeners were able to achieve nearly perfect performance in a speech identification task when the masking phrase was presented in a different ear than a target phrase at the same level, and were correct approximately 70% of the time when the target and masking phrases were presented in the same ear. However, speech identification scores dropped to about 60% when a different masking phrase was presented to each ear, indicating that the listeners were susceptible to interference from a masker presented in the ear contralateral to the target when a second masker was presented to the same ear as the target speech.

Brungart and Simpson initially hypothesized that this "across-ear interference" effect represented an attentional resource limitation [e.g., (Wickens, 1984)] that was directly dependent on the relative difficulty of the listening task in the listener's target ear. Specifically, a relatively simple speech segregation task in the target ear would require few attentional resources and would thus allow for the devotion of greater resources to suppressing the contralateral masker. Likewise, a more difficult speech segregation task in the target ear would require greater resources and thus would leave fewer resources for contralateral suppression. Thus, one might expect listeners to be able to perform a relatively easy multitalker listening task in the target ear without significant interference from a masking talker in the unattended ear, but not a relatively difficult one. This argument was bolstered by the fact that listeners in the study were much more sensitive to across-ear interference when the target-ear signal-to-noise ratio was negative than when it was positive.

In a later study, Kidd *et al.* (2003) examined a similar set of target-masker configurations in a non-speech detection task and found results that were not consistent with a model that assumes that across-ear interference is driven by the difficulty of the listening in the target ear. In that study, listeners were asked to detect the presence of a series of 1 kHz tones

[a]Electronic mail: douglas.brungart@wpafb.af.mil

presented in the context of two different types of maskers: a random-frequency "multiple-bursts different" maskers, which qualitatively sounded much different than the fixed-frequency target tone and thus resulted in relatively low detection thresholds in a monaural listening task, and a fixed-frequency "multiple-bursts same" masker, which qualitatively sounded similar to the fixed-frequency target tone and resulted in relatively high detection thresholds in a monaural listening task. The listeners experienced significant levels of across-ear interference when they heard the different-sounding MBD masker in the target ear (i.e., an easier segregation task) and the similar-sounding MBS masker in the unattended ear, but almost no across-ear interference when they heard the similar-sounding MBS masker in the target ear (i.e., a more difficult segregation task) and the different-sounding MBD masker in the unattended ear.

These results do not seem to be consistent with the model proposed by Brungart and Simpson (2002), because that model would always predict a difficult listening task in the target ear (such as that resulting from the task with the MBS masker) to be at least as susceptible to interference from an across-ear masker as an easier listening task in the target ear (such as that with the MBD masker). However, the Kidd *et al.* (2003) data could be explained by an alternative model of dichotic selective attention, which we will call the "integrated strategy" model, that assumes that the listener can choose to focus attention using a single listening strategy that is applied more generally to the combined signal arriving at both ears. In a dichotic listening task with the target in one ear and the masker in the other ear, the listener would presumably choose the strategy of listening in the "target ear," and no substantial across-ear interference would be expected. However, in most cases, the strategy would be driven by the acoustic characteristics of the most destructive interferer in the listening environment, which typically would be the masker located in the same ear as the target.

This integrated strategy model could easily explain the results found in the Kidd *et al.* (2003) study. First, consider the condition with the random-frequency MBD masker in the target ear and the fixed-frequency MBS masker in the unattended ear. In this case, the impact of the MBD masker may be reduced by a target detection strategy in which one listens for the tone that "does not change" in the target ear during the stimulus presentation. However, according to the model, this strategy cannot be directed to the target ear only but rather is implemented in a more general sense. Thus, the model would predict that such a strategy would allow for interference from the MBS stimulus in the unattended ear, which also does not change in frequency and thus could easily be confused with the target in the combined dichotic signal. Next consider the case with the fixed-frequency MBS signal in the target ear and the random-frequency MBD signal in the unattended ear. In that case, where both the target and the MBS masker in the target ear are constant over time, the most reasonable detection strategy would involve the listener selectively attending to the narrow "protected" frequency band in which the target could occur. This frequency-based segregation strategy would also exclude the off-frequency masking components of the MBD masker in the contralateral ear, so the model would predict relatively little across-ear interference in this case. Thus, it seems that the results of the Kidd *et al.* (2003) study could be explained by a model that predicts best performance when a within-ear segregation strategy is adopted by the listener that also reduces interference from the across-ear masker.

Clearly there are large differences between the stimuli used in the Kidd *et al.* (2003) study and the speech stimuli used in the Brungart and Simpson (2002) study. In order to determine whether the integrated strategy model that accounts for the results from Kidd *et al.* (2003) might also apply for dichotic speech perception tasks, it is necessary to construct a dichotic speech perception experiment that systematically varies two important factors of the auditory stimulus: the relative difficulty of the within-ear listening task, and the relative similarity of the target talker to the within- and across-ear maskers. If the "shared resource" model of dichotic attention is correct, one would expect across-ear interference to depend primarily on the difficulty of the within-ear listening task. However, if the integrated strategy model is correct, one would expect performance to vary systematically with within- and across-ear target-masker similarity. Specifically, one would expect the most across-ear interference to occur when the across-ear masker is more similar to the target talker than the within-ear masker, because the best strategy to segregate the target from the masker in the attended ear would not be an effective strategy for eliminating interference from the more target-like masker in the unattended ear.

As it turns out, both within-ear task difficulty and target-masker similarity can be examined relatively easily by manipulating the voice characteristics of the within- and across-ear maskers in a speech identification task using the coordinate response measure (CRM). Previous studies using these speech stimuli have shown that changes in the similarity of the target and masker voices have a substantial impact on the difficulty of a two-talker monaural listening task: the performance is best when the masking phrase is spoken by a talker who is different in sex than the target talker, somewhat worse when the masking phrase is spoken by a different talker of the same sex, and worse still when the target and masking phrases are both spoken by the same talker (Brungart and Simpson, 2002). Therefore it should be possible to use similarity between the target and masking voices in the target ear to systematically probe the relationship between task difficulty in the target ear, within-ear and across-ear target-masker similarity, and susceptibility to across-ear interference from an unrelated speech masker in the unattended ear.

The present study consists of a series of experiments designed to explore the role that target-masker similarity plays in dichotic listening. In the Brungart and Simpson (2002) study, only cases in which the target phrase, target-ear masking phrase, and unattended-ear masking phrase were all spoken by different same-sex talkers were considered. To this point, we are aware of only one other experiment (Wightman and Kistler, 2005) that has examined the role of target-masker similarity in this dichotic paradigm. However, that experiment was limited to only two cases: one with male

target and masking voices in one or both ears, and one with a male target voice and female masking voice in one or both ears. In this experiment, we extend the same dichotic listening paradigm to explore same-talker, same-sex, and different sex maskers both in the target and unattended ears. The next section describes the experiment in more detail.

II. EXPERIMENT 1: DICHOTIC SIMILARITY IN A HYBRID MONAURAL-DICHOTIC COCKTAIL-PARTY TASK

A. Methods

The experiment was based on the CRM, a call-sign based intelligibility test that has proven useful for measuring performance in listening with two or more simultaneous talkers (Brungart, 2001a, b). The CRM phrases were taken from the publicly available CRM speech corpus for multitalker communications research (Bolia *et al.*, 2000), which contains phrases of the form "ready (call sign) go to (color) (number) now," spoken by four male and four female talkers with all possible combinations of eight call signs ("Arrow," "Baron," "Charlie," "Eagle," "Hopper," "Laker," "Ringo," "Tiger"); four colors ("blue," "green," "red," "white"); and eight numbers (1–8).

The stimulus presented to the right (target) ear always consisted of a mixture of two simultaneous phrases from the corpus: a target phrase, randomly selected from the phrases containing the call sign Baron, and a masking phrase, randomly selected from all the phrases that were different in call sign, color, and number from the target phrase. The level of the target phrase was scaled relative to the masking phrase to produce one of five different target-to-masker (TMRs) (−8, −4, 0, 4, or 8 dB). The stimulus presented to the left (unattended) ear consisted either of silence or of a second phrase that was randomly selected from all the phrases in the CRM containing a different call sign, color, and number than either of the two phrases in the target ear. When present, this contralateral masking phrase was presented at the same level as the masking phrase in the target ear.

Prior to each trial, the target talker was randomly selected from the eight talkers in the corpus. Then, depending on the experimental condition, the masking talkers in the target and contralateral ears were selected from one of three different categories: same-talker (T), where the masking talker was the same talker used in the target phrase; same-sex (S) where the masking talker was a different talker who was the same sex as the target phrase; and different-sex (D), where the masking talker was a different talker who was different in sex from the target talker. This resulted in the 12 different stimulus conditions shown in Fig. 1. Once the correct target and masking phrases were selected, the waveforms were digitally combined and played at a comfortable listening level (roughly 65 dB SPL) through stereo headphones (AKG-240) connected to a 50 kHz 24-bit D/A card (Sound-Blaster Audigy).

The experiment was conducted by listeners seated in front of the CRT of one of three identical control computers located in three different quiet listening rooms. Prior to the experiment, the listeners were instructed to always listen in their right ear for the target phrase containing the call sign Baron, and to respond by selecting the color and number coordinates contained in that target phrase from an array of colored digits displayed on the screen of the control computer. The data collection was divided into blocks of 60 trials, with one repetition of each of the 12 listening configurations at each of the 5 target-ear TMR values in each block. Each of the 10 listeners participated in a total of 48 blocks of trials in the experiment, for a total of 2880 trials per listener.

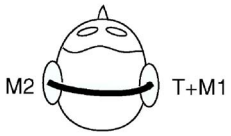

Condition	Designation	M1	M2
1	TT	Same-Talker	None
2	TT-T	Same-Talker	Same-Talker
3	TT-S	Same-Talker	Same-Sex
4	TT-D	Same-Talker	Different-Sex
5	TS	Same-Talker	None
6	TS-T	Same-Sex	Same-Talker
7	TS-S	Same-Sex	Same-Sex
8	TS-D	Same-Sex	Different-Sex
9	TD	Different-Sex	None
10	TD-T	Different-Sex	Same-Talker
11	TD-S	Different-Sex	Same-Sex
12	TD-D	Different-Sex	Different-Sex

FIG. 1. (Color online) Conditions tested in the experiment

B. Results

Figure 2 shows the percentage of correct color and number identifications as a function of target-ear TMR for each of the 12 conditions tested in the experiment. Each panel in Fig. 2 represents a different type of masker in the target ear, and the symbols within each panel show the results with different types of maskers in the unattended ear. The designations in the legends of each panel correspond to the designations assigned to each of the 12 conditions in Fig. 1.

The arcsine-transformed proportions of correct responses from the individual listeners in each condition were

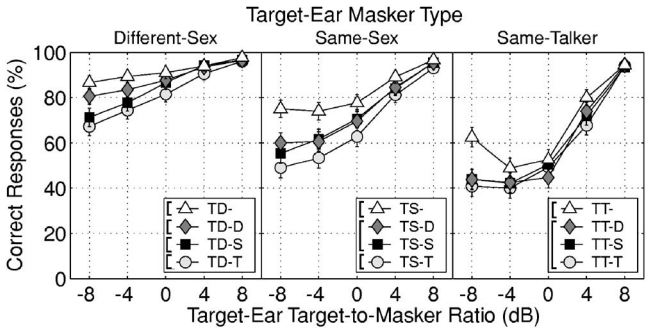

FIG. 2. Percentage of correct color and number identifications in each condition of the experiment. Each panel represents a different type of masker in the target ear, and the different symbols within each panel represent different types of maskers in the unattended ear. The error bars represent the 95% confidence intervals for each data point, calculated from the pooled raw data across all ten subjects. The braces in the legends of each panel indicate groups of conditions that were not significantly different from one another at the $p<0.05$ level (as calculated from a Bonferroni-corrected post-hoc t-test on the interaction between target-ear masker type and unattended-ear masker type).

TABLE I. Within-subject repeated-measures analysis of variance for Experiment 1.[a]

Effect	SS	dF	MS	F	p
INTERCEPT	700.169	1	700.169	914.738	0.000
Error	6.889	9	0.765		
TMR	18.94	4	4.734	52.3	0.000*
Error	3.260	36	0.091		
CONTRA	1.49	3	0.496	32.4	0.000*
Error	0.414	27	0.0153		
IPSI	10.11	2	5.054	506.8	0.000*
Error	0.179	18	0.010		
TMR*CONTRA	0.51	12	0.042	5.4	0.000*
Error	0.856	108	0.008		
TMR*IPSI	1.68	8	0.210	21.6	0.000*
Error	0.703	72	0.0098		
CONTRA*IPSI	0.12	6	0.020	3.3	0.008*
Error	0.339	54	0.0063		
TMR*CONTRA*IPSI	0.15	24	0.006	1.1	0.321
Error	1.208	216	0.0056		

TMR=target-ear TMR value; CONTRA=unattended-ear masker type; and IPSI=target ear masker type. See the text for details.

TABLE II. Uncorrected p values obtained for two-tailed t-tests for paired comparisons between the conditions of Experiment 1. The bold indicates conditions that are significantly different at the $p<0.05$ level when the data are Bonferroni corrected to account for the 18 pairwise comparisons represented here.

	Different-sex target-ear masker			
Condition	TD-	TD-D	TD-S	TD-T
TD-	···	**0.0001**	**0.0000**	**0.0000**
TD-D	**0.0001**	···	**0.0016**	**0.0000**
TD-S	**0.0000**	**0.0016**	···	**0.0018**
TD-T	**0.0000**	**0.0000**	**0.0018**	···
	Same-sex target-ear masker			
Condition	TS-	TS-D	TS-S	TS-T
TS-	···	**0.0000**	**0.0000**	**0.0000**
TS-D	**0.0000**	···	0.6461	**0.0000**
TS-S	**0.0000**	0.6461	···	**0.0000**
TS-T	**0.0000**	**0.0000**	**0.0000**	···
	Same-talker target-ear masker			
Condition	TT-	TT-D	TT-S	TT-T
TT-	···	**0.0000**	**0.0000**	**0.0000**
TT-D	**0.0000**	···	0.7017	0.2907
TT-S	**0.0000**	0.7017	···	0.1499
TT-T	**0.0000**	0.2907	0.1499	···

also analyzed with a three-factor within-subjects analysis of variance on the factors of target-ear TMR (−8, −4, 0, 4, or 8 dB), unattended-ear masker type (same-talker, same-sex, different-sex, and none), and target-ear masker type (same-talker, same-sex, and different sex). The ANOVA results shown in Table I indicate that all the main effects and two-way interactions in the experiment were statistically significant at the $p<0.005$ level. Additional post-hoc two-tailed t-tests were conducted to compare the overall effect of unattended ear masker type across the four curves shown in each panel of Fig. 2. The raw p values obtained from these analyses are shown in Table II, and the bold values in the table indicate pairs that were significantly different at the $p<0.05$ level after Bonferroni correction to account for the 18 pairwise comparisons (a total of six comparisons across the four curves within each of the three panel). The results of this pairwise comparison test are shown by the brackets on the left sides of the legends in Fig. 2: conditions that were not significantly different from one another are grouped together into the same bracket, and conditions that were significantly different from one another are grouped into separate brackets.

As the post-hoc t-test results indicate, all three of the independent variables tested in the experiment had a significant impact on performance in the dichotic listening task. Looking from left to right across the three panels of Fig. 2, it is apparent that performance systematically decreased as the target-ear masker changed from a different-sex voice that was qualitatively much different than the target talker to a same-talker voice that was identical to the target talker. This trend is consistent with previous studies that have shown that performance in the two-talker CRM listening task is better with a different-sex masker than with a same-sex masker and better with a same-sex masker than with a same-talker masker (Brungart, 2001b).

Looking from left to right within the individual panels of Fig. 2, it is also apparent that performance varied systematically with the TMR value in the target-ear. When the TMR value was greater than 0 dB, performance consistently increased with increasing TMR. When the TMR value was less than 0 dB, however, there were cases where decreasing TMR had little or no effect on performance (as in the TS-, TT-D, TT-S, and TT-T conditions) and one case where performance actually increased with decreasing TMR (the TT-condition shown by the triangles in the right-hand panel of Fig. 2). In the conditions with no unattended-ear masker (i.e. the TS- and TT- conditions shown by the triangles in the right-hand-most two panels of the figure), the plateau in performance that occurred at negative TMR values can be attributed to the use of level difference cues to help distinguish between the target and masking voices. For example, the increase in performance that occurred at −8 dB in the TT-condition probably occurred because the listeners were able to perform the task by listening for the quieter of the two talkers in the stimulus. Similar results have been reported in previous studies that have examined two-talker listening tasks in monaural listening environments (Brungart, 2001b; Egan *et al.*, 1954).

The characteristics of the unattended-ear masker also had an impact on performance. A comparison across the four curves within each panel indicates that performance was consistently degraded when a masking voice was added to the unattended ear and that, in general, the amount of degradation was greatest when the masking voice in the unattended ear was qualitatively similar to the target voice. However, the degree to which listeners were affected by the similarity between the target voice and the unattended-ear masking voice varied across the three different target-ear masking conditions. When a different-sex masking voice was present in the target ear, all four of the unattended-ear masking conditions were significantly different from one another [as indicated by

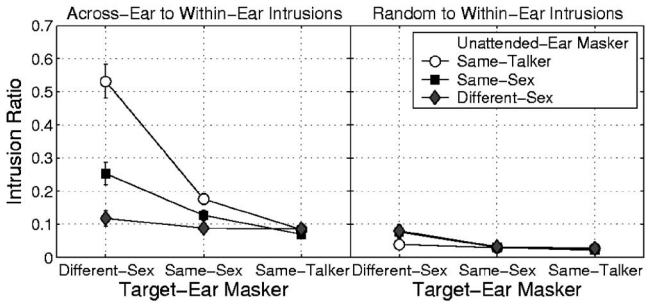

FIG. 3. Analysis of within-ear and across-ear intrusions in Experiment 1. In this context, a within-ear intrusion is assumed to occur when either the color response or the number response in a given trial matches the color or number word spoken by the masking talker in the target ear. Similarly, an across-ear intrusion occurs when either the response color or response number matches the phrase spoken by the masking talker in the unattended ear. The left-hand panel shows the ratio of across-ear to within-ear intrusions in each condition of the experiment. The right-hand panel shows the ratio of random responses (where the response contained a color or number word that was not spoken by any talker in the stimulus) to within-ear intrusions. The error bars show the ±1 standard error around each data point.

the results of a Bonferroni-corrected post-hoc t-test at the $p < 0.05$ level (Table II)]. This is illustrated by the four non-overlapping brackets in the legend of that panel. When a same-sex masking voice was present in the target ear, performance was best with no unattended-ear masker and worst with a same-talker unattended-ear masker, but there was statistically no difference between a same-sex or different-sex masker in the unattended ear. Finally, when a same-talker masking voice was present in the target ear, the addition of a masking phrase to the unattended ear caused the same amount of degradation independent of its vocal characteristics.

Further insights into the results can be obtained by more closely examining the pattern of errors produced in the experiment. Figure 3 shows an analysis of the "intrusions" that occurred in the experiment, where an intrusion is defined as a trial where the color or number response of the subject matched one of the masking phrases in the stimulus rather than the target phrase. The values in the left panel of the figure represent the ratio of the proportion of trials where an across-ear intrusion occurred (the response color or number matched the masking phrase in the unattended ear) to the proportion of trials where a within-ear intrusion occurred (the response color or number matched the masking phrase in the target-ear). The right-hand panel of Fig. 3 shows the ratio of the proportion of random responses (where either the response color or the response number did not match any of the CRM phrases in the stimulus) to the proportion of trials where a within-ear intrusion occurred. As in previous experiments (Brungart and Simpson, 2002; Wightman and Kistler, 2005), these results show that within-ear intrusions are responsible for the majority of the incorrect responses in the dichotic listening task, occurring more than 10 times as frequently as random errors that fail to match any of the color and number key words presented in the stimulus. However, the proportion of across-ear intrusions varied systematically with the target and masker configuration in a manner that seemed to directly mirror the across-ear target-masker similarity seen in Fig. 2. When a different-sex masking voice was present in the target ear, the proportion of across-ear intrusions increased dramatically as the unattended ear masker became more similar to the target voice, with nearly five times as many across-ear intrusions for the TD-T condition than for the TD-D condition, and more than twice as many for the TD-S condition than for the TD-D condition. When a same-sex masking voice was present in the target ear, the proportion of across-ear intrusions showed the same pattern, but less dramatically than in the different-sex target-ear masking conditions. And when a same-talker masking voice was present in the target ear, the voice characteristics of the masker in the unattended ear had no effect on the number of across-ear confusions.

C. Discussion

The results from Experiment 1 cannot be accounted for by the shared resource model in which performance is mediated by the difficulty of the segregation task in the target ear. For example, even when a condition was presented in which the monaural segregation task was relatively easy (i.e., the TD condition) performance was differentially affected by the contralateral masker depending upon its relative similarity to the speech phrases in the target ear. Moreover, in the most difficult condition (the TT condition) listeners were generally least susceptible to across ear interference.

However, the somewhat complicated relationship between the amount of across-ear interference caused by a speech masker in the unattended ear, and the similarity between that speech masker and the target speech signal does appear to be well predicted by the integrated strategy model of dichotic attention. When the within-ear masker was qualitatively different from the target, the amount of across-ear interference systematically increased with the similarity between the across-ear masker and the target. However, as the within-ear masker became more similar to the target speech, similarity between the across-ear masker and the target had less of an effect on performance. In the limit, when the within-ear masker was identical to the target talker, variations in the qualitative similarity of the across-ear masker and the target talker had little or no measurable effect on performance. These findings are consistent with the integrated strategy model, which generally predicts that the amount of across-ear masking should be influenced not simply by the similarity between the target talker and the across-ear masker, but rather by the extent to which the across-ear masker is *more* similar to the target speech than the within-ear masker is.

To elaborate, under the integrated strategy model, we assume that the listener is forced to adopt a single listening strategy that will most effectively segregate the target speech phrase from all of the interfering voices present in the combined dichotic stimulus. As the within-ear masker generally causes the most interference, one would typically expect the listener to adopt the strategy that makes it easiest to extract the target-ear speech from the target-ear masker. The amount of across-ear interference is then determined by the extent to which this segregation strategy can be used to attenuate the interference from the masker in the unattended ear. For ex-

ample, consider the case where the target talker is male and the masking talker in the same ear is female. The best segregation strategy is one that eliminates as much of the female masker as possible while retaining as much of the male target as possible. If an additional female voice is presented in the unattended ear, the listener will still be able to maintain a high level of performance because the segregation strategy adopted to eliminate the same-ear masker is also effective at eliminating the across-ear masker. If the across-ear talker is male, however, the listener is likely to confuse it with the target talker and thus will experience a decrease in performance due either to the failure of the listening strategy or to the necessity to adopt a less efficient listening strategy than one based on gender differentiation in the target ear.

Next consider the case where the target talker is male and there is a same-sex masker in the target ear. In this case, the listener will have to focus his or her attention on the more subtle differences that can be used to identify a particular male talker, including mean F0 value, vocal tract length, and speaking style. If a female voice is presented in the unattended ear, performance is only slightly degraded because that talker's F0 values, vocal tract length, and speaking style will not match those of the target talker. However, if a same-talker masker is added to the unattended ear, it will match these characteristics and again the listener will experience a marked decrease in performance.

Finally consider the case where the same voice is used for both the target and masker phrases in the target ear. Now the listener only has access to very weak prosodic continuity cues to connect the target call sign to the subsequent color and number combination occurring in the target phrase. Even if the unattended-ear masker also has the same voice as the target talker, the listener is not severely impaired by this across-ear masker similarity because the same-talker masker will not have the same prosodic pattern as the target phrase. Similarly, he or she will gain no improvement in performance if the unattended-ear masker happens to be a different sex talker, because he or she is listening specifically for prosodic patterns and not for gender differences in the voices.

Note that this integrated strategy model has direct parallels to the ideas of early and late selection outlined in the multimode theory of attention of Johnston and Heinz (1978). They suggested that target information is selected at the level of sensory analysis by early modes of attention but not until after semantic analysis by late modes. They also suggest that, as the perceptual-processing system shifts from early to late modes of attention, it collects more information from nontarget sources but requires more capacity to focus on a specific target source. In the context of our results, this might suggest that the preferred mode of attention is set by the masking talker in the target ear, and that the listener will be susceptible to additional interference from the masker in the unattended ear if the information from that ear needs to be selected at a later stage of attention than the information in the target ear. For example, in a condition with the different-sex target-ear masker, listeners may be relying primarily on early selection to extract the target speech signal from the target-ear masker. This may make them susceptible to interference from a perceptually-similar masker in the unattended ear, which requires processing on the more detailed semantic level associated with late selection to be successfully disentangled from the target speech. In the condition with a same-talker ipsilateral masker, they are relying on late selection for the target-ear listening task, and this requires more resources overall and results in lower performance, but it allows the target speech to be successfully extracted from the contralateral masker even when that masker is perceptually similar to the target talker.

One aspect of the results which was not directly addressed by either the shared-resource model or the integrated strategy model is the presence of a significant amount of across-ear intrusions in the TD-T conditions of the experiment. These kinds of intrusions are perfectly consistent with the integrated strategy model, and, depending on how the "within-ear segregation" and "across-ear segregation" processes are structured, they could also occur under the shared-resource model of attention. However, they do seem to preclude the possibility that "across-ear" segregation and "within-ear" segregation could be *sequential* processes, whereby the listener first uses some attentional resources to fully switch attention to the ear containing the target signal, and then uses the remaining attentional resources to extract the target signal from the remaining target-ear signal on the basis of voice characteristics and other monaural factors. If the dichotic attention process used this kind of sequential structure, one would predict (1) that similarities between the target talker and the across-ear masker would have little or no effect on the amount of across-ear interference and (2) that across-ear intrusions would almost never occur in any stimulus condition. The results of Experiment 1 clearly refute the first prediction: similarities between the target talker and the across-ear masker had a significant and in some cases a substantial impact on the amount of across-ear interference in the experiment. The increased numbers of across-ear intrusions that occurred in the TS-T and TD-T conditions also seem to refute the second prediction. One could attribute the small number of intrusions that occurred in the other conditions of the experiment (and those that in earlier experiments that used similar stimuli (Brungart and Simpson, 2002; Wightman and Kistler, 2005) to short lapses of listener attention, but the systematic increase in intrusions that occurred in the TS-T and TD-T conditions can only be explained by a model in which the signals from the listener's left and right ears are, on some level, combined prior to the extraction of the target speech on the basis of the vocal characteristics of the talkers. It is also perhaps worth noting that the significantly increased of across-ear intrusions that occurred when the across-ear masking voice was identical to the target voice is consistent with an earlier finding by Treisman (1964b) that showed that listeners who were asked to repeat the words spoken by a female talker in the right ear almost never mistakenly reported the words spoken by an interfering male talker in the left ear ($<1\%$), but frequently reported the words spoken by the same female talker in the left ear ($\approx 20\%$). Thus, it seems that listeners have some difficulty in completely ignoring a masking voice in the unattended ear when it is very similar in character to the target voice.

Although the results of Experiment 1 consistently sup-

port the predictions of the integrated strategy model of dichotic attention, they represent only a small fraction of the possible combinations that could occur in dichotic listening. Further, many of the effects found in the experiment were quite small in magnitude, suggesting they might not be consistently repeatable. And, perhaps most importantly, they only covered a range of conditions where listeners performed reasonably well in the CRM task (>40%), suggesting that some of the effects might have been very different if the listeners performance were closer to chance performance. In order to address these potential issues, a second experiment was conducted where the experimental conditions of Experiment 1 were made more difficult by adding a second interfering talker to the same ear as the target speech. The next section describes this experiment in more detail.

III. EXPERIMENT 2: A DICHOTIC LISTENING TASK WITH TWO INTERFERING TALKERS IN THE TARGET EAR

A. Methods

The methods used in Experiment 2 were virtually identical to those used in Experiment 1, with one major exception. In Experiment 2, the target speech signal presented to the listener's right (target) ear was masked by two independent CRM phrases, rather than the single interfering CRM phrase used in Experiment 1. Both of the interfering CRM phrases in the target ear were selected to have the same level of qualitative similarity to the target speech (i.e., both were spoken by the target talker, both were spoken by different same-sex talkers, or both were spoken by different different-sex talkers). Both interfering talkers were also scaled to have the same overall root-mean-square (RMS) level, and then the target speech was scaled relative to this level to produce one of five different TMR ratios: −3, 0, +3, +6, and +9 dB. In some conditions, an additional randomly selected CRM phrase was scaled to the same level as the masking phrase in the target ear and presented to the listener's left (unattended) ear. Again, depending on the condition, this talker was either the same talker who spoke the target phrase, a different talker of the same sex, or a talker who was different in sex than the target talker. Note that, as in the first experiment, the maskers were selected to ensure that they did not contain the same color or number keywords as the target phrase.

Nine of the ten listeners who participated in Experiment 1 also served as subjects in Experiment 2. The data were collected in blocks of 96–108 trials, with each block taking approximately 5 min to complete. In the first 24 blocks, the TMR values ranged from 0 to +9 dB, but in the last 6 blocks this range was expanded to include the data point at −3 dB. This resulted in a total of 2952 trials per listener, with 30 trials in each of the 12 target-masker configurations at an TMR of −3 dB, and 54 trials in each of the 12 target-masker configurations at each TMR value greater than 0 dB.

B. Results

Figure 4 shows the results of Experiment 2 in the same general format used in Fig. 2. All three independent variables and their interactions were found to be significant in a three-factor within-subjects ANOVA (Table III). Although the overall level of performance was lower in Experiment 2 than it was in Experiment 1, the pattern of performance was remarkably similar. As expected, overall performance decreased systematically with target-masker similarity in the target ear (moving from left to right across the panels), and increased systematically with increasing target-to-masker ratio (moving from left to right within each panel). There was also evidence of the same significant interaction between target-masker similarity in the target ear and the unattended ear that occurred in Experiment 1. As in Fig. 2, the brackets in the legends of the panels in Fig. 4 indicate conditions that were determined to be significantly different from one another with a bonferonni-corrected post-hoc t-test (Table IV). When a different-sex masking voice was present in the target ear, all four of the unattended-ear masking conditions were

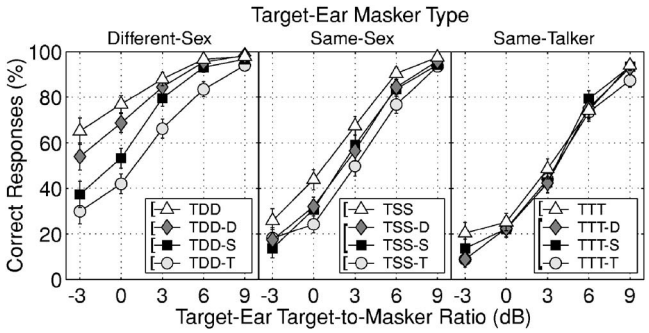

FIG. 4. Percentage of correct color and number identifications in each condition of Experiment 2, where there were two interfering talkers in the listener's right (target) ear, and either zero or one interfering talkers in the listener's left (unattended) ear. Each panel represents a different type of masker in the target ear, and the different symbols within each panel represent different types of maskers in the unattended ear. The error bars represent the 95% confidence intervals for each data point, calculated from the pooled raw data across all 9 subjects. The braces in the legends of each panel indicate groups of conditions that were not significantly different from one another at the $p<0.05$ level (as calculated from post-hoc Bonferroni-corrected paired-comparison t-test).

TABLE III. Within-subject repeated-measures analysis of variance for the arcsine-transofrmed individual subject scores in Experiment 2.[a]

Effect	SS	dF	MS	F	p
INTERCEPT	463.409	1	463.409	1107.257	0.000
Error	3.348	8	0.419		
TMR	54.18	4	13.54	742.5	0.000*
Error	0.584	32	0.018		
CONTRA	2.08	3	0.69	58.4	0.000*
Error	0.284	24	0.012		
IPSI	9.53	2	4.76	159.4	0.000*
Error	0.478	16	0.030		
TMR*CONTRA	0.25	12	0.02	3.9	0.000*
Error	0.513	96	0.005		
TMR*IPSI	1.35	8	0.17	26.5	0.000*
Error	0.409	64	0.006		
CONTRA*IPSI	0.76	6	0.13	17.2	0.000*
Error	0.353	48	0.007		
TMR*CONTRA*IPSI	0.39	24	0.02	2.6	0.000*
Error	1.208	192	0.006		

TMR=target-ear target-to-masker ratio; CONTRA=unattended-ear masker type; IPSI=target ear masker type. See the text for details.

TABLE IV. Uncorrected p values obtained for two-tailed t-tests for paired comparisons between the across-ear masking conditions of Experiment 2. The bold text indicates conditions that are significantly different at the $p < 0.05$ level when the data are Bonferoni corrected to account for the 18 pairwise comparisons represented here.

Different-sex target-ear maskers				
Condition	TDD-	TDD-D	TDD-S	TDD-T
TDD-	···	**0.0001**	**0.0000**	**0.0000**
TDD-D	**0.0001**	···	**0.0000**	**0.0000**
TDD-S	**0.0000**	**0.0000**	···	**0.0000**
TDD-T	**0.0000**	**0.0000**	**0.0000**	···
Same-sex target-ear maskers				
Condition	TSS-	TSS-D	TSS-S	TSS-T
TSS-	···	**0.0000**	**0.0000**	**0.0000**
TSS-D	**0.0000**	···	0.6224	**0.0003**
TSS-S	**0.0000**	0.6224	···	**0.0019**
TSS-T	**0.0000**	**0.0003**	**0.0019**	···
Same-talker target-ear maskers				
Condition	TTT-	TTT-D	TTT-S	TTT-T
TTT-	···	0.0237	0.2273	**0.0019**
TTT-D	0.0237	···	0.2920	0.3999
TTT-S	0.2273	0.2920	···	0.0580
TTT-T	**0.0019**	0.3999	0.0580	···

significantly different from one another; when a same-sex masking voice was present in the target ear, performance was best with no unattended-ear masker and worst with a same-talker unattended-ear masker, but there was no difference between a same-sex or different-sex masker in the unattended ear; and when a same-talker masking voice was present in the target ear, the vocal characteristics of the masker in the unattended ear had no significant effect on the resulting degradation in performance.

The pattern of within-ear and across-ear intrusions in Experiment 2 was consistent with the pattern found in Experiment 1. Figure 5 shows an analysis of intrusions that is similar to the one shown in Fig. 3, but limited to intrusions related to incorrect number responses rather than number or color responses (in the four-talker stimuli of Experiment 2 all four colors were always present in every stimulus, so there is no way to distinguish between random errors and intrusions in the color responses of that experiment). The data in the figure are somewhat more variable than those from Experiment 1, but the same basic trends are evident: (1) the majority of the errors are the result of within-ear intrusions, rather than across-ear intrusions or random responses and (2) the ratio of across-ear intrusions to within-ear intrusions is the same for all types of unattended-ear maskers when there are same-sex maskers in the target-ear, but is much higher for a same-talker unattended-ear masker when there are different-sex maskers in the target ear.

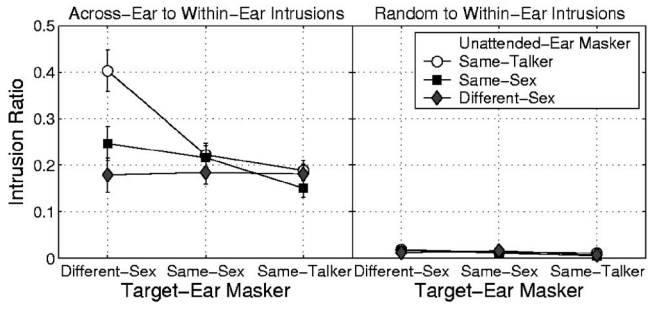

FIG. 5. Analysis of within-ear and across-ear intrusions in Experiment 2. These intrusions were calculated as in Fig. 3, but the data were analyzed only for number errors only, and not for both number and color errors (all four colors were present in every stimulus presentation, so an analysis of color errors is not meaningful in this context). The error bars show the ±1 standard error around each data point.

C. Discussion

The results of Experiment 2 provide additional support for all of the major conclusions of Experiment 1. The first of these conclusions was that there is not an increasing relationship between the difficulty of within-ear segregation and the amount of across-ear interference in a dichotic listening task. In Experiment 2, the TDD condition was by far the easiest within-ear segregation condition, but the TDD-S and TDD-T conditions produced more across-ear masking than any of the other dichotic conditions. Similarly, the TTT condition was the most difficult within-ear segregation condition, but the TTT-D, TTT-S, and TTT-T conditions produced almost no measurable across-ear interference at all. From these results and those of Experiment 1, it is very clear that the qualitative difficulty of the within-ear segregation task cannot be used to reliably predict the amount of across-ear interference in a dichotic speech identification task.

The second major conclusion of Experiment 1 was that the amount of across-ear interference varied in a complex but systematic way depending on how similar the within-and across-ear maskers were to the target talker. Again, the results of Experiment 2 fully support this conclusion. The amount of across-ear interference was generally greatest, and varied least with the voice characteristics of the across-ear masker, in the TDD-conditions, and the amount of across-ear interference was generally smallest, and varied the least with the voice characteristics of the across ear masker, in the TTT-conditions.

The final major conclusion of Experiment 1 was that the number of across-ear intrusions depended on the target-masker similarity of the within- and across-ear maskers, and that the largest number of intrusions occurred when there was a different-sex masker in the target ear and a same-talker masker in the unattended ear. Again, the results of Experiment 2 exactly match this pattern of results.

Although the magnitudes of the effects were, in some cases, very small, the fact that all the major performance trends related to within- and across-ear target-masker similarity were almost exactly the same in Experiments 1 and 2 gives some confidence that these trends reflect real properties in the underlying processes involved in dichotic speech perception. Thus, the evidence seems to be mounting that dichotic speech segregation can be conceptually modeled by an "integrated strategy model" where the amount of across-ear interference can be predicted by the extent to which the listener's optimal strategy for extracting the target speech

signal from the masking talker in the target ear can be effectively applied to suppress the interference from the masking talker in the unattended ear. If one assumes that speech signals differ from one another on some continuum, and that the optimal strategy for speech segregation is to choose the least conservative listening strategy that will reliably differentiate the target speech from the masker, then one could summarize the predictions of the model with the relatively simple heuristic that the amount of across-ear interference is insensitive to target-masker similarity when the within-ear masker is at least as similar to the target talker as the across-ear masker is, but that across-ear interference systematically increases when the across-ear masker becomes more similar to the target talker than the within-ear masker is.

To this point, all of the available data seem to be consistent with this heuristic. However, these data have only examined a very limited number of cases. In order to further test the integrated strategy hypothesis, a third experiment was conducted that examined the effect of time-reversing the speech maskers in the target and unattended ear. This condition was designed to build on one of the major results from Brungart and Simpson (2002), namely that the presence of a time-reversed talker in the unattended ear can cause as much across-ear interference as a normal talker in the unattended ear. As the contralaterally presented time-reversed speech in this condition was qualitatively less similar to the target speech than the normal masker in the target ear, this result is again consistent with the integrated strategy model for predicting the effects of across-ear interference. However, we did not test the closely related condition with a reversed within-ear masker and a normal across-ear masker, which, if the listeners were applying a within-ear segregation strategy of "listening to the non-reversed talker," would be predicted to produce a greater amount of across-ear interference than a condition with reversed maskers in both ears. Experiment 3 was conducted to more fully explore the effect of time reversal on dichotic listening performance.

IV. A DICHOTIC LISTENING TASK WITH TIME-REVERSED WITHIN- AND ACROSS-EAR MASKERS

A. Methods

The methods used in the third experiment were again similar to those used in the TS and TS-S listening conditions of the first experiment. As in Experiment 1, the target phrase in each trial was randomly selected from all the phrases in the CRM corpus with the call sign Baron, and the masking phrases were chosen from all the phrases in the corpus that had different call signs, colors, and numbers than the target phrase and were spoken by a different talker of the same sex as the target talker. Also, as before, the RMS value of the phrase presented in the target ear was scaled to one of five different TMR values relative to the level of the masking phrase in that ear (−8, −4, 0, +4, or +8 dB). The primary difference in Experiment 3 was that, in addition to the standard conditions with a same-sex masker in the target ear (the TS condition) or in both ears (the TS-S condition), three new conditions were conducted with the same-sex masking phrase time-reversed either in the same ear as the target speech (the TR and TR-S conditions), the ear opposite the target speech (the TS-R condition), or in both ears (the TR-R condition).

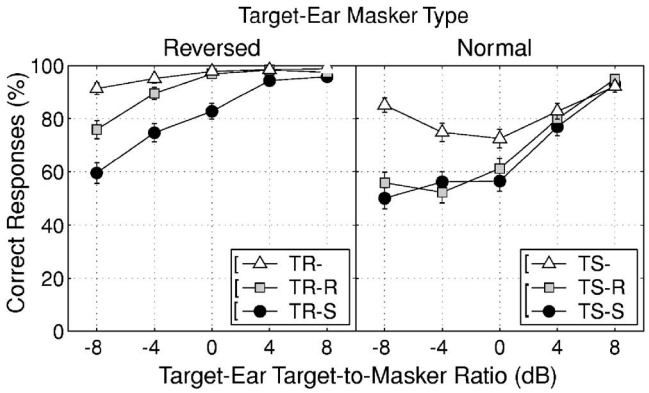

FIG. 6. Percentage of correct color and number identifications in each condition of Experiment 3, where there was a single normal or reversed interfering talker in the listener's right (target) ear, and either zero or one interfering normal or reversed talkers in the listener's left (unattended) ear. Each panel represents a different type of masker in the target ear, and the different symbols within each panel represent different types of maskers in the unattended ear. The error bars represent the 95% confidence intervals for each data point, calculated from the pooled raw data across all 9 subjects. The braces in the legends of each panel indicate groups of conditions that were not significantly different from one another at the $p<0.05$ level (as calculated from post-hoc Bonferroni-corrected pairwise t-tests.)

A total of nine paid volunteer listeners participated in the study, including seven of the nine listeners from Experiment 2. The data collection was divided into blocks of 110 trials, with each block containing 10 trials in each of the six conditions listed previously.[1] Each subject participated in a total of 36 blocks over a two week period, resulting in a total data collection of 360 trials per subject in each of the six conditions.

B. Results

Figure 6 shows the results of Experiment 3 in a format similar to the one used in Figs. 2 and 4. Not surprisingly, the results show that performance was substantially better when the target-ear masker was time-reversed (left-hand panel) than when it was presented normally (right-hand panel). Also, comparing the curves in the right panel, it is clear that the listeners performed almost identically in the TS-S and TS-R listening configurations, just as they did in the earlier experiment by Brungart and Simpson (2002). However, the results in the left-hand panel clearly show that time-reversal of the contralaterally-presented stimulus *did* have a large impact on performance when the target-ear masker was time reversed. In fact, performance at low TMR values was approximately 15 percentage points worse in the TR-S condition than in the TR-R condition. A Bonferroni-corrected post-hoc t-test test performed on results confirmed that the TR, TR-R, and TR-S conditions were all significantly different from one another, but that the TS-R and TS-S conditions were not (as illustrated by the brackets in the legends in Fig. 6).

C. Discussion

The data from Experiment 3 again reinforce the two major conclusions of Experiment 1. First, they provide further evidence that the amount of across-ear interference is unrelated to the difficulty of the listening task in the target ear. When the target-ear TMR value was 0 dB, for example, performance was nearly perfect in the TR condition, and only about 75% in the TS condition, but the addition of a same-sex across-ear masker produced roughly the same decrease in performance (20 percentage points) in both conditions.

The data also provide additional support for the notion that across-ear interference in dichotic listening depends on the target-masker similarity of the across-ear masker only when that masker is more similar to the target speech than the within-ear masker is. In the case of Experiment 3, time reversing the across-ear masker to make it more distinct from the target speech improved performance when the within-ear masker was also reversed, but not when the within-ear masker was normal speech. Conceptually, one could interpret this to mean that the listener in the TR condition was adopting a within-ear strategy of "listening to the non-reversed taller," and that this strategy was disrupted more in the presence of a normal across-ear masker (which would not be filtered out by the within-ear strategy) than by the presence of a time-reversed across-ear masker (who would be filtered out by the within-ear strategy). Similarly, in the TS case the listener adopts a within-ear-segregation strategy-based on specific voice characteristics (F0, Vocal Tract, etc.) that would be just as effective on the time-reversed across-ear masking speech as it would be on the normal across-ear masking speech. Thus, the listener's performance is not significantly different across the TS-S and TS-R conditions of the experiment.

V. CONCLUSIONS

In this paper, we have presented three experiments examining the role that target-masker similarity plays in within-ear and across-ear interference in dichotic listening. As in previous studies, these results have shown that within-ear selective attention degrades when the target and masking voice characteristics become more similar. However, there was no evidence that the amount of across-ear interference was directly related to the difficulty of the within-ear listening task. In many cases, the listeners were most susceptible to across-ear interference in the conditions with the most easily segregated different-sex masking talker in the target ear. There were, however, strong indications that there is a consistent relation between within-ear target-masker similarity, across-ear target-masker similarity, and the amount of across-ear masking in a dichotic listening task. In all the conditions we tested, the amount of across-ear interference increased with the similarity of the across-ear masker to the target voice only when the across-ear masker was more similar to the target than the within-ear masker was. Further, this increased across-ear interference was associated with an increased number of across-ear intrusions where the listener inadvertently responded with the color and number keywords spoken by the masker in the unattended ear.

These results provide strong support for an integrated strategy model of dichotic attention in which the sounds from the attended and unattended ears are, in some way, integrated together into a single perceptual image prior to the point where the voices are actually segregated into different streams of speech. Thus, the listener is forced to choose a single general speech segregation strategy that is effectively applied to the combined signal containing all the competing voices in the dichotic stimulus. However, one issue that remains unresolved is how the signal from the unattended ear is really represented in this combined signal. In her Attenuation Filter Theory, Treisman (1964a) suggested that selective attention to a single ear has the effect of attenuating, but not eliminating, the acoustic information arriving at the unattended ear, and that the attenuated message from the unattended ear is in effect combined with the message from the attended ear prior to semantic processing. This would suggest that the voice from the unattended ear is present in the combined signal prior to the extraction of the target phrase, but that it produces less interference than it would if it were presented in the same ear as the target speech. This certainly seems like a reasonable assumption, but from the results we have obtained thus far it is difficult to know just how much "attenuation" occurs in the signal from the unattended ear. Of course, performance in the dichotic listening task is generally worse when the second interfering masker is presented in the same ear as the target speech than when it is presented in the opposite ear, but much of this effect could be accounted for by additional energetic masking due to the spectral overlap of the competing talkers in the target ear. And there is at least one exception to this rule: when the second interfering masker is much quieter than the other two talkers, it can actually produce more interference when it is added to the unattended ear than when it is added to the target ear (Brungart and Simpson, 2005). Before a truly comprehensive model of dichotic spatial attention can be developed, it will be necessary to gain a greater understanding of how the "attenuated" image of the across-ear masker is really perceived in relation to the unattenuated image of the speech signal in the target ear.

ACKNOWLEDGMENTS

The authors would like to thank Nandini Iyer for her helpful comments on the manuscript. Funding for this effort was provided, in part, by AFRL Grant No. 01-HE-01-COR.

[1]Each block also contained ten trials in each of five other conditions that are not discussed here.

Abouchacra, K., Tran, T., Besing, J., and Koehnke, J. (**1997**). "Performance on a selective attention task as a function of stimulus presentation mode," Proceedings of the Midwinter Meeting of the Association for Research in Otolaryngology, St. Petersburg Beach, FL.

Bolia, R., Nelson, W., Ericson, M., and Simpson, B. (**2000**). "A speech corpus for multitalker communications research," J. Acoust. Soc. Am. **107**, 1065–1066.

Brungart, D. (**2001a**). "Evaluation of speech intelligibility with the coordi-

nate response measure," J. Acoust. Soc. Am. **109**, 2276–2279.
Brungart, D. (**2001b**). "Informational and energetic masking effects in the perception of two simultaneous talkers," J. Acoust. Soc. Am. **109**, 1101–1109.
Brungart, D., and Simpson, B. (**2002**). "Within-channel and across-channel interference in the cocktail-party listening task," J. Acoust. Soc. Am. **112**, 2985–2995.
Brungart, D., and Simpson, B. (**2005**). "Evidence for a "reverse cocktail party effect" in a three-talker dichotic listening task," Acustica **91**, 564–566.
Cherry, E. (**1953**). "Some experiments on the recognition of speech, with one and two ears," J. Acoust. Soc. Am. **25**, 975–979.
Drullman, R., and Bronkhorst, A. (**2000**). "Multichannel speech intelligibility and talker recognition using monaural, binaural, and three-dimensional auditory presentation," J. Acoust. Soc. Am. **107**, 2224–2235.
Egan, J., Carterette, E., and Thwing, E. (**1954**). "Factors affecting multichannel listening," J. Acoust. Soc. Am. **26**, 774–782.
Johnston, W., and Heinz, S. (**1978**). "Flexibility and capacity demands of attention," J. Exp. Psychol. Gen. **30**, 656–674.
Kidd, G. J., Mason, C., Arbogast, T., Brungart, D., and Simpson, B. (**2003**). "Informational masking caused by contralateral stimulation," J. Acoust. Soc. Am. **113**, 1594–1603.
Moray, N. (**1959**). "Attention in dichotic listening: affective cues and the influence of instructions," Q. J. Exp. Psychol. **9**, 56–60.
Moray, N. (**1969**). *Listening and Attention* (Penguin, Baltimore, MD).
Treisman, A. (**1964a**). "The effect of irrelevant material on the efficiency of dichotic listening," Am. J. Psychol. **77**, 533–546.
Treisman, A. (**1964b**). "Verbal cues, language, and meaning in attention," Am. J. Psychol. **77**, 206–214.
Wickens, C. D. (**1984**). "The structure of attentional processes," in *Varieties of Attention*, edited by R. Parasuraman and D. Davies (Academic, Orlando, FL).
Wightman, F., and Kistler, D. (**2005**). "Informational masking of speech in children: Effects of ipsilateral and contralateral distracters," J. Acoust. Soc. Am. **118**, 3164–3176.
Wood, N., and Cowan, N. (**1995**). "The cocktail party phenomenon revisited: Attention and memory in the classic selective listening procedure of cherry," J. Exp. Psychol. Gen. **124**, 243–262.

Subglottal coupling and its influence on vowel formants

Xuemin Chi[a] and Morgan Sonderegger[b]
Speech Communication Group, RLE, MIT, Cambridge, Massachusetts 02139

(Received 25 September 2006; revised 14 June 2007; accepted 15 June 2007)

A model of acoustic coupling between the oral and subglottal cavities is developed and predicts attenuation of and discontinuities in vowel formant prominence near resonances of the subglottal system. One discontinuity occurs near the second subglottal resonance (*SubF*2), at 1300–1600 Hz, suggesting the hypothesis that this is a quantal effect [K. N. Stevens, J. Phonetics **17**, 3–46 (1989)] dividing speakers' front and back vowels. Recordings of English vowels (in /hVd/ environments) for three male and three female speakers were made, while an accelerometer attached to the neck area was used to capture the subglottal waveform. Average speaker *SubF*2 values range from 1280 to 1620 Hz, in agreement with prior work. Attenuation of 5–12 dB of second formant prominence near *SubF*2 is found to occur in all back-front diphthongs analyzed, while discontinuities in the range of 50–300 Hz often occur, in good agreement with the resonator model. These coupling effects are found to be generally stronger for open-phase than for closed-phase measurements. The implications for a quantal relation between coupling effects near *SubF*2 and [back] are discussed.
 [DOI: 10.1121/1.2756793]

PACS number(s): 43.70.Bk [BHS] Pages: 1735–1745

I. INTRODUCTION

An important question lies at the intersection of phonetics and feature-based phonology: What is the precise connection between the acoustic properties of sounds and their phonological feature values? One proposal addressing this question is quantal theory (QT) (Stevens, 1972, 1989), in which features arise from nonlinear articulatory-acoustic relations in speech production when an acoustic parameter of the speech signal shifts from one stable region to another for a linear articulatory movement (schematized in Fig. 1).

These are termed "quantal relations"; possible quantal relations for most distinctive features are given in Stevens (1989). Experimental studies that address QT (Stevens and Blumstein, 1975; Ladefoged and Bhaskararao, 1983; Pisoni, 1981; Perkell and Cohen, 1989) generally have not examined particular quantal relations, focusing instead on whether a phonetic data set is "quantal" in the broad sense that it shows variation in articulation of a particular sound structured so as to minimize variation in its acoustic realization. However, almost no work so far has directly tested the central claim of QT, that certain acoustic-articulatory nonlinearities are used as quantal relations. A direct test of QT would have to address two questions about a particular acoustic-articulatory relation proposed as a quantal relation for [feature]: First, does the nonlinearity occur robustly in real speech? Second, if it does, is it used by speakers to distinguish sounds with + and − values of [feature]? Without direct tests of individual quantal relations, it is unclear whether QT should be seen as a theoretical construct, a set of constraints on speech sounds, or the fundamental basis of phonetic categories. This paper takes a first step toward testing QT by analyzing a nonlinear acoustic-articulatory relation proposed as a quantal relation in detail, and thus answering the first question, that of occurrence and robustness.

This paper examines second formant frequency discontinuity and amplitude attenuation in diphthongs near the second subglottal resonance (*SubF*2) due to coupling between the oral and subglottal cavities ("subglottal coupling"). Subglottal resonances have been measured in a number of studies using both invasive (Ishizaka *et al.*, 1976; Cranen and Boves, 1987) and noninvasive (Fant *et al.*, 1972; Henke, 1974; Stevens *et al.*, 1975; Hanson and Stevens, 1995; Cheyne, 2002) methods. *SubF*2 usually lies in the range of 1300–1600 Hz, depending on the speaker. This frequency range is also approximately the dividing line between the second formant (*F*2) of front ([−back]) and back ([+back]) vowels. What determines the boundary, between front and back vowels is unknown. QT provides one possibility, that speakers will avoid putting formants in the acoustically unstable region around *SubF*2, which will then be used as a dividing line between front and back vowels.

In this paper, a theoretical model is first presented to explain the occurrence of subglottal coupling effects, followed by analysis of the occurrence and size of these effects, namely attenuation of the second formant amplitude (*A*2) and a discontinuity in second formant frequency near *SubF*2, and finally discussion of the implications for testing QT.[1]

II. MODELING ORAL-SUBGLOTTAL COUPLING

Coupling between the oral and subglottal cavities can usually be ignored in acoustic modeling of the vocal tract transfer function, but becomes non-negligible when an oral cavity formant approaches a subglottal resonance in frequency. General properties of coupled resonators (discussed in the following) then predict that the formant prominence amplitude will be attenuated, and its prominence frequency will appear to "jump," skipping the subglottal resonance fre-

[a]Electronic mail: xuemin@speech.mit.edu
[b]Electronic mail: morgan@speech.mit.edu

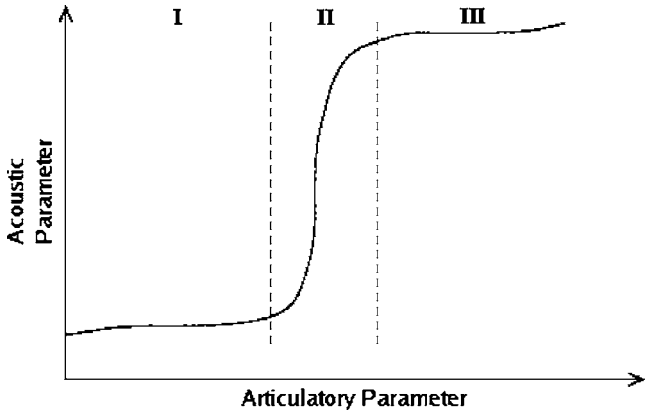

FIG. 1. Schematic of a quantal relation. Regions I and III correspond to [+feature] and [−feature] values, region II is the abrupt transition between them.

quency. The latter effect can often be observed as a discontinuity in the $F2$ track for back-front diphthongs near the second subglottal resonance, as in Fig. 2. These attenuation and frequency jump effects, together called "subglottal coupling effects," can be understood through the acoustic model of the oral-subglottal system described in the following. This model predicts formant frequency jumps and $A2$ attenuation due to subglottal coupling, and suggests a positive correlation between the amount of a speaker's subglottal coupling and the size of that speaker's frequency jump and amplitude attenuation effects.

A. Description of the acoustic model

In this section, an acoustic model of coupling between the oral and subglottal cavities is developed in order to understand the occurrence of subglottal coupling effects seen in some back-front diphthongs. Interaction between the oral and subglottal cavities can be modeled by the circuit shown in Fig. 3.

In this circuit, the volume velocity output of the glottis, U_0, is filtered by the circuit's transfer function, $T(\omega)$, to give U_m, the volume velocity at the lips. This setup deviates from

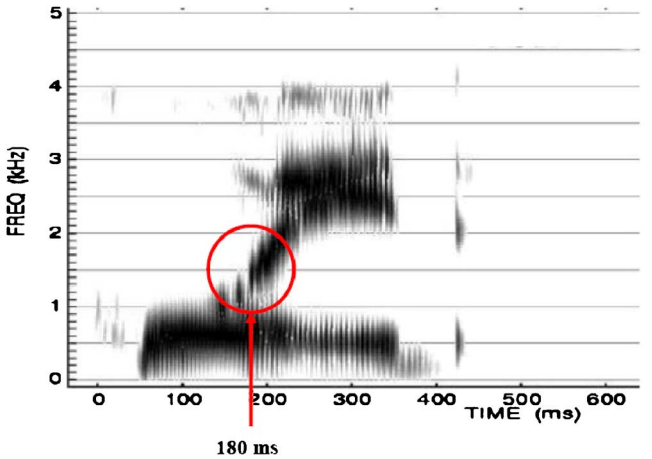

FIG. 2. (Color online) Spectrogram for an /ɔɪ/ diphthong spoken by a male speaker (M1). As shown in the circled region at 180 ms, attenuation of $F2$ prominence and discontinuity in the $F2$ track occur near the second subglottal resonance, at 1370 Hz.

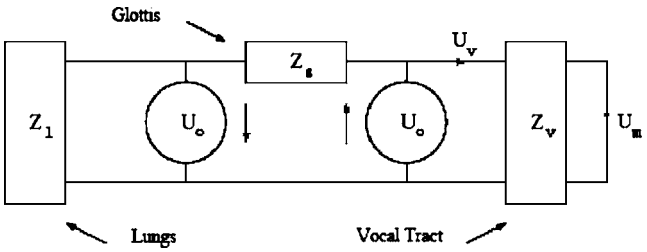

FIG. 3. Equivalent circuit model of the oral and subglottal cavities. Z denotes impedances. Adapted from Hanson and Stevens (1995).

the standard source-filter model only in incorporating the subglottal cavity, via coupling to the vocal tract through the glottis, into the transfer function, which is conventionally determined only by the vocal tract.

In Fig. 3, Z_l is the impedance of the subglottal system, approximated here by a tube of length l_l and area A_l terminated in a lossy capacitance (acoustic compliance) Z_c, following an approximation suggested in Ishizaka *et al.* (1976) to capture the damping effect of the lung bronchi. This approximation is acceptable when an accurate model of only one subglottal formant is required, as in this paper.[2]

Z_g is the glottal impedance, modeled by

$$Z_g = R_g + j\omega M_g, \tag{1}$$

with $R_g = 12\mu h_g / l_g d_g^3 + K_\rho U_g / (l_g d_g)^2$ and $M_g = \rho h_g / l_g d_g$, where μ and ρ are the glottal coefficients of viscosity and density, l_g, d_g, h_g are the glottal length, width, and thickness, U_g is the glottal volume velocity, and K is a constant taken to be ≈ 1 (Rösler and Strube, 1989; Stevens, 1998, p. 165). U_g is periodic, but since its period is small compared to the time scale of formant transitions, it can be approximated here by its average value without affecting the model behavior, allowing a linear system analysis. The dipole configuration of two volume velocity sources U_0 separated by impedance Z_g in Fig. 3 is a good approximation for the glottal source (Zhao *et al.*, 2002).

Z_v, the impedance looking into the vocal tract from the glottis, is computed here using the two-tube model of the vocal tract shown in Fig. 4. This model is sufficiently accurate to predict $F1$ and $F2$, which characterize different vowels (along the height and backness dimensions). Vocal tract wall impedances are neglected for simplicity, but to give the vocal tract formants some bandwidth in the frequency range

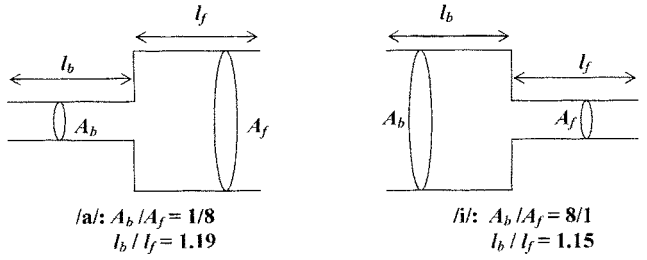

FIG. 4. Two-tube models of the vocal tract configuration for /ɑ/ and /i/, adapted from Fant (1960), p. 66. For /ɑ/, A_b=1 cm^2, A_f=8 cm^2, l_b =10.7 cm, and l_f=9.0 cm. For /i/, A_b=8 cm^2, A_f=1 cm^2, l_b=7.9 cm, and l_f=6.9 cm. Z_f is the impedance looking into the front cavity and Z_r is the radiation impedance at the lips.

of interest, an output resistance was added in series with the radiation impedance for the simulations described in Sec. II B.

In Fig. 4, Z_r is the radiation impedance at the lips and Z_f is the impedance looking into the front cavity. For the frequency range simulated here, Z_r can be approximated as

$$Z_r = \frac{\rho\omega^2}{4c}K_s(\omega) + j\frac{\omega\rho(0.8a)}{A_m}, \tag{2}$$

where $\pi a^2 = A_m$, the area of the mouth opening. $K_s(\omega)$ is a numerical factor accounting for the baffling effect of the head, which can be approximated as 1 at low frequencies, rising to 1.7 by 2000 Hz, and 1.5 for frequencies above 2000 Hz (Stevens, 1998, p. 153).

The impedance looking down a tube of length l and area A terminated in an impedance Z is (Kinsler and Frey, 1962, p. 201)

$$Z_0(l,A,Z) = \frac{\rho c}{A}\cdot\frac{Z + j\frac{\rho c}{A}\tan kl}{\frac{\rho c}{A} + jZ\tan kl}, \tag{3}$$

where c is the speed of sound. For the two tube model, in Fig. 4, Eq. (3) thus gives $Z_f = Z_0(l_f, A_f, Z_r)$ and $Z_v = Z_0(l_b, A_b, Z_f)$.

To determine the transfer function, $T(\omega) = U_m/U_0$, in Fig. 3, $T(\omega)$ is decomposed into

$$T(\omega) = \frac{U_m}{U_v}\frac{U_v}{U_0}, \tag{4}$$

where U_v is the airflow into the vocal tract, and the two ratios of volume velocities are first solved individually.

U_m/U_v is determined by impedance matching at the entrances to the front and back cavities, which leads to

$$\frac{U_m}{U_v} = \frac{[K_b\cos(\omega l_b/c) - j\sin(\omega l_b/c)Z_f]}{K_b} \times \frac{[K_f\cos(\omega l_f/c) - j\sin(\omega l_f/c)Z_v]}{K_f}, \tag{5}$$

after some calculation, where $K_f = \rho c/A_f$ is the characteristic impedance of the front cavity and K_b is defined similarly.

Solving the circuit in Fig. 3 gives

$$\frac{U_v}{U_0} = \frac{Z_g}{Z_g + Z_v + Z_l}, \tag{6}$$

where U_v is the airflow into the vocal tract. Under the usual assumption of zero oral-subglottal coupling, $Z_g = \infty$, U_v/U_0 is unity and contributes no poles or zeros to the transfer function $T(\omega)$. As shown in Sec. II C, when coupling is assumed, numerical calculation of Eq. (6) using the expressions for Z_g, Z_v, and Z_l given earlier shows that a zero-pole pair is added to the transfer function at each subglottal resonance, with the zero at the subglottal resonance (when Z_l has a local maximum) and the pole at the local minimum of $(Z_g + Z_v + Z_l)$. The simulations in Sec. II C show that each pole lies above its associated zero, and the distance in frequency between the zero and pole in each pair is correlated with the glottal area, and thus inversely correlated with the magnitude of Z_g. The emergence of a zero-pole pair can be understood more clearly by considering the limiting case where $Z_l = \infty$, in which case Eq. (6) has a zero at each subglottal resonance. In sum, the net effect of adding subglottal coupling to a source-filter model is an extra zero-pole pair at each subglottal resonance.

B. Model calculations

Using the model developed in previous sections, a simulation was performed to show how the added zero (at the frequency of the second subglottal resonance) resulting from subglottal coupling and its associated pole lead to the frequency jump and amplitude attenuation effects seen in speech spectra. Taking account of radiation from the mouth, the pressure spectrum of an /aɪ/ diphthong for a male speaker was simulated by changing dimensions linearly between the tube shapes approximating the vocal tract configurations of /ɑ/ and /i/ shown in Fig. 4. The dimensions used were $A_b = 1$ cm^2, $A_f = 8$ cm^2, $l_b = 10.7$ cm, $l_f = 9.0$ cm for /ɑ/, and $A_b = 8$ cm^2, $A_f = 1$ cm^2, $l_b = 7.9$ cm, $l_f = 6.9$ cm for /i/. The lossy capacitance Z_c was taken to be a resistance in series with a capacitance and another resistance in parallel. The values of these parameters were empirically chosen to approximate the subglottal spectrum near *SubF2*.

Using values within the ranges for a male speaker, we set $U_g = 200$ cm^3 s^{-1} (Holmberg *et al.*, 1988), $l_g = 1.5$ cm, $d_g = 0.045$ cm, $h_g = 0.3$ cm (Li *et al.*, 2006), $M_g = 0.0082$ g cm^{-4}, $R_g = 128.3$ dyn s cm^{-5} (Rösler and Strube, 1989; Stevens, 1998, p. 165), $l_l = 19.35$ cm, $A_l = 2.5$ cm^2 (Ishizaka *et al.*, 1976), and $A_g = 0.0675$ cm^2 (Stevens, 1971). A_g, defined here as $l_g d_g$, is taken to represent the average value of the glottal area over one glottal cycle. With the understanding that the true glottal area is continuously changing, A_g will be referred to as "glottal area" for simplicity.

To simulate *F2* tracks, one last step was taken: a resistance of 1.5 acoustic ohms was added in series to Z_r to give the vocal tract formant peak some bandwidth. This was done as an alternative to adding wall impedances to facilitate finding modeled values of *F2*, since without wall impedances the vocal tract formant will always dominate any poles or zeroes arising from subglottal coupling. With this added resistance and with the above given parameter settings, the simulated track of the second formant prominence frequency matches one recorded by hand, using methods described in Sec. V A, for a male speaker's /aɪ/ utterance. This track is shown in Fig. 5, and does show a frequency jump effect near *SubF2*. Also shown in Fig. 5 is a simulated *F2* track using the same parameter values, but with no oral-subglottal coupling ($Z_g = \infty$). No jump occurs in this track, showing that the frequency jump observed in the coupled case arises directly from subglottal coupling, rather than this particular set of parameter values.

The frequency jump effect arises as the second formant peak passes through the zero pole pair introduced by subglottal coupling. The dynamics of this effect can be understood through the schematic pole-zero plot shown in Fig. 6. As

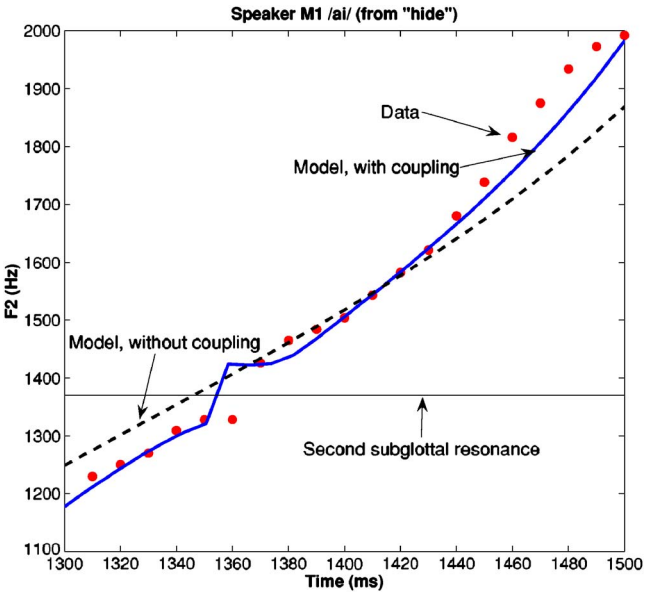

FIG. 5. (Color online) Observed and modeled $F2$ tracks (with and without coupling) for an /aɪ/ diphthong spoken by a male speaker (M1). The modeled track with coupling shows a jump in $F2$ near *SubF*2, while the modeled track without coupling shows no discontinuities. Data were taken once per pitch period, with window length of one glottal cycle.

discussed in Sec. II A, the subglottal pole lies above the subglottal zero in frequency. As the pole associated with the second formant prominence approaches the zero located at *SubF*2, the second formant peak amplitude is attenuated. The second formant peak then becomes associated with the higher pole and resumes its normal linear trajectory. The discontinuity seen in the $F2$ track is a result of this switch in the formant peak's pole affiliation. A frequency discontinuity near *SubF*2 thus arises directly from subglottal coupling in this model. As can be seen in Fig. 6, the size of this discontinuity will be approximately equal to the frequency difference between the subglottal zero and its associated pole.

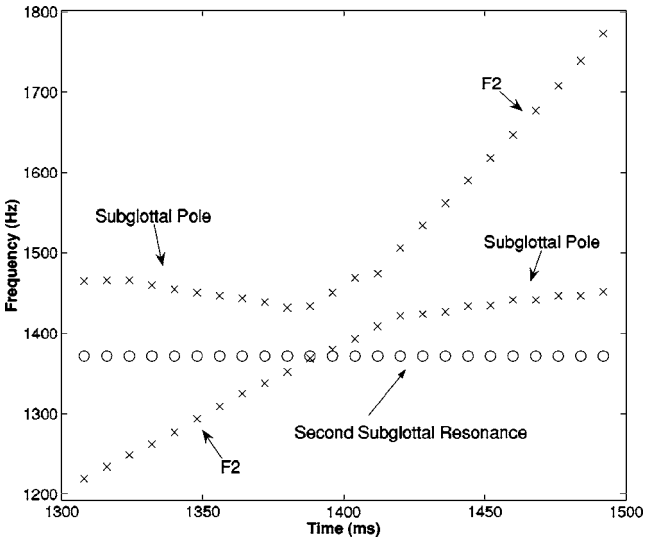

FIG. 6. Schematic of pole-zero plot corresponding to a simulated back-front diphthong with subglottal coupling. As the lower pole approaches the zero, the formant peak amplitude is attenuated and the peak frequency switches affiliation to the higher pole, which moves away from the zero.

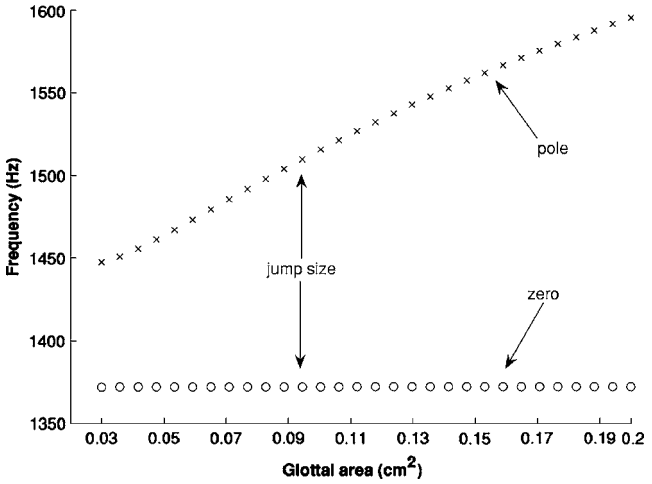

FIG. 7. Simulated frequencies of the zero-pole pair due to subglottal coupling near the second subglottal resonance frequency, where the zero is located. As glottal area increases from 0.03 to 0.2 cm^2 the zero-pole separation increases from 75 to 225 Hz, implying larger observed "jumps" in the second formant prominence frequency.

C. Model predictions

This model predicts the occurrence of subglottal coupling effects; it also predicts patterns of cross-speaker variation in these effects. As discussed in Sec. II A, subglottal coupling increases as the magnitude of Z_g decreases, giving rise to greater separation between the pole and zero introduced by subglottal coupling. This leads to increased attenuation of the second formant prominence, $A2$ (due to the more prominent zero, as the pole moves away), and an increased jump size in $F2$ (due to the increased zero-pole distance). Because Z_g varies inversely with glottal area ($l_g d_g$) [Eq. (1)], a larger glottal opening implies greater subglottal coupling. Speakers with breathier voices (larger glottal area) are thus expected to show greater frequency jump and amplitude attenuation.

To examine the effect glottal area (and thus Z_g) has on the size of the frequency separation of the zero-pole pair of U_v/U_0 introduced by coupling (and thus predicted $F2$ jump size), the pole and zero were calculated for a range of A_g. The influence of the vocal tract due to coupling was ignored by setting $Z_v=0$, so that the only variable is the average glottal area A_g. As A_g is increased from 0.03 to 0.2 cm^2 for normal modal voicing (Stevens, 1998, p. 35), predicted jump size, shown in Fig. 7, increases from 75 to 225 Hz as Z_g decreases, causing an increase in subglottal coupling and a resulting increase in the zero-pole distance.

To examine the effect glottal area (and thus Z_g), has on predicted $A2$ attenuation near *SubF*2, simulations of the vocal tract output for an /aɪ/ diphthong, as described in Sec. II B, were performed for a range of A_g. Increasing A_g from 0.03 to 0.2 cm^2 predicts an increase in $A2$ attenuation from 5 to 13 dB, as shown in Fig. 8, with larger A_g causing greater attenuation near *SubF*2. Because the model neglects wall impedances and uses a simple model for the subglottal imped-

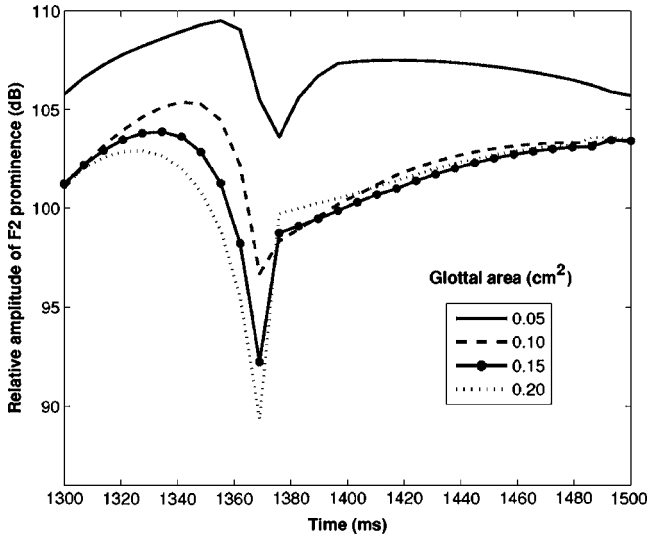

FIG. 8. Simulated *F*2 amplitude trajectories for /aɪ/ diphthongs using glottal areas of 0.05, 0.10, 0.15, and 0.20 cm^2. The amplitude attenuation seen in these trajectories occurs as the second formant peak crosses *SubF*2 at around 1370 ms. When glottal area is 0.05 cm^2, an attenuation of about 5 dB is observed in the F2 prominence. For a larger glottal area of 0.20 cm^2, the attenuation increases to 12 to 13 dB. Increased glottal area leads to greater zero-pole separation. The zero then becomes more prominent, causing greater amplitude attenuation to the F2 prominence.

ance, these attenuation values are only approximate. These simplifications affect bandwidths, but not the general prediction of a positive correlation between glottal area and the strength of subglottal coupling effects.

Note that the 1.5 acoustic ohm added resistance described in Sec. II B was not used in the calculations for Fig. 7 because the vocal tract was decoupled, and was not used in Fig. 8 because it would affect measurement of the *A*2 dip near *SubF*2.

Variation in the parameters used in this model will lead to variation in the extent of subglottal coupling effects for different speakers. The bulk of this paper shows the robustness of subglottal coupling effects across speakers and accounts for the differences observed in the strength of the coupling effects across speakers.

III. PROCEDURES

A. Data collection

Acoustic data were collected from three male and three female speakers, labeled M1–M3 and F1–F3. All speakers were native speakers of American English except M1, a native speaker of Canadian English. Subjects were recorded saying the phrase "hVd, say hVd again" five times for each of the American English monophthongs and diphthongs shown in Table I. The sentences were presented in a random order and prompted on a computer screen.

All utterances were recorded in a sound-isolated chamber using an Electro-Voice model DO54 omni-directional microphone (for audio data) and an accelerometer (for subglottal data). The microphone signal was first amplified by a mixer, then low-pass filtered at 4.8 kHz to avoid aliasing. It was digitized into a PC using the MARSHA[3] program at a sampling rate of 10 kHz, which is above the Nyquist rate.

TABLE I. American English vowel IPA symbols, carrier words used, and [back] value.

Vowel	English word	[+/−back]
/i/	"heed"	−
/ɪ/	"hid"	−
/ɛ/	"head"	−
/æ/	"had"	−
/ɑ/	"hodd"	+
/ɔ/	"hawed"	+
/o/	"hoed"	+
/ʌ/	"hud"	+
/ʊ/	"hood"	+
/u/	"who'd"	+
/ɝ/	"heard"	+
/aʊ/	"how'd"	+/+
/aɪ/	"hide"	+/-
/ɔɪ/	"hoid"	+/−
/ju/	"hued"	−/+
/eɪ/	"hade"	−/−

B. Measuring the subglottal resonances

The subglottal resonances for each speaker were measured using an EMkay BU-1771 accelerometer glued 1 in. above the sternal notch. This method is noninvasive and gives a spectrum sufficiently clear to accurately determine subglottal resonant frequencies (Henke, 1974; Stevens *et al.*, 1975; Cheyne, 2002). Because of its small mass (300 mg), the accelerometer does not have a significant impact on the system to which it is attached.

For a typical speaker, the accelerometer voltage signal ranges from 10 to 15 mVPP. A noninverting amplifier with a gain of 10 was built to amplify this voltage signal before it was fed to a mixer, and then digitized into a computer. A low offset, low drift LF411 operational amplifier was used to eliminate additional dc offset that came from the accelerometer output. The ac-coupled mixer removed the dc bias from the signal before it was digitized by the computer at 10 kHz. The digitized accelerometer signal was then bandpass filtered around the *SubF*2 region to emphasize the second subglottal resonance, with a bandwidth of 600 Hz for male speakers and 800 Hz for female speakers.[4] A wider bandwidth was used for female speakers due to their generally breathier voices, which give wider *SubF*2 peaks (Klatt and Klatt, 1990; Hanson, 1997). A sample spectrogram and DFT of the accelerometer output for the word "heed" (spoken by speaker M1), taken at midvowel using a 10 ms window, are displayed in Fig. 9. The subglottal resonances for this utterance are at 550 and 1360 Hz.

IV. SECOND SUBGLOTTAL RESONANCE ANALYSIS

*SubF*2 values from the accelerometer data were first found for all vowels for all speakers. Although only diphthongs will be examined in the remainder of this paper, *SubF*2 values for both monophthongs and diphthongs were measured to explore the overall distribution of speakers' *SubF*2 values. Previous studies, listed in the following, have reported fewer than 10 *SubF*2 measurements per speaker, on one to three different vowels.

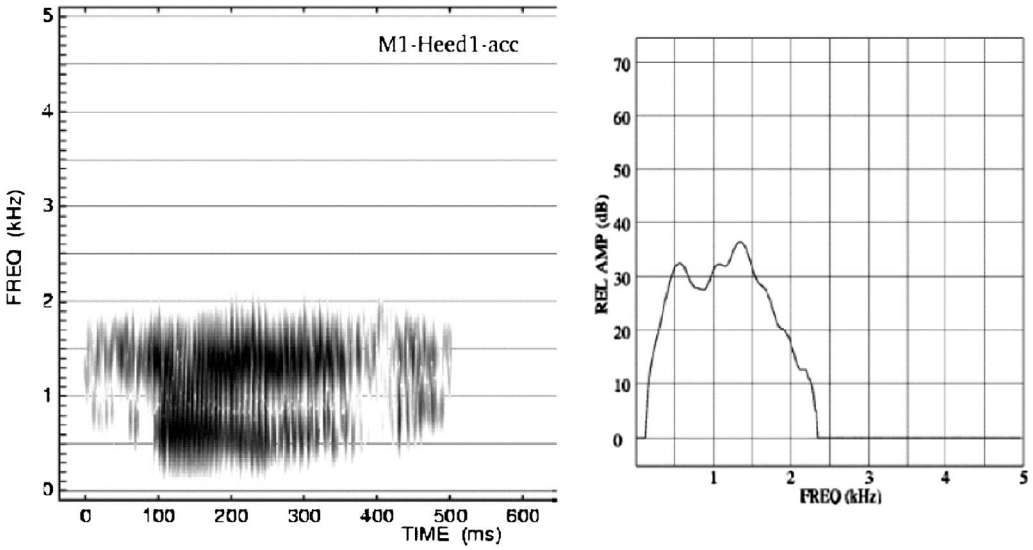

FIG. 9. Sample spectrogram and DFT of M1's accelerometer signal for "heed." The DFT was taken around 240 ms with a window size of 10 ms. Spectral peaks are visible at 550 Hz *(SubF*1*)* and 1360 Hz *(SubF*2*)*. A small peak around 1000 Hz can be seen in the accelerometer spectrum. This peak is a result of coupling to the supraglottal tract, and is not captured by our simple model of the subglotal system. For a more detailed model accounting for such peaks, see Lulich (2006).

Because *SubF*2 stays relatively constant during phonation, its values for all monophthongs were determined using a formant tracker. Means of data taken using the tracker were found to agree with hand-taken data for several test vowels and also with those measured by hand in the diphthong analysis in Sec. V. Statistics on each speaker's *SubF*2 distribution are shown in Table II. Histograms of *SubF*2 values for all speakers conform reasonably well to normal distributions and agree with previously reported *SubF*2 values found using invasive techniques. Ishizaka *et al.* (1976) reported means "around 1400 Hz" for five speakers (male and female), and Cranen and Boves (1987) reported a mean of 1355 Hz for two male speakers, while mean values for this study's speakers fall between 1280 and 1620 Hz.[5]

V. DIPHTHONG ANALYSES

Back-front diphthongs of the six speakers were examined for coupling effects (formant frequency jump and amplitude attenuation) predicted by the theoretical model when the second formant peak passes *SubF*2. *F*2, second formant frequency, *A*2, amplitude of second formant prominence, and *SubF*2, second subglottal resonance, were measured by hand in two different ways in three steps. A Hamming window with length of one pitch period was first used to take measurements from consecutive pitch periods for four diphthong tokens of each of the six speakers. Next, the window size was changed to slightly longer than half of each glottal period, and measurements on the same tokens were taken twice per pitch period to compare the open and closed phases of the glottal cycle. As open-phase measurements showed stronger evidence of subglottal coupling effects, open-phase measurements were finally made on six additional diphthong tokens for each speaker, totaling ten open-phase tokens per speaker.

TABLE II. Mean, standard deviation (σ), number of tokens (N), and normal distribution chi-squared for speakers' *SubF*2 distributions, across monophthongs and diphthongs.

Speaker	$\bar{x}$ (Hz)	σ (Hz)	N	χ^2_ν
M1	1374	12	168	1.3
M2	1310	20	160	0.86
M3	1280	18	158	1.0
F1	1620	28	160	0.70
F2	1469	23	170	0.80
F3	1447	30	170	1.1

A. Analysis by pitch period

Measurements described in Sec. V were taken by hand at consecutive pitch periods with a window size of one pitch period over the audio and accelerometer data for the diphthongs /aɪ/ ("hide") and /ɔɪ/ ("hoid"). Two repetitions of each diphthong were analyzed, for a total of four vowel tokens for each of the six speakers.

*F*2, *A*2, and *SubF*2 time trajectories were plotted to examine *F*2 and *A*2 behavior near *SubF*2. An example is shown in Fig. 10. Beginning around 1320 ms, *F*2 for speaker M2 jumps approximately 200 Hz as it passes through *SubF*2, while *A*2 falls 6.7 dB, then rises 4 dB. The jump size falls within the range of 75–225 Hz predicted by the theoretical model and the attenuation falls within the predicted 5–13 dB range. Table III summarizes the average size of frequency jumps and *A*2 attenuation for the six speakers. The size of the *F*2 jump (0–249 Hz) and, to a lesser extent, the amount of *A*2 attenuation (−8.5 to −6.4 dB; 5.6 to 8 dB) are speaker dependent because the distance between the zero-pole pair from subglottal coupling depends on an individual's glottal impedance, as described in Sec. II C.

As seen in Table III, an obvious jump in *F*2 could not be observed for some tokens and speakers, but attenuation in *A*2 near the frequency crossing was observed for all tokens and

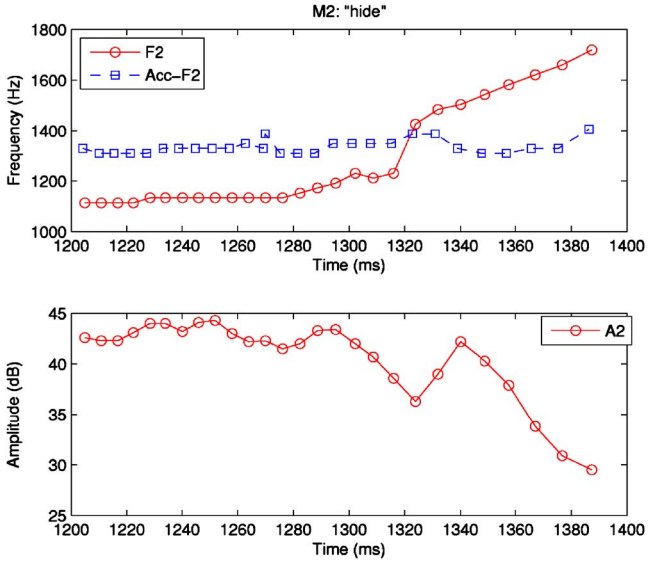

FIG. 10. (Color online) Time trajectories of *F*2, *SubF*2, and *A*2, measured with pitch-period window length, for a "hide" token spoken by a male speaker (M2). The *F*2 track shows a jump of 200 Hz and the *A*2 track shows a dip of −6.7 dB and rise of 4.0 dB at approximately 1320 ms.

speakers. In the above-mentioned diphthong analysis, tokens were marked "no jump" if a jump did occur, but did not cross *SubF*2. In tokens where this happened, the jump always occurred just above *SubF*2. This type of jump may be explainable in terms of the theoretical model. In the simulations of *F*2 tracks described in Sec. II B, if no resistance is added in series with Z_r, a frequency jump still occurs but generally takes place just above *SubF*2. Referring to Fig. 6, this corresponds to the lower pole having sufficiently low bandwidth and high amplitude to dominate the higher pole, even as the lower pole approaches *SubF*2. As the higher pole moves away from *SubF*2, the formant peak switches affiliation to the higher pole and a jump is observed above *SubF*2.

B. Open/closed phase analysis

A second method of analysis was used to determine whether *F*2 and *A*2 measurements would differ during parts of each pitch period when the glottis was more open or more closed. Since greater glottal area leads to greater coupling, one would expect greater coupling during the more open glottis phase than during the phase where the glottis is narrower. The window size was therefore adjusted to be slightly longer than one-half pitch period to better capture changes within each glottal cycle.

TABLE III. *F*2 jump and *A*2 attenuation measurements (falling and rising values) for backfront diphthongs near *SubF*2, averaged across four tokens per speaker. Window size set at pitch period length. Data ranges are in parentheses.

		Average change in *A*2 at jump (dB)	
Speaker	Average jump in *F*2 (Hz)	Falling	Rising
M1	141 (78–195)	6.4(3.5–8.0)	7.4(3.5–10.0)
M2	220 (156–371)	8.5(5.4–13.6)	5.6(3.3–8.2)
M3	None	8.2(6.0–9.2)	8.0(6.0–8.9)
F1	None	7.0(5.0–8.0)	7.0(5.0–8.0)
F2	64 (0–254)	7.5(2.6–13.8)	6.5(2.1–12.8)
F3	249 (176–312)	6.7(3.4–10)	7.6(5.1–10)

Measurements were taken by hand at two points within each pitch period on the same set of tokens as presented earlier, with window placement determined so that most of the windowed waveform would closely approximate either the more closed or more open portion of the glottal cycle under normal speech circumstances. Closed-phase measurements were taken with the window centered over the biggest peak in the pitch period, and open-phase measurements were taken with the window centered over the lowest amplitude part of the pitch period, before the largest peak in the next pitch period, as demonstrated in Fig. 11. It is recognized that the glottis may be closed for less than 50% of the glottal cycle, and that speakers with breathier voices might even never have complete glottal closure, but "open phase" and "closed phase" remain useful idealizations, to be understood here as the portion of a pitch period where the glottis is more open and more closed.

In attempting to track the effect of *SubF*2 on the *F*2 and *A*2 tracks, a very small Hamming window was used to select

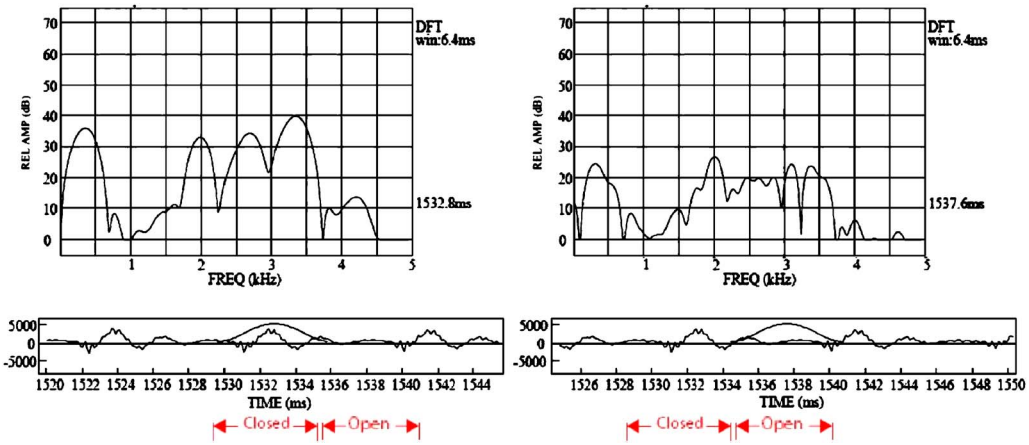

FIG. 11. (Color online) Spectra from two window placements within one pitch period of the vowel /i/. The left spectrum window is centered on the closed phase of the waveform. *F*1 and *F*2 are located at 350 and 2000 Hz. The right spectrum window is centered on the open phase of the waveform. Average spectral amplitude is lower during the open phase than during the closed phase.

either the open or closed phase of the glottal cycle. Such a short time window corresponds to poor resolution in the frequency domain. According to Rayleigh's criterion, the minimum distance between two frequency peaks that can be resolved by a window is half of the window's main lobe width. Hamming windows have a main-lobe width of $8\pi/N$, where N is the number of points of the window. Given window time duration t, the main-lobe width is found to be $w=4/t$ (Hz) (Oppenheim and Schafer, 1999, p. 471). A 4 ms Hamming window at a rate of 10 kHz thus has a width of 1000 Hz, and theoretically is only able to resolve peaks that are 500 Hz apart. However, it was empirically found that peaks separated by 400 Hz could also be resolved. By the same calculation, a 6.4 ms Hamming window would resolve two peaks that are 312 Hz apart. This frequency resolution is still too poor to resolve two peaks that correspond to *F*2 and the pole introduced by trachea coupling, when they come too close together. Given such a small window, it can only be concluded that the single *F*2 peak in the audio spectrum is the smoothed result of two peaks that are close together. Because the window itself is symmetric, the peak of the windowed signal would lie closer in frequency to the peak that has a higher amplitude. One can thus conclude that the frequency jump size given by the measured *F*2 is actually smaller than or equal to the actual frequency jump, making the observed frequency jump a conservative estimate.

To track the effect of *SubF*2 on *F*2 and *A*2 during the open and closed phases of the glottal cycle, *F*2 values recorded (from the audio data) during the closed phase (*F*2_*closed*), and during the open phase (*F*2_*open*), together with the second subglottal frequency (from the accelerometer data) taken during the closed phase (*SubF*2_*closed*), were all plotted against time. *SubF*2_*closed* was used because *SubF*2 should be less affected by subglottal coupling when the glottis is more closed, and thus more accurate. The example in Fig. 12 illustrates how measurements taken during the two phases can differ. In this example, a frequency jump near *SubF*2 and a corresponding amplitude dip occur in open-phase measurements, but not in closed-phase measurements. *A*2_*open* is also consistently lower than *A*2_*closed* in Fig. 12, as expected because there is more energy during the initial glottal closure. From examination of the decaying waveform within a pitch period, it can be seen that the open-phase signal amplitude is approximately 9 dB lower than the closed-phase signal amplitude.[6]

Table IV summarizes the size of observed frequency jumps and *A*2 attenuation during the open and closed phases. For all open-phase and most closed-phase measurements, *A*2 attenuation occurs when *F*2 comes close to *SubF*2, in agreement with the results in Sec. V A. Little difference was found in the amount of attenuation between open and closed-phase measurements, but the only instances where attenuation did not occur were in a few closed-phase measurements, and in this sense attenuation was slightly more prevalent in open-phase measurements. The size of frequency jumps is generally greater for open-phase measurements, as expected if frequency jumps arise from subglottal coupling. Frequency jumps can still occur during closed-phase measurements because the size of the glottal opening within each period is highly speaker-dependent, and some speakers might maintain a glottal chink throughout the entire utterance.

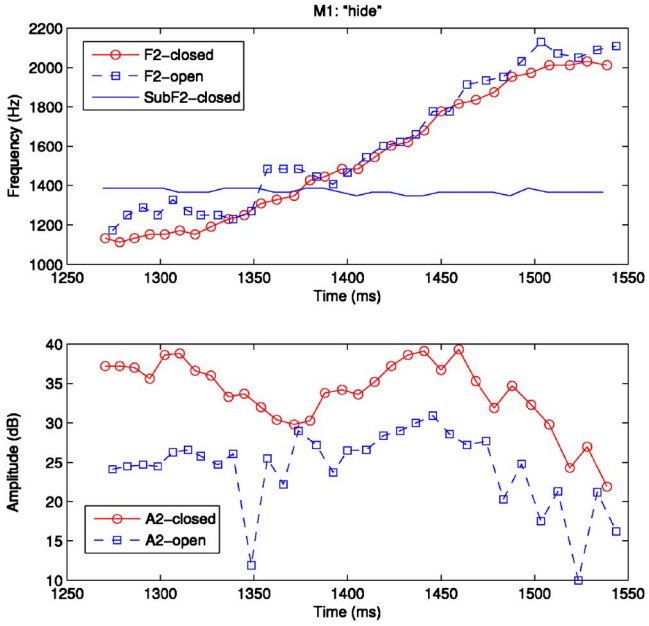

FIG. 12. (Color online) Time trajectories of *F*2_*closed*, *F*2_*open*, *SubF*2_*closed*, *A*2_*closed*, *A*2_*open* for a version of "hide" produced by a female speaker (F1). In the top panel, the curve with circles represents closed-phase *F*2. Assuming the glottis is completely closed, no interference on *F*2 from subglottal coupling near *SubF*2 should be seen. The closed-phase curve rises smoothly during the /aɪ/ diphthong, as expected. The open-phase *F*2 trajectory, by contrast, is greatly affected by the zero-pole pair from subglottal coupling, resulting in a frequency jump (of 210 Hz) near *SubF*2. The lower panel shows the corresponding amplitude trajectories. The closed-phase *A*2 trajectory has greater amplitude due to the presence of more energy in the initial closing of the glottis, while the open-phase trajectory shows an amplitude dip (of 14 dB) near the frequency jump, due to attenuation near the zero introduced by subglottal coupling.

The comparison of open and closed-phase measurements confirms that open-phase measurements are better indicators of the effect of subglottal coupling on formant frequencies, and to some extent on amplitudes. Open-phase measurements were thus taken for six additional diphthong tokens per speaker (totaling five "hide" and five "hoid" tokens per speaker). Table V lists average open-phase *F*2 jump and *A*2 attenuation values for each of the six speakers.

C. Discussion of diphthong results

The results of the diphthong analysis in Tables III–V show that as the second formant crosses *SubF*2, there is often

TABLE IV. Amount of *F*2 jump and *A*2 attenuation in back-front diphthongs due to sub-glottal coupling, measured during open and closed phases of the glottal cycle. Averaged across four tokens for each speaker. Data ranges are in parentheses.

	Average *F*2 jump (Hz)		Average *A*2 attenuation (dB)	
Speaker	Closed phase	Open phase	Closed phase	Open phase
M1	141 (74–176)	224(176–273)	7.1 (3–14)	12.4 (5–22)
M2	229(137–350)	220 (97–274)	6.4 (2–12)	8.9 (4–18)
M3	103 (0–410)	196 (78–313)	6.8 (0–13)	5.2 (0.5–9)
F1	68 (0–273)	327(234–390)	6.3 (0–17)	7.4 (1–15)
F2	49 (0–196)	171(137–215)	10.4(1.5–17)	6.5 (1–12)
F3	103 (0–410)	131 (0–349)	8.6(2.1–16)	8.0(1.5–15)

TABLE V. Open-phase *F*2 jumps and *A*2 attenuation (falling and rising values) in diphthongs near *SubF*2, averaged over ten tokens (5 /aɪ/ and 5 /ɔɪ/). The correlation between each speaker's jump size and *A*2 attenuation amount (average of falling and rising values) and the correlation significances are shown in the rightmost columns.

Speaker	Average Jump in *F*2 (Hz)	Average $\Delta A2$ at jump (dB)	Corr. (r)	Corr. significance
M1	299	−8.3, +7.5	−0.46	$p=0.18$
M2	348	−8.0, +6.5	−0.45	$p=0.19$
M3	237	−5.6, +6.5	0.58	$p=0.08$
F1	294	−8.5, +9.4	−0.53	$p=0.12$
F2	252	−8.4, +6.2	0.05	$p=0.89$
F3	201	−6.2, +8.3	−0.60	$p=0.07$

a discontinuity in the *F*2 track due to subglottal coupling. A more robust cue for this coupling is *A*2 attenuation near *SubF*2, which occurs regardless of whether there is an observable frequency jump. The ranges for the frequency jump and amplitude attenuation vary among speakers due to differences in glottal impedance.

Frequency jumps were found to be around 50–300 Hz, and most data fell within the predicted jump size range of 75–225 Hz. However, some jump size measurements fell above the predicted range, a discrepancy which could be due to the lack of finite, frequency-dependent vocal tract wall impedances in simulating jump sizes in Fig. 7. Finite, frequency-dependent wall impedances would increase the simulated formant's bandwidth and decrease its amplitude, causing it to be canceled by the subglottal zero sooner and to reemerge once its pole affiliation is switched later, leading to larger observed frequency discontinuities between these two events.

Some diphthong tokens showed no frequency jump. This may occur because of variation in the bandwidths, amplitudes, and separation of the subglottal pole and zero by speaker and utterance: Unless the pole and zero are sufficiently sharp and separated, their effect on the spectrum will be indistinguishable from noise. By this argument, only frequency jumps above some lower limit should be observed; otherwise no jump will be observed. This is consistent with the diphthong data, where very few jumps of less than 100 Hz were observed.

While the 5–12 dB *A*2 attenuation observed in the analyses agrees well with the predicted range of 5–13 dB, using a more accurate subglottal system model that incorporates bronchi structure (see Ishizaka *et al.*, 1976; Lulich, 2006) and adding wall impedances to the vocal tract would give understanding of how model parameter values affect the size of subglottal coupling effects.

A weak negative correlation (though not always statistically significant) exists between a speaker's *F*2 jump size and the corresponding *A*2 attenuation for four of the six speakers. This can be explained by the velocity with which the formant moves across the region of the spectrum containing the zero-pole pair introduced by subglottal coupling. Given the fixed number of measurement points at every glottal cycle, the faster the formant passes through the zero-pole region in time, the larger the observed frequency jump size, and the smaller the observed *A*2 attenuation due to the short amount of time the formant is affected by subglottal coupling in the zero-pole region.

VI. IMPLICATIONS FOR QUANTAL THEORY

This paper's findings can be seen as part of the larger project of testing QT directly by testing a proposed quantal relation. One aspect of QT predicts that speakers will avoid putting formants in an acoustically unstable region, which will then be used as a dividing line between sounds having + or − values of a phonological feature. Showing that this acoustic-articulatory nonlinearity occurs robustly across speakers is a necessary condition, and thus the first step, for testing whether it is used as a quantal relation. The diphthong analyses carried out earlier show that subglottal coupling effects occurred robustly for all six speakers. In another study, Lulich (2006) observed the same unstable region in a data set of 400 CV transitions from one English speaker. Both findings suggest that the frequency range near *SubF*2 forms an acoustically unstable region which could be used by speakers to separate front and back vowels.

The next step, testing whether the acoustically unstable region *is* used in this way, requires study of vowel production and perception near *SubF*2 and comparison of the quantal hypothesis to alternative hypotheses. This step is not addressed in this paper's analysis, but has been in recent work. Sonderegger (2004) used a larger version of the current data set, containing monophthong (shown in Table I) and *SubF*2 data for 14 English speakers, to examine whether *F*2 fell below or above *SubF*2 for all monophthongs for all speakers. *F*2 was always significantly ($p<0.05$) above *SubF*2 for front vowels and almost always significantly below ($p<0.05$) *SubF*2 for back vowels, showing a pattern which supports the quantal hypothesis. On the perception side, a recent study (Lulich *et al.*, 2007; Lulich, 2006) analyzed the effect of *SubF*2 location on the categorization of vowel tokens as [+back] or [−back] by varying the frequency of the subglottal zero in synthesized vowel tokens. The data supported the hypothesis that speakers use the location of *SubF*2 (manifested as a zero in the vowel spectrum) to distinguish front and back vowels. In addition, the quantal hypothesis was tested against several alternative hypotheses, and was found to be more consistent with the data.

An important but more involved part of testing a quantal relation is studying whether it holds cross-linguistically. This study and those mentioned earlier all focus only on English vowels. However, quantal relations are hypothesized to be language independent, because speakers of different languages should have the same nonlinear acoustic-articulatory relations.

While more work is needed before subglottal coupling effects near *SubF*2 can be said to be "tested" as a quantal relation for [back], the current paper, together with the above-described studies, support the hypothesis that (1) subglottal coupling effects near *SubF*2 lead to an acoustically unstable region and (2) these coupling effects form a quantal relation dividing front and back vowels, at least in English and predicted cross-linguistically.

VII. CONCLUSION

Accelerometer measurements of the second subglottal resonance agreed well with previously reported values from invasive studies, confirming that an accelerometer glued below the glottal area can be used for noninvasive and relatively accurate measurements of subglottal resonances. When averaged across all tokens for all American English monophthongs and diphthongs, male speakers had mean *SubF*2 values ranging from 1280 to 1374 Hz, female speakers from 1447 to 1620 Hz.

The effect of oral-subglottal coupling on the second formant was predicted using a theoretical model and simulation of *A*2 attenuation and *F*2 jumps near *SubF*2 in back-front diphthongs. For all speakers, the back-front diphthongs /aɪ/ and /ɔɪ/ consistently showed *A*2 attenuation of 5–12 dB when *F*2 approached *SubF*2, often accompanied by a frequency jump in the range of 50–300 Hz in *F*2; otherwise no jump occurred. Attenuation was present in nearly all diphthongs, even when jumps were not. Jumps (when present) were within or above the range predicted by the theoretical model and the predicted and observed ranges of attenuation were almost exactly the same, so that the subglottal coupling effects observed were in a sense stronger than predicted. Both attenuation and jumps were generally stronger in measurements taken during the open phase of the glottal cycle than during the closed phase, as expected if these effects result from subglottal coupling.

The coupling effects examined have potential relevance for speech synthesis and recognition systems, as well as further research on the role of subglottal resonances in speech. Inserting disturbances due to oral-subglottal coupling into the open phase of a pitch period could enhance the naturalness of synthesized speech. Subglottal coupling effects near the first and third subglottal resonances could also be examined, both for general understanding and for possible quantal effects involving the first and third vowel formants. A recent dissertation (Lulich, 2006) uses acoustic models and perception experiments to examine the role of lower airway resonances in defining distinctive feature contrasts via the zero-pole pairs they contribute to the transfer function.

The procedure used in this paper to examine the second subglottal resonance and its effects on the front-back division in vowel space forms part of a general methodology for studying articulatory-acoustic nonlinearities and testing whether they serve as quantal relations for phonological features. First, an acoustic model was used to explain how the hypothesized nonlinear effects (in this case attenuation effects and frequency jump near *SubF*2) could occur. Second, data were examined in detail to check whether the predicted effect occurred robustly across speakers. This lays the basis for studying whether the robust effect is indeed quantal, in this case separating front from back vowels. More generally, this method offers a way of investigating articulatory-acoustic nonlinearities which constrain the possible acoustics of linguistic sounds. This paper aims to show the value of investigating one such nonlinearity from acoustic phonetic and linguistic perspectives; its methodology could be used in further research to understand the many nonlinearities found in human speech and their practical implications for speech research.

ACKNOWLEDGMENTS

First and foremost, we would like to thank Professor Ken Stevens for his knowledge, support, and advice. We also thank John Rodriguez, Harold Cheyne, Martin Hughes, John Sweeney, Arlin Mason, and members of the Speech Communication group for help with the experiment, as well as our subjects. We are grateful to Steven Lulich, Elisabeth Hon, and Yoko Saikachi for comments and discussion. This work was supported in part by NIH Grant No. DC00075 and the MIT UROP Program.

[1]The measurement designated *F*2 refers to the frequency of the spectrum peak corresponding to the second formant, which may deviate slightly from the actual natural frequency of the formant because of the influence of the zero arising from coupling to the subglottal tract. Likewise *A*2 is the amplitude of the spectrum peak that is labeled as *F*2.

[2]The tube's length and impedances can be adjusted to fit an empirically measured subglottal spectrum peak's center frequency and bandwidth.

[3]Written by Mark Tiede of the MIT Speech Communication Group. MARSHA allows the user to record and digitize multiple channels of input at once (in this case the audio and accelerometer signals).

[4]The bandpass filter was used to emphasize the frequency range around *SubF*2 mainly because the frequency range below *SubF2* has much higher energy. This is why there is still some low-frequency energy present after filtering.

[5]Independent of the measurements of *SubF2* taken from the subglottal tracks, it was found that one quick way to approximate a speaker's second subglottal resonance without the aid of an accelerometer is by inspecting the spectrum of a front vowel such as /i/, where *F*2 is located far above *SubF*2. The pole from the zero-pole pair due to oral-subglottal coupling is visible in the speech spectrum and lies above *SubF*2. Its distance from *SubF*2 is dependent on the glottal impedance, Z_g.

[6]For speaker F1, the bandwidth of the first formant, B1, is approximately 160 Hz; $B1 = 1/\tau\pi$, where τ is the time constant of the decaying waveform envelope. In this case $\tau = 0.002$ s, the time it takes for the amplitude of the wave to decrease by a factor of *e*, or 8.69 dB.

Cheyne, H. (**2002**). "Estimating glottal voicing source characteristics by measuring and modeling the acceleration of the skin on the neck," Ph.D. thesis, Massachusetts Institute of Technology, Cambridge, MA.

Cranen, B., and Boves, L. (**1987**). "On subglottal formant analysis," J. Acoust. Soc. Am. **84**, 734–746.

Fant, G., Ishizaka, K., Lindqvist, J., and Sundberg, J. (**1972**). "Subglottal formants," KTH Speech Transmission Laboratory Quarterly Progress and Status Report 1, 1–12.

Fant, G. (**1960**). *Acoustic Theory of Speech Production* (Mouton, The Hague).

Hanson, H. (**1997**). "Glottal characteristics of female speakers: Acoustic correlates," J. Acoust. Soc. Am. **101**, 466–481.

Hanson, H., and Stevens, K. N. (**1995**). "Sub-glottal resonances in female speakers and their effect on vowel spectra," *Proceedings of the XIIIth International Congress of Phonetic Sciences*, Stockholm, vol. **3**, pp. 182–185.

Henke, W. L. (**1974**). "Signals from external accelerometers during phonation: Attributes and their internal physical correlates," Technical Report, Massachusetts Institute of Technology, RLE Cambridge, MA.

Holmberg, E., Hillman, R., and Perkell, J. (**1988**). "Glottal airflow and transglottal air pressure measurements for male and female speakers in soft, normal, and loud voice," J. Acoust. Soc. Am. **84**, 511–529.

Ishizaka, K., Matsudaira, M., and Kaneki, T. (**1976**). "Input acoustic-impedance measurement of the subglottal system," J. Acoust. Soc. Am. **60**, 190–197.

Kinsler, L., and Frey, A. (**1962**). *Fundamentals of Acoustics*, 3rd ed. (Wiley, New York).

Klatt, D., and Klatt, L. (**1990**). "Analysis, synthesis and perception of voice quality variations among male and female talkers," J. Acoust. Soc. Am. **87**, 820–856.

Ladefoged, P., and Bhaskararao, P. (**1983**). "Non-quantal aspects of consonant production: A study of retroflex consonants," J. Phonetics **11**, 291–302.
Li, S., Scherer, R., Wan, M., and Wang, S. (**2006**). "The effect of three-dimensional glottal geometry on intraglottal quasi-steady flow distributions and their relationship with phonation," Sci. China, Ser. C: Life Sci. **49**, 82–88.
Lulich, S. (**2006**). "The role of lower airway resonances in defining feature contrasts," Ph.D. thesis, Massachusetts Institute of Technology, Cambridge, MA.
Lulich, S., Bachrach, A., and Malyska, N. (**2007**). J. Acoust. Soc. Am. (in press).
Oppenheim, A., and Schafer, R. (**1999**). *Discrete-Time Signal Processing* (Prentice-Hall, Englewood Cliffs, NJ).
Perkell, J., and Cohen, M. (**1989**). "An indirect test of the quantal nature of speech in the production of the vowels /i/, /a/ and /u/," J. Phonetics **17**, 123–133.
Pisoni, D. (**1981**). "Variability and the quantal theory of speech: A first report," Phonetica **37**, 285–305.
Rösler, S., and Strube, H. (**1989**). "Measurement of the glottal impedance with a mechanical model," J. Acoust. Soc. Am. **86**, 1708–1716.
Sonderegger, M. (**2004**). "Subglottal coupling and vowel space: An investigation in quantal theory," Physics B.S. thesis, Massachusetts Institute of Technology, Cambridge, MA.
Stevens, K. (**1971**). "Airflow and turbulence noise for fricative and stop consonants: Static considerations," J. Acoust. Soc. Am. **50**, 1180–1192.
Stevens, K. (**1972**). "The quantal nature of speech: Evidence from articulatory-acoustic data," in *Human Communication: A Unified View*, edited by E. David and P. Denes, (McGraw Hill, New York), pp. 51–66.
Stevens, K. (**1989**). "On the quantal nature of speech," J. Phonetics **17**, 3–46.
Stevens, K. (**1998**). *Acoustic Phonetics* (MIT, Cambridge, MA).
Stevens, K., and Blumstein, S. (**1975**). "Quantal aspects of consonant production and perception: A study of retroflex stop consonants," J. Phonetics **3**, 215–233.
Stevens, K., Kalikow, D., and Willemain, T. (**1975**). "A miniature accelerometer for detecting glottal waveforms and nasalisation," J. Speech Hear. Res. **18**, 594–599.
Zhao, W., Zhang, C., Frankel, S., and Mongeau, L. (**2002**). "Computational aeroacoustics of phonation. I. Computational methods and sound generation mechanisms," J. Acoust. Soc. Am. **112**, 2147–2154.

Acoustic and perceptual cues for compound-phrasal contrasts in Vietnamese

Anh-Thu T. Nguyễn[a] and John C. L. Ingram[b]
School of English, Media Studies, and Art History, University of Queensland, St Lucia, QLD 4072, Australia

(Received 4 January 2006; revised 31 March 2007; accepted 11 May 2007)

This paper reports two series of experiments that examined the phonetic correlates of lexical stress in Vietnamese compounds in comparison to their phrasal constructions. In the first series of experiments, acoustic and perceptual characteristics of Vietnamese compound words and their phrasal counterparts were investigated on five likely acoustic correlates of stress or prominence (f0 range and contour, duration, intensity and spectral slope, vowel reduction), elicited under two distinct speaking conditions: a "normal speaking" condition and a "maximum contrast" condition which encouraged speakers to employ prosodic strategies for disambiguation. The results suggested that Vietnamese lacks phonetic resources for distinguishing compounds from phrases lexically and that native speakers may employ a phrase-level prosodic disambiguation strategy (juncture marking), when required to do so. However, in a second series of experiments, minimal pairs of bisyllabic coordinative compounds with reversible syllable positions were examined for acoustic evidence of asymmetrical prominence relations. Clear evidence of asymmetric prominences in coordinative compounds was found, supporting independent results obtained from an analysis of reduplicative compounds and tone sandhi in Vietnamese [Nguyễn and Ingram, 2006]. A reconciliation of these apparently conflicting findings on word stress in Vietnamese is presented and discussed. [DOI: 10.1121/1.2747169]

PACS number(s): 43.70.Fq, 43.71.Es, 43.70.Bk, 43.70.Kv [PEI] Pages: 1746–1757

I. INTRODUCTION

Compounding is a highly productive process in Vietnamese and in many languages. Compounding may be characterized as a device for creating words (new lexical items) from phrases (compositional syntactic constructions). Phonologically, this may involve a prosodic contrast in which the prosodic characteristics of the phrasal construction are altered to conform to the prosodic template of the word. This is evidenced in many languages which mark the distinction between compound words and their phrasal counterparts prosodically, in ways that are language specific and possibly related to their prosodic type (see Nguyễn *et al.*, in press). In English, where words tend to take initial stress (Cutler and Carter, 1987), this is achieved by assigning left-edge prominence to compounds, in contrast to the right-edged prominence of a phrase. Along with their characteristic left prominence, most English compounds also take on the prosodic characteristics of a word, deaccenting and temporally compressing the second element so as to conform to rhythmic constraints of stress-timing (e.g., *blackberry* versus *black berry*; Nguyễn *et al.*, in press). In tone languages such as Mandarin Chinese (Shen, 1993) and Hmong (Ratliff, 1992), compounds are prosodically distinguished from phrases on the basis of lexical tone sandhi. In Vietnamese, tone sandhi is restricted to reduplications (Thompson, 1965; Ngô, 1984; among others); therefore, in the absence of a general rule of tone sandhi in Vietnamese compounds, it is questioned whether there is an independent prosodic mechanism for distinguishing Vietnamese compounds from their phrasal counterparts, or whether listeners are required to rely exclusively on context to disambiguate phrasal from compound constructions.

The aim of our research was to examine whether there is any prosodically distinctive marking of compound words in Vietnamese (in relation to their corresponding phrases). Two series of experiments were conducted to test (a) whether there is any prominence related contrastive pattern between compounds and phrases in Vietnamese such as one observes in compound phrasal pairs such as *black-bird* versus *black bird* in stress based languages like English, and (b) whether compounds in Vietnamese as disyllabic word forms show any evidence of prosodic asymmetry, such as deaccenting one of the syllables of a disyllabic word.

In the first series, acoustic evidence from native speaker production and perception was sought as to whether there is acoustical and perceptual evidence for contrastive stress patterns in Vietnamese (strong–weak in noun phrases versus weak–strong in compounds). Native speaker production and perceptual discrimination of compounds and phrases was tested under two speaking conditions: (1) a condition of "maximal contrast," where subjects were asked to produce minimal prosodic pairs of the target stimuli in a manner that would "bring out the differences in meaning" between a compound and its corresponding phrase; and (2) in a "picture naming task," where there was no particular focus upon the possible differentiating phonetic features of the compound-phrasal contrast. The maximal contrast condition was in-

[a]Electronic mail: thunguyen@uq.edu.au
[b]Electronic mail: j.ingram@uq.edu.au

tended to test whether the language provides a way of prosodically marking distinctions in meaning between syntactically generated phrases and their corresponding lexical compounds. The picture naming task asks the same question but under conditions intended to more faithfully reflect circumstances of normal speech production.

In a second series of experiments, bisyllabic coordinating compounds which have a free variation form with reversed constituent syllable positions (e.g., *bàn*[table] *ghế*[chair] versus *ghế*[chair] *bàn*[table]: furniture) were used to investigate prosodic asymmetry (left or right prominence) at the level of the disyllabic word.

The patterns of syllable comparisons consist of a paradigmatic contrast between homophonous syllables of a compound and a phrase (e.g., *hoa hồng*: noun phrase: a pink flower and *hoa hồng*: compound: a rose) and a crossover contrast between homophonous syllables in a coordinative compound (*bàn ghế*) and its free variation form (*ghế bàn*). Thus, in the first series of experiments, a set of paradigmatic comparisons could be made to test for acoustic correlates of a possible stress contrast between compound and phrasal minimal prosodic pairs and to assess the perceptual impact of such a contrast, under two conditions of elicitation. In a second experiment, syntagmatic comparisons could be made between the first and second position within a class of coordinative compounds that happen to be freely reversible in phonological form. In both cases, it was possible to control for effects of speaker, speech rate, tonal and segmental composition in making the comparisons, but obviously, in the second case it was not possible to test for a compound-phrasal perceptual contrast, as both forms were allomorphs of the same compound word.

A. Compounding in Vietnamese

Vietnamese noun phrases and compounds are, of course, contrastive in terms of meanings (compositional versus noncompositional) and morphosyntactic structures (phrases versus words). There are different types of compounds in Vietnamese. Thompson (1965) identified six different types, namely, idiom compounds, generalizing coordinative compounds, specializing compounds, reinforcing compounds, attributive compounds, and pseudocompounds. The present study restricts itself to the investigation of prosodic features of two compound types: (1) specializing adjunctive compounds whose meanings are "fundamentally related to the meanings of the corresponding phrases but are generally highly specialized in reference" (e.g., *hoa hồng*: noun phrase: *a pink flower* versus compound: *a rose*) (Thompson, 1965, p. 129), and (2) generalizing coordinative compounds made up of two coordinative bases/heads which denote a general class (e.g., *bàn ghế* versus *ghế bàn*: compound: *furniture*); In terms of syntactic structure, Vietnamese compounds and phrases have a reversed word order from English (e.g., Vietnamese: head noun +adjective modifier: *hoa*[flower] *hồng*[pink] versus English: Adjective+Noun: *black berry*). Phonologically, it is claimed by some linguists that the pattern of prominence in Vietnamese compounds, particularly specializing compounds, is the reverse of the English pattern; that is *weak-strong* for compounds "with weak stress on their first base/syllable" (Thompson, 1965; Trần, 1969; Ngô, 1984) and *strong-weak* for noun phrases (Thompson, 1965, p. 121). By contrast, there are contradictory views about the stress patterns of coordinating compounds. According to Thompson (1965), this compound type "frequently occurs with weak stress on their first syllable" (p. 128), while Ngô (1984) and Cao (2003), relying on the "morphosyntactic weight" of the syllable, claimed that, "both constituents received strong stress" (Ngô, 1984, p. 275). Nevertheless, whether the contrastive pattern of prominence of Vietnamese compounds and noun phrases is acoustically supported and whether Vietnamese compounds show evidence of prosodic asymmetry (e.g., deaccenting one of the syllables of a disyllabic word) needs to be investigated.

B. Stress in Vietnamese

Lexical stress has been found to be instantiated by a variety of phonetic cues, i.e., duration, pitch (fundamental frequency—F0), intensity, and vowel quality (Beckman, 1986; among others). It is widely agreed that stress is phonetically realized in a language-specific way. Stress in a tone language such as Mandarin Chinese was shown to affect duration and the surface output of lexical tones in Mandarin: F0 range is expanded in stressed (i.e., focused) syllables and narrower or compressed in unstressed or postfocal contexts (Xu, 1999). In Vietnamese, a tone language, no system of lexical word stress has been found; nevertheless, it is widely accepted that there is stress in the sense of accentual prominence at the phrasal level (Thompson, 1965; Nguyễn, 1970). Some studies have attempted to investigate the phonetic correlates of Vietnamese stress, but mostly in the sense of phrase level accentual prominence and generally based on auditory impressions. Đỗ (1986) has shown that duration and intensity are important parameters for describing stress in Vietnamese. Chaudhary (1983) remarks that intensity is one stable acoustic correlate of Vietnamese stress. Some other authors, such as Hoàng and Hoàng (1975), or Gsell (1980) consider that full tonal realization of accented syllables is one of the positive marks of accent. Jones and Huỳnh (1960) remark that normally stresses in a Vietnamese utterance are conditioned by junctures.

A review of the literature shows that previous studies of stress in Vietnamese (Cao, 2003; Ngô, 1984; among others) have been largely based on a notion of "morphosyntactic" weight of syllables (e.g., "Assign[stress] to the core of a morphosyntactic category" Ngô, 1984, p. 101) and "stress" in the sense of phrase level accentual prominence (Thompson, 1965; Nguyễn, 1970; Chaudhary, 1983; Hoàng and Hoàng, 1975; Jones and Huỳnh, 1960), but have not addressed the question of stress at the word level, from the perspective of acoustic phonetics and native speakers' perception, which is the aim of this study.

II. EXPERIMENT 1. COMPOUND AND PHRASAL STRESS PRODUCTION

In this section, we report the first series of experiments involving minimal prosodic pairs of compound words and their corresponding phrasal constructions elicited under different conditions of "maximal contrast" and "picture naming." We report an analysis of the acoustic characteristics that might be expected to differentiate compounds and phrases if speakers are producing them in a manner that distinguishes the two forms. This is followed (in Sec. III) by a perceptual experiment that assessed the discriminability of the compound-phrasal pairs by native Vietnamese listeners, from tokens obtained under the two conditions of elicitation.

Two competing hypotheses are evaluated in these experiments;

(1) Hypothesis 1: This hypothesis is to test whether there is acoustical evidence of contrastive stress patterns (strong-weak in noun phrases versus weak-strong in compounds). This hypothesis predicts that the vowel of the first element (V1) in a noun phrase will have longer duration, stronger intensity, larger F0 range, possibly higher F0, and fuller vowel quality than the same vowel in a compound and vice versa, the vowel in the second element (V2) of the compound will have longer duration, stronger intensity, larger F0 range, possibly higher F0, and fuller vowel quality than the same vowel of the phrase.
(2) Hypothesis 2: This hypothesis predicts that in case no strong evidence of duration, intensity, and pitch as cues to the contrastive stress patterns is found, a junctural pause between two constituents of the phrase may serve (under special conditions of maximal contrast) as the acoustic and perceptual cue to the distinction between compounds and noun phrases in Vietnamese. If hypothesis 2 turns out to be correct, it raises the question of whether a compound-phrasal prosodic contrast is part of the phonology of Vietnamese or whether Vietnamese speakers are making use of a prosodic device for syntactic phrase disambiguation (juncture) which is available universally. "Juncture" as a phonological category is probably a complex phonetic construct, cued by preboundary lengthening, pausing, and possibly also pitch contour modification (though this may well be much less prominent in a tone language). In this study, the pausing between the two constituent syllables of the test items and the prepausal lengthening of the first elements are examined in order to decide whether or not there is a juncture.

A. Linguistic materials

Fifteen pairs of two-syllable compounds and their corresponding phrases were constructed from three types of compounds, formed on the basis of their grammatical structures: noun-adjective (NA type), noun-verb (NV type), and noun-noun (NN type), illustrated in Table I.

There is an important distinction between the phrase types that correspond to three types of compound used in the experiment. The NA and NV compounds derive from syntactic constituents that form a clause and are dominated by an S node in standard syntactic representation. The NN compounds, on the other hand, derive from noun phrases, dominated by the lower-ranked syntactic constituent NP. It is well known from prosodic phonology that juncture breaks are much more likely to occur between major clausal constituents than within a phrasal constituent, such as an NP (Selkirk, 1986; Nespor and Vogel, 1986).

TABLE I. Type of compound, source phrase, and syntactic rank.

Type	Example	Compound	Phrase	Rank
N-A	hoa hồng	*Rose*	*Flower [is] pink*	Clause
N-V	bò cày	*Ox-plough*	*Ox [is] ploughing*	Clause
N-N	chân vịt	*Propellar*	*Duck's foot*	NP

B. Subjects and test conditions

Two groups of native speakers ($n_1=30$, $n_2=15$), aged 18–22, balanced for selection by gender and by the three major dialect regions of Vietnam (northern: Hanoi, central: Hue, and southern: Saigon) were separately tested for production of compound and phrasal constructions under two elicitation conditions.

Under the *maximal contrast* condition, subjects were asked to read minimal sentence pairs in a natural way, such that listeners could distinguish between the meaning of a compound and its corresponding phrase. Subjects in this experiment were 30 first-year university students in Vietnam (speakers of Hanoi [$n=10$], Hue [$n=10$], and Saigon dialects [$n=10$); half males and half females in each dialect group, age ranged 18–22). The test items were embedded in sentences having the same grammatical structure and word order. All test items occurred in utterance nonfinal position. Examples of these sentences are:

Compound: ***Hoa hồng*** thì đẹp (A *rose* is beautiful)

Phrase: ***Hoa hồng*** thì đẹp (A *pink flower* is beautiful)

For the *picture naming* task, a different group of 15 overseas Vietnamese students (speakers of Hanoi [$n=5$], Hue [$n=5$] and Saigon [$n=5$]; nine females and six males, age ranged 22–45) at the University of Queensland were asked to describe a picture, using a constant carrier sentence to ensure that the target phrase or compound word appeared in nonfinal position in an utterance with the same number of words, tone coarticulation, and speaking rate effects. Two examples:

Có(there is/are)+numeral/classifier
+compound/phrase+ ở đây (here)

Có một bông **hoa hồng** ở đây (There is a rose here)

Có hai con **cá mập** ở đây (There are two sharks here)

Recordings were made in a quiet room using sound recording and editing computer software (PRAAT, Boersma and Weenink, 2007), at 20 kHz sampling rate and 16 bit precision.

C. Measurements

The test items were segmented via the Emu Speech Tools, (Cassidy, 1999). First, the Emu Labeller was used to

TABLE II. Percentages of juncture pauses in noun phrases elicited under minimal pair sentence and picture naming tasks by phrase types and dialects.

	Minimal pair sentence			Picture naming		
	Hanoi	Hue	Saigon	Hanoi	Hue	Saigon
NA	84	80	82	0	0	0
NN	16	14	15	0	0	0
NV	66	60	66	0	0	0

mark the edges of the target syllables and vowels, relying primarily on the spectrographic display in the Labeller. The segmentation criteria were generally based on the major discontinuities of the energy distribution over frequency and time visible on the spectrograms. Then, the Emu-R statistical software was used to extract vowel duration (ms), vowel formant (Hz), intensity (db), spectral tilt, and fundamental frequency (Hz). The following acoustic parameters were measured:

(1) Duration of first and second syllables (onset[$O1O2$], vowel[$V1V2$], coda[$C1C2$], and whole syllable[$S1S2$]); duration of the pause (if longer than 100 ms) between the syllable constituents of the phrases/compounds.
(2) First formant and second formant of both first and second syllables ($S1F1$, $S1F2$, $S2F1$, and $S2F2$). Formant at vowel midpoint was taken for monophthongs while formant at ten equidistant points of the formant trajectory was taken for diphthongs/triphthongs.
(3) Tone range (F0range=$F0$max-F0min): $S1F0range$ and $S2F0range$.
(4) Mean of vowel intensity (db) at four equidistant points ($V1$ *intensity mean and* $V2$ *intensity mean*).
(5) Vowel spectral tilt (H1-A3): third formant is compared with the first harmonic using Stevens and Hanson's model (1995) ($V1$ *spectral tilt and* $V2$ *spectral tilt*). An acoustic correlate of greater vocal effort (and thus stress) is expected to be a decrease of a negative spectral tilt (more gradual fall of the spectrum).

D. Statistical analysis of stress contrasts

Rather than regarding the maximal contrast (minimal pair) and picture naming production tasks as levels of a single treatment factor in a unified factorial design, the two conditions were analyzed in separate experiments. Different subjects were required so that the effects of exposure to one elicitation condition did not contaminate or bias responses elicited under the other condition. There were unequal numbers of subjects under the minimal pair [$n=30$] and picture naming tasks [$n=15$]. Also, the two experiments were undertaken separately, with the picture naming experiment conceived as a replication and extension of the original experiment which was conducted under conditions of maximal contrast elicitation.

A mixed (fixed and random) effects analysis of variance (ANOVA) model, using the restricted maximum likelihood method to estimate variance components was applied in all of the foregoing analyses. The fixed effects included prosodic type (compound versus phrase), compound type (NA, NN, NV), dialects (Hanoi, Hue, and Saigon), and their two- and three-way interactions. The random effects were speakers and words. A Tukey post-hoc test was then conducted to determine the significant differences among levels of the main fixed factors and their interaction effects.

In addition, a ratio measure of the dependent variable in a phrase over its corresponding compound (e.g., for the duration parameter: duration $S1_{phrase}$/ duration $S1_{compound}$) was calculated for presentation in graphs. Thus, values greater than 1.0 reflect a higher magnitude for the phrasal token on a given acoustic parameter, and conversely, a value significantly less than 1.0, a greater magnitude for the compound token than its corresponding phrase. In this way, any effects upon the acoustic parameter of interest caused by intrinsic segmental composition, tone type, or speaker were controlled for in testing for the effects of prosodic type.

Spectrographic analysis was used to identify and measure any juncture pauses (defined as breaks longer than 100 ms) that tended to occur between constituents of a phrase under the maximal contrast elicitation condition.

E. Results on juncture pauses

Juncture pauses were only observed in the maximal contrast elicitation condition and appeared mainly in two types of noun phrase constructions: noun-adjective and noun-verb, not in noun-noun phrases. Table II shows the percentage of juncture pauses used in phrases by phrase types. Juncture pauses occurred in approximately 80% of the noun-adjective phrase constructions, about 65% of the noun-verb phrase constructions, but in only 15% of the noun-noun phrase constructions. Pausing was *never* used (0%) in compounds and in the picture naming task, regardless of prosodic type (compound nor phrase).

These results strongly suggest that the speakers were employing a juncture (phrase boundary) marking strategy to differentiate phrases and compounds in the maximal contrast (minimal pair) condition, but were not doing so under the picture naming elicitation condition. We sought to confirm this and to determine whether any *other* mechanism might be operative from a series of ANOVAs of the paradigmatic comparisons on the five prosodic parameters described earlier.

F. Statistical results of prosodic parameters

The effects of interest to this study are prosodic type (compound versus phrase), and its interaction with the fac-

TABLE III. Summary of the patterns of acoustic difference between CP and PH. Symbol < >: sig. at $p<0.01$, Ns.: insignificant.

Acoustic cues	MAX-S1	MAX-S2	PIC-S1	PIC-S2
Duration	PH>CP		Ns.	Ns.
F0 range	PH>CP	CP>PH: inconclusive	Ns.	Ns.
Formant F1	PH>CP		Ns.	Ns.
Intensity	PH<CP	PH<CP	Ns.	Ns.
Spectral tilt	Ns.	Ns.	Ns.	Ns.

tors compound type (NA, NN, NV) and dialect (Hanoi, Hue, Saigon). The main effects of compound type and dialect, while of some intrinsic interest, are not central to the hypotheses tested in this paper if significant. Particularly, the significant main effect of prosodic type was shown to be consistent across speakers of the three dialects in a preliminary analysis; therefore, dialectal variation is discussed only when relevant. The pattern of significant effects of the ANOVA results (Table III) closely paralleled the distribution of junctural pauses (Table II), providing *prima facie* support for the hypothesis that *all* the prosodic effects which differentiate compounds from phrases are linked to the distribution of junctural pauses (phrase boundary effects).

There were no significant effects observed under the picture naming elicitation (PIC), whereas robust main effects of prosodic type and interactions between prosodic type and compound type were found under the maximal contrast elicitation for the dependent variables of syllable duration, F0 range, and vowel first formant. Intensity yielded a main effect for the phrasal-compound contrast under minimal pair elicitation (the maximal contrast condition, MAX) but no interaction effect with compound type. We turn now to a detailed consideration of these effects in terms of each acoustic parameter type, which is reported in two main sections: (1) results of the PIC experiment and (2) the results of the MAX experiment.

1. Results of the picture naming experiment

There were no significant main or interaction effects for any factors of the picture-naming task. This is illustrated in the PH/CP ratio measurement in Fig. 1 that there was no significant difference in any acoustic parameters between compounds and phrases across three compound types indicated by the PH/CP ratio clustering around a value of 1 (unity).

2. Results of the maximal contrast experiment

The statistical results and ratio measurements (Fig. 2) showed that there were highly significant main effects of prosodic type for syllable duration, F0 range, intensity, and vowel first formant (F1) for the first syllable in the minimal pair sentence task, while there were no or very marginally significant effects for the second syllable.

a. S1 duration. The ANOVA results showed that the first syllable (S1) had a significant main effect of prosodic type ($F(1,860)=971.16$, $p<0.0001$) and its interaction with compound type ($F(2,860)=19.21$, $p<0.0001$). Tukey post-hoc comparisons and a plot of mean phrase/compound (PH/CP) ratios by compound types (Fig. 2) showed that the first syllables of all three word/phrase types (NA, NN, NV) of the phrase was significantly longer than that of the corresponding compound (mean PH/CP ratio >1). Nevertheless, Fig. 2 also shows that the magnitude of lengthening was much greater for NA and NV than NN constructions, indicated by greater PH/CP mean ratios. Further examination of the duration of onset, vowel, and coda of the first syllables showed that all segments (onset, vowel, and coda) of the first syllable of the phrase were significantly longer than their counterparts in the compound ($p<0.01$).

b. S2 duration. There was a significant main effect of prosodic type ($F(1,859)=8.61$, $p<0.01$) and two-way interactions not only with compound type ($F(2,859)=20.93$, $p<0.0001$) but also with dialect ($F(2,859)=9.68$, $p<0.0001$). Post hoc tests showed that significant effects for the second syllables were only found for the NV construction (CP >PH: mean PH/CP ratio <1, Fig. 2). Examination of the syllable constituents showed that while the onset of the second syllable of the phrase was longer than its counterpart in the compound across the three compound types, a significant effect (compound>phrase, $p<0.01$) was found for only the vowel and coda of the NV compound type, this is argued to be an artifact of the juncture that separated the compound from its following preposition phrase (see Sec. V E). Post-hoc pairwise examination of the interaction of prosodic type and dialect showed a dialectal effect that the second syllable of the NA and NN noun phrases of only the Hanoi speakers was significantly longer than its compound counterpart (PH >CP: mean PH/CP ratio >1).

To sum up, the duration results showed that all segments (onset, vowel, and coda) of the first syllable of the phrase under maximal contrast elicitation were significantly longer than their counterparts in the compound across the three dialects and three compound types (though NN had smaller lengthening magnitude than NV and NA). By contrast, only the vowel and coda of the second syllable of the NV compound was longer than its counterpart in phrases. There was also a dialectal effect that in the northern (Hanoi) dialect, the second syllable of the NN and NA noun phrase was longer than its compound counterpart, suggesting that Hanoi speakers seem to place emphasis on both syllables of the noun phrase. Further discussion on duration results is presented in Sec. V E.

c. S1 F0 range. The first syllable (S1) had a significant main effect for the factor prosodic type ($F(1,858)=24.94$, $p<0.0001$), its two-way interaction (prosodic type ×compound types: $F(2,858)=20.11$, $p<0.0001$), and three-way interaction (prosodic type×compound types×dialects: $F(4,858)=3.8$, $p<0.01$). Post hoc pairwise comparisons sup-

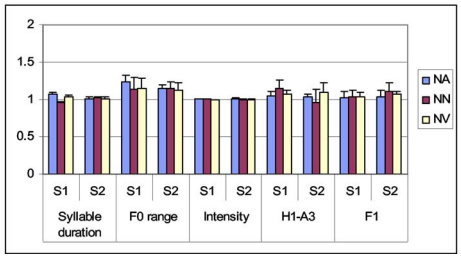

FIG. 1. (Color online) Mean of PH/CP ratios of the acoustic parameters by syllables (S1 and S2) and compound types (NA, NN, NV) of the picture naming experiment.

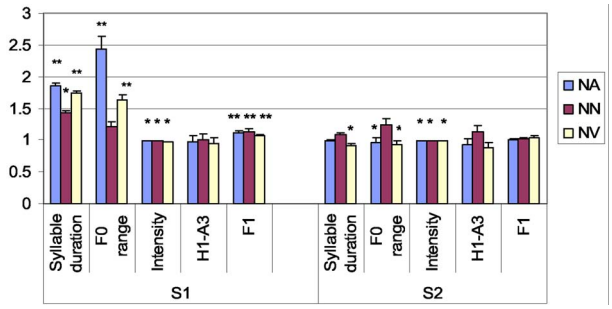

FIG. 2. (Color online) Mean of PH/CP ratios of the acoustic parameters by syllables (S1 and S2) and compound types (NA, NN, NV) of the maximal contrast experiment. (**) significant at $p<0.0001$, (*) $p<0.01$.

ported by a graphical display of the mean of PH/CP ratio by compound types (Fig. 2) showed significant compound-phrase differences for the NA and NV compound types only, with no significant effect for the NN type. The first syllable of the NA and NV noun phrase had a significantly greater F0 range than its counterpart in compounds (PH/CP ratio >1) across the three dialects. A detailed analysis of the common tone types (falling, dropping, level, rising) across three compound types showed that the tonal range expansion was found for the falling and rising tones only (PH$>$CP, $p<0.01$), while the level and the dropping tone did not show significant effects, possibly due to articulatory constraints on their F0 expansion (level is a flat tone; drop tends to end with creakiness).

d. S2 F0 range. The ANOVA results showed a significant main effect of prosodic type ($F(1,859)=22.78$, $p<0.0001$), a two-way interaction (prosodic type$\times$dialect: $F(2,859)=4.92$, $p<0.01$) and a weak three-way interaction (prosodic type$\times$compound types$\times$dialects: $F(4,859)=2.39$, $p<0.05$). Post hoc results showed that the second syllable of the NA and NV compound had significantly greater F0 range than that of the phrase (PH/CP ratio <1, Fig. 2). However, detailed analysis by the common tone types (curve, falling, rising) showed significant effects for the curve tone and the falling tone of the NA type (CP$>$PH, $p<0.01$) while no significant difference was found for the same falling tone of the NV type. The significant effect of the falling tone of the NA compound types can be explained as an artifact effect of tonal coarticulation in the compound pattern, due to the high level and rising tone of the preceding syllables (*áo*, *bánh*, *cá*, *hoa*); this is well-supported by a statistically significant difference in the starting F0 of this falling tone between (compound and phrase, $F(1,90)=3.4$, $p<0.03$). The significant effect of the curve tone of the NV compound types was found to be contributed by the Southern dialect only (Southern: $F(1,60)=5.6$, $p<0.03$; Central: $F(1,30)=1.5$, $p=0.2$ ns., Northern: $F(1,30)=0.9$, $p=0.3$ ns). Examination of the F0 contour showed that the Southern speakers produced the curve tone in the compound with a higher rising tail after the creakiness than in the phrase, probably due to more articulatory space given by a following juncture break after the compound pattern of this NV compound type, which will be discussed in detail in Sec. V E on the duration effect.

An examination of the three-way interaction effect (prosodic type$\times$compound type$\times$dialects) on the second syllable showed that the Southern (Saigon) speakers had significantly greater F0 range expansion than speakers of the other two dialects. This is consistent with the findings of previous cross-dialect tonal studies that the Southern dialect has greater F0 range than the Northern and Central dialects (Seitz, 1986).

In summary, the F0 range results showed a robust effect (PH$>$CP) for the first syllable across the three dialects, while the effect for the second syllable appears to be only an artifact of tonal coarticulation.

e. Intensity and spectral tilt. The ANOVA results on mean intensity of four equidistant points along the vowel showed a significant main effect of prosodic type for both syllables (S1: $F(1,860)=19.64$, $p<0.0001$; S2: $F(1,859)=7.54$, $p<0.01$). Mean PH/CP ratios by compound types (Fig. 2) showed that mean intensity of both syllables (S1 and S2) of compound patterns were significantly greater than their counterparts in the phrase (mean PH/CP ratio <1). Further examination of the four equidistant points on the intensity contour showed that there were significant differences (CP$>$PH) in the last two points of the first syllable and in the first three points of the second syllable (statistical significance at $p<0.01$).

Spectral tilt: The spectral *slope* measurements (H1-A3) showed no significant effects.

f. Vowel formants. The ANOVA analysis of F1 and F2 formant values of both syllables (S1 and S2) showed only a significant main effect of prosodic type (PH$>$CP, Fig. 2) for the first syllable ($F(1,860)=22.51$, $p<0.0001$). As confirmed in the monophthong vowel plots (Fig. 3), the raising of the F1 of the vowel of the phrases in comparison with that of the compound was found only in the first syllable under the minimal pair sentence task [MAX-S1: Fig. 3(a)] across three dialects, while vowels of both prosodic types (CP and PH) in the second syllable [MAX-S2, Fig. 3(b)] tend to assemble in the same region of the vowel space.

An examination of the formant trajectories of the diphthongs/triphthongs showed similar patterns; there was a significant difference in formant trajectory between phrase and compound for the first vowel of the minimal pair sentence task only (MAX-S1) in comparison to the formant trajectories of diphthongs under the three other positions (MAX-S2, PIC-S1, and PIC-S2). The diphthong/triphthongs /aw/(in *áo*) of the first syllable of the phrase had significantly lower F2 in the offglide than its counterpart in compound, the diphthong /wa/ (in *hoa*) had a significantly higher F2, and the triphthong /ɯɤi/(in *ngu'ò'i*) had a lower F2 in the onglide /ɯ/ portion and higher F2 in the offglide.

G. Discussion

1. Duration

The duration results showed that all segments (onset, vowel, and coda) of the first syllable of a phrase were significantly longer than their counterparts in a compound across the three dialects and three compound types (though NN had a smaller lengthening effect than NV and NA)—but only under the maximal contrast elicitation condition. The lengthening of the first syllable of the phrases seemed to bear a close relationship with the juncture pause between the constituents of that phrase (Table II) elicited under the minimal pair sentence task: The NN word/phrase type is different from the other two phrase types NA and NV. There were very few junctures between two syllables of the NN type and

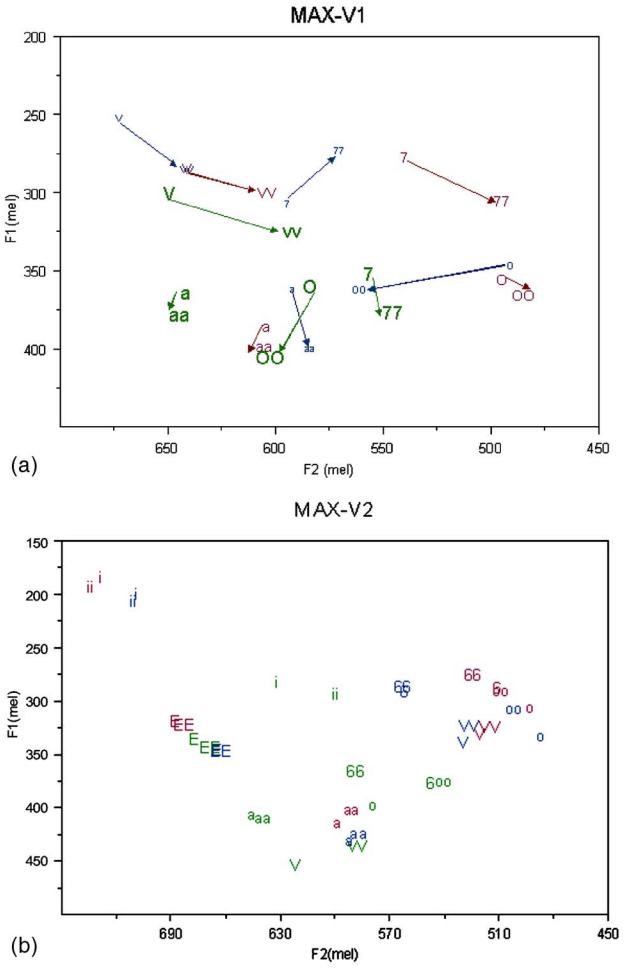

FIG. 3. (Color online) (a), (b) Formant plots of monothong by dialects and prosodic type. Vowels are represented in SAMPA symbols. Single character: CP, double character: PH. Legends for dialects: Largest font: Southern [Saigon], smaller font: Northern [Hanoi]; smallest font: Central[Hue]. Vowel symbols: V: /ʌ/, 7: /ɤ/, a:/a/, 0:/ɔ/ (fig. a), o:/o/ (fig. b), E:/ɛ/, i:/i/.

the lengthening effect on V1 of the NN type was less than that of the NA and NV types (Fig. 2). In fact, as mentioned previously and discussed below, juncture is not allowed between elements of the NN type. The few junctures that were found in this type appear to be the result of some speakers' carry-over effect from the NA and NV types. The absence of a juncture between the constituents of the items in the NN group and the lengthening to a smaller extent of the first constituent in comparison to that of the NA and NV types can be explained on the basis of prosodic boundary strength in the theory of prosodic phonology (Nespor and Vogel, 1986 or Selkirk, 1986). The following diagram shows the syntactic trees of the three phrase types.

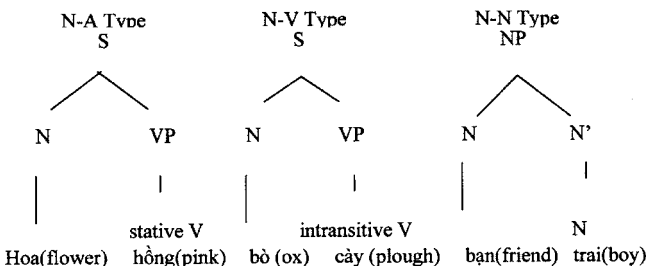

The propensity to prosodically mark a constituent boundary by a juncture pause or by preboundary lengthening is related to the rank of the syntactic constituent so marked. The boundary between two phrases in a clause, outranks any boundary between two constituents of a noun phrase. Vietnamese requires an intervening copular verb "*là*" (e.g., *bạn trai*: bạn *là* nam: friend *is* boy/male) or a verb phrase (nhà đá: nhà được *làm bằng* đá: house *is made of* stone) to form a predicative phrase from a sequence of two nouns.

Another effect of duration is the significant lengthening of the second constituent of compounds compared with their counterparts in noun phrases, but this only applied to compounds of the NV type. Supported by evidence that only the vowel and the coda of the compound was significantly lengthened in comparison to their counterparts in the phrase, it can be argued that this lengthening could be due to an artifact of a juncture pause that most speakers made between the compounds and its following prepositional phrase, which occurred in all five sentences of this phrase type (NV) but not in the two other phrase types (NA and NN).

There was also a dialectal effect on duration. In the northern (Hanoi) dialect, the second syllable of NN and NA noun phrases was significantly longer than their compound counterparts, suggesting that Hanoi speakers may put emphasis on both syllables of the noun phrases to distinguish it from compounds.

2. F0 range

The first syllable of the NA and NV noun phrase had significantly greater F0 range than its counterpart in compounds across three dialects. By contrast, the significant effect for the second syllable is only an artifact of tonal coarticulation. Combined with other acoustic correlates (duration, vowel quality, and intensity), the greater F0 range only on the first syllable of the phrase in comparison to compounds suggests a fuller tone realization thanks to prepausal syllable lengthening. This is supported by the fact that for the NN word/phrase types, there was almost no juncture and thus less syllable lengthening, no significant difference was found for F0 range between phrase and compound.

3. Intensity and spectral tilt

Both syllables of the phrase in the minimal pair sentence task had lower intensity (db) in comparison to their counterparts in the compound. This suggests an effect of speaking rate deceleration and gesture diminution at a phrase boundary. Again, the effect is confined to the maximal contrast elicitation and appears to be a by-product of a juncture pause distinguishing the phrase from the compound.

4. Vowel formants

The raising of the F1 of the vowel of a phrase in comparison to that of a compound was confined to the first syllable of the maximal contrast elicitation across the three dialects. This is arguably an effect of jaw lowering in response to syllable lengthening.

Taken together, as shown in Table III, the differences between phrases and compounds seem to be confined mainly to the first syllable of the phrase in the minimal pair sentence task, which is accompanied by a junctural pause. The results suggest a boundary-induced lengthening effect which is supported by not only duration but also intensity and vowel formant results. However, the evidence of a more fully realized tone and a lengthening of all syllable segments (including onset) also seems to be indicative of an additional accentual effect which may have been "conditioned by juncture," as observed previously by Jones and Huỳnh (1960) that "normally the stresses in a Vietnamese utterance are conditioned by junctures." Speakers might have intended to put more emphasis on the grammatical head noun of the noun phrase (which is also parsed as the subject of the adjective clause or the communicative theme) to distinguish it from the compound word. This is consistent with the dialectal effect that Northern (Hanoi) speakers lengthened both words of the phrase to distinguish it from the compound.

In summary, the acoustic analysis shows that Hypothesis 1 is not supported: there was no significant effect on any of the acoustic parameters between compounds and noun phrases elicited under the picture naming task, which more closely represents spontaneous natural speech. Even under conditions of maximal contrast in the minimal pair sentence task, there was no consistent significant asymmetrical prominence in terms of spectral tilt, intensity, or duration and F0 range to distinguish between contrastive elements of compounds and noun phrases. Only a phrase-level junctural effect, prepausal lengthening, and expanded F0 range on the first syllable was found between phrasal constituents, supporting hypothesis 2. No evidence was found of an independent word prosody to distinguish compounds from phrases, such as operates in a stress language like English. Given that the only acoustic features in native speakers' production that appear to distinguish compounds from phrases in Vietnamese emerged under conditions of maximal contrast and apparently involved a "juncture marking strategy," it remained to be investigated whether a parallel situation pertained in the domain of perception of compound–phrase contrasts. The answer to this question was the purpose of the following perception experiment.

III. PERCEPTION EXPERIMENT

Having argued on the basis of acoustic analysis of production data that Vietnamese speakers rely on juncture to mark phonological contrasts between compounds and phrasal constructions under conditions of maximal contrast, it remains to show that Vietnamese listeners may only be able to distinguish between phrasal and compound constructions when junctural cues are provided by the speaker. There is evidence (from the production experiment) that the junctural cues are not possible in NN phrasal constructions. The prediction is, therefore, that even under conditions of maximal perceptual contrast (minimal prosodic pair discrimination) Vietnamese listeners will fail to distinguish compounds from NN phrases.

A. Subjects

Eighteen subjects (six Hanoi, six Hue, and six Saigon; ten females) with no known auditory deficiencies, participated in the perception experiment. Only three of the listeners were also speakers for the production experiments. Since Hanoi dialect is a prescribed national standard in instruction and national broadcasting, listeners from other dialects, particularly the well-educated ones, generally have no difficulty understanding Hanoi dialects, but the reverse does not hold. Listeners of this study are all tertiary students at the University of Queensland and have been in Australia from 4 months to 1.5 years.

B. Stimuli

Stimuli of four Hanoi female speakers from the production experiment (two speakers from the picture-naming task and two from the minimal pair sentence task) were used for the perception study. The criteria used for the selection of stimuli were that all four speakers spoke standard Hanoi dialects and had an easy-to-hear voice, which was judged to be clear, loud enough to hear, and easy to understand for speakers of other dialects by the experimenter. The two speakers from the minimal pair sentence task consistently produced a juncture break between syllables of the NA and NV noun phrases but no juncture between the NN noun phrases and compound stimuli. The two speakers from the picture-naming tasks consistently produced no pause, gap, break, or whatever between syllables of phrases and compounds.

There were two types of stimuli: (1) compounds/phrases in isolation and (2) compounds/phrases embedded in contextual sentences. The test items in isolation were segmented from the contextual sentences via speech analysis software (PRAAT). There were in total 240 tokens: 15 test items $\times 2$ prosodic types (CP vs PH) $\times 4$ speakers (2 in picture naming task versus 2 in minimal pair sentence task) $\times 2$ stimulus types (compounds/phrases in isolation versus compounds/phrases in contextual sentence). The tokens were put in random order each with two immediate repetitions in block of ten with a gap of about 6 s between each item. There were in total 24 blocks (12 blocks of target items in isolation and 12 blocks of contextual sentences containing the target items).

C. Procedures

The listening identification test consisted of two parts: in part one, listeners heard the target items presented in isolation; in part two they heard a contextual sentence containing the target item. Part one was performed before part two to avoid a carry-over effect of contextual sentence perception. Two different meanings of the target item were given in the answer sheet: one as a compound and one as a noun phrase. The subjects' task was to choose the meaning which they judged was expressed by the speaker by circling the letter corresponding to their response in the answer sheet.

The experiment was delivered online so that subjects could either perform the test via their personal computer at home or at the researcher's office.

D. Results

A five-way fixed effect ANOVA (2 prosodic types [CP vs PH] ×2 experiments [MAX vs PIC] ×2 task types [word/phrase vs sentence] ×3 compound types [NA, NN, NV] ×3 dialects [HN, HU, SG]) was conducted on the percentage number of correct responses (the number of listeners over the total listeners in a dialect group who chose the correct response for a testing item). It is worth noting that a preliminary analysis showed that there was no significant difference between two speakers in the same experiment (MAX and PIC), and thus speakers as a factor was excluded from this analysis. Significant main effects were obtained for all factors except dialects (prosodic types: $F(1,1)=258$, $p<0.0001$, experiments: $F(1,1)=144$, $p<0.0001$; task types: $F(1,1)=17$, $p<0.0001$, compound types: $F(1,2)=10$, $p<0.0001$, dialects: $F(1,2)=0.3$ ns). Five significant two-way interaction effects were found including, prosodic types ×experiments: $F(1,1)=137$, $p<0.0001$, prosodic types ×compound types: $F(1,2)=9.35$, $p<0.0001$, prosodic types×dialects: $F(1,2)=11.93$, $p<0.0001$, prosodic types ×tasks: $F(1,1)=11.24$, $p<0.001$ and experiments ×compound types: $F(1,2)=18.15$, $p<0.0001$. The significant three-way interactions consisted of prosodic types ×experiments×compound types: $F(1,2)=40.32$, $p<0.0001$, prosodic types×compound types×tasks: $F(1,2)=4.69$, $p<0.01$, and a four-way interaction prosodic types ×experiments×compound types×tasks: $F(1,2)=11.27$, $p<0.0001$. Examination of the five main effects showed that compounds had significantly more correct response than phrases (mean scores: 73.5% vs 47.3%, $p<0.01$). The test items elicited under the maximal contrast experiment (MAX) also had more accurate responses than those elicited under the picture naming task (PIC) (mean: 70 vs 50.6, $p<0.01$). Test items embedded in a contextual sentence (S) yielded more correct responses than those presented in isolation (W) (mean: 63.7 vs 57.0, $p<0.01$). The NA and NV compound types with a juncture break between syllables of the phrase had more correct responses than the NN type (NA: 64.9, NV: 60.3, NN: 56, $p<0.01$). In contrast, there was no significant difference in correct perception scores among the three dialectal groups of listeners (HN: 59, HU: 60, SG: 61).

Examination of the prosodic types×dialects interaction showed that Northern (Hanoi) listeners had more correct compound responses but fewer correct phrase responses than listeners in the other two dialects (mean percentage scores compound versus phrase, respectively: Hanoi: 78 vs 40, Hue: 73 vs 51; Saigon: 70 vs 50, $p<0.01$), indicating that they misclassified phrases more for compounds even though they were listening to speakers of their own dialects.

Examination of the four-way interaction effect prosodic types×experiments×compound types×tasks (Fig. 4) showed three things which were consistent with the main effects. (1) The compound stimulus items from the PIC experiment had significantly more correct responses than the phrase, indicating a response bias toward the compound form and that the phrase in this experiment tended to be misclassified as compound due to the absence of a juncture break. (2) This is further supported by evidence that the phrase of the NN word/phrase type from the MAX experiment, which also lacks a juncture break between its two syllables, was more misheard as compound, indicating that listeners expected a juncture pause between components of phrases as a distinction from compounds. In addition, performance for stimuli with an absence of a juncture between constituents of the phrase was at chance level (clustering around 50%), indicating listeners' confusion between the compounds and phrases. In contrast, in patterns that have a juncture between syllables of phrases (NA and NV under MAX experiment), identification was better, though not optimal (approximately 70%) and had equal rate of success between the compound and phrase patterns. (3) Generally, there was a very marginal difference between items embedded in a contextual sentence and items presented in isolation, indicated by similar patterns of variation across three compound types for both the MAX and the PIC experiments. This further strengthened the finding that a juncture break between the two components of the phrase is essential for the distinction between phrase and compound regardless of whether they were presented in context or isolation. In other words, to listeners, the presence of a junctural break is more important than the contextual sentence in assisting the discrimination between meanings. This also lends further support to the acoustic results of the production experiment in indicating that there is neither acoustic nor perceptually salient evidence for a prosodically distinctive prominence contrast between the phrase and compound in Vietnamese, except for a juncture break between two components of the phrase but only under maximal contrast conditions. The difference between the NN and the other two compound/phrase types NA and NV under condition of maximal contrast also indicated speakers' parsing strategy in trying to convey the distinction between phrase and compound by relying on syntactic structure. The adjectives are also stative verbs in Vietnamese and thus the adjective in NA and the verb in NV constructions can be parsed as verb phrases of the adjective clauses while the noun cannot.

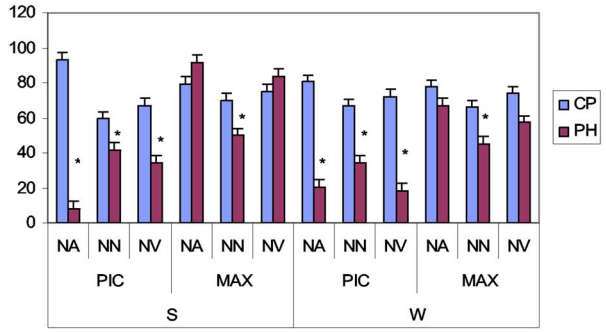

FIG. 4. (Color online) Mean of responses by four way interactions: prosodic types×compound types×experiments×task types. (*) sig. $p<0.01$.

IV. CONCLUSION: COMPOUNDS AND PHRASES IN PRODUCTION AND PERCEPTION

The results of the production experiments indicate that Vietnamese speakers only produce consistent acoustic cues to distinguish compounds from phrases when required to do so by speaking under conditions of maximal contrast and do

so by employing a juncture marking strategy that is probably universally available. Consistent with this strategy, the first components of the phrasal constructions were lengthened in comparison with their corresponding compounds accompanied by an expanded tone range, intensity dropping, and jaw lowering, which suggests a prepausal articulatory effect. No conclusive evidence of enhanced fundamental frequency, duration, or intensity prominence was found on the second components of compounds. Compound words as a whole were not temporally compressed in comparison to their phrasal counterparts as in English, a stressed language.

The results of the perception experiments indicate that listeners relied only on the juncture between the two components of noun phrases as a cue to distinguish between noun phrases and compounds. The results that listeners failed to distinguish noun phrases from compounds in the NN types and in stimuli elicited under picture-naming task where there is no juncture between the two constituents and performed better in patterns that have a juncture between syllables of noun phrases (NA and NV under MAX experiment) regardless of whether they were presented in context or isolation strengthens the case that there is neither significant acoustic nor perceptual evidence of contrastive stress patterns (strong-weak versus weak-strong) between noun phrases and compounds, contrary to previous claims in the literature (Thompson, 1965; Trần, 1969; among others). There was no significant dialectal variation in the production or perception of compound — phrasal contrasts. Hanoi speakers differed from speakers of the other two dialects in lengthening both syllables of the phrase in comparison to compound but were not more successful than listeners of Hue and Saigon in perceptually distinguishing compounds and phrases produced by speakers of their own dialect.

The acoustic and perceptual evidence appears to converge and is consistent with native speaker intuitions that phrases and their corresponding compounds are usually pronounced identically in Vietnamese, even in careful speech. However, it must be conceded that the *paradigmatic comparisons* upon which the acoustic evidence of the foregoing experiments rely is less than ideal to investigate this question. Prosodic features, particularly lexical stress patterns, probably rest heavily on *syntagmatic* comparisons between syllable sized units in the speech stream. Such comparisons were not possible given the phonetic structure of the compound phrasal constructions examined in this experiment. But Vietnamese provides us with another subclass of compound expressions—coordinative compounds with a free variation of reversible syllable constituents, which provide segmental feature control that enables a sensitive evaluation of asymmetries of prosodic prominence between adjacent syllables of disyllabic words.

V. EXPERIMENT 3: COORDINATIVE COMPOUNDS

In this experiment, essentially the same acoustic parameters as experiment 1 were analyzed, including syllable duration (onset, nucleus, and coda), F0 range, F0 contour, vowel intensity, spectral tilt, and vowel formant structure, to determine which syllable of the two (the first or second in a crossover contrast (e.g., in *bàn ghế* vs. *ghế bàn*) is more prominent.

A. Hypothesis

The basic hypothesis for testing was that coordinative compounds in Vietnamese are right headed i.e., show signs of acoustic prominence on the second syllable. But it could be argued that any acoustic prominence observed on the second syllable of a disyllabic compound may simply be a (word) boundary effect (such as final lengthening), rather than an accentual prominence effect. To meet this objection, the fine-structure of the temporal organization of the target syllable (including onset, vowel, and coda) will be examined. Accentual prominence characterized by vocal and articulatory gesture enhancement on a syllable might be expected to express itself as much in the onset as the coda, whereas word boundary lengthening may be expected to differentially lengthen the coda (Edwards and Beckman, 1988). Therefore, apart from other accompanying acoustic correlates (e.g., a larger tone range, greater intensity, and/or a full/unreduced vowel), the second syllable (S2) is considered to be more acoustically/accentually prominent than its corresponding syllable in the first position (S1) if it has a longer duration across all segment constituents including onset, vowel, and coda. By contrast, if only the syllable coda gets lengthened, the effect may be simply a preboundary lengthening.

B. Method

Ten minimal pairs of coordinative compounds were used in this experiment to elicit speech from the same subjects and using the same procedure as in the picture naming task; i.e., the same 15 subjects were asked to describe a picture, using the target word in a constant carrier sentence.

C. Analysis

Signal processing and measurements of fundamental frequency, duration, intensity, spectral tilt, and vowel formant were identical to those reported in experiment 1 (Sec. II C).

The statistical analysis involved a mixed model ANOVA, with two fixed factors: Syllable position (S1 and S2) and dialects (Hanoi, Hue, and Saigon), and two random factors: syllables (20 syllables) and speakers (15 speakers). The acoustic parameters (listed in Sec. II C) were the dependent variables. In addition, a ratio measure of S2/S1 (e.g., for the duration parameter: S2 duration/S1 duration) was also calculated and presented in graphs.

D. Results

The ANOVA results showed a significant main effect of syllable position for syllable duration and its constituent segments (syllable: $F(1,1551)=175.48$, $p<0.0001$, onset: $F(1,1524)=6.08$, $p<0.02$, vowel: $F(1,1551)=281.98$, $p<0.0001$, coda: $F(1,1153)=8.56$, $p<0.01$), tone duration: $F(1,1551)=156.59$, $p<0.0001$, F0 range: $F(1,1551)=19.39$, $p<0.0001$, mean intensity: $F(1,1551)=7.03$, $p<0.01$ and vowel first formant: $F(1,1551)=7.8$, $p<0.01$.

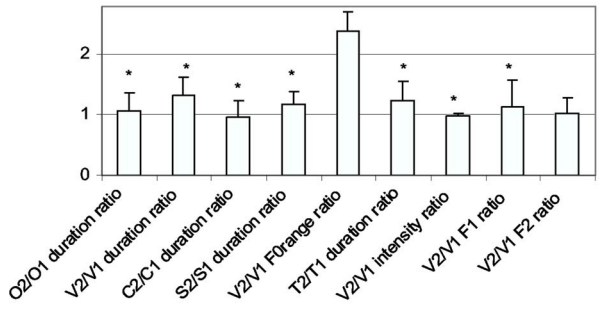

FIG. 5. (Color online) Mean S2/S1 acoustic values of coordinative compounds. (*) sig. $p < 0.01$. Legend: O2/O1: onset, V2/V1: vowel, C2/C1: coda, T2/T1: tone.

No significant effect was found for the factor of dialect or its interaction with syllable positions. There was no significant effect for spectral tilt values. Mean ratio in Fig. 5 showed that the constituent syllable of the coordinative compound has longer syllable duration (longer onset and vowel but shorter coda), longer tones, larger tone range, and higher vowel first formant (except a lower intensity value) when it is in the second position than in the first position.

1. Duration

The second syllable was shown (Fig. 5) to have significantly longer duration than the first syllable. Examination of the lengthening mechanism of the constituent segments of syllables that have an onset, vowel, and coda (e.g., bạn, chồng, quần, sách, vịt, xuồng, Fig. 6) showed that the syllable in the second position had significantly longer onset (O duration), vowel (V duration) and overall syllable duration (S duration) but a marginally shorter coda (C duration) than the same syllable in the first position. This evidence, particularly the negative effect of final lengthening on the coda, is counterindicative of a preboundary lengthening effect but supportive of the hypothesis of a right-headed accentual effect, which is also supported by other acoustic cues: F0 range and shape and vowel formant measurements (indicative of F1—F2 space expansion).

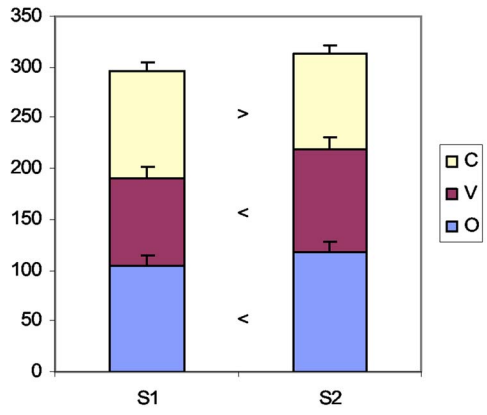

FIG. 6. (Color online) Duration of segments (onset, vowel, coda) of syllables in coordinative compounds. ⟨or⟩: significant patterns at $p < 0.01$.

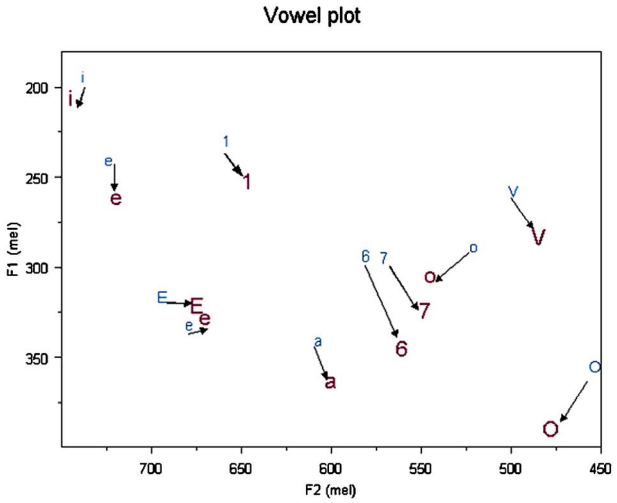

FIG. 7. (Color online) Vowel plots of coordinative compounds. Symbols: V: /ʌ/, 7: /ɤ/, a:/a/, O:/ɔ/, o:/o/ E:/ɛ/, e:/e, i:/i/, l:/ɨ/, 6:/ɐ/. Smaller font: first syllable, larger font: second syllable. The vowel /ɨ/ produced by Southern (Saigon) speakers.

2. F0 contour and F0 range

The examination of F0 contour showed that a syllable in the second position has a longer and fuller tonal shape in addition to a larger tonal range than one in the first position. For example, the second rising (sac) tone rose higher. The second falling (huyen) tone fell more sharply and lower. The second curve(hoi) and drop(nang) tone fell more sharply and lower (across three dialects) and then rose higher than its first position counterpart in the Southern dialect, consistent with findings from previous studies about the effect of stress on the surface output of lexical tones (Xu, 1999; Gsell, 1980; Hoàng and Hoàng, 1975).

3. Vowel formants

Figure 7 shows that the vowel in the second syllable has higher F1 than its first position counterparts, suggesting an articulatory gesture enhancement with larger mouth opening and jaw lowering which have been shown by previous researchers (Erickson, 2002; Van Summers, 1987) to be indicative of stress or prosodic strengthening.

4. Intensity and spectral tilt

No significant effect was found for spectral tilt. The second syllable had a marginally lower intensity value (dB) than the first syllable, suggesting a possible diminuation of vocal effort word or phrase finally at word boundaries.

E. Discussion

The results of this experiment showed that the second syllables of coordinative compounds are more acoustically prominent than first syllables, evidenced by a longer duration, larger tone range, fuller tonal shape, and gesture enhancement, suggesting a right-headed stress pattern. This supports Thompson's observation (1965) and discredits the prediction of Cao (2003) and Ngô (1984) of an "equivocal"

stress pattern for coordinative compounds on the ground of "morphosyntactic weight." Moreover, the results of this experiment are consistent with our recent findings on reduplicative compounds which were shown to have a right-headed prominence pattern on both phonetic and phonological grounds (Nguyễn and Ingram, in press). Taken together, these results strongly suggest a word-level stress pattern in Vietnamese.

VI. CONCLUSION

There is superficial tension (but no underlying inconsistency) between the principal findings reported in this paper. From the first series of experiments, it is clear that Vietnamese speakers only produce, and listeners only consistently hear phonetic contrasts between compounds and phrases under conditions of maximal contrast, in which speakers mark a phrasal construction with a juncture between the left and right elements of the phrase, to distinguish it from the compound word—something that they would not normally do unless specific demands of communication require it. Vietnamese apparently lacks the equivalent of a word level "compound rule" such as English and many other languages possess, which assigns a distinctive stress pattern to compound words via a mechanism such as lexical deaccentuation.

On the other hand, from the second experiment, involving syntagmatic comparisons in reversible adjunctive compounds (and other special compound constructions (Nguyễn and Ingram, in press) there was clear acoustic evidence that Vietnamese disyllabic word forms are not symmetrical in terms of accentual prominence, but "right-headed" or biased in weight toward the second element. These findings address a long-standing controversy over the existence of word stress in Vietnamese and more recently, the question of the "prosodic word" in a highly syllable oriented tone language such as Vietnamese. It is possible that word stress levels exist only as a phonetic tendency in Vietnamese, upon which no distinctive phonological contrasts depend. This is a matter of active inquiry, with theoretical implications for a typology of prosodic systems and of practical interest for phonetic and phonological transfer effects in second language learning.

ACKNOWLEDGMENTS

The postdoctoral research fellowship granted to T. A. T. N. by the University of Queensland is gratefully acknowledged. We would like to thank our subjects for their voluntary participation. We are grateful to the anonymous reviewers of the previous manuscript for their constructive criticisms and the anonymous reviewers of the current journal for their valuable comments and suggestions. Thanks to Dr. Bert Remijsen for sharing his praat scripts and N. H. N. for his statistical advice.

Beckman, M. E. (**1986**). *Stress and Non-Stress Accent* (Foris, Dordrecht).
Boersma, Paul & Weenink, David (2007). Praat: doing phonetics by computer (Version 4.6.09) [Computer program]. Retrieved June 24, 2007, from http://www.praat.org/
Cao, X. H. (**2003**). *Tiếng Việt: Mấy Vấn đề Ngữ âm ngữ Pháp Ngữ nghĩa*, Vietnamese: issues of phonology, syntax, and semantics (Giáo dục Press, Danang).
Cassidy, S. (**1999**). "Compiling multi-tiered speech databases into the relational model: Experiments with the Emu system," Proceedings of Eurospeech '99, Budapest, September 1999.
Chaudhary, C. C. (**1983**). "Word stress in Vietnamese: A preliminary investigation," Indian Linguist. **44**, 1–10.
Cutler, A., and Carter, D. M. (**1987**). "The predominance of strong initial syllables in the English vocabulary," Comput. Speech Lang. **2**, 133–142.
Đỗ, T. D. (**1986**). "Elements pour une e'tude comparative de l' intonation en Francais et en Vietnamien: L'accent de mots en Vietnamien (Elements for a comparative studies of intonation in French and in Vietnamese: the accent of words in Vietnamese)," Memoire de DEA, Universite' de Paris 3 ILPGA, Paris.
Edwards, J., and Beckman, M. E. (**1988**). "Articulatory timing and the prosodic interpretation of syllable duration," Phonetica **45**, 156–174.
Erickson, D. (**2002**). "Articulation of extreme formant patterns for emphasized vowels," Phonetica **59**, 134–149.
Gsell, R. (**1980**). "Remarques sur la structure de l' espace tonal en Vietnamien du sud (Parler de Saigon)," (Remarks on the structure of tonal space in Southern Vietnamese (spoken in Saigon)), Cahiers d'etudes Vietnamiennes, 4, Universite'de Paris 7.
Hoàng, T., and Hoàng, M. (**1975**). "Remarques sur la structure phonologique du Vietnamien. Essais Linguistiques (Remarks on the phonological structure of Vietnamese)," Etudes Vietnamiennes (Vietnamese studies), Vol. **40**, Hanoi.
Jones, R. B., and Huýnh, S. T. (**1960**). *Introduction to Spoken Vietnamese* (American Council of Learned Societies, Washington, DC).
Nespor, M., and Vogel, I. (**1986**). *Prosodic Phonology* (Foris, Dordrecht).
Ngô, T. N. (**1984**). "The syllabeme and pattern of word formation in Vietnamese," Ph.D dissertation, New York University, New York.
Nguyễn, D. L. (**1970**). "A contrastive phonological analysis of English and Vietnamese," *Pacific Linguistics Series* (Australian National University, Canberra), Vol. **8**.
Nguyễn, T. A. T., and Ingram, J. (**2006**). "Reduplication and word stress in Vietnamese," Proceedings of the 11th Australian International Conference on Speech Science & Technology, University of Auckland, New Zealand, 6–8 December.
Nguyễn, T. A. T., Ingram, J., and Pensalfini, R. (**2008**). "Prosodic transfer in Vietnamese acquisition of Vietnamese contrastive stress patterns," J. Phonetics **36**.
Ratliff, M. (**1992**). "Meaningful tone: A study of tonal morphology in compounds, form classes, and expressive phrases in White Hmong," in *Monograph Series on Southeast Asia* (Northern Illinois University Center for Southeast Asian Studies, DeKalb, IL), Vol. **27**.
Seitz, P. (**1986**). "Relationships between tones and segments in Vietnamese," Ph.D. thesis, University of Pensylvania (UMI).
Selkirk, E. (**1986**). "On derived domains in sentence phonology," Phonology Yearbook **3**, 371–405.
Shen, X. S. (**1993**). "On the temporal dimension of Mandarin," Acta-Llinguistica-Hafniensia **26**, 143–159.
Stevens, K. N., and Hanson, H. M. (**1995**). "Classification of glottal vibration from acoustic measurements," in *Vocal Fold Physiology: Voice Quality Control*, edited by O. Fujimura and H. Hirano (Singular, San Diego).
Thompson, L. (**1965**). *A Vietnamese Reference Grammar* (University of Hawaii Press, Honolulu).
Trần, H. M. (**1969**). "Stress, tone and intonation in South Vietnamese," Ph.D thesis. Australian National University, Malden.
van Summers, W. (**1987**). "Effects of stress and final-consonant voicing on vowel production: Articulatory and acoustic analyses," J. Acoust. Soc. Am. **82**, 847–863.
Xu, Y. (**1999**). "Effects of tone and focus on the formation and alignment of F0 contours," J. Phonetics **27**, 55–105.

Spectral and temporal cues for phoneme recognition in noise

Li Xu[a] and Yunfang Zheng
School of Hearing, Speech and Language Sciences, Ohio University, Athens, Ohio 45701

(Received 18 June 2006; revised 28 June 2007; accepted 6 July 2007)

Cochlear implant users receive limited spectral and temporal information. Their speech recognition deteriorates dramatically in noise. The aim of the present study was to determine the relative contributions of spectral and temporal cues to speech recognition in noise. Spectral information was manipulated by varying the number of channels from 2 to 32 in a noise-excited vocoder. Temporal information was manipulated by varying the low-pass cutoff frequency of the envelope extractor from 1 to 512 Hz. Ten normal-hearing, native speakers of English participated in tests of phoneme recognition using vocoder processed consonants and vowels under three conditions (quiet, and +6 and 0 dB signal-to-noise ratios). The number of channels required for vowel-recognition performance to plateau increased from 12 in quiet to 16–24 in the two noise conditions. However, for consonant recognition, no further improvement in performance was evident when the number of channels was ⩾12 in any of the three conditions. The contribution of temporal cues for phoneme recognition showed a similar pattern in both quiet and noise conditions. Similar to the quiet conditions, there was a trade-off between temporal and spectral cues for phoneme recognition in noise. © *2007 Acoustical Society of America.* [DOI: 10.1121/1.2767000]

PACS number(s): 43.71.Es, 43.66.Ts [KWG] Pages: 1758–1764

I. INTRODUCTION

Cochlear implants have provided hearing for thousands of patients with severe to profound sensorineural hearing loss. Speech recognition is remarkably good in most patients, with average sentence recognition better than 80% correct in quiet (see Zeng, 2004 for a review). However, reduced speech recognition in noise is one of the most common problems faced by every cochlear implant user. Skinner *et al.* (2002) reported that about one third of their 62 postlingually deafened cochlear implant users scored ⩽75% correct on CUNY sentences presented in multiple-talker babble noise at a fairly moderate +10 dB signal-to-noise ratio (S/N).

Spectral cues and temporal cues in cochlear implant speech processors are represented by the number of channels and the low-pass cutoff frequency of the envelope extractor, respectively. Several previous studies have examined the effects of spectral cues or temporal cues or both on speech recognition in quiet. Fu and Shannon (2000) examined the contribution of temporal cues for phoneme recognition in normal-hearing subjects. The low-pass cutoff frequency of the noise-excited vocoder (Shannon *et al.*, 1995) was varied, and the results demonstrated that with a low-pass cutoff frequency of 20 Hz, the subjects reached a performance plateau for both consonant and vowel recognition. These results were consistent with the data from earlier work (Van Tassel *et al.*, 1987; Drullman *et al.*, 1994a, b; Shannon *et al.*, 1995). In terms of spectral cues for speech recognition, there is converging evidence that 4 to 8 channels are sufficient to achieve good (i.e., >85% correct) speech recognition depending on the speech materials used (e.g., vowel, consonant, or sentence) and listening conditions (Shannon *et al.*, 1995, 2004; Dorman *et al.*, 1997; Loizou *et al.*, 1999; Xu *et al.*, 2002; Zeng, *et al.*, 2005). In a recent study of English phoneme recognition in quiet, Xu *et al.* (2005) systematically varied both the number of channels and the low-pass cutoff frequency of the envelope extractor. Results showed that the temporal envelope information required for consonant and vowel recognition to reach a performance plateau was 16 and 4 Hz, respectively. The spectral information required for the performance plateau in consonant and vowel recognition was 6–8 channels and 12 channels, respectively. Finally, there was a trade-off between the two speech cues in quiet. In other words, in order to achieve a certain level of phoneme recognition performance, the number of channels increased as the required low-pass cutoff frequency decreased. The range over which the trade-off for consonant recognition occurred was ⩽12 channels in the spectral domain and ⩽32 Hz of low-pass cutoff frequencies in the temporal domain. For vowel recognition, the trade-off occurred when the number of channels was ⩾4 and the low-pass cutoff frequency was ⩽4 Hz.

A few studies have investigated spectral and/or temporal cues for speech recognition in cochlear implant users. In a recent study, Nie *et al.* (2006) covaried the number of channels and the stimulation pulse rate to evaluate the spectral and temporal cues in cochlear implant speech recognition. They confirmed the trade-off effect between spectral and temporal cues for speech recognition in cochlear implant users. However, little is known about the contributions of spectral and temporal cues to speech recognition in noise. Friesen *et al.* (2001) found that a larger number of channels was required in noise conditions for cochlear implant users to achieve performance equivalent to that in quiet conditions. Similar results were obtained in Fu *et al.* (1998) and Dorman *et al.* (1998). Therefore, higher spectral resolution appears to be necessary for speech recognition in noise. On the other

[a]Author to whom correspondence should be addressed. Electronic mail: xul@ohio.edu

hand, the temporal envelope cue might be particularly susceptible to the interference of background noise. It is thus important to know whether the use of temporal cues differs substantially under noise conditions.

The present study was designed to examine spectral and temporal cues processed through a cochlear implant speech-processing simulation and to determine their contributions to speech recognition in noise. Spectral cues were manipulated by varying the number of channels in a noise-excited vocoder, whereas temporal cues were manipulated by varying the low-pass cutoff frequency of the envelope extractor. We attempted to test whether the relative contributions of spectral and temporal cues are similar in noise and quiet conditions and whether there is a trade-off between spectral and temporal cues for speech recognition in noise as demonstrated in quiet.

II. METHOD

A. Subjects

Ten subjects (5 males and 5 females, age 24.3±2.8, mean±s.d.) were recruited from the Ohio University student population. They were normal-hearing, native speakers of English with pure-tone air-conduction thresholds ≤20 dB HL at octave frequencies from 250 to 8000 Hz. All subjects scored ≥95% correct on English consonant and vowel recognition tests using the unprocessed original speech materials. None of subjects had a history of ear disease. The use of human subjects was reviewed and approved by the Ohio University Institutional Review Board.

B. Stimuli

Two tests (i.e., consonant test and vowel test) were conducted to assess phoneme recognition. The consonant test had 20 initial consonants that included "ba," "cha," "da," "fa," "ga," "ja," "ka," "la," "ma," "na," "pa," "ra," "sa," "sha," "ta," "tha," "va," "wa," "ya," and "za" (Shannon *et al.*, 1999). One male talker (No. 3) and one female talker (No. 3) of the multitalker cohort were used, resulting in 40 tokens (20×2=40) for each consonant test. The vowel test used 12 hVd vowels that included "had," "haid," "hawed," "head," "heed," "hid," "heard," "hoed," "hod," "hood," "hud," and "who'd" (Hillenbrand *et al.*, 1995). Two male talkers (Nos. 48 and 49) and two female talkers (Nos. 39 and 44) of the multitalker cohort were used, resulting in 48 tokens (12×4=48) for each vowel test.

C. Signal processing

A noise-excited vocoder technique (Shannon *et al.*, 1995) was applied in stimulus signal processing, using MATLAB (MathWorks, Natick MA) software. Before signal processing, the speech signal was mixed digitally with the speech-shaped noise (Nilsson *et al.*, 1994) with S/N of +6 and 0 dB. The rms amplitude of each speech token was calculated and the speech-shaped noise with a rms amplitude equal to 50% (+6 dB S/N) or 100% (0 dB S/N) of that of the speech token was added to the original speech. In the noise-excited vocoder (see Xu *et al.*, 2002, 2005 for details), the original speech signals or the speech signals mixed with the noise were passed through a bank of analysis filters that varied between 2 and 32 (2, 4, 6, 8, 12, 16, 24, and 32) in number of channels. The overall bandwidth was 5350 Hz (from 150 to 5500 Hz). Half-wave rectification and low-pass filtering were used to extract the temporal envelope of each analysis band. The low-pass filter was a second-order Butterworth filter with a roll-off of 12 dB/octave. The low-pass cutoff frequency was varied between 1 and 512 Hz in 1 octave steps. A white noise bandpassed through the same analysis filters was modulated by the extracted temporal envelope of each band. Whereas the process of modulation might introduce sidebands that might overlap with adjacent bands, the effects of such on speech recognition were found negligible in our pilot experiments. Finally, the modulated noise bands were summed and then stored in the computer hard disk for later presentation.

D. Procedure

The signals were presented monaurally through a circumaural headphone (Sennheiser, HD 265) at the ear of preference in an IAC sound booth. The intensity was adjusted to the most comfortable level for each subject. For our subjects, this level was around 65 dB (A). Custom programs written in MATLAB were used to present the stimuli. In the programs, two graphical user interfaces (GUIs) were created to present the consonants and the vowels, respectively. In the GUIs, the phonemic symbols (20 initial consonants or 12 hVd vowels) were represented in alphabetical order in a grid on a computer screen. The consonant or vowel stimuli were presented acoustically in random order. The subjects were instructed to use a computer mouse to select the button that represented the consonant or vowel that they had heard.

For both consonant and vowel tests, there were 80 combinations of number of channels and low-pass cutoff frequency (8 numbers of channels×10 low-pass cutoff frequencies) and each combination was tested in three conditions (quiet, and S/N of +6 and 0 dB). Thus, in the consonant test there were 9600 responses collected from each subject (20 tokens×2 talkers×80 combinations ×3 conditions), and in the vowel test there were 11520 responses (12 tokens×4 talkers×80 combinations ×3 conditions). All subjects participated in a training session of about 3 h by listening to the processed speech materials in order to familiarize themselves with the experiment. Four combinations [i.e., (1) 24 channels, 128 Hz low-pass cutoff; (2) 12 channels, 32 Hz low-pass cutoff; (3) 6 channels, 8 Hz low-pass cutoff; and (4) 2 channels, 2 Hz low-pass cutoff] were used during the training in such a sequence. Feedback was provided during training. During experimental testing, no feedback was provided. The order of the 80 combinations of number of channels and low-pass cutoff frequency and the 3 noise conditions were randomized. The experiment was scheduled for blocks of 1, 2, or 3 h, and each subject took approximately 25 h to complete the experiment.

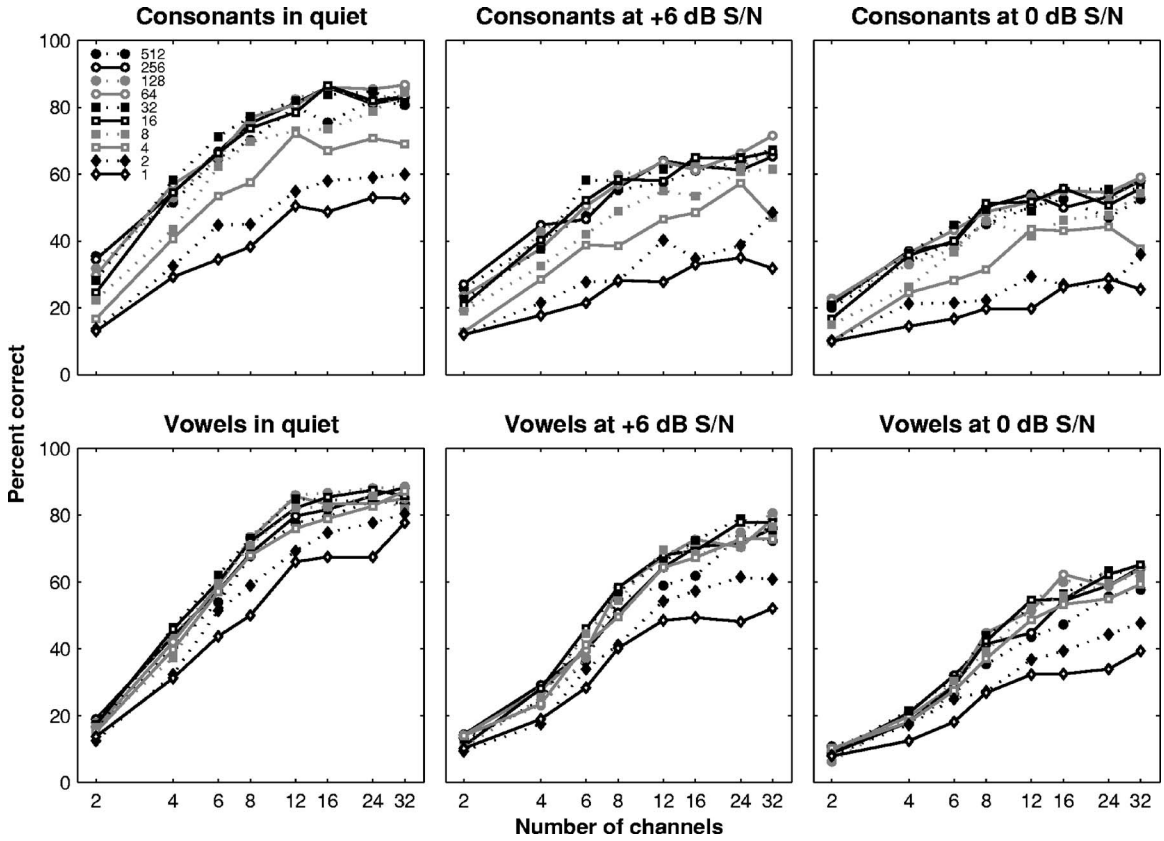

FIG. 1. Consonant and vowel recognition as a function of number of channels under three conditions (quiet, S/N of +6 and 0 dB). The data were the mean scores across all ten subjects. In each panel, each line represents data using one of the ten low-pass cutoff frequencies as indicated by the legend in the upper-left panel.

III. RESULTS

In the present study, there were three independent variables (i.e., number of channels, low-pass cutoff frequency, and noise level) and two dependent variables (consonant and vowel recognition scores). For the results of both consonant and vowel tests, a three-way ANOVA with repeated measures revealed that all three main factors (number of channels, low-pass cutoff, and stimulus type) were significant (all $p=0.000$). The grand mean scores for both consonant and vowel recognition averaged across all 80 combinations of number of channels and low-pass cutoff frequency showed a decrease of 14.7 percentage points from quiet to +6 dB S/N, and a decrease of 9.7 percentage points from +6 to 0 dB S/N.

Figure 1 shows the group-mean phoneme recognition score as a function of number of channels for the consonant (upper panels) and vowel (lower panels) tests under the three conditions (quiet, S/N of +6 and 0 dB). The standard deviation of the recognition scores averaged across all testing conditions for all ten subjects was 9.44 percentage points. Each line represents data using one of the ten low-pass cutoff conditions. In both noise and quiet conditions the recognition scores increased as the number of channels increased. In the quiet condition, the required number of channels to reach performance plateau was about 12 for both consonant and vowel tests; however, in the vowel test the required number of channels for performance plateau increased to 16–24 in the noise conditions. In the consonant test, an increase in the number of channels beyond 12 did not consistently improve speech recognition scores in noise conditions.

Figure 2 shows the group-mean phoneme recognition score as a function of low-pass cutoff frequency for the consonant (upper panels) and vowel (lower panels) tests under the three conditions (quiet, S/N of +6 and 0 dB). Each line represents one of the eight numbers of channels. In general, phoneme recognition improved as a function of low-pass cutoff frequency. The low-pass cutoff frequencies required to reach performance plateau, in both quiet and noise conditions, were about 16 and 4 Hz for consonants and vowels, respectively. Thus, the contributions of temporal cues to phoneme recognition in quiet and in the two noise conditions did not appear to be significantly different from each other.

Figure 3 shows the phoneme recognition score as a function of both number of channels and low-pass cutoff frequency for the consonant (left column) and vowel (right column) tests under the three conditions (quiet, S/N of +6 and 0 dB). Each gray-scale shaded area represents a phoneme recognition score for a particular range of numbers of channels and low-pass cutoff frequencies.

An exponential function, $y=ae^{b(x+c)}+d$, where y is the percent correct scores and x is the number of channels (or low-pass cutoff frequency) was used to fit each of the group-mean score curves shown in Figs. 1 and 2. The values of the parameters of the exponential function were derived based on a method of ordinary least squares and were found to be in the following ranges: a (−1.5 to −0.9), b (−0.6 to −0.1), c

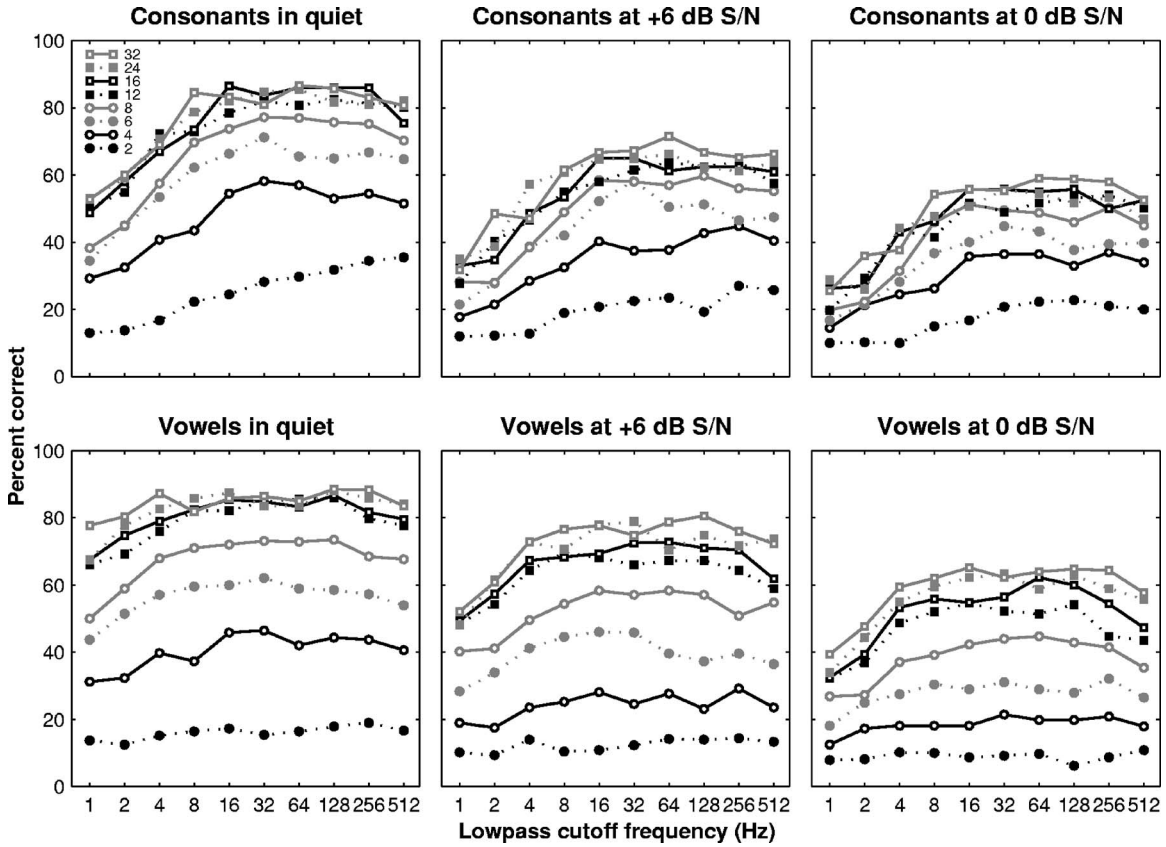

FIG. 2. Consonant and vowel recognition as a function of low-pass cutoff frequency under three conditions (quiet, S/N of +6 and 0 dB). The data were the mean scores across all ten subjects and were exactly the same as in Fig. 1 but plotted in a different format. In each panel, each line represents data using one of the eight numbers of channels as indicated by the legend in the upper-left panel.

(−5 to −2), and d (0.11 to 0.89). From each of the fitting curves, the knee point, defined as the number of channels (or low-pass cutoff frequency) at which 90% of the performance plateau is reached, was then obtained. Those data are also presented in Fig. 3 by the two lines that overlie the contour plots. The vertical line represents the number of channels at which the recognition performance became asymptotic. The number of channels at which the consonant recognition reached plateau was around 12 for both quiet and noise conditions, indicating that an increase of spectral information beyond 12 channels did not improve consonant recognition in noise. On the other hand, the number of channels required to reach vowel recognition plateau was around 12 in quiet and between 16 and 24 in the noise conditions, indicating that vowel recognition in noise benefited from the increased spectral information. The horizontal line represents the low-pass cutoff frequency at which the recognition performance became asymptotic. Note that for both quiet and noise conditions, the low-pass cutoff frequencies for the performance plateau were between 8 and 16 Hz for consonant recognition and around 4 Hz for vowel recognition (Fig. 3).

The two lines also divide each of the contour plots in Fig. 3 into four quadrants. The upper-right quadrant represents the number of channels and the low-pass cutoff frequency at which the performance plateau was reached. The performance was essentially the same at any point in that spectral and temporal space. The upper-left quadrant represents the number of channels before the performance reached plateau but the low-pass cutoff frequency after the performance reached plateau. Therefore, the performance in that space depended only on the number of channels. On the contrary, the lower-right quadrant represents the low-pass cutoff frequency before the performance reached plateau but the number of channels after the performance reached plateau. Therefore, the performance in that space depended only on the low-pass cutoff frequency. Of particular interest is the lower-left quadrant. It represents the number of channels and low-pass cutoff frequency before the performance plateau. Thus, the performance depended on both the number of channels and the low-pass cutoff frequency in that space. It was also the space where there was a trade-off between the spectral and the temporal cues for phoneme recognition. It was evident that the trade-off existed for consonant and vowel recognition in both quiet and noise conditions. Note that the range over which the trade-off occurred was different for consonant and vowel recognition. The trade-off for consonant recognition occurred with the number of channels $\leqslant$12 and the low-pass cutoff frequency $\leqslant$16 Hz. Correspondingly, the trade-off for vowel recognition occurred with the number of channels $\geqslant$4 and the low-pass cutoff frequency $\leqslant$4 Hz (Fig. 3).

IV. DISCUSSION

Noise has a detrimental effect on speech recognition. In the present study, the mean scores for both consonant and

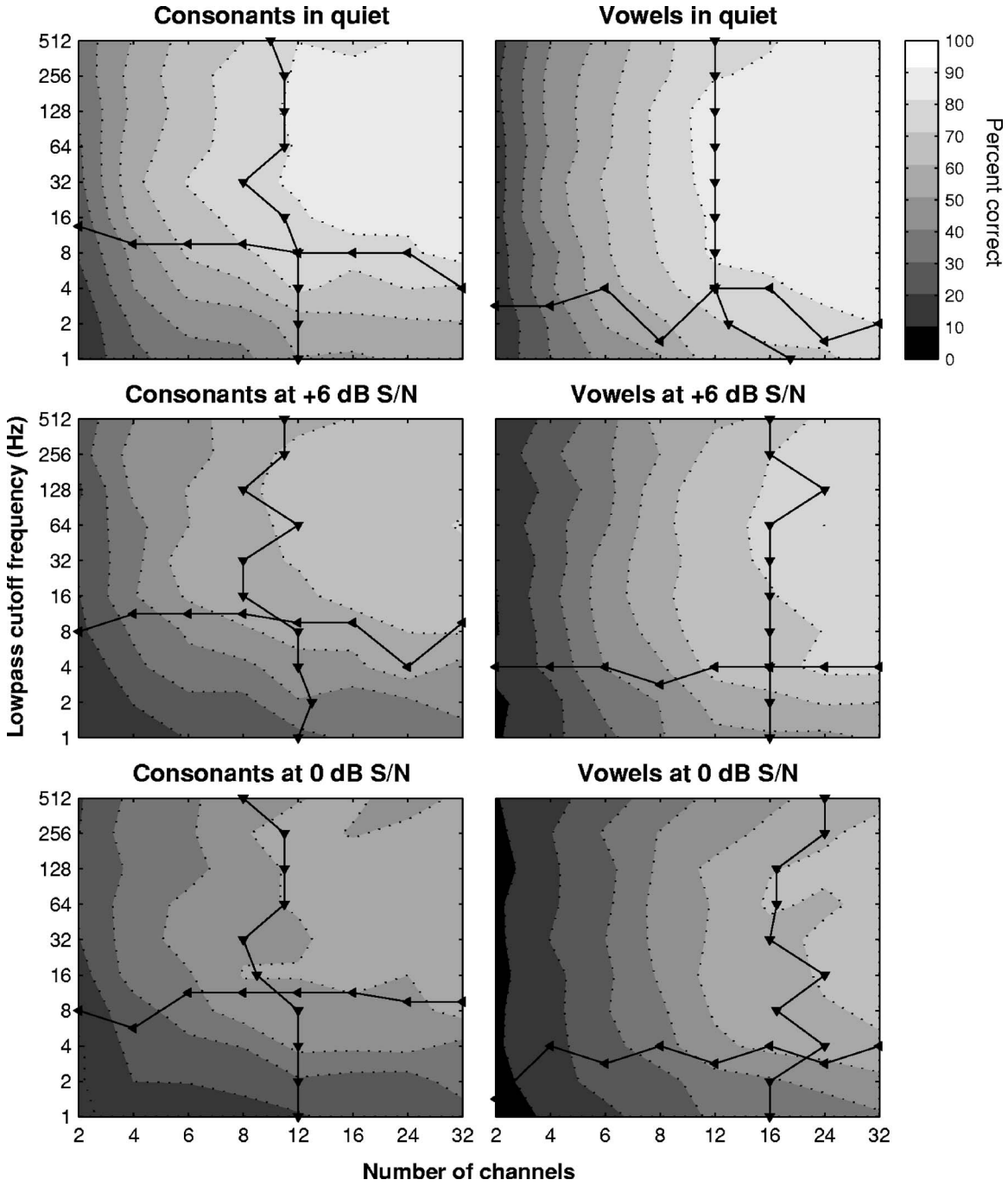

FIG. 3. Group-mean phoneme recognition as a function of both number of channels (abscissa) and low-pass cutoff frequency (ordinate) under three conditions (quiet, S/N of +6 and 0 dB) for consonant (left) and vowel (right) tests. The data were the same as in Figs. 1 and 2. Each gray scale represents a certain percent correct score as indicated in the scale bar on the right. The vertical line and inverted triangle represent the knee point (i.e., the number of channels at which the recognition performance is turning into plateau) using the corresponding low-pass cutoff frequency indicated on the ordinate. The horizontal line and the left closed triangle represent the knee point (i.e., the low-pass cutoff frequency at which the recognition performance is turning into plateau) using the corresponding number of channels indicated on the abscissa.

vowel recognition using the vocoder processed speech tokens showed a decrease of about 15 percentage points from quiet to +6 dB S/N, and a decrease of 10 percentage points from +6 to 0 dB S/N. These results are in close agreement with those of Fu *et al.* (1998), who tested four normal-hearing subjects listening to unprocessed and vocoder processed speech sound under ten different noise conditions from +24 to −15 dB S/N. With the unprocessed stimuli, the subjects' performance started to decrease when the S/N decreased to 0 dB. When the subjects listened to the vocoder processed stimuli, their performance started to decrease at about +12 dB S/N. The performance score for consonant and vowel recognition decreased about 15 percentage points from S/N of +24 to +6 dB, and about 10 percentage points from +6 to 0 dB S/N. A study of sentence recognition by Stickney *et al.* (2004) showed similar results. In addition, they also found that a single-talker masker exerted a stronger masking effect than did the steady-state noise with eight

channels. This might be because the single-talker masker introduced more informational masking (central competition between the speech signal and the masker).

In the present study, we found that an increase in the number of channels in noise conditions beyond the point of plateau performance in quiet improved vowel recognition but not consonant recognition. As shown in Figs. 1 and 3, the knee points (the points where performance began to plateau) for consonant recognition were almost the same (i.e., 12 channels) in both quiet and noise conditions. For vowel recognition, however, the number of channels required to reach the performance plateau increased in the noise conditions (16–24 channels) compared to that in quiet (12 channels). This might be due to the fact that vowel recognition relies more on spectral cues than consonant recognition does (Peterson and Barney, 1952). Parikh and Loizou (2005) performed acoustic analysis of the vowels in noise and showed that F1 could be detected more reliably than F2, suggesting that listeners had access to correct F1 information but vague F2 information. Therefore, a higher spectral resolution as a result of a larger number of channels might help resolve the formants better in noise conditions. It is worth noting that the observed benefit of an increased number of channels for vowel recognition in noise might be due to the ceiling effects on vowel recognition in quiet. Although the highest mean scores of all subjects were 88.5% correct with the vocoder processed vowels (lower than the 95–100% correct scores with unprocessed vowels), we could not exclude the possibility that ceiling effects had caused the vowel recognition to reach performance plateau at a lower number of channels. On the other hand, consonants inhabit an auditory/acoustical space that is more multidimensional than that inhabited by vowels. Some features of consonants, such as the place of articulation, rely more on spectral cues, as shown by Xu *et al.* (2005). Due to a limited number of subjects and experiment repetitions, the analysis of information transmission was not performed in the present study. In future studies, it would be interesting to evaluate the effects of number of channels and low-pass cutoff frequency on transmission of various phonemic features in noise.

Another important finding from the present study is that temporal cues contributed to phoneme recognition similarly in both quiet and noise conditions. As illustrated in Figs. 2 and 3, the knee points of the low-pass cutoff frequencies were almost constant in the three conditions for consonant (16 Hz) and vowel (4 Hz) recognition. Fu and Shannon (2000) examined phoneme recognition of both cochlear implant listeners and normal-hearing listeners in quiet, and found that when the low-pass cutoff frequency was at 20 Hz, subjects reached a performance plateau. Xu *et al.* (2005) demonstrated similar results in quiet: The low-pass cutoff frequencies required for performance plateau were 16 and 4 Hz for consonant and vowel recognition, respectively. Therefore, when the low-pass cutoff frequency is higher than 16 or 20 Hz, the auditory system might not be sensitive to the differences with added temporal cues for speech recognition. There are several possible reasons for this. First, noise may obscure temporal cues, which makes the cues less effective. It should be pointed out that we used a steady-state speech-shaped noise. Conceivably, if a temporal-modulated noise or a single-talker noise (Qin and Oxenham, 2003; Stickney *et al.*, 2004) were used, the interference of the noise on the temporal envelopes would be greater, rendering the temporal cues even less effective. Second, there is a trade-off between temporal and spectral cues in both quiet and noise conditions as shown in Fig. 3. Thus, when the spectral cues are sufficient, only a limited low-pass cutoff frequency is required for recognition task. Third, the auditory system might not be able to utilize additional temporal cues even if they are available. Psychoacoustical experiments by Bacon and Viemeister (1985) showed a low-pass characteristic in the temporal modulation transfer function (TMTF). Although the cutoff of the TMTF was found to be around 50–60 Hz, human listeners are most sensitive to the temporal modulation at an even lower frequency.

There are a number of implications for auditory prostheses based on the results of the present study. We showed that increased spectral information can improve vowel recognition in noise whereas increased temporal information does not improve phoneme recognition in noise. Current cochlear implant systems provide limited frequency resolution. A typical cochlear implant user may have only 6–10 functional channels (Fishman *et al.*, 1997; Garnham *et al.*, 2002; Kong *et al.*, 2004). Therefore, increasing the effective number of channels might be a key to improving speech recognition in noise for cochlear implant users. Current-steering (or virtual-channel) technique, coupled with reduced channel interaction, might provide more effective channels for cochlear implant users. Another implication is related to presentation of the temporal information in the cochlear implant system. We showed that a low-pass cutoff frequency of 16 Hz was sufficient to achieve a speech recognition performance plateau both in quiet and in noise. Current cochlear implant devices typically use a low-pass cutoff frequency of around 400–500 Hz. Such a relative high low-pass cutoff might not be optimal. If the low-pass cutoff frequency is set at a lower value, a lower stimulation pulse rate will be sufficient to represent the temporal envelope information. Middlebrooks (2005) studied temporal information transmission in the guinea pig cortex and found that a low pulse rate instead of a high pulse rate resulted in significantly better temporal envelope detection. Perceptual studies in cochlear implant users also showed that a low rate stimulation yielded a better modulation detection threshold than a high rate stimulation (Galvin and Fu, 2005; Pfingst *et al.*, 2007). Therefore, we speculate that a low low-pass cutoff frequency and a low rate stimulation might achieve better speech recognition in quiet and noise for cochlear implant users. However, this speculation requires testing in cochlear implant users.

V. CONCLUSIONS

In this study, we systematically varied the number of channels and the low-pass cutoff frequency of the envelope extractor to examine the relative contributions of spectral and temporal cues to phoneme recognition in noise. Results demonstrated that noise reduced speech recognition performance, and an increase in the number of channels beyond

that required for plateau performance in quiet could only improve vowel recognition in noise. Temporal cues contributed to phoneme recognition similarly in both quiet and noise conditions. There was a trade-off between temporal and spectral cues for speech recognition in noise as well as in quiet. It is suggested that future cochlear implant design focus more on increasing the spectral resolution so as to provide better speech recognition in noise for implant users.

ACKNOWLEDGMENTS

We are grateful to Bryan Pfingst, Fan-Gang Zeng, Associate Editor Ken Grant, and an anonymous reviewer for their constructive comments. This research was funded by a Scholarly Activity Award from the College of Health and Human Services at Ohio University.

Bacon, S. P., and Viemeister, N. F. (**1985**). "Temporal modulation transfer functions in normal-hearing and hearing impaired listeners," Audiology **24**, 117–134.

Dorman, M. F., Loizou, P. C., Fitzke, J., and Tu, Z. (**1998**). "The recognition of sentences in noise by normal-hearing listeners using simulations of cochlear-implant signal processors with 6–20 channels," J. Acoust. Soc. Am. **104**, 3583–3585.

Dorman, M. F., Loizou, P. C., and Rainey, D. (**1997**). "Speech intelligibility as a function of the number of channels of stimulation for signal processors using sine-wave and noise-band outputs," J. Acoust. Soc. Am. **102**, 2403–2411.

Drullman, R., Festen, J. M., and Plomp, R. (**1994a**). "Effect of temporal envelope smearing on speech perception," J. Acoust. Soc. Am. **95**, 1053–1064.

Drullman, R., Festen, J. M., and Plomp, R. (**1994b**). "Effect of reducing slow temporal modulations on speech reception," J. Acoust. Soc. Am. **95**, 2670–2680.

Fishman, K. E., Shannon, R. V., and Slattery, W. H. (**1997**). "Speech recognition as a function of the number of electrodes used in the SPEAK cochlear implant speech processor," J. Speech Lang. Hear. Res. **40**, 1201–1215.

Friesen, L. M., Shannon, R. V., Baskent, D., and Wang, X. (**2001**). "Speech recognition in noise as a function of the number of spectral channels: Comparison of acoustic hearing and cochlear implants," J. Acoust. Soc. Am. **110**, 1150–1163.

Fu, Q. J., and Shannon, R. V. (**2000**). "Effect of stimulation rate on phoneme recognition by Nucleus-22 cochlear implant listeners," J. Acoust. Soc. Am. **107**, 589–597.

Fu, Q.-J., Shannon, R. V., and Wang, X. S. (**1998**). "Effects of noise and spectral resolution on vowel and consonant recognition: Acoustic and electric hearing," J. Acoust. Soc. Am. **104**, 3586–3596.

Galvin, J. J., III, and Fu, Q.-J. (**2005**). "Effects of stimulation rate, mode and level on modulation detection by cochlear implant users," J. Assoc. Res. Otolaryngol. **6**, 269–279.

Garnham, C., O'Driscoll, M., and Ramsden, S. (**2002**). "Speech understanding in noise with a Med-El COMBI 40+ cochlear implant using reduced sets," Ear Hear. **23**, 540–552.

Hillenbrand, J., Getty, L. A., Clark, M. J., and Wheeler, K. (**1995**). "Acoustic characteristics of American English vowels," J. Acoust. Soc. Am. **97**, 3099–3111.

Kong, Y. Y., Cruz, R., Jones, J. A., and Zeng, F. G. (**2004**). "Music perception with temporal cues in acoustic and electric hearing," Ear Hear. **25**, 173–185.

Loizou, P. C., Dorman, M., and Tu, Z. (**1999**). "On the number of channels needed to understand speech," J. Acoust. Soc. Am. **106**, 2097–2103.

Middlebrooks, J. C. (**2005**). "Transmission of temporal information from a cochlear implant to the auditory cortex," Assoc. Res. Otolaryngol. Abst. **28**, 91.

Nie, K., Barco, A., and Zeng, F. G. (**2006**). "Spectral and temporal cues in cochlear implant speech perception," Ear Hear. **27**, 208–217.

Nilsson, M., Sali, S. D., and Sullivan, J. A. (**1994**). "Development of the Hearing in Noise Test for the measurement of speech reception thresholds in quiet and in noise," J. Acoust. Soc. Am. **95**, 1085–1099.

Parikh, G., and Loizou, P. (**2005**). "The influence of noise on vowel and consonant cues," J. Acoust. Soc. Am. **118**, 3874–3888.

Peterson, G. E., and Barney, H. L. (**1952**). "Control methods used in a study of the vowels," J. Acoust. Soc. Am. **24**, 175–184.

Pfingst, B. E., Xu, L., and Thompson, C. S. (**2007**). "Effect of carrier pulse rate and stimulation site on modulation detection by subjects with cochlear implants," J. Acoust. Soc. Am. **121**, 2236–2246.

Qin, M. K., and Oxenham, A. J. (**2003**). "Effects of simulated cochlear implant processing on speech reception in fluctuating maskers," J. Acoust. Soc. Am. **114**, 446–454.

Shannon, R. V., Fu, Q.-J., and Galvin, J. (**2004**). "The number of spectral channels required for speech recognition depends on the difficulty of the listening situation," Acta Oto-Laryngol., Suppl. **552**, 50–54.

Shannon, R. V., Jensvold, A., Padilla, M., Robert, M. E., and Wang, X. (**1999**). "Consonant recordings for speech testing," J. Acoust. Soc. Am. **106**, L71–74.

Shannon, R. V., Zeng, F.-G., Kamath, V., Wygonski, J., and Ekelid, M. (**1995**). "Speech recognition with primarily temporal cues," Science **270**, 303–304.

Skinner, M. W., Arndt, P. L., and Staller, S. J. (**2002**). "Nucleus 24 advanced encoder conversion study: Performance vs. preference," Ear Hear. **23**, 2S–25S.

Stickney, G. S., Zeng, F.-G., Litovsky, R., and Assmann, P. (**2004**). "Cochlear implant speech recognition with speech maskers," J. Acoust. Soc. Am. **116**, 1081–1091.

Van Tassel, D. J., Soli, S. D., Kirby, V. M., and Widin, G. P. (**1987**). "Speech waveform envelope cues for consonant recognition," J. Acoust. Soc. Am. **82**, 1152–1161.

Xu, L., Thompson, C. S., and Pfingst, B. E. (**2005**). "Relative contributions of spectral and temporal cues for phoneme recognition," J. Acoust. Soc. Am. **117**, 3255–3267.

Xu, L., Tsai, Y., and Pfingst, B. E. (**2002**). "Features of stimulation affecting tonal-speech perception: Implications for cochlear prostheses," J. Acoust. Soc. Am. **112**, 247–258.

Zeng, F.-G. (**2004**). "Trends in cochlear implants," Trends in Amplification **8**, 1–34.

Zeng, F.-G., Nie, K., Stickney, G. S., Kong, Y.-Y., Vongphoe, M., Bhargave, A., Wei, C., and Cao, K. (**2005**). "Speech recognition with amplitude and frequency modulations," Proc. Natl. Acad. Sci. U.S.A. **102**, 2293–2298.

The role of fundamental frequency contours in the perception of speech against interfering speech

Christine Binns[a] and John F. Culling
Department of Psychology, University of Cardiff, Tower Building, Park Place, Cardiff, CF10 3AT, Wales

(Received 9 February 2006; revised 8 March 2007; accepted 1 June 2007)

Four experiments investigated the effect of the fundamental frequency (F0) contour on speech intelligibility against interfering sounds. Speech reception thresholds (SRTs) were measured for sentences with different manipulations of their F0 contours. These manipulations involved either reductions in F0 variation, or complete inversion of the F0 contour. Against speech-shaped noise, a flattened F0 contour had no significant impact on SRTs compared to a normal F0 contour; the mean SRT for the flattened contour was only 0.4 dB higher. The mean SRT for the inverted contour, however, was 1.3 dB higher than for the normal F0 contour. When the sentences were played against a single-talker interferer, the overall effect was greater, with a 2.0 dB difference between normal and flattened conditions, and 3.8 dB between normal and inverted. There was no effect of altering the F0 contour of the interferer, indicating that any abnormality of the F0 contour serves to reduce intelligibility of the target speech, but does not alter the masking produced by interfering speech. Low-pass filtering the F0 contour increased SRTs; elimination of frequencies between 2 and 4 Hz had the greatest effect. Filtering sentences with inverted contours did not have a significant effect on SRTs. © *2007 Acoustical Society of America.* [DOI: 10.1121/1.2751394]

PACS number(s): 43.71.Es, 43.71.Gv [MSS] Pages: 1765–1776

I. INTRODUCTION

Intonation is known to have many functions in language, including helping with syntactic disambiguation (Cutler *et al.*, 1997), distinguishing between new and given information (Cutler *et al.*, 1997), syllable stress (Lehiste, 1970), segmentation (Liss *et al.*, 1998) as well as voicing cues (Haggard *et al.*, 1981) and cues to vowel identity (Traunmüller, 1981). Less is known about the overall impact of intonation on speech intelligibility.

The following set of experiments aims to investigate the impact of intonation on speech intelligibility under different listening conditions—speech-shaped noise and a single-talker interferer. The effect will be measured using speech reception thresholds while manipulating the F0 contour, either by reducing the amount of F0 variation incrementally or by F0 inversion.

Previous experiments have explored the role of intonation in speech recognition by flattening the F0 contour and comparing the intelligibility of these utterances to normally intonated ones in a quiet listening environment, with a background of white noise or against a competing talker (Wingfield *et al.*, 1984; Assmann, 1999; Laures and Weismer, 1999). These studies showed a detrimental effect of flattening the F0 contour on sentence intelligibility.

In the study by Laures and Weismer (1999), two male speakers read nine low-predictability sentences selected from the Speech Perception in Noise test with a pronounced prosody. Each of these sentences was resynthesized using the LPC resynthesis technique. The F0 contour of the voiced segments was flattened by adjusting their F0 value to the mean F0 of the sentence. Ten listeners were presented with both normally intonated and monotonous sentences in a background of white noise and asked to transcribe them. On a second presentation of the stimuli, listeners were asked to rate the sentences for intelligibility on a scale of 1–7, with 1 being unintelligible and 7 being highly intelligible. A significant difference between the normally intonated and monotonous sentences was found for both the number of words transcribed correctly and rated intelligibility. Among the explanations proposed for these findings was that the rise and fall of the F0 contour has been found to direct the listener's attention to the content words of the utterance (Cutler and Foss, 1974); therefore without these cues, the intelligibility of the utterance is lowered.

Another contributing factor may be the presence of F0 movement. Culling and Summerfield (1995) investigated the effect of frequency modulation on the identification of concurrent vowel sounds presented concurrently with interfering vowels. Listeners were asked to report both the presentation intervals and the identity of a target vowel in conditions where the target vowel was modulated halfway through the stimulus and either none, one, or two of the interfering vowels were modulated throughout. The modulation of the target vowel was deferred since a pilot study showed that this enhances the effect of frequency modulation on vowel prominence. Results showed that F0 modulation increases the perceptual salience and identification of vowels against the background of other unmodulated vowels. These results suggest that frequency modulation can enhance the target by making it more salient than the competing sound.

Our studies aim to further investigate these effects by decreasing the amount of F0 variation gradually with the inclusion of conditions where the contour retains only half or a quarter of the total variation present in a standard contour,

[a]Electronic mail: binnsc@cf.ac.uk

along with an inverted F0 condition. An inverted F0 contour retains the variation present in a standard F0 contour, but these variations are reversed so that where there would be a rise in the normally intonated contour, there is now a fall, and vice versa. Inverted F0 contours have been found to detrimentally affect the intelligibility of an utterance by Culling *et al.* (2003) in experiments investigating the effect of reverberation on listeners' abilities to separate two competing voices. This result indicates that it is not simply the movement *per se* of the F0 contour that aids the listener in his/her comprehension of the utterance, since this is still available in the inverted F0 contour, but perhaps more that the new contour is linguistically misleading. In a normally intonated sentence, content words are highlighted by a number of cues, including their F0. Since this F0 cue is inverted in an inverted contour, it is possible that the listener's expectations of which words are important will be confused and hence sentence intelligibility will be compromised. Hillenbrand (2003) has also experimented with monotonized and inverted F0 contours. He measured the intelligibility of synthetic speech presented in quiet. When the F0 contour was flattened there was a reduction in intelligibility, but when it was inverted there was no further effect. However, when the sentences were low-pass filtered at 2 kHz to reduce their overall intelligibility before manipulating the F0 contours, he found that the effect of manipulating the contours was larger and a difference between the monotonous and inverted conditions began to emerge. These results imply that the F0 contour's contribution to speech intelligibility increases in adverse listening conditions. In our experiments, adverse listening conditions will be created through the presence of background noise in an effort to further investigate these effects.

A number of stimulus features are known to produce different effects on speech intelligibility. The choice of stimuli, both targets and interferers, for these experiments will be motivated through the discussion of these features. In terms of interferers, there are three factors that we feel need to be analyzed: the role of F0 differences, dip-listening effects, and informational masking.

First, the identification of target speech is better when it differs in F0 from the interfering speech. Previous experiments have shown that listeners are better able to segregate two speech sources if they differ in mean F0 (Brokx and Nooteboom, 1982; Bird and Darwin, 1998; Assmann, 1999; Drullman and Bronkhorst, 2004). Brokx and Nooteboom (1982), using monotonous target and interfering speech, found that word recognition rates increased from approximately 40% correct at 0 semitones difference to roughly 60% correct at 3 semitones difference. A further measurement taken at a 12 semitone difference showed a decline in the F0 segregation advantage, compared to the 3 semitone difference, with approximately 50% correct word recognition. Also using monotonized speech, Bird and Darwin (1998) have shown that the segregation advantage increases beyond the 3 semitone difference found by Brokx and Nooteboom up to 8 semitones. Assmann (1999) has replicated these findings for both intoned and monotonous speech, showing a steady increase in speech intelligibility from 0 semitone difference up to 8 semitone difference between the target and interferer. Drullman and Bronkhorst (2004) found that listeners' performance gradually improves with increasing F0 difference up to 12 semitones when the speech retains naturally modulated F0s, as opposed to the speech with fixed F0s used by Brokx and Nooteboom. In naturally modulated speech, the F0 fluctuations within the speech would mean that, although the mean F0 difference between the target and interferer is fixed, the difference at any point in time would vary around this mean. Therefore, it seems that in the case of naturally modulated speech, a greater difference in mean F0 between the target and interferer produces a larger segregation advantage for the listener due to the increased chance of the target and interferer F0 values not overlapping.

In terms of F0 segregation, de Cheveigné (1993) proposed a neural-cancellation model whereby harmonic sounds could be segregated by isolating the F0 of the interfering sounds and canceling them. Hence, according to the model, a listener's ability to identify target speech more readily when it differs in F0 from the interfering speech is due to a cancellation process that perceptually removes the interfering speech on a particular F0. In this model, there is no limit, in principle, to the number of interfering harmonic sounds at different F0's that can be perceptually canceled. However, Culling *et al.* (2005), found that when target speech was presented against two interfering speech sources, the listener was best able to identify the target speech when the interfering voices were monotonized at a different F0 to the target speech, but at the same F0 as each other. When the interfering voices were on different F0's to each other as well as to the target speech, only a minimal advantage was seen compared to when all voices were monotonized on the same F0. This implies that a cancellation mechanism exists but that it can remove sounds at only one F0, as opposed to multiple sounds at different F0's. Therefore, a single-talker interferer will produce less masking than multiple speech interferers on different F0's.

Second, continuous white noise is a more effective masker than modulated noise, which, in turn, tends to produce more masking than a single-talker interferer (Carhart *et al.*, 1969; Festen and Plomp, 1990). The difference between white noise and modulated noise is that modulated noise permits dip listening whereas white noise does not. Dip listening is where the listener is given glimpses of the target speech through the interfering noise because of the natural dips and pauses present in the speech wave form. Noise that is modulated like speech therefore inherits these fluctuations, enabling the listener to dip listen. Modulated noise still produces more masking than a single-talker interferer because the speech interferer contains F0 information.

Third, informational masking is said to occur when the effect of masking cannot be attributed to energetic masking. Decreasing target-masker similarity tends to reduce the informational masking effects of the stimulus (Festen and Plomp, 1990; Durlach *et al.*, 2003; Brungart *et al.*, 2001). Brungart *et al.* (2001) showed that using the same talker for the target as for the interferer generated more masking than using a different talker of the same sex, which, in turn, created more of a masking effect than using a talker of the

opposite sex. Informational masking tends to occur in impoverished listening conditions, with few grouping cues, such as when both voices come from the same location or are within the same F0 range. The fact that more informational masking occurs when the voices are perceived to come from the same location has been found to decrease as the number of talkers increases from 3 to 4 to 6 to 10, although the spatial difference advantage does not completely disappear (Freyman *et al.*, 2004). Hence, with one or two interfering voices, recognition performance improves when the target and interferer appear to be from different locations, but as the number of interfering talkers from separate directions is increased, this cue no longer aids recognition performance. This effect is proposed to be due to the rise of informational masking as the number of voices is initially increased to two voices, and then a consequent fall as the number of voices increases to three. As the number of talkers in the interferer increases, it is possible that they begin to mask each other and hence enable the listener to pay more attention to the target voice.

A combination of all three of these factors can be seen in experiments using multiple-talker interferers. As the number of interfering talkers is increased, the amount of masking also increases (Peissig and Kollmeier, 1996; Drullman and Bronkhorst, 2004). The more background talkers present, the greater the chance of the dips in one talker's speech being filled by another talker and the less effect of F0 difference there is. As noted earlier, informational masking is also more likely to occur in situations using two or three voice interferers (Carhart *et al.*, 1975; Freyman *et al.*, 2004), and becomes less prominent as the number of voices increases above this amount.

Given the above-mentioned factors concerning the types of interferer used, speech-shaped noise and a single talker interferer will be used to simulate the effect of listening to speech in a speech background in the following experiments. The single-talker interferer will be a different talker to the target speech, and placed outside the target's F0 range in order to minimize any effects of informational masking. Speech-shaped noise acts as a speech-type background without producing the informational masking effects that would potentially be present if multiple talkers with similar characteristics were used.

The nature of the target speech can also affect intelligibility. Notably the predictability of the speech materials is an important factor affecting the intelligibility of the utterances. Boothroyd and Nittrouer (1988) found that phonemes placed in nonsense words were harder to recognize than phonemes placed in real words. Random sequences of words (e.g., "girls white car blink") were also less easily recognized than words in grammatically correct sentences with few contextual cues (e.g., "ducks eat old tape"). These were, in turn, harder to correctly identify than words placed in grammatically correct sentences with contextual cues (e.g., "most birds can fly"). Low-predictability sentences will be used in this experiment to ensure than the listeners can make relatively little use of contextual cues to predict the words in the sentences. Due to the need for continuously voiced sentences in Experiment 4, not all sentences are from the same corpus, but they do maintain a low-level of predictability.

The following experiments measure the impact of F0 cues in the intelligibility of speech against noise. Reducing the F0 incrementally from the variation present in a normally intonated contour to a monotonous contour, with no variation, will enable us to see whether the more variation in the contour, the more intelligible the speech or whether it is the case that just a small amount of F0 variation can give the listener enough cues to correctly transcribe the target speech. If it is the case that the listener extracts information from the F0 contour to enhance speech intelligibility, placing inverted F0 contours on the speech should mislead the listener because the F0 cues will now be incorrect.

II. EXPERIMENT 1

A. Method

1. Listeners

Twenty paid participants were recruited from the Cardiff University Participation Panel. All were native speakers of English and normal hearing (self-report). None of the listeners were familiar with the sentences used in the study.

2. Stimuli

The set of sentences used in this experiment was from the Harvard IEEE corpus (Rothauser *et al.*, 1969). The recordings, made at M.I.T. of male voice DA, were digitized at 20 kHz sampling rate with 16 bit quantization. All the sentences were low predictability and included five nominated key words. For example, "a WISP of CLOUD HUNG in the BLUE AIR."

Each sentence was manipulated using the Praat PSOLA speech analysis and resynthesis package. The F0 contour of each sentence was manipulated using Eq. (1); m is the coefficient for the particular manipulation; $\overline{F0}$ is the mean fundamental frequency. The mean F0 of the target speaker was 107 Hz, with an average pitch range of 120 Hz. By inverting the F0 contour, there were times when the F0 reached below the acceptable range allowed by Praat; Praat cannot synthesize F0 values lower than about 70 Hz, hence when inversion produced values below this limit, Praat incorrectly synthesized the F0 at a higher value. For this reason, the F0 contour of each sentence was multiplied by 1.5 in order to raise the mean F0 so that the F0 contour could be inverted without falling below the permitted F0 range for the Praat software package. The F0 range of different voices is approximately equivalent on a logarithmic scale (Graddol, 1986; Traunmuller and Branderud, 1989; Nolan, 2003), hence this was considered preferential for manipulating the F0 contour across sentences to a linear scale. After this, each of the sentences was resynthesized,

$$F0' = [1.5\overline{F0}\exp(m\ln(F0/\overline{F0}))]. \quad (1)$$

Five different manipulation coefficients (m) of the F0 contour were applied (1, 0.5, 0.25, 0, and −1), corresponding to the five conditions (standard, half, quarter, monotone, and inverse), see Fig. 1. The standard contour refers to the nor-

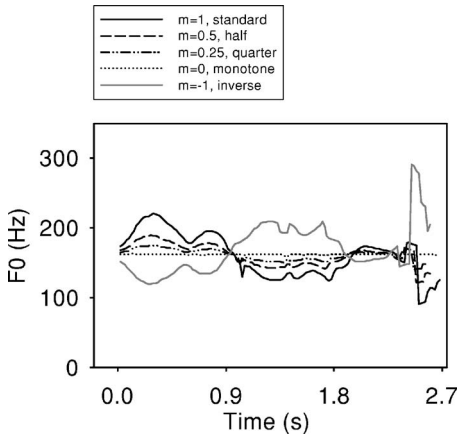

FIG. 1. Manipulations (m) of the F0 contour for an example sentence ("Greet the new guests and leave quickly") from Experiment 1. Manipulations are $m=1$, 0.5, 0.25, 0, and −1, corresponding to the five conditions of the experiment: standard, half, quarter, monotone, and inverse, respectively.

mal intonation placed upon that sentence by the speaker. The half and quarter conditions follow the same general shape of the standard contour, but the amount of variation in both is reduced; in the half condition this variation is half that of the standard contour and in the quarter, it is quarter. The monotone condition refers to a monotonized F0 contour, and the inverse to an inverted contour.

Speech-shaped noise was created by processing white noise with a digital filter whose magnitude response was equal to the long-term average spectrum of the entire set of unmanipulated target sentences. This noise was used as the interferer and edited to be, on average, 0.1 s longer than the speech targets so that no part of the speech target was unmasked at any stage.

3. Procedure

Participants were seated in an IAC single-walled sound-attenuated booth in front of a computer screen visible through the booth window. They listened to stimuli over Sennheiser HD-590 headphones and responded to them using a keyboard placed inside the booth.

Speech reception thresholds (SRTs) were measured for each condition in the experiments (Plomp and Mimpen, 1979; Culling and Colburn, 2000). In the first phase of a SRT measurement, the sound level of the target started low at –28 SNR. The listener's instructions were to attend to the voice and ignore the interfering noise. The listener was allowed to hear the same target sentence and interferer repeatedly at the start of each run by pressing the return key on the keyboard. Each time this key was pressed, the level of the target sentence was increased by 4 dB. Once the listener believed that they could hear more than half the sentence correctly, they typed out their transcript. The correct sentence was then displayed underneath the listener's transcript, containing five capitalized keywords. The listener compared these words to those in their own sentence and entered the number of key words that they had heard correctly (0–5). The second phase of the measurement then began. The sound level of the target was set according to their performance on the first sentence. Thus if the listener heard three or more words correctly, the level was 2 dB below that of the initial level set by the listener in the first phase by pressing the return key. If the listener achieved less than three words correct, the level was raised by 2 dB. The listener could now only hear the sentence once and an SRT was measured using a one-up/one-down adaptive SRT technique whereby if the listener heard three or more words correctly, the level of the target speech was decreased by 2 dB; otherwise it was increased by 2 dB. Listeners were presented with a new sentence on each trial, even if they heard none of the key words correctly. The SRT measurement was complete once the listener had heard and written out their transcript for all ten target sentences. The measured SRT for the trial was taken as the average signal-to-noise ratio for sentences three to ten.

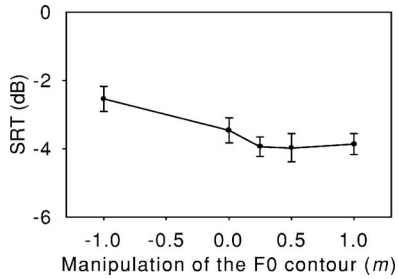

FIG. 2. Mean SRT measurements (dB) across all listeners for the different manipulations of the F0 contour (m) in Experiment 1. Manipulations $m=1$, 0.5, 0.25, 0, and −1 correspond to the following conditions: Standard, half, quarter, monotone, and inverse. Error bars represent ±1 s.d.

The session began with two practice SRT measurements with normally intonated sentences played against speech-shaped noise interferers. This practice familiarized the listener with the task. Ten further SRT measurements were made. Two SRT measurements were made for each condition (standard, half, quarter, monotone, and inverse). The order of the presentation of the conditions was rotated for each listener, while the sentence material stayed in the same order. Thus, the sentence order remained independent of the condition, with participants starting with the same sentence list, but different conditions. This ensured that each of the 100 target sentences was presented to every listener in the same order and contributed equally to each condition as well as making sure that each condition was presented in each position within the session, counterbalancing order effects.

B. Results and discussion

Figure 2 shows that there was a slight increase in SRTs as m was reduced, from the standard targets ($m=1$) to the monotonous ($m=0$) targets, with a greater increase for targets with an inverted F0 contour ($m=-1$). The difference between speech with a standard contour ($m=1$) and monotonous speech ($m=0$) was 0.4 dB and was 1.3 dB between standard speech ($m=1$) and speech with an inverted F0 contour ($m=-1$). However, the difference was smaller than the 4 dB difference between normal and inverted F0 contours found by Culling *et al.* (2003), who used speech as an interferer. A repeated measures ANOVA found a significant main effect of the F0 contour ($F(4,76)=3.525; p<0.02$). Post-hoc Tukey HSD tests, which include corrections for multiple comparisons, showed there to be a significant difference be-

tween the standard, half, and quarter conditions ($m=1,0.5,0.25$) and the inverted condition ($m=-1$) at the 0.05 significance level. No other comparisons were significant.

These results show that flattening the F0 contour causes a reduction in SRT; however, since this effect was nonsignificant, the results do not reflect those of earlier studies where flattening the F0 contour has proved significantly detrimental to speech intelligibility (e.g., Assmann, 1999; Laures and Weismer, 1999; Laures and Bunton, 2003). Inverting the contour, on the other hand, significantly reduced the intelligibility of the target speech. The fact that the quarter and half conditions did not substantially reduce the sentence intelligibility, whereas inverting the contour did, implies that as long as there is only a small amount of F0 modulation in the "correct" direction, the intelligibility of the utterance is almost unaffected.

The inverted condition produced a statistically significant decrement but still one that was smaller than observed by Culling *et al.* (2003). One difference between the current experiment and that of Culling *et al.* (2003) was that a single-talker interferer was used in their experiment instead of speech-shaped noise. Single-talker maskers have been shown to produce less masking than speech-shaped noise, which is thought to be due in part to the listener's ability to exploit the dips in the temporal envelope of the speech, which are not present in the noise (Festen and Plomp, 1990; Peissig and Kollmeier, 1997). However, the differences in fundamental frequency and intonation contours between the target and masker can be used to perceptually segregate the two talkers, hence it could be that the fundamental frequency contours are more important to sentence intelligibility against a single-talker interferer than a noise masker. For this reason, a single-talker interferer was used in the second experiment in order to see whether this larger difference could be replicated by changing the type of interferer. As seen earlier, inverting the F0 contour of the target speech detrimentally affected the intelligibility of the utterance. Culling *et al.* (2003) also manipulated the F0 contour of the speech interferer in their experiment by inverting it. Manipulating the F0 contour of the interfering speech as well as that of the target speech prevents an effect on the mean F0 difference. It is unclear whether the greater effect seen in the Culling *et al.* (2003) paper was due to the inversion of the target or the interferer. Therefore, the F0 contour of the target and the interferer were manipulated parametrically in this experiment in order to investigate whether the large effect observed by Culling *et al.* (2003) was an effect of adjusting the target, the interferer, or both.

III. EXPERIMENT 2

A. Method

1. Listeners

Eighteen undergraduate Psychology students were used as participants in this experiment. All were normally hearing native speakers of English. None of the participants were familiar with the sentences used, or had they taken part in the previous experiment.

2. Stimuli

The set of sentences used here was selected from the same corpus as in the previous experiment. However, the recordings of another male voice, CW, were used instead of DA.[1] This voice was also digitized at 20 kHz with 16 bit quantization. The sentences were once again manipulated using Praat PSOLA. The following formula was applied to the F0 contour of each sentence before resynthesis, adjusting the average F0 of all the target sentences to 125 Hz to enable a consistent 9 semitone difference to be set between the target and interfering sentences,

$$F0' = [125 \exp(m \ln(F0/\overline{F0}))]. \quad (2)$$

Only three values of m were used this time ($m=1,0,-1$) corresponding to the three conditions (standard, monotone, and inverse).

Speech interferers were used instead of noise and were created using ten sentences from the Harvard IEEE corpus. The recorded voice used was DA. The F0 contour of the interferers was manipulated using Praat PSOLA as for the target sentences. Equation (3), which results in a fixed mean F0 of 210.25 Hz, a 9 semitone difference between the target and interferers, was applied to the sentences before resynthesis,

$$F0' = [210.25 \exp(m \ln(F0/\overline{F0}))]. \quad (3)$$

Thus, the mean F0 of the interferers was set at an average of 9 semitones higher than that of the target sentences. This was done to avoid potentially confounding effects of the F0 difference (Assmann, 1999; Brokx and Nooteboom, 1982; Culling and Darwin, 1994; Bird and Darwin, 1998). For instance, if both the target and interferer were monotonized with the same F0, there would be no F0 differences to exploit, but if the target had a normal F0 contour and the interferer was monotonous, the differences in instantaneous F0 could be used to differentiate between the two at the points in time where the normal F0 contour deviates from the mean.

By introducing a constant difference in mean F0, we sought to minimize differences in mean F0 difference between the various conditions of contour manipulation. Bird and Darwin (1998) showed there to be a steady increase in sentence identification from 0 to 8 semitone F0 difference between the target and masker. In the experiment by Brokx and Nooteboom (1982), the advantage of the F0 difference was found to decrease at one octave (12 semitones). However, no research has indicated what happens between 8 and 12 semitones using monotonized F0s. The 9 semitone difference used here was felt to be as large a difference as could be employed without encountering the decline in the F0 difference advantage found by Brokx and Nooteboom (1982), while at the same time being large enough to reduce the chance of overlap of the F0 contours. This ensured that any effect found from manipulating the contour was due to the contour change itself and not the difference in F0 between the target and interferer. Figure 3 shows the different manipulations of both the target and interferer contours, around their F0 means.

Nine conditions were set up, using each possible combination ($m=1,0,-1$) of both the target and interfering F0

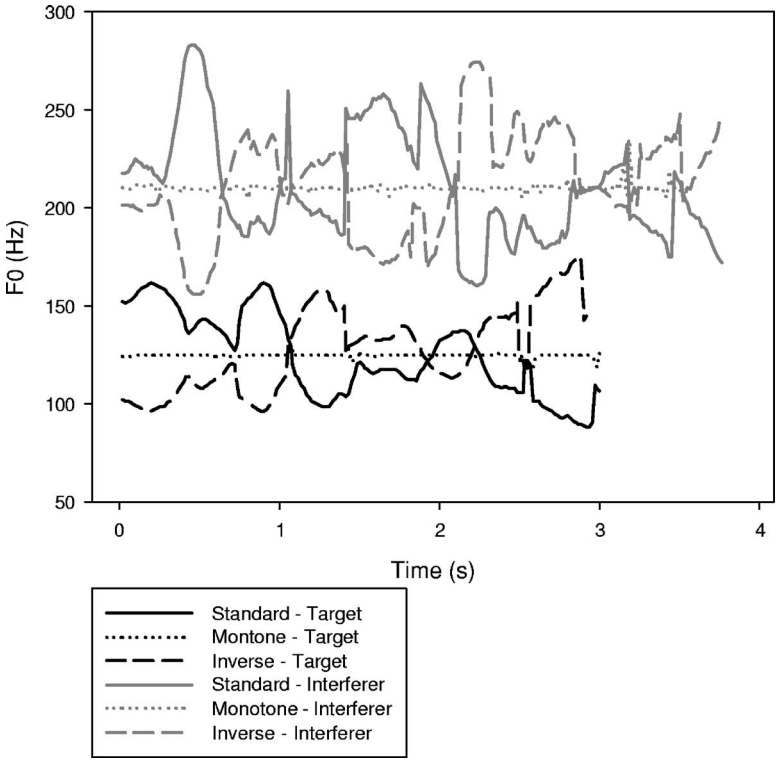

FIG. 3. Manipulations (m) of the F0 contour for both the target and interferer sentences in Experiment 2. The target speech is "Where were they when the noise started?" and the interfering sentence is "A ridge on a smooth surface is a bump or flaw." The interfering sentence in this case is 0.6 s longer than the target sentence. The mean F0 of the target is set to 125 dB, with the mean of the interferer being 9 semitones higher, at 210.25 dB. Manipulations are $m=1$, 0, and −1 for both the target and interfering contours, corresponding to the standard, monotone, and inverse conditions, respectively.

contour. Hence the target F0 contour was manipulated in three ways to create a standard, monotonous, and inverse condition for the target. The interferer F0 contour was also manipulated to be standard, monotonous, or inverse.

3. Procedure

The procedure was similar to that in Experiment 1, measuring SRTs for each of the conditions within the experiment. Each experiment, therefore, consisted of nine runs, each with ten sentences, along with a practice run at the start of the experiment to familiarize the listener with the task.

As in the previous experiment, at the start of each run, the target level would be set low at –28 SNR, whereas the interferer level was set high. The interfering sentence remained the same in both content and manipulation throughout each run. However, in order to differentiate the target from the interferer, the listener was instructed to pay attention to the quieter sentence (target) at the start of the run and ignore the louder sentence (interferer). The listener typed out their transcript, as in Experiment 1, as soon as they judged they could hear more than half of the target sentence and scored the number of words they heard correctly. SRTs were recorded for each condition. Once again, the order of the conditions was rotated for each listener, while the sentence material stayed in the same order.

B. Results and discussion

Figure 4 shows that there was a larger difference in SRT between the normally intonated, monotonous, and inverted target speech than in Experiment 1, where the interferer was speech-shaped noise. The difference between normally intonated speech and monotonous speech was 2.0 dB, and was 3.8 dB between normally intonated speech and speech with an inverted F0 contour.

A repeated measures ANOVA found a significant main effect of the target F0 contour ($F(2,24)=18.288$; $p<0.001$). Post-hoc Tukey HSD tests showed there to be a significant difference between the standard ($m=1$) target F0 condition and inverse ($m=-1$) condition ($p<0.01$). The difference between the monotone ($m=0$) and inverse ($m=-1$) conditions, and the monotone ($m=0$) and standard ($m=1$) conditions was also significant ($p<0.05$). There was no effect of varying the F0 contour of the interferer, indicating that the inversion effect is not mediated by the interferer.

Analyses of the listener's transcripts showed no errors from intrusions from the interfering speech. Instead, errors were unrelated errors in the target sentences, such as mis-

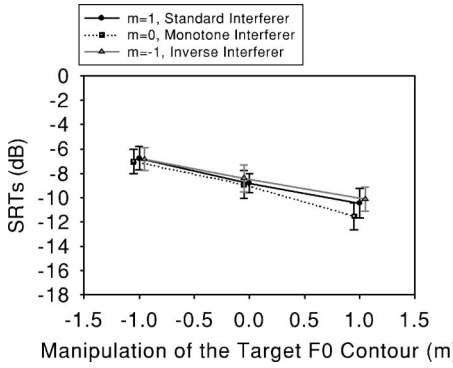

FIG. 4. Mean SRT measurements across all listeners for each of the nine conditions in Experiment 2. The three lines represent the manipulations ($m=1$, 0, −1; standard, monotone, and inverse) of the F0 contour for the interferer, with the x axis representing manipulations ($m=1$, 0, −1; standard, monotone, and inverse) of the target F0 contour. Error bars represent ±1 s.d.

heard and missing words. The implication of this is that the listeners were better able to follow and interpret the target speech where they had an increased amount of correct F0 information, rather than becoming confused by the content of the interfering speech.

As mentioned earlier, the fact that there was a larger difference between the conditions in this experiment than in Experiment 1 implies that there is something about a speech background that requires the listener to rely more heavily on the F0 contour of the target sentence in order to understand it. Mattys (2004) has also found that different cues are used in different circumstances. He found that coarticulation cues were more prominent than stress cues in quiet, whereas stress cues became more important than coarticulation cues when the speech was presented in a white noise background. Hence, it could be the case that cues that do not normally influence speech intelligibility greatly in certain conditions become more important as the conditions change. In the same way as the stress cues becoming more salient in white noise compared to quiet, cues from the F0 contour may have a greater impact on speech intelligibility in a background of speech, where the listener is required to select and follow one of two voices, rather than in a speech-shaped noise background.

Having established that a robust effect of the F0 contour is observed when the target is manipulated and presented against a speech interferer, the next experiment returned to the manipulations performed in the first experiment, where the F0 variation was reduced systematically, hence it included the half and quarter conditions used previously. These conditions were repeated, but this time against interfering speech.

IV. EXPERIMENT 3

A. Method

1. Listeners

Ten paid participants were recruited from the Cardiff University Participation Panel. All were normally hearing native speakers of English. None of the listeners were familiar with the sentences used in the study or had they taken part in either of the previous experiments.

2. Stimuli

The target sentences used here were from the same corpus as in Experiment 2, using the same speaker, CW. The interferer sentences were spoken by DA, as in Experiment 2. The same equations as used in Experiment 2 were applied to the target and interfering speech in order to achieve the different F0 means, 125 and 210.25 Hz, respectively. The interferer remained normally intonated ($m=1$), since altering the F0 contour of the interferer did not make a difference in Experiment 2. The same F0 modulations as used in Experiment 1 were employed for the target speech ($m=1, 0.5, 0.25, 0, -1$) to represent the five different conditions (standard, half, quarter, monotone, and inverse) (see Fig. 5). The same procedure was followed as in Experiment 2.

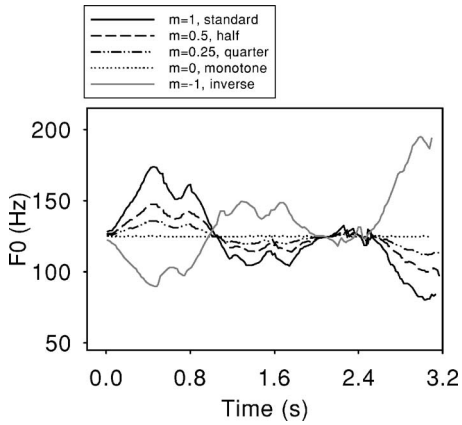

FIG. 5. Manipulations (m) of the F0 contour for an example of the target speech from Experiment 3. The sentence corresponding to the F0 contour is "All sat frozen and watched the screen." Manipulations are $m=1$, 0.5, 0.25, 0, and −1, corresponding to the five conditions of the experiment: Standard, half, quarter, monotone, and inverse, respectively.

B. Results and discussion

Figure 6 shows that there were again larger differences between each of the conditions than in Experiment 1. This confirms the results from Experiment 2 that using speech as the interferer increases the importance of the F0 contour in understanding the target speech.

No difference was found between the standard and half conditions. There was a 1.4 dB difference between the half and the quarter conditions, a further 0.2 dB difference between the quarter and the monotone conditions, and a 0.9-dB difference between the monotone and inverted conditions. A repeated-measures ANOVA showed a significant main effect of the F0 contour ($F(4,36)=3.722$; $p<0.05$). Post-hoc Tukey HSD tests showed a significant difference ($p<0.05$) between the standard ($m=1$) and inverse condition ($m=-1$), and the half ($m=0.5$) and inverse condition ($m=-1$).

The significant effect of F0 modulation implies that it is easier for the listener to separate and understand the target sentence from the single-talker interferer if the target F0 contour follows an appropriate F0 pattern. The lack of difference in decibels between the standard ($m=1$) and half ($m=0.5$) conditions implies that F0 variation can be reduced to a certain degree without hindering the intelligibility of the utter-

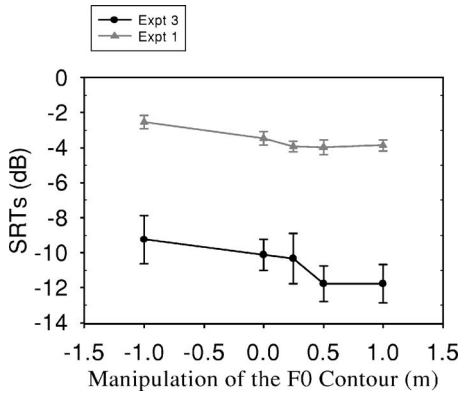

FIG. 6. Mean SRT measurements (dB) for the different manipulations ($m=1$, 0.5, 0.25, 0, −1; standard, half, quarter, monotone, and inverse) of the F0 contour in both Experiments 1 and 3. Error bars represent ±1 s.d.

ance. The difference in SRT levels between the standard ($m=1$) and quarter ($m=0.25$) conditions has become more marked than in Experiment 1, but remains insignificant. This larger difference, combined with the very slight difference between the quarter ($m=0.25$) and monotone ($m=0$) conditions, indicates that a small amount of variation in the F0 contour does not aid the listener much above the monotone. Hence it seems that, although reducing the amount of F0 variation has a progressively detrimental effect on speech intelligibility, a stronger effect is seen with F0 inversion, indicating that it is more important to have a "correct" F0 contour highlighting the important syllables in an utterance than having F0 variation.

V. EXPERIMENT 4

The previous experiments have shown that reducing variation in the F0 contour, and inverting the F0 contour cause detrimental effects to sentence intelligibility. What has not been shown by these experiments is where the important modulation frequencies for this effect lie. Low-pass filtering removes the high-frequency components of the F0 contour while retaining the low-frequency components. By progressively removing the higher frequencies, the frequencies most important for intelligibility can be revealed. Thus, rather than acting as a means for comparison with Experiments 1–3, this experiment will contribute to their results providing information on the whereabouts of frequencies involved in the F0 inversion effect.

Low-pass filtering the amplitude modulation spectrum of speech has shown that the important frequencies for the modulation of the speech signal as a whole lie between 4 and 16 Hz (Drullman *et al.*, 1994), with the most important frequency being 4 Hz, the syllable rate of speech. English is a stress-timed language (Cruttenden, 1986), which means it involves the rhythmic alternation of stressed and unstressed syllables. Therefore, the shape of the F0 contour is dependent on the accents placed on these syllables. For this reason, it would seem likely that the most important modulation frequencies for the F0 contour will lie around the syllable rate of speech, 4 Hz. The following experiment will test this prediction through low-pass filtering the F0 contour of the speech.

A. Method

1. Listeners

Twenty paid participants were recruited from the Cardiff University Participation Panel. All were normally hearing native speakers of English. None of the listeners were familiar with the sentences used in this study or had they taken part in Experiments 1–3.

2. Stimuli

In order to low-pass filter an F0 contour, it needs to be an uninterrupted wave form. For the F0 contour to be uninterrupted, the speech used needs to be continuously voiced. For this reason, 100 continuously voiced sentences were created. The key words were selected from the MRC psycholinguistic database to contain only vowels, nasals, liquids and voiced fricatives, and on the basis of their Francis and Kucera (1982) frequency being under 1000. The sentences were written in the style of the IEEE sentences in that they each contained five key words by which the listeners would rate their responses and using connecting words that were also fully voiced. Due to the limitations on the sentence construction for these stimuli, that they need to be continuously voiced, the sentences tended to be less contextually coherent than the Harvard sentences, although this was not tested. The fewer contextual cues present, the harder it is for the listener to follow the sentences (Boothroyd and Nittrouer, 1988), hence SRT values were expected to be higher for these stimuli. The list of continuously voiced sentences can be found in the Appendix.

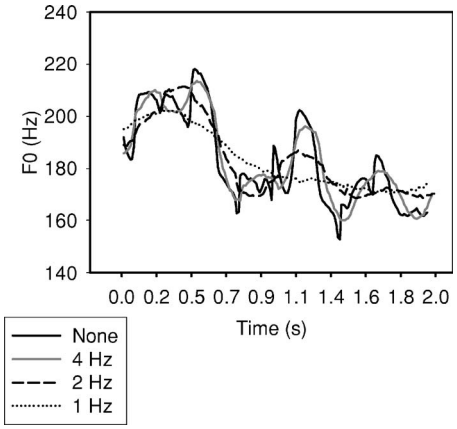

FIG. 7. Low-pass filtered F0 contours compared to an unfiltered F0 contour for the same continuously voiced sentence from Experiment 4. The sentence is "The raven rose over the rim of the ravine." The contour is filtered at 1, 2, and 4 Hz.

The sentences were then recorded using a Sennheiser K6 microphone with an ME62 omnidirectional capsule. The signals were conditioned and digitized using Tucker Davis Technologies equipment (an MA1 microphone amplifier and a DD1 digital-to-analogue converter) at 20 kHz with 16 bit quantization. The F0 contours of the sentences were extracted and low-pass filtered at cut-off frequencies of 1, 2, and 4 Hz (see Fig. 7), and, if required, inverted, before resynthesis using the Praat PSOLA speech analysis and resynthesis package as in the previous experiments.

The following formula was applied before resynthesis, setting all the sentences at an average F0 of 210 Hz,

$$F0' = [210 \exp(m \ln(F0/\overline{F0}))]. \quad (4)$$

In this experiment m was set to either 1 or −1, so that both the standard and inverse conditions could be compared when low-pass filtered.

Speech interferers were used once again and were created using ten sentences from the Harvard IEEE corpus. The recorded voice used was DA's. The following formula was applied to the interferers, setting their average F0 to 125 Hz, hence allowing a 9 semitone difference between the target and interferer contours, as in both Experiments 2 and 3, the target F0 was placed higher than the interferer F0. This was because the different target voice used in Experiment 4 had a naturally highter F0 than the voices in earlier experiments.

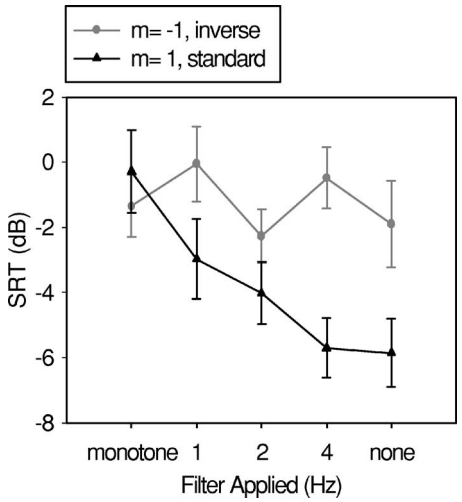

FIG. 8. Mean SRT measurements (dB) across all listeners in Experiment 4. The black line corresponds to results for the manipulated normally intonated ($m=1$) sentences, whereas the gray line represents results for the sentences with an inverted F0 contour ($m=-1$). The low-pass filtering applied to the sentences (1, 2, and 4 Hz), along with monotone ($m=0$) and standard ($m=1$) F0 manipulations, are on the x axis. Error bars represent ±1 s.d.

$$F0' = [125 \exp(m \ln(F0/\overline{F0}) \ ]. \quad (5)$$

The variable m was set to 1 to allow for a standard contour.

Both normally intonated ($m=1$) and inverse ($m=-1$) conditions were compared for the target speech, in each of the five low-pass-filtering conditions (0, 1, 2, 4 Hz and unfiltered), giving ten conditions in total. The same procedure was followed as in Experiments 2 and 3.

B. Results and discussion

The detrimental effect of inverting the F0 contour detailed in Experiments 1–3 was replicated in this experiment ($F(1,19)=51.063$, $p<0.001$), supporting the conclusions drawn that having the correct F0 cues on the appropriate syllables aids speech intelligibility against an interfering voice.

Low-pass filtering the F0 contour was found to degrade the intelligibility of the speech ($F(4,76)=4.740$, $p<0.005$), Figure 8 shows that low-pass filtering the F0 contour produced a greater increase in SRT for the standard F0 contour than for the inverse F0 contour. This reflects the significant linear trend that was found between the F0 manipulation and low-pass filtering conditions ($F(1,19)=4.609$, $p<0.05$). That is, low-pass filtering detrimentally affected the normally intonated contour ($F(1,19)=13.243$, $p<0.001$), but did not have a significant effect on the inverse F0 contour ($F(1,19)=1.337$, $p>0.05$).

The most important frequencies for the normally intonated contour seem to lie between 2 and 4 Hz, with a 2.5 dB difference in SRT between these two conditions. However, enough information is retained in the 1 Hz filtered condition to improve the intelligibility of the utterance relative to the monotone condition, with a further 2 dB difference between these conditions. Pairwise comparisons showed that, for the standard contour, there was a significant difference ($p<0.02$) between the monotonous condition and hoth the standard condition and the standard contour filtered at 4 Hz.

The strongest effect of filtering the F0 contour was found when the frequencies between 2 and 4 Hz were removed. This implies that the most important frequencies for the F0 contour lie at or below the syllable rate of speech. Accents within the F0 contour are placed on syllables in the speech, and as shown in the above-mentioned experiments, when accents are misplaced on these syllables, as in the inverted F0 contour, speech intelligibility decreases. Indeed, deliberately mis-stressing syllables within English words has been reported to decrease response time in comparison to correctly stressed words (Cutler and Clifton, 1984). Thus, it seems that the syllable is an important unit in the F0 contour.

By reducing the amount of information in the inverse contour, it was expected that the intelligibility of the utterance would improve, since less misleading pitch information would be supplied to the listener. This prediction followed from the previous three experiments where the inverted F0 contour caused a greater detriment to speech intelligibility than a monotone F0 contour. Hence, as the inverted F0 contour is increasingly low-pass filtered, its shape tends toward a flattened or monotone F0 contour, implying that its effect on speech intelligibility would decrease. However, this did not occur.

An interesting point to note is that the difference between the monotone and standard conditions was larger with the continuously voiced sentences than in the previous experiment. On the other hand, the difference between the monotone and inverse conditions is no longer significant. There are two ways to interpret this result. The effect of the inverse F0 contour may have disappeared using continuously voiced materials. It could, be for instance, that part of the inversion effect is mediated by stop closures; the presence of onset and offset cues may serve to confuse the listener further when presented with the incorrect F0 cues in inverse contour, and, hence, once these cues are removed, the inverse contour causes no greater effect than the monotonous contour. Alternatively, it may be masked by some interaction between combined use of continuous voicing and complete monotonization of the F0 contour, which elevates thresholds in this particular condition. The latter suggestion is supported by fact that the difference between the inverse and normally intonated contours remained the same as in previous experiment (at around 4 dB). It could be that the lack of onset and offset cues from stop closures combined with the lack of variation in the F0 contour in the monotone condition is particularly detrimental to understanding and yielding SRTs that are similar to those produced by inversion.

Thus, it is unclear as to why the difference between the monotone and inverse conditions has decreased by using these continuously voiced materials. It is interesting to note that in the Hillenbrand (2003) experiment, where synthesized speech was used, a small difference was found between the monotone and inverse conditions only when the stimuli had been low-pass filtered to impair their intelligibility, suggesting that the choice of materials may influence observation of the effect.

VI. GENERAL DISCUSSION

A reduction of F0 modulation was found to have a detrimental effect on speech intelligibility, confirming previous findings (Laures and Weismer, 1999; Assmann, 1999; Laures and Bunton, 2003; Culling *et al.*, 2003). Even a small amount of F0 modulation ($m=0.25$) increased the intelligibility of the sentences against a single-talker interferer, indicating that it is the contour shape that is important to speech recognition. The fact that an inverted F0 contour caused a greater deficit than a monotonous contour implies that it is perhaps false information within the contour caused by its inversion that reduces its intelligibility over that of removing the variation from the contour through monotonization. There are a number of related ways to account for these effects: the incorrect cuing of content words, the disruption of lexical access, and the F0 contour shape in general.

A. Disrupted cuing of accented words

In a normally intonated sentence, important content words will be accented, tending to be above the average F0 of the sentence. This factor, along with the content words generally being louder and articulated more slowly, contribute to making these words acoustically clearer than the surrounding words (Lehiste, 1970). In a monotonous sentence, none of the words in the sentence are accented and all are at the same F0; therefore, there are fewer cues as to the whereabouts of the content words. In a sentence with an inverted F0 contour, however, the accented content words will now be accented in the opposite direction, for instance, a rise will become a fall and vice versa. Equally, words that were previously above the average F0 will now be below. Therefore, whereas in a monotonous sentence no F0 cues will highlight important words, in a sentence with an inverted contour, these F0 cues will be misleading and highlight words that are not particularly important to the meaning of the sentence. Not only are accented words acoustically clearer, but listeners have also been shown to use the F0 contour in order to anticipate upcoming accented words within a sentence (Cutler, 1976). For these reasons, a sentence with an inverted contour would be found to be less intelligible than a monotonous contour due to its misleading accents.

Supporting this argument is the fact that when speech is degraded, the F0 contours are relied on more heavily. Hillenbrand (2003) found that when the speech had been low-pass filtered at 2 kHz, an intelligibility difference was found between the monotone and inverted F0 conditions, implying that the misleading information in the inverted F0 contour had a greater effect when the words lost some clarity and, hence, that the F0 contour is relied upon more heavily as speech quality becomes corrupted.

B. Disruption of lexical access

Low-pass filtering the standard contour indicated that the most important frequencies for a normally intonated sentence lie between 2 and 4 Hz; when these frequencies were removed from the contour, the SRTs increased the most, corresponding to a decrease in sentence intelligibility. These frequencies are at or below the syllable rate of the sentence. Since English is a stress-timed language (Cruttenden, 1986), it involves the rhythmic alternation of stressed and unstressed syllables. Thus, it makes sense that the syllable rate is important to the intonation contour of the sentence, since it is the syllables that are assigned the particular accents. This particular result therefore implies that the clarity of the accents placed on the syllables within the sentence is important for speech intelligibility and reinforces the idea that listeners actively search for the accents within the sentence, and in doing so look to the syllables for these accents.

C. Importance of contour shape

Filtering the F0 contour also showed that a reduction of information in the normally intonated contour decreases its intelligibility, but even the lowest frequency components of a contour in the "right" direction (1 Hz filter) improved the intelligibility relative to the monotone condition. This supports the conclusion from the previous experiments implying that the contour shape is important to speech intelligibility. As mentioned earlier, the focus (accented word) of the sentence is searched for by the subject in order to quickly gain an understanding of the utterance. The F0 contour surrounding the focused word directs the listener's attention to that particular word (Cutler, 1976; Cutler and Fodor, 1979). Therefore, where there is an F0 contour in the right direction, the focused words may remain focused, to some degree, and the surrounding contour still guides the listener toward those words more readily than in a monotone condition where the variation has been removed. Hence, there are two cues present in a contour in the normally intonated condition, the accent and the surrounding contour, guiding the listener to the content words, which are not present in the monotone condition and are misleading in the inverted condition. This potentially explains why an F0 contour filtered at the 1 Hz level is more intelligible than a monotonous contour despite not containing much variation. Low-pass filtering the inverse F0 contour of sentences did not affect the intelligibility. It is not clear whether the lack of a difference between the monotone and inverse conditions is due to a decreased inversion effect or an increased monotone effect with the continuously voiced sentences.

Overall, it seems that the F0 contour is an important factor in speech intelligibility for degraded speech. Reducing the amount of F0 variation through monotonization decreases the intelligibility of speech. An inverted F0 contour causes a greater deficit than a monotonous contour, implying that it perhaps contains false information, which depresses its intelligibility. These results confirm findings from Cutler (1976) that there are two cues present in an F0 contour in the normally intonated condition, the accent and the surrounding contour guiding the listener to the content words, which are not present in the monotonous condition and are misleading in the inverted condition.

APPENDIX

the YELLOW LION WORE an IRON MUZZLE
EVERY MAN WON a LEMON RAZOR
the OILY RIVER RAN in the RURAL VALLEY

the WEARY WOMAN LAY on the MAIN LAWN
the MEAN ARMY WON EVERY WAR
a LOVELY WELL is NEAR the WOOL MILL
YOUR LAWYER is AWARE of the VALUE of the VAN
MOVE the LIME WIRE over the NEW RAIL
NINE MEN OWE ME MONEY
AIM the ARROW OVER the LOW WALL
ALLOW the LOYAL ANIMAL a WARM LAIR
the ENEMY is AWARE of YOUR INNER ZONE
WARM RAIN RAN over the IVORY MIRROR
MANY WOMEN LIVE a MILE AWAY
WARN OUR MEN of the EARLY ALARM
NONE of THEM RAN VIA the MARINA
EVEN the LIVELY EARL was AWAY ILL
NEARLY ALL the NAVY was WARY of the MAYOR
the EVEN WAVES will OVERWHELM the LONELY MARINER
ROYAL LOONIES were ALL OVER the MOOR
ELEVEN REMOVAL MEN were in the LOWER ROOM
the WARNING of NAVAL INVASION was a MARVELOUS RUSE
an ARRAY of RAW MELON is ALWAYS on the MENU
WEAVE your LINEN on the LARGE NARROW LOOM
the EVIL VILLAIN ALWAYS LIES and is EVASIVE
WOMEN RARELY MARRY in a YELLOW VEIL
the RAVEN ROSE OVER the RIM of the RAVINE
the RARE RHYTHM was the ENEMY of ALL REASON
LAZY LIMBS LAY OVER the WEIR
the WILLOWS WAVE OVER the LEISURELY LAKE
RAISE the ALARM WHENEVER the LEVEL RISES
a NORMAL MALE loses NINE ENAMEL MOLARS
in the ARENA, ROMANS EARN MANY ENEMIES
we MOVE AWAY the REVELERS in the MAUVE ROOM
SMALL MARINE MAMMALS were EVERYWHERE in the MUSEUM
we ALL WOVE WARM WOOLIES in the MILL
we KNEW of the ANIMAL'S LOW EYES and EARS
ALL LOVE UNRULY REVELRY in the EVENING
their ZEAL is ONLY the ILLUSION of EARLY RISING
MOTHER was NEVER in the VILLA with OTHER WOMEN
MINERAL EROSION REMAINS the MAIN WORRY
you will NEVER LEAN EASILY on a LAME LIMB
my MEMOIRS are VENOMOUS in EVERY LINE or WORD
MEASLES are MAINLY a MALAISE of the VERY YOUNG
the REASON WHY we were ALUMNAE was ALWAYS UNKNOWN
REAL MAYONNAISE is LOVELY or MELLOW on the NOSE
ANYONE WHO is EARLY will VIEW the MARE
the NEWS of the RALLY INVOLVES NEARLY EVERYONE
the NEW MOVIE REVEALS our ONLY ERROR
REMOVE the RIVAL MILLER ALIVE in the MORNING
LONELY MEN ROAM EVERY REALM
we OIL the REAR RAILWAY ALL YEAR
EVEN a MINIMAL WIN ALARMS MANY
EVERY VOLUME VARIES in a NOVEL WAY
our LONE MEMORY of ONE WARREN was VIVID
the MILLIONAIRE'S MANOR is OVER the NORMAN RIVER
ALL WHO OWN NAVY are NORMAL
we LEARN NEARLY ALL our MANNERS in YOUTH
NORMALLY the LEAN ROWERS WEAR LEATHER
RAW LIVER as a MEAL WORRIES ME
my MORAL LOVER is UNAWARE of the MINER'S NAME
the NERVE in your ARM NEVER ANNOYS YOU
RELY on the WARY EYE of the VAIN ALIEN
you VALUE YOUR REVOLVER MORE than ME
MOREOVER the IRONY of the NOVEL was VERY MINIMAL
RAISE the OLIVE LEVER NEAR YOU
the MINI WALL MURAL is OVER THERE
THESE ROSES LINE the AVENUE EVENLY
NO ONE KNOWS the NUN is REALLY a LIAR
we will LOSE YOU in the ZOO'S NARROW MAZE
the NEW ROYALS REIGN EVILY over the REALM
ZOOM in ANYWHERE on the NEW MOON NOW
MIRROR MY EVERY MOVE in the ROOM
the MEN'S MORALE was NEVER a WORRY of MINE
HAVE the ANNUAL REUNION in LOVELY VIENNA
they will MOAN if you REMOVE THEIR LEISURE HOUR
EARLIER the LEAVES were on the REALLY WORN LANE
USE the NEON NAIL in THEIR URN
they will MOURN the LOSS of ONE as MERRY as YOU
NEVER KNEEL on ANY WALL in the VENUE
WEIGH the ONIONS THERE NEAR the VEAL
the LOAN will RELIEVE ALL YOUR MONEY WORRIES
SLOWLY ROLL the WHEEL THROUGH the RYE
the WEATHER is USUALLY VERY RAINY in ROME
ILL ANIMALS WALLOW or ROLL in MUD
the WILL of MY MUM AMUSES MANY
i RUN MORE MILES on a MEAL of MUESLI
RENEW your VOWS of LOVE in EARLY MAY
the RAVENOUS LLAMA MAULS ALL in VIEW
in the VILE RAIN, our ONLY EWE was MAIMED
the MELLOW ROAR of the RIVER LULLS US
the ROW OVER the NEW MALL is WEAK
their AIM MERELY NUMBS MY KNEE
LAYERS of OIL OOZE over the NEW ROAD
the MEN YELL as the RAM RUINS the MINE

the ARRIVAL of the MAIL ALWAYS LEAVES them LOW

a RISE in EARNINGS will EASE THEIR WOE
you are NEVER ILL WHEN YOU are IMMUNE
ONE WOMAN'S ROLE was VERY ONEROUS
AIR YOUR VIEWS ORALLY in the UNION

[1]Speakers were changed from Experiment 1 to Experiment 2 due to the change in interferer type. In Experiment 2, a single-talker interferer needed to be used. The interferer needed to be placed at a substantially different F0 from the target speech. DA's voice sounded more natural than CW's when the mean F0 was adjusted to allow for this difference.

Assmann, P. F. (**1999**). "Fundamental frequency and the intelligibility of competing voices," Proceedings of the 14th International Congress of Phonetic Sciences, San Francisco, 1–7, August **1999**, pp. 179–182.

Bird, J., and Darwin, C. J. (**1998**). "Effects of a difference in fundamental frequency in separating two sentences," in *Psychophysical and Physiological Advances in Hearing*, edited by A. R. Palmer, A. Rees, Q. Summerfield, and R. Meddis, Whurr, London, pp. 263–269.

Boothroyd, A., and Nittrouer S., (**1988**). "Mathematical treatment of context effects in phoneme and word recognition," J. Acoust. Soc. Am. **84**, 101–114.

Brokx, J. P. L., and Nooteboom, S. G. (**1982**). "Intonation and the perceptual separation of simultaneous voices," J. Phonetics **10**, 23–36.

Brungart, D. S., Simpson, B. D., Ericscon, M. A., and Scott, K. R., (**2001**). "Informational and energetic masking effects in the perception of multiple simultaneous talkers." J. Acoust. Soc. Am. **110**, 2527–2538.

Carhart, R., Tillman, T. W., and Greetis, E. S. (**1969**). "Perceptual masking in multiple sound backgrounds," J. Acoust. Soc. Am. **45**, 694–703.

Carhart, R., Tillman, T. W., and Greetis, E. S., (**1969**).

Cruttenden, A. (**1986**). *Intonation* (Cambridge University Press, New York).

Culling, J. F., and Colburn, H. S. (**2000**). "Binaural sluggishness in the perception of tone sequences and speech in noise," J. Acoust. Soc. Am. **107**, 517–527.

Culling, J. F., and Darwin, C. J. (**1994**). "Perceptual separation of simultaneous vowels: Cues arising from low-frequency beating," J. Acoust. Soc. Am. **95**, 1559–1569.

Culling, J. F., and Summerfield, Q. S. (**1995**). "Perceptual segregation of concurrent speech sounds: Absence of across-frequency grouping by common interaural delay." J. Acoust. Soc. Am. **98**(2), 785–797.

Culling, J. F., Hodder, K. I., and Toh, C. Y. (**2003**). "Effects of reverberation on perceptual segregation of competing voices," J. Acoust. Soc. Am. **114**, 2871–2876.

Culling, J. F., Linsmith, G. M., and Caller, T. L. (**2005**). Evidence for a cancellation mechanism in perceptual segregation by differences in fundamental frequency." J. Acoust. Soc. Am. **117**(4), 2600.

Cutler, A. (**1976**). "Phoneme-monitoring reaction times as a function of preceding intonation contour," Percept. Psychophys. **20**, 55–60.

Cutler, A., and Clifton, C. E. (**1984**). "The use of prosodic information in word recognition," in *Control of Language Processes*, Attention and Performance Vol. **X**, edited by H. Bouma and D. G. Bouwhuis (Erlbaum, Hillsdale, NJ) pp. 183–196.

Cutler, A., Dahan, D., and van Donselaar, W. (**1997**). "Prosody in the comprehension of spoken language: A literature review," Lang Speech **40**, 141–201.

Cutler, A., and Fodor, J. A. (**1979**). "Semantic focus and sentence comprehension," Cognition **7**, 49–59.

Cutler, A., and Foss, D. J. (**1977**). "On the role of sentence stress in sentence processing." Language and Speech, **20**, 1–10.

de Cheveigné, A. (**1993**). "Separation of concurrent vowel identification harmonic sounds: Fundamental frequency estimation and a time-domain cancellation model of auditory processing," J. Acoust. Soc. Am. **93**, 3271–3290.

Drullman, R., and Bronkhorst, A. W. (**2004**). "Speech perception and talker segregation: Effects of level, pitch, and tactile support with multiple simultaneous talkers," J. Acoust. Soc. Am. **116**, 3090–3098.

Drullman, R., Festen, J. M., and Plomp, R. (**1994**). "Effect of reducing slow temporal modulations on speech reception," J. Acoust. Soc. Am. **95**, 2670–2680.

Durlach N. I. Mason, C. R., Shinn-Cunningham, B. G., Arbogast, T. L., Colburn, S., and Kidd, G. (**2003**). "Informational masking: Counteracting the effects of stimulus uncertainty by decreasing target-masker similarity." J. Acoust. Soc. Am. **114**(1), 368–379.

Festen, J. M., and Plomp, R. (**1990**). "Effects of fluctuating noise and interfering speech on the speech-reception threshold for impaired and normal hearing," J. Acoust. Soc. Am. **88**, 1725–1736.

Francis, W. N., and Kucera, H. (**1982**). *Frequency Analysis of English Usage: Lexicon and Grammar* (Houghton-Mifflin, Boston).

Freyman, R. L., Balakrishnan, U., and Helfer, K. S. (**2004**). "Effect of number of masking talkers and auditory priming on informational masking in speech recognition," J. Acoust. Soc. Am. **115**, 2246–2256.

Graddol, D. (**1986**). "Discourse specific pitch behaviour." in *Intonation in Discourse*, edited by C. Johns-Lewis (Croom Helm, London), pp. 221–237.

Haggard, M., Summerfield, Q., and Roberts, M. (**1981**). "Psychoacoustical and cultural determinants of phoneme boundaries: Evidence from trading F0 cues in the voiced-voiceless distinction," J. Phonetics **9**, 49–62.

Hillenbrand, J. M. (**2003**). "Some effects of intonation contour on sentence intelligibility," J. Acoust. Soc. Am. **114**, 2338.

Laures, J. S., and Bunton, K. (**2003**). "Perceptual effects of a flattened fundamental frequency at the sentence level under different listening conditions," J. Appl. Photogr. Eng. **36**, 449–464.

Laures, J. S., and Weismer, G. (**1999**). "The effects of a flattened fundamental frequency on intelligibility at the sentence level," J. Speech Lang. Hear. Res. **42**, 1148–1156.

Lehiste, I. (**1970**). *Suprasegmentals* (MIT, Cambridge, MA).

Liss, J., Spitzer, S., Caviness, J., Adler, C., and Edwards, B. (**1998**). "Syllabic strength and lexical boundary decisions in the perception of hypokinetic dysarthritic speech," J. Acoust. Soc. Am. **104**, 2457–2466.

Mattys, S. L. (**2004**). "Stress versus coarticulation: Toward an integrated approach to explicit speech segmentation," J. Exp. Psychol. Hum. Percept. Perform. **30**, 297–408.

Nolan, F. (**2003**). "Intonational equivalence: An experimental evaluation of pitch scales," Proceedings of the 15th International Congress of Phonetic Sciences, Barcelona, 771–774.

Peissig, J., and Kollmeier, B. (**1997**). "Directivity of binaural noise reduction in spatial multiple noise-source arrangements for normal and impaired listeners," J. Acoust. Soc. Am. **101**, 1660–1670.

Plomp, R., and Mimpen, A. M. (**1979**). "Speech-reception thresholds for sentences as a function of age and noise level," J. Acoust. Soc. Am. **66**, 1333–1342.

Rothauser, E. H., Chapman, W. D., Guttman, N., Nordby, K. S., Silbiger, H. R., Urbanek, G. E., and Weinstock, M. (**1969**). "I.E.E.E. recommended practice for speech quality measurements." I.E.E.E. Trans. Audio Electroacoust., **17**, 227–246.

Traunmüller, H. (**1981**). "Perceptual dimension of openness in vowels," J. Acoust. Soc. Am. **69**, 1465–1475.

Traunmüller, H., and Branderud, P. (1989). "Paralinguistic speech signal transformations," STL-QPSR, pp. 63–68.

Wingfield, A., Lombardi, L., and Sokol, S. (**1984**). "Prosodic features and the intelligibility of accelerated speech: Syntactic versus periodic segmentation," J. Speech Hear. Res. **27**, 128–134.

A comparative intelligibility study of single-microphone noise reduction algorithms

Yi Hu and Philipos C. Loizou[a)]
The University of Texas at Dallas, Department of Electrical Engineering, P.O. Box 830688, Richardson, Texas 75083, USA

(Received 9 May 2007; revised 3 July 2007; accepted 4 July 2007)

The evaluation of intelligibility of noise reduction algorithms is reported. IEEE sentences and consonants were corrupted by four types of noise including babble, car, street and train at two signal-to-noise ratio levels (0 and 5 dB), and then processed by eight speech enhancement methods encompassing four classes of algorithms: spectral subtractive, sub-space, statistical model based and Wiener-type algorithms. The enhanced speech was presented to normal-hearing listeners for identification. With the exception of a single noise condition, no algorithm produced significant improvements in speech intelligibility. Information transmission analysis of the consonant confusion matrices indicated that no algorithm improved significantly the place feature score, significantly, which is critically important for speech recognition. The algorithms which were found in previous studies to perform the best in terms of overall quality, were not the same algorithms that performed the best in terms of speech intelligibility. The subspace algorithm, for instance, was previously found to perform the worst in terms of overall quality, but performed well in the present study in terms of preserving speech intelligibility. Overall, the analysis of consonant confusion matrices suggests that in order for noise reduction algorithms to improve speech intelligibility, they need to improve the place and manner feature scores. © *2007 Acoustical Society of America.*
[DOI: 10.1121/1.2766778]

PACS number(s): 43.72.Kb, 43.72.Qr, 43.72.Ar [DOS] Pages: 1777–1786

I. INTRODUCTION

The objective of noise reduction (also called speech enhancement) algorithms is to improve one or more perceptual aspects of noisy speech, most notably, quality and intelligibility. Improving quality, however, might not necessarily lead to improvement in intelligibility. In fact, in some cases improvement in quality might be accompanied by a decrease in intelligibility. This is due to the distortion imparted on the clean speech signal resulting from excessive suppression of the noisy signal.

In some applications, the main goal of speech enhancement algorithms is to improve speech quality, with a secondary goal to preserve, at the very least, speech intelligibility. Hence, much of the focus of most speech enhancement algorithms has been to improve speech quality. Only a small number of algorithms have been evaluated using formal intelligibility tests (Boll, 1979; Lim, 1978; Tsoukalas *et al.*, 1997; Arehart *et al.*, 2003), and in those studies, only a single speech enhancement algorithm was evaluated and in a limited number of noise conditions. Also, in most of these studies, no statistical tests were run to assess whether the differences among algorithms were statistically significant. It therefore remains unclear as to which of the many speech enhancement algorithms proposed in the literature performs well in terms of speech intelligibility. At the very least, we would like to know which algorithm(s) preserve or maintain speech intelligibility in reference to the noisy (unprocessed) speech, and which algorithm(s) impair speech intelligibility, particularly in extremely low signal-to-noise ratio (SNR) conditions. Given the absence of accurate and reliable objective measure to predict the intelligibility of speech processed by enhancement algorithms, we must resort to formal listening tests to answer the above questions.

In this paper, we report on the intelligibility evaluation of eight speech enhancement methods encompassing four classes of algorithms: spectral subtractive, subspace, statistical-model based and Wiener-type algorithms. Phonetically balanced sentences and consonants were corrupted by four different types of noise commonly encountered in daily life, and processed by the above enhancement algorithms. The enhanced speech files were presented to normal-hearing subjects for identification in a double-walled soundproof booth. The present intelligibility study is a followup study to the one we reported in Hu and Loizou (2007b), with two main differences. First, we increased the number of subjects who participated on the sentence recognition task from 24 to 40. This was done to increase the power of the statistical tests used to assess significant differences between algorithms. Second, we now test subjects on the consonant recognition task. While the sentence test is attractive and practical as it reflects real-world communicative situations, it cannot be used to understand why some algorithms do not perform well or understand how to design algorithms that would improve intelligibility. For that reason, we chose to complement the sentence recognition task with the consonant recognition task. The consonant task was included for its diagnostic value and is similar in many respects to the diagnostic rhyme test (Voiers, 1983). More specifically, informa-

[a)]Author to whom correspondence should be addressed. Electronic mail: loizou@utdallas.edu

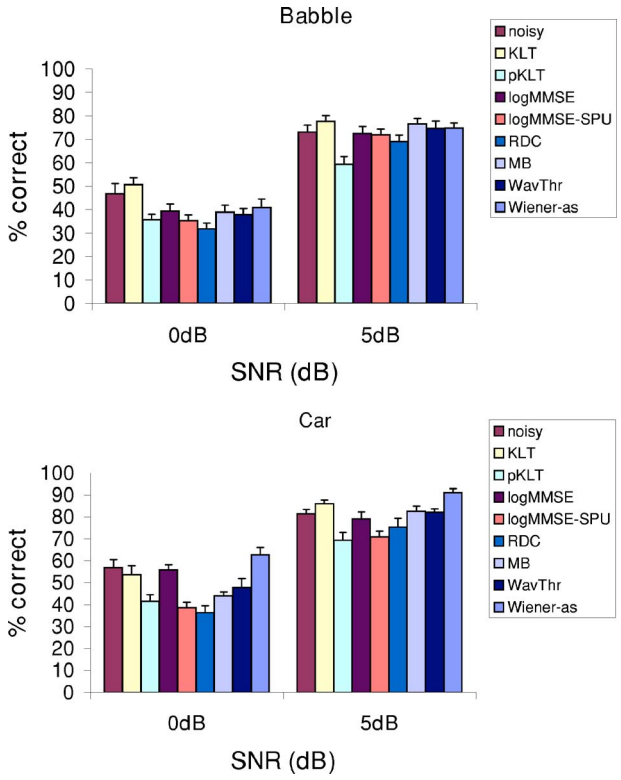

FIG. 1. (Color online) Mean sentence intelligibility scores for eight speech enhancement algorithms in the babble and car noise conditions at 0 and 5 dB SNR.

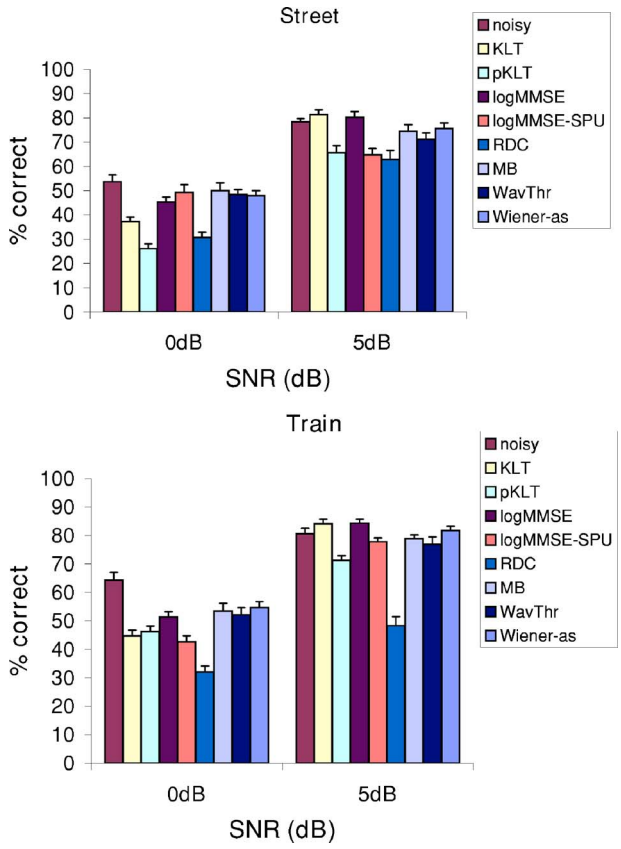

FIG. 2. (Color online) Mean sentence intelligibility scores for eight speech enhancement algorithms in the street and train noise conditions at 0 and 5 dB SNR.

tion transmission analysis, as per Miller and Nicely (1955), is used in the present study to analyze the consonant confusion matrices in terms of information transmitted for three articulatory features: place of articulation, manner of articulation and voicing. The information transmission analysis is important, because the detailed analysis of the feature scores can help us identify the limitations of existing algorithms as well as pinpoint the type of spectral/temporal distortions introduced by current enhancement algorithms. If, for instance, a particular algorithm yields low place feature scores, that would suggest that the spectral cues (e.g., formant transitions) are not adequately preserved and are perhaps distorted by the noise reduction algorithm. If a particular algorithm yields low manner or voicing feature scores, that would suggest that the gross temporal envelope cues (e.g., short-time energy, consonant/vowel energy ratio) are not adequately preserved by the noise reduction algorithm. The feature analysis of consonant confusion matrices thus provides valuable information that can help us identify the weaknesses of existing noise reduction algorithms and consequently help us design better noise reduction algorithms capable of improving speech intelligibility.

II. INTELLIGIBILITY STUDY

A. Methods

1. Materials and subjects

IEEE sentences (IEEE, 1969) and consonants in /a C a/ format were used for the intelligibility studies. The IEEE database was selected as it contains phonetically balanced sentences with relatively low word-context predictability. The consonant test included 16 consonants recorded in /a C a/ context, where C=/p, t, k, b, d, g, m, n, dh, l, f, v, s, z, sh, jh/. All consonants were produced by a female speaker, and all sentences were produced by a male talker. The IEEE sentences and consonants were recorded in a soundproof booth using Tucker Davis Technologies recording equipment. The sentences and consonants were originally sampled at 25 kHz and downsampled to 8 kHz. These recordings are available in Loizou (2007). To simulate the receiving frequency characteristics of telephone handsets, the speech and noise signals were filtered by the modified intermediate reference system (IRS) filters used in ITU-T P.862 (2000) for evaluation of the PESQ measure.

A total of 40 native speakers of American English were recruited for the sentence intelligibility tests. Ten additional listeners were recruited for the consonant tests. All subjects were paid for their participation.

2. Noise reduction algorithms

Noise was artificially added to the sentences as follows. The IRS filter was independently applied to the clean and noise signals to bandlimit the signals to 3.2 kHz. The active speech level of the filtered clean speech signal was first determined using the method B of ITU-T P. 56. A noise segment of the same length as the speech signal was randomly cut out of the noise recordings, was appropriately scaled to reach the desired SNR level and finally added to the filtered

TABLE I. Results from statistical comparisons between algorithms on sentence recognition. Algorithms indicated with asterisks performed equally well.

		Subspace		Statistical-model		Spectral subtractive		Wiener type	
Noise	SNR	KLT	pKLT	logMMSE	logMMSE-SPU	RDC	MB	WavThr	Wiener-as
Car	0 dB			*					*
Babble		*							
Street				*	*		*	*	*
Train				*			*	*	*
Car	5 dB	*							*
Babble		*		*	*		*	*	*
Street		*		*			*		*
Train		*		*			*		*

clean speech signal. The noise signals were taken from the AURORA database (Hirsch and Pearce, 2000) and included the following recordings from different places: babble, car, street, and train. The noise signals were added to the speech signals at SNRs of 0 and 5 dB.

The noise-corrupted sentences were processed by eight different speech enhancement algorithms which included: the generalized KLT approach (Hu and Loizou, 2003), the perceptual KLT approach (pKLT) (Jabloun and Champagne, 2003), the Log Minimum Mean Square Error (logMMSE) algorithm (Ephraim and Malah, 1985), the logMMSE algorithm with speech presence uncertainty (logMMSE-SPU) (Cohen and Berdugo, 2002), the spectral subtraction algorithm based on reduced delay convolution (RDC) (Gustafsson *et al.*, 2001), the multiband spectral subtraction algorithm (MB) (Kamath and Loizou, 2002), the Wiener filtering algorithm based on wavelet-thresholded (WavThr) multitaper spectra (Hu and Loizou, 2004), and the Wiener algorithm based on *a priori* SNR estimation (Wiener-as) (Scalart and Filho 1996). With the exception of the logMMSE-SPU algorithm which was provided by the author (Cohen and Berdugo, 2002), all other algorithms were based on our own implementation. The parameters used in the implementation of these algorithms were the same as those published unless stated otherwise.

A statistical-model based voice activity detector (VAD) was used in all (but the subspace methods) algorithms to update the noise spectrum during speech-absent periods (Sohn *et al.*, 1999). The subspace methods used the VAD method proposed in Mittal *et al.* (2000) with the threshold value set to 1.2. Detailed description of the eight algorithms tested can be found in Hu and Loizou (2007a) and Loizou (2007). MATLAB implementations of all noise reduction algorithms tested in the present study are available in Loizou (2007).

3. Procedure

A total of 40 native speakers of American English were recruited for the sentence intelligibility tests. The 40 listeners were divided into four panels (one per type of noise), with each panel consisting of ten listeners. Each panel of listeners listened to sentences corrupted by a different type of noise. This was done to ensure that no subject listened to the same sentence twice. Each subject participated in a total of 19 listening conditions (=2 SNR levels $\times$8 algorithms +2 noisy references +1 quiet). Two sentence lists (ten sentences per list) were used for each condition. The presentation order of the listening conditions was randomized among subjects. Subjects were asked to write down all the words they heard.

An additional ten native speakers of American English were recruited for the consonant recognition task. There were six repetitions of each consonant. The presentation of the 16 consonants was completely randomized. The test session was preceded by one practice session in which the identity of the consonants (in quiet) was indicated to the listeners. To collect responses, a graphical interface was used that allowed the subjects to identify the consonants they heard by clicking on the corresponding button in the graphical interface.

TABLE II. Statistical comparisons between the intelligibility of noisy (unprocessed) sentences and enhanced sentences. Algorithms indicated with "E" were found to be equally intelligible to noisy speech, algorithms indicated with "L" yielded lower intelligibility scores and algorithms indicated with "B" improved intelligibility.

		Subspace		Statistical model		Spectral subtractive		Wiener type	
Noise	SNR	KLT	*p*KLT	logMMSE	logMMSE-SPU	RDC	MB	WavThr	Wiener-as
Car	0 dB	E	L	E	L	L	L	L	E
Babble		E	L	E	L	L	E	L	E
Street		L	L	L	E	L	E	E	E
Train		L	L	L	L	L	L	L	L
Car	5 dB	E	L	E	L	E	E	E	B
Babble		E	L	E	E	E	E	E	E
Street		E	L	E	L	L	E	E	E
Train		E	L	E	E	L	E	E	E

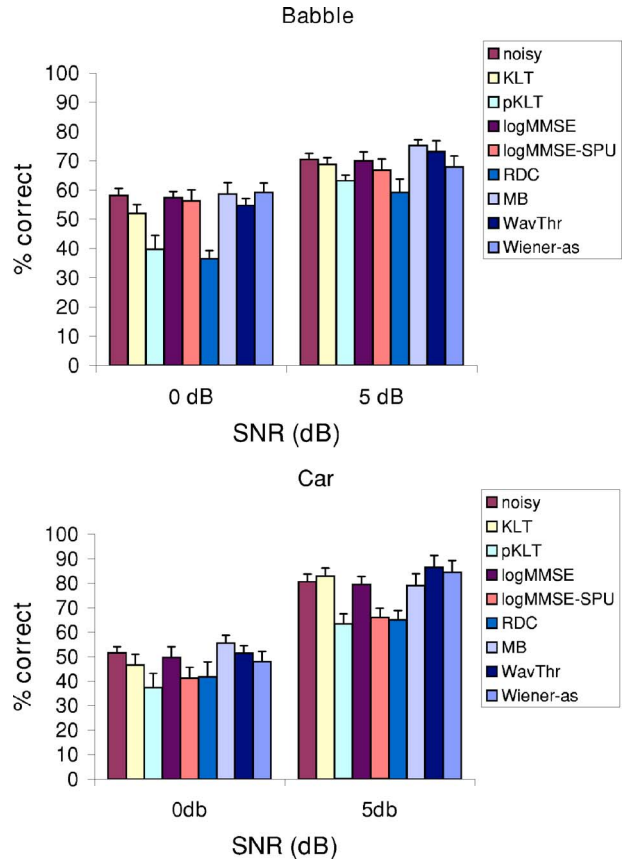

FIG. 3. (Color online) Mean consonant intelligibility scores for eight speech enhancement algorithms in the babble and car noise conditions at 0 and 5 dB SNR.

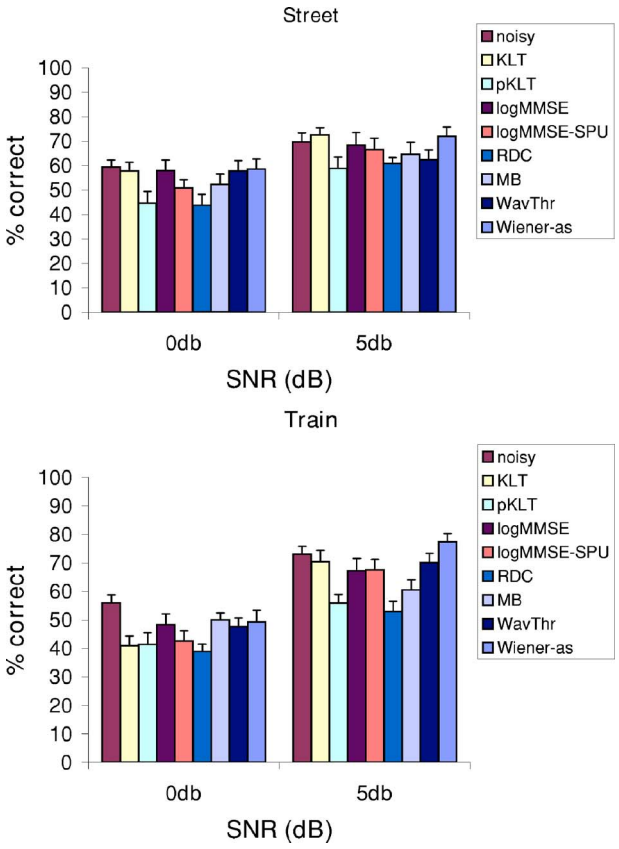

FIG. 4. (Color online) Mean consonant intelligibility scores for eight speech enhancement algorithms in the street and train noise conditions at 0 and 5 dB SNR.

The processed speech files (sentences/consonants), along with the clean and noisy speech files, were presented monaurally to the listeners in a double-walled soundproof booth via Sennheiser's (HD 250 Linear II) circumaural headphones at a comfortable level. Tests were conducted in multiple sessions with each session lasting no more than 2 h. The subjects were allowed to take a break during the listening session to reduce fatigue.

III. RESULTS

Listening tasks involved sentence and consonant recognition in noise. Speech intelligibility was assessed in terms of percentage of words identified correctly. All words were considered in the scoring. We report the results on sentence and consonant recognition separately.

A. Sentence recognition

Figure 1 shows the mean intelligibility scores for babble and car noises, and Fig. 2 shows the mean scores for street and train noises. The error bars in the figures give the standard errors of the mean. The intelligibility scores of noisy (unprocessed) speech are also given for comparative purposes. Of all the conditions tested, algorithms performed the worst (i.e., yielded lowest intelligibility scores) in multitalker babble.

We present comparative analysis at two levels. At the first level, we compare the performance of the various algorithms across all classes aiming to find the algorithm(s) that performed the best across all noise conditions. At the second level, we compare the performance of all algorithms in reference to the noisy speech (unprocessed). This latter comparison will provide valuable information as to which, if any, algorithm(s) significantly improve the intelligibility of noisy speech. If no improvement is obtained, we can learn at the very least which algorithm(s) maintain speech intelligibility and which algorithm(s) diminish speech intelligibility.

In order to assess significant differences between the intelligibility scores obtained from each algorithm, we subjected the scores of the 40 listeners to statistical analysis. Analysis of variance (ANOVA) indicated a highly significant effect ($p < 0.005$) of speech enhancement algorithms on speech intelligibility (a highly significant effect was found in all SNR conditions and types of noise). Following the ANOVA, we conducted multiple comparison statistical tests according to Fisher's LSD test to assess significant differences between algorithms. Differences between scores were deemed significant if the obtained p value (level of significance) was smaller than 0.05.

1. Intelligibility comparison among algorithms

Statistical analysis was performed to assess significant differences in performance between algorithms. Multiple paired comparisons (Fisher's LSD) were conducted between the algorithm with the highest score against all other algorithms. Table I reports the results from the statistical analysis.

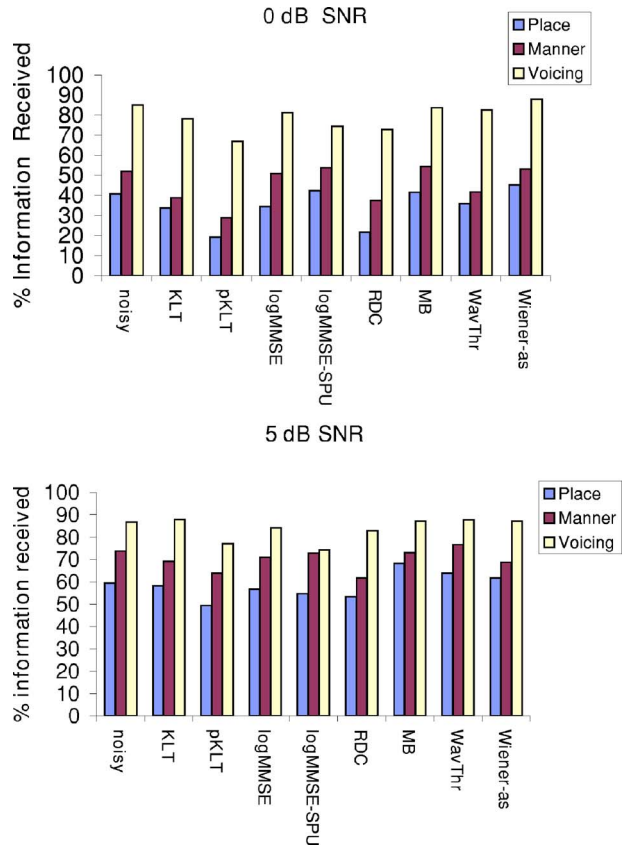

FIG. 5. (Color online) Mean percent information received for the multitalker babble conditions at 0 and 5 dB SNR.

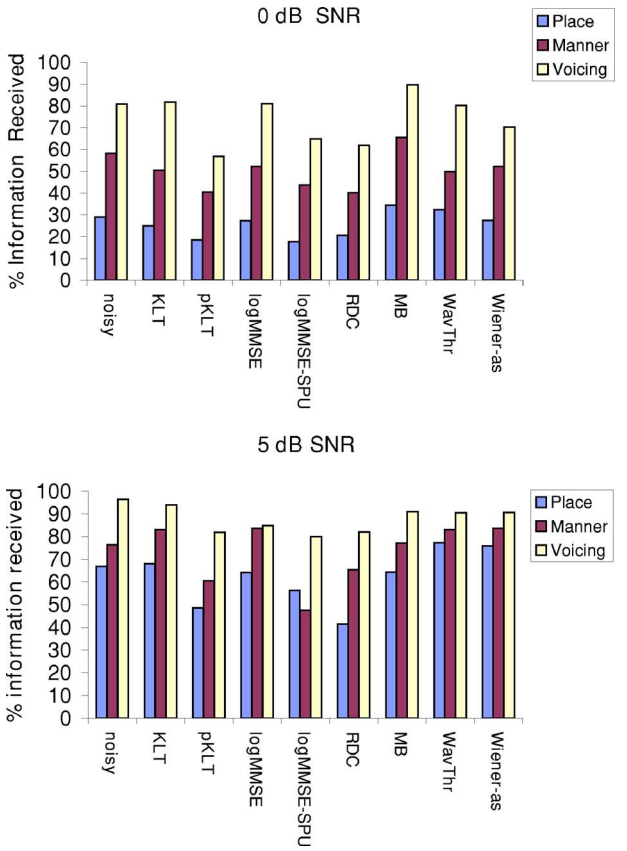

FIG. 6. (Color online) Mean percent information received for the car conditions at 0 and 5 dB SNR.

The algorithms denoted by asterisks in Table I performed equally well. At 5 dB SNR, the KLT and Wiener-as algorithms performed equally well in all conditions. This was followed by the logMMSE and MB algorithms. The pKLT, RDC, logMMSE-SPU and WavThr algorithms performed poorly. At 0 dB SNR, the Wiener-as and logMMSE algorithms performed equally well in most conditions. This was followed by the MB and WavThr algorithms. The KLT algorithm performed poorly except in the babble condition in which it performed the best among all algorithms. Considering all conditions, the Wiener-as algorithm performed consistently well in nearly all conditions, followed by the logMMSE algorithms which performed well in six of the eight noise conditions, followed by the KLT and MB algorithms which performed well in five conditions.

2. Intelligibility comparison against noisy speech

Further analysis was performed to find out whether intelligibility is improved or at least maintained (i.e., speech was equally intelligible) in reference to noisy (unprocessed) speech. Multiple paired comparisons (Fisher's LSD) were conducted between the intelligibility scores obtained with noisy speech (unprocessed) samples and the scores obtained with sentences enhanced by the various algorithms. The results from the statistical analysis are given in Table II. Algorithms indicated with "E" yielded equal intelligibility to noisy speech, algorithms indicated with "L" yielded lower intelligibility, and algorithms indicated with "B" improved speech intelligibility. The Wiener-as algorithm maintained speech intelligibility in six of the eight noise conditions tested, and improved intelligibility in 5 dB car noise. Good performance was followed by the KLT, logMMSE and MB algorithms which maintained speech intelligibility in six conditions. All algorithms produced a decrement in intelligibility in train noise at 0 dB SNR. The pKLT and RDC algorithms significantly reduced the intelligibility of speech in most conditions.

B. Consonant recognition

Figure 3 shows the mean consonant recognition scores for babble and car noises, and Fig. 4 shows the mean scores for street and train noises. The error bars in the figures give the standard errors of the mean. The intelligibility scores of noisy (unprocessed) consonants are also given for comparative purposes. Of all the conditions tested, the train condition at 0 dB SNR was the most challenging, with most algorithms performing worse than the unprocessed (noisy) consonants.

The consonant confusion matrices were subjected to information transmission analysis (Miller and Nicely, 1955) to obtain the percent information transmitted for three articulatory features: place of articulation, manner of articulation and voicing. The mean feature scores are plotted in Figs. 5–8 for the four different types of noise tested. Overall, the place scores were the lowest and the voicing scores were the highest. This outcome is consistent with the findings in Miller and Nicely (1955) with noisy (unprocessed) consonants presented at various SNR levels.

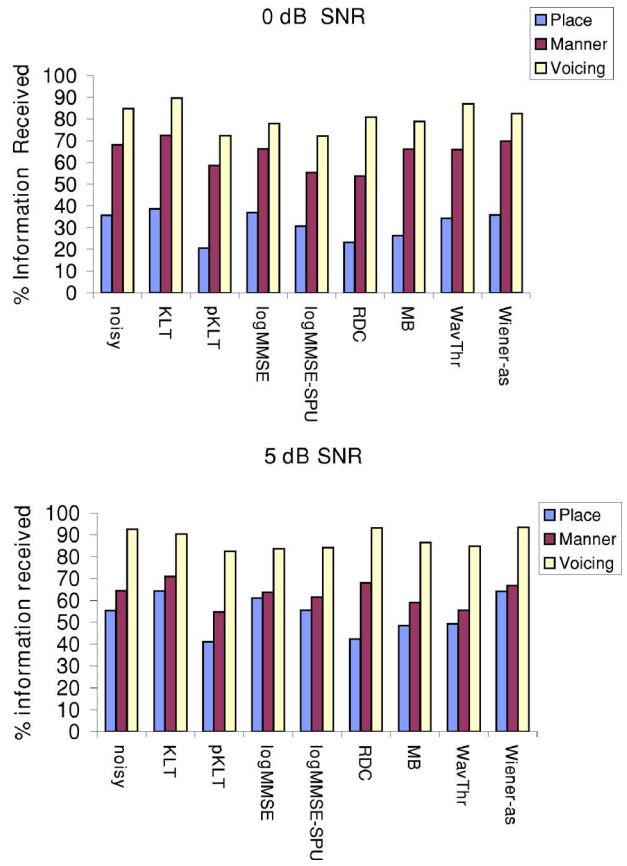

FIG. 7. (Color online) Mean percent information received for the street conditions at 0 and 5 dB SNR.

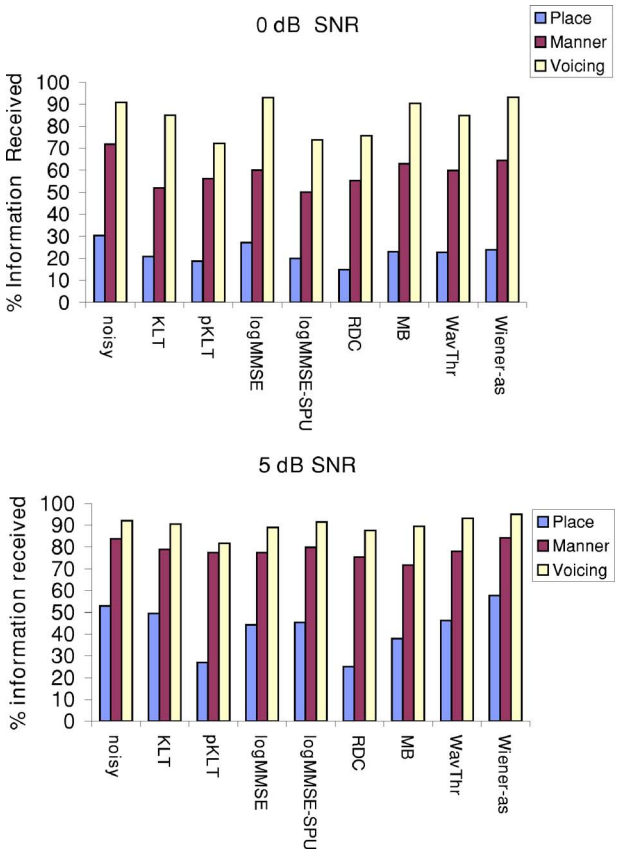

FIG. 8. (Color online) Mean percent information received for the train conditions at 0 and 5 dB SNR.

As before, we present comparative analysis at two levels. At the first level, we compare the performance of the various algorithms across all classes aiming to find the algorithm(s) that performed the best across all noise conditions. At the second level, we compare the performance of all algorithms in reference to the noisy consonants (unprocessed).

1. Consonant intelligibility comparison among algorithms

Statistical analysis was performed to assess significant differences in performance between algorithms. Multiple paired comparisons (Fisher's LSD) were conducted between the algorithm with the highest score against all other algorithms. Table III reports the results from the statistical analysis. Asterisks in the table indicate absence of statistically significant difference (i.e., $p > 0.05$) between the algorithm with the highest score and the denoted algorithm. That is, the algorithms denoted by asterisks in Table III performed equally well. At 5 dB SNR, with the exception of a few algorithms (pKLT and RDC), most algorithms performed equally well. A similar pattern was also observed at 0 dB SNR. The KLT, logMMSE, MB and Wiener-as algorithms performed equally well in most conditions. The logMMSE-SPU performed well in most conditions except in car noise. Overall, the Wiener-type algorithms (Wiener-as and WavThr) and the KLT algorithm performed consistently well in all conditions, followed by the logMMSE and MB algorithms. The RDC and pKLT algorithms performed poorly relative to the other algorithms, and the underlying causes are investigated in the next section.

2. Consonant intelligibility comparison against noisy consonants

Further analysis was performed to find out whether consonant intelligibility is improved or at least maintained in reference to the intelligibility of noisy (unprocessed) consonants. Multiple paired comparisons (Fisher's LSD) were conducted between the intelligibility scores obtained with noisy speech (unprocessed) samples and the scores obtained with consonants enhanced by the various algorithms. The results from the statistical analysis are given in Table IV. In this table, algorithms indicated with E yielded equal consonant intelligibility to noisy consonants and algorithms indicated with L yielded lower intelligibility. Statistical analysis revealed that the Wiener-type algorithms (Wiener-as and WavThr) and the logMMSE algorithm preserved consonant intelligibility in all eight conditions. That is, enhanced consonants were found to be as intelligible as that of noisy (unprocessed) consonants. This was followed by the KLT and MB algorithms, which maintained consonant intelligibility in seven of the eight conditions. The RDC and pKLT algorithms produced a decrement in consonant intelligibility in a number of conditions.

Next, we used the data from feature transmission analysis to examine why some algorithms performed poorly with

TABLE III. Results obtained form the comparative statistical analysis of intelligibility scores of /a*C*a/ syllables. Algorithms indicated by asterisks performed equally well, in terms of speech intelligibility. Algorithms with no asterisks performed poorly.

		Subspace		Statistical model		Spectral subtractive		Wiener type	
Noise	SNR	KLT	*p*KLT	logMMSE	logMMSE-SPU	RDC	MB	WavThr	Wiener-as
Car	0 dB	*		*			*	*	*
Babble		*		*	*		*	*	*
Street		*		*	*		*	*	*
Train		*	*	*	*		*	*	*
Car	5 dB	*		*			*	*	*
Babble		*		*	*		*	*	*
Street		*		*	*		*	*	*
Train		*			*			*	*

TABLE IV. Statistical comparisons between the intelligibility of noisy (unprocessed) consonants and enhanced consonants. Algorithms indicated with "E" were found to be equally intelligible to noisy speech. Algorithms indicated with "L" obtained lower intelligibility scores than noisy consonants.

		Subspace		Statistical model		Spectral subtractive		Wiener type	
Noise	SNR	KLT	*p*KLT	logMMSE	logMMSE-SPU	RDC	MB	WavThr	Wiener-as
Car	0 dB	E	L	E	E	E	E	E	E
Babble		E	L	E	E	L	E	E	E
Street		E	L	E	E	L	E	E	E
Train		L	L	E	L	L	E	E	E
Car	5 dB	E	L	E	L	L	E	E	E
Babble		E	E	E	E	L	E	E	E
Street		E	E	E	E	E	E	E	E
Train		E	L	E	E	L	L	E	E

TABLE V. Place feature transmission comparison with respect to noisy (unprocessed) consonants.

		Subspace		Statistical-model		Spectral subtractive		Wiener type	
Noise	SNR	KLT	*p*KLT	logMMSE	logMMSE-SPU	RDC	MB	WavThr	Wiener-as
Car	0 dB	E	E	E	E	E	E	E	E
Babble		E	L	E	E	L	E	E	E
Street		E	E	E	E	E	E	E	E
Train		E	E	E	E	L	E	E	E
Car	5 dB	E	L	E	E	L	E	E	E
Babble		E	E	E	E	E	E	E	E
Street		E	E	E	E	E	E	E	E
Train		E	L	E	E	L	L	E	E

TABLE VI. Manner feature transmission comparison with respect to noisy (unprocessed) consonants.

		Subspace		Statistical model		Spectral subtractive		Wiener type	
Noise	SNR	KLT	*p*KLT	logMMSE	logMMSE-SPU	RDC	MB	WavThr	Wiener-as
Car	0 dB	E	L	E	L	L	E	E	E
Babble		L	L	E	E	L	E	E	E
Street		E	E	E	L	L	E	E	E
Train		L	L	E	L	L	E	E	E
Car	5 dB	E	L	E	L	E	E	E	E
Babble		E	E	E	E	E	E	E	E
Street		E	E	E	E	E	E	E	E
Train		E	E	E	E	E	L	E	E

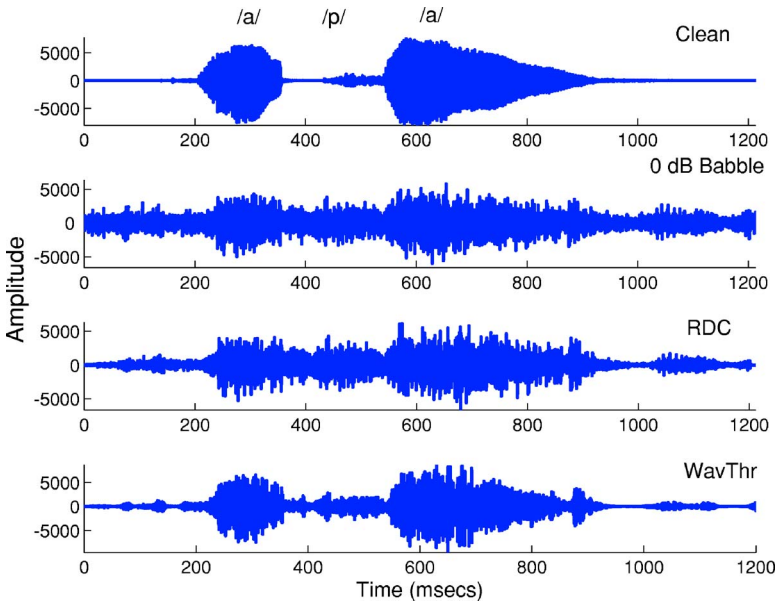

FIG. 9. (Color online) Example consonant waveforms processed by the RDC and WavThr algorithms. The top two panels show the /a p a/ waveform in quiet and in 0 dB babble, respectively.

respect to noisy speech. Statistical analysis was conducted separately for each of the three articulatory features (place, manner, and voicing). Multiple paired comparisons (Fisher's LSD) were conducted between the feature scores obtained with noisy consonant (unprocessed) samples and the feature scores obtained with consonants enhanced by the various algorithms. The comparative results (with respect to the feature scores obtained for noisy consonants) from the statistical analysis are given in Tables V–VII for place, manner and voicing respectively.

From Table IV, we see that the KLT algorithm performed poorly in only one condition, 0 dB SNR train noise. According to Table VI, this was attributed to manner confusion errors. The place and voicing features were preserved. The logMMSE-SPU algorithm performed poorly in the 0–dB SNR train condition and in the 5 dB SNR car condition. From Tables VI and VII, we observe that this was due to manner and voicing errors. Lastly, the RDC and pKLT algorithms performed poorly on consonant recognition (see Table IV) due to place, manner and voicing errors. The majority of the feature errors, however, made by the RDC and pkLT algorithms at 0 dB SNR were caused by manner confusion errors (Table VI).

The manner confusion errors were found to be quite common in most algorithms (Table VI), particularly at low SNR levels (0 dB). The manner errors are produced when enhancement algorithms do not adequately preserve the gross temporal envelope of speech. The stop consonant /p/, for instance, is characterized by a brief silence (closure) followed by a short burst and a low-energy aspiration segment (see example in Fig. 9, top panel). Preserving the silence in /p/ prior to the occurrence of the burst is critical for accurate perception of the stop consonant /p/. Any errors made by enhancement algorithms in preserving the low-energy characteristics of stop consonants will undoubtedly cause manner (or voicing) confusion errors. Figure 9 shows an example waveform of /a p a/ that caused a manner confusion error when the noisy signal was processed by the RDC algorithm at 0 dB SNR. As can be seen, the RDC algorithm enhanced poorly the /p/ segment of the word, as the energy (and gross envelope) of the enhanced /p/ segment was as large as the preceding vocalic segment /a/. Consequently, the enhanced consonant /p/ was not perceived as /p/ by listeners but as /f/, thus contributing to a manner of articulation error. In direct contrast, Fig. 9 (bottom panel) shows /a p a/ enhanced by an algorithm (WavThr) that did not produce as many manner confusion errors as the RDC algorithm. In this example, the WavThr algorithm preserved the low-energy characteristics of /p/.

IV. DISCUSSION AND CONCLUSIONS

This paper compared the intelligibility of speech produced by eight different enhancement algorithms operating in several types of noise and SNR conditions. Based on the statistical analysis of the sentence and consonant intelligibility scores, we can draw the following conclusions:

1. With the exception of a single noise condition (car noise at 5 dB SNR), no algorithm produced significant improvements in speech intelligibility. The majority of the algorithms (KLT, logMMSE, MB, WavThr, Wiener-as) tested were able to maintain intelligibility at the same level as that of noisy speech.
2. When comparing the performance of the various algorithms, we found that the Wiener-as algorithm performed consistently well in nearly all conditions for both sentence and consonant recognition tasks. Following the Wiener-as algorithm, the KLT (subspace), MB and logMMSE algorithms performed comparably well on sentence recognition. On consonant recognition, the Wiener-as, KLT, and WavThr algorithms performed equally well, followed by the logMMSE and MB algorithms.
3. The algorithms that were found in our previous study (Hu and Loizou, 2007a) to perform the best in terms of overall quality were not the same algorithms that performed the best in terms of speech intelligibility. The KLT (subspace) algorithm was found in Hu and Loizou (2007a) to perform the worst in terms of overall quality, but performed

TABLE VII. Voicing feature transmission comparison with respect to noisy (unprocessed) consonants.

Noise	SNR	Subspace		Statistical-model		Spectral subtractive		Wiener type	
		KLT	*p*KLT	logMMSE	logMMSE-SPU	RDC	MB	WavThr	Wiener-as
Car	0 dB	E	L	E	E	L	E	E	E
Babble		E	E	E	E	E	E	E	E
Street		E	E	E	E	E	E	E	E
Train		E	L	E	L	L	E	E	E
Car	5 dB	E	E	E	L	E	E	E	E
Babble		E	E	E	E	E	E	E	E
Street		E	E	E	E	E	E	E	E
Train		E	L	E	E	E	E	E	E

well in the present study in terms of preserving speech intelligibility. In fact, in babble noise (0 dB SNR), the KLT algorithm performed significantly better than the logMMSE algorithm (see Table I), which was found in Hu and Loizou (2007a) to be among the algorithms with the highest overall speech quality.

4. The Wiener-as algorithm performed the best in terms of preserving speech intelligibility (in one case, it improved intelligibility). We believe that this is due to the fact that it applies the least amount of attenuation to the noisy signal, and thus introduces negligible speech distortion. This is done, however, at the expense of introducing noise distortion (residual noise). At the other extreme, the pKLT approach significantly reduces the noise distortion but introduces a great deal of speech distortion, which in turn impairs speech intelligibility. In between the two extremes of speech/noise distortion lie the KLT and logMMSE algorithms. The WavThr and MB algorithms also fall between the two extremes of speech/noise distortion, and preserve consonant intelligibility in nearly all conditions.
5. Analysis of the consonant confusion matrices revealed that the majority of the confusions are due to place of articulation errors, followed by manner of articulation errors and voicing errors. The manner confusion errors were found to be quite common in most algorithms (Table VI), particularly at low SNR levels (0 dB). This suggests that most algorithms do not adequately preserve the low-energy characteristics of consonants at low-SNR environments.
6. The performance of speech enhancement algorithms, in terms of speech intelligibility, seems to be dependent on the temporal/spectral characteristics of the noise, and this dependence is more evident in the low-SNR conditions (0 dB in our case). In the 0 dB babble condition, for instance, the subspace algorithm performed the best but did not perform as well in the other conditions (car, street and train environments). In the 0 dB train condition, none of the evaluated speech enhancement algorithms preserved speech intelligibility (see Table II). The same algorithms, however, did preserve speech intelligibility in other noise conditions (same SNR).

The analysis of consonant confusion matrices provided some insight as to why none of the enhancement algorithms improved speech intelligibility. As shown in Figs. 5–8 (and Table V) none of the enhancement algorithms improved the place feature scores, which are critically important for conveying formant frequency information (Borden *et al.*, 1994). The place scores were found to be the lowest, about 30% at 0 dB SNR across the various types of noise. For an enhancement algorithm to improve intelligibility, it needs to significantly improve the place of articulation feature score. This can be done by designing algorithms that preserve spectral information, and particularly formant frequency information. The manner feature scores, which were the second lowest (about 50–70% at 0 dB SNR across conditions) also need to improve. This can be done by designing techniques that preserve the gross temporal envelope and low-energy characteristics of consonants.

Finally, it is important to point out that the disappointing conclusion drawn from this study that single-microphone enhancement algorithms do not improve speech intelligibility is only applicable to normal-hearing listeners and not necessarily to hearing-impaired listeners wearing hearings aids (Arechart *et al.*, 2003) or cochlear implants (Loizou *et al.*, 2005). In a different study (Loizou *et al.*, 2005), we showed that the KLT algorithm can significantly improve speech intelligibility in cochlear implant users. Further research is therefore needed to investigate the performance of existing speech enhancement algorithms in hearing-impaired listeners.

ACKNOWLEDGMENTS

The authors would like to thank Jessica Dagley for her help in collecting the data. The authors also would like to thank Dr. Israel Cohen for providing the MATLAB implementation of the log-MMSE method with speech presence uncertainty. Research was supported by Grant No. R01 DC007527 from the National Institute of Deafness and other Communication Disorders, NIH.

Arehart, K. H., Hansen, J. H., Gallant, S., and Kalstein, L. (**2003**). "Evaluation of an auditory masked threshold noise suppression algorithm in normal-hearing and hearing-impaired listeners," Speech Commun. **40**, 575–592.

Boll, S. F. (**1979**). "Suppression of acoustic noise in speech using spectral subtraction," IEEE Trans. Acoust., Speech, Signal Process. **ASSP-27**, 113–120.

Borden, G., Harris, K. and Raphael, L. (**1994**). *Speech Science Primer: Physiology, Acoustics, and Perception of Speech* (Williams and Wilkins, Baltimore).

Cohen, I., and Berdugo, B. (**2002**). "Noise estimation by minima controlled recursive averaging for robust speech enhancement," IEEE Signal Process. Lett. **9**, 12–15.

Ephraim, Y., and Malah, D. (**1985**). "Speech enhancement using a minimum mean-square error log-spectral amplitude estimator," IEEE Trans. Acoust., Speech, Signal Process. **ASSP-33**, 443–445.

Gustafsson, H., Nordholm, S., and Claesson, I. (**2001**). "Spectral subtraction using reduced delay convolution and adaptive averaging," IEEE Trans. Speech Audio Process. **9**, 799–807.

Hirsch, H., and Pearce, D. (**2000**). "The aurora experimental framework for the performance evaluation of speech recognition systems under noisy conditions," in *ISCA Tutorial and Research Workshop ASR2000*, Paris, France.

Hu, Y., and Loizou, P. C. (**2003**). "A generalized subspace approach for enhancing speech corrupted by colored noise," IEEE Trans. Speech Audio Process. **11**, 334–341.

Hu, Y., and Loizou, P. C. (**2004**). "Speech enhancement based on wavelet thresholding the multitaper spectrum," IEEE Trans. Speech Audio Process. **12**, 59–67.

Hu, Y., and Loizou, P. C. (**2007a**). "Subjective comparison and evaluation of speech enhancement algorithms," Speech Commun. **49**, 588–601.

Hu, Y., and Loizou, P. C. (**2007b**). "A comparative intelligibility study of speech enhancement algorithms," in *Proc. IEEE int. Conf. Acoust., Speech, Signal Processing*, Honolulu, Hawaii, pp. 561–564.

IEEE Subcommittee (**1969**). "IEEE recommended practice for speech quality measurements," IEEE Trans. Audio Electroacoust. **17**, 225–246.

ITU-T P.862 (**2000**). *Perceptual evaluation of speech quality (PESQ), and objective method for end-to-end speech quality assessment of narrowband telephone networks and speech codecs*, (ITU-T Recommendation P.862).

Jabloun, F., and Champagne, B. (**2003**). "Incorporating the human hearing properties in the signal subspace approach for speech enhancement," IEEE Trans. Speech Audio Process. **11**, 700–708.

Kamath, S., and Loizou, P. C. (**2002**). "A multi-band spectral subtraction method for enhancing speech corrupted by colored noise," in *Proc. IEEE Int. Conf. Acoust., Speech, Signal Processing*, Orlando, FL.

Lim, J. S. (**1978**). "Evaluation of a correlation subtraction method for enhancing speech degraded by additive white noise," IEEE Trans. Acoust., Speech, Signal Process. **26**, 471–472.

Loizou, P. (**2007**). *Speech Enhancement: Theory and Practice* (CRC, Boca Raton, FL).

Loizou, P. C, Lobo, A., and Hu, Y. (**2005**). "Subspace algorithms for noise reduction in cochlear implants," J. Acoust. Soc. Am. **118**, 2791–2793.

Miller, G., and Nicely, P. (**1955**). "An analysis of perceptual confusions among some English consonants," J. Acoust. Soc. Am. **27**, 338–352.

Mittal, U., and Phamdo, N. (**2000**). "Signal/noise KLT based approach for enhancing speech degraded by colored noise," IEEE Trans. Speech Audio Process. **8**, 159–167.

Scalart, P, and Filho, J. (**1996**). "Speech enhancement based on a priori signal to noise estimation," in *Proc. IEEE Int. Conf. Acoust., Speech Signal Processing*, Atlanta, GA, pp. 629–632.

Sohn, J., Kim, N., and Sung, W. (**1999**). "A statistical model-based voice activity detection," IEEE Signal Process. Lett. **6**, 1–3.

Tsoukalas, D. E., Mourjopoulos, J. N., and Kokkinakis, G. (**1997**). "Speech enhancement based on audible noise suppression," IEEE Trans. Speech Audio Process. **5**, 479–514.

Voiers, W. (**1983**). "Evaluating processed speech using the diagnostic rhyme test," Speech Technol. **Jan./Feb.**, 30–39.

Analysis and modeling of piano sustain-pedal effects[a)]

Heidi-Maria Lehtonen,[b)] Henri Penttinen, Jukka Rauhala, and Vesa Välimäki
[1]*Helsinki University of Technology, Laboratory of Acoustics and Audio Signal Processing, Espoo, Finland*

(Received 11 September 2006; revised 6 June 2007; accepted 13 June 2007)

This paper describes the main features of the sustain-pedal effect in the piano through signal analysis and presents an algorithm for simulating the effect. The sustain pedal is found to increase the decay time of partials in the middle range of the keyboard, but this effect is not observed in the case of the bass and treble tones. The amplitude beating characteristics of piano tones are measured with and without the sustain pedal engaged, and amplitude envelopes of partial overtone decay are estimated and displayed. It is found that the usage of the sustain pedal introduces interesting distortions of the two-stage decay. The string register response was investigated by removing partials from recorded tones; it was observed that as the string register is free to vibrate, the amount of sympathetic vibrations is increased. The synthesis algorithm, which simulates the string register, is based on 12 string models that correspond to the lowest tones of the piano. The algorithm has been tested with recorded piano tones without the sustain pedal. The objective and subjective results show that the algorithm is able to approximately reproduce the main features of the sustain-pedal effect. © *2007 Acoustical Society of America.* [DOI: 10.1121/1.2756172]

PACS number(s): 43.75.Mn, 43.75.Zz, 43.75.Wx [NHF] Pages: 1787–1797

I. INTRODUCTION

Modern pianos have either two or three pedals. The right pedal is always the sustain pedal (or the resonance pedal), which lifts all the dampers and allows the strings to vibrate due to sympathetic coupling. The left pedal is called the *una corda* pedal, and its purpose is to make the output sound softer and give it a "lyrical" quality.[1] The purpose of the possible middle pedal can vary depending on the instrument; it can be the bass sustain pedal or the practice pedal, which softens the sound of the instrument. The sustain pedal, however, is the most important and widely used. It has primarily two purposes. First, it acts as "extra fingers" in situations where *legato* playing is not possible with any fingering. Second, since all the strings are free to vibrate, enrichment of the tone is obtained. The usage of the sustain pedal needs synchronization between the hands and foot, and Repp[2,3] has found that its timing is influenced by the tempo of the performance.

The purpose of this study is to provide information on the sustain-pedal effect through signal analysis and to present an algorithm for modeling the effect. A preliminary version of this work was presented as a part of a Master's thesis.[4] Now, some modifications and improvements to the algorithm are suggested. In addition, the signal analysis given is in more depth.

The acoustics and the sound of the piano have been widely addressed in the literature. Excellent reviews of the topic are given, for example, in the text book edited by Askenfelt[5] and in the article series by Conklin.[6–8] Recently, research has focused on specific topics, such as the dispersion phenomenon,[9–11] the longitudinal vibrations,[12,13] and the grand piano action.[14] In addition, the physics-based sound synthesis of the piano has gained much popularity during the last two decades. The digital waveguide approach[15–17] is an efficient way to produce realistic piano tones in real time. Another popular approach is the finite difference method; the modeling of the hammer-string interaction[18,19] and the simulation of the piano string vibration[20] have been interesting research topics. Recently, Giordano and Jiang[21] presented a complete finite difference piano model, which consisted of several interacting submodels, such as the hammers, strings, and the soundboard.

Despite the importance of the sustain pedal, only few studies considering the modeling of the effect have been published. De Poli *et al.*[22] presented a model, which is based on the string register simulation with 18 string models of fixed length and ten string models of variable length. The fixed-length strings correspond to the 18 lowest tones of the piano, and the usage of the variable-length strings depends on the situation. For example, some of them can be used to increase the amount of string models in the set of fixed-length strings. In this case, their lengths are set to correspond to the notes subsequent to those of the fixed-length strings. The output from the two junctions is first lowpass filtered and then multiplied with a coefficient that determines the degree of the effect of the sustain pedal. With this system De Poli *et al.* were able to produce a resonance pedal effect for digital electronic pianos.

The problem can be approached also from a theoretical point of view. Carrou *et al.*[23] presented a study that discussed sympathetic vibrations of several strings. They constructed an analytical model of a simplified generic string instrument, in which the instrument body is modeled as a beam to which

[a)]Portions of this work were presented in "Analysis and parametric synthesis of the piano sound," Master's thesis, Helsinki University of Technology, 2005.

[b)]Author to whom correspondence should be addressed. Electronic address: heidi-maria.lehtonen@tkk.fi

the strings are attached. With this model, Carrou *et al.* obtained results that are applicable to real instruments with many strings, such as the harp. Basically, the situation is similar in the case of the piano, where sympathetic coupling between the strings is a known phenomenon.[1,24,25] However, in the case of the sustain pedal, the number of vibrating strings is nearly 250, and an analytical approach would lead to an extremely complex mathematical problem as well as a heavy computational modeling. In contrast, in this study, the goal is to obtain an efficient model-based synthesis algorithm with a low computational cost, and the approach taken here is rather phenomenological than physical.

Van Duyne and Smith[26] proposed that the sustain-pedal effect can be synthesized by commuting the impulse response of the soundboard and open strings to the excitation point. This approach provides an efficient and accurate way to simulate the sustain-pedal effect.

Jaffe and Smith[27] proposed that sympathetic vibrations can be simulated with a bank of sympathetic strings parallel to a plucked string. Later, some authors have suggested that the sustain pedal could be simulated with a reverberation algorithm,[16] which is often used in room simulations[28,29] and instrument body modeling.[30–32]

The approach taken in this paper follows the aforementioned ideas; the freely vibrating string register is simulated with a set of string models, which are designed to correspond to the lowest tones in the piano. On the other hand, the proposed system can be interpreted as a reverberation algorithm, since the number of modes in the system is very high.

This paper is organized as follows. In Sec. II the recording setup and equipment are described. Section III reports the results of the signal analysis and in Sec. IV the synthesis algorithm with examples and perceptual evaluation of the proposed model are presented. Finally, Sec. V concludes the paper.

II. RECORDINGS

In order to study features of the sustain-pedal effect, recorded piano tones with and without the sustain pedal were analyzed. Obviously, the best choice for the recording place would be an anechoic chamber, but unfortunately this option was out of the question. The next best choice is to carry out the recordings in a maximally absorbent recording studio. Single tones from the bass, middle, and treble range of the piano were played both with and without the sustain pedal.

A. Recording setup and equipment

The recordings were carried out at the Finnvox recording studio in Helsinki, Finland, in February 2006. The instrument was a Yamaha concert grand piano (serial number 3070800) with 88 keys, and it was tuned just before the recording session. The signals that were used in the analysis were recorded on two channels, and the microphones (Danish Pro Audio 4041 with Danish Pro Audio HMA 4000 preamplifier) were positioned 32 cm above the string register. The microphones corresponding to the left and right channels were located 80 cm from the keyboard end and 71 cm from the other end, respectively, and the positions were kept constant throughout the session. Another option for the microphone locations would have been a few meters away from the instrument. This choice would have provided information about the phenomenon from the listener's point of view. On the other hand, our goal was to analyze the effect and gather accurate information for synthesis. Since a better signal-to-noise ratio is obtained when the effects of the transmission path are minimized, it was decided to place the microphones close to the strings.

FIG. 1. Illustration of the microphone positioning above the string register. The letters L and R indicate the locations of the microphones corresponding to the left and right channel, respectively.

Figure 1 illustrates the recording setup. The microphone locations for the left and right channels are indicated with the letters L and R, respectively. The signals were recorded with the sampling rate of 44.1 kHz and 16 bits. Finally, only the right channel was chosen for the analysis, since it provided a slightly better signal-to-noise ratio.

B. Recorded tones

An extensive set of bass, middle, and treble tones were played several times without the sustain pedal and then with the sustain pedal, and finally the features of five of them were selected to be shown in the present study. The dynamics of the tones were determined to be *mezzo forte* in all cases. It is assumed that the soundboard and the sympathetically resonating string register behave linearly, and thus the model that is calibrated based on signal analysis performed to *mezzo forte* tones is also suitable for playing with different dynamics.

In order to keep the dynamics as constant as possible during the whole session, a weight of 0.5 kg was used to press down the keys in the low and middle range of the piano. A pile of small coins attached to each other made up the weight used. For the highest range, that is, the 17 uppermost keys of the piano, the method proved to produce a pronounced sound effect while depressing the key, when the key touched the front rail and the key frame under the keyboard. Thus, the highest keys were played manually in the conventional way while keeping the dynamic level as constant as possible.

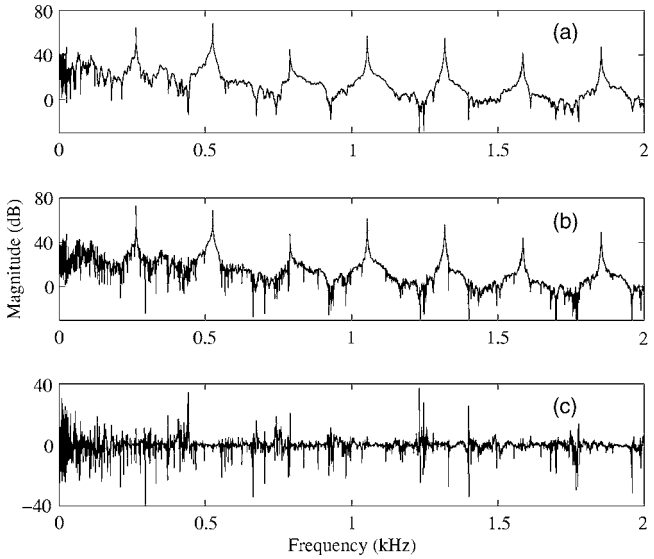

FIG. 2. Tone C4 (a) without and (b) with the sustain pedal in frequency domain. (c) shows the difference between the magnitude spectra in (a) and (b).

In addition, the proportion of the energy of sympathetic vibrations was investigated by first playing the tone with the sustain pedal and then damping the string group that corresponds to the key that was pressed down. After damping the string group, the string register still keeps ringing due to sympathetic coupling, and it is possible to obtain information on the relation between the energy of the direct sound and sympathetic vibrations. This experiment was carried out for several keys from the bass, middle, and treble tones, and each case was repeated a couple of times.

A visualization of the effect of the sustain pedal on the piano tone is shown in Fig. 2. Figures 2(a) and 2(b) illustrate the spectrum of the tone C4 (key index 40, f_0=262.7 Hz) when the sustain pedal is not used and when it is used, respectively. It can be seen that when the tone is played with the sustain pedal, the spectrum contains additional components between the partials. In order to better see these additional components, the difference between the magnitude spectra of Figs. 2(a) and 2(b) is presented in Fig. 2(c). The spectra are computed with a 2^{20} point fast Fourier transform (FFT) using a rectangular window.

III. SIGNAL ANALYSIS

In this section, the signal analysis procedure is described. First, the sustain-pedal effect is analyzed by extracting single partials from recorded tones played with and without the sustain pedal and their features are compared in Sec. III A. Second, in Sec. III B, the residual signals are investigated by canceling all partials from tones that were played with and without the sustain pedal. The residual signal energies were measured in critical bands[33] in order to study in which frequency ranges there are differences. Additionally, possible physical explanations for the observed features are discussed.

TABLE I. The fundamental frequencies and the inharmonicity coefficients of the example tones.

Tone	f_0 (Hz)	B
C2	65.6	3.8×10^{-5}
C3	131.2	1.1×10^{-4}
C4	262.7	3.3×10^{-4}
D5	589.1	1.2×10^{-3}
C6	1052.8	2.3×10^{-3}

A. Extracted partials

Recorded signals were analyzed by extracting single partials by bandpass filtering tones with and without the sustain pedal. In general, three features of the partials were of interest: the possible differences in initial levels, decay times, and amplitude beating characteristics. These features were investigated in the case of the five example tones listed in Table I with their fundamental frequencies and inharmonicity coefficients.[34] These parameters can be estimated from tones manually, or by using some specific algorithm, e.g., the inharmonic comb filter method presented by Galembo and Askenfelt.[35] In the present study, the fundamental frequencies and the inharmonicity coefficients of the example tones were estimated using a simple algorithm based on a peak picking technique. In this algorithm, local maxima of the whitened spectrum of a piano tone are searched and the corresponding frequencies are used as estimates for the harmonic component locations. The theoretical partial frequencies are computed using Eq. (1)[36]

$$f_m = m f_0 \sqrt{1 + m^2 B}, \tag{1}$$

where m is the partial index and f_m is the corresponding frequency. The best B and f_0 estimates are obtained by finding the minimum mean-square error between the partial frequencies and the theoretical partial frequencies obtained from Eq. (1) with different values of f_0 and B. The initial guesses for these parameters are based on the key index information.

In the case of the piano, the harmonics exhibit a complicated decay process because of the two-stage decay and beating.[1] In order to obtain an approximation of the decay times of the tones, a straight line was fitted to the first six seconds of signal log envelopes in a least squares sense.[37,38] After this, estimates for T_{60}-times, that is, the time it takes for a partial to decay 60 dB, were computed based on the slope of the fitted straight line. Additionally, the same procedure was repeated for partials that correspond to the fundamental frequencies of the tones.

The results for the five example tones are listed in Tables II and III, giving the overall decay rates and the decay rates of the partials corresponding to the fundamental frequencies, respectively, along with their initial levels. As can be seen, the decay times in general are larger in those cases where the sustain pedal is used, especially in the middle range of the piano. In the treble range, there are no remarkable differences in the decay times, while in the bass tones the overall decay time seems to be even slightly decreased, but the decay time of the first partial is increased when the sustain

TABLE II. The overall T_{60}-times and the initial levels of the tones without (N) and with (P) the sustain pedal.

Tone	T_{60}/N (s)	T_{60}/P (s)	Level/N (dB)	Level/P (dB)
C2	20.3	18.1	−7.5	−7.0
C3	12.5	14.8	−7.3	−7.3
C4	9.5	15.3	−6.8	−6.6
D5	14.7	18.3	−5.0	−4.5
C6	12.0	12.0	−4.3	−3.7

pedal is used. The changes in initial levels of the partials are minor, within 1 dB, which implies that these changes are, in general, difficult to hear.

There are several possible physical explanations for the observed changes in decay times presented in Tables II and III. The bass strings are attached to a separate bridge, which inhibits the energy from leaking to the middle and treble strings and, thus, the decay times are not altered substantially when the bass tones are played with the sustain pedal compared to the situation where the sustain pedal in not engaged. In the middle region, on the other hand, the number of strings is higher because of the duplets and triplets, and the middle and treble strings are attached to the same bridge, which enables more coupling to surrounding strings. It is likely that some of the surrounding strings have modes near the modes of the strings corresponding to the struck key, and when these modes are not damped by the damper, the decay time of the played tone increases. In the treble region the decay times are not likely to increase, since the harmonic structure is sparse. Even if the frequency of a partial of a high tone is nearly the same as some of the partials of the lower tones, the high tone does not contain much energy for exciting the lower strings. Moreover, the high strings are relatively far away from the more energetic middle strings.

The relevance of the increased decay times from the perceptual point of view is a more complicated question. Järveläinen and Tolonen[39] presented perceptual tolerances for decay parameters and concluded that decay time variations are inaudible if the change is between 75% and 140%. Despite the fact that the reported perceptual tolerances were determined for synthetic tones that resemble guitar plucks, they can be expected to indicate that the human hearing is similarly inaccurate in analyzing the decay process of piano tones. In this light, the decay time difference seems to be audible only in the case of the tone C4, since the T_{60} time is 161% of the original T_{60} time when the sustain pedal is engaged.

TABLE III. The T_{60}-times of the fundamental frequencies with the initial levels for five example tones without (N) and with (P) the sustain pedal.

Tone	T_{60}/N (s)	T_{60}/P (s)	Level/N (dB)	Level/P (dB)
C2	9.3	14.8	−14.1	−13.7
C3	10.0	14.3	−10.3	−9.9
C4	10.3	17.0	−13.8	−14.2
D5	14.2	16.0	−5.2	−4.5
C6	9.0	8.3	−4.4	−3.8

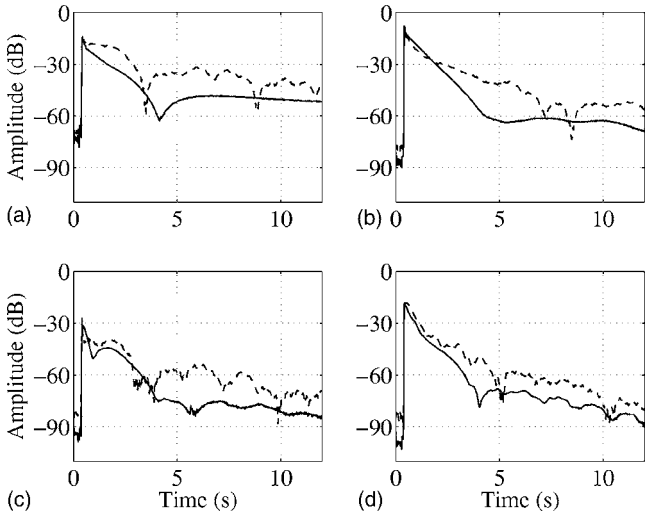

FIG. 3. Envelopes of the partials (a) 1, (b) 2, (c) 3, and (d) 4 of the tone C4. The solid and dashed lines represent the tones without and with the sustain pedal, respectively.

The amplitude beating in the partials is slightly increased, as is shown in Fig. 3, which presents the envelopes of the partials Nos. 1–4 of the tone C4. The solid and dashed lines represent the tones with and without the sustain pedal, respectively. The differences in the noise floors, which are visible before the onset of the tones, are due to the contact sound between the dampers and the strings when the sustain pedal is pressed down before pressing down the key. The amplitude beating characteristics are similar also in the bass and treble tones.

The increased beating results from the energy transfer from the excited string group to the string register via the bridge. As all the dampers are lifted and the string register is allowed to vibrate freely, the modes near those of the excited string group gain energy.

Another observation is that the two-stage decay structure of the partials becomes less obvious when the tone is played with the sustain pedal compared to the situation when the sustain pedal is not engaged. This feature is also due to the energy leakage from the string register, and it depends on the admittance of the bridge.

B. String register hammer response

When the hammer hits a string group, the freely vibrating string register and the soundboard are excited by the impulse of the hammer. The behavior of the undamped string register was studied by removing the partials from recorded tones corresponding to the struck key. The aim was to compare the residual signals of the tones with and without the sustain pedal in the frequency domain.

The frequency analysis was done with a 2048 point FFT applying a Hanning window having 512 samples with a hop size of 256 samples. Figures 4(a) and 4(b) illustrate the time-frequency plot of the residual signals obtained from the tone C4 without and with the sustain pedal, respectively. It can be seen that when the tone is played with the sustain pedal the level of the residual signal during the time interval 1–5 s is approximately 10 dB higher than in the reference case. The

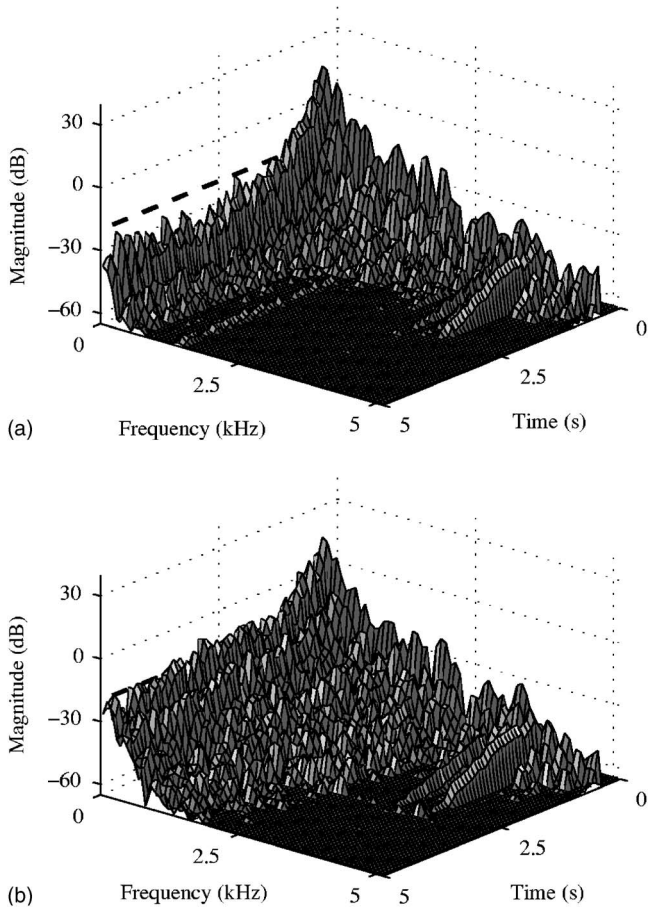

FIG. 4. Time-frequency plot of the residual signal obtained from tone C4 (a) without and (b) with the sustain pedal. The dashed line in (a) indicates the corresponding residual signal magnitude 5 s after the excitation when the tone is played with the sustain pedal (b).

dashed line in Fig. 4(a) illustrates the corresponding level of the residual signal when the sustain pedal is used [see Fig. 4(b)]. The trend is similar when the analysis is performed on lower and higher tones.

The energies of the residual signals were measured on the Bark scale.[33] The Bark scale was chosen because it provides information from the psychoacoustical point of view, which is important for perceptually meaningful synthesis of the sustain pedal effect. Figure 5 illustrates the energies of the residual signals for the tone C4 with and without the sustain pedal. The energies were computed from a 1 s excerpt 110 ms after the excitation. Figure 6 presents the difference of the two curves of Fig. 5 as well as the corresponding differences for the tones C2 and C6. As a conclusion, the residual signal energy is increased 5–30 dB on Bark bands 1–14, which correspond to the frequency range 0–2.5 kHz.

The aforementioned frequency range affected by the sustain-pedal effect seems reasonable from the physical point of view. It can be seen in Fig. 5 that the differences between the residual signal energies start to decrease around 1.5 kHz, and finally roll off towards 0 dB around 2.5 kHz. This frequency range is approximately the same where the strings do not have dampers anymore. As a result, the highest strings are more or less excited always, regardless of the usage of the sustain pedal.

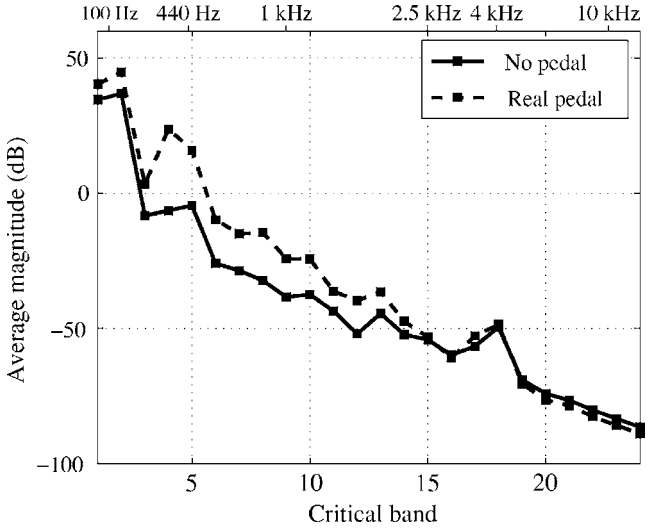

FIG. 5. Energies of the residual signals as a function of frequency on the Bark scale. The solid and dashed lines represent the cases where the tone C4 is played without and with the sustain pedal, respectively.

IV. SYNTHESIS ALGORITHM DESIGN

The main idea of the proposed reverberation algorithm is to approximate the string register with 12 simplified digital waveguide string models[40] that correspond to the 12 lowest strings of the piano. The proposed structure is basically an extension to the algorithm presented by De Poli *et al.*,[22] where 18 fixed length and ten variable length strings were used to simulate the string register.

In addition, in the present study a dispersion filter $A_k(z)$ and a lowpass filter $H_k(z)$, where k represents the key index, are included in every string model. The design processes of these filters are described in Secs. IV A 1 and IV A 2, respectively. The input to the string models is filtered with a tone corrector filter $R(z)$ and their summed output is multiplied with a mixing coefficient, which is then added to the input tone. The tone corrector filter and the mixing coefficient are discussed in Secs. IV A 4 and IV A 5, respectively. A sche-

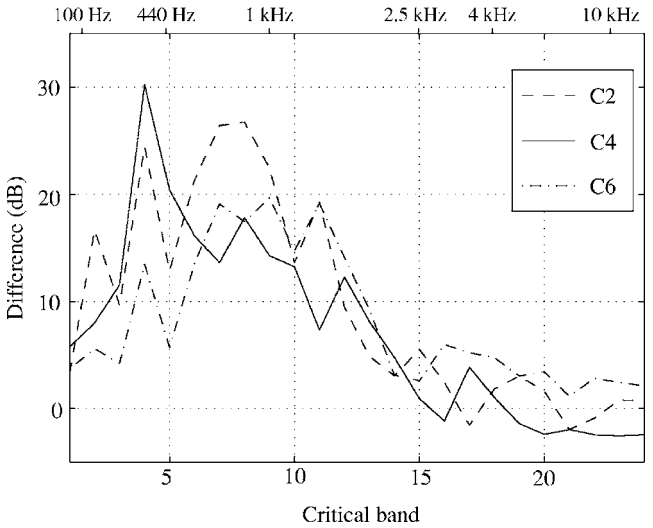

FIG. 6. Differences of the residual signal energies in the case of tones C2, C4, and C6 as a function of frequency on the Bark scale.

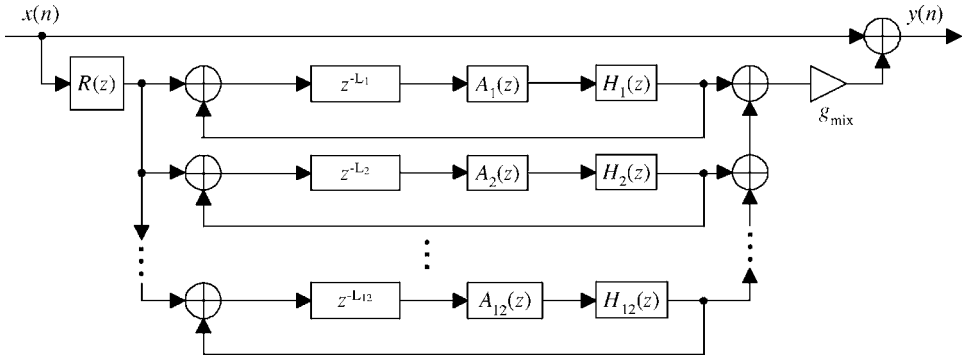

FIG. 7. Block diagram that shows the structure of the sustain-pedal algorithm.

matic view of the algorithm is presented in Fig. 7. In the following, the choice of the algorithm parameters is discussed. The synthesis algorithm is designed with the MATLAB software using a 44.1 kHz sampling rate and a double-precision floating-point arithmetic.

A. Algorithm parameters

1. Delay line lengths

In theory, nearly 250 string models are needed in order to accurately imitate the string register. This choice is, however, not feasible for real-time processing. Thus, the number of string models must be reduced. Since the lowest tones contain more partials than the highest tones, it is advantageous to choose the delay line lengths according to the N lowest tones. When the value of the parameter N is chosen to be 12, the string register is simulated with the first octave of the piano, and the partials of these tones roughly approximate the higher octaves.

The values of the delay line lengths $L_1,\ldots,L_{12}$ are defined by the frequencies indicated in Table IV with the following rounding operation:

$$L_k = \mathrm{floor}\left(\frac{f_s}{f_{0,k}} + \frac{1}{2}\right), \tag{2}$$

where floor is the greatest integer function, f_s is the sampling frequency, and $f_{0,k}$ refers to the fundamental frequency of the tone that corresponds to the key index k. The rounding operation is performed, because the ratio of the sampling frequency and the fundamental frequency is usually not an integer. This makes a slight error to the delay line length, which is ordinarily compensated with an allpass fractional delay filter.[27,41,42] In this case, however, this compensation is not necessary, since only the lowest tones with long delay lines are dealt with. The fractional part is about 0.05% of the whole delay line length, and thus this minor error is inaudible.

TABLE IV. Parameters for the sustain-pedal algorithm.

Key index k	f_0 (Hz)	L	B	a_1	g
1	27.5	1602	3.0×10^{-4}	−0.974	0.9918
2	29.2	1511	2.9×10^{-4}	−0.972	0.9903
3	30.9	1428	2.7×10^{-4}	−0.971	0.9942
4	32.7	1349	2.6×10^{-4}	−0.969	0.9928
5	34.6	1273	2.5×10^{-4}	−0.966	0.9929
6	36.8	1199	2.4×10^{-4}	−0.964	0.9941
7	38.9	1134	2.3×10^{-4}	−0.961	0.9941
8	41.2	1070	2.2×10^{-4}	−0.959	0.9954
9	43.7	1009	2.1×10^{-4}	−0.956	0.9947
10	46.3	952	2.0×10^{-4}	−0.953	0.9958
11	49.1	899	1.9×10^{-4}	−0.949	0.9938
12	52.1	847	1.8×10^{-4}	−0.946	0.9929

2. Dispersion filter design

The stiffness of the piano strings, making the strings dispersive, produces inharmonic tones. It is known that the inharmonicity is a perceptually important phenomenon in the bass range of the piano as it adds "warmth" to the sound.[36] In the proposed sustain-pedal algorithm, however, the purpose of the dispersion filters is not to produce inharmonicity, but to spread the harmonic components of the string models more randomly in the sympathetic spectrum. This approach follows the idea of Väänänen *et al.*,[43] where the authors used comb-allpass filters cascaded with delay lines in the reverberator algorithm in order to obtain a dense response for room acoustics modeling. In the present work, the dispersion filters have an effect especially on the tonal quality of the sound decay. When the dispersion filters are excluded from the model, the decay process may sound somewhat too regular or metallic.

In this model, the dispersion filters are designed with the tunable dispersion filter method.[44,45] The original tunable dispersion filter method offers closed-form formula to design a second-order dispersion filter. This method has been extended to an arbitrary number of first-order filters in cascade,[45] which is used in this work to design a single first-order dispersion filter. The transfer function of the dispersion filter can be denoted as

$$A_k(z) = \frac{a_{1,k} + z^{-1}}{1 + a_{1,k}z^{-1}}, \tag{3}$$

where k is the index of the string model and $a_{1,k}$ is the filter coefficient, which can be calculated as[27,42]

$$a_{1,k} = \frac{1 - D_k}{D_k + 1}, \tag{4}$$

where D_k is the phase delay value at dc. Roughly speaking, increase in the D_k value corresponds to increase in the inharmonicity coefficient value. This is applied in the tunable dispersion filter method, which provides a closed-form formula to determine the D_k value based on the desired fundamental

frequency and the desired inharmonicity coefficient value.[44,45]

The parameter values used in this work are shown in Table IV. The inharmonicity coefficient values used in the dispersion filter design are realistic values for the first 12 keys of the piano.[35,46] The delay at the $f_{0,k}$, produced by the dispersion filter, can be approximated with[45] D_k.

3. Lowpass filter design

As the purpose of the algorithm is to simulate real strings, also the frequency-dependent losses in the string are approximated by digital means. A first-order lowpass filter is used for modeling the losses. This filter is often applied in physical modeling of string instruments, because it is easy to design, efficient to implement, and it sufficiently brings about the slow decay of low-frequency partials and fast decay of high-frequency partials at the same time.[38] The transfer function of $H_k(z)$ is given as[38]

$$H_k(z) = \frac{b_k}{1 + cz^{-1}}, \tag{5}$$

where $b_k = g_k(1+c)$. The losses of the string are simulated so that the parameters g_k and c control the overall decay and the frequency-dependent decay, respectively. In this work, the parameters g_k are calibrated based on the 12 lowest tones played without the sustain pedal, and they are listed in Table IV. The c parameter, which controls the frequency-dependent decay, is designed as an approximation based on several tones for the middle, and treble tones. This procedure was found suitable, since especially the treble tones decay fast compared to bass tones. If the parameter was calibrated for bass tones, the decay process of the middle and treble tones with synthetic sustain pedal would be too long. Thus, the c parameter is set to -0.197 for all the strings.

4. Tone corrector

The tone corrector $R(z)$ is designed based on the information obtained from residual signal analysis. In Sec. III B it was concluded that the energy increases mainly in the frequency band 0–2.5 kHz, and in the highest frequency range there is no significant increase in the energy of the residual signal due to strings without the dampers. This is visible also in Fig. 6. In order to design the tone corrector filter $R(z)$, differences of the residual signal energies were computed for several bass, middle, and treble tones. Then, a second-order filter consisting of a dc blocking filter and a lowpass filter was fitted manually to the average of the energy differences. The transfer function can be written as

$$R(z) = \frac{0.1164(1 - z^{-1})}{1 - 1.880z^{-1} + 0.8836z^{-2}}. \tag{6}$$

The average energy difference and the magnitude spectrum of the tone corrector are shown in Fig. 8 with a dashed and solid lines, respectively. The maximum error in the fit is about 5 dB.

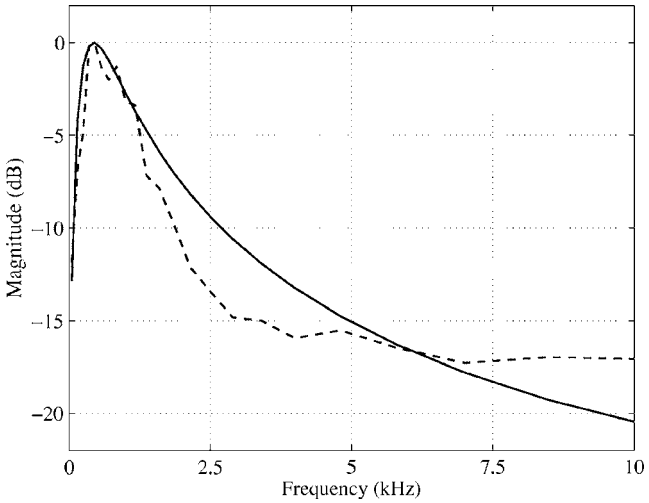

FIG. 8. The average energy difference (dashed line) and the magnitude spectrum of the tone corrector $R(z)$ (solid line).

5. Mixing coefficient

In order to determine the value of the mixing coefficient g_{mix}, the proportion of the energy of sympathetic vibrations has been investigated from the recordings. The tone was played with the sustain pedal, but after the sound had decayed 1–2 s, the string group corresponding to the tone was damped while the rest of the string register still kept ringing. The energies of two 500 ms excerpts were calculated 200 and 3000 ms after the onset of the tone, and the relation of the energies was computed. The first and the second excerpt corresponds to the tone before and after the damping, respectively. It was found that the energy difference before and after the damping is approximately −30 dB for the lowest tones and −45 dB for the highest tones.

In order to find an appropriate mixing coefficient value that produces a similar relation between the direct and artificially reverberated sound, the algorithm has been tested with input tones that are truncated after 2 s from the onset. This approximately simulates the situation, in which the strings are damped about 2 s after the onset of the tone. Based on this analysis, we have found that appropriate mixing coefficient values g_{mix} that yield similar relations between energies of the direct and reverberated sound are 0.015 for the lowest range and 0.005 for the highest range of the piano. Table V lists the used mixing coefficient values as a function of the key index.

It should be pointed out that the exact mixing coefficient value g_{mix} is not a critical issue; small changes in the value do not produce drastic changes to the output sound, provided that the value is chosen from the aforementioned range.

TABLE V. Mixing coefficient values used in the sustain-pedal algorithm.

Key index k	g_{mix}
1–16	0.015
17–28	0.01
29–40	0.008
41–54	0.006
55–88	0.005

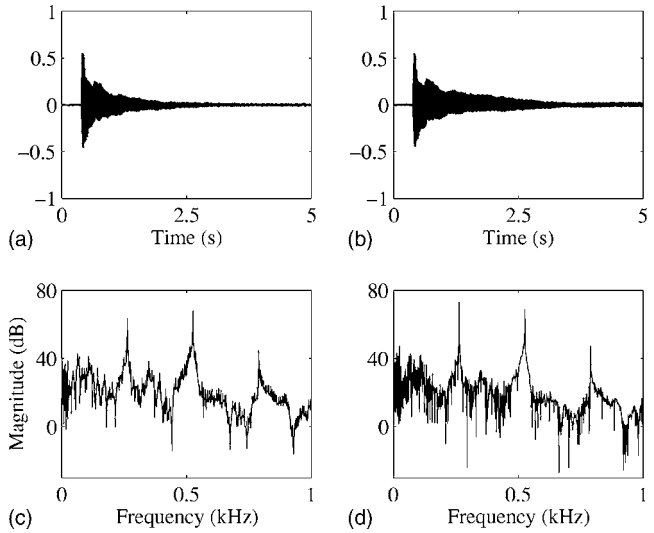

FIG. 9. Tone C4 (a) with the synthetic sustain pedal and (b) with the real sustain pedal. In (c) and (d) the magnitude spectra of the same signals are presented.

B. Results

The algorithm has been tested with recorded piano tones without the sustain pedal, and the processed tones have been compared to recorded tones with the real sustain pedal, Figures 9(a) and 9(b) illustrate the tone C4 with the synthetic and real sustain pedals in the time domain, and (c) and (d) depict the same signal in the frequency domain, respectively. The spectrum is computed with a 2^{20} point FFT using a rectangular window. As can be seen, the algorithm is able to approximately reproduce the additional spectral content between the partials. This effect was noted in Fig. 2, where the spectra of the tones with and without the sustain pedal were compared. The results are similar also in the bass and treble regions.

Additionally, the residual signals of the tones with the synthetic sustain pedal were computed and analyzed. Figure 10(a) presents the time-frequency plot of the residual signal obtained from the tone C4 with the synthetic sustain pedal. For comparison, the residual signal of the tone played with the real sustain pedal is illustrated in Fig. 10(b). The differences between the synthetic and real sympathetic vibration, the T_{60} times were measured in frequency bands 0–2000 Hz, 2000–4000 Hz, and 4000–6000 Hz. These results are listed in Table VI for three example tones: C2, C4, and C6. The T_{60} times are computed in the same way as described in Sec. III A, except that the straight line was fitted to the first 2 s of the signals. For the two highest frequency bands of the tone C6, the straight line was fitted to the first second of the signal, however, because of the fast decay.

Additionally, the residual signal energies were measured in critical bands. In Fig. 11, the solid and dashed lines represent the situation that was depicted in Fig. 5 and the dash-dotted line represents the energy of the residual signal of the tone with the synthetic sustain pedal.

In Fig. 12, the differences of the residual signal energies of the tones without and with the synthetic sustain pedal are presented in the cases of the example tones C2 (dashed line), C4 (solid line), and C6 (dash-dotted line).

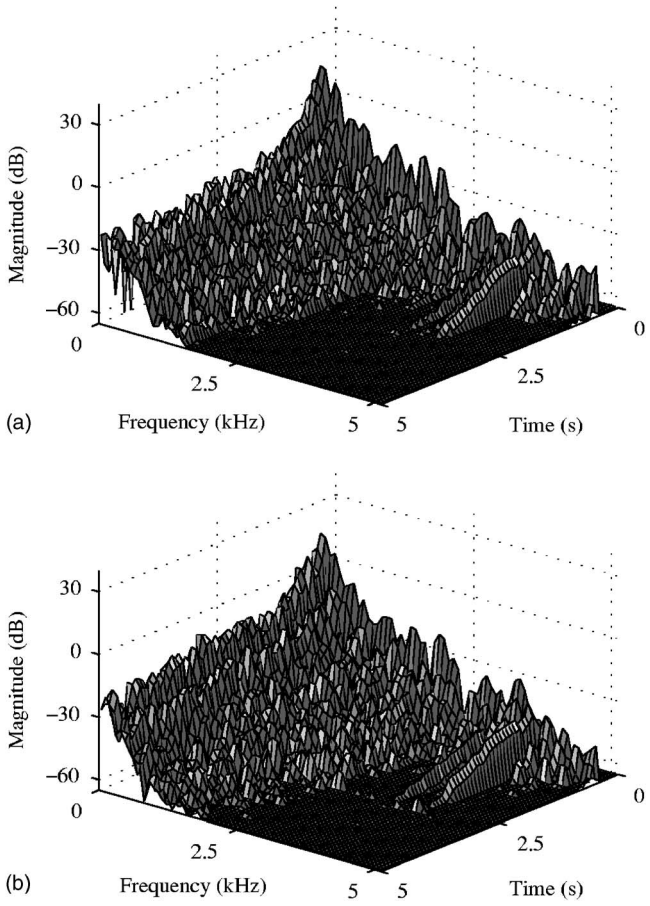

FIG. 10. Time-frequency plot of the residual signal obtained from tone C4 (a) with the synthetic sustain pedal and (b) with the real sustain pedal.

While the algorithm seems to be able to approximate the overall behavior of the real sustain-pedal device, the details of the phenomenon are not modeled perfectly. For example, the partial decay times remain the same in some cases. On the other hand, in Sec. III A it was concluded that the change in the partial decay times is generally inaudible except in the case of the tone C4. If, however, lengthening of partial decay times is of interest, it could be taken into account, for example, with an envelope generator. If the aim is to process synthetic piano sounds, the longer decay times can be taken into account already in the synthesis phase.

Tones with the synthetic sustain pedal and examples of residual signals are available for listening at the web page http://www.acoustics.hut.fi/publications/papers/jasa-piano-pedal/.

TABLE VI. Decay times T_{60} of the synthetic and real sympathetic vibrations in three frequency bands.

Tone	0–2000 Hz	2000–4000 Hz	4000–6000 Hz
C2, synthetic	8.0 s	7.0 s	6.5 s
C2, real	5.8 s	7.3 s	6.4 s
C4, synthetic	5.0 s	4.4 s	5.0 s
C4, real	5.4 s	4.7 s	5.2 s
C6, synthetic	7.4 s	1.7 s	1.8 s
C6, real	5.2 s	1.8 s	1.8 s

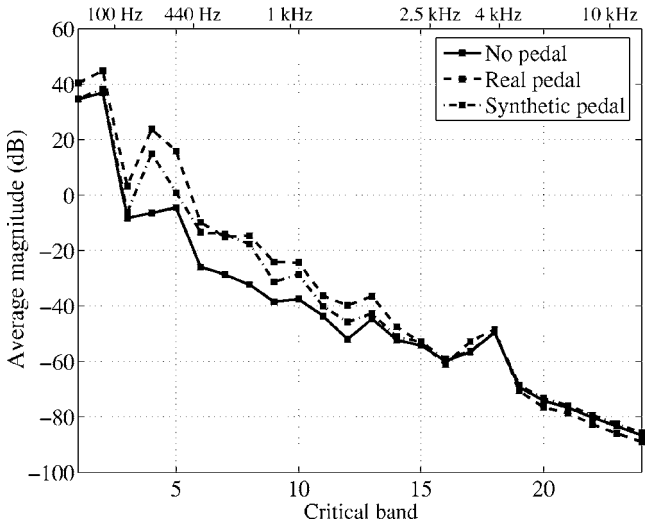

FIG. 11. Energies of the residual signals as a function of frequency on the Bark scale. The solid and dashed lines represent the cases where the tone C4 is played without and with the sustain pedal, respectively. The dash-dotted line represents the residual signal energy of the tone that has been processed with the proposed sustain-pedal algorithm.

C. Perceptual evaluation

In order to evaluate the performance of the proposed algorithm from the perceptual point of view, a listening test was conducted. In addition, the proposed algorithm was compared against a reference algorithm having 28 string models without the dispersion filters. The lowpass filters were replaced with a constant coefficient 0.998, which corresponds to that presented by De Poli *et al.*[22] Also the amount of string models is the same as the maximum amount of string models used by De Poli *et al.*[22] The mixing coefficient was chosen to be half of that used in the proposed model, and the tone corrector was the same in both algorithms.

The main goal of the test was to investigate the indistinguishability between the original tones with the sustain pedal and processed sounds with the synthetic sustain pedal in the two cases. Six subjects all having background in music and audio signal processing took the test. None of the subjects reported a hearing defect, and all had previous experiences from psychoacoustic experiments. The subjects were between 23 and 28 years of age.

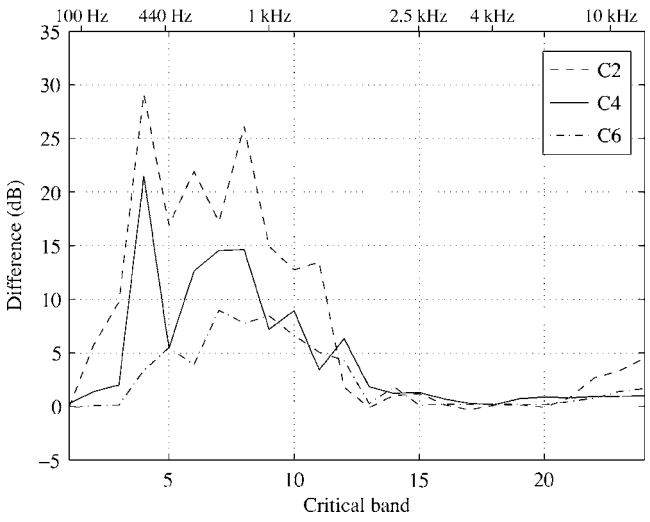

FIG. 12. Differences of the residual signal energies in the case of tones C2, C4, and C6 without the sustain pedal and with the proposed sustain-pedal algorithm as a function of frequency on the Bark scale. These results can be compared to those of Fig. 6, where the same analysis is performed to tones with and without the real sustain pedal.

The test included tones from two instruments. The first instrument (denoted as instrument No. 1) was the same grand piano that was used in the analysis part of this study, and the other one (denoted as instrument No. 2) was another Yamaha grand piano, recorded in a rehearsal room of Espoo Music School. Altogether ten tones were included in the test: tones F2, Gb3, A4, Ab5, and G7 from the instrument No. 1 and tones C1, C2, C4, C5, and G6 from the instrument No. 2. Each tone, with three types per tone (real sustain pedal, synthetic sustain pedal using 12 string models with dispersion filters and lowpass filters, and synthetic sustain pedal using 28 string models with frequency-independent damping coefficients) were repeated five times during the test in a pseudorandom order, making a total of 150 sound samples.

The listening test was conducted in a quiet room and the sound samples were presented to the subjects through Sennheiser HD 580 headphones. In the beginning of the test, the subjects took two rehearsal tests. In the first rehearsal test, they were able to familiarize themselves with five tones with the real sustain pedal and synthetic sustain pedals. The second rehearsal test simulated the actual test, where single tones were played and the subject was asked to determine whether the sustain pedal used in the tones was real or synthetic. The results from the rehearsal tests were not saved. In the actual test, after listening to each sound sample twice, they were asked whether they thought the sustain pedal was real or synthetic.

Following the procedure used by Wun and Horner,[47] the perceived quality of a synthetic sustain pedal was measured with a discrimination factor d defined as

$$d = \frac{P_c - P_f + 1}{2}, \tag{7}$$

where P_c and P_f are the proportions of correctly identified tones with synthetic sustain pedal and tones with real sustain pedal misidentified as tones with synthetic sustain pedal, respectively. The proportions are normalized in the range [0, 1]. Following the convention of Wun and Horner,[47] the tones with synthetic sustain pedal are considered to be nearly indistinguishable from the tones with the real sustain pedal, if the d factor falls below 0.75. Table VII shows the results for the tones used in the test.

From the results it can be seen that the proposed algorithm works well for the low and high range of the piano. In most cases it performs better than the reference algorithm. In the middle range the synthetic sustain pedal is distinguished from the real sustain pedal. In fact, the reference algorithm seems to work slightly better for the tones Gb3 and C4. This is reasonable, since using more string models in the algorithm yields a denser harmonic structure, which is important especially in the middle range, where the amount of relatively energetic strings is high. On the other hand, especially

TABLE VII. Results of the listening test. P and R refer to the results of the proposed and the reference model, respectively. The values that fall below 0.75 are bold for clarity.

Tone	Key index	f_0 (Hz)	Instrument	d factor/P	d factor/R
C1	4	32.8	2	**0.67**	0.82
C2	16	66.1	2	**0.50**	**0.65**
F2	21	87.4	1	**0.53**	**0.53**
Gb3	34	185.7	1	0.80	0.75
C4	40	264.6	2	0.78	0.75
A4	49	441.7	1	0.80	0.90
C5	52	526.4	2	0.83	0.93
Ab5	60	833.8	1	**0.57**	**0.68**
G6	71	1570.5	2	**0.70**	0.83
G7	83	3158.8	1	**0.57**	0.87

in the highest range the decay of the simulated sympathetic vibrations is too long if the frequency-dependent damping is not taken into account. This is probably the reason for the high d factors of the reference algorithm in highest frequency range.

After the listening test most of the subjects reported that the most difficult cases were the bass tones. The middle-range tones were the easiest ones, where the regular and metallic-sounding decay revealed the synthetic cases. In the highest region, the processed tones were judged as synthetic, if the decay process was too long and noisy.

V. CONCLUSIONS

In this paper, the effect of the sustain-pedal device in the grand piano was analyzed. Also, an algorithm for reproducing the effect was proposed. Physically, pressing the sustain pedal lifts dampers which otherwise damp a large bank of sympathetically resonating strings. From the signal analysis it was found that the energy of the residual signal increases when the sustain pedal is used, because the string register is allowed to vibrate freely. Moreover, when the sustain pedal is engaged, the decay times of the tones are longer in the middle range of the piano. This phenomenon was not, however, observed in the case of the bass and treble tones. The initial levels of the harmonics are not substantially changed when the sustain pedal is used; the observed change remains within 1 dB in all example cases. On the other hand, the amplitude beating is slightly increased, and the two-stage decay structure of the tone is not as clear as in the case where the sustain pedal is not engaged.

The proposed algorithm is based on 12 digital waveguide string models corresponding to the 12 lowest tones of the piano, and they consist of delay lines, dispersion filters, and lowpass filters. It was found that the algorithm is able to approximately reproduce the sustain-pedal effect, but the details of the sustain-pedal effect are not modeled perfectly.

A listening test was conducted in order to investigate the naturalness of tones processed with the proposed sustain-pedal algorithm. The result was that the synthetic sustain pedal in low and high tones is perceptually indistinguishable from the real sustain pedal. In the middle range, however, the synthetic sustain pedal is detected from unnaturally regular and metallic decay characteristics. In general, the proposed algorithm performs better than the reference algorithm. The results indicate that by decreasing the amount of string models and including loss filters and dispersion filters the performance of the algorithm is the same or even better than with a larger amount of string models without any filters.

At the moment, the algorithm has been tested only with recorded piano tones. In the future, the aim is to also process synthetic tones. In order to do this, the algorithm needs to be tested and properly calibrated for the synthetic tones.

ACKNOWLEDGEMENTS

This work was funded by the Academy of Finland (Project No. 104934). Heidi-Maria Lehtonen is supported by the GETA graduate school, Tekniikan edistämissäätiö, the Emil Aaltonen Foundation, and the Finnish Cultural Foundation. The work of Henri Penttinen has been supported by the Pythagoras Graduate School of Sound and Music Research. Jukka Rauhala is supported by the Nokia Foundation. Special thanks go to Risto Hemmi and Finnvox Studios for giving us the opportunity to carry out the recordings. In addition, Hannu Lehtonen is acknowledged for helping us with the recordings.

[1]G. Weinreich, "Coupled piano strings," J. Acoust. Soc. Am. **62**, 1474–1484 (1977).
[2]B. Repp, "Pedal timing and tempo in expressive piano performance: A preliminary investigation," Psychol. Music **24**, 199–221 (1996).
[3]B. Repp, "The effect of tempo on pedal timing in piano performance," Psychol. Res. **60**, 164–173 (1996).
[4]H.-M. Lehtonen, "Analysis and parametric synthesis of the piano sound," Master's thesis, Helsinki University of Technology, Espoo, Finland (2005), available at http://www.acoustics.hut.fi/publications/. Last viewed Sept. 1, 2006.
[5]A. Askenfelt, editor, *Five Lectures on the Acoustics of the Piano* (Royal Swedish Academy of Music) (1990), available at http://www.speech.kth.se/music/5-lectures/. Last viewed Feb. 15, 2007.
[6]H. A. Conklin, Jr., "Design and tone in the mechanoacoustic piano. Part I. Piano hammers and tonal effects," J. Acoust. Soc. Am. **99**, 3286–3296 (1996).
[7]H. A. Conklin, Jr., "Design and tone in the mechanoacoustic piano. Part II. Piano structure," J. Acoust. Soc. Am. **100**, 695–708 (1996).
[8]H. A. Conklin, Jr., "Design and tone in the mechanoacoustic piano. Part III. Piano strings and scale desing," J. Acoust. Soc. Am. **100**, 1286–1298 (1996).
[9]H. Järveläinen, V. Välimäki, and M. Karjalainen, "Audibility of the timbral effects of inharmonicity in stringed instrument tones," ARLO **2**, 79–84 (2001).
[10]H. Järveläinen, V. Välimäki, and T. Verma, "Perception and adjustment of pitch in inharmonic string instrument sounds," J. New Music Res. **31**, 311–319 (2003).
[11]B. E. Anderson and W. J. Strong, "The effect of inharmonic partials on pitch of piano tones," J. Acoust. Soc. Am. **117**, 3268–3272 (2005).
[12]H. A. Conklin, Jr., "Generation of partials due to nonlinear mixing in a stringed instrument," J. Acoust. Soc. Am. **105**, 536–545 (1999).
[13]B. Bank and L. Sujbert, "Generation of longitudinal vibrations in piano strings: From physics to sound synthesis," J. Acoust. Soc. Am. **117**, 2268–2278 (2005).
[14]W. Goebl, R. Bresin, and A. Galembo, "Touch and temporal behavior of grand piano actions," J. Acoust. Soc. Am. **118**, 1154–1165 (2005).
[15]J. O. Smith and S. A. Van Duyne, "Commuted piano synthesis," in *Proceedings of the International Computer Music Conference*, 335–342 (Banff, Canada) (1995), available at http://www-ccrma.stanford.edu/~jos/cs.html. Last viewed Feb. 15, 2007.
[16]B. Bank, F. Avanzini, G. Borin, G. De Poli, F. Fontana, and D. Rocchesso, "Physically informed signal processing methods for piano sound synthesis: A research overview," EURASIP J. Appl. Signal Process. **10**, 941–952 (2003).
[17]É. Ducasse, "On waveguide modeling of stiff piano strings," J. Acoust.

Soc. Am. **118**, 1776–1781 (2005).
[18]A. Chaigne and A. Askenfelt, "Numerical simulations of piano strings. I. A physical model for a struck string using finite difference methods," J. Acoust. Soc. Am. **95**, 1112–1118 (1994).
[19]J. Bensa, O. Gipouloux, and R. Kronland-Martinet, "Parameter fitting for piano sound synthesis by physical modeling," J. Acoust. Soc. Am. **118**, 495–504 (2005).
[20]J. Bensa, S. Bilbao, R. Kronland-Martinet, and J. O. Smith, "The simulation of piano string vibration: From physical models to finite difference schemes and digital waveguides," J. Acoust. Soc. Am. **114**, 1095–1107 (2003).
[21]N. Giordano and M. Jiang, "Physical modeling of the piano," EURASIP J. Appl. Signal Process. **7**, 926–933 (2004).
[22]G. De Poli, F. Campetella, and G. Borin, "Pedal resonance effect simulation device for digital pianos," U.S. Patent No. 5,744,743 (1998).
[23]J. Carrou, F. Gautier, N. Dauchez, and J. Gilbert, "Modelling of sympathetic string vibrations," Acta. Acust. Acust. **91**, 277–288 (2005).
[24]B. Capleton, "False beats in coupled piano string unisons," J. Acoust. Soc. Am. **115**, 885–892 (2003).
[25]B. Cartling, "Beating frequency and amplitude modulation of the piano tone due to coupling of tones," J. Acoust. Soc. Am. **117**, 2259–2267 (2005).
[26]S. A. Van Duyne and J. O. Smith, "Developments for the commuted piano," in *Proceedings of the International Computer Music Conference*, 319–326 (Banff, Canada) (1995), available at http://www-ccrma.stanford.edu/~jos/cs.html. Last viewed Feb. 15, 2007.
[27]D. A. Jaffe and J. O. Smith, "Extensions of the Karplus-Strong plucked-string algorithm," Comput. Music J. **7**, 56–69 (1983).
[28]J.-M. Jot and A. Chaigne, "Digital delay networks for designing artificial reverberators," in *Proceedings of the 90th AES Convention*, Paris, France (1991).
[29]W. G. Gardner, "Reverberation algorithms," in *Applications of Digital Signal Processing to Audio and Acoustics*, edited by M. Kahrs and K. Brandenburg, 85–131 (Kluwer Academic, Boston, 1998).
[30]D. Rocchesso and J. O. Smith, "Circulant and elliptic feedback delay networks for artificial reverberation," IEEE Trans. Speech Audio Process. **5**, 51–63 (1997).
[31]H. Penttinen, M. Karjalainen, T. Paatero, and H. Järveläinen, "New techniques to model reverberant instrument body responses," in *Proceedings of the International Computer Music Conference*, 182–185, Havana, Cuba (2001).
[32]V. Välimäki, H. Penttinen, J. Knif, M. Laurson, and C. Erkut, "Sound synthesis of the harpsichord using a computationally efficient physical model," EURASIP J. Appl. Signal Process. **7**, 934–948 (2004).
[33]E. Zwicker and R. Feldtkeller, *The Ear as a Communication Receiver* (The Acoustical Society of America, Melville, NY) (1999).
[34]Note that one of the example tones is a D tone (D5) and the others are C tones from different octaves. C5 was not included in the set of recorded tones.
[35]A. Galembo and A. Askenfelt, "Signal representation and estimation of spectral parameters by inharmonic comb filters with application to the piano," IEEE Trans. Speech Audio Process. **7**, 197–203 (1999).
[36]H. Fletcher, E. D. Blackham, and R. Stratton, "Quality of piano tones," J. Acoust. Soc. Am. **34**, 749–761 (1962).
[37]M. Karjalainen, V. Välimäki, and Z. Jánosy, "Towards high-quality sound synthesis of the guitar and string instruments," in *Proceedings of the International Music Conference*, 56–63, Tokyo (1993).
[38]V. Välimäki, J. Huopaniemi, M. Karjalainen, and Z. Jánosy, "Physical modeling of plucked string instruments with application to real-time sound synthesis," J. Audio Eng. Soc. **44**, 331–353 (1996).
[39]H. Järveläinen and T. Tolonen, "Perceptual tolerances for decay parameters in plucked string synthesis," J. Audio Eng. Soc. **49**, 1049–1059 (2001).
[40]J. O. Smith, "Physical modeling using digital waveguides," Comput. Music J. **16**, 74–91 (1992).
[41]M. Karjalainen and U. K. Laine, "A model for real-time sound synthesis of guitar on a floating-point signal processor," in *Proceedings of the IEEE International Conference on Acoust. Speech Signal Processing*, 3653–3656, Toronto, Canada (1991).
[42]T. I. Laakso, V. Välimäki, M. Karjalainen, and U. K. Laine, "Splitting the unit delay tools for fractional delay filter design," IEEE Signal Process. Mag. **13**, 30–60 (1996).
[43]R. Väänänen, V. Välimäki, J. Huopaniemi, and M. Karjalainen, "Efficient and parametric reverberator for room acoustics modeling," in *Proceedings of the International Computer Music Conference*, 200–203, Thessaloniki, Greece (1997).
[44]J. Rauhala and V. Välimäki, "Tunable dispersion filter design for piano synthesis," IEEE Signal Process. Lett. **13**, 253–256 (2006).
[45]J. Rauhala and V. Välimäki, "Dispersion modeling in waveguide piano synthesis using tunable allpass filters," in *Proceedings of the ninth International Conference on Digital Audio Effects*, 71–76, Montreal (2006), available at http://www.dafx.ca/proceedings/papers/p-071.pdf. Last viewed Feb. 18, 2007.
[46]A. Askenfelt and A. S. Galembo, "Study of the spectral inharmonicity of musical sound by the algorithms of pitch extraction," Acoust. Phys. **46**, 121–132 (2000).
[47]C. Wun and A. Horner, "Perceptual wavetable matching for synthesis of musical instrument tones," J. Audio Eng. Soc. **49**, 250–262 (2001).

Numerical simulations of fluid-structure interactions in single-reed mouthpieces

Andrey Ricardo da Silva[a] and Gary P. Scavone
Computational Acoustic Modeling Laboratory, Schulich School of Music, McGill University, Montreal, Quebec, Canada

Maarten van Walstijn
Sonic Arts Research Centre, School of Electronics, Electrical Engineering, and Computer Science, Queen's University Belfast, Belfast, United Kingdom

(Received 23 April 2007; revised 18 June 2007; accepted 21 June 2007)

Most single-reed woodwind instrument models rely on a quasistationary approximation to describe the relationship between the volume flow and the pressure difference across the reed channel. Semiempirical models based on the quasistationary approximation are very useful in explaining the fundamental characteristics of this family of instruments such as self-sustained oscillations and threshold of blowing pressure. However, they fail at explaining more complex phenomena associated with the fluid-structure interaction during dynamic flow regimes, such as the transient and steady-state behavior of the system as a function of the mouthpiece geometry. Previous studies have discussed the accuracy of the quasistationary approximation but the amount of literature on the subject is sparse, mainly due to the difficulties involved in the measurement of dynamic flows in channels with an oscillating reed. In this paper, a numerical technique based on the lattice Boltzmann method and a finite difference scheme is proposed in order to investigate the characteristics of fully coupled fluid-structure interaction in single-reed mouthpieces with different channel configurations. Results obtained for a stationary simulation with a static reed agree very well with those predicted by the literature based on the quasistationary approximation. However, simulations carried out for a dynamic regime with an oscillating reed show that the phenomenon associated with flow detachment and reattachment diverges considerably from the theoretical assumptions. Furthermore, in the case of long reed channels, the results obtained for the *vena contracta* factor are in significant disagreement with those predicted by theory. For short channels, the assumption of constant *vena contracta* was found to be valid for only 40% of the duty cycle.
 [DOI: 10.1121/1.2759166]

PACS number(s): 43.75.Pq, 43.75.Ef [NHF] Pages: 1798–1809

I. INTRODUCTION

The study of the acoustical properties of single-reed instruments has followed a paradigm first proposed by Helmholtz,[1] with these systems divided into linear and nonlinear components representing the instrument's bore and mouthpiece-reed, respectively.

Previous research on the resonator component has provided an extensive list of experimental and theoretical studies since the pioneering work of Bouasse.[2] Much light has been shed on the behavior of this system and, consequently, many satisfactory models have been proposed.

Conversely, the amount of available literature on the mouthpiece-reed component is considerably smaller and the majority of models rely on the quasistationary approximation to describe the flow behavior. That is, the flow in a mouthpiece with an oscillating reed is assumed to be equal, at any instant, to the flow in a mouthpiece with a static reed having the same configuration.[3] Moreover, the flow is considered to be frictionless and incompressible. Consequently, the dependence of the volume flow U on the pressure difference across the reed Δp and on the reed opening h is normally described by the Bernoulli obstruction theory based on the stationary Bernoulli equation, given by

$$U_B = hw\sqrt{\frac{2|\Delta p|}{\rho}}\,\mathrm{sgn}(\Delta p), \tag{1}$$

where w is the channel's width and ρ is the density of the fluid.

This approach was first presented by Backus,[4] whose semiempirical model was limited to low blowing pressure regimes. Years later, Worman[5] presented a more complex model addressing, in further detail, phenomena such as threshold of pressure and Bernoulli forces acting on the reed. Wilson and Beavers[6] coupled the previous model to an idealized cylindrical resonator. More recent models involving the same approach were developed by Fletcher,[7,8] Saneyoshi *et al.*[9] Kergomard,[10] and Olivier.[11]

The quasistationary approximation has also been used to derive a steady viscous flow representation by Hirschberg *et al.*[12] Their semiempirical model was based on the results obtained from the simulation of flow in a two-dimensional (Borda) tube based on the theory of potential flow. They noticed that, for Reynolds numbers $\mathrm{Re} > 10$, two patterns of

[a]Electronic mail: andrey.dasilva@mail.mcgill.ca

flow may occur simultaneously, depending on the ratio l/h, where l is the length of the channel and h is its height. The flow is fully detached along the channel, for short channels ($l/h<1$), whereas for long channels ($l/h>3$) the flow is reattached at a roughly fixed point, l_r, measured from the channel's entrance. They also observed that, in the case of short channels, the vena contracta factor $\alpha=T_j/h$ was approximately constant with a value $\simeq 0.6$, where T_j is the thickness of the jet formed at the detached portion of the flow.

van Zon *et al.*[13] provided an experimental validation of Hirschberg's model using an idealized prototype of the mouthpiece with a static reed and assuming the flow to be two dimensional. They also derived a more sophisticated flow model in which the transition between fully separated to attached flow is represented by a boundary layer solution. Other stationary measurements using realistic mouthpieces have found the same flow behavior, such as those conducted by Valkering[14] and by Dalmont *et al.*,[15] in the case of clarinet, and by Maurin,[16] in the case of saxophones.

However, previous attempts to characterize flow in dynamic regimes,[13,17] i.e., flow in a mouthpiece with a moving reed, have suggested that the stationary behavior observed by van Zon *et al.* is unrealistic. This is particularly evident in the case of the steadiness associated with the detachment/reattachment phenomenon, which is strongly affected by subtle modifications of the reed channel geometry as the reed moves. The unsteadiness of the flow modulates the aerodynamic forces acting on the reed and plays an important role in the reed's behavior. In fact, this unsteadiness is responsible for the self-sustained oscillations in systems whose acoustic coupling between the resonator and the exciter is weak or even absent. This is the case in the harmonium,[18] in the accordion,[19] and in the human phonatory system.[20–24] Moreover, the unsteadiness of the flow can explain why small modifications in a mouthpiece geometry can correspond to enormous changes in the transient behavior and the steady-state sound of single-reed instruments.[25,26]

Unfortunately, the accurate quantification and visualization of a dynamic flow controlled by a moving boundary (in this case, the reed) is a rather complicated task. For this reason, previous attempts to do so are limited to qualitative outcomes.[13,17] Similar difficulties are found when tackling the problem with unsteady numerical flow simulations using traditional computational fluid dynamic (CFD) techniques based on the *continuum* theory.[27,28]

The objectives of this paper are the presentation of a numerical model of fully coupled fluid-structure interaction in a single-reed mouthpiece in order to address the major aspects of dynamic flow and its dependency on the reed channel geometry and to verify the validity of the quasistationary theory in dynamic regimes. To accomplish that, we implement a two-dimensional dynamic model of a single-reed mouthpiece based on a hybrid numerical approach involving the lattice Boltzmann method (LBM), to represent the fluid and acoustic domains, and on a finite difference scheme to resolve the distributed model of the reed with varying cross section, as proposed by Avanzini and van Walstijn.[29] The main advantage of this approach consists in its simplicity in providing solutions of second-order accuracy to represent the fluid-structure interaction involving a moving boundary.[30] This simplicity is contrasted with the complexity and high computational demand associated with traditional CFD techniques. Furthermore, the LBM can solve the different scales associated with the flow and acoustic fields in a single calculation, thus allowing the direct representation of the acoustic-flow interaction.[31]

The influence of the player's lip and the coupling of the proposed system with the instrument's bore and player's vocal tract is not considered in this paper. Furthermore, the contribution of aeroacoustic sources on the instrument's sound content due to undisturbed flow will be left to future work.

This paper is organized as follows: Section II describes the model by presenting the lattice Boltzmann technique used, as well as the finite difference scheme to resolve the distributed reed model and the coupling between both techniques. Section III compares the results obtained from a stationary simulation with those provided by the quasistationary theory. Section IV evaluates the characteristics of a dynamic flow in a reed-mouthpiece system without acoustic coupling for three different reed channel geometries and compares the results with those expected by the quasistationary theory. Finally, the conclusions and remarks for future investigations are presented in Sec. V.

II. THE REED-MOUTHPIECE MODEL

The following describes the implementation of the two-dimensional model of the mouthpiece-reed system. The mouthpiece is represented by the LBM, which includes solid static boundaries associated with the mouthpiece walls (face, rails, and cavity walls) and the fluid domain, described in terms of acoustic and fluid fields. The moving boundary associated with the reed is represented by a distributed model of a clamped-free bar with varying cross section and resolved with an implicit finite difference scheme, as proposed by Avanzini and van Walstijn.[29]

A. The lattice Boltzmann method

The LBM is classified as a *particle* or *nonequilibrium* technique. It simulates the space-temporal evolution of fluid-acoustic systems based on a time-space discretization of the Boltzmann equation, known as the lattice Boltzman equation (LBE) [see Eq. (2)].

Xe and Luo[32] have demonstrated that the Navier-Stokes and continuity equations can be fully recovered from the LBE for low Mach numbers, namely ($\mathrm{Ma}<0.2$), by applying the Chapman-Enskog expansion, thus providing a physical validity for the method. Detailed descriptions of the LBM are provided by Succi[33] and Gladrow.[34]

The LBE controls two essential operations: advection and collision of fluid particles. These particles are described in terms of velocity distribution functions and can propagate in a discrete set of directions within the lattice.

In this paper we use an isothermal two-dimensional model known as D2Q9, after Qian *et al.*[35] In this sense, the lattice grid is represented by squared two-dimensional lattice

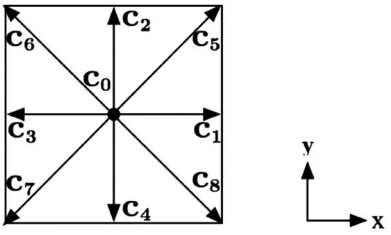

FIG. 1. The squared grid for the D2Q9 lattice Boltzmann model.

cells containing nine sites each (eight propagation directions and one rest site), as depicted in Fig. 1. Each cell connects to eight neighbor cells by the unity vectors $\mathbf{c}_i$, where $i=1,2,\ldots,8$, indicates the propagation direction associated with each site. The null vector $\mathbf{c}_0$ is associated with a nonpropagating site and plays an important role in improving the accuracy of the model by removing the unphysical velocity dependency of pressure.[36]

The two main operations, namely, advection and collision, are controlled by the LBE,

$$f_i(\mathbf{x}+c_i\Delta t,t+\Delta t)-f_i(\mathbf{x},t)=-\frac{1}{\tau}(f_i-f_i^M), \tag{2}$$

where f_i is the distribution function associated with the propagation direction i at the site $\mathbf{x}'$ and time t'. τ is the relaxation time or collision period, which acts to control the kinematic viscosity of the fluid, and f_i^M is the equilibrium distribution function for direction i, which depends on the local fluid velocity $\mathbf{u}'(\mathbf{x}',t')$ and local fluid density $\rho'(\mathbf{x}',t')$. Here and in the following, variables indicated with a prime are adimensional. The general expressions of the equilibrium function f_i^M associated with the D2Q9 model are

$$f_i^M=\begin{cases}\rho'\epsilon_i\left[1+3\mathbf{c}_i\cdot\mathbf{u}'+\dfrac{9}{2}(\mathbf{c}_i\cdot\mathbf{u}')^2-\dfrac{3}{2}\mathbf{u}'^2\right] & \text{for } i=1,2,\ldots,8\\ \rho'\left[\dfrac{4}{9}-\dfrac{2}{3}\mathbf{u}'^2\right] & \text{for } i=0\end{cases} \tag{3}$$

with $\epsilon_1=\epsilon_2=\epsilon_3=\epsilon_4=1/9$ and $\epsilon_5=\epsilon_6=\epsilon_7=\epsilon_8=1/36$.

The left-hand side of Eq. (2) represents the advection operation and determines the diffusion of the distribution functions f_i over the lattice grid. The right-hand term determines the rate at which f_i change due to intermolecular collisions between particles. This term is defined by a simplified collision function, known as BGK, after Bhatnagar, Grass, and Krook,[37] which is controlled by a single relaxation time τ for all the advection directions i. This process, known as relaxation, forces f_i toward equilibrium and restitutes the viscosity of the fluid, recovering its nonlinear form whereby the continuity and Navier-Stokes equations are satisfied.

The local macroscopic variables ρ' and $\mathbf{u}'$ are obtained in terms of moments of the local distribution functions f_i by

$$\rho'(\mathbf{x},t)=\sum_i f_i(\mathbf{x},t),\quad \rho'(\mathbf{x},t)\mathbf{u}'(\mathbf{x},t)=\sum_i f_i(\mathbf{x},t)\mathbf{c}_i. \tag{4}$$

Other macroscopic parameters such as lattice pressure p', lattice viscosity ν', and lattice speed of sound c_0' are obtained by expanding the LBE into the Navier-Stokes equation and are expressed by

$$p'=\frac{\rho'}{3},\quad \nu'=\frac{2\tau-1}{6},\quad c_0'=\frac{1}{\sqrt{3}}. \tag{5}$$

The adimensional lattice variables ρ', p', $\mathbf{u}'$, $\mathbf{x}'$, t', and ν' can be easily related to their respective physical counterparts ρ, p, $\mathbf{u}$, $\mathbf{x}$, t, and υ by the following relations: $\rho=\rho'$, $p=\rho c_0^2$, $\mathbf{u}=\mathbf{u}'c_0/c_0'$, $\mathbf{x}=\mathbf{x}'\Delta_x$, $t=\Delta_x(c_0'/c_0)t'$, and $\nu=(c_0/c_0')\Delta_x\nu'$, where c_0 is the physical speed of sound.

B. The mouthpiece model

The mouthpiece model was implemented in a lattice grid containing 1002×502 cells. The physical dimensions of the system are depicted in Fig. 2, as well as the dimensions of the grid. The lattice pitch was $\Delta x=4\times10^{-5}$ m and the time step $\Delta t=6.792\times10^{-8}$ s. As a matter of convenience, we have opted to use an undisturbed fluid density $\rho_0'=\rho_0=1.0$ kg/m^3. The relaxation time τ was chosen to be 0.505, which implies a lattice viscosity $\nu'=1.68\times10^{-3}$ and a physical kinematic viscosity $\nu=3.95\times10^{-5}$ m^2/s, using $c_0=340$ m/s as the reference speed of sound.

Although the choice of values for ρ_0 and ν differ considerably from those of air in normal playing conditions, the dynamic similarity with the real system is obtained by forcing Re$\simeq$1200 for a maximum Ma=0.1. These parameters also allow the two essential criteria of the lattice Boltzmann BGK model to be met: the maximum compressibility (Ma

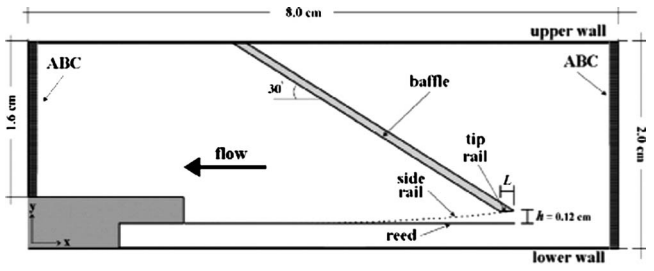

FIG. 2. Lattice grid representing the two-dimensional model of the mouthpiece-reed system.

TABLE I. Characteristics of a plastic reed (Plasticover) obtained by Avanzini and van Walstijn (Ref. 29).

Length	$L_{\text{reed}}=34\times10^{-3}$ m
Width	$w=10\times10^{-3}$ m
Density	$\rho_{\text{reed}}=500$ kg/m^3
Young's modulus	$Y=5.6\times10^{9}$ N/m^2
Viscoelastic const.	$\eta=6.0\times10^{-7}$ s
Fluid damping coef.	$\gamma_{\text{air}}=100$ s^{-1}

<0.1) before numerical instabilities[34] and a minimum grid resolution (5.6 lattices per wavelength) to avoid spurious dispersion and dissipation effects associated with the numerical bulk viscosity, as described by Crouse *et al.*[38]

C. The reed model

The reed is represented as a clamped-free bar with nonuniform thickness $b(x)$, constant width w, and driven by a force $F(x,t)$. The partial differential equation describing the vertical displacement $y(x,t)$ as a function of $F(x,t)$ is given by

$$\rho_r A(x)\frac{\partial^2 y}{\partial t^2}(x,t)+\frac{\partial^2}{\partial x^2}\left[YI(x)\left(1+\eta\frac{\partial}{\partial t}\right)\frac{\partial^2 y}{\partial x^2}(x,t)\right]=F(x,t), \tag{6}$$

where $x\in[0,L]$ is the horizontal position, $A(x)=wb(x)$ is the cross section, ρ_r is the material density, Y is the Young's modulus, $I(x)$ is the moment of area about the longitudinal axis, and η is the viscoelastic damping coefficient. Table I shows the values used in the simulation, obtained experimentally by Avanzini and van Walstijn.[29] Equation (6) considers only reed motion associated with flexural waves in the vertical direction and, thus, torsional and longitudinal modes are neglected. This is similar to the approach used by Chaigne and Doutaut[39] to simulate xylophone bars. In our model, a term associated with the energy dissipation of the reed due to the work exerted on the surrounding fluid is neglected in Eq. (6). However, this is taken into account implicitly by the fully coupled fluid-structure interaction scheme presented in Sec. II E.

Equation (6) is solved by performing a space-temporal discretization based on an implicit finite difference scheme described by Chaigne and Doutaut.[39] This results in a matricial difference equation in which the spatial coordinate is vectorialized,

$$\mathbf{y}(n+1)=\mathbf{A}_0\cdot\mathbf{y}(n)+\mathbf{A}_1\cdot\mathbf{y}(n-1)+\mathbf{A}_F\cdot\mathbf{F}(n), \tag{7}$$

where $\mathbf{y}(n+1)$, $\mathbf{y}(n)$, and $\mathbf{y}(n-1)$ represent the displacement vector at successive time instants and $\mathbf{A}_0$, $\mathbf{A}_1$, and $\mathbf{A}_F$ are coefficient matrices. $\mathbf{F}(n)$ is a vector representing the longitudinally distributed force on the reed. The interaction between the reed and the mouthpiece lay is considered to be inelastic. This is achieved by nullifying the kinetic energy of those reed sections that collide with the mouthpiece side rail, which presents an upper boundary to the reed. The inelastic assumption for the reed/lay interaction is discussed and justified in Ref. 29.

D. Initial and boundary conditions

The algorithm assumes a no-slip condition of flow at the walls by implementing a bounce-back scheme proposed by Bouzidi *et al.*[40] The bounce-back scheme works to invert the direction of propagation of a distribution function f_i just before it reaches a solid boundary. This procedure creates a null fluid velocity at the walls and provides second-order accuracy to represent viscous boundary layer phenomena.

The problem of a moving boundary, the reed, within the lattice is tackled by using an interpolation scheme proposed by Lallemand and Luo.[30] This technique preserves second-order accuracy in representing the no-slip condition and the transfer of momentum from the boundary to the flow. One constraint of this approach is the velocity limit defined by $\text{Ma}<0.5$, $\text{Ma}=u_b/c_0$, u_b being the velocity of the boundary. However, such a limitation does not represent a problem in our simulation because it corresponds to values of velocity much higher than those found for reeds at normal playing conditions.

The mean flow is initiated by using a fairly well known technique in CFD called absorbing boundary conditions (ABC). This technique has been adapted to LBM by Kam *et al.*[41] and consists in using a buffer between the fluid region and the open boundary to create an asymptotic transition toward a target flow defined in terms of target distribution functions f_i^T. This is done by adding an extra term to Eq. (2) to represent the transition region,

$$f_i(\mathbf{x}+c_i\Delta t,t+\Delta t)-f_i(\mathbf{x},t)=-\frac{1}{\tau}(f_i-f_i^M)-\sigma(f^M-f_i^T), \tag{8}$$

where $\sigma=\sigma_m(\delta/D)^2$ is the absorption coefficient, σ_m is a constant, normally equal to 0.3, is the distance measured from the beginning of the buffer zone, and D is the width of the buffer. The f_i^T is constant and can be obtained in the same manner as f_i^M using Eq. (3), where the local velocity $\mathbf{u}'$ and local density ρ are replaced by the desired target flow u^T and target density ρ^T, respectively. Another desired feature of this technique is the anechoic characteristic that avoids any reflection or generation of spurious waves at the open boundaries.

E. Numerical procedures

Seven different operations are executed at every time step in order to couple the lattice Boltzmann model with the finite difference scheme. The sequence of operations is depicted as a flowchart in Fig. 3. Before the simulation begins, the initial conditions associated with the fluid and reed variables are set and the definition of solid boundaries within the lattice are defined. The reed variables such as displacement $y(x,0)$, velocity $\dot{y}(x,0)$, and force $F(x,0)$ are set to zero, as well as the variables associated with the fluid domain, such as the local fluid velocities $\mathbf{u}$. The initial fluid variables are used to define the initial distribution functions based on Eq. (3), so that, in the first time step $f_i=f_i^M$. The flow is started by prescribing a target pressure difference at the ABC layer, defined as $\Delta p^T=(\rho_{\text{in}}^T-\rho_{\text{out}}^T)c_0^2$, where the indexes "in" and

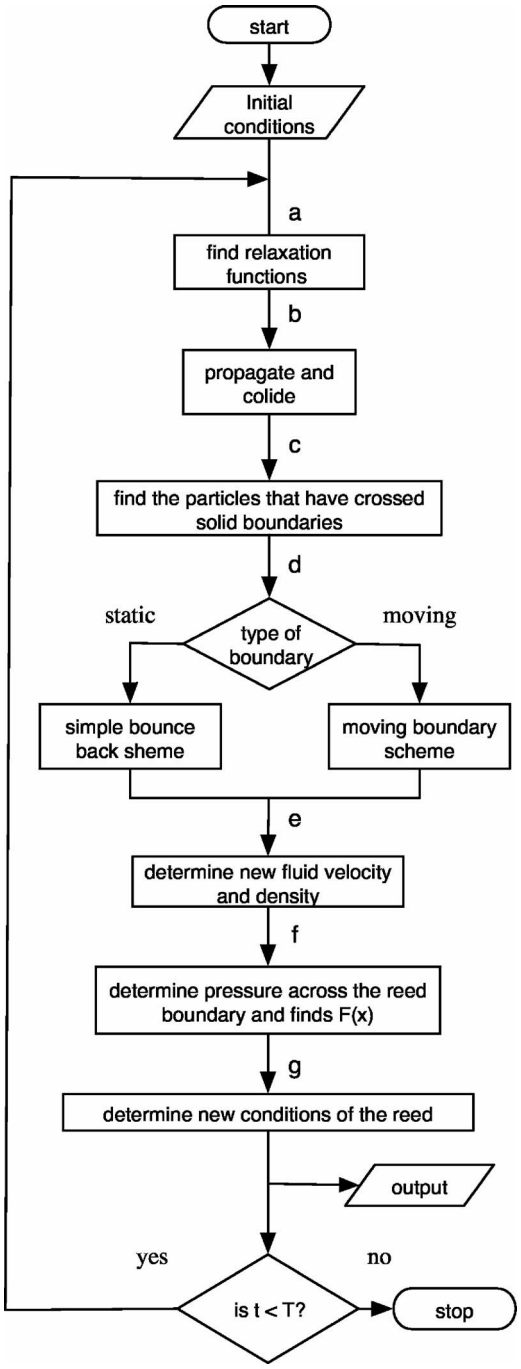

FIG. 3. Flowchart of the integrated algorithm.

"out" indicate inlet and outlet, respectively. The values of Δp^T depend on the type of simulation being conducted and are described in the next sections of this paper.

With respect to the flowchart in Fig. 3, the following operations take place after the initial conditions are set: (a) calculate the relaxation functions f_i^M's using Eq. (3); (b) propagate f_i to all directions, ignoring the presence of predefined solid boundaries and perform their relaxation based on Eq. (2); (c) find the lattice positions of f_i that have crossed solid boundaries during the propagation step in (b); (d) replace f_i found by the previous operator with new values based on two different interpolation strategies: f_i at crossed static boundaries are replaced by values calculated using the simple bounce-back scheme, proposed by Bouzidi *et al.*[40] Otherwise, f_i are replaced by values calculated using the moving boundary scheme proposed by Lallemand and Luo.[30] In this case, the calculation of the new f_i requires the actual values of $\dot{y}(x,t)$ in order to take into account the transfer of momentum from the reed to the flow; (e) determine new values of $\mathbf{u}'$ and ρ' using Eq. (5); (f) evaluate the new distributed force $F(x,t)$ on the reed model based on local lattice pressures across the reed boundary; and (g) calculate the reed's new position $y(x,t)$ and velocity $\dot{y}(x,t)$.

III. QUASISTATIC MODEL

The following compares the results obtained for a stationary simulation (static reed) using the model described in Sec. II with the results provided by the quasistationary approximation for two-dimensional flows in single-reed mouthpieces with constant channel cross section, as proposed by van Zon *et al.*[13] The model was based on the results from a stationary measurement involving an idealized two-dimensional prototype of the mouthpiece-reed system. Similar measurements using real mouthpieces have found identical results and were conducted by Valkering[14] and Dalmont,[15] in the case of a clarinet, and by Maurin,[16] for the saxophone.

A. Overview of the analytical model

Hirschberg *et al.*[12] derived a semiempirical analytical model for the viscous steady flow in a two-dimensional single-reed mouthpiece channel with constant height. The model was based on the numerical study of a two-dimensional channel (Borda tube) using a potential flow scheme.

They observed two types of flow for Reynolds numbers $\mathrm{Re} > 10 (\mathrm{Re} = U/w\upsilon)$, depending on the ratio between the channel height h and its length l. In both cases, a jet is formed at the sharp edges of the channel's entrance. For small ratios $(l/h \leqslant 1)$, the jet does not reattach along the channel walls, whereas, for high ratios $(l/h \geq 3)$, the jet reattaches at a fixed point $l_r \simeq h$ measured from the channel's entrance.

Thus, in the case of short channels, the flow is described by the Bernoulli equation [Eq. (1)] scaled with a constant vena contracta factor α, whereas, in the case of long channels, the detached segment is represented by the Bernoulli flow and the reattached part is represented by the Poisseuille flow.

These results were confirmed experimentally by van Zon *et al.*[13] who derived a more accurate steady flow model in which the transition between fully separated to Poisseuille flow is described by a boundary layer flow. In this case, the velocity profile $u(x,y)$ within the boundary layer of thickness $\delta(x)$ is assumed to increase linearly with the distance y from the wall.

Similar to the model proposed by Hirschberg *et al.*, the flow in short channels $(l/h \leqslant 1)$ is given by

$$U = \alpha U_B, \tag{9}$$

where U_B is the Bernoulli flow given by Eq. (1) and α, $0.5 \leqslant \alpha \leqslant 0.61$ is the constant vena contracta factor whose value depends on the external geometry of the mouthpiece.

For long channels ($l/h \geq 4$) and $\delta(l) > \delta_c$, where δ_c is the critical boundary layer thickness, van Zon *et al.* describe the volume flow by

$$U = \frac{\nu w}{ch}(l_c - l_r). \tag{10}$$

The term $(l_c - l_r)$ is the length of the transition between fully separated flow to Poisseuille flow, given by

$$\frac{l_c - l_r}{l - l_r} = \frac{12c(1-\delta^*)^2}{24c-1}\left[1 - \sqrt{1 - \frac{h^4(24c-1)\Delta p}{72\rho\nu^2(l-l_r)^2(1-\delta^*)^2}}\right], \tag{11}$$

where δ^* is the generalization of the critical boundary layer thickness δ_c for a channel of arbitrary height h, expressed by

$$\delta^* = \frac{\delta_c}{h} = \frac{4}{9}\left(1 - \sqrt{\frac{5}{32}}\right) = 0.2688 \tag{12}$$

and

$$c = \frac{1}{6}\left[4\delta^* + 9\ln(1-\delta^*) + \frac{5\delta^*}{1-\delta^*}\right] = 0.01594. \tag{13}$$

B. Stationary results

The stationary simulations were conducted for different cases involving geometries with the same characteristics as that shown in Fig. 2, but with different channel profiles as depicted in Fig. 4. For each geometry, different steady-state values of U are achieved by prescribing different target pressure values Δp^T from 0 to 9 kPa. The simulations used the same characteristics described in Sec. II in terms of initial and boundary conditions, lattice discretization, and fluid properties. However, in this case the reed is maintained fixed (or static) throughout the simulations.

Figure 5(a) presents the numerical results obtained for the three cases in terms of vena contracta factor $\alpha = U/U_B$ as a function of the modified Reynolds number proposed by van Zon *et al.*[13] These results are compared with those predicted by the quasistationary model presented in the previous section. For short channels, the values of α were chosen to represent two geometry cases, namely, a slit in an infinite wall and a tube with sharp edges (Borda tube). According to potential flow theory,[42] α is determined by the turning angle of the upstream flow into the channel, which depends on the characteristics of the external geometry. For the slit in an infinite wall, one finds $\alpha = 0.61$, whereas for the Borda tube $\alpha = 0.5$. Therefore, in the case of a short single-reed mouthpiece channel ($l/h \leqslant 1$), one should expect an intermediate value between the two extreme cases, i.e., $0.5 \leqslant \alpha \leqslant 0.61$. Figure 5(b) plots the same simulation results in terms of volume flow U as a function of the pressure difference Δp and compares that with the theory provided for short and long channels as presented in Sec. III A.

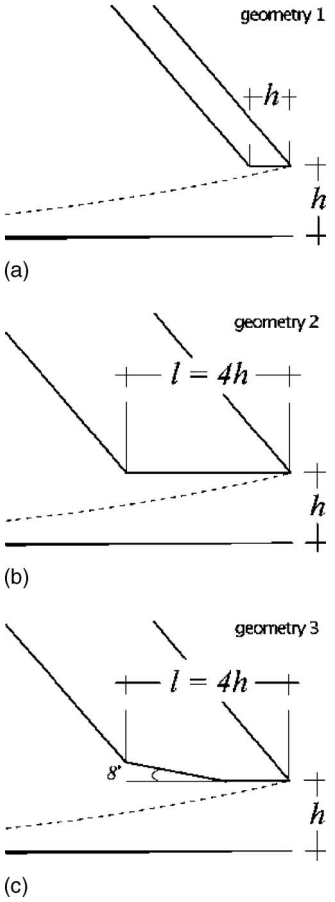

FIG. 4. Different reed channel profiles used in the simulation: (a) $L/h = 1$, (b) $L/h = 4$, and (c) $L/h = 4$ with a chamfer.

In general, Figs. 5(a) and 5(b) show that the results obtained for geometries 1, 2, and 3 agree very well with the theory presented in Sec. III A. However, Fig. 5(a) shows that the result for geometry 1 is in considerable disagreement for $h\,\mathrm{Re}/(l-s) < 60$ when compared with the limits provided by the theory for short channels and fully detached flow ($0.5 \leqslant \alpha \leqslant 0.61$). This type of disagreement is commonly reported in the literature and is attributed to the influence of viscous effects at low Reynolds numbers, as described by Durrieu *et al.*[43] and Blevins.[44] Curiously, the results obtained for geometry 2 are very similar to those found for geometry 3 and agree very well with those predicted by the theory for long channels [Eq. (10)], despite the fact that geometry 3 has a rather diverging channel profile due to the presence of the chamfer.

The flow profiles were found to be roughly constant for all geometries. In the first geometry, the flow remained fully separated for $\mathrm{Re} > 30$, whereas in geometries 2 and 3 the flow separated at the beginning of the channel and reattached at $l_r \simeq 2h$ for $\mathrm{Re} > 60$.

IV. DYNAMIC RESULTS

The goal of the following is to investigate the main aspects of the fluid-structure interaction in dynamic regimes by using the same geometries investigated in Sec. III (Fig. 4). We also intend to substantiate the validity of quasistationary theory by evaluating the main assumptions associated with

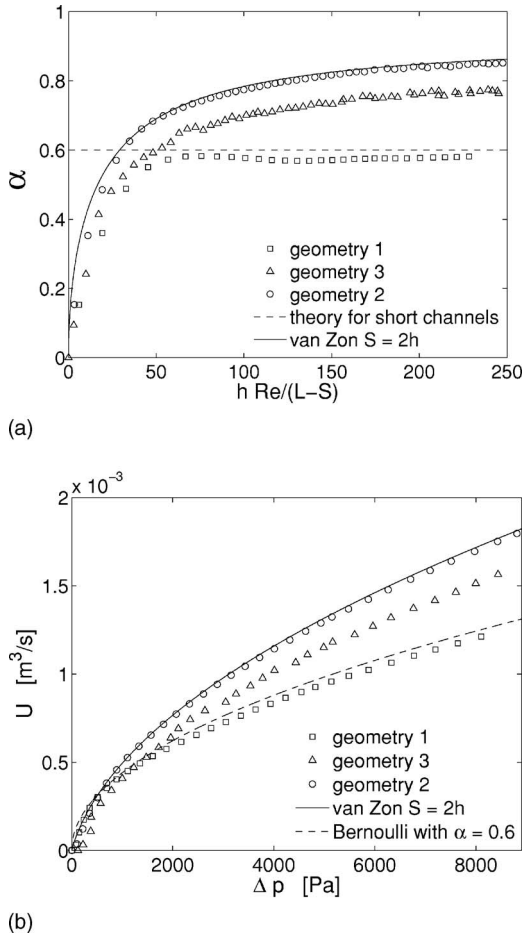

FIG. 5. Comparison between theory and numerical results for a stationary reed: (a) Vena contracta factor as a function of the modified Reynolds number and (b) pressure difference across the reed channel as a function of the volume flow.

the steadiness of the flow reattachment point and steadiness of the vena contracta factor when the oscillation of the reed is taken into account.

For all three cases, we use the same initial and boundary conditions described in Sec. II. The flow is initiated by prescribing $\Delta p^T = 5$ kPa. This value corresponds to a middle point between the threshold of oscillation and the maximum pressure found for a clarinet mouthpiece.[15] It must be stressed that the ABC scheme used at the inlet and outlet of the system (Fig. 2) provides a complete anechoic behavior, which avoids any sort of acoustic coupling between the reed and the upstream and downstream chambers. Therefore, the reed can only move if an aerodynamic force F_B exists due to flow detachment with an ensuing reattachment.[25] This aerodynamic force can explain the movement of the reed during the transient state of the flow but its existence alone is, however, insufficient to explain a self-sustained oscillatory regime. This can only happen when the net energy exchanged between the flow and the reed during one duty cycle is positive: $E = \int_0^T \overline{F_B} \cdot \dot{y}_{\text{tip}} > 0$, where $\overline{F_B}$ is the space averaged aerodynamic force on the reed and $\dot{y}_{\text{tip}}$ is the velocity of the reed measured at its tip. In other words, the amount of energy absorbed by the reed from the flow during one duty cycle has to be greater than the energy imparted to the flow by the reed. As explained by Hirschberg,[25] in the absence of acoustic coupling, a positive net energy after one duty cycle is possible due to several reasons: (a) the difference in the reed channel geometry between opening and closing phase; (b) the inertia of the flow in the channel;[18] and (c) variability of the separation/reattachment point behavior.[21]

A. General results

Figure 6 depicts the time histories associated with displacement of the reeds measured at their tips for all geometries. The self-sustained oscillation regime is achieved for all geometries in Fig. 4. The long channel geometries depicted in Figs. 4(b) and 4(c) present very similar behavior with high oscillation amplitudes, which forces the tip of the reed to close the channel completely. For the geometry with the short channel [Fig. 4(a)], the reed oscillation is roughly

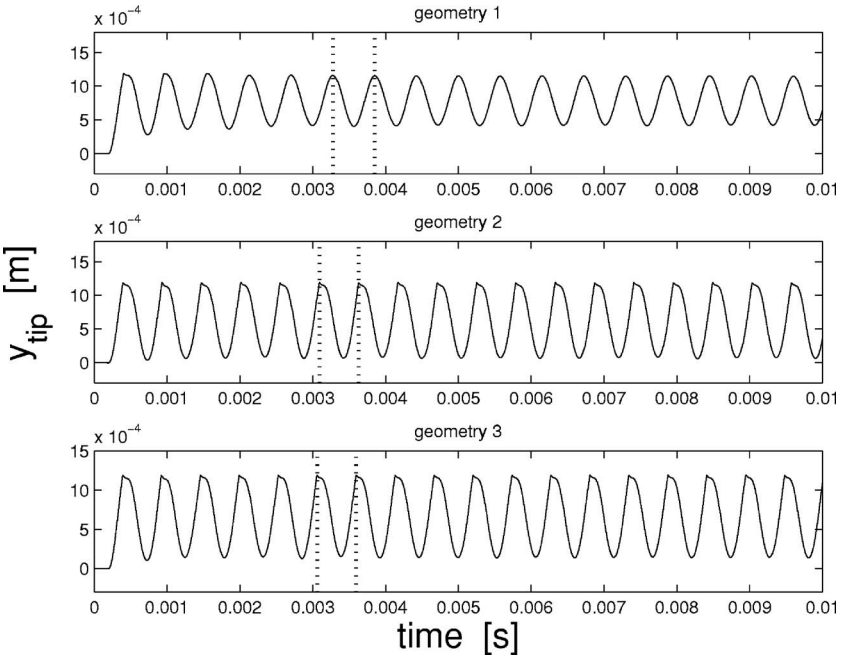

FIG. 6. Time histories of the reed displacement measured at the tip for different channel geometries.

sinusoidal and the average value of the tip displacement $y_{tip} \simeq 8.0 \times 10^{-4}$ m. Long-channel geometries present similar oscillation periods that are $\simeq 6.5\%$ shorter than those found for the short-channel geometry. This vibratory behavior at a frequency close to the reed's first natural frequency f_0 was expected, given the absence of acoustic coupling between the reed and the downstream and upstream cavities.

Further analysis was carried out by investigating the dynamic characteristics of one single oscillation period. The selected duty cycles are related to the sixth oscillation period of each case and are indicated between dashed lines in Fig. 6.

Figure 7(b) shows the normalized energy flows $\dot{E} = \overline{F_B} \dot{y}_{tip}$ as a function of time in terms of fraction of one duty cycle. The negative areas indicate transfer of energy to the flow due to the work of the reed. They take place during the phases associated with the opening of the reed, as shown in Fig. 7(a). Conversely, the positive areas in Fig. 7(b) take place when the reed is closing and represent the energy absorption by the reed due to flow work. In the regions of negative energy flow, $\dot{y}_{tip}$ and $\overline{F_B}$ are out of phase but become in phase as the reed starts to close again. In all cases, the shift from negative to positive energy flow also coincides with the maximum volume flow U, shown in Fig. 7(c). These results present the same behavior found in the experiments conducted by Thomson[23] for an idealized model of the human larynx.

The high amplitudes of oscillation found in the case of long-channel geometries are explained by the higher ratios between absorbed E^+ and lost energy E^- during one cycle, as shown in Table II. The excess of energy given to the reed is dissipated internally by the viscous damping predicted by the third term on the right-hand side of Eq. (6) and by the inelastic collision of the reed against the side lays of the mouthpiece. Furthermore, Fig. 7(b) shows that the reeds in the long-channel geometries start to receive energy from the flow at 0.6 T of the duty cycle, which represents a delay of 0.13 T compared to the short channel geometry. This is due to a higher flow inertia caused by larger fluid volume within long channels and due to the effect of flow driven by the moving reed, as will be discussed later in this paper. Table II presents some aspects related to the oscillation frequencies achieved by each geometry, as well as aspects related to the energy exchange between the flow and the reed.

Figure 8 provides a better understanding of the results presented in Figs. 7(a)–7(c) by depicting snapshots of the normalized velocity field $u_{norm} = (u_x^2 + u_y^2)^{1/2} / \max(u_x)$ in the mouthpiece models, taken at four different instants within the same duty cycle.

In all cases, a jet is formed at the channel's entrance as the reed starts to open. At this point, the jet rapidly adheres to the rail tip but remains detached elsewhere. This situation continues until the gradient of pressures between the jet and the reed is enough to force the jet to attach to the reed's surface. The gradient is originated by the entrainment of flow between the jet and the reed wall due to viscous momentum transfer and it is proportional to the downstream volume flow. This phenomenon, known as the Coanda effect, plays

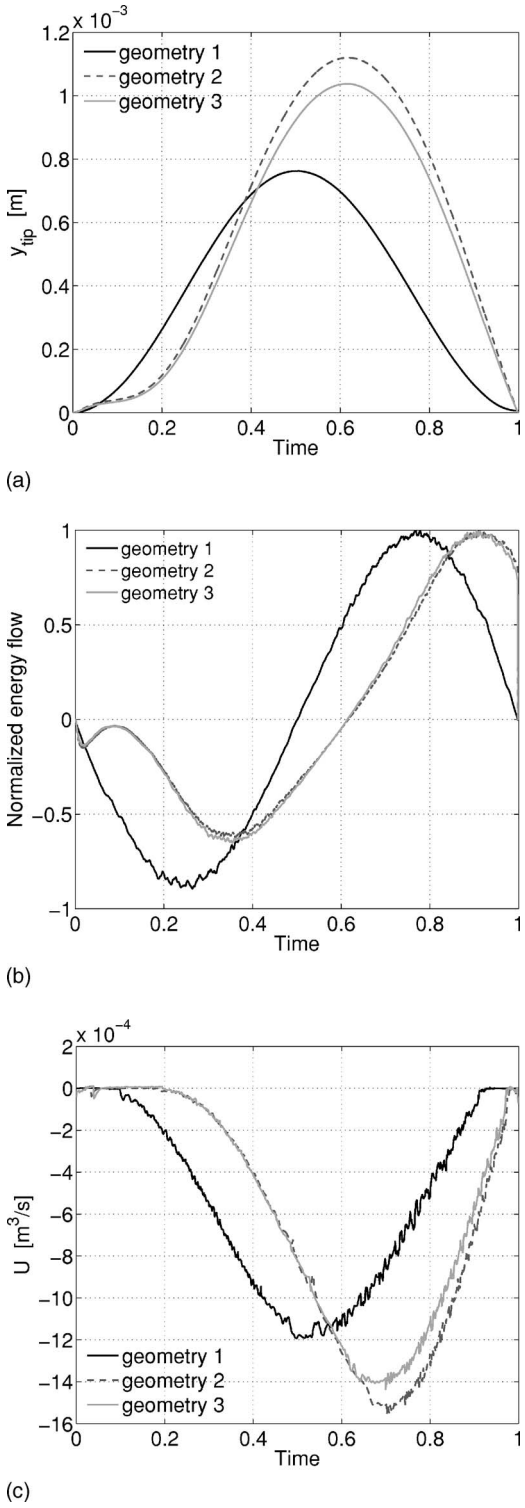

FIG. 7. Oscillation characteristics as function of time in terms of fraction of one duty cycle: (a) channel aperture, (b) normalized energy flow, and (c) volume flow.

an important role in the self-sustained oscillations in vocal folds[20–24] and in reed instruments such as the accordion[19] and the harmonium.[18]

During the opening stage the volume flow U in the short channel accelerates earlier into the mouthpiece chamber. In fact, for the same channel aperture y_{tip}, the volume flow into the short channel is much higher than that into the long-

TABLE II. Aspects of dynamic flow in the different channel profiles.

	L/h	f(Hz)	f/f_0	E	$\lvert E^+/E^- \rvert$
Geometry 1	1	1760.3	1.00	120.28	1.10
Geometry 2	4	1877.2	1.07	188.59	1.24
Geometry 3	4	1855.7	1.06	179.30	1.22

channel geometries, as shown in Figs. 7(a) and 7(c). The early acceleration provides the necessary pressure gradient for the jet to detach from the rail tip and adhere on the reed at $\simeq$0.5 T, in contrast with the long channel geometries in which the same phenomenon happens at $\simeq$0.7 T, as depicted in Fig. 8. The separation/adhesion phenomenon is confirmed by the determination of the skin friction based on the shear stress on the reed surface.

As already mentioned, there are two explanations for the early volume acceleration in the case of the short channel. First, the fluid volume within the channel has a reduced inertia. The second reason is attributed to the effect of the flow driven by the reed U_{wall}. This is because, in the case of a dynamic regime, the effective volume flow can be expressed by $U=U_{\Delta p}+U_{\text{wall}}$, where $U_{\Delta p}$ is the flow driven by the pressure difference Δp across the reed channel. Thus, during the opening stage the reed exerts work on the flow by pulling it out of the mouthpiece chamber in the upstream direction, which means that $U_{\Delta p}$ and U_{wall} are out of phase. In short channels, the influence of U_{wall} on the effective flow U is much smaller than in the case of long channels, which explains the early acceleration.

The effect of U_{wall} also becomes significant at instants near the complete closure of the channel ($0.9T \leqslant t \leqslant 1$). During this period, $U_{\Delta p}$ and U_{wall} are in phase and U_{wall} may become higher than $U_{\Delta p}$, which could explain the considerable unsteadiness of the flow at this fraction of the duty cycle. This phenomenon has been reported by Deverge *et al.*[45] in the case of experiments involving prototypes of the human glottis. In their observations, however, the effect of U_{wall} seems to be more evident in channels with constant

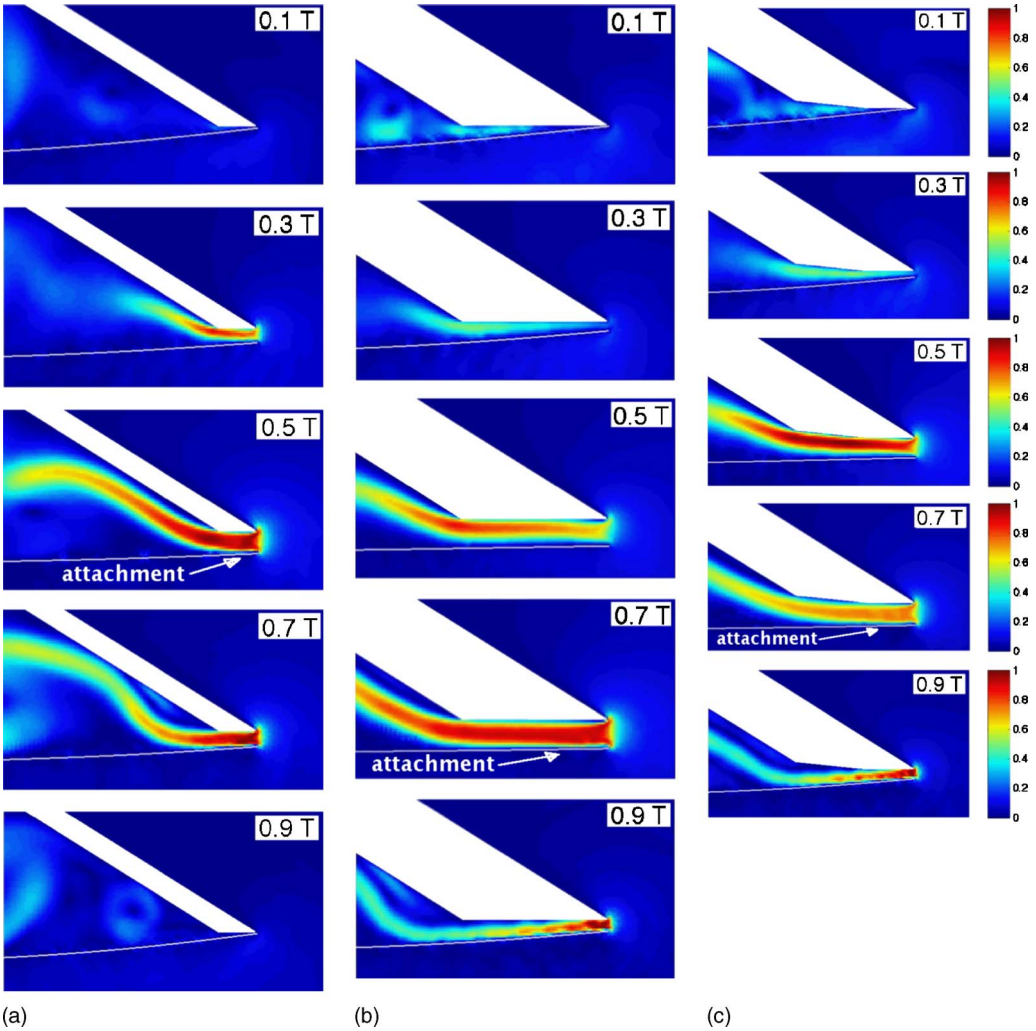

FIG. 8. (Color online) Snapshots of the velocity field for different instants within the same duty cycle: (a) $L/h=1$, (b) $L/h=4$, and (c) $L/h=4$ chamfered.

height. This fact contrasts with our case in which the reed channel becomes divergent near the closure stage.

Furthermore, the aerodynamic force F_B caused by the pressure gradient increases when the jet attaches to the reed and becomes proportional to the attachment length. This explains the higher oscillation amplitudes in geometries 2 and 3. The increase in F_B acts to decelerate the reed until it stops. At this point, $\dot{y}_{\text{tip}}$ and $\overline{F_B}$ become in phase and the reed starts to receive energy from the flow. The stronger F_B in long channels also explains the positive pitch shift in these geometries, because a stronger F_B forces the reed to close more rapidly.

B. Discrepancy from the quasistationary predictions

The snapshots of flow during one duty cycle depicted in Fig. 8 show some fundamental deviations between the quasistationary assumptions and the numerical results regarding the detachment/adhesion phenomenon. In the case of the short channel geometry, Fig. 8(a), the constant fully separated flow assumed in the quasistationary theory has not been observed. In fact, for the first half of the duty cycle the flow is detached from the reed but remains attached to the rail tip. For the second half of the duty cycle the flow attaches to both reed and rail tip.

The results for geometries 2 and 3, Figs. 8(b) and 8(c), are very self-similar. The presence of a chamfer in geometry 3 did not play a significant role on the stability of the attachment phenomenon. In those cases, the flow remains detached from the reed for nearly $\simeq$70% of the duty cycle. At $\simeq$0.7 T, the flow adheres to the reed and gradually detaches from the rail tip until the complete channel closure. This pattern contrasts with the theory, which assumes a constant separation region between the channel's entrance and $l_r=2h$ and full attachment of the flow afterwards.

As expected, the numerical results for the vena contracta factor also diverge considerably from the theoretical predictions. Figure 9 depicts the comparison between numerical and theoretical values for α along one duty as a function of the modified Reynolds number proposed by van Zon *et al.* The hysteresis observed for all cases in Fig. 9 agrees qualitatively with that found in a dynamic flow measurement conducted by van Zon *et al.*[13] The hysteresis observed in the short channel geometry [Fig. 9(a)] is much smaller than that observed in the remaining cases [Figs. 9(b) and 9(b)]. This is probably due to a less significant influence of the flow driven by the reed U_{wall}, as previously discussed. Furthermore, the flow adhesion segment is much shorter in the case of geometry 1, which minimizes the contribution of shear dissipation on the hysteresis. Figure 10 depicts the numerical values of α as a function of time in terms of fraction of a duty cycle. For the short channel, the values of α remain constant for only 35% of the duty cycle, namely $0.50\ \text{T} \leqslant t \leqslant 0.85\ \text{T}$. The values of α become very unstable as the reed approaches the closed position. As already discussed, this characteristic is attributed to the effect of U_{wall}, which becomes higher than the flow driven by the pressure difference across the reed channel.

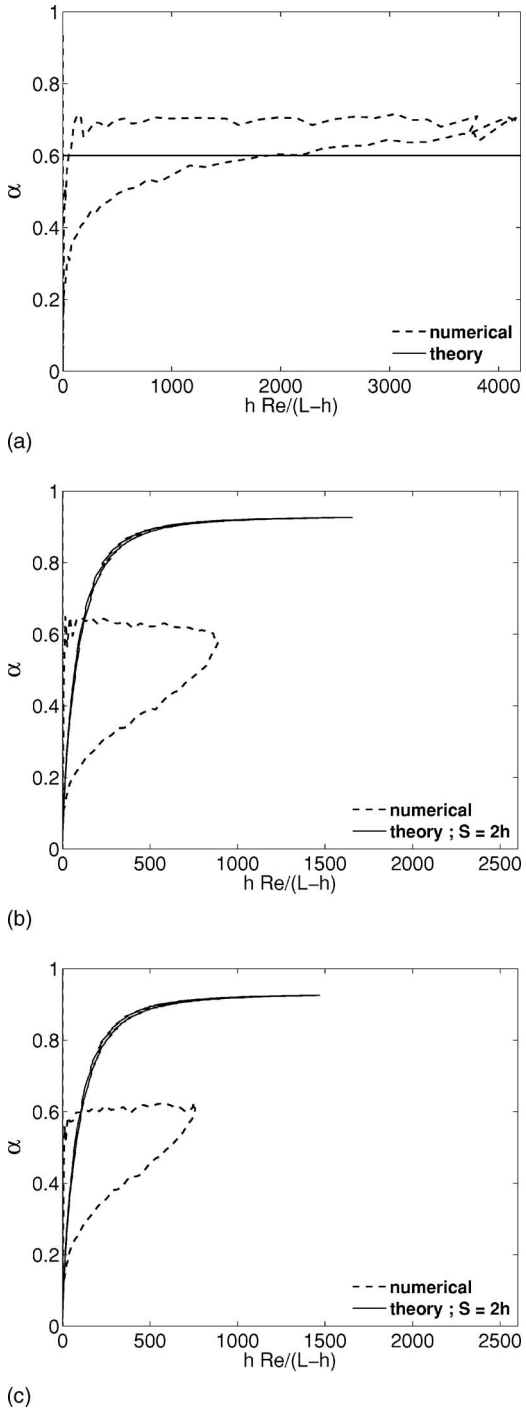

FIG. 9. Numerical and theoretical results for the vena contracta factor as function of the modified Reynolds number: (a) geometry 1, (b) geometry 2, and (c) geometry 3.

V. CONCLUSIONS

We propose a numerical technique based on the lattice Boltzmann and finite difference methods to represent the problem of fully coupled fluid-structure interaction in single reed mouthpieces. The model provides second-order accuracy at representing boundary layer phenomena and was used to evaluate the behavior of three different reed channel geometries in two types of regimes, namely, stationary and dynamic. The stationary results agree very well with those predicted by the quasistationary theory, in terms of volume flow

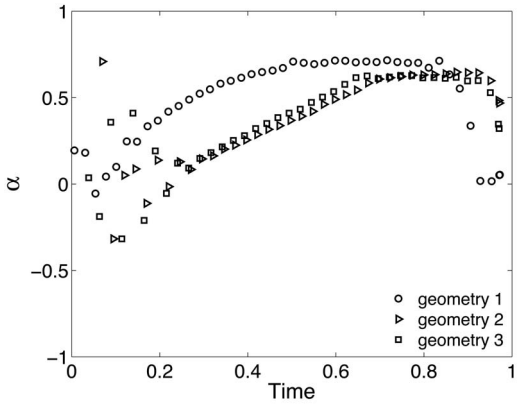

FIG. 10. Numerical values for the vena contracta factor as function of time for one duty cycle.

and vena contracta factor. Furthermore, we observed the same behavior found experimentally by van Zon *et al.*,[13] associated with the steadiness of the vena contracta factor for different Reynolds numbers, in the case of short channels, and with the steadiness of the detachment / reattachment phenomenon in long channels.

However, the results obtained during the dynamic simulations are very different from those predicted by the quasistationary theory. For the short channel geometry, α was found to be constant for only $\simeq$40% of the duty cycle, and for long channels, the values of α were in stark disagreement with the quasistationary predictions. Moreover, the patterns observed in stationary measurements such as fully detached flow, in the case of short reed channels, and the twofold pattern, in the case of long channels, were not observed in the dynamic simulations. The main difference in the flow behavior between short and long channels was found to be the time taken by the flow to adhere on the reed wall within one duty cycle. This characteristic was attributed to the effect of inertia associated with different fluid volumes within the reed channel and to the flow driven by the reed. The results also show that different levels of self-sustained oscillations can be achieved in the absence of acoustic feedback due to the complexity of hydrodynamic forces acting on the reed, which supports the hypothesis proposed by Hirschberg *et al.*[12,25] in the case of single reed mouthpieces.

The two-dimensional nature of our numerical approach restricts the results to a qualitative analysis. Another limitation is associated with the lack of acoustic feedback, which neglects eventual influences of the acoustic field on the flow within the reed channel. Nevertheless, we feel it is worthwhile to focus on the aerodynamicaly oscillating situation presented in this paper. The widespread assumptions made in modeling wind instrument reeds that have been reported many times in this journal and others are based on a quasistationary assumption that itself does not take into account the influence of the acoustic field on the flow behavior. The simulations reported in this paper show that there are significant deviations from these long held assumptions that call into question the validity of the currently accepted model. These deviations might easily be obscured in the presence of acoustic feedback. Furthermore, the approach presented in this paper contributes to our understanding of the behavior of dynamic flow in single-reed mouthpieces and its dependency on the characteristics of the reed channel geometry.

More investigations are needed in order to understand the behavior of the dynamic flow when the acoustic coupling between mouthpiece-reed system and resonator is taken into account. Another interesting step could be taken in order to investigate the mechanisms of energy transfer between flow and the acoustic field, as well as the characterization of aeroacoustic sources in the mouthpiece and its contribution to the instrument's sound content.

ACKNOWLEDGMENTS

The authors would like to thank Professor Luc Mogeau and the anonymous reviewers of this paper for their helpful suggestions. A.R.d.S wishes to thank CAPES (Funding Council of the Brazilian Ministry of Education) for supporting his doctoral research.

[1] H. L. F. Helmholtz, *On the Sensations of Tone as a Physiological Basis for the Theory of Music* (Dover, New York, 1877).
[2] H. Bouasse, *Instruments à Vent (Wind Instruments)* (Blanchard, Paris, 1929), Vols. I and II.
[3] S. S. Chen, "A general theory for dynamic instability of tube arrays in crossflow," J. Fluids Struct. **1**, 35–53 (1987).
[4] J. Backus, "Small-vibration theory of the clarinet," J. Acoust. Soc. Am. **35**, 305–313 (1963).
[5] W. E. Worman, "Self-sustained nonlinear oscillations of medium amplitude in clarinet-like systems," Ph.D. thesis, Case Western Reserve University, Cleveland, OH, 1971.
[6] T. A. Wilson and G. S. Beavers, "Operating modes of the clarinet," J. Acoust. Soc. Am. **56**, 653–658 (1974).
[7] N. H. Fletcher and T. D. Rossing, *The Physics of Musical Instruments* (Springer, New York, 1998).
[8] N. H. Fletcher, "Air flow and sound generation in musical instruments," Annu. Rev. Fluid Mech. **11**, 123–146 (1979).
[9] J. Saneyoshi, H. Teramura, and S. Yoshikawa, "Feedback oscillations in reed woodwind and brasswind instruments," Acustica **62**, 194–210 (1987).
[10] J. Kergomard, "Elementary considerations on reed-instruments oscillations," in *Mechanics of Musical Instruments*, edited by A. Hirschberg, J. Kergomard, and G. Weinreich (Springer, Wien, 1995).
[11] S. Ollivier, "Contribution á l'étûde des oscillations des instruments à vent à anche simple: Validation d'un modèle élémentaire (Contribution to the study of oscillations in single-reed instruments: Validation of an elementary model)," Ph.D. thesis, University of Maine, Maine, 2002.
[12] A. Hirschberg, R. W. A. van der Laar, J. P. Marrou-Mauriere, A. P. J. Wijnands, H. J. Dane, S. G. Kruijswijk, and A. J. M. Houtsma, "A quasi-stationary model of air flow in the reed channel of single-reed wind instruments," Acustica **70**, 146-154 (1990).
[13] J. van Zon, A. Hirschberg, J. Gilbert, and A. P. J. Wijnands, "Flow through the reed channel of a single reed instrument," in *Congrs Franais d'Acoustique* Sup. J. Phys. Colloque de Physique, Paris, Vol. **54**, pp. 821-824 (1990).
[14] A. M. C. Valkering, "Characterization of a clarinet mouthpiece," Technical Report No. R-1219-S, Vakgroep Transportfysica, TUE, Eindhoven, 1993.
[15] J. P. Dalmont, J. Gilbert, and S. Ollivier, "Nonlinear characteristics of single-reed instruments: Quasistatic volume flow and reed opening measurements," J. Acoust. Soc. Am. **114**, 2253–2262 (2003).
[16] L. Maurin, "Confrontation théorie-expérience des grandeurs d'entrée d'un excitateur à anche simple (Theoretical and experimental comparisons of input variables in a single-reed oscillator)," Ph.D. thesis, University of Maine, Main, 1992.
[17] J. Gilbert, "Étude des instruments de musique à anche simple (A study of single-reed musical instruments)," Ph.D. thesis, University of Maine, Maine, 1991.
[18] A. O. St-Hilaire, T. A. Wilson, and G. S. Beavers, "Aerodynamic excitation of the harmonium reed," J. Fluid Mech. **49**, 803–816 (1971).
[19] D. Ricot, R. Causse, and N. Misdariis, "Aerodynamic excitation and sound production of a blown-closed free reeds without acoustic coupling: The

example of the acordion reed," J. Acoust. Soc. Am. **117**, 2279–2290 (2005).
[20]X. Pelorson, A. Hirschberg, R. R. van Hassel, A. P. J. Wijnands, and Y. Auregan, "Theoretical and experimental study of quasisteady-flow separation within the glottis during fonation. Application to a modified two-mass model," J. Acoust. Soc. Am. **96**, 3416–3431 (1994).
[21]B. D. Erath and M. W. Plesniak, "The occurrence of the coanda effect in pulsatile flow through static models of the human vocal folds," J. Acoust. Soc. Am. **120**, 1000–1011 (2006).
[22]S. L. Thomson, L. Mongeau, and S. H. Frankel, "Aerodynamic transfer of energy to the vocal folds," J. Acoust. Soc. Am. **118**, 1689–1700 (2005).
[23]S. L. Thomson, "Fluid-structure interactions within the human larynx," Ph.D. thesis, Purdue University, West Lafayette, IN, 2004.
[24]I. R. Titze, "The physics of small-amplitude oscillations of the vocal folds," J. Acoust. Soc. Am. **83**, 1536–1552 (1988).
[25]A. Hirschberg, J. Gilbert, A. P. Wijnands, and A. M. C. Valkering, "Musical aero-acoustics of the clarinet," J. Phys. IV **4**, 559–568 (1994).
[26]A. H. Benade, *Fundamentals of Musical Acoustics* (Oxford University Press, New York, 1976).
[27]W. Shyy, *Computational Fluid Dynamics with Moving Boundaries*, Series in Computational Methods and Physical Processes in Mechanics and Thermal Sciences (Taylor and Francis, New York, 1995).
[28]M. Liefvendahl and C. Troeng, "Deformation and regeneration of the computational grid for cfd with moving boundaries," in *Proceedings of the 45th AIAA Aerospace Science Meeting*, Nevada, 2007.
[29]F. Avanzini and M. van Walstijn, "Modelling the mechanical response of the reed-mouthpiece-lip system of a clarinet. 1. A one-dimensional distributed model," Acta Acust. **90**, 537–547 (2004).
[30]P. Lallemand and L. S. Luo, "Lattice Boltzmann method for moving boundaries," J. Comput. Phys. **184**, 406–421 (2003).
[31]X. M. Li, R. C. K. Leung, and R. So, "One-step aeroacoustics simulation using lattice Boltzmann method," AIAA J. **44**, 78–89 (2006).
[32]X. He and L. S. Luo, "Theory of the lattice Boltzmann method: From the Boltzmann equation to the lattice Boltzmann equation," Phys. Rev. E **56**, 6811–6817 (1997).
[33]S. Succi, *The Lattice Boltzmann Equation for Fluid Dynamics and Beyond* (Oxford University Press, Oxford, 2001).
[34]D. A. Wolf-Gladrow, *Lattice Gas Cellular Automata and Lattice Boltzmann Models: An Introduction*, Lecture Notes in Mathematics, Vol. 1725 (Springer, Berlin, 2004).
[35]Y. Qian, D. d'Humires, and P. Lallemand, "Lattice BGK models for the Navier-Stokes equation," Europhys. Lett. **17**, 479–484 (1992).
[36]Y. Qian, S. Succi, and S. A. Orszag, "Recent advances in lattice Boltzmann computing," Annu. Rev. Comput. Phys. **3**, 195–242 (1995).
[37]P. L. Bhatnagar, E. P. Gross, and M. Krook, "A model for collision processes in gases. I. Small amplitude processes in charged and neutral one-component systems," Phys. Rev. **94**, 511–525 (1954).
[38]B. Crouse, D. Freed, G. Balasubramanian, S. Senthooran, P. Lew, and L. Mongeau, "Fundamental capabilities of the lattice Boltzmann method," in *Proceedings of the 27th AIAA Aeroacoustics Conference*, Cambridge, 2006.
[39]A. Chaigne and V. Doutaut, "Numerical simulations of xylophones. 1. Time-domain modeling of the vibrating bars," J. Acoust. Soc. Am. **101**, 539–557 (1997).
[40]M. Bouzidi, M. Firdaouss, and P. Lallemand, "Momentum transfer of a Boltzmann-lattice fluid with boundaries," Phys. Fluids **13**, 3452–3459 (2001).
[41]E. W. S. Kam, R. M. C. So, and R. C. K. Leung, "Non-reflecting boundary for one-step lbm simulation of aeroacoustics," in 27th AIAA Aeroacoustics Conference, Cambridge, MA, 2006, pp. 1–9.
[42]R. H. Kirchhoff, *Potential Flows*, *Mechanical Engineering* (CRC, New York, 1985).
[43]P. Durrieu, G. Hofmans, G. Ajello, R. Boot, Y. Aurégan, A. Hirchberg, and M. C. A. M. Peters, "Quasisteady aero-acoustic response of orifices," J. Acoust. Soc. Am. **110**, 1859–1872 (2001).
[44]R. D. Blevins, *Applied Fluid Dynamics Handbook* (Van Nostrand Heinhold, New York, 1984).
[45]M. Deverge, X. Pelorson, C. Vilain, P.-Y. Lagreé, F. Chentouf, J. Willems, and A. Hirschberg, "Influence of collision on the flow through in-vitro rigid models of the vocal folds," J. Acoust. Soc. Am. **114**, 3354–3362 (2003).

Effect of porosity on effective diagonal stiffness coefficients (c_{ii}) and elastic anisotropy of cortical bone at 1 MHz: A finite-difference time domain study

Cécile Baron,[a] Maryline Talmant, and Pascal Laugier
Université Pierre et Marie Curie-Paris 6, Laboratoire d'Imagerie Paramétrique, Paris F-75005, France and CNRS, LIP, Paris F- 75006, France

(Received 16 March 2007; revised 12 June 2007; accepted 21 June 2007)

Finite-difference time domain (FDTD) numerical simulations coupled to real experimental data were used to investigate the propagation of 1 MHz pure bulk wave propagation through models of cortical bone microstructures. Bone microstructures were reconstructed from three-dimensional high resolution synchrotron radiation microcomputed tomography (SR-μCT) data sets. Because the bone matrix elastic properties were incompletely documented, several assumptions were made. Four built-in bone matrix models characterized by four different anisotropy ratios but the same Poisson's ratios were tested. Combining them with the reconstructed microstructures in the FDTD computations, effective stiffness coefficients were derived from simulated bulk-wave velocity measurements. For all the models, all the effective compression and shear bulk wave velocities were found to decrease when porosity increases. However, the trend was weaker in the axial direction compared to the transverse directions, contributing to the increase of the effective anisotropy. On the other hand, it was shown that the initial Poisson's ratio value may substantially affect the variations of the effective stiffness coefficients. The present study can be used to elaborate sophisticated macroscopic computational bone models incorporating realistic CT-based macroscopic bone structures and effective elastic properties derived from μCT-based FDTD simulations including the cortical porosity effect. © *2007 Acoustical Society of America.* [DOI: 10.1121/1.2759165]

PACS number(s): 43.80.Ev, 43.80.Qf, 43.80.Jz, 43.80.Vj [FD] Pages: 1810–1817

I. INTRODUCTION

Quantitative ultrasound has received considerable interest in recent years for its potential to assess different bone properties that are relevant to predict bone fragility.

Axial transmission is a generic term to designate a variety of techniques devised to assess cortical bone using a linear arrangement of ultrasound emitters and receivers placed on top of the overlying soft tissue. A part of the ultrasonic energy is guided along the cortex and can be radiated at the interface between soft tissue and bone. Various technical implementations of the technique have been proposed at different frequencies in the range 250 kHz–1.25 MHz.[1–4]

Several wave types contribute to the total pressure field sensed by the receivers. The first arriving signal (FAS) is of special interest for *in vivo* assessment of cortical bone because it arrives prior to all other contributions, and therefore, can be easily determined from time-of-flight measurements of the signals received at different positions parallel to the interface.[5] The nature of the wave associated with the first arriving signal was found to change with increasing cortical thickness to wavelength ratio (Cort.Th/λ) from an S_0 Lamb mode for Cort.Th/$\lambda \ll 1$ to a lateral wave for Cort.Th/$\lambda \gg 1$.[6]

Recently, axial transmission approaches have been described that work in a low frequency range and exploit a later arriving signal, a slow guided wave mode, in addition to the FAS.[4,7,8] This guided wave mode is well described by the theory for guided waves in plate [fundamental antisymmetric (or flexural) guided wave].[2]

Clinical trials revealed the ability of these techniques in discriminating normal and osteoporotic subjects.[1,8,9] Clinical performances were enlightened by *in vitro* experiments. Experimental studies on excised human radii demonstrate the sensitivity of FAS velocity to porosity and degree of mineralization[5] and also to intrinsic elastic properties.[10] In addition, the velocity of the fundamental antisymmetric guided wave shows an exquisite sensitivity to cortical thickness.[11,12]

Another approach used to give insight into clinical performances is the modeling of ultrasound propagation in axial transmission configuration. Bone finite-difference time domain (FDTD) studies, using either a generic model of the structure (plate or tube models)[6,12] or bone structures reconstructed from three-dimensional x-ray tomography data, provided valuable insights into the relationships between ultrasound propagation characteristics (e.g., velocity of FAS or flexural mode) and bone properties such as cortical thickness and porosity. However, in these previous works, the models ignore the true local material properties, generic values were used instead.

We assume that the prediction capabilities of the computed tomography (CT) based finite-difference simulations may be enhanced with further refinements such as incorporating in the model individualized material properties.

[a]Electronic mail: norabelic@yahoo.fr

Bone is a poroelastic medium with a porous network filled with a fluid-like medium (marrow) embedded in an elastic tissue matrix. Cortical porosity mainly consists in an oriented network of Haversian canals of typically 50 μm diameter approximately aligned with the long axis of the bone and of resorption cavities around 50–200 μm in diameter. At a smaller scale, small transverse canaliculi and osteocytes lacunae (typically less than 10 μm diameter) also contribute to cortical porosity. Each Haversian canal is surrounded by a layered cylindrical structure, called osteon, of typically 200 μm diameter and between the osteons is the highly mineralized interstitial tissue. The wavelength in axial transmission is much longer than the typical size of these structures and the material properties required as input into the bone computational models are effective properties, the values of which are determined by the anisotropic elastic properties of the bone tissue matrix and by the oriented cortical porosity. First, the presence of pores inside the cortex induces a decrease of whole bone stiffness and density compared to stiffness and density of the bone matrix.[13] Second, due to its preferential orientation, the porous network contributes to the mechanical anisotropy of bone.[14] Progress in CT-based FDTD models requires knowing the effective individual material properties in which the effects of both cortical porosity and anisotropic elasticity are properly taken into account.

Scarce data on porosity-related anisotropic stiffness can be found in literature. Several experimental studies have investigated the impact of porosity on the longitudinal Young's modulus.[15–18] As these studies were reduced to axial direction, they did not provide any information on the contribution of porosity to the anisotropy. A few studies, based on experiments or micromechanics models have examined the dependence of effective anisotropic stiffness coefficients on tissue properties and especially on porosity. Dependence on porosity of four elastic moduli of cortical bone assumed to be transversally isotropic has been reported in a single experimental study.[13] Micromechanics provided comprehensive models of effective elastic properties of bone using various hypotheses to describe elastic properties of the bone matrix and the pore network.[14,19] In particular, Sevostianov *et al.*[14] have depicted the effect of porous network on overall stiffness coefficients of cortical bone assuming an isotropic bone matrix and identifying the effect of pore distribution. In the related field of composite media with unidirectional pores, a similar analysis was performed by Ichitsubo *et al.*[20] with an anisotropic matrix.

In this study, we report on microcomputed tomography (μCT) based FDTD simulations whereby the effective elastic properties are directly computed for individualized porous network of 19 cortical bone microstructures reconstructed from high resolution synchrotron radiation microtomography (SR-μCT). The bone matrix was modeled as a homogeneous anisotropic medium. As the elastic properties of the bone matrix were only partially documented in our samples, four built-in models were used for each specimen. The computational bone model for ultrasonic propagation in bone and the basis of the SR-μCT-based FDTD simulations are described in Sec. II. In Sec. III the results of the effective elastic properties are examined as a function of porosity for the different bone models. We close with a discussion of the limitations and potential extension of the current study.

II. MATERIALS AND METHODS

A. Samples

In this study we use a subset of 19 samples from a collection of human radii with soft tissue removed and previously assessed by different experimental techniques such as SR-μCT and scanning acoustic microscopy (SAM), which provided accurate data for cortical bone microstructure and estimates of material properties (density, stiffness) that were used to build the cortical bone models developed in the present paper.

Assessment of the microstructure was reported in Ref. 5. Small portions were cut in the postero-lateral zone of the distal radius. The dimensions were typically 10 mm long in the direction parallel to the bone axis and 8 mm long in the circumferential direction. These volumes were imaged by SR-μCT[21] at the European Synchrotron Radiation Facility (ESRF, Grenoble, France). The radiographs [two-dimensional (2D) projections] were recorded on a 1024×1024 charge-coupled device-based 2D detector and the voxel size was set to $10 \times 10 \times 10$ μm^3. From sets of 2D projections under different angles of view, three-dimensional reconstructions of the microstructure were obtained by tomography algorithm. The amount of mineral was 1082 ± 16 mg/cm^3 in the whole collection of samples.

Among the 19 samples considered in this study, 10 were previously studied by scanning acoustic microscopy at 50 MHz with a spatial resolution of 23 μm and a spatial sampling rate of 20 μm $\times$ 20 μm.[22] The section adjacent to the samples investigated by SR-μCT was scanned and a mapping of the acoustic impedance was provided. It was shown that the setup resolved Haversian canals larger than 25 μm. As a consequence, these measurements were representative of the impedance of the bone matrix at a scale of 20 μm. The acoustical impedance averaged over the whole set of specimens was found to be 8.1 ± 0.5 MRa.

B. Configuration of the simulation

Propagation of transient 1 MHz plane waves in the 3D reconstructed bone microstructures was computed using a FDTD code, SIMSONIC, developed in the laboratory and detailed elsewhere,[6,23] which computes a numerical solution to the 3D linear elastic wave propagation. The algorithm is based on Virieux scheme,[24] and uses first-order derivative in space and time.

The code requires the simulation box to be defined as right angle volume. Therefore, parallelepipedic volumes were extracted from the 3D SR-μCT reconstructed volumes (Fig. 1). The volume of the blocks analyzed in simulation with a spatial step of 20 μm varies from 9 to 36 mm^3, depending on the thickness of the sample.

A combination of symmetric boundary conditions (tangential velocities equal on both sides of the boundary and normal velocities null on the boundary) and/or antisymmetric boundary conditions (tangential velocities null on the bound-

FIG. 1. Three-dimensional porous network (pores are in grey) in a parallelepipedic block extracted from the μCT reconstructed bone structure. On the right-hand side are shown a transverse and longitudinal cross section through the three-dimensional porous network. The preferential orientation of the pores is along the bone axis.

ary and normal velocities equal on both sides of the boundary) on the simulation domain was applied to ensure the propagation of compression and/or shear plane bulk waves. Perfectly matched layers (PML) on sides and edges of the simulation domain were used to avoid unphysical reflections.[25]

SimSonic provides the transient signals associated with transmission of 1 MHz bulk compression or shear waves through the reconstructed volumes. Typical signals are shown in Fig. 2. Plane bulk waves velocities were deduced from time of flight measurements by detection of first signal maximum.

C. Derivation of effective stiffness

Effective stiffness coefficients were derived from velocities of simulated pure bulk wave propagating in principal directions and from effective mass density. For cortical bone the general degree of anisotropy is that of orthotropic material symmetry,[26] which is characterized by nine independent stiffness coefficients. The stiffness matrix can expressed as follows using the abbreviated subscript notation:[27]

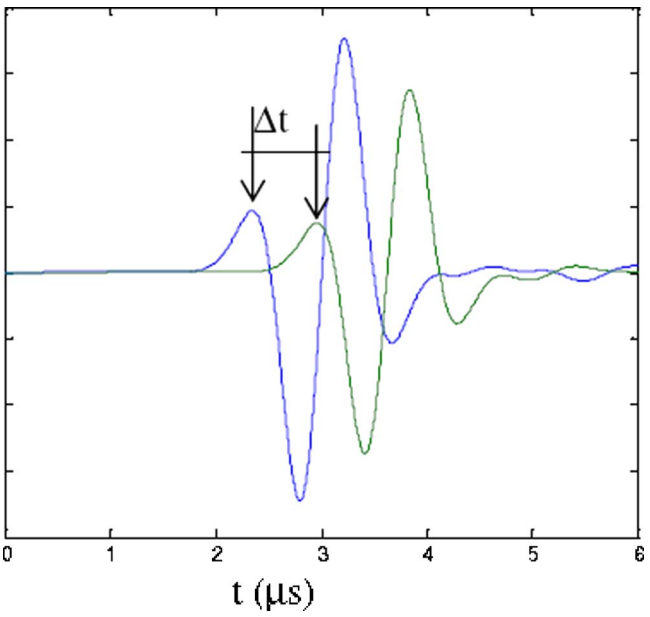

FIG. 2. (Color online) Velocity evaluation from the first maximum signal detection.

$$C = \begin{pmatrix} c_{11} & c_{12} & c_{13} & 0 & 0 & 0 \\ c_{12} & c_{22} & c_{23} & 0 & 0 & 0 \\ c_{13} & c_{23} & c_{33} & 0 & 0 & 0 \\ 0 & 0 & 0 & c_{44} & 0 & 0 \\ 0 & 0 & 0 & 0 & c_{55} & 0 \\ 0 & 0 & 0 & 0 & 0 & c_{66} \end{pmatrix} \quad \begin{matrix} \mathrm{X} \leftrightarrow 1 \\ \text{with } \mathrm{Y} \leftrightarrow 2, \\ \mathrm{Z} \leftrightarrow 3 \end{matrix} \quad (1)$$

where the X direction corresponds to the radial direction (i.e. thickness direction), the Y direction is the circumferential direction, and the Z direction is along the bone axis. But, as described by Katz,[28] the Haversian cortical bone is transverse isotropic in nature because of the locally uniaxial architecture of osteons. Consequently, numerous studies[29–31] assumed the cortical bone as a transverse isotropic elastic solid medium, which reduces the number of independent coefficients of the stiffness matrix to five. Considering transverse isotropy with (XY) as the isotropic plane,[32–34] the stiffness coefficients of $\mathbf{C}$ verify $c_{13}=c_{23}$, $c_{22}=c_{11}$, $c_{44}=c_{55}$, and $c_{66}=(c_{11}-c_{12})/2$.

When the waves propagate along principal directions of symmetry, the diagonal terms of the stiffness matrix c_{11}, c_{12}, and c_{33} are related to the phase velocity of compression-bulk wave which propagates along the X, Y, and Z direction, respectively, with

$$V_x = \sqrt{\frac{c_{11}}{\rho}}, \quad V_y = \sqrt{\frac{c_{22}}{\rho}}, \quad V_z = \sqrt{\frac{c_{33}}{\rho}}. \quad (2)$$

The stiffness coefficients c_{44} and c_{55} are related to the phase velocity of shear wave which propagate in Z direction and c_{66} in the transverse plane according to

$$V_{yz} = \sqrt{\frac{c_{44}}{\rho}}, \quad V_{xz} = \sqrt{\frac{c_{55}}{\rho}}, \quad V_{xy} = \sqrt{\frac{c_{66}}{\rho}}. \quad (3)$$

The effective stiffness coefficients were deduced from Eqs. (2) and (3) calculating the effective mass density ρ with the following rule of mixture:

$$\rho = \rho^0(1-p) + p\rho_w, \quad (4)$$

where ρ^0 is the mass density of the tissue matrix, ρ_w is the mass density of the fluid filling the pores (water), and p is the porosity.

D. Numerical bone models

Maps of the mass density and of the stiffness coefficients were used as input data in the software. The cortical bone was modeled as a two-phase medium constituted by the bone matrix and the fluid filling the pores. Each phase was supposed to be homogeneous within and between the samples. The spatial variation of density and stiffness in the simulation volume (spatial step of 20 μm) relies on the presence of the pores. Both components were clearly delineated by segmentation of the original reconstructed SR-μCT data and were defined by fixed mass density and stiffness coefficients.

TABLE I. Four bone matrix models.

	c_{33}^0 (GPa)	c_{11}^0 (GPa)	c_{33}^0/c_{11}^0	c_{13}^0/c_{11}^0	c_{55}^0/c_{11}^0	c_{66}^0/c_{11}^0
Model 1	34.3	34.3	1	0.43	0.29	0.29
Model 2	34.3	30.6	1.12	0.42	0.34	0.29
Model 3	34.3	27.3	1.26	0.42	0.38	0.31
Model 4	34.3	22.9	1.5	0.41	0.45	0.30

Ideal nonviscous fluid (water) was assumed to fill the pores. The mass density was (ρ_f=1 g/cm^3), and the stiffness coefficients were calculated from the following Lame's constants values (λ=2.25 GPa, μ=0 GPa).

Simulations in each bone sample microstructure were conducted with four different models of bone matrix shown in Table I. For the isotropic case (model 1), two independent stiffness coefficients are required (c_{33}^0, c_{13}^0) to define the elasticity of the bone matrix, and in the three transversely isotropic models (models 2–4), five independent stiffness coefficients are needed (c_{11}^0, c_{33}^0, c_{55}^0, c_{13}^0, and c_{12}^0). Here, the subscript zero is used to denote the intrinsic stiffness of the tissue matrix.

In all the models, the axial stiffness c_{33}^0 was taken close to 34 GPa, the overall mass density ρ^0 of the bone matrix mass 1.91 g/cm^3. These values were derived from SR-μCT and SAM data averaged over the samples that were investigated with these techniques. In Ref. 22, the mass density of the solid matrix was related by a second-order polynomial fit to the mineral amount. According to this, the mass density in our study was approximated to a value of 1.91 mg/cm^3, considering the mean value of mineralization previously measured and neglecting the intersample variations. The axial stiffness c_{33}^0=34.3 GPa was derived from acoustic impedance (Z=8.1 MRa) values measured at 50 MHz, with a resolution of 23 μm well adapted to spatial grid of the simulation (20 μm). The axial stiffness was derived using the relation

$$c_{33}^0 = \frac{Z^2}{\rho^0} \tag{5}$$

between acoustical impedance and density, with ρ^0 =1.91 g/cm^3. Because the standard deviation of the acoustic impedance over the samples was small and the variations of the mean value of the acoustic impedance were weak between the different regions investigated, a fixed value of c_{33}^0 was adopted within and between specimens. We choose to couple the numerical simulations to experimental data obtained on the same set of specimens investigated by both scanning acoustic microscopy and μCT. This might have resulted in stiffness values slightly higher than values reported in the literature.[13,35] We do not expect the trends reported here to be accurate in an absolute sense. However, since our main conclusion is based on the comparative performance of the models, the general trends reported here are expected to hold in a relative sense. All four models are built around the same value of c_{33}^0. It would be interesting to carry out a parametric study on the influence of this absolute value.

With models 2–4, transversely isotropic bone matrices with various degrees of anisotropy were explored. The value of the anisotropy ratio $AR_0=c_{33}^0/c_{11}^0$ was chosen in the range 1–1.5. The value of c_{11}^0 was therefore determined from the selected anisotropy ratio value. Moreover, for the three transversely isotropic matrix (models 2–4), the shear stiffness coefficient c_{55}^0 was fixed to 10.4 GPa.[36]

The other stiffness coefficients, c_{13}^0 and c_{12}^0, were derived from the relationship between Poisson's ratio and stiffness, assuming the bone matrix to be either isotropic (model 1) or transversely isotropic (models 2–4), with the following relationships:

$$\nu_L^0 = \frac{c_{13}^0}{c_{11}^0 + c_{12}^0}, \quad \nu_T^0 = \frac{c_{33}^0 c_{12}^0 - (c_{13}^0)^2}{c_{33}^0 c_{11}^0 - (c_{13}^0)^2}. \tag{6}$$

The longitudinal ν_L^0 and the transverse ν_T^0 Poisson's ratios were equal and set to a value of 0.3, a commonly used value in the literature.[37–39] Model 2 was build with AR^0=1.12, a value reported in Hofmann *et al.*[36] In model 3, a ratio of anisotropy c_{33}^0/c_{11}^0=1.26 was adopted, according to Turner's report.[37] In addition, we kept in this model the value of the longitudinal shear modulus given in Ref. 36 providing c_{55}^0.

Model 4 was used to enlarge the range of anisotropy ratio and AR^0 reaches the value of 1.5, the value of c_{33}^0 and c_{55}^0 remaining the same as in models 2 and 3.

E. Pore size and porosity

Figure 2 shows a typical 3D reconstruction of the porous network. To perform numerical simulation, the original grey scale reconstructions were segmented to yield binary mappings of the porous network. The segmentation threshold laid between the two well-separated distributions of pixel values

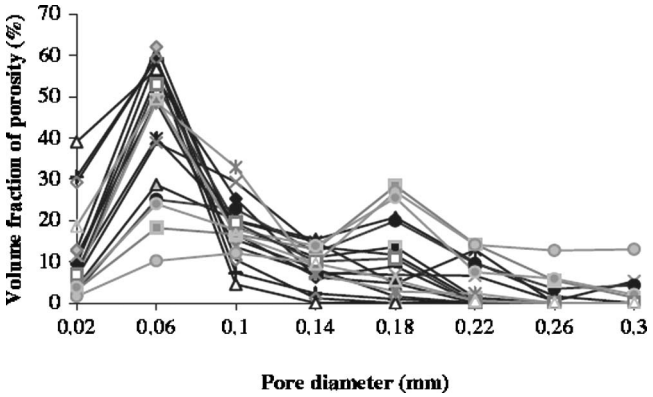

FIG. 3. Distribution of pores diameter through the 19 samples.

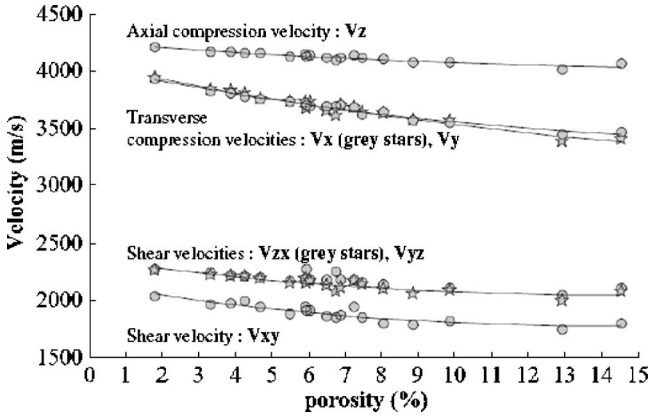

FIG. 4. Effective compression and shear bulk wave velocities deduced from FDTD simulations as a function of cortical porosity (model 2). The grey stars represent V_x and V_{zx}.

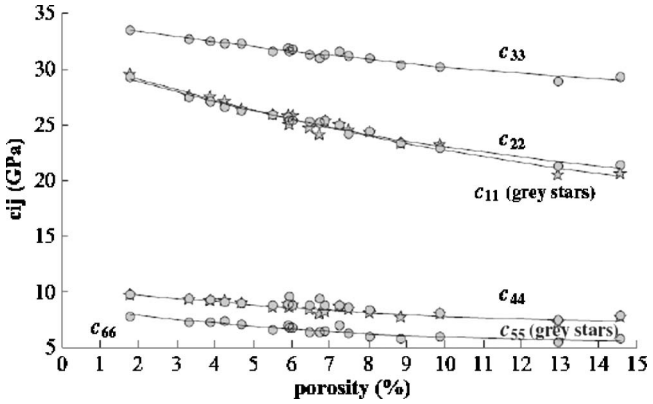

FIG. 5. Effective diagonal stiffness coefficients as a function of porosity (model 2).

corresponding to the bone tissue and to the empty pores. The porosity was defined for each specimen as the ratio of the volume of pores to the total bone volume. The pore area related to different pore diameters was estimated in each reconstructed tomographic cross section, and then the pore areas were summed over the cross sections and multiplied by the spatial step increment between two consecutive slices to obtain the porosity. The distribution of the porosity as function of pore diameters was deduced from the morphological analysis of the 19 reconstructed microstructures. In addition, structural parameters such as mean pore density (number of detected pores per mm^2) and mean pore diameter (the equivalent diameter was determined from the area of the individual canals) were extracted.

III. RESULTS

A. Pore size and porosity

Each of the 19 samples had a porosity falling in the range 2%–15%. The distribution of diameters for the 19 specimens illustrated in Fig. 3 shows a bimodal distribution with two pore classes, the 60- and the 180-μm-diam groups, as contributors to the porosity (Fig. 3). The spatial resolution of SR-μCT was not sufficient to resolve the smallest pores (osteocytes lacunae, canaliculi) of a few microns in diameter. A higher resolution (<10 μm) is needed to consistently visualize all cortical pores in human bone.[40]

The average porosity in these samples was about 7%, the average pore number density was 15 mm^{-2}, and the mean pore diameter was about 80 μm. These results are consistent with previous morphological studies on human cortical bone.[22,41]

B. Effective velocities and stiffness coefficients as a function of cortical porosity

Velocities of compression and shear bulk plane waves along the three principal axes of symmetry were computed for the 19 bone specimens and the 4 models. Figure 4 presents results for model 2. All the effective compression and shear bulk wave velocities decrease when porosity increases. However, the decrease was less pronounced for propagation along the long axis of the bone compared to the transverse directions. For a 10% increase in porosity, waves that propagate in the transverse plane undergo a decrease of 12% (470 m/s) for compression waves and 17% (370 m/s) for shear waves, while waves that propagate in the Z direction are reduced by 4% (160 m/s) for compression waves and 11% (260 m/s) for shear waves.

Similar trends of velocity variation versus porosity were observed for the four bone matrix models (Table II).

As a consequence of the decrease of both the effective mass density [Eq. (4)] and bulk wave velocities (Fig. 4) with the porosity, all the effective diagonal stiffness coefficients decline with the porosity as illustrated for model 2 in Fig. 5.

In all the bone models, a quadratic law between stiffness coefficients and porosity (ap^2+bp+c) was a better fit than a linear regression, although the first coefficient of the polynomial was small (see Table III).

TABLE II. Absolute (relative variation) of compression and shear waves velocities for a 10% increase of porosity (from 0 to 10%).

(m/s)	Compression waves in the transverse plane V_x and V_y	Compression wave in the axial direction V_z	Shear wave in the transverse plane V_{xy}	Shear waves in the axial direction V_{zx} and V_{yz}
Model 1	530 (12%)	190 (4.5%)	380 (17%)	250 (11%)
Model 2	470 (12%)	160 (4%)	370 (17%)	260 (11%)
Model 3	420 (11%)	150 (3.5%)	355 (17%)	200 (9%)
Model 4	350 (10%)	130 (3%)	320 (11%)	270 (11%)

TABLE III. Quadratic law variations of the diagonal stiffness coefficients vs porosity $c_{ii}=a(p\%)^2+bp\%+c$.

$AR^0=1.12$	c_{11}	c_{22}	c_{33}	c_{44}	c_{55}	c_{66}
a	0.024	0.026	0.011	0.004	0.013	0.014
b	−1.088	−1.047	−0.527	−0.232	−0.398	−0.412
c	31.15	30.82	34.37	10.14	10.47	80.60
R^2	0.97	0.98	0.96	0.80	0.88	0.88

C. Porosity contribution to effective anisotropy

The influence of porosity on effective stiffness is weaker in the axial direction (i.e., for c_{33} and for c_{44} and c_{55}) compared to the transverse directions (i.e., for c_{11} and c_{22} and for c_{66}), a result that contributes to the increase of the effective anisotropy as a function of porosity compared to the original elastic anisotropy of the bone matrix.

The effective anisotropy ratio ($AR=c_{33}/c_{11}$) normalized by the intrinsic anisotropy ratio of the bone matrix ($AR^0=c_{33}^0/c_{11}^0$) is plotted as a function of porosity for the four different bone models in Fig. 6. Normalized anisotropy ratios are consistently found to be greater than one and increasing with the porosity. The data indicate that the porosity contributes to the overall effective elastic anisotropy of bone structure. The higher the porosity, the higher its contribution to the bone elastic anisotropy. A 10% increase of porosity (from 0 to 10%) results in a relative increase of anisotropy ranging between 16% (for $AR^0=1.5$) and 20% (for the isotropic case) for the four bone matrix models studied.

Furthermore, the effective shear anisotropy ratio ($AR'=c_{55}/c_{66}$) increases with the porosity: For a 10% increase of porosity, the AR' is 16% greater for the isotropic case (model 1), 14% greater for models 2 and 3, and 12% greater for model 4.

The relative contribution of porosity to structural anisotropy of cortical bone is all the more important because the bone matrix is weakly anisotropic.

On the other hand, the other anisotropy ratios assessed by FDTD simulations (c_{ii}/c_{11}) were found to remain almost unchanged with the porosity.

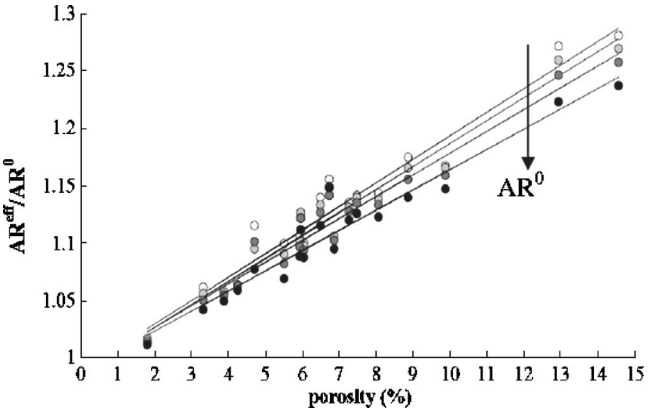

FIG. 6. Normalized effective anisotropy ratio (AR/AR_0) as a function of porosity for the different bone matrix models. Open circles correspond to the isotropic case (model 1), the light grey circles to model 2 ($AR^0=1.12$), the dark grey circles to model 3 ($AR^0=1.26$), and the closed circles to model 4 ($AR^0=1.5$).

IV. DISCUSSION

Our results suggest that the porous network introduces or reinforces transverse isotropy, as expected owing to its preferential orientation parallel to the bone axis. Indeed, it is noteworthy that the effect of porosity is similar for c_{11} and c_{22}, and for c_{44} and c_{55}. As pictured by Fig. 5, the differences between c_{11} and c_{22} and between c_{44} and c_{55} induced by the porous network were subtle: for example, $(c_{11}-c_{22})/c_{11}\leqslant 2\times10^{-4}$ for $p\leqslant 10\%$ and $(c_{11}-c_{22})/c_{11}\approx 4\times10^{-2}$ for $p\geqslant 10\%$. Therefore, if either isotropic (model 1) or transversely isotropic symmetry (models 2–4) is assumed for the tissue matrix, the introduction in the bone model of the oriented porous network resulted in a structure with effective transversely isotropic elastic properties. The result is consistent with the well-known effective macroscopic transverse isotropy of human cortical bone.[34,42–44]

However, two additional conditions, $c_{13}=c_{23}$ and $c_{66}=(c_{11}-c_{12})/2$, required by this symmetry could not be checked here because mixed-indices stiffness coefficients were not evaluated. The evaluation of the mixed-indices stiffness coefficients c_{12}, c_{13}, and c_{23} requires one either to rotate the sample or to record angular variation of transmitted bulk wave. In the first case, it would be necessary to modify the software to implement capabilities of working with material of more general anisotropy than orthotropy, and in the second case it would be necessary to implement a more sophisticated signal processing. As these tasks were not under the scope of this study, the stiffness coefficients c_{12}, c_{13}, and c_{23} were not evaluated. However, note that under the reasonable assumption of a macroscopic transverse anisotropy, c_{12} can be simply derived from the knowledge of c_{11} and c_{66} with $c_{66}=(c_{11}-c_{12})/2$.

Coupling μCT-based models of bone microstructure with FDTD simulations is a powerful means to compute the effect of porosity on effective stiffness and elastic anisotropy of bone. The high spatial resolution reached by SR-μCT allows an accurate determination of the porous network. However, the bone computational model also requires input data for the stiffness of the bone tissue matrix. Because the complete set of real data (five stiffness coefficients and mass density) for the bone matrix was not known, some hypotheses were made. The Poisson's ratios are not easy to determine experimentally and therefore are not known with accuracy, and an *a priori* value of 0.3 for the Poisson's ratios was assumed, following a commonly adopted assumption in many studies, especially finite element analyses,[45] despite the rather wide range of values, between 0.12 and 0.63, reported in literature.[31,42] Thus, one limitation of our study is related to the assumption adopted regarding the values of the

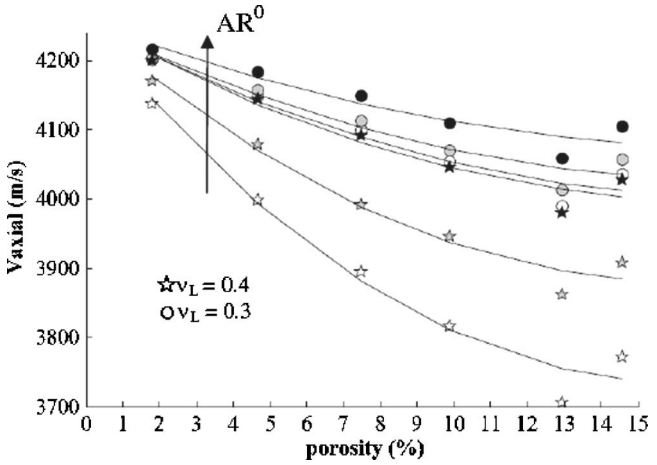

FIG. 7. Influence of the longitudinal Poisson's ratio on the dependence of the axial velocity on the cortical porosity. The stars represent the data obtained for ν_L=0.4 and the circles represent the data related to ν_L=0.3. The colors from white to black correspond to increasing AR^0 (model 1, model 2, and model 4).

Poisson's ratios, as mentioned in Raum *et al.*[22] Here, in a first step we have investigated the influence of the longitudinal Poisson's ratio value on the axial velocity as a function of porosity for model 1 (model 1 is isotropic, the longitudinal and transverse Poisson's ratios are equal), model 2, and model 4. For these bone models, the computations have been run with an input Poisson's ratio value of 0.4 instead of 0.3. The new Poisson's ratio value was properly taken into account by modifying the value of the stiffness coefficients c_{12}^0 and c_{13}^0 according to Eq. (6).

The influence of the Poisson's ratio value on the axial velocity is presented in Fig. 7. The increase of Poisson's ratio from 0.3 to 0.4 induces a stronger impact of porosity on axial velocity and a better differentiation of the behavior between the different anisotropy models. For a longitudinal Poisson's ratio of 0.3 and a 10% increase of porosity, the axial velocity decreases by 190 m/s (4%) for model 1, 165 m/s (4%) for model 2, and 130 m/s (3%) for model 4. When the longitudinal Poisson's ratio is fixed to 0.4, the impact of a 10% increase of porosity on the axial velocity is of 430 m/s (10%) for model 1, 300 m/s (7%) for model 2, and 200 m/s (5%) for model 4. Consequently, an accurate estimation of the Poisson's ratios or of the related stiffness coefficients, especially the mixed-indices ones, at the matrix level is critical for a reliable prediction of relative variation of ultrasound velocities as function of porosity. Advances in this field have been published recently.[31,45]

The present study permits a direct assessment of the effect of porosity on the stiffness coefficients of cortical bone. However, the morphology of the porous network is complex and requires several parameters to be fully characterized, including the size of the pores, pore density (number of pores per unit of area), spatial distribution of the pores, and shape of the pores.[46] The question arises as to whether these properties are determinant factors of the effective stiffness and the elastic anisotropy of cortical bone. Simplified models of porous networks were numerically built in order to better understand these effects for fixed values of porosity. Preliminary results (not shown here) suggest that the influence of morphological parameters is small. For example, with a simplified model with a periodic spatial distribution of cylindrical inclusions embedded in the bone matrix, with their axis parallel to the axis of the bone, only subtle difference of 2% in the axial compression velocity could be observed. However, more work is required to explore the consequences of morphological variations in the cortical porosity on effective elastic properties.

The results of the present study can be used to elaborate sophisticated macroscopic computational bone models incorporating realistic CT-based macroscopic bone structures and effective elastic properties derived from μCT-based FDTD simulations taking into account the effect of cortical porosity. These macroscopic computational bone models are of considerable interest as they can be used in order to evaluate the effect of porosity and of macroscopic bone structure on measured velocities in axial transmission. The frequency bandwidth (around 1 MHz) in this study is in the range of that typically used in some of the clinical settings. However, as mentioned in Sec. I, other devices are working at lower frequencies (around 250 kHz). Work on velocity frequency dispersion in cortical bone is sparse. Studying the frequency dependence of stiffness coefficients is potentially important. Therefore, specific attention must be paid in future works to the determination of phase velocity and amplitude in different frequency ranges.

V. CONCLUSION

The effect of oriented cortical bone porosity on ultrasound plane bulk wave velocities and elastic stiffness coefficients was investigated using transient numerical simulation of ultrasound plane bulk waves in 3D reconstructed microstructure of cortical bone samples. The effective stiffness coefficients were found to decrease with increasing porosity. The preferential orientation of the pore network along the bone axis induced an additional anisotropy (16%–20%) of the effective medium compared to the initial anisotropy of the bone tissue matrix. With initial Poisson's ratios values of 0.3, the variation of the effective anisotropy ratio was found to be fairly the same whatever the original anisotropy of the bone matrix was. However, the Poisson's ratio of the elastic bone matrix was found to be a critical determinant of the evaluation of relative variation of effective velocities and in turn of effective stiffness coefficients as a function of porosity.

[1]D. Hans, S. K. Srivastav, C. Singal, R. Barkmann, C. F. Njeh, E. Kantorovitch, C. C. Gluer, and H. K. Genant, "Does combining the results from multiple bone sites measured by a new quantitative ultrasound device improve discrimination of hip fracture?," J. Bone Miner. Res. **14**, 644–651 (1999).
[2]P. Moilanen, P. H. F. Nicholson, T. Kärkkäinen, Q. Wang, J. Timonen, and S. Cheng, "Assessment of the tibia using ultrasonic guided waves in pubertal girls," Osteoporosis Int. **14**, 1020–1027 (2003).
[3]E. Bossy, M. Talmant, M. Defontaine, F. Patat, and P. Laugier, "Bidirectional axial transmission can improve accuracy and precision of ultrasonic velocity measurement in cortical bone: A validation on test materials," IEEE Trans. Ultrason. Ferroelectr. Freq. Control **51**, 71–79 (2004).
[4]A. Tatarinov, N. Sarvazyan, and A. Sarvazyan, "Use of multiple acoustic wave modes for assessment of long bones: Model study," Ultrasonics **43**, 672–680 (2005).

[5]E. Bossy, M. Talmant, F. Peyrin, L. Akrout, P. Cloetens, and P. Laugier, "An in vitro study of the ultrasonic axial transmission technique at the radius: 1-MHz velocity measurements are sensitive to both mineralization and intracortical porosity," J. Bone Miner. Res. **19**, 1548–1556 (2004).
[6]E. Bossy, M. Talmant, and P. Laugier, "Three-dimensional simulations of ultrasonic axial transmission velocity measurement on cortical bone models," J. Acoust. Soc. Am. **115**, 2314–2324 (2004).
[7]F. Lefebvre, Y. Deblock, P. Campistron, D. Ahite, and J. J. Fabre, "Development of a new ultrasonic technique for bone and biomaterials in vitro characterization," Biomedical Materials Res. Part B, (Applied Biomaterials) **63**, 441–446 (2002).
[8]P. H. F. Nicholson, P. Moilanen, T. Kärkkäinen, J. Timonen, and S. Cheng, "Guided ultrasonic waves in long bone: Modelling, experiment and in vivo application," Physiol. Meas **23**, 755–768 (2002).
[9]R. Barkmann, E. Kantorovich, C. Singal, D. Hans, H. K. Genant, M. Heller, and C. C. Glüer, "A new method for quantitative ultrasound measurements at multiple skeletal sites: First results of precision and fracture discrimination," Clinical Densitometry **3**, 1–7 (2000).
[10]K. Raum, I. Leguerney, F. Chandelier, E. Bossy, M. Talmant, A. Saied, F. Peyrin, and P. Laugier, "Bone microstructure and elastic tissue properties are reflected in QUS axial transmission measurements," Ultrasound Med. Biol. **31**, 1225–1235 (2005).
[11]M. Muller, P. Moilanen, E. Bossy, P. H. F. Nicholson, V. Kilappa, J. Timonen, M. Talmant, S. Cheng, and P. Laugier, "Comparison of three ultrasonic axial transmission methods for bone assessment," Ultrasound Med. Biol. **31**, 633–642 (2005).
[12]P. Moilanen, V. Kilappa, P. Nicholson, J. Timonen, and S. Cheng, "Thickness sensitivity of ultrasound velocity in long bone phantoms," Ultrasound Med. Biol. **30**, 1517–1521 (2004).
[13]X. N. Dong and X. E. Guo, "The dependence of transverse elasticity of human femoral cortical bone on porosity," J. Biomech. **37**, 1281–1287 (2004).
[14]I. Sevostianov and M. Kachanov, "Impact of the porous microstructure on the overall elastic properties of the osteonal cortical bone," J. Biomech. **33**, 881–888 (2000).
[15]D. R. Carter and W. C. Hayes, "The compressive behaviour of bone as a two phase porous material," J. Bone Jt. Surg., Am. Vol. **59**, 954–962 (1977).
[16]J. D. Currey, "The effect of porosity and mineral content on the Young's modulus of elasticity of compact bone," J. Biomech. **21**, 131–139 (1988).
[17]T. S. Keller, Z. Mao, and D. M. Spengler, "Young's modulus, bending strength, and tissue physical properties of human compact bone," J. Orthop. Res. **8**, 592–603 (1990).
[18]S. Bensamoun, J.-M. Gherbezza, J.-F. de Belleval, and M.-C. Ho Ba Tho, "Transmission scanning acoustic imaging of human cortical bone and relation with the microstructure," Clin. Biomech. (Los Angel. Calif.) **19**, 639–647 (2004).
[19]X. N. Dong and X. E. Guo, "Prediction of cortical bone elastic constants by a two-level micromechanical model using generalized self-consistent method," J. Biomech. Eng. **128**, 309–316 (2006).
[20]T. Ichitsubo, M. Tane, O. Hirotsugu, M. Hirao, T. Ikeda, and H. Nakajima, "Anisotropic elastic constants of lotus-type porous copper: Measurements and micromechanics modeling," Acta Mater. **50**, 4105–4115 (2002).
[21]M. Salome, F. Peyrin, P. Cloetens, C. Odet, A.-M. Laval-Jeantet, J. Baruchel, and P. Spanne, "A synchrotron radiation microtomography system for the analysis of trabecular bone samples," Med. Phys. **26**, 2194–2204 (1999).
[22]K. Raum, R. O. Cleveland, F. Peyrin, and P. Laugier, "Derivation of elastic stiffness from site-matched mineral density and acoustic impedance maps," Phys. Med. Biol. **51**, 747–758 (2006).
[23]E. Bossy, F. Padilla, F. Peyrin, and P. Laugier, "Three-dimensional simulation of ultrasound propagation through trabecular bone structures measured by Synchrotron tomography," Phys. Med. Biol. **50**, 5545–5556 (2005).
[24]J. Virieux, "P-SV wave propagation in heterogeneous media: Velocity-stress finite-difference method," Geophysics **51**, 889–901 (1986).
[25]F. Collino and C. Tsogka, "Application of the PML absorbing layer model to the linear elastodynamic problem in anisotropic heterogeneous media," Geophysics **66**, 294–307 (2001).
[26]R. B. Ashman, S. C. Cowin, W. C. Van Burskirk, and J. C. Rice, "A continuous wave technique for the measurement of the elastic properties of cortical bone," J. Biomech. **17**, 349–361 (1984).
[27]B. A. Auld, *Acoustic Fields and Waves in Solids*, Rob E. Krieger Publishing Company (Malabar, FL 1973).
[28]J. L. Katz and K. Ukraincik, "On the anisotropic elastic properties of hydroxyapatite," J. Biomech. **4**, 221–227 (1971).
[29]H. S. Yoon and J. L. Katz, "Ultrasonic wave propagation in human cortical bone. II. Measurement of elastic properties and microhardness," J. Biomech. **9**, 459–462 (1976).
[30]J. L. Katz, "Anisotropy of Young's modulus of bone," Nature (London) **283**, 106–107 (1980).
[31]M. Pithioux, P. Lasaygues, and P. Chabrand, "An alternative ultrasonic method for measuring the elastic properties of cortical bone," J. Biomech. **35**, 961–968 (2002).
[32]W. C. Van Burskirk, S. C. Cowin, and R. N. Ward, "Ultrasonic measurements of orthotropic elastic constants of bovine femoral bone," J. Biomech. Eng. **103**, 67–71 (1981).
[33]J. L. Katz, H. S. Yoon, S. Lipson, R. Maharidge, A. Meunier, and P. Christel, "The effects of remodeling on the elastic properties of Bone," Calcif. Tissue Int. **36**, S31–S36 (1984).
[34]J. Y. Rho, "An ultrasonic method for measuring the elastic properties of human tibial cortical and cancellous bone," Ultrasonics **34**, 717–783 (1996).
[35]K. Hasegawa, C. H. Turner, and D. B. Burr, "Contribution of collagen and mineral to the elastic anisotropy of bone," Calcif. Tissue Int. **55**, 381–386 (1994).
[36]T. Hofmann, F. Heyroth, H. Meinhard, W. Fränzel, and K. Raum, "Assessment of composition and anisotropic elastic properties of secondary osteon lamellae," J. Biomech. **39**, 2282–2294 (2006).
[37]C. H. Turner, J. Y. Rho, Y. Takano, T. Y. Tsui, and G. M. Pharr, "The elastic properties of trabecular and cortical bone tissues are similar: Results from two microscopic measurement techniques," J. Biomech. **32**, 437–441 (1999).
[38]J. Y. Rho, P. Zioupos, J. D. Currey, and G. M. Pharr, "Microstructural elasticity and regional heterogeneity in human femoral bone of various age examined by nano-indentation," J. Biomech. **35**, 189–198 (2002).
[39]C. E. Hoffler, X. E. Guo, P. K. Zysset, and S. A. Goldstein, "An application of nano-indentation technique to measure bone tissue lamellae properties," J. Biomech. Eng. **127**, 1046–1053 (2005).
[40]D. M. L. Cooper, J. R. Matyas, M. A. Katzenberg, and B. Hallgrimson, "Comparison of microcomputed tomographic and microradiographic measurements of cortical bone porosity," Calcif. Tissue Int. **74**, 437–447 (2004).
[41]D. M. L. Cooper, A. L. Turinsky, C. W. Sensen, and B. Hallgrimsson, "Quantitative 3D analysis of the canal network in cortical bone by microcomputed tomography," Anat. Rec. **274B**, 169–179 (2003).
[42]D. T. Reilly and A. H. Burstein, "The elastic and ultimate properties of compact bone tissue," J. Biomech. **8**, 393–405 (1975).
[43]A. Ambardar and C. D. Ferris, "Compact anisotropic bone: Elastic constants, in vitro aging effects and numerical results of a mathematical model," Acta Biol. Acad. Sci. Hung. **29**, 81–94(1978).
[44]S. Lipson and J. L. Katz, "The relationship between elastic and microstructure of bovine cortical bone," J. Biomech. **17**, 231–240 (1984).
[45]R. Shahar, P. Zaslansky, A. A. Fiesem, J. D. Currey, and S. Weiner, "Anisotropic Poisson's ratio and compression modulus of cortical bone determined by speckle interferometry," J. Biomech. **40**, 252–264 (2007).
[46]D. M. L. Cooper, A. L. Turinsky, C. W. Sensen, and B. Hallgrimson, "Effect of voxel size on 3D micro-CT analysis of cortical bone porosity," Calcified Tissue Int. **80**, 211–219 (2007).

Ultrasonically determined thickness of long cortical bones: Two-dimensional simulations of *in vitro* experiments

Petro Moilanen[a] and Maryline Talmant
Université Pierre et Marie Curie - Paris 6, Laboratoire d'Imagerie Paramétrique UMR7623, Paris, F-75005, France

Valerie Bousson
Service de Radiologie Osteo-Articulaire, Hopital Lariboisiere, Paris, F-75010, France

Patrick H. F. Nicholson, Sulin Cheng, and Jussi Timonen
Departments of Physics and Health Sciences, University of Jyväskylä, Jyväskylä, FIN-40014, Finland

Pascal Laugier
Université Pierre et Marie Curie - Paris 6, Laboratoire d'Imagerie Paramétrique UMR7623, Paris, F-75005, France

(Received 19 December 2006; revised 14 June 2007; accepted 14 June 2007)

Previously it has been demonstrated that cortical bone thickness can be estimated from ultrasonic guided-wave measurements, in an axial transmission configuration, together with an appropriate analytical model. This study considers the impact of bone thickness variation within the measurement region on the ultrasonically determined thickness (UTh). To this end, wave velocities and UTh were determined from experiments and from time-domain finite-difference simulations of wave propagation, both performed on a set of ten human radius specimens (29 measurement sites). A two-dimensional numerical bone model was developed with tunable material properties and individualized geometry based on x-ray computed-tomography reconstructions of human radius. Cortical thickness (CTh) was determined from the latter. UTh data for simulations were indeed in a excellent accordance (root-mean-square error was 0.26 mm; $r^2=0.94$, $p<0.001$) with average CTh within the measurement region. These results indicate that despite variations in cortical thickness along the propagation path, the measured phase velocity can be satisfactorily modeled by a simple analytical model (the A_0 plate mode in this case). Most of the variability (up to 85% when sites were carefully matched) observed in the *in vitro* ultrasound data was explained through simulations by variability in the cortical thickness alone. [DOI: 10.1121/1.2756758]

PACS number(s): 43.80.Ev, 43.80.Vj, 43.80.Jz, 43.80.Qf [CCC] Pages: 1818–1826

I. INTRODUCTION

In recent years, there has been a growing interest in using axial transmission of ultrasonic guided waves for characterizing human long bones such as the radius and tibia. The first *in vitro* study to investigate propagation of a flexural type of guided wave in long-bone cortex dates back over 20 years (Jansons *et al.*, 1984). Since then, several related *in vitro* (Lefebvre *et al.*, 2002; Lee and Yoon, 2004; Muller *et al.*, 2005; Tatarinov *et al.*, 2005) and *in vivo* studies (Oranov *et al.*, 1988; Tatarinov *et al.*, 1990; McCarthy *et al.*, 2000; Moilanen *et al.*, 2003) have been published. Guided waves are believed to yield increased diagnostic information over the speed-of-sound of the fast first-arriving signal used in the existing axial-transmission devices for long-bone assessment, since guided modes are particularly sensitive to both material and geometrical aspects of bone cortex (Nicholson *et al.*, 2002), which are known to play an important role in the strength of long bones.

A few recent studies have shown interest in developing noninvasive methods for assessing cortical bone thickness, because reduced cortical thickness has been shown to relate to decreased bone strength and increased fracture risk (Augat *et al.*, 1996; Turner, 2002). Basically, two different approaches have been proposed recently: a direct pulse-echo measurement (Wear, 2003) and a model-based inversion of axial guided-wave transmission data (Moilanen *et al.*, 2006). Both approaches yielded excellent estimations of cortical thickness. One potential benefit of the pulse-echo approach is that it provides mapping of local (punctual) thickness, whereas the guided-wave approach reflects an average thickness within a finite (linear) range along the long axis of bone. The guided-wave approach can thus be considered a robust method describing directly the average thickness of the measurement region.

The uncertainties in ultrasonically determined thickness (UTh) measurements, as discussed in previous phantom and *in vitro* studies (Moilanen *et al.*, 2006; 2007), can be explained by the unavoidable limitations of scanning length, and by variation in elastic properties and geometry of bone samples. In particular, an analytical model of a homogeneous

[a]Electronic mail: pemoilan@cc.jyu.fi

elastic plate or axisymmetric tube with fixed elastic parameters (and tube diameter for the tube model), used for UTh determination, was found to be the source for some of the estimator uncertainties, due to variation in material properties and diameter between the bone samples (Moilanen *et al.*, 2007). This study (Moilanen *et al.*, 2007) also suggested, based on measurements made in nonaxisymmetric bone phantoms, that the impact of such slight irregularities in bone geometry is only moderate, and analytical theory could satisfactorily model the velocity of flexural guided wave in real bone. This part of the study was, however, made in phantoms with simplified bone geometry. In particular, it did not take into account any variation in the direction of the long axis of bone, and the impacts of geometrical irregularities on ultrasonic measurements were not quantified. Thereby, the suitability of an analytical plate or tube model for determination of UTh is not completely established yet.

Due to the lack of a well-defined theoretical model to describe guided-wave propagation in a complex structure such as long bones, it is not possible to accurately describe results measured for bone. Despite its potential, the approach of guided waves has not yet gained a rapid success as a novel method of long-bone characterization. The gap between guided wave theory and guided waves measured in the bone structure could, however, be filled by using numerical simulation of wave propagation as a tool. This requires development and validation of a numerical bone model that takes into account the real macrostructure and material properties of bone.

Numerical simulations based on the finite-difference method have been previously used to study axial transmission of the fast first-arriving signal in long bones (Bossy *et al.*, 2002; 2004). However, there are very few papers on numerical simulation of guided-wave propagation in long bones. Recently, simulations based on the finite-element method were used to investigate the ability of guided waves to monitor fracture healing in long bones (Protopappas *et al.*, 2006). This study, however, described bone as a two-dimensional plate. To our knowledge, the present paper is thus the first one to model guided-wave propagation in long bones by using the finite-difference method, and the first one to study this propagation in a virtual bone model that is developed on the basis of realistic and individualized long-bone geometry.

The purposes of this study were to develop a two-dimensional (2D) numerical bone model, which describes realistic macrostructural geometry of long bones in the direction of the bone's long axis, and to use this bone model (a) to evaluate the effect of sample-specific variations in cortical thickness on the accuracy of using Lamb wave theory (Lamb, 1917) to predict measured *in vitro* ultrasound data, and (b) to evaluate the extent to which the 2D bone model explains variability observed in real *in vitro* ultrasound data. To this end, the simulated ultrasound data for virtual bones were compared (a) to analytical and numerical plate models and (b) to real *in vitro* ultrasound data.

II. MATERIALS AND METHODS

A. *In vitro* study

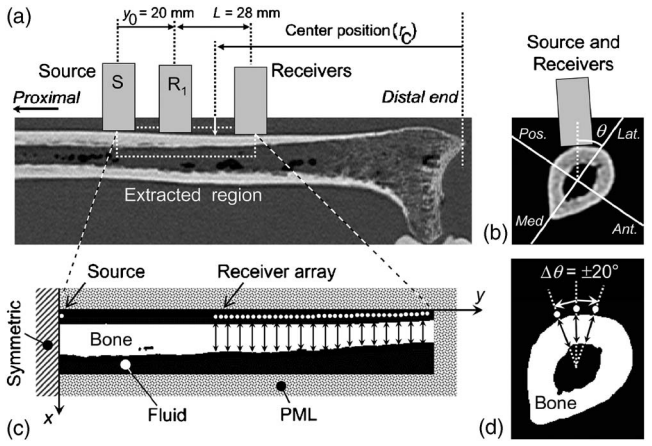

FIG. 1. Longitudinal cross section (a) and transverse cross section (b) of a 3D x-ray computed tomography (CT) reconstruction of a human radius bone. Physical probes were positioned based on a given longitudinal site marker (center position) and the anatomical directions shown. Simulation maps were created from extracted CT volumes corresponding to measurement regions. Binarized longitudinal cross section of bone (c) was used as a 2D simulation map. Materials, boundary conditions, and positions of point source and receivers are shown. Determination of local cortical thickness (CTh) is shown by arrow markers. Uncertainty of tangential positioning of extraction is shown superimposed with a transverse cross section of binarized CT volume (d).

1. Bone samples

Ten fresh and intact human-radius specimens, with soft tissues removed, were used for the *in vitro* study.

2. Low-frequency ultrasound assessments

A low-frequency ultrasound scanner (f_c=200 kHz), introduced by previous studies (Nicholson *et al.*, 2002; Moilanen *et al.*, 2004; 2006), was used to record ultrasonic velocity v_2. Two similar PZT contact transducers, one source and one receiver, were placed on the same side of long bone, perpendicular to its long axis, in a given source-receiver distance [Fig 1(a)]. The source was fixed and excited by a short pulse, with a center frequency of excitation of f_c=200 kHz and a 300 kHz bandwidth (−16 dB). Ultrasonic gel was used as contact agent. The signal was received sequentially at 40 different source-receiver distances ranging from 20 to 48 mm. Recorded signals were then observed in the time-distance plane, which enabled observation of at least two distinct wave modes, fast first arriving signal (also referred to as Wave 1) and a slower guided wave contribution (also referred to as Wave 2). In this study we focused on Wave 2 and its phase velocity v_2, as this was the basis for a previously introduced inversion scheme to estimate cortical thickness from the recorded velocity of ultrasound (Moilanen *et al.*, 2006, 2007).

Positioning of the ultrasonic source and receivers with respect to a given anatomical site marker r_c is illustrated in Fig. 1(a). Reproducibility of measurements was evaluated from two repeated measurements for each sample and position.

Each bone sample was measured at four different sites, including three axial positions (1, 2, and 3) and two circumferential positions (A and C). The axial positions r_c were measured from the distal end and were located, respectively,

TABLE I. Reference cortical thickness ($\theta=0°$).

	Mean ± s.d.	Range
CTh (mm)	3.03±0.70	2.00–4.93

at 5/25, 7/25, and 9/25 of the length of the whole sample. Tangential position θ was measured from the lateral anatomical direction, approximately, $\theta=35°$ (to posterior) for site A and $\theta=-60°$ (to anterior) for site C [Fig. 1(b)]. Note that position 2A was in accordance with the site typically used for clinical ultrasonic assessments of human radius. Because we did not have CT scans (Sec. II C 2) available for all of the ultrasonically measured bone sites, we only considered ultrasonic measurements performed for a number of these positions (Table I). This yielded a total sample size of $n=29$.

B. Numerical simulations

1. Algorithm

Propagation of transient signal was simulated numerically using a finite-difference time-domain method. Simulations were performed by using a custom-made code developed previously in LIP (Bossy *et al.*, 2004). In this code, discretization of the linear elastic wave equations is made according to the Virieux scheme (Virieux, 1986; Graves, 1996), which provides a good implementation of fluid-solid interfaces and attenuating layers, referred to as perfectly matched layers to avoid numerical reflection artifacts. The grid step used for all simulations was $h=100$ μm, which represented $\lambda_c^L/200$, $\lambda_c^T/90$ and $\lambda_c^F/30$, where λ_c is the center wavelength, and superscripts L, T, and F refer, respectively, to longitudinal and transverse bulk velocity in solid, and bulk velocity in fluid. The grid step satisfied the condition $h<\lambda_{\min}15$, where $\lambda_{\min}$ is the minimum wavelength propagating in the system.

2. Transducers and signal modeling

One point source was used to excite a short Gaussian-distributed excitation pulse with a center frequency of $f_c=200$ kHz and a bandwidth of 300 kHz (−16 dB). An array of 40 point receivers with the closest source-receiver distance $y_0=20$ mm and a pitch of 0.7 mm was used to simulate the ultrasonic scan made by the experimental receiver [Fig. 1(c)]. The length of the receiver array was thus approximately $L=28$ mm. Thereby, realistic excitation and reception was simulated with the exception of the geometry of transducer elements. Point elements were used in order to generate and receive any propagating wave modes, because this has essentially been the approach of developing the experimental measurement. The physical transducers used have a finite diameter, however, so, based on simulations made in a few randomly chosen samples, we checked to see that the choice of using point elements instead of finite-sized ones did not affect significantly the recorded ultrasound velocities. Simulated source and receivers were located in ambient liquid, 1 mm apart from the solid substrate. A time history of 50 μs was recorded at the receivers.

C. Materials modeling

1. Ambient fluid

The objective was to simulate *in vitro* experiments, thus bone should be considered as a free waveguide. However, bone has curved boundaries, but using the finite-difference code available at our laboratory, we were restricted to using (free) boundary conditions for orthogonal boundaries only. Therefore, it was necessary to immerse the bone sample in a fluid medium to cut orthogonal boundaries. This caused leakage of ultrasonic waves into the ambient fluid, which affects attenuation and alters phase-velocity dispersion of guided waves.

It is well known that radiation into surrounding fluid is proportional to the density ratio between the fluid and solid substrate (Viktorov, 1967). The effect of fluid loading thus decreases with decreasing fluid density. On the other hand, to be able to distinguish the leaky A_0 wave from bulk waves in a fluid, it is preferable to have the bulk velocity of the fluid lower than the phase velocity of A_0 wave in solid. Thus, if the density and bulk velocity of the ambient fluid are low enough, compared to those of the solid, the effect of fluid loading can be neglected, and the solid structure immersed in such a fluid can simulate a free waveguide. After several trials with different fluid properties, we ended up using properties of a nonphysical, arbitrary light ambient fluid. The chosen fluid had the density $\rho_F=0.5$ g/cm^3 and the bulk velocity $c_F=632$ m/s.

2. Cortical bone model

a. Material parameters Bone was considered as a homogeneous, isotropic elastic medium. Its material parameters were considered fixed throughout the samples. Values $c_L=4000$ m/s, $c_T=1800$ m/s, and $\rho=1.85$ g/cm^3 were used for bone, consistent with Bossy *et al.* (2004).

b. Geometry The actual macrostructural geometry was considered for each sample and was extracted from three-dimensional x-ray computed-tomography (CT) reconstructions (Fig. 1). The CT reconstructions were produced using Somaton 4 Plus (Siemens). A symmetric voxel of 100 μm was obtained by linear interpolation from the original 200 μm longitudinal and, approximately, 100 μm transverse resolution.

Extraction of bone geometry for 2D simulation maps was started by positioning the ultrasonic probes to match the positions used in experimental *in vitro* measurements. To this end, the longitudinal axis of bone was determined by a straight line fitted to the center-of-mass points of transverse cross sections, and the transverse anatomical directions were then used to fix the remaining two Cartesian coordinate axes. The ultrasonic probes were positioned in this coordinate system of bone, 1 mm apart of the periosteal surface.

Longitudinal axis together with a path drawn by the ultrasonic probes defined a plane of the longitudinal cross section. A given threshold level was then used to transform the corresponding gray-level CT cross section into a two-color simulation map, representing bone wall and ambient fluid [Fig. 1(c)].

The physical ultrasonic probe was relatively large compared to the diameter of radius bone shaft and, therefore,

exact positioning of simulated point probes to match the positions of physical probes was not possible. To evaluate the uncertainty of positioning the simulated probes, simulations were performed for five longitudinal cross sections within $\theta = \pm 20°$ from the default position [Fig. 1(d)].

3. Plate models

a. Uniform plate Simulations on plates with constant thickness were used to evaluate the accuracy of the whole method of velocity measurement, when the model used for inversion is identical to wave propagation and when the thickness is known and constant. Material properties of the plates were considered fixed and concordant with those of the inversion scheme (Sec. II G).

b. Nonuniform plates Plates with linear thickness variation and plates with rough bottom surface were used as simplified models on the aspects of thickness variation observed for the bone model. Based on bones' reference thickness data (Sec. II D), linear thickness variation was modeled in simulations in plates by thickness decreasing linearly with increasing source-receiver distance, and surface roughness in plates by rough lower ("endosteal") surface. Elastic properties of the thickness variation models were the same as those used for the bone model.

D. Reference thickness assessment

Reference cortical bone thickness (CTh; Table I) was deduced from the binarized simulation maps (2D longitudinal cross sections). For each sample, CTh was defined as an average of cortical thickness $e_{\text{cortical}}(y,\theta)$ within a finite volume determined by the longitudinal range covered by the receiver array ($\Delta y = L = 28$ mm) and across five circumferential angles $\Delta\theta = \pm 20°$ for each sample [Figs. 1(c) and 1(d)].

Cortical thickness $e_{\text{cortical}}(y)$ was observed to decrease gradually for all the samples with increasing source-receiver distance y. Proportional linear axial variation in cortical thickness was given by

$$\Delta e_{\text{axial}} = \frac{e_{\text{cortical}}(y_0 + L) - e_{\text{cortical}}(y_0)}{e_{\text{cortical}}(y_0 + 1/2L)}, \quad (1)$$

where y_0 is the position of first receiver and L the length of receiver array. Linear axial variation in e was assessed by using linear regression and Eq. (1) between $e(y)$ and y points $(y = y_0, \ldots, y_0 + L)$, and the rms sample mean ± standard deviation was 35±20%. Surface roughness was assessed as the residual of the linear regression between $e(y)$ and y, and the rms value ± standard deviation for all samples was 6.5±2.5%.

E. Visualization of signals

Temporal snapshots were used to visualize simulated wave field. Each simulation snapshot represents absolute values of the displacement-velocity wave field, using a logarithmic gray scale combined with transparency effects to visualize bone (e.g., Fig. 2).

Distance-time diagrams were used to illustrate signals measured at the array of receivers. This diagram illustrates absolute values of normal (perpendicular) particle velocity, using a gray scale, as functions of source-receiver distance and time history [e.g., Fig. 3(a)].

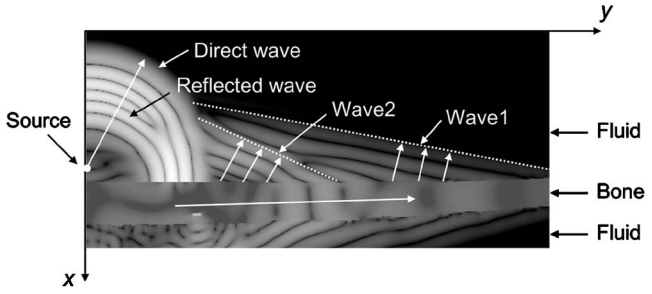

FIG. 2. A snapshot of simulated ultrasonic waves propagating through a real cortical bone geometry obtained from 3D x-ray computed tomography (grey frame) and immersed in ambient fluid (black background). The width of the simulation area shown is approximately 50 mm. Different wave modes identified are "direct" wave emitted in the fluid, wave "reflected" from the interface of fluid and bone, and first arriving signal (Wave 1) and slower second wave (Wave 2) propagating in bone and leaking from bone to surrounding fluid.

F. Signal analysis

Phase velocity v_2 of Wave 2 was assessed by using the two-dimensional fast Fourier transform (2D-FFT) (Alleyne and Cawley, 1991). A method called group-velocity filtering was used prior to 2D-FFT to extract Wave 2 from the temporal signal (Moilanen *et al.*, 2006). This has been reported to enhance identification of Wave 2. Phase velocity $v_2 = v_2(f_i, c_{\text{gr}}, t_w, t_d)$ of Wave 2 was thus a function of frequency f_i and three parameters, group velocity c_{gr}, time width t_w, and time delay t_d, of group-velocity filtering.

In this study, dispersion of v_2 was assessed within a frequency range of 50–350 kHz. Fixed (across the samples) and constant (with regards to frequency) group-velocity, time-width, and time-delay parameters were used for group-velocity filtering, and thus the phase-velocity results were independent of variation in filtering parameters (Fig. 3). Fixed values of filtering parameters were chosen after a study on reference waveguides (uniform plates, Sec. II C 3). As a result, the value chosen for the group velocity parameter was approximately consistent with the group velocity of an A_0 Lamb mode.

G. Inversion scheme

Ultrasonic cortical thickness estimate, UTh, was deduced from the measured phase velocity v_2 by using fundamental antisymmetric Lamb mode (A_0) as the inversion model (Moilanen *et al.*, 2006). The choice of inversion model was based on a good accordance obtained by previous phantom and *in vitro* studies between v_2 and phase velocity of A_0 (Nicholson *et al.*, 2002; Moilanen *et al.*, 2006; Lefebvre *et al.*, 2002; Lee and Yoon, 2004), and the particular sensitivity of A_0-mode phase velocity to wall thickness.

UTh, was obtained by minimization of cost function

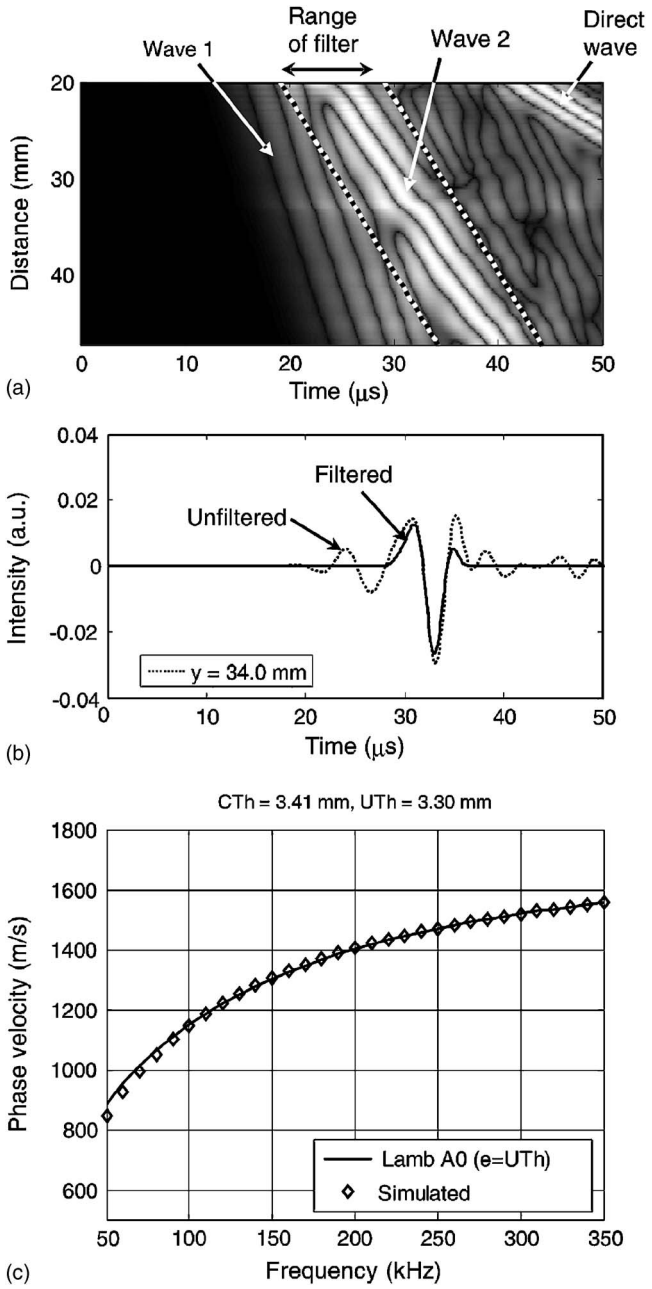

FIG. 3. Analysis of Wave 2: Results for a simulated *in vitro* measurement. (a) Distance-time diagram: Identified wave modes and the range of group-velocity filter are shown. (b) Recorded (dashed line) and group-velocity filtered (solid line) signal. (c) Phase velocity of Wave 2 (markers) and fitted phase velocity of A_0 (line).

$$J(e) = \sum_{i=1}^{N} |d_i(f_i, e)|, \tag{2}$$

where

$$d_i(f_i, e) = v_2(f_i) - c_{\mathrm{ph}}^{A_0}(f_i, e) \tag{3}$$

is the residual between the phase velocities of Wave 2 (v_2) and A_0 ($c_{\mathrm{ph}}^{A_0}$) at frequency f_i for plate thickness e. Thickness e was the fitting parameter and UTh$\equiv e$ when Eq. (2) converges to its minimum. The phase velocity of A_0 is $c_{\mathrm{ph}}^{A_0} = c_{\mathrm{ph}}^{A_0}(f_i, e, c_L, c_T)$, where c_L and c_T are, respectively, the compression and shear bulk velocity. Parameters c_L and c_T were chosen fixed (nonindividualized) for all the bone samples according to proper reference values reported in the literature and, for simplicity, are not shown explicitly in Eqs. (2) and (3).

In this study, the bulk-velocity parameters of Eq. (3) represented isotropic elastic material and the values were the same as those used for a numerical bone model and reference plate waveguides (Sec. II C).

A recent *in vitro* study in human radii (Moilanen *et al.*, 2007) reported that an F_{11} tube mode was more suitable than A_0 as the inversion model for tubular bone geometry. Using A_0 was observed to yield overestimated UTh as compared to reference cortical bone thickness, particularly when the sample had a thick wall with respect to its outer diameter. In the present study, however, the 2D simulations did not take tubularity into account and A_0 was expected to model best the simulated v_2. For consistency, the A_0 model was also used for experimental *in vitro* data.

An example of UTh determination based on A_0 is illustrated in Fig. 3(c). For the clarity, different symbols and abbreviations used for velocity and thickness are summarized in an appendix.

H. Data analysis

Linear regression analysis (Snedecor, 1976) and Bland-Altman plots (Bland and Altman, 1986) were used to compare cortical thickness estimate data with true cortical thickness and physical *in vitro* data with simulated *in vitro* data.

III. SIMULATION RESULTS

A. Results

Four wave modes, the first-arriving signal (Wave 1), slower second wave (Wave 2), direct wave, and reflected wave, were identified in a snapshot of simulated *in vitro* measurement (Fig. 2). These wave modes were also observed in a recorded distance-time diagram [Fig. 3(a)], although the reflected wave interfered with the direct wave and was not identified separately.

Figure 3(c) shows an example of velocity v_2 (f =50–350 kHz) for one virtual bone sample. It was consistent with the phase velocity $c_{\mathrm{ph}}^{A_0}$ of an A_0 mode (e=CTh). For the center frequency (f_c=200 kHz) and throughout all the virtual bone samples, v_2 followed the same trend as $c_{\mathrm{ph}}^{A_0}$, however, v_2 was slightly lower than $c_{\mathrm{ph}}^{A_0}$ (Fig. 4). A root-mean-squared error (rmse) between v_2 for the bone model and $c_{\mathrm{ph}}^{A_0}$ (through all the samples and frequencies f =50–350 kHz) was 33 m/s. Velocity v_2 for the bone model was also consistent with v_2 simulated for plates (e=CTh) (Fig. 4). We observed, however, that v_2 for plates differed slightly from $c_{\mathrm{ph}}^{A_0}$, particularly in thicker samples. Therefore, $c_{\mathrm{ph}}^{A_0}$, but not v_2 for plates, was used as the reference.

UTh data for virtual bone samples yielded a strong linear correlation with CTh (r^2=0.94, $p<0.001$), but UTh data lay slightly below the identity line [Fig. 5(a)]. (rmse) between UTh and CTh was 0.26 mm and a relative difference between UTh and CTh was −6±5% (−18±15 mm for the average CTh=3 mm) [Fig. 5(b)].

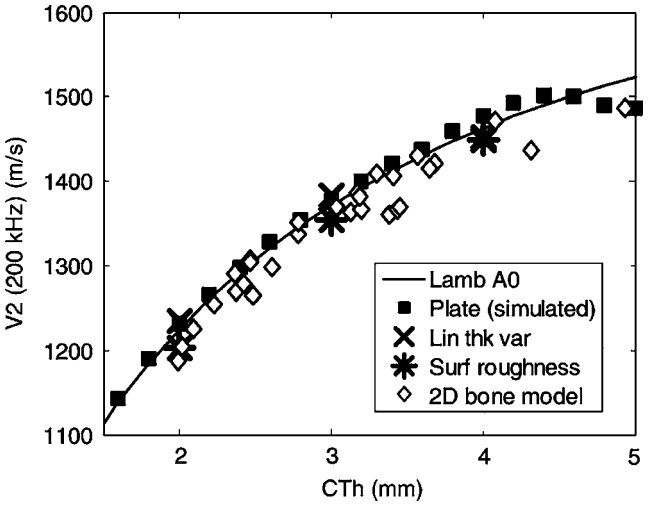

FIG. 4. Simulated v_2 for plates, linear thickness-variation model (Lin thk var), surface-roughness model (Surf roughness), and bone geometry. Phase velocity of Lamb A_0 is shown for comparison with v_2.

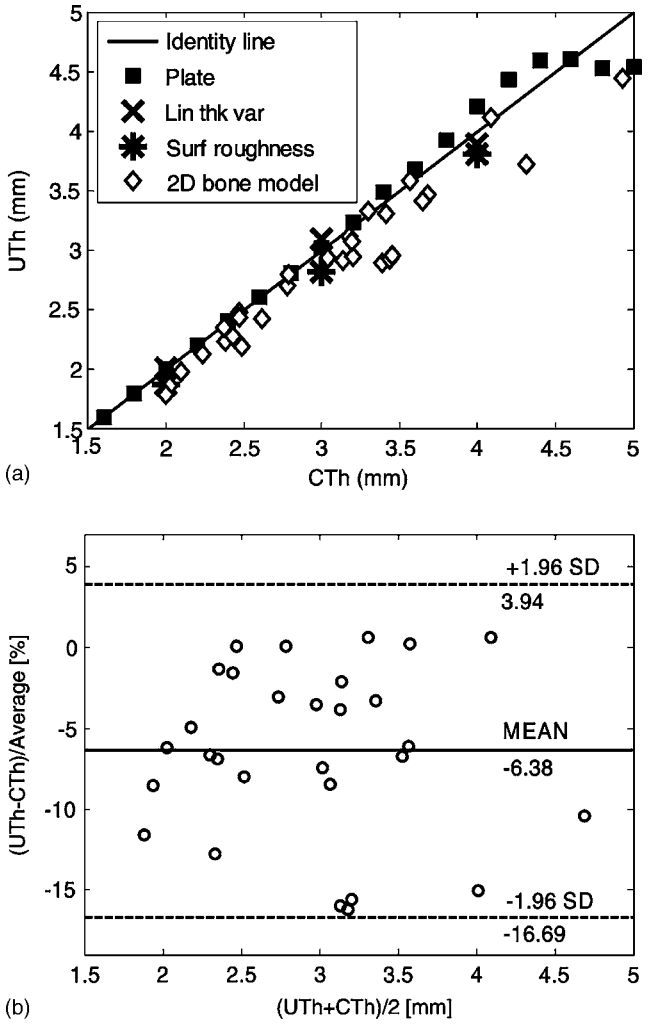

FIG. 5. (a) UTh data with respect to CTh for simulations on uniform plates (square markers), plates with linear thickness variation (crosses), plates with rough bottom surface (stars) and structures obeying bone geometry (diamonds). Identity line is shown for the reference. (b) Bland-Altman plot shows the relative accuracy error between UTh and CTh data for bone geometry.

TABLE II. Descriptive statistics of measured ultrasound data (n=29).

	Mean± s.d.	Range	rms CoV (%)
Simulation results			
v_2 100 kHz (m/s)	1078±94	894–1268	2.0
v_2 200 kHz (m/s)	1345±78	1187–1487	1.3
UTh (A_0) (mm)	2.85±0.66	1.78–4.45	5.1
Experimental results			
v_2 100 kHz (m/s)	1136±156	863–1444	1.2
v_2 200 kHz (m/s)	1358±118	1143–1610	0.8
UTh (A_0) (mm)	3.27±1.43	1.56–7.69	3.4

When a UTh measurement with repeatability error of 5.1% (assessed by means of root-mean-square coefficient of variation, Table II) was used in a linear regression model as a predictor for true cortical thickness, the precision error of a single thickness estimate was PE_{ThkEst}=0.25±0.01 mm.

B. Discussion

As we in this paper studied the impact of realistic axial 2D geometry alone, the accordance between simulation results and reference thickness (r^2=0.94) was expectedly better than that reported previously for experimental *in vitro* data in human radii (r^2=0.81) (Moilanen *et al.*, 2007).

It was thus shown that all the low-frequency ultrasonic velocities for virtual bone were in a general accordance with those for plates. These results justified the use of simple plate theory as the basis of inverse schemes for ultrasonic estimators (here UTh) of bone properties (here CTh). Indeed, the UTh data were shown to be strongly related to CTh, in agreement with a previous *in vitro* study (Moilanen *et al.*, 2007). In this simulation study, however, the ultrasonic data were affected by realistic geometry of the virtual bone model alone, whereas the *in vitro* ultrasound data were also affected by variation in material properties of the bone samples. Any discrepancy shown between simulations on virtual bone and plate of constant thickness thus purely represented the impact of axially varying cortical thickness.

On the other hand, agreement between plate results and virtual bone was only modest. For both velocities and UTh, a general tendency of ultrasonic data for bone model was to be lower than those for plate with a constant thickness of e=CTh. We attempted to explain this difference by simulation modeling in plates with linearly varying thickness and in plates with rough bottom surface. Linear thickness variation is expected to cause propagation of so-called adiabatic modes (Ech-Cherif El-Kettani *et al.*, 2004), which adapt themselves locally to slowly varying thickness of the waveguide. It is also well known that characteristics of guided waves are sensitive to the condition (roughness) of the guiding surfaces (Lobkis and Chimenti, 1997a,b; Sheard and Spivak, 1995). Thus, surface roughness is also expected to affect the signal. The bone samples were observed to have systematically a linearly decreasing thickness component with respect to increasing source-receiver distance (Sec. II D). On the other hand, they also had some surface roughness. Simple simulation models, taking into account the average linear and nonlinear thickness variation of the bone samples,

gave predictions for the impact of thickness variation for three average plate thicknesses (e=2, 3, and 4 mm, $e \equiv$CTh) (Figs 4 and 5). Linearly decreasing thickness was observed to overestimate ultrasound results as compared to those for a plate model, and surface roughness seemed to underestimate them (Figs 4 and 5). These initial results thus suggest that the negative offset between results for bone model and plate model can be explained mostly by surface roughness.

We did not perform an explicit quantitative analysis of the impact of thickness variation by using these simplified models of uneven thickness, because for v_2 and UTh it was not possible to extract purely the impact of sample geometry. This can be observed as a discrepancy between simulated v_2 data on plates and $c_{\mathrm{ph}}^{A_0}$ (Fig. 4), and between simulated UTh on plates and true plate thickness e (Fig 5). This occurred because A_0 is often (particularly for thicker plates) influenced by interferences with other wave modes, such as S_0, and the signal analysis used cannot, for a realistic receiver array length ($L \cong 30$ mm), unambiguously separate such interfering signal contributions (Moilanen *et al.*, 2006). Because interferences are characteristic of the system analyzed, the results shown here for limited signal-processing accuracy for plates do not represent generic results for other sample geometries. As we had no analytical results available for the numerical models of uneven thickness, the impact of interferences on v_2 and UTh data for these sample geometries could not be accurately modeled and separated.

As a conclusion, a simple plate model can be used to describe well the average cortical thickness of long bones within a limited range (here y_0=20 mm and L=28 mm). Discrepancy between the plate model and ultrasonic results for virtual bone was then 33 m/s for v_2 and 0.26 mm for UTh. Final estimation for the precision on which a UTh measurement (with $\mathrm{PE}_{\mathrm{ThkEst}}$=0.25 mm) can discriminate changes in true cortical bone thickness is given by the least significant difference, which at the 95% confidence level is 2.8 $\mathrm{PE}_{\mathrm{ThkEst}}$=0.70 mm. These results are strictly limited to *in vitro* measurements and the 2D model presented. Any fundamental alteration of the sample or measurement system [*in vitro*/*in vivo*, 2D/three-dimensional (3D), frequency range, probe positions, array length, type of long bone, etc.] may affect the accuracy differently, and requires a new assessment of the validity of using a simplified model to represent ultrasonic data for bone. To this end, numerical simulations in related virtual bone models will provide a powerful tool.

IV. SIMULATED VERSUS EXPERIMENTAL DATA

A. Results

Distributions of ultrasound variables determined for the simulated and experimental measurements are summarized in Table II. (rms) coefficient of variation represents uncertainty of positioning for simulated data and repeatability for experimental data.

Simulated ultrasound velocity v_2 was significantly correlated with experimental v_2 (Fig. 6). The simulated v_2 explained approximately 80% of the variation in the experimental v_2. Accordingly, simulated and experimental UTh were significantly correlated, and simulated UTh data explained 77% of the variability in experimental UTh data.

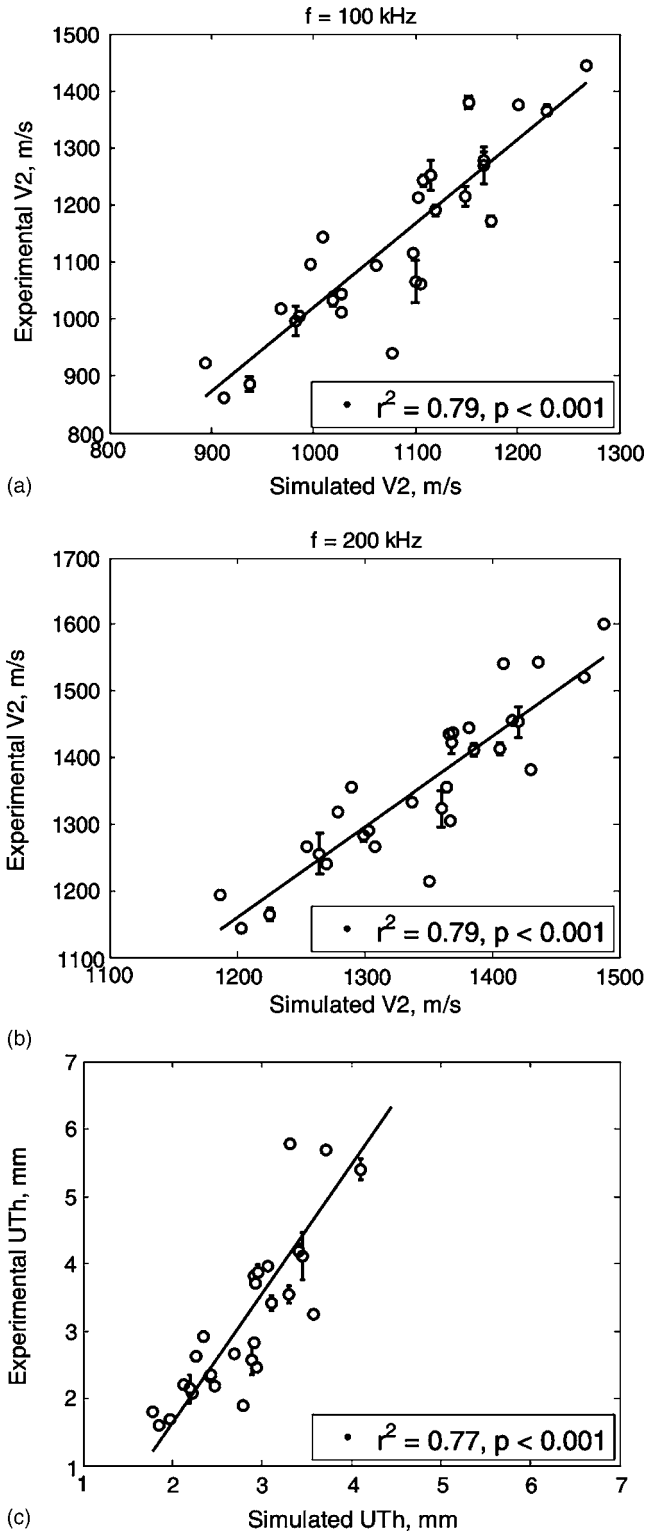

FIG. 6. Correlations between simulated and experimental ultrasound results. The error bars shown express the uncertainty of probes positioning.

B. Discussion

Despite the simplicity of the 2D bone model, variability in simulated data explained 80% of the variability in experimental data. This confirms that variation in cortical thick-

ness, which was the only property in common between the numerical bone model and real bone, was the major contributor to the variability in low-frequency axial ultrasound velocities. Any discrepancy between simulated and experimental results is expected to relate to uncertainty of probe positioning, limited reproducibility of experiments, and to such bone properties and property variations that were not included in the bone model.

Ranges and sample means of experimental v_2 and UTh data were slightly greater than those for simulations. This difference can be explained as the experimental *in vitro* measurements considered the bone shaft to be tubular, but the simulations modeled bone as a flat plate. The phase velocity of the fundamental flexural tube mode, F_{11}, is known to be slightly higher than that of the A_0 plate mode, and this can directly explain the difference observed in v_2 results. When the A_0 mode is used to fit v_2 data for a three-dimensional tubular bone geometry, this accordingly yields overestimated UTh (Moilanen *et al.*, 2007). We, however, did not include the F_{11} inversion model in this work so that our UTh results relying on A_0 model fit represented purely the differences between the numerical bone model and real bone.

The variability in simulated data thus explained 80% of the variability in experimental data. To test whether uncertainties of simulated and experimental ultrasound data explained some of the unexplained variability, the uncertainty of simulated and experimental data was first quantified and the impact of this uncertainty was then numerically evaluated.

Variation in axial cortical thickness was the only property in common with the numerical bone model and real bone, whereas variation in bone diameter and material properties between the samples related only to real bones. Variation in bone diameter and material properties should thus be considered as uncertainties (Moilanen *et al.*, 2007) when comparing the simulated and experimental data of the present paper. The purpose of this paper was, however, to study the impact of 2D (axial) geometry alone, thus we did not take into account the variation in bone-shaft diameter and material properties. We considered the physical experiments to be affected by limited reproducibility alone (rms CoV in Table II), and simulated data by uncertainty of probe positioning (rms CoV in Table II).

Impact of uncertainties on r^2 values between simulated and experimental data was evaluated numerically on initially perfectly correlated sets of variables ($r^2=1$, rmse=0). The uncertainties of each point were individually randomized based on the normal distribution with standard deviation corresponding to uncertainties quantified for ultrasonic results (rms CoV, Table II). The results were obtained after a thousand iterations (Table III). The impact of uncertainties was obtained as a reduction of these correlations, by $1-r^2$. Thus, in general, uncertainties explained 5% of the variability between simulated and experimental results. Given the error bounds, we thereby explained 85±2% (v_2) and 82±2% (UTh) of the variability between simulated and experimental data. The rest, 15% for v_2 and 18% for UTh, can be explained by variation in bone material properties and outer diameter of bone shaft. In addition, some of the uncertainty is expected to relate to the limited accuracy of Wave 2 signal analysis (see Sec. IV).

TABLE III. Correlations between initially perfectly matched experimental and simulation results with randomized errors. rms CoV is considered as the uncertainty in simulations and experiments.

	R square	sd *R* square	*p*
v_2 (100 kHz)	0.94	0.02	<1E-5
v_2 (200 kHz)	0.94	0.02	<1E-5
UTh (A_0)	0.95	0.02	<1E-5

V. CONCLUSION

We developed a 2D numerical bone model and used it to investigate the impact of realistic bone geometry on ultrasonic cortical-thickness evaluation. It was shown that, despite geometrical variation in the plane of longitudinal cross section, the low-frequency axial ultrasound velocities can be modeled by simple plate theory with acceptable error bounds. Thus, ultrasonically determined thickness (UTh) based on fitting with the plate model provides a valid estimate of cortical bone thickness in 2D. Experimental data were influenced by measurement uncertainty and aspects of bone-property variation not taken into account by the 2D bone model. The advantage of developing a numerical bone model was, thereby, that it enabled analysis of sensitivity independently for different aspects of bone-property variation. The complexity of the model can later be progressively increased toward more realistic representation, and this is expected to yield detailed insight into the sensitivity of ultrasonic parameters to different structural properties. This makes numerical simulation a powerful tool for optimization and further improvement of accuracy of this and related quantitative ultrasound methods.

We limited this study to simulations of 2D bone geometry, as cortical thickness assessment can well be modeled in two dimensions and 2D simulations are significantly faster to compute than three-dimensional ones. Despite the simplicity of the model, the simulated ultrasound data were well in agreement with the real *in vitro* data. Some of the unexplained variability between simulations and experiments was explained by uncertainties related to repeatability and positioning, and the rest related to the accuracy with which the elastic and geometrical properties of real bones were modeled. Upgrading the bone model into three dimensions is expected to yield an improved representation of the *in vitro* measurements. Modeling the clinical application and final estimation of accuracy limits of the method described remain additional challenges for future studies.

ACKNOWLEDGMENTS

This work was supported by the French Ministry of Education, the Academy of Finland, and the Franco-Finnish Association for Scientific Research and Technique.

APPENDIX: SYMBOLS AND ABBREVIATIONS

Different symbols and abbreviations used for velocity and thickness are summarized in the following.

A special symbol v_2 was used for the velocity of Wave 2 to separate this property of a recorded signal from any theoretical, computational, or reference value of velocity, expressed by c. Symbols c_L and c_T were used to refer, respectively, to compression and shear bulk velocity, and c_{ph} and c_{gr} denoted, respectively, the phase and group velocity.

Symbol e was used for the plate thickness parameter of Lamb wave theory and e_{cortical} for the cortical thickness. A special abbreviation CTh was used for the average cortical thickness determined across a finite volume, corresponding specifically to the region of ultrasonic measurement. The abbreviation UTh was used for the ultrasonic cortical thickness estimate.

Alleyne, D., and Cawley, P. (**1991**). "A two-dimensional Fourier transform method for the measurement of propagating multimode signals," J. Acoust. Soc. Am. **89**, 1159–1168.

Augat, P., Reeb, H., and Claes, L. E. (**1996**). "Prediction of fracture load at different skeletal sites by geometric properties of the cortical shell," J. Bone Miner. Res. **11**, 1356–1363.

Bland, J. M., and Altman, D. G. (**1986**). "Statistical methods for assessing agreement between two methods of clinical measurement," Lancet **1**, 307–310.

Bossy, E., Talmant, M., and Laugier, P. (**2002**). "Effect of bone cortical thickness on velocity measurements using ultrasonic axial transmission: A 2D simulation study," J. Acoust. Soc. Am. **112**, 297–307.

Bossy, E., Talmant, M., and Laugier, P. (**2004**). "Three-dimensional simulations of ultrasonic axial transmission velocity measurement on cortical bone models," J. Acoust. Soc. Am. **115**, 2314–2324.

Ech-Cherif El-Kettani, M., Luppé, F., and Guillet, A. (**2004**). "Guided waves in a plate with linearly varying thickness: Experimental and numerical results," Ultrasonics **42**, 807–812.

Graves, R. W. (**1996**). "Simulating seismic wave propagation in 3D elastic media using staggered-grid finite differences," Bull. Seismol. Soc. Am. **86**, 1091–1106.

Jansons, H., Tatarinov, A., Dzenis, V., and Kregers, A. (**1984**). "Constructional peculiarities of the human tibia defined by reference to ultrasound measurement data," Biomaterials **5**, 221–226.

Lamb, H. (**1917**). "On waves in an elastic plate," Proc. R. Soc. London, Ser. A **93**, 114–128.

Lee, K. I., and Yoon, S. W. (**2004**). "Feasibility of bone assessment with leaky Lamb waves in bone phantoms and a bovine tibia," J. Acoust. Soc. Am. **115**, 3210–3217.

Lefebvre, F., Deblock, Y., Campistron, P., Ahite, D., and Fabre, J. J. (**2002**). "Development of a new ultrasonic technique for bone and biomaterials in vitro characterization," J. Biomed. Mater. Res. **63**, 441–446.

Lobkis, O. I., and Chimenti, D. E. (**1997a**). "Elastic guided waves in plates with surface roughness. I. Model calculation," J. Acoust. Soc. Am. **102**,143–149.

Lobkis, O. I., and Chimenti, D. E. (**1997b**). "Elastic guided waves in plates with surface roughness. II. Experiments," J. Acoust. Soc. Am. **102**, 150–159.

McCarthy, I., Goodship, A., Herzog, R., Oganov, V., Stussi, E., and Vahlensieck, M. (**2000**). "Investigation of bone changes in microgravity during long and short duration space flight: Comparison of techniques," Eur. J. Clin. Invest **30**, 1044–1054.

Moilanen, P., Nicholson, P. H., Kärkkäinen, T., Wang, Q., Timonen, J., and Cheng, S. (**2003**). "Assessment of the tibia using ultrasonic guided waves in pubertal girls," Osteoporosis Int. **14**, 1020–1027.

Moilanen, P., Kilappa, V., Nicholson, P. H., Timonen, J., and Cheng, S. (**2004**). "Thickness sensitivity of ultrasound velocity in long bone phantoms," Ultrasound Med. Biol. **30**, 1517–1521.

Moilanen, P., Nicholson, P. H. F., Kilappa, V., Cheng, S., and Timonen, J. (**2006**). "Measuring guided waves in long bones: Modelling and experiments in free and immersed plates," Ultrasound Med. Biol. **32**, 709–719.

Moilanen, P., Nicholson, P. H. F., Kilappa, V., Cheng, S., and Timonen, J. (**2007**). "Assessment of the cortical bone thickness using ultrasonic guided waves: Modelling and in vitro study," Ultrasound Med. Biol. **33**, 254–262.

Muller, M., Moilanen, P., Bossy, E., Nicholson, P., Kilappa, V., Timonen, J., Talmant, M., Cheng, S., and Laugier, P. (**2005**). "Comparison of three ultrasonic axial transmission methods for bone assessment," Ultrasound Med. Biol. **31**, 633–642.

Nicholson, P. H. F., Moilanen, P., Kärkkäinen, T., Timonen, J., and Cheng, S. (**2002**). "Guided ultrasonic waves in long bones: Modelling, experiment and in vivo application," Physiol. Meas **23**, 755–768.

Oranov, V. S., Rakhmanov, A. S., Morukov, B. V., Ianson, Kh. A., and Tatarinov, A. M. (**1988**). "Bone examination by noninvasive methods during prolonged hypokinesia," Kosm. Biol. Aviakosm. Med. **22**, 30–33 (in Russian).

Protopappas, V. C., Fotiadis, D. I., and Malizos, K. N. (**2006**). "Guided ultrasound wave propagation in intact and healing long bones," Ultrasound Med. Biol. **32**, 693–708.

Sheard, J. D., and Spivak, M. (**1995**). "Wave scattering in a rough elastic layer adjoining a fluid half-space," J. Acoust. Soc. Am. **97**, 72–83.

Snedecor, G. W. (**1976**). *Statistical Methods*, 6th ed. (The Iowa State University Press, Ames, IA).

Tatarinov, A., Sarvazyan, N., and Sarvazyan, A. (**2005**). "Use of multiple acoustic wave modes for assessment of long bones: Model study," Ultrasonics **43**, 672–680.

Tatarinov, A. M., Dubonos, S. L., Ianson, Kh. A., Oganov, V. S., Dzenis, V. V., and Rakhmanov, A. S. (**1990**). "Ultrasonic diagnosis of the changes in human tibia during 370-day antiorthostatic hypokinesia," Kosm. Biol. Aviakosm. Med. **24**, 29–31 (in Russian).

Turner, C. H. (**2002**). "Biomechanics of bone: Determinants of skeletal fragility and bone quality," Osteoporosis Int. **13**, 97–104.

Viktorov, I. A. (**1967**). *Rayleigh and Lamb Waves*, Plenum, New York.

Virieux, J. (**1986**). "P-SV wave propagation in heterogenous media: Velocity-stress finite-difference method," Geophysics **51**, 889–901.

Wear, K. A. (**2003**). "Autocorrelation and cepstral methods for measurement of tibial cortical thickness," IEEE Trans. Ultrason. Ferroelectr. Freq. Control **50**, 655–660.

High frequency ultrasonic characterization of human vocal fold tissue

Chih-Chung Huang[a)]
NIH Resource on Medical Ultrasonic Transducer Technology, Department of Biomedical Engineering, University of Southern California, Los Angeles, California 90089, and Department of Biomedical Engineering, Chung Yuan Christian University, Chung Li, Taiwan 32023

Lei Sun
NIH Resource on Medical Ultrasonic Transducer Technology, Department of Biomedical Engineering, University of Southern California, Los Angeles, California 90089

Seth H. Dailey
Division of Otolaryngology, Department of Surgery, University of Wisconsin-Madison, Madison, Wisconsin 53792

Shyh-Hau Wang
Department of Biomedical Engineering, Chung Yuan Christian University, Chung Li, Taiwan 32023

K. Kirk Shung
NIH Resource on Medical Ultrasonic Transducer Technology, Department of Biomedical Engineering, University of Southern California, Los Angeles, California 90089

(Received 12 April 2007; revised 5 June 2007; accepted 14 June 2007)

Recently, endolaryngeal sonography at frequencies ranging from 10 to 30 MHz has been found to be useful in diagnosing diseases of the vocal folds (VFs). However, image resolution can be further improved by ultrasound at higher frequencies, necessitating the measurement of high-frequency acoustic properties of VF tissue. The ultrasonic parameters of integrated backscatter, sound velocity, and frequency-dependent attenuation coefficient were measured in both the lamina propria (LP) and vocalis muscle (VM) of human VFs using a 47 MHz high-frequency ultrasonic transducer. The integrated backscatter was -173.44 ± 6.14 (mean±s.d.) and -195.13 ± 3.58 dB in the LP and VM, respectively, the sound velocity was 1667.68 ± 44.9 and 1595.07 ± 39.33 m/s, and the attenuation coefficient at 47 MHz was 8.28 ± 1.72 and 7.17 ± 1.30 dB/mm. The difference between these ultrasonic parameters may be attributed to variations in the structure and fiber concentrations in VF tissue. These results could serve as a useful clinical reference for the further development of high-frequency ultrasound devices for endolarynx sonography applications. © *2007 Acoustical Society of America.* [DOI: 10.1121/1.2756759]

PACS number(s): 43.80.Vj [CCC] Pages: 1827–1832

I. INTRODUCTION

The vocal folds (VFs) are located side by side in the larynx, just above the trachea. Vocal fold vibration is achieved when the VFs are entrained into self-sustained oscillation by the tracheal airstream during exhalation. Human VFs are typically 10–15 mm long and 2–4 mm thick. The VF is a laminated structure consisting of nonkeratinizing stratified squamous epithelium, the lamina propria (LP), and the vocalis muscle (VM). The viscoelastic components of the LP (e.g., hyaluronic acid) are critical as they modulate oscillation of the VFs during phonation.[1] Common diseases of the LP such as nodules, polyps, cysts, and scarring all influence the function of the VFs.[2]

Office-based or surgical endoscopy is currently the most frequently used technique to diagnose diseases of the VFs. However, diagnoses based on endoscopy are hindered by the shortcoming of this technique only providing images of the surface of the VFs, and not yielding quantitative information about deeper layers. Several medical imaging modalities including computed tomography (CT),[3] magnetic resonance imaging (MRI),[4] and optical coherence tomography (OCT)[5] have also been used to diagnose problems of the VFs. However, the resolution of CT and MRI is limited, and OCT can only penetrate living tissue by approximately 2 mm.[5] Recently, ultrasound has been shown to be useful in diagnosing diseases of the larynx and VFs due to its low cost, high resolution, real-time, and noninvasive capabilities. Friedman[6] used a 7 MHz ultrasonic scanner to study the properties of the VFs in animal models and humans, with the transducer positioned outside the larynx. Rudorf *et al.*[7] used a linear array of 10 MHz ultrasonic transducers to assess laryngeal paralysis in dogs, and Rubin *et al.*[8] investigated differences between solid and cystic swelling in human VFs. Hsiao *et al.*[9] used color Doppler imaging to measure the elasticity of human VFs. Furthermore, high-frequency ultrasound up to 30 MHz has been used for endolaryngeal sonography applications due to its high resolution. Arens *et al.*[10]

[a)]Electronic mail: j648816n@ms23.hinet.net

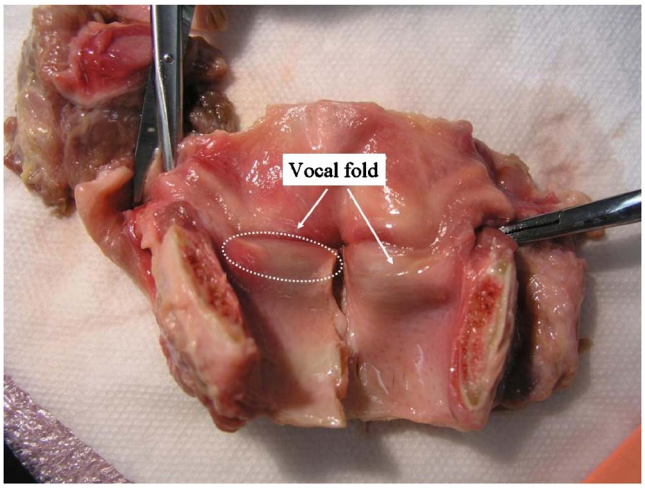

FIG. 1. (Color online) A photo of a human larynx split open in midsaggital section. The location of the VFs is indicated by the arrows.

developed a high-frequency ultrasound transducer placed on the tip of a small endoluminal catheter for imaging the structure of the larynx, which allowed exact 360° cross sections of the larynx to be obtained. Arens and Glanz[11] also demonstrated that high-frequency ultrasound allowed clinicians to evaluate the size and infiltration of laryngeal lesions and perform a more accurate preoperative staging than when using CT or MRI. Moreover, Tamura *et al.*[12] characterized the properties of VF nodules, polyps, cysts, and cancer using 30 MHz endolarynx sonography. Tamura *et al.*[13] reported that the epithelium, LP, and VM of the VFs could be visualized by 30 MHz endolarynx sonography. However, it is possible to further improve the resolution of ultrasound image in VF tissue by using even higher frequency ultrasound. As ultrasound frequency is increased to 50 MHz, an axial and lateral resolution of better than 20 and 100 μm can be achieved, respectively.[14] Depending on the frequency used, the anatomical structures could be visualized up to a depth of 5 mm at a frequency of 50 MHz, which is suitable for imaging VF tissue (the thickness is typically 2–4 mm). Consequently, the high-frequency acoustic properties of VF tissue need be characterized before high-frequency imaging can be applied to clinical applications.

In this study, the quantitative acoustic parameters of integrated backscatter, frequency-dependent attenuation coefficient, and sound velocity were measured at 47 MHz in the LP and VM of VFs obtained from human cadavers. All experiments were carried out using a high-resolution ultrasound biomicroscope (UBM) system. The ultrasonic parameters obtained for the LP and VM are discussed.

II. MATERIALS AND METHODS

A. VF samples

The present study was approved by Institutional Review Boards of both the University of Southern California and University of Wisconsin-Madison. Larynges were obtained from human cadavers at the University of Wisconsin-Madison, School of Medicine's Department of Anatomy within 1 h after death. Four larynges (8 vocal folds) obtained from individuals without vocal fold pathology ranging in age from 40 to 73 (64±19) years old from four caucasian males were included in this study. The larynges were split in the midsagittal plane to yield two hemi larynges with easily accessed VFs. The VFs were then cut away from the attached cartilaginous framework of the larynx and the LP surgically divided from the VM along the long axis of the vocal fold. Both the LP and VM were approximately 1 mm thick. Figure 1 shows a photo of human larynx, and the location of VFs is indicated by arrows.

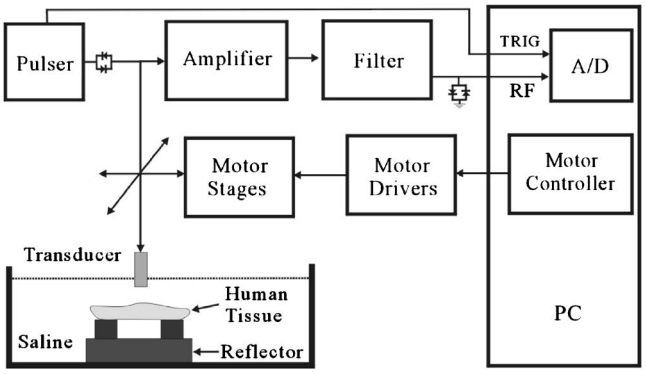

FIG. 2. Block diagram of the experimental setup.

B. Experimental arrangement and UBM system

The experimental arrangement is shown in Fig. 2. Prior to the measurements, the VF tissues were placed on a rectangular polyurethane board with a square acoustic window for the transmission and reception of ultrasound energy. A quartz flat reflector was placed under the tissue, where the distance from the transducer to the reflector is 8 mm. The distance between transducer and tissue is approximately 5.5 mm. A high-frequency ultrasonic transducer (NIH Ultrasonic Transducer Resource Center, USC) with a center frequency of 47 MHz was used in the measurements. The characteristics of the transducer are listed in Table I. Figure 3 shows the pulse-echo wave form and spectrum from the transducer used in this study. Both the ultrasonic transducer and the VF tissues were placed in a saline solution and all measurements were performed at a room temperature of 25.0 °C.

The schematic diagram of the high-resolution UBM system is shown in Fig. 2. The ultrasonic transducer was held on a motor stage (Parker Hannifin Corp., Cleveland, OH) and the *B*-mode image was acquired as the transducer was moved linearly in the sweep scan mode in which the motor stage was controlled by a motor controller. A high-voltage pulser (AVB2-TB-C, Avtech Electrosystems Ltd., Ottawa, Ontario, Canada) was used to produce a cycle of sinusoidal wave with

TABLE I. Characteristics of the transducer.

Center frequency	47 MHz
Fractional bandwidth	23%
F-number	1.8
Focal length	5.5 mm
Diameter	3 mm

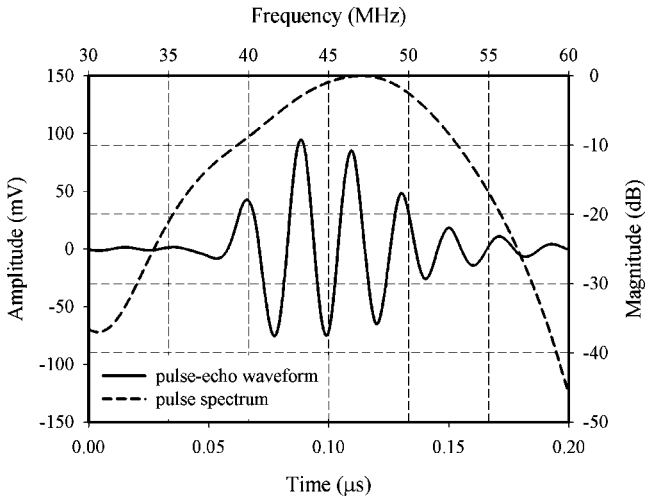

FIG. 3. Pulse-echo wave form and spectrum of the transducer.

an output voltage up to 400 V peak-to-peak. The pulse proceeded through an expander (Matec Instruments Company, Northborough, MA) to remove low amplitude noise, and then through a T-junction to drive the transducer. The received rf signals backscattered from human tissue were amplified by a low noise amplifier (Miteq 1166, Miteq Inc., Hauppauge, NY) at a noise figure of 1.2 dB, and then a bandpass filter (Model BIF-50, Mini-Circuits, Brooklyn, NY) was used to remove the noise out of the main bandwidth. The rf signals were passed through an electronic limiter (Matec Instruments Company, Northborough, MA) for protection purposes. Subsequently, the rf signals were digitized using a 14 bit analog-to-digital converter (CS14200, Gage Applied Technologies, Inc., Lachine, Quebec, Canada) with a maximum sampling frequency of 200 MHz housed in a personal computer. The *B*-mode images were obtained from envelopes corresponding to each *A* line of the rf backscattered signals calculated using the Hilbert transform. For each *B*-mode image, the image size was 7 mm × 10 mm, corresponding to 800 *A*-line signals being acquired.

C. Parameter analysis

1. Integrated backscatter

Integrated backscatter is defined as the frequency average of the backscattering transfer function of a volume of tissue over the bandwidth of the transducer normalized relative to that from a flat reflector. The integrated backscatter (IB) is given by[15]

$$\mathrm{IB} = \frac{1}{f_2 - f_1} \sum_{f_1}^{f_2} \frac{|S_r(f)|^2}{|S_{\mathrm{ref}}(f)|^2}, \tag{1}$$

where f_1 and f_2 denote the lower and upper frequencies of the −6 dB bandwidth of the ultrasonic spectrum, respectively, and $S_r(f)$ and $S_{\mathrm{ref}}(f)$ represent the spectra corresponding to backscattered signals returned from the VF tissues and an echo received from a quartz flat reflector in the distilled water, respectively. For each measurement, the rf signals corresponding to a 1.0-mm-long gated window in the focal zone of the transducer were acquired.

2. Sound velocity

A pulse-echo approach was used to measure the sound velocity in the VF tissues, which eliminates the need to measure its thickness.[16] This method is based on the measurement of four times of flight from different positions. Assume that T_m and T_w are the times of flights with and without the sample in the propagation path from the reflector, respectively, and t_1 and t_2 are the times of flight for the pulse to travel from the transducer to the front and rear faces of the VF tissues, respectively. The sound velocity (V) in the VF tissues was calculated using

$$V = C\left(\frac{T_w - T_m}{t_2 - t_1} + 1\right), \tag{2}$$

where C is the sound velocity in saline solution. After the sound velocity was calculated, the accurate thickness (D) of tissue can be estimated using

$$D = \frac{V(t_2 - t_1)}{2}. \tag{3}$$

3. Frequency-dependent attenuation coefficient

The ultrasonic frequency-dependent attenuation coefficient was calculated using[17]

$$\alpha(f) = \frac{20}{2D}\left(\log_{10}\frac{A_1(f)}{A_2(f)}\right), \tag{4}$$

where D is the thickness of the tissue, and $A_1(f)$ and $A_2(f)$ are the amplitude spectra computed from echoes received from the reflector in saline and the reflector with tissue interposed, respectively, using a 1024-point fast Fourier transform. The thickness of tissue at different positions along the cross section of *B*-mode images were estimated corresponding to each echo received from the reflector to calculate the frequency-dependent attenuation coefficient. The frequency-dependent attenuation coefficient was calculated in the frequency range from 35 to 54 MHz. A total of 400 *A*-lines of radio frequency signals were acquired respectively from three different sections of tissue to calculate ultrasonic parameters.

III. RESULTS

Figure 4 shows typical 47 MHz *B*-mode images of the LP and VM from the same human VF sample. The image size is 4 mm × 6 mm, and both the LP and VM appear to be homogeneous. Figure 5 shows the frequency dependence of the attenuation coefficient of the LP and VM. Linear fitting was implemented within the frequency range from 35 to 54 MHz to estimate the frequency-dependent attenuation coefficient. It is evident from Fig. 5 that the difference in the attenuation coefficient between LP and VM increased with increasing ultrasound frequency. The paired student *t*-tests were used to compare the acoustic parameters from LP and VM. All data were expressed as means and standard error of the mean. Statistical significance was chosen as $p < 0.05$. The integrated backscatter of the LP and VM was −173.44±6.14 and −195.13±3.58 dB, respectively, relating

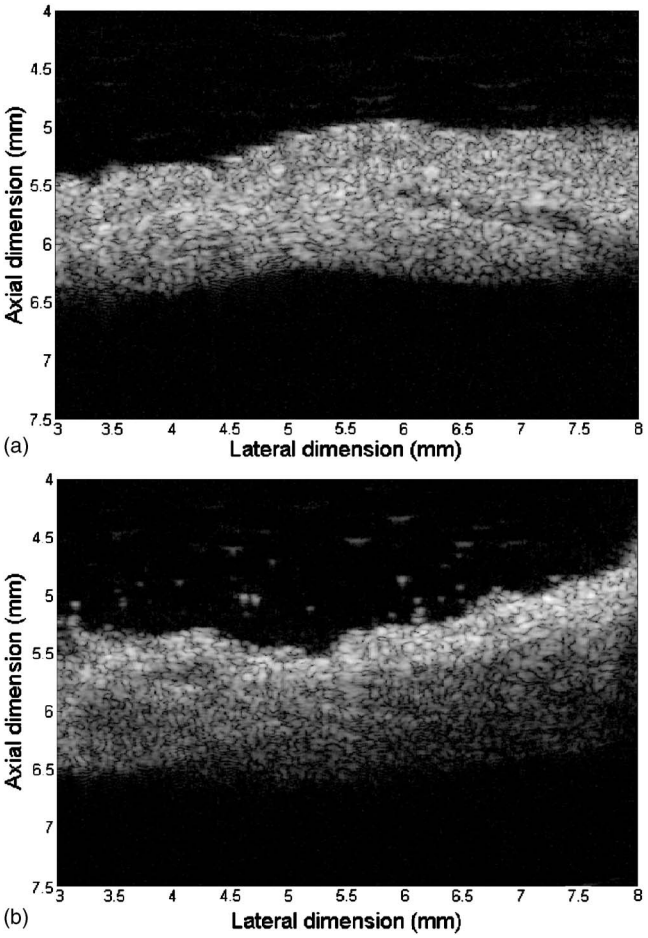

FIG. 4. Typical *B*-mode images of the (a) lamina propria (LP) and (b) vocalis muscle (VM).

to that from a flat reflector ($p<0.05$). The sound velocity in the LP and VM was 1667.68±44.9 and 1595.07±39.33 m/s, respectively ($p<0.05$), and the attenuation coefficient at 47 MHz was 8.28±1.72 and 7.17±1.30 dB/mm ($p>0.05$). These values of the integrated backscatter, sound velocity, and attenuation coefficient are summarized in Fig. 6.

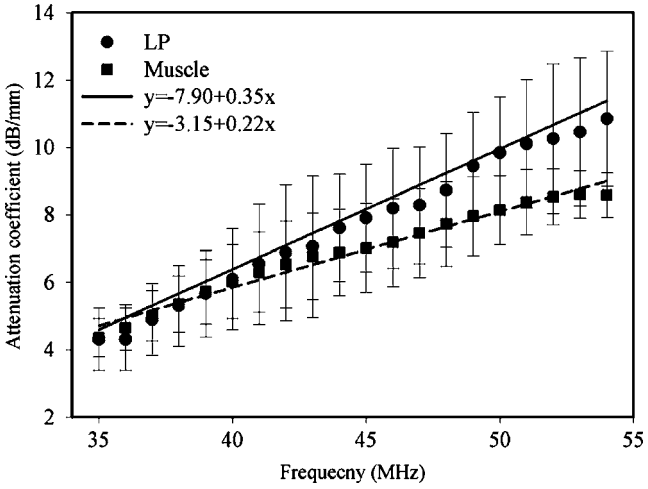

FIG. 5. Frequency-dependent attenuation coefficients of the LP and VM. Mean and s.d. values are shown.

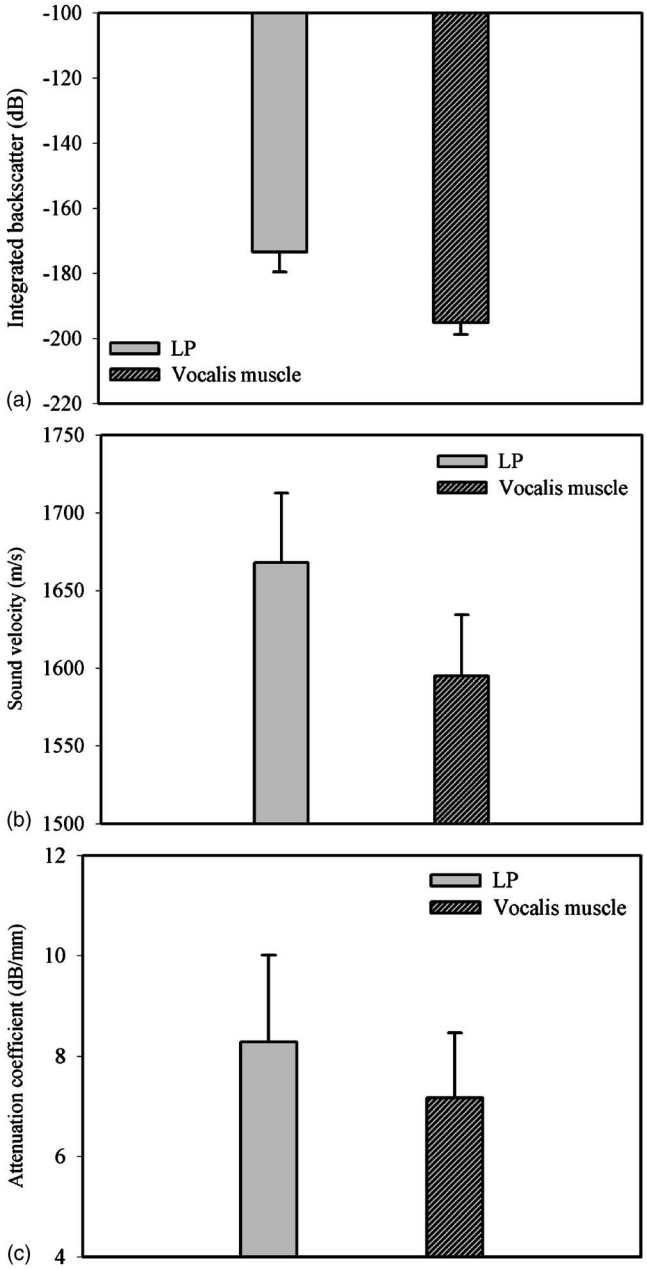

FIG. 6. Acoustic parameters of the LP and VM: integrated backscatter (a), sound velocity (b), and (c) attenuation coefficient at 47 MHz. Mean and s.d. values are shown.

IV. DISCUSSION AND CONCLUSION

The LP of human VFs is crucial to phonation, and it is susceptible to many pernicious inflammatory laryngeal conditions, such as laryngitis, nodules, cysts, polyps, and scarring.[18] In addition, excessive phonation and deleterious environment factors such as tobacco smoke, alcohol, radiation, and refluxed stomach contents can also damage the LP. In order to understand functional and characteristic changes caused by these laryngeal conditions, it is necessary to study the normal properties of LP and then determine how the abnormal conditions differ.

It has been shown theoretically that the scattering of an acoustic wave from densely distributed small scattering elements is dependent on several physical parameters, namely

the size of the scatterers relative to the wavelength, the scatterer acoustic properties such as their density and compressibility relative to those of the surrounding medium, and the concentration and distribution of the scatterers.[19–21] In adult human VFs, the VM tissue comprises cylindrical muscle fiber elements that have an average diameter of 20–26 μm.[22] Given that the wavelength of 47 MHz ultrasound is approximately 34 μm, it was hypothesized that the muscle fibers in VM tissue are the anatomic structure responsible for ultrasound scattering. The LP is a type of connective tissue that consists mainly of collagen fibers, elastin fibers, hyaluronic acid and fibroblasts.[18] Our experimental results, as listed in Table I, indicated that the integrated backscatter from the LP (−173.44±6.14 dB) was higher than that from the VM (−195.13±3.58 dB), which may be attributable to the structure of collagen fibers differing between the LP and the VM. A picrosirius-polarization visualization method revealed that the collagen fibers in the LP form an intertwined network arranged in the form of a wicker basket.[2] These fibers were found to be highly branched and anastomosed, not forming bundles but instead forming a delicate three-dimensional network whose empty spaces were filled with glycoproteins, glycosaminoglycans, and elastic fibers. However, this network arrangement was not observed in the VM.[2] Consequently, the higher integrated backscatter from the LP may be due to the denser aggregation and arrangement of collagen fibers in LP tissue resulting in a different effective structure of ultrasound scatterers.

Elastic fibers confer elasticity on many tissues and can be stretched up five times their original size. In the VFs, such fibers are concentrated in the LP, and the elastic properties of the LP are determined by both elastic and collagen fibers.[23] According to our experimental results, the sound velocity in LP (1667.68±44.9 m/s) is greater than it is in VM (1595.07±39.33 m/s). The measurement of sound velocity from blood vessel walls indicated that the sound velocity in tissues increased, corresponding to the increase of collagen and elastin concentration.[24,25] Consequently, the higher sound velocity in LP may be attributed to the concentration of elastic and collagen fibers in LP being higher than VM. These fibers guarantee tensile strength while at the same time conferring the vocal ligament with an elasticity that enables it to support the tension of the intrinsic musculature of the larynx during phonation by balancing the tension in the LP.[26] Although soft tissues are generally anisotropic, viscoelastic, and nonlinear, most analyses simplify them to linear, elastic, and isotropic materials. The bulk modulus (K) is commonly used to characterize the elastic properties of materials, and is related to Young's modulus (E) and Poisson's ratio (ν) according to $K=E/3(1-2\nu)$. Many soft tissues are nearly incompressible, with a Poisson's ratio close to 0.5.[27] The bulk modulus, which is the reciprocal of the compressibility of the substance, can also be estimated from the sound velocity (V) and material density (ρ) according to $K=\rho V$.[2] The density of the LP is similar to that of the VM, at approximately 1.043 g/cm^3.[28] Table I indicates that the sound velocity was approximately 4.3% higher in the LP than in the VM. Consequently, the LP appears to exhibit higher elasticity due to its higher concentration of elastic and collagen fibers.[2,29] Comparing our results with previous studies, Lockwood *et al.* reported velocities ranging from 1572 to 1628 m/s for frozen/thawed human arteries measured at 37 °C[30] and Saijo *et al.* published a value of 1614 m/s for frozen/thawed fixed normal human aortic media.[31] These studies indicated that the sound velocity in elastic tissue is somewhat greater than average value of 1540 m/s assumed for most soft tissue. However, the sound velocity in LP is approximately 1667.68 m/s, which implied that the LP is much more elastic and has a higher content of elastic and collagen fibers than some elastic tissue.

An ultrasound wave propagating in a heterogeneous biological tissue is attenuated by absorption and scattering, with the former having the greatest effect and increasing with frequency.[14] It is evident from Fig. 5 that the attenuation coefficients in both the LP and VM increased with the ultrasound frequency, with the difference in the attenuation coefficient between the LP and VM increasing with frequency. There is experimental evidence that ultrasonic absorption in biological materials is affected by molecular interactions.[32–34] In addition, the acoustic impendence (Z) of tissue can be estimated from the sound velocity (V) and tissue density (ρ) according to $Z=\rho V$. According to our measurements, the sound velocity in the LP and VM is 1667.68±44.9 and 1595.07±39.33 m/s, respectively. Assume that the density of the LP and VM is approximately 1.043 g/cm^3. The acoustic impendence of LP and VM is 1.739 and 1.663 MRa, respectively. The reflection coefficient (R), which is the ratio of reflected pressure (p_r) to incident pressure (p_i) of ultrasonic wave, can be estimated from the acoustic impendence of tissue (Z_2) and surrounding media (Z_1)according to $R=p_r/p_i=(Z_2-Z_1)/(Z_2+Z_1)$ (assume that the incident angle is zero). The acoustic impendence of water is 1.48 MRa,[14] the reflection coefficient of LP and VM to the water is 0.08 and 0.058, respectively. Consequently, the higher attenuation in the LP may be due to the presence of higher concentrations of elastic and collagen fibers, high elasticity, higher reflection coefficient, and other frictional factors that consume energy, which is lost as heat.[35] This would make physiologic sense given that the LP acts in part as a shock absorber.

In conclusion, a high-resolution UBM system was designed and used to measure ultrasonic parameters in human LP and VM tissue using a 47 MHz high-frequency ultrasonic transducer. Due to differences in structure and fiber concentration, the LP exhibits higher integrated backscatter, sound velocity, and attenuation coefficient. These results could be useful clinical references for the further development of high-frequency ultrasound devices for endolarynx sonography applications.

ACKNOWLEDGMENT

This work has been supported by NIH Grant No. P41-EB2812.

[1]K. Ishii, K. Yamashita, M. Akita, and H. Hirose, "Age-related development of the arrangement of connective tissue fibers in the lamina propria of the human vocal fold," Ann. Otol. Rhinol. Laryngol. **109**, 1055–1064 (2000).
[2]E. C. Madruga de Melo, M. Lemos, X. F. J. Aragao, L. U. Sennes, P. H. Nascimento Saldiva, and D. H. Tsuji, "Distribution of collagen in lamina

propria of the human vocal fold," Laryngoscope **113**, 2187–2191 (2003).
[3]V. A. Kumar, J. S. Lewin, and L. E. Ginsberg, "CT assessment of vocal cord medialization," AJNR Am. J. Neuroradiol. **26**, 1643–1646 (2006).
[4]M. Ahmad, J. Dargaud, A. Morin, and F. Cotton, "Function morphology of phonation evaluated by dynamic MRI," Surg. Radiol. Anat. **28**, 481–485 (2006).
[5]N. A. Nassif, W. B. Armstrong, F. J. de Boer, and B. J. F. Wong, "Measurement of morphologic changes induced by trauma with the use of coherence tomography in porcine vocal cords," Otolaryngol.-Head Neck Surg. **133**, 845–850 (2005).
[6]E. M. Friedman, "Role of ultrasound in the assessment of vocal cord function in infants and children," Ann. Otol. Rhinol. Laryngol. **106**, 199–209 (1997).
[7]H. Rudorf, F. J. Barr, and J. G. Lane, "The role of ultrasound in the assessment of laryngeal paralysis in the dog," Vet. Radiol. Ultrasound **42**, 338–343 (2001).
[8]J. S. Rubin, S. Lee, J. McGuinness, I. Hore, D. Hill, and L. Berger, "The potential role of ultrasound in differentiating solid and cystic swellings of true vocal fold," J. Voice, **18**, 231–235 (2004).
[9]T. Y. Hsiao, C. L. Wang, C. N. Chen, F. J. Hsieh, and Y. W. Shau, "Elasticity of human vocal folds measured in vivo using color Doppler imaging," Ultrasound Med. Biol. **29**, 1145–1152 (2002).
[10]C. Arens, B. Eistert, H. Glanz, and W. Waas, "Endolaryngeal high-frequency ultrasound," Eur. Arch. Otorhinolaryngol. **255**, 250–255 (1998).
[11]C. Arens and H. Glanz, "Endoscopic high-frequency ultrasound of the larynx," Eur. Arch. Otorhinolaryngol. **256**, 316–322 (1999).
[12]E. Tamura, S. Kitahara, and N. Kohno, "Clinical assessment of intralaryngeal ultrasonography," Laryngoscope **111**, 1767–1770 (2001).
[13]E. Tamura, S. Kitahara, and N. Kohno, "Intralaryngeal application of a miniaturized ultrasonic probe,' Acta Oto-Laryngol. **122**, 92–95 (2002).
[14]K. K. Shung, *Diagnostic Ultrasound: Imaging and Blood Flow Measurements* (CRC Press, Boca Raton, FL, 2006).
[15]C. C. Huang, S. H. Wang, and P. H. Tsui, "Detection of blood coagulation and clot formation using quantitative ultrasonic parameters," Ultrasound Med. Biol. **31**, 1567–1573 (2005).
[16]I. Y. Kuo, B. Hete, and K. K. Shung, "A novel method for the measurement of acoustic speed," J. Acoust. Soc. Am. **88**, 1679–1682 (1990).
[17]C. C. Huang and S. H. Wang, "Characterization of blood properties from coagulating blood of different hematocrits using ultrasonic backscatter and attenuation," Jpn. J. Appl. Phys., Part 1 **45**, 7191–7196 (2006).
[18]M. Catten, S. D. Gray, T. H. Hammond, R. Zhou, and E. Hammond, "Analysis of cellular location and concentration in vocal fold lamina propria," Otolaryngol.-Head Neck Surg. **118**, 663–667 (1998).
[19]B. Hete and K. K. Shung, "Scattering of ultrasound from skeletal muscle tissue," IEEE Trans. Ultrason. Ferroelectr. Freq. Control **40**, 354–365 (1993).
[20]K. K. Shung and G. A. Thieme, *Ultrasonic Scattering in Biological Tissues* (CRC Press, Boca Raton, FL, 1993).
[21]C. Y. Wang and K. K. Shung, "Variation in ultrasonic backscattering from skeletal muscle during passive stretching," IEEE Trans. Ultrason. Ferroelectr. Freq. Control **45**, 504–510 (1998).
[22]Y. Sato and H. Tauchi, "Age changes in human vocal muscle," Mech. Ageing Dev. **18**, 67–74 (1982).
[23]T. H. Hammond, S. D. Gray, and J. E. Butler, "Age and gender-related elastin distribution changes in human vocal folds," Otolaryngol.-Head Neck Surg. **119**, 314–322 (1998).
[24]K. K. Shung and J. M. Reid, "Ultrasound velocity in major bovine blood vessel walls," J. Acoust. Soc. Am. **64**, 692–694 (1978).
[25]J. V. Geleskie and K. K. Shung, "Further studies on acoustic impedance of major bovine blood vessel walls," J. Acoust. Soc. Am. **71**, 467–470 (1982).
[26]T. H. Hammond, S. D. Gray, and J. E. Butler, "Age and gender-related collagens distribution changes in human vocal folds," Ann. Otol. Rhinol. Laryngol. **109**, 913–920 (2000).
[27]J. Ophir, S. K. Alam, B. S. Garra, F. Kallel, E. E. Konofagou, T. Krouskop, C. R. B. Merritt, R. Righetti, R. Souchon, S. Srinivasan, and T. Varghese, "Elastography: Imaging the elastic properties of soft tissues with ultrasound," J. Med. Ultrason. **29**, 155–171 (2002).
[28]A. L. Aerlman, I. R. Titze, and D. S. Cooper, "Elasticity of canine vocal fold tissue," J. Speech Hear. Res. **27**, 212–219 (1984).
[29]S. D. Gray, K. J. Chan, and B. Turner, "Dissection plane of the human vocal fold lamina propria and elastin fiber concentration," Acta Oto-Laryngol. **120**, 87–91 (2000).
[30]G. R. Lockwood, L. K. Ryan, J. W. Hunt, and F. S. Foster, "Measurement of the ultrasonic properties of vascular tissue and blood from 35-65 MHz," Ultrasound Med. Biol. **17**, 653–666 (1991).
[31]Y. Saijo, H. Sasaki, H. Okawai, S. Nitta, and M. Tanaka, "Acoustic properties of atherosclerosis of human aorta obtained with high frequency ultrasound," Ultrasound Med. Biol. **24**, 1061–1064 (1998).
[32]F. W. Kremkau, E. L. Carstensen, and W. G. Aldridge, "Macromolecular interaction in the absorption of ultrasound in fixed erythrocytes," J. Acoust. Soc. Am. **53**, 1448–1451 (1973).
[33]K. K. Shung, M. Y. Lee, and J. M. Reid, "Effect of oxygen tension and pH on the ultrasonic absorption properties of sickle cell," Blood **54**, 451–458 (1979).
[34]K. K. Shung, M. Rocco, and J. O. Ballard, "Ultrasonic absorption in deer blood," J. Acoust. Soc. Am. **70**, 664–668 (1981).
[35]D. A. Christensen, *Ultrasonic Bioinstrumentations* (Wiley, New York, 1988).

Erratum: Retrofocusing techniques in a waveguide for acoustic communications (L) [J. Acoust. Soc. Am. 121(6), 3277–3279 (2007)]

H. C. Song[a)]
Marine Physical Laboratory, Scripps Institution of Oceanography, La Jolla, California 92093-0238, USA

S. M. Kim
Marine and Ocean Engineering Research Institute, Daejun, Korea

(Received 8 June 2007; revised 5 July 2007; accepted 6 July 2007)
[DOI: 10.1121/1.2766999]

PACS number(s): 43.10Vx, 43.60.Dh, 43.60.Gk, 43.60.Fg

In the subject paper, the curves in Fig. 2 that are labeled as "Approach 3" are incorrect. A suitably revised figure (now labeled Fig. 1) with the correct curves is given here.

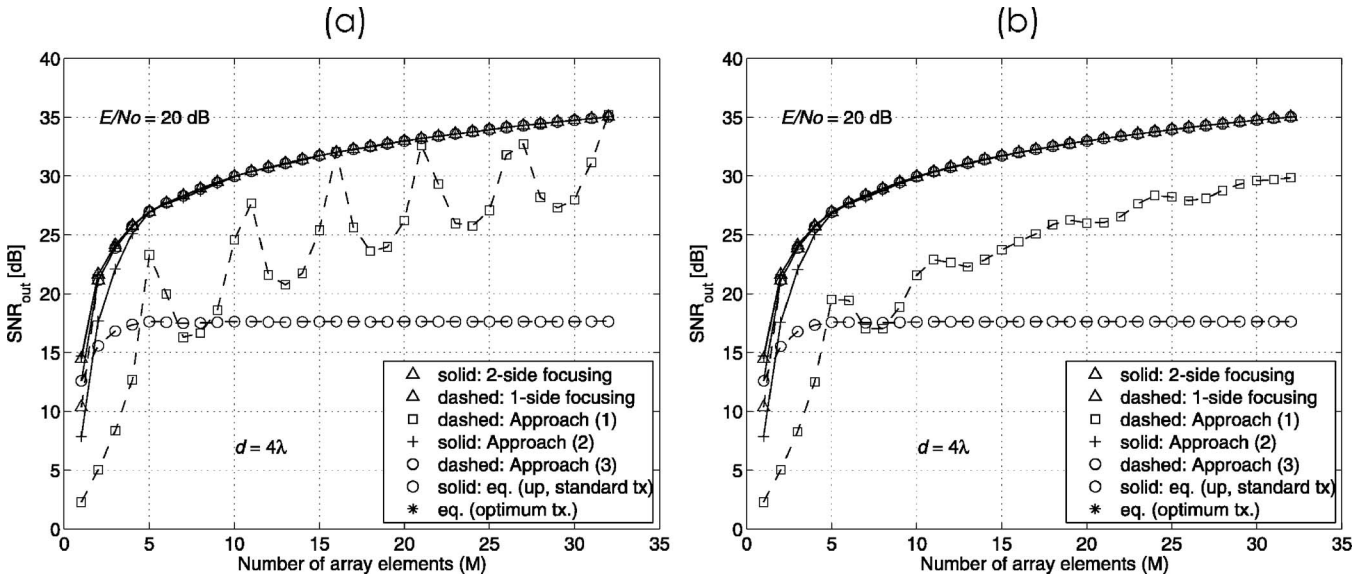

FIG. 1. Performance of various techniques on the example channel: output SNR versus M for fixed symbol SNR$=E/N_0=20$ dB. (a) $d=4\lambda$ without the channel normalization $q(0)=1$ imposed. Note the aperture of $M=35$ elements array is 17 m in 75-m-deep water. (b) Reproduction of plot (a) when the phase delay is frequency dependent such that $\phi(f)=2\pi(d/\lambda)\sin\theta$.

[a)]Electronic mail: hcsong@mpl.ucsd.edu

 0001-4966/2007/122(3)/1833/1/$23.00

Erratum: "Theory of frequency dependent acoustics in patchy-saturated porous media" [J. Acoust. Soc. Am. 110(2), 682–694 (2001)]

David Linton Johnson[a)]
Schlumberger-Doll Research, One Hampshire St., Cambridge, Massachusetts 02139

(Received 30 May 2007; accepted 14 June 2007)
[DOI: 10.1121/1.2756792]

PACS number(s): 43.20.Jr, 43.10.Vx [PEB]

There is a typographical error in Eq. (40): R_0 should be R_b.

Equation (41) is correct, as written, but with the convention that L_1 and L_2 refer to the half-widths of the two layers and not to the full widths as claimed in the text. For the sake of consistency with the rest of the manuscript, it should be rewritten in terms of the full widths as

$$T = -\frac{K_{BGW}\phi^2}{24k(L_1+L_2)}\{\eta_1 g_1^2 L_1^3 + 3\eta_1 g_1 g_2 L_1^2 L_2 + 3\eta_2 g_1 g_2 L_1 L_2^2 + \eta_2 g_2^2 L_2^3\}. \quad (41)$$

The surface-to-volume ratio, for this geometry, as well as the caption to Fig. 1(c) are given correctly in terms of the full widths of the two layers.

[a)]Electronic mail: johnson10@slb.com

